UNIVERSIDAD DE SALAMANCA

FACULTAD DE FARMACIA

Departamento de Ciencias Farmacéuticas

NOVEL INDOLE-BASED ANTIMITOTIC AGENTS: DESIGN, SYNTHESIS AND STUDY OF THE ANTITUMOR MECHANISM OF ACTION

MEMORIA PARA OPTAR AL GRADO DE DOCTOR

ALBA VICENTE BLÁZQUEZ

Bajo la dirección de

Dr. Faustino Mollinedo, Dr. Rafael Peláez

Centro de Investigaciones Biológicas Margarita Salas (CSIC)

2020

NOVEL INDOLE-BASED ANTIMITOTIC AGENTS: DESIGN, SYNTHESIS AND STUDY OF THE ANTITUMOR MECHANISM OF ACTION

VNiVERSiDAD D SALAMANCA

CAMPUS DE EXCELENCIA INTERNACIONAL

Trabajo presentado para optar al grado de Doctor en Farmacia con Mención Internacional por la Universidad de Salamanca por:

Firmado por VICENTE BLAZQUEZ ALBA - 70913894H el día 21/07/2020 con un certificado emitido por AC FNMT Usuarios

D.ª Alba Vicente Blázquez

El **Dr. Faustino Mollinedo García**, Profesor de Investigación del Consejo Superior de Investigaciones Científicas (CSIC) en el Centro de Investigaciones Biológicas Margarita Salas y el **Dr. Rafael Peláez Lamamié de Clairac Arroyo**, Profesor Titular de Química Orgánica del Departamento de Ciencias Farmacéuticas de la Universidad de Salamanca,

CERTIFICAN

Que el trabajo de tesis titulado "**Novel indole-based antimitotic agents: design, synthesis and study of the antitumor mechanism of action**", presentado por la Graduada en Farmacia por la Universidad de Salamanca **D.ª ALBA VICENTE BLÁZQUEZ** para optar al Grado de Doctor en Farmacia con Mención Internacional por la Universidad de Salamanca, ha sido realizado bajo su dirección en el CIB Margarita Salas y en el Laboratorio de Química Farmacéutica del Departamento de Ciencias Farmacéuticas de la Universidad de Salamanca. Considerando que cumple con las condiciones necesarias, autorizan su presentación a fin de que pueda ser defendido ante el tribunal correspondiente.

Y para que así conste a efectos oportunos, expiden y firman el presente certificado en Salamanca, a 21 de julio de 2020.

Firmado por MOLLINEDO GARCIA FAUSTINO - DNI 02494012F el día 22/07/2020 con un certificado emitido por AC

Fdo. Dr. Faustino Mollinedo

PELAEZ LAMAMIE CLAIRAC ARROYO RAFAEL - 07870367C

Firmado digitalmente por PELAEZ LAMAMIE CLAIRAC ARROYO RAFAEL - 07870367C
Fecha: 2020.07.21 20:43:06 +02'00'

Fdo. Dr. Rafael Peláez

I greatly appreciate the funding support received towards my Ph.D. by Graduate student contracts “Formación de Profesorado Universitario FPU” from the Spanish Ministry of Education, Culture and Sports (FPU2015/02457). The grant “Ayudas FPU para Estancias Breves y Traslados Temporales" (EST18/00016) allowed me to conduct a three-month stay at Dr. DeCicco-Skinner’s laboratory at the Department of Biology at American University (Washington, DC, USA) in 2019. I would also like to thank the “Academia de Farmacia de Castilla y León” for the Prize of the Spanish Association against Cancer (AECC) in 2018, and Spanish Society of Medicinal Chemistry (SEQT) for the “Ramón Madroñero” award, granted at the XIX Call for Novel Researchers Prizes in 2019.

The research conducted in this Ph.D. thesis has been financially supported by the following research projects:

i. Alternativas terapéuticas a los benzimidazoles para las zoonosis parasitarias mediante diseño basado en la diana. RTI2018-099474-B-I00 (Spanish Ministry of Science, Innovation, and Universities 2019-2021).

ii. Diseño, síntesis y evaluación de análogos de combretastatina funcionalizados para su inclusión en sistemas de liberación dirigida. Fundación Memoria de D. Samuel Solórzano Barruso 2019.

iii. Combinación de nuevos agentes antitubulina y análogos alquilfosfolípidos como una nueva estrategia frente a cáncer y Leishmaniosis. SA262P28 (Consejería de Educación de la Junta de Castilla y León and FEDER Funds 2018-2021).

iv. Lipid rafts y entorno tumoral inflamatorio en la terapia del cáncer: análogos alquilfosfolípidos como agentes dirigidos frente a lipid rafts e inflamación con múltiples indicaciones terapéuticas. SAF2017-89672-R (Spanish Ministry of Science, Innovation, and Universities 2018-2020).

v. Nuevos agentes antimitóticos activos frente a células resistentes. SA030U16 (Consejería de Educación de la Junta de Castilla y León and FEDER Funds 2016-2018).

vi. Lipid rafts, cancer stem cells y microentorno tumoral inflamatorio en la terapia del cáncer: análogos alquilfosfolípidos como agentes líder en terapias dirigidas a lipid rafts. SAF2014-59716-R (Spanish Ministry of Science, Innovation, and Universities 2015-2017).

vii. Optimización de antitumorales inhibidores de tubulina por mejora de las propiedades farmacocinéticas. SA147U13 (Consejería de Educación de la Junta de Castilla y León and FEDER Funds 2013-2015).

The manuscripts with the results of this work are currently being prepared for submission. Further work carried out during this period has contributed to the following publications:

i. Jiménez, C.; Ellahioui, Y.; Álvarez, R.; Aramburu, L.; Riesco, A.; González, M.; Vicente, A.; Dahdouh, A.; Ibn Mansour, A.; Jiménez, C.; Martín, D.; Sarmiento, R. G.; Medarde, M.; Caballero, E.; Peláez, R. Exploring the size adaptability of the B ring binding zone of the colchicine site of tubulin with para-nitrogen substituted isocombretastatins. *Eur. J. Med. Chem.* **2015**, *100*, 210–222.

ii. Álvarez, R.; Aramburu, L.; Puebla, P.; Caballero, E.; González, M.; Vicente, A.; Medarde, M.; Peláez, R. Pyridine based antitumour compounds acting at the colchicine site. *Curr. Med. Chem.* **2016**, *23* (11), 1100–1130.

iii. Vicente-Blázquez, A.; González, M.; Álvarez, R.; Del Mazo, S.; Medarde, M.; Peláez, R. Antitubulin sulfonamides: The successful combination of an established drug class and a multifaceted target. *Med. Res. Rev.* **2019**, *39* (3), 775–830.

iv. González, M.; Ellahioui, Y.; Álvarez, R.; Gallego-Yerga, L.; Caballero, E.; Vicente-Blázquez, A.; Ramudo, L.; Marín, M.; Sanz, C.; Medarde, M.; Pelaéz, R. The Masked Polar Group Incorporation (MPGI) strategy in drug design: Effects of nitrogen substitutions on combretastatin and isocombretastatin tubulin inhibitors. *Molecules* **2019**, *24* (23), 4319.

v. Álvarez, R.; Aramburu, L.; Gajate, C.; Vicente-Blázquez, A.; Mollinedo, F.; Medarde, M.; Peláez, R. Potent colchicine-site ligands with improved intrinsic solubility by replacement of the 3,4,5-trimethoxyphenyl ring with a 2-methylsulfanyl-6-methoxypyridine ring. *Bioorg. Chem.* **2020**, *98*, 103755.

ABSTRACT

Cancer is the second leading cause of death, accountable for about 1 in 6 deaths globally. There is massive investment in the development of novel therapeutic strategies, although brand-new chemotherapy faces several handicaps such as lack of clinical efficacy, pharmacokinetic problems, or the appearance of resistance mechanisms. In this work, we focused on the design of novel compounds aimed to interact with the protein tubulin, which is a validated target in cancer chemotherapy and arguably one of the most successful ones. i) It has proven effective as a therapeutic target since some of the antitumor drugs currently at the forefront in clinical use (e.g. paclitaxel), act by binding to tubulin. ii) It is an essential protein, barely susceptible to relevant mutations that would affect its proper functioning.

Microtubules are built up by the lateral association of protofilaments, which in turn, are formed by the head-to-tail polymerization of α,β-tubulin. Microtubules are highly dynamic structures that fulfill a vast range of pivotal functions, such as chromosome segregation during cell division, vesicle transport, or maintenance of cell shape. These roles make them an appealing target in cancer chemotherapy since minor disturbance of their dynamics leads to an antimitotic effect and eventually cell death. Many tubulin binding drugs also exert antivascular activities hampering the growth of solid tumors by shutting down the supply of oxygen and nutrients. Among the several binding pockets described in microtubules to date, we have focused on the colchicine domain. Although some colchicine site ligands are quite advanced in clinical trials, none has yet reached clinical approval. The ligands that bind to this pocket mostly show simple chemical structures, so constructing an extensive library of compounds to explore the impact of structural changes on the antitumor activity is attainable.

The colchicine domain has been considered as an ensemble of three consecutive zones (1-2-3) based on the X-ray structures of protein-ligand complexes. Most of the known ligands bind to two zones, and only a few of them interact simultaneously with the three zones of the domain. The primary goal of this work is to obtain compounds with advantageous properties that are able to interact with the colchicine domain, as promising pharmacological agents in cancer therapy. To this end, the design has been approached by parts considering the data provided by PDB structures and structure-activity relationship data of compounds with no X-ray reports, under the presumption of their binding mode. We have designed compounds directed to zones 1-2, 2-3, and 1-2-3, leveraging the common zone 2 in the different approaches by designing common structural elements for this zone that can be later combined with residues in zones 1 and 3.

This work has yielded a series of indole-based compounds with two aromatic rings connected by sulfonamide or tetrazole groups that preferentially adopt folded conformations that are required for the interaction with zones 1-2 of the colchicine domain. These compounds bind to the colchicine domain in β-tubulin and preclude the *in vitro* polymerization of microtubules, inducing disorganization of the tubulin cytoskeleton. Our results expose that these compounds exert antimitotic and antivascular activities. The antimitotic mechanism of action leads to antiproliferative potencies in the submicromolar or nanomolar range against several tumor and non-tumorigenic cell lines. We have studied the mechanism of action and the induction of cell death in the human epithelial cervical carcinoma HeLa cells caused by some representative lead compounds and compared their behavior with other cell lines. This research contributes to further unraveling the molecular processes, both reversible or irreversible, that are involved in the transition from microtubule depolymerization to cell death.

Contents

LIST OF ABBREVIATIONS AND ACRONYMS

A

aa	aminoacid
AB	assembly buffer
Ab-1	primary antibody
Ab-2	secondary antibody
Ac	acetyl
ACD	accidental cell death
acetone-D6	deuterated acetone
ACN	acetonitrile
Ac_2O	acetic anhydride
AcOH	acetic acid
ADC	antibody-drug conjugate
ADP	adenosine diphosphate
AIDS	acquired immune deficiency syndrome
AIF	apoptosis-inducing factor
AMPK	AMP-activated protein kinase
ANT	adenine nucleotide translocase
AnV	annexin V
Apaf-1	apoptotic protease activating factor 1
APC/C	anaphase promoting complex or cyclosome
Ar	aryl
ATCC	American Type Culture Collection
Atg	autophagy-related genes
ATP	adenosine triphosphate
ATPase	adenosine triphosphatase

B

Bad	Bcl-2 associated agonist of cell death
Baf	bafilomycin A1
Bak	Bcl-2 homologous antagonist killer
Bax	Bcl-2 associated X
Bcl-2	B-cell lymphoma 2
Bcl-xL	B-cell lymphoma extra large
BCRP	breast cancer resistance protein
bd	broad doublet
BH3	Bcl-2 homology domain 3
Bid	BH3 interacting domain death agonist
Bik	Bcl-2 interacting killer
Bim	Bcl-2 interacting mediator of cell death
BIM	benzimidazol-5-yl
BIR	baculoviral IAP repeat domain
BME	basement membrane extract
Bn	benzyl
BnNCO	benzyl isocyanate
Bok	Bcl-2 related ovarian killer
bs	broad singlet
BSA	Bovine Serum Albumin
bt	broad triplet
Bub	budding uninhibited by benzimidazole

C

[c]	concentration
c.a.	commercially available
CA4	combretastatin A4
CAD	caspase-activated DNase
CAK	Cdk-activating kinase
CARD	caspase-associated recruitment domain
casp	caspase
CCCP	carbonyl cyanide *m*-chlorophenyl hydrazone
CDI	1,1'-carbonyldiimidazole
Cdk1	cyclin-dependent kinase 1
c-FLIP	cellular FLICE-inhibitory protein
CHX	cycloheximide
cIAP	cellular inhibitor of apoptosis protein
CKII	casein kinase II
cl	cleaved
ClBn	benzyl chloride
COSY	Correlation Spectroscopy
CQ	chloroquine
CRD	cysteine-rich domain
CSI	chlorosulfonyl isocyanate
Ctl	control
CYLD	cylindromatosis
cyt c	cytochrome c

D

d	doublet
dADP	deoxyadenosine diphosphate

DAMPs	danger-associated molecular patterns
DAPI	4',6-diamino-2-phenylindole
dATP	deoxyadenosine triphosphate
DCI	*N*,*N'*-dicyclohexylcarbodiimide
dd	doublet of doublets
DD	death domain
DDQ	2,3-dichloro-5,6-dicyano-1,4-benzoquinone
DED	death effector domain
DFCP1	double FYVE-containing protein 1
DFT	density functional theory
DHE	dihydroethidium
DHI	2,6-dihydroxyisonicotinoyl
DIC	differential interference contrast
$DiOC_6[3]$	3,3'-dihexyloxacarbocyanine iodide
DISC	death-inducing signaling complex
DMEM	Dulbecco's Modified Eagle Medium
DMF	dimethylformamide
DMSO	dimethyl sulfoxide
DMSO-D6	deuterated dimethyl sulfoxide
DNA	deoxyribonucleic acid
DNase	deoxyribonuclease
DPBS	Dulbecco's phosphate-buffered saline
DR	death receptor
DTT	dithiothreitol

E

EB	extraction buffer
EDC	1-ethyl-3-(3-dimethylaminopropyl) carbodiimide
EDTA	ethylene diamine tetraacetic acid
e.g.	for example
EGTA	ethylene glycol tetraacetic acid
Elac	elacridar
EMA	European Medicines Agency
eq	equivalent
ER	endoplasmic reticulum
Erk	extracellular signal-regulated kinase
Et	ethyl
et al.	and others
EtBr	ethyl bromide
$(EtCO)_2O$	propionic anhydride
Et_3N	triethylamine
EtNCO	ethyl isocyanate
EtOAc	ethyl acetate
EtOH	ethanol

F

FADD	Fas-associated death domain protein
FAK	focal adhesion kinase
FasL	Fas ligand
FBS	Fetal Bovine Serum
FC	flow cytometry
FDA	Food and Drug Administration
Fig.	Figure
FIP200	FAK family kinase-interacting protein
FITC	fluorescein isothiocyanate
FS	forward scatter

G

G418	geneticin
GC	gas chromatography
GDP	guanosine diphosphate
GLUD1	glutamate dehydrogenase 1
GLUL	glutamate-ammonia ligase
GTP	guanosine triphosphate
GTPase	guanosine triphosphatase

H

h	hour
HEPES	4-(2-hydroxyethyl)-1-piperazineethane sulfonic acid
Hex	hexane
HMBC	Heteronuclear Multiple Bond Correlation
HRMS	High-Resolution Mass Spectrometry
HRP	horseradish peroxidase
Hsp90	heat shock protein 90
HSQC	Heteronuclear Single Quantum Coherence

I and J

IAP	inhibitor of apoptosis protein
IC	indolecombretastatin
IC_{50}	half-maximal inhibitory concentration
ICAD	inhibitor of CAD
i.e.	that is

IF	immunofluorescence
IKK	IκB kinase
ILP-2	IAP-like protein 2
IR	infrared
i.v.	intravenous
J	coupling constant
JNK	c-Jun N-terminal kinase

K and L

kb	kilobase
K_b	binding constant
LC3	microtubule-associated protein light chain 3
LIR	LC3-interacting region
L-L	liquid-liquid
LLM	laulimalide
LPC	lysophosphatidylcholine
LUBAC	linear ubiquitin chain assembly complex

M

m	*meta*
m	multiplet
M^+	molecular ion
Mad	mitotic arrest deficient
MAPs	microtubule-associated proteins
MCC	mitotic checkpoint complex
Mcl-1	myeloid cell leukemia 1
MDAs	microtubule destabilizing agents
MDR	multiple drug resistance
Me	methyl
MeOH	methanol
MES	2-(*N*-morpholino)ethanesulfonic acid
min	minute
MLC	myosin light chain
ML-IAP	melanoma IAP
MLKL	mixed lineage kinase domain-like protein
MMAE	monomethyl auristatin E
MMP	matrix metalloproteinase
MOMP	mitochondrial outer membrane permeabilization
Mp	melting point
MPF	maturation promoting factor
MS	mass spectrometry
MSAs	microtubule stabilizing agents
MST1	macrophage stimulating 1
MTBE	methyl *tert*-butyl ether
MTOC	microtubule organizing center
mTORC1	mammalian target of rapamycin complex
MTP	microtubular protein
Mw	molecular weight

N

n	number of experimental replicates
NBR1	neighbor of BRCA1
NBS	*N*-bromosuccinimide
$n Bu_4N^+HSO_4$	tetrabutylammonium hydrogen sulfate
NCCD	Nomenclature Committee on Cell Death
NCD	non-communicable diseases
n.d.	not determined
Nec-1	necrostatin-1
NEMO	NF-κB essential modulator
NF-κB	nuclear factor kappa light chain enhancer of activated B cells
n.i.	non-isolated
NIAP	neuronal IAP
*N*MeIND	*N*-methyl-indol-5-yl
NMR	Nuclear Magnetic Resonance
No.	number
n.o.	not obtained
nOe	nuclear Overhauser effect
NOESY	nOe Spectroscopy
n.r.	no reaction
ns	not significant
NSCLC	non-small cell lung cancer

O and P

o	*ortho*
O/N	overnight
p	*para*
P	phospho
PAGE	polyacrylamide gel electrophoresis
PAK2	p21-activated kinase 2
PARP	poly (ADP-ribose) polymerase
PAS	phagophore assembly sites

PBS	phosphate-buffered saline
PCD	programmed cell death
PDB	Protein Data Bank
Pd/C	palladium on activated charcoal
PDH	pyruvate dehydrogenase
p-DMAP	4-dimethylaminopyridine
PE	phosphatidylethanolamine
PEL	peloruside A
PFA	paraformaldehyde
P-gp	P-glycoprotein
Ph	phenyl
PhNCO	phenyl isocyanate
Ph_3P	triphenylphosphine
P_i	inorganic phosphate
PI	propidium iodide
PI3K	phosphatidylinositol 3-kinase
PI3P	phosphatidylinositol-3-phosphate
PIPES	piperazine-*N*,*N*′-bis(2-ethanesulfonic acid)
PKC	protein kinase C
PMSF	phenylmethylsulfonyl fluoride
PP2A	protein phosphatase 2A
ppm	parts per million
procasp	procaspase
pSFFV	spleen focus-forming virus plasmid
PtdSer	phosphatidylserine
PTMs	post-translational modifications
Puma	p53-upregulated modulator of apoptosis
PYGL	glycogen phosphorylase
pyr	pyridine

Q and R

q	quartet
Ref	reference
RHIM	RIP homotypic interaction motif
RIPK	receptor-interacting protein kinase
RNA	ribonucleic acid
RNase	ribonuclease
ROCK	Rho-associated coiled coil-containing protein kinase 1
ROS	reactive oxygen species
rpm	revolutions per minute
rt	room temperature

S

s	singlet
SAC	spindle assembly checkpoint
SAPK2	stress-activated protein kinase 2
SAR	structure activity relationship
SD	standard deviation
SDS	sodium dodecyl sulfate
Smac	second mitochondria-derived activator of caspase
s/n	supernatant
SNARE	soluble NSF attachment protein receptor
SPLB	soluble protein loading buffer
SQSTM1	sequestosome 1
SS	side scatter

T

t	triplet
TAB	TAK1 binding protein
TAK1	TGFβ-activated kinase 1
TB	transport buffer
TBDs	tubulin binding drugs
tBid	truncated Bid
TBS	Tris-buffered saline
TBS-T	Tris-buffered saline with Tween 20
t-BuOH	*tert*-butanol
td	triplet of doublets
THF	tetrahydrofuran
TLC	thin layer chromatography
TM	2,3,4-trimethoxyphenyl
TNF	tumor necrosis factor
TNFR	tumor necrosis factor receptor
TOCSY	Total Correlation Spectroscopy
TPI	tubulin polymerization inhibition
TRADD	TNF receptor-associated death domain protein
TRAF	TNF receptor-associated factor
TRAIL	TNF-related apoptosis-inducing ligand
TRAIL-R	TRAIL receptor
TsOH	*p*-toluenesulfonic acid

U-Z	
UBD	ubiquitin binding domain
ULK	Unc-51-like autophagy activating kinase
UV	ultraviolet
VDAs	vascular disrupting agents
Vera	verapamil
Vps	vacuolar protein sorting
WB	Western blot
WCE	whole-cell extract
WHO	World Health Organization
WIPI	WD-repeat domain phosphoinositide-interacting protein
WT	wild type
XIAP	X-linked inhibitor of apoptosis protein

Symbols	
2n	diploid
4n	tetraploid
δ	chemical shift
Δ	heat/reflux
$\Delta\Psi_m$	mitochondrial transmembrane potential
ε	molar extinction coefficient
λ	wavelength
µW	microwave

Chapter 1

INTRODUCTION

CANCER AT A GLANCE

The human being has experienced a striking increase in life expectancy within the last century, reaching over 70 years as a global average. Undoubtedly, this value deeply differs between countries. The population of Europe, Canada, Japan, or Australia is expected to live further than 80 years.[1] It is not only the rise in life expectancy but also the improved quality thereof (although intimately linked), what has changed the leading causes of death. Decades ago, people tended to suffer from infectious diseases, which is still the case of underdeveloped countries, whereas nowadays, people tend to die from non-communicable diseases (NCD) comprising chronic and age-related disorders (e.g. cancer). Our DNA and repairing systems are not prepared to remain intact for so long, so cancer is one of the prices the human being has to pay to live longer.

The term cancer does not refer to a single disorder, but it rather clusters a group of many diseases that share the feature of harboring genetic basis although non inherited.[2] The fundamental hallmarks of cancer are the ability to skip proliferation, differentiation, and cell death control mechanisms, culminating in the out-of-control growth of abnormal cells within a given tissue. Most malignant neoplasms (primary tumor) can spread to nearby tissues through either blood or lymph systems to establish a secondary tumor mass known as metastasis, which is the prominent cause of death by cancer.[3] Even though the disease is not inherited, genetic susceptibility might be. Cancer disease emerges as a slow development process due to the gradual accumulation of mutations in tumor suppressor genes, oncogenes, or susceptibility genes, that are progressively acquired during a lifetime. Granted, malignification may be accelerated when one is exposed to carcinogens such as ionizing radiation.

According to the World Health Organization (WHO), cancer rises as the second leading cause of death worldwide, accounting for around 9.6 million deaths in 2018.[4] One out of three people will develop cancer during their lifetime, which turns it into a major public health issue. Lung and breast cancers are the most frequently diagnosed and the ones that cause most of the deaths in males and females, respectively.[5] Many efforts are gathered in fighting cancer progression and in developing early detection strategies. First thought as homogeneous, the reality is that individual cells within a tumor mass are highly heterogeneous. Following Darwinian selection, a single cell might acquire a particular mutation whereby it gains survival chances over other cells lacking “improved” features. The mutated genes are therefore transmitted by clonal expansion, creating a dominant population of cells that can in turn acquire further mutations. The altered proliferation and compromised cell cycle checkpoints make tumor cells more prone to keep on dividing and bypassing control mechanisms in the presence of genomic damage in which a healthy cell would not be able to do so. This results in highly mutated and dreadful cells that exhibit genomic instability and complex karyotypes.

Chemotherapy has already demonstrated effectiveness in fighting cancer progression to some extent, but there is no panacea for curing cancer.[6,7] Moving from bench to bedside in the development of new antitumor drugs is a difficult task for many reasons, such as the lack of clinical efficacy, pharmacokinetic problems, or acquisition of resistance, to name a few.[8] Drugs have to reach tumor cells in sufficient concentrations, but the blood vessel network that irrigates a solid tumor is abnormal and occasionally poorly perfused.[9] Even hitting the bullseye, there are on- and off-target mechanisms for resistance that can be inherent or acquired along the path. As aforementioned, tumor cells are very prone to find an alternative pathway to bypass the threaten. We have thus focused on the protein tubulin, which is a validated target in current cancer chemotherapy and barely allows relevant mutations.

TUBULIN AS ANTITUMOR TARGET

The cytoskeleton of eukaryotic cells is formed by the actin network (microfilaments), intermediate filaments, and microtubules, the latter made of tubulin protein. Polar fibers of actin and tubulin are both able to self-assemble and show cytomotive properties. By contrast, this self-assembly behavior is not observed for intermediate filaments. Unlike actin, whose fibers grow steadily, microtubules alternate periods of growth and shrinkage in a stochastic manner.[10,11] Tubulin is an essential protein that fulfills a wide variety of functions, all of them fundamental for the cell to survive: cell division, maintenance of cell shape, and intracellular transport of vesicles and organelles. Microtubules are key components of the mitotic spindle that plays a paramount role in ensuring proper chromosome segregation during cell division. They also provide a track for motor proteins such as kinesins and dyneins to transport different cargoes throughout the cell and form the backbone of motile structures (cilia and flagella).

Targeting tubulin offers a considerable number of advantages. It is a validated target that has proven to be an effective strategy in fighting cancer. Tubulin binding drugs (TBDs) are arguably one of the most successful chemotherapy strategies, such as some taxanes and vinca alkaloids approved by the FDA, which are effective and extensively used in clinic, alone or in combination.[12–14] Tubulin is not susceptible to meaningful mutations given its high degree of conservation. However, it is expressed in all cells, so the appearance of on-target toxicity is a recurrent drawback, mainly manifested as bone marrow disorders and neurotoxicity. Several TBDs cause vascular disruption at low doses, and can be used in combination with other drugs to minimize toxicity. Tubulin-targeting therapy usually exhibits pharmacokinetic problems and acquired resistance associated with MDR transporters.

Microtubule structure

Tubulin is a globular-shaped protein that can be found either as soluble free subunits of α- and β-tubulin dimers, or as part of organized polymers named microtubules. If unspecified, tubulin usually refers to the 8 nm dimer of α and β subunits, whose sequences share some 40% similarity.[15] Both monomers have a molecular mass of around 50 kDa each, also exhibiting a very similar tertiary structure (Fig. 1A). The GTP-dependent head-to-tail binding of α,β-tubulin leads to protofilaments. Microtubules arise from the lateral association of adjacent protofilaments, whose interaction is much weaker than that observed for the longitudinal polymerization of dimers (Fig. 1B).[16] *In vivo* microtubules are typically formed by 13 protofilaments, although in some cases, 9 to 16 protofilaments could be found constituting microtubules *in vitro*.[17–19] Monomers that belong to neighboring protofilaments are slightly staggered, disposed into a 3-start left-handed helix that runs in parallel.[20] This arrangement creates a 25 nm diameter tubular lattice with an inner distance of 15 nm. Microtubules are therefore cylindrical hollow tubes that exhibit a highly dynamic behavior following a polar trend.

In 1998 K. H. Downing's group reported a high-resolution model of the microtubule, later refined in a wide range of X-ray structures.[21–26] The tubulin dimer has two differentiated regions: a major structured globular domain and an unstructured tail. The globular region includes the GTPase domain near the N-terminus and the activation (or intermediate) domain, both providing the tubulin core, whereas the unstructured tail is defined by the long C-terminal helix. These acidic C-terminal tails are negatively charged and protrude from the surface of the microtubule. The dimer is precisely stacked in the microtubule; β-tubulins crown the plus-end, whereas the minus-end is capped by α-tubulins as illustrated in Fig. 1.[22,27]

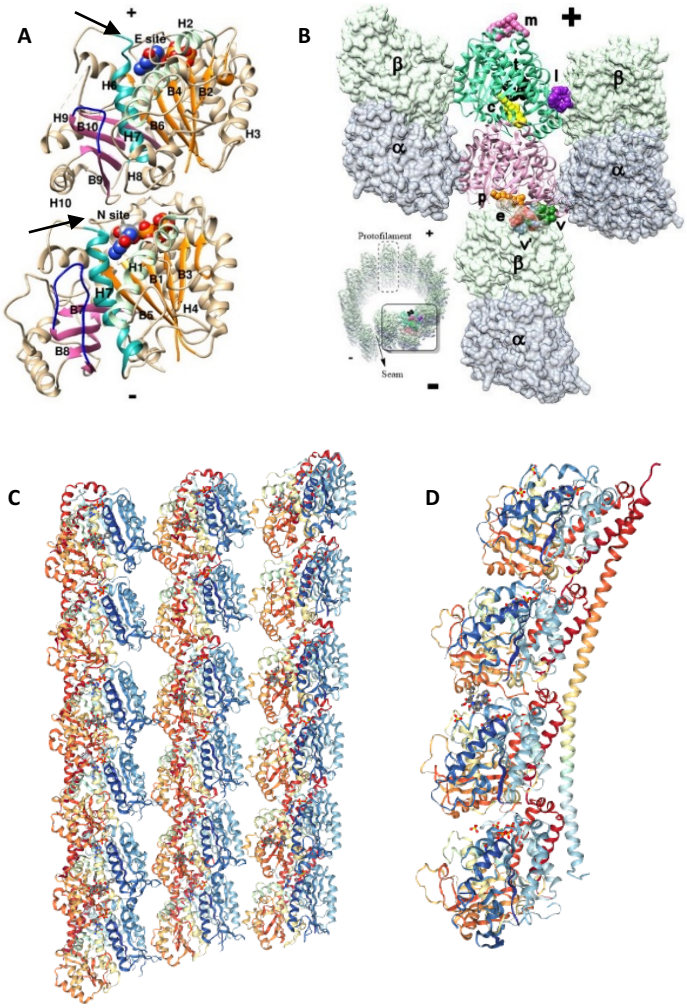

Figure 1. **A.** Structure of a tubulin dimer with the β-tubulin on top, towards the plus-end (+) and the minus-end (-) at the bottom. The E site is located in the β-tubulin neighboring the interdimer space and the N site is found near the intradimer surface. Both sites are found in a cleft in GTPase domains. The location of E and N sites is indicated by arrows. **B.** Representation of the lateral and longitudinal contacts between tubulin dimers. The seven binding sites for exogenous ligands described so far (later discussed) are indicated by the cpk models of those ligands. **C.** Straight conformation of the tubulin lattice captured for the X-ray structure embracing paclitaxel (PDB ID: 3J6G).[28] **D.** Curved conformation of the stathmin-like tubulin complex obtained for the X-ray structure with vinblastine (PDB ID: 4EB6).[29] NGL viewer was used for the visualization of large complexes.[30]

Microtubule dynamics

As mentioned above, these cytomotive polymers are polar structures that exhibit a highly dynamic behavior, experiencing continuous assembly and withdrawal of subunits.[31–33] This behavior is slightly different between edges; plus-ends are intrinsically more dynamic than minus-ends, meaning that the rate of growing-shrinkage is faster due to a more rapid assembly and disassembly of subunits. The polymerization process relies on the hydrolysis of GTP, fine-tuned by many proteins.[34] Two nucleotide binding sites can be distinguished within the dimer: E site and N site, both in combination with Mg^{2+} (Fig. 1A).[20–23] The N site (non-exchangeable), which binds non-hydrolyzed GTP, is found in the α-tubulin. The E site (exchangeable) is located in the β-tubulin and points towards the solvent at the plus-end, binding either GTP, GDP, or GDP + P_i. The GTP at the E site is hydrolyzed shortly after receiving an incoming dimer, releasing P_i and retaining GDP, which stays buried. The incoming dimer places its activation domain from the α-tubulin close to the phosphates of the GTP bound to the E site from the previous β-tubulin.[23] The acidic glutamate E254 in that α-monomer, deemed as the catalytic residue, is essential for the activation of the GTPase at the β subunit via a molecule of water that attacks the γ-phosphate of the GTP (E site).[21] A lysine residue is found at the β-tubulin instead of the acidic glutamate, so the GTP loaded at the N site will never be hydrolyzed.[10,23]

Free soluble dimers exist as either GDP- or GTP-bound tubulin regarding the E site, whose exchange occurs freely in physiological conditions.[35,36] Only soluble GTP-bound dimers are suitable for polymerization, but the features that make them the ones compatible with the microtubule are poorly understood.[37–39] In a simplistic approach, tubulin can be disposed in straight or curved conformations, the latter induced by the bending between monomers (Fig. 1C-D). According to the "allosteric model" firstly proposed, GDP favors the bent conformation, whereas the presence of GTP induces straighter dispositions.[40,41] Later on, the "lattice model" refuted that theory, expounding that the straightening occurs while polymerizing, not before (i.e. not in soluble GTP-bound dimers).[42–47]

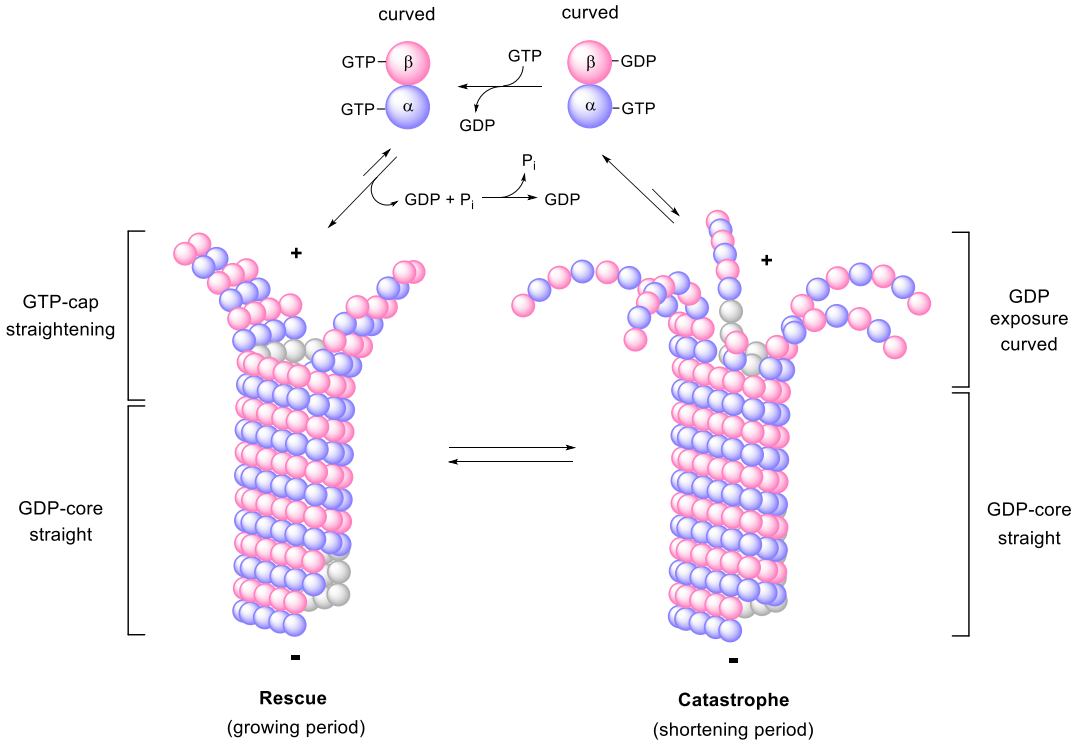

Figure 2. Schematic representation of growing and shrinkage processes within microtubules. The guanine nucleotide of the E site is freely exchanged in soluble dimers, transitioning from GDP- to GTP-tubulin. Growing microtubules show uneven tapered plus-ends with a GTP-cap that straightens the GDP-core, otherwise unstable. The length of this GTP-cap varies depending on the hydrolysis rate and the P_i release. The exposure of GDP or not enough stabilization of the GDP-core results in the peeling outward of protofilaments due to the loss of lateral contacts. Withdrawal of tubulin dimers is around 100 times faster in microtubules exposing GDP than those capped by GTP-tubulin.[33] Dynamic instability consists of the transition from growing periods to disassembly (catastrophe) or the other way (rescue).

The current model states that tubulin shows two conformations related to its state: curved in soluble dimers and straight in microtubules.[43] Upon binding to growing edges, curved GTP-bound tubulin undergoes a progressive straightening (Fig. 2). The hydrolysis of the exchangeable GTP occurs when the dimer is fully straightened in the protofilament, permitting the interaction of the catalytic residue in α-tubulin with the γ-phosphate of the GTP in β-tubulin.[48] This gradual transition gives rise to a stabilizing region called GTP-cap. The GDP core of microtubules is unstable and more prone to depolymerize, but it is constrained by the lateral and longitudinal contacts into a straight conformation. Not enough stabilization results in the peeling of protofilaments. This tension is stored as conformational energy that will be released when depolymerization occurs.

The GTP-cap consisting of GTP and GDP + P_i - bound dimers, restrains the straight conformation of the protofilament, promoting polymerization rather than depolymerization.[49] By contrast, the exposure of GDP at the plus-end induces a curved conformation, therefore weakening lateral interactions that eventually leads to disassembly of tubulin subunits (Fig. 2).[50] Depolymerization may occur not only in GDP-loaded microtubules but also in GTP-protofilaments, although the energy cost is remarkably higher in the second case. Whether the plus-end exposes GTP (strong interaction) or GDP (weak interaction) governs the stability of the microtubule.[22,51,25] Growing microtubules show a flared plus-end with a stabilizing GTP-cap. In this scenario, protofilament edges composed of recently incorporated tubulin are uneven while polymerizing and slightly outward from the tube.[10] Withdrawal of subunits involves the bending of protofilaments that peel outward without lateral interactions (Fig. 2).[45,52]

The self-assembly of tubulin filaments occurs through a nucleation-elongation mechanism. First, a small nucleus of tubulin is slowly constituted, followed by rapid assembly of dimers into both ends.[13] Microtubules radiate from the microtubule organizing center (MTOC) or centrosome, anchored by their minus-ends. MTOCs are basically constituted by γ-tubulin that shares 28-35% sequence with α- and β-tubulins.[53] The growing-shrinkage processes are promoted by two main mechanisms designated as treadmilling and dynamic instability.[10,54] Treadmilling refers to the addition of soluble tubulin to the plus-end while the minus-end disassembles, thereby establishing a continuous flux. This occurs if the critical concentration at the plus-end is lower than that at the minus-end, resulting in the overall addition of dimers to the growing edge. By contrast, dynamic instability consists of the co-existence of long periods of slow growing and short periods of quick shrinkage stochastically occurring at both ends.[13] The net result switches from growing to withdrawal of dimers (catastrophe) or the opposite (rescue). Exposure of GTP stabilizes the end that continues growing, whereas exposure of GDP causes rapid loss of dimers (Fig. 2).

Tubulin heterogeneity

Microtubules give rise to specialized networks to bear the scheduled functions in each specific tissue, which entails changes in behavior and morphological features to fulfill the roles as required.[55] For example, interphase microtubules are up to 4-100 fold less dynamic than those functioning during mitosis, which turnover with the free tubulin pool every 10-30 seconds.[56] The versatile microtubule architecture relies on tubulin heterogeneity, which tunes their physical properties, dynamics, and the interaction with microtubule-associated proteins (MAPs). These fine-settings modulate both microtubule behavior and functions.[55] Tubulin heterogeneity is confered by two mechanisms, namely the expression of different α- and β-tubulin isotypes (genetically encoded)[15] and post-translational modifications (PTMs).[57] These modifications together open a staggering range of combinations known as the “tubulin code”, although the way this code is precisely written and read by cellular effectors remains unraveled.[58–61]

A. Tubulin isotypes

There are eight α-tubulin and nine β-tubulin isotypes known in humans so far (Table 1).[55,62] These monomers intermingle freely into α,β-heterodimers that will build the mosaic-like microtubule lattice.[63] Most microtubules are enriched in certain isotypes that coexist depending on the cell type, rather than being restricted to one single isotype. The genes encoding these isotypes are located in different chromosomes and their expression is stereotyped regarding each tissue. Some of them, such as αIa, αIb and αIc are ubiquitously expressed whereas others are restricted to a specific tissue (e.g. βIIa and βIIb are mainly expressed in the nervous system). The expression pattern is tightly related to some biased functions, such as βVI-tubulin, which gives rise to the marginal band found in platelets.[64]

The primary sequences for α- and β-tubulin do not remarkably differ between isotypes.[15] The globular core is highly conserved, allowing little variation. The minor changes exhibited in this compactly folded region modulate microtubule stability. Most aminoacid alterations are clustered in the C-terminal flexible chain, especially in the last 15-20 residues (Fig. 3). Since flexible C-terminal motifs are exposed at the outer surface of the microtubule, they are closely involved in the interaction with MAPs.[65] The specific pattern of primary sequences and PTMs serve as a cue for recruiting and recognition of MAPs and effectors, which in turn regulate microtubule dynamics.[66] Hence, C-terminal tails of each isotype establish a crosstalk to fulfill specific microtubule functions. Indeed, some *in vivo* studies suggested that tubulin isotypes are functionally non-interchangeable.[67] The composition in isotypes affects microtubule dynamics. Thus, βIII-tubulin shows a higher dynamic behavior than βII or βIV isotypes.[26,68]

Isotype	Gene	Gene location	No. aa	Gene expression
αIa	TUBA1A	12q13.12	451	Ubiquitous expression
αIb	TUBA1B	12q13.12	451	Ubiquitous expression
αIc	TUBA1C	12q13.12	449	Ubiquitous expression
αIIIc	TUBA3C	13q12.11	450	Restricted in testis
αIIId	TUBA3D	2q21.1	450	Restricted in testis
αIIIe	TUBA3E	2q21.1	450	Restricted in testis
αIVa	TUBA4A	2q35	448	Broad expression (skin, brain, bone marrow)
αVIII	TUBA8	22q11.21	449	Biased in heart. Also testis and brain
βI	TUBB	6p21.33	451	Ubiquitous expression
βIIa	TUBB2A	6p25.2	445	Mainly expressed in nervous system
βIIb	TUBB2B	6p25.2	445	Mainly expressed in nervous system
βIII	TUBB3	16q24.3	450	Nervous system (brain), lower in testis
βIVa	TUBB4A	19p13.3	444	Biased in brain. Also testis and adrenal
βIVb	TUBB4B	9q34.3	445	Broad expression, especially testis (cilia)
βV	TUBB6	18p11.21	444	Ubiquitous expression
βVI	TUBB1	20q13.32	446	Biased in hematopoietic: bone marrow, spleen
βVIII	TUBB8	10p15.3	444	Oocytes and early embryo

Table 1. Human α- and β-tubulin isotypes. Gene loci are indicated using the standard nomenclature. The first digits refer to the number of the chromosome where the gene is located. Whether it is placed in the longer arm (q arm) or the shorter one (p arm) is indicated with "q" and "p" letters, respectively. The numbers before the period mark the region and band, and the numbers after the period, the sub-bands.

Certain isotypes play distinct functions depending on the particular location. Mutations in the genes encoding those isotypes or altered expression thereof may cause pathological disorders. The loss of βVI-tubulin, which gives rise to the marginal band in platelets, has been related to thrombocytopenia and abnormal bleeding.[69] Mutations in TUBB3 that encodes for βIII-tubulin lead to polymicrogyria, since it is preferentially expressed in the nervous system.[70] Likewise, disorders in oocyte maturation have been observed upon TUBB8 mutations.[71] Several tubulin isotypes have also been reported to be upregulated in many different neoplasms such as the overexpression of αIb-tubulin in mantle cell lymphoma. The altered expression levels frequently correlate with poor prognosis and aggressive diseases. Overexpression of certain isotypes is also related to the development of resistance to some anticancer agents. Increased levels of β I-V tubulins, especially βIII, have been found to confer resistance to taxane drugs (e.g. paclitaxel or docetaxel).[55,72]

B. Post-translational modifications

PTMs encompass a vast number of alterations, most of them reversible: tyrosination/detyrosination cycle, glycylation, glutamylation, methylation, phosphorylation, acetylation, polyamination, *S*-nitrosylation, palmitoylation, sumoylation, Δ2- and Δ3-tubulin, ubiquitination (Fig. 3).[61,73,74] PTMs are preferentially clustered in the unstructured C-terminal tails that are hotspots for cellular effectors.[65] The length of these tails varies from around 10 to 22 residues; β-tubulins exhibit longer tails than α-tubulins. Post-translational modifications (e.g. incorporation of long branched glutamate chains on internal glutamate sites) strikingly affect steric and electrostatic properties. A few modifications have been reported to ensue in the globular core, perturbing behavior and functions of the microtubule: acetylation, phosphorylation, polyamination, or methylation, to name a few (Fig. 3).[75] Like isotype expression, the incidence of PTMs depends on functional requirements, being stereotyped concerning the tissue and microtubule structure. Most PTMs are harbored in polymeric tubulins rather than in soluble dimers. Still, phosphorylation and polyamination arise in the soluble pool of free tubulin, which is then incorporated into the microtubule lattice.[76,77]

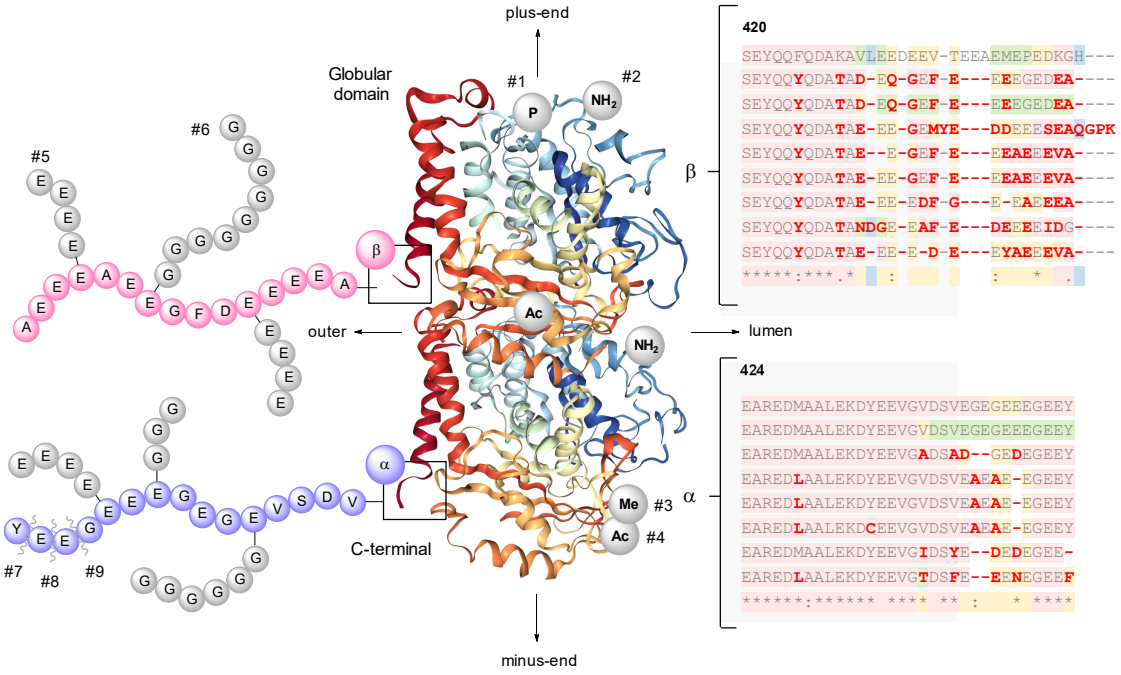

Figure 3. The "tubulin code". The dimer in the middle corresponds to the straight co-crystalline structure of tubulin with paclitaxel (PDB ID: 1TUB).[21] C-terminal tails are boxed both in α- and β-tubulin. Sequences on the left represent the last 15 residues for βI (**pink**) and αIa (**blue**) isotypes. Some PTMs are schematically indicated in the C-terminal tails and the tubulin core: phosphorylation (#1), polyamination (#2), methylation (#3), acetylation (#4), polyglutamylation (#5), polyglycylation (#6), detyrosination (#7), Δ2-tubulin (#8), Δ3-tubulin (#9). The terminal sequence for every tubulin isotype is clustered on the right: there are nine β-tubulin and eight α-tubulin isotypes. The aminoacid sequences were structurally aligned using T-Coffee Multiple Sequence Alignment Server (Expresso).[78] The last line of each alignment corresponds to the clustal consensus: "*" (identical residue), ":" (conservative substitution) or "." (less conservative substitutions). The aminoacids that differ from the sequence used as template (βI and αIa) are marked in **red**. The sequences were obtained in FASTA format from the NCBI database.

The incorporation of polyamines (putrescine, spermine, spermidine) into glutamines within α- and β-tubulin cores is an irreversible modification that confers stability to the lattice. Acetylation of the lysine K40 within the α-tubulin subunit is the only modification that takes place in the microtubule lumen.[79] Additional acetylation sites have been recently discovered in β-tubulin. Acetylated residues are enriched in axonal microtubules, basal bodies, and long-lived microtubules. Glutamate residues are overrepresented in C-terminal tails (Fig. 3), endowing them with negative net charge. These residues can anchor polyglutamate and polyglycine chains, resulting in branched tails. The first aminoacid is bonded through the γ-carboxyl group of the canonic glutamate and the next incoming residues will be incorporated through peptidic bonds. Axonemes of cilia and flagella are heavily glutamylated and glycylated.[80]

Most α-tubulin C-terminal motifs are capped by a tyrosine aminoacid, except for αIVa and αVII. Those tails can be labeled with a tyrosine (tyrosination) or alternatively removed (detyrosinated). Tyrosinated microtubules are typically more dynamic and show high turnover, whereas long-lived microtubules are enriched in detyrosinated tails.[81] Tyrosination/detyrosination state is involved in the recruitment of cellular effectors. After the tyrosine residue, the removal of one or two glutamates leads to Δ2- or Δ3-tubulin, respectively. These irreversible modifications prevent tubulin from being tyrosinated and are tightly related to microtubule stability.

Tubulin binding sites and partnering drugs in clinical use

Aside from antitumor properties, several tubulin ligands have been reported to display antiparasitic and herbicide effects (e.g. oryzalin), many of them extracted from natural sources.[82–84] Based on those natural discoveries, extensive research has been conducted to develop drug candidates. Seven distinct binding sites for exogenous ligands have been characterized within the tubulin dimer so far, named after their first discovered interacting compound. They are often classified into two subsets according to their net effect on the tubulin lattice: microtubule stabilizing agents (MSAs) or microtubule destabilizing agents (MDAs).[85]

On the one hand, MSAs preferentially bind at the dimers composing the microtubule, promoting polymerization rather than depolymerization. They exert a stabilization effect by reinforcing lateral contacts between neighboring protofilaments (Fig. 4). Indeed, the MSA paclitaxel can even promote the incorporation of GDP-loaded free tubulin dimers into the microtubule.[86] On the other hand, MDAs preferentially bind at the soluble dimers prior to their merger into the tube, therefore impeding polymerization (Fig. 4).

The modulation of the polymer mass was initially thought to be the prime mechanism of action: MSAs increase microtubule mass, whereas MDAs trigger a decline. This theory was overturned by the fact that changes in the microtubule mass are only caused by high drug doses. Yet, microtubule-interfering agents abolish the well-orchestrated polymer dynamics with unaltered microtubule mass at 10-100 fold lower doses, irrespective of whether they are pigeonholed as MSAs or MDAs.[13] This suppressor effect culminates in the blockage of the cell cycle transition between metaphase and anaphase, committing the cell to die. Two binding domains for MSAs have been described to date: the taxoid site and the laulimalide/peloruside site.[87,88] The other five binding sites are allocated to MDAs, and encompass vinca alkaloid, eribulin, maytansine, pironetin, and - the one in hand – colchicine interaction domains (Fig. 4).

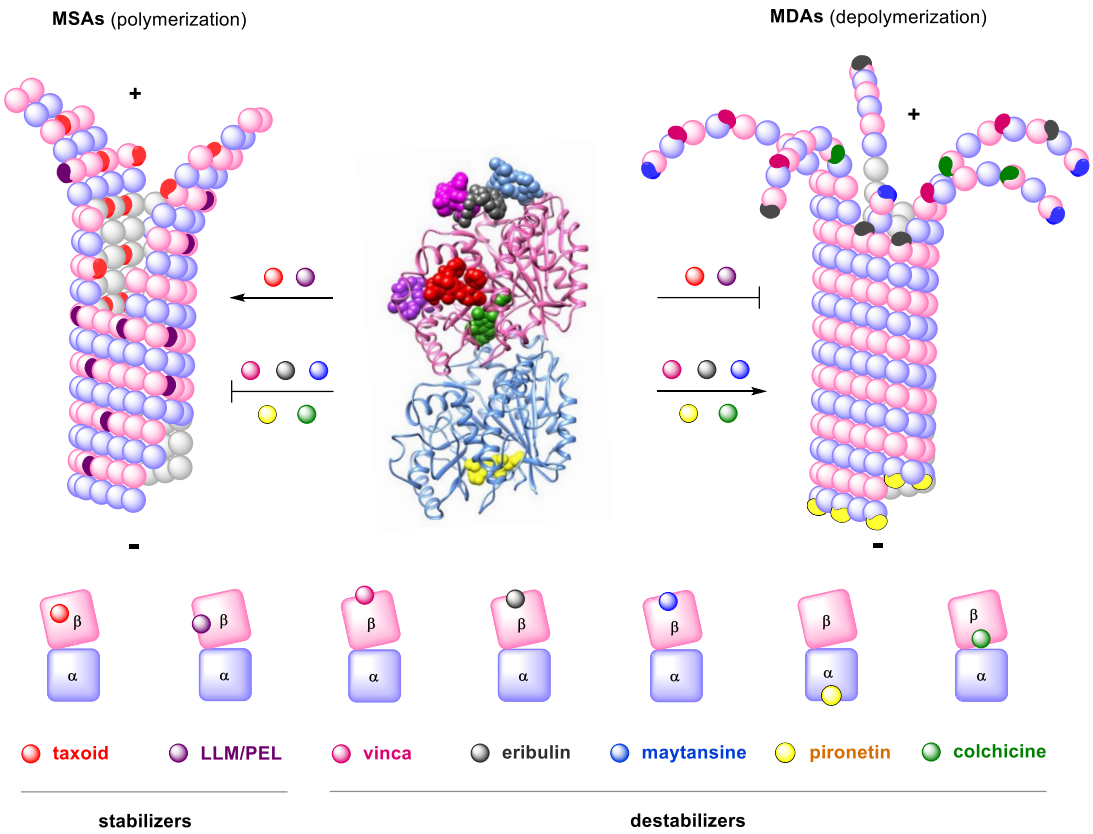

Figure 4. Depiction of tubulin binding domains. The interaction of MSAs with the **taxoid** or the **LLM/PEL** domains in β-tubulin stabilizes the M-loop and reinforces lateral contacts between neighboring protofilaments. MDAs perturb the longitudinal contacts along protofilaments within the same dimer or between consecutive dimers. **Vinca** domain ligands act as a wedge between dimers, hence impeding the longitudinal straightening of interdimer interfaces. Additionally, the engagement of the vinca site may stabilize ring-shaped tubulin oligomers, which are not compatible with microtubules. **Maytansine** and **eribulin** site ligands are preferentially found in the plus-end. They cause depolymerization by either inactivation of free dimers in a non-compatible state at high concentrations or by preventing the assembly of incoming dimers at substoichiometric concentrations. The occupation of the **pironetin** site hinders the incorporation of dimers into the minus-end or turns soluble tubulin into an incompetent state for the binding. **Colchicine** site ligands bind at the intradimer interface and hamper the curved-to-straight transition required for GTP hydrolysis.

A. Microtubule stabilizing agents (MSAs)

The taxoid binding domain is a deep hydrophobic cleft in β-tubulin facing the microtubule luminal surface (Fig. 5).[87] The access to that internal region occurs by the transitory pass through microtubule pores. Indeed, the external pore type I may be an additional binding site for these ligands, leading to microtubule stabilization. The binding of taxanes and related drugs to its innate domain or the external pore is widely accepted to be mutually exclusive, the latter considered as a step in the diffusion towards the luminal domain.[89,90] The occupation of the taxoid domain tethers adjacent protofilaments by stabilizing lateral contacts (Fig. 4). There are many compounds that bind to the taxoid domain*:* taxanes, taccalonolides, epothilones, cyclostreptin, dictyostatin, discodermolide, eleutherobin, sarcodictyins, zampanolide, dactylolide.[91,92]

Drug	Trademark	Formulation	FDA approved indications	Date
paclitaxel	Taxol®	i.v. infusion	Advanced ovarian carcinoma	1992
			Metastatic breast cancer	1994
			AIDS-related Kaposi sarcoma	1997
			Locally advanced or metastatic NSCLC	1998
	Abraxane®	i.v. infusion (nanoparticle)	Refractory, metastatic or relapsed breast cancer	2005
			Locally advanced or metastatic NSCLC	2012
			Late-stage metastatic pancreatic cancer	2013
docetaxel	Taxotere®	i.v. infusion	Locally advanced or metastatic breast cancer	1996
			Locally advanced of metastatic NSCLC	1999
			Metastatic hormone-refractory prostate cancer	2004
			Squamous cell carcinoma of head and neck	2006
			Advanced gastroesophageal adenocarcinoma	2006
cabazitaxel	Jevtana®	i.v. infusion	Metastatic hormone-refractory prostate cancer	2010
ixabepilone	Ixempra®	i.v. infusion	Locally advanced or metastatic breast cancer	2007
vincristine	Oncovin®	i.v. infusion (salt)	Acute lymphocytic leukemia	1963
			Hodgkin lymphoma	1963
			Non-Hodgkin lymphoma	1963
			Neuroblastoma	1963
			Rhabdomyosarcoma	1963
			Wilms tumor	1963
	Marqibo®	i.v. (liposome)	Acute lymphoblastic leukemia	2012
vinblastine	Velban®	i.v. infusion (salt)	Breast cancer	1965
			Choriocarcinoma	1965
			Hodgkin lymphoma	1965
			Non-Hodgkin lymphoma	1965
			AIDS-related or classic Kaposi sarcoma	1965
			Mycosis fungoides	1965
			Advanced testicular cancer	1965
vinorelbine	Navelbine®	i.v. infusion (salt)	Locally advanced of metastatic NSCLC	1994
vinflunine	Javlor®	i.v. infusion	Metastatic transitional urothelium carcinoma	2009
MMAE	Adcetris®	i.v. infusion (ADC)	Hodgkin lymphoma	2011
			Systemic anaplastic large cell lymphoma	2011
			Cutaneous anaplastic large cell lymphoma	2017
			Mycosis fungoides	2017
			Peripheral T-cell lymphoma	2018
	Polivy®	i.v. infusion (ADC)	Relapsed diffuse large B-cell lymphoma	2019
	Padcev®	i.v. infusion (ADC)	Locally advanced or metastatic urothelial cancer	2019
eribulin	Halaven®	i.v. infusion (salt)	Metastatic breast cancer	2010
			Unresectable or metastatic liposarcoma	2016
emtansine	Kadcyla®	i.v. infusion (ADC)	HER2-positive metastatic breast cancer	2013
colchicine	Colcrys®	oral	Prophylaxis and treatment of acute gout flares	1961
			Familial Mediterranean fever	1961

Table 2. Tubulin-binding drugs approved by the Food and Drug Administration (FDA) for cancer treatment as for February 2020. Vinflunine (Javlor®) has been approved by the European Medicines Agency (EMA) but not by the FDA. The information registered in the table was retrieved from the National Cancer Institute of the NIH.[93]

Paclitaxel is a diterpene first isolated in the 60s from the bark of the Pacific yew tree *Taxus brevifolia*, and the first molecule identified as a MSA (Fig. 5).[94] The FDA approved it in 1992 under the trademark Taxol®, and it has been extensively used in clinic since then for the treatment of severe neoplasms (Table 2).[95] Its hydrophobic profile and considerable size contribute to its high affinity for unspecific efflux pumps (e.g. P-glycoprotein).[96] The second prime resistance mechanism fighting taxanes treatment back is mediated by the overexpression of specific tubulin isotypes (e.g. βIII).[55] These two mechanisms hamper the full effectiveness of taxane's clinical use, as does the acute toxicity (e.g. severe neutropenia or leucopenia, and neurotoxicity).[97] There is a nanodroplet formulation containing albumin-stabilized paclitaxel (Abraxane®) with fewer side effects (Table 2).[95]

Two other taxanes have also been approved by the FDA. Docetaxel (Taxotere®) shows improved efficacy compared to paclitaxel in some cases, although the two resistance mechanisms above apply to both taxanes.[95] Cabazitaxel (Jevtana®) displays a feeble affinity for P-glycoprotein as a significant advantage and is used against prostate cancer previously treated with docetaxel-prednisone.[98] The only non-taxane drug in clinical use is the aza-epothilone B derivative ibaxepilone (Ixempra®) for locally advanced or metastasized breast cancer alone or in combination with capecitabine.[99]

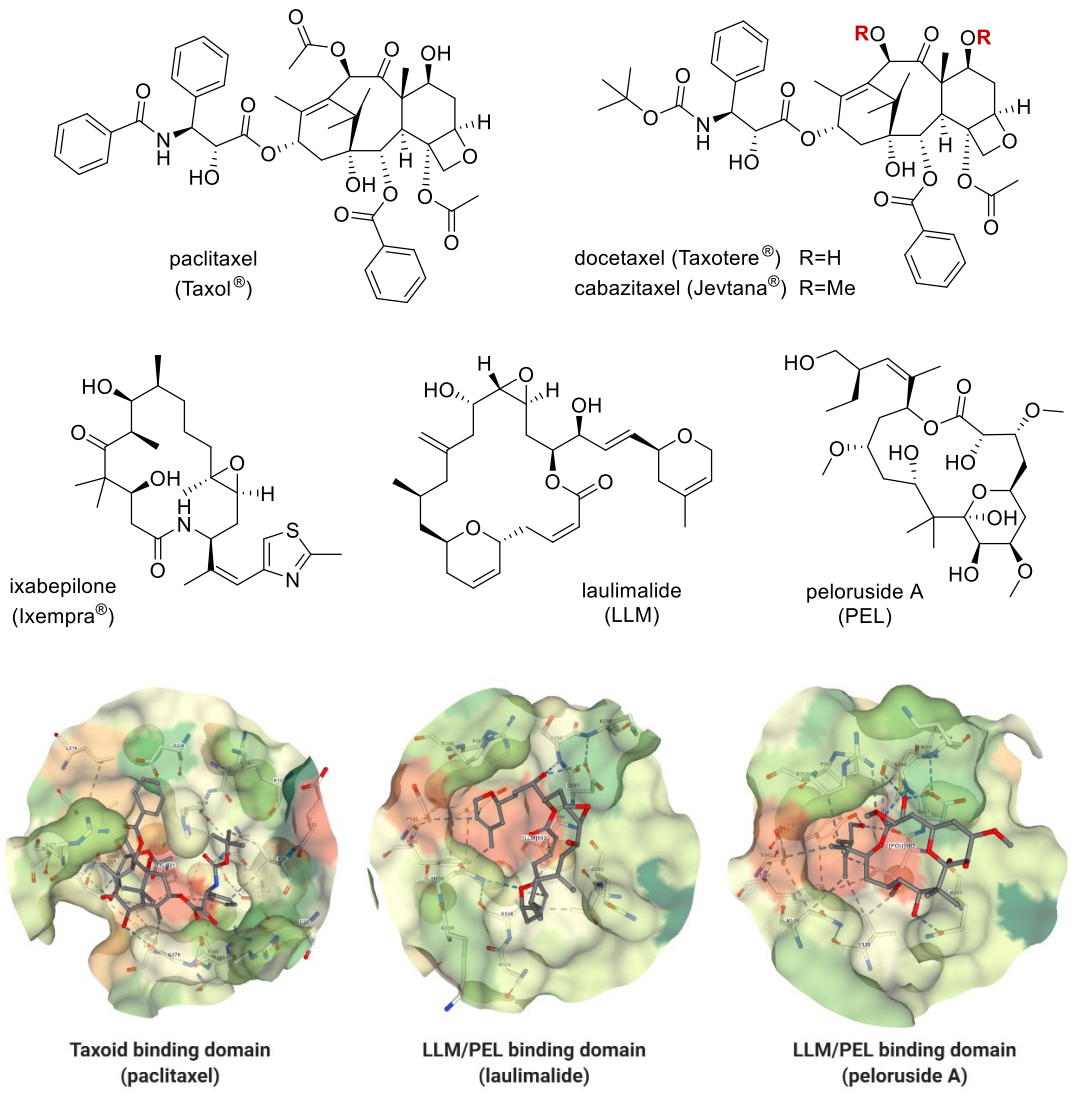

Figure 5. Chemical structures of reference MSAs. The interacting poses of paclitaxel (PDB ID: 1TUB),[21] LLM (PDB ID: 4O4H),[100] and PEL (PDB ID: 4O4J)[100] into their respective binding domains are depicted at the bottom.

A second binding pocket for MSAs was identified on the outer surface of β-tubulin for two macrocyclic lactones: laulimalide and peloruside A (Fig. 5).[101–103] Laulimalide (LLM) was isolated from *Cacospongia mycofijiensis* and peloruside A (PEL) from the New Zealand sponge *Mycale hentscheli*. The ligation of the LLM/PEL domain promotes the lateral interaction with the adjacent β subunit by stabilizing the M-loop (Fig. 4). This M-loop stabilization effect is common to all MSAs that bind to the taxoid domain and the LLM/PEL domain.[104] The bridging of neighboring protofilaments reinforces and stabilizes the microtubule lattice.[100] Moreover, the interaction at the LLM/PEL pocket simultaneously stabilizes the taxoid domain in an allosteric fashion and vice versa.[105] There are a couple of X-ray structures of LLM and PEL in complex with tubulin, either alone or concurrently with epothilone A.[100] Altogether, this observation suggests a synergistic mechanism of stabilization or crosstalk upon engagement of both sites, that might be profitably evaluated in clinical trials. Both macrolactones have been reported to maintain their cytotoxic activity in MDR-overexpressing cell lines *in vitro*.[106]

B. Microtubule destabilizing agents (MDAs)

The vinca alkaloids turned the clinical market upside down from the moment the FDA approved vincristine and vinblastine in the 60s (Fig. 6). These drugs were the first tubulin-targeting ligands that made it to the clinic for cancer treatment and, even nowadays, are among the most used chemotherapy strategies against hematological tumors.[107] These compounds were isolated in the 50s from the leaves of the periwinkle plant *Catharanthus roseus* or *Vinca rosea*, hence their name. Gigant *et al.* determined the structure of the vinca domain in 2005, embedded at the interdimer interface, sharing interacting residues from both β-tubulin and the α-tubulin of the incoming dimer.[108] Vinca alkaloids (e.g. vinblastine) bind close to the E site mainly at microtubule edges, preferentially the plus-end, and restrain the hydrolysis of the GTP loaded in the β-tubulin.[109] The microtubule destabilizing effect observed upon treatment with these compounds stems from their wedge effect between dimers, thereby inducing a curved conformation prone to depolymerize rapidly. It impedes the straightening of protofilament tips, which is required for the assembly of competent microtubules. The interaction at the vinca domain may alternatively stabilize those protofilaments into bent ring-shaped oligomers at higher concentrations of the ligands.[108,110]

There are three vinca alkaloids approved by the FDA to date (vinblastine, vincristine, and vinorelbine), and a fourth semisynthetic one by the EMA (vinflunine), as illustrated in Table 2.[111,112] There is a liposomal formulation with vincristine sulfate (Marqibo®) that exhibits ameliorated pharmacokinetic profile and effectiveness.[113] Despite they have proven effectiveness, non-desirable side effects are quite common after treatment (e.g. peripheral neuropathy and reversible myelosuppression),[114] as do resistances shared with taxanes (e.g. MDR-mediated resistance and altered β-isotype expression).[115] Extensive research has been conducted seeking for an ameliorated outcome.

Many natural or semisynthetic ligands have been reported to bind at the vinca domain, such as auristatins or tubulysins.[116,117] Although their narrow therapeutic windows leave no room for clinical expectations when used as free drugs, some of them have been evaluated as drug cargoes in antibody-drug conjugates (ADCs), such as monomethyl auristatin E (MMAE), approved by the FDA as a payload on ADC. Surprisingly, a family of triazolopyrimidines has been recently reported to bind at the vinca site (Fig. 6), though displaying stabilizing activity by promoting longitudinal contacts between dimers within the protofilament, as opposed to classical MSAs, which reinforce lateral contacts.[118]

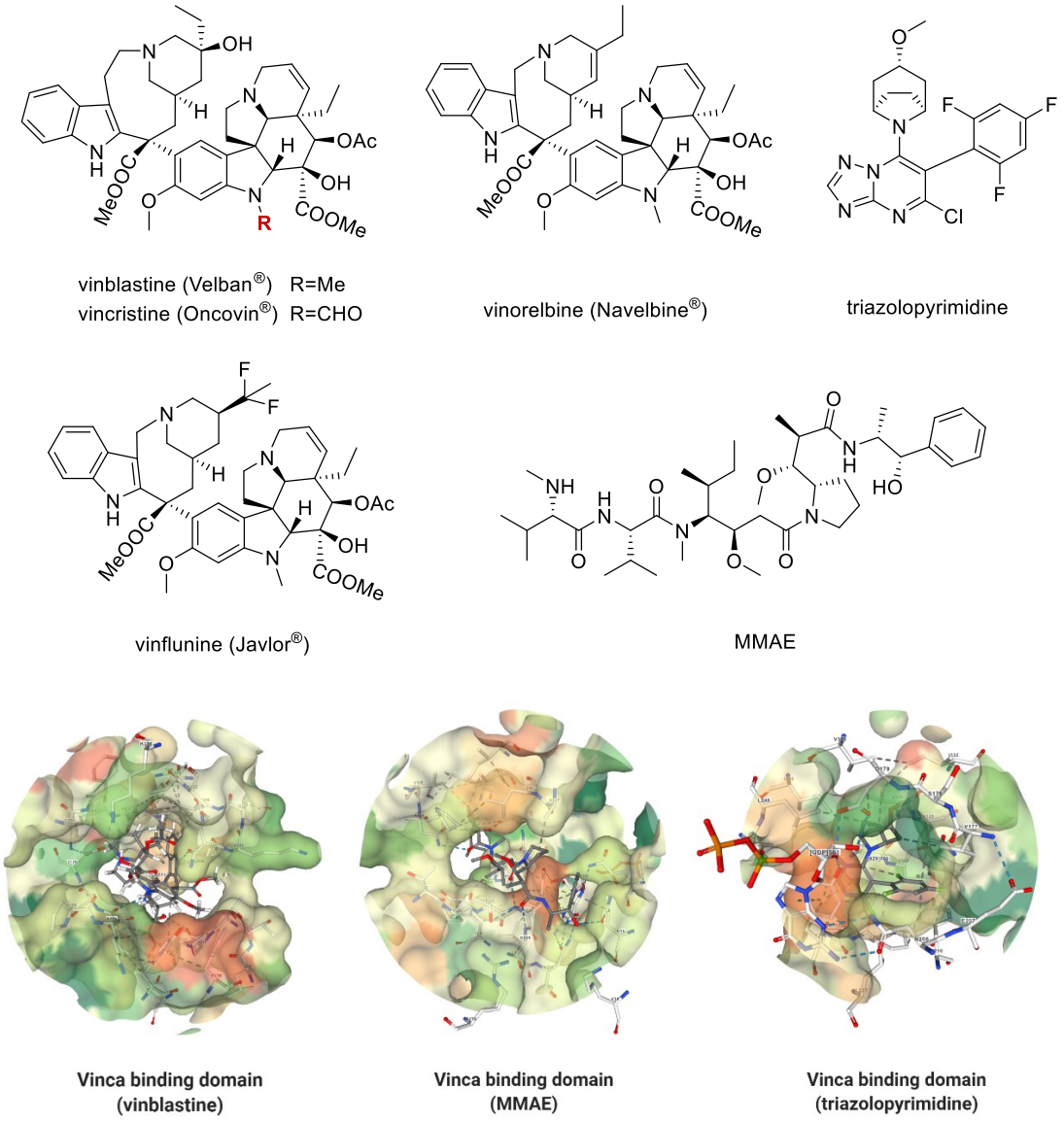

Figure 6. Chemical structures of vinca alkaloids and related ligands. The interacting poses of vinblastine (PDB ID: 5J2T),[117] MMAE (PDB ID: 5IYZ),[117] and triazolopyrimidine (PDB ID: 5NJH)[118] into their domain are depicted at the bottom.

Apart from the vinca alkaloids mentioned above, eribulin (Halaven®) is the only non-conjugated MDA currently in clinical use for cancer treatment (Table 2). The FDA has approved it formulated as a mesylate salt for the treatment of metastatic breast cancer and advanced liposarcoma. Eribulin binds to the soluble tubulin pool, then incorporated into the growing edges of microtubules impeding polymerization. Eribulin binding domain is located at the interface between a β subunit and the incoming α-tubulin, near the vinca domain, and almost overlapping the E site (Fig. 7).[119] The occupation of the eribulin pocket suppresses microtubule growth at plus-ends by hampering the incorporation of novel dimers and turning soluble dimers into a non-compatible state although it barely affects minus-end dynamics.[120] It impedes GTP hydrolysis and the occupation of the vinca domain due to steric hindrance.[121] Some researchers consider vinca and eribulin domains as a single entity since they partially share an interacting region.

The maytansine/rhizoxin binding domain has also been framed close to the E site and the vinca site at the β-tubulin, hindering the formation of longitudinal interactions in protofilaments upon ligation (Fig. 7).[122] Although rhizoxin clinical trials did not fulfill the hype expectations,[123] the ADC consisting of trastuzumab combined with the maytansine analogue emtansine reached clinical use for the treatment of HER2-positive breast cancer (Kadcyla®) exhibiting adequate tolerance (Table 2).[124] Yet, resistance mechanisms have already been reported.[125] As it occurs upon eribulin binding, vinblastine interaction with its own binding pocket is impeded upon engagement of the maytansine site, given the spatial proximity.[122] Alternatively, the occupation of the vinca domain hampers the access to eribulin and maytansine pockets. Both eribulin and maytansine domain ligands exert their destabilizing effect by either "inactivating" free dimers at high concentrations or by impairing longitudinal interactions at lower doses. This mechanism differs from the one employed by vinca domain ligands.

In a similar way, the natural compound pironetin disturbs the longitudinal tubulin-tubulin contacts by binding to a pocket located in the α-tubulin close to the interdimer interface (Fig. 7). It establishes a covalent bond with cysteine C316α through Michael addition to the α,β-unsaturated carbonyl. Maytansine and pironetin cap microtubules, maytansine at the plus-end and pironetin at the minus-end.[126,127]

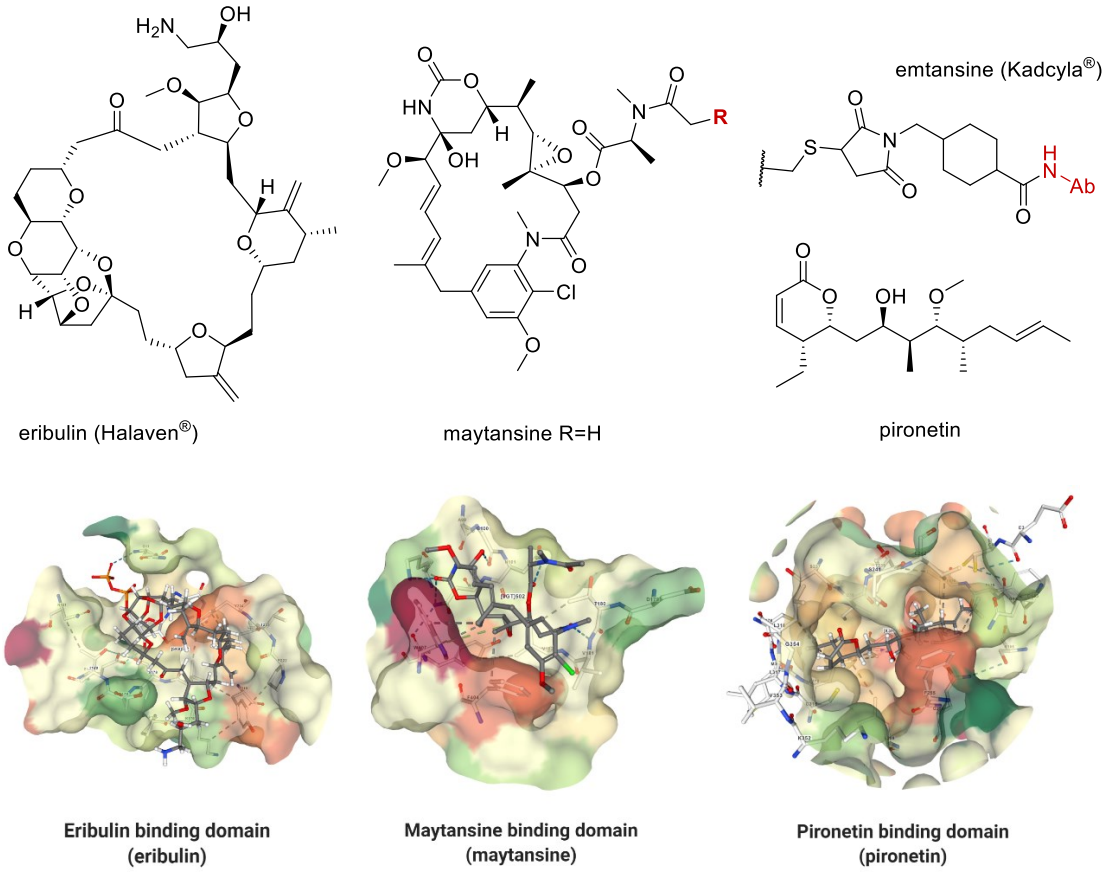

Figure 7. Chemical structures of the MDAs eribulin, maytansine, emtansine, and pironetin. The interacting poses of eribulin (PDB ID: 5JH7),[119] maytansine (PDB ID: 4TV8),[122] and pironetin (PDB ID: 5LA6)[126] into their respective binding domain are represented at the bottom.

THE COLCHICINE DOMAIN

The overall purpose of the present work is primarily obtaining putative colchicine site ligands and further studying their mechanism of action, which are the reasons why the colchicine domain is reviewed in a distinct section from other MDAs. Colchicine is a tricyclic alkaloid from the poisonous meadow saffron *Colchicum autumnale*.[128] The therapeutic properties of this plant have been known for centuries, but it was not until 1820 when Pelletier and Caventou first isolated colchicine. It is the first discovered tubulin binding drug and allowed the identification of tubulin itself in 1967.[129] The structure of the colchicine site was determined by Ravelli *et al.* in 2004 by X-ray diffraction. It is a hydrophobic cavity located at the α-β intradimer interface,[25] mostly buried into the β-tubulin with a shallow region facing the α-tubulin close to the N site (Fig. 8).[130] The mostly hydrophobic nature of the domain may condition the design of novel drug-like agents.

The occupation of the colchicine site hampers the transition between the curved and the straight conformation of the tubulin dimer, which is required for its stable incorporation into the microtubule. Colchicine site ligands thus block the polymerization and destabilize the microtubule lattice (Fig. 4).[131] The colchicine domain is sterically occluded in straight protofilaments, so the ligands preferentially bind to free soluble dimers, then incorporated into microtubule ends.[132,133] Colchicine exerts an allosteric effect upon binding to its domain, resulting in an increased GTPase activity of the β-tubulin leading to "inactivated" GDP-bound dimers.[134] Colchicine binding also induces a conformational change of the M-loop in the β-tubulin involved in lateral contacts between adjacent protofilaments, thus destabilizing the microtubule.[25]

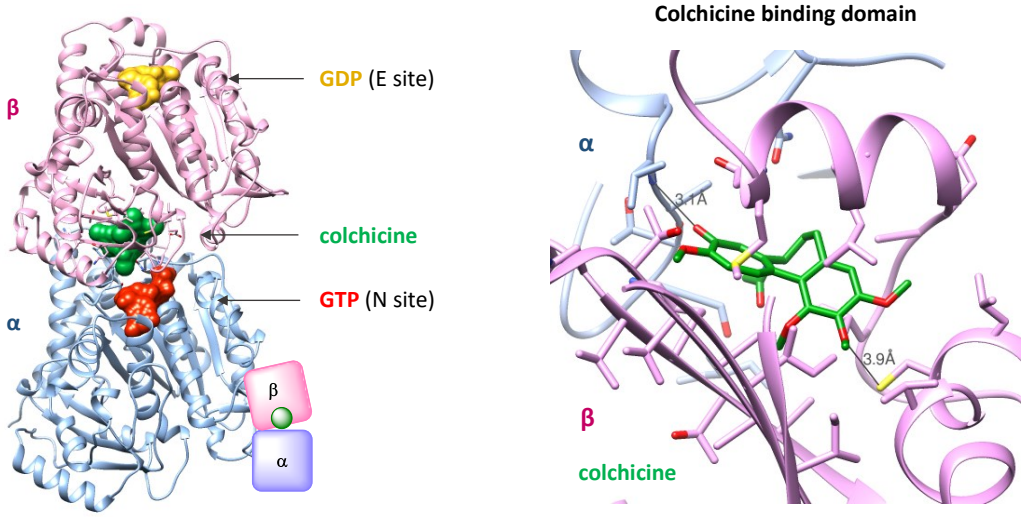

Figure 8. X-ray structure of the tubulin-colchicine complex (PDB ID: 4O2B).[135] Both E and N nucleotide binding sites are indicated by arrows, loading **GDP** and **GTP**, respectively. The α-tubulin is colored in **blue**, the β-tubulin in **pink**, and colchicine in **green**.

Despite its high potency as cytotoxic agent, colchicine is not used as an antitumor drug due to the high-toxicity profile and the narrow therapeutic window (e.g. bone marrow toxicity).[136,137] Notwithstanding, it has been approved by the FDA in the prophylaxis and treatment of acute gout flares and familial Mediterranean fever at lower doses than those needed to exert cytotoxic activity (Table 2).[138–140] The high toxicity may be partially related to its slow kinetics in the tubulin binding, which is a two-step process. The initial low-affinity interaction evolves into a tight interaction after a conformational change in the tubulin

dimer.[132] Many alternatives have emerged seeking for ameliorated drug-like properties. However, none of them has yet surpassed clinical trials and reached clinical use to date.[141] Current efforts are invested in the discovery of more hydrosoluble compounds with improved potency and reduced toxicity. The hub key relies on the comprehensive understanding of the domain and how it accommodates to the ligand.[142]

The colchicine site offers an enticing chance for drug design for several reasons. First, compared to most TBDs that interact with the other domains, colchicine site ligands are structurally small molecules, which is attainable in synthetic terms. Developing a vast chemical library of colchicine site derivatives based on ligand-protein interactions is rather easy compared to the huge and complex structures of taxanes or vinca alkaloids. This simpler structure permits to avoid resistance mediated by MDR transporters since P-gp efflux pumps preferentially export bigger and more hydrophobic molecules.[143] MDR-mediated resistance entails, or at least, is related to the therapeutic failure of many drugs (e.g. paclitaxel). Another reason to pick the colchicine site as a drug target draws from the vascular disrupting activity displayed by some ligands interacting in this pocket, which shut the blood flow to the inner core of a solid tumor culminating in necrosis.[144] This significant advantage will be further discussed later.

Colchicine site interacting ligands

Ravelli *et al.* described the colchicine domain in 2004 through the X-ray structures of DAMA-colchicine (PDB ID: 1SA0) and podophyllotoxin (PDB ID: 1SA1) in complex with tubulin.[25] Since then, the number of crystal complexes grows every year. It has been boosted mainly since the group of Steinmetz reported a crystallization strategy based on the stabilization by RB3 and tubulin tyrosine ligase, which improved resolution.[145] These structures include a vast diversity of compounds (Table 3, Fig. 9-12). The emerging picture of these complexes is a broad and deep pocket, considered as a binding domain rather than just a "site".[146] This domain is usually divided into three consecutive zones, referred to as zones 1-3 (Fig. 9). Zone 1 contacts the α-tubulin, although embedded in the β subunit. Aromatic rings such as the *p*-methoxyphenyl in combretastatin A4 (CA4, Fig. 9) or the tropolone ring in colchicine (Fig. 10) occupy this region. It gives way to zone 2 through a region exposed towards the solvent that can shelter variable-length bridges connecting the moieties harbored in zones 1 and 2. Zone 2 is an interacting region shared by most of the ligands, frequently occupied by a trimethoxyphenyl ring as in CA4 (Fig. 9) or colchicine (Fig. 10). Zone 3 is a less hydrophobic pocket deeply buried into β-tubulin that accommodates ligands such as MI-181 (Fig. 9).[146]

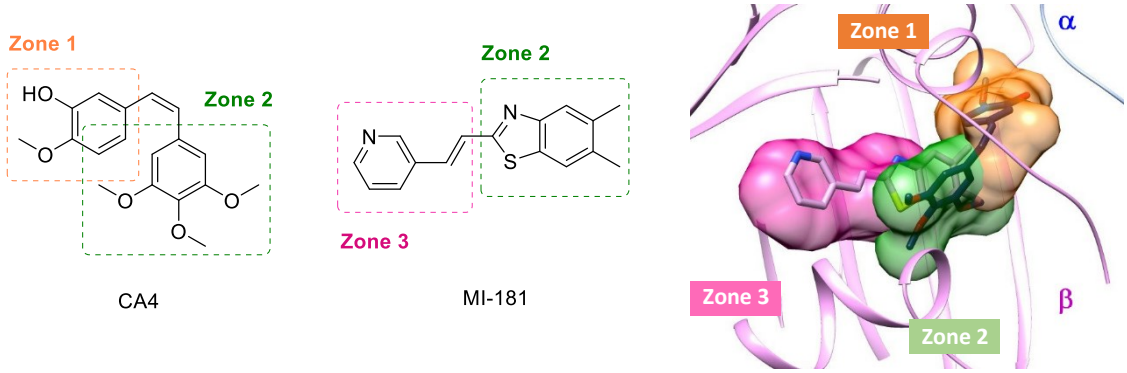

Figure 9. Chemical structures of CA4 and MI-181. Structure of the colchicine domain with CA4 (dark blue) occupying zones 1 (**orange**) and 2 (**green**), and MI-181 (light pink) occupying zones 2 (**green**) and 3 (**pink**).

In recent years, many compounds have been designed and evaluated as tubulin polymerization inhibitors aimed to bind at the colchicine site. The following overview is only focused on the colchicine site ligands with X-ray structures deposited in Protein Data Bank (Table 3). Although the simple chemical structures of these ligands can be seen as an advantage for drug design, it is not easy to extract a common pharmacophore model due to rather different interacting modes. Most of the ligands interact in zones 1-2, others in zones 2-3, and there are only three structures (ABT-751,[133] lexibulin,[148] and MT189[149]) that occupy zones 1-2-3, although one of them only partially. The ligands in zones 1-2 and zones 2-3 share zone 2, but interact in a substantially different way. Many of the compounds binding to zones 1-2 bear a trimethoxyphenyl (e.g. colchicine, MTC, podophyllotoxin, CA4), and are usually referred to as classical ligands. Many others have rather different moieties (e.g. ABT-751, BAL27862, BKM120, and especially all the compounds that do not occupy zone 1) (Fig. 11).

The structural diversity in zone 2 is probably related to the structural requirements to access with the remaining fragments to the alternatives zones 1 or 3. Bulky groups such as trimethoxyphenyl bend the leucine L255β in the frontier between zones 2-3, blocking the access to zone 3.[142] Moieties with different geometrical requirements allow to reallocate the side chain of L255β thus opening a gorge towards zone 3 (e.g. pyridylendiamine in ABT-751).

PDB ID	Drug	Group	Zones	Å	Date	Ref
1SA0	DAMA-colchicine	col	1-2	3.58	2004	25
1SA1	podophyllotoxin	podo	1-2	4.20	2004	25
3HKE	T138067	covalent	1-2	3.60	2009	133
4O2A	BAL27862	other	1-2	2.50	2014	135
4O2B	colchicine	col	1-2	2.30	2014	135
4YJ3	C2	CA4-ext	1-2	3.75	2015	147
5CB4	tivantinib	CA4-het	1-2	2.19	2015	148
5JVD	TUB092	CA4-ext	1-2	2.39	2016	149
5LP6	thiocolchicine	col	1-2	2.90	2016	150
5M7E	buparlisib	other	1-2	2.05	2017	151
5M7G	MTD147	other	1-2	2.25	2017	151
5M8D	MTD265-R1	other	1-2	2.25	2017	151
5M8G	MTD265	other	1-2	2.15	2017	151
5LYJ	combretastatin A4	CA4	1-2	2.40	2017	152
5GON	CA4 β-lactam	CA4-het	1-2	2.48	2017	153
5XLZ	9(10*H*)-anthracenone	CA4-short	1-2	2.30	2017	154
5JCB	YJTSF1	podo	1-2	2.30	2017	155
5NFZ	MTC	col	1-2	2.10	2017	156
5OV7	rigosertib	other	1-2	2.40	2017	157
5XLT	4'-deMe-epipodophyllotoxin	podo	1-2	2.81	2017	158
5H7O	DJ101	podo	1-2	2.80	2017	159
5OSK	quinazolinone 7j	CA4-short	1-2	2.11	2017	160
5XAF	CA4 β-lactam Z1	CA4-het	1-2	2.55	2017	161
5XAG	CA4 β-lactam Z2	CA4-het	1-2	2.56	2017	161
5YL2	SKLB028	CA4-ext	1-2	2.09	2018	162
5YLJ	millepachine	CA4-ext	1-2	2.70	2018	162
5YLS	SKLB050	CA4-ext	1-2	3.00	2018	162
5XIW	colchicine	col	1-2	2.90	2018	162

Table 3. Continued

PDB ID	Drug	Group	Zones	Å	Date	Ref
5XKE	demecolcine	col	1-2	2.60	2018	-
5XKF	verubulin	CA4-short	1-2	2.80	2018	163
5XKG	SKLB060	CA4-short	1-2	2.20	2018	163
5XKH	CF1	CA4-short	1-2	2.25	2018	-
6BR1	pyrido[2,3-d]pyrimidine	CA4-short	1-2	2.30	2018	164
6BRF	pyrido[3,2-d]pyrimidine	CA4-short	1-2	2.50	2018	164
6BRY	furo[3,2-d]pyrimidine	CA4-short	1-2	2.70	2018	164
6BS2	oxazolo[5,4-d]pyrimidine	CA4-short	1-2	2.65	2018	164
6D88	VERU-111 analogue 13f	CA4-ext	1-2	2.85	2018	165
6GJ4	benzoxazepine	CA4-ext	1-2	2.40	2018	166
6F7C	acylhydrazone 12	CA4-ext	1-2	2.00	2018	167
6H9B	carbazole 4f	CA4-short	1-2	2.75	2018	168
5Z4P	4,5-dihydroindazole	CA4-het	1-2	2.50	2019	-
5Z4U	1*H*-pyrazole	CA4-het	1-2	3.18	2019	-
6HX8	STX3451	CA4-ext	1-2	2.40	2019	169
6JCJ	crolibulin	podo	1-2	2.50	2019	170
6GF3	jerantinine B acetate	other	1-2	2.40	2019	171
6NNG	DJ95	CA4-ext	1-2	2.40	2019	172
6O5M	ABI analogue 10bb	CA4-ext	1-2	2.30	2019	173
6O5N	ABI analogue 10ab	CA4-ext	1-2	3.00	2019	173
6O61	ABI-231	CA4-ext	1-2	2.60	2019	173
6QQN	TH588	other	1-2	2.30	2019	174
6AGK	ABI analogue 4v	CA4-ext	1-2	2.80	2019	175
6EG5	pyrido[2,3-d]pyrimidine	CA4-short	1-2	2.45	2019	176
6N47	pyrido[3,2-d]pyrimidine	CA4-short	1-2	2.60	2019	176
6K9V	D64	CA4-short	1-2	2.54	2019	177
3HKD	TN16	dione	2-3	3.70	2009	133
3N2G	G2N	pterin	2-3	4.00	2010	42
3N2K	G2K	pterin	2-3	4.00	2010	42
5C8Y	plinabulin	dione	2-3	2.59	2015	148
5CA1	nocodazole	biaryl	2-3	2.40	2015	148
4YJ2	MI-181	biaryl	2-3	2.60	2015	147
5O7A	QA_1	other	2-3	2.50	2017	178
5XHC	87U	dione	2-3	2.75	2017	-
5XI5	MBRI-001	dione	2-3	2.81	2017	179
5XI7	PO7	dione	2-3	2.99	2017	-
5YL4	8WR	dione	2-3	2.64	2017	-
6FKJ	TUB075	dione	2-3	2.15	2018	180
6FKL	TUB015	dione	2-3	2.10	2018	180
5YZ3	MP-HJ-1c	biaryl	2-3	2.54	2018	181
6KNZ	tirbanibulin	other	2-3	2.47	2019	182
3HKC	ABT-751	-	1-2-3	3.80	2009	133
5CA0	lexibulin	-	1-2-3	2.50	2015	148
5ZXH	MT189	-	1-2-3	2.80	2019	183

Table 3. PDB IDs of the X-ray structures of tubulin with ligands that bind at the colchicine domain. These ligands are clustered according to the binding zones they interact with. The resolution of the complex is indicated in Å. Col = colchicinoids; podo = podophyllotoxin and related; CA4-ext = CA4 derivatives with extended bridge; CA4-het = heterocycles on the bridge; CA4-short = non-isomerizable one-atom bridge.

A. Ligands that occupy zones 1 and 2

The classical ligands of zones 1-2 are composed of two non-coplanar aromatic rings connected by a bridge with variable length. However, there is broad structural variability represented by colchicinoids, podophyllotoxins, combretastatins, and numerous variations on the bridge. Other less classical variations include azines such as buparlisib (BKM120) or TH588, BAL27862, rigosertib, and the covalent ligand T138067 (Fig. 10). Some of these structures barely related to classical ligands correspond to an original design for other therapeutic targets but have been recently described to bind to the colchicine domain, and some of them are already in advanced phases of clinical trials. These ligands have shown that structurally unrelated moieties can successfully replace the once considered essential 3,4,5-trimethoxyphenyl ring.[184,185] The classical ligands of the colchicine domain, despite their structural diversity, harbor common structural elements that were summarized in a pharmacophore that includes seven pharmacophoric points: three hydrogen bond acceptors (A1-A3), one donor (D1), two hydrophobic centers (H1-H2), and a planar group (R1), canvassed in two planes with a relative angle of 45°, corresponding to those of the aromatic rings.[186]

Colchicinoids are biaryls with atropoisomerism (Fig. 10). The C ring of colchicine (tropolone ring) binds at zone 1, whereas the A ring harboring a trimethoxy substitution pattern interacts with zone 2. The presence of the B ring in colchicine implies that its binding and dissociation kinetics to tubulin are slow, what has been related to its high toxicity. MTC lacks that ring, shows rapid binding kinetics and fluoresces when bound to the colchicine domain, so it can be used in competition assays to determine the binding of compounds to the colchicine domain. Podophyllotoxin is a natural product isolated from *Podophyllum sp.* and binds to tubulin similarly to colchicine. Podophyllotoxin and related compounds are highly toxic despite their rapid binding kinetics. The configuration of the podophyllotoxin lactone is important for the activity because it conditions the axial disposition of the trimethoxyphenyl ring, required for the binding to the colchicine domain.

Combretastatin A4 (CA4) is a natural product originally isolated from the root bark of *Combretum caffrum*,[187] but nowadays it is obtained by chemical synthesis (Fig. 10). Its poor solubility has propitiated that several prodrugs emerge as ameliorated alternatives. It is the case of the phosphate prodrug fosbretabulin or the serine-derivative AVE-8062 (ombrabulin), currently under phase III clinical trials.[188–191] Structurally, CA4 is a *cis*-stilbene that readily isomerizes to the less active *trans* isomer.[192,193] Recently, the isomerization in combretastatins has been exploited to prepare compounds that isomerize under UV radiation to the active isomer, allowing to perform photodynamic therapy.[194] The isomerization of CA4 occurs spontaneously upon physical factors (heat, light, and acidic pH) and *in vivo* by metabolic reactions.[195] The phenolic group of CA4 is the anchoring point for prodrug formulation due to the low intrinsic solubility but suffers from rapid metabolic inactivation and elimination.[196] Its pharmacokinetic profile, low efficacy, and short lifespan have limited clinical success.

Several strategies have been applied in order to avoid the inactivating isomerization of the olefin in CA4, including the formation of heterocycles (CA4-het), the constriction of the bridge to a single non-isomerizable atom (CA4-short), and the elongation associated or not to the formation of cycles that do not isomerize (CA4-ext). The most explored strategy to lock the *cisoid* configuration of the bridge has probably been its integration into heterocyclic systems of four (β-lactams),[153,161] five (azoles and related), and six members, the latter considerably less successful. A related strategy is the formation of chalcones (TUB092) or bigger heterocyclic systems on the bridge (e.g. C2, ABI analogues). A more recent strategy has been the reduction of the two-carbon bridge of CA4 to non-isomerizable one-atom

versions, such as aryl ketons (e.g. phenstatins),[197] the one-carbon biaryl isomers of combretastatins (e.g. isocombretastatins),[198,199] and biarylamines such as verubulin in phase II clinical trials (Fig. 10).[200]

Among the less classical variations, the azine buparlisib (BKM120) was initially designed as PI3K inhibitor,[201] currently in phase III clinical trials.[202] The redefinition of buparlisib's mechanism of action, which mainly allocates the cytotoxic effect to its microtubule destabilizing activity rather than to PI3K inhibition, in the context of its promising clinical expectation, further validates tubulin as an enticing target for the design of antitumor drugs with real odds towards clinical use. Compound TH588 was designed as MTH1 inhibitor,[203] BAL27862 was discovered by optimization of high-throughput screening hits,[135] and rigosertib is considered an inhibitor of Ras effector pathways.[204]

T138067 is a synthetic sulfonamide with a pentafluorinated benzene ring. The carbon in *para* position with respect to the sulfone reacts with the thiol group of the cysteine C241β of zone 2,[205] involved in the binding of the trimethoxyphenyl ring in classical ligands. The X-ray structure of T138067 reveals one covalently-bound unit traced outside of the colchicine domain, and a second one binding non-covalently to zones 1-2.[133] Covalent ligands have emerged as an appealing possibility in cancer chemotherapy since they avoid resistance mediated by transport proteins once bound to their targets.[206]

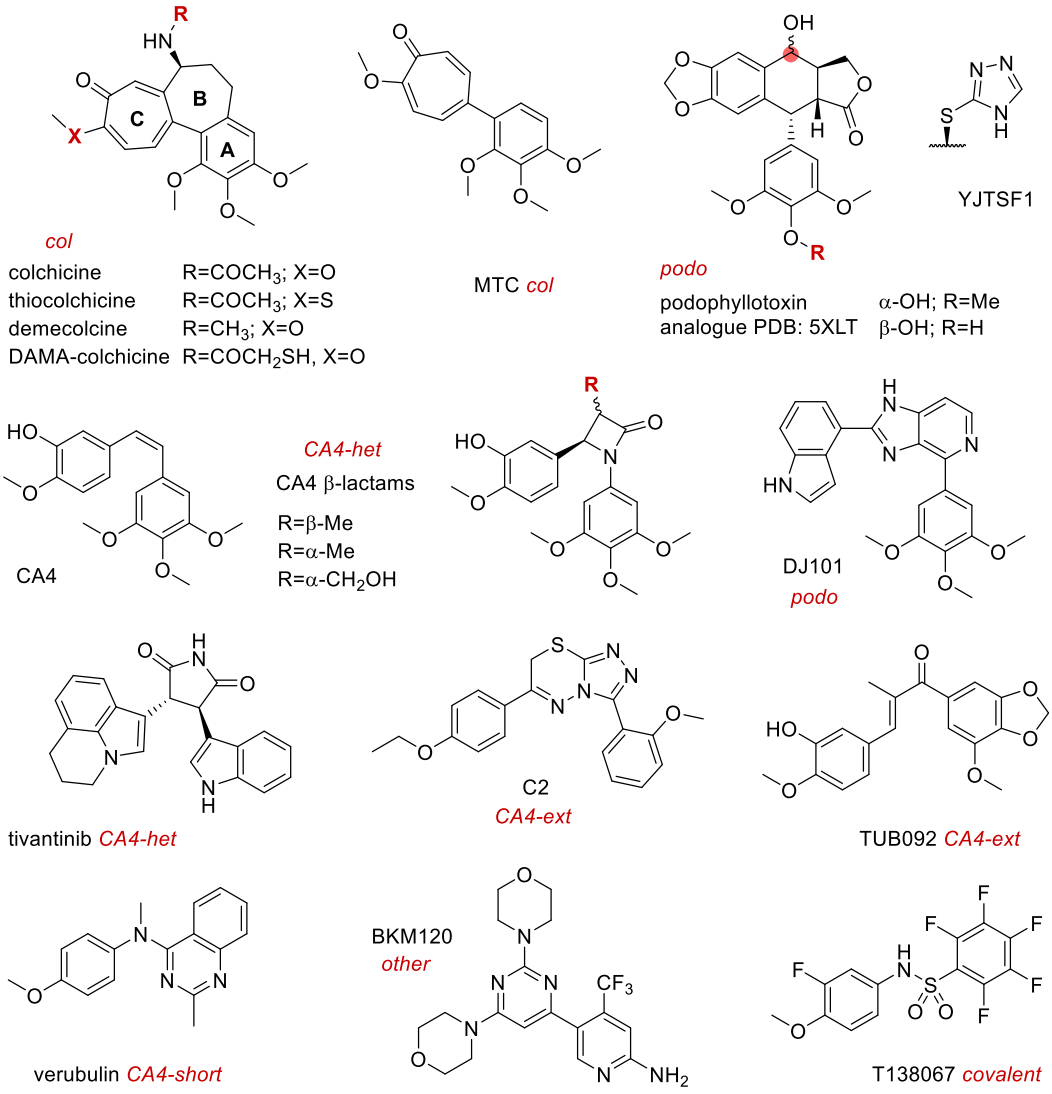

Figure 10. Continued

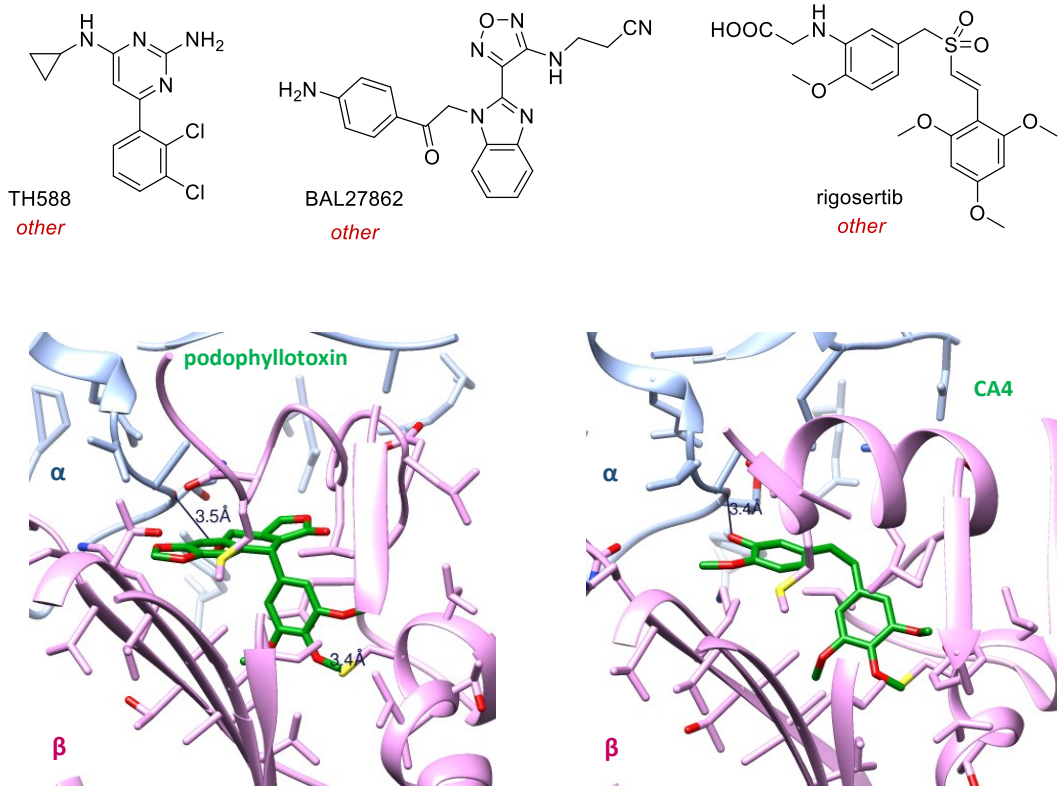

Figure 10. Top. Chemical structures of several compounds that bind to zones 1 and 2 of the colchicine domain. The structural group according to Table 3 is indicated in **red**. **Bottom.** X-ray structures of podophyllotoxin (left; PDB ID: 1SA1)[25] and combretastatin A4 (right; PDB ID: 5LYJ)[152] in complex with tubulin. The α-tubulin is colored in **blue**, the β-tubulin in **pink**, and the ligands in **green**.

B. Ligands that occupy zones 2 and 3

TN16 was the first colchicine site ligand reported to bind to zones 2 and 3 (PDB ID: 3HKD).[133] It competes with colchicine for binding tubulin,[207] but there is just a partial overlapping revealed when superimposed with the colchicine-tubulin complex in the region accommodating the trimethoxyphenyl ring of colchicine (zone 2). Several other ligands with little structural similarity but sharing a similar elongated and flattened conformation have also been shown to bind to zones 2-3 (Fig. 11): the cyclic diones plinabulin and related analogues,[148] and two cyclohexanediones (TUB015 and TUB075),[180] the biaryls MI-181,[147] nocodazole,[148] and MP-HJ-1c,[181] the pterin analogues G2N and G2K,[42] and other more flexible structures such as the quinolinoxyacetamide derivative QA_1[178] and tirbanibulin.[182]

Cyclic diones bind all as the enol tautomers, thus forming a hydrogen bond with glutamate E200β, with the rest of the moieties in a very similar disposition. Analogues of pterins G2N and G2K despite an apparently very different structure, also make akin interactions, with the aminopyridine acting as an equivalent of the enols and the carbamate mimicking the phenyl groups of cyclic diones. The biaryl compounds share a flat disposition by means of conjugation. The different lengths and positions of the bridges between the aryls are in turn translated into different aryl sizes, but they all occupy a very similar region. Tirbanibulin and QA_1 despite their more flexible and different structures, bind in an analogous way, although the first presents an extension directed outside the colchicine domain. Tirbanibulin is an SRC inhibitor whose antitubulin profile has been recently shown.[182] It is currently in phase II clinical trials as an orally bioavailable antitumor drug.

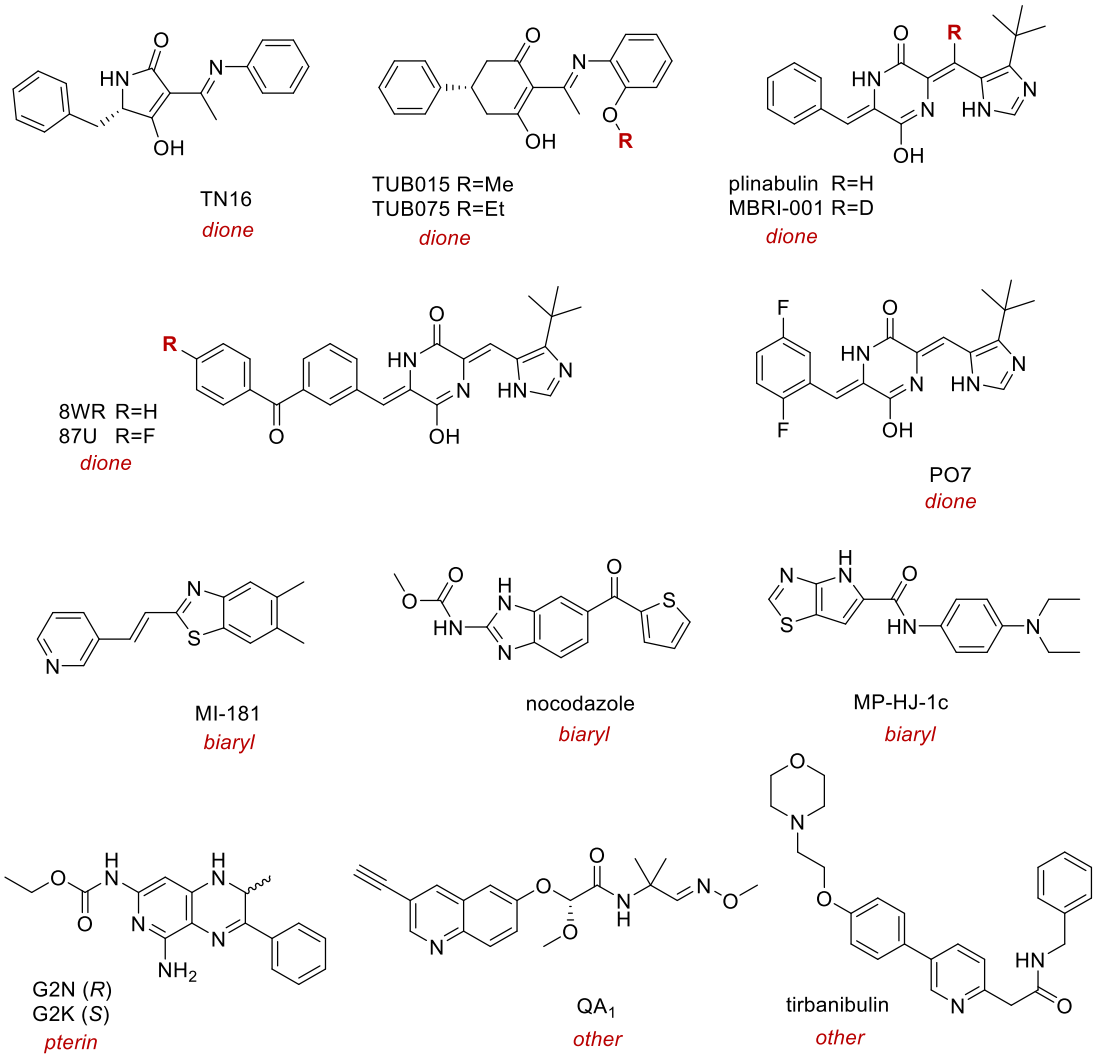

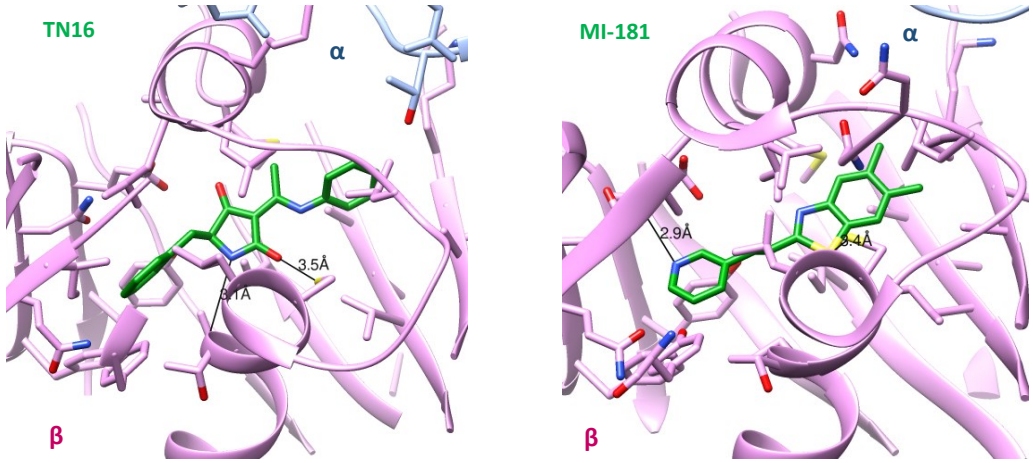

Figure 11. Top. Chemical structures of the compounds that bind to zones 2 and 3 of the colchicine domain. The structural group according to Table 3 is indicated in **red**. **Bottom.** X-ray structures of TN16 (left; PDB ID: 3HKD)[133] and MI-181 (right; PDB ID: 4YJ2)[147] in complex with tubulin. The α-tubulin is colored in **blue**, the β-tubulin in **pink**, and the ligands in **green**.

C. Ligands that occupy zones 1, 2, and 3

There are three compounds that bind to the three zones of the colchicine domain, although partially to at least one of them: ABT-751, MT189, and lexibulin. E7010, renamed ABT-751, is a tricyclic synthetic sulfonamide that emerged in 1992 as a cytotoxic compound (Fig. 12),[208] later described as colchicine site ligand.[209] Its *p*-methoxyphenyl ring is accommodated in zone 1, whereas the pyridylendiamine moiety interacts with zone 2. The phenolic ring goes in zone 3, although there is only a partial occupation.[133] ABT-751 underwent multiple clinical trials for cancer treatment as an orally available drug reaching phase II, either alone or in combination, but did not prove as effective as expected. Many other sulfonamide-based colchicine site ligands have emerged in an attempt to achieve ameliorated bioavailability and improved clinical outcomes.[27] It is the case of A-293620 and its prodrugs A-318315, that presumably bind to zones 1-2.[210]

MT189 binds to the colchicine site in a very similar way to ABT-751, as observed by their structural similarity, the major difference being the replacement of the pyridine by an imidazopyridine ring. It has low aqueous solubility and limited *in vivo* activity.[211] The structure of lexibulin is rather different compared to the other two ligands, but like ABT-751, it shows good oral availability. It broadly occupies zone 3, although partially zones 1 and 2. Its clinical development was suspended after phase II clinical trials.

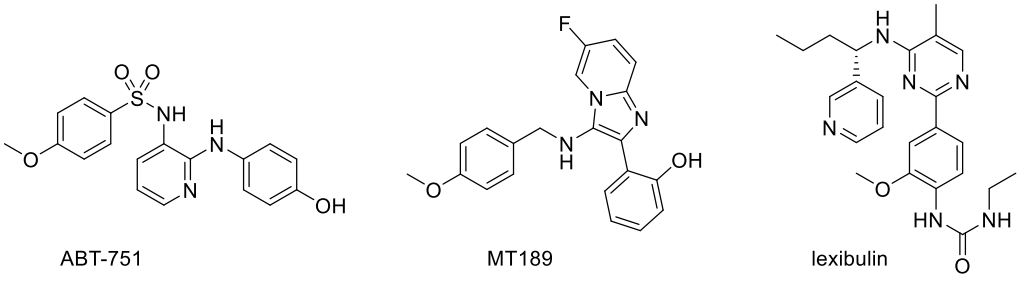

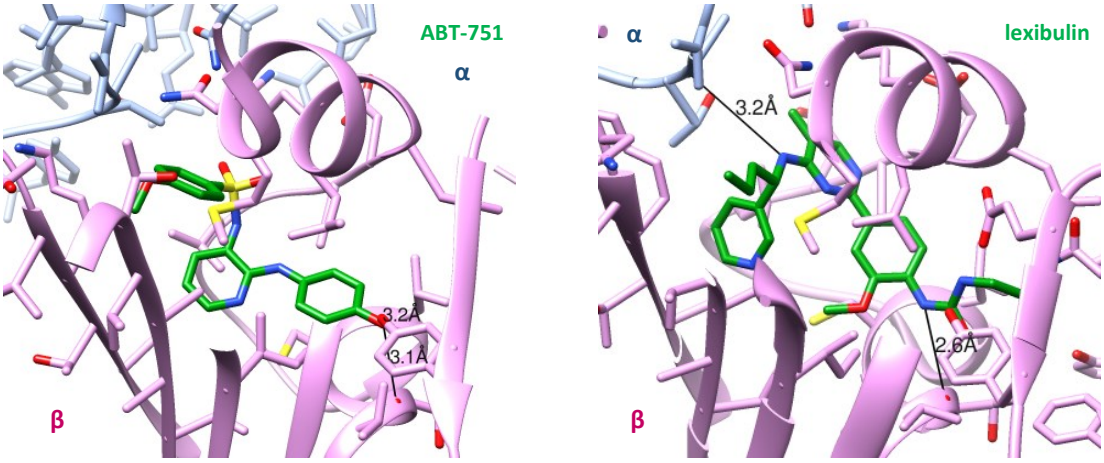

Figure 12. Top. Chemical structures of the compounds that bind to the three zones of the colchicine domain. They interact with zones 1-2-3 although partially with at least one of them. **Bottom.** X-ray structures of ABT-751 (left; PDB ID: 3HKC)[133] and lexibulin (right; PDB ID: 5CA0)[148] in complex with tubulin. The α-tubulin is colored in **blue**, the β-tubulin in **pink**, and the ligands in **green**.

CELL DEATH ROUTINES

Cell death plays a decisive role in ensuring the survival of multicellular organisms and handling homeostasis. Cell death phenomena not only respond to critical damage by eradicating aberrant or injured cells but also participate in healthy embryo development, tissue renewal, or immune homeostasis. Cell demise has been traditionally considered as either programmed (PCD), routinely linked to apoptosis, or circumstantial (ACD), deemed as necrosis. This categorical statement is far from being entirely true since regulation has also been found for a specific subset within necrotic death, called necroptosis.[212] Although some other classifications have been proposed, the Nomenclature Committee on Cell Death (NCCD) established standard criteria: regarding the molecular mechanisms driving to the death condition and the morphological features of the dying cells, cell death falls into three main categories: apoptosis (type I), autophagy (type II), and necrosis (type III).[213–215] Granted, this is a simplistic approach, since there are several other death pathways, although less frequent: pyroptosis, paraptosis, ferroptosis, etc. Responding to the objective of characterizing the cell death mechanism triggered upon treatment with the novel designed molecules in the present work, those three major cell death pathways, type I, II, and III, are briefly reviewed below.

Apoptotic cell death (type I)

The term apoptosis was coined in 1972 by Kerr *et al.* referring to a well-characterized death mechanism that is programmed rather than chaotic and is finely regulated in cells.[216,217] Apoptosis is a cell-specific process that only affects cells meant to die in a coordinated way with no plasma release.[218] Thus, no inflammation response is triggered.

There are many stimuli able to induce apoptotic cell death, which can be mostly initiated either via mitochondrial alterations (intrinsic pathway) or via death receptor ligation (extrinsic pathway). Mitochondria are deemed as the hub that commits a cell to die, either directly by the intrinsic route or as an amplification loop following death receptor engagement.[219] Both pathways converge in the activation of caspase proteases that eventually trigger the apoptotic phenotype. Besides these two signaling pathways, some authors have included the inflammasome-dependent route and the so-called PIDDosome pathway as alternative cues for apoptosis. Nevertheless, they are generally excluded from the apoptosis concept and categorized as different forms of regulated cell death. The inflammasome pathway or pyroptosis is triggered upon activation of caspases 1 and 5 that typically arises mostly in inflammatory cells in response to infection and eventually favors a lytic death.[220] On the other hand, the PIDDosome pathway occurs as a consequence of caspase 2 activation due to heat shock or DNA damage.[221]

There is a series of hallmark features that characterize apoptotic cells.[222] These cells show chromatin condensation, also known as pyknosis, together with cell shrinkage and dismantling of the nuclear envelope. The condensed DNA material is subsequently fragmented in a process termed karyorrhexis.[223] The characteristic cleavage pattern (DNA laddering) allows to detect apoptosis induction by electrophoresis on an agarose gel.[224] The blebbing of the plasmatic membrane is unequivocally associated with apoptosis. Cells are transformed into apoptotic bodies that are eventually engulfed by phagocytic cells in a process known as efferocytosis, without releasing danger-associated molecular patterns (DAMPs).[225] Thus, there is barely any affectation of neighboring cells. Phagocytosis is prompted in response to “find-me” signals and “eat-me” signals, acting as labels to assist in the guidance and recognition between phagocytes and apoptotic bodies.

The release of soluble lysophosphatidylcholine (LPC) functions as a "find-me" cue.[226] The prime example of an "eat-me" signal is the selective exposure of phosphatidylserine (PtdSer) at the surface of apoptotic cells. In healthy cells, phosphatidylserine is exposed in the inner leaflet of the plasma membrane. As a consequence of the apoptotic machinery, it flips its orientation inside out towards the extracellular space as a claim to be eaten. This feature is commonly studied by flow cytometry as an apoptotic marker using labeled annexin-V protein that binds to the outer PtdSer in a calcium-dependent manner.[227] Failed or dysfunctional phagocytosis of apoptotic corpses winds up in secondary necrosis (also known as late apoptosis) due to the loss of membrane integrity and pouring of the intracellular content.

The nuclear events that are executed following damage stimuli rely on caspase activation, the key players of the apoptotic response.[228] Human caspases are a group of twelve cysteine-dependent endoproteases that are constitutively present in the cytosol as inactive zymogens.[229] The activation occurs by dimerization and/or proteolytic cleavage, giving rise to the active forms that in turn specifically cleave multiple intracellular substrates after aspartate residues. Apoptotic caspases are usually classified into initiator (caspases 8, 9, and 10) or effector (caspases 3, 6, and 7).[230] Beyond apoptotic caspases, there are some others related to the cell cycle (caspase 2), cell differentiation (caspase 14), or caspases that play distinct roles in inflammation processes (caspases 1, 4, and 5).[231] Both initiator and effector apoptotic caspases consist of a variable in length N-terminal domain and a catalytic domain, the latter with a large subunit (p20) towards the N-terminal region and a small subunit (p10). Initiator caspases contain an additional domain at the N-terminus: CARD (caspase-associated recruitment domain) for caspase 9, and DED (death effector domain) for caspases 8 and 10. Monomeric initiator procaspases are self-activated by close spatial proximity when enlisted in recruitment platforms assembled with adaptor molecules that also harbor death fold domains (CARD or DED).[232] Activation is triggered upon dimerization and a subsequent conformational change, leading to the exposure of catalytic sites.[233] In contrast, effector caspases exist as dimeric zymogens that are activated by upstream initiator caspases after cleavage between the larger and the small subunits, turning into an active tetramer (two large and two small subunits).[234]

A. Mitochondria-mediated apoptosis (intrinsic pathway)

Cells have evolved apoptosis as the logical response to damage that, in the case of the intrinsic pathway, may be ER stress, growth-factor deprivation, oxidative stress, impairing in DNA repair, or DNA damage, to name a few.[235] This route occurs as a consequence of mitochondrial outer membrane permeabilization (MOMP), followed by the irreversible leakage of soluble proapoptotic factors from the mitochondria to the cytosol, which initiates the caspase cascade.[236] Mitochondrial integrity is tightly governed by the Bcl-2 protein family members clustered in three functional subgroups.[237,238] Two out of those three regulator types are multidomain proteins, showing either prosurvival (Bcl-2, Bcl-xL, Mcl-1, Bcl-w) or proapoptotic roles (Bax, Bak, Bok). In regular conditions, Bcl-2 and Bcl-xL ensure the integrity of the mitochondrial membrane by hijacking Bax and Bak into heterodimers, what prevent them from piercing the mitochondrial outer membrane.[239] After an apoptotic stimulus, the cramped equilibrium between proapoptotic and prosurvival cues gets imbalance, leading to the attainment of MOMP that commits the cell to die.[240] The third group corresponds to BH3-only domain apoptosis initiators (Bid, Bad, Bim, Bik, Noxa, Puma) able to activate proapoptotic proteins and/or inhibit prosurvival ones.[239] On the one hand, Bid, Bim, and Puma activate Bax and Bak.[241] On the other hand, Noxa and Bad (also referred to as sensitizers) inhibit Bcl-2, Mcl-1, and Bcl-xL by mutual sequestration.[242]

Bak is usually found in the mitochondria, whereas Bax is prominently cytosolic, but they freely commute back and forth. Released Bax and Bak are able to assemble into oligomeric structures that embed into the mitochondrial membrane creating leaking channels by the merge of both leaflets. The loss of mitochondrial integrity eases the release of cytochrome c from the intermembrane mitochondrial space to the cytosol to activate the caspase machinery (Fig. 13).[243] Several proteins translocate to the cytosol at the same time as cytochrome c, namely Smac/Diablo, Omi/HtrA2, and ARTS/Sept4.[244]

The activation of the initiator caspase that launches intrinsic apoptosis (caspase 9) is assisted by the recruitment platform termed apoptosome.[245] The apoptosome is a wheel-shaped heptameric complex consisting of a core with seven units of the cytosolic ATPase Apaf-1, which binds cytochrome c at the external edges (Fig. 13). The nucleotide exchange activity of Apaf-1 is switched on after cytochrome c binding, which firstly induces the hydrolysis of the dATP cofactor embedded in Apaf-1. The energy provided in this hydrolysis is required so that the inactive monomeric Apaf-1-dADP/ADP can undergo a conformational change turning into the active state, binding exogenous dATP/ATP once again. The formation of the oligomeric structure subsequently follows it.[246]

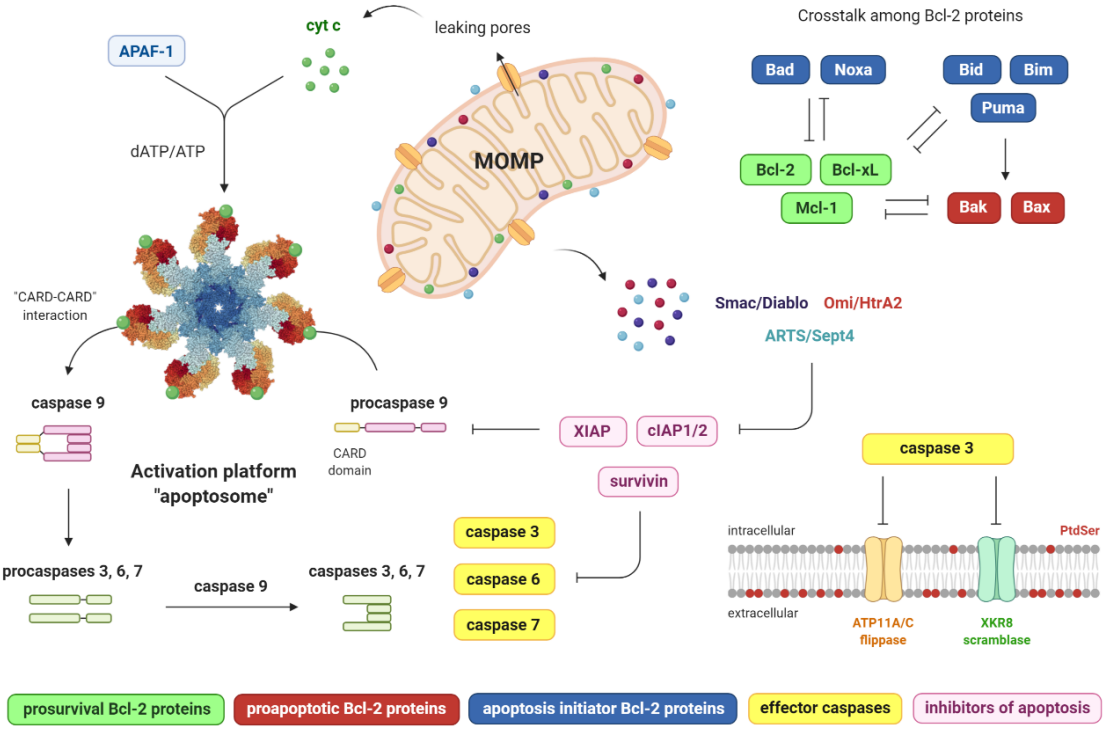

Figure 13. Intrinsic apoptotic pathway. Bcl-2 family proteins dictate cell fate by controlling the induction of mitochondria-dependent apoptosis. This family encompasses prosurvival (Bcl-2, Bcl-xL, Mcl1), proapoptotic proteins (Bax, Bak), and apoptosis initiators (Bad, Bid, Bim, Noxa, Puma). The sensitizer proteins Bad and Noxa bind to and inhibit prosurvival ones, which sequester apoptosis initiators and proapoptotic proteins into inactivating dimers. The imbalance between pro and antiapoptotic cues culminates in MOMP due to the formation of mitochondrial pores by Bax/Bak oligomers. MOMP results in the leakage of cytochrome c and antagonists of IAPs (Smac, Omi, ARTS). Cytochrome c and Apaf-1 assemble into a heptameric complex termed apoptosome that functions as a caspase recruitment platform. The recruitment of the initiator procaspase 9 via CARD domains leads to its self-activation induced by proximity. Once catalytically competent, caspase 9 cleaves and hence activates effector caspases 3, 6, and 7. The exposure of PtdSer at the outer leaflet of the membrane ("eat-me" signal) is mediated by the caspase 3-dependent inactivation of ATP11A/C flipasse and XKR8 scramblase.

Apaf-1 operates as an adaptor molecule harboring a CARD domain.[247] The activation of procaspase 9 into the active homodimer is induced by proximity when recruited to the apoptosome by CARD-CARD interactions.[248] Caspase 9 may afterward catalytically cleave itself, although it is not a compulsory requirement for activation.[249] The cleavage is involved in the exposure of a binding site for the inhibitor of apoptosis XIAP, therefore serving as a regulatory mechanism. It is also related to the release of caspase 9 from the apoptosome since cleaved caspase 9 shows lower affinity for the apoptosome as well as decreased cleaving activity. Indeed, once dissociated, it cannot be rebound.[250–252] Dimeric caspase 9, preferentially the one bound to the apoptosome, activates downstream caspases 3, 6, and 7 by proteolytic cleavage, therefore executing apoptosis. Although all these three effector caspases perform a cascade of cleaving events, caspase 3 is widely deemed as the main hub for the commitment of nuclear alterations. Active caspase 3 elicits the inactivation of ATP11A and ATP11C flippases that in healthy cells confine PtdSer to the inner membrane leaflet.[253] At the same time the activation of XKR8 scramblase is also triggered by caspase 3, promoting PtdSer translocation to the outer leaflet.[254,255]

B. Death receptor-mediated apoptosis (extrinsic pathway)

In general terms, extrinsic apoptosis ensues when cells face an extracellular threat. It is mediated by the so-called death receptors, belonging to the TNF receptor superfamily.[256–258] These proteins are identified as type I transmembrane molecules, mostly prearranged as trimers embedded in the plasma membrane that transduce extracellular stimulation into caspase activation. They contain an extracellular domain enriched in cysteine residues (CRD) that defines the ligand specificity, and a cytosolic death domain (DD) of around 80 aminoacids to recruit adaptor molecules in order to constitute the caspase activating platform.[259] TNF receptors are usually divided according to the adaptor molecule recruited by the DD, falling into two groups. The first subset comprises Fas/CD95/Apo1, TRAIL-R1/DR4, and TRAIL-R2/DR5, that directly activate apoptosis upon interaction with their cognate ligands: Fas ligand (FasL) and TRAIL, respectively (Fig. 14). Most death ligands are primarily expressed as type II transmembrane trimers that preferentially bind to the receptors when still anchored to the membrane. True enough, they can be occasionally found as soluble cytokines after cleavage by proteases or directly produced by alternative splicing, thus activating death receptors, although less efficiently.[260] The adaptor molecule of these death receptors is FADD, which is indispensable for the activation of the initiator caspases 8 and 10.[261] FADD exhibits two domains: a death domain (DD) and a death effector domain (DED). Upon ligation of Fas and TRAIL-R, cytosolic FADD is recruited to the intracellular region of the receptor by DD-DD homotypic interactions. In turn, the presence of the DED in FADD enables the recruiting of procaspases 8 and 10, or c-FLIP, via their DED motifs.

Death receptors experience a conformational change in the intracellular domain induced by ligation, that results in the oligomerization thereof, followed by the recruitment of FADD. The altogether docking of Fas (or TRAIL-R), FADD, and procaspase 8 or 10 at the inner leaflet constitutes the so-called death-inducing signaling complex (DISC).[262] DISC is the caspase recruitment platform for activating initiator procaspases 8 and 10, serving the role of the apoptosome but in the extrinsic pathway. Alike caspase 9, initiator caspases 8 and 10 are self-activated by proximity when the local concentration increases in the recruitment platform DISC.[263] Monomeric zymogens turn into catalytically active caspases 8 and 10 by dimerization. Dimeric forms may be additionally processed by cleavage between the large and small subunits. Self-cleavage regulates the stability, although it is not indispensable for being catalytically active.[263]

Caspase 8 can either form homodimers or heterodimers with its inactive homolog c-FLIP, which serves as a regulation mechanism blocking the boost of the apoptotic cascade, putatively by preventing the processing and/or competing with the caspase 8 homodimer for the interaction at the DISC.[264] Activation of caspase 8 results in the subsequent cleavage of effector caspases 3, 6, and 7 into active enzymes. Moreover, ligation of TRAIL-R and Fas may induce the dissociation of FADD, caspase 8 and c-FLIP from the receptor-bound DISC, giving rise to the cytosolic complex II or secondary complex (Fig. 14).[265,266] Altogether, death receptors can also be internalized by clathrin-mediated endocytosis to assembly the DISC in cytosolic compartments.[267,268] Both cytosolic complexes are meant to boost the activation of effector caspase 8, although the role of TRAIL-R endocytosis remains controversial.

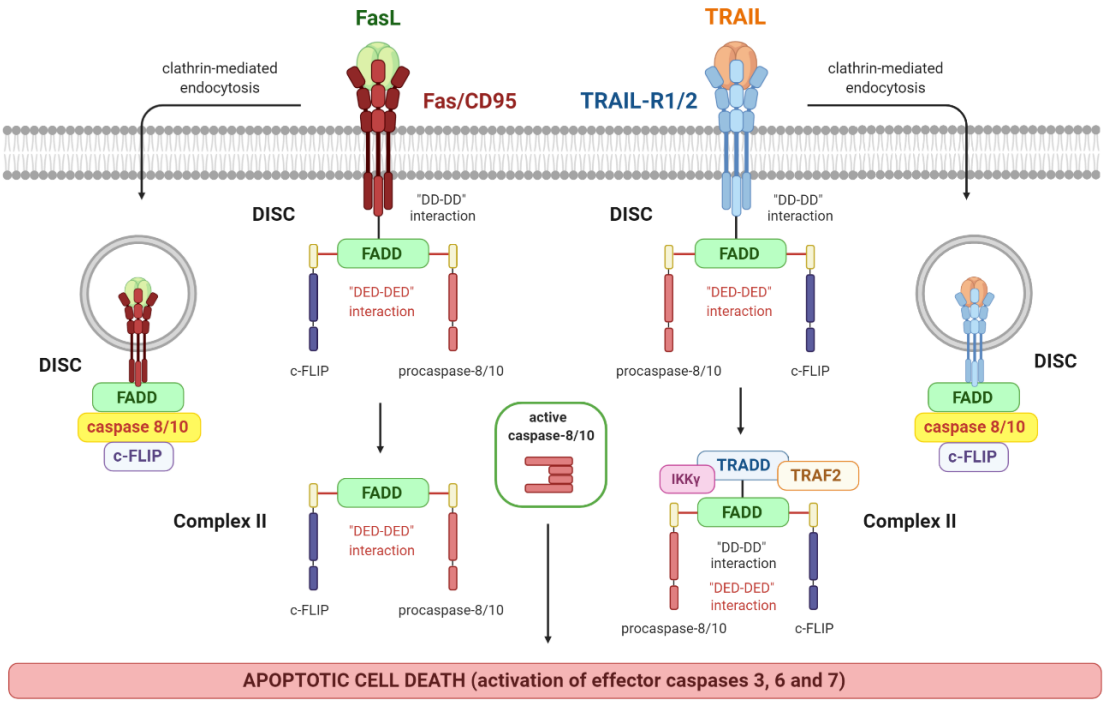

Figure 14. Engagement of Fas and TRAIL-R1/2. The interaction of these death receptors with their cognate ligands induces the oligomerization and further recruitment of FADD adaptor. It interacts with the cytosolic tails of the receptor via DD interactions. The DED motif endows FADD with the ability to interact with DED-containing procaspases 8 and 10, as well as with c-FLIP. The altogether ensemble of these components forms the complex DISC. Upon Fas and TRAIL-R ligation, a secondary cytosolic complex may stem from the DISC, composed of FADD, procaspase 8, and c-FLIP in the case of FasL-dependent signaling. This secondary complex functions as an amplification platform for caspase activation. The cytosolic complex that arises from the membrane-bound TRAIL-R-DISC is formed by FADD, caspase 8, TRAF2, and IKKγ (NEMO). Aside from the membrane-bound complex and the cytosolic complex, the efficient activation of initiator caspases 8 and 10 arises from the DISC found in endosomes after clathrin-mediated endocytosis of Fas and TRAIL-R1/2.

The second subset of death receptors gathers TNFR1, DR3/Apo3, and DR6. Engagement of TNFR1 by its ligand TNF-α results in the recruitment of complex I. It may indirectly induce apoptosis, necroptosis, or even cell survival. Besides, it is also involved in inflammation responses and cytokine production. Less is known about DR3 and DR6. TNFR1 is mirrored by TNF-α, stimulating the DD-mediated recruitment of the adaptor molecule TRADD in the cytosol, what may end in either cell demise or cell survival (Fig. 15).[269,270]

When bound to TNFR1, TNF-α induces a conformational rearrangement of the receptor enabling the docking of the cytosolic complex I, devoid in initiator caspases and FADD.[271] TNFR1 recruits TRADD and the DD-containing kinase RIPK1 subsequently joins the cluster. Complex I is fulfilled after assembly of cIAP1/2 and TRAF2/5.[272,273] On the one hand, RIPK1 is modified with poly-ubiquitin chains firstly by the E3 ubiquitin ligases cIAP1 and cIAP2, then by LUBAC.[274–276] Ubiquitinated RIPK1 induces the assembly of TAB2, TAB3 and TAK1, therefore activating survival signaling pathways mediated by JNK, p38, and Erk.[277] RIPK1 also recruits and bring together the IKK complex, formed by IKKα, IKKβ, and IKKγ (NEMO). [278] This complex induces the phosphorylation of the NF-κB inhibitor IκBα,[279] so that free NF-κB translocates into the nucleus promoting the transcription of antiapoptotic proteins (e.g. Bcl-xL, XIAP, cIAPs and c-FLIP).[280] Therefore, both the activation of JNK, p38, and Erk signaling pathways, as well as the IKK-dependent activation of NF-κB play a protective and prosurvival role. Ligation of TNFR1 may also prompt different types of cell death, by either formation of complex IIa or IIb as follows.[271] Alike Fas and TRAIL-R, TNFR1 may be internalized in clathrin-coated endosomes and eventually recruits FADD, TRADD and caspase 8.[281]

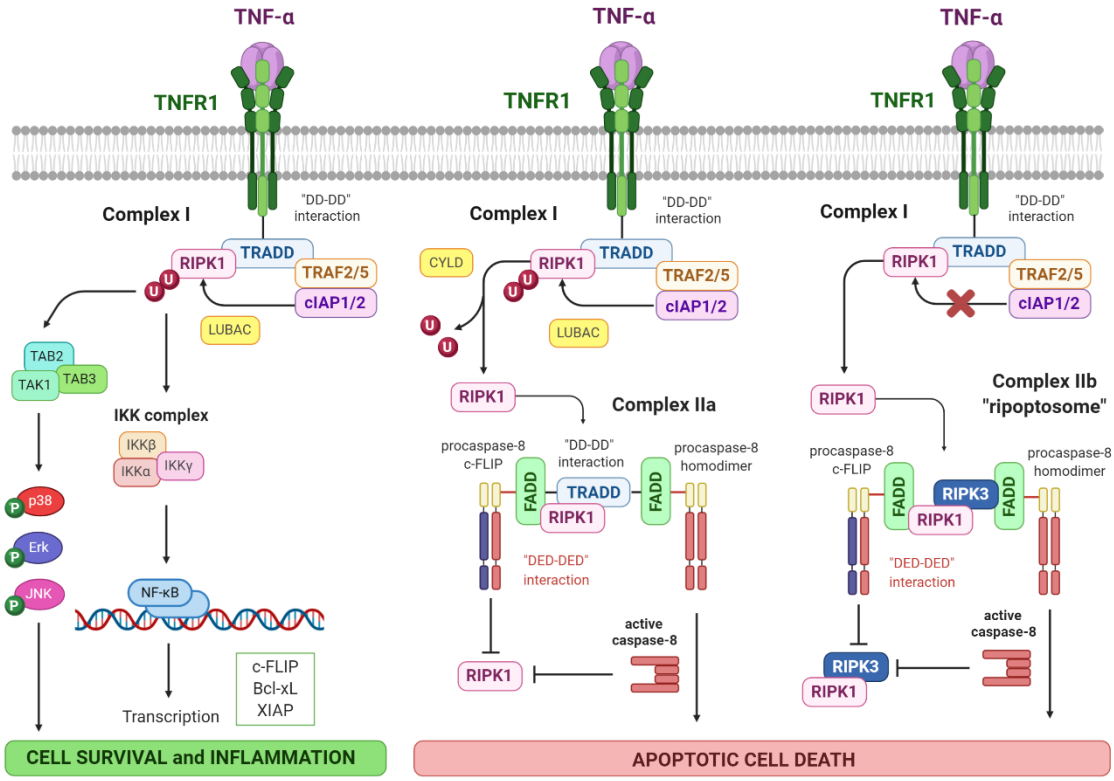

Figure 15. TNFR1 signaling pathway. Interaction of TNFR1 with its cognate ligand TNF-α induces the recruitment of the TRADD adaptor to the cytosolic tail of the receptor, both harboring a DD interacting domain. The initial membrane-bound complex I is constructed by TNFR1, TRADD, TRAF2/5, RIPK1, and cIAP1/2. The latter, together with LUBAC, induces the ubiquitination of RIPK1, which eventually mediates cell survival responses via JNK and NF-κB signaling pathways. If inefficient ubiquitination of RIPK1, it disassembles from the membrane complex and constructs two cytosolic molecular complexes lacking TNFR1: complex IIa (upon CYLD-mediated RIPK1 deubiquitination) and complex IIb or ripoptosome (when ubiquitinating systems are compromised). These two distinct complexes boost the activation of initiator caspases 8 and 10, which inactivate both RIPK1 and RIPK3, thus preventing necroptosis, as discussed later.

The ubiquitination state of RIPK1 is crucial for the cell outcome upon TNFR1 ligation, functioning as a switch towards survival or cell death (Fig. 15).[282–285] In regular conditions, modified RIPK1 with multiple ubiquitin chains is assembled in complex I. The loss of ubiquitin residues mainly mediated by the deubiquitinating CYLD enzyme results in the destabilization of complex I and renders the disjunction of RIPK1, now free to constitute complex IIa.[286] This secondary complex is formed by TRADD, FADD, procaspase 8 homodimer, and procaspase 8/c-FLIP heterodimer. After inactivation of RIPK1 by the c-FLIP containing heterodimer, procaspase 8 is self-activated and mobilizes the apoptotic machinery via proteolytic activation of effector caspases.

The depletion of cIAP1/2 by any means triggers the assembly of complex IIb or ripoptosome. cIAPs do not transfer ubiquitin residues to RIPK1 in the first place, which disengages from complex I and induces the assembly of cytosolic TRADD-independent complex IIb. Besides RIPK1, it contains FADD, procaspase 8 homodimer, procaspase 8/c-FLIP heterodimer, and RIPK3. Similarly to complex IIa, proteolytic inactivation of RIPK1 within complex IIb (so does RIPK3) is required so that active caspase 8 can induce downstream effector caspases. This is triggered by the procaspase 8/c-FLIP heterodimer or the mature caspase 8.

C. Crosstalk between intrinsic and extrinsic pathways

In some cell types, categorized as type I (e.g. lymphocytes), the onset of the extrinsic pathway is sufficient to provoke cell demise by proteolytic cleavage of effector caspases 3, 6, and 7 due to a sufficient activation of caspase 8.[287] However, type II cells (e.g. hepatocytes) require a pipeline activation of the intrinsic pathway after death receptor ligation, putatively due to reduced levels of DISC. The BH3-only protein Bid is truncated by the mature form of caspases 8 and 10 into tBid. This cleaved protein translocates to the mitochondria, enabling Bax and Bak to form oligomers that stack into the mitochondrial outer membrane creating leaking channels.[288–290] Therefore, caspase 8 is able to induce MOMP, switching on the intrinsic pathway as a death amplification loop. Actually, the crosstalk with the mitochondria occurs in both type I and type II cells. The difference being that overexpression of prosurvival proteins Bcl-2 and Bcl-xL prevents type II cells from dying after extrinsic pathway activation, but not type I cells.[291] This supporting signaling appears to be crucial to induce apoptosis in type II cells, whereas in type I cells, it functions as an amplification loop.

D. Regulation by IAPs and antagonists of IAPs

Apoptosis procurement is tightly modulated. It additionally shows negative regulation by a series of proteins allocated to the inhibitors of apoptosis family (IAPs), which encompasses XIAP, cIAP1, cIAP2, NIAP, survivin, Bruce (also referred to as Apollon), ML-IAP and ILP-2.[292] As the name implies, proteins belonging to this family block the catalytic activity of caspases, thus halting the apoptotic machinery.[293] IAPs have BIR domains involved in the binding and inhibition of caspase enzymes.[294] Most IAPs additionally harbor a RING domain with E3 ubiquitin ligase activity, thus able to label the antagonist of apoptosis Smac and caspases for subsequent degradation via the proteasome.[295] Yet, XIAP is the only member capable of directly inhibiting caspases, besides via its ubiquitin ligase activity that marks caspases for their later degradation.[296] It binds caspase 9 preventing its activation and subsequent cleavage of caspase 3.[297] XIAP additionally inhibits the catalytic activity of caspases 3 and 7 directly. IAPs other than XIAP majorly exert their antiapoptotic activity by ubiquitination of many substrates, among them, caspases.[298]

There are antagonists of those inhibitors of apoptosis, closely related to the mitochondria. Smac/Diablo and Omi/HtrA2 are early released from the intermembrane space together with cytochrome c by the leaking channels generated during mitochondrial outer membrane alteration.[299,300] Smac and Omi block the XIAP-mediated inhibition of caspases 3 and 9 by directly binding to XIAP.[301] Besides, while Smac induces self-ubiquitination of IAPs, such as cIAP1/2, the serine protease activity of Omi directly triggers the irreversible degradation of cIAP1/2 and XIAP.[302] ARTS/Sept4 is located in the mitochondrial outer membrane, therefore able to execute its proapoptotic role regardless of the consecution of MOMP. Even so, translocation of ARTS to the cytosol is achieved almost immediately after the apoptotic stimulus.[303] It is able to bind and degrade XIAP and the prosurvival protein Bcl-2.[304]

E. Nuclear events and other effects downstream of caspases

The caspase machinery operates as a bridge linking extracellular or intracellular damage stimuli with a series of nuclear events, which arise in late stages of the apoptotic signaling. Once active, caspases cleave multiple intracellular substrates - more than 1000 proteins.[305] The three effector caspases have been proposed to play redundant roles, although some might be distinct, such as the role of caspase 7 in cell detachment.[306] The cleavage of cellular structures results in the shrinkage of organelles and the rounding of the cell. The characteristic rounded shape of apoptotic cells stems from gelsolin, PAK2, and ROCK cleavage, which triggers cytoskeletal alterations and induces aberrant actin rearrangement.[307,308] The caspase 7-mediated cleavage of FAK gives rise to loss of focal adhesions and retraction from the tissue where the cell is embedded.[309] The cleavage of lamins A, B, and C leads to nuclear envelope disintegration. The cleaved form of p75, a component of the electron transport chain complex I, disturbs the mitochondrial potential and diminishes ATP production.[310]

DNA fragmentation is linked to chromatin condensation. Caspase 3 activates the kinase MST1, which phosphorylates histones H2B and H2AX, leading to chromatin condensation.[311,312] Multiple nucleases participate in DNA fragmentation. The cleavage of ICAD by caspase 3 releases CAD from the CAD-ICAD inhibitory complex. Free CAD therefore gets activated and cleaves double-stranded DNA, giving rise to 50-300 kb DNA fragments that are further processed by both exo and endonucleases into 200 base pairs fragments.[313] Two assisting nucleases are endonuclease G and AIF, released from the mitochondria for the final steps of the impending apoptotic outcome.[314,315] These two enzymes work in a caspase-independent manner, in contrast to the caspase-dependent role of CAD. The ultimate effector of apoptotic cues is PARP, cleaved, and hence inactivated by effector caspases. PARP cleavage prevents ATP depletion, which is a cue for necroptosis induction (a regulated form of type III cell death). PARP cleavage is therefore a useful tool to detect apoptosis induction by immunoblotting.

Autophagy and autophagy-induced cell death (type II)

The autophagy term refers to a catabolic “self-eating” process aimed to remove unwanted cellular components by lysosomal degradation.[316] Cells degrade via autophagy damaged or dysfunctional organelles, altered proteins, or long-lived components that either require a turnover or are no longer useful.[317] Autophagy is primarily involved in survival and adaptation when cells encounter stressful environments such as starvation, energy depletion, or ER stress. It is crucial for maintaining homeostasis and for recycling aminoacids and other nutrients that can be later reused as building blocks for macromolecules or as sources of energy gained as ATP.[318] This process also functions as a quality control mechanism, especially in neurons, and participates in tissue development.

Autophagy encompasses three subsets: macroautophagy, microautophagy,[319] and chaperone-mediated autophagy,[320] that share lysosome-conducted degradation. Macroautophagy is the major form, hereafter alluded to as autophagy. First thought as non-specific, autophagy can actually selectively mediate the degradation of intracellular or extracellular structures.[321] Therefore, macroautophagy is an "umbrella term" that gathers many forms of autophagy, named after what is in fact processed (e.g. mitophagy hints mitochondria degradation). Nevertheless, those forms share the signaling pathway and regulation mechanism regardless of the cargo nature.

A. Autophagosome formation

The autophagy-mediated waste clearance eventually stems from the fusion between a lysosome and a double-membrane vesicle known as autophagosome that encloses the damaged cargo. Autophagosomes move using microtubules as traffic tracks towards lysosome-enriched MTOCs whereby their contents are delivered into lysosomes for breakdown, forming the single-membrane autolysosome. This is a very dynamic process; autophagosomes are rapidly formed and fused within less than 10 minutes.[322] The whole multi-step process, including initiation, nucleation, elongation, maturation, and fusion, is tightly regulated by proteins belonging to the Atg family that stands for autophagy-related genes (Fig. 16).[323]

The initiation step occurs at multiple phagophore assembly sites (PAS) with the formation of a C-shaped isolation membrane termed preautophagosome or phagophore.[324] This double-membrane fragment buds off from regions of the ER enriched in DFCP1 protein and PI3P (omegasome) to which different-origin membrane pieces are recruited to form the initial hijacking structure.[325,326] There are two molecular complexes that control the first steps of autophagy: ULK and PI3K complexes.[327] Autophagy initiation is assisted by the ULK complex, which is the most upstream hub and comprises the kinase ULK1, Atg13, FIP200, and Atg101 (Fig. 16).[328] This complex is negatively regulated by mTORC1,[329] which dissociates upon an autophagy stimulus, allowing the ULK complex to anchor to PAS, where multiple Atg proteins will cluster. Active ULK1 phosphorylates Atg13, FIP200, and itself once translocated to the PAS, hence launching the nucleation step of multiple Atg protein and lipids to generate the isolation membrane.

Additionally, ULK1 mediates the phosphorylation-dependent activation of Beclin-1, which is part of the second regulatory complex, the class III PI3K complex that participates in the nucleation step at the PAS. The proteins Vps15/p150, Atg14L, and Vps34 partner Beclin-1, with Vps34 harboring the PI3 kinase activity to produce PI3P.[330] The increasing levels of PI3P at the omegasome recruit downstream effectors such as DFCP1 and WIPI proteins (WIPI1/2), and support the final closure into the mature vesicle. WIPI proteins are found at the isolation membrane that stems from the omegasome and are involved in inducing curvature and in the recruitment of further players such as p62/SQSTM1 or NBR1.[331]

There are two ubiquitin-like conjugation systems involved in the wrapping of the isolation membrane to form the mature autophagosome.[332] The first one relies on Atg7 and Atg10 that bring together a triple complex composed of Atg5/12/16L (Fig. 16). A crucial step in the formation of the autophagosome is the lipidation of LC3. Cytosolic pro-LC3 is first cleaved by Atg4 into LC3-I. A subsequent lipidation step by incorporation of phosphatidylethanolamine (PE) is conducted by the second ubiquitin-like conjugation system formed by Atg7 and Atg3, assisted in turn by the Atg5/12/16L complex.[333] Lipidated LC3 (LC3-II) is found embedded in both autophagosome leaflets and participates in the recruitment of

specific cargoes, by tethering autophagy receptors to which those cargoes are bound to.[334] The cargo-specific degradation depends on the recognition between ubiquitin binding domains (UBD) present in autophagy receptors (e.g. p62), which will all be degraded in the autolysosome, and the ubiquitinated target structure to be embraced by the closing double-membrane.[334,335] Those autophagy receptors are in turn anchored to LC3 by LIR motifs. The elongation of the double-membrane is achieved by recruitment of lipids, mediated by Atg9.[336] The autophagosome then fuses with the lysosome, assisted by SNARE proteins. Once encountered, the outer leaflet of the autophagosome membrane docks with that of the lysosome, which degrades both the inner leaflet and the enclosed content by lysosomal hydrolases (e.g. cathepsin). This degradative process relies on the acidification of the autolysosome lumen owing to the V-type ATPase. The resulting building blocks return to the cytoplasm by membrane permeases.

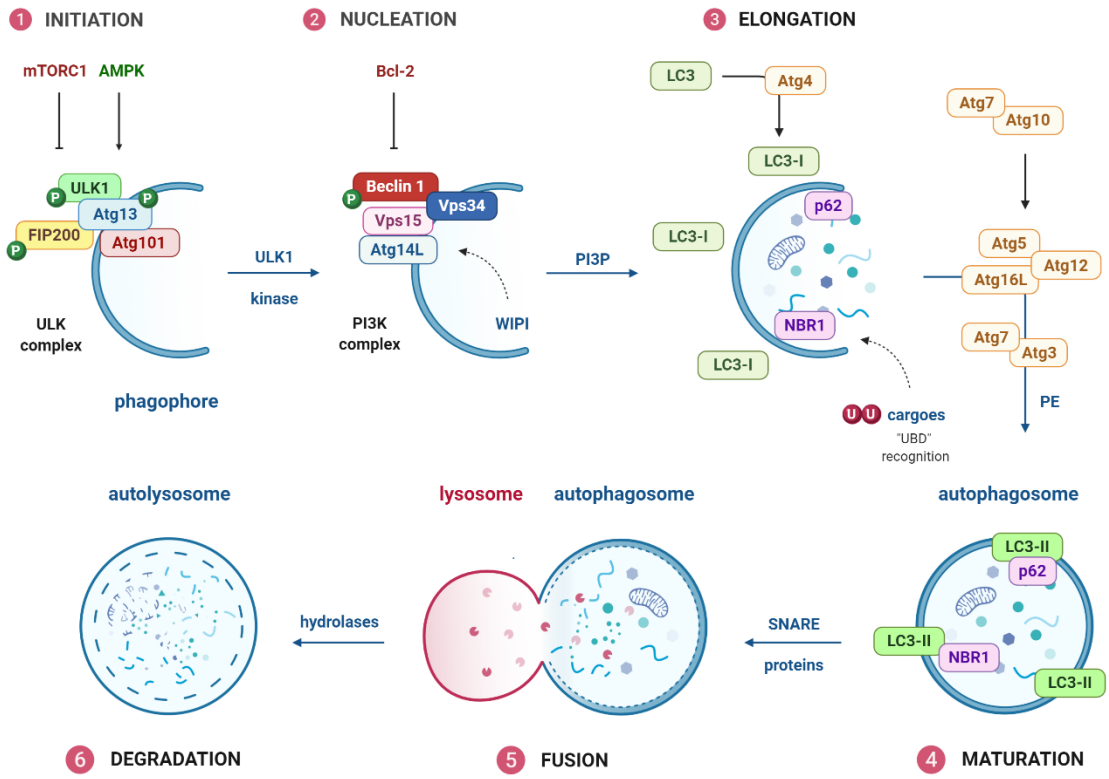

Figure 16. Autophagy signaling pathway. The initiation step is conducted by the ULK complex (ULK1, FIP200, Atg13, and Atg101), sensitive to the nutrient status of the cell. In healthy metabolic conditions, mTORC1 prevents ULK activation by phosphorylation of ULK1 and Atg13. Upon ATP depletion, AMPK turns on autophagy directly by ULK1 activation and indirectly by mTORC1 inhibition. ULK1 promotes the activation of the class III PI3K complex, resulting in increased levels of PI3P. There are two ubiquitin-like protein conjugation systems that participate in the elongation and maturation steps. Atg7 and Atg10 assist the conjugation of Atg5/12/16L, which stabilizes the phagophore. Atg4 mediates the cleavage of proLC3 to cytosolic LC3-I. Its later lipidation is mediated by Atg7, Atg3, and Atg5/12/16L, and results in the formation of LC3-PE or LC3-II, involved in the delivery of autophagosomes to lysosomes. The latter step is the fusion into an autolysosome, which degrades the engulfed cargoes. Selective autophagy involves the incorporation of specific ubiquitin-containing substrates into the autophagosome by autophagy receptors, such as p62 or NBR1, anchored to LC3.

B. Autophagic cell death and crosstalk with other death routines

The energy status is a key regulator of the cell outcome. Thus, low ATP levels induce autophagy by activating AMPK, which is a sensor of bioenergetics that positively regulates the ULK complex.[337] The other pathway that monitors the nutritional status of the cells is mediated by mTORC1, which prevents ULK activation. Likewise, low energy environments prevent apoptosis to be triggered, since the apoptotic cascade relies on energy consumption. There is a fine crosstalk between autophagy and other types of regulated cell death, such as apoptosis.[338,339] Proautophagy mediators are among the many substrates cleaved by active caspases, as it is the case of Beclin-1, cleaved by caspases 3 and 8.[340] Prosurvival proteins from the Bcl-2 family (e.g. Bcl-2, Bcl-xL, Mcl-1) prevent the assembly of Beclin-1 with the PI3K complex,[341] hence inhibiting the autophagic response, whereas proapoptotic mediators (e.g. Bad, Bid, Noxa) function as autophagic induction cues.[342] Moreover, the apoptosis inhibitory protein c-FLIP hampers the Atg3-mediated processing of LC3.[343] Apoptosis might also be launched after autophagy-mediated degradation of cIAP1/2.[344]

Autophagy arises as an early survival mechanism. Oddly enough, these phenomena are a double-edged sword considered as the type II cell death since occasionally, autophagy promotes cell death under certain circumstances.[345,346] It harbors the consideration of autophagy-induced cell death if halted in the presence of autophagy inhibitors rather than rushed,[347] excluding the cases when its manipulation impacts on other forms of regulated cell death. Sustained accumulation of autophagosomes and autolysosomes culminates in the induction of cell death that morphologically differs from apoptosis and necrosis. It has not been fully unraveled whether sustained autophagy causes cell demise, or it is a mere escort preceding cell death. Within this instance, cell demise is accompanied by extensive intracellular vacuolization and an increased autophagic flux.[348]

Necrotic cell death (type III)

Cell death has been classically divided into apoptotic or necrotic based on morphological features, although overturned by the recent and not-so-recent description of distinct forms of regulated cell death (e.g. pyroptosis or autophagy). Rather than programmed, necrosis occurs as an accidental consequence of lethal injury or exposure to non-physiological conditions such as ischemia, hypoxia, or ionizing radiation. When transiently exposed to an injury or damage, cells might undergo a series of adaptive changes to endure those harsher conditions. An overwhelming injury beyond repair and sustained in time results in necrosis by default. Cell and organelle swelling is the hallmark of necrosis, as opposed to the distinctive shrinkage observed in cells undergoing apoptosis. Membrane permeabilization is followed by the rupture of the membrane. Cellular content and organelles are spilled out, and intracellular DAMPs and cytokines are therefore released, causing local inflammation and damage of the nearby tissue.[349] The nuclear events that take place upon apoptotic stimuli are not observed for necrotic cell death.

A subset of necrosis has been recently reported to show regulation rather than being accidental: necroptosis. Necroptosis was first described in 2000 as a caspase-independent regulated cell death.[350] It shares the morphological hallmark features of necrosis and the proinflammatory profile.[351] Yet, necroptosis relies on the formation of the necrosome complex when the proteolytic activity of caspase 8 is abrogated, hence considered as a back-up process.[352]

A. Necroptosis

Necroptosis can be driven by the engagement of extracellular death receptors, toll-like receptors, or intracellular receptors. The most broadly characterized pathway is the one mediated by death receptors, especially TNFR1. As already discussed, pleiotropic TNF-α signaling can drive cell outcome towards survival or death, being the ubiquitination state of RIPK1 decisive in controlling this duality (see Fig. 15). When ubiquitinated, RIPK1 elicits the complex I-mediated activation of the canonical NF-κB signaling, resulting in nuclear transcription of prosurvival cues. If deubiquitinated, complex II arouses in the cytosol by the recruitment of FADD, RIPK1, procaspase 8 and/or c-FLIP. Both RIPK1 and RIPK3 are degraded by caspase 8 alone or complexed with c-FLIP, triggering apoptosis.[284]

Necroptosis has garnered enticing interest as a therapeutic target.[353] Its implication in the pathogenesis of several diseases (e.g. stroke or neurodegeneration)[354] has been recently reviewed by Choi *et al.*[355] There are two prerequisites for necroptosis: i) removal of ubiquitin chains from RIPK1 and ii) pharmacological or genetically encoded inactivation of caspase 8 that leads to an inefficient cleavage of RIPK1 and RIPK3. Regardless, the critical determinant of whether a cell is biased to undergo apoptosis or necroptosis has not been fully mastered yet. There are other conditioning factors, such as depletion of cIAP1/2 that makes cells more prone to die from necroptosis if caspase 8 activity is compromised, otherwise the choice would be undergoing apoptosis.[356,357] When catalytically active, RIPK1 and RIPK3 kinases assemble through their RHIM domains into the complex IIc or necrosome.[358] RIPK1 was the first described performer exhibiting a role in the necroptosis signaling.[350] Notwithstanding, RIPK1-independent necroptosis has already been reported, being RIPK3 and its downstream pseudo-kinase MLKL the two indispensable players for the commitment of this regulated type of death. Though termed caspase-independent, it is negatively regulated by the active form of caspase 8, which switches cell fate towards apoptosis.[359]

In regard to the molecular mechanism, RIPK1 and RIPK3 are phosphorylated by the latter, or they can conduct self-phosphorylation, a process that is fundamental for the formation of the necrosome complex (Fig. 17).[356,360] The necrosome is arranged after phosphorylation-dependent oligomerization of RIPK3 into amyloid microfilaments, which is sufficient to trigger necroptosis. Phosphorylated RIPK3 can be found either alone (RIPK1-independent necroptosis) or escorted by RIPK1 (RIPK1-dependent necroptosis). This first phosphorylation step is critical for RIPK3 to recruit and phosphorylate its downstream partner-in-crime MLKL.[361,362] The association of multiple phosphorylated MLKL molecules gives rise to the translocation to the membrane and subsequently permeabilization by creating pores, committing the cell to die (Fig. 17).[363,364] Currently, two trends are aiming to explain the executioner mechanism of MLKL. On the one hand, MLKL might bind to phosphatidylinositol phosphates directly, promoting the formation of leaking pores. On the other hand, calcium, sodium, and potassium ion channels might be recruited.[365–367]

Additionally, RIPK3 has also been reported to orchestrate mitochondrial disorders by activating metabolic enzymes and increasing ROS production (Fig. 17).[368] RIPK3-dependent activation of glycogen phosphorylase (PYGL) and pyruvate dehydrogenase (PDH) boosts aerobic respiration, and hence ROS production following enhanced glycogenolysis and glycolysis.[369,370] RIPK3 moreover promotes glutaminolysis and local ammonia accumulation by activating glutamate-ammonia ligase (GLUL) and glutamate dehydrogenase 1 (GLUD1), contributing to ROS generation. Indeed, mitochondrial ROS production induces the self-phosphorylation of RIPK1, therefore easing the formation of the necrosome.[371] Activation of RIPK3 within the necrosome induces caspase 1-mediated pyroptosis, a type

of cell death featured by the formation of the inflammasome, that also contributes to increase ROS and cytokine production.[372] It has been disclosed that oxidative stress promotes autophagy responses.[373] In addition to cytokine production, the massive leakage of DAMPs and alarmins after membrane disruption aggravates the inflammatory response.[374–376]

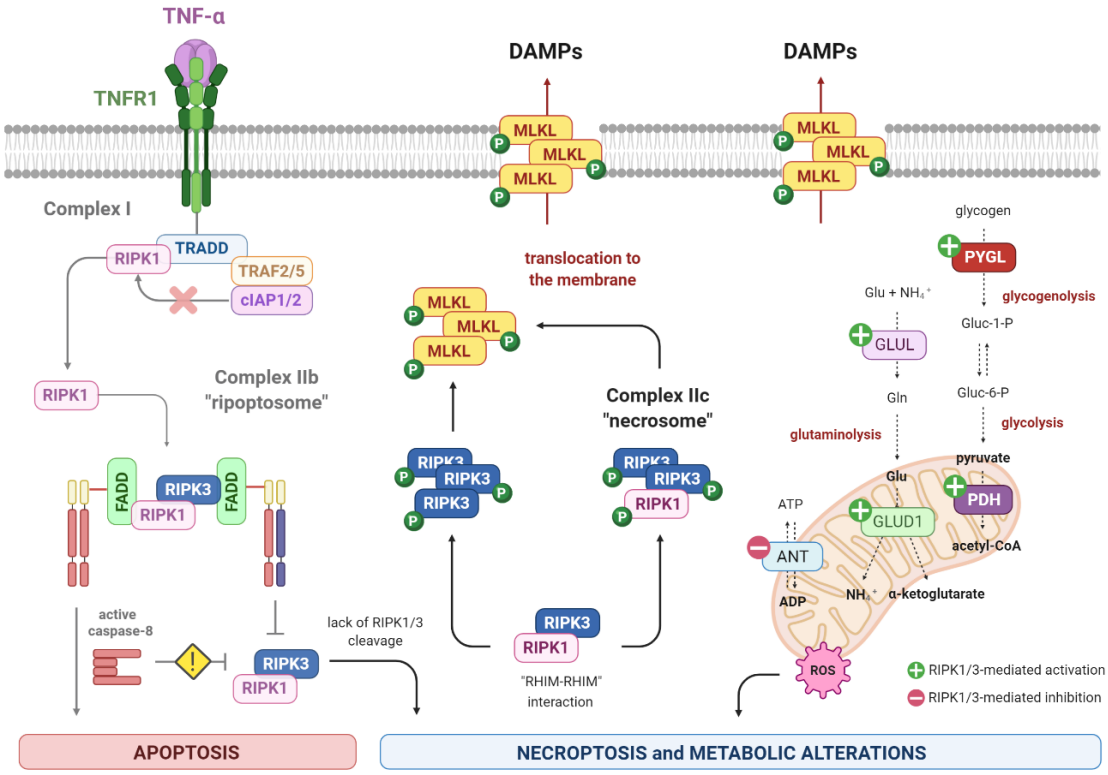

Figure 17. Cell death signaling upon TNFR1 ligation. When the proteolytic activity of caspase 8 is compromised by any means, TNFR1 ligation induces necroptosis rather than apoptosis. The cytosolic complex IIb or ripoptosome is recruited when RIPK1 lacks ubiquitin chains, resulting in the activation of apical caspase 8, which prevents necroptosis by cleaving and hence inactivating necroptotic players RIPK1 and RIPK3. If caspase 8-mediated cleavage of RIPK1 and RIPK3 is abolished, both kinases are phosphorylated and form an amyloid-like complex or necrosome. RIPK1-independent necroptosis accomplishment has also been reported. The phosphorylated RIPK3 form in turn phosphorylates MLKL, which prompts the formation of leaking pores when translocated to the plasma membrane. The release of DAMPs and cytokines induces local inflammatory response, aggravated by the elevated production of mitochondrial ROS. RIPK3 directly binds and activates metabolic enzymes (e.g. PYGL, PDH, GLUL, and GLUD1) and RIPK1 downregulates the mitochondrial adenine nucleotide translocase (ANT), resulting in reduced levels of cytosolic ATP. RIPK3-dependent activation of glycogen phosphorylase (PYGL) boosts the formation of glucose-1-phosphate from glycogen (glycogenolysis), later transformed into the glycolysis substrate glucose-6-phosphate. The upregulated activity of PDH, the bridge enzyme between glycolysis and aerobic respiration, eventually leads to augmented ROS production. Higher levels of ROS and oxidative stress caused by RIPK3 activation feeds back the formation of the necrosome complex.[377] GLUL and GLUD1 enzymes catalyze the conversion of cytosolic glutamate into ammonia and α-ketoglutarate that feeds the Krebs cycle. Increased aerobic respiration correlates with higher oxidative stress. The altogether combination of ROS, lipid peroxidation, metabolic alterations, and ATP depletion contributes to the alarm state and necrotic death.

CELL DEATH BY TBDs

Extensive research has been conducted to fulfill the gaps relative to the study of the mechanism of action that underlies the treatment with tubulin binding drugs. Notwithstanding, the spindle poisons tale has not yet been fully unraveled, with just a few highlights known so far.[33] Cytotoxic drugs, as it is the case of tubulin binding agents, cause cellular demise by killing cells that are subject to rapid proliferation.[378] It has been widely accepted that the preferential targeting of antimitotic agents towards neoplastic cells is gained from their boosted proliferation rate in comparison with healthy cells in the body. This statement is primarily backed up by the high-incidence increased toxicity elicited in tissues that manifest rapid turnover (e.g. gastrointestinal epithelium or bone marrow). This accepted explanation has been disputed in the strengthened "proliferation rate paradox" theory.[379] According to this theory, tumor regression caused by drugs that affect dividing cells is doubtfully based on the enhanced proliferation, as many clinical neoplasms responding to chemotherapy show low division rates.

The prime route of administration in cancer therapy is intravenous infusion. The drugs are infused to the patient during a certain period, then cleared from the body. In theory, only cells that enter mitosis whilst the drug is still circulating (reaching the tumor taken for granted) in fair concentration would be disturbed, whereas non-dividing cells would be spared.[379] Several non-exclusive putative explanations using paclitaxel as a model have been put forward by Mitchinson.[379] On the one hand, paclitaxel might be retained longer than expected, so even days after administration, it can trigger cell demise in quiescent cells as they slowly enter division. These quiescent cells may be additionally affected without division by paclitaxel-induced effects on interphase microtubules. On the other hand, the tumor microenvironment may also be compromised when challenged with paclitaxel. Targeting non-tumor cells within the neoplasm could potentially be related to the long-term response. As it occurs upon treatment with colchicine site ligands, endothelial cells within the blood vessels that irrigate solid tumors might be affected, as well as cells from the immune system. Bystander killing has also been speculated to influence tumor recession.[379]

The effects of TBDs have been classified in two major groups: mitosis-dependent cell death and mitosis-independent tumor regression. Indeed, the "proliferation rate paradox" is supported by data suggesting that mitosis-independent actions after disturbance of interphase events are vital components of the clinical response.[380,381] When reaching cytotoxic concentrations, tubulin targeting drugs hamper proper cell division due to the malfunctioning of the mitotic spindle, a common characteristic among tubulin ligands, irrespective of their cognate binding domain.[33] A second mechanism of action has been enlightened for several tubulin ligands: vascular disrupting activity.[144,382–384] This is one of the reasons why designing molecules that bind at the colchicine domain is in vogue. Vascular disrupting agents (VDAs) exert this unique effect at lower doses than those required to induce the mitosis-dependent killing of tumor cells directly.[385,386] This may lessen the acute toxic side effects manifested upon conventional chemotherapy and opens a vast range of clinical opportunities in combination regimens.

Many ligands that bind to the colchicine domain in tubulin have shown an antiangiogenic profile (e.g. CA4) at low concentrations.[387–389] The impairment of new sprout formation is related to the Rho/ROCK-dependent upregulation of the connective tissue growth factor (CTGF), and hindrance in VE-cadherin/β-catenin pathway. Therefore, the ligands perturb the proper adhesion, chemotaxis, and migration of the endothelial cells required to constitute novel tubes.[390–392] Some other molecules are involved in the antiangiogenic response, such as Rac1, Cdc42, Hsp90, and PKC.[393–395] In addition, metastasis prevention has been reported upon treatment. This effect arises from induced alterations in the transport of matrix

metalloproteinases (MMP).[396,397] MMPs are proteolytic enzymes associated with the cleavage of the extracellular matrix, allowing tumor cells to enter the bloodstream. Once circulating either by blood or lymph, tumor cells may settle a secondary tumor mass in a distant location. The two primary mechanisms, namely mitosis inhibition and vascular disrupting activity are briefly discussed below.

Mitotic blockage and cell death

The malfunctioning of the spindle microtubules induces a sustained mitotic arrest.[398] Irrespective of the stabilizing (MSAs) or destabilizing (MDAs) effect exerted by these drugs in the microtubule lattice, both subsets impair the proper functioning of microtubules.[33] The effect of spindle poisons is primarily manifested in highly dynamic microtubules, as mitotic microtubules. Hence, cells that are submitted to high proliferation rates would be more severely challenged. It is the case of bone marrow tissue, which often suffers toxicity upon treatment with antimitotic drugs. The term mitotic catastrophe has been coined to refer to this situation whereby a cell arrested in mitosis may eventually undergo apoptosis, become senescent, or conduct slippage.[399] The latter concept involves that the cell is able to circumvent the mitotic checkpoint and reach G_1 phase, becoming tetraploid after an aberrant cell division.[400,401] Mitotic catastrophe has occasionally been considered as a type of cell death, although the hallmark features fit in apoptosis. The overall consensus defines mitotic catastrophe as a pre-lethal status ensuing from mitotic failure caused by unrepaired DNA damage or compromised spindle.[402]

During metaphase, the chromosomes are situated along the equator of the cell, organized in sister chromatids whose cohesion is ensured by a multimeric ring-shaped protein known as cohesin (Fig. 18).[403] Concomitantly, the mitotic spindle irradiates from MTOCs located at both poles of the cells. These highly dynamic microtubules are meant to establish proper attachments with chromosomes to pursue their eventual segregation by traction forces. The tether of microtubules and chromosomes is bipolar and amphitelic and occurs in the kinetochores.[404,405] In order to prevent chromosome missegregation, the presence of a single unattached kinetochore is enough to activate a mitotic checkpoint named spindle assembly checkpoint (SAC).[406] Its purpose is to delay the anaphase onset once mitosis is underway to ensure accurate anchorages between the chromosomes and the spindle.[407–410]

The activation of the SAC arises temporally at the early stages of metaphase in a normal mitosis and during a drug-induced blockage of microtubule dynamics. The transient arrest is alleviated after the establishment of every single kinetochore attachment, what does not occur to treated cells.[411] There are several proteins from Mad and Bub families that are recruited to kinetochores during the SAC. They form the mitotic checkpoint complex (MCC), an ensemble of Mad2, Bub3, BubR1, and Cdc20.[412,413] The recruitment of the MCC blocks APC/C^{Cdc20} (anaphase promoting complex or cyclosome) from activation by inducing a locked conformation.[414] APC/C^{Cdc20} is the molecular machinery involved in the degradation of mitotic substrates.[415–417] It harbors E3 ubiquitin ligase activity and targets cyclin B1 and securin for ubiquitination to be degraded via the proteasome 26S (Fig. 18).[418] The inactive APC/$C^{Cdc20\text{-}MCC}$ is no longer able to label substrates for degradation (Fig. 19).[419] Therefore, the blockage of its E3 ubiquitin ligase activity entails two main consequences. On the one hand, securin upregulation prevents separase, a proteolytic enzyme, from targeting cohesin for degradation,[420] guaranteeing the integrity of the cohesion between chromatids.[421] On the other hand, the sustained levels of cyclin B1 result in the permanent activation of a cyclin B1/Cdk1 complex (MPF, maturation promoting factor). Anaphase entrance would not be triggered since a drop in cyclin B1 levels is required to conduct it.[415] Eventually, there is a prolonged G_2/M arrest that can be monitored by flow cytometry.

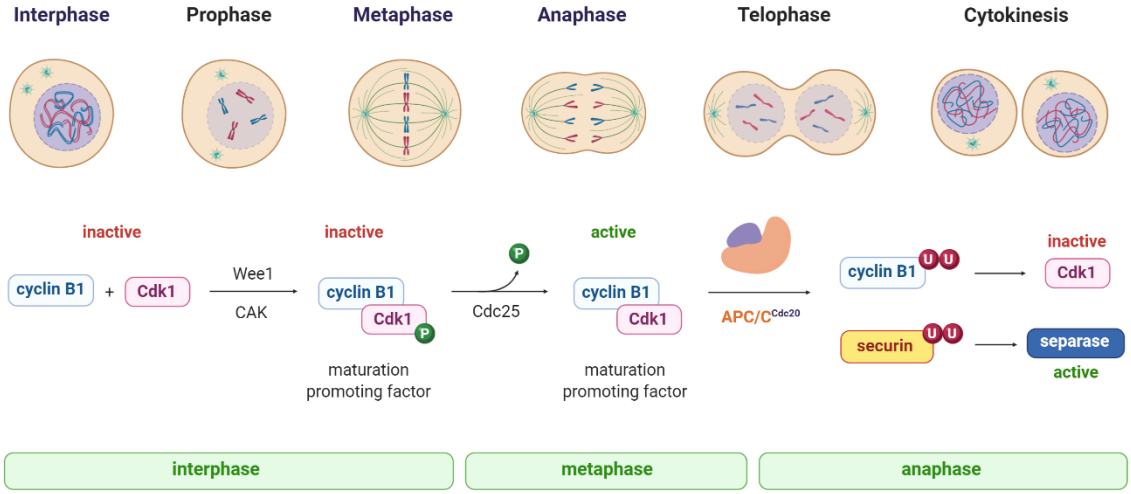

Figure 18. Status of the maturation promoting factor (MPF) during the cell cycle. Cyclin B1 and Cdk1 form a complex called MPF, which is phosphorylated mainly by the kinases Wee1 and CAK. In order to turn it active, the phosphatase Cdc25 removes the phosphate groups, marking metaphase. The active form of Cdk1 triggers a phosphorylation cascade of mitotic substrates. The onset of anaphase is conducted upon degradation of cyclin B1. The E3 ubiquitin ligase APC/C labels cyclin B1 and securin for proteasome-dependent degradation. Therefore, cyclin B1 is no longer able to form the active complex with Cdk1. Securin displays a protective role in the integrity of the cohesion between sister chromatids. Downregulation of securin implies the degradation of cohesin by the proteolytic enzyme separase.

There is mounting evidence showing that once the mitotic arrest is underway, cells will presumably die by apoptosis.[422] Still, the mitotic catastrophe has been long considered as the type of cell death that ensues antimitotic therapy, as mentioned above. The cell death that follows mitotic arrest shares most of the hallmark features of apoptosis, although the loss of membrane integrity has also been reported, which is allocated to necrosis.[423,424] Gajate *et al.* reported that the pharmacological inhibition of caspases prevents the apoptotic cell death induced by the colchicine domain ligand MTC in leukemic cells, as does the overexpression of the antiapoptotic proteins Bcl-2 and Bcl-xL.[425] How the sustained arrest in metaphase commits the cell to die remains unclear. It has been reported that the prolonged cell arrest is not enough for the cell to die. Experimental data suggest that the high levels of active Cdk1 complexed with cyclin B1, are responsible for switching cell fate from mitotic arrest to apoptosis through a phosphorylation cascade.[426] Many Bcl-2 protein family members, such as Bad, Bcl-xL, Bcl-2, and Mcl-1 are phosphorylated upon Cdk1 activation, eliciting substantially different consequences (Fig. 19).[427]

As explained earlier, Bad already displays a proapoptotic role, which is promoted upon its Cdk1-dependent phosphorylation.[428] Mcl-1, Bcl-xL, and Bcl-2 belong to the prosurvival subset of proteins within the Bcl-2 family.[429–431] Phosphorylation of Mcl-1 entails a cue for conducting its degradation and abrogates Bak from the hijacking dimer, thus triggering a proapoptotic effect.[426,432–434] Choi *et al.* showed that the increase in Bcl-xL phosphorylation, but not in Bcl-2, promotes apoptosis through the intrinsic pathway.[435,436] The relevance of Bcl-2 phosphorylation generates controversy. Some authors defend that the phosphorylation of Bcl-2 may boost apoptosis, putatively by reducing the interaction of Bcl-2 with proapoptotic Bak.[437–439] Some others defend that Bcl-2 phosphorylation stimulates its inherent prosurvival effect.[440–442] Bcl-2 phosphorylation has been reported to display a protective effect against its degradation.[443]

The altogether phosphorylation status of the Bcl-2 family members might putatively dictate the cell fate. It has been described that Mcl-1 is the main Bcl-2 family member involved in bridging mitotic arrest and cell death.[411,444] Unlike the other Bcl-2 members, Cdk1-mediated Mcl-1 phosphorylation favors its ubiquitination and subsequent degradation.[432] Downregulation of Mcl-1 preferentially impairs Bak sequestration, which belongs to the proapoptotic subset of Bcl-2 proteins.[445]

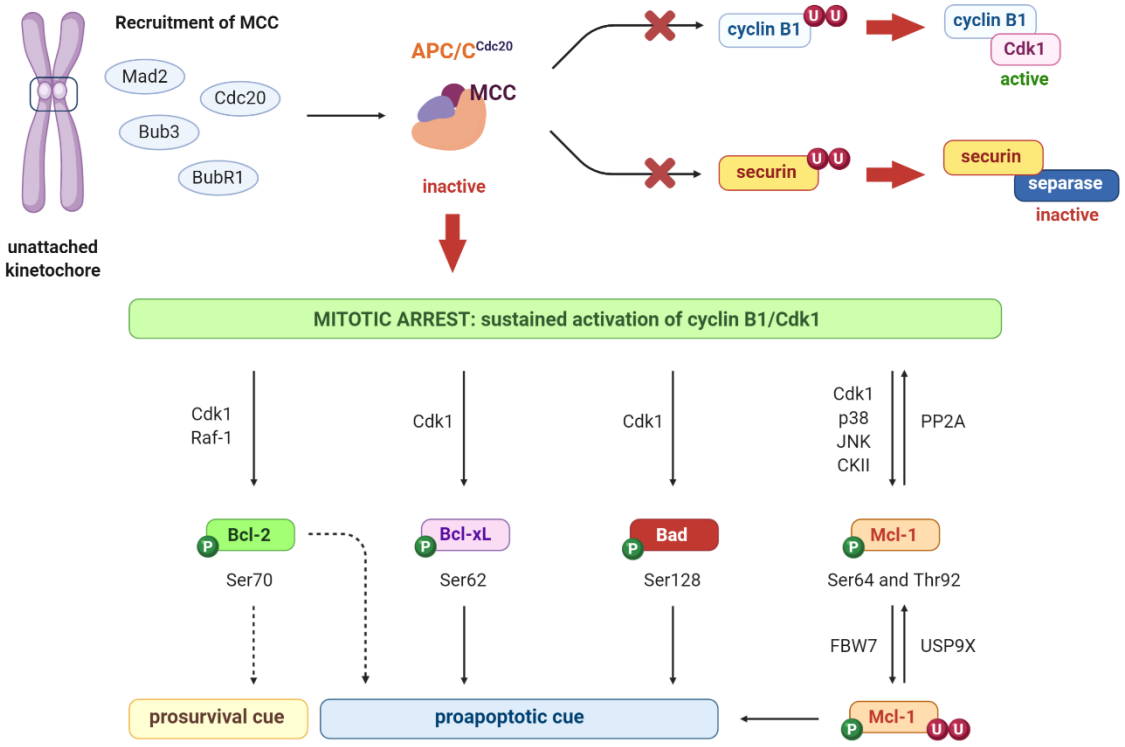

Figure 19. Spindle assembly checkpoint (SAC). TBDs impair the establishment of bipolar attachments between microtubules and kinetochores. Therefore, Mad2, Bub3, Cdc20, and BubR1 are recruited to the unattached kinetochores during the active SAC to constitute the mitotic checkpoint complex (MCC). MCC-mediated inactivation of APC/C^{Cdc20} elicits that Cdk1 in complex with cyclin B1 is permanently active and that cohesin would not be compromised due to the inactivation of the separase enzyme. The sustained levels of active cyclin B1/Cdk1 trigger a phosphorylation cascade of several Bcl-2 protein family members: Bcl-2, Bcl-xL, Bad, and Mcl-1. The phosphorylation of Bcl-xL, Bad, and Mcl-1 entails a proapoptotic effect, whereas the role of phosphorylated Bcl-2 remains controversial.

There is growing evidence that whether cells undergo apoptosis or slippage depends on an imbalance between the degradation rates of cyclin B1 and Mcl-1.[411] Under an active checkpoint, APC/C$^{Cdc20\text{-}MCC}$ does not label cyclin B1 for degradation. However, it is not a full impairment, so there is a gradual drop in the levels of cyclin B1 occurring very slowly.[446] If cyclin B1 drops below the threshold needed to commit the anaphase onset before Mcl-1 drops to levels leading to apoptosis, cells exit mitosis and undergo slippage. The slipped cells reenter anaphase without splitting DNA and become tetraploid cells.[447] Otherwise, if the levels of Mcl-1 decrease to the point that Bax and Bak proteins induce MOMP before cyclin B1 levels drop low enough, cells undergo apoptosis. Withal, overexpression of Mcl-1 is not sufficient to prevent vincristine-induced apoptosis.[448] The crosstalk between mitotic arrest, cell death, and slippage is hence poorly understood. There is a putative interplay between a bunch of many proteins transducing survival and death cues, with the mitochondria as the hub player that controls cell fate.

Vascular disrupting therapy

Targeting the tumor vasculature as a therapeutic approach has recently regained notable interest. Drugs that target the vascular endothelium are particularly promising to dampen the growth of solid tumors. The establishment of a whole tumor-associated vascular network is required to provide tumor cells with oxygen and nutrients.[449,450] Otherwise, the tumor mass would not surpass beyond 1-2 mm^3 size. Besides, the bloodstream could carry invasive tumor cells from the primary locus as a track whereby they can settle a secondary tumor in a distant spot. Vascular disrupting agents prominently affect endothelial cells from the tumor neovasculature. These healthy cells are more genetically stable compared to tumor cells, which are very prone to mutate and bypass a threat when challenged with chemotherapy.[451] That, together with the low turnover rate of non-tumor-associated endothelial cells, would presumably minimize the toxic effects on healthy vessels and the incidence of resistance-mediated therapeutic failure.[452,453] The arduous access to the tumor core is one of the hardships to be faced in order to ensure drug delivery precisely. Hence, targeting the easily accessible microvasculature that irrigates the tumor may favor the prognosis and clinical outcome.[454]

Vascular-targeting drugs group two different approaches: angiogenesis inhibition and vascular disruption, which differ not only in the mechanism but also in the dosage schedule.[455–459] Drugs that inhibit angiogenesis prevent the foremost creation of blood vessels and restrict tumor growth. Their cytostatic effect warrants the chronic administration and utility in the first stages of the tumor. By contrast, vascular disrupting agents (VDAs) exert an indirect cytotoxic mechanism by destroying the vessels that had been previously created in response to proangiogenic cues arising from the tumor.[460] These agents halt the blood flow by inducing a rapid collapse and further cause massive necrosis of the inner core within 24 hours right after acute administration. Prompting ischemia by vascular disruption is therefore an opportunity to fight solid tumors with a considerable size. These advanced cancerous masses require an extensive blood vessel network to guarantee the vital supplies and are frequently resistant to conventional chemotherapy strategies. Even so, it is not easy to find drugs that purely exert angiogenesis inhibition or vascular disruption. These effects are often intermingled.

Despite targeting non-tumor cells, VDAs selectively affect the newly-created microvessels that irrigate the tumor.[461] Just a mild transient depletion in blood flow is observed in healthy tissues upon treatment.[462] The basis of this selectivity relies on the architecture of the vascular endothelium, which differs between healthy tissues and the tumor environment (Fig. 20).[463–465] Healthy tissues are extensively crossed by a mature well-structured vascular network, which is permeable to oxygen and nutrients. This blood system is over and over dissected into branches following a disciplined hierarchy. The development of the normal vasculature is fine-tuned by pro and antiangiogenic molecules, conditioned to the demands of each tissue. Under physiological conditions, the inner lumen of the blood vessel is fully covered by endothelial cells arranged in a single layer. The flat shape of endothelial cells eases the laminar blood flow and avoids the adherence of circulating cells. These cells are firmly tethered through adherens and tight cell-to-cell junctions that ensure the integrity of the vessel. Otherwise, the basal membrane would be exposed to the bloodstream providing a thrombogenic surface. Endothelial cells covering normal vessels are almost quiescent, with a lifespan of around 120 days.[466] Therefore, the finely orchestrated wall of the blood vessel functions as a barrier separating the bloodstream from the underlying tissue. This structure is additionally reinforced by the presence of smooth muscle cells termed pericytes. By contrast, the urgency of tumor cells to settle a vascular system results in highly disordered, fragile, and thin-walled vessels.[467] This is due to the overproduction of proangiogenic cues by the tumor microenvironment, together with the higher proliferation rate of endothelial cells compared to those that are not associated with tumors.

The resulting irregular vascular network is very immature and chaotically arranged in tortuous ducts often capped by blind sprouts.[468] The endothelial cells are frequently devoid of adherens and tight junctions that bring them together and exhibit an abnormal morphology. This entails an increase in vascular permeability and the exposure of a weakened basal membrane.[469] Most of the pericytes that cover the outer surface of the blood vessels are lacking.[470] Taken altogether, these physiological alterations contribute to the fragility of the tumor microvessels, which are highly susceptible to VDAs. This tumor neovasculature is highly sensitive to subtle alteration in the blood flow that would not perturb the proper irrigation throughout normal vasculature.[471]

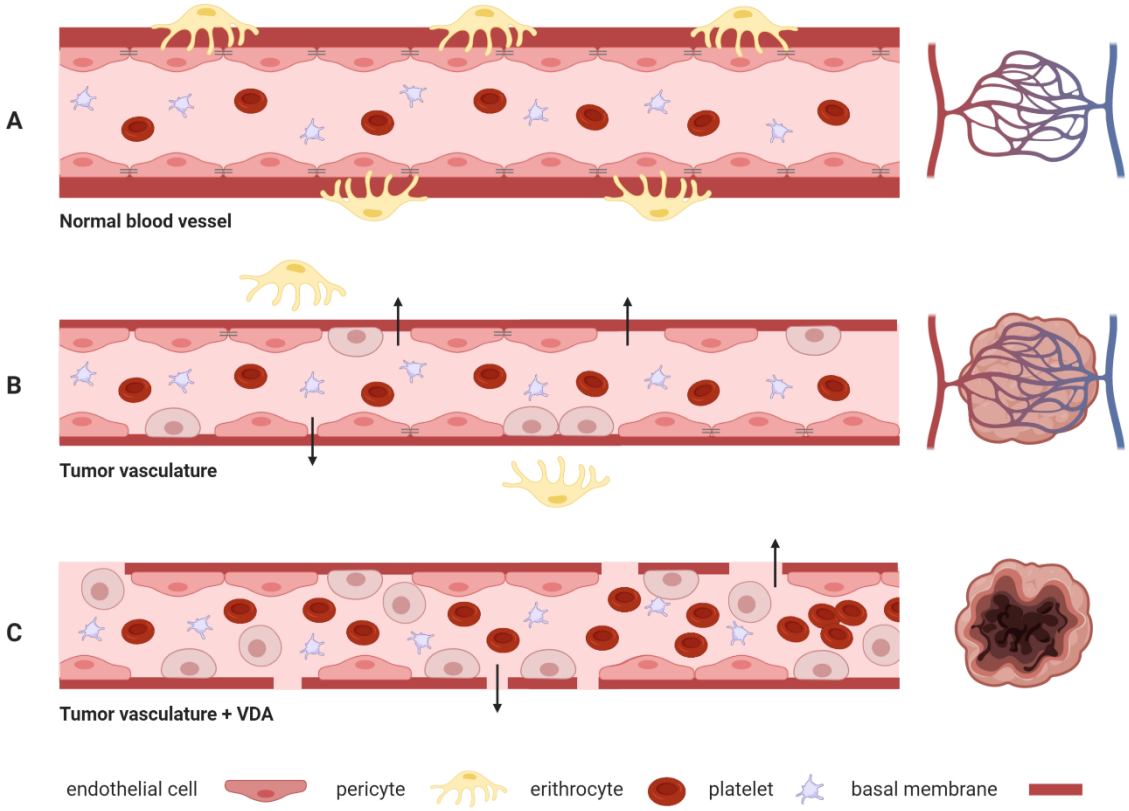

Figure 20. Comparative architecture of blood vessels. **A.** Normal blood vessel irrigating healthy tissues **B.** Thin microvessel formed upon tumor growth. This vasculature exhibits thinner walls and compromised cell-to-cell junctions. Many endothelial cells show abnormal morphology, which results in the partial exposure of the basement membrane. Pericytes detach from these immature blood vessels, and intravasation of metastatic tumor cells may occur. **C.** Effect of vascular disrupting agents on the tumor vasculature. Cytoskeletal alterations result in rounded endothelial cells able to detach from the basal membrane, which is compromised. There is extravasation of macromolecules accompanied by plasma leakage. As a result, higher hematocrit may cause clumps. The inner tumor core dies by necrosis upon the shutdown of the blood flow.

CA4 was the first modulator of microtubule dynamics that proved selective toxicity towards the tumor vasculature with a broad therapeutic window.[144] The antivascular potential of tubulin ligands is evidenced by the selective targeting of the endothelial cells that cover the inner lumen of tumor microvessels.[472] These compounds compromise the vessel integrity by perturbing the endothelial cell shape upon cytoskeleton disruption.[455] At such low doses, microtubule dynamics failure orchestrates the activation of the small GTPase Rho and the subsequent Rho/ROCK pathway, a kinase that coordinates the F-actin and microtubule cytoskeleton.[473] However, high drug concentrations are toxic for the rapidly proliferating endothelial cells within the tumor vasculature, which undergo caspase-dependent apoptosis.[474] The

induction of the Rho GTPase activity triggers a downstream phosphorylation cascade that eventually culminates in the collapse of the vascular network.[475] Hemorrhage and clotting processes contribute to the profound damage, finally leading to oxidative stress, hypoxia, and ischemia.[476] The widespread failure of the vascular network is rapidly achieved after drug infusion. Therefore, the supply of bloodstream to the solid tumor is suddenly interrupted, causing massive necrosis within the inner tumor core due to oxygen and nutrient deprivation.[477] Nonetheless, the thin outer rim of cells may stand undamaged since the normal vasculature from the nearby tissues can ensure their vital demands.[478,479] Combination strategies have to be addressed in this scenario. Otherwise, the viable cells of the outer rim may restore the inner tumor mass easily. VDAs can be administered concomitantly with conventional cytotoxic chemotherapy (e.g. carboplatin or paclitaxel), radiotherapy, or antiangiogenic molecules (e.g. bevacizumab), arising as really promising in combinations.[480,481] The combination of VDAs with cytotoxic drugs would boost the antitumor effect and at the same time, restrict the incidence of toxic side effects due to the lower doses of both drugs.[482–484]

The abnormal shape of the endothelial cells upon treatment stems from the phosphorylation of myosin light chain (MLC) by Rho kinase (Fig. 21).[485] The phosphorylation status of MLC enhances the assembly of actin-myosin fibers and the subsequent contraction-retraction dynamics.[486] The stress F-actin fibers cluster into focal adhesions. Altogether, the resulting increased cellular tension gives rise to membrane blebbing and an overall round-shaped phenotype.[487] The flat monolayer of endothelial cells that constitutes the luminal wall of the vessel under normal conditions eases the blood flow, whereas the rounded endothelial cells that protrude towards the lumen offer geometric resistance to blood flow.[473,488] Downstream from Rho kinase, the activation of stress-activated protein kinase 2 (SAPK2) is involved in the misassembly of stress fibers at the periphery of the cell.[489] Together with the accumulation of F-actin around the cytoplasm, stress fibers contribute to the contractile tension and eventual blebbing. The FAK-dependent formation of focal adhesions, as well as the disassembly of cell-to-cell junctions through interference with vascular endothelial-cadherin/β-catenin/Akt pathway, contribute to a drop in cell adherence and a weakening of the vessel wall.[490–493]

Rho-dependent morphology changes of the discontinuous endothelial layer trigger dramatic osmotic forces alterations that contribute to the shutdown of the blood flow.[494] A raise in vascular permeability, which is innately higher in tumor vasculature, elicits the leakage of macromolecules to the underlying tissue with the potential increase in the interstitial pressure.[495–497] That is accompanied by plasma reduction, leading to higher local hematocrit. This impairs blood flow by increasing viscous resistance what might cause stagnation and rouleaux formation due to the clumping of erythrocytes.[498] The thrombogenic scenario is aggravated by the exposure of the basement membrane after adherence disturbance and loss of cells, inducing the clotting cascade and recruitment of platelets with vasoconstrictor serotonin release. Widespread collapse of the damaged vascular network with occlusive and hemorrhagic processes cuts the sluggish flow to the tumor core that undergoes necrotic cell death.[385]

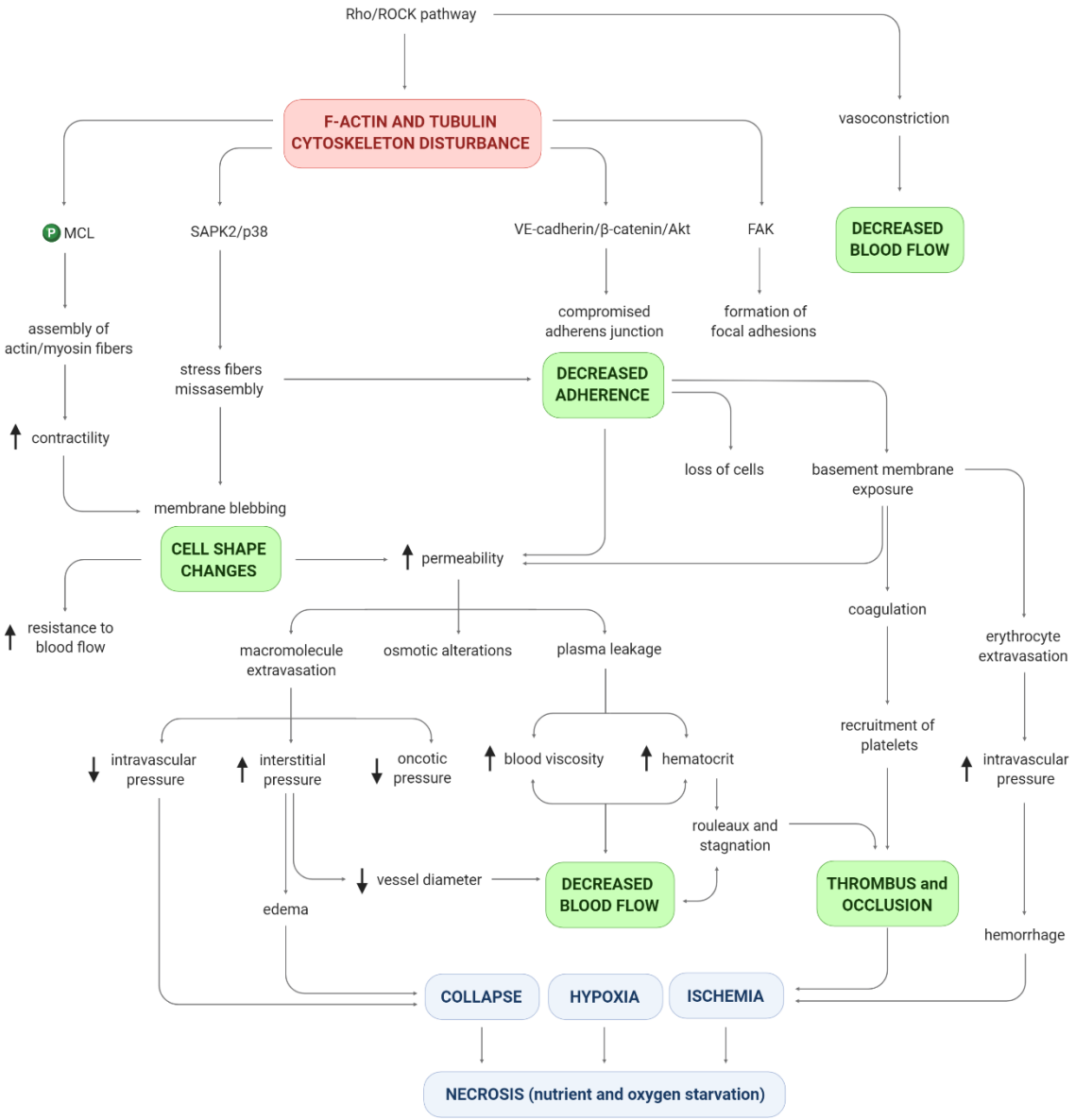

Figure 21. Pathophysiological cascade triggered by vascular disrupting agents, culminating in necrotic death of the cells restricted to the inner tumor core.

Chapter 2

OBJECTIVES

GENERAL AIM

Tubulin is an essential protein that plays crucial roles during the lifespan of a cell, especially during mitosis. This, together with the fact that it is not susceptible to relevant mutations that would affect its proper functioning, make it enticing in cancer chemotherapy. It is a well-validated target since two of the most important classes of antitumor drugs approved by the FDA - taxanes and vinca alkaloids - exert their cytotoxic effect by impeding microtubule dynamics. However, since tubulin is ubiquitously expressed and its roles are critical in healthy cells, tubulin-based chemotherapy entails severe toxic effects that mainly manifest in high turnover tissues such as bone marrow, or neurotoxicity as a consequence of alterations in axonal transport. Many TBDs exhibit a dual mechanism of action: through direct cytotoxic effect in tumor cells and by affecting healthy endothelial cells located in tumor-associated vessels, also referred to as VDAs. Vascular disrupting activity is usually achieved at lower doses than those needed to kill tumor cells.[386] A combination strategy with VDAs and conventional chemotherapy allows a reduction of doses and therefore, may lessen toxic effects.

Despite their widespread use in clinic, taxanes and vinca alkaloids manifest resistance issues associated with MDR transport and pharmacokinetic limitations because of their big size and hydrophobicity. Among the many binding domains described within the tubulin dimer, we have thus chosen the colchicine interaction pocket to design novel compounds with improved properties. Although a few colchicine site ligands are quite advanced in clinical trials, none of them has yet reached clinical approval. Colchicine domain ligands offer a clear advantage over taxanes and vinca alkaloids: they are structurally smaller, and therefore are not usually substrates of MDR transporters. A simpler structure allows the development of compounds with improved pharmacokinetic profiles and more accessible in synthetic terms.

Accordingly, the overall goal of this Ph.D. is to obtain bioactive molecules that bind to the colchicine site of tubulin, thus displaying antitumor properties. We aim to gather a series of compounds with advantageous properties to study, after a preliminary evaluation, whether structural changes cause differences in the mechanism of action. With this broad topic in mind, we pursued two main objectives that will be considered independently regarding the “Results” chapter.

First objective. Design, synthesis, and characterization of novel compounds aimed to bind to the colchicine domain in β-tubulin.

Second objective. Study of the antitumor potential and mechanism of action underlying treatment with the compounds resulting from the first objective, and the effect of structural modifications on the activity.

DESIGN APPROACH

The design has been approached following a combined strategy. We have used the information provided by X-ray structures (although there are limited ligands) in combination with structure-activity relationship data of compounds with no X-ray reports, under the presumption of their binding mode. Based on X-ray structures, the colchicine domain has been divided into three interaction regions, termed zones 1, 2, and 3. Most of the crystal structures so far correspond to ligands accommodated in zones 1-2, fewer in zones 2-3, and there are only three compounds that interact with the three zones concomitantly (see Table 3). Those compounds, ABT-751, MT189, and lexibulin, occupy at least one zone only partially. There are hardly any ligands that bind to the three zones, possibly because the structural requirements to engage the whole domain simultaneously are unknown.

Taking that into account, the search for compounds that interact with the three zones was approached part by part. We designed molecules biased to bind at either zones 1-2 or zones 2-3, trying to have common structural elements in zone 2, so the moieties in zones 1 and 3 can be later combined. We have likewise attempted a full interaction with zone 3, taking ABT-751 as a template by extending the part that partially occupies that region. This overall approach tries to generate preliminary data whereby the structure-activity relationship studies may provide input for further development of molecules interacting at zones 1, 2, and 3 as a future perspective.

A. Design of molecules aimed to bind at zones 1-2 – Analogues of CA4 and related

For this purpose, we have selected CA4, ABT-751, and A-293620 as model scaffolds (Fig. 22). CA4 harbors two phenyl rings linked by an olefin moiety with *cis* configuration. The phenolic ring (B ring) binds at zone 1 of the colchicine domain, and the 3,4,5-trimethoxyphenyl ring (A ring) adopts a non-coplanar disposition relative to the B ring and interacts at zone 2.[152] CA4 and ABT-751 share a common moiety in zone 1 and contain the interchangeable structural elements we aim to combine for zones 2-3. Given the pharmacokinetic problems frequently associated to TBDs, we have focused on sulfonamides such as ABT-751, which can be administered orally. A-293620 and its prodrug A-318315 also bear a sulfonamide bridge with a modification of the B ring: an indole moiety. These compounds have no X-ray complexes with tubulin, but have proven effective against *in vitro* tubulin polymerization. A-293620 is structurally related to some other indole derivatives that resemble CA4, such as indolecombretastatins (Fig. 22).[499] Substitutions at the indole 3-position may positively contribute to the potency and aqueous solubility. Taking together these data, we proposed the design of the compounds as follows:

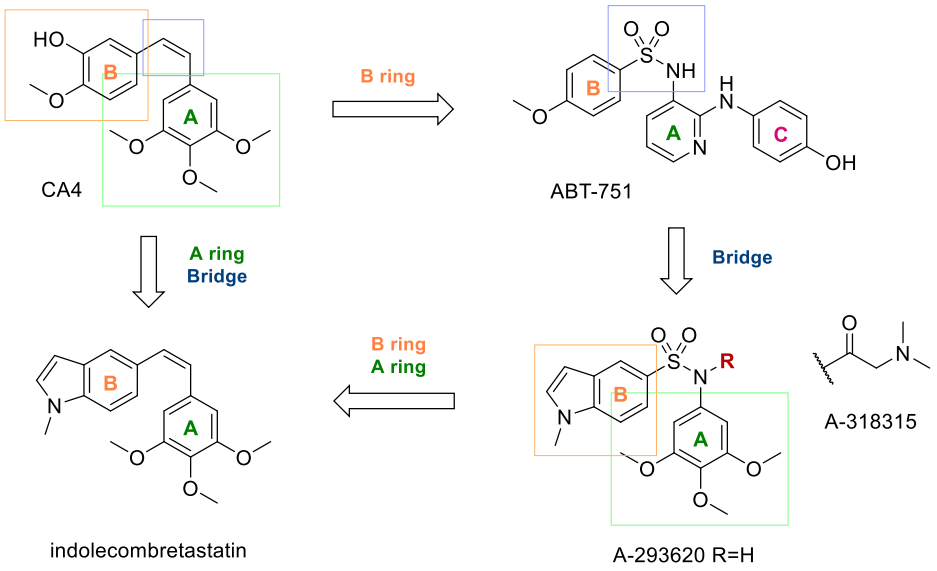

Figure 22. Chemical structures of CA4, ABT-751, A-293620 and its prodrug A-318315, and indolecombretastatin.

B ring. CA4 and ABT-751 share a *p*-methoxybenzene group as B ring accommodated in zone 1, which is one of the most permissive regions for structural modifications (Fig. 22). The 3-hydroxy group of CA4 is engaged in at least one hydrogen bond with the protein,[152] and is used as an anchoring point for prodrug formulation, as it is the case of the phosphate prodrug fosbretabulin. The removal of the hydroxyl group overcomes the rapid clearance after conjugation metabolism,[196] but at the same time impedes the

formulation of prodrugs to increase aqueous solubility. Hence, solubilizing polar groups should be introduced in other parts of the scaffold to counteract losing the OH.

Our group at the University of Salamanca has previously reported that the replacement of this phenolic ring in combretastatins and isocombretastatins by bicyclic moieties, such as naphthalene or indole rings, endows the compounds with antiproliferative activity akin to that observed for CA4.[499–505] We have selected the *N*-methyl-5-indolyl moiety present in A-293620 and indolecombretastatins as B ring because this group positively contributes to the antitubulin profile.[506] This choice allows the introduction of modifications at the indole 3-position pursuing to increase the aqueous solubility and potency and to explore the putative interactions with the residues in zone 1 of the colchicine domain.

Bridge. The classical ligands of zones 1-2 of the colchicine domain accommodate their aromatic moieties in a non-coplanar and *cisoid* conformation. The olefin bridge endows CA4 with chemical instability afforded by *cis-trans* isomerization. It readily isomerizes into the *trans* olefin, which is thermodynamically more stable.[152] The spontaneous isomerization of *cis*- to *trans*-CA4 is accompanied by a considerable reduction in potency (Fig. 23). As an alternative, we propose a sulfonamide moiety, which is a privileged scaffold in medicinal chemistry, or tetrazole rings.[27] The tetrazole group functions as a sulfonamide bioisostere and locks the aromatic rings into a restricted *cisoid* disposition (Fig. 24). Sulfonamides are in continuous rotation but preferentially adopt a *cisoid* conformation in solution (Fig. 23). Therefore, the presence of the sulfonamide avoids the chemical instability allocated to the *cis*-olefin of CA4. The sulfonamide hydrogen can be replaced by solubilizing groups to explore the interface between zones 1-2 and to improve pharmacokinetic and/or pharmacodynamic properties, thus replacing the phenolic OH group removed from the B ring.

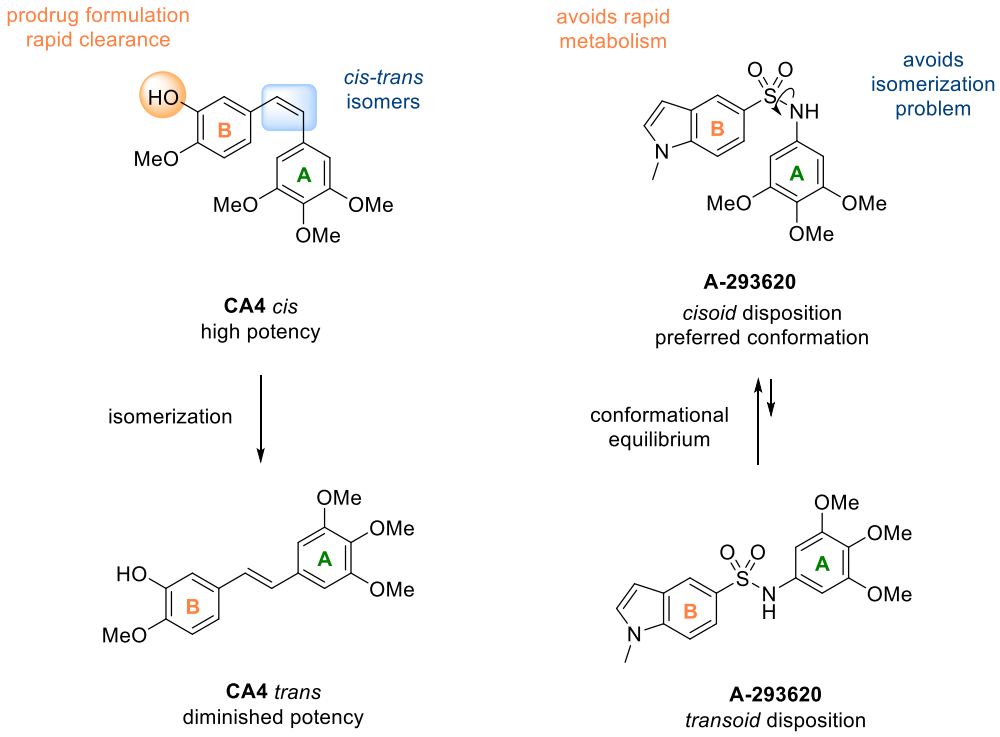

Figure 23. Chemical structures of CA4 and A-293620. The isomerization of the *cis* olefin of CA4 leads to reduced potency. It may arise during the storage process or after *in vivo* administration. The sulfonamide A-293620 shows two conformational clusters regarding the relative disposition of rings B and A that are in continuous interchange, although folded conformations are energetically more stable, hence more favorable.

Substitutions at the indole 3-position remarkably improve the antiproliferative activity and allow to introduce solubilizing polar groups, although in some cases, turned indolecombretastatins into MDR1 efflux pump substrates.[499] This effect is apparently conditioned by the bridge nature.[499,505] By changing the olefin bridge in indolecombretastatins by a sulfonamide or a tetrazole, we additionally seek to avoid MDR-mediated resistance when introducing substituents at the indole 3-position. Both sulfonamide and tetrazole bridges will be considered in their two possible orientations: the nitrogen directly bound to the A ring or the B ring (Fig. 24).

In the case of tetrazole derivatives, *p*-methoxyphenyl and *N,N*-dimethylaminophenyl moieties are additionally proposed as B rings to study the impact of *N*-methyl-5-indolyl versus benzene rings on the activity (Fig. 23).

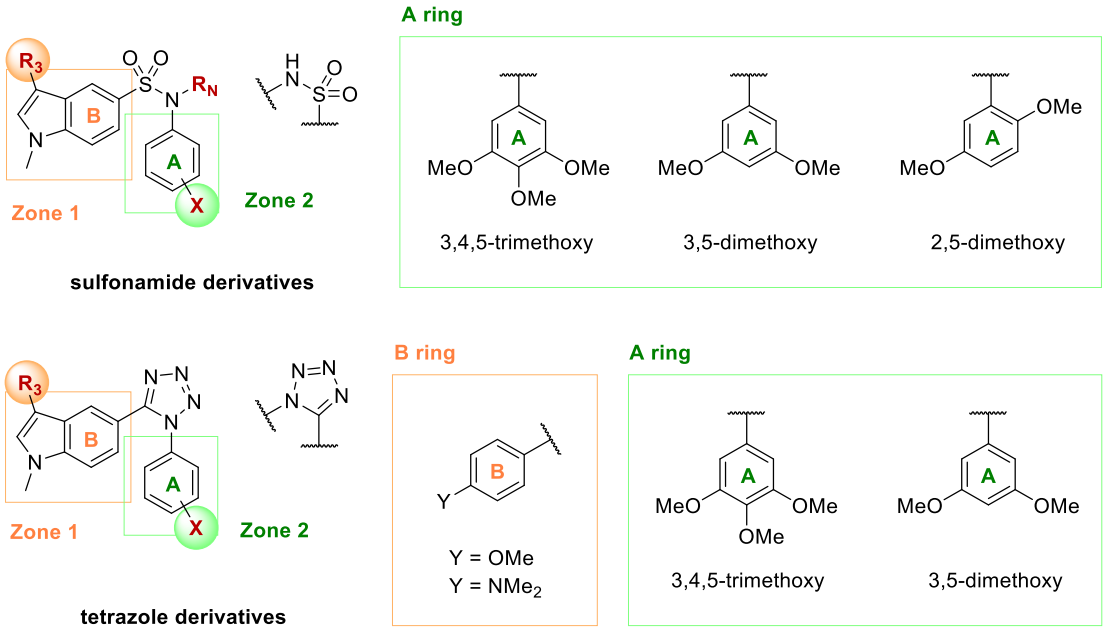

Figure 24. Proposed scaffolds aimed to bind at zones 1-2 of the colchicine domain. These compounds are structurally related to A-293620, with a sulfonamide or tetrazole bridge linking the rings B and A. *N*-methyl-5-indolyl will serve as B ring, together with *p*-methoxyphenyl and *N,N*-dimethylaminophenyl groups for tetrazole derivatives. We will explore the effect of 3,4,5-trimethoxy, 3,5-dimethoxy, and 2,5-dimethoxy substitutions on the A ring.

A ring. The 3,4,5-trimethoxyphenyl ring that binds to zone 2 has been long considered essential for the antitubulin activity. Nevertheless, it is a bulky and hydrophobic group that decreases the overall aqueous solubility of the compound and suffers metabolism by O-demethylation of 4-methoxy group, which favors the isomerization of the olefin bridge in CA4.[195] The replacement of the olefin by the bulkier sulfonamide or tetrazole moieties leads to bigger sizes. The protein-ligand interaction might be hampered due to steric hindrance. Taking that into account, we will explore the structure-activity relationship while changing the position of the methoxy groups to reduce the volume of the A ring, counteracting the gain in the bridge region. We will study the impact on the activity of 3,5-dimethoxy, 2,5-dimethoxy, and 3,4,5-trimethoxyphenyl moieties as A rings (Fig. 24).

Retrosynthetic analysis. The preparation of sulfonamides will be approached by the reaction between a sulfonyl chloride and the corresponding aromatic amines. The modifications at the highly reactive indole 3-position will be further conducted on the sulfonamide scaffold, as well as substitutions at the

sulfonamide nitrogen. An analogous methodology is proposed for tetrazole derivatives. Since the tetrazole moiety is prepared from its counterpart amide, we will first form the amide bond between carboxylic acids and aromatic amines. The modifications at the indole 3-position will be pursued on both tetrazole and amide scaffolds (Fig. 25).

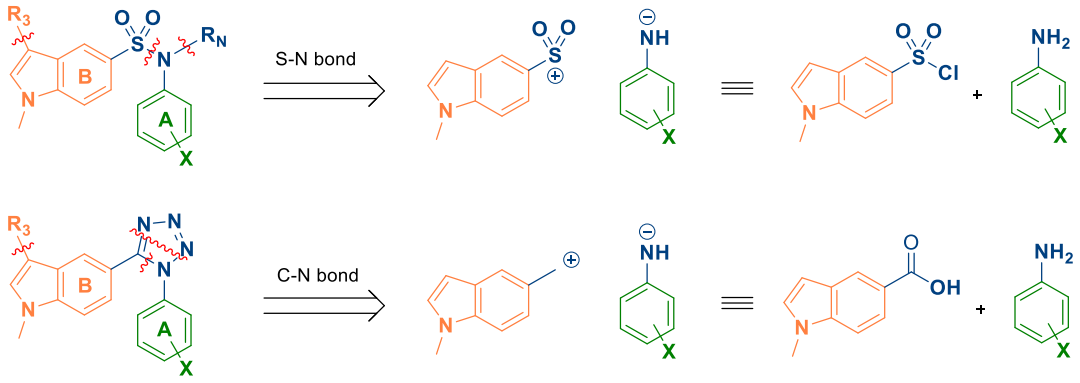

Figure 25. Retrosynthetic analysis of the proposed scaffolds into synthons. Sulfonamides will be formed between sulfonyl chlorides and amines. Tetrazole rings will be obtained from amides, in turn constructed between carboxylic acids and amines. A similar procedure will be followed for sulfonamides and tetrazoles with reversed orientation. Afterward, the modification of the sulfonamide nitrogen and the indole 3-position will be pursued. The structural moieties are colored according to the zone they are aimed to occupy: **orange** for zone 1 (B ring), **green** for zone 2 (A ring), and **blue** for the bridge. The disconnections between bonds are shown in **red**.

B. Design of molecules aimed to bind at zones 2-3 – Analogues of MI-181

Senese *et al.* identified the benzothiazole MI-181 as a tubulin targeting drug.[507] Its X-ray structure in complex with tubulin showed the interaction with zones 2 and 3 of the colchicine domain, lacking direct contacts with the α-tubulin (PDB ID: 4YJ2).[147] The binding of MI-181 in a deeper region of the β-tubulin completely differs from that of CA4, which interacts with zones 1-2 closer to the α subunit. Nevertheless, the benzothiazole group of MI-181 occupies zone 2, as does the 3,4,5-trimethoxyphenyl residue of CA4 (Fig. 26). There is a common feature among the ligands that bind to zones 2-3 of the colchicine domain: their extended and flattened conformation to fit into that deeper region of the pocket. Intending to mimic the binding pose of MI-181, herein we raise the design of two distinct series of compounds (Fig. 27).

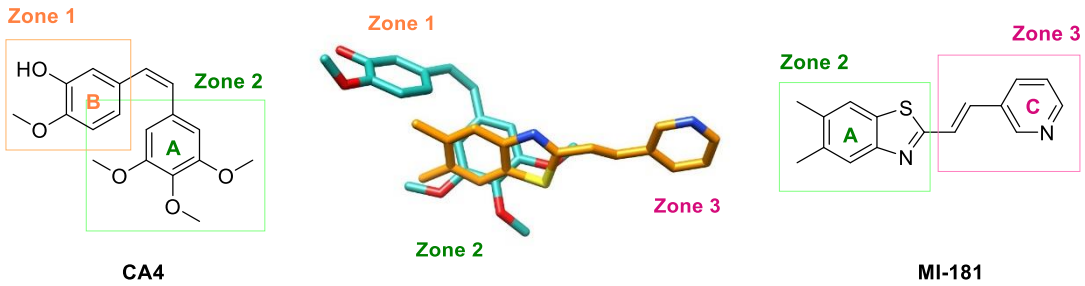

Figure 26. Chemical structures of CA4 and MI-181. Their binding poses in their respective X-ray complexes are superimposed in the middle. CA4 is colored in **blue**, and MI-181 in **orange**.

On the one hand, we propose hybrid molecules between CA4 and MI-181. We will preserve the trimethoxyphenyl ring of CA4 in replacement of the benzothiazole ring of MI-181, although with altered anchoring. A 2,3,4-trimethoxy substitution pattern will be studied instead of a 3,4,5-trimethoxybenzene. This arrangement intends to direct the additional ring towards the deeper zone 3 of the colchicine domain. The first choice as the moiety to bind the zone 3 will be a pyridine ring as that of MI-181, with an additional amino group to explore its derivatization. The *trans*-olefin of MI-181 will be replaced by an amide, which exhibits similar geometry, increases the aqueous solubility, and provides additional interacting sites with the protein. Further modifications will be conducted: alteration of the methoxy groups position, linkers other than amide, or replacement of the pyridine ring by other alternatives.

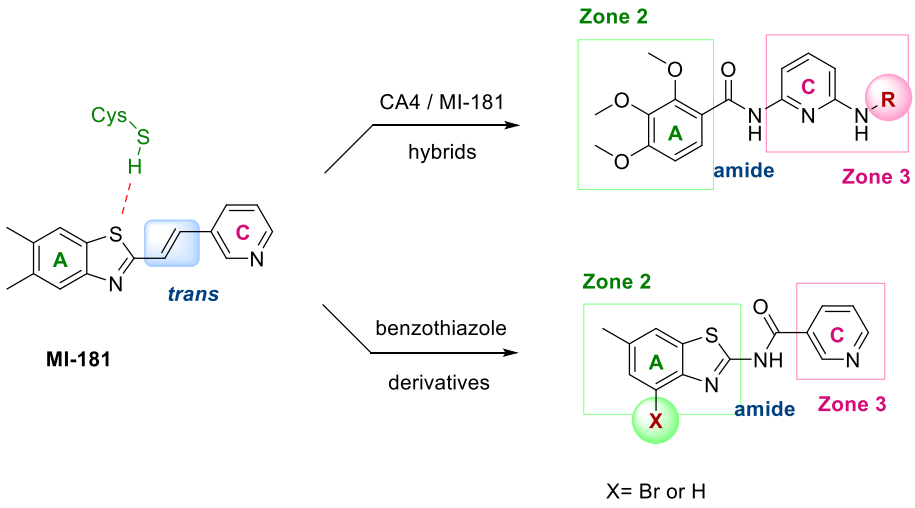

Figure 27. Proposed scaffolds aimed to bind at zones 2-3 of the colchicine domain. These compounds are structurally related to MI-181. The first scaffold consists of an amide bridging a polymethoxylated A ring (different possibilities) and a C ring aimed to bind at zone 3. The second scaffold preserves the benzothiazole core as in MI-181 with an amide linker (also urea, carbamate, and alkyl amine) instead of the *trans* olefin.

The thiazole ring is in close proximity to the thiol group of the cysteine C241β in zone 2, frequently proposed to hydrogen bonds with many ligands that bind to the colchicine domain. It suggests a weak interaction between an acceptor thiazole sulfur and a donor thiol group.[147] Thus, we propose novel benzothiazole derivatives carrying only one methyl group with an extra bromo substituent directed towards the bridge region. The *trans*-olefin between the benzothiazole and pyridine rings in MI-181 will be replaced by planar amides or longer linkers (carbamate, urea, alkylamine) that may increase the aqueous solubility of the compounds. Aside from the edging pyridine, we will also probe for alkyl chains or a phenyl ring.

Retrosynthetic analysis. The formation of the linker between the moieties that would putatively occupy zones 2 and 3 will be conducted depending on the linker nature (Fig. 28). For zone 2, we will use 2-aminobenzothiazole (brominated or not) or polymethoxylated carboxylic acids. The other fragment will be a carboxylic acid or an aromatic amine (for amides), an isocyanate (for ureas), a chloroformate (for carbamates), or an aldehyde (for alkylamines). The derivatization of the unsubstituted amino group on the C ring will be carried out as the last step.

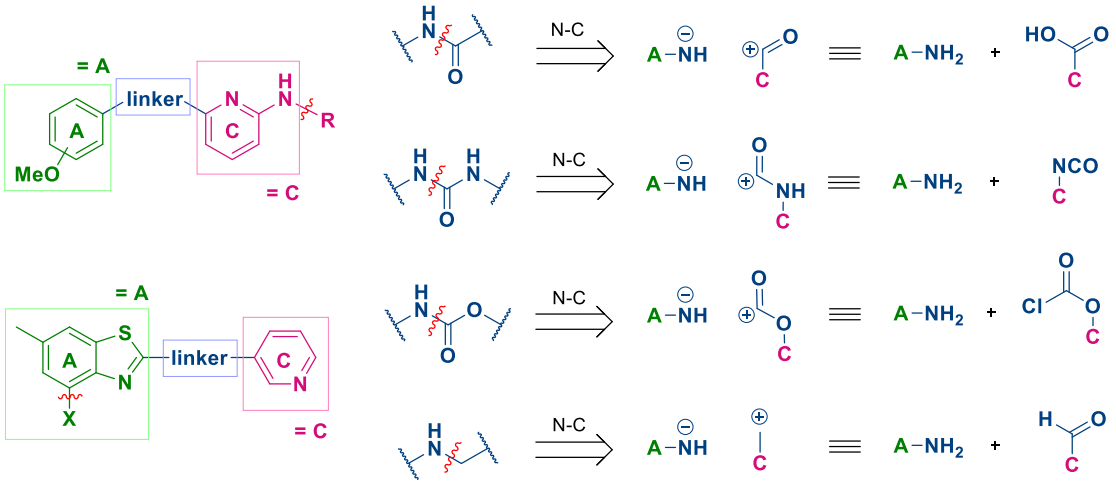

Figure 28. Retrosynthetic analysis of the proposed scaffolds into synthons. The structural moieties are colored according to the zone they are aimed to occupy: **green** for zone 2 (A ring), **pink** for zone 3 (C ring) and **blue** for the linker. The disconnections between bonds are shown in **red**.

C. Design of molecules aimed to bind at zones 1, 2, and 3 – Analogues of ABT-751

Among the three compounds that bind to the three zones of the colchicine domain, ABT-751 and MT189 show structural similarity and occupy zones 1 and 2, and zone 3 partially, whereas lexibulin occupies zone 3 and partially zones 1 and 2. Lexibulin shows very little similarity with other ligands of the colchicine domain, making it difficult to use for the design of molecules aimed to bind at zones 1, 2, and 3.

We have therefore selected the synthetic sulfonamide ABT-751 as a template to design novel ligands. It underwent phase II clinical trials, although did not prove effective enough to reach phase III.[508–510] In contrast to the majority of drugs used in cancer chemotherapy, ABT-751 allows oral administration, an enormous advantage. ABT-751 and CA4 share a 4-methoxyphenyl moiety as B ring (zone 1). The 2,3-disubstituted pyridine (A ring) interacts with zone 2, coinciding with the trimethoxybenzene group of CA4. However, the phenolic ring (C ring) of ABT-751 is buried deeper than colchicine in the β-subunit. The superimposition of ligand complexes that occupy zones 2-3 (e.g. nocodazole) with ABT-751 suggests that different substitution patterns regarding the pyridine ring may ease the access to zone 3 (Fig. 29). We propose analogues of ABT-751 as follows (Fig. 30):

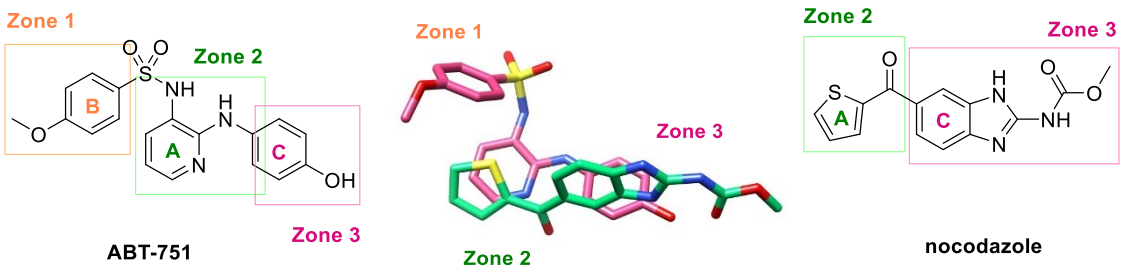

Figure 29. Chemical structures of ABT-751 and nocodazole. Their binding poses in their respective X-ray complexes are superimposed in the middle. ABT-751 is colored in **pink**, and nocodazole in **green**.

B ring. ABT-751 has a 4-methoxybenzene group as B ring that binds to zone 1. This moiety will be preserved in the novel ligands for two main reasons. First, it is also present in potent compounds (e.g. CA4) that bind to the colchicine domain. The second reason falls in practicality. The synthetic route to obtain the final compounds implies several steps. Hence, the 4-methoxybenzenesulfonyl chloride is a right choice as starting material as it is commercially available.

Bridge. The sulfonamide group confers ABT-751 optimal pharmacokinetic properties and contributes to the oral bioavailability of this drug. As mentioned before, biaryl sulfonamides prefer a folded conformation, the one locked in tubulin-ABT-751 crystals. Therefore, we will use the sulfonamide to bridge B and A rings.

A ring. To explore the geometry required so that the capping groups on the C ring may access the deepest region of the domain, we will alter the substitution pattern exhibited by ABT-751 regarding the A ring. In replacement of the 2,3-diaminopyridine, we will probe for 1,3-diaminobenzene and 2,6-diaminopyridine. Both options might putatively confer akin geometry, although the presence of a CH over a nitrogen could modify the pharmacokinetic properties. Although different from that of ABT-751, the 1,3-disubstituted A ring may confer proper geometry, so that the C ring points towards the deep zone 3.

C ring. This substitution is based on ligands of zone 3 such as TN16 because the phenolic ring in ABT-751 barely contacts the zone 3. Initially, we chose phenyl groups in view to their similarity with other zone 3 ligands. To afford fully access, the novel ligands will harbor different-length linkers between A-C rings to confer flexibility besides improved aqueous solubility: benzylamines, benzamides, phenylacetamides, or phenylsulfonamides. We will explore several substituents on the C ring to establish hydrogen bonds with the residues of the deepest region of the cavity, which is enriched in polar residues compared to the highly hydrophobic nature of zones 1 and 2.

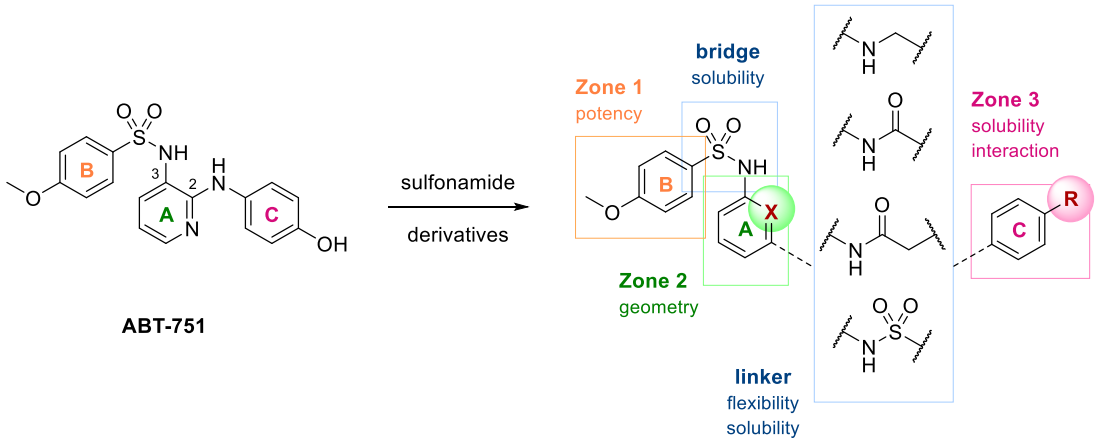

Figure 30. Proposed general scaffold structurally related to ABT-751 to bind at zones 1-2-3 of the colchicine domain. The novel compounds will harbor a conservative 4-methoxybenzene sulfonamide core with a *meta* disubstituted benzene or its counterpart pyridine moiety. Different linkers between A and C rings will permit to explore the adaptability of the domain and to give access to zone 3.

Retrosynthetic analysis. The conservative biaryl core (rings B and A) will be constructed in the first place by a reaction between 4-methoxybenzenesulfonyl chloride and the corresponding amine. This amine might have already been linked to the C ring. Then, the other amino group not engaged in the sulfonamide bond will be modified to generate the four series of compounds corresponding to the four different linkers between A-C rings. The substituent on the C ring will be further modified (Fig. 31).

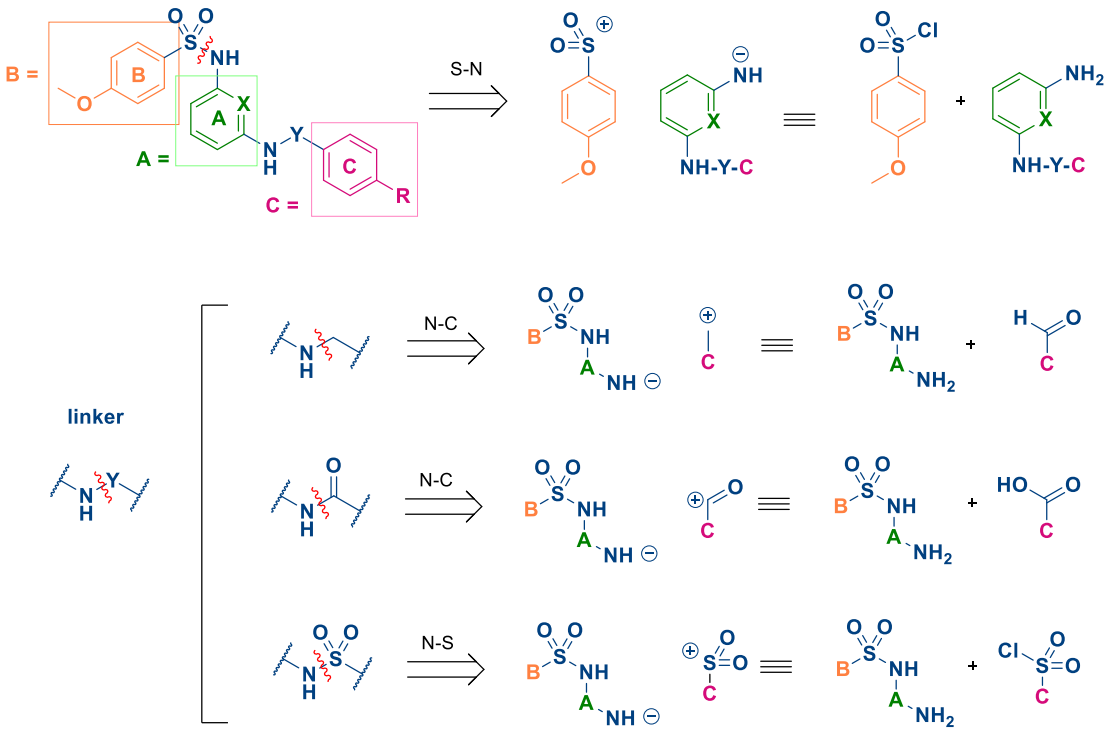

Figure 31. Retrosynthetic analysis of the proposed scaffolds into synthons. The structural moieties are colored according to the zone they are aimed to occupy: **orange** for zone 1 (B ring), **green** for zone 2 (A ring), **pink** for zone 3 (C ring) and **blue** for the sulfonamide bridge and the linker between rings A-C. The disconnections between bonds are shown in **red**.

As depicted in the retrosynthetic analysis, there are many reaction types shared between the different structural families. For an easier understanding of the results concerning the synthesis of the ligands, the compounds will be classified by synthetic analogy into sulfonamides (intended to bind at zones 1-2 and zones 1-2-3), tetrazoles (zones 1-2), amides containing a polymethoxylated benzene (zones 2-3), and benzothiazole derivatives (zones 2-3).

OBJECTIVES

First objective. Design, synthesis, and characterization of novel compounds aimed to bind to the colchicine domain in β-tubulin. This chemistry section will be disclosed in the chapter "Results I".

- ✓ To synthesize sulfonamides and related compounds.
- ✓ To synthesize tetrazoles and their amide precursors.
- ✓ To synthesize amides, ureas, and carbamates.
- ✓ To prepare benzothiazole derivatives.

Second objective. Study of the antitumor potential and mechanism of action underlying treatment with the compounds resulting from the first objective. The experiments conducted for this purpose will be disclosed in the chapter "Results II". This second general objective gathers the following specific aims:

- ✓ To evaluate the *in vitro* antiproliferative activity of the synthesized compounds against tumor and non-tumorigenic cell lines, and to establish a structure-activity relationship (SAR).
- ✓ To examine the effect of the compounds on mitotic microtubules and to elucidate whether tubulin is the molecular target behind the observed drug response.
- ✓ To study whether the compounds exert antivascular effects *in vitro* using endothelial cells.
- ✓ To characterize the cell death mechanism upon treatment and the interplay thereof: apoptosis (type I), autophagy (type II), or necrosis (type III).
- ✓ To evaluate whether the effect of the compounds *in vitro* can be reversed.

Chapter 3

RESULTS I

GENERAL CHEMICAL TECHNIQUES

The chemical section followed a standard workflow. First, the reactions were carried out, each one in specific conditions, according to literature or later optimization. The reaction progress was monitored by TLC unless otherwise indicated. Then, the compounds were isolated by L-L extraction or precipitation, followed by purification thereof using column chromatography, crystallization, or preparative TLC. Isolated compounds were characterized by ^{1}H- and ^{13}C-NMR, IR spectra, HRMS analysis, and melting points (just for crystals). Additionally, 1D-nOe and 2D-homonuclear (COSY, NOESY, TOCSY) or heteronuclear (HSQC, HMBC) experiments confirmed the structural proposals or assisted in signal assignments. Chemical results are divided into four main groups:

- ✓ Synthesis of sulfonamides and related compounds.
- ✓ Synthesis of tetrazoles and their amide precursors.
- ✓ Synthesis of amides, ureas, and carbamates.
- ✓ Preparation of benzothiazole-based derivatives.

SYNTHESIS OF SULFONAMIDES AND RELATED COMPOUNDS

The sulfonamides were designed to bind to zones 1-2 (analogues of CA4), or zones 1-2-3 (analogues of ABT-751) of the colchicine domain. This first section thus clusters compounds with a sulfonamide moiety linking either two monocyclic rings (benzene-benzene [scaffold **A**] or benzene-pyridine [scaffold **B**]), or a bicyclic ring and a monocyclic one (indoline-benzene [scaffold **C**] and indole-benzene [scaffold **D**]) (Fig. 32).

Scaffolds **A** and **B** were individually synthesized, and scaffold **D** was prepared in two steps from scaffold **C** by transformation of the indoline ring. Furthermore, the direction of the sulfonamide bridge within scaffold **D** was also reverted, with the sulfur right next to the benzene and the nitrogen directly bound to the indole. In that case, the resulting compounds do not derive from scaffold **C** but an indole-based starting material.

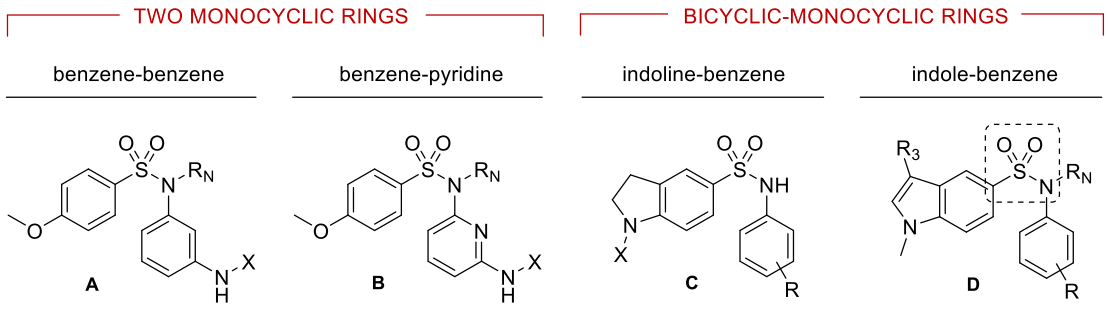

Figure 32. General chemical structures of sulfonamide derivatives. Sulfonamides linking two monocyclic rings are divided into benzene-benzene (scaffold **A**) and benzene-pyridine (scaffold **B**) sub-types. Concerning sulfonamides linking a bicyclic ring and a monocyclic one, there are indoline-benzene (scaffold **C**) and indole-benzene (scaffold **D**) derivatives, the latter directly synthesized from their indoline-benzene counterparts (scaffold **C**).

The sulfonamide bond was formed by a reaction between a sulfonyl chloride and a primary aromatic amine in the presence of a base: triethylamine, pyridine, or $NaHCO_3$ (Fig. 33).[511] Different solvents and conditions were tested to optimize reaction yields, especially in those cases where more than one product might be obtained because of the presence of two amino groups (scaffolds **A** and **B**). Some of the sulfonyl chloride and amine precursors used in the preparation of sulfonamides had to be previously synthesized (see "Preparation of synthetic precursors").

Once the sulfonamide moiety was obtained, four different structural modifications (**SM**) were conducted (Fig. 33), not necessarily exclusive of each other:

- ✓ **SM-1**: Aromatization of indolines (scaffold **C**) to indoles (scaffold **D**) by means of a redox reaction.
- ✓ **SM-2**: Substitutions at the sulfonamide nitrogen (R_N) by alkylation with either short-chain alkanes or bulkier groups (scaffolds **A**, **B**, and **D**).
- ✓ **SM-3**: Substitutions on the aromatic rings (R_2 and/or R_3) and transformation of functional groups (scaffolds **A**, **B**, and **D**).
- ✓ **SM-4**: Appendage of a third aromatic ring (Ar_3) linked through different types of spacers (Z). This modification was pursued for scaffolds **A** and **B**, the analogues of ABT-751 intended to bind to the three regions of the colchicine domain.

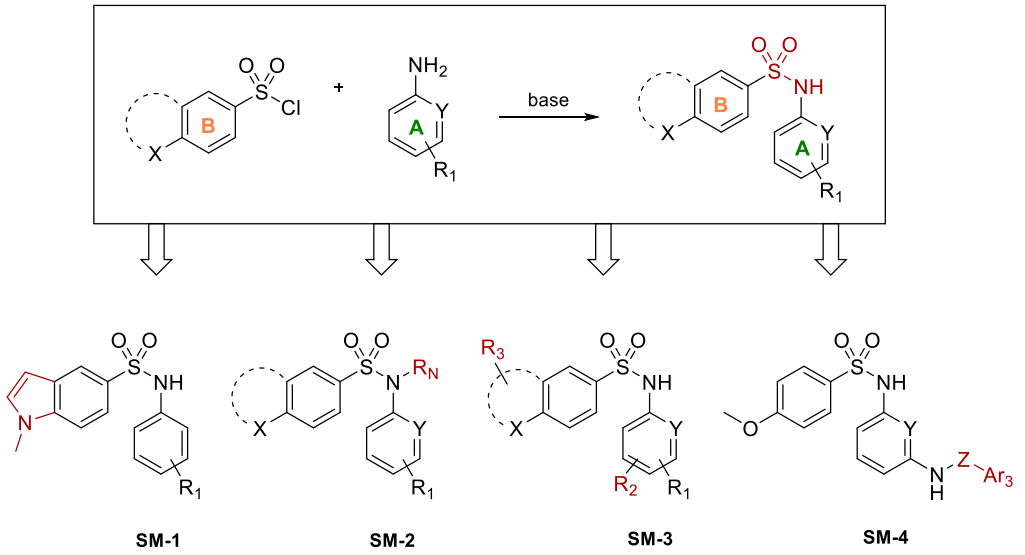

Figure 33. General procedure for the synthesis of sulfonamides and structural modifications following the preparation of the sulfonamide core. **SM-1**: Aromatization of indolines to indoles. **SM-2**: Alkylation of the sulfonamide nitrogen (R_N). **SM-3**: Substitutions on the aromatic rings (R_2 and R_3). **SM-4**: Incorporation of a third aromatic ring (Ar_3) bound through different linkers (Z). Structural changes are marked in **red**. The ring aimed to bind at zone 1 is indicated in **orange** (B ring), and the one aimed to bind at zone 2 in **green** (A ring).

Preparation of synthetic precursors

Some of the starting materials needed for preparing scaffolds **C** and **D** were not available and had to be synthesized from simpler compounds (Fig. 34).

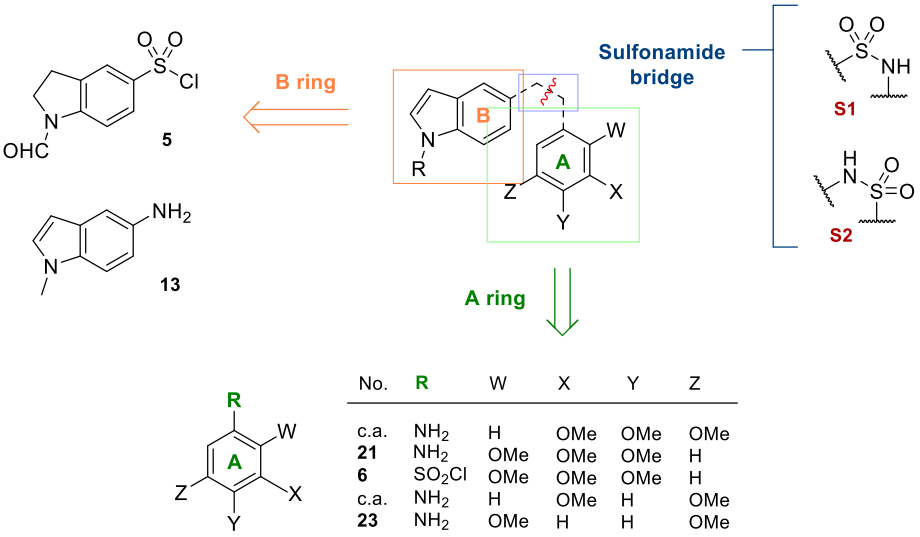

Figure 34. General chemical structure of indole-sulfonamides and summary of the reagents used in their preparation (scaffolds **C** and **D**). The starting materials **5** and **13** were synthesized as **B rings**, and compounds **21**, **6**, and **23** as **A rings**. We considered two different **sulfonamide bridges**: the sulfur linked to the **B ring** (bridge **S1**), and alternatively, to the **A ring** (bridge **S2**). c.a.= commercially available.

A. Preparation of sulfonyl chlorides 5 and 6

Indoline-sulfonamides (scaffold **C**, **S1**) were prepared from the synthetic precursor **5** by reaction with the corresponding amines (Fig. 34). The preparation of indole-sulfonamides (scaffold **D**) with **S2** bridges required the sulfonyl chloride on the A ring (**6**) to react with amine **13** (Fig. 34).

The sulfonyl chloride is needed in position 5 of indoline to obtain the sulfonamides **S1**. The chlorosulfonation step has to be conducted on indolines rather than indoles because the sulfonyl chloride would be introduced at position 3 of indole, which is the most reactive one in electrophilic aromatic substitution reactions. In indolines, the reaction should occur at position 5 due to the directing effect of the nitrogen. Two options were considered for that purpose (Scheme 1): i) to attempt a direct functionalization of indoline by electrophilic aromatic substitution with chlorosulfonic acid, or ii) the formation of indoline amides (acetyl or formyl) to mask the nucleophilicity and basicity of the amino group, followed by the functionalization at position 5.

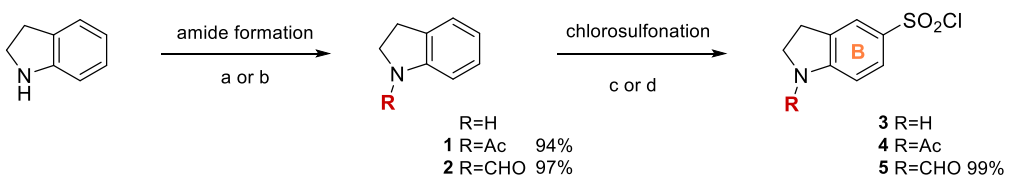

Scheme 1. Preparation of compounds **1**-**5**. Reagents and conditions: (a) Ac_2O, CH_2Cl_2, rt, 15 min. (b) HCOOH, CH_2Cl_2, rt, 22 h. (c) HSO_3Cl, CH_2Cl_2, 4 °C, 6 h, N_2. (d) HSO_3Cl, $SOCl_2$, 1,2-dichloroethane, 4-70 °C, 5 h, N_2.

The reaction of indoline with chlorosulfonic acid did not provide indoline-5-sulfonyl chloride **3** (Scheme 1). This may occur because the amine reacts with chlorosulfonic acid or by protonation of the amine that reduces the nucleophilicity of the aromatic ring. Indoline acetylation (**1**) and formylation (**2**) were carried out to later introduce the sulfonyl chloride at position 5 with chlorosulfonic acid (**4** and **5**). Formyl product **2** can be directly reduced to methyl. In the case of the acetyl derivative **1**, deacetylation is required previously to the methylation of the NH group once formed the indole ring.

Acetylation and formylation of indoline provided **1** and **2** in excellent yields (94-97%), respectively, as the mixture of two rotamers because of the slow rotation of the amide bond. This observation additionally applies to all *N*-formylindoline compounds (**5**, **78**, **101**, and **120**). The major formyl isomer is the one with the hydrogen near the aromatic ring (*E*), in 3:1 proportion (Fig. 35). Given that formamides have planar geometry, the ring current effect deshields the formyl proton of the major isomer (8.95 ppm in *E*-**2**), and not the minor one (8.46 ppm in *Z*-**2**). For the same reason, the proximity between the electron pair of the minor carbonyl group and the H7 proton reduces the shielding of H7 (7.95 ppm in *Z*-**2** versus 7.33 ppm in *E*-**2**). DFT calculations of the two rotamers in CH_2Cl_2 found the *E*-**2** isomer as more stable than the *Z*-**2** isomer by 2.86 kJ/mol, in line with the NMR data.

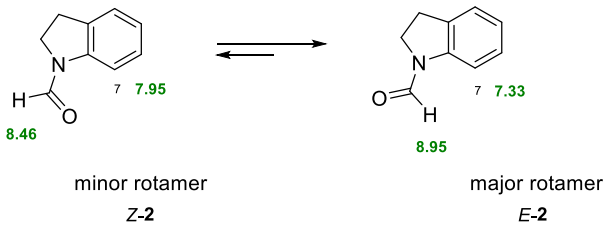

Figure 35. Equilibrium between *E*-**2** and *Z*-**2** rotamers. (*E*)-*N*-formyl-indolines were obtained in major proportion than (*Z*)-*N*-formyl-indolines. ^{1}H-NMR chemical shift values (ppm) in $CDCl_3$ are indicated in **green**.

In the case of the acetamide, *Z*-**1** was obtained as the major rotamer in ten-fold higher proportion than *E*-**1**, with less noticeable differences in chemical shifts. This agrees with DFT calculations predicting a difference in stability by 3.20 kJ/mol. Although chlorosulfonation of **1** did not provide indoline **4**, compound **2** led to sulfonyl chloride **5** in excellent yield (99%).[210]

Chlorosulfonation of 1,2,3-trimethoxybenzene produced 2,3,4-trimethoxybenzenesulfonyl chloride **6** (Scheme 2). The chlorosulfonation position can be deduced by the *ortho* coupling constants between the two aromatic protons. This position is the most activated in electrophilic aromatic substitutions but the opposite regiochemistry to what has been observed in the nitration reaction on the same substrate.

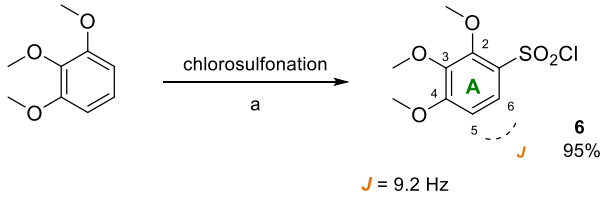

Scheme 2. Preparation of compound **6** as **A ring**. Reagents and conditions: (a) HSO_3Cl, $SOCl_2$, 1,2-dichloroethane, 4 °C-rt, 2 h, N_2. The coupling constant (*J*) is indicated in **orange**.

B. Preparation of amines 13, 21, and 23

Indole amine **13** and anilines **21** and **23** (Fig. 34) were prepared from nitro derivatives **12**, **18**, and **22**, respectively.

5-Aminoindoles were needed to obtain *N*-indol-5-yl-benzene sulfonamides. In a similar way to the strategy followed in the chlorosulfonation of indolines, we conducted the nitration of indoline, *N*-acetyl (**1**) and *N*-formyl (**2**) indolines to prepare compounds **7**, **8**, and **10**, respectively (Scheme 3). Neither 5-nitroindoline (**7**) nor 5-nitroindoline-1-carbaldehyde (**10**) were obtained. Compound **8** was obtained in good yield (72%), and also compound **9** (12%), nitrated at position 7 (Scheme 3). Attempts to aromatize the mixture of regioisomers were unsuccessful.

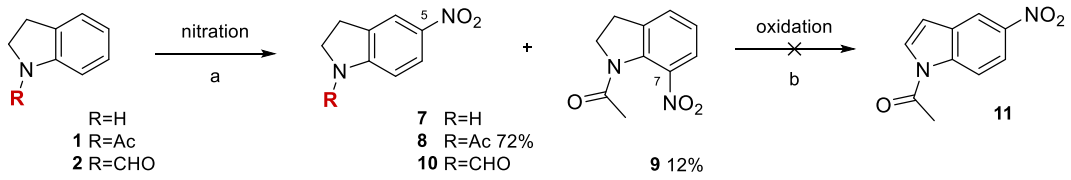

Scheme 3. Preparation of compounds **7-11**. Reagents and conditions: (a) HNO_3, AcOH or CH_2Cl_2, 4 °C, 9 h-5 days. (b) DDQ, toluene/CH_2Cl_2 or dioxane, rt-reflux, 7 days.

Amine **13** was eventually obtained from commercial 5-nitroindole (Scheme 4). The indole amino group is weakly acidic and was methylated by nucleophilic substitution in basic media. Previous studies had shown that an *N*-methyl group potentiates the inhibitory effect of indole-based combretastatins and phenstatins on the *in vitro* tubulin polymerization.[501,506] The *N*-methylation of 5-nitro-1*H*-indole to provide **12** was conducted in acetonitrile with KOH to form the anion and methyl iodide as the alkylating agent. The use of ACN and KOH allowed us to avoid the phase transfer catalyst that makes the purification more difficult.

The methylation of 5-nitroindole to **12** and the subsequent catalytic hydrogenation to **13** provided the products in quantitative yields (99%) and did not require further purification (Scheme 4). Compound **13** displays IR bands in 3407 and 3335 cm^{-1} that correspond to stretching vibrations of N-H bonds. The reduction of the nitro to the amino group shields protons H4 and H6 that move upfield from 8.13/8.59 ppm to 6.69/6.92 ppm (Scheme 4).

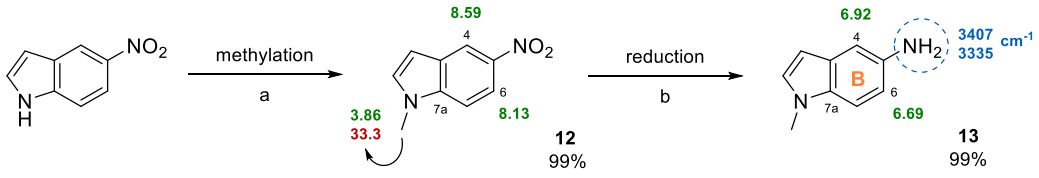

Scheme 4. Preparation of **13** as **B ring**. Reagents and conditions: (a) CH_3I, KOH, ACN, rt, 24 h, N_2. (b) Pd/C, EtOAc/MeOH, rt, 14 h, H_2. IR vibrational frequencies of the amino group are in **blue**, ^{1}H-NMR chemical shift values (ppm) in **green**, and ^{13}C-NMR chemical shift values (ppm) in **red**.

Aniline **21** is required to obtain the sulfonamides **S1** with a 2,3,4-trimethoxyphenyl ring. We attempted the nitration of 1,2,3-trimethoxybenzene because its chlorosulfonation gave the substituted product at position 4, but the nitration reaction instead gave 1,2,3-trimethoxy-5-nitrobenzene (**19**). Then, we attempted the nitration of 5-bromo-1,2,3-trimethoxybenzene because the aimed position is the one available, but it gave mixtures.

In light of these results, we nitrated 2,3-dimethoxyphenol (Scheme 5). The phenol is the directing group in the nitration reaction. Whether it directs to *ortho* (**16**, major regioisomer, 6:4) or *para* (**17**) positions, both provided the same product after methylation of the phenol group (**18**), so they were not separated one from the other. The reduction of the nitro group was conducted in hydrogen atmosphere leading to compound **21** in 91% yield. The chemical shifts of its aromatic protons are upfield compared to those observed for nitro compound **18**, especially the *ortho* proton with respect to the amino group (7.69 versus 6.52 ppm).

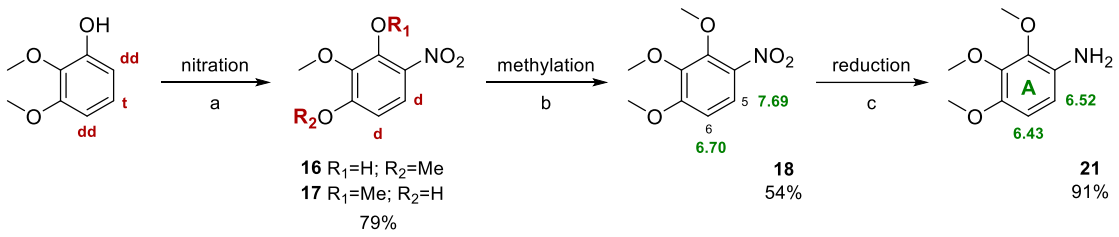

Scheme 5. Preparation of **21** as **A ring**. Reagents and conditions: (a) HNO_3, AcOH, CH_2Cl_2, 4 °C, 72 h. (b) $(CH_3O)_2SO_2$, K_2CO_3, acetone, 50 °C, 21 h, N_2. (c) Pd/C, CH_2Cl_2/MeOH, rt, 72 h, H_2. ^{1}H-NMR chemical shift values (ppm) are in **green**, and the splitting pattern is indicated in **red**.

2,5-Dimethoxyaniline (**23**) was obtained in excellent yield from 1,4-dimethoxybenzene by nitration (**22**), followed by hydrogenation of the nitro to an amino group (Scheme 6). The mono-nitration of symmetric 1,4-dimethoxybenzene implies an alteration of the ^{1}H-NMR splitting pattern in **22** (non-symmetric product). The formation of aniline **23** can be checked by IR bands of the amino group and the shielding of the aromatic protons (Scheme 6).

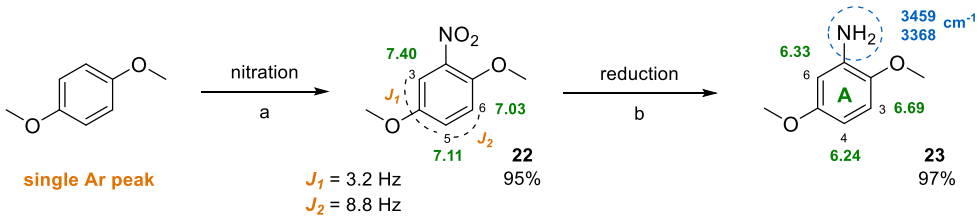

Scheme 6. Preparation of **23** as **A ring**. Reagents and conditions: (a) HNO_3, AcOH, 4 °C, 30 min. (b) Pd/C, EtOAc/MeOH, rt, 6 days, H_2. IR vibrational frequencies of the amino group are in **blue**, ^{1}H-NMR chemical shift values (ppm) in **green** and coupling constants (*J*) are indicated in **orange**.

Formation of the sulfonamide bond

Sulfonamides were synthesized from sulfonyl chlorides and primary aromatic amines (Table 4). This reaction releases HCl, which needs to be neutralized with a base. We employed pyridine or triethylamine in monophasic reactions, or $NaHCO_3$ for biphasic reactions.[511] Table 4 collects the conditions tested in the preparation of sulfonamides, as well as byproducts obtained in the reaction, if applicable.

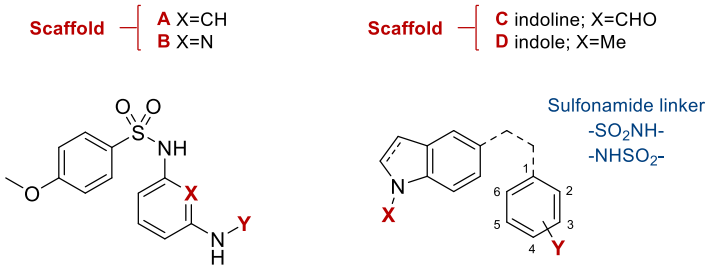

No.	Scaffold	Linker	Y	Solvent	Base	Conditions	Yield	Byproduct
35	**A**	SO_2NH	H	CH_2Cl_2	pyr	rt, 24 h	31%	**36** (67%)
35	**A**	SO_2NH	H	CH_2Cl_2	Et_3N	rt, 16 h	81%	**36** (7%)
35	**A**	SO_2NH	H	MeOH	Et_3N	rt, 24 h	76%	**36** (10%)
38	**A**	SO_2NH	4-NO_2PhSO_2	CH_2Cl_2	Et_3N	rt, 17 h	39%	**39-41** (5-26%)
62	**B**	SO_2NH	H	CH_2Cl_2	pyr	rt, 4 h	no reaction	
62	**B**	SO_2NH	H	MeOH	Et_3N	rt-Δ, 72 h	no reaction	
62	**B**	SO_2NH	H	CH_2Cl_2	Et_3N	Δ, 24 h	78%	**63** (15%)
65	**B**	SO_2NH	4-NO_2PhSO_2	CH_2Cl_2	Et_3N	rt-Δ, 96 h	complex spectra	
78	**C**	SO_2NH	3,4,5-$(MeO)_3$	EtOAc/H_2O	$NaHCO_3$	rt, 4 h	83%	none
98	**C**	SO_2NH	2,3,4-$(MeO)_3$	EtOAc/H_2O	$NaHCO_3$	rt, 4 h	no reaction	
99	**D**	$NHSO_2$	2,3,4-$(MeO)_3$	CH_2Cl_2	Et_3N	rt, 24 h	47%	none
101	**C**	SO_2NH	3,5-$(MeO)_2$	EtOAc/H_2O	$NaHCO_3$	rt, 14 h	77%	none
101	**C**	SO_2NH	3,5-$(MeO)_2$	CH_2Cl_2	pyr	rt, 19 h	91%	none
120	**C**	SO_2NH	2,5-$(MeO)_2$	EtOAc/H_2O	$NaHCO_3$	rt, 6 h	79%	none

Table 4. General chemical structures of the synthesized sulfonamides. The table summarizes the conditions tested in the synthesis of each derivative and the result: yield of the desired product and whether some other byproduct was obtained in the synthetic process.

The reaction of 4-methoxybenzenesulfonyl chloride with diamines (*m*-phenylenediamine or 2,6-diaminopyridine) gave sulfonamides **35** and **62**, but also disulfonamides **36** and **63**, respectively (**SM-4**), due to the reaction between two molecules of sulfonyl chloride per molecule of diamine.

Sulfonamide and disulfonamide derivatives can be distinguished by the integration of ^{1}H-NMR signals and the splitting pattern of the diamine A ring. ^{1}H-NMR spectra of disulfonamides show that the signals corresponding to 4-methoxyphenyl groups have twice relative intensity than monosulfonamides with respect to the protons of the pyridine ring (Fig. 36). The aromatic protons of the A ring H3' and H5' are different in monosulfonamides and chemically equivalent in disulfonamides (Fig. 36).

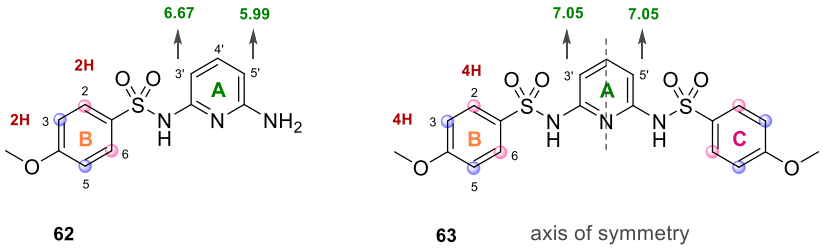

62 63

Figure 36. Chemical structures of compounds **62** and **63**. ^{1}H-NMR chemical shift values (ppm) are indicated in **green**, and the relative integral of the B ring protons are in **red**. The protons that are chemically equivalent are indicated by balls of the same color (**blue** or **pink**). This likewise applies to **35** versus **36**.

To minimize the formation of disulfonamides, we added the sulfonyl chloride dropwise to an excess of the diamine in order to keep a low local concentration of sulfonyl chloride. The ratio between mono/di sulfonamides thus varies depending on the experimental conditions (Table 4).

When using pyridine as a base in the preparation of **35** (Table 4, row 1), *m*-phenylenediamine precipitated. The ratio of sulfonyl chloride per diamine goes up, thus favoring the formation of **36** in 67% yield over 31% of **35**. Pyridine is not basic enough to prevent the protonation of *m*-phenylenediamine and keep it in solution. The use of a stronger base such as triethylamine reduces the protonation of amines and increases the yield of the monosulfonamide product (Table 4, rows 2-3). Following this synthetic strategy, compound **35** was the major product in CH_2Cl_2 (81%) as in methanol (76%) with 7-10% of **36**, and they were separated from each other by column chromatography or selective crystallization. Similar results were obtained in the preparation of **62**.

The reaction of **35** with *p*-nitrobenzenesulfonyl chloride gave the sulfonation product on the free amino group (**38**). The formation of disulfonamides on the same nitrogen was also observed (Fig. 37, **39**-**41**), even in the presence of an unsubstituted amino group (**40**). This suggests that the higher electrophilicity of *p*-nitrobenzenesulfonyl chloride reduces the chemoselectivity. The structure of disulfonamide **38** was established based on the signals corresponding to the *p*-methoxy and *p*-nitrophenyl rings (doublets at 6.87/7.70 ppm and 7.90/8.20 ppm, respectively), and the non-symmetrical diamine A ring. Compound **39** shows two different *p*-nitrophenyl groups in ^{1}H- and ^{13}C-NMR spectra, only compatible with a sulfonamide on one nitrogen and a disulfonamide on the other. Compound **40** has one *p*-methoxy and one *p*-nitrophenyl group but lacks the signals of the NH groups observed in **38**. Additionally, **41** shows two symmetrical *p*-nitrophenyl rings beside the *p*-methoxyphenyl group.

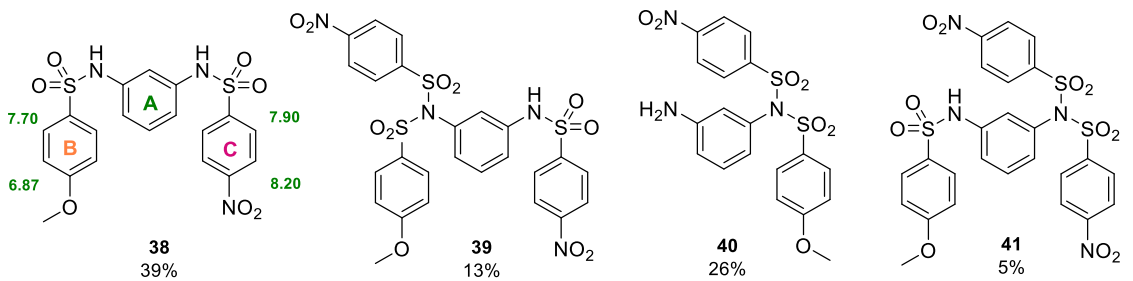

38 39%
39 13%
40 26%
41 5%

Figure 37. Chemical structures of compounds **38**-**41** obtained when treating **35** with *p*-nitrobenzenesulfonyl chloride.

The reaction between sulfonyl chloride **5** and anilines in EtOAc/water provided sulfonamides **78**, **101**, and **120** isolated by precipitation in good yields.[210] The presence of the *N*-formyl results in two sets of signals in the NMR spectra due to the formamide rotamers. The relative area of formyl proton peaks reveals a major *trans* isomer (2:1 proportion), whose chemical shifts (8.93-8.96 ppm) are deshielded compared to those of the *cis* isomer (8.51-8.54 ppm). Signal assignment was based on 2D-NMR experiments: COSY, TOCSY, HSQC, and HMBC. The TOCSY experiment for **120** is shown in Fig. 38, where the cross peaks between the formamide protons represent exchange cross peaks.

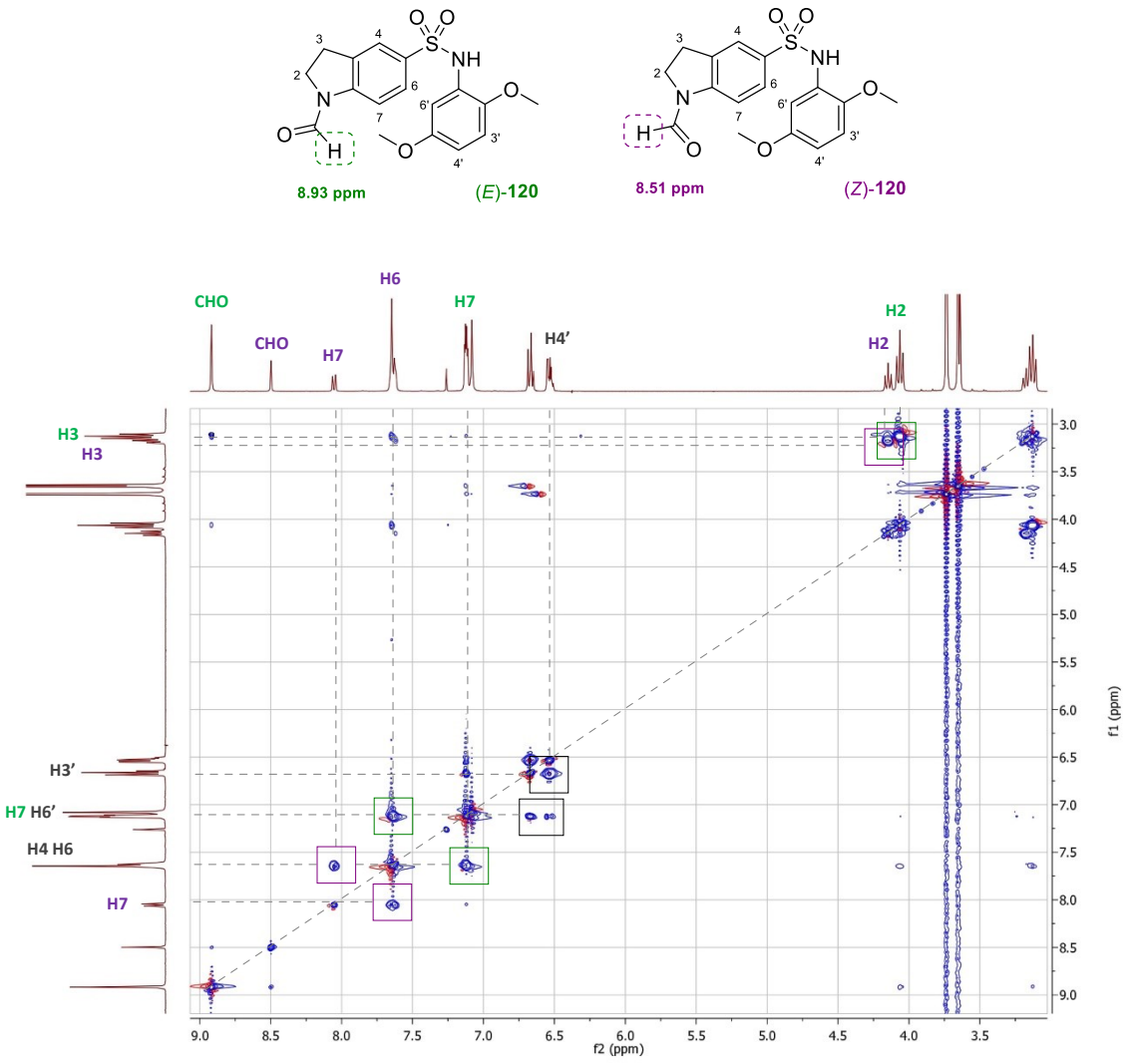

Figure 38. TOCSY experiment of **120**. Cross peaks are generated for protons within the same spin system. **H4'** (X axis) is coupled to **H3'** (Y axis) by 8.8 Hz. Both signals (X axis) correlate with the peak at 7.13 ppm (**H6'**, Y axis). **Black** indicates that no difference was observed in the chemical shift for *trans* and *cis* conformers. **H3'**, **H4'**, and **H6'** are so close that they cannot be resolved. Signals that are specific for (*E*)-**120** signals are in **green**, and (*Z*)-**120** signals are in **purple**. **H7** (X axis) correlates with the multiplet at 7.65 ppm (**H4** and **H6**, Y axis). It has two other cross peaks with **H3'** and **H4'** because **H6'** resonates at the same chemical shift as **H7** (multiplet). *Cis* **H7** (X axis) correlates with the same peak at 7.65 ppm (Y axis, **H4** and **H6**), meaning that **H4** and **H6** resonate as a single peak regardless of the conformer. The diagonal line interconnects the correlation of ^{1}H peaks with themselves.

Modifications on scaffolds A and B

We conducted the following modifications on scaffolds **A** and **B**: methylation of the sulfonamide, the appendage of additional aromatic rings, and substitutions on the aromatic rings.

A. Methylation of the sulfonamide nitrogen (SM-2)

Methylations of **35** and **62** were carried out by nucleophilic substitution using a base to form the anion, which is more nucleophilic to attack the electrophile (methyl iodide). Compound **37** was obtained in homogeneous phase with KOH in acetonitrile and compound **64** with phase transfer catalyst in moderate yields (Scheme 7). The methyl protons resonate at 3.11 and 3.20 ppm for **37** and **64**, respectively.

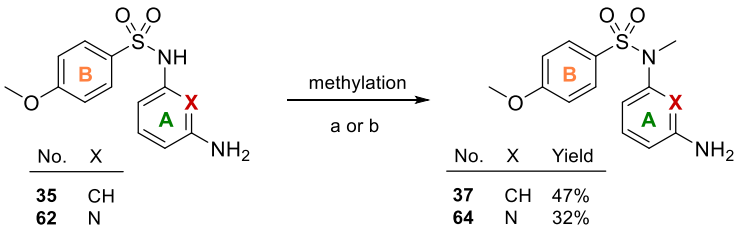

Scheme 7. Preparation of compounds **37** and **64**. Reagents and conditions: (a) CH_3I, KOH, ACN, rt, 3 days, N_2. (b) CH_3I, NaOH, $n Bu_4N^+HSO_4^-$, CH_2Cl_2, rt, 3 days, N_2.

B. Incorporation of a third aromatic ring (SM-4)

A third aromatic ring was appended to the free amine group through spacers other than sulfonamide (for disulfonamides see "Formation of the sulfonamide bond"): methylamines or amides. Two different approaches were attempted for the preparation of these three-ring compounds (Fig. 39): A. Preparation of sulfonamides **35**, **62**, and **64** (step 1), followed by the incorporation of the third ring (step 2). B. Reaction between the diamine (*m*-phenylenediamine or 2,6-diaminopyridine) and an aldehyde (for methylamine spacer) or a carboxylic acid (for amide spacer) (step 1), followed by the formation of the sulfonamide (step 2).

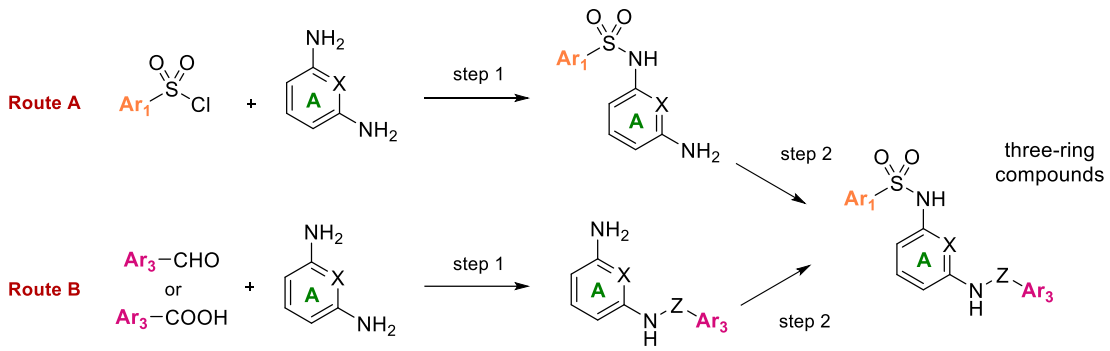

Figure 39. Two approaches were envisioned for the preparation of three-ring compounds. **Route A.** Formation of the sulfonamide bond first, then incorporation of the third aromatic ring (Ar_3). **Route B.** Reductive amination or amide formation with the diamine, followed by reaction with a sulfonyl chloride. The moieties aimed to bind at zones **1**, **2**, and **3** are indicated in **orange**, **green**, and **pink**, respectively.

Benzylamines were formed by reductive amination. The nucleophilic addition of a primary amine to an aromatic aldehyde gives the intermediate imine, subsequently reduced to the corresponding methylamine derivative by treatment with a reducing agent: $NaBH_4$ or $NaBH_3CN$. This procedure can be conducted in one-pot or two steps. Different conditions were tested when preparing derivatives listed in Table 5. The characteristic signal of the reductive amination products is the benzylic methylene at 4.21-4.42 ppm in ^{1}H-NMR and 46.3-46.6 ppm in ^{13}C-NMR spectra.

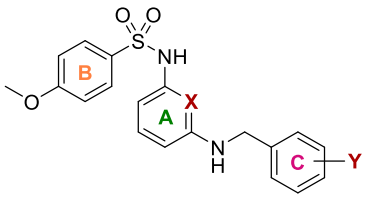

No.	X	Y	Route	Media	Solvent	Conditions	Reducer	Result
43	CH	4-NO_2	**B**	-	CH_2Cl_2	rt	$NaBH_3CN$	mixtures
43	CH	4-NO_2	**B**	HCl	CH_2Cl_2	rt	$NaBH_3CN$	mixtures
43	CH	4-NO_2	**A**	HCl	CH_2Cl_2	rt	$NaBH_3CN$	rearrangement
43	CH	4-NO_2	**A**	-	CH_2Cl_2/MeOH	Δ/4 °C	$NaBH_4$	**43** (97%)
53	CH	4-AcNH	**A**	-	CH_2Cl_2/MeOH	Δ/4 °C	$NaBH_4$	**53** (44%)
67	N	3-NO_2	**B**	HCl	THF	rt-Δ	$NaBH_3CN$	**66** (64%)
68	N	4-NO_2	**A**	HCl	CH_2Cl_2/MeOH	Δ/4 °C	$NaBH_3CN$	no reaction
68	N	4-NO_2	**A**	HCl	THF/MeOH	rt	$NaBH_3CN$	no reaction
69	N	4-AcNH	**A**	HCl	THF	Δ	$NaBH_3CN$	mixtures

Table 5. General chemical structure of the benzylamines. The table summarizes the conditions tested in the preparation of each derivative and the result with the yield of the product if obtained. The **route** refers to the synthetic methodology depicted in Figure 39. **Route A** corresponds to systems with **B**-**A**-**C** rings (step 2), and **route B** corresponds to systems with **A**-**C** rings (step 1).

Firstly, we attempted the preparation of **43** by reductive amination in one-pot (**route B**), but we obtained mixtures of the benzylamine and unreduced imines in neutral and acidic media (Table 5, rows 1-2). Hence, we did not attempt the second step to form the sulfonamide.

Reductive amination of sulfonamide **35** (**route A**, one-pot, row 3) led to Fries-like rearrangement and hydrolysis products (Fig. 40, compounds **44**-**46**). In **44**, there is only one *p*-disubstituted system corresponding to 4-methoxyphenyl with the methyl protons at 3.82 ppm and a 1,3,4-trisubstituted A ring as a result of a Fries-like rearrangement from **35** at the *para* position of the free amino group (Fig. 40). The NMR spectra of **45** and **46** do not show *p*-methoxyphenyl rings, indicating that the sulfonamide was hydrolyzed. **46** is the result of a reductive monoamination on the non-symmetrical A ring, whereas in **45**, the double reductive amination gives a product the NMR spectra of which are consistent with a symmetrical A ring and double relative integral of 4-nitrophenyl moieties. The Fries-like rearrangement takes place when sulfonamide **35** is treated with HCl in the presence of the aldehyde and $NaBH_3CN$.

Compounds **43** and **53** were obtained in two steps. The imine forms slowly and was prepared in refluxing CH_2Cl_2, later reduced with $NaBH_4$ in moderate to good yields (44-97%). More electrophilic aldehydes result in higher yields. Nevertheless, this procedure was unsuccessful for those compounds bearing a pyridine as A ring (Table 5, X=N). Benzylamine **43** shows two pairs or aromatic doublets of *para*-disubstituted benzenes corresponding to *p*-methoxy and *p*-nitrophenyl groups.

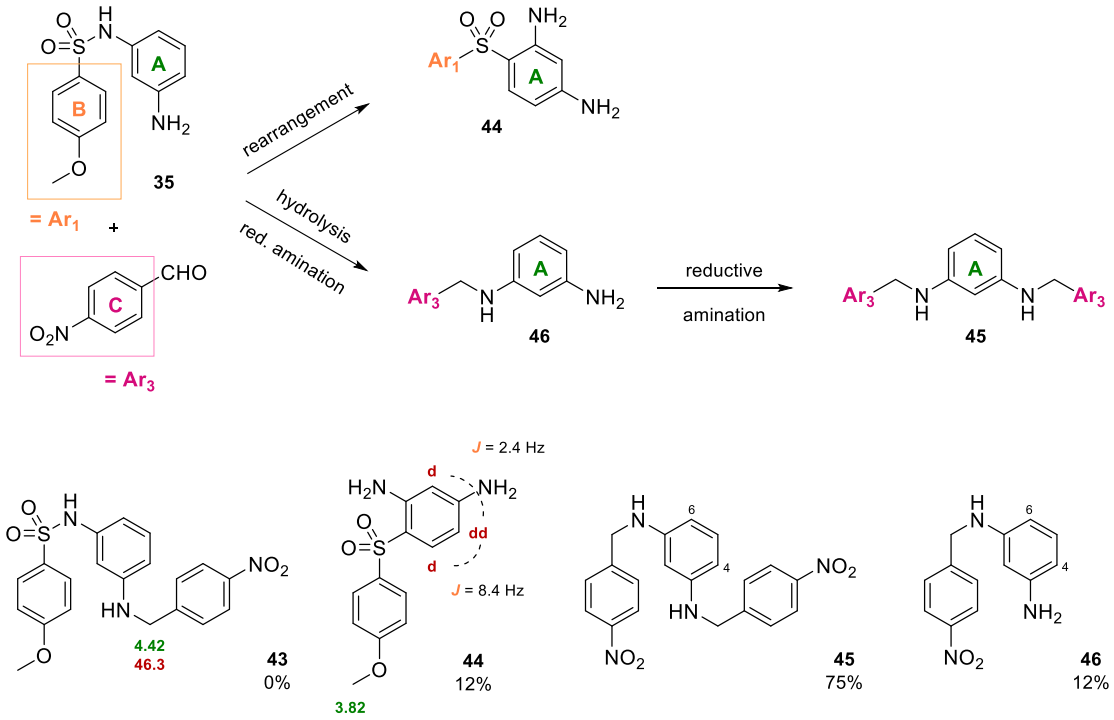

Figure 40. Reductive amination of **35** leading to compounds **44**-**46**. ^{1}H-NMR chemical shifts are in **green**, ^{13}-NMR chemical shifts in **red**, and coupling constants are in **orange**.

The synthesis of derivatives with an amide spacer connecting rings A and C was attempted by the reaction between an aromatic amine (*m*-phenylenediamine, **35**, **62**, or **64**) and carboxylic acids (Table 6). These reactions follow an addition-elimination mechanism and require the previous activation of the acid to increase its reactivity. Two different procedures were used for this purpose: coupling agents or the formation of acyl chlorides (Fig. 41).[512] The formation of the amide bond can be ensured by the carbonyl IR band around 1650 cm^{-1} and the chemical shift around 165-170 ppm in ^{13}C-NMR.

We have used 4-nitro, 4-ureido, and 4-acetamidobenzoic acids, citrazinic acid, and benzimidazole-5-carboxylic acid (Table 6). The acids 4-ureidobenzoic **27** and 4-acetamidobenzoic **29** were prepared from methyl 4-aminobenzoate (Scheme 8). The derivatization of the amino group was carried out first to urea **26** and amide **28** in good yields (80-88%). The urea was prepared by treatment with KOCN at 40 °C, whose carbonyl resonates at 155.9 ppm upfield from that of the ester. The formation of the amide group in **28** was accomplished using acetic anhydride in pyridine, with the methyl protons at 2.20 ppm. Saponification of the methyl ester of **26** and **28** provided free acids **27** and **29**, respectively, with the disappearance of the methyl ester at 3.83 ppm and the deshielding of the carbonyl carbon (Scheme 8).

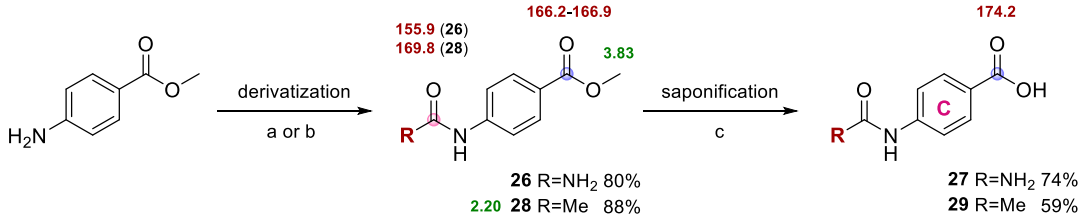

Scheme 8. Preparation of **27** and **29** as **C ring**. Reagents and conditions: (a) KOCN, water/AcOH, 40 °C, 24 h, N_2. (b) Ac_2O, pyr, rt, 4 h. (c) NaOH, MeOH, rt/Δ, 30 min-3 h. ^{1}H-NMR shift values (ppm) are in **green**, and **red** for ^{13}C-NMR.

As our first option, we chose to use coupling agents. It is noteworthy that their reactivity is less than that of acyl chlorides, although more easily handled. We employed 1,1'-carbonyldiimidazole (CDI) or, in most cases, carbodiimides DCI or EDC·HCl. The carboxylate nucleophile that is formed in the presence of *p*-DMAP adds to the carbodiimide to form an intermediate O-acylisourea. The amine reagent is subsequently added, followed by elimination of an activated leaving group as urea (Fig. 41).

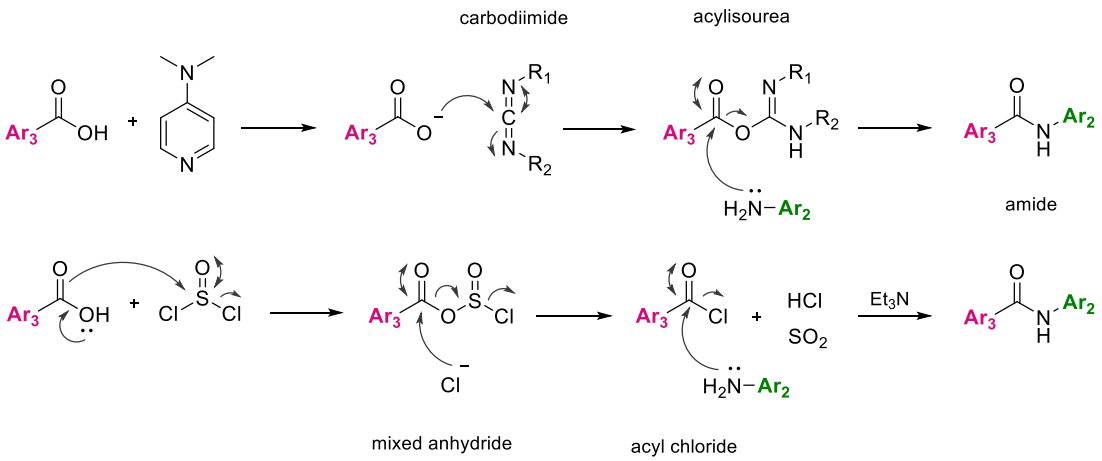

Figure 41. Mechanism of reaction between carboxylic acids and amines to form an amide bond: using carbodiimides as coupling agents (first row) or with thionyl chloride to form the acyl chloride (second row).

The overall outcome was not successful. DCI reaction occurs pretty slowly at room temperature. Upon heating, compound **58** was obtained in 38% yield. Yields are significantly reduced due to the difficult chromatographic separation from the urea byproduct. Therefore, we replaced DCI by EDC·HCl, whose urea is easily eliminated by L-L extraction, but yields were highly variable. Microwave irradiation at 130 °C diminished reaction times from hours or even days to minutes, but the yields were not much higher.

When we applied this methodology to obtain compounds with pyridine as A ring (Table 6, X=N) yields dropped even further (e.g. 7% of **70**). We therefore turned to acyl chlorides to activate the carboxylic acid (Fig. 41), testing many experimental conditions. The formation of the acyl chloride from the carboxylic acid and thionyl chloride was carried out in a sealed tube a 70 °C. Then, the excess of thionyl chloride was removed under vacuum and the amides were rapidly formed by the dropwise addition of the acyl chloride to a solution of the amine with triethylamine.

This procedure afforded better results than those using coupling agents. Nevertheless, the yields are far from being optimal, and we did not obtain all the proposed compounds. The critical step seems to be the proper formation of the acyl chloride rather than the second step in which the amide is prepared. One of the conditions tested when preparing compound **70** led to the formation of **71** by the reaction of two molecules of acyl chloride per molecule of amine because we added 3 eq of the carboxylic acid.

The compounds with a triaryl scaffold exhibited very poor solubility in most organic solvents. In light of the discouraging synthetic difficulties with such low yields and the fact that these compounds did not prove effective against *in vitro* cell proliferation, we decided to move to the design and preparation of compounds that putatively bind to zones 1-2 and 2-3. Later on, we would combine the best structural moieties that confer the bioactive profile in the design of molecules that might engage the three zones of the colchicine domain.

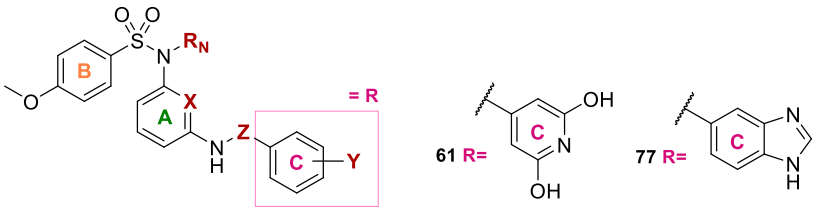

No.	R_N	X	Y	Z	Route	Solvent	Conditions	Activation	Result
54	H	CH	4-NO_2	CO	**B**	CH_2Cl_2	rt	CDI	no reaction
54	H	CH	4-NO_2	CO	**A**	CH_2Cl_2	rt	DCI	mixtures
54	H	CH	4-NO_2	CO	**A**	CH_2Cl_2	rt	EDC·HCl	**54** (63%)
54	H	CH	4-NO_2	CO	**A**	CH_2Cl_2	µW, 130 °C	EDC·HCl	**54** (32%)
54	H	CH	4-NO_2	CO	**A**	CH_2Cl_2/DMF	70 °C/rt	$SOCl_2$	**54** (36%)
57	H	CH	4-urea	CO	**A**	CH_2Cl_2	µW, 130 °C	EDC·HCl	**57** (13%)
58	H	CH	4-NO_2	$COCH_2$	**A**	CH_2Cl_2	rt	EDC·HCl	no reaction
58	H	CH	4-NO_2	$COCH_2$	**A**	CH_2Cl_2/THF	rt-Δ	DCI	**58** (38%)
58	H	CH	4-NO_2	$COCH_2$	**A**	CH_2Cl_2	µW, 130 °C	EDC·HCl	**58** (69%)
61	H	CH	DHI	CO	**A**	CH_2Cl_2	70 °C/rt	$SOCl_2$	no reaction
61	H	CH	DHI	CO	**A**	DMF	4 °C/rt	$SOCl_2$	no reaction
61	H	CH	DHI	CO	**A**	DMF	100 °C	DCI	no reaction
70	H	N	4-NO_2	CO	**A**	CH_2Cl_2	µW, 130 °C	EDC·HCl	**70** (7%)
70	H	N	4-NO_2	CO	**A**	toluene	Δ	$SOCl_2$	no reaction
70	H	N	4-NO_2	CO	**A**	DMF/toluene	4 °C/rt	$SOCl_2$	no reaction
70	H	N	4-NO_2	CO	**A**	DMF	4 °C/rt	$SOCl_2$	mixtures
70	H	N	4-NO_2	CO	**A**	CH_2Cl_2	Δ/rt	$SOCl_2$	**70** (27%)
70	H	N	4-NO_2	CO	**A**	CH_2Cl_2	70 °C/rt	$SOCl_2$	**70** (impure)
70	H	N	4-NO_2	CO	**A**	CH_2Cl_2/DMF	70 °C/rt-Δ	$SOCl_2$	no reaction
70	H	N	4-NO_2	CO	**A**	CH_2Cl_2	70 °C/rt	$SOCl_2$	**71** (48%)
70	H	N	4-NO_2	CO	**A**	CH_2Cl_2	70 °C/rt	$SOCl_2$	**70** (16%)
73	H	N	4-AcNH	CO	**A**	CH_2Cl_2	µW, 130 °C	DCI	mixtures
74	Me	N	4-NO_2	CO	**A**	CH_2Cl_2	70 °C/rt	$SOCl_2$	**74** (30%)
75	H	N	4-NO_2	$COCH_2$	**A**	CH_2Cl_2	70 °C/rt	$SOCl_2$	**75** (36%)
76	Me	N	4-NO_2	$COCH_2$	**A**	CH_2Cl_2	70 °C/rt	$SOCl_2$	**76** (33%)
77	H	N	BIM	CO	**A**	CH_2Cl_2	70 °C/rt	$SOCl_2$	no reaction
77	H	N	BIM	CO	**A**	CH_2Cl_2	Δ	EDC·HCl	no reaction

Table 6. General chemical structure of benzamides and phenylacetamides. The table summarizes the conditions tested and the result with the product yield if obtained. The **route** refers to the synthetic methodology depicted in Figure 39. DHI = 2,6-dihydroxyisonicotinoyl; BIM = benzimidazol-5-yl. DHI and BIM represent R instead of Y.

C. Functional groups on the aromatic rings (SM-3)

With the aim of studying the putative interactions with the residues at the deepest region of zone 3 in the colchicine domain, we have explored different substituents on the C ring: nitro, amino, urea, or bromo groups, to name a few. Some substituents were already introduced along with the incorporation of the C ring. Other substituents were introduced later on, or formed by derivatization of amines.

Preparation of amino groups: Catalytic reduction of aromatic nitro groups **38**, **43**, **54**, **58**, and **70** provided the corresponding amines **42**, **47**, **55**, **59**, and **72**, respectively, in most cases with moderate yields (Table 7). The reduction of the nitro group shields the *ortho* protons.

Hydrogenation of **54** gave **55** in only 26% yield. Complex mixtures were obtained from the reduction of **58** to **59**. Unexpectedly, the reduction of the nitro group in **38** with Pd/C gave dimethylamino derivative **42** in 32% yield, being the putative source of methyl groups the methanol used as co-solvent. The double methylation of the primary amine was confirmed by nOe between the methyl groups of dimethylamino and the aromatic protons in a NOESY experiment.

The reduction of nitro derivative **54** with iron in acidic media led to **35** as hydrogenolysis product, although compound **72** was successfully obtained in 48% yield following that methodology.[513,514] Reduction with $SnCl_2$ in refluxing EtOAc[515] with or without microwave irradiation yielded anilines **55** and **59** in good yields (77-78%), but required labor-intensive elimination of the stannous salts. We did not apply the hydrogenation to benzylamine **43** because it would undergo hydrogenolysis. Reduction of **43** with $SnCl_2$ gave **47** in 46% and the hydrogenolysis product **35** in 41% yield.

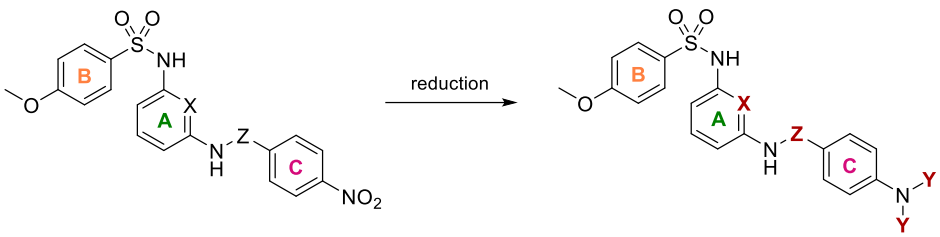

No.	X	Y	Z	Method	Solvent	Conditions	Result
42	CH	Me	SO_2	H_2, Pd/C	CH_2Cl_2/MeOH	rt, 4 days	**42** (32%)
47	CH	H	CH_2	$SnCl_2{\cdot}2H_2O$	EtOAc	Δ, 18 h	**47** (46%) **35** (41%)
55	CH	H	CO	H_2, Pd/C	CH_2Cl_2/MeOH	rt, 24 h	**55** (26%)
55	CH	H	CO	Fe, HCl	AcOH/EtOH/H_2O	Δ, 30 min	**35** (59%)
55	CH	H	CO	$SnCl_2{\cdot}2H_2O$	EtOAc	rt-Δ, 21 h	**55** (78%)
55	CH	H	CO	$SnCl_2{\cdot}2H_2O$	EtOAc	μW 120 °C, 15 min	**55** (impure)
59	CH	H	$COCH_2$	H_2, Pd/C	CH_2Cl_2/MeOH	rt, 3 days	mixtures
59	CH	H	$COCH_2$	$SnCl_2{\cdot}2H_2O$	EtOAc	Δ, 10 h	**59** (77%)
72	N	H	CO	Fe, HCl	AcOH/EtOH/H_2O	100 °C, 15 h	**72** (48%)

Table 7. Experimental conditions tested in the preparation of amino derivatives from nitro groups and the result including the yield of the desired product if obtained.

Bromination of the C ring: Br_2 is a liquid with high density, highly fuming, and toxic by inhalation. Because of that, we used *N*-bromosuccinimide as bromo source because it is more easily handled than bromine. We used previously synthesized anilines **47** and **55** as starting materials (Scheme 9). The amino group promotes and directs the electrophilic aromatic substitution at its *ortho* (and *para*, irrelevant in this case as it is already occupied) position, which is strongly activated by resonance with the amino lone pair of electrons.

Bromination of benzylamine **47** did not give **48** but the Fries-like rearrangement product **49** (28%) and debenzylated compound **50** in 14% yield (Scheme 9). ^{1}H-NMR spectra of **49** show two *para*-disubstituted benzenes (rings B and C), and two aromatic singlets allocated to a tetrasubstituted A ring with the two protons in *para*-disposition in respect to each other, resulting from the bromination of position 6. Compound **50** shows identical A and B ring substitutions and the loss of the benzyl group corresponding to the C ring.

Bromination of **55** provided **56** in 49% yield. The position of the bromine atom is evidenced by the splitting pattern of the C ring in ^{1}H-NMR spectra, changing from a *para*-disubstituted in **55** to a trisubstituted one in **56**. The electron-withdrawing effect of the benzoyl in **55** makes the A ring less electron-rich, and therefore less prone to Fries rearrangements and electrophilic aromatic substitutions by bromine than the benzylic ring in **47**.

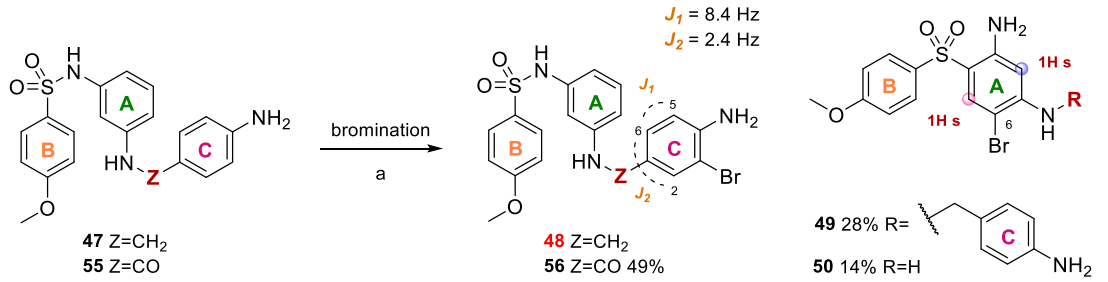

Scheme 9. Preparation of compounds **49**, **50**, and **56**. Reagents and conditions: (a) NBS, CH_2Cl_2, 4 °C, 1-2 h, N_2. Coupling constants (*J*) are in **orange**.

Derivatization of the amino group: We unsuccessfully tried to transform the amino terminal into urea and guanidine (Scheme 10). To form the unsubstituted urea, aniline **47** was treated with potassium cyanate in a mixture of water and acetic acid and heated at 40 °C. This procedure successfully yielded **26** from methyl 4-aminobenzoate, but in this case **51** was not obtained. Similarly, complex mixtures were obtained from the reaction of **58** with benzyl isocyanate in refluxing CH_2Cl_2 to form compound **60**. Treatment of **47** with cyanamide also led to complex mixtures.

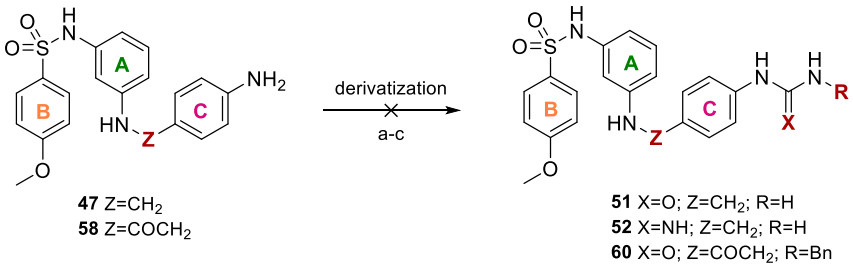

Scheme 10. Preparation of compounds **51**, **52**, and **60**. Reagents and conditions: (a) KOCN, water/AcOH, 40 °C, 2 h, N_2. (b) NH_2CN, water/AcOH, 40-80 °C, 24 h, N_2. (c) Benzyl isocyanate, CH_2Cl_2, reflux, 24 h, N_2.

Modifications on scaffolds C and D

Regarding scaffolds **C** and **D**, we have conducted the aromatization of the indoline ring to indole, alkylations at the sulfonamide, and substitutions on the aromatic rings.

A. Aromatization of the indoline ring (SM-1)

N-formyl-indolines **78**, **101**, and **120** were reduced to the *N*-methyl counterparts **79**, **102**, and **121**, which were subsequently oxidized to indoles **80**, **103**, and **122** (Scheme 11). The first step was achieved using $NaBH_4$ as the reducing agent in acidic media provided by trichloroacetic acid, leading to *N*-methyl-indolines in high yields (88-91%).[210] These compounds display only one set of signals with the *N*-methyl group resonating at 32.1-34.2 ppm in ^{13}C-NMR and around 2.79 ppm in ^{1}H-NMR spectra. The reduction of the formyl groups shields the 2-methylene in ^{1}H-NMR and deshields it in ^{13}C-NMR.

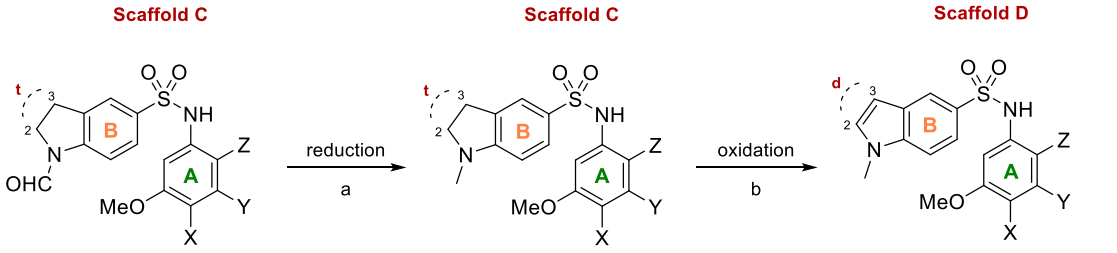

No.	X	Y	Z
78	OMe	OMe	H
101	H	OMe	H
120	H	H	OMe

No.	X	Y	Z	Yield
79	OMe	OMe	H	89%
102	H	OMe	H	88%
121	H	H	OMe	91%

No.	X	Y	Z	Yield
80	OMe	OMe	H	70%
103	H	OMe	H	78%
122	H	H	OMe	72%

Scheme 11. Preparation of **80**, **103**, and **122**. Reagents and conditions: (a) $NaBH_4$, Cl_3CCOOH, THF, 4 °C-rt, 4-72 h, N_2. (b) DDQ, THF, 4 °C-rt, 24-72 h, N_2. Splitting patterns of protons H2 and H3 are indicated in **red** in each scaffold: triplet (t) or doublet (d).

Oxidation of indolines with DDQ in THF gave indoles in good yields (70-78%) after precipitation with MTBE, hence avoiding chromatographic techniques (Scheme 11).[210] The aromatization of indolines into indoles results in a downfield shift of C2 and C3 methines to the aromatic region and resonate as doublets coupled by 3.2 Hz.

B. Alkylation of the sulfonamide nitrogen (SM-2)

The introduction of substituents at the sulfonamide nitrogen was accomplished following two different procedures that led to the alkylated compounds listed in Table 8. The two methods follow a standard nucleophilic substitution mechanism but differ in the choice of solvent and base. Some modifications were introduced on compounds that had already been modified at the indole 3-position (**SM-3**), whose synthesis will be discussed in the next section. Hence, the starting material of the alkylation reaction is likewise indicated in Table 8.

For one- or two-carbon substituents, herein considered short-chain alkanes (methyl or ethyl), the anion was formed with KOH in acetonitrile, then treated with methyl iodide or ethyl bromide. Bulkier groups (ester, nitrile, or benzyl derivatives) were successfully introduced using DMF as solvent and K_2CO_3 as the base by treatment with ethyl bromoacetate, chloroacetonitrile, benzyl chloride, or 4-fluorobenzyl chloride.

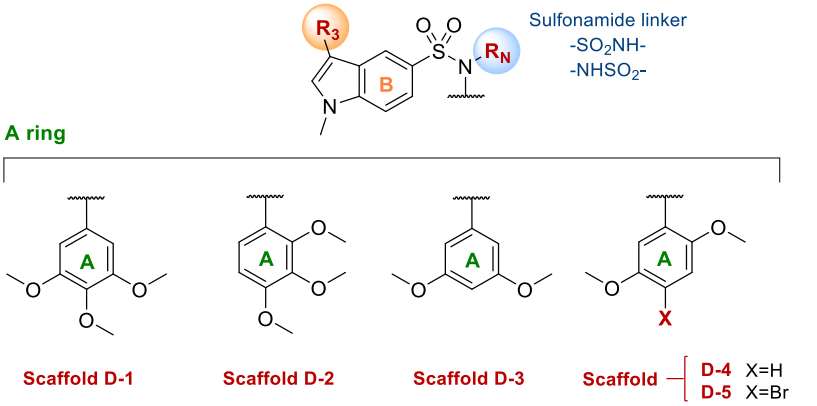

No.	Scaffold	R_3	Linker	R_N	St. mat.	Conditions	Yield
81	**D-1**	H	SO_2NH	Me	**80**	2.1 eq, 19 h	91%
82	**D-1**	H	SO_2NH	Et	**80**	2.0 eq, 72 h	84%
83	**D-1**	H	SO_2NH	COOEt	**80**	2.0 eq, 8 h	n.r.
84	**D-1**	H	SO_2NH	CH_2COOEt	**80**	2.0 eq, 72 h	91%
86	**D-1**	H	SO_2NH	CH_2CN	**80**	2.5 eq, 3 h	70%
90	**D-1**	CHO	SO_2NH	Me	**89**	2.0 eq, 48 h	91%
93	**D-1**	CHO	SO_2NH	Et	**89**	2.3 eq, 6 days	11%
100	**D-2**	H	$NHSO_2$	Me	**99**	2.0 eq, 3 h	97%
104	**D-3**	H	SO_2NH	Me	**103**	2.0 eq, 19 h	91%
105	**D-3**	H	SO_2NH	Et	**103**	2.0 eq, 8 days	79%
106	**D-3**	H	SO_2NH	CH_2COOEt	**103**	2.0 eq, 1 week	94%
107	**D-3**	H	SO_2NH	CH_2CN	**103**	2.0 eq, 15 h	84%
108	**D-3**	H	SO_2NH	CH_2CH_2CN	**103**	2.0 eq, 4 days	n.r.
109	**D-3**	H	SO_2NH	Bn	**103**	2.0 eq, 4 days	80%
110	**D-3**	H	SO_2NH	4-F-Bn	**103**	2.3 eq, 48 h	85%
111	**D-3**	H	SO_2NH	4-NO_2-Bn	**103**	2.2 eq, 1 week	mixtures
123	**D-4**	H	SO_2NH	Me	**122**	2.1 eq, 24 h	94%
124	**D-4**	H	SO_2NH	Et	**122**	4.0 eq, 5 days	48%
125	**D-4**	H	SO_2NH	CH_2COOEt	**122**	2.4 eq, 10 days	60%
126	**D-4**	H	SO_2NH	CH_2CN	**122**	8.6 eq, 5 days	47%
127	**D-4**	H	SO_2NH	Bn	**122**	2.2 eq, 10 days	62%
133	**D-4**	CHO	SO_2NH	Me	**132**	2.0 eq, 24 h	89%
129	**D-5**	Br	SO_2NH	Me	**128**	2.0 eq, 72 h	49%

Table 8. General chemical structure of indole-sulfonamide derivatives (scaffold **D**). Depending on the substitution pattern of the benzene (**A ring**), compounds have been divided into five groups: 3,4,5-trimethoxyphenyl (scaffold **D-1**), 2,3,4-trimethoxybenzene (scaffold **D-2**), 3,5-dimethoxybenzene (scaffold **D-3**), 2,5-dimethoxybenzene (scaffold **D-4**), and 4-bromo-2,5-dimethoxybenzene (scaffold **D-5**). The table summarizes the alkylation products, the starting material, conditions, and yields. St. mat. = starting material; n.r. = no reaction.

The alkylated compounds with scaffolds **D-1**, **D-2**, and **D-3** were obtained in overall excellent yields. The outcome was not that good for scaffolds **D-4** and **D-5**, possibly due to steric hindrance with the 2-methoxy group. Accordingly, the highest yields were obtained for methyl substituents. Reaction of **89** with ethyl bromide afforded **93** in 11% yield, because two other products were obtained, as explained below. The acid **85** was obtained by saponification of **84** (Scheme 12).

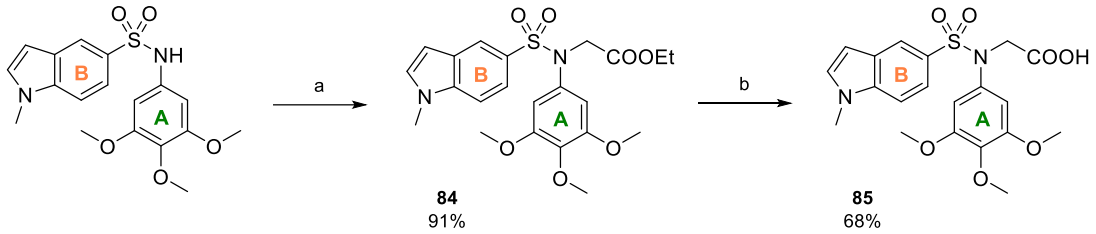

Scheme 12. Preparation of compound **85**. Reagents and conditions: (a) Ethyl bromoacetate, K_2CO_3, DMF, rt, 72 h, N_2. (b) KOH, MeOH, rt, 30 min.

Nevertheless, not every attempt turned out successful. The reaction of **103** with 1-(chloromethyl)-4-nitrobenzene gave complex mixtures, and the formylation of **80** with ethyl chloroformate and alkylation of **103** with 3-bromopropanenitrile were unsuccessful (Table 8).

The stretching of a carbonitrile group typically gives an IR band at around 2200 cm^{-1}. However, the introduction of a CH_2CN group (in **86**, **107** and **126**) cannot be searched by IR since there is no carbonitrile absorption feature for aminoacetonitriles.[516]

C. Substitutions on the aromatic rings (SM-3)

Based on the good results obtained for substituted indolecombretastatins,[499] different groups were introduced at the indole 3-position: bromine atom, aldehyde, or amide groups. Additionally, aromatic nitriles and propenenitriles were obtained from aldehydes (Scheme 13).

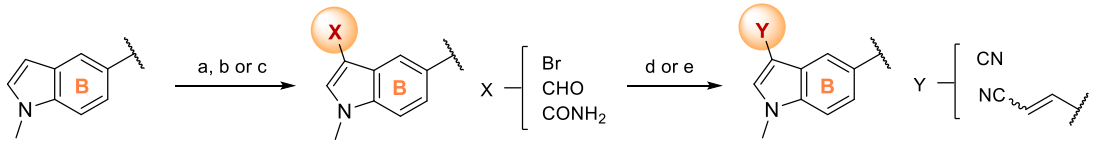

Scheme 13. Substitutions at the indole 3-position. Reagents and conditions: (a) X=Br: NBS, CH_2Cl_2, 4 °C, 15 min-3 h, N_2. (b) X=CHO: i) $POCl_3$, DMF, 4 °C, 30 min, N_2; ii) indolic compound, DMF, 4 °C, 5 min-1 h, N_2. (c) X=$CONH_2$: CSI, $C_2H_4Cl_2$, 4 °C-rt, 3-24 h, N_2. (d) Y=CN: i) $NH_2OH{\cdot}HCl$, pyr, MeOH, reflux, 12-48 h, N_2; ii) Ac_2O, pyr, 130 °C, 30 h-4 days, N_2. (e) Y=CHCHCN: KOH, ACN, rt, 6-7 days, N_2.

Bromination reactions: The bromination reaction was carried out with NBS at low temperature. The bromine atom was introduced at the indole 3-position when unsubstituted. Compounds with a 2,5-dimethoxyphenyl ring (scaffold **D-4**, Table 8) were brominated at position 4 of the phenyl ring (scaffold **D-5**) when either of these two conditions applies: the indole 3-position is already occupied (**134** and **135**) or at least two equivalents of NBS are added to the reaction (**128** and **131**). Bromination products are included in Table 9. The second bromine in compound **130** was introduced at indole 2-position, then the third one reacts with the benzene (**131**).

Bromination of the indole 3-position shields the ipso carbon (C3) and H2 proton resonates as singlet. The bromination of 2,5-dimethoxyphenyl gives two aromatic singlets corresponding to H3 and H6 protons.

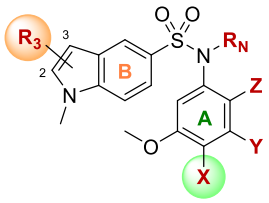

No.	R_3	R_N	X	Y	Z	Conditions	Yield
87	3-Br	H	OMe	OMe	H	1.2 eq NBS, 3 h	61%
88	3-Br	Et	OMe	OMe	H	1.2 eq NBS, 1 h	78%
128	3-Br	H	Br	H	OMe	2.2 eq NBS, 15 min	50%
130	2,3-Br_2	CH_2CN	H	H	OMe	2.1 eq NBS, 3 h	n.i.
131	2,3-Br_2	CH_2CN	Br	H	OMe	8.5 eq NBS, 72 h	n.i.
134	3-CHO	Me	Br	H	OMe	1.2 eq NBS, 24 h	35%
135	3-CHO	H	Br	H	OMe	1.1 eq NBS, 30 min	68%

Table 9. General chemical structure of brominated indole derivatives and conditions employed in the preparation of each compound, together with the yield. n.i. = non-isolated.

The indole 3-position is more reactive to electrophilic aromatic substitutions than benzenes, so that bromination cannot be selectively conducted on the A ring concomitantly to an unsubstituted indole. Thus, we tried to build the sulfonamide with the aniline previously brominated by reacting 4-bromo-2,5-dimethoxyaniline (**24**) with sulfonyl chloride **5** (Scheme 14). Bromination of 2,5-dimethoxyaniline **23** gives a product that rapidly decomposes even in the absence of light. Therefore, we attempted bromination of 1,4-dimethoxybenzene to provide **25**, which would be later nitrated. 1,4-Dimethoxybenzene did not react with NBS in CH_2Cl_2, and we added the Lewis acid $FeCl_3$ as catalyst with unsuccessful results so that nitration was not attempted.

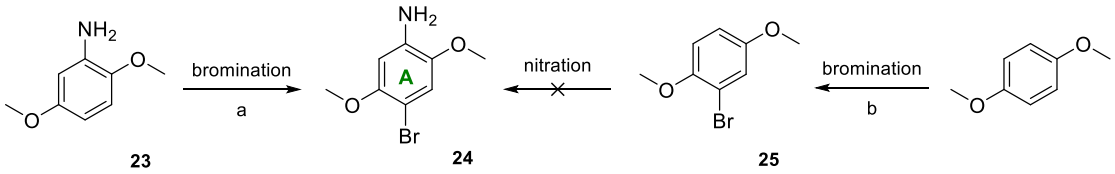

Scheme 14. Preparation of compounds **24** and **25** as **A ring**. Reagents and conditions: (a) NBS, CH_2Cl_2, 4 °C, 7 h, N_2. (b) NBS, $FeCl_3$, CH_2Cl_2, 4 °C, 48 h, N_2.

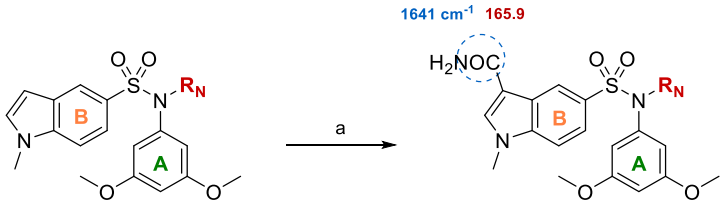

No.	R_N
103	H
104	Me

No.	R_N	Yield
112	H	58%
113	Me	-

Scheme 15. Introduction of an amide group at the indole 3-position. Reagents and conditions: (a) CSI, $C_2H_4Cl_2$, 4 °C-rt, 3-24 h, N_2. ^{13}C-NMR chemical shift value (ppm) of the amide carbon is shown in **red**, and the IR absorption of the amide group is in **blue**.

Preparation of carboxamides: The reaction of **103** with chlorosulfonyl isocyanate gave the indole-carboxamide **112** in 58% yield (Scheme 15).[517] However, **113** could not be obtained from **104** under the same conditions. The indole amide in **112** resonates at 165.9 ppm in ^{13}C-NMR and gives an IR band at 1641 cm^{-1}.

Formylation of the indole ring: The formylation of the indole 3-position was conducted following Vilsmeier-Haack procedure (Fig. 42).[518] The first step between $POCl_3$ and dry DMF provides the iminium salt known as the Vilsmeier reagent, which is the electrophile for the electrophilic aromatic substitution that takes place. The mixture of $POCl_3$ and DMF was subsequently poured into the indolic derivative, generating an intermediate compound, which is hydrolyzed to afford the aldehyde.

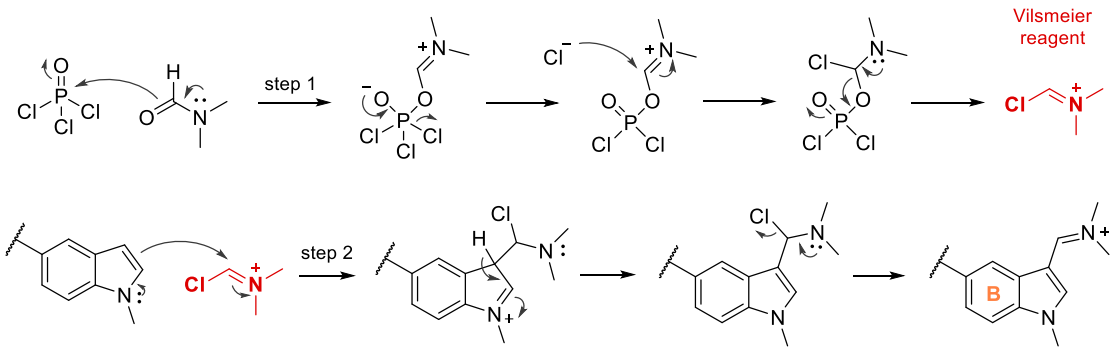

Figure 42. Mechanism of Vilsmeier-Haack reaction. The reaction between $POCl_3$ and dry DMF gives the so-called Vilsmeier reagent, which is an iminium salt. In a second step, this reagent is added to the indole, providing an intermediate compound. When poured into water with sodium acetate, it is hydrolyzed to the aldehyde.

The Vilsmeier-Haack methodology successfully gave indole-carbaldehyde derivatives in high yields ranging from 82% to 97% (Table 10). The formyl groups are characterized by the signals at 184 ppm in ^{13}C-NMR and display stretching absorptions at around 1644-1663 cm^{-1}. The formyl proton resonates as a singlet at approximately 10.00 ppm.

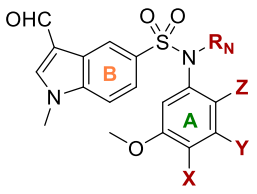

No.	R_N	X	Y	Z	Yield
89	H	OMe	OMe	H	95%
114	H	H	OMe	H	n.o.
115	Me	H	OMe	H	82%
116	Bn	H	OMe	H	97%
132	H	H	H	OMe	96%

Table 10. General chemical structure of formyl-indole derivatives and yields obtained for each compound. n.o. = not obtained.

The Vilsmeier-Haack procedure thus gave very good yields, but compound **114** could not be obtained. The reaction was monitored by TLC and suggested the consumption of **103** but the product did not precipitate in water at 4 °C and L-L extraction gave no crude residue in any pH.

Preparation of carbonitriles: The preparation of carbonitriles from carbaldehydes was accomplished in two consecutive steps. First, aldehydes were treated with a large excess of hydroxylamine with pyridine in refluxing methanol to provide the oximes by nucleophilic addition-elimination.[503,504] Oximes were obtained as mixtures of *E* and *Z* isomers and were transformed into carbonitriles by reaction with an excess of acetic anhydride in pyridine at 130 °C (Table 11) to achieve the thermal elimination of the intermediate acetate.[499] The yields are reduced due to the need for two consecutive steps of product isolations. The triple bond of a nitrile group gives an IR absorption around 2220 cm^{-1}, and upfield shifts the ipso carbon in ^{13}C-NMR spectra down to 86.8-87.6 ppm.

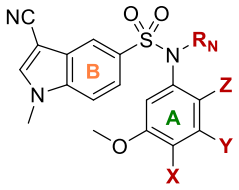

No.	R_N	X	Y	Z	Yield
96	H	OMe	OMe	H	28%
97	Me	OMe	OMe	H	63%
117	Me	H	OMe	H	24%
118	Bn	H	OMe	H	27%
136	H	Br	H	OMe	19%
139	H	H	H	OMe	28%
140	Ac	H	H	OMe	27%

Table 11. General chemical structure of nitrile-indole derivatives and the yield obtained for each compound.

Aldehyde **132** gave nitriles **139** (28%) and **140** (27%). Acetylation of the sulfonamide occurs under the harsh elimination conditions used in the oxime acetate elimination step, favored by the presence of the 2-methoxy group (Scheme 16). The same behavior was not observed for the brominated analogue **135**. The structure of **140** was confirmed by mass spectrometry (M+Na^+, 436.0938), the presence of the nitrile band in 2219 cm^{-1}, and the acetate methyl group that resonates at 1.82 ppm in ^{1}H-NMR and 23.9 ppm in ^{13}C-NMR.

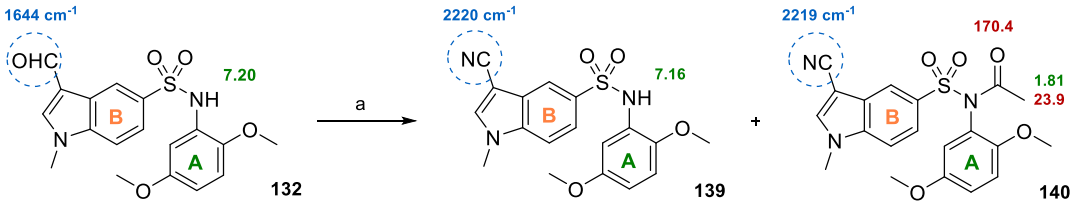

Scheme 16. Preparation of **139** and **140**. Reagents and conditions: (a) i) $NH_2OH{\cdot}HCl$, pyr, MeOH, reflux, 24 h, N_2; ii) Ac_2O, pyr, 130 °C, 30 h, N_2. IR bands are in **blue**, ^{1}H-NMR chemical shift values (ppm) in **green**, and ^{13}C-NMR in **red**.

Formylation of **103** was unsuccessful, failed to produce aldehyde **114** and therefore nitrile **119** could not be obtained (Scheme 17). However, the methylated and benzylated sulfonamides **115** and **116** with a formyl group at the indole 3-position were obtained in good yields. We therefore attempted to obtain **119** from the benzylated nitrile **118** by means of a debenzylation reaction. Nitrile **118** was obtained in poor yield from aldehyde **116** but debenzylation reaction could not be achieved (Scheme 17).

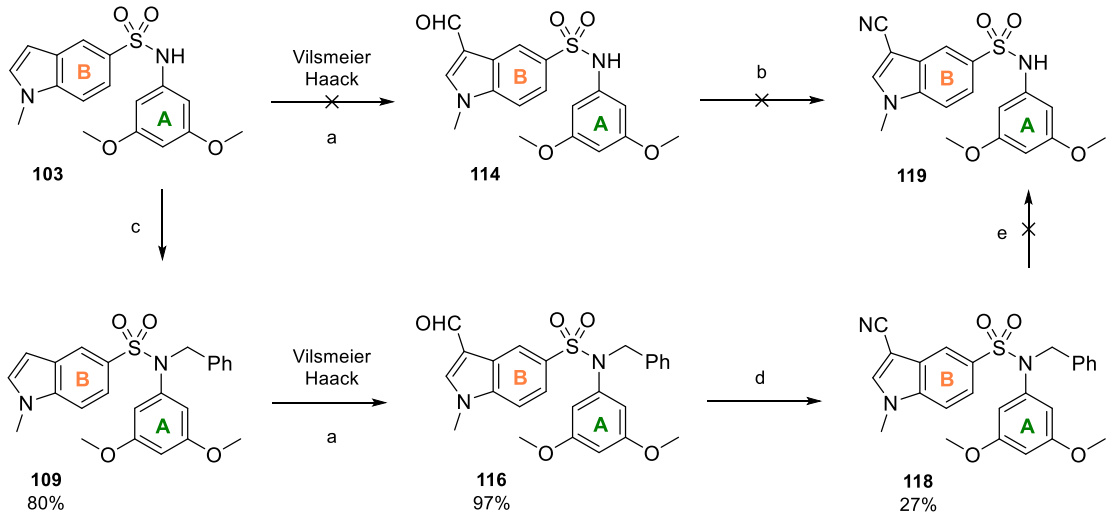

Scheme 17. Synthetic strategy to obtain compound **119**. Reagents and conditions: (a) i) $POCl_3$, DMF, 4 °C, 30 min-1 h, N_2; ii) **103**, DMF, 4 °C, 1-3 h, N_2. (b) Non-attempted. (c) Benzyl chloride, K_2CO_3, DMF, rt, 4 days. (d) i) $NH_2OH{\cdot}HCl$, pyr, MeOH, reflux, 24 h, N_2; ii) Ac_2O, pyr, 130 °C, 72 h, N_2. (e) Pd/C, AcOH, CH_2Cl_2, rt, 24 h, H_2.

Preparation of propenenitriles: Propenenitriles were obtained from aldehyde derivatives by aldol condensation with acetonitrile in basic media. Simultaneous addition of methyl iodide or ethyl bromide gave the alkylated products in one-pot (Scheme 18). Low yields were obtained due to incomplete aldehyde reaction.

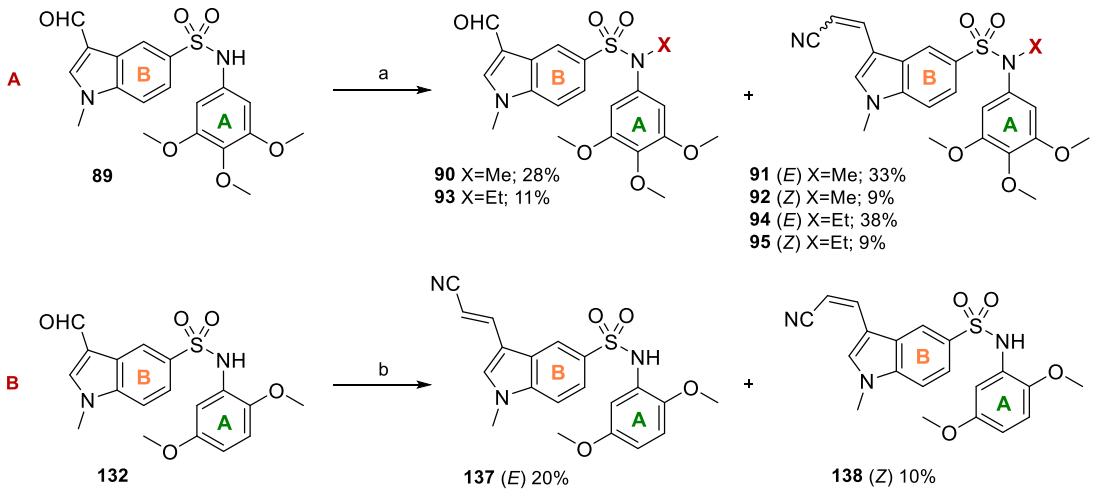

Scheme 18. Preparation of compound **90**-**95**, **137**, and **138**. Reagents and conditions: (a) Methyl iodide or ethyl bromide, KOH, ACN, rt, 6 days, N_2. (b) KOH, ACN, rt, 7 days, N_2.

The mixtures of *E* and *Z* propenenitriles were resolved by preparative TLC. Propenenitriles show an IR band at around 2200 cm^{-1} and can be distinguished one from the other by the coupling constant between the olefin protons: around 12 Hz and 16 Hz for *cis* and *trans* isomers, respectively. Upon standing in $CDCl_3$ solution, the *cis* isomer partially isomerizes to the thermodynamically more stable *trans* olefin, which is the predominant in the reaction. The chemical shift of the H2 proton of the indole ring is downfield in the *cis* isomer compared to the *trans* isomer by the configuration of the olefin (Table 12).

Treatment of **89** with methyl iodide or ethyl bromide gave formyl derivatives **90** and **93** and propenenitriles *E*+*Z* (**91**, **92**, **94**, and **95**) (Scheme 19). Compound **132** provided propenenitriles **137** and **138** in the absence of an alkylating agent.

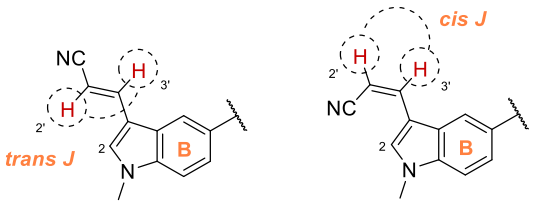

E isomer *Z* isomer

No.	Isomer	H2'	H3'	*J* H2'-H3'	H2
91	*E*	5.67	7.47	16.4	7.46
92	*Z*	5.26	7.33	11.6	8.31
94	*E*	5.66	7.44	16.8	7.80
95	*Z*	5.26	7.34	12.0	8.31
137	*E*	5.60	7.41	16.4	7.32
138	*Z*	5.27	7.35	12.0	8.28

Table 12. IR spectroscopy and ^{1}H-NMR data of the indicated groups and positions thereof. All the spectra were acquired in $CDCl_3$. **^{1}H-NMR** chemical shift values are indicated in ppm. The **coupling constants** (*J*) between olefin protons H2' and H3' are expressed in Hz.

SYNTHESIS OF TETRAZOLES AND THEIR AMIDE PRECURSORS

The synthesis of compounds consisting of two aromatic rings (two benzenes or indole-benzene) linked by a tetrazole bridge was approached by preparing the amide precursors in the first place, which were used as the starting materials for the tetrazole formation reaction (Scheme 19). Further modifications were carried out on the amides or alternatively, on the tetrazoles.

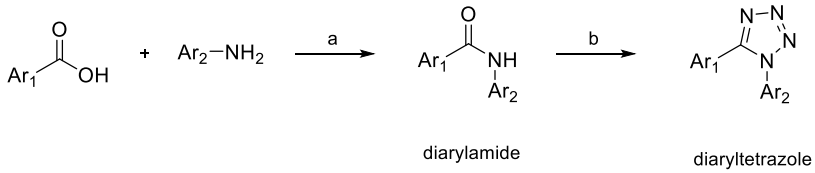

Scheme 19. General synthetic procedure of tetrazole derivatives. Reagents and conditions: (a) i) Ar_1-COOH, EDC·HCl, *p*-DMAP, CH_2Cl_2, reflux, 1-3 h, N_2; ii) Ar_2-NH_2, reflux, 6 h-9 days, N_2. (b) NaN_3, $SiCl_4$, ACN, 80-90 °C, 3-6 days. Amides, and therefore tetrazoles, were considered in their two possible orientations. This means that Ar_1 can serve as **B ring**, and Ar_2 as **A ring**, or vice versa.

Preparation of synthetic precursors

The first step is the formation of the amide that connects Ar_1 and Ar_2 between carboxylic acids and amines. Among the starting materials used in the preparation of amide compounds, most carboxylic acids (4-methoxy-, 3,5-dimethoxy-, 4-nitrobenzoic-, 4-dimethylamino- and 2,5-dichloro- benzoic acids) and aromatic amines (3,5-dimethoxy-, 4-methoxy- and 4-nitro- anilines) were commercially available, except for 1-methyl-1*H*-indole-5-carboxylic acid (**31**) and 1-methyl-1*H*-indol-5-amine (**13**), the latter prepared as already described in the section "Synthesis of sulfonamides". Aniline **33** was also prepared in the search for alternative synthetic routes towards **159** (see "Modifications on the biaryl amide scaffold").

N-methyl-indole-5-carboxylic acid **31** was prepared from 1*H*-indole-5-carbaldehyde in two steps (Scheme 20). The alkylation of the acidic proton of the indole ring was conducted in phase transfer conditions providing **30** in 93% yield. Aldehyde **30** was then converted to acid **31** in 76% yield by Pinnick oxidation using $NaClO_2$ and NaH_2PO_4 that generate the oxidating agent $HClO_2$.[519] The oxidation of aldehyde **30** shields the carbonyl carbon that resonates at 170.4 ppm in **31**, and results in the disappearance of the formyl singlet of **30** at 9.98 in ^{1}H-NMR spectra.

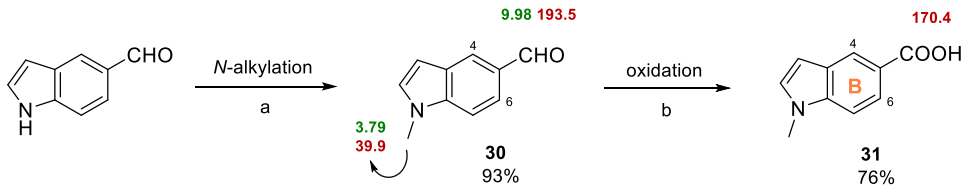

Scheme 20. Preparation of **31** as **B ring**. Reagents and conditions: (a) i) NaOH, $nBu_4N^+HSO_4^-$, CH_2Cl_2, rt, 1 h; ii) CH_3I, 48 h, N_2. (b) $NaClO_2$, $NaH_2PO_4·H_2O$, 2-methyl-2-butene, H_2O/*t*-BuOH, 4 °C-rt, 24 h, N_2. ^{1}H-NMR chemical shift values (ppm) in **green**, and ^{13}C-NMR chemical shift values (ppm) in **red**.

Preparation of biaryl amides

The amide formation was accomplished by the reaction between carboxylic acids and primary aromatic amines in the presence of EDC·HCl and *p*-DMAP (Table 13). The amide displays a characteristic IR band around 1650 cm^{-1} and a ^{13}C-NMR signal at 163.2-166.3 ppm.

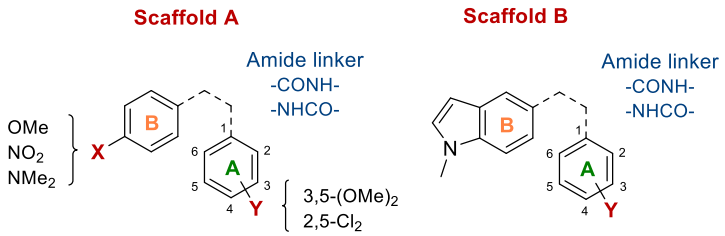

No.	Scaffold	X	Linker	Y	Conditions	Yield
141	**A**	OMe	CONH	3,5-$(OMe)_2$	Δ, 16 h	83%
148	**A**	OMe	NHCO	3,5-$(OMe)_2$	Δ, 14 h	77%
153	**A**	NO_2	CONH	3,5-$(OMe)_2$	Δ, 72 h	52%
155	**A**	NMe_2	CONH	3,5-$(OMe)_2$	Δ, 7 days	75%
157	**A**	NO_2	NHCO	3,5-$(OMe)_2$	Δ, 9 days	97%
160	**A**	OMe	NHCO	2,5-Cl_2	Δ, 24 h	22%
161	**A**	NO_2	NHCO	2,5-Cl_2	Δ, 30 h	45%
162	**B**	-	CONH	3,5-$(OMe)_2$	Δ, 6 h	n.i.
163	**B**	-	NHCO	3,5-$(OMe)_2$	Δ, 4 days	86%

Table 13. General structure of the synthesized biaryl amides with two benzenes (**Scaffold A**) or indole/benzene (**Scaffold B**). The table summarizes the experimental conditions and yields. n.i.= non-isolated.

Modifications on the biaryl amide scaffold

The modification of the nitro group at phenyl 4-position was carried out prior to the formation of the tetrazole ring. Compounds **153** and **157** were reduced under H_2 atmosphere to anilines **154** and **158**, respectively, in moderate to excellent yields (Scheme 21). The electron-withdrawing nitro group deshields the *ortho* protons in the ^{1}H-NMR spectra, which are upfield shifted in the corresponding amines.

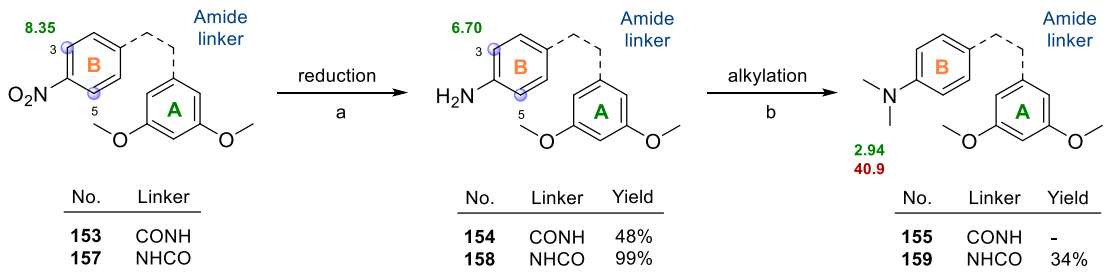

Scheme 21. Modification of the nitro group at the **B ring**. Reagents and conditions: (a) Pd/C, EtOAc/MeOH, rt, 24-72 h, H_2. (b) i) PFA, AcOH, MeOH, reflux, 12 h, N_2; ii) $NaBH_3CN$, MeOH, rt, 12 h, N_2. Compound **155** was not synthesized following procedure (b). The NMR shift values (ppm) in the scheme correspond to **153**, **154**, and **159**. ^{1}H-NMR chemical shift values (ppm) are indicated in **green**, and those for ^{13}C-NMR in **red**.

The amino group of **158** was then subjected to a reductive amination to obtain **159**, a double alkylated product. This reaction was conducted with PFA in refluxing methanol in the presence of acetic acid. Then, the mixture was treated with $NaBH_3CN$ at room temperature to obtain dimethylamino derivative **159** in 34% yield (Scheme 21). Compound **154** was prepared by reduction of **153**, but the product of the reductive amination (**155**) was not prepared from **154** but directly by amide formation.

Therefore, the critical step is the reductive amination with PFA. We evaluated the effect of inverting the sequential synthetic steps: first the methylation of 4-nitroaniline followed by catalytic hydrogenation of the nitro group previous to the formation of the amide (Scheme 22). 4-Nitroaniline was converted with PFA at room temperature into dimethyl derivative **32** in 86% yield. Reduction of **32** to **33** also occurred in excellent yields (94%), thus validating this alternative synthetic route.

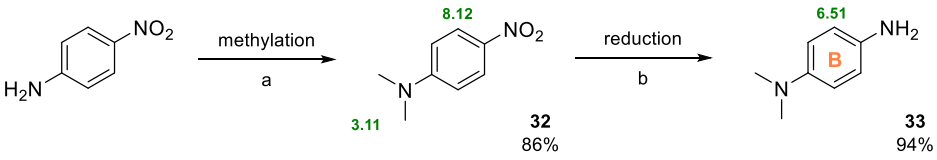

Scheme 22. Preparation of compound **33** as **B ring**. Reagents and conditions: (a) i) PFA, AcOH, MeOH, rt, 1.5 h, N_2; ii) $NaBH_3CN$, MeOH, rt, 7 days, N_2. (b) Pd/C, EtOAc/MeOH, rt, 24 h, H_2.

The second type of modifications on amides is the bromination reaction. For compounds with benzene as B ring (**Scaffold A**), the bromine was introduced at the A ring, irrespective of the amide orientation. Bromination took place on the *N*-methylindole when present (**Scaffold B**). Amide derivatives were treated with NBS at different temperatures to provide mono- or poly- brominated compounds (Table 14).

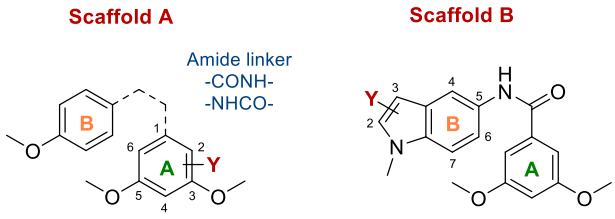

Reagent	Product	Scaffold	Linker	Y	Conditions	Yield
141	**142**	**A**	CONH	2,4-Br_2	4.4 eq NBS, rt, 48 h	55%
	143			2,6-Br_2		17%
148	**149**	**A**	NHCO	2,6-Br_2	2.1 eq NBS, Δ, 5 min	84%
163	**164**	**B**	-	3-Br	1.1 eq NBS, 4 °C, 3 h	90%
164	**165**	**B**	-	2,3-Br_2	1.1 eq NBS, 4 °C, 4 days	93%

Table 14. General structure of the synthesized bromo derivatives with two benzenes (**Scaffold A**) or indole/benzene (**Scaffold B**). The table summarizes the substituents of these compounds, conditions, and yields resulting from the reaction.

The gradual addition of NBS to amide **141** resulted in the formation of two dibrominated compounds: **142** and **143**, with bromine atoms at 2,4- and 2,6- positions, respectively. Time-course ^{1}H-NMR spectra of the reacting mixture showed that **142** and **143** are simultaneously formed, being **142** the major product (4:1 proportion). The 2,6-dibromo-3,5-dimethoxybenzene A ring in **143** is symmetrical, so the two methoxy

groups display a single peak in ^{1}H-NMR (3.94 ppm) and ^{13}C-NMR spectra (56.7 ppm). The same applies to benzene carbons C3 and C5. However, methoxy groups are asynchronous in **142** because they are not chemically equivalent. Bromination of **148** under reflux conditions led to **149** as a single product with the bromine atoms in positions 2 and 6.

Bromination of indole-containing amides occurred preferentially at the indole 3-position. Additional bromination took place at position 2, as evidenced by the NMR splitting pattern of the product **165**. The two reactions exhibited very good yields.

Conversion of amides into 1,5-disubstituted tetrazoles

Amides were transformed into tetrazoles by treatment with sodium azide and silicon tetrachloride in acetonitrile at 80-90 °C (Fig. 43).[520] For safety reasons, small-scale reactions (< 300 mg) were carried out in sealed tubes, but larger ones (> 300 mg) were carried out with regular refluxing equipment. The reactions are slow and take 3-6 days to complete, but proceed in excellent yields around 78-98% (Table 15).

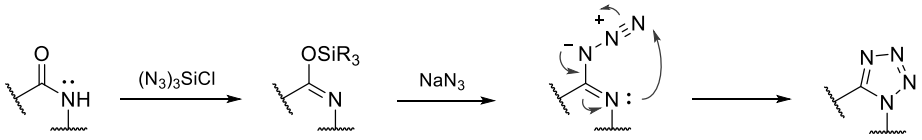

Figure 43. Mechanism of tetrazole formation reaction. Reaction between $SiCl_4$ and NaN_3 gives triazidochlorosilane $(N_3)_3SiCl$ (azide transfer reagent) that reacts with the amide oxygen. It is subsequently substituted by azide providing the tetrazole ring after intramolecular rearrangement.

Amides and tetrazoles show quite similar ^{1}H- and ^{13}C-NMR spectra, with the main difference being the disappearance of the IR absorption bands of the NH group (~3282-3420 cm^{-1}) and amide carbonyl (~ 1640-1682 cm^{-1}), the carbonyl carbon at 165-166 cm^{-1}, and also by the mass spectra.

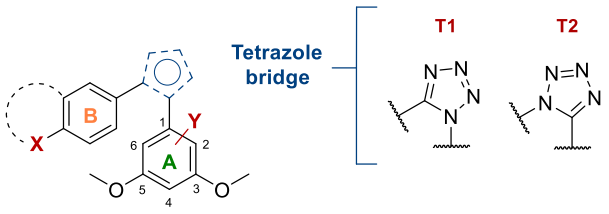

Reagent	Product	X	Bridge	Y	Conditions	Yield
141	**144**	OMe	**T1**	H	sealed tube, 3 days	78%
142	**147**	OMe	**T1**	2,4-Br_2	sealed tube, 5 days	98%
148	**150**	OMe	**T2**	H	sealed tube, 3 days	94%
155	**156**	NMe_2	**T1**	H	sealed tube, 4 days	78%
163	**166**	*N*MeIND	**T2**	H	reflux system, 4 days	96%

Table 15. General chemical structure of the synthesized tetrazoles. The table summarizes the starting amide used in the reaction, conditions, and yields.

Modifications on the 1,5-biaryl tetrazole scaffold

We performed two types of electrophilic aromatic substitutions: brominations and formylations at the indole 3-position. Carbaldehydes were later converted into carbonitriles via intermediate oximes in similar conditions to those previously described.

A. Benzenic B rings

Bromination of tetrazole derivatives **144** and **150** led to compounds listed in Table 16 by treatment with NBS. As previously observed with amides, the bromination products are independent of the tetrazole orientation. Reaction of **144** at room temperature occurred slowly and required an excess of NBS to complete, providing monobrominated compound **145**. Under refluxing conditions, **144** led to dibrominated product **146** at positions 2 and 6 (Scheme 23).

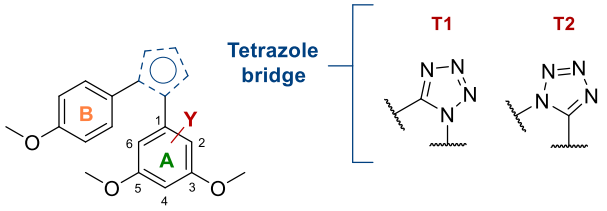

Reagent	Product	Bridge	Y	Conditions	Yield
144	**145**	**T1**	2-Br	3.6 eq NBS, rt, 24 h	78%
144	**146**	**T1**	2,6-Br_2	3.4 eq NBS, Δ, 24 h	91%
150	**151**	**T2**	2-Br	3.9 eq NBS, 4 °C, 72 h	n.i.
	152		2,6-Br_2		61%

Table 16. General chemical structure of the brominated tetrazoles. The table summarizes the starting material used in the reaction, conditions, and yields. n.i. = non-isolated.

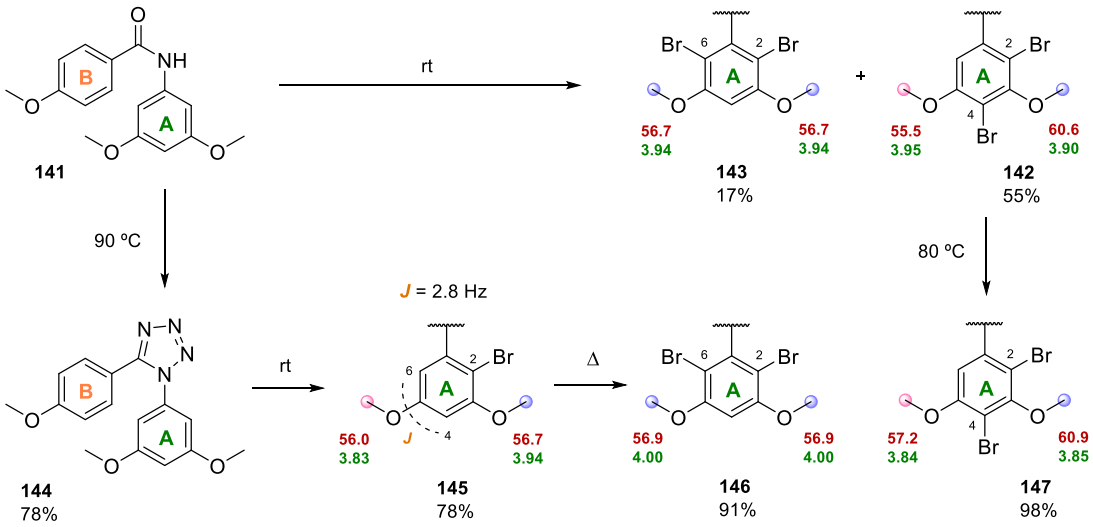

Scheme 23. Summary of brominations on amide and tetrazole scaffolds with the nitrogen on the **A ring**. Compound **146** is obtained from **144**, but time-course ^{1}H-NMR indicates that monobrominated **145** is formed first. ^{1}H-NMR chemical shift values (ppm) are in **green**, those for ^{13}C-NMR in **red**, and the coupling constant (*J*) is indicated in **orange**. Chemically equivalent nuclei are indicated by balls of the same color (**blue** or **pink**).

The result of **144** bromination contrasts with that of its counterpart amide **141**. Bromination of **141** at room temperature gave **142** and **143** (Scheme 23), with two bromines in 2,4- and 2,6-positions, respectively. Nevertheless, 2,4-dibrominated amide **142** was obtained in higher proportion, whereas 2,6-dibrominated tetrazole **146** was provided as a single product. Its regioisomer **147** with bromines in 2 and 4 positions of the A ring was obtained from **142** by forming the tetrazole ring (Scheme 23).

Similarly, low-temperature monobromination of **150** led to **151**, which could not be isolated. We first tried its crystallization in methanol and CH_2Cl_2, but **152** was obtained. The second bromine was introduced because of the excess of NBS that remained in the crude residue. Heating the solution for crystallization may have favored the introduction of the second bromine. Alternatively, we attempted a preparative TLC to isolate **151**, also obtaining **152**. The two methoxy groups of **151** A ring are asynchronous, resonating at 3.81 and 3.87 ppm, in agreement with bromination at position 2 of the A ring. However, the two aromatic protons of A ring are synchronous, even if they are chemically non-equivalent. The NMR spectra for **152** coming from **151** show an axially symmetric A ring, therefore confirming the initial bromination at position 2.

B. Indolic B rings

Concerning tetrazoles with an indole moiety, we conducted brominations on both B and A rings, as well as indole formylation. Compounds **167** and **168** were obtained by bromination of **166** (Scheme 24). The indole 3-position reacts with the first equivalent of NBS, and when NBS was added in excess, the positions 2 of indole and benzene get brominated as well (**168**).

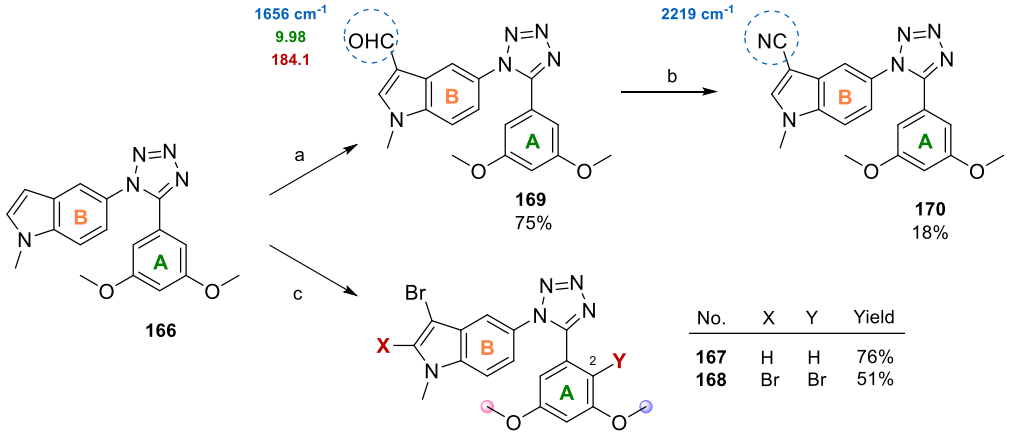

Scheme 24. Preparation of compounds **167**-**170**. Reagents and conditions: (a) i) $POCl_3$, DMF, 4 °C, 30 min, N_2; ii) **166**, 4 °C, 2 h, N_2. (b) i) $NH_2OH{\cdot}HCl$, MeOH, pyr, reflux, 48 h, N_2; ii) Ac_2O, pyr, 130 °C, 72 h, N_2. (c) NBS, CH_2Cl_2, 4 °C (**167**), or rt (**168**), 5-16 h, N_2. IR absorption frequencies are depicted in **blue**. ^{1}H-NMR chemical shift values (ppm) are in **green**, and those for ^{13}C-NMR are in **red**.

Compound **166** was formylated by Vilsmeier-Haack procedure by reaction with $POCl_3$ and dry DMF in ice.[518] Precipitation in water with sodium acetate yielded **169**, as indicated by the signals of the carbonyl carbon at 184.1 ppm, the formyl proton at 9.98 ppm, and the carbonyl IR band at 1643 cm^{-1} (Scheme 24). Carbaldehyde **169** was subsequently transformed into carbonitrile derivative **170** with low yield (18%), displaying an IR band at 2219 cm^{-1}.

We attempted the preparation of 5-amino-1-methyl-1*H*-indole-3-carbonitrile to be used as the starting material for biaryl amides that will eventually lead to tetrazole derivatives, bearing the cyano group from the beginning (Scheme 25). Attempts to nitrate 1*H*-indole-3-carbaldehyde or 1-methyl-1*H*-indole-3-carbaldehyde with nitric acid were unsuccessful. Nitration of indole-3-carbaldehyde with $NaNO_3$ in acidic media at 4 °C allowed us to obtain **15** in low yields. Therefore, this alternative route was dismissed.

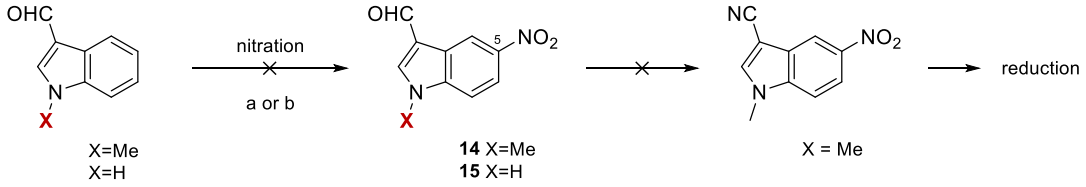

Scheme 25. Preparation of compounds **14** and **15**. Reagents and conditions: (a) HNO_3, AcOH, CH_2Cl_2, 4 °C. (b) $NaNO_3$, H_2SO_4, 4 °C, 1.5 h, N_2

Additionally, we included compounds **171**-**190** for the evaluation of the biological effect (Fig. 44). These ligands were prepared by Sara del Mazo as part of her Master's thesis and Dr. Pilar Puebla at the Department of Pharmaceutical Sciences (University of Salamanca),[521] which is why their synthesis and characterization is not discussed in this Ph.D. dissertation.

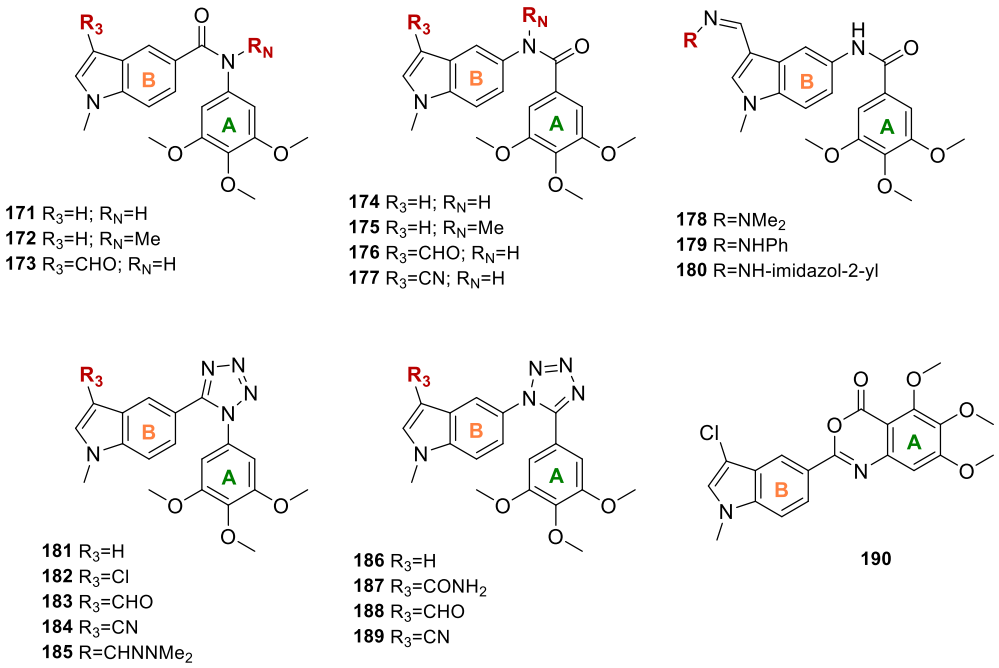

Figure 44. Chemical structures of compounds **171**-**190**. Synthetic procedures and characterization of the compounds are available in the thesis entitled "New antimitotic compounds based on natural products" defended in July 2017.

SYNTHESIS OF AMIDES, UREAS, AND CARBAMATES

This family of compounds was designed as hybrids between CA4 and MI-181, aimed to bind at zones 2 and 3 of the colchicine domain. The trimethoxyphenyl ring of CA4 is important for the interaction with tubulin and is frequently engaged in a hydrogen bond with cysteine C241β, as X-ray models suggest. This moiety is linked to the B ring of CA4 by the *para* position with respect to the central methoxy group (position 5). We have replaced that anchoring position by position 4 to direct the rest of the scaffold towards the deepest region of the colchicine domain. Besides a 2,3,4-trimethoxyphenyl ring, we additionally tested different polymethoxylated benzenes: 2,3-dimethoxy, 3,4-dimethoxy, 2,4-dimethoxy, and 2,5-dimethoxy substitution patterns (Fig. 45).

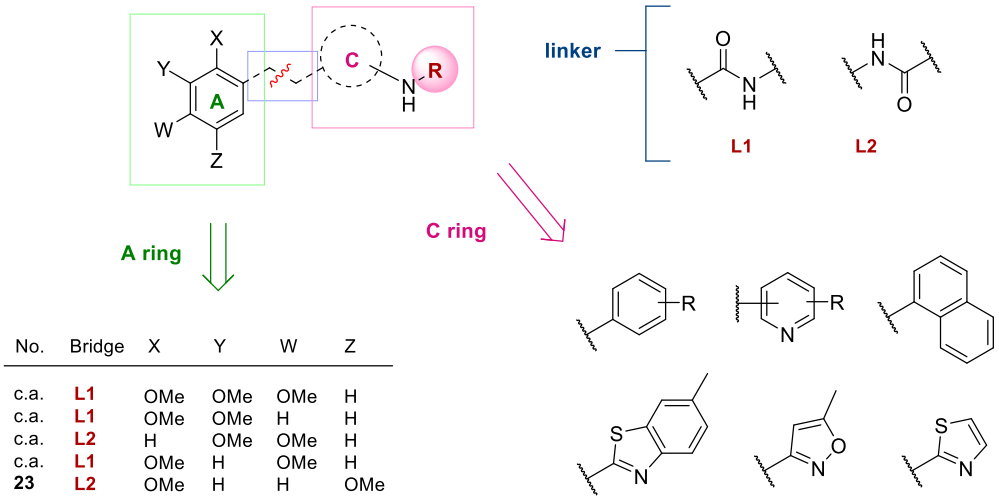

No.	Bridge	X	Y	W	Z
c.a.	L1	OMe	OMe	OMe	H
c.a.	L1	OMe	OMe	H	H
c.a.	L2	H	OMe	OMe	H
c.a.	L1	OMe	H	OMe	H
23	L2	OMe	H	H	OMe

Figure 45. Summary of the compounds clustered in the present section. All the starting materials required to construct the linker were commercially available except for 2,5-dimethoxyaniline (**23**), prepared as previously described. We considered two different **linkers**: the amide carbon linked to the **A ring** (linker **L1**), and alternatively, to the **C ring** (linker **L2**). c.a.= commercially available.

MI-181 accommodates a pyridine ring (C ring) at zone 3, linked to the A ring through a *trans* olefin. We replaced the olefin by amide linkers to maintain a *transoid* disposition of the aromatic rings. We prepared compounds with the two possible linker orientations (**L1** and **L2**). Polymethoxylated benzoic acids led to amides **L1** when reacting with amines, and polymethoxylated anilines afforded amides **L2** by reaction with the corresponding carboxylic acids (Fig. 45). Anilines were used as the starting materials to prepare ureas and carbamates (**L2**-like linker). Amides are linear, whereas ureas and carbamates allow some more flexibility to explore different dispositions.

We combined polymethoxylated benzenes with different aryl and heteroaryl groups as C rings: benzene, naphthalene, pyridine, pyrimidine, isoxazole, thiazole, and benzothiazole. In order to explore the interactions with the residues of zone 3, we introduced several modifications on compounds with C rings bearing unsubstituted amino groups. The linker (amide, urea, or carbamate) was formed in the first place to obtain the biaryl scaffold. Then, we conducted the modification of the amino group on the C ring. Additionally, we tested the effect of introducing an alkyl group on the amide linker and the bromination of the A ring.

Preparation of biaryl amides

Biaryl amides were constructed by reaction between a carboxylic acid and a primary amine (Table 17). Most of the carboxylic acids we used are linked to the A ring and therefore led to amides with a linker **L1** (Fig. 45). Those acids encompass 2,3,4-trimethoxy, 2,3-dimethoxy, and 2,4-dimethoxybenzoic acids. Reversed amides **L2** were obtained from carboxylic acids on the C ring: picolinic, nicotinic, and isonicotinic acids. Carboxylic acids need to be activated in order to form amide bonds, with coupling agents or by forming the acyl chloride, which was our first choice.

Polymethoxylated benzoyl chlorides were easily obtained by treating the acids with $SOCl_2$. The acyl chloride was then added dropwise to a solution of the amine in the presence of triethylamine to neutralize HCl released during the reaction. Nicotinoyl and isonicotinoyl chlorides precipitate in CH_2Cl_2, what reduces the reaction yields.

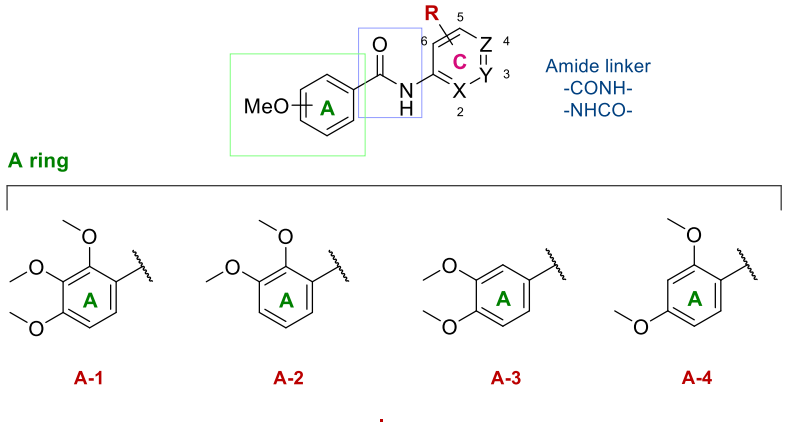

No.	A ring	Linker	X	Y	Z	R	Conditions	Yield
191	A-1	CONH	CH	CH	CH	2-NH_2	$SOCl_2$, rt, 72 h	49%
193	A-1	CONH	CH	CH	CH	3-NH_2	$SOCl_2$, rt, 15 h	26% + **194** (22%)
195	A-1	CONH	CH	CH	CH	4-NH_2	$SOCl_2$, rt, 14 h	54%
199	A-1	CONH		1-naphthyl		-	$SOCl_2$, rt, 6 h	85%
200	A-1	CONH	N	CH	CH	-	$SOCl_2$, 4 °C, 16 h	0% + **201** (57%)
200	A-1	CONH	N	CH	CH	-	DCI, µW, 130 °C, 2 h	54%
202	A-1	CONH	N	CH	CH	5-Me	EDC·HCl, Δ, 72 h	55%
204	A-1	CONH	N	CH	CH	5-Br	EDC·HCl, Δ, 48 h	73%
206	A-1	CONH	N	CH	CH	4-Br	EDC·HCl, Δ, 1 week	44%
207	A-1	CONH	N	CH	CH	4-NO_2	$SOCl_2$, rt, 24 h	14% + **208** (23%)
207	A-1	CONH	N	CH	CH	4-NO_2	EDC·HCl, Δ, 1 week	58%
209	A-1	CONH	N	CH	CH	3-NH_2	$SOCl_2$, rt, 5 h	74% + **210** (7%)
223	A-1	CONH	CH	N	CH	-	$SOCl_2$, rt, 1 h	64%
225	A-1	CONH	CH	N	CH	2-NH_2	$SOCl_2$, rt, 3.5 h	56%
226	A-1	CONH	CH	N	CH	4-OMe	$SOCl_2$, rt, 1 h	68%
228	A-1	CONH	CH	N	CH	4-NH_2	$SOCl_2$, rt, 4 days	69%
236	A-1	CONH	CH	CH	N	2-NH_2	$SOCl_2$, rt, 16 h	79%
241	A-1	CONH	CH	CH	N	-	$SOCl_2$, rt, 15 h	85%

Table 17. Continued

No.	A ring	Linker	X	Y	Z	R	Conditions	Yield
243	**A-1**	CONH	pyrimidin-2-yl			-	DCI, µW, 100 °C, 2 h	mixtures
244	**A-1**	CONH	5-Me-isoxazol-3-yl			-	$SOCl_2$, rt, 5 h	30% + **245** (49%)
246	**A-1**	CONH	thiazol-2-yl			-	$SOCl_2$, rt, 48 h	72%
247	**A-1**	CONH	6-Me-benzothiazol-2-yl			-	$SOCl_2$, rt, 72 h	70%
248	**A-2**	CONH	CH	N	CH	-	$SOCl_2$, rt, 15 h	61%
249	**A-2**	CONH	CH	CH	N	-	$SOCl_2$, rt, 2 h	67%
250	**A-3**	NHCO	N	CH	CH	-	$SOCl_2$, rt, 8 h	64%
251	**A-3**	NHCO	CH	N	CH	-	$SOCl_2$, rt, 1.5 h	83%
253	**A-3**	NHCO	CH	CH	N	-	$SOCl_2$, rt, 10 h	88%
261	**A-4**	CONH	N	CH	CH	-	$SOCl_2$, rt, 15 h	mixtures
261	**A-4**	CONH	N	CH	CH	-	DCI, µW, 130 °C, 2 h	19%
262	**A-4**	CONH	CH	N	CH	-	$SOCl_2$, rt, 14 h	30%
263	**A-4**	CONH	CH	CH	N	-	$SOCl_2$, rt, 24 h	43%

Table 17. General chemical structure of biaryl amides. Depending on the substitution pattern of the polymethoxylated benzene (**A ring**), compounds have been divided into four groups: 2,3,4-trimethoxyphenyl (**A-1**), 2,3-dimethoxyphenyl (**A-2**), 3,4-dimethoxyphenyl (**A-3**), and 2,4-dimethoxyphenyl (**A-4**). The table summarizes the products, conditions, and yields. The reagent used to activate the acid is indicated in Conditions, with the time and temperature used for the amide formation step.

Amides are characterized by the absorption band of the carbonyl group at 1648-1693 cm^{-1} and the resonance at 161.7-164.1 ppm in ^{13}C-NMR. The overall yields were good, although moderated in some cases. The main problem is the aqueous solubility, so that part of the product is not extracted during the reaction treatment. The differences in the isolated yields correspond to the difficulties in the purification process.

Bifunctional amines (i.e. *o*-, *m*-, *p*-phenylenediamines and 2,3-, 2,5-, 2,6-, 3,4-diaminopyridines) were used in excess to avoid or minimize the formation of diamides. Even so, the reaction between 2,3,4-trimethoxybenzoyl chloride and *m*-phenylenediamine or 2,6-diaminopyridine gave amides **193** and **209**, and diamides **194** and **210** as the result of the two amino groups reacting with one molecule of acyl chloride each (Scheme 26). However, these byproducts were not obtained in the reaction with *o*- and *p*-phenylenediamines, 2,3-, 2,5-, and 3,4-diaminopyridines.

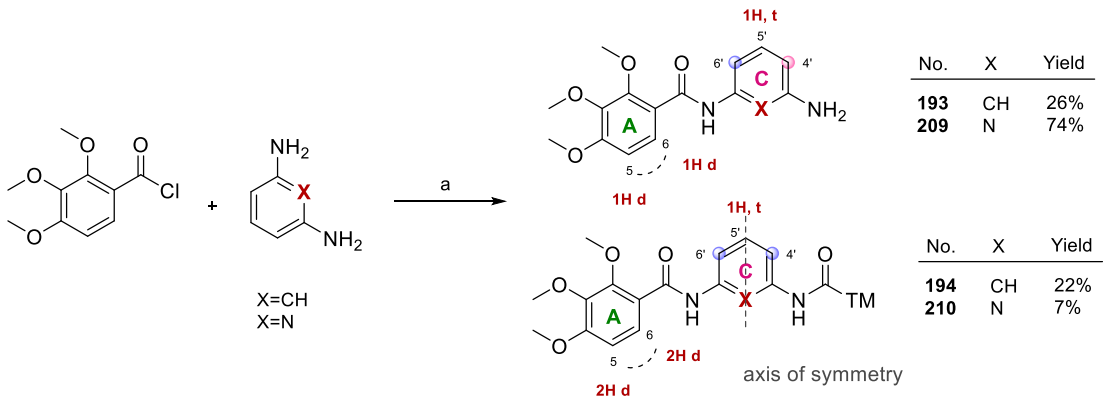

Scheme 26. Preparation of compounds **193**, **194**, **209**, and **210**. Reagents and conditions: (a) Et_3N, CH_2Cl_2, rt, 5-15 h, N_2. Chemically equivalent protons are indicated by balls of the same color (**blue** or **pink**).

The formation of amides reduces the nucleophilicity of the amines in *ortho* and *para* positions, thus less reactive, and diamides are not obtained in those cases. The resonance effect does not apply in the case of amines in 1,3 relative positions, thus the amide formation in one NH_2 group does not decrease the nucleophilic character of the other, explaining the formation of diamides. The A ring protons of diamides show twice integration values compared to H5' of the C ring. H4' and H6' are chemically equivalent in diamides but resonate differently in monoamides, indicating that each acyl chloride reacted with a different amino group of the starting diamine (Scheme 26).

The reaction of benzoyl chlorides with aromatic amines in the *ortho* position of pyridine-like nitrogens (i.e. 2-aminopyridine, 2-amino-5-nitropyridine, 5-methylisoxazol-3-amine) additionally gave imides **201**, **208**, and **245** resulting from the formation of two amide bonds on the same nitrogen (Table 17, Scheme 27). The reaction of 2,3,4-trimethoxybenzoyl chloride with 2-aminopyridine gave imide **201** in 57% yield, and with 2-amino-5-nitropyridine provided monoamide **207** (14%) and imide **208** (32%). The reaction of 5-methylisoxazol-3-amine with the same benzoyl chloride gave **244** (30%) and **245** (49%). This behavior is not observed when the benzoic acids were activated with carbodiimides (Scheme 27). The two imide benzoyl groups are chemically equivalent, and thus give rise to only one set of signals with twice the intensity than monoamides, but two IR bands corresponding to the carbonyls. The second benzoyl group shields protons H6 and H3' (Scheme 27).

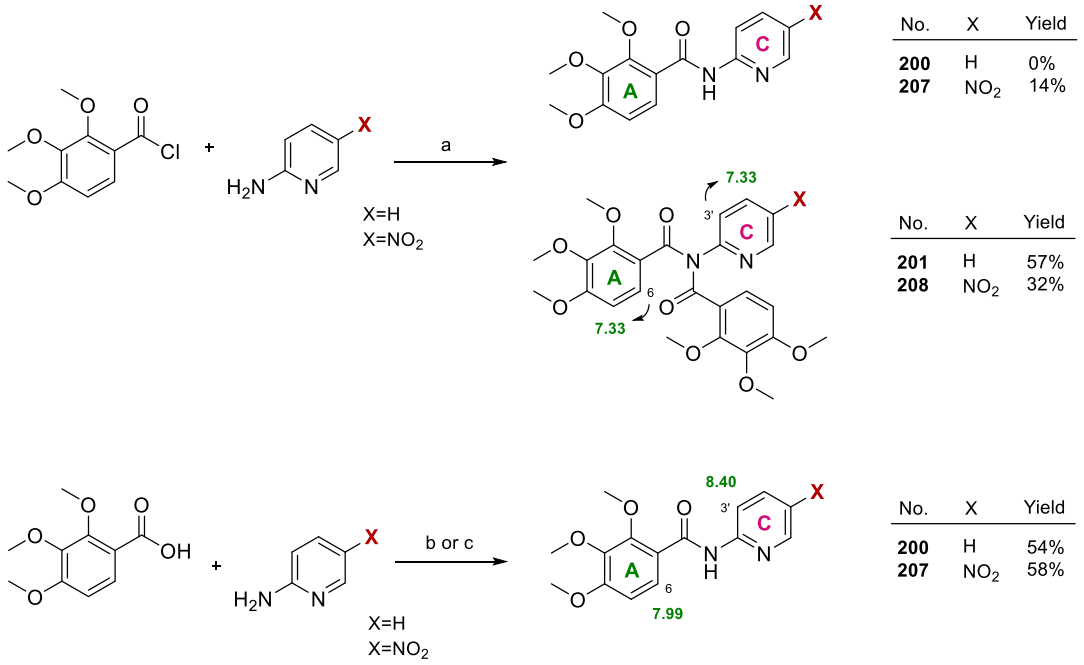

No.	X	Yield
200	H	0%
207	NO_2	14%

No.	X	Yield
201	H	57%
208	NO_2	32%

No.	X	Yield
200	H	54%
207	NO_2	58%

Scheme 27. Preparation of compounds **200**, **201**, **207**, and **208**. Reagents and conditions: (a) Et_3N, CH_2Cl_2, 4 °C, 16-24 h, N_2. (b) DCI, *p*-DMAP, CH_2Cl_2, µW, 130 °C, 2 h. (c) EDC·HCl, *p*-DMAP, CH_2Cl_2, reflux, 1 week, N_2. ^{1}H-NMR chemical shift values (ppm) of **200** and **201** are in **green**.

We hypothesized that this distinct reactivity could rely on tautomerism (Fig. 46). The acylation of the amino group increases its acidity and reduces the energetic difference between the more stable amide (Fig. 46, left) and the imine (Fig. 46, middle). The endocyclic NH group may establish an intramolecular hydrogen bond with the amide carbonyl or with the acyl chloride, but not in the case of carbodiimides due to the higher size of the acylisourea. This only occurs with amino groups in position 2 with respect to a pyridine-like nitrogen, but not in 3-amino or 4-aminopyridines.

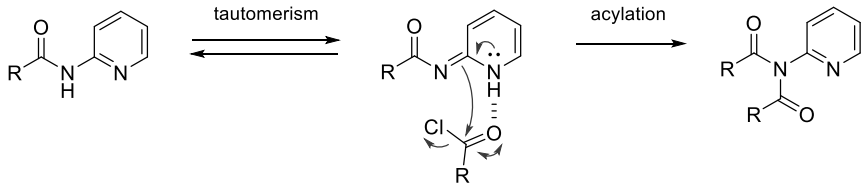

Figure 46. Tautomeric equilibrium in 2-aminopyridine derivatives. The tautomer on the left is energetically more stable, but the relative energy between the two tautomers decreases when the NH_2 is acylated compared to unsubstituted 2-aminopyridine.

When using the coupling agents DCI or EDC·HCl to form **200** and **207**, the yields improved (54-58%) compared to the reaction with acyl chlorides (0-14%) because imides are not formed (Scheme 27). Therefore, we applied this methodology by default to obtain 2-aminopyridine derivatives **202**, **204**, **206**, and **261**. The reactions with carbodiimides give similar overall yields to those with acyl chlorides, and microwave irradiation notably reduces the reaction time.

The reaction of acyl chlorides with diaminopyridines could provide two products, depending on which of the two amino groups reacts. We assumed that 2,3,4-trimethoxybenzoyl chloride reacted with the amino group in position 3 of 2,3-diaminopyridine to provide **225** (Fig. 47) because of the deshielding of proton H4 (7.76 ppm) compared to the starting pyridine (6.92 ppm). We proposed the reaction with 2,5-diaminopyridine by the amine in position 5, yielding **228**, based on the chemical shifts of the pyridine protons. Proton H5 resonates as doublet upfield from the doublet of doublets corresponding to H4, consistent with the proximity of the electron-donating amino group. Compound **236** is presumably forming the amide by the 4-amino group, given the deshielding of proton H5 (7.75 ppm) compared to the diamine (6.40 ppm), and also the deshielding of proton H2 upon acylation of the free amino group of **236** (compounds **237** and **238**), later discussed.

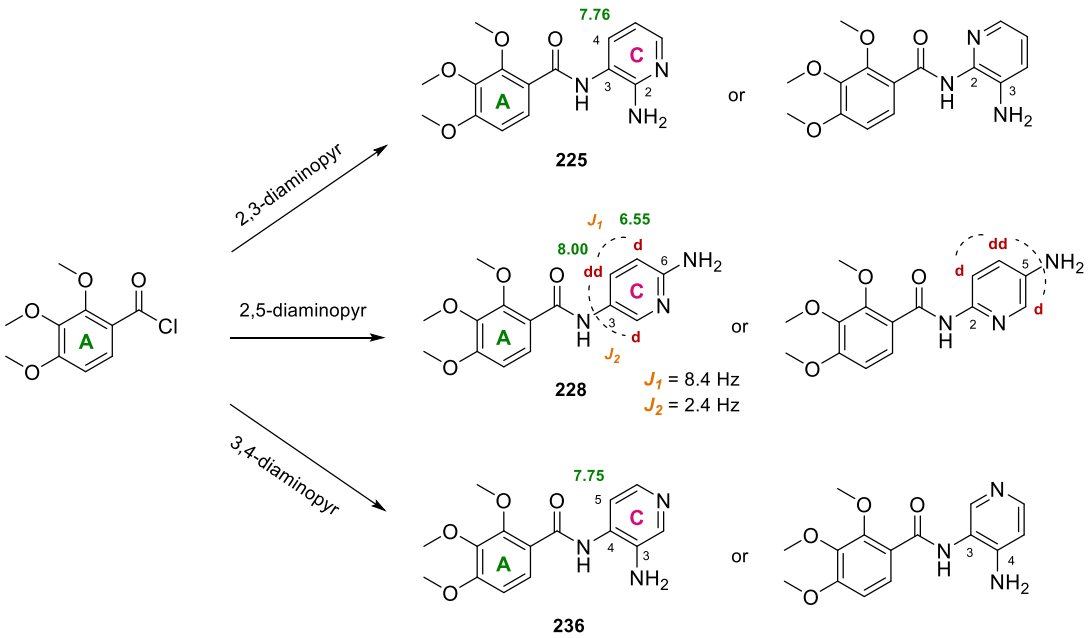

Figure 47. Possible outcomes resulting from the reaction of 2,3,4-trimethoxybenzoyl chloride and 2,3-, 2,5-, or 3,4-diaminopyridines. The number of the product indicates the proposed result of the reaction. ^{1}H-NMR chemical shifts are in **green**, coupling constants (*J*) in **orange**, and splitting patterns in **red**.

Preparation of ureas and carbamates

Urea derivatives were prepared from 4-aminoveratrole and 2,5-dimethoxyaniline **23**. The reaction of these starting materials with ethyl, phenyl, and benzyl isocyanate gave compounds shown in Scheme 28. Compounds **255** and **265** lack the C ring. Although these ethyl ureas linked to the A ring might be too short to engage the zone 3 of the colchicine domain, we addressed the three alternatives (ethyl, phenyl, and benzyl) to explore the effect on the activity.

4-Aminoveratrole gave derivatives **255**, **257**, and **258** in very good yields (84-91%), higher than those for compounds that arise from **23** (49-71%), possibly because of the steric hindrance of the 2-methoxy group. Ureas are characterized by the carbonyl band at 1640 cm^{-1}, and the carbon resonance at 153.2-158.4 ppm. Compound **23** was treated with phenyl chloroformate to provide carbamate **268** through an addition-elimination mechanism. The preparation of ethyl and benzyl carbamates from **23** was sluggish or led to mixtures.

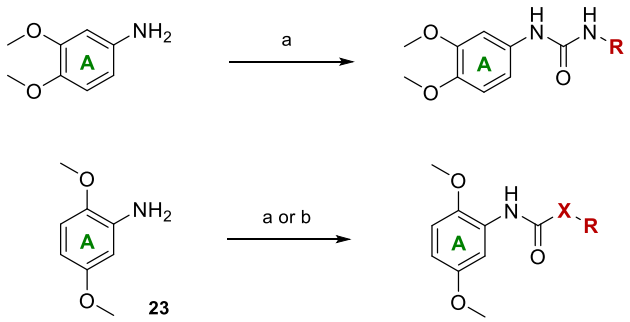

No.	R	Yield
255	Et	84%
257	Ph	91%
258	Bn	84%

No.	X	R	Yield
265	NH	Et	71%
266	NH	Ph	49%
267	NH	Bn	57%
268	O	Ph	54%

Scheme 28. Preparation of urea and carbamate derivatives from 4-aminoveratrole and aniline **23**. Reagents and conditions: (a) ethyl, phenyl, or benzyl isocyanate, CH_2Cl_2, rt, 24 h-1 week, N_2. (b) phenyl chloroformate, Et_3N, CH_2Cl_2, rt, 24 h, N_2.

Bromination of the A ring

In order to modify the conformation of **255** and **258**, we brominated the A ring (Scheme 29). Compounds **256** and **259** were obtained in excellent yields (92-93%). Bromination occurs at the *ortho* position of the amino and *para* of the 3-methoxy group, as evidenced by the two remaining aromatic protons that resonate as singlets in ^{1}H-NMR, in line with a *para*-relative disposition. Attempts to introduce a second bromine on **259** led to complex mixtures.

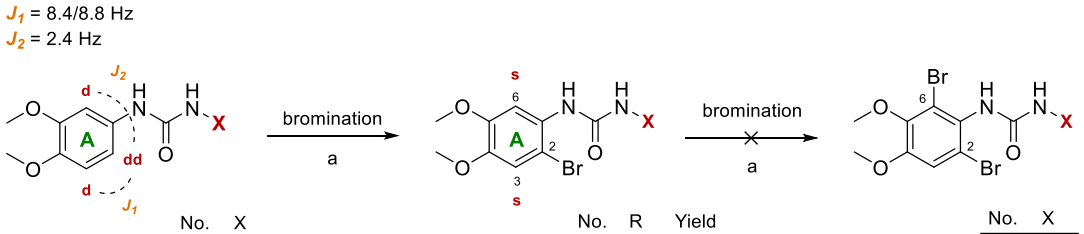

No.	X
255	Et
258	Bn

No.	R	Yield
256	Et	92%
259	Bn	93%

No.	X
260	Bn

Scheme 29. Preparation of brominated derivatives **256** and **259**. Reagents and conditions: (a) NBS, CH_2Cl_2, 4 °C-rt, 30 min-24 h, N_2. Coupling constants (*J*) are indicated in **orange** and the splitting pattern in **red**.

Methylation of the amide linker

Conformational analysis of 2,3,4-trimethoxyphenyl amides suggested the formation of an intramolecular hydrogen bond between the amide and the 2-methoxy group. Alkylation of the amide was pursued in order to modify the conformational preference of the compounds (Table 18).

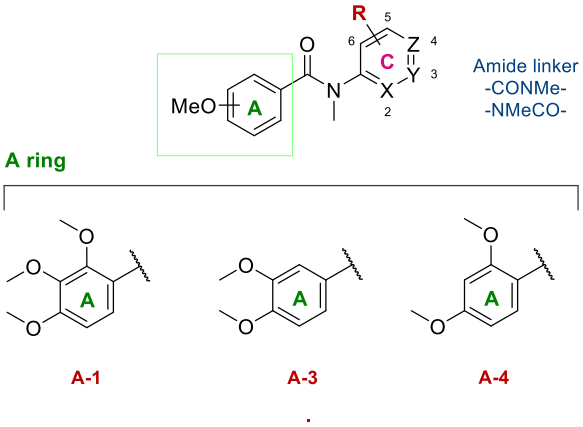

Reagent	Product	A ring	Linker	Conditions	Yield
202	**203**	**A-1**	CONMe	KOH, ACN, rt, 6 days	38%
223	**224**	**A-1**	CONMe	KOH, ACN, rt, 24 h	55%
226	**227**	**A-1**	CONMe	KOH, ACN, rt, 24 h	42%
241	**242**	**A-1**	CONMe	NaOH, CH_2Cl_2, rt, 48h	n.o.
241	**242**	**A-1**	CONMe	NaH, THF, 4 °C, 72 h	38%
251	**252**	**A-3**	NMeCO	KOH, ACN, rt, 72 h	46%
253	**254**	**A-3**	NMeCO	KOH, ACN, rt, 72 h	68%
263	**264**	**A-4**	CONMe	KOH, ACN, rt, 72 h	51%

Table 18. Methylation products obtained from amides in Table 17 (reagents). Conditions and yields are illustrated in the table. n.o. = not obtained.

Methylation of **241** in phase transfer conditions barely showed progress. We then tried with stronger conditions: NaH in dry THF in ice. Hydride is a strong base that gives off hydrogen gas when the amide is deprotonated. It is therefore an irreversible acid-base reaction. This procedure provided **242** in 38% yield. The methylated product is characterized by the chemical shifts of the methyl group, around 3.40 ppm in ^{1}H-NMR, and 35.3-38.4 ppm in ^{13}C-NMR.

Derivatization of the amino group on the C ring

The presence of an amino group on the C ring allowed us to introduce different substituents in order to explore the interaction with the colchicine domain. Compounds **191**, **195**, **209**, **228**, and **236** were subjected to reactions under conditions that had already been discussed, yielding products shown in Table 19.

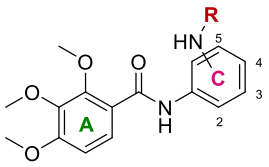

Reagent	NH_2	C ring	Product	Conditions	R	Yield
191	2- NH_2	Ph	**192**	Ac_2O, pyr, CH_2Cl_2, rt, 5 days	Ac	16%
			196	MeOH, Ph_3P, DDQ, CH_2Cl_2, rt	Me	no reaction
195	4- NH_2	Ph	**197**	Ac_2O, pyr, CH_2Cl_2, rt, 3 h	Ac	72%
			198	PhNCO, CH_2Cl_2, rt, 5.5 h	urea-Ph	71%
			211	$(MeO)_2SO_2$, K_2CO_3, acetone, 50 °C	Me	28%
			212		Me_2	29%
			213	$ClSO_2CH_3$, Et_3N, CH_2Cl_2, rt, 72 h	$(SO_2CH_3)_2$	72%
			214	Ac_2O, pyr, CH_2Cl_2, rt, 3 h	Ac	91%
			215	$(CF_3CO)_2O$, pyr, rt, 36 h	$COCF_3$	unstable
			216	$(EtCO)_2O$, pyr, rt, 4 h	COEt	64%
209	3- NH_2	2-pyr	**217**	PhCOCl, Et_3N, CH_2Cl_2, rt, 24 h	COPh	98%
			218	BnCOCl, Et_3N, CH_2Cl_2, rt, 30 h	COBn	80%
			219	KOCN, H_2O/AcOH, 40 °C, 4 h	urea	no reaction
			220	EtNCO, CH_2Cl_2, Δ, 4 days	urea-Et	43%
			221	PhNCO, CH_2Cl_2, rt, 48 h	urea-Ph	89%
			222	ClCOOEt, CH_2Cl_2, rt, 18 h	COOEt	24%
			229	Ac_2O, pyr, CH_2Cl_2, rt, 24 h	Ac	14%
			230	$(EtCO)_2O$, pyr, CH_2Cl_2, rt, 34 h	COEt	25%
			231	PhCOCl, Et_3N, CH_2Cl_2, rt, 48 h	$(COPh)_2$	63%
228	4- NH_2	3-pyr	**232**	EtNCO, CH_2Cl_2, rt, 5 days	urea-Et	55%
			233	PhNCO, CH_2Cl_2, rt, 24 h	urea-Ph	50%
			234	BnNCO, CH_2Cl_2, rt, 1 week	urea-Bn	mixtures
			235	ClCOOEt, Et_3N, CH_2Cl_2, rt, 24 h	COOEt	mixtures
			237	Ac_2O, CH_2Cl_2, rt, 5 days	Ac	54%
			238	PhCOCl, Et_3N, CH_2Cl_2, rt, 48 h	COPh	11%
236	2- NH_2	4-pyr	**239**	EtNCO, CH_2Cl_2, rt, 1 week	urea-Et	59%
			240	PhNCO, CH_2Cl_2, rt, 4 h	urea-Ph	76%

Table 19. Summary of the derivatization products obtained from unsubstituted NH_2 groups, conditions, and yields.

Aromatic amines can be selectively monoalkylated with alcohols using Ph_3P and DDQ at room temperature.[522] However, compound **196** was not obtained under these conditions. Methylation of **209** with dimethyl sulfate provided a mixture of methylamine **211** and dimethylamine **212** in 28% and 29% yields, respectively.

Amides were obtained in variable yields by reaction with anhydrides or acyl chlorides. The trifluoroacetamide of **209** was unstable and decomposed in silica. Urea and carbamate derivatives were obtained with the corresponding isocyanates and chloroformates. Ethyl isocyanate tends to react slowly with reaction times ranging from 4-7 days, compared to phenyl isocyanate that reacts within 4-48 hours at room temperature. The formation of unsubstituted urea **219** was approached by treatment of **209** with potassium cyanate in a mixture of water and acetic acid at 40 °C, but the starting material was fully recovered.

Disulfonamide **213** was obtained from **209** with mesyl chloride. Two molecules of mesyl chloride reacted with the amino group on the C ring. Similarly, compound **231** reacted with two equivalents of benzoyl chloride affording **228**. This behavior is similar to that previously observed for benzoylations of 2-aminopyridines.

Additionally, we intended to obtain compounds akin to **209** derivatives (NH groups in 1,3-relative position) with a different location of the pyridine nitrogen. We attempted a nucleophilic aromatic substitution reaction of the bromine in **204** by an amino group in **205**, but the treatment with ammonia was unsuccessful (Scheme 30).

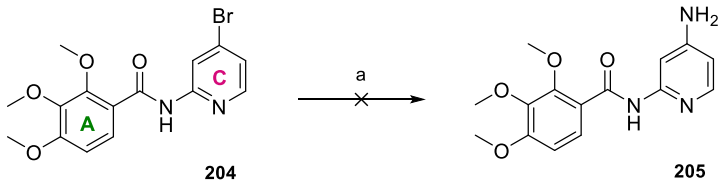

Scheme 30. Preparation of compounds **205**. Reagents and conditions: (a) NH_4OH, $MeOH/H_2O$, 50 °C, 2 weeks.

Compounds **237**-**240** were obtained from **236** by acetylation, benzoylation, and reaction with isocyanates. We tried to deduce the position of the 2,3,4-benzoyl group by means of spectroscopic experiments on these derivatives. Irradiation of ethyl protons of **239** did not give detectable nOe with any pyridine protons but with the 2- and 3-methoxy groups, thus suggesting that ethyl urea is directed towards the A ring. nOe experiments on **237** did not provide the desired information either.

PREPARATION OF BENZOTHIAZOLE-BASED DERIVATIVES

The last family of compounds is based on MI-181, which interacts with zones 2 and 3 of the colchicine domain. It harbors a 5,6-dimethylbenzothiazole group as A ring, with a *trans* olefin connecting this moiety to a pyridine C ring. We prepared a whole series of compounds derived from 6-methylbenzo[d]thiazol-2-amine (Fig. 48). Additionally, brominated analogues on the benzothiazole ring were also synthesized, conducting the bromination in the first place on the amine used as the starting material.

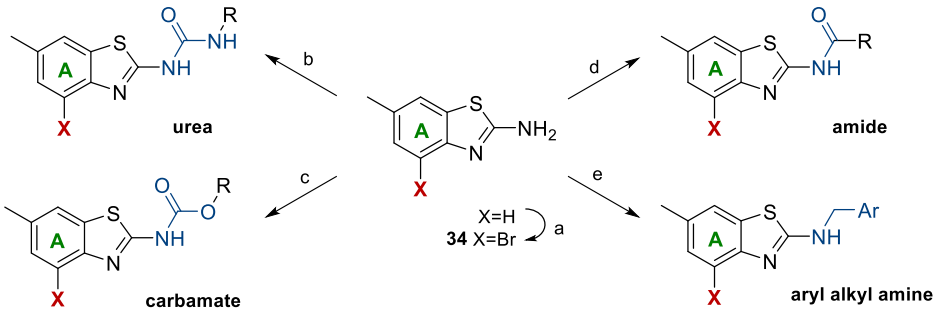

Figure 48. Summary of the general modifications carried out from 6-methylbenzo[d]thiazol-2-amine and **34**. Reagents and conditions: (a) NBS, CH_2Cl_2, 4 °C, 4 h, N_2. (b) R-isocyanate, CH_2Cl_2, rt, 5 h-1 week, N_2. (c) R-chloroformate, Et_3N, CH_2Cl_2, rt, 5-24 h, N_2. (d) i) $SOCl_2$, rt, 24 h; ii) R-COCl, Et_3N, CH_2Cl_2, rt, 3 h-5 days, N_2. (e) i) TsOH, Ar-CHO, toluene, reflux, 4-48 h, N_2; ii) $NaBH_4$, EtOH, rt, 30 min-5 days, N_2.

Then, ureas, carbamates, amides, and aryl alkyl amines were prepared from both benzothiazole amines, either 4-bromo-6-methylbenzo[d]thiazol-2-amine (**34**) or the non-brominated version 6-methylbenzo[d]thiazol-2-amine (Fig. 48). These spacers aim to mimic the conformational behavior induced by the *trans* olefin, which disposes MI-181 rings into an extended conformation one respect to the other to fit into the deepest region of the colchicine domain.

Synthesis of brominated benzothiazole 34

6-Methylbenzo[d]thiazol-2-amine was treated with NBS providing compound **34** in low isolated yield (29%) (Scheme 31). The formation of a brominated benzothiazole can be assessed by the change in the splitting pattern of the aromatic protons. Bromination occurs at position 4, as shown by 1D-nOe experiment, with nOe effects between the two aromatic singlets H5 and H7 and the methyl at position 6.

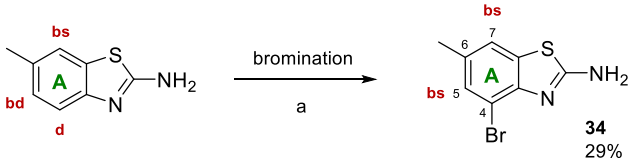

Scheme 31. Preparation of compound **34** as **A ring**. Reagents and conditions: (a) NBS, CH_2Cl_2, 4 °C, 4 h, N_2. The splitting pattern is indicated in **red**.

Formation of ureas and carbamates

Ureas were obtained by reaction between the corresponding amine and ethyl, phenyl, or benzyl isocyanates, and into carbamates with ethyl, phenyl, or benzyl chloroformates with good to excellent yields (except **274** and **280**-**282**), providing compounds listed in Table 20.

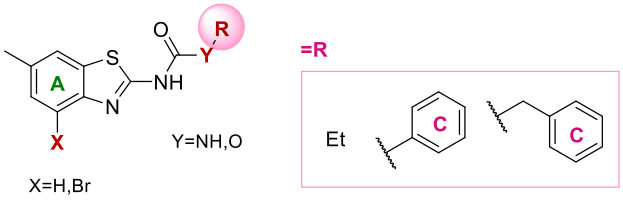

No.	X	Y	R	Conditions	Yield
269	H	NH	Et	rt, 24 h	50%
270	Br	NH	Et	rt, 1 week	63%
271	H	NH	Ph	rt, 5 h	81%
274	Br	NH	Ph	rt, 5 days	13%
275	H	NH	Bn	rt, 5 h	92%
276	Br	NH	Bn	rt, 72 h	65%
277	H	O	Et	rt, 20 h	81%
278	Br	O	Et	rt, 24 h	79%
279	H	O	Ph	rt, 22 h	80%
280	Br	O [bis]	Ph [bis]	rt, 5 h	22%
281	H	O	Bn	rt, 23 h	13%
282	Br	O	Bn	rt, 21 h	mixtures

Table 20. General chemical structure of benzothiazole derivatives containing urea or carbamate moieties. The table summarizes the substituents of the obtained compounds, conditions and yields.

The reaction between **34** and phenyl chloroformate did not lead to the expected carbamate but to compound **280** with two carbamate moieties as evidenced by the integration values in ^{1}H-NMR spectra and the exact mass analysis by HRMS (Scheme 32).

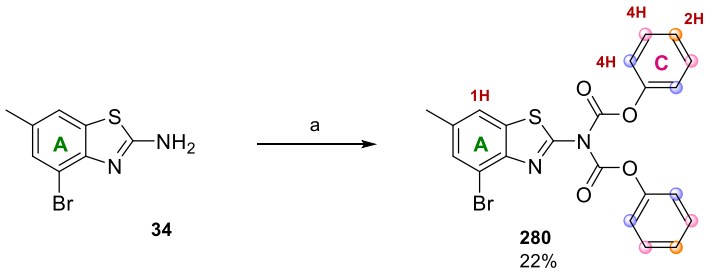

Scheme 32. Preparation of **280**. Reagents and conditions: (a) phenyl chloroformate, Et_3N, CH_2Cl_2, rt, 5 h, N_2. The protons that are chemically equivalent are indicated by balls of the same color (**blue**, **pink**, or **orange**).

In order to lock the conformation of urea derivative **271**, we tried to enclose the urea moiety in a five-membered ring, but imidazolinone **272** was not obtained in phase transfer conditions with NaOH or with NaH. Methylation of **271** with NaH and methyl iodide gave dimethylated derivative **273** in 35% yield, as shown by the two methyl groups that resonate at 3.51 ppm in ^{1}H-NMR and 31.5 and 37.5 ppm in ^{13}C-NMR, distinct than the methyl in position 6 of the benzothiazole ring (Scheme 33).

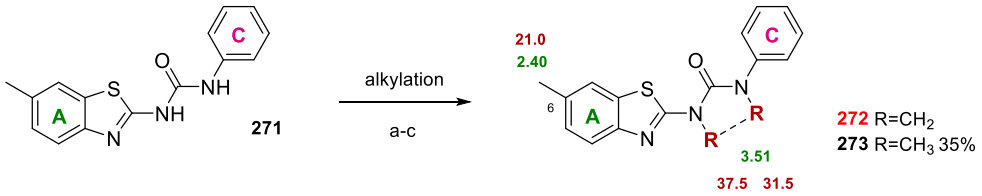

Scheme 33. Preparation of compounds **272** and **273**. Reagents and conditions: (a) 1,2-dibromoethane, NaOH, THF, rt, 4 days, N_2. (b) 1,2-dibromoethane, NaH, THF, 4 °C, 72 h, N_2. (c) CH_3I, NaH, THF, 4 °C, 10 days, N_2. ^{1}H-NMR chemical shifts (ppm) are indicated in **green**, and those for ^{13}C-NMR are in **red**.

Formation of amide derivatives

The preparation of amides **283**-**289** from benzothiazole amines was accomplished by reaction with the corresponding acyl chlorides (Table 21). Benzamides **283** and **284** and phenyl acetamides **285** and **286** were formed with commercial acyl chlorides. Pyridine amides **287**, **288**, **289**, and **293** were obtained with previously formed acyl chlorides or by reaction with carboxylic acids and EDC. The formation of the amide gives a characteristic IR band, and the carbonyl carbon resonates downfield from 160 ppm.

Pyridinecarboxylic acids hamper the reaction because their acyl chlorides are pretty insoluble, so we got yields as low as 16% (**288**), or even complex crudes as it is the case of **289**. This product was neither obtained via EDC hydrochloride in refluxing CH_2Cl_2. The irradiation of the proton peak in **288** corresponding to the methyl group gave nOe with the two broad singlets at 7.50 and 7.59 ppm, which are therefore at positions 5 and 7, so bromine is indeed at position 4.

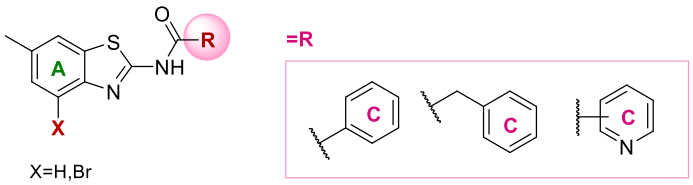

No.	X	R	Conditions	Yield
283	H	Ph	PhCOCl, Et_3N, CH_2Cl_2, rt, 5 days	74%
284	Br	Ph	PhCOCl, Et_3N, CH_2Cl_2, rt, 24 h	mixtures
285	H	Bn	BnCOCl, Et_3N, CH_2Cl_2, rt, 5 days	72%
286	Br	Bn	BnCOCl, Et_3N, CH_2Cl_2, rt, 23 h	57%
287	H	2-pyr	(RCOOH, $SOCl_2$), Et_3N, CH_2Cl_2, rt, 3 h	79%
288	Br	2-pyr	(RCOOH, $SOCl_2$), Et_3N, CH_2Cl_2, rt, 28 h	16%
289	H	3-pyr	(RCOOH, $SOCl_2$), Et_3N, CH_2Cl_2, rt, 22 h	mixtures
289	H	3-pyr	EDC·HCl, *p*-DMAP, CH_2Cl_2, Δ, 3 weeks	n.o.
293	H	4-pyr	(RCOOH, $SOCl_2$), Et_3N, CH_2Cl_2, rt, 30 min	n.o.

Table 21. General chemical structure of benzothiazole derivatives containing amide spacers. The table summarizes conditions and yields. n.o. = not obtained.

Formation of aryl alkyl amines

The aryl alkylation of the benzothiazole amine was conducted via two-step reductive amination using pyridine aldehydes (picolinaldehyde, nicotinaldehyde, or isonicotinaldehyde). We first tried to synthesize **291** following the procedure established for sulfonamide-based compounds. The amine was mixed with picolinaldehyde in refluxing CH_2Cl_2 slightly acidic. The second step was conducted at room temperature in methanol and $NaBH_4$, but led to complex mixtures. Thus, we sought for an alternative protocol.

The eventual procedure also consists of two steps. First, the amine reacts with the aryl aldehyde in the presence of *p*-toluenesulfonic acid in refluxing toluene, yielding the imine. Toluene permits heating at higher temperature than CH_2Cl_2 and water removal. Then, the imine was reduced with $NaBH_4$ to methylamine yielding compounds **290**-**292** in poor yields (19-26%), whose benzylic methylenes resonate at 4.59-4.81 ppm in ^{1}H-NMR and 46.5-48.3 ppm in ^{13}C-NMR (Scheme 34).

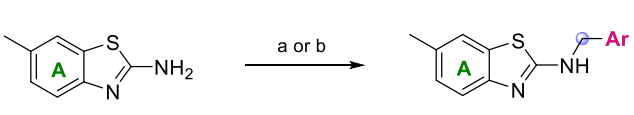

No.	Ar	Yield
290	2-pyr	19%
291	3-pyr	26%
292	4-pyr	9%

Scheme 34. Preparation of compounds **290**-**292**. Reagents and conditions: (a) i) picolinaldehyde, HCl, CH_2Cl_2, reflux, 1 week, N_2; ii) $NaBH_4$, MeOH, rt, 72 h, N_2. (b) i) R-CHO, TsOH, toluene, reflux, 4-48 h, N_2; ii) $NaBH_4$, EtOH, rt, 30 min-5 days, N_2.

Surprisingly, the reaction that yielded **292** provided a second product in 9% yield: amide **293**, which was not obtained with isonicotinoyl chloride. Isonicotinaldehyde may have been partially oxidized containing traces of the acid when we used it in the reaction aimed to obtain just **292**.

Chapter 4

RESULTS II

CHARACTERIZATION OF THE ANTIPROLIFERATIVE ACTIVITY

We have screened all the compounds resulting from the previous chapter to determine their *in vitro* antiproliferative activity. Cell proliferation was assessed by a colorimetric reaction using XTT, MTT, or WST-1 reagents. This procedure is based on the conversion of those tetrazolium salts into colored formazan crystals by metabolically-active cells. The formation of the formazan compounds can be quantified and correlates with the relative number of viable cells. The effect of the compounds was first evaluated at 1 µM, and IC_{50} values were determined by dose-response curves for those inhibiting cell proliferation by at least 50% in two independent experiments. For this purpose, we used the human tumor cell lines HeLa (cervix adenocarcinoma), HT-29 (colorectal adenocarcinoma), and HL-60 (acute myeloid leukemia). The metabolization of tetrazolium salts was measured after 72-h treatments.

None of the sulfonamides **35**-**77** aimed to bind to the three zones of the colchicine domain showed antiproliferative activity at 1 µM against those three tumor cell lines. Amide derivatives and related compounds **191**-**268** and benzothiazole-based compounds **269**-**293** initially designed to bind to zones 2 and 3 did not affect cell proliferation at 1 µM either. The only compound that affected cell viability was 1-(4-bromo-6-methylbenzo[d]thiazol-2-yl)-3-ethylurea (**270**). It showed an IC_{50} value of 484.0 ± 23.1 nM against HeLa cells and no proliferation inhibition at 1 µM against HT-29 and HL-60 cell lines.

SAR of indole sulfonamide derivatives

Most of the sulfonamides **80**-**140** aimed to bind to zones 1 and 2 proved effective at 1 µM against HeLa, HT-29, and HL-60 cells. Based on those results, we decided to evaluate their effect on proliferation in the human tumor cell line AGS (human gastric adenocarcinoma) and the non-tumorigenic cell line HEK-293 from human embryonic kidney. The results for half-maximal inhibitory concentrations (IC_{50}) are summarized in Table 22 in nanomolar units. These compounds exerted antiproliferative activity with IC_{50} values in the submicromolar range, displaying akin potencies against the different assayed cell lines, although HT-29 adenocarcinoma was slightly more resistant, consistently with previous reports.[499] Subtle variations in potency were found for tumor versus non-tumorigenic cell lines.

The structure activity relationship evidences the importance of the substitution pattern on the polymethoxylated benzene (**A ring**). The overall IC_{50} values for 3,4,5-trimethoxyphenyl derivatives (scaffold D-1, compounds **80**-**97**) are around one order of magnitude lower than those for compounds with a 3,5-dimethoxyphenyl group (scaffold D-3, **103**-**118**), which in turn showed higher potency than 2,5-dimethoxyphenyl derivatives (scaffolds D-4 and D-5, **122**-**140**). The comparison of D-4 and D-5 reveals that the introduction of bromine at 4-position of the A ring improves the antiproliferative activity (see **133** and **139** versus **134** and **136**, respectively).

Compounds **99** and **100** (scaffold D-2) that harbor a reversed sulfonamide did not show any effect on cell proliferation below 1 µM, in contrast with their highly potent counterparts **80** and **81** (scaffold D-1). The diminished antitumor potency of D-2 compared to D-1 compounds is in agreement with the results published for indolecombretastatins.[499] In order to discern whether the loss of activity is due to the altered location of the methoxy groups in 2,3,4-positions, or the reversed sulfonamide, we tried to combine the scaffold D-2 with the sulfonamide orientation of series D-1, but compound **98** was not obtained. The lack of activity could putatively be due to the altered substitution pattern of the A ring, as some previous reports found the bridge reversal increasing the antitumor activity in sulfonate derivatives.[523]

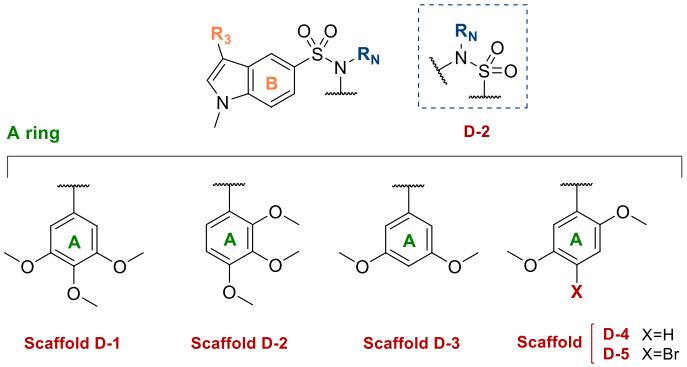

No.	A ring	R_3	R_N	HeLa -	HeLa Elac 0.1 µM	HeLa Vera 1 µM	HeLa Vera 10 µM	HT-29	HL-60	AGS	HEK-293	G_2/M arrest 10 nM	G_2/M arrest 100 nM	G_2/M arrest 1 µM
80		H	H	10.8 ± 3.4	10.9 ± 1.7	11.1 ± 1.5	8.4 ± 1.6	51.0 ± 7.8	10.9 ± 4.9	12.9 ± 4.2	6.4 ± 1.0	-	+	+
81		H	Me	2.4 ± 0.4	3.3 ± 0.6	2.1 ± 0.6	1.9 ± 0.9	4.3 ± 0.9	1.1 ± 1.0	3.3 ± 0.8	2.3 ± 0.4	+	+	+
82		H	Et	22.1 ± 5.8	2.3 ± 0.9	3.0 ± 0.8	2.7 ± 0.6	14.4 ± 8.2	10.8 ± 4.7	8.2 ± 4.5	6.0 ± 1.1	+/-	+	+
84		H	CH_2COOEt	28.8 ± 7.3	10.7 ± 3.5	10.7 ± 1.5	10.0 ± 1.3	53.3 ± 8.9	15.2 ± 2.6	26.5 ± 7.8	6.6 ± 2.1	-	+	+
85		H	CH_2COOH	> 1000	n.d.	n.d.	n.d.	> 1000	> 1000	n.d.	n.d.	-	-	-
86		H	CH_2CN	13.7 ± 3.5	11.5 ± 1.1	12.8 ± 2.1	9.6 ± 2.6	47.7 ± 5.2	26.7 ± 7.5	5.6 ± 1.8	5.1 ± 2.8	-	+	+
87		Br	H	48.2 ± 4.9	13.2 ± 2.6	18.5 ± 4.8	17.0 ± 2.5	249.9 ± 46.3	28.0 ± 5.0	78.9 ± 8.4	24.1 ± 6.5	-	+	+
88		Br	Et	30.0 ± 5.9	18.9 ± 5.6	12.6 ± 3.5	14.8 ± 8.1	52.8 ± 8.2	24.1 ± 8.9	53.1 ± 2.6	24.1 ± 6.5	-	+	+
89		CHO	H	206.5 ± 38.6	285.3 ± 52.1	332.4 ± 50.0	286.7 ± 43.7	623.8 ± 140.6	209.8 ± 83.9	213.2 ± 33.6	229.4 ± 22.3	-	-	+
90		CHO	Me	41.2 ± 4.9	34.9 ± 4.7	40.3 ± 8.3	44.7 ± 11.0	385.2 ± 48.2	89.3 ± 14.0	35.3 ± 3.6	39.9 ± 5.6	-	+	+
91	D-1	CH=CH-CN (*E*)	Me	35.4 ± 7.6	16.7 ± 3.4	13.3 ± 3.1	12.2 ± 2.1	78.3 ± 15.7	14.4 ± 9.0	18.0 ± 1.2	9.7 ± 0.5	-	+	+
92		CH=CH-CN (*Z*)	Me	44.6 ± 8.5	18.5 ± 4.1	17.6 ± 6.8	15.7 ± 8.5	107.1 ± 15.6	23.0 ± 9.6	22.6 ± 1.5	11.4 ± 1.0	-	+	+
93		CHO	Et	178.5 ± 60.6	184.6 ± 76.0	131.0 ± 90.0	130.0 ± 63.6	606.4 ± 84.7	123.2 ± 89.1	157.8 ± 22.3	175.7 ± 23.5	-	-	+
94		CH=CH-CN (*E*)	Et	68.6 ± 15.1	37.6 ± 4.6	38.3 ± 5.4	41.8 ± 14.3	342.3 ± 48.8	120.4 ± 69.1	162.8 ± 18.3	156.0 ± 15.6	-	+	+
95		CH=CH-CN (*Z*)	Et	188.0 ± 27.7	46.2 ± 9.4	43.5 ± 6.8	40.7 ± 5.6	336.3 ± 47.6	258.0 ± 47.7	196.6 ± 29.9	161.5 ± 19.6	-	+	+
96		CN	H	21.4 ± 2.7	24.9 ± 5.2	23.2 ± 3.2	25.5 ± 6.1	55.2 ± 11.8	16.2 ± 6.3	11.2 ± 1.7	13.8 ± 1.4	-	+	+
97		CN	Me	12.3 ± 4.0	10.6 ± 2.8	10.7 ± 1.5	18.3 ± 3.6	51.9 ± 9.8	20.1 ± 8.3	19.4 ± 5.8	6.8 ± 19.6	-	+	+
99	D-2	H	H	~ 1000	n.d.	n.d.	n.d.	> 1000	> 1000	n.d.	n.d.	-	-	-
100		H	Me	~ 1000	n.d.	n.d.	n.d.	> 1000	> 1000	n.d.	n.d.	-	-	-

Table 22. Continued

No.	A ring	R_3	R_N	HeLa				HT-29	HL-60	AGS	HEK-293	G_2/M arrest		
				-	Elac 0.1 µM	Vera 1 µM	Vera 10 µM					10 nM	100 nM	1 µM
103	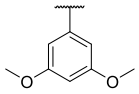 D-3	H	H	1401.8 ± 188.8	n.d.	n.d.	n.d.	> 1000	> 1000	n.d.	n.d.	-	-	-
104		H	Me	20.1 ± 2.7	32.2 ± 4.5	29.2 ± 4.5	29.0 ± 4.3	42.6 ± 7.8	23.5 ± 5.0	30.5 ± 3.9	11.8 ± 3.0	-	+	+
105		H	Et	55.2 ± 8.3	130.9 ± 12.0	89.5 ± 15.4	90.2 ± 8.6	153.6 ± 17.7	41.0 ± 6.8	263.0 ± 44.6	87.8 ± 5.9	-	+	+
106		H	CH_2COOEt	320.7 ± 24.2	326.3 ± 26.6	455.9 ± 27.0	313.7 ± 34.0	593.4 ± 30.9	328.3 ± 26.8	529.8 ± 37.6	431.8 ± 50.0	-	-	+
107		H	CH_2CN	68.6 ± 8.7	201.4 ± 15.8	138.7 ± 16.3	125.8 ± 10.3	230.8 ± 20.6	104.7 ± 6.8	199.6 ± 31.0	111.5 ± 30.0	-	+/-	+
109		H	Bn	273.2 ± 20.0	266.0 ± 25.8	259.7 ± 52.5	267.7 ± 61.8	369.6 ± 35.2	246.8 ± 26.4	266.9 ± 40.3	177.0 ± 42.5	-	-	+
110		H	Bn-4-F	278.6 ± 22.4	249.6 ± 36.3	287.4 ± 45.4	295.7 ± 41.6	326.8 ± 76.0	229.2 ± 43.2	207.4 ± 20.1	222.0 ± 96.1	-	-	+
112		$CONH_2$	H	1770.2 ± 546.6	n.d.	n.d.	n.d.	1504.7 ± 598.7	> 1000	n.d.	n.d.	-	-	-
115		CHO	Me	> 1000	n.d.	n.d.	n.d.	> 1000	> 1000	n.d.	n.d.	-	-	-
116		CHO	Bn	> 1000	n.d.	n.d.	n.d.	> 1000	> 1000	n.d.	n.d.	-	-	-
117		CN	Me	551.4 ± 21.2	643.0 ± 17.0	711.9 ± 22.8	641.8 ± 34.8	713.0 ± 30.8	512.8 ± 18.3	433.8 ± 90.6	573.7 ± 38.3	-	-	+
118		CN	Bn	794.3 ± 34.4	796.4 ± 29.0	943.0 ± 44.2	911.0 ± 28.0	993.0 ± 74.6	754.5 ± 33.9	789.4 ± 71.5	680.5 ± 55.8	-	-	+
122	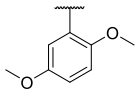 D-4	H	H	320.2 ± 49.0	254.8 ± 91.7	360.5 ± 102.3	321.6 ± 79.5	898.0 ± 92.6	262.2 ± 67.5	454.1 ± 49.2	451.5 ± 47.8	-	-	+
123		H	Me	169.2 ± 34.0	138.4 ± 24.2	164.4 ± 33.0	140.5 ± 26.7	613.1 ± 82.2	233.8 ± 37.0	149.5 ± 20.4	126.9 ± 11.4	-	+/-	+
125		H	CH_2COOEt	1020.2 ± 30.1	n.d.	n.d.	n.d.	> 1000	> 1000	n.d.	n.d.	-	-	-
126		H	CH_2CN	220.5 ± 99.1	168.1 ± 58.3	224.9 ± 43.7	186.0 ± 80.2	435.4 ± 81.7	160.4 ± 81.3	247.3 ± 36.5	182.8 ± 32.3	-	+/-	+
127		H	Bn	818.0 ± 68.4	719.9 ± 47.5	793.6 ± 27.5	709.1 ± 34.6	948.4 ± 41.0	899.7 ± 53.5	840.9 ± 53.1	584.0 ± 83.7	-	-	+
132		CHO	H	> 1000	n.d.	n.d.	n.d.	> 1000	> 1000	n.d.	n.d.	-	-	-
133		CHO	Me	> 1000	n.d.	n.d.	n.d.	> 1000	> 1000	n.d.	n.d.	-	-	-
137		CH=CH-CN (*E*)	H	319.5 ± 49.1	367.8 ± 55.3	720.2 ± 71.9	655.4 ± 72.5	545.8 ± 85.6	250.6 ± 59.6	786.0 ± 53.7	854.1 ± 52.5	-	-	+
138		CH=CH-CN (*Z*)	H	469.0 ± 54.1	425.3 ± 102.6	797.8 ± 83.5	478.3 ± 121.6	775.9 ± 143.1	400.7 ± 105.8	885.2 ± 35.6	990.2 ± 51.0	-	-	+
139		CN	H	~ 1000	n.d.	n.d.	n.d.	> 1000	> 1000	n.d.	n.d.	-	-	-
140		CN	Ac	> 1000	n.d.	n.d.	n.d.	> 1000	> 1000	n.d.	n.d.	-	-	-
128	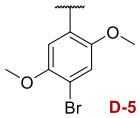 D-5	Br	H	369.0 ± 91.9	234.8 ± 79.7	266.2 ± 66.2	253.7 ± 51.8	343.4 ± 65.5	155.7 ± 83.4	410.4 ± 49.1	393.7 ± 72.1	-	-	+
129		Br	Me	273.5 ± 27.8	146.5 ± 24.9	136.2 ± 17.3	78.2 ± 16.3	417.6 ± 64.7	203.7 ± 97.4	210.7 ± 32.3	354.9 ± 88.2	-	+/-	+
134		CHO	Me	765.3 ± 102.7	759.7 ± 76.0	758.5 ± 68.7	763.8 ± 83.4	611.5 ± 120.9	206.6 ± 90.2	518.6 ± 34.8	502.5 ± 22.8	-	-	+
135		CHO	H	> 1000	n.d.	n.d.	n.d.	> 1000	> 1000	n.d.	n.d.	-	-	-
136		CN	H	320.2 ± 72.5	282.8 ± 59.1	287.5 ± 44.1	279.3 ± 45.4	417.2 ± 87.0	329.1 ± 56.3	~ 1000	> 1000	-	-	+
IC^{501}	D-1	H	-	n.d.	n.d.	n.d.	n.d.	360	n.d.	n.d.	n.d.	n.d.	+/-	+

Table 22. Antiproliferative activity of biaryl sulfonamides against the human cell lines HeLa, HT-29, HL-60, and AGS (tumor), and HEK-293 (non-tumorigenic). IC_{50} values are expressed in nanomolar and were measured after 72 h of incubation (n = 3-7). The G_2/M arrest was evaluated in HeLa cells at 10 nM, 100 nM, and 1 µM concentrations after 24, 48, and 72 h treatments and is indicated qualitatively based on the 24 h results in Table 25. Elac = elacridar; Vera = verapamil; n.d. = not determined; IC = indolecombretastatin; + = > 50%; +/- = 35-50%; - = no effect.

Sulfonamides **80**, **81**, **82**, **84**, and **86** show nanomolar potencies against different cell lines comparable or even higher than those of indolecombretastatins[499] (e.g. **80** displayed seven-fold higher activity against HT-29 than IC; Table 22). This indicates that the sulfonamide moiety is a suitable replacement over the olefin bridge. The impact of **sulfonamide** substituents on the activity depends on the nature of the A ring. In general, these modifications retained the antiproliferative potency for 3,4,5-trimethoxy and some 2,5-dimethoxyphenyl derivatives. However, it resulted in an exacerbated cytotoxic profile within 3,5-dimethoxyphenyl compounds, up to around 70-fold enhancement in **104** compared to **103**. Irrespective of the A ring they harbor, the sulfonamide methylation provided the most potent compounds within each series (**81**, **104**, and **123**), showing higher activity than their unsubstituted counterparts (**80**, **103**, and **122**). This observation also applies to sulfonamide pairs with modifications on the indole 3-position (see **89**, **96**, **128**, and **135** versus **90**, **97**, **129**, and **134**). The saponification of **84** to **85** led to the loss of the activity at 1 µM, which might be related to the fact that carboxylic acids are predominantly ionized at physiological pH. The introduction of ethyl, ethyl acetate, or acetonitrile substituents on **80** (D-1) led to similar IC_{50} values. Regarding D-3 and D-4 series, the incorporation of ethyl and acetonitrile groups (**105**, **107**, and **126**) gave the best results after methyl sulfonamides, followed by benzyl derivatives (**109**, **110**, and **127**), which in turn resulted more potent than those bearing an ethyl acetate group (**106** and **125**).

Substitutions at the **indole 3-position**, which greatly improve the antiproliferative potencies of indolecombretastatins,[499] are detrimental in indole sulfonamides. The introduction of aldehyde groups led to weaker cytotoxic activity, the same trend observed for indolecombretastatins. Derivatives with bromine (**87**, **88**, **128**, and **129**) and amide groups (**112**) at the indole 3-position barely showed changes on IC_{50} values with respect to their unsubstituted counterparts. However, in the case of compounds **128** and **129** (D-5), the negative contribution of the indole substitution might be masked by the positive effect of a bromine group on the A ring. Nitrile groups did not improve the antiproliferative effect of unsubstituted indoles either, but considerably enhanced the cytotoxic activity compared to their formyl counterparts, (e.g. **89**, **135** versus **96**, **136**, respectively). Propenenitriles led to IC_{50} values akin to those observed for aldehyde groups within 3,4,5-trimethoxyphenyl series (D-1), whereas the incorporation of this group into 2,5-dimethoxyphenyl derivative **122** (D-4) retained the activity (**137** and **138**). The overall activity of the *E* isomers was slightly higher than that of *Z* isomers, although the latter isomerize to the more favorable *E* configuration, at least in part.

SAR of tetrazoles and related amides

Many of the compounds belonging to this group aimed to bind to zones 1 and 2 inhibited cell proliferation at 1 µM concentration against HeLa, HT-29, and HL-60, then additionally tested against AGS and HEK-293 (Table 23). Tetrazoles and amides can be divided into two groups depending on the **B ring**: derivatives with benzene (**141**-**161**) or *N*-methylindol-5-yl (**162**-**190**) as B ring.

Most of the compounds with benzene as B ring harbor a 3,5-dimethoxyphenyl as A ring (scaffold D-3). None of these amides affected cell proliferation at 1 µM irrespective of the substituent in position 4 of the B ring (MeO, NO_2, NH_2, or NMe_2) or the presence of bromine atoms on the A ring. The orientation of the amide bridge (A1 and A2) did not make any difference either. The two amides **160** and **161** with a 2,5-dichlorophenyl group (scaffold D-6) as **A ring** did not prove effective at 1 µM. Regarding tetrazole derivatives, three compounds showed IC_{50} values in the submicromolar range against all the tested cell lines. The most potent among them is **156** bearing a dimethylamino group on the **B ring**. It showed five-fold higher potency in HeLa cells than its counterpart **144** with a methoxy group, both sharing the tetrazole

orientation T1. The reversed orientation of the **tetrazole bridge** (T2) translates into a three-fold decrease in the antiproliferative activity (**144** versus **150**).

The bromination of **144** and **150** gave compounds **146**, **147**, and **152** with two bromine groups each on the **A ring**, and a complete loss of activity. The putative unfavorable interaction with the protein may arise from the overall conformation of the brominated products. Conformational analysis studies performed with **144** and **150** predicted that B ring and A ring planes in the least energetic conformations are respectively around 30° and 45° angles bent compared to the tetrazole plane. The introduction of a bromine group at position 2 of the A ring (**146**, **147**, and **152**) has two main consequences: it affects the orientation of the vicinal methoxy group and forces the A ring to twist up to 90° with respect to the tetrazole plane.

The majority of the compounds with an *N*-methylindol-5-yl moiety as B ring showed IC_{50} values in the submicromolar range, and a few of them nanomolar. Most of them experienced a remarkable drop in cytotoxic potency against HT-29 compared to the other cell lines, which responded similarly to treatments. The decreased activity is more evident for compounds with a 3,4,5-trimethoxyphenyl as A ring (scaffold D-1), as it is the case of **184** with 17-fold higher IC_{50} value against HT-29 (548 nM) than HeLa cells (32 nM). For all the pairs differing in the **bridge** (A1, A2 versus T1, T2), the activity of amide derivatives was weaker than their tetrazole counterparts, whatever the substituents on the indole ring (e.g. **163**, **171**, and **174** versus **166**, **181**, and **186**, respectively).

The effect of the bridge orientation on the antiproliferative activity differs between amides and tetrazoles. The amides with the nitrogen bound to the B ring (A2) exhibited increased potencies than amides A1 for unsubstituted indoles. Amides **171** and **172** (A1) showed no cell proliferation inhibition at 1 µM, whereas their reversed analogues **174** and **175** (A2) displayed IC_{50} values of 20 nM and 414 nM against HeLa cells, respectively. The impact of the amide reversal in substituted indoles is at best moderate based on the data we have (see **173** versus **176**). By contrast, tetrazole derivatives **181** and **186** with an unsubstituted indole ring showed akin potency, around 2-3 nM in HeLa cells, irrespective of the tetrazole orientation T1 or T2. The main difference resides in the activity against HT-29 cells: the IC_{50} value of **181** (T1) is around 30-fold lower than that of **186** (T2). Concerning tetrazoles with substituents on the indole 3-position, the T1 orientation led to improved potency compared to T2 analogues (**183**, **184** versus **188**, **189**), the opposite trend to amides.

There is no clear pattern regarding the impact on the activity of removing the 4-methoxy group of the **A ring**. Amide **163** with a 3,5-dimethoxyphenyl group (scaffold D-3) is around ten-fold less potent than its counterpart **174** with a 3,4,5-trimethoxyphenyl moiety (scaffold D-1). However, tetrazole derivatives D-3 with no substituent or carbonitrile on the indole 3-position showed increased activity than D-1 compounds (**166**, **170** versus **186**, **189**). A formyl substituent induces the opposite effect (**169** versus **188**).

In general, the introduction of substituents on the **B ring** has a negative effect on the antiproliferative activity of the compounds, except for brominated amides **164** and **165** that retained the potency of **163** (D-3). In amides D-1, nitrile derivative **177** showed 15-fold lower activity than the unsubstituted indole, a 45-fold decrease in the case of the formyl group (**176**). Larger hydrazine substituents **178**-**180** resulted in the loss of activity. The effect of the substituents on the activity showed differences between series regarding tetrazole compounds, although all of them are detrimental for the cytotoxic activity.

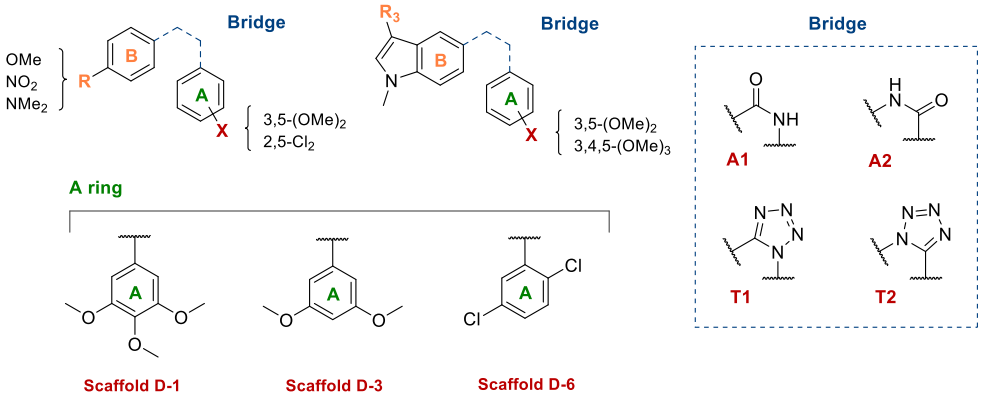

No.	B ring/A ring	R	Bridge	HeLa -	HeLa Elac 0.1 μM	HeLa Vera 1 μM	HeLa Vera 10 μM	HT-29	HL-60	AGS	HEK-293	G_2/M arrest 10 nM	G_2/M arrest 100 nM	G_2/M arrest 1 μM
141		4-Meo	A1	>1000	n.d.	n.d.	n.d.	>1000	>1000	n.d.	n.d.	-	-	-
142		4-MeO-2′,4′-Br_2	A1	>1000	n.d.	n.d.	n.d.	>1000	>1000	n.d.	n.d.	-	-	-
143		4-Meo-2′,6′-Br_2	A1	>1000	n.d.	n.d.	n.d.	>1000	>1000	n.d.	n.d.	-	-	-
144		4-Meo	T1	48.5 ± 5.0	79.7 ± 5.8	77.1 ± 7.7	74.4 ± 10.6	104.8 ± 8.0	47.2 ± 4.4	63.8 ± 7.9	75.3 ± 3.8	-	+/-	+
146		4-MeO-2′,6′-Br_2	T1	>1000	n.d.	n.d.	n.d.	>1000	>1000	n.d.	n.d.	-	-	-
147		4-Meo-2′,4′-Br_2	T1	>1000	n.d.	n.d.	n.d.	>1000	>1000	n.d.	n.d.	-	-	-
148		4-MeO	A2	>1000	n.d.	n.d.	n.d.	>1000	>1000	n.d.	n.d.	-	-	-
150		4-Meo	T2	147.3 ± 11.5	163.5 ± 16.6	139.9 ± 19.4	145.3 ± 22.8	200.9 ± 20.9	141.1 ± 16.6	150.8 ± 18.9	171.8 ± 33.4	-	+/-	+
152		4-MeO-2′,6′-Br_2	T2	>1000	n.d.	n.d.	n.d.	>1000	>1000	n.d.	n.d.	-	-	-
153		4-NO_2	A1	>1000	n.d.	n.d.	n.d.	>1000	>1000	n.d.	n.d.	-	-	-
154		4-NH_2	A1	>1000	n.d.	n.d.	n.d.	>1000	>1000	n.d.	n.d.	-	-	-
155		4-Me_2N	A1	>1000	n.d.	n.d.	n.d.	>1000	>1000	n.d.	n.d.	-	-	-
156		4-Me_2N	T1	10.9 ± 2.2	12.8 ± 3.1	8.9 ± 0.9	9.5 ± 1.3	32.8 ± 4.6	9.6 ± 101	12.0 ± 1.0	5.3 ± 1.9	-	+	+
157		4-NO_2	A2	>1000	n.d.	n.d.	n.d.	>1000	>1000	n.d.	n.d.	-	-	-
158		4-NH_2	A2	>1000	n.d.	n.d.	n.d.	>1000	>1000	n.d.	n.d.	-	-	-
159		4-Me_2N	A2	>1000	n.d.	n.d.	n.d.	>1000	>1000	n.d.	n.d.	-	-	-
160	D-6	4-MeO	A2	>1000	n.d.	n.d.	n.d.	>1000	>1000	n.d.	n.d.	-	-	-
161	D-6	4-NO_2	A2	>1000	n.d.	n.d.	n.d.	>1000	>1000	n.d.	n.d.	-	-	-

D-3

Table 23. Continued

No.	B ring/A ring	R	Bridge	HeLa				HT-29	HL-60	AGS	HEK-293	G_2/M arrest		
				-	Elac 0.1 µM	Vera 1 µM	Vera 10 µM					10 nM	100 nM	1 µM
163	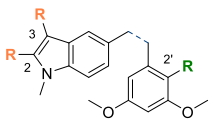 D-3	H	**A2**	195.3 ± 15.7	329.8 ± 70.9	229.7 ± 19.7	193.6 ± 43.9	260.6 ± 32.8	200.7 ± 17.9	221.0 ± 43.1	241.7 ± 39.6	-	-	+
164		Br	**A2**	284.0 ± 53.4	290.4 ± 29.5	363.0 ± 44.1	289.8 ± 28.4	393.8 ± 46.0	199.4 ± 24.3	300.5 ± 39.5	185.1 ± 51.0	-	-	+
165		2,3-Br_2	**A2**	279.8 ± 62.6	279.9 ± 51.9	323.1 ± 21.2	286.9 ± 55.5	453.1 ± 20.1	317.6 ± 24.2	372.4 ± 23.6	180.1 ± 42.1	-	-	+
166		H	**T2**	0.8 ± 0.5	1.0 ± 0.4	0.7 ± 0.4	0.7 ± 0.5	1.0 ± 0.1	0.10 ± 0.06	22.1 ± 9.9	5.6 ± 0.7	+	+	+
167		Br	**T2**	44.9 ± 7.3	51.2 ± 6.6	43.2 ± 9.6	36.0 ± 3.7	116.4 ± 12.6	45.9 ± 9.2	82.5 ± 3.4	102.8 ± 20.0	-	+	+
168		2,3,2'-Br_3	**T2**	314.1 ± 51.3	362.7 ± 93.9	415.0 ± 56.8	388.6 ± 41.4	670.2 ± 29.8	600.5 ± 41.2	702.8 ± 46.4	583.0 ± 53.1	-	-	+
169		CHO	**T2**	244.9 ± 22.7	378.4 ± 23.6	310.4 ± 35.4	225.7 ± 14.5	524.4 ± 39.2	199.8 ± 18.9	192.9 ± 24.3	366.6 ± 70.5	-	-	+
170		CN	**T2**	53.3 ± 10.2	59.8 ± 8.5	76.6 ± 5.0	66.1 ± 6.7	114.6 ± 10.3	32.3 ± 3.7	54.0 ± 6.3	41.7 ± 6.3	-	+	+
171		H	**A1**	>1000	n.d.	n.d.	n.d.	>1000	>1000	n.d.	n.d.	-	-	-
172		H	**A1***	>1000	n.d.	n.d.	n.d.	>1000	>1000	n.d.	n.d.	-	-	-
173		CHO	**A1**	>1000	n.d.	n.d.	n.d.	>1000	>1000	n.d.	n.d.	-	-	-
174		H	**A2**	20.3 ± 8.1	30.2 ± 6.6	30.0 ± 5.5	34.4 ± 8.1	188.0 ± 50.1	42.1 ± 9.0	64.9 ± 6.6	31.5 ± 2.4	-	+	+
175		H	**A2***	414.2 ± 59.5	378.0 ± 30.4	362.0 ± 28.1	389.2 ± 37.1	893.0 ± 215.5	462.6 ± 70.0	485.0 ± 71.0	370.0 ± 81.4	-	-	+
176		CHO	**A2**	903.0 ± 9.4	1018.1 ± 15.3	928.4 ± 77.8	820.9 ± 82.1	1630.1 ± 111.8	973.3 ± 42.7	n.d.	n.d.	-	-	+
177		CN	**A2**	300.0 ± 24.8	253.0 ± 19.8	156.3 ± 11.0	125.6 ± 23.9	274.0 ± 129.7	62.8 ± 10.2	523.3 ± 34.1	355.5 ± 27.4	-	-	+
178	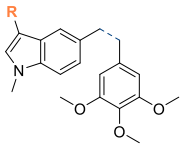 D-1	CH=N-NMe_2	**A2**	>1000	n.d.	n.d.	n.d.	>1000	>1000	n.d.	n.d.	-	-	-
179		CH=N-NH-Ph	**A2**	>1000	n.d.	n.d.	n.d.	>1000	>1000	n.d.	n.d.	-	-	-
180		CH=N-NH-Imid	**A2**	>1000	n.d.	n.d.	n.d.	>1000	>1000	n.d.	n.d.	-	-	-
181		H	**T1**	2.3 ± 0.9	2.4 ± 1.1	5.5 ± 2.1	2.4 ± 1.0	1.2 ± 0.3	2.3 ± 1.1	2.5 ± 0.1	2.0 ± 0.2	+/-	+	+
182		Cl	**T1**	30.0 ± 13.5	29.8 ± 7.2	27.5 ± 7.6	20.9 ± 4.3	261.0 ± 35.3	25.7 ± 5.1	22.6 ± 1.1	12.1 ± 1.5	-	+	+
183		CHO	**T1**	52.0 ± 18.2	33.3 ± 12.0	36.1 ± 8.9	34.2 ± 9.9	780.0 ± 277.9	23.2 ± 6.4	14.5 ± 1.4	5.6 ± 1.1	-	+	+
184		CN	**T1**	32.0 ± 2.2	44.0 ± 7.8	22.9 ± 9.1	14.1 ± 3.7	547.9 ± 56.3	12.6 ± 1.6	16.8 ± 3.3	6.4 ± 1.0	-	+	+
185		CH=N-NMe_2	**T1**	130.0 ± 20.0	277.1 ± 26.7	266.9 ± 38.9	265.2 ± 37.2	1103.3 ± 77.6	116.3 ± 14.3	241.2 ± 24.0	145.9 ± 33.6	-	-	+
186		H	**T2**	2.8 ± 1.3	3.1 ± 1.2	3.8 ± 1.6	2.9 ± 1.1	30.7 ± 7.3	7.6 ± 1.0	3.1 ± 0.3	1.5 ± 0.4	+/-	+	+
187		$CONH_2$	**T2**	240.0 ± 69.7	143.4 ± 16.9	112.0 ± 6.5	34.6 ± 3.8	350.0 ± 124.2	124.2 ± 50.2	67.8 ± 5.7	85.3 ± 3.4	-	+/-	+
188		CHO	**T2**	82.0 ± 6.9	135.8 ± 18.5	121.7 ± 11.5	121.6 ± 12.2	586.0 ± 77.8	113.0 ± 25.3	74.7 ± 5.4	87.0 ± 5.9	-	+/-	+
189		CN	**T2**	220.0 ± 78.7	218.6 ± 18.1	163.3 ± 20.0	148.5 ± 46.4	470.0 ± 73.9	124.4 ± 15.7	113.8 ± 11.7	97.6 ± 6.5	-	-	+
190		Cl	other	>1000	n.d.	n.d.	n.d.	>1000	>1000	n.d.	n.d.	-	-	-
CA4[499]	**D-1**	-	-	3	n.d.	n.d.	n.d.	32	13	n.d.	n.d.	n.d.	+	+

Table 23. Antiproliferative activity of biaryl amides and tetrazoles against the human cell lines HeLa, HT-29, HL-60, and AGS (tumor), and HEK-293 (non-tumorigenic). IC_{50} values are expressed in nanomolar and were measured after 72 h of incubation (*n* = 3-6). The G_2/M arrest was evaluated in HeLa cells at 10 nM, 100 nM, and 1 µM after 24, 48, and 72 h and is indicated qualitatively based on the 24 h results in Table 25. Elac = elacridar; Vera = verapamil; n.d. = not determined; IC = indolecombretastatin; * = *N*-Me; Imid = imidazol-2-yl; + = > 50%; +/- = 35-50%; - = no effect.

Comparison between sulfonamide, amide, and tetrazole bridges

The structure activity relationship deduced from Table 23 indicates that the tetrazole moiety leads to highly more potent compounds that their amide precursors. The conversion of amides into tetrazole derivatives locks the *cisoid* disposition of the aromatic rings. The amide moiety shows apparent structural similarity with the sulfonamide group, but they harbor different geometry. The sulfonamide sulfur is tetrahedral, and the nitrogen exhibits pyramidal geometry.[524,525] The carbon and nitrogen of amides, by contrast, bear sp^2 hybridization, which makes amides trigonal planar. The conformational analysis of biaryl sulfonamides **80**-**140** points out that the *cisoid* disposition of the aromatic rings is more favorable than the *transoid* conformation. However, the opposite is true for amides collected in Table 23. The methylation of the bridge has contrary contributions to the inhibitory concentration: it remarkably increases the potency of sulfonamide compounds whereas the methylation of amide **174** induced a 20-fold decrease in potency in **175**.

Amides A1 (**171**-**173**) and tetrazoles T1 (**181**-**185**) with a 3,4,5-trimethoxyphenyl ring (D-1) mimic the orientation of the bridge in sulfonamides D-1 (**80**-**97**). Although those amides displayed no effect, the highly active tetrazoles **181** and **183** proved more potent than unsubstituted sulfonamides **80** and **89**. The antiproliferative activity of compounds with a tetrazole bridge T1 is akin to that of methylated sulfonamides (**81** and **90**). The introduction of a carbonitrile at the indole 3-position led to more potent sulfonamides than tetrazoles, whatever the sulfonamide substitution (H or Me). There are no sulfonamide pairs matching tetrazole derivatives T2 because the sulfonamide nitrogen is bound to the A ring in series D-1 and D-3, that would correspond to A1 and T1 bridges.

In summary, the introduction of substituents at the indole 3-position decreases the potency of the compounds irrespective of the bridge. In sulfonamides, the overall activity of 3,4,5-trimethoxyphenyl derivatives (D-1) is higher than that of 3,5-dimethoxyphenyl compounds (D-3), followed by less potent compounds with a 2,5-dimethoxyphenyl group (D-4 and D-5). The introduction of a methyl group on the sulfonamide nitrogen markedly improves the activity compared to unsubstituted sulfonamides. The effect of replacing the D-1 in amides and tetrazoles by a D-3 moiety depends on the rest of the modifications on the scaffold. Regardless, tetrazole derivatives show higher potency than amides.

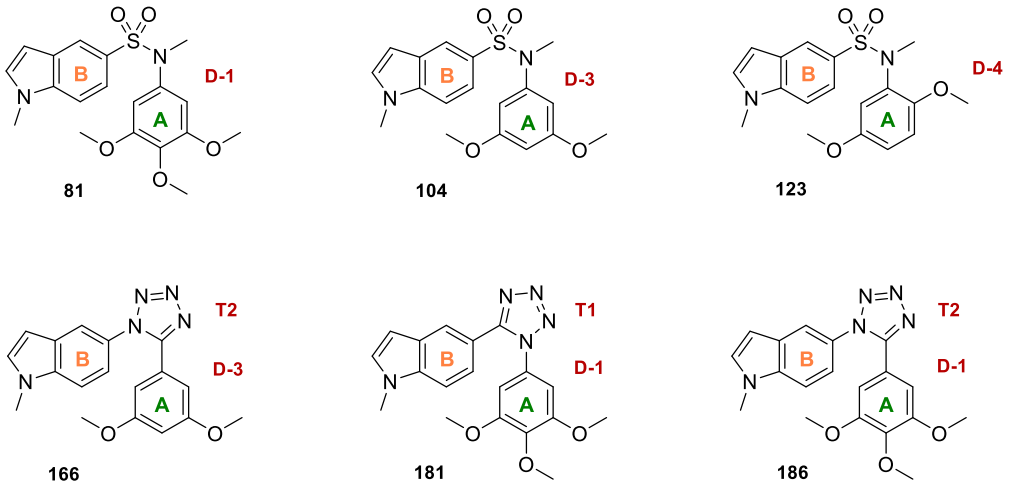

Figure 49. Chemical structure of the proposed lead compounds whose mechanism of action has been further studied in detail in the present work. For NMR spectra visualization see Supplementary Material on CD.

In order to select a few lead compounds for the evaluation of the mechanism of action and discern whether structural modifications could affect their antitumor profile, we divided the active compounds in Tables 22 and 23 into structural families. According to their A ring, sulfonamides were divided into D-1, D-3, and D-4/5 groups. Tetrazole derivatives were classified related to their bridge orientation and A ring: D-3 tetrazoles (T2), and D-1 tetrazoles with bridges T1 and T2. We selected the most potent compound within each group, all of them with no modifications on the indole ring: methylated sulfonamides **81**, **104**, and **123**, and tetrazoles **166**, **181**, and **186** (Fig. 49).

Besides the cell lines collected in Tables 22 and 23, the lead compounds were additionally assayed against the human tumor cell lines SNU-1 (human gastric adenocarcinoma), RPMI-8226 and U266 (human multiple myeloma), and the non-tumorigenic cell line 3B-11 from murine vascular epithelium. We also isolated murine fibroblasts from dermises of newborn mice pups to evaluate the effect of the compounds in primary cells (Table 24). Despite some differences, the overall sensitivity of the tested tumor and non-tumorigenic cell lines was somewhat similar. We selected HeLa cells to conduct the upcoming experiments as the tumor model for the present work.

Cell line	81	104	123	166	181	186
HeLa	2.4 ± 0.4	20.1 ± 2.7	169.2 ± 34.0	0.8 ± 0.5	2.3 ± 0.9	2.8 ± 1.3
HT-29	4.3 ± 0.9	42.6 ± 7.8	613.1 ± 82.2	1.0 ± 0.1	1.2 ± 0.3	30.7 ± 7.3
HL-60	1.1 ± 1.0	23.5 ± 5.0	233.8 ± 37.0	0.10 ± 0.06	2.3 ± 1.1	7.6 ± 1.0
AGS	3.3 ± 0.8	30.5 ± 3.9	149.5 ± 20.4	22.1 ± 9.9	2.5 ± 0.1	3.1 ± 0.3
SNU-1	7.3 ± 1.1	36.4 ± 5.9	136.3 ± 33.9	1.7 ± 0.7	3.9 ± 1.7	4.0 ± 1.0
RPMI-8226	10.1 ± 0.4	71.3 ± 3.0	200.2 ± 36.7	9.2 ± 1.5	5.4 ± 0.9	11.9 ± 2.4
U266	4.2 ± 1.5	48.4 ± 4.4	97.6 ± 5.9	1.5 ± 0.2	1.2 ± 0.5	11.2 ± 5.6
HEK-293	2.3 ± 0.4	11.8 ± 3.0	126.9 ± 11.4	5.6 ± 0.7	2.0 ± 0.2	1.5 ± 0.4
3B-11	7.3 ± 0.8	95.6 ± 2.4	301.7 ± 38.8	14.4 ± 0.4	3.7 ± 0.3	31.6 ± 2.5
Fibroblasts	3.4 ± 0.3	94.8 ± 5.5	323.2 ± 30.3	6.6 ± 0.8	2.9 ± 0.4	20.8 ± 1.5

Table 24. IC_{50} values (nM) of the lead compounds **81**, **104**, **123**, **166**, **181**, and **186** against the indicated cell lines after 72-h treatments (*n* = 3-7). The first seven correspond to human tumor cell lines, and the later three are non-tumorigenic cells, either human (HEK-293) or murine (3B-11 and primary fibroblasts).

Susceptibility to MDR transporters

MDR proteins cluster several efflux pumps frequently related to the failure of cancer chemotherapy.[526] These membrane proteins recognize multiple structurally-unrelated substrates and export them outside the cell. MDR transporters, especially P-glycoprotein, are involved in resistance to many TBDs such as paclitaxel and vinca alkaloids, preferentially exporting big and hydrophobic molecules.[96,115] To study whether the active compounds are substrates of MDR proteins, we evaluated their antiproliferative activity against HeLa cells in co-treatment with the MDR modulators verapamil and elacridar (Tables 22 and 23). Verapamil is a calcium channel blocker and a first-generation MDR pump inhibitor based on competition,[527] whereas elacridar is a third-generation drug that selectively inhibits P-gp and BCRP.[528]

We incubated HeLa cells with verapamil (1 and 10 µM) and elacridar (0.1 µM) for 2 h, then exposed to the synthesized compounds for 72 h. If MDR transporters are pumping the compounds, their combination with verapamil and elacridar will maintain the intracellular concentrations, manifested by higher sensitivity to the ligands. These two drugs themselves showed no effect on cell proliferation at the working concentrations.

Mild effects were observed with the combination of MDR inhibitors and sulfonamide derivatives, exhibiting approximately a two-fold increase in the activity of **84**, **87**, **88**, **91**, **92**, **94**, **95**, and **129**. The activity of ethyl derivative **82** was restored up to 7-11 times when blocking MDR-mediated transport. Overall, 8 out of the 16 active compounds with a 3,4,5-trimethoxyphenyl ring (scaffold D-1) showed enhanced cytotoxic activity in combination with MDR inhibitors, whereas IC_{50} changes were only observed in one compound within 2,5-dimethoxyphenyl series (scaffolds D-4/5) and none with a 3,5-dimethoxyphenyl ring (scaffold D-3). Since these compounds seem to have in common the presence of bulky and/or hydrophobic groups such as bromine or propenenitriles, the hydrophobic volume might be related to the susceptibility for MDR transport. Regarding tetrazole derivatives, only compounds **177**, **183**, and **187** showed some improvement in potency. Nevertheless, none of the lead compounds (sulfonamides **81**, **104**, **123**, and tetrazoles **166**, **181**, **186**) seem to be substrates of MDR proteins.

Our group has previously reported that pretreatment with verapamil remarkably increased the potency against A549 human lung carcinoma of some indolecombretastatins with an aldehyde (100-fold) or nitrile (10-fold) groups at the indole 3-position.[499] Based on the elicited results, the replacement of the olefin by a sulfonamide moiety avoids the overall MDR transport, because neither aldehyde **89** nor nitrile **96** derivatives are exported.

Inhibition of colony formation in HeLa cells

We evaluated the capacity of the six lead compounds to hamper the growth of HeLa cells in an anchorage-independent environment. For this purpose, we conducted a soft agar colony formation assay.[529] HeLa cells were seeded embedded in 0.3% agarose gel containing the treatments on top of a 0.6% agarose layer, and fed with an extra 0.3% layer supplemented with the treatments once a week. After 14 days under standard growth conditions, the resulting colonies were counted (Fig. 50A), and images were captured in phase contrast (Fig. 50B) and after cell staining with MTT (Fig. 50C).

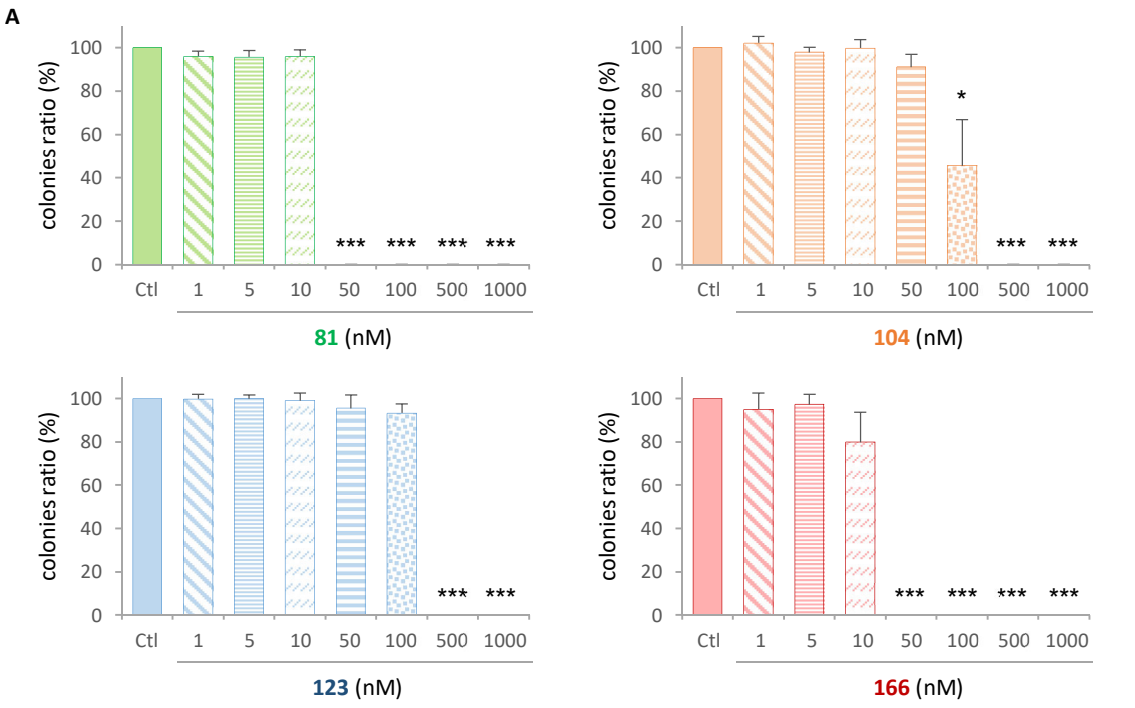

Figure 50. Continued

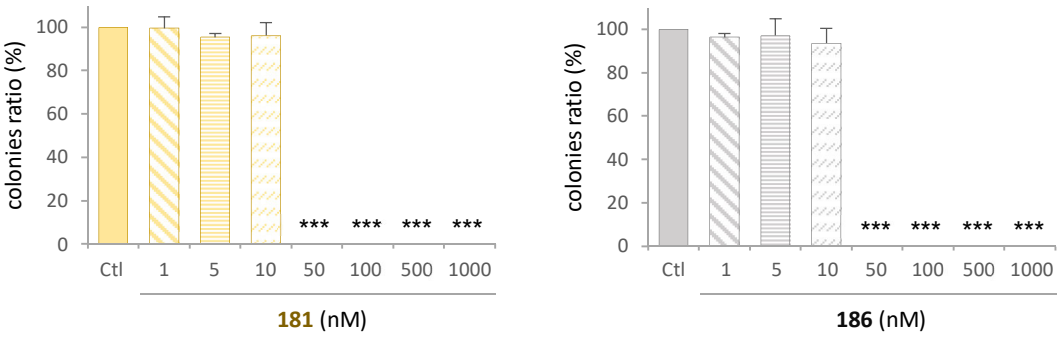

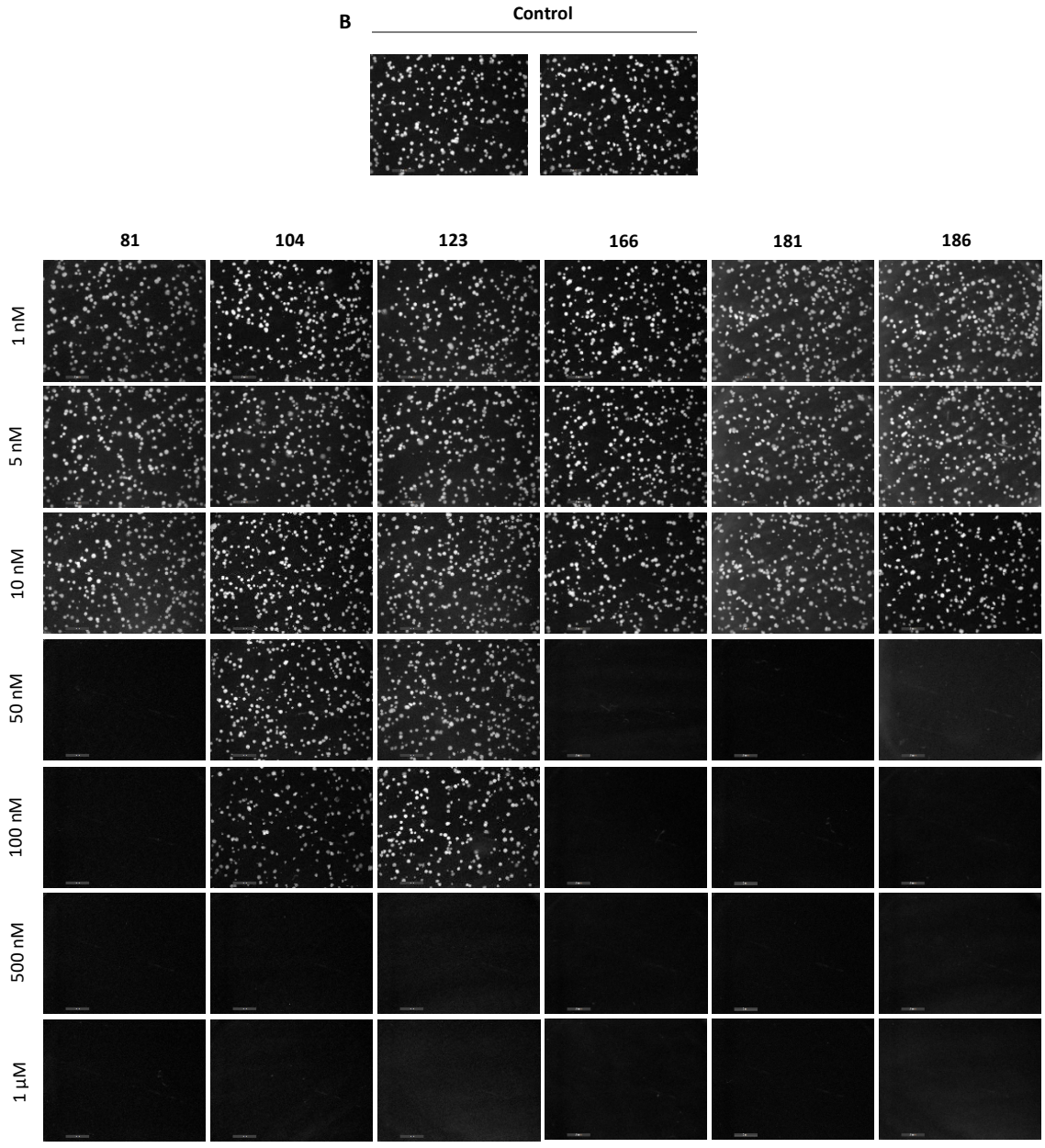

Figure 50. Continued

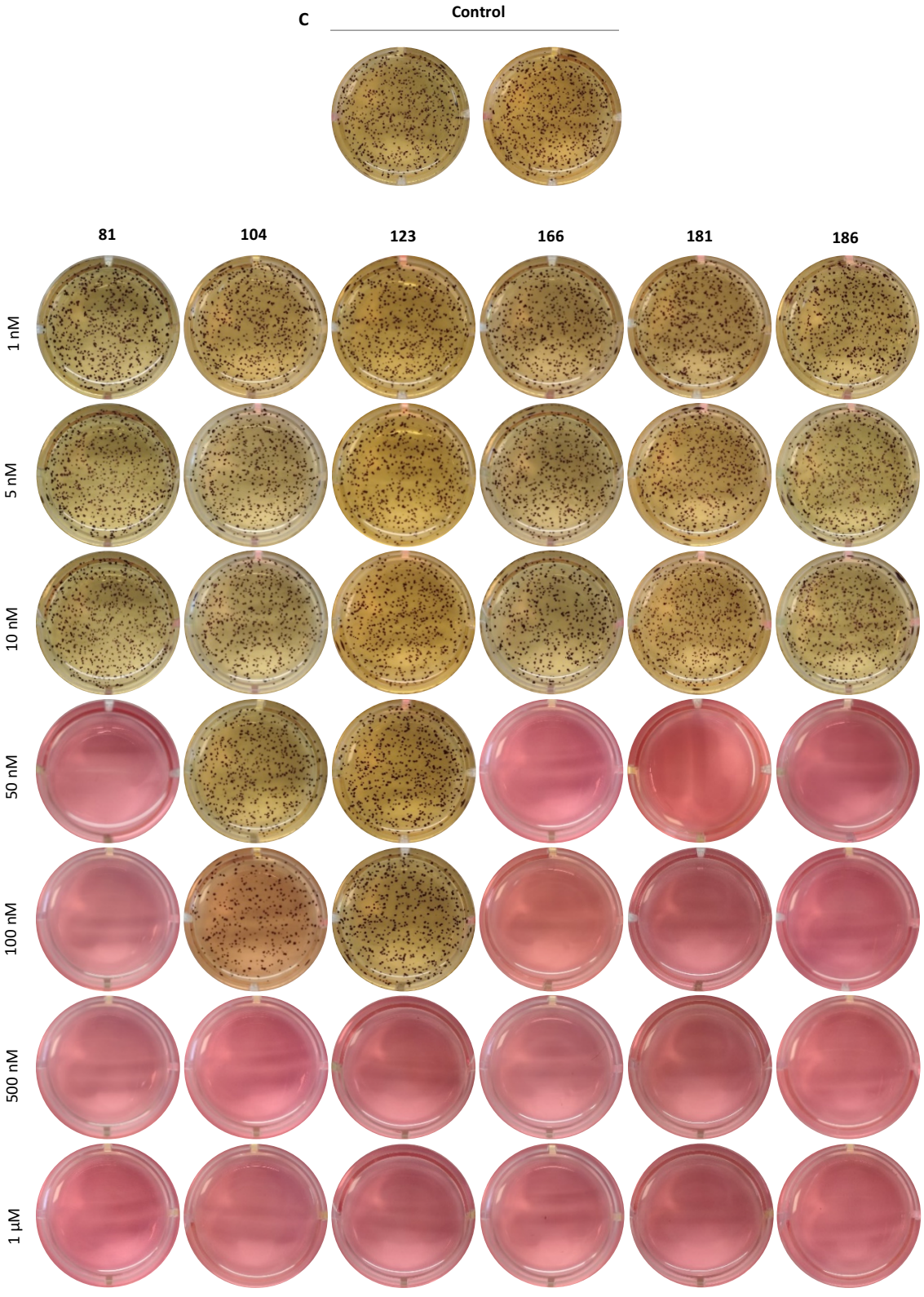

Figure 50. Soft agar colony formation assay. HeLa cells (10^3) were seeded in 0.3% agarose gel with increasing concentrations of the lead compounds and incubated for 14 days under standard conditions. **A.** Analysis of the number of colonies in the presence of the drugs, expressed as the ratio referred to the colonies in untreated samples (100%). The colonies were counted after MTT staining by two independent observers ($n = 4$; * $p < 0.05$; *** $p < 0.001$). **B.** Representative phase-contrast images for each condition. **C.** Representative images of MTT-stained colonies.

In view of the results, the six lead compounds inhibited the formation of HeLa colonies. There is a dose-dependent effect that correlates with the potency order observed in cell proliferation assays (Table 24).

EFFECT ON THE CELL CYCLE DISTRIBUTION

In order to study the mechanism of action of the compounds, we first evaluated their effect on the cell cycle progression. Both MSAs and MDAs impede or delay the anaphase onset, which would manifest as an accumulation of cells in the G_2/M population. The cell cycle distribution was monitored in HeLa cells by flow cytometry using the fluorescent dye propidium iodide (PI), which is an intercalating agent that labels DNA. Cells were previously fixed in 70% ethanol to permeabilize them to PI entrance and incubated with RNase to avoid RNA interference. The red fluorescence emitted by PI relates to the DNA relative content of the cells within a sample, depicted in a histogram as the DNA profile. Three populations can be distinguished in a diploid cycle: G_0/G_1, S, and G_2/M. Cells in G_2 or M phases (4n) are twice as bright as cells in G_0/G_1 (2n), whereas cells in S phase show fluorescence intensity in between G_0/G_1 and G_2/M because they are in the process of doubling their DNA content. There is a population of cells to the left of the G_0/G_1 peak termed $SubG_0/G_1$, which corresponds to apoptotic cells that underwent DNA condensation and fragmentation (hypodiploid peak).

The cell cycle profile was evaluated in HeLa cells after 24 h, 48 h, and 72 h of incubation with all the compounds listed in Tables 22 and 23. Each compound was tested at three concentrations (10 nM, 100 nM, and 1 µM) to determine if the potency exhibited in the cell proliferation assay matches the potency observed for cell cycle alterations. The percentages of cells in $SubG_0/G_1$ and G_2/M regions are collected in Table 25 for each condition (the results obtained for compounds with IC_{50} > 1 µM are not shown). The cell cycle arrest was qualitatively categorized according to the 24 h data as + (G_2/M > 50%), +/- (G_2/M = 35-50%), and – (no effect), compared to G_2/M = 25% in untreated cells (Tables 22 and 23).

The compounds that proved effective in the proliferation assay also exhibited a sustained increase in the percentage of cells in the G_2/M peak compared to untreated samples (Ctl), which is compatible with the mechanism of action of tubulin binding drugs. The sustained mitotic arrest was already noticed 24 h after treatment and evolved towards a striking increase in the percentage of cells in the $SubG_0/G_1$ population (Table 25). Compounds with IC_{50} values against HeLa cells around 10^{-7} M caused G_2/M arrest at 1 µM (e.g. **122**), those with IC_{50} values around 10^{-8} M showed effect at 100 nM (e.g. **80**), and compounds with IC_{50} around 10^{-9} M induced the accumulation of cells in the G_2/M region even at 10 nM (**81**, **166**, **181**, and **186**). The akin SAR and potency in the two experiments suggest that inhibition of cell proliferation is closely related to the halt of the G_2/M-to-G_1 transition.

Compounds **81** and **166**, which exhibit the lowest IC_{50} values among sulfonamides and tetrazoles, respectively, are the most potent ones regarding the G_2/M arrest (Table 25), increasing the percentage of cells in the G_2/M peak at 10 nM up to 63.6% and 66.0% after 24 h compared to untreated samples (21.7%). Compound **82** also showed partial effects (+/-) at that concentration. *Cis*-propenenitrile **95** with an IC_{50} value against HeLa cells of 188.0 nM caused G_2/M arrest at 100 nM, which disagrees with the previous observation. It could be due to a partial isomerization to the more potent *trans*-propenenitrile **94** (IC_{50} = 68.6 nM) that induces cell cycle arrest at 100 nM concentration.

		24 h		48 h		72 h				24 h		48 h		72 h	
No.	[c]	SubG$_0$/G$_1$	G$_2$/M	SubG$_0$/G$_1$	G$_2$/M	SubG$_0$/G$_1$	G$_2$/M	No.	[c]	SubG$_0$/G$_1$	G$_2$/M	SubG$_0$/G$_1$	G$_2$/M	SubG$_0$/G$_1$	G$_2$/M
	10 nM	1.7 ± 0.4	21.7 ± 1.0	1.7 ± 0.4	21.7 ± 1.0	2.1 ± 0.5	19.7 ± 1.1		10 nM	2.2 ± 0.0	28.8 ± 1.3	1.9 ± 0.1	26.5 ± 1.2	2.5 ± 1.0	19.5 ± 2.6
Ctl	100 nM	2.1 ± 0.7	24.2 ± 1.2	1.6 ± 0.6	23.0 ± 1.5	1.6 ± 0.6	19.5 ± 1.4	**91**	100 nM	6.8 ± 2.5	77.4 ± 2.2	16.4 ± 2.9	69.1 ± 4.8	31.9 ± 4.8	51.7 ± 5.5
	1 µM	2.2 ± 0.5	26.2 ± 1.4	1.7 ± 0.6	23.3 ± 2.6	1.8 ± 0.7	19.0 ± 1.6		1 µM	6.3 ± 1.5	70.1 ± 1.5	13.3 ± 1.0	71.0 ± 1.2	22.4 ± 2.2	59.6 ± 2.5
	10 nM	3.4 ± 1.4	31.6 ± 2.4	3.5 ± 0.7	31.4 ± 1.1	3.9 ± 1.7	26.9 ± 3.6		10 nM	2.2 ± 0.4	29.1 ± 1.1	1.8 ± 0.3	26.3 ± 1.2	2.6 ± 1.0	22.2 ± 0.9
80	100 nM	6.8 ± 1.1	81.5 ± 1.3	17.0 ± 1.3	68.4 ± 2.6	32.7 ±1.8	47.7 ± 1.6	**92**	100 nM	7.0 ± 1.8	78.0 ± 3.3	18.4 ± 2.9	67.8 ± 2.1	32.8 ± 1.8	44.5 ± 3.0
	1 µM	8.8 ± 0.4	72.7 ± 2.3	16.8 ± 2.0	68.8 ± 3.6	25.2 ± 3.3	58.7 ± 3.1		1 µM	6.6 ± 1.4	69.9 ± 1.8	13.8 ± 1.9	71.1 ± 3.2	28.3 ± 5.4	50.1 ± 3.8
	10 nM	10.9 ± 3.6	63.6 ± 7.9	22.8 ± 6.2	48.8 ± 3.1	35.0 ± 3.2	36.8 ± 1.7		10 nM	2.3 ± 0.3	27.6 ± 1.2	1.9 ± 0.4	23.9 ± 0.1	2.5 ± 1.3	17.7 ± 1.9
81	100 nM	9.1 ± 3.3	70.2 ± 2.0	14.5 ± 2.1	70.5 ± 4.6	26.6 ± 4.0	60.5 ± 5.6	**93**	100 nM	3.5 ± 1.3	31.4 ± 4.9	2.7 ± 0.3	19.6 ± 1.7	2.4 ± 0.4	22.1 ± 2.0
	1 µM	11.3 ± 4.8	67.9 ± 3.7	19.0 ± 5.7	62.7 ± 8.8	25.2 ± 1.9	55.2 ± 2.8		1 µM	6.8 ± 1.7	79.6 ± 2.5	20.7 ± 3.9	62.8 ± 4.9	33.2 ± 4.3	47.1 ± 5.8
	10 nM	4.2 ± 1.6	41.4 ± 5.5	7.8 ± 3.0	40.1 ± 5.7	12.1 ± 4.5	37.8 ± 2.6		10 nM	2.0 ± 0.2	27.4 ± 1.1	1.8 ± 0.1	25.3 ± 2.9	1.9 ± 0.5	18.1 ± 1.2
82	100 nM	9.5 ± 3.4	71.1 ± 1.4	19.5 ± 5.3	64.6 ± 4.9	29.4 ± 4.3	50.4 ± 7.5	**94**	100 nM	12.0 ± 1.7	61.5 ± 5.2	22.9 ± 4.2	49.3 ± 4.3	33.3 ± 7.1	36.1 ± 3.5
	1 µM	8.0 ± 1.3	70.1 ± 2.5	19.8 ± 6.1	64.1 ± 8.7	22.8 ± 1.4	60.9 ± 1.9		1 µM	10.2 ± 6.5	70.2 ± 3.2	15.6 ± 3.7	68.5 ± 5.9	24.5 ± 5.1	56.6 ± 7.4
	10 nM	1.9 ± 0.5	29.9 ± 1.4	1.7 ± 0.3	26.9 ± 1.3	2.7 ± 1.0	20.6 ± 2.1		10 nM	1.9 ± 0.4	27.0 ± 2.4	1.8 ± 0.1	26.4 ± 2.9	2.3 ± 0.2	19.1 ± 2.9
84	100 nM	6.2 ± 0.6	76.3 ± 1.6	17.0 ± 3.5	68.3 ± 4.1	25.2 ± 2.1	58.4 ± 2.9	**95**	100 nM	8.1 ± 2.2	53.6 ± 7.7	14.9 ± 2.5	48.9 ± 5.9	17.4 ± 3.6	37.7 ± 5.2
	1 µM	6.2 ± 1.6	70.9 ± 1.8	14.2 ± 1.3	69.3 ± 0.4	26.0 ± 2.5	56.9 ± 2.1		1 µM	8.1 ± 1.9	71.6 ± 3.5	19.2 ± 4.4	65.6 ± 6.3	31.8 ± 8.3	51.4 ± 7.1
	10 nM	3.9 ± 1.2	33.9 ± 7.9	4.5 ± 2.2	31.3 ± 6.3	3.8 ± 2.2	25.9 ± 4.4		10 nM	2.2 ± 0.8	26.4 ± 2.5	2.4 ± 0.8	25.4 ± 1.2	2.3 ± 0.2	21.7 ± 1.3
86	100 nM	8.1 ± 1.4	70.9 ± 6.3	22.0 ± 6.9	63.2 ± 8.1	30.1 ± 7.6	52.5 ± 5.7	**96**	100 nM	11.0 ± 2.1	74.4 ± 1.3	23.4 ± 3.8	55.5 ± 4.6	47.0 ± 10.2	34.4 ± 8.4
	1 µM	7.9 ± 0.7	67.5 ± 5.2	19.0 ± 6.7	64.7 ± 7.4	27.0 ± 5.2	53.3 ± 5.8		1 µM	7.8 ± 1.6	75.0 ± 1.9	16.4 ± 2.2	68.4 ± 4.5	36.3 ± 3.5	45.1 ± 1.2
	10 nM	2.3 ± 0.5	27.9 ± 2.6	2.2 ± 0.5	28.6 ± 3.8	2.6 ± 1.1	21.1 ± 1.1		10 nM	1.9 ± 0.1	32.2 ± 1.2	2.1 ± 0.3	29.9 ± 3.0	2.4 ± 0.7	22.4 ± 2.7
87	100 nM	9.9 ± 2.3	74.8 ± 3.2	24.2 ± 4.4	55.0 ± 5.6	38.2 ± 5.1	36.8 ± 6.6	**97**	100 nM	5.8 ± 1.2	81.8 ± 1.3	18.5 ± 2.6	68.0 ± 1.8	33.4 ± 2.9	48.4 ± 3.1
	1 µM	7.3 ± 1.6	76.9 ± 2.2	16.4 ± 2.5	69.1 ± 2.9	29.8 ± 5.1	53.0 ± 4.4		1 µM	6.7 ± 1.2	71.3 ± 2.6	14.8 ± 2.4	70.4 ± 1.6	24.9 ± 1.7	58.0 ± 2.0
	10 nM	1.9 ± 0.4	28.5 ± 0.2	2.7 ± 0.7	24.8 ± 2.1	2.8 ± 0.2	23.1 ± 2.6		10 nM	1.2 ± 0.2	23.6 ± 0.1	1.0 ± 0.4	22.5 ± 3.6	1.4 ± 0.1	22.0 ± 0.1
88	100 nM	9.2 ± 1.3	72.4 ± 2.6	19.0 ± 4.5	66.5 ± 4.6	28.4 ± 3.5	52.3 ± 4.4	**103**	100 nM	1.1 ± 0.1	25.4 ± 4.1	1.2 ± 0.3	24.7 ± 1.4	1.2 ± 0.2	22.9 ± 0.8
	1 µM	8.9 ± 2.0	66.6 ± 2.5	22.3 ± 6.6	62.7 ± 6.7	28.0 ± 4.2	54.9 ± 5.6		1 µM	1.4 ± 0.4	33.2 ± 2.1	2.4 ± 1.8	34.3 ± 4.7	4.6 ± 2.4	36.4 ± 1.5
	10 nM	2.3 ± 0.3	24.1 ± 1.3	2.1 ± 0.1	22.4 ± 0.6	1.8 ± 0.4	18.1 ± 1.4		10 nM	0.9 ± 0.1	28.3 ± 3.5	1.5 ± 0.4	24.9 ± 2.9	1.6 ± 0.3	20.2 ± 0.1
89	100 nM	2.2 ± 0.7	28.6 ± 0.9	2.1 ± 0.3	27.7 ± 2.2	1.9 ± 0.3	21.7 ± 1.8	**104**	100 nM	6.4 ± 0.6	70.9 ± 6.3	21.9 ± 3.8	47.4 ± 7.0	38.6 ± 9.3	33.6 ± 9.4
	1 µM	8.6 ± 2.1	72.1 ± 3.0	21.4 ± 2.4	52.9 ± 3.7	42.4 ± 6.5	30.4 ± 5.4		1 µM	4.0 ± 1.3	87.8 ± 3.2	23.2 ± 7.4	61.7 ± 7.6	33.7 ± 9.4	46.2 ± 9.4
	10 nM	1.8 ± 0.2	27.7 ± 0.8	1.7 ± 0.3	23.1 ± 0.4	2.0 ± 0.4	18.3 ± 1.4		10 nM	0.9 ± 0.2	27.4 ± 2.2	1.4 ± 0.7	24.4 ± 2.2	1.7 ± 0.4	20.8 ± 1.4
90	100 nM	7.2 ± 0.9	58.2 ± 2.2	18.2 ± 3.5	48.3 ± 3.0	25.4 ± 3.6	41.2 ± 1.2	**105**	100 nM	3.3 ± 0.4	54.7 ± 4.9	11.2 ± 4.0	48.8 ± 2.6	18.2 ± 5.4	40.9 ± 5.2
	1 µM	7.0 ± 1.2	76.4 ± 0.3	19.0 ± 3.0	67.2 ± 3.6	32.3 ± 0.6	48.3 ± 3.3		1 µM	3.1 ± 0.8	86.1 ± 4.9	12.1 ± 4.2	76.1 ± 4.8	41.5 ± 8.2	38.6 ± 9.4

Table 25. Continued

		24 h		48 h		72 h				24 h		48 h		72 h	
No.	[c]	SubG$_0$/G$_1$	G$_2$/M	SubG$_0$/G$_1$	G$_2$/M	SubG$_0$/G$_1$	G$_2$/M	No.	[c]	SubG$_0$/G$_1$	G$_2$/M	SubG$_0$/G$_1$	G$_2$/M	SubG$_0$/G$_1$	G$_2$/M
	10 nM	0.8 ± 0.1	27.6 ± 0.6	1.1 ± 0.1	25.2 ± 1.0	1.6 ± 0.2	20.4 ± 1.4		10 nM	1.5 ± 1.3	26.8 ± 2.2	1.6 ± 0.7	26.9 ± 0.5	1.8 ± 0.4	20.7 ± 1.5
106	100 nM	1.1 ± 0.6	29.0 ± 2.6	1.2 ± 0.3	26.3 ± 2.0	1.6 ± 0.3	21.6 ± 2.3	**128**	100 nM	3.8 ± 0.6	31.4 ± 3.3	4.2 ± 0.6	31.1 ± 3.0	4.9 ± 2.1	28.8 ± 2.1
	1 µM	4.9 ± 1.7	86.8 ± 3.9	21.0 ± 3.9	62.0 ± 5.3	39.2 ± 4.1	37.8 ± 5.4		1 µM	11.9 ± 1.5	74.7 ± 3.5	28.0 ± 6.5	51.1 ± 4.9	39.0 ± 6.1	33.7 ± 6.5
	10 nM	1.0 ± 0.2	26.6 ± 2.0	0.9 ± 0.3	24.0 ± 2.3	1.1 ± 0.5	22.1 ± 1.1		10 nM	1.6 ± 0.2	28.5 ± 1.4	1.5 ± 0.1	26.4 ± 0.9	1.8 ± 0.4	22.2 ± 0.9
107	100 nM	1.7 ± 0.6	40.0 ± 5.3	4.0 ± 2.3	37.1 ± 4.5	5.5 ± 3.3	30.7 ± 4.4	**129**	100 nM	6.1 ± 2.2	42.8 ± 2.1	8.5 ± 1.6	38.7 ± 4.6	12.7 ± 4.4	35.5 ± 0.4
	1 µM	4.0 ± 2.0	89.2 ± 3.4	18.9 ± 3.9	65.1 ± 6.0	39.1 ± 5.6	41.2 ± 5.5		1 µM	8.8 ± 2.1	77.3 ± 3.8	16.7 ± 2.7	66.8 ± 7.5	35.3 ± 2.9	47.5 ± 1.9
	10 nM	2.0 ± 0.7	26.7 ± 2.3	1.2 ± 0.5	22.6 ± 3.1	1.2 ± 0.3	20.9 ± 1.2		10 nM	1.7 ± 0.2	28.4 ± 0.5	1.5 ± 0.1	24.6 ± 1.7	1.9 ± 0.9	18.6 ± 1.9
109	100 nM	1.1 ± 0.7	27.5 ± 2.0	1.4 ± 0.3	27.0 ± 0.8	1.6 ± 0.2	22.3 ± 1.8	**134**	100 nM	2.1 ± 0.4	28.7 ± 0.2	2.1 ± 0.8	23.6 ± 2.0	2.0 ± 0.4	20.1 ± 1.6
	1 µM	4.2 ± 1.6	88.4 ± 3.4	18.6 ± 3.3	68.8 ± 4.8	30.9 ± 5.8	44.7 ± 8.3		1 µM	8.9 ± 0.3	73.5 ± 2.6	22.6 ± 2.4	50.3 ± 1.2	34.1 ± 4.7	33.0 ± 4.1
	10 nM	0.9 ± 0.3	24.8 ± 0.8	1.0 ± 0.3	21.8 ± 1.6	1.0 ± .03	20.6 ± 0.6		10 nM	1.7 ± 0.4	27.0 ± 0.7	1.3 ± 0.5	24.4 ± 3.3	1.8 ± 0.3	19.7 ± 1.9
110	100 nM	1.0 ± 0.4	27.7 ± 0.8	1.5 ± 0.8	24.1 ± 0.6	1.1 ± 0.6	21.5 ± 1.6	**136**	100 nM	2.8 ± 1.0	28.2 ± 1.2	2.6 ± 1.0	25.6 ± 1.5	3.2 ± 0.7	22.4 ± 3.6
	1 µM	4.2 ± 1.2	88.7 ± 2.5	20.8 ± 5.1	64.8 ± 6.8	26.3 ± 5.8	49.0 ± 8.1		1 µM	9.7 ± 1.2	73.7 ± 1.0	34.0 ± 8.5	44.7 ± 8.4	38.3 ± 2.5	34.1 ± 2.7
	10 nM	0.8 ± 0.5	26.3 ± 1.0	1.1 ± 0.3	21.6 ± 1.1	1.4 ± 0.2	21.0 ± 1.4		10 nM	1.7 ± 0.6	25.0 ± 2.4	1.6 ± 0.2	23.8 ± 1.5	2.8 ± 0.6	19.5 ± 2.8
117	100 nM	1.1 ± 0.2	25.0 ± 0.3	1.3 ± 0.4	24.6 ± 0.8	1.2 ± 0.5	20.9 ± 0.1	**137**	100 nM	2.0 ± 1.1	25.6 ± 3.2	2.1 ± 0.32	25.2 ± 1.6	2.7 ± 0.3	21.8 ± 1.3
	1 µM	9.2 ± 1.8	69.5 ± 2.9	20.3 ± 3.1	50.8 ± 8.0	28.5 ± 5.3	42.9 ± 6.1		1 µM	10.9 ± 2.4	67.1 ± 2.5	31.3 ± 7.1	46.4 ± 6.3	41.7 ± 5.0	35.0 ± 4.6
	10 nM	1.2 ± 0.6	26.9 ± 1.4	1.5 ± 0.6	23.6 ± 3.6	1.0 ± 0.5	19.0 ± 1.2		10 nM	1.3 ± 0.8	26.1 ± 0.8	1.4 ± 0.1	23.6 ± 1.4	1.6 ± 0.3	21.4 ± 0.6
118	100 nM	1.7 ± 0.8	27.3 ± 1.1	1.5 ± 0.8	23.6 ± 2.2	1.2 ± 0.5	19.4 ± 1.1	**138**	100 nM	2.2 ± 0.8	25.7 ± 1.1	1.9 ± 0.6	24.8 ± 0.7	2.5 ± 0.7	22.1 ± 2.3
	1 µM	5.1 ± 2.7	54.3 ± 3.8	13.7 ± 2.6	47.7 ± 3.6	19.5 ± 5.2	41.5 ± 6.1		1 µM	9.5 ± 2.4	63.3 ± 3.4	31.7 ± 7.0	40.4 ± 7.7	35.3 ± 4.4	37.5 ± 3.5
	10 nM	1.6 ± 0.5	27.7 ± 0.7	1.8 ± 0.5	24.5 ± 1.0	2.0 ± 0.9	19.8 ± 0.9		10 nM	1.1 ± 0.1	23.8 ± 2.6	1.4 ± 0.5	20.1 ± 1.9	1.4 ± 0.4	19.9 ± 1.7
122	100 nM	4.5 ± 2.9	27.8 ± 1.6	3.8 ± 0.9	26.8 ± 3.0	2.6 ± 0.5	24.1 ± 3.5	**144**	100 nM	2.8 ± 1.0	45.5 ± 6.2	6.4 ± 2.3	41.0 ± 7.2	10.2 ± 2.6	39.4 ± 4.5
	1 µM	12.9 ± 3.7	69.1 ± 4.0	31.7 ± 9.1	46.3 ± 9.2	41.0 ± 7.1	34.5 ± 6.8		1 µM	4.8 ± 1.6	85.7 ± 3.3	20.8 ± 5.5	64.4 ± 8.0	34.9 ± 5.8	32.0 ± 7.9
	10 nM	1.6 ± 0.4	27.4 ± 0.9	1.4 ± 0.4	24.8 ± 0.4	1.8 ± 0.5	22.6 ± 0.9		10 nM	1.2 ± 0.3	22.6 ± 2.1	1.4 ± 0.5	21.3 ± 1.2	1.9 ± 0.2	18.6 ± 0.3
123	100 nM	6.2 ± 1.3	40.8 ± 6.7	8.1 ± 2.7	37.4 ± 5.5	10.2 ± 3.8	32.8 ± 4.0	**150**	100 nM	1.6 ± 0.6	36.0 ± 3.1	2.9 ± 1.3	35.7 ± 5.3	4.3 ± 2.3	31.2 ± 5.4
	1 µM	8.7 ± 2.5	75.2 ± 5.2	22.5 ± 2.5	62.4 ± 4.4	37.1 ± 6.9	42.4 ± 8.0		1 µM	6.2 ± 1.6	83.5 ± 3.0	24.4 ± 5.8	54.7 ± 4.7	37.2 ± 5.2	42.8 ± 6.2
	10 nM	1.7 ± 0.2	27.4 ± 2.9	1.3 ± 0.2	25.6 ± 0.4	1.6 ± 0.2	21.9 ± 1.1		10 nM	1.5 ± 0.6	26.9 ± 2.1	1.3 ± 0.7	26.1 ± 1.6	1.7 ± 0.9	23.2 ± 1.4
126	100 nM	3.6 ± 0.8	35.7 ± 3.7	6.4 ± 2.0	35.4 ± 3.5	6.4 ± 3.1	31.2 ± 2.6	**156**	100 nM	5.9 ± 1.8	81.6 ± 7.8	22.7 ± 5.1	55.1 ± 3.2	33.4 ± 6.9	36.3 ± 5.8
	1 µM	7.9 ± 1.3	80.6 ± 3.8	23.7 ± 3.6	57.9 ± 4.0	35.4 ± 7.1	43.8 ± 9.5		1 µM	4.5 ± 0.8	88.1 ± 1.8	16.4 ± 4.0	71.3 ± 5.1	38.2 ± 7.0	44.2 ± 6.5
	10 nM	1.2 ± 0.7	25.7 ± 0.3	1.2 ± 0.6	23.4 ± 0.7	1.2 ± 0.4	20.0 ± 0.8		10 nM	1.2 ± 0.2	24.4 ± 2.8	1.4 ± 0.2	22.2 ± 0.8	1.8 ± 0.8	18.0 ± 1.6
127	100 nM	1.3 ± 0.2	26.6 ± 0.1	1.2 ± 0.5	23.2 ± 1.9	1.5 ± 0.2	20.2 ± 1.2	**163**	100 nM	1.4 ± 0.4	28.3 ± 4.2	2.2 ± 1.2	31.9 ± 6.3	3.0 ± 1.5	26.9 ± 4.5
	1 µM	8.4 ± 1.1	61.8 ± 6.0	19.6 5.2	47.8 ± 5.0	33.7 ± 6.4	36.3 ± 5.9		1 µM	6.5 ± 1.1	81.6 ± 3.9	26.7 ± 4.8	51.2 ± 4.1	40.2 ± 6.3	37.2 ± 6.8

Table 25. Continued

		24 h		48 h		72 h				24 h		48 h		72 h	
No.	**[c]**	**SubG$_0$/G$_1$**	**G$_2$/M**	**SubG$_0$/G$_1$**	**G$_2$/M**	**SubG$_0$/G$_1$**	**G$_2$/M**	**No.**	**[c]**	**SubG$_0$/G$_1$**	**G$_2$/M**	**SubG$_0$/G$_1$**	**G$_2$/M**	**SubG$_0$/G$_1$**	**G$_2$/M**
	10 nM	1.0 ± 0.2	24.7 ± 3.0	1.1 ± 0.4	24.0 ± 1.4	1.3 ± 0.2	21.3 ± 0.8		10 nM	1.2 ± 0.6	27.0 ± 1.3	1.3 ± 0.6	20.6 ± 0.4	1.2 ± 0.2	18.9 ± 0.7
164	100 nM	1.0 ± 0.2	27.6 ± 2.6	1.5 ± 0.5	29.8 ± 1.9	1.4 ± 0.7	22.7 ± 1.0	**177**	100 nM	1.6 ± 0.6	34.9 ± 2.2	3.7 ± 2.1	35.1 ± 0.9	3.5 ± 1.1	30.7 ± 4.0
	1 µM	6.2 ± 1.0	83.8 ± 1.8	25.6 ± 5.5	54.8 ± 8.5	40.5 ± 8.2	36.9 ± 7.2		1 µM	4.8 ± 1.6	86.7 ± 4.4	23.4 ± 5.9	62.0 ± 8.0	34.6 ± 5.7	47.9 ± 7.2
	10 nM	0.8 ± 0.2	25.4 ± 3.6	1.1 ± 0.6	24.0 ± 2.1	1.1 ± 0.4	21.4 ± 0.3		10 nM	4.2 ± 2.1	41.8 ± 4.7	8.6 ± 2.7	42.6 ± 5.4	9.9 ± 0.8	39.7 ± 3.0
165	100 nM	1.2 ± 0.2	27.2 ± 2.4	1.5 ± 0.5	25.7 ± 3.2	1.6 ± 0.5	23.1 ± 2.3	**181**	100 nM	4.5 ± 1.1	82.2 ± 5.3	13.2 ± 2.8	74.4 ± 4.9	25.2 ± 3.1	56.2 ± 6.6
	1 µM	5.2 ± 1.8	87.0 ± 1.9	19.3 ± 3.5	64.4 ± 7.3	39.1 ± 9.9	37.6 ± 8.5		1 µM	5.4 ± 1.4	81.4 ± 6.1	11.8 ± 2.5	76.2 ± 3.7	27.1 ± 2.6	56.6 ± 6.4
	10 nM	5.2 ± 1.4	66.0 ± 6.6	14.3 ± 3.0	51.2 ± 8.7	31.8 ± 6.0	35.3 ± 6.8		10 nM	1.3 ± 0.5	26.9 ± 1.7	1.4 ± 0.8	24.1 ± 1.6	1.3 ± 0.6	23.8 ± 1.8
166	100 nM	3.2 ± 0.5	88.3 ± 4.0	16.8 ± 3.1	70.6 ± 7.2	36.2 ± 5.9	43.6 ± 9.5	**182**	100 nM	3.5 ± 0.6	86.4 ± 2.2	13.5 ± 2.5	73.2 ± 4.2	29.1 ± 1.0	53.3 ± 0.1
	1 µM	3.4 ± 0.9	83.8 ± 4.9	12.1 ± 3.3	74.8 ± 7.8	37.3 ± 9.3	39.4 ± 6.7		1 µM	4.2 ± 1.0	83.1 ± 4.7	14.9 ± 6.3	71.2 ± 9.2	34.6 ± 6.1	47.8 ± 5.3
	10 nM	1.4 ± 0.7	25.6 ± 0.6	1.3 ± 0.4	23.4 ± 1.2	1.4 ± 0.2	21.4 ± 2.7		10 nM	1.0 ± 0.6	24.5 ± 3.4	1.0 ± 0.3	22.8 ± 1.4	1.1 ± 0.4	22.6 ± 1.4
167	100 nM	6.8 ± 0.7	73.6 ± 5.3	21.9 ± 5.1	47.3 ± 7.0	31.5 ± 5.6	34.1 ± 5.3	**183**	100 nM	5.7 ± 0.9	68.4 ± 2.6	16.6 ± 2.5	51.2 ± 7.7	25.7 ± 5.5	43.0 ± 9.8
	1 µM	3.8 ± 0.8	88.2 ± 2.8	18.1 ± 5.5	67.1 ± 6.3	29.3 ± 7.1	57.8 ± 3.0		1 µM	4.2 ± 0.7	84.3 ± 3.3	10.2 ± 2.6	77.0 ± 2.9	21.8 ± 4.9	61.0 ± 5.4
	10 nM	1.0 ± 0.4	24.5 ± 2.9	1.0 ± 0.6	22.2 ± 1.8	1.0 ± 0.5	20.8 ± 0.8		10 nM	1.2 ± 0.1	26.4 ± 2.6	1.3 ± 0.5	20.6 ± 0.8	1.4 ± 0.6	19.6 ± 0.5
168	100 nM	1.0 ± 0.3	26.7 ± 3.0	1.6 ± 0.5	24.0 ± 2.2	1.6 ± 0.5	21.6 ± 3.0	**184**	100 nM	8.8 ± 1.7	71.8 ± 4.9	24.1 ± 7.6	49.0 ± 9.6	29.2 ± 7.2	45.6 ± 6.6
	1 µM	7.0 ± 1.1	80.8 ± 3.9	22.6 ± 3.5	59.6 ± 5.7	33.8 ± 3.0	38.8 ± 6.0		1 µM	5.4 ± 1.2	82.2 ± 6.1	13.9 ± 4.6	72.4 ± 9.6	21.8 ± 4.6	64.3 ± 6.9
	10 nM	1.2 ± 0.3	25.2 ± 2.4	1.4 ± 0.3	22.1 ± 0.2	1.4 ± 0.2	20.9 ± 0.3		10 nM	1.2 ± 0.4	25.2 ± 2.4	1.1 ± 0.5	20.6 ± 1.5	1.8 ± 0.6	20.0 ± 1.0
169	100 nM	1.4 ± 0.4	27.9 ± 1.9	1.8 ± 0.6	26.6 ± 3.9	1.9 ± 0.4	21.8 ± 3.1	**185**	100 nM	1.0 ± 0.3	31.4 ± 2.1	2.1 ± 1.4	36.2 ± 7.5	4.7 ± 2.3	37.7 ± 7.1
	1 µM	7.9 ± 0.9	76.2 ± 5.9	23.4 ± 4.4	51.4 ± 6.2	33.5 ± 4.2	38.9 ± 7.1		1 µM	6.3 ± 2.6	85.0 ± 4.6	26.7 ± 6.0	58.7 ± 5.2	31.1 ± 7.3	52.9 ± 6.7
	10 nM	1.6 ± 0.4	26.2 ± 0.7	1.4 ± 0.5	22.6 ± 0.4	1.5 ± 0.2	21.3 ± 0.3		10 nM	2.4 ± 1.0	39.0 ± 4.8	4.0 ± 2.9	38.3 ± 4.2	4.9 ± 3.0	34.1 ± 4.3
170	100 nM	5.1 ± 2.0	61.4 ± 6.5	14.1 ± 3.0	50.7 ± 4.5	23.1 ± 6.7	41.7 ± 7.7	**186**	100 nM	5.2 ± 0.6	83.7 ± 3.2	13.3 ± 3.1	74.7 ± 4.7	24.7 ± 5.9	58.6 ± 4.7
	1 µM	5.1 ± 2.5	86.3 ± 4.9	16.1 ± 3.3	71.5 ± 6.0	31.7 ± 3.2	57.5 ± 2.1		1 µM	6.2 ± 1.2	80.6 ± 4.8	16.6 ± 3.8	70.7 ± 6.6	27.0 ± 3.8	53.5 ± 9.6
	10 nM	1.0 ± 0.3	25.4 ± 3.0	1.1 ± 0.5	23.5 ± 2.3	1.3 ± 0.2	20.9 ± 1.2		10 nM	1.1 ± 0.3	24.5 ± 2.2	1.2 ± 0.6	23.8 ± 1.8	1.1 ± 0.4	21.9 ± 1.5
174	100 nM	4.2 ± 0.5	60.9 ± 2.8	12.5 ± 3.0	51.7 ± 3.1	20.6 ± 5.7	40.5 ± 6.2	**187**	100 nM	2.8 ± 1.4	36.4 ± 2.2	4.1 ± 2.9	34.0 ± 3.3	4.2 ± 2.5	28.8 ± 2.9
	1 µM	4.2 ± 0.9	87.0 ± 3.3	12.2 ± 3.0	74.8 ± 3.6	26.7 ± 6.0	55.1 ± 2.8		1 µM	4.9 ± 1.2	85.6 ± 3.8	16.7 ± 1.2	69.5 ± 3.2	26.5 ± 3.4	55.2 ± 7.8
	10 nM	1.5 ± 0.3	23.3 ± 2.0	1.0 ± 0.3	20.8 ± 1.5	1.1 ± 0.3	19.4 ± 0.8		10 nM	1.4 ± 0.7	25.0 ± 2.7	1.1 ± 0.1	22.4 ± 2.6	1.3 ± 0.3	20.5 ± 3.3
175	100 nM	1.1 ± 0.2	24.7 ± 1.9	1.4 ± 0.5	22.3 ± 0.9	0.9 ± 0.4	21.1 ± 1.6	**188**	100 nM	2.5 ± 0.5	40.0 ± 5.4	4.7 ± 1.5	37.7 ± 4.3	5.4 ± 2.6	34.9 ± 5.4
	1 µM	8.3 ± 1.7	71.2 ± 3.8	26.3 ± 5.5	54.1 ± 8.0	31.4 ± 8.1	41.7 ± 0.1		1 µM	5.8 ± 0.8	85.2 ± 2.6	16.5 ± 3.6	69.1 ± 5.2	36.4 ± 7.7	46.3 ± 8.8
	10 nM	1.1 ± 0.5	26.1 ± 2.4	1.2 ± 0.1	21.6 ± 3.5	1.9 ± 0.5	19.6 ± 1.3		10 nM	1.4 ± 0.3	23.4 ± 1.5	1.1 ± 0.3	21.9 ± 1.6	1.4 ± 0.6	20.9 ± 0.7
176	100 nM	0.8 ± 0.1	25.6 ± 4.1	1.0 ± 0.1	21.4 ± 2.9	1.6 ± 0.2	20.2 ± 0.7	**189**	100 nM	1.5 ± 0.5	30.3 ± 3.4	2.5 ± 1.5	29.0 ± 5.3	2.6 ± 2.0	28.1 ± 4.2
	1 µM	3.3 ± 0.8	50.7 ± 5.1	8.9 ± 2.0	45.2 ± 5.7	16.6 ± 2.2	40.4 ± 6.4		1 µM	5.0 ± 0.7	85.6 ± 3.0	14.1 ± 0.3	73.1 ± 2.4	27.0 ± 4.2	56.4 ± 3.2

Table 25. Percentages of HeLa cells in the SubG$_0$/G$_1$ and G$_2$/M populations following treatment with the indicated compounds. All the compounds were tested at 10 nM, 100 nM, and 1 µM, and the cell cycle distribution was measured after 24 h, 48 h, and 72 h of treatment (n = 3-6). We tested three control conditions (Ctl) by adding the equivalent amount of DMSO (< 0.05%).

Based on these data, we selected a working concentration of the lead compounds **81**, **104**, **123**, **166**, **181**, and **186** to normalize the effect for the upcoming experiments conducted in HeLa cells based on their respective potencies. Among the three concentrations tested in Table 25 (10 nM, 100 nM, and 1 µM), we selected the lower dose inducing the arrest of HeLa cells in G_2/M by at least 70%. All of them were then used at a concentration of 100 nM (**81, 104**, **166**, **181**, and **186**), except for sulfonamide **123** at 1 µM.

Most of the cells accumulated in the G_2/M region after an incubation of 24 h with the compounds. To evaluate the timeline towards the consecution of the G_2/M arrest, we performed a time-course in HeLa cells with compound **81** (100 nM) every two hours up to one day (Fig. 51). The effect on the cell cycle is time-dependent, with an evident G_2/M arrest 8 h after treatment and a parallel reduction in G_0/G_1.

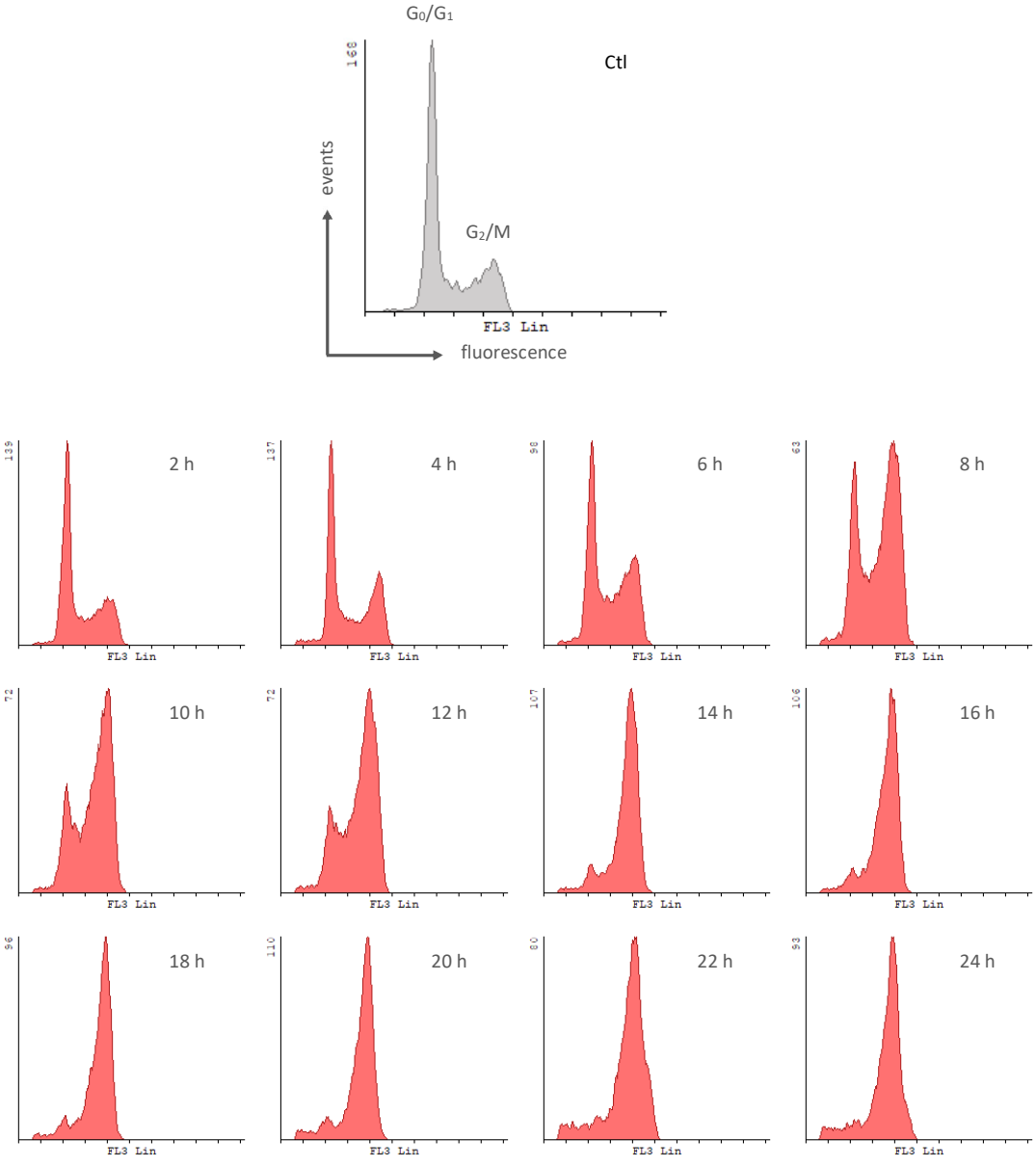

Figure 51. Cell cycle histograms of HeLa cells in a time-course treatment with compound **81** at 100 nM (red histograms). The peaks corresponding to G_0/G_1 and G_2/M populations are indicated on the control histogram (Ctl, grey histogram). Cells in the G_2/M region show twice fluorescence intensity than those in G_0/G_1. The S phase corresponds to the region between those two populations. The region to the left of the G_0/G_1 peak is called $SubG_0/G_1$ (hypodiploidy). Flow cytometry profiles are representative of three independent experiments.

In light of the time-dependent accumulation of cells in G_2/M induced by **81** (Fig. 51), we selected some representative time-points to study the distribution of the cells in the different populations upon treatment with the lead compounds at the working concentrations: 9 h, 15 h, 24 h, 48 h, and 72 h (Fig. 52).

Figure 52. Analysis of cell cycle populations (**SubG$_0$/G$_1$**, **G$_0$/G$_1$**, **S**, and **G$_2$/M**) in HeLa cells after treatment with the lead compounds at the indicated concentrations. The statistical analysis was carried out for the data relative to the G_2/M population respect to untreated samples (Ctl) after the same incubation period (n = 4-15; *** $p < 0.001$).

The six lead compounds exhibited a similar trend (Fig. 52). The differences in the G_2/M percentage 9 h after treatment compared to untreated samples (Ctl) are statistically significant ($p < 0.001$) in all cases. The maximum value was reached after 24 h in the case of compounds **81**, **166**, **181**, and **186** (83.1-87.1%). Compound **123** showed a slight decrease in the percentage of cells in the G_2/M region after 24 h (83.7 %) compared to 15 h (87.1%), but this difference is considered to be not statistically significant. The arrest induced by compound **104** was achieved faster in time, with an accumulation after a 15 h-incubation of 87.0% of the cells in G_2/M. This value significantly differs from the 66.6% after 24 h ($p < 0.001$). This drop in the percentage of cells in the G_2/M peak occurs at expense of an increase in the $SubG_0/G_1$ and G_0/G_1 regions ($p < 0.001$), especially the latter (5.5% versus 19.6%), meaning that at least part of the cell population is able to bypass the arrest and reenter G_0/G_1. After reaching the maximum G_2/M percentage, all the treatments showed a reduction of this peak with a concomitant increase in the number of cells in the $SubG_0/G_1$ region over time.

The cells in G_2 and M phases have equivalent amounts of DNA, and therefore cannot be distinguished by this procedure. To determine that the G_2/M arrest elicited after treatment was based on an accumulation of cells in mitosis rather than G_2, we performed a Western blot analysis in HeLa cells to detect MPM-2 signal. This primary antibody recognizes a phosphorylated epitope (S/T)P present in many phosphoproteins that are phosphorylated at the onset of mitosis. The detected signal correlates with the mitotic burden in the lysate. The lead compounds were tested at their respective working concentrations and incubated for 9 h, 15 h, 24 h, 32 h, and 48 h (Fig. 53). The immunoblot images show time-dependent expression levels of mitotic phosphoproteins, with increased signal after 9 h of treatment, that drops after 48 h, coinciding when the $SubG_0$/G1 population starts increasing (Fig. 52).

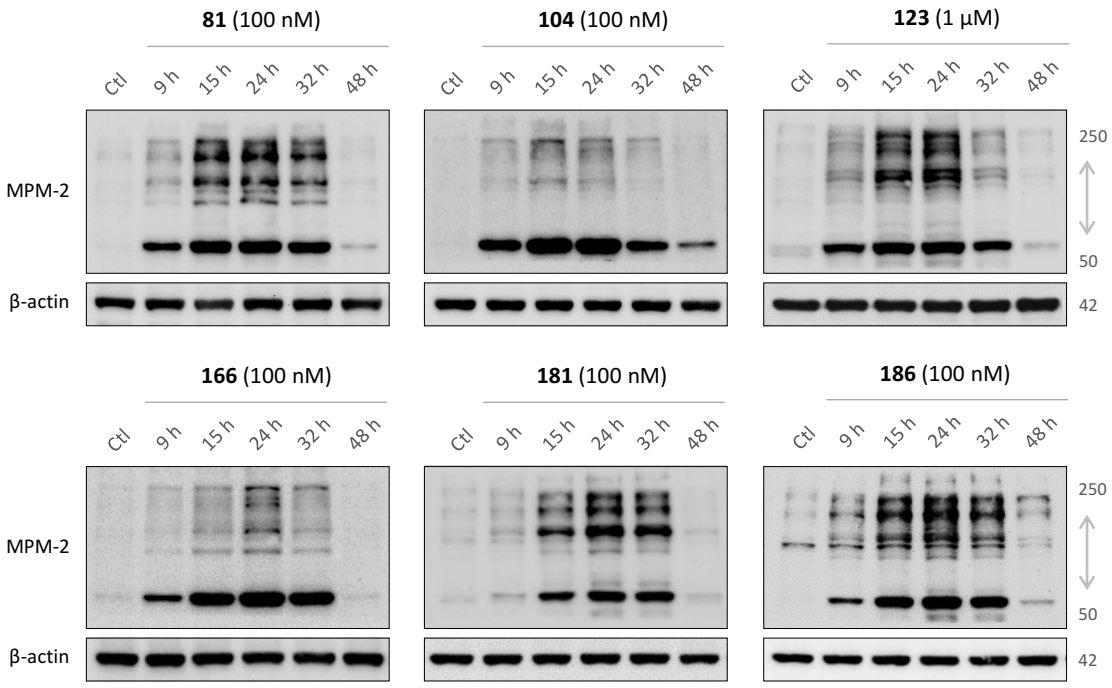

Figure 53. Immunoblots of HeLa cell lysates: time-course of the expression levels of phosphorylated mitotic proteins (MPM-2) after treatment with the lead compounds compared to untreated samples (Ctl). β-actin was used as a loading control. Molecular weights are indicated in kDa. Western blot images are representative of three independent experiments.

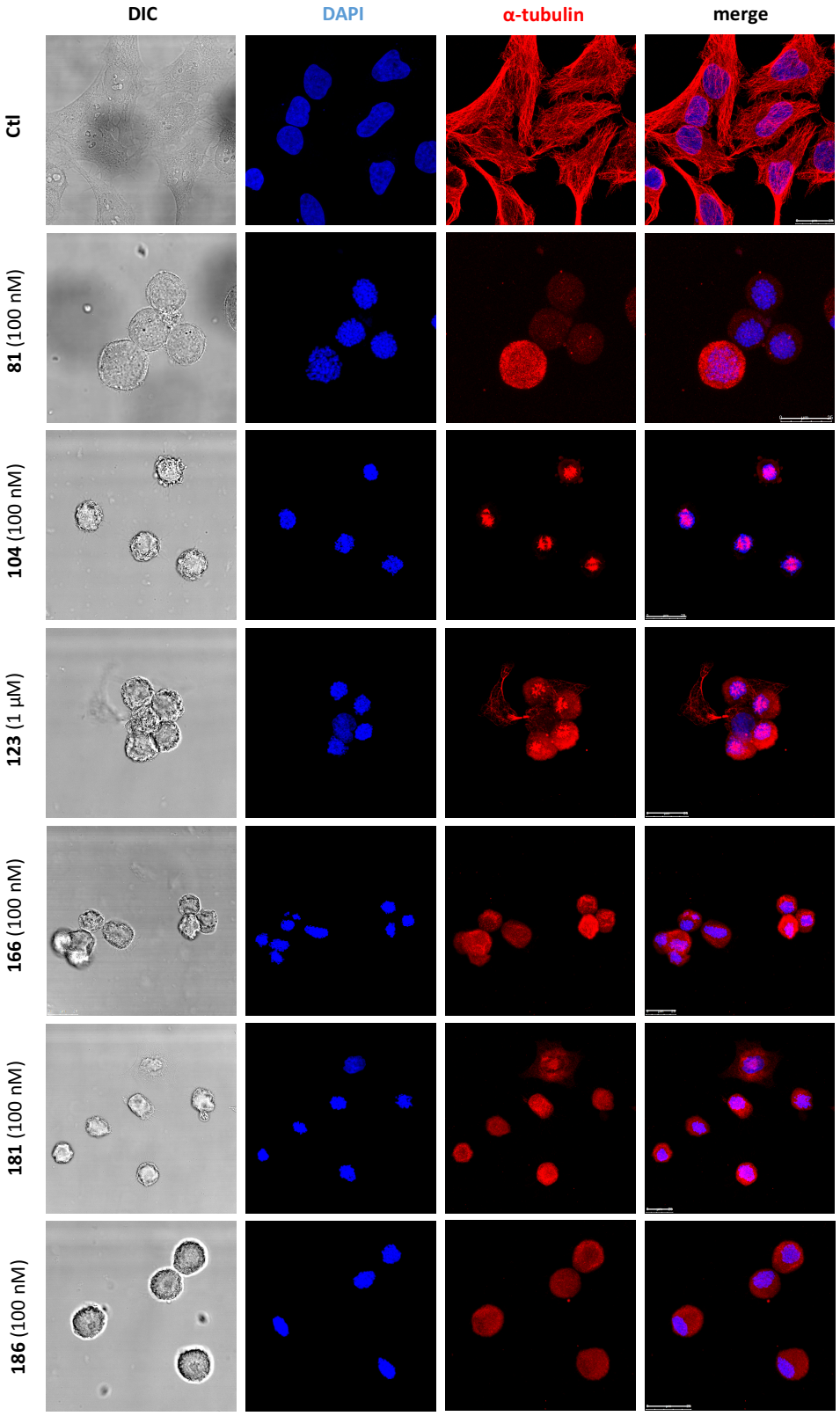

Figure 54. Confocal immunofluorescence microscopy of HeLa cells for visualization of the microtubule network. Cells were incubated in the absence (Ctl) or in the presence of the lead compounds at the indicated concentrations for 24 h. Cells were captured by differential interference contrast (DIC). **Nuclei** were stained with DAPI in blue fluorescence and **α-tubulin** was visualized in red fluorescence (CY3-conjugated Ab-2). Scale bar: 25 µm. Photomicrographs are representative of three independent experiments.

EFFECT ON MICROTUBULES *IN VITRO*

Tubulin cytoskeleton in HeLa cells

Cell cycle profiles, together with the increased detection of MPM-2 signal, points out that the synthesized compounds may act as antimitotic drugs. To verify that the antimitotic effect is achieved upon alteration of the tubulin cytoskeleton, we performed confocal immunofluorescence microscopy experiments in HeLa cells. For the visualization of the tubulin network, we selected a 24-hour incubation period since the maximal cell cycle disturbance with minimal cell death is occurring based on previous data (Fig. 52). To this end, cells were incubated in the presence of the compounds at the working concentration, then fixed and processed. DAPI was used to stained the nuclei (blue fluorescence), and α-tubulin was labeled with red fluorescence using a CY3-conjugated secondary antibody. This procedure was carried out for several ligands among those collected in Tables 22 and 23 with similar results, so the lead compounds have been chosen for representative analysis.

The compounds caused a complete microtubule network disruption in HeLa cells with tubulin protein dispersed throughout the cytosol compared to untreated samples, which exhibit an organized network with filamentous tubulin fibers (Fig. 54). This structural feature is in agreement with a destabilizing effect and differs from MSAs that typically induce the formation of microtubule bundles.[530] We observed some multinucleated cells (photomicrographs not shown). The halt in mitosis is responsible for the round-shaped morphology of the treated HeLa cells that can be seen with the naked eye, utterly different than the flattish spreading shape observed in untreated samples. These overall results support a mechanism of action based on the destabilization of the tubulin cytoskeleton.

Tubulin polymerization assay

Once established that the tested compounds disorganize the tubulin cytoskeleton, we conducted a biochemical assay to study the effect on tubulin polymerization *in vitro*, and therefore assess the proposed microtubule destabilizing effect. We purified microtubular protein (MTP) from calf brain following Shelanski procedure as described in Materials and methods.[531,532] This methodology is based on the distinct property of MTP to polymerize at 37 °C in a GTP buffer and depolymerize at 4 °C, yielding a mixture of approximately 70% tubulin and 30% MAPs.

We incubated the compounds at an initial concentration of 10 μM with 1.0 mg/mL MTP at 20 °C for 20 min to ensure the binding in case any compound shows slow binding kinetics like colchicine, then cooled at 4 °C to make sure the protein is depolymerized. The negative control was set with DMSO, a maximum amount of 4%, which has been reported not to interfere with the assembly process.[533] The polymerization was monitored when switching the temperature to 37 °C by measuring the absorbance at 450 nm related to the turbidity due to polymerization, where the compounds do not absorb. The polymerization percentage was calculated by comparing the amplitude of tubulin-ligand curves from 4-37 °C with the amplitude observed for the negative control, considered as 100% of polymerization. MDAs will exhibit lower polymerization than ligand-free samples, whereas MSAs usually induce increased polymerization. Tubulin polymerization inhibition (TPI) percentages at 10 μM are indicated in Tables 26 and 27. IC_{50} values were calculated by dose-response curves for those compounds that inhibited polymerization by at least 50% at 10 μM in two independent experiments to compare the potency of the active compounds. Lack of cell proliferation inhibition does not necessarily indicate the lack of effect against *in vitro* polymerization, so we tested the compounds irrespective of their antiproliferative activity.

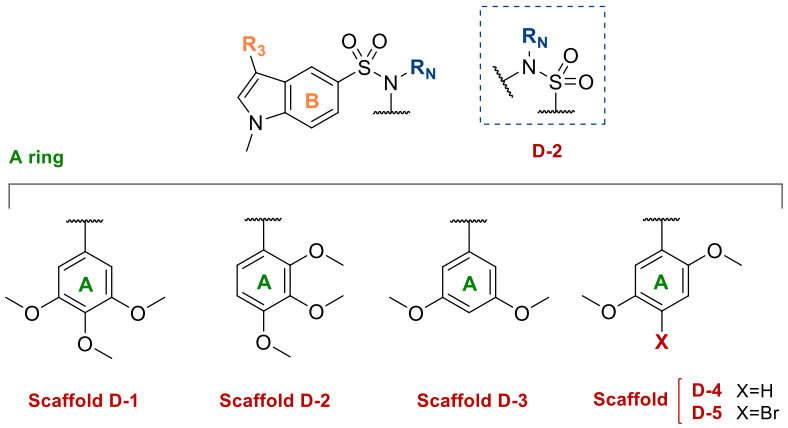

No.	A	R_3	R_N	TPI	IC_{50}	No.	A	R_3	R_N	TPI	IC_{50}
80		H	H	43	-	**110**		H	Bn-4-F	24	-
81		H	Me	100	2.1	**112**		$CONH_2$	H	0	-
82		H	Et	96	2.2	**115**	D-3	CHO	Me	2	-
84		H	CH_2COOEt	86	4.2	**116**		CHO	Bn	14	-
85		H	CH_2COOH	22	-	**117**		CN	Me	13	-
86		H	CH_2CN	56	9.7	**118**		CN	Bn	15	-
87		Br	H	42	-	**122**		H	H	6	-
88		Br	Et	68	5.4	**123**		H	Me	20	-
89	D-1	CHO	H	13	-	**125**		H	CH_2COOEt	4	-
90		CHO	Me	19	-	**126**		H	CH_2CN	16	-
91		*E*-CHCHCN	Me	99	5.6	**127**	D-4	H	Bn	11	-
92		*Z*-CHCHCN	Me	56	8.8	**132**		CHO	H	32	-
93		CHO	Et	9	-	**133**		CHO	Me	55	10.1
94		*E*-CHCHCN	Et	74	6.3	**137**		*E*-CHCHCN	H	0	-
95		*Z*-CHCHCN	Et	26	-	**138**		*Z*-CHCHCN	H	0	-
96		CN	H	24	-	**139**		CN	H	43	-
97		CN	Me	52	10.0	**140**		CN	Ac	8	-
99	D-2	H	H	7	-	**128**		Br	H	12	-
100		H	Me	0	-	**129**		Br	Me	25	-
103		H	H	0	-	**134**	D-5	CHO	Me	8	-
104		H	Me	10	-	**135**		CHO	H	0	-
105	D-3	H	Et	16	-	**136**		CN	H	0	-
106		H	CH_2COOEt	14	-	**IC**[499]	D-1	H	-	-	2.0
107		H	CH_2CN	11	-	**CA4**[499]		-	-	-	3
109		H	Bn	13	-						

Table 26. Effect of sulfonamide derivatives on tubulin polymerization *in vitro*. Tubulin polymerization inhibition (TPI) at 10 µM concentration is indicated in percentage (n = 2). IC_{50} values (µM) against tubulin polymerization were measured for the ligands that showed TPI over 50%.

The overall results showed a destabilizing activity for many of the ligands, in line with the disintegration of the microtubule network shown in confocal immunofluorescence experiments (Fig. 54). Some compounds (**81**, **82**, **91**, **166**, **167**, and **181**) exerted almost complete (> 90%) TPI at 10 µM. The concentration of 10 µM was selected based on previous results of our research group, which permits to easily discriminate between compounds that exert a strong inhibitory effect from those that do not. Most of the ligands belonging to the family of indolecombretastatins, highly structurally related to the compounds of this work, showed IC_{50} values against tubulin polymerization below 10 µM.[499] The

unsubstituted indolecombretastatin (IC) shows an IC_{50} value of 2.0 µM, more potent than CA4 (Table 26). Compounds **81** and **82** displayed IC_{50} values of 2.1 and 2.2 µM, respectively, proving more potent than CA4, and as potent as indolecombretastatin. Most of the ligands that belong to the family of indolecombretastatins and display cytotoxic activity against HeLa cells in the submicromolar range also inhibit tubulin polymerization with IC_{50} values below 5 µM.[499] However, sulfonamides with akin TPI values exert milder effects on tubulin polymerization (Table 22).

There is an acceptable correlation between TPI and the antiproliferative activity for all the cell lines, and therefore, similar SARs can be deduced from the antitubulin and the antiproliferative activities. The 3,4,5-trimethoxyphenyl series exhibited overall enhanced TPI at 10 µM than structures with other A-ring patterns. Substituents at the sulfonamide led to increased TPI (e.g. **81, 82**, **84**, **86** versus **80**). Modifications at the indole 3-position are detrimental for the antitubulin effect, leading to 3 to 5-fold higher IC_{50} values when the indole ring of **81** (IC_{50} = 2.1 µM) was modified with nitrile or propenenitrile substituents in compounds **91**, **92**, and **97** (IC_{50} = 5.6, 8.8, and 10.0 µM, respectively). Similar trends were found for ethyl derivatives **88** and **94**, showing around 2.5-fold lower activity than that observed for **82**. Based on these observations, compounds triggering a greater cytotoxic response show remarkable tubulin assembly inhibition. Tetrazoles **166**, **167**, **181**, and **186** strongly inhibited tubulin polymerization at 10 µM, with IC_{50} values of 5.2 µM and 4.3 µM in the case of **166** and **167** (Table 27), although the latter displayed notably weaker antiproliferative activity than **166**, the most potent compound regarding the proliferation assay.

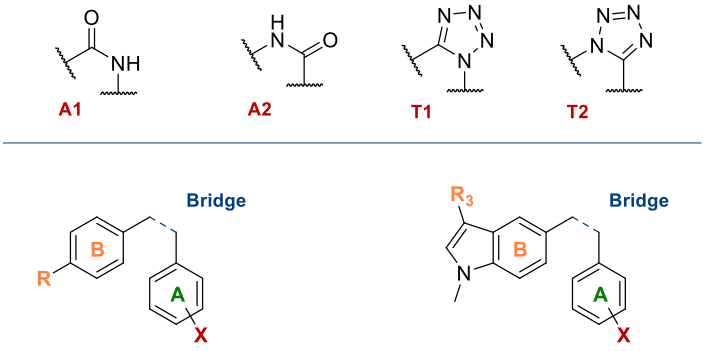

No.	A	Bridge	TPI	IC_{50}	No.	A	Bridge	TPI	IC_{50}
141		A1	0	-	**160**	**D-6**	A2	0	-
144		T1	8	-	**161**		A2	2	-
148		A2	0	-	**163**		A2	0	-
150		T2	10	-	**164**		A2	2	-
152		T2	0	-	**166**	**D-3**	T2	92	5.2
154	**D-3**	A1	0	-	**167**		T2	98	4.3
155		A1	0	-	**169**		T2	19	-
156		T1	45	-	**181**		T1	100	n.d.
157		A2	0	-	**183**	**D-1**	T1	5	-
158		A2	0	-	**186**		T2	74	n.d.
159		A2	0	-					

Table 27. Effect of amide and tetrazole derivatives on tubulin polymerization *in vitro*. Tubulin polymerization inhibition (TPI) at 10 µM concentration is indicated in percentage (n = 2). IC_{50} values (µM) against tubulin polymerization were measured for the ligands that showed TPI over 50%. n.d. = not determined.

MTC competition assay

As evidenced by the polymerization assay, these compounds prevent tubulin from polymerizing in a dose-dependent manner, which is compatible with the mechanism of action of MDAs. However, the polymerization inhibition does not necessarily mean that the molecular target of the drugs is tubulin. The polymerization assay was conducted on microtubular protein so that the inhibition could be related to MAPs or tubulin selective targeting. In order to elucidate whether the polymerization inhibition is due to tubulin binding, we performed a competition assay at the colchicine binding domain in the laboratory of Dr. Fernando Díaz at CIB Margarita Salas (Madrid).

To this end, we used bovine brain tubulin and MTC as a fluorescent probe (λ_{exc} = 350 nm, λ_{em} = 423 nm). MTC binds to the colchicine domain with a known binding constant ($K_b = 4.7 \cdot 10^5\ M^{-1}$) and fluoresces when bound, showing negligible emission in its free state (**light blue**, Fig. 55).[534] The competition can be detected by comparing the emission spectra of MTC + tubulin (10 µM each) at 25 °C in the presence of increasing concentrations of ligands. The fluorescence of the MTC-tubulin complex (**red**, Fig. 55) decreases in the presence of competitive inhibitors of the colchicine domain.[535] This method not only shows the binding of ligands to the domain but also the affinity (K_b) by measuring the fractional saturation values.[536]

For a first screening, we selected several compounds that did not absorb at 350 nm and recorded the emission spectra of MTC-tubulin with increasing concentrations of ligands from 360 nm to 550 nm (Fig. 55). Those spectra registered two peaks, a first peak at 397 nm, and the second at 423 nm, the maximum emission of the MTC-tubulin complex. All the tested compounds caused decay of the fluorescence emission and therefore bind to the colchicine domain of tubulin. The fluorescence observed at 423 nm converted into fractional saturation values allowed us to measure the binding constants of the compounds (Table 28). The association of **81** and **104** with tubulin (K_b = 1.3 and $1.1 \cdot 10^7\ M^{-1}$) is as strong as that of colchicine ($K_b = 1.16 \cdot 10^7\ M^{-1}$ at 37 °C)[537] under these conditions. Using MTC as a probe is not the optimal strategy to calculate the binding constants of those two compounds accurately, which requires a reference ligand with a higher affinity than MTC for the colchicine domain. The binding constant for **166** could not be determined because it insolubilizes at 5 µM (**dark blue**, Fig. 55). The fluorescence intensity reduction at 2.5 µM (**yellow**, Fig. 55) is greater than that observed for any of the other tested compounds, suggesting that the affinity of **166** might be stronger than the others.

No.	K_b
80	$4.0 \cdot 10^6\ M^{-1}$
81	$1.3 \cdot 10^7\ M^{-1}$
82	$2.9 \cdot 10^6\ M^{-1}$
84	$6.2 \cdot 10^6\ M^{-1}$
90	$4.0 \cdot 10^5\ M^{-1}$
104	$1.1 \cdot 10^7\ M^{-1}$
123	$9.7 \cdot 10^5\ M^{-1}$
166	n.d.
colchicine[537]	$1.2 \cdot 10^7\ M^{-1}$
podophyllotoxin[538]	$1.8 \cdot 10^6\ M^{-1}$
MTC	$4.7 \cdot 10^5\ M^{-1}$

Table 28. Binding constants (K_b) determined at 25 °C based on the fluorescence emission at 423 nm for the ligands in Figure 55. The colchicine binding constant was measured at 37 °C.

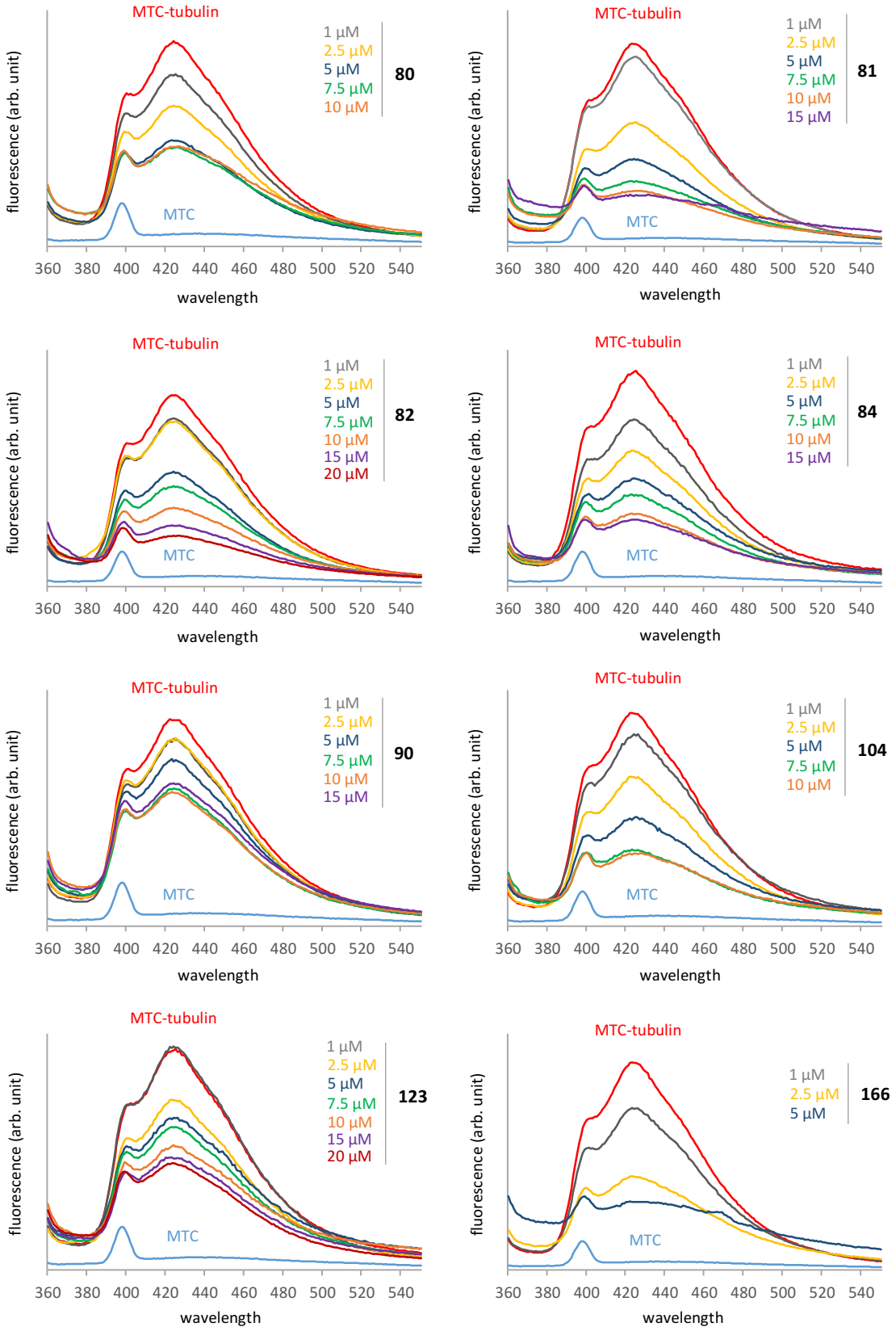

Figure 55. Displacement of MTC from the colchicine domain: fluorescence emission spectra of 10 µM MTC and 10 µM tubulin at 25 °C in the absence (**red**) or in presence of increasing concentrations of **80**, **81**, **82**, **84**, **90**, **104**, **123**, and **166**. The spectra of MTC was recorded as the blank (**light blue**), showing negligible emission at 423 nm.

STUDY OF THE ANTIVASCULAR EFFECT *IN VITRO*

In a preliminary approach to study the antivascular potential of the lead compounds, we conducted a tube formation assay[539] at Dr. DeCicco-Skinner's laboratory (Washington, DC, USA) during a short-term stay. It is a rapid and quantifiable procedure to measure the angiogenesis *in vitro* with endothelial cells that form capillary-like structures when plated on basement membrane extract (BME) in the presence of proangiogenic cues. To this end, mouse 3B-11 endothelial cells were starved overnight, then stained with calcein AM (green fluorescence) and seeded in stem cell conditioned media on top of reduced growth factor basement membrane matrix (≥ 10 mg/mL). 3B-11 cells were incubated in the absence (Ctl) or the presence of the lead compounds at three different concentrations. Endothelial cells began to align themselves after 1-2 h, then tube-like structures appeared as lumens enclosed by endothelial cells. After 6 hours, the vascular network was captured (Fig. 56A) and measured regarding the number of nodes, meshes, and segments using ImageJ with the Angiogenesis Analyzer plugin (Fig. 56B).

The drug concentrations tested to evaluate the antivascular profile were chosen based on the potency of the lead compounds against HeLa cells. The working concentration was set at 100 nM by default for compounds **81**, **104**, **166**, **181**, and **186**, so we tested that value (100 nM) and two lower doses (50 nM and 10 nM) for this experiment. Compound **123**, less potent against HeLa cells, was tested at its working concentration (1 µM) and additionally at 0.5 µM and 100 nM. All of the compounds caused a dose-dependent inhibition of tube formation.

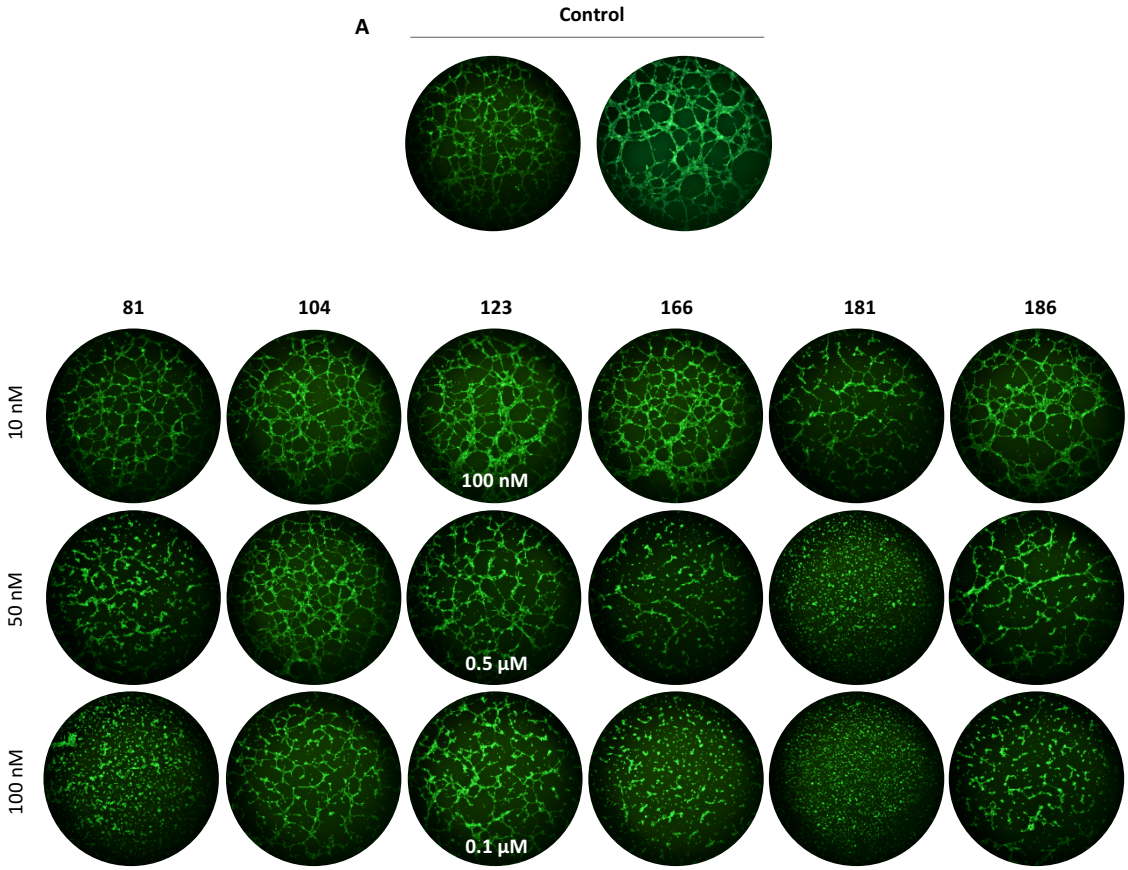

Figure 56. Continued

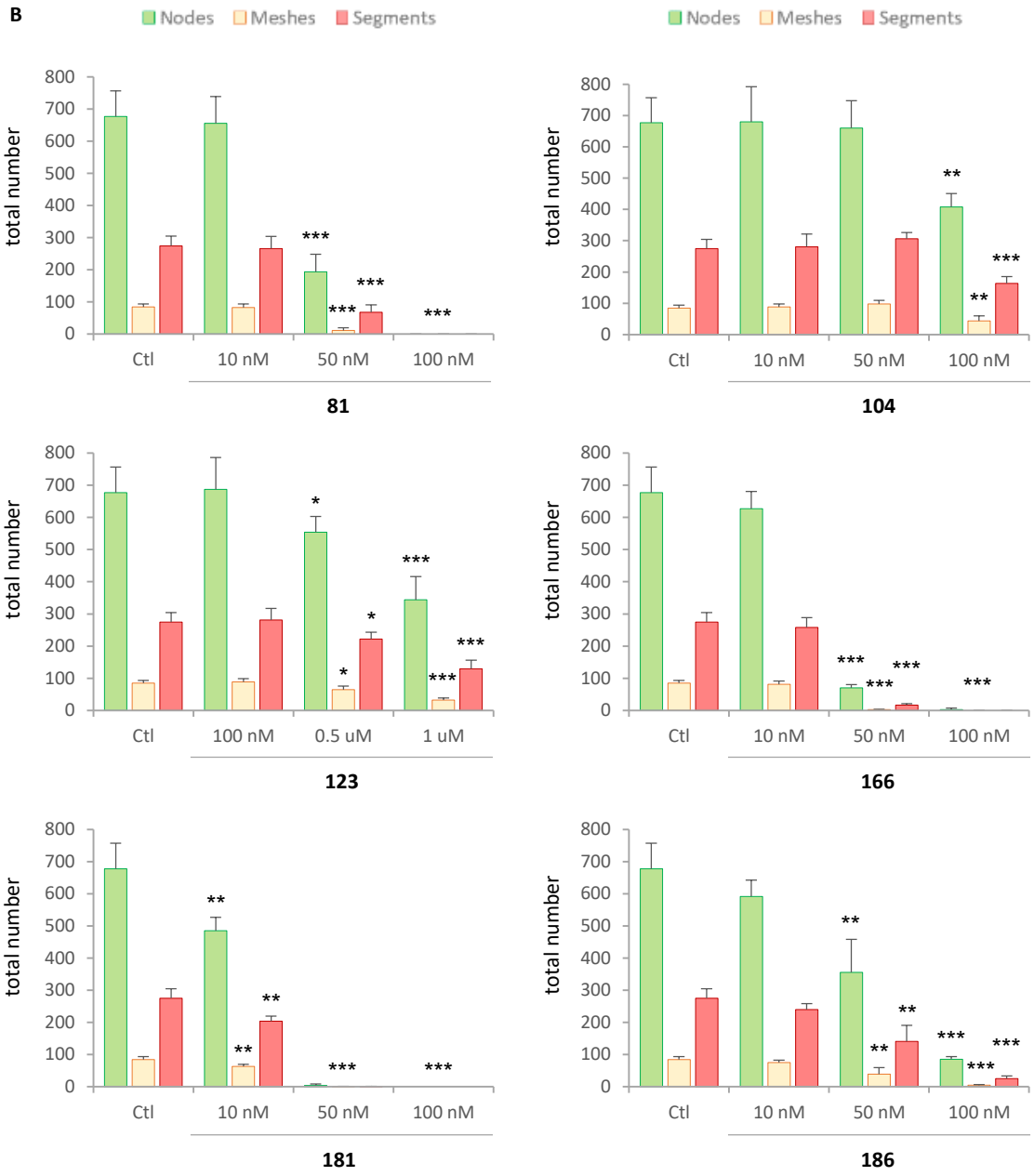

Figure 56. Tube formation assay in 3B-11 endothelial cells. **A.** Images of the capillary-like network stained with calcein AM (green fluorescence). The images are representative of four independent experiments. **B.** Quantitative analysis of the total number of **nodes**, **meshes**, and **segments** observed in the absence (Ctl) and the presence of the lead compounds ($n = 4$; * $p < 0.05$; ** $p < 0.01$; *** $p < 0.001$).

The potency of the compounds is in agreement with the IC_{50} values against 3B-11 cell proliferation (Table 24). Tetrazole **181** (3.7 nM) was the most potent ligand, showing effect at the lowest concentration of 10 nM ($p < 0.01$), followed in potency by **166** (14.4 nM) and **81** (7.3 nM), whose effects at such low dose were considered to be not statistically significant. Despite the structural similarity of tetrazoles **181** and **186** differing only in the bridge orientation, **186** (31.6 nM) showed considerably reduced potency. Compounds **104** (95.6 nM) and **123** (301.7 nM) showed tube formation inhibition at higher concentrations (Fig. 56).

STUDY OF THE CELL DEATH INDUCED AFTER TREATMENT

Induction of apoptosis in HeLa cells

The three main cell death routines are apoptosis (type I), autophagy (type II), and necrosis (type III). We analyzed whether the mitotic arrest was followed by cell death in HeLa cells and characterized the type of death. Following cell cycle analysis, we found that the percentage of treated cells in G_2/M decreased from 24 h onwards (Fig. 52). The decay we observed is due to the increasing number of cells in the $SubG_0/G_1$ region, which corresponds to apoptotic cells with DNA fragmentation. The time-dependent increase of the $SubG_0/G_1$ peak points out that cells underwent apoptosis after the mitotic arrest (Fig. 57). Likewise, we studied the plasma membrane permeability in a time-course experiment to determine its evolution during cell demise (Fig. 57).

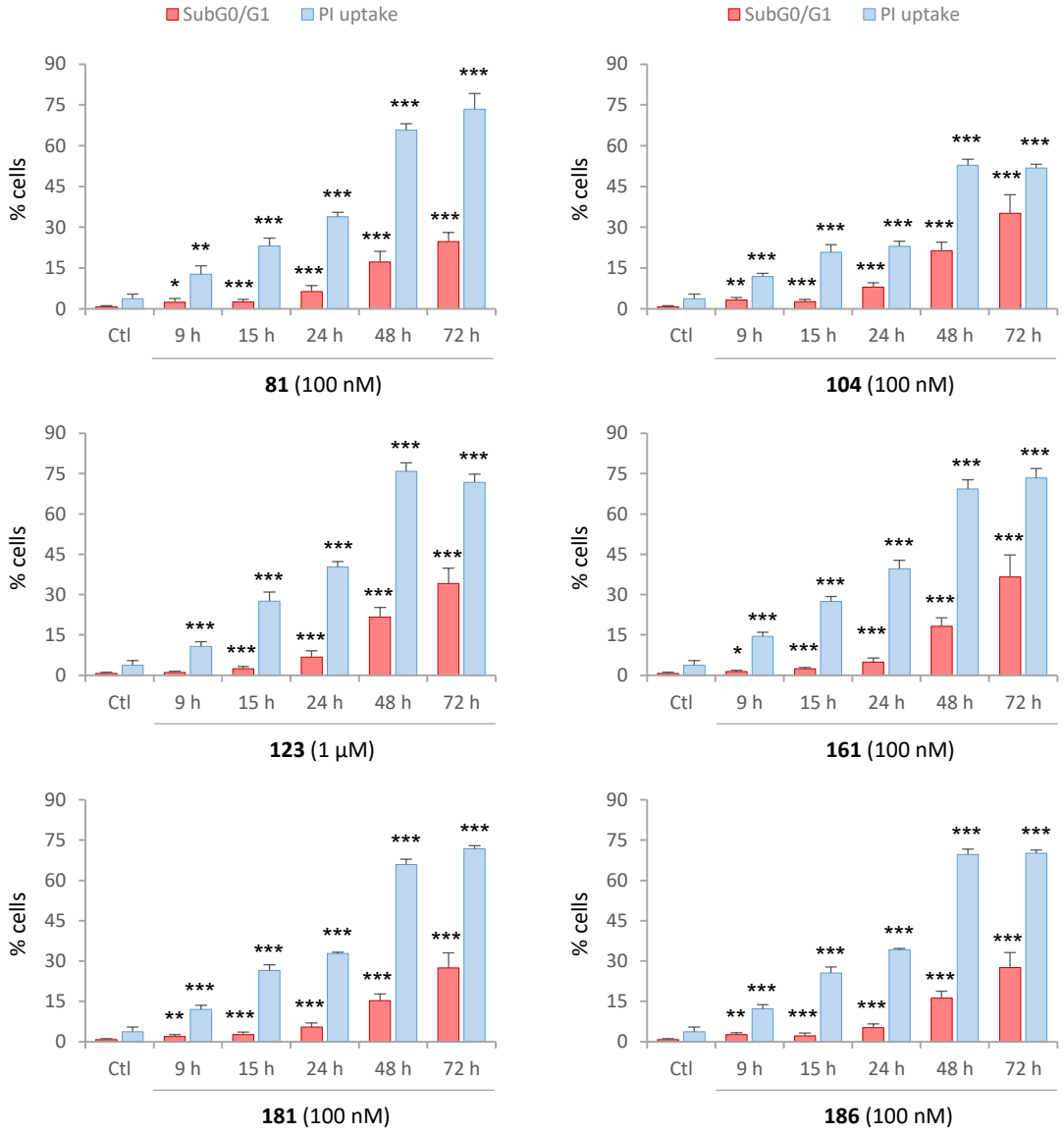

Figure 57. Time-course of HeLa cells in the absence (Ctl) or the presence of the lead compounds. The graphs represent the percentage of cells in **$SubG_0/G_1$** population measured by cell cycle analysis (n = 4-15; * $p < 0.05$; ** $p < 0.01$; *** $p < 0.001$), and the percentage of **PI-positive cells** in non-permeabilized samples (n = 4).

The integrity of the plasma membrane can be easily studied by flow cytometry in a PI exclusion assay (red fluorescence) in non-permeabilized cells following treatment. The appearance of a PI-positive population is indicative of membrane permeabilization. The loss of membrane integrity is a hallmark of necrotic cell death, but this feature may occur under other circumstances. As depicted in Figure 57, all of the compounds induced time-dependent permeabilization of the plasma membrane, assessed by the increasing number of cells with red fluorescence (**blue bars**). This effect is statistically significant at early incubation times (10.7-14.4% after 9 h compared to 3.7% in control), as does the accumulation of apoptotic cells in the $SubG_0/G_1$ region (**red bars**). Although those two parameters are not comparable, the loss of membrane integrity occurred either to a larger extent or earlier than DNA fragmentation, and reached a plateau after 48-h incubation. There was no plateau, but an increasing trend regarding the $SubG_0/G_1$ percentage. Nevertheless, we did not evaluate longer incubation periods because the number of cells strikingly decreased after 72-h treatments, noticed with the naked eye and by the number of events recorded by flow cytometry. The pace of membrane permeabilization and apoptosis is similar for compounds **81**, **123**, **166**, **181**, and **186**. However, compound **104** exhibited milder effects on membrane integrity compared to the other ligands, with an akin percentage of cells in $SubG_0/G_1$ (Fig. 58).

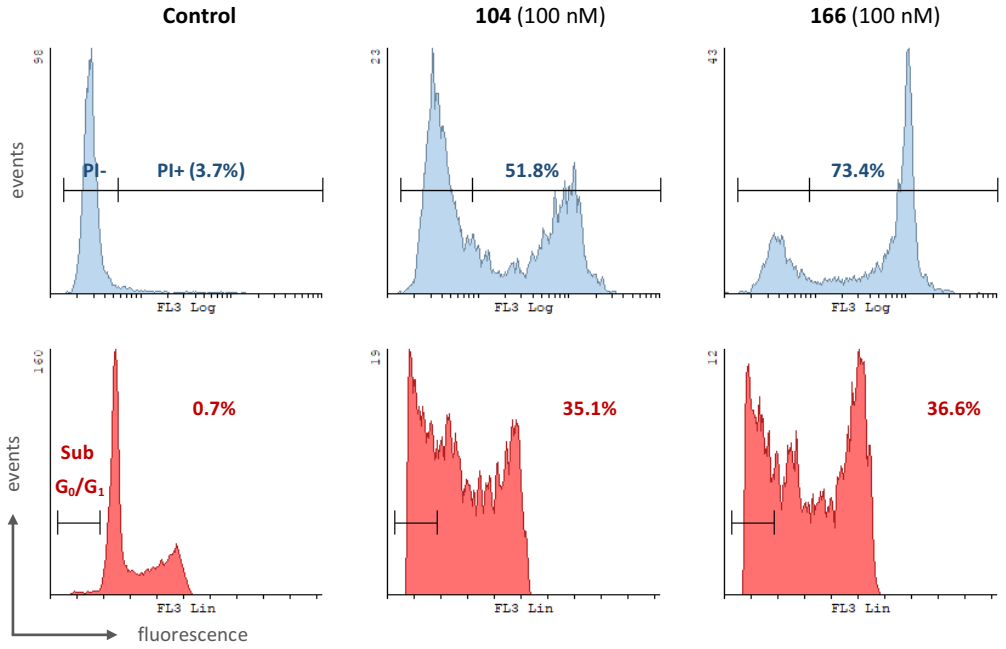

Figure 58. Histograms of HeLa cells in control conditions or treated with **104** and **166** at 100 nM for 72 h. The Y axis corresponds to the number of cells and the X axis is the red fluorescence of PI in non-permeabilized samples (first row, **PI uptake**) or in fixed samples (second row, **cell cycle**). The histograms are representative of at least four independent experiments. The percentage of **PI-positive** cells indicates the permeabilization rate within the samples and the percentage of the **$SubG_0/G_1$** population correlates with the number of apoptotic cells.

The strong membrane permeabilization arising upon treatment may correspond to necrotic death, either pure necrosis or apoptosis that evolved towards necrosis, given the lack of phagocytic cells in the culture media. When comparing the percentages of $SubG_0/G_1$ population and PI-positive cells in Figure 57, it is clear that the percentage of cells permeable to PI is much higher than those exhibiting DNA fragmentation ($SubG_0/G_1$). One may think that secondary necrosis would manifest later than apoptosis. However, it should be taken into account that the activation of apoptosis and the induction of caspases occur earlier than chromatin condensation and DNA fragmentation.

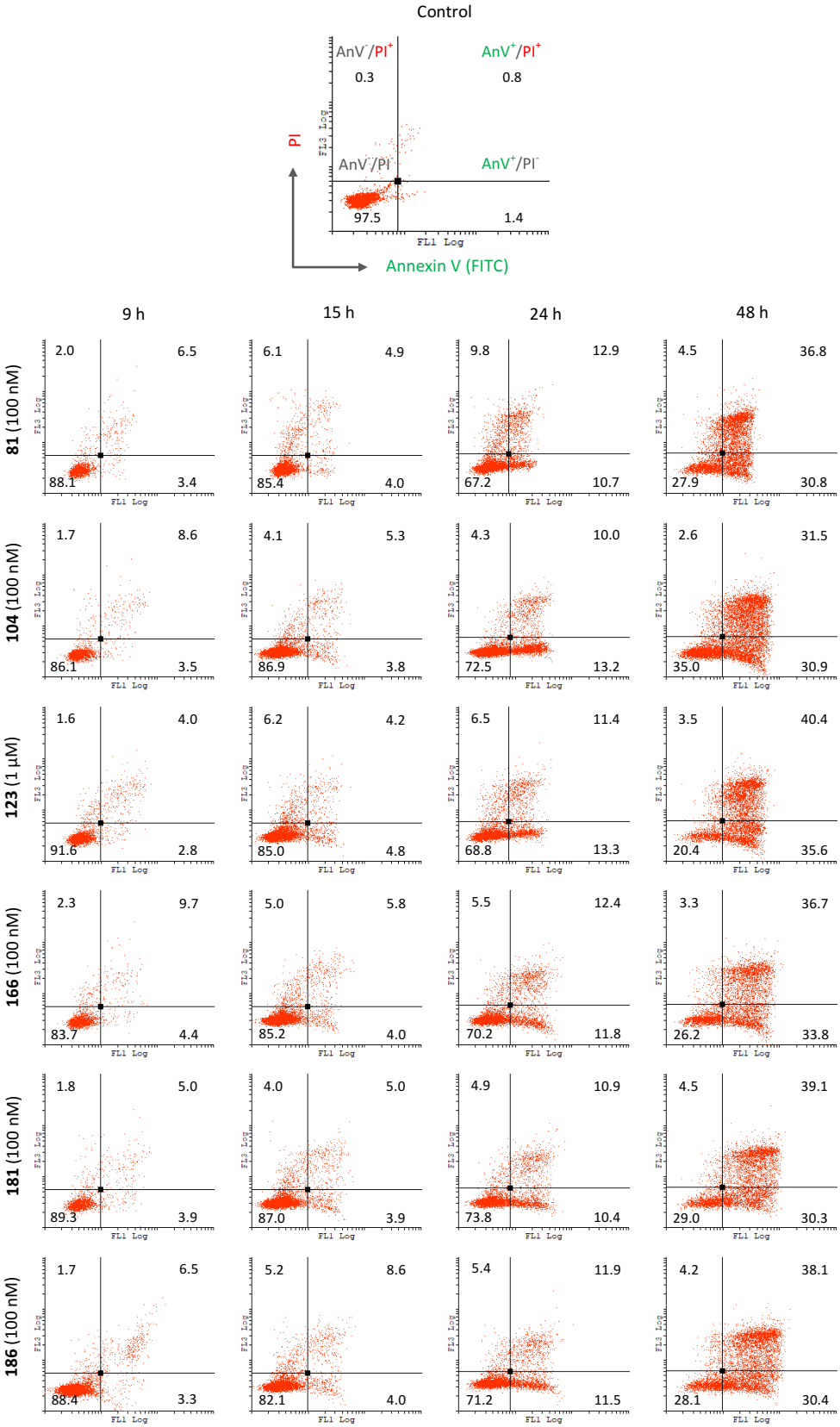

Figure 59. Dot plots of non-permeabilized HeLa cells treated with the lead compounds for 9 h, 15 h, 24 h, and 48 h. According to their distribution along the X axis (**Annexin V-FITC**, green fluorescence) and the Y axis (**PI**, red fluorescence), cells can be categorized as AnV^-/PI^- (live cells), AnV^+/PI^- (early apoptosis), AnV^-/PI^+ (necrosis) and AnV^+/PI^+ (late apoptosis or necrosis secondary to apoptosis), expressed as the mean in percentage (n = 3). Dot plots are representative of three independent experiments.

The percentage of $SubG_0/G_1$ is indicative that apoptosis is occurring at least to that extent. Moreover, cells dying while in G_2/M (4n) progressively transition from being twice as bright as G_1 cells towards the $SubG_0/G_1$ region whilst DNA degradation occurs, and will not be considered as such in early stages.

In order to understand the significance of the PI-positive population and trace its origin, we conducted a time-course flow cytometry experiment in HeLa cells (non-permeabilized) with double staining of PI (red fluorescence), and Annexin V conjugated with FITC (green fluorescence), which labels the PtdSer redistributed into the outer leaflet of the plasma membrane in early apoptosis (Fig. 59). There are four populations: double negatives AnV^-/PI^- (lower left, live cells), AnV^+/PI^- (lower right, early apoptosis), AnV^-/PI^+ (upper left, necrosis), and double positives AnV^+/PI^+ (upper right, late apoptosis or necrosis secondary to apoptosis). There are hardly any AnV^-/PI^+ cells, suggesting that the majority of HeLa cells treated with the lead compounds did not die by necrosis. The percentage of live cells AnV^-/PI^- significantly decreased after 24-h treatment, with exacerbated cell death after 48 h. For those incubation times, the overall dying cells are gathered in two populations on the right (AnV^+/PI^- and AnV^+/PI^+) that appeared concomitantly. The presence of single positive AnV^+/PI^- endorses the induction of an apoptotic response. The appearance of double positive cells AnV^+/PI^+, presumably independent of necrosis because they do not come earlier from single positive AnV^-/PI^+ cells, thus indicates late apoptosis. These results proved similar to the effect of 0.5 µM staurosporine, an apoptosis inducer used as a positive control (data not shown).

The apoptotic cell death was easily visualized by phase-contrast videomicroscopy in a time-lapse experiment upon treatment of HeLa cells with **81** and **166** at 100 nM (Fig. 60). The morphological changes began early upon treatment when the cells got arrested in mitosis, including the rounding-up of the cells that lost the adhesion to the plate surface. The characteristic membrane blebbing of apoptotic cells was clearly observed from 18 h after the addition of the drugs, and evolved towards the fragmentation into apoptotic blebs (Fig. 60, magnification).

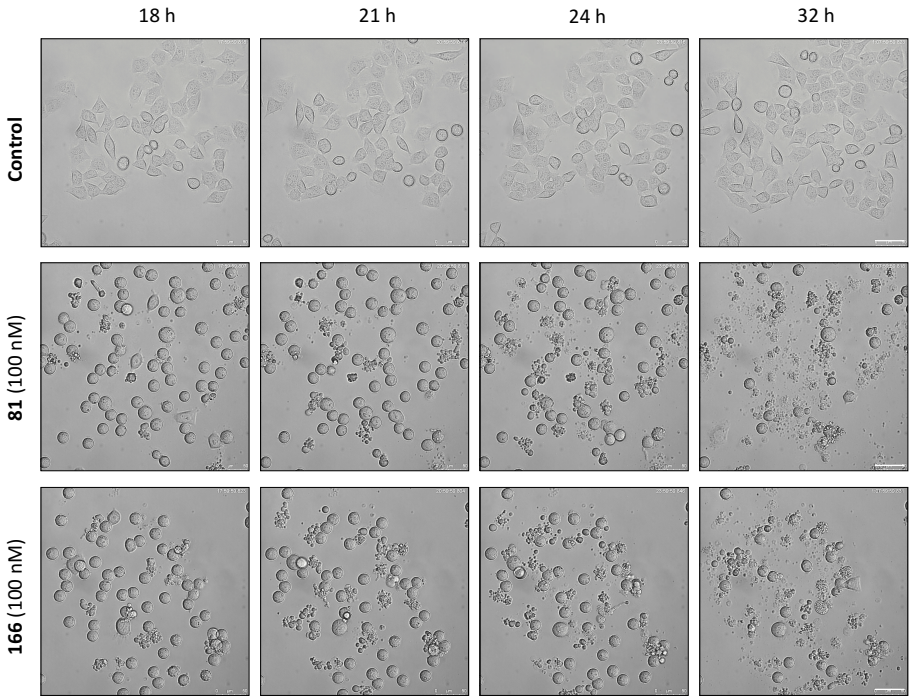

Figure 60. Continued

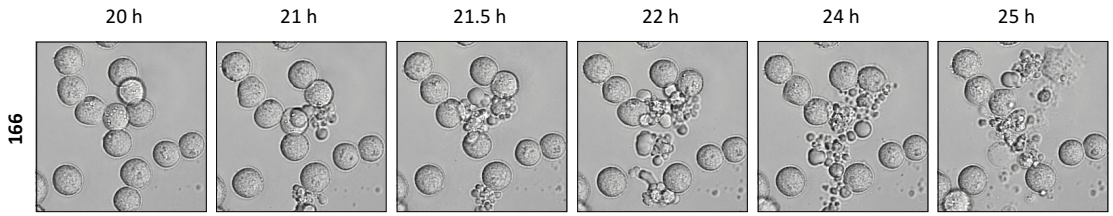

Figure 60. Phase-contrast time-lapse videomicroscopy frames from HeLa cells in control conditions or treated with **81** and **166** at 100 nM. The elapsed time is indicated on top of each frame. The videos were recorded for 72 h taking frames every 30 min. For complete visualization, see Supplementary Video HeLa on CD.

The induction of apoptosis by the lead compounds was assessed by the appearance of the cleaved fragments of caspase 3 (17 and 19 kDa), corresponding to the active form of the enzyme (Fig. 61). The immunoblots showed time-dependent caspase 3 cleavage, primarily induced after 32 and 48-h incubations, consistent with the increase in the $SubG_0/G_1$ population by cell cycle analysis. The higher levels of cleaved-caspase 3 coincided in time with the processing of poly (ADP-ribose) polymerase PARP (116 kDa), a major caspase 3 substrate, into its cleaved 89 kDa fragment. To determine the implication of the mitochondria in the apoptotic death, we separated the mitochondrial fraction from the cytosolic lysate and probed for cytochrome c (Fig. 62). The immunoblots revealed the release of cytochrome c from the mitochondria upon treatment with the tested compounds **81**, **104**, and **123**. Moreover, we detected the activation of caspase 9, as assessed by the appearance of the 35 kDa cleaved form. This initiator caspase is activated when recruited to the apoptosome and cleaves effector caspases (e.g. caspase 3).

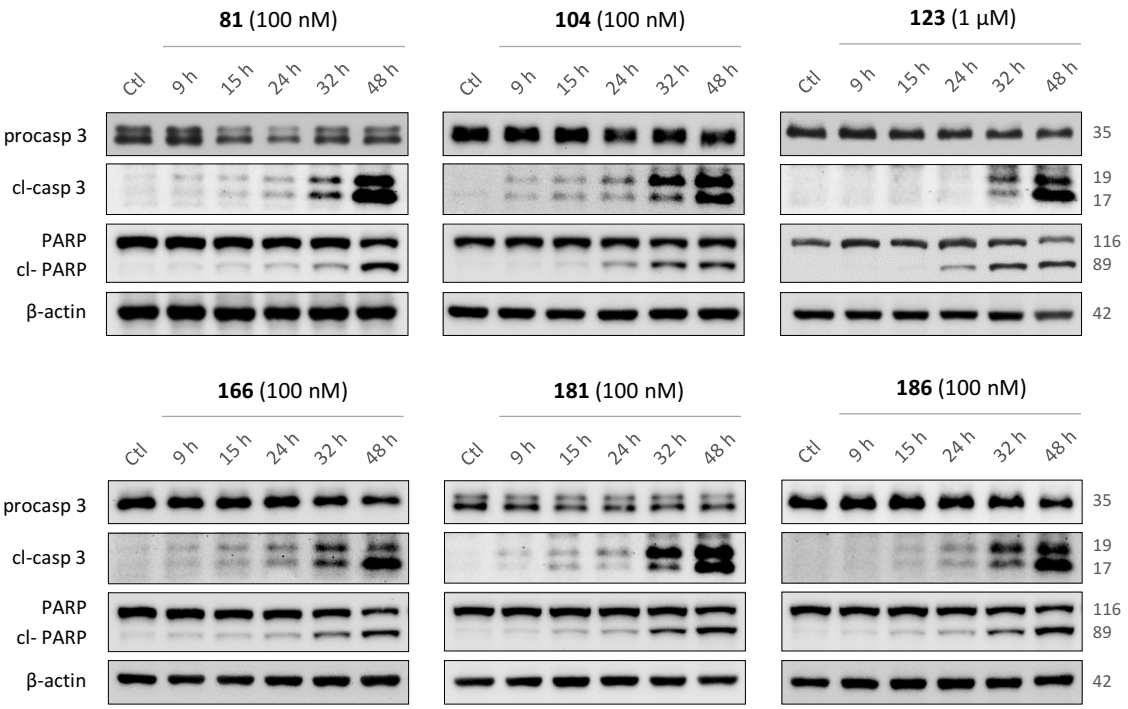

Figure 61. Immunoblots of HeLa cell lysates: time-course of the expression levels of apoptotic proteins after treatment with the lead compounds compared to untreated samples (Ctl). We used specific antibodies against caspase 3, cleaved-caspase 3, and PARP. β-actin was used as a loading control. Molecular weights are indicated in kDa. Western blot images are representative of three independent experiments.

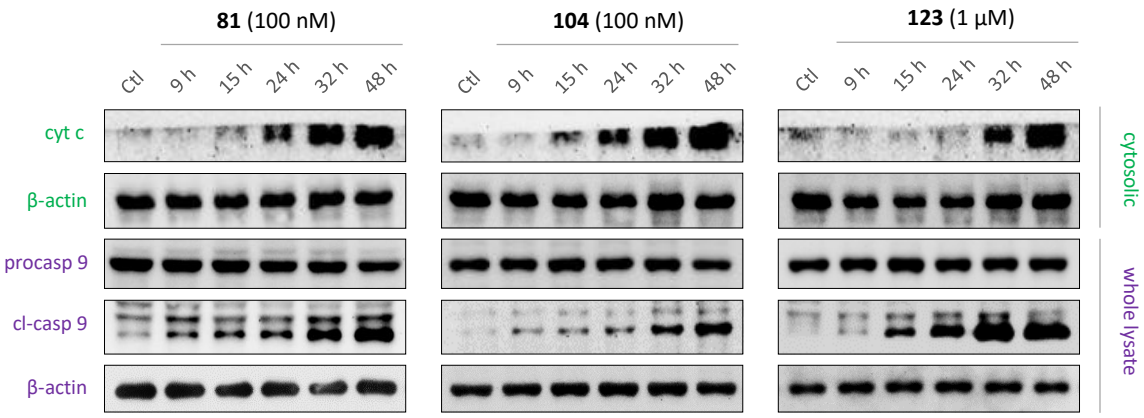

Figure 62. Immunoblots of HeLa cell lysates: time-course of the expression levels of apoptotic proteins after treatment with the lead compounds compared to untreated samples (Ctl). We separated the **cytosolic fraction** from mitochondrial protein and used anti-cytochrome c antibody to detect its release to the cytosol. The specific antibodies against caspase 9 and cleaved-caspase 9 were used in the **whole cellular lysate**. β-actin was used in both cases as a loading control. Western blot images are representative of two independent experiments.

In addition, the incubation of HeLa cells with the pan-caspase inhibitor Z-VAD-fmk (100 μM) blocked the apoptotic response elicited after 48-h treatments, indicating that the cell demise is caspase-dependent. It was evidenced by the decrease in the percentage of cells in the $SubG_0/G_1$ region (Fig. 63A) and in the number of Annexin V-positive cells (AnV^+/PI^- and AnV^+/PI^+, Fig. 64). The number of PI-positive cells was also reduced in a similar extent (Fig. 63B). The ratio between PI uptake and $SubG_0/G_1$ upon co-treatment with Z-VAD-fmk and the ligands matches that observed in Figure 57 for incubation times of around 9-15 h. This suggests that the membrane permeabilization occurred as a consequence of apoptotic induction. However, the combination of Z-VAD-fmk with compound **104** led to a milder decrease in $SubG_0/G_1$ (19.3% versus 8.2%), compared to the strong inhibition observed for the other ligands (15.4-20.2% versus 2.6-3.8%).

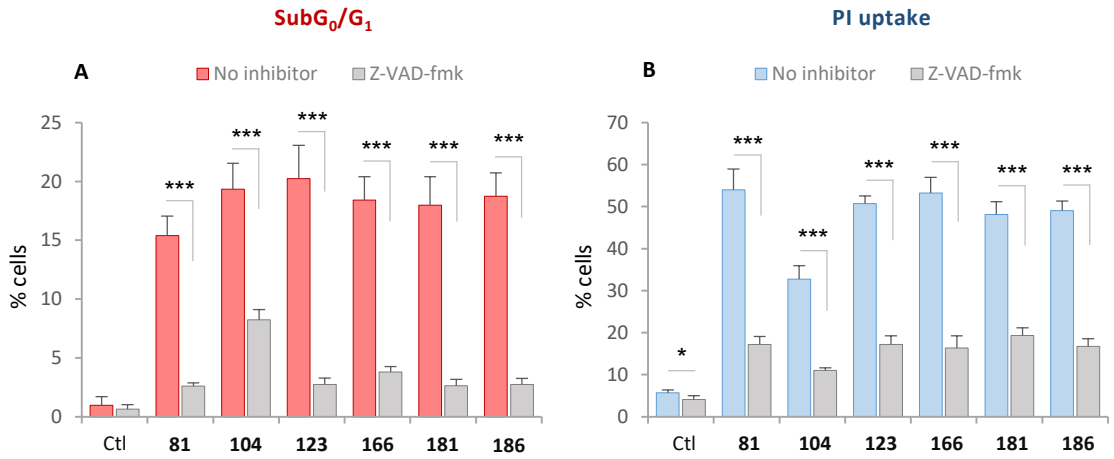

Figure 63. HeLa cells in the absence (Ctl) or the presence of the lead compounds, in combination or not with the pan-caspase inhibitor Z-VAD-fmk (100 μM). The compounds were tested at the working concentration: 100 nM in the case of **81**, **104**, **166**, **181**, and **186**, and 1 μM **123** and incubated for 48 h. **A.** Quantification of the percentage of cells in the **$SubG_0/G_1$** region was measured by cell cycle analysis (n = 5-6; * $p < 0.05$; *** $p < 0.001$). **B.** Number of **PI-positive cells** in the PI exclusion assay with non-permeabilized cells (n = 3-4).

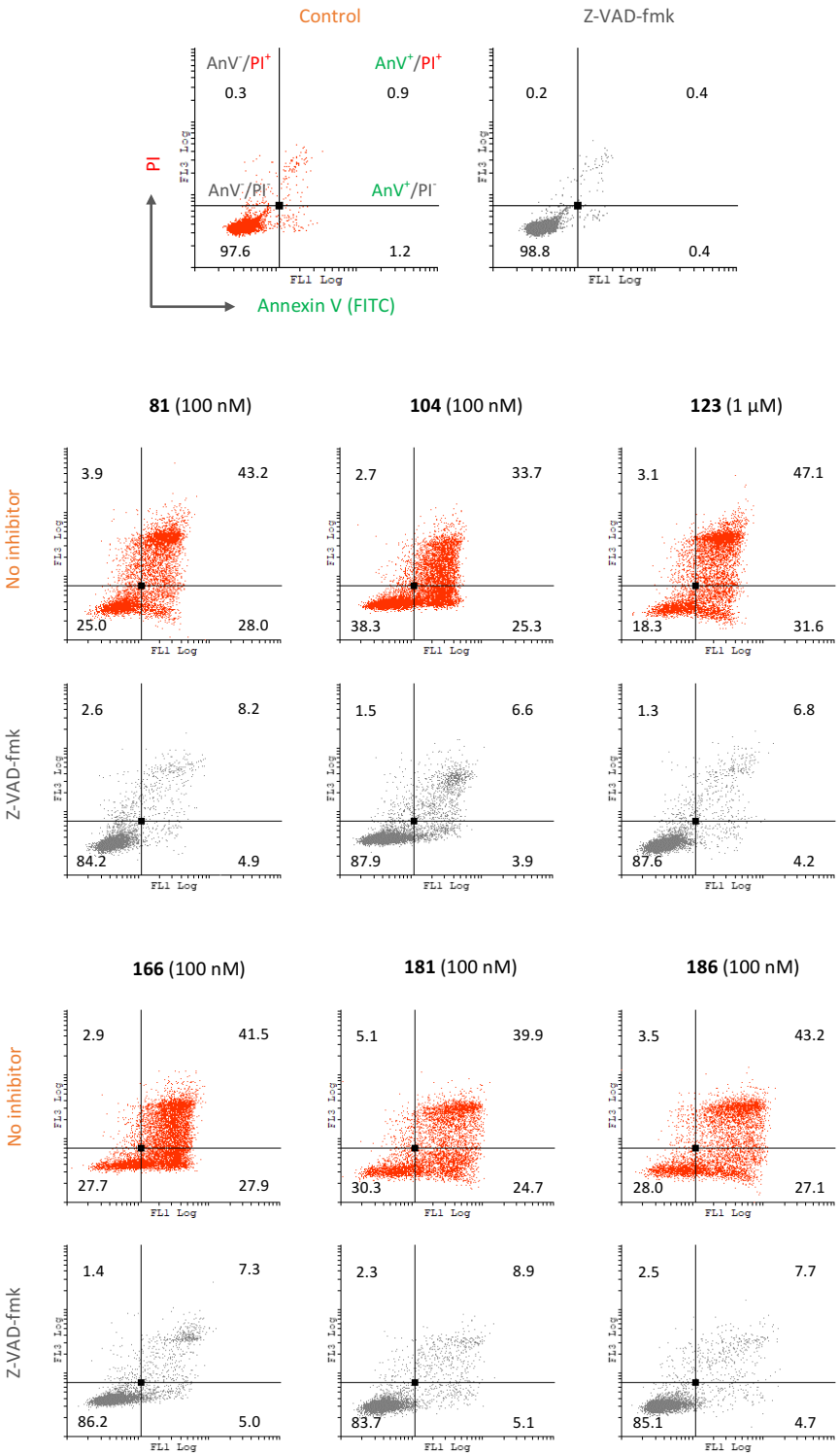

Figure 64. Dot plots of non-permeabilized HeLa cells stained with **Annexin V-FITC** (green fluorescence, X axis) and **PI** (red fluorescence, Y axis). The cells were incubated without (**orange dot plots**) or with 100 µM of the pan-caspase inhibitor Z-VAD-fmk (**grey dot plots**) for 2 h prior to the addition of the lead compounds. The cells were analyzed after 48-h incubation with the indicated ligands. The population in each quadrant is expressed as the mean in percentage (n = 4) regarding the groups AnV^-/PI^- (live cells), AnV^+/PI^- (early apoptosis), AnV^-/PI^+ (necrosis) and AnV^+/PI^+ (late apoptosis or necrosis secondary to apoptosis). Dot plots are representative of four independent experiments.

Z-VAD-fmk completely blocked the cleavage of PARP, as observed by the presence of a single band in the lysates corresponding to **81** and **166** in combination with the inhibitor (Fig. 66). Z-VAD-fmk however, was unable to prevent the rounding-up of HeLa cells that occurred early upon treatment and the accummulation of cells in mitosis (Fig. 65 and 66). We detected a higher signal of mitotic proteins using the MPM-2 antibody in HeLa cells treated for 48 h with **81** and **166** than the control. The combination of those drugs with Z-VAD-fmk, in turn, showed increased mitotic burden compared to the treatments alone (Fig. 66). The percentages of cells in the G_2/M peak supported this observation (Fig. 65). The increased accumulation of cells in mitosis with Z-VAD-fmk is due to the reduction of apoptotic cells, as evidenced by the lack of PARP cleavage and the scarce $SubG_0/G_1$ population. These observations support that the mitotic arrest occurs before the onset of cell death.

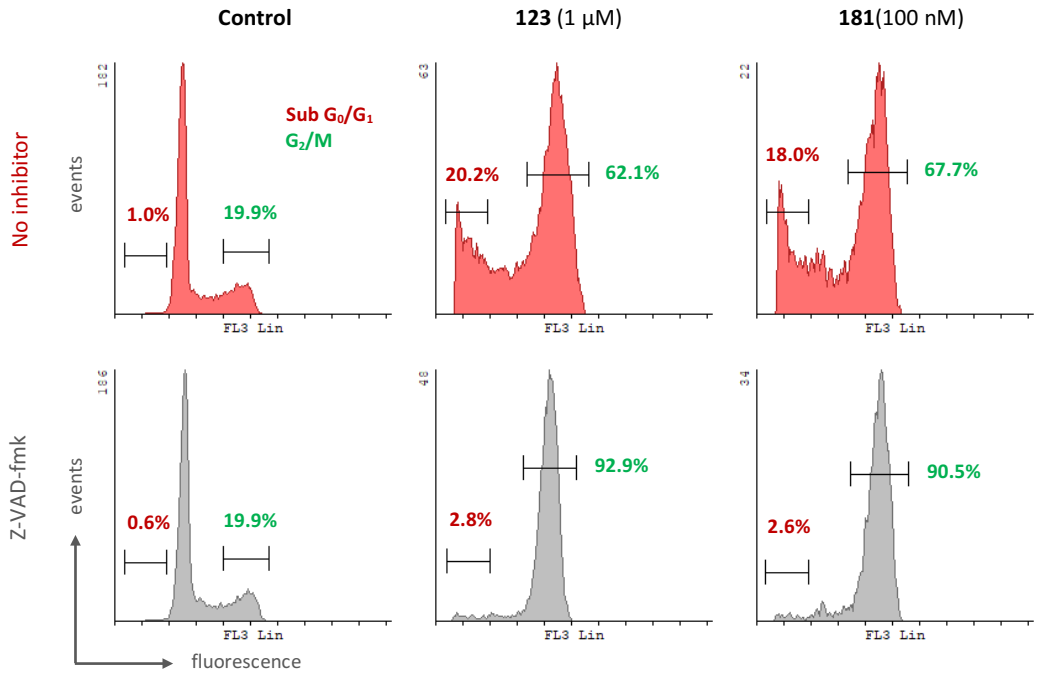

Figure 65. Cell cycle histograms of HeLa cells in control conditions or treated with **123** and **181** for 48 h, alone (no inhibitor) or in combination with the broad-spectrum caspase inhibitor Z-VAD-fmk (100 µM). The Y axis corresponds to the number of cells and the X axis is the red fluorescence of PI. The histograms are representative of at least five independent experiments. The percentages of cells in the **$SubG_0/G_1$** and **G_2/M** regions are indicated next to their gates.

We found that Z-VAD-fmk prompted the upregulation of caspase 9 cleavage when incubated in combination with **81** and **166**, what has been previously described in etoposide-treated embryonic fibroblasts.[540] This induction is accompanied with lower expression of the uncleaved form of caspase 9 (Fig. 66). Z-VAD-fmk prevented the effective cleavage of the inactive procaspase 3 into the active enzyme formed by the 17 and 19 kDa fragments. However, we observed a modified cleavage pattern of caspase 3 upon combined treatment. There is an upper cleaved form of caspase 3 of around 20 kDa, which might be an incomplete cleavage product, hence catalytically inactive because it failed to degrade PARP. The antibody against cleaved-caspase 3 recognized an unidentified additional band of 25 kDa, which disappeared with Z-VAD-fmk. It does not correspond to procaspase 3 (35 kDa). Taken altogether, these data suggest that HeLa cells undergo a caspase-dependent apoptotic death following mitotic arrest and that the apoptotic response can be prevented by inhibiting effector caspases.

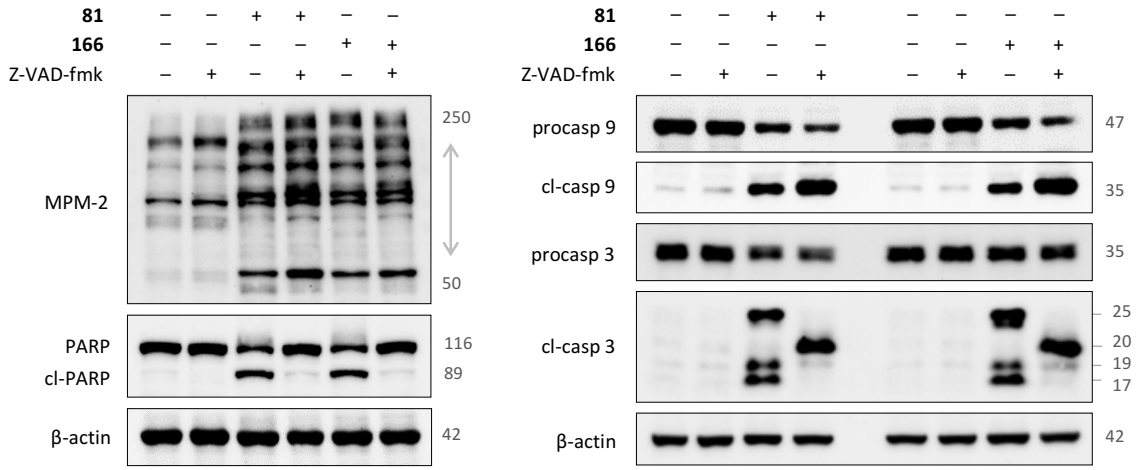

Figure 66. Immunoblots of HeLa cell lysates: expression levels of mitotic (MPM-2) and apoptotic proteins after treatment with the lead compounds for 48 h compared to untreated samples in combination or not with the caspase inhibitor Z-VAD-fmk (100 μM). β-actin was used as a loading control. Molecular weights are indicated in kDa. Western blot images are representative of two independent experiments.

Induction of autophagy in HeLa cells

Autophagy plays a cytoprotective role by recycling dysfunctional or damaged cellular components. It is mainly induced in response to multiple stresses that eventually lead to apoptosis. Newer research has revealed that it can contribute to cell demise. According to the NCCD, the concept of autophagic cell death refers to type II cell death, coursing with the activation of the autophagic pathway that precipitates the consecution of cell death, whose manipulation does not impact on other routines of regulated death.[347]

We studied the fluctuations of autophagy upon treatment with the lead compounds to evaluate whether HeLa cells were able to prompt an autophagic response in the presence of the drugs, and if so, its purpose related to cell death either as a prosurvival mechanism or as autophagic cell death. The hallmark of autophagy is the formation of autophagosomes, which can be studied by monitoring the levels of LC3 protein.[541] The cytosolic LC3-I form is lipidated by covalent attachment of PE, giving rise to LC3-II localized on autophagosome membranes. LC3-I and LC3-II can be distinguished one from the other because the latter shows faster electrophoretic mobility in acrylamide gels. Time-course experiments in HeLa cells showed that the treatments induced minor differences in LC3-II levels with no clear trend (Fig. 67).

Autophagy is a highly dynamic process that occurs very rapidly; autophagosomes are formed and their content degraded in about 10 min.[542] The overall levels of LC3-II reflect the number of autophagosomes in static time points, but do not inform of the global autophagy activity. Therefore, the measurements of LC3-II in steady state are inconclusive when taken alone. By contrast, the flux through the autophagic pathway is a more reliable indicator.[541] In order to study the autophagic flux, we compared the baseline levels of LC3-II with those in the final stages of the pathway in the absence of lysosomal degradation.[543] To this end, we incubated HeLa cells with bafilomycin A1 (Baf) before adding the treatments. It is an inhibitor of the vacuolar H^+-ATPase, thus blocks lysosomal degradation and ultimately impedes fusion, causing the accumulation of autophagosomes.[544,545]

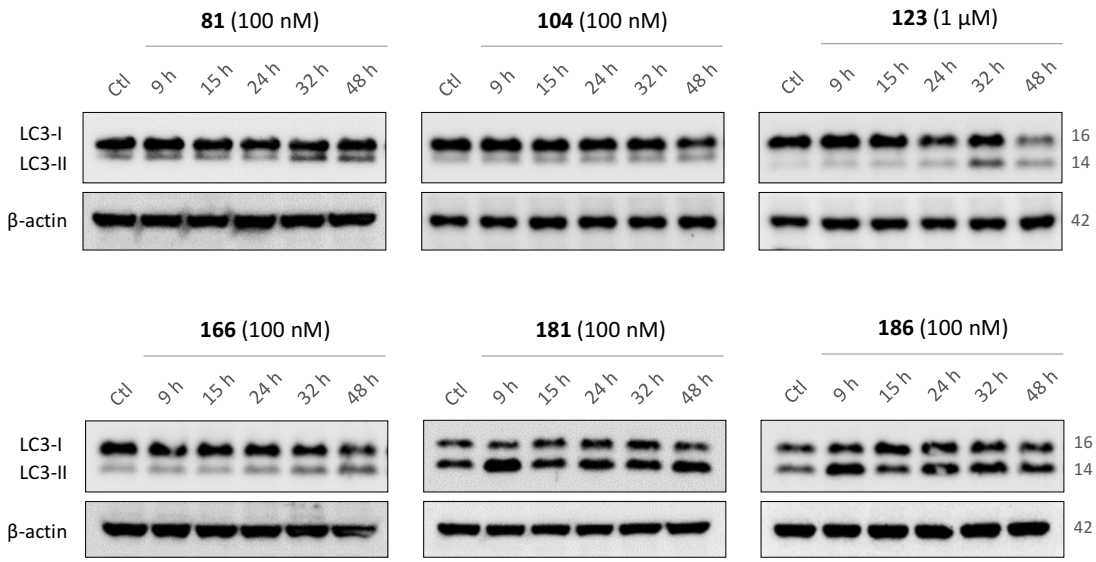

Figure 67. Immunoblots of HeLa cell lysates: time-course of the expression levels of free LC3-I (16 kDa) and autophagosome-bound LC3-II (14 kDa) after treatment with the lead compounds compared to untreated samples (Ctl). β-actin was used as a loading control. Molecular weights are indicated in kDa. Western blot images are representative of three independent experiments.

HeLa cells were treated with the lead compounds for 48 h alone or in combination with 15 nM bafilomycin A1 to monitor the autophagic flux, that can be inferred based on the levels of LC3-II.[543] Cells incubated with bafilomycin A1 alone showed higher LC3-II levels compared to control samples (Fig. 68A), indicating that there is ongoing autophagic flux in HeLa cells. The treatments alone induced a very slight increase in LC3-II, which is compatible with an enhanced autophagosome formation or a reduced clearance thereof, whereas the combination with bafilomycin A1 caused an additive or a supra-additive effect (Fig. 68A). Similar results were observed by indirect immunofluorescence of LC3 (green fluorescence) in HeLa cells after 24-h incubation with the drugs, alone or in combination with bafilomycin A1 (Fig. 68B). Altogether, these data may suggest that the ligands enhanced the autophagic flux,[541] what does not necessarily mean that there is a proficient fusion or lysosomal degradation.

In order to explore whether the autophagic response could be involved in cell death after treatment, we studied the effect in HeLa cells of the compounds combined with bafilomycin A1 compared to the treatments alone. Initially, we selected a 48-h incubation with the drugs that induced DNA degradation ($SubG_0/G_1$ population) of around 15-20% of the HeLa cells. The inhibition of late stages of autophagy with bafilomycin A1 decreased the overall cell viability in terms of the percentage of double negative AnV^-/PI^- cells compared to steady-state measurements (Fig. 69 and 70A, 71.8% versus 97.3%, $p < 0.001$) and enhanced DNA degradation (Fig. 70B, 3.8% versus 0.6%, $p < 0.01$). However, the combination with the ligands scarcely affected cell viability (Fig. 69 and 70A). Only the co-treatment of bafilomycin A1 with compounds **104** and **123** exhibited a statistically significant positive effect in cell viability compared to the treatments alone ($p < 0.05$, Fig. 70A). This effect correlated with a reduced percentage of cells in the $SubG_0/G_1$ region when inhibiting autophagy (Fig. 70B). The overall results for the $SubG_0/G_1$ apoptotic population elicited in the cell cycle assay are consistent with the rate of PARP cleavage (Fig. 71) and the cleaved forms of caspases 9 and 3 (see Appendix Fig. I).

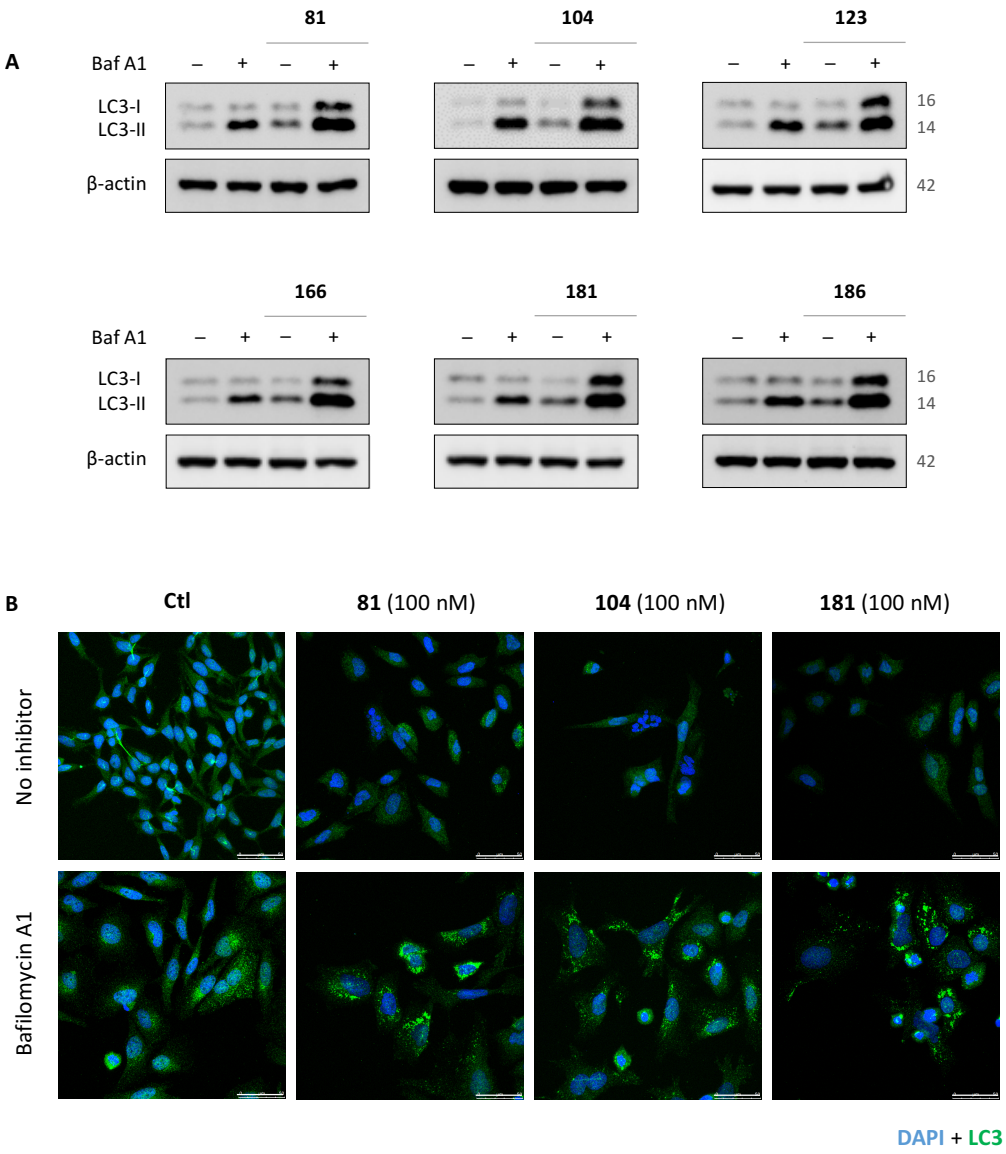

Figure 68. Expression of LC3 in HeLa cells in the absence (Ctl) or the presence of the indicated compounds alone or in combination with 15 nM bafilomycin A1. The ligands were used at 100 nM except for **123** at 1 µM. **A.** Immunoblots of HeLa cell lysates: expression levels of LC3 after 48-h incubations. β-actin was used as a loading control. Molecular weights are indicated in kDa. Western blot images are representative of three independent experiments. **B.** Confocal immunofluorescence microscopy of HeLa cells. Cells were incubated in the absence (Ctl) or the presence of the lead compounds at the indicated concentrations for 24 h. **Nuclei** were stained with DAPI in blue fluorescence, and **LC3** was stained in green fluorescence (Alexa 488-conjugated Ab-2). Scale bar: 50 µm. Photomicrographs are representative of two independent experiments.

The combination of bafilomycin A1 and the lead compounds therefore showed a different effect on cell demise regarding each treatment. We repeated the cell cycle analysis and Annexin V-FITC/PI staining for an incubation period of 24 h (see Appendix Fig. II and III). After a shorter exposure to bafilomycin A1, none of the differences between the combination and the treatments alone were considered to be statistically significant, although exhibited a similar trend to that in Figures 69 and 70.

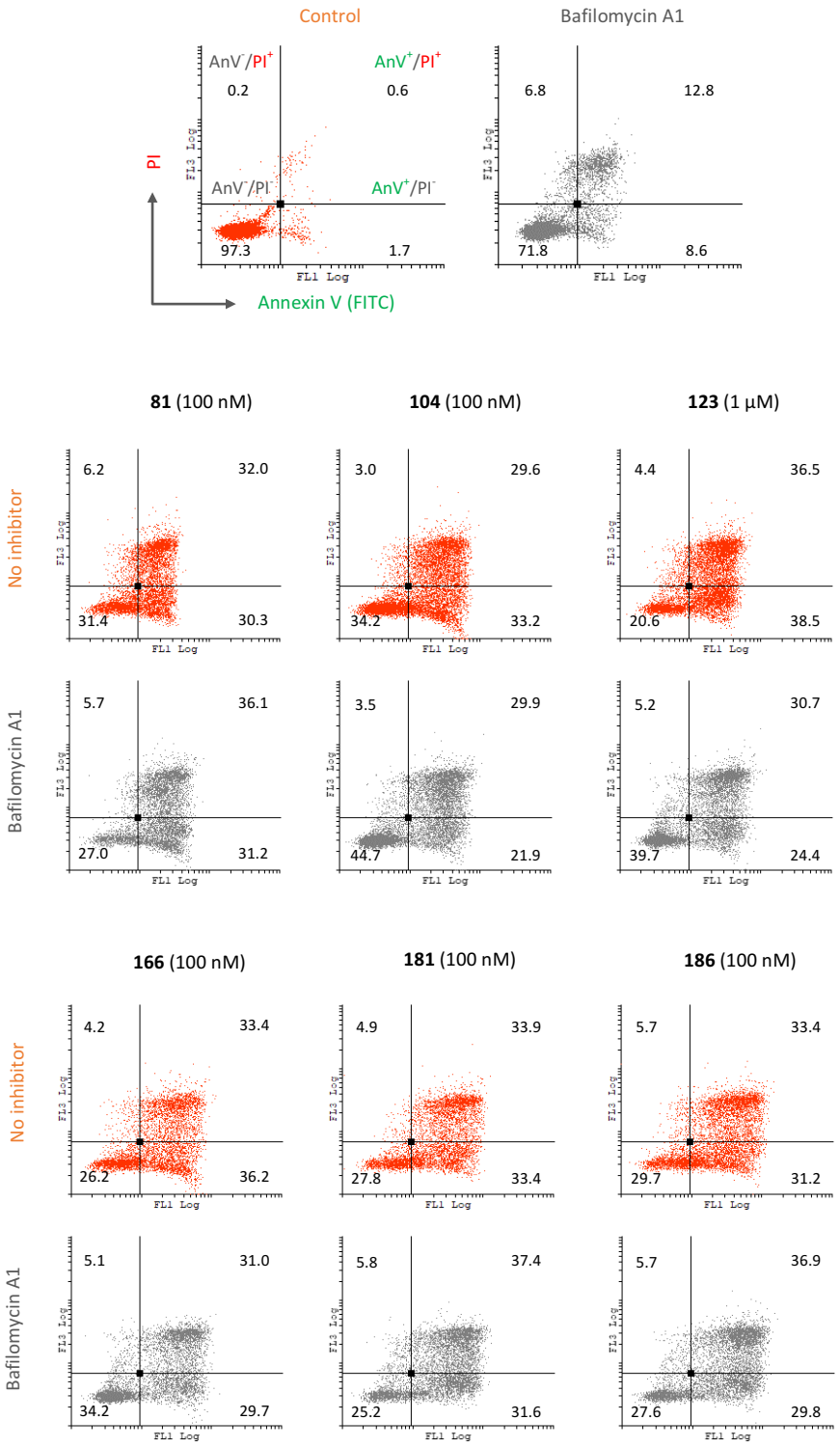

Figure 69. Dot plots of non-permeabilized HeLa cells stained with **Annexin V-FITC** (green fluorescence, X axis) and **PI** (red fluorescence, Y axis). The cells were incubated without (**orange dot plots**) or with 15 nM of the autophagy inhibitor bafilomycin A1 (**grey dot plots**) for 2 h prior to the addition of the lead compounds. The cells were analyzed after 48-h incubation with the indicated ligands. The population in each quadrant is expressed as the mean in percentage (n = 3) regarding the groups AnV^-/PI^- (live cells), AnV^+/PI^- (early apoptosis), AnV^-/PI^+ (necrosis) and AnV^+/PI^+ (late apoptosis or necrosis secondary to apoptosis). Dot plots are representative of three independent experiments.

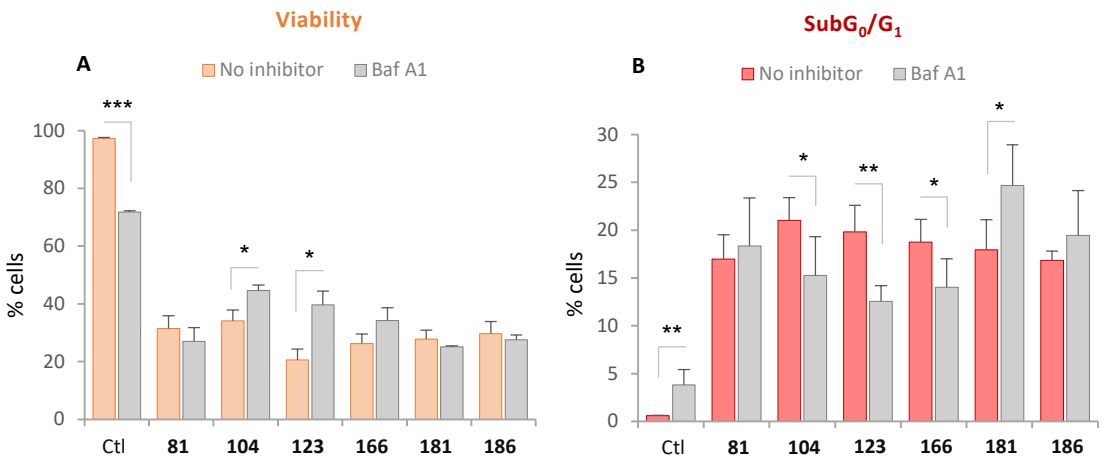

Figure 70. HeLa cells in the absence (Ctl) or the presence of the lead compounds, in combination or not with the autophagy inhibitor bafilomycin A1 (15 nM). The compounds were tested at the working concentration: 100 nM except **123** at 1 μM, and incubated for 48 h. **A.** Percentage of **double negative An^-/PI^- cells** (viable cells) related to the dot plots in Figure 68 (n = 3; * $p < 0.05$; ** $p < 0.01$; *** $p < 0.001$). **B.** Quantification of the percentage of cells in the **$SubG_0/G_1$** region was measured by cell cycle analysis (n = 5).

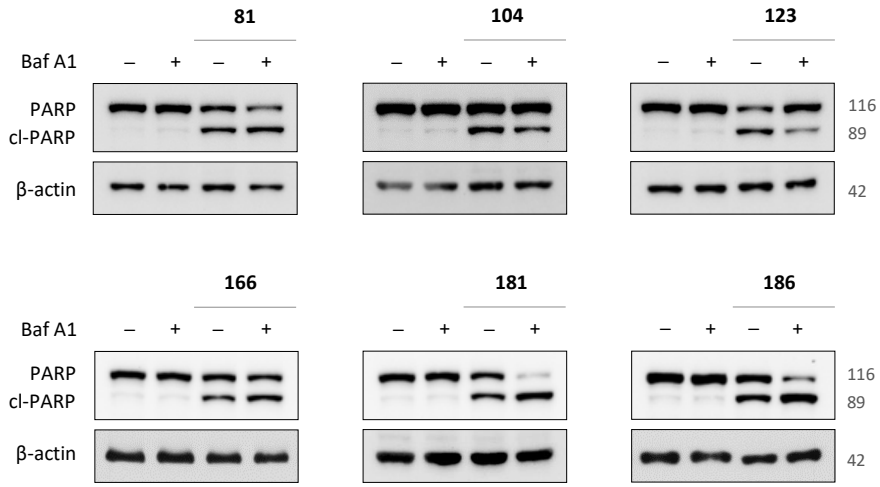

Figure 71. Immunoblots of HeLa cell lysates: detection of PARP cleavage after treatment with the indicated compounds for 48 h, in combination or not with bafilomycin A1 (15 nM). The ligands were used at 100 nM except for **123** at 1 μM. β-actin was used as a loading control. Molecular weights are indicated in kDa. Western blot images are representative of two independent experiments.

Given the effect disparity on cell death caused by using bafilomycin A1 to inhibit the late stages of autophagy, we additionally used chloroquine (CQ) to block the late stages of autophagy. It increases the lysosomal pH and decreases the fusion between autophagosomes and lysosomes.[546,547] A concentration of 20 μM of chloroquine caused the accumulation of autophagosomes, as assessed by the increased levels of LC3-II (Fig. 72A), but neither DNA degradation (Fig. 72B) nor membrane permeabilization (Fig. 72C) manifested any statistically significant differences when combined with the lead compounds for 48 h. Cell cycle was also analyzed after 24-h treatments (see Appendix Fig. IV). Based on these shreds of evidence, the enhanced autophagic flux upon treatment presumably implies a limited impact on cell demise.

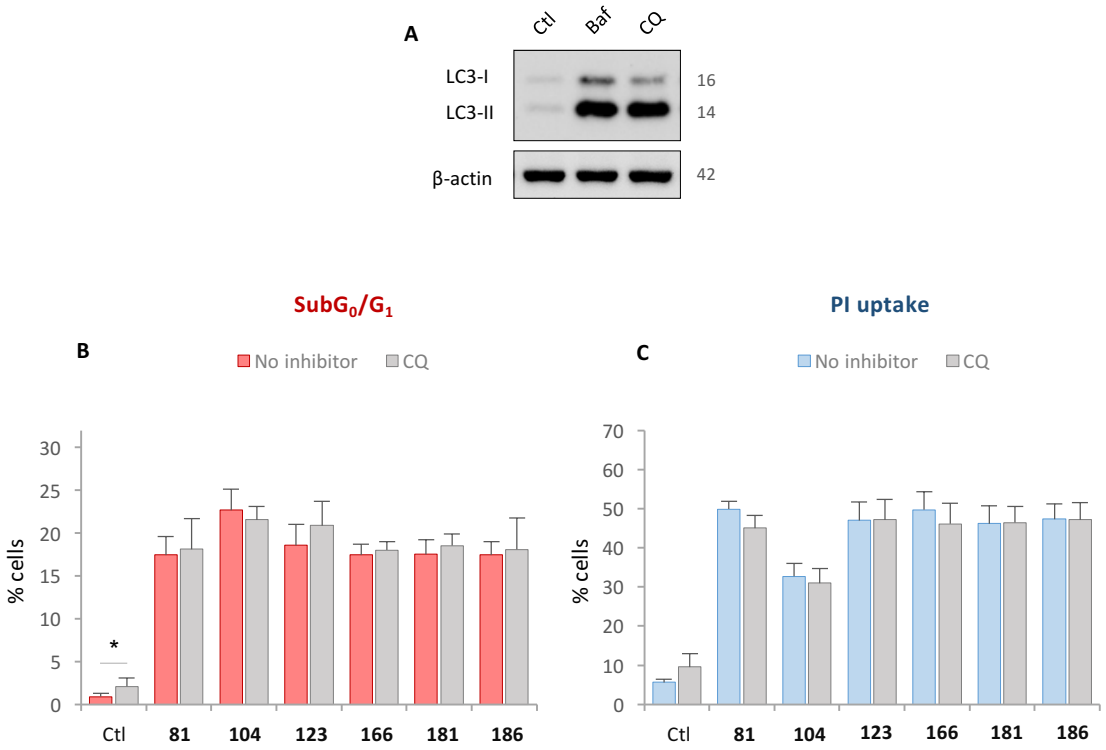

Figure 72. A. Immunoblot of HeLa cell lysates: expression levels of LC3 in steady-state and after incubation with 15 nM bafilomycin A1 (Baf) and 20 µM chloroquine (CQ). β-actin was used as a loading control. Molecular weights are indicated in kDa. **B.** Quantification of the percentage of HeLa cells in the **SubG$_0$/G$_1$** region by cell cycle analysis after 48-h incubation with the lead compounds at 100 nM (except **123** at µM) in combination or not with 20 µM chloroquine (n = 5; * p < 0.05). **C.** Percentage of **PI-positive cells** in the PI exclusion assay with non-permeabilized HeLa cells treated with the lead compounds for 48 h, alone or in combination with chloroquine (n = 4).

Induction of necrosis in HeLa cells

The results above showed that HeLa cells underwent apoptotic cell death upon treatment with the lead compounds, with a discrete increase in the autophagic flux that has no decisive impact on the percentage of dying cells. We observed no necrotic cells under the microscope, but rather a clear apoptotic morphology as assessed by time-lapse videomicroscopy (Fig. 60). In time-course experiments, we observed the steady rounding-up of cells early after treatment because of the mitotic arrest, remaining refringent up until 24 h. The presence of dying cells was primarily detected from 24 h onwards. Many of the apoptotic Annexin V-positive cells however became permeable to PI (Fig. 59), suggesting that the membrane permeabilization occurs in parallel to the induction of apoptosis but does not correspond to a necrotic phenotype given the lack of single PI-positive cells in time-course experiments (Fig. 59). The results obtained in this experiment were similar to that of staurosporine, included as a positive control for apoptosis detection. In addition, the permeabilization was significantly prevented (p < 0.001) when blocking apoptosis with Z-VAD-fmk (Fig. 63B and 73). These data suggest that necrosis hardly contributed to the overall cell demise.

To further validate this observation, we next examined whether regulated necrosis or necroptosis was involved in the response of HeLa cells to the drugs. To this end, we treated HeLa cells with the lead compounds with or without 200 µM of necrostatin-1 (Nec-1), a specific inhibitor of RIPK1.[548]

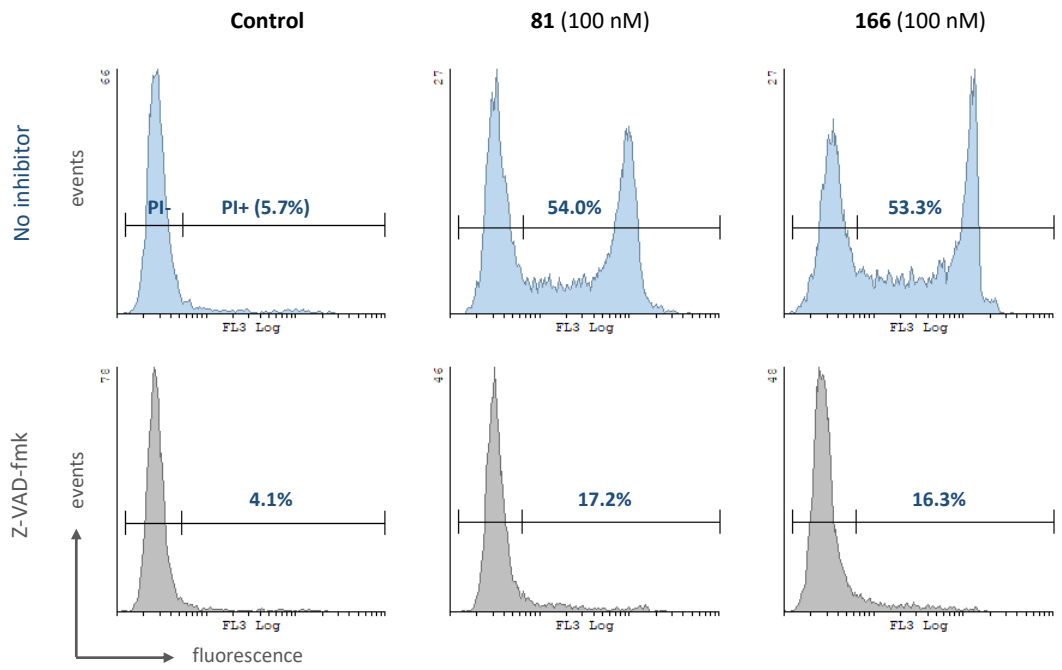

Figure 73. Histograms of HeLa cells in control conditions or treated with **81** and **166** at 100 nM for 48 h alone (no inhibitor) or in combination with Z-VAD-fmk (100 µM). The Y axis corresponds to the number of cells, and the X axis is the red fluorescence of PI in non-permeabilized samples. The histograms are representative of at least three independent experiments.

The combination of the lead compounds with necrostatin-1 did not impact on the apoptotic death in HeLa cells upon treatment, assessed by DNA degradation (Fig. 74A). It was confirmed by the equivalent PARP cleavage in samples treated with **81** and **166** alone or combined with Nec-1, and did not affect the mitotic arrest either (Fig. 75). The addition of Nec-1 instead increased the incorporation of PI in non-permeabilized cells compared to the treatments alone, with statistically significant differences (Fig. 74B).

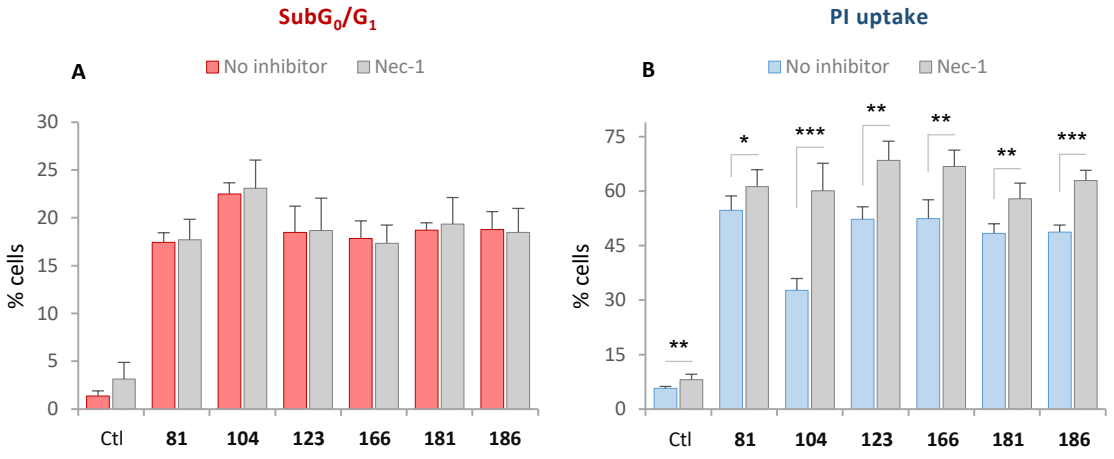

Figure 74. HeLa cells in the absence (Ctl) or the presence of the lead compounds, in combination or not with the necroptosis inhibitor Nec-1 (200 µM). The compounds were tested at 100 nM except **123** at 1 µM, and incubated for 48 h. **A.** Quantification of the percentage of cells in the **SubG$_0$/G$_1$** region, measured by cell cycle analysis (n = 5). **B.** Number of **PI-positive cells** in non-permeabilized samples (n = 5; * $p < 0.05$; ** $p < 0.01$; *** $p < 0.001$).

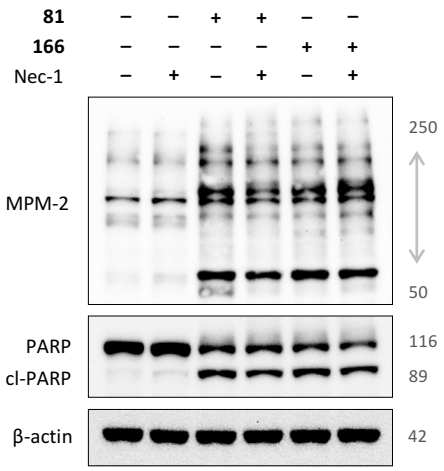

Figure 75. Immunoblots of HeLa cell lysates: detection of mitotic proteins (MPM-2) and PARP cleavage after treatment with **81** and **166** for 48 h, in combination or not with necrostatin-1 (200 μM). β-actin was used as a loading control. Molecular weights are indicated in kDa. Western blot images are representative of two independent experiments. A specific antibody against PARP was used to detect the constitutive (116 kDa) form and the cleaved form (89 kDa).

MITOCHONDRIA-RELATED CHANGES

The altogether results relative to the induction of cell death in HeLa cells after treatment pointed out that the sustained mitotic arrest triggered apoptotic cell death with a scarce contribution of autophagy and necrosis to the overall cell demise. The release of cytochrome c from the mitochondria to the cytosol and the cleavage of caspase 9 (see Fig. 62) evidenced the implication of mitochondrial changes on the consecution of the apoptotic phenotype. Mitochondria have been shown to play a central role in most apoptotic models, either as the initiation of the intrinsic pathway or as an amplification loop of the extrinsic pathway to propagate the apoptotic response. The presence of mitochondrial leaking channels is usually linked to the depolarization of the transmembrane potential ($\Delta\Psi_m$) either by Bax/Bak oligomers during apoptosis or by the opening of mitochondrial permeability transition pores in necrotic death.[549] The depletion of $\Delta\Psi_m$ therefore suggests the loss of mitochondrial membrane integrity and reflects the initiation of apoptosis. In order to monitor the status of the mitochondria upon treatment with the lead compounds, we measured the mitochondrial transmembrane potential and the generation of ROS in HeLa cells after 15, 24, and 48-h incubations with the ligands to see the evolution at three time-points that have previously shown increasing percentages of $SubG_0/G_1$, PtdSer exposure, and PARP cleavage, as assessed by cell cycle analysis, AnnexinV-FITC labeling, and immunoblotting, respectively.

The transmembrane potential and the levels of ROS were measured in parallel by flow cytometry in non-permeabilized HeLa cells previously treated with the lead compounds. We used the lipophilic cationic probe $DiOC_6[3]$ (green fluorescence) that accumulates first into the cytosol and then into mitochondria of live cells at low concentrations as a function of its potential $\Delta\Psi_m$. DHE was used as a sensor to detect ROS in live cells (preferentially intracellular superoxide), by its oxidization to ethidium that labels nucleic acids (red fluorescence). $DiOC_6[3]$ uptake detects mitochondrial function in live and early apoptotic cell populations, considered as viable cells. The loss of plasma membrane integrity in necrotic or late apoptotic cells (PI-positive cells) may distort the results mimicking a depolarized mitochondrial status, as $DiOC_6[3]$ accumulation is driven by electrochemical gradient. For this reason, it is important to pay attention to proper gating. Selecting the whole population of cells will translate into a mixture of viable and non-viable cells that are permeable. Thus, the more cells with membrane permeabilization, the more loss of mitochondrial potential will be detected. However, in order to study the changes in mitochondrial potential before membrane permeabilization occurred, non-viable cells should be excluded.

$DiOC_6[3]$ uptake (green fluorescence) was monitored together with DHE (red fluorescence), so PI (red fluorescence) could not be used as an exclusion staining to gate viable cells selectively. When plotting an untreated sample into complexity (SS) versus size (FS) analysis, cellular debris can be dismissed from cells within **Gate 1** (Fig. 76A), showing a major homogeneous normal-sized population of cells. Upon treatment (Fig. 76B), there are two easily differentiated populations inside **Gate 1**: population in **Gate 2**, comparable in SS and FS to that observed in panel A, and population in **Gate 3**, as an effect of the treatment. The sample in panel B was stained with PI, plotting the number of events versus red fluorescence underneath (Fig. 76C-F). The full fluorescence profile is represented in panel C (grey histogram), corresponding to cells within **Gate 1** in panel B (**Gate 2** + **Gate 3**). When plotting the cells within **Gate 2** (panel D, blue histogram) and **Gate 3** (panel E, red histogram) separately, superimposed in panel F, it is evident that the population in **Gate 2**, also that of the control, corresponds to viable cells that are PI-negative, whereas the population in **Gate 3**, scarcely present in the control, corresponds to non-viable cells that are PI-positive. Therefore, given the technical limitations to the triple staining $DiOC_6[3]$, DHE, and PI, we selected the viable cells based on these observations to analyze the double staining $DiOC_6[3]$ and DHE.

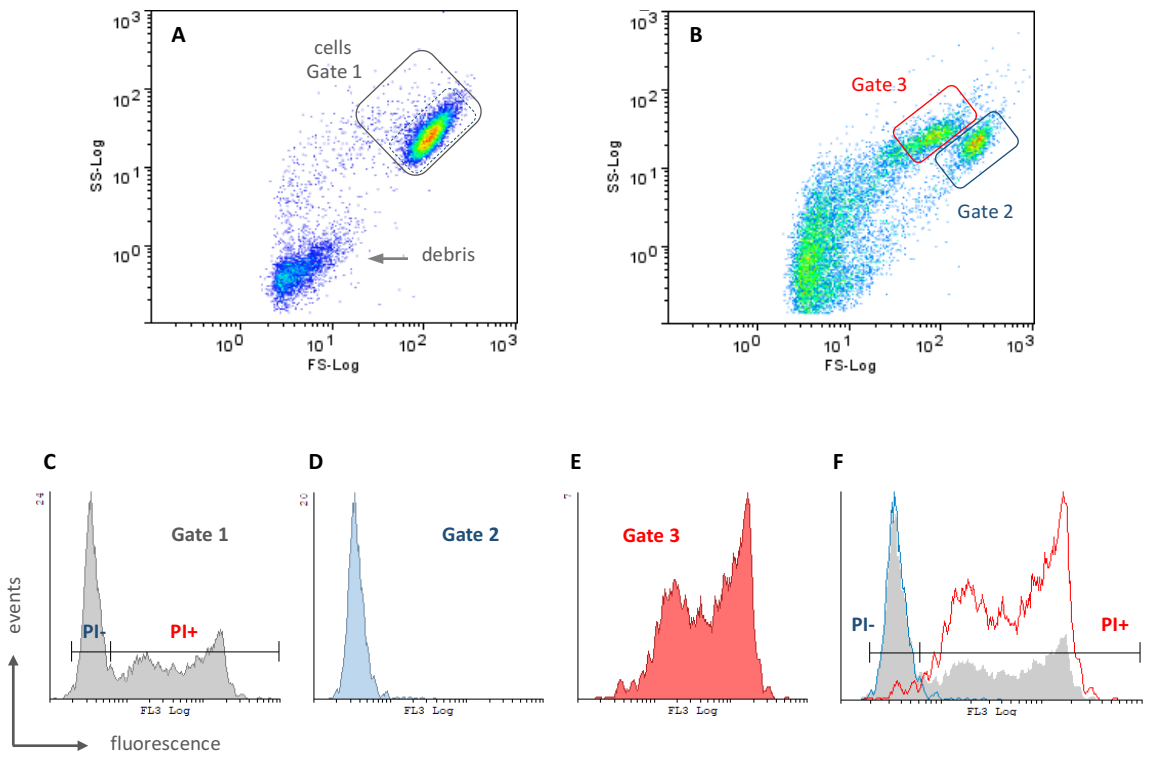

Figure 76. Analysis of a PI exclusion assay (red fluorescence) by flow cytometry in non-permeabilized HeLa cells without treatment (**A**) or treated with **81** at 100 nM for 48 h (**B**-**F**). **A** and **B.** Dot plots representing complexity (SS, Y axis) versus cellular size (FS, X axis) in control conditions (**A**) or after 48-h incubation with **81** (**B**). These dot plots are useful to distinguish cells (**Gate 1**) from cellular debris. Panels **C**-**F** correspond to the treated sample in dot plot **B**. **C.** Cells of **Gates 2** + **3** (equals **Gate 1**) plotted on a histogram representing the number of events (Y axis) versus red fluorescence (X axis), indicating PI-positive (PI^+) and PI-negative (PI^-) cells. **D.** Histogram of cells coming from **Gate 2**. **E.** Histogram of cells coming from **Gate 3**. **E.** Overlay of histograms **C** (**grey**), **D** (**blue**), and **E** (**red**) showing that the PI-negative cells (PI^-) are located within **Gate 2** in dot plot **B**, and the PI-positive cells (PI^+) are located within **Gate 3** in dot plot **B**, with little overlay between populations.

Regarding PtdSer exposure run in parallel, Annexin V-FITC positive cells fall into the two gates mentioned above, although the discrimination is not that broad as that of PI in Fig. 76: single positive AnV^+/PI^- cells are found in **Gate 2**, together with double negative cells, and double positive AnV^+/PI^+ cells are found in **Gate 3** (Fig. 77).

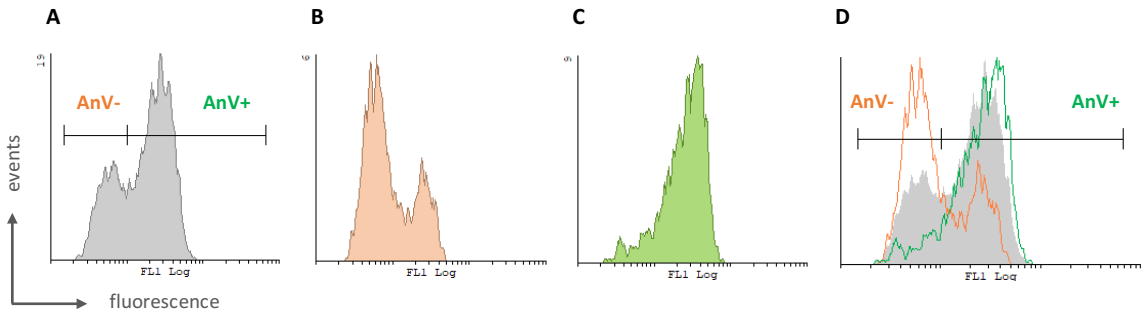

Figure 77. Analysis of PtdSer exposure in an Annexin V-FITC staining experiment (green fluorescence) by flow cytometry in non-permeabilized HeLa cells treated with **81** at 100 nM for 48 h (see Fig. 76B). Panels **A**-**D** correspond to the treated sample in dot plot from Fig. 76B. **A.** Cells of **Gates 2** + **3** (equals **Gate 1**) plotted on a histogram representing the number of events (Y axis) versus green fluorescence (X axis), indicating AnV-positive (AnV^+) and AnV-negative (AnV^-) cells. **B.** Histogram of cells coming from **Gate 2**. **C.** Histogram of cells coming from **Gate 3**. **D.** Overlay of histograms **A** (**grey**), **B** (**orange**), and **C** (**green**), showing that AnV-negative cells (AnV^-) are mostly located within **Gate 2** (AnV^-/PI^-) and AnV-positive cells (AnV^+) are located within **Gate 2** (AnV^+/PI^-) and **Gate 3** (AnV^+/PI^+).

The results for $DiOC_6[3]$ and DHE signals are depicted in Figures 78 and 79, respectively, represented as overlay histograms comparing the fluorescence of the treated samples (green and red histograms) with that of the untreated controls (grey filled histograms), with similar results irrespective of each individual treatment. Regarding the transmembrane potential (Fig. 78), the overlay of the green fluorescence upon 15-h incubation and the untreated samples showed no differences. However, the left-skewed histogram obtained after 24-h treatments revealed an incipient depolarization in viable cells, when the exposure of PtdSer began to be detectable. The major difference was elicited for the 48-h incubation period that showed a clear increase of cells in the $SubG_0/G_1$ region, and a rise in single positive AnV^+/PI^- and double positive AnV^+/PI^+ cells (see Fig. 59).

We observed two populations of HeLa cells after 48-h treatments: a group of cells that fluoresces brighter than the control (right peak), and a second group of cells that showed lower fluorescence than the control, suggesting depolarization (left peak). The appearance of depolarization in viable cells after 48 h, coincident in time with an increased apoptotic signal, is not surprising since we observed an enhanced detection of cytochrome c in the cytosol (see Fig. 62). By gating only viable cells we observed the loss of the mitochondrial potential in cells with integral membranes, in agreement with the increased detection of single AnV^+/PI^- cells. The biological significance of the brighter population is unclear. It might correspond to hyperpolarized cells or be caused by differences in mitochondrial dye loading.

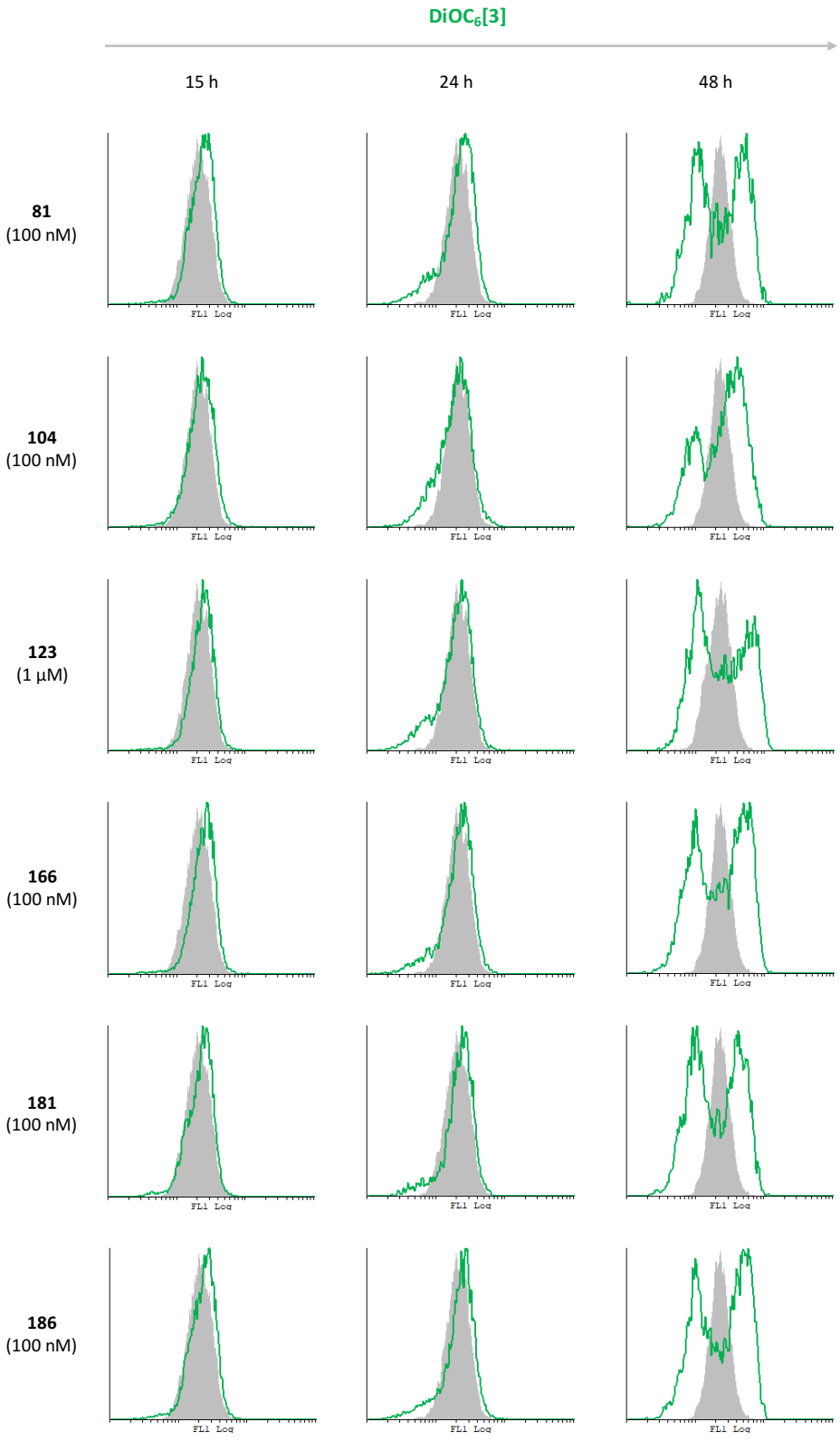

Figure 78. Overlay histograms of HeLa cells representing the mitochondrial transmembrane potential ($\Delta\Psi_m$) in control conditions (**grey histograms**) or treated with the indicated compounds for 15 h, 24 h, or 48 h (**green histograms**). The Y axis corresponds to the number of cells and the X axis is the green fluorescence of $DiOC_6[3]$ in non-permeabilized samples. The histograms are representative of three independent experiments.

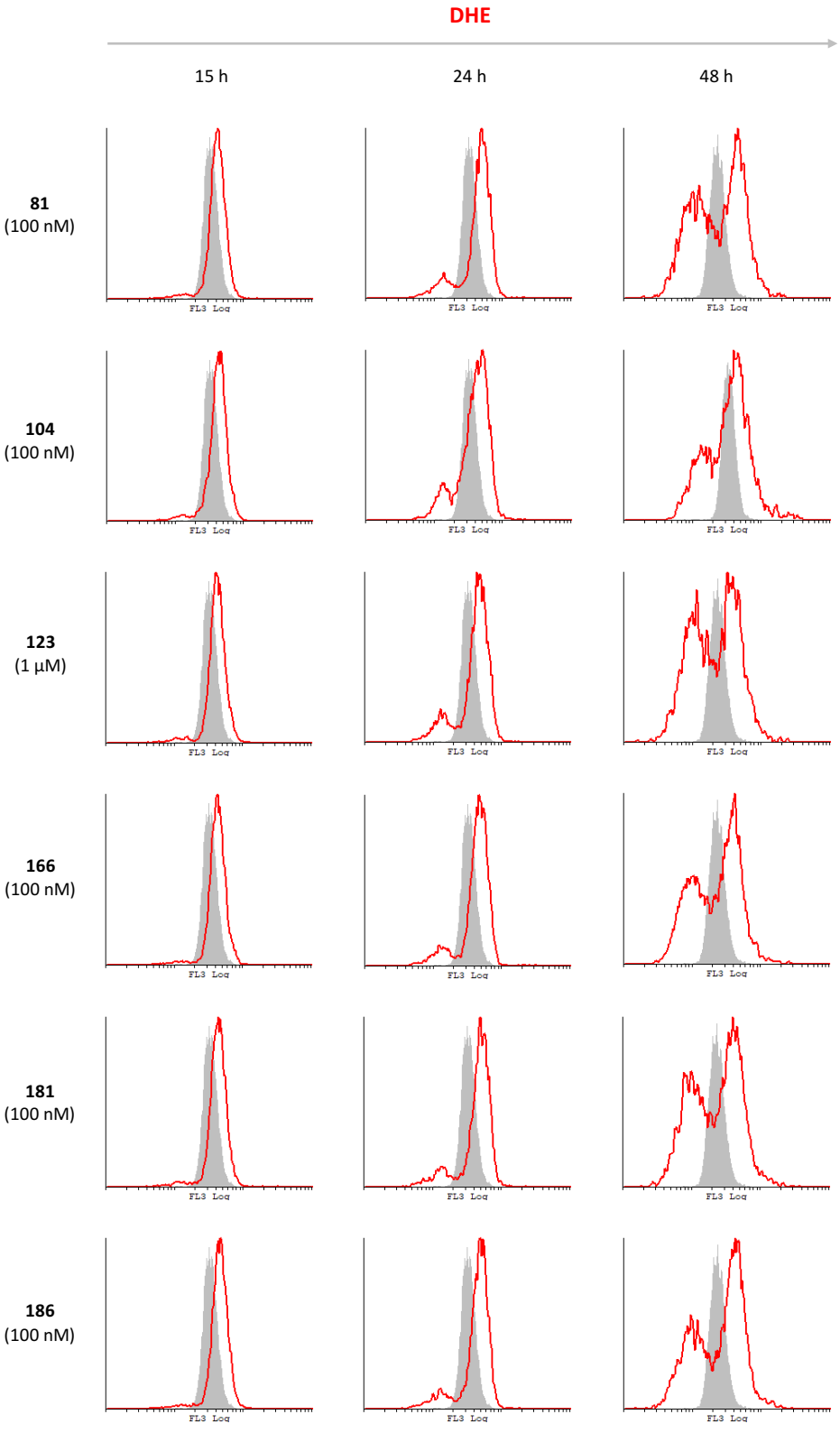

Figure 79. Overlay histograms of HeLa cells representing the levels of reactive oxygen species (ROS) in control conditions (**grey histograms**) or treated with the indicated compounds for 15 h, 24 h, or 48 h (**red histograms**). The Y axis corresponds to the number of cells and the X axis is the red fluorescence of DHE when oxidized by intracellular superoxide in non-permeabilized samples. The histograms are representative of three independent experiments.

The mitochondria are the main source of reactive oxygen species (ROS) that target DNA, lipids, and proteins. We observed an increase in ROS levels, assessed by the displacement of the histogram of treated cells (red) towards the right respect to the control untreated samples run in parallel (Fig. 79). This increase was already evidenced after a 15-h incubation, sustained during longer periods of exposure to the ligands. A population of cells with lower ROS content started to appear after 24 h, with a higher representation to the total population after 48 h. The evolution of the changes on the transmembrane potential and the intracellular concentration of ROS followed a similar trend, although the augmented ROS production was detected in cells incubated with the ligands for 15 h, which did not show altered $\Delta\Psi_m$. This suggests that the enhanced production of ROS occurred earlier and may contribute to mitochondrial damage. The population that exhibited increased $DiOC_6[3]$ fluorescence after 48 h mostly corresponded to cells with increased levels of ROS (Fig. 80). High levels of ROS can promote the intrinsic apoptotic pathway and are also involved in the execution phases of necrosis.[550]

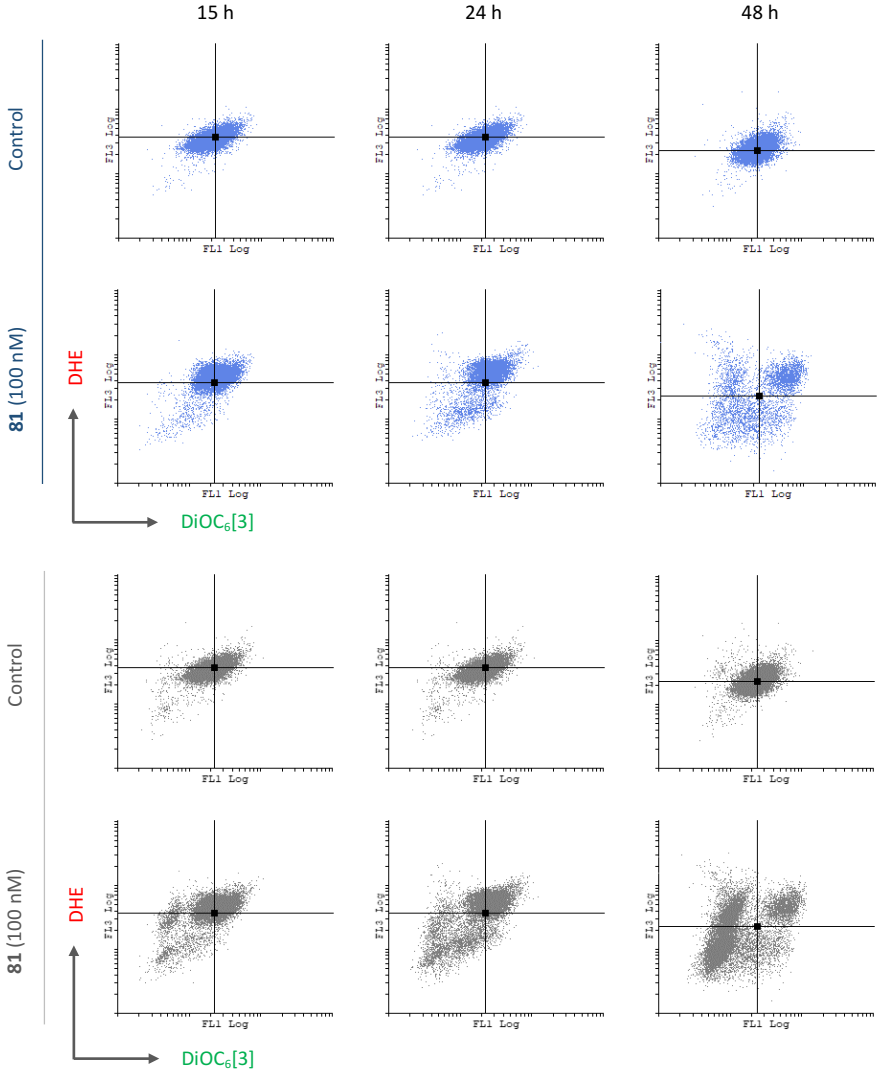

Figure 80. Dot plots of HeLa cells labeled with **$DiOC_6[3]$** (X axis, green fluorescence) and **DHE** (Y axis, red fluorescence) in control conditions or treated with **81** at 100 nM for 15 h, 24 h, and 48 h. Dot plots in blue come from samples when gating SS versus FS on viable cells (**Gate 2**, see Figure 76) and dot plots in grey come from the same samples when gating viable and non-viable cells (**Gate 1** = **Gate 2** + **Gate 3**, see Figure 76).

Given the compromised mitochondrial integrity, we subsequently analyzed the expression levels of the anti-apoptotic proteins from the Bcl-2 family. These proteins have been reported to display a role in linking the sustained mitotic arrest upon treatment to the induction of cell death, although the precise molecular mechanism that dictates cells to enter apoptosis remains unsolved. We observed no changes in Bcl-2 expression in HeLa cells after treatment with the lead compounds (Fig. 81). However, the phosphorylation of this protein was clearly induced 9 h after adding the drugs and even increased during longer periods of exposure. Bcl-xL expression exhibited a similar trend in the time-course experiment. The levels of Mcl-1 were also increased early upon treatment, although compared to P-Bcl-2 and Bcl-xL, Mcl-1 showed a decreasing tendency rather soon, from 9 h or 15 h onwards. Therefore, P-Bcl-2, Bcl-xL, and Mcl-1 experienced a transient induction at early stages after treatment, followed by a progressive attenuation that occurred earlier in the case of Mcl-1, and after around 32 h in the case of P-Bcl-2 and Bcl-xL (Fig. 81).

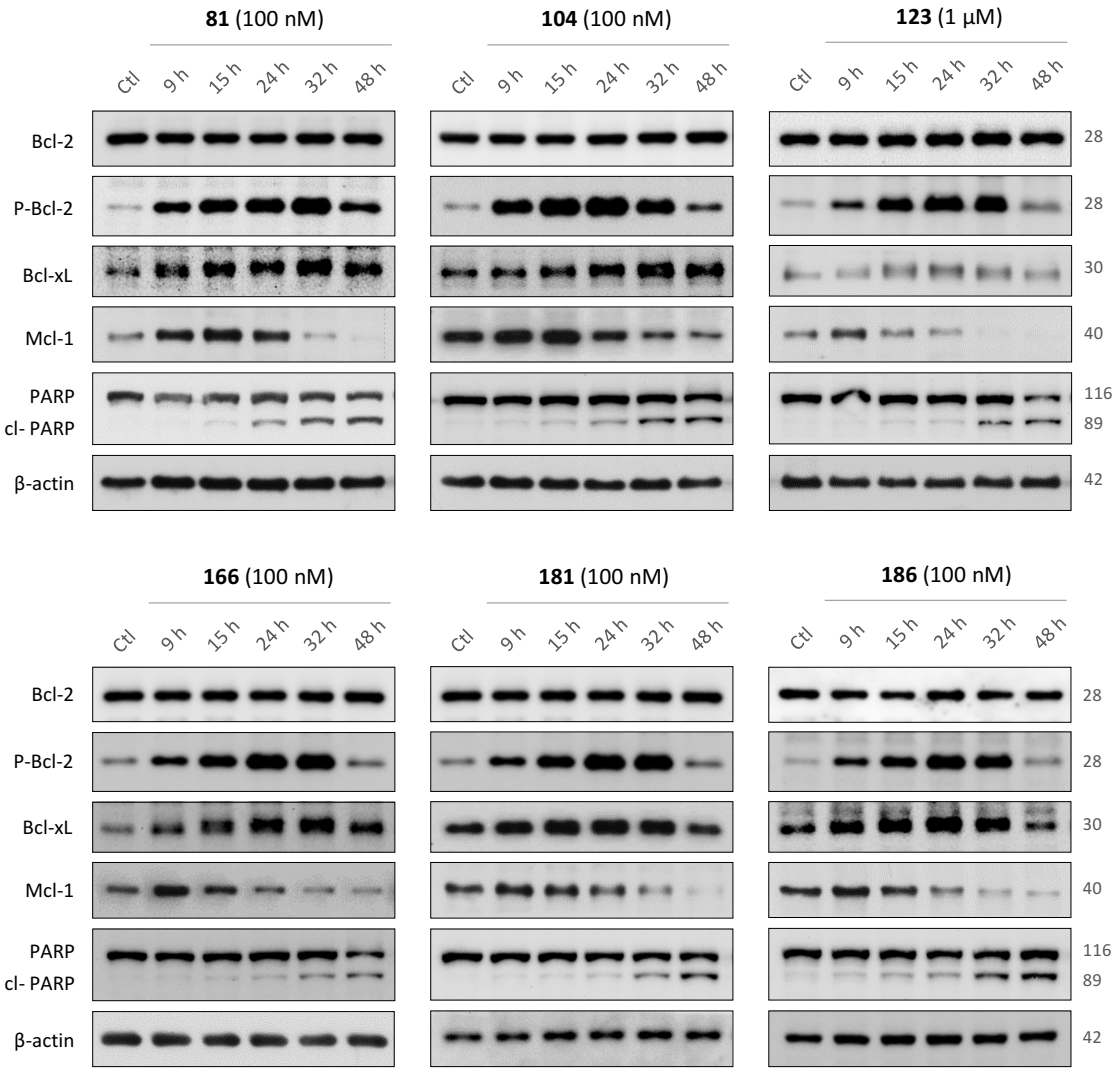

Figure 81. Immunoblots of HeLa cell lysates: time-course of the expression levels of proteins from the Bcl-2 family and PARP cleavage after treatment with the lead compounds compared to untreated samples (Ctl). β-actin was used as a loading control. Molecular weights are indicated in kDa. Western blot images are representative of three independent experiments.

This time-dependent modulation may suggest that the transient overexpression of these proteins could be related to an initial protective response that at some point failed in protecting the cells from dying. This ended up with reduced levels of the proteins, in parallel with the increasing apoptotic response, assessed by PARP cleavage (Fig. 81).

Based on those results, we decided to study whether Bcl-2 and Bcl-xL, which showed to be expressed in high levels for longer periods than Mcl-1 up until the boosted induction of apoptosis after 32 h, could prevent drug-induced apoptosis in HeLa cells if maintaining sustained high levels in a stable manner. That has already been reported for the colchicine site ligand MTC in erythroleukemic cell line HEL.[425] To this end, we used in our laboratory HeLa cells that had been stably transfected by Dr. Consuelo Gajate with the expression vector pSFFV-*bcl-2* (HeLa Bcl-2) or pSFFV-*bcl-xL* (HeLa Bcl-xL), containing the human *bcl-2* or *bcl-xL* open reading frame. The cells were cultured in the presence of G418 to allow the selective proliferation of transfected cells. We initially used HeLa cells transfected with the empty vector (HeLa Neo) as transfection control, but since no differences were observed compared to the non-transfected cells (HeLa WT), we used the latter as the parallel control for the upcoming experiments. The overexpression of Bcl-xL and Bcl-2 was characterized periodically by flow cytometry (Fig. 82A) and immunoblotting (Fig. 82B) relative to the expression in HeLa WT, showing that the overall increased expression comes from a single homogeneous population.

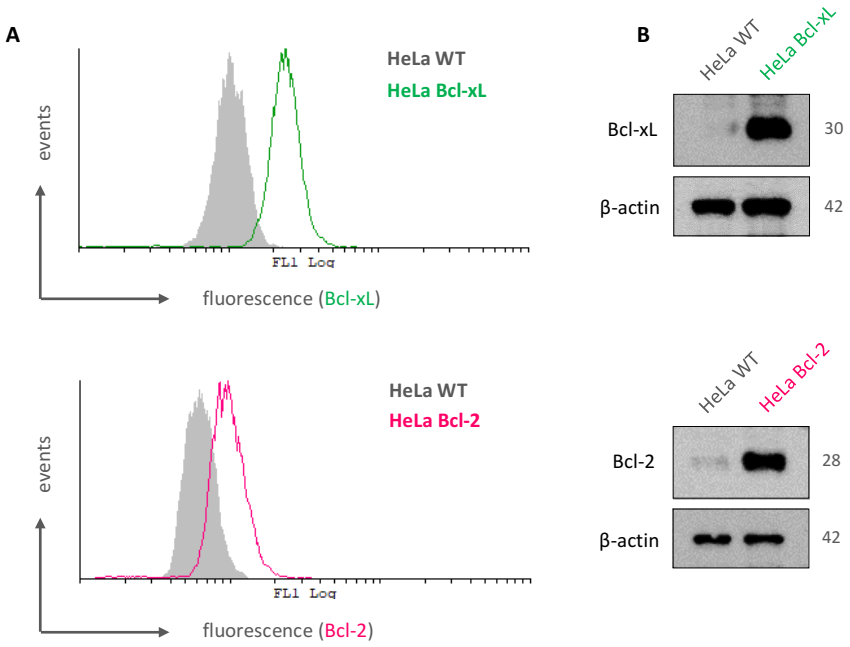

Figure 82. Expression of Bcl-xL and Bcl-2 proteins. **A.** Expression analysis by flow cytometry. HeLa cells were fixed, and labeled with Ab-1 against Bcl-xL or Bcl-2 and with Alexa488-conjugated Ab-2 anti-rabbit. The histograms represent the number of events versus green fluorescence in non-transfected HeLa cells (**HeLa WT**) or in HeLa cells transfected with Bcl-xL (**HeLa Bcl-xL**) or Bcl-2 (**HeLa Bcl-2**). **B.** Immunoblots of HeLa cell lysates coming from wild type cells or transfected cells. β-actin was used as a loading control. Molecular weights are indicated in kDa. Histograms and Western blot images are representative of periodic measures.

The overexpression of Bcl-xL or Bcl-2 led to a cell cycle arrest upon treatment with the lead compounds, similar to that of wild type cells, as assessed by time-course cell cycle analysis (Fig. 83 and 84, **green bars**) and the disruption of the microtubule network evidenced by confocal immunofluorescence (Fig. 85).

Figure 83. Analysis of cell cycle populations (**SubG$_0$/G$_1$**, **G$_0$/G$_1$**, **S**, and **G$_2$/M**) in HeLa cells overexpressing Bcl-xL (**HeLa Bcl-xL**) protein after treatment with the lead compounds at the indicated concentrations. The statistical analysis was carried out for the data relative to the G$_2$/M population respect to untreated samples (Ctl) after the same incubation period (n = 5-11; *** p < 0.001).

Figure 84. Analysis of cell cycle populations (**SubG$_0$/G$_1$**, **G$_0$/G$_1$**, **S**, and **G$_2$/M**) in HeLa cells overexpressing Bcl-2 (**HeLa Bcl-2**) protein after treatment with the lead compounds. The statistical analysis was carried out for the data relative to the G$_2$/M population respect to untreated samples (Ctl) after the same incubation period (n = 3-7; *** $p < 0.001$).

The time-dependent consecution of the mitotic arrest in transfected cells was similar to that showed in wild type HeLa cells (see Fig. 52), although the percentage of cells in the G$_2$/M region was higher in the case of transfected cells at long incubation times, especially 48 h and 72 h, at the expense of a reduction in DNA fragmentation (SubG$_0$/G$_1$). By representing the SubG$_0$/G$_1$ population observed in time-course experiments (Fig. 86) it is clear that the six lead compounds induced DNA degradation in both HeLa Bcl-xL and HeLa Bcl-2 cells, although in a milder manner than the induction of apoptosis in wild type HeLa cells.

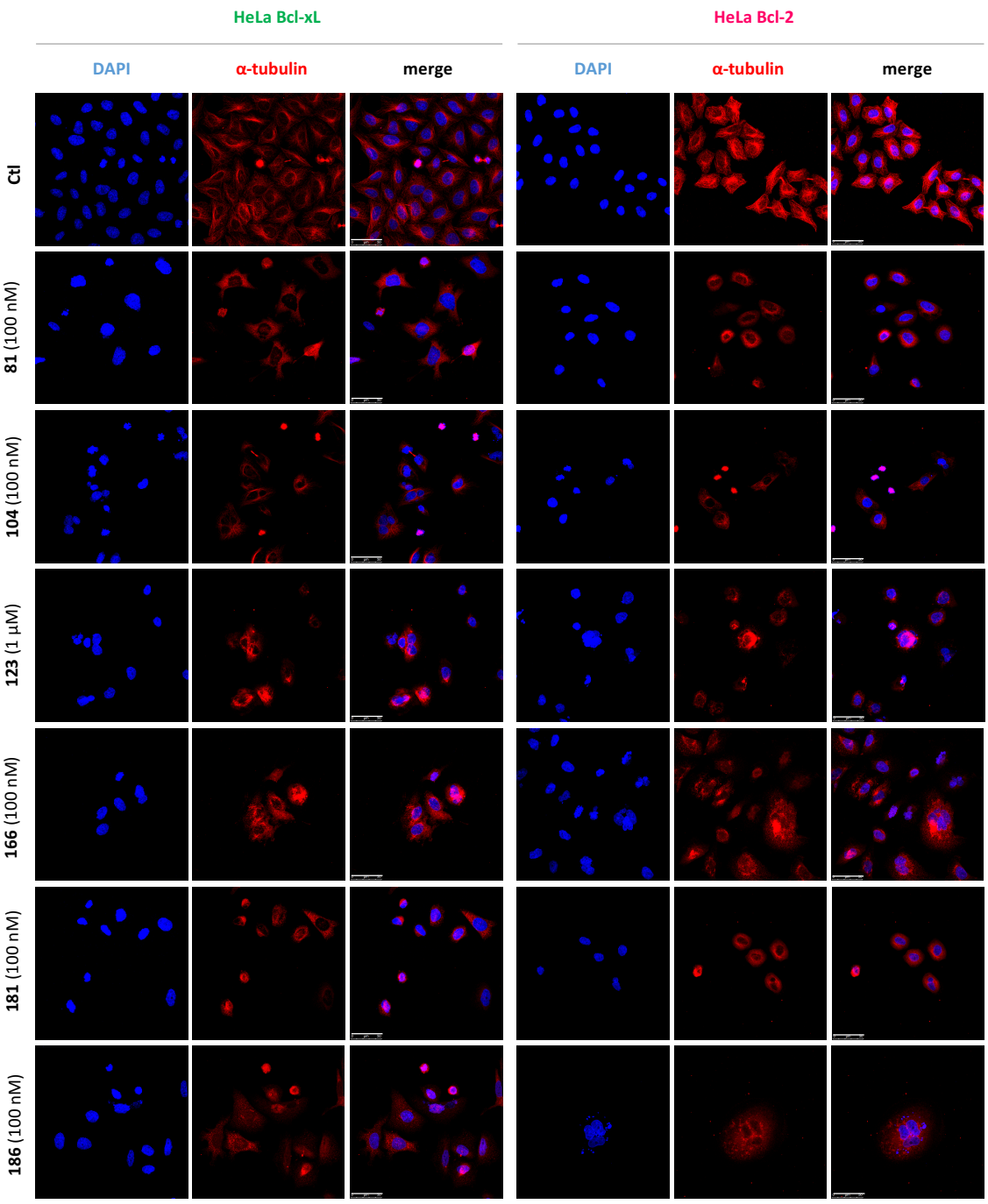

Figure 85. Confocal immunofluorescence microscopy of **HeLa Bcl-xL** and **HeLa Bcl-2** cells for visualization of the microtubule network. Cells were incubated in the absence (Ctl) or in the presence of the lead compounds at the indicated concentrations for 24 h. **Nuclei** were stained with DAPI in blue fluorescence and **α-tubulin** was visualized in red fluorescence (CY3-conjugated Ab-2). Scale bar: 50 µm. Photomicrographs are representative of two independent experiments.

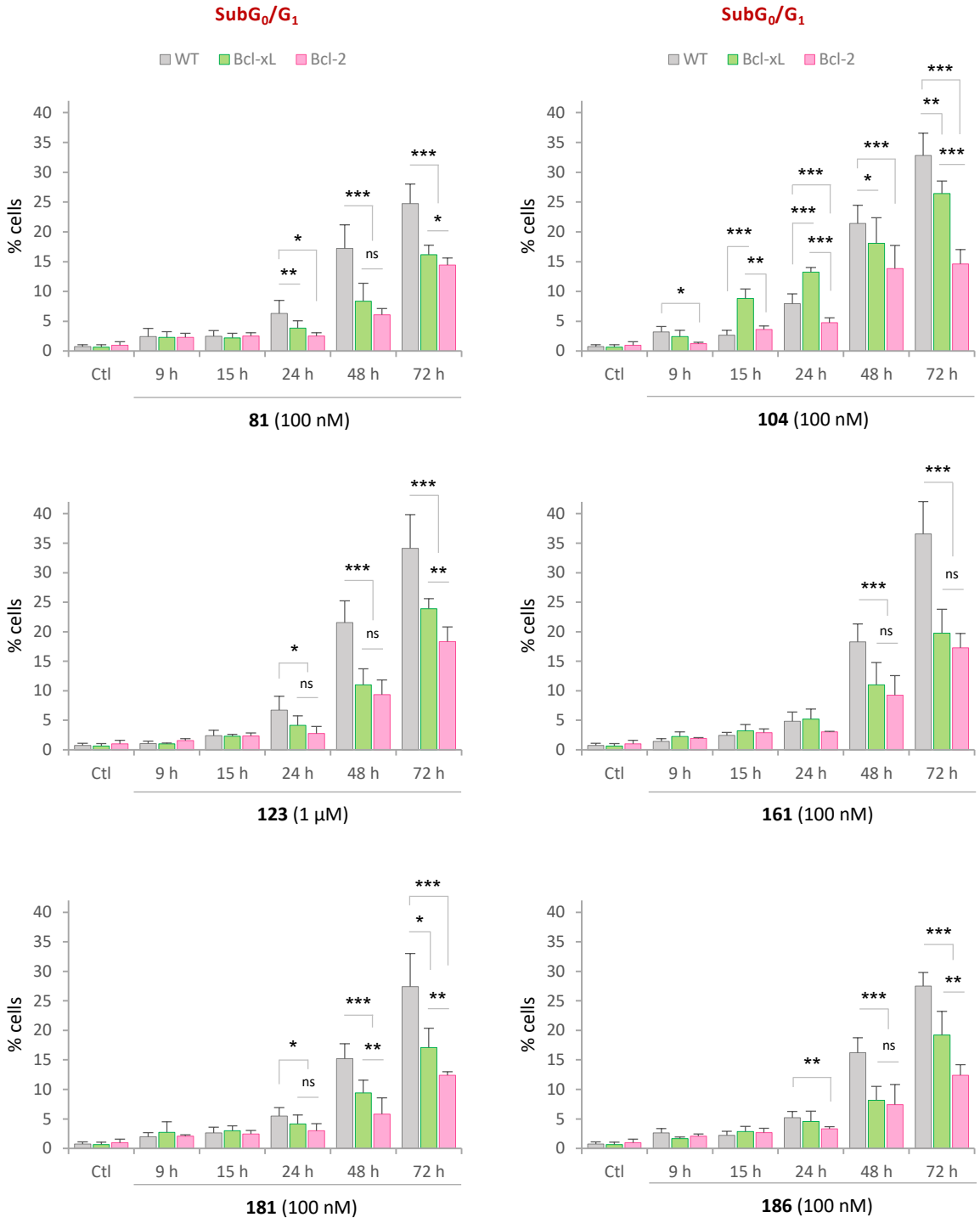

Figure 86. Time-course experiment representing the percentage of cells in the **SubG$_0$/G$_1$** in HeLa cells: **HeLa WT** (WT), **HeLa Bcl-xL** (Bcl-xL), and **HeLa Bcl-2** (Bcl-2). Cells were incubated in the absence (Ctl) or the presence of the lead compounds at the indicated concentrations. The statistical analysis was carried out comparing the data relative to the **SubG$_0$/G$_1$** population between the three cell types at the same time-point (n = 3-15; * $p < 0.05$; ** $p < 0.01$; *** $p < 0.001$).

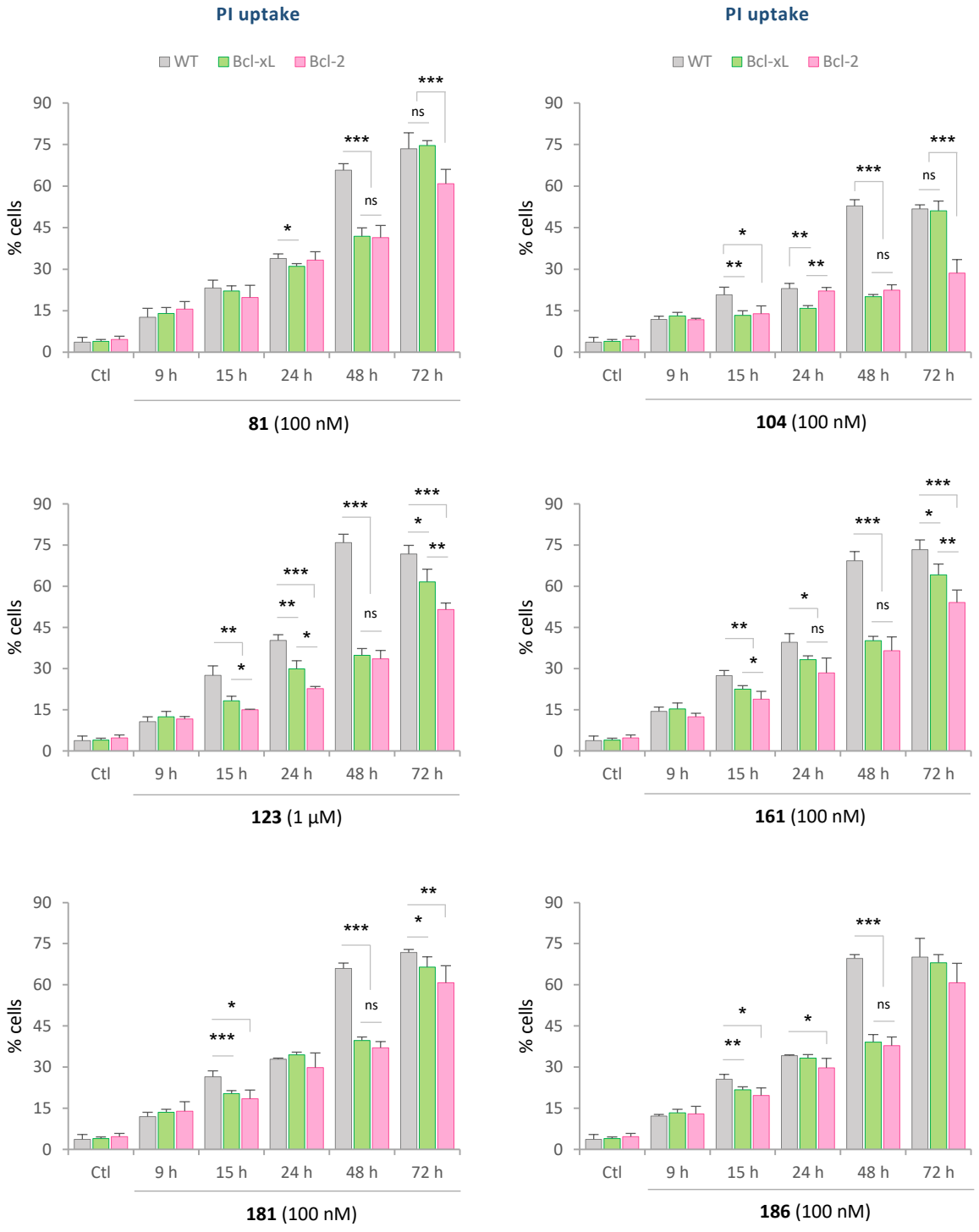

Figure 87. Time-course experiment respresenting the percentage of PI-positive cells in non-permeabilized samples (**PI uptake**) of HeLa cells: **HeLa WT** (WT), **HeLa Bcl-xL** (Bcl-xL), and **HeLa Bcl-2** (Bcl-2). Cells were incubated in the absence (Ctl) or the presence of the lead compounds at the indicated concentrations. The statistical analysis was carried out comparing the data relative to the **PI-positive** population between the three cell types at the same time-point (n = 3-7; * $p < 0.05$; ** $p < 0.01$; *** $p < 0.001$).

Although all the cells experienced some degree of apoptotic death gradually increasing over time, transfected HeLa cells appeared more resistant, undergoing cell death to a lesser degree than wild type cells. In HeLa WT cells, as already commented, the apoptotic boost was seen after 48-h incubations, assessed by the remarkable increase in the percentage of cells in the $SubG_0/G_1$ region (Fig. 86). In contrast, the overexpression of Bcl-xL and Bcl-2 by gene transfer prompted apoptosis in a lesser extent with statistically significant differences for all the compounds. The Hill slopes observed for the augmentation of apoptosis as a function of time in transfected cells were less pronounced compared to wild type cells. The percentage of cells within HeLa Bcl-xL and Bcl-2 samples that showed DNA degradation at 72 h after treatment, was quantitatively similar to the apoptotic response elicited in wild type cells 48 h after treatment. Based on these observations, there is a delay in the onset of apoptosis of roughly a day, meaning that the enhanced expression of prosurvival proteins Bcl-xL and Bcl-2 partially protects the cells from dying, but it is not enough to prevent cell death. HeLa cells transfected with Bcl-2 showed a lower DNA degradation than those overexpressing Bcl-xL, with statistically significant differences for all the compounds except for **166**, which caused higher variability. The differences were mainly observable at long incubation times.

We analyzed the membrane permeabilization in parallel to cell cycle experiments by measuring the percentage of PI-positive cells (Fig. 87). As expected, the compounds induced time-dependent membrane permeabilization in HeLa Bcl-xL and HeLa Bcl-2, at a similar pace to the induction of DNA fragmentation (Fig. 86). Similarly, the number of permeable cells mostly differed after 48-h incubations, although the values reached those observed for wild type cells after 72 h. The extension of PI uptake in transfected cells upon 48-h treatments was akin to the percentage of permeable wild type cells after 24 h. It agrees with a delay in cell death, as observed for DNA degradation, rather than an overall reduction of the apoptotic rate, although there are still statistically significant differences in the rate of membrane permeabilization, and especially in the $SubG_0/G_1$ region 72 h after adding the ligands. The diminished apoptotic response was confirmed after 48-h treatments by measuring PARP cleavage (Fig. 88).

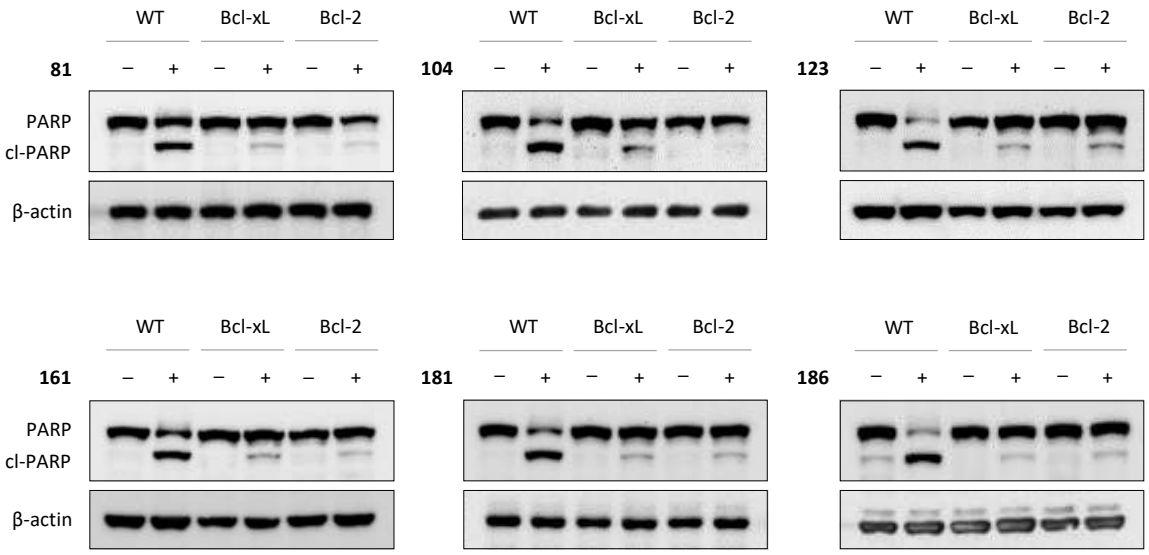

Figure 88. Immunoblots of HeLa cell lysates: analysis of PARP cleavage after 48-h incubation with or without the compounds at 100 nM except **123** at 1 μM in **HeLa WT** (WT), **HeLa Bcl-xL** (Bcl-xL), and **HeLa Bcl-2** (Bcl-2) cells. β-actin was used as a loading control. Western blot images are representative of three independent experiments.

ROLE OF AKT, ERK, AND JNK KINASES

We studied the implication of kinases Akt, Erk1/2, and JNK in response to treatment. These kinases are important regulators of cell survival and proliferation, among many processes. We performed time-course experiments in HeLa cells to determine the expression levels of these proteins and their phosphorylated forms by immunoblotting, revealing no clear changes upon treatment with the lead compounds (Fig. 89).

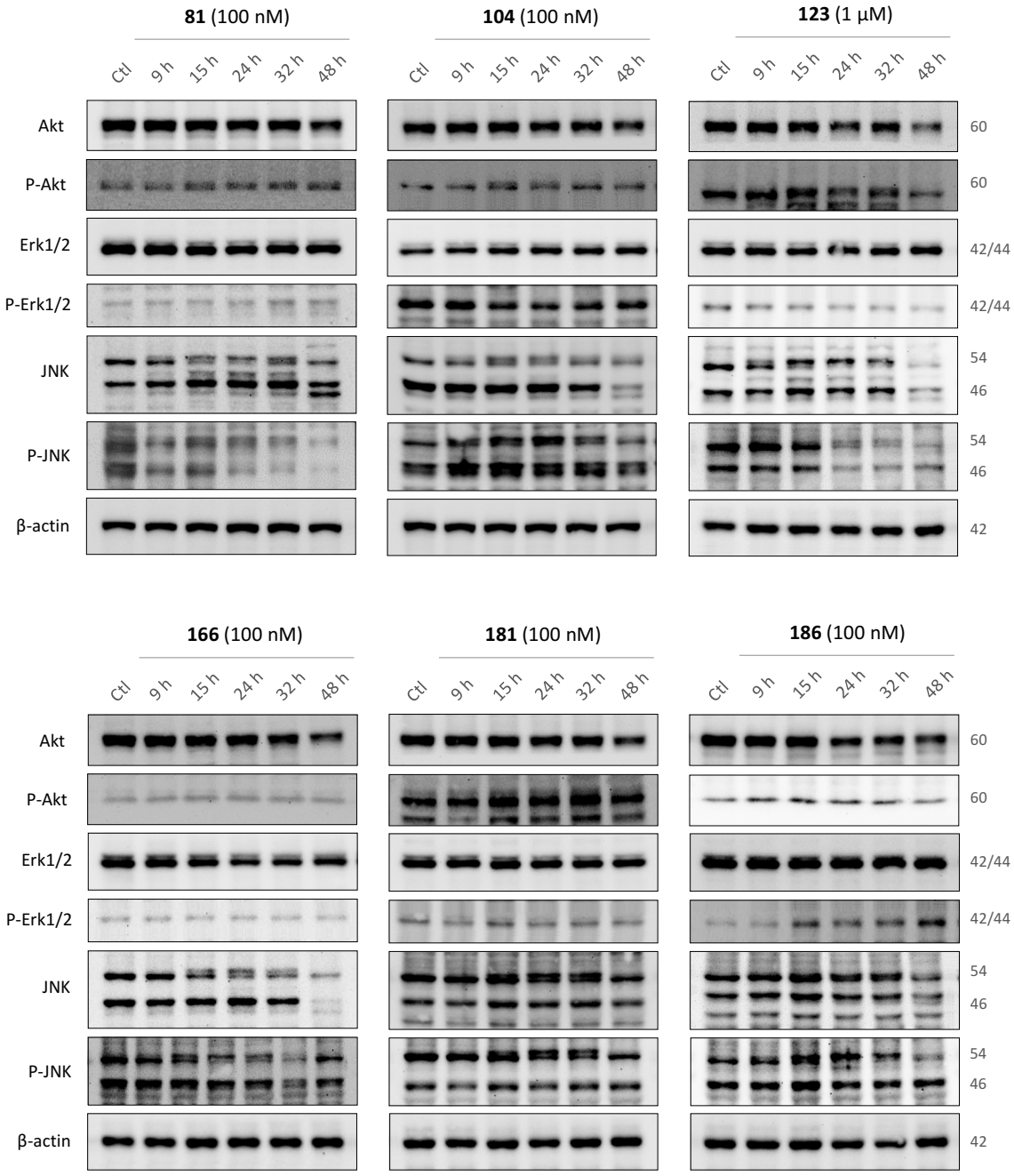

Figure 89. Immunoblots of HeLa cell lysates: time-course of the expression levels of Akt, Erk1/2, JNK, and their phosphorylated forms after treatment with the lead compounds compared to untreated samples (Ctl). β-actin was used as a loading control. Molecular weights are indicated in kDa. Western blot images are representative of three independent experiments.

The role of Erk1/2 was further explored by treating the cells with the MEK inhibitor U0126 (10 µM) that inhibits the phosphorylation of Erk1/2. HeLa cells were incubated in the absence or the presence of the lead compounds in combination or not with U0126 for 48 h (Fig. 90). The results relative to the percentage of cells in the $SubG_0/G_1$ region and cells permeable to PI showed no statistically significant differences when adding U0126, suggesting that the Erk1/2 pathway does not play a relevant role in cell death commitment upon treatment with the lead compounds. The incubation for 24 h did not cause any differences either (see Appendix Fig. V).

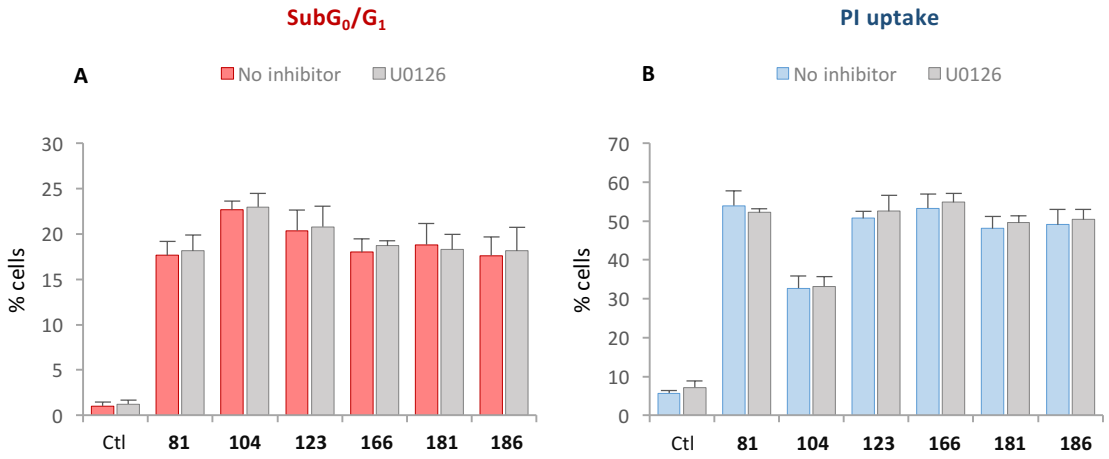

Figure 90. HeLa cells in the absence (Ctl) or the presence of the lead compounds, in combination or not with the MEK inhibitor U0126 (10 µM). The compounds were tested at 100 nM except **123** at 1 µM and incubated for 48 h. **A.** Quantification of the percentage of cells in the **$SubG_0/G_1$** region, measured by cell cycle analysis (n = 5). **B.** Number of **PI-positive cells** in non-permeabilized samples (n = 4). None of the pairs showed statistically significant differences.

The Western blot analysis also evidenced no changes in PARP cleavage upon 48-h treatment with **81** and **166** alone or in combination with U0126 (Fig. 91).

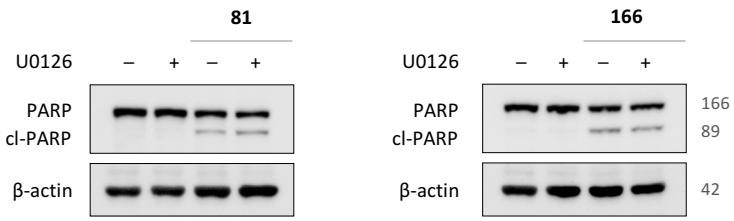

Figure 91. Immunoblots of HeLa cell lysates: detection of PARP cleavage after treatment with **81** and **166** at 100 nM for 48 h, in combination or not with U0126 (10 µM). β-actin was used as a loading control. Molecular weights are indicated in kDa. Western blot images are representative of two independent experiments.

REVERSIBILITY OF THE DRUG-INDUCED RESPONSE

Once added to the culture media, the lead compounds induced the progressive accumulation of cells in G_2/M noticeable with 9-h incubations that reached the maximum response after 15-24 h, assessed by cell cycle analysis (see Fig. 51 and 52), detection of MPM-2 signal (see Fig. 53), and microtubule disruption visualized by immunofluorescence (see Fig. 54). In order to study whether the mitotic arrest can be alleviated after drug removal from the culture media, we conducted a series of reversibility experiments to determine the distribution of cell populations by cell cycle analysis after washing out the compounds. To do so, we selected three incubation periods that caused a complete accumulation of cells in the G_2/M region in different stages of the apoptotic response. HeLa cells were incubated in the the presence of the lead compounds for 15 h, 24 h, or 48 h (0 h after rescue), then washed three times with PBS and re-seeded in drug-free culture media. Samples were taken 24 h, 48 h, and 72 h after the rescue to monitor the cell cycle evolution.

The six compounds prompted a roughly complete mitotic arrest in HeLa cells (Fig. 92) with increasing percentages of the SubG_0/G_1 population after 15 h (2.3-3.2%), 24 h (5.3-8.8%), and 48 h (17.9-23.3%). As depicted in Figure 92, the cells that had been exposed to 15-h treatments completely recovered from the mitotic arrest irrespective of each compound. The 15-h incubation with compound **123** at 1 μM resulted in 4.6% G_0/G_1 and 88.4% G_2/M, showing a partial reversion of the drug-induced arrest 24 h after the rescue (42.0% G_0/G_1 and 42.9 % G_2/M). These values turned roughly normal upon longer time spans, similar between 48 h and 72 h (50.6% and 52.5% G_0/G_1, 26.1% and 25.4% G_2/M, respectively). There was a transient and slight initial increase of the SubG_0/G_1 population after rescue regardless of the incubation period, presumably caused by the washing process because it was also observed for untreated HeLa cells (data not shown, 0.5% versus 2.0%, $p < 0.01$). Despite this initial increase, the percentage of cells in the SubG_0/G_1 region experienced a gradual decrease after removing the 15-h treatments with no statistically significant differences in DNA degradation observed at the 15-h time-point, or even lower apoptosis. Based on these data, the drug-induced arrest can be lifted when removing the treatments after 15-h incubation, abrogating the apoptotic response.

The transient post-rescue increase in cell death was exacerbated after exposing cells to the compounds for 24 h, putatively because in that instance, the cells were affected by the treatments in more extent and partially sensitized to stress stimuli such as repeated washes. The G_2/M population decreased when the ligands were removed, and the opposite was observed for the G_0/G_1 phase, with a decreasing trend in cell death over time. However, the percentage of cells in the SubG_0/G_1 region 72 h after rescue showed statistically significant differences with that at the 24-h time-point, suggesting a partially reversible effect. HeLa cells previously treated with compound **104** however showed a full recovery after 24-h and also 48-h incubation periods. By contrast, the effects induced by the other five compounds after 48 h were not reverted after drug removal. The percentages of cells in the G_2/M region decreased at expense of apoptosis, enhanced as time went by (Fig. 92).

Altogether, these data back up the previous observation that the mitotic arrest occurs long before the boosting of the apoptotic response. The irreversible commitment of DNA breakdown depends on the initial incubation period. The mitotic arrest elicited after 15-h incubation can be alleviated by microtubule re-polymerization after drug removal, as assessed by confocal immunofluorescence (Fig. 93). Detached rounded cells arrested in mitosis got attached to the surface when removing the drug, and recovered the original shape of untreated cells with a functional microtubule network spreading throughout the cell.

Figure 92. Continued

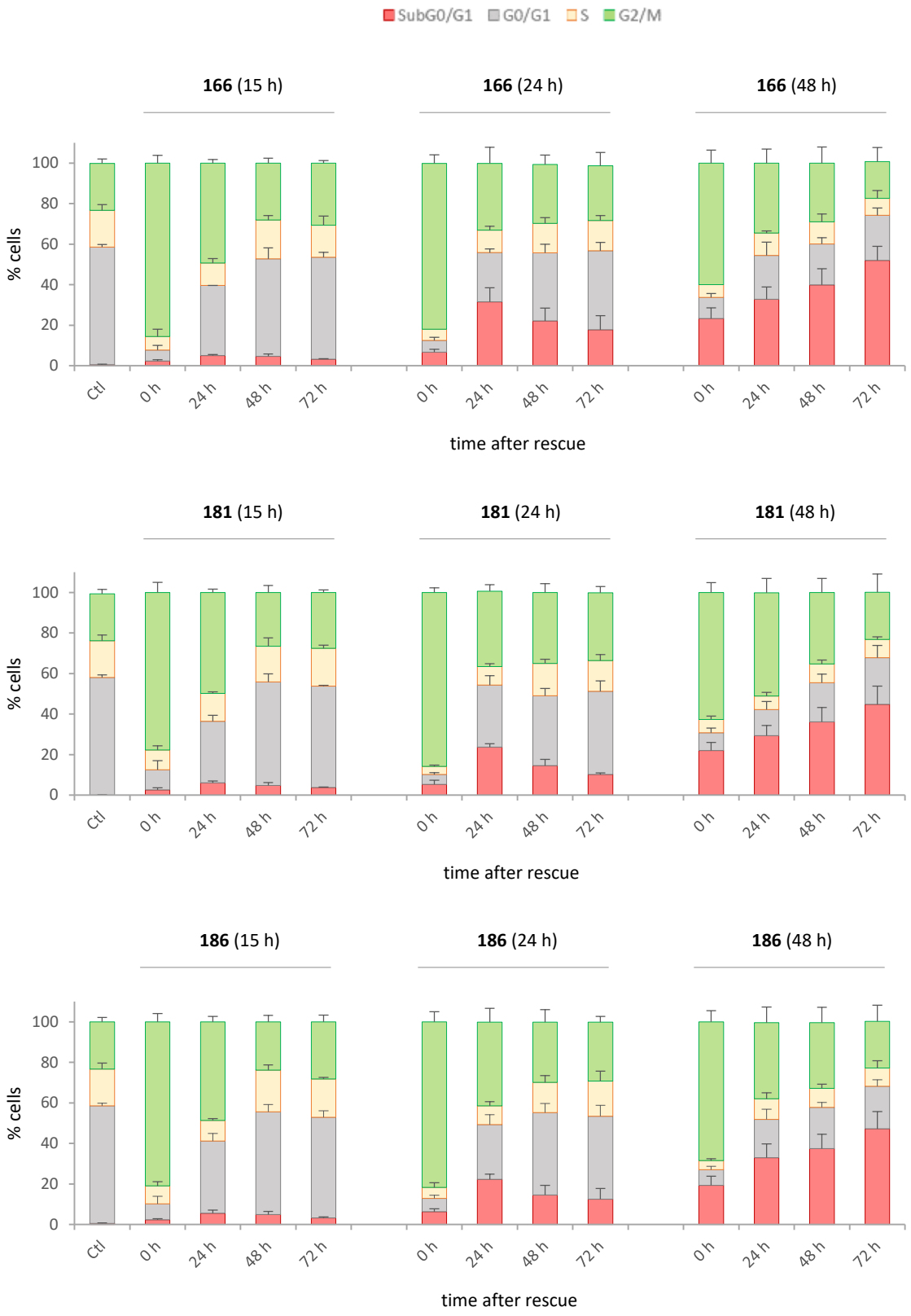

Figure 92. Analysis of cell cycle populations (**SubG$_0$/G$_1$**, **G$_0$/G$_1$**, **S**, and **G$_2$/M**) in HeLa cells after treatment with the lead compounds for 15 h, 24 h, or 48 h (0 h after rescue) at 100 nM or 1 µM in the case of **123**. Then, cells were harvested, washed three times with PBS and plated in fresh media. Samples were collected 24 h, 48 h, and 72 h after the rescue (n = 4).

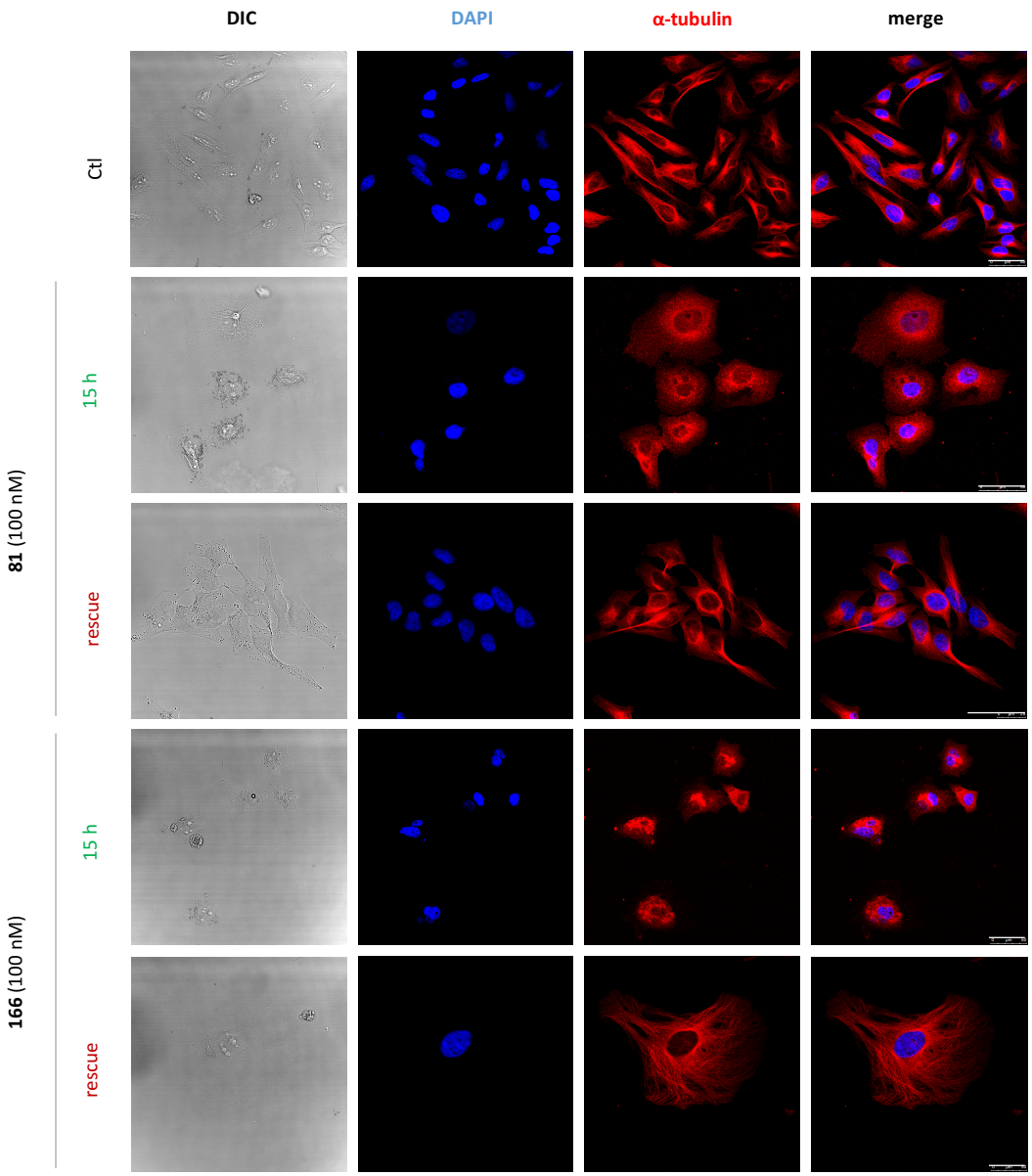

Figure 93. Confocal immunofluorescence microscopy of HeLa cells for visualization of the microtubule network. Cells were incubated in the absence (Ctl) or the presence of **81** and **166** at 100 nM for 15 h. The drugs were then removed from the culture media by washing three times with PBS. Cells were plated in fresh culture media and processed 24 h after the rescue. **Nuclei** were stained with DAPI in blue fluorescence and **α-tubulin** was visualized in red fluorescence (CY3-conjugated Ab-2). Scale bar: 50 µm. Photomicrographs are representative of two independent experiments.

After 15-h incubation with **81** and **166**, HeLa cells were deprived of a steady microtubule network, which was restored in fresh media. By that time (24 h), there were approximately half of the cells in G_0/G_1 and the other half in G_2/M. In order to monitor how fast these changes became evident by cell cycle analysis, we incubated HeLa cells with the lead compounds for 15 h and monitored a time span from as shorter as 30 min after rescue (Fig. 94). The recovery occurred at a similar pace after incubation with the six compounds. It was noticeable 6 h after the rescue with an evident increase in the G_0/G_1 population at the expense of the cells in G_2/M. The cell cycle profile was considered normal 48 h after rescue.

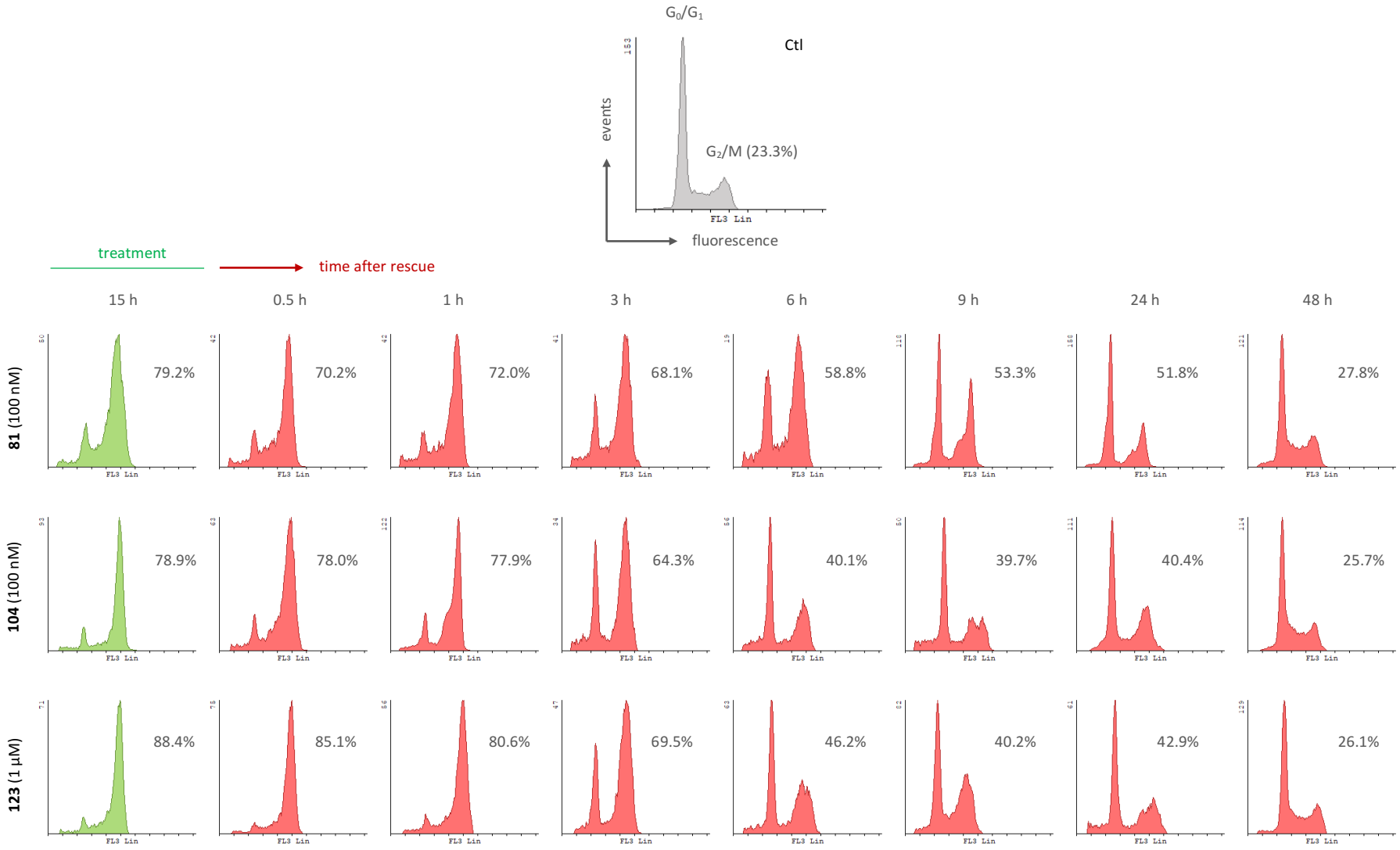

Figure 94. Continued

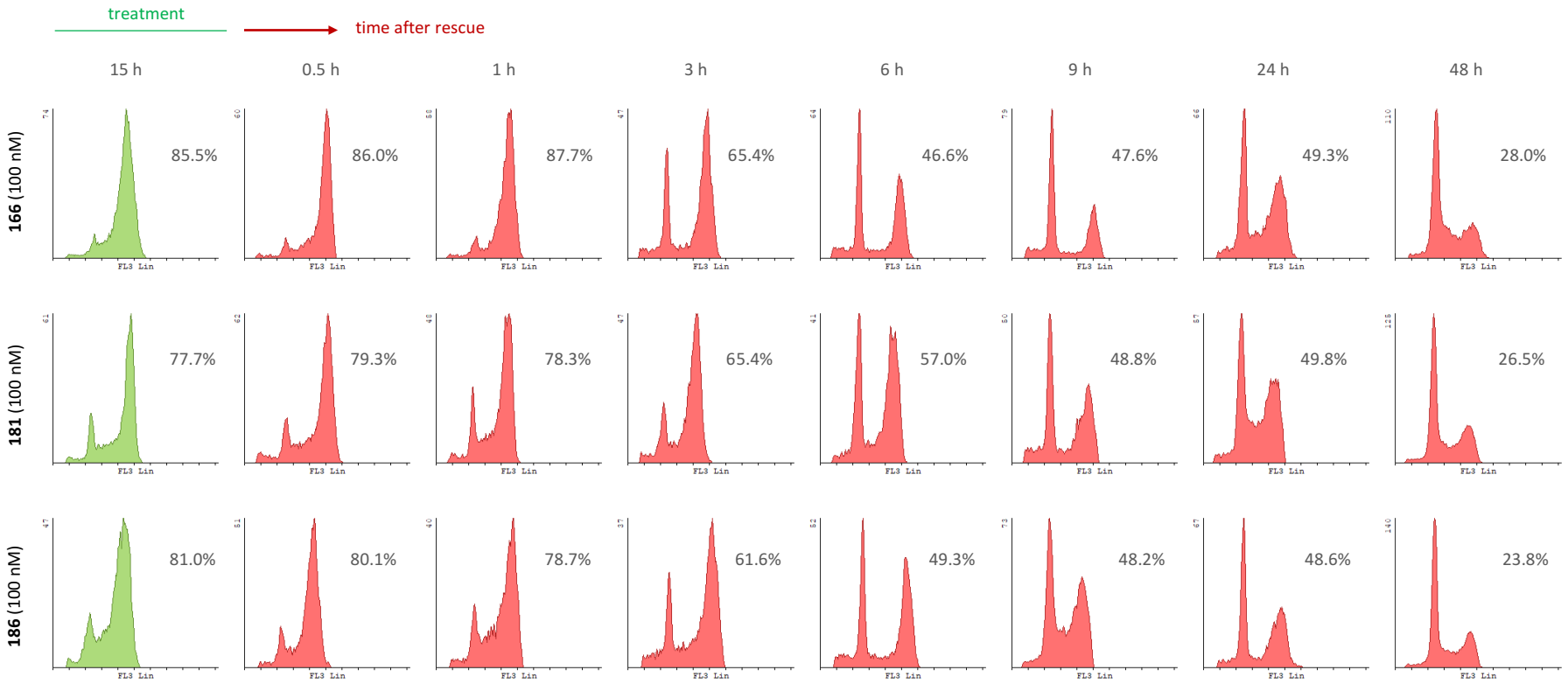

Figure 94. Cell cycle histograms relative to a rescue experiment in HeLa cells treated with the compound at the indicated concentrations for 15 h (green histograms). The peaks corresponding to G_0/G_1 and G_2/M populations are indicated on the control histogram (Ctl, grey histogram). After that incubation period, both adherent and suspended cells were brought together and washed three times with PBS, then re-seeded in drug-free culture media. Samples were taken at the indicated time-points after the rescue (red histograms). The percentages of cells in the G_2/M region are indicated on the right side of each histogram. Flow cytometry profiles are representative of three independent experiments.

We evaluated whether the changes that occurred after the rescue impact on cell death. As observed in Figure 92, HeLa cells recovering from 15-h treatments with the lead compounds showed little modification of the DNA fragmentation rate ($SubG_0/G_1$ population), whereas 24-h treatments resulted in enhanced apoptosis when removing the drugs with a decreasing tendency. By contrast, cells could not recover from 48-h treatments and experienced a dramatic increase in DNA fragmentation, except in the case of 100 nM **104**. These results were confirmed by double staining HeLa cells with Annexin V-FITC and PI after incubation with **166** for 15 h, 24 h, and 48 h. The drug was subsequently removed, and the washed samples were analyzed two days after the rescue (Fig. 95). In line with cell cycle analysis, 15-h incubation did not affect the overall viability of the cells upon rescue, although the percentage of apoptotic cells remarkably increased following the rescue of 24-h treatment. The contribution of late apoptosis to the overall demise was augmented upon rescue compared to the 48-h time-point even with roughly similar viability, which agrees with the higher percentage of cells in the $SubG_0/G_1$ region. The other five lead compounds gave similar results (see Appendix Fig. VI).

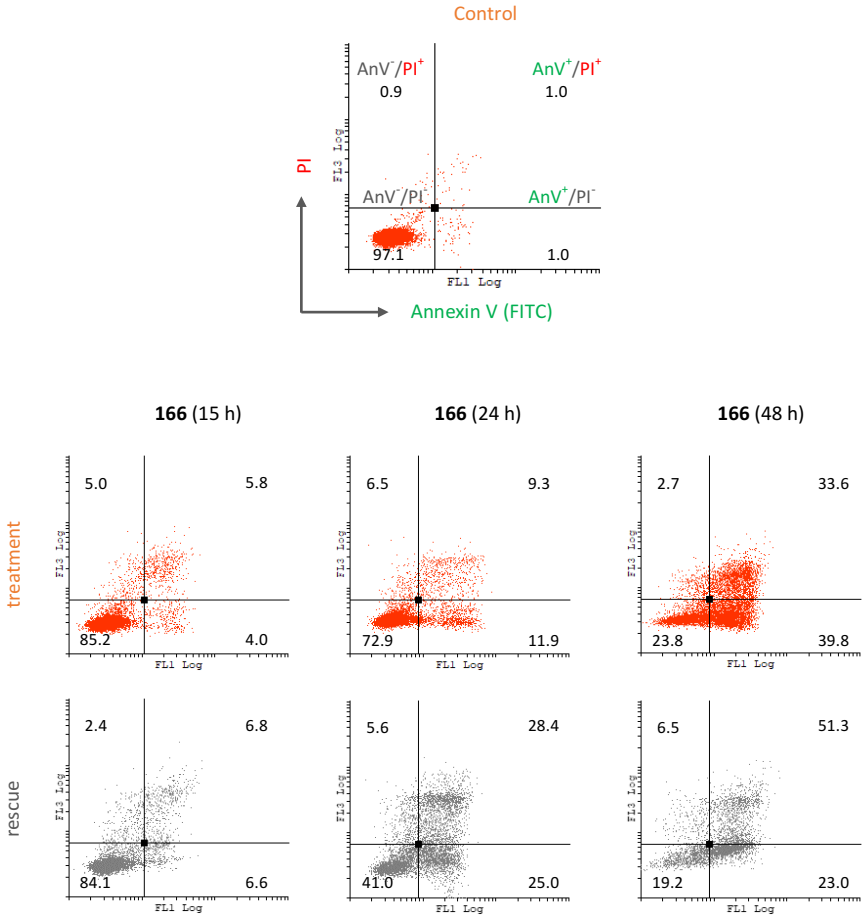

Figure 95. Dot plots of non-permeabilized HeLa cells treated with **166** at 100 nM for 15 h, 24 h, or 48 h (treatment). The cells were washed three times with PBS and re-seeded in drug-free culture media, then analyzed 48 h after removing the treatment (rescue). According to their distribution along the X axis (**Annexin V-FITC**, green fluorescence) and the Y axis (**PI**, red fluorescence), cells can be categorized as AnV^-/PI^- (live cells), AnV^+/PI^- (early apoptosis), AnV^-/PI^+ (necrosis) and AnV^+/PI^+ (late apoptosis or necrosis secondary to apoptosis), expressed as the mean in percentage (*n* = 3). Dot plots are representative of three independent experiments.

The status of the transmembrane mitochondrial potential ($\Delta\Psi_m$) and the levels of ROS were monitored by flow cytometry in parallel to cell cycle analysis. HeLa cells were incubated for 15 h, 24 h, or 48 h with the lead compounds, then removed and cultured for 48 h after rescue. Given the full recovery of the cells after 15-h incubations, mitochondrial changes were also monitored in that case 24 h and 72 h after drug removal besides the 48 h time span. The results are given as overlay histograms comparing the detected fluorescence of treated or washed samples with that of untreated cells at each time-point. $DiOC_6[3]$ was used as a probe for the detection of mitochondrial potential (green fluorescence, Fig. 96) and DHE as a sensor of intracellular ROS (red fluorescence, Fig. 97). As explained above, only viable cells were gated and plotted into histograms.

As a result of 15-h incubation with the lead compounds, the cells showed a strong arrest with scarce apoptosis. The transmembrane mitochondrial potential was not affected in this instance compared to untreated cells, whereas there was a slight increase in the intracellular levels of ROS, evidenced by the displacement of the population distribution towards brighter fluorescence values (Fig. 97). When washing out the ligands, the cell cycle profile went back progressively to the normal cell cycle distribution, considered normal around 48 h after the rescue, with steady levels of apoptosis, very minor. The little increase observed in the levels of ROS right after treatment was reverted to the baseline levels. However, the cells that recovered from the mitotic arrest experienced a slight increase in the mitochondrial transmembrane potential 48 h and 72 h after rescue (Fig. 96).

A similar outcome occurred after 24-h incubation with the drugs. The mitotic arrest was accompanied by enhanced DNA degradation. The arrest was alleviated after removing the treatments with a transient increase in the $SubG_0/G_1$ region that went down over time, although even at 72 h after rescue, it surpassed the apoptosis rate observed right after the 24-h treatment. The higher levels of ROS found after treatment were reduced when the cells were washed, although in a lesser extent than after 15-h treatments. We found an augmented signal coming from $DiOC_6[3]$ after the rescue, suggesting an increase in the transmembrane potential, a similar situation to that of rescued cells after 15-h treatments.

The arrest found after 48-h treatments was not abrogated after the rescue, but the cells kept on dying, except after treatment with compound **104**, from which the cells did recover by cell cycle analysis. Regarding the mitochondria, we found two populations of cells as already commented. There are cells with lower fluorescence (pressumably depolarized) and others with higher fluorescence (pressumably hyperpolarized) than untreated cells at that time-point. The same observation applies to ROS levels. The fluorescence profile of DHE barely changed after the rescue compared to that after 48-h incubation, except in the case of **104**. Removing the treatments resulted in a displacement towards the right of the $DiOC_6[3]$ fluorescence signal, with the disappearance of the depolarized population found after 48 h. Taking into account that we are only considering viable cells, it may suggest that the apoptosis was that advanced that depolarized cells still located in the viable cell region after 48-h treatments got permeabilized and shifted towards the non-viable cell region, therefore not gated.

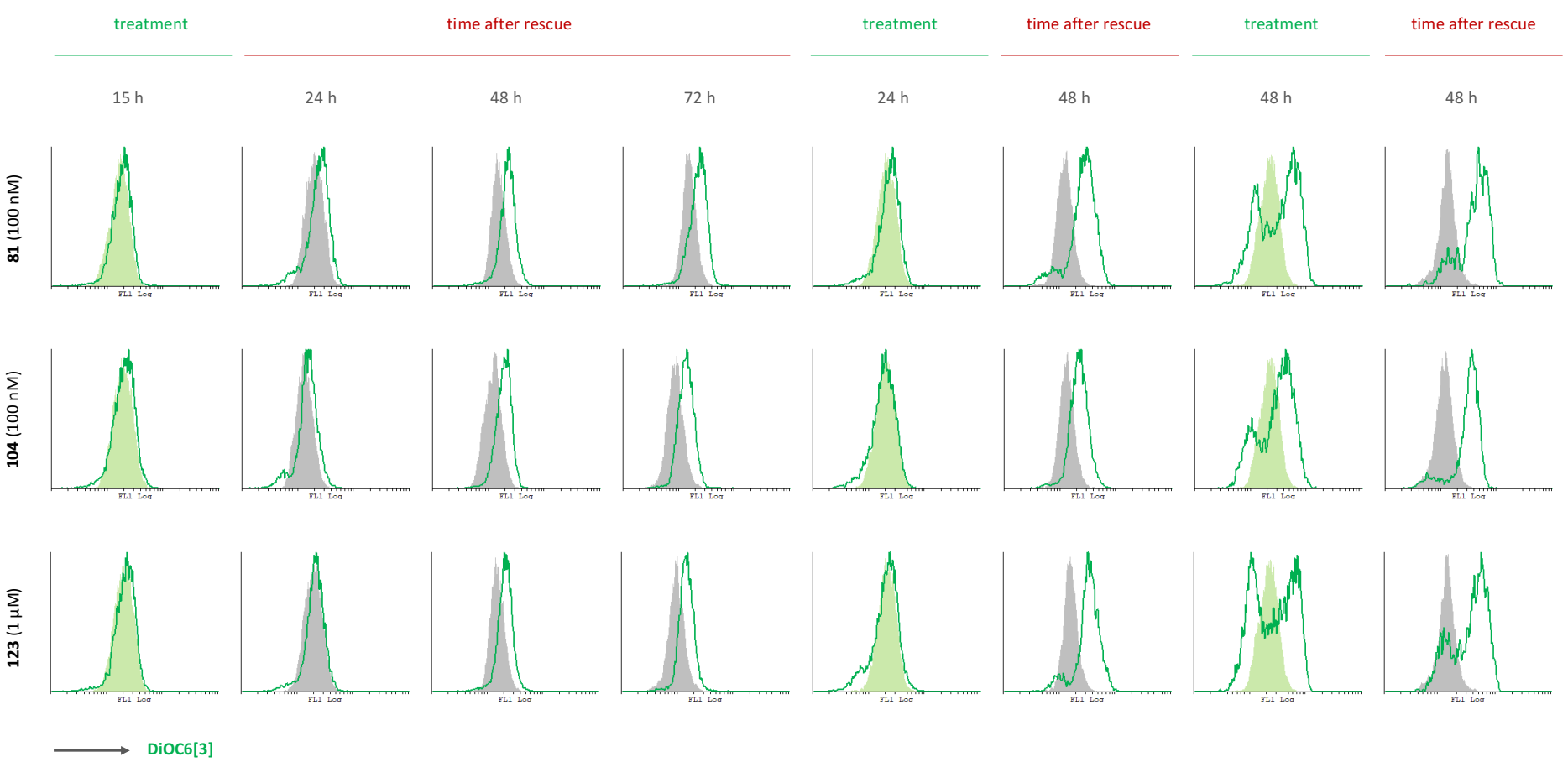

Figure 96. Continued

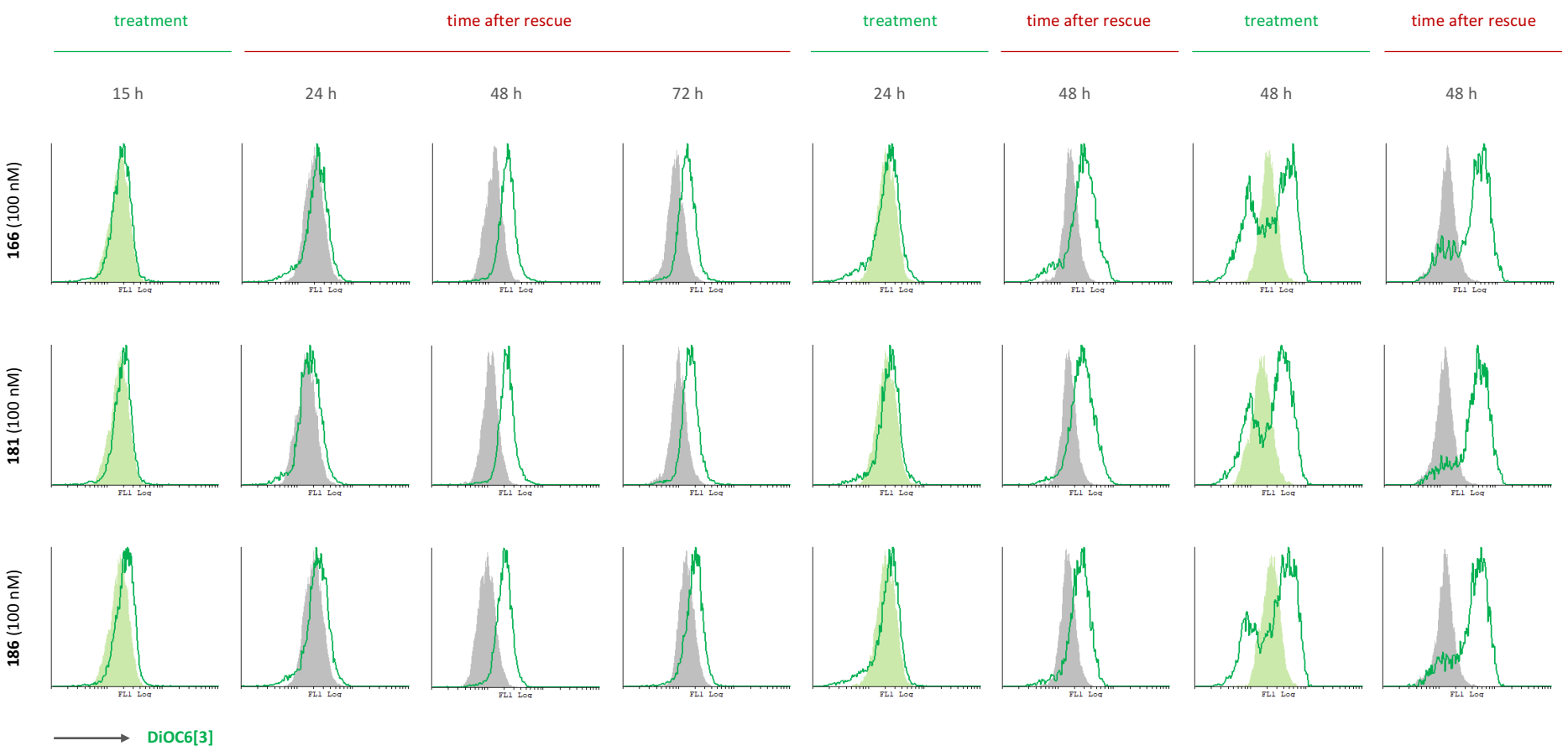

Figure 96. Overlay histograms of HeLa cells representing the mitochondrial transmembrane potential ($\Delta\Psi_m$) in control conditions (filled histograms) or treated with the indicated compounds for 15 h, 24 h, and 48 h, or after rescue (**unfilled green histograms**). The Y axis corresponds to the number of cells and the X axis is the green fluorescence of $DiOC_6[3]$ in non-permeabilized samples. The histograms are representative of three independent experiments.

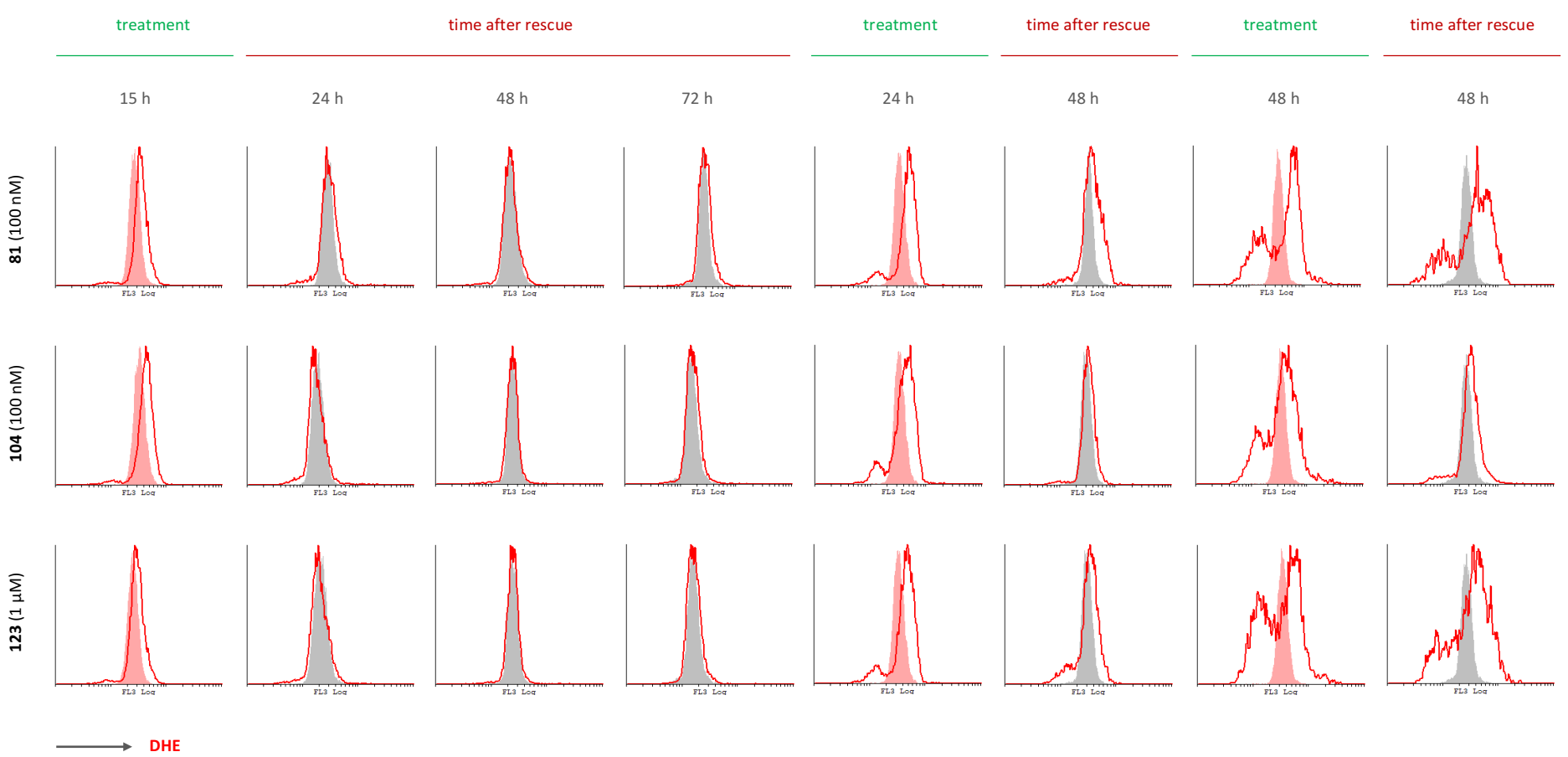

Figure 97. Continued

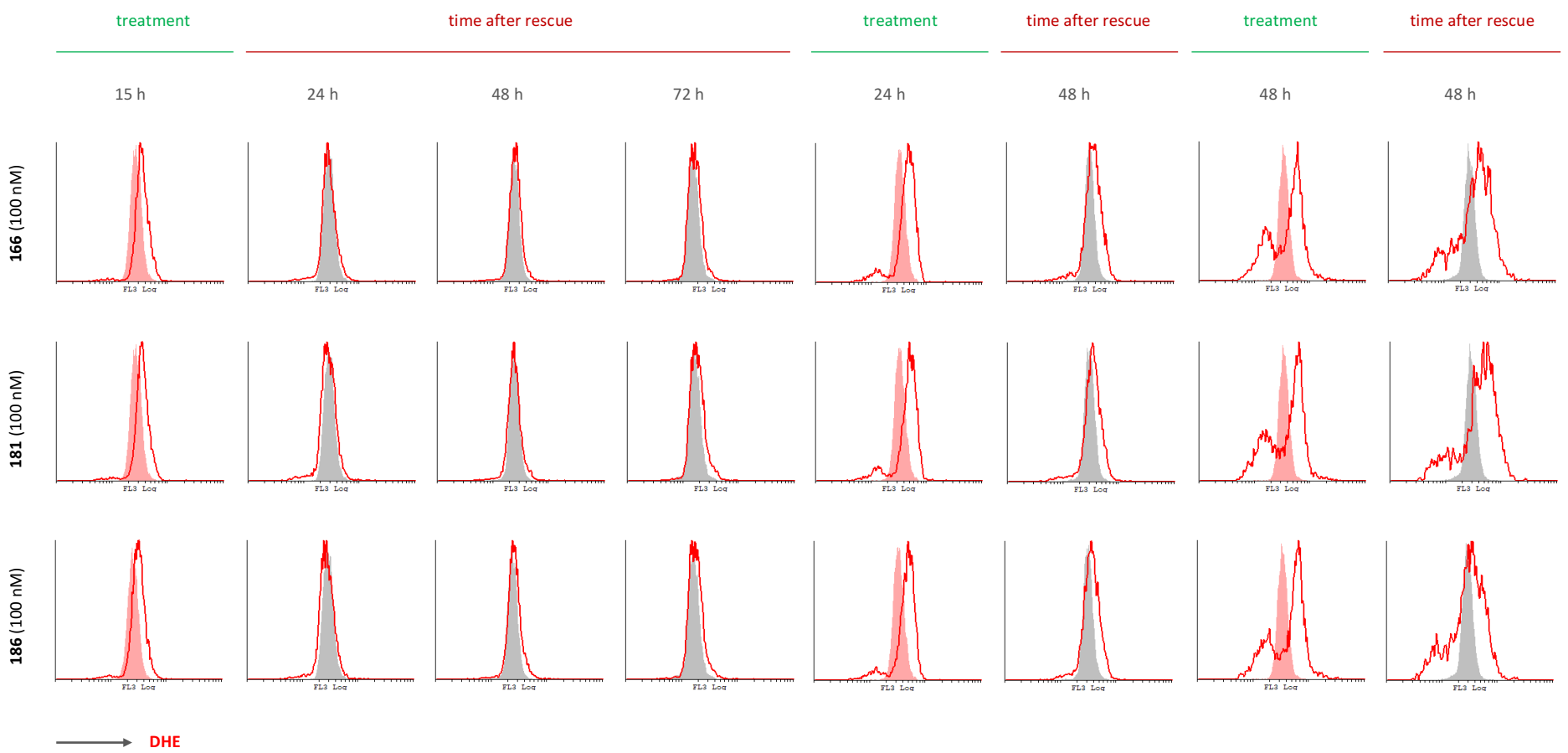

Figure 97. Overlay histograms of HeLa cells representing the levels of reactive oxygen species (ROS) in control conditions (filled histograms) or treated with the indicated compounds for 15 h, 24 h, and 48 h, or after rescue (**unfilled red histograms**). The Y axis corresponds to the number of cells and the X axis is the red fluorescence of DHE when oxidized by intracellular superoxide in non-permeabilized samples. The histograms are representative of three independent experiments.

All the previous data together point out that drug-induced effects can be reverted after 15-h incubation by re-polymerization of the microtubule cytoskeleton after removing the drugs from the culture media. We investigated whether the unlocking of the mitotic arrest and the reconstruction of the microtubule network depended on the synthesis of proteins. HeLa cells were incubated with **81** and **166** at 100 nM for 15 h, then washed three times with PBS. At that point, the samples were re-seeded in drug-free fresh culture media in the presence or the absence of the protein synthesis inhibitor cycloheximide (CHX, 75 µM) and we monitored the evolution of the cell cycle profile from 3 h up to 32 h after the rescue (Fig. 98).

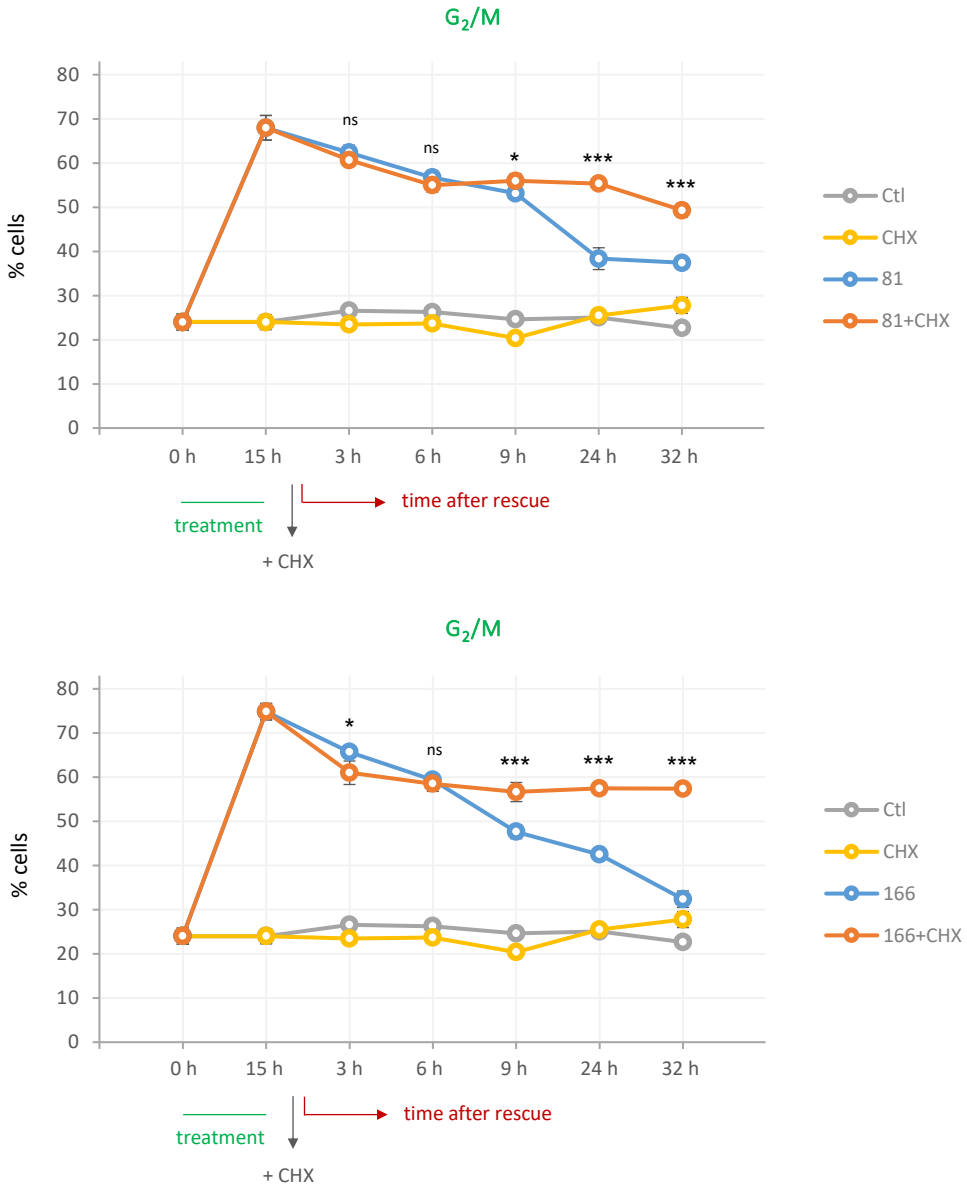

Figure 98. Percentages of HeLa cells in the G_2/M region. Cells were incubated with **81** and **166** at 100 nM for 15 h (treatment), then washed three times with PBS and re-seeded in drug-free culture media in the presence or the absence of 75 µM CHX. Samples were collected at the indicated time-points after rescue. The statistical analysis was carried out comparing the percentage of G_2/M in drug+CHX samples (orange) and only-drug samples (blue) (n = 4; * $p < 0.05$; *** $p < 0.001$).

The gradual decrease in the G_2/M population after removing **81** and **166** (blue curves) was not observed when adding CHX to the culture media (orange curves). There was an initial slight reduction in the percentage of cells in G_2/M that remained constant over time, suggesting that the abrogation of the mitotic arrest is at least in part dependent on the synthesis of proteins. We decided to let the cells grow for longer than 32 h after rescue to evaluate whether the attenuated recovery was a delay or an actual blockage in mitosis in the absence of protein synthesis. However, cells should not be exposed to CHX for longer than 24 h to avoid effects on viability due to CHX rather than the tested conditions. Because of that, we conducted the same experiment in HeLa cells overexpressing Bcl-xL and Bcl-2 by gene transfer that partially protects cells from apoptosis (Fig. 99).

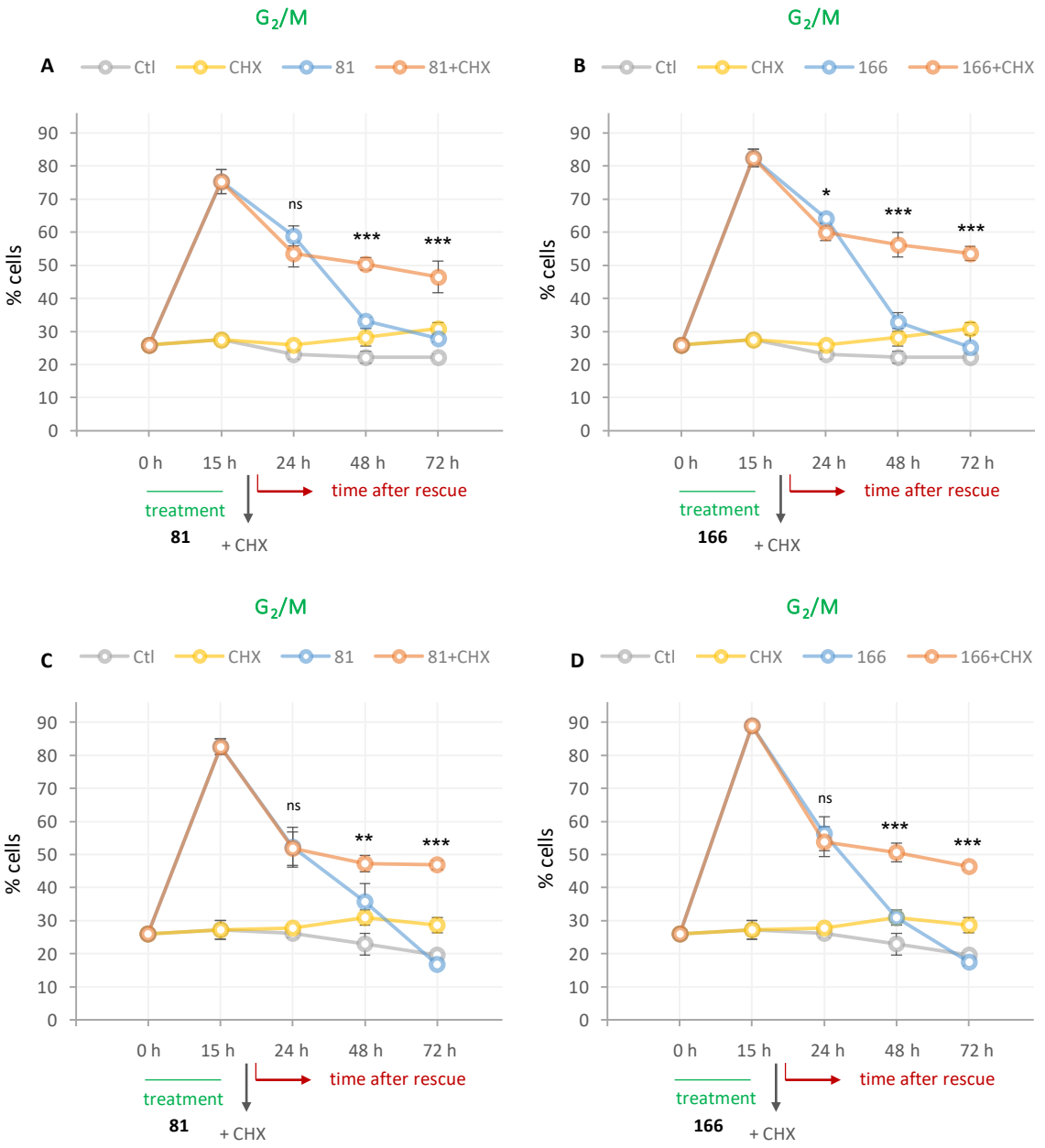

Figure 99. Percentages of HeLa Bcl-xL (**A** and **B**) and HeLa Bcl-2 (**C** and **D**) in G_2/M. Cells were incubated with **81** (**A** and **C**) and **166** (**B** and **D**) at 100 nM for 15 h (treatment), then washed and seeded with or without 75 µM CHX. Samples were collected at the indicated time-points after rescue. The statistical analysis was carried out comparing G_2/M in drug+CHX (orange) samples and only-drug samples (blue) (n = 4; * p < 0.05; ** p < 0.01; * p < 0.001).

After a 15-h incubation with **81** and **166** followed by drug removal, cells were re-seeded, and the cell cycle evolution was monitored 24 h, 48 h, and 72 h after the rescue. As depicted in Figure 99, transfected HeLa cells were not able to recover from the mitotic arrest in the presence of CHX, similar to the results obtained in wild type cells.

The reversible mitotic arrest was confirmed by immunoblotting when probing for MPM-2. There was a dramatic increase of mitotic proteins after 15-h incubation with **81** and **166**, as already demonstrated, that progressively decayed early after rescue. The signal detected 3 h after removing the treatments was lower than that at the 15-h time-point, reaching similar levels to those of untreated samples 24 h after drug removal (Fig. 100). The analysis of several other proteins revealed clear changes in the phosphorylation rate of Bcl-2. Phospho-Bcl-2 showed enhanced levels after 15-h treatment than control conditions with a gradual decrease to normal levels at around 24-48 h after rescue, with no modification of Bcl-2 expression (Fig. 100).

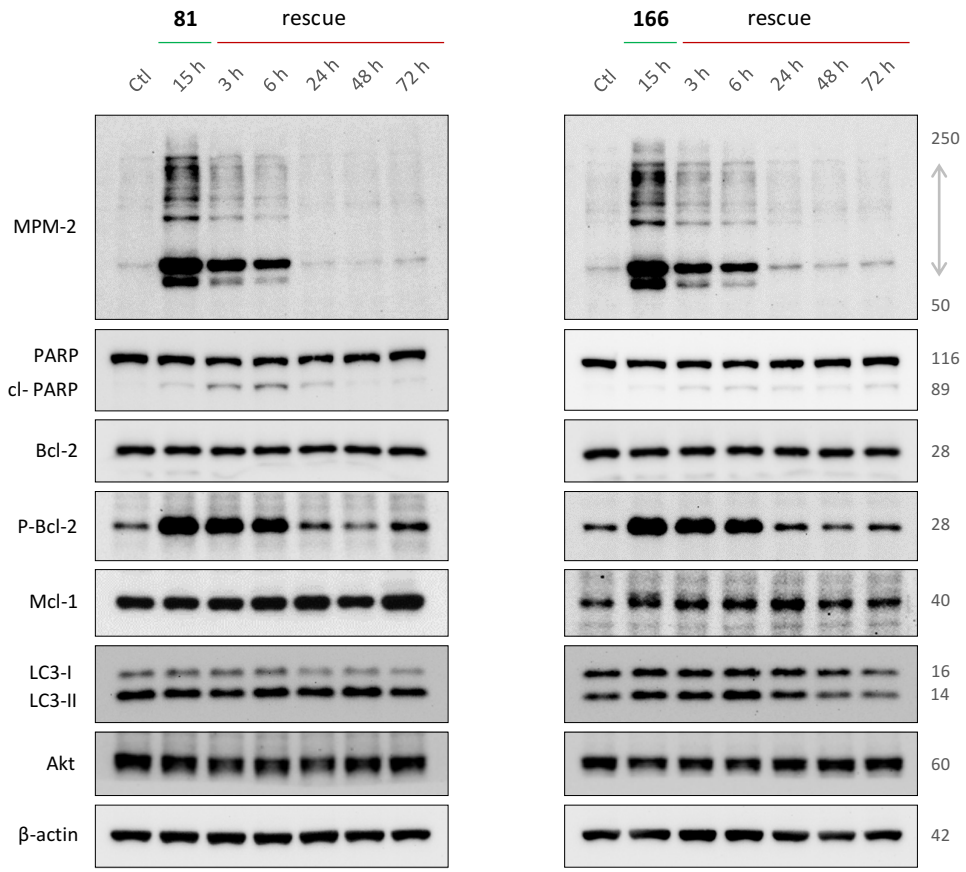

Figure 100. Immunoblots of HeLa cell lysates: cells were incubated in the absence (Ctl) or the presence of **81** and **166** at 100 nM for 15 h. The compounds were subsequently removed and the cells were plated on drug-free culture media, monitoring the time after rescue since that moment. β-actin was used as a loading control. Molecular weights are indicated in kDa. Western blot images are representative of two independent experiments.

In view of the mitochondrial changes observed upon rescue from 15-h treatments, we decided to study whether the increase of the transmembrane potential could protect the cells when challenged with the compounds in an additional treatment cycle, or on the contrary, whether cells are sensitized. To this purpose, the experiments were designed as depicted in Figure 101. HeLa cells were incubated in the absence or the presence of compounds **81** and **166** at 100 nM for 15 h, and subsequently washed three times with PBS to remove the treatments (1st cycle). Cells were re-seeded in drug-free culture media and grew for 48 h so that the mitotic arrest is completely alleviated (rescue). After that period, compounds **81** and **166** were added again at the same concentration (2nd cycle), monitoring the percentage of cells in the $SubG_0/G_1$ region as an apoptosis indicator and the percentage of cells that are permeable to PI.

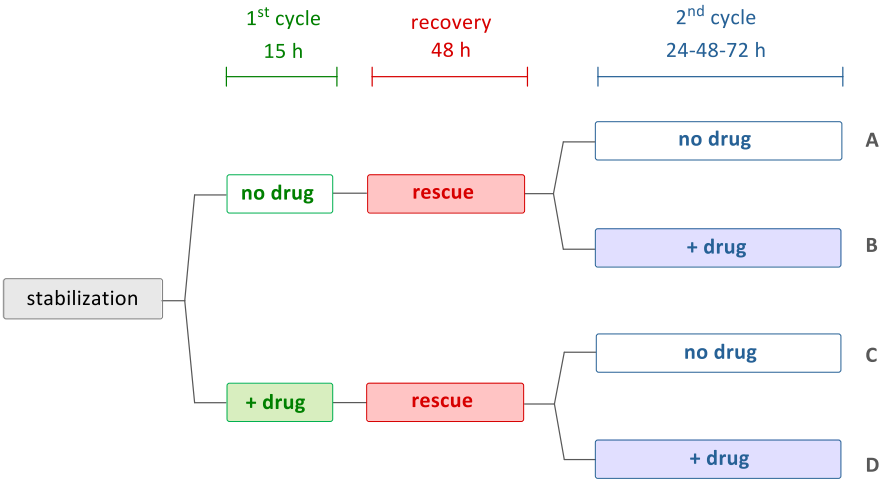

Figure 101. Experimental design to study the effect of a second cycle of treatment in HeLa cells previously treated and recovered from 15-h incubation with the compounds. We compared four conditions. **A.** Control: HeLa cells cultured in the absence of drugs, only subjected to the washing process (rescue). **B.** HeLa cells subjected to the washing process and then treated with **81** or **166** (rescue + 2nd cycle). **C.** HeLa cells incubated for 15 h with **81** or **166**, then washed and cultured in drug-free media (1st cycle + rescue). **D.** HeLa cells incubated for 15 h with **81** or **166**, then washed and re-seeded. After 48 h, **81** was added to cells previously treated with **81**, and **166** to cells previously treated with **166**, harvesting samples 24 h, 48 h, and 72 h after adding the drugs for the second time (1st cycle + rescue + 2nd cycle).

The exposure of HeLa cells to 15-h treatments with **81** and **166** led to a statistically significant increase in DNA degradation and membrane permeabilization (Fig. 102). After removing the drugs from the culture media letting the cells grow for 48 h, those differences decreased, considered to be not statistically significant in the case of the percentage of $SubG_0/G_1$. The number of permeable cells to PI was steadily higher than untreated cells, even though the cell cycle recovery was complete (blue curves). By comparing the cells exposed to the 1st and the 2nd cycles of treatment (Fig. 101: D, Fig. 102: orange curves) with those only exposed to the 2nd cycle (Fig. 101: B, Fig. 102: yellow curves), we observed a significant increase in apoptosis and PI uptake in cells that had been preincubated with the drugs with respect to those treated with the compounds for the first time. These observations pointed out that, although the cells treated for 15 h with the compounds are able to fully recover from the cell cycle arrest with hardly cell death, they turn more sensitive to a second cycle of treatment, indicating that the increase in mitochondrial transmembrane potential is not related to resistance to the treatment.

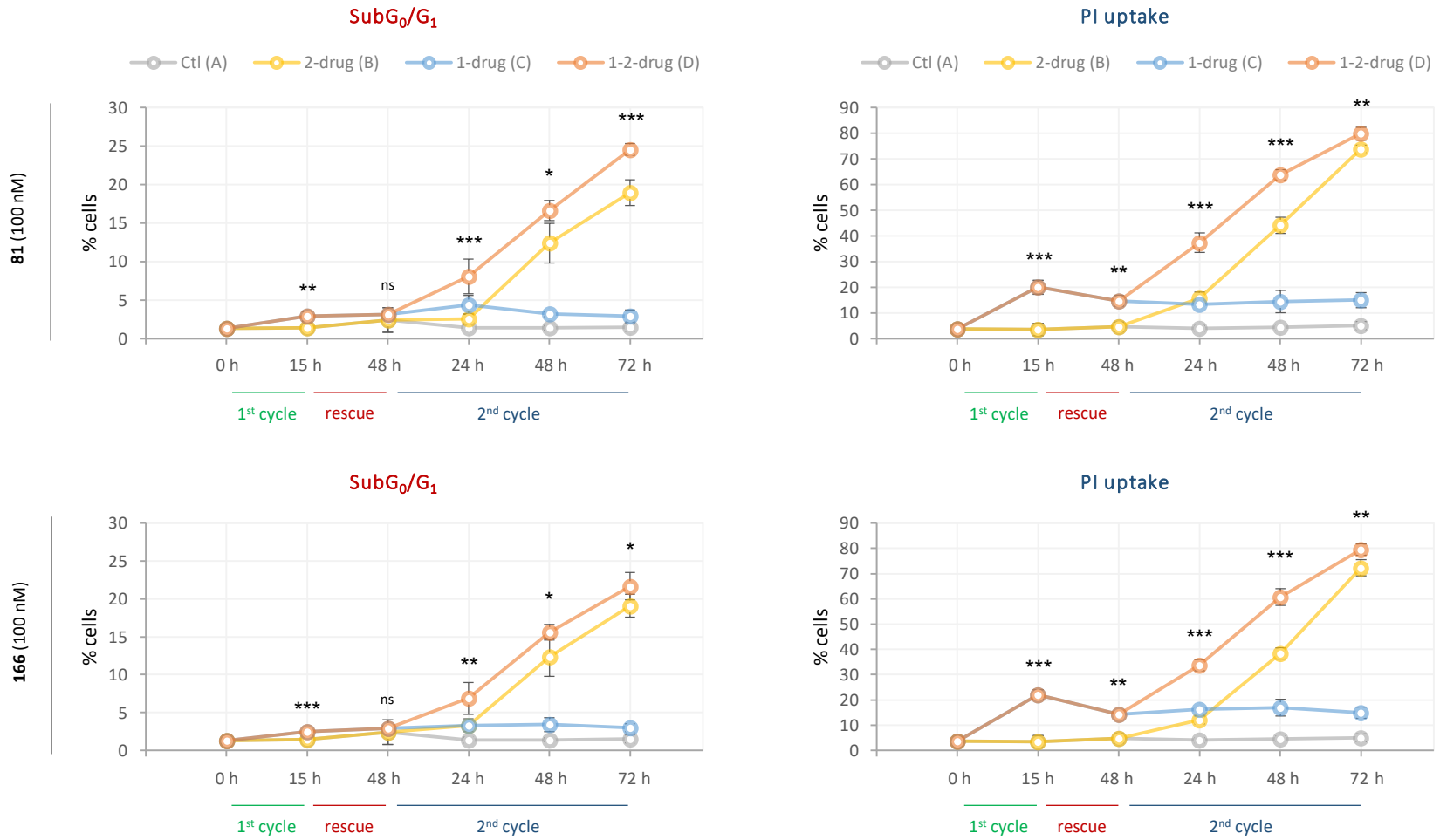

Figure 102. Percentages of HeLa cells in the **SubG$_0$/G$_1$** region (left) and **permeable to PI** (right). Cells were incubated with **81** (top) and **166** (bottom) at 100 nM for 15 h (1st cycle, see Fig. 101), then washed and grown for 48 h (rescue). After that period, the drugs were added to the cells (2nd cycle), monitoring the evolution for 24-72 h. The statistical analysis was carried out comparing 1-drug (B, yellow curves) with 1-2-drug (D, orange curves) (n = 6; * $p < 0.05$; ** $p < 0.01$; * $p < 0.001$).

EFFECT OF THE LEAD COMPOUNDS IN OTHER CELL LINES

The overall sensitivity of the cell lines tested in the proliferation assay was somewhat similar. However, the antiproliferative activity of the compounds does not necessarily translate into cell death in all the cell lines, since distinct outcomes may result from the treatments. We selected the human non-tumorigenic cell lines HEK-293 from embryonic kidney (Fig. 103) and HPNE from pancreas duct (Fig. 104) to evaluate the mitotic arrest of the lead compounds at the same working concentrations used against HeLa cells.

The lead compounds caused a rapid mitotic arrest in HEK-293 cells after 9 h, reaching the maximum percentage of cells in the G_2/M region after 15-24 h (Fig. 103). However, the treatment with compound **104** exhibited a similar effect to that observed in HeLa cells, showing a decrease in the G_2/M population (85.5% at 9 h versus 78.4% at 15 h, $p < 0.05$) at time-points when the mitotic arrest keeps on increasing after treatment with the other five compounds (9-24 h). The percentage of cells in the G_0/G_1 phase increased considerably from 9 h to 15 h after treatment (5.4% at 9 h versus 14.1% at 15 h, $p < 0.001$) with a minor, although statistically significant, increase in the $SubG_0/G_1$ region (2.1% at 9 h versus 3.7% at 15 h, $p < 0.01$). The G_0/G_1 increase accounts for the reduction of the G_2/M peak, suggesting that some cells can bypass the mitotic arrest and reenter the diploid cell cycle. The apoptotic cell death was attenuated compared to HeLa cells; the extent of the $SubG_0/G_1$ population of HEK-293 cells after 7 days of treatment (20.8-31.6%) was similar or even lower than the effect of 72-h treatments in HeLa cells (24.7-36.6%).

The pace at which HPNE cells got arrested in mitosis was much slower than HeLa and HEK-293 cells (Fig. 104). The maximum percentage of cells in G_2/M was only observed 72 h or 4 days after adding the drugs. HPNE experienced a strikingly reduced apoptosis rate compared to HeLa and HEK-293 cells, even at longer incubation periods. Only 2.9-8.3% of the cells underwent DNA fragmentation after 7 days of treatment. Compound **104** caused neither mitotic arrest nor apoptosis in HPNE cells at 100 nM. The percentage of cells in G_2/M decreased over time after 48 h-7 days of treatment with **104**, but also it occurred in untreated cells. When added at 1 µM instead of 100 nM, it did induce mitotic arrest similar to the other five compounds (see Appendix Fig. VII), indicating that the lack of effect at 100 nM is due to the lower potency of **104** in HPNE cells compared to HeLa cells. The mitotic arrest induced after treatment with the lead compounds was assessed by confocal microscopy in HEK-293 and HPNE cells after 24-h treatments (Fig. 105 and 106), showing disruption of the tubulin cytoskeleton, except in the case of **104** at 100 nM.

In order to study whether the capacity of the cells to recover from the mitotic arrest depends on how advanced apoptosis is, we conducted a reversibility experiment in HEK-293 cells that experienced cell death to a lesser extent than HeLa cells. The cells were incubated with the lead compounds for 9 h, 15 h, 24 h, 48 h, and 72 h. The drugs were subsequently washed out from the media, and the cells were grown for 48 h, considered as the period required for a total recovery in HeLa cells (Fig. 107). The mitotic arrest was totally alleviated after incubation periods of 9 h and 15 h with the drugs. Removing the compounds after 24-h treatments led to a partial decrease of the G_2/M population at the expense of a G_0/G_1 increase, together with a moderate rise in the $SubG_0/G_1$ region. However, the effect induced by 48- and 72-h treatments could not be reverted when removing the ligands. Around 15.2-21.6% of HeLa cells exhibited DNA fragmentation after 48-h treatments versus 2.7-7.2% in HEK-293 cells at the same time-point (16.8% after treatment with **104**). Cell death in HEK-293 after 48 h (non-reversible arrest) was similar to that observed in HeLa cells after 15-24 h (reversible arrest), suggesting that the lack of apoptosis does not necessarily translate into a recovery when removing the compounds. HPNE cells barely showed apoptosis when treated with the compounds for 7 days, but the arrest could not be reverted (see Appendix Fig. VII).

Figure 103. Analysis of cell cycle populations (**SubG$_0$/G$_1$**, **G$_0$/G$_1$**, **S**, and **G$_2$/M**) in HEK-293 cells after treatment with the lead compounds at the indicated concentrations. The statistical analysis was carried out for the data relative to the G$_2$/M population with respect to untreated samples (Ctl) after the same incubation period (n = 4-11; *** p < 0.001).

Figure 104. Analysis of cell cycle populations (**SubG$_0$/G$_1$**, **G$_0$/G$_1$**, **S**, and **G$_2$/M**) in HPNE cells after treatment with the lead compounds at the indicated concentrations. The statistical analysis was carried out for the data relative to the G$_2$/M population with respect to untreated samples (Ctl) after the same incubation period (n = 6-12; * $p < 0.05$; ** $p < 0.01$; *** $p < 0.001$).

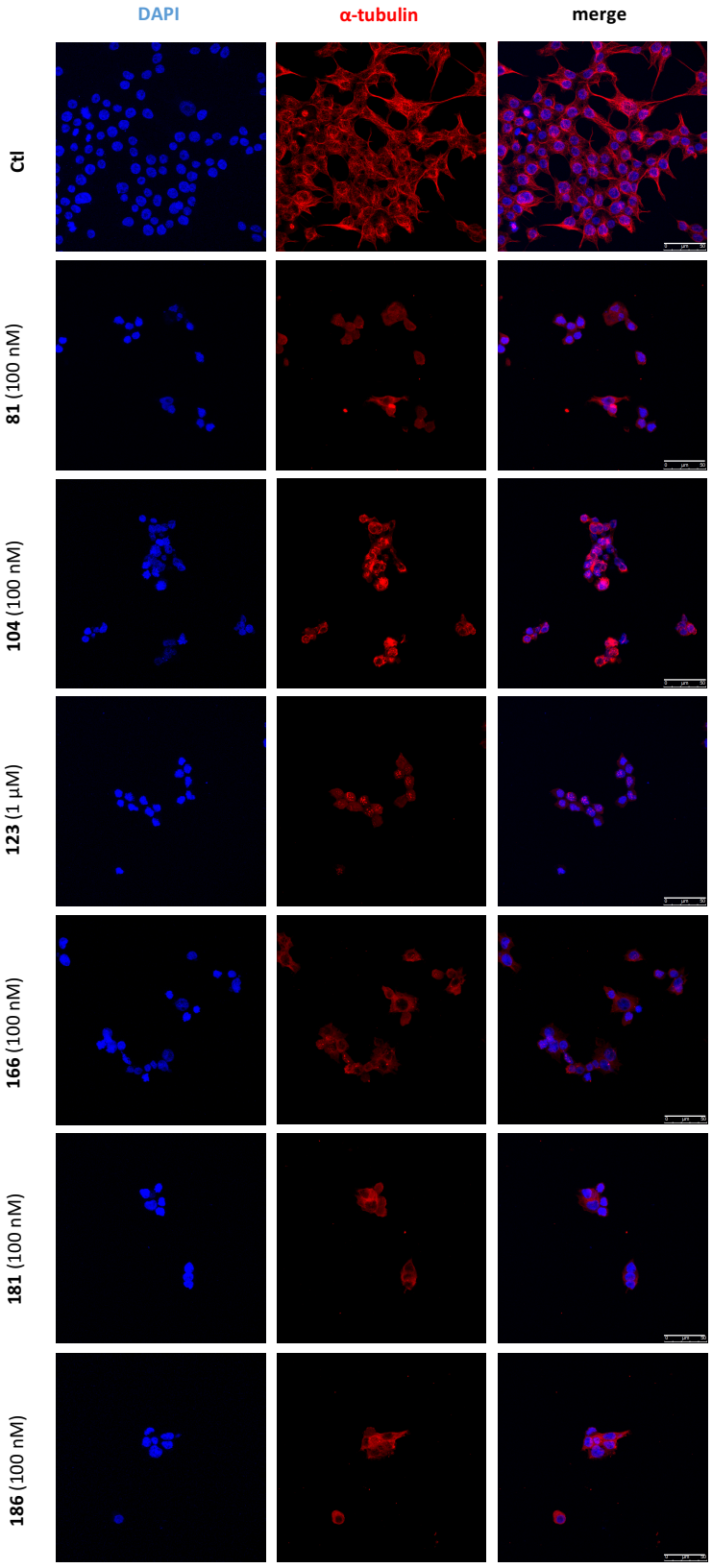

Figure 105. Confocal immunofluorescence microscopy of HEK-293 cells for visualization of the microtubule network. Cells were incubated in the absence (Ctl) or the presence of the lead compounds at the indicated concentrations for 24 h. **Nuclei** were stained with DAPI in blue fluorescence and **α-tubulin** was visualized in red fluorescence (CY3-conjugated Ab-2). Scale bar: 50 µm. Photomicrographs are representative of two independent experiments.

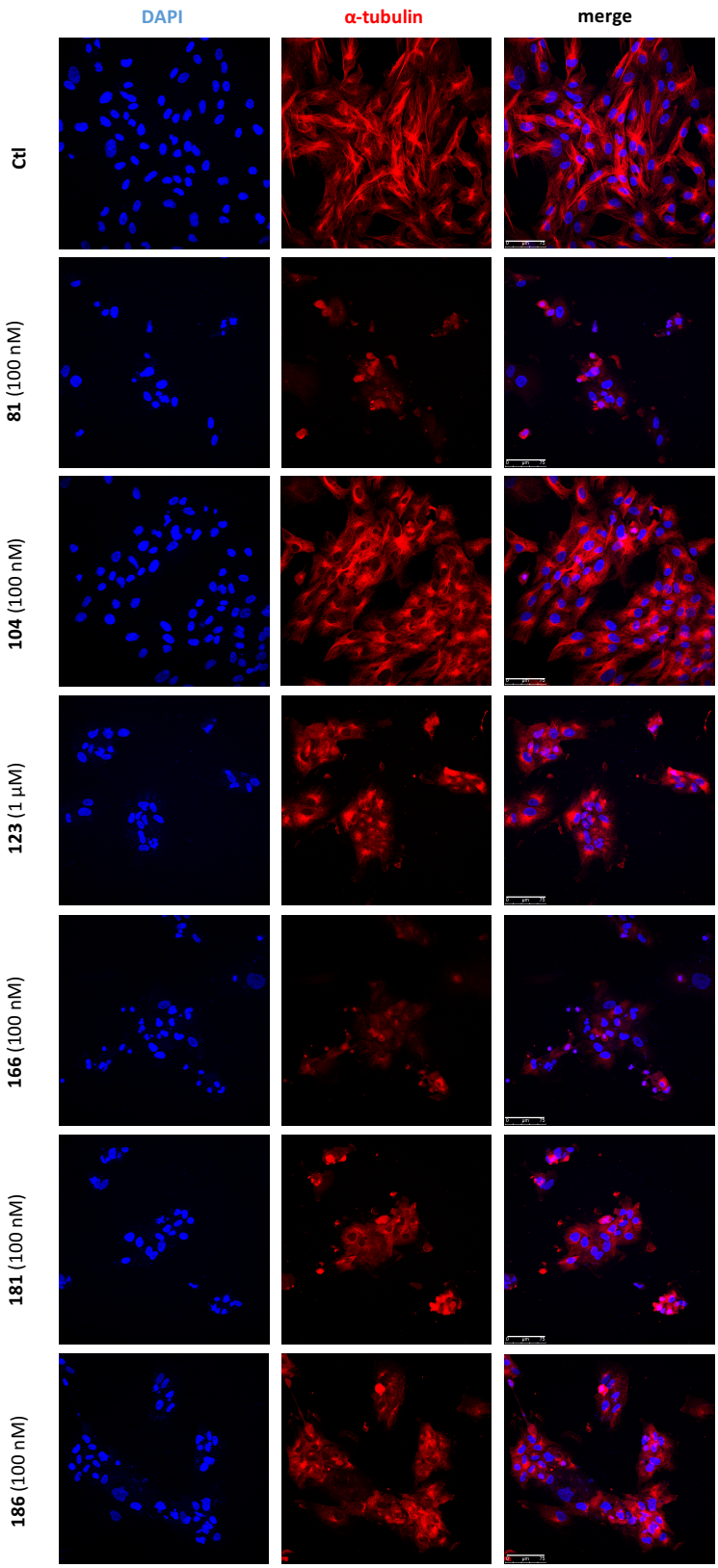

Figure 106. Confocal immunofluorescence microscopy of HPNE cells for visualization of the microtubule network. Cells were incubated in the absence (Ctl) or the presence of the lead compounds at the indicated concentrations for 24 h. **Nuclei** were stained with DAPI in blue fluorescence and **α-tubulin** was visualized in red fluorescence (CY3-conjugated Ab-2). Scale bar: 75 µm. Photomicrographs are representative of two independent experiments.

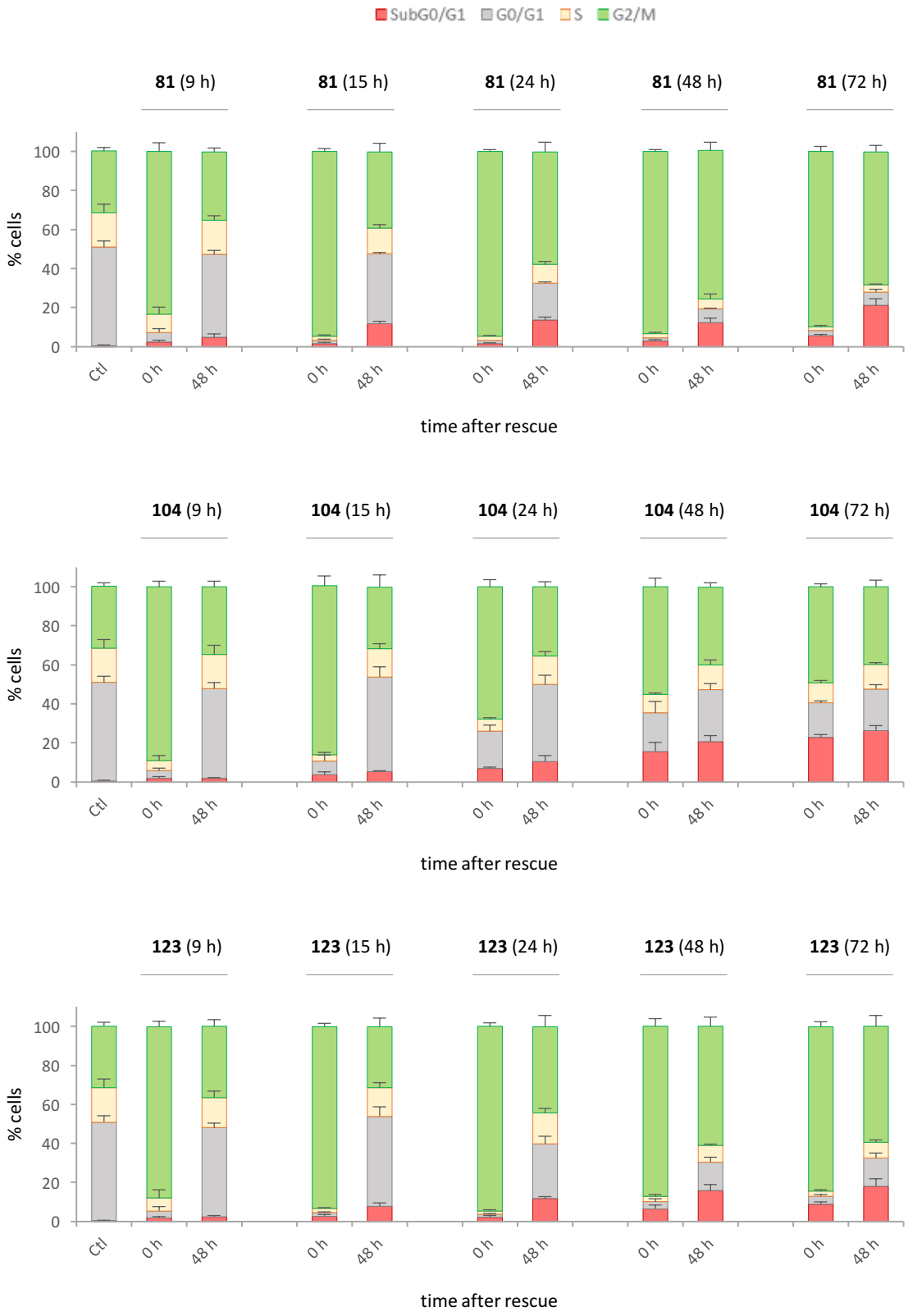

Figure 107. Continued

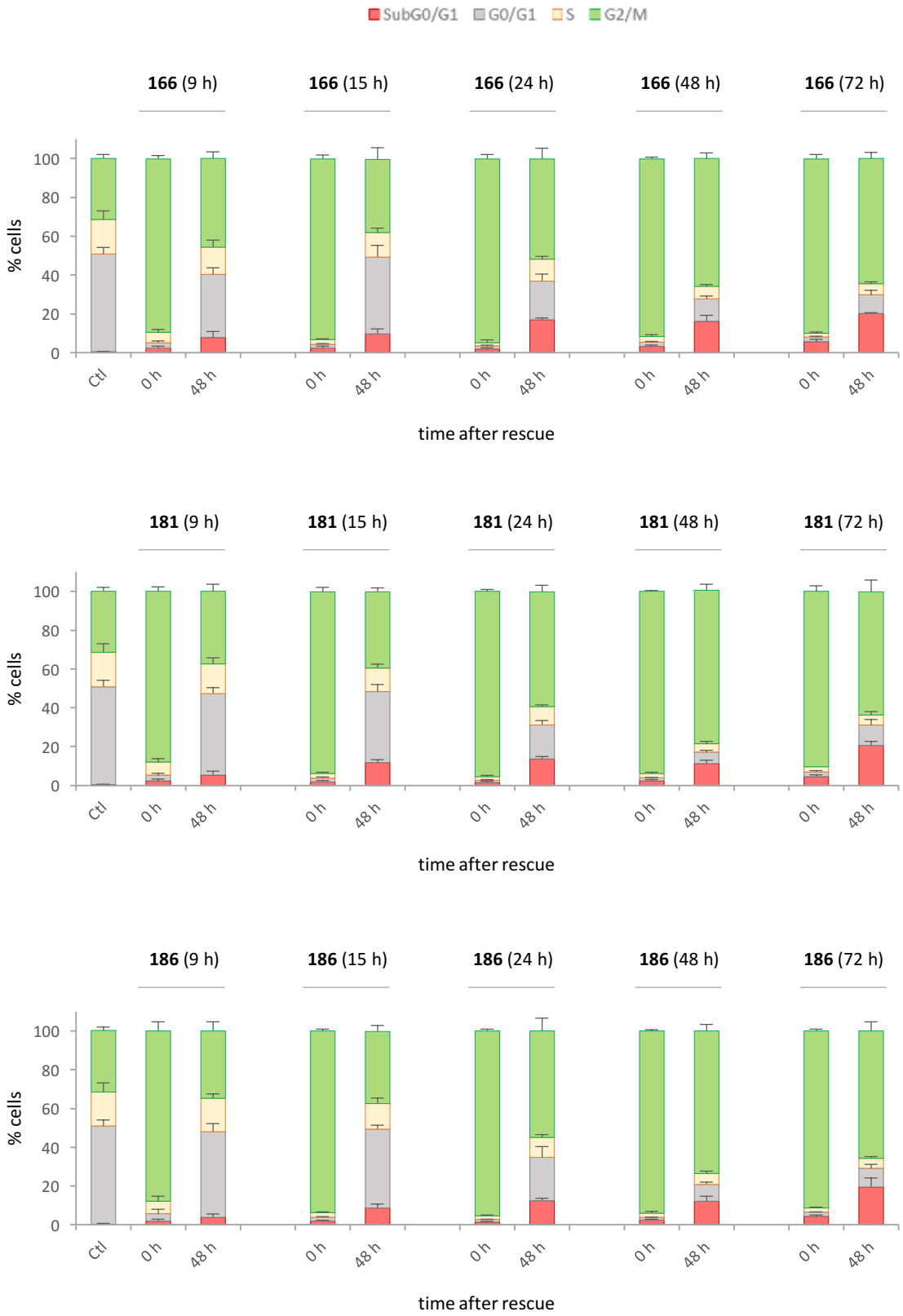

Figure 107. Analysis of cell cycle populations (**SubG$_0$/G$_1$**, **G$_0$/G$_1$**, **S**, and **G$_2$/M**) in HEK-293 cells after treatment with the lead compounds for 9 h, 15 h, 24 h, 48 h, or 72 h (0 h after rescue) at 100 nM or 1 µM in the case of **123**. Then, cells were harvested, washed three times with PBS and plated in drug-free culture media. Samples were collected 48 h after the rescue (*n* = 5).

Given the scarce cell death induced with the lead compounds in HPNE cells, we tested the effect of different tubulin binding drugs and staurosporine after 72 h (Fig. 108). After treatment with staurosporine (Fig. 108B), 34.9% of HPNE cells showed DNA fragmentation. However, the treatment with the tubulin binding drugs paclitaxel, colchicine, nocodazole, and vincristine (Fig. 108C-F) led to 0.8-7.3% of cells in the $SubG_0/G_1$ region, together with mitotic arrest. The scarce apoptosis induced by TBDs was similar to the effect of **81** and **166**, even at higher concentrations than the standard 100 nM (Fig. 108G-J). The fact that staurosporine and the lead compounds caused cell death in HeLa cells but only staurosporine led to apoptosis in HPNE cells suggests that different cell lines may undergo different outcomes after treatment with microtubule interfering agents.

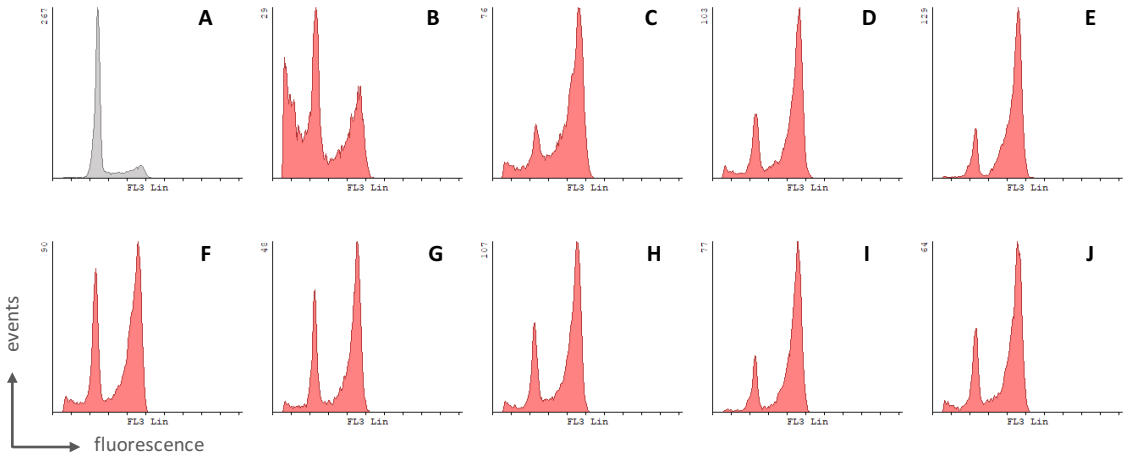

Figure 108. Cell cycle histograms of HPNE cells in the absence of treatment (panel **A**, grey histogram, Ctl) or after 72-h incubation (panels **B**-**J**, red histograms) with the following compounds. **B.** 0.5 µM staurosporine. **C.** 1 µM paclitaxel. **D.** 1 µM colchicine. **E.** 1 µM nocodazole. **F.** 1 µM vincristine. **G.** 100 nM **81**. **H.** 1 µM **81**. **I.** 100 nM **166**. **J.** 1 µM **166**. Flow cytometry profiles are representative of three independent experiments.

We conducted time-course experiments in tumor versus non-tumorigenic cell lines by treatment with the lead compounds for 9 h, 15 h, 24 h, 48 h, and 72 h, analyzing the percentage of cells in the $SubG_0/G_1$ region (Fig. 109A) and the percentage of PI-positive cells (Fig. 109B) in parallel. We used the human tumor cell lines HeLa (cervix adenocarcinoma), AGS and SNU-1 (gastric adenocarcinoma), MIA PaCa-2 (pancreatic carcinoma), U2OS (osteosarcoma), and Huh-7 (hepatocellular carcinoma). Besides the human non-tumorigenic cell lines HEK-293 and HPNE, we evaluated the effect in hamster fibroblasts BHK and mouse fibroblasts L929. As illustrated in Figure 109, the effect of the lead compounds differs between tumor and non-tumorigenic cell lines. The four non-tumorigenic cell lines we tested showed reduced apoptosis compared to tumor cells in general terms, unrelated to a lack of effect since all the compounds induced mitotic arrest in all the cell lines (except **104** that did not affect HPNE cells at 100 nM but at 1 µM). The tumor cell lines U2OS and Huh-7 proved more resistant to the treatments than HeLa, AGS, SNU-1, and MIA PaCa-2 cell lines, especially Huh-7 cells that exhibited $SubG_0/G_1$ and PI uptake profiles similar to those of non-tumorigenic cells upon treatment with the ligands.

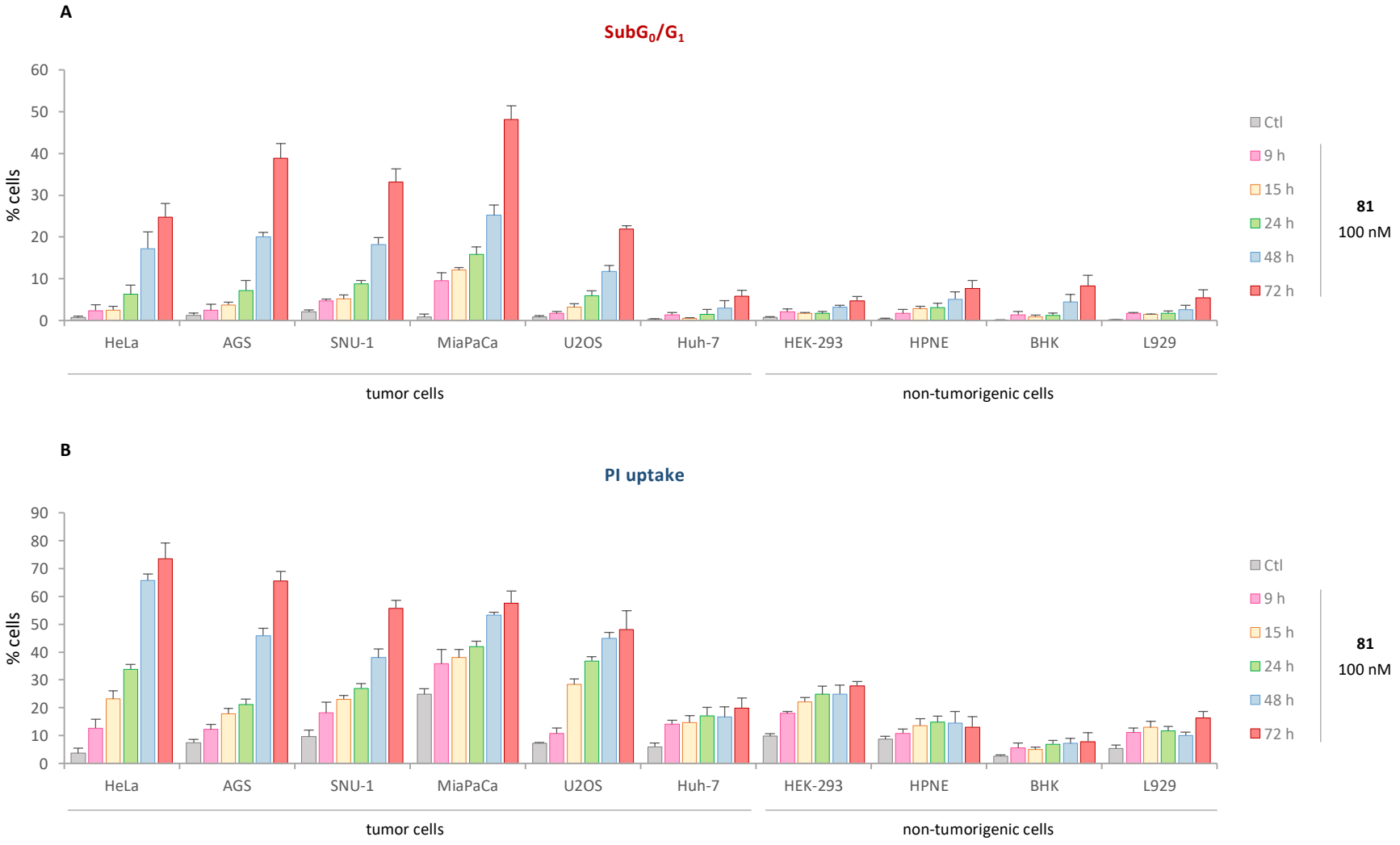

Figure 109. Continued

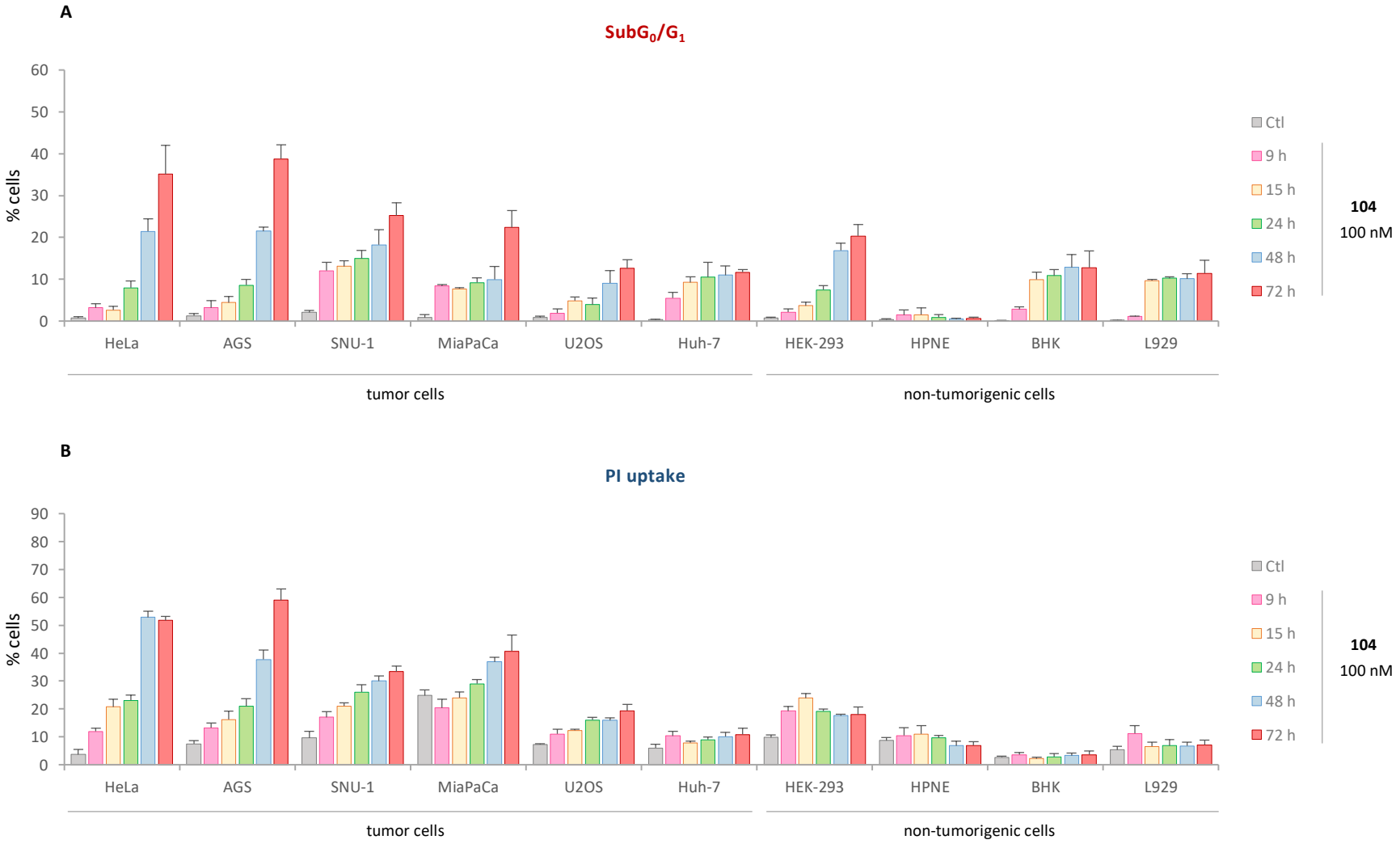

Figure 109. Continued

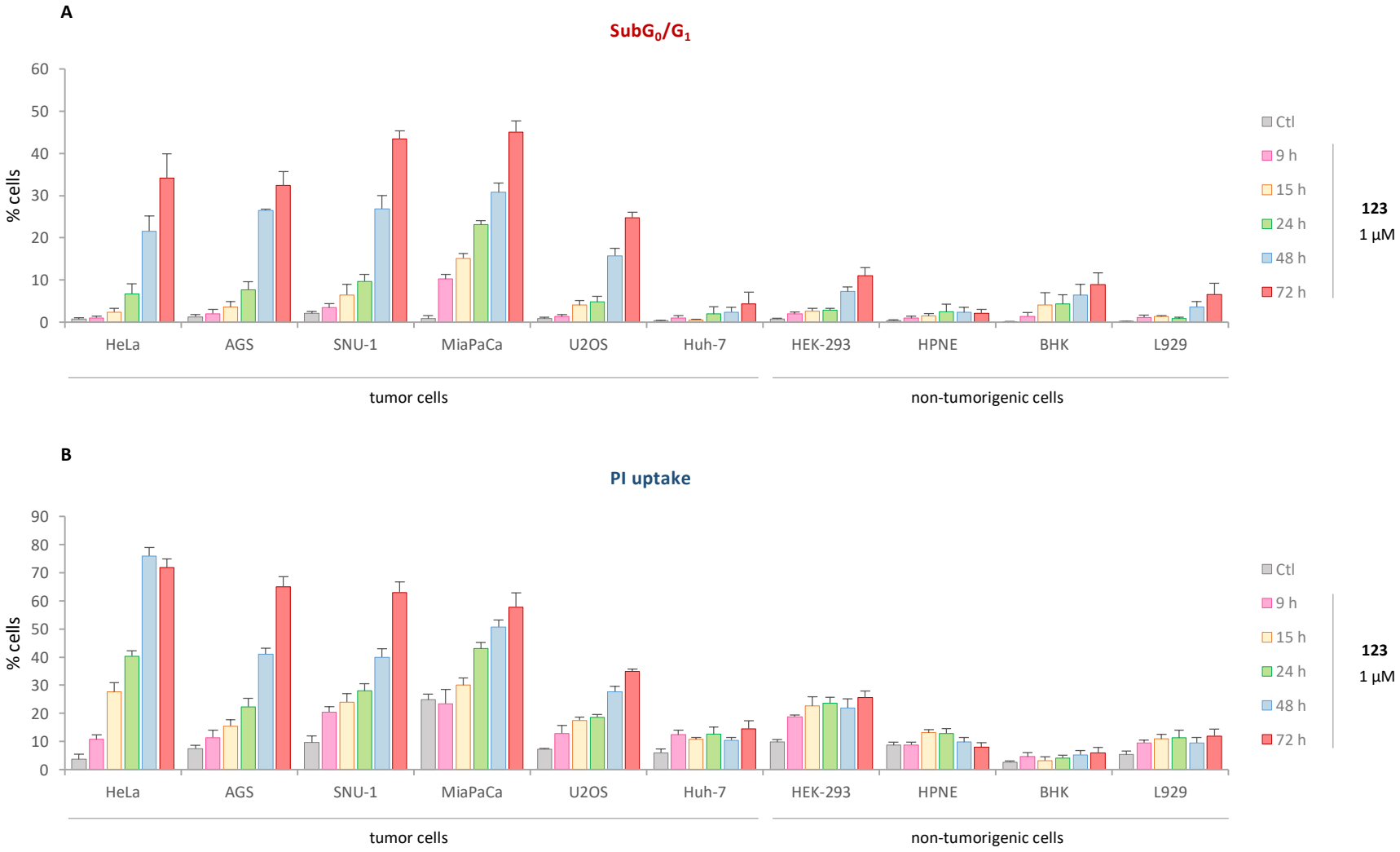

Figure 109. Continued

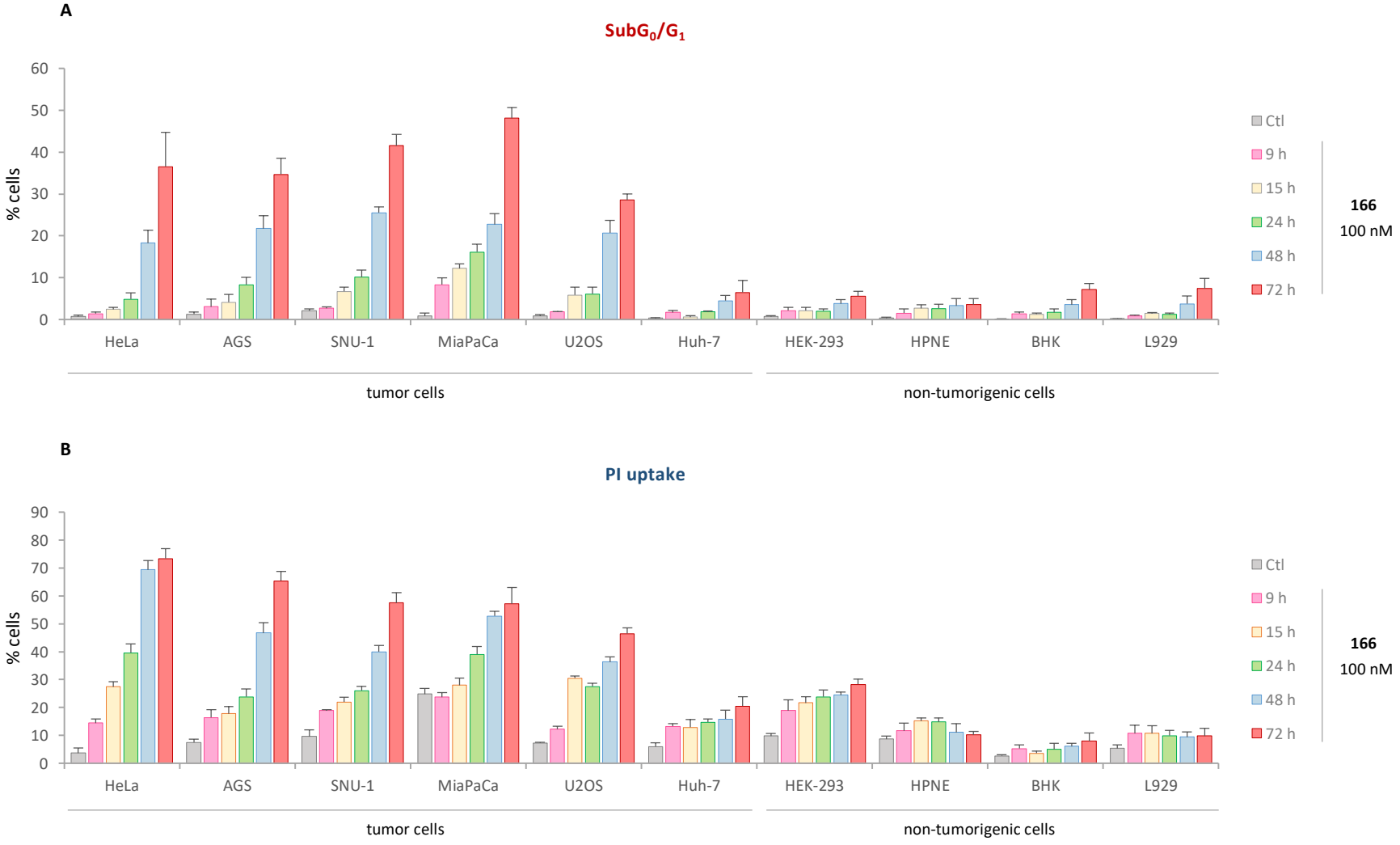

Figure 109. Continued

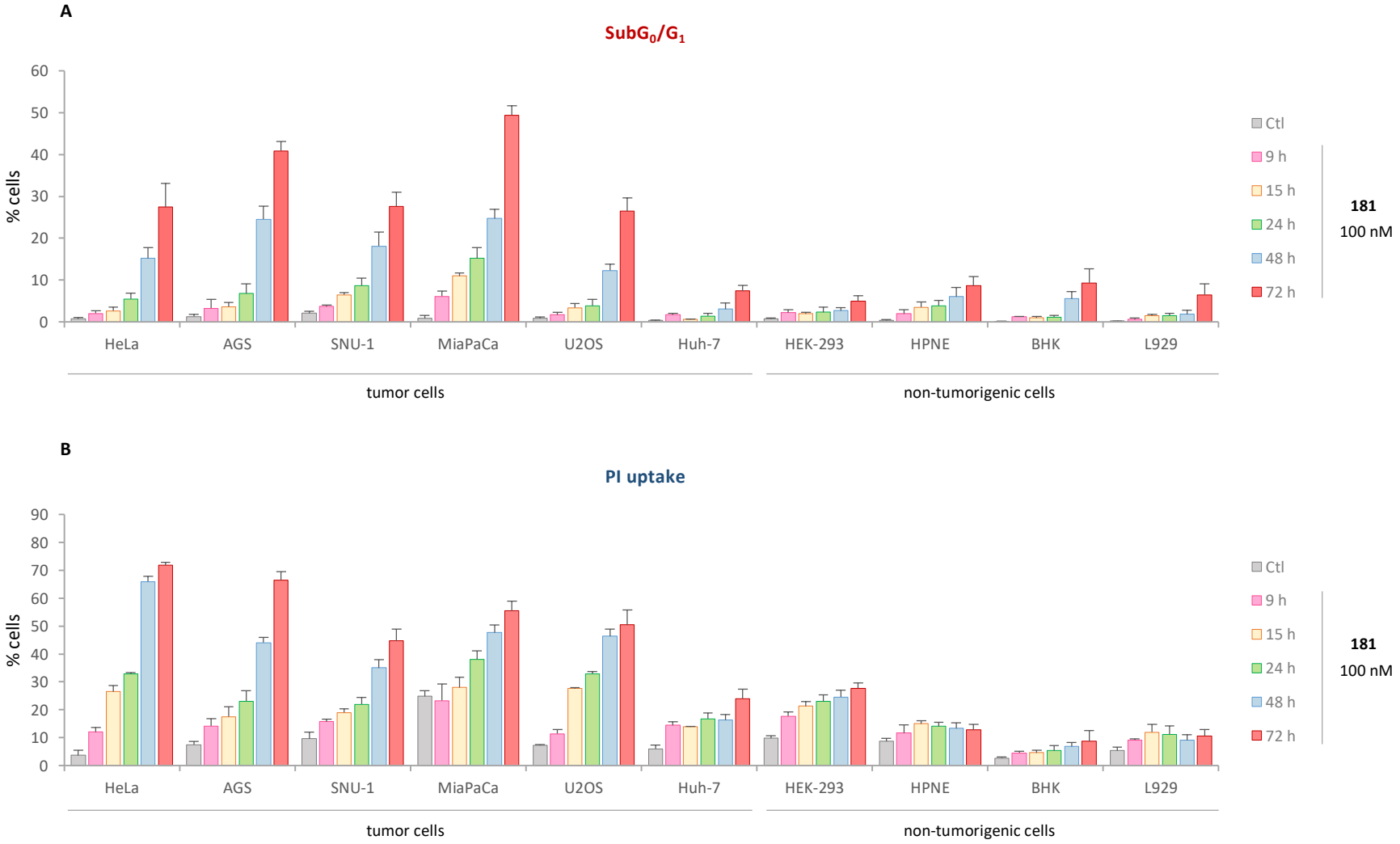

Figure 109. Continued

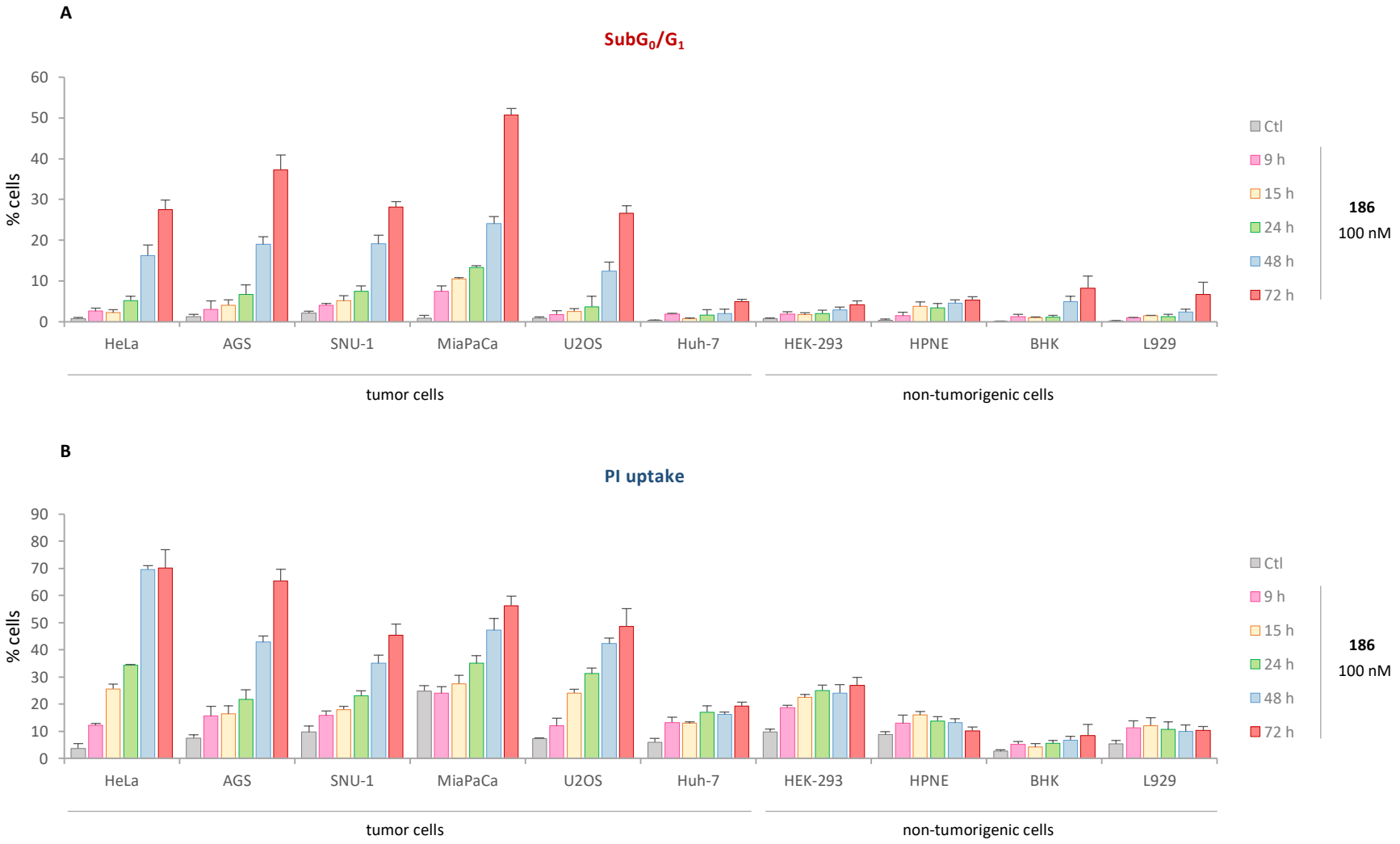

Figure 109. Time-course experiments representing the effect of the lead compounds in tumor cell lines (HeLa, AGS, SNU-1, MIA PaCa-2, U2OS, and Huh-7) and non-tumorigenic cell lines (HEK-293, HPNE, BHK, and L929). **A.** Percentage of cells in the **SubG$_0$/G$_1$** region. **B.** Percentage of **PI-positive cells** (*n* = 3-15).

Chapter 5

DISCUSSION

SULFONAMIDE DERIVATIVES AIMED TO BIND TO ZONES 1-2-3

Given the structural diversity of the few ligands that simultaneously occupy the three zones of the colchicine domain with known binding modes, pursuing an effective interaction with the whole domain is challenging. Taking that into account, we have approached the design of compounds based on the structure of the sulfonamide ABT-751 with changes as minor as possible. The *p*-methoxyphenyl group (B ring) of ABT-751 interacts in zone 1, and the pyridine (A ring) sits in zone 2. The 1,2-substitution pattern of the pyridine moiety directs the third aromatic ring (C ring) towards zone 3 with partial occupation (Fig. 110).

The superimposition of the interacting modes of ABT-751 and nocodazole (see Fig. 29) made us consider a different substitution pattern of the pyridine ring to ease the access to zone 3. We have changed the 1,2-substitution of the A ring in ABT-751 by a 1,3-substitution pattern in pyridine or benzene rings (Fig. 110). Aiming to occupy zone 3 completely, the amino linker of ABT-751 that connects the pyridine and the phenolic ring has been replaced by more extended groups that may confer adaptability to access zone 3. We have introduced hydrogen bond donor substituents on the C ring seeking to increase the antimitotic potency and hydrosolubility. However, the evaluation of the resulting compounds has revealed no effects against cell proliferation at 1 µM concentrations. Unpublished data from our group have shown that compounds with analogous linkers and *o*-phenylenediamine (1,2-substitution) as A ring are also inactive against HeLa cell proliferation at 1 µM.[551] Altogether, this suggests that the occupation of zones 1 and 2 hinders the access to zones 3 due to the geometry conferred by the A ring substitution or the extended linkers.

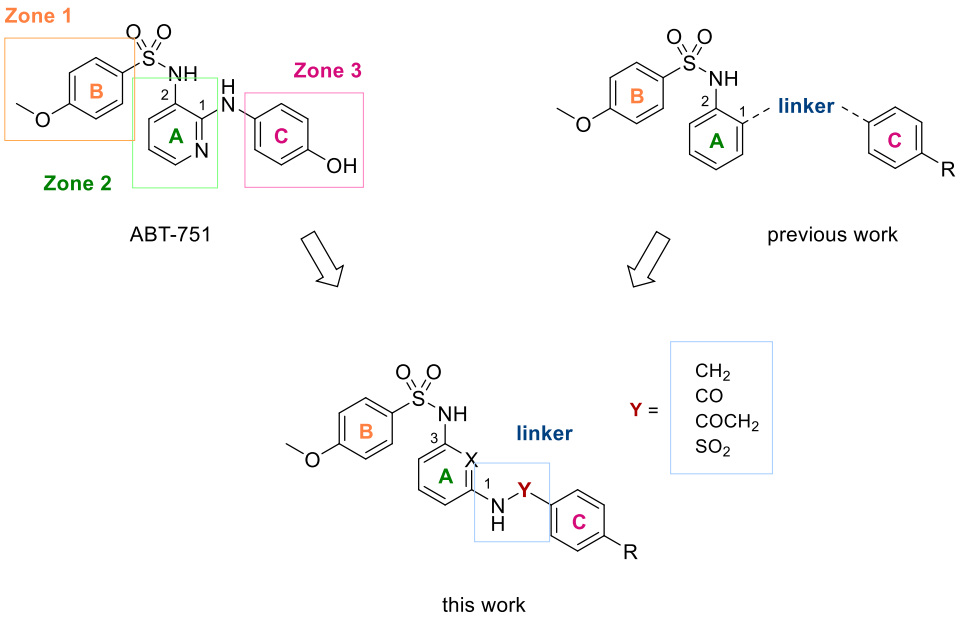

Figure 110. Chemical structure of ABT-751 and general scaffolds of three-ring sulfonamides designed as part of previous work in our group (*o*-phenylenediamine as A ring) and those described in this work (*m*-phenylenediamine or 2,6-diaminopyridine as A rings).

AMIDE AND BENZOTHIAZOLE DERIVATIVES AIMED TO BIND TO ZONES 2-3

We have designed two families of compounds aimed to bind to zones 2 and 3 of the colchicine domain: polymethoxyphenyl amides and benzothiazole derivatives. The first family is based on the chemical structures of CA4 and MI-181 (Fig. 111). CA4 binds to zones 1-2 of the domain, and MI-181 binds to zones 2-3. The superimposition of their binding modes at the interaction pocket shows overlapping between the trimethoxyphenyl of CA4 and the benzothiazole of MI-181 (A rings). Considering this, we have used different polymethoxylated benzenes as A rings, connected to aryl or heteroaryl groups in zone 3 by amide linkers (Fig. 111). Amides show trigonal planar geometry similar to the *trans* olefin of MI-181 and place the residues in zones 2 and 3 in an extended and flattened conformation, which is a common feature among the compounds that bind to these zones of the domain.

None of the synthesized compounds displays antiproliferative activity at 1 µM. Computational and 1D-nOe studies suggest that the least energetic conformations of compounds with a 2-methoxy group (2,3,4-trimethoxy, 2,3-dimethoxy, 2,4-dimethoxy) place the NH group towards the oxygen in an intramolecular hydrogen bond. The methyl carbon of the 2-methoxy group is thus oriented in the opposite direction (Fig. 111). This may result in steric hindrance with the lateral chains in zone 2 of the colchicine domain. However, the removal of the 2-methoxy in reversed amides with 3,4-dimethoxyaniline as A ring does not lead to cytotoxic activity. Since neither benzamides nor *N*-phenyl amides display biological activity, we thought the amide linker might be too short to access zone 3. Its elongation with urea linker, which is also planar, does not provide active compounds either.

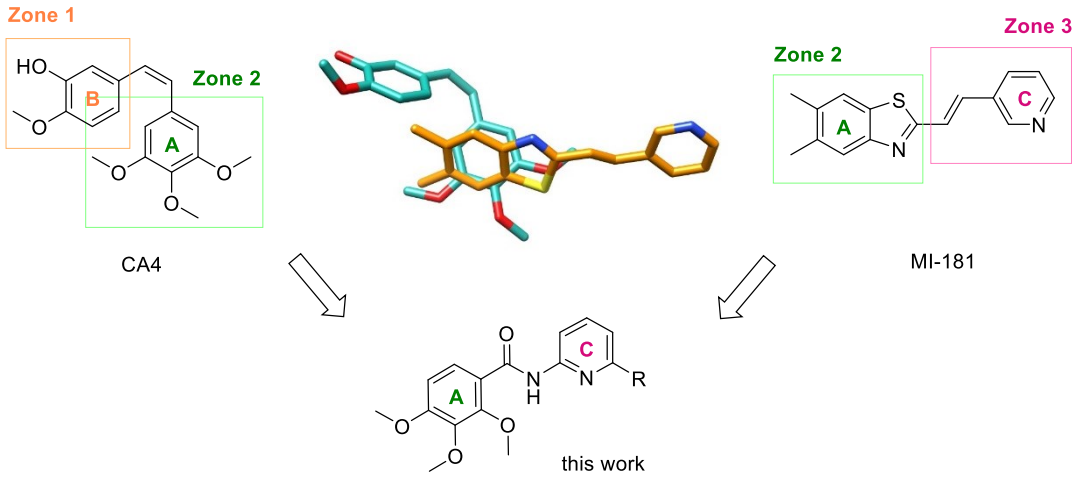

Figure 111. Chemical structures of CA4 and MI-181. Their binding poses in their respective X-ray complexes are superimposed in the middle (CA4 in **blue**, MI-181 in **orange**). The general scaffold of 2,3,4-trimethoxyphenyl amides is shown underneath.

The second family of compounds designed to bind to zones 2 and 3 is based on MI-181. We have conserved the benzothiazole residue as A ring, combined with benzenes or pyridines as C rings. The *trans* olefin connecting A-C rings in MI-181 has been replaced by amides, methylamines, ureas, or carbamates that may establish additional interactions with the side chains of the domain. Similar groups are also present in cyclic diones that bind as the enol tautomers in zones 2 and 3 of the colchicine domain (e.g. TN16, TUB015, plinabulin). The superimposition of benzothiazoles and these diones shows analogous positioning of the NH and carbonyl groups (Fig. 112). Nevertheless, our results have revealed that benzothiazole derivatives do not display *in vitro* antiproliferative activity at 1 µM (only **270** in HeLa cells).

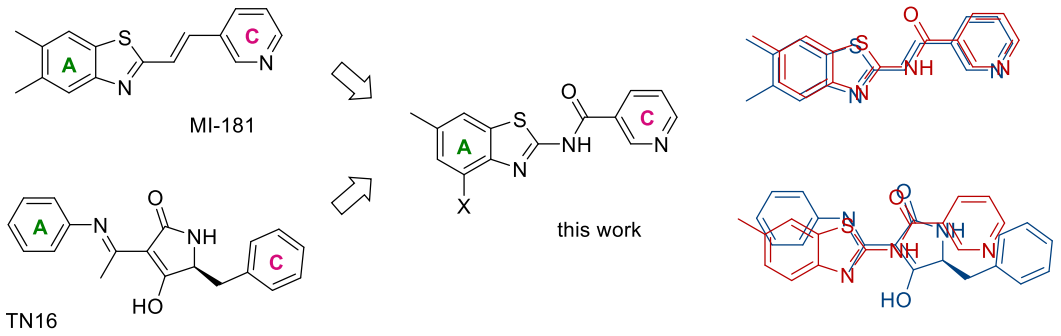

Figure 112. Chemical structures of MI-181 and TN16. Their superimposition in 2D with a representative benzothiazole of this work is depicted on the right: benzothiazole-amide in **red**, MI-181 and TN16 in **blue**.

MI-181 binds with the two aromatic rings in the same plane due to the *trans* olefin conjugation with both benzothiazole and pyridine rings (Fig. 113). Amides are also conjugated with the benzothiazole and adopt a similar geometry to olefins. However, the preferred conformation of MI-181 modified with an amide group (-NHCO-) instead of olefin places the pyridine ring 32° tilted compared to the amide plane (Fig. 113). This angle is even higher in the case of methylamines because of the tetrahedral geometry of the sp^3 carbon. The replacement of the *trans* olefin by an amide group (-NHCO-) impedes the effective interaction at the colchicine domain. Although we cannot rule out that the reversed amide orientation (-CONH-) may result in active ligands, computational analyses suggest a different disposition of the pyridine ring. The aromatic rings are coplanar in the least energetic conformation with the amide hydrogen near the benzothiazole nitrogen, resulting in different spatial occupation than MI-181 (Fig. 113).

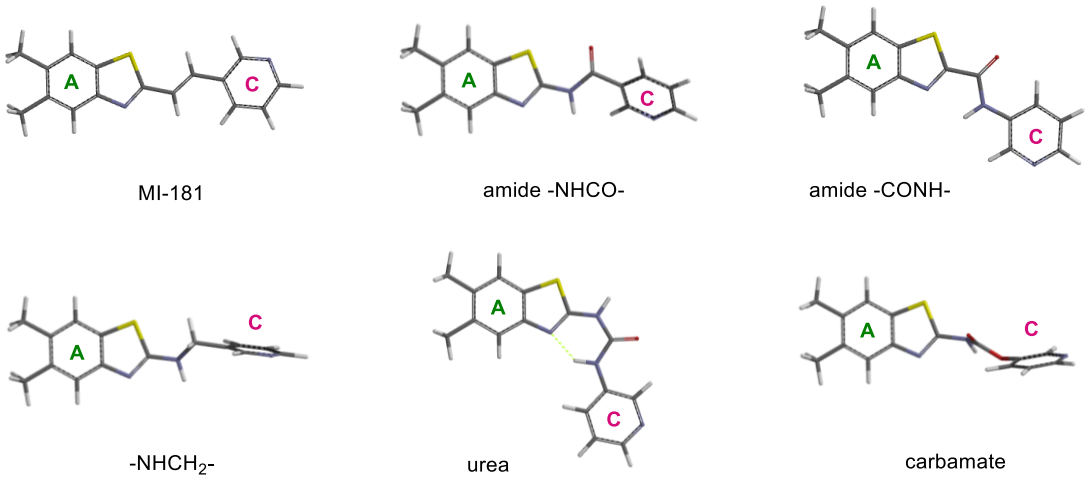

Figure 113. Conformational effects of the replacement of the *trans* olefin in MI-181 by amide, methylamine, urea, and carbamate. Compounds with amides -CONH- have not been prepared in this work.

Ureas and carbamates are one-atom longer than amides. Ureas are also planar but adopt a *cisoid* conformation to establish an intramolecular hydrogen bond between the furthest NH group and the nitrogen of the benzothiazole (Fig. 113), which harbors the highest electron density within the ring. This results in a non-extended disposition or the aromatic rings that might explain the lack of biological activity. The replacement of the amino group in ureas by oxygen in carbamates leads to an elongated conformation that places the aromatic rings in different planes due to the carbamate geometry (Fig. 113).

SULFONAMIDE AND TETRAZOLE DERIVATIVES AIMED TO BIND TO ZONES 1-2

Structure activity relationship and conformational studies

Among the colchicine site ligands, combretastatins have served as model scaffolds for the design of many compounds with ameliorated properties, especially combretastatin A4. One of the colchicine domain requirements for an adequate accommodation of ligands in zones 1 and 2 is a *cisoid* disposition of the aromatic rings. In the case of CA4, this disposition is achieved by the *cis* configuration of the olefin bridge (Fig. 116). However, CA4 shows several liabilities related to its chemical structure, which limit clinical success. The first one belongs to the nature of that bridge. The *cis* olefin readily isomerizes into the thermodynamically more stable *trans* isomer with a dramatic drop in the cytotoxic activity.[152] The second drawback is the low aqueous solubility, tackled by the formulation of highly soluble prodrugs on the phenolic ring of CA4. The hydroxyl group that serves as the anchor for prodrugs is a target for rapid phase II metabolic inactivation.[196,552]

To address the chemical instability issue, we proposed the substitution of the olefin bridge by sulfonamide and tetrazole groups. In the first case, the sulfonamide bond is in continuous rotation, which creates an equilibrium between two main conformational clusters relative to the aromatic rings, adopting one *transoid* or two *cisoid* dispositions (Fig. 114). Conformational analyses for all the sulfonamide-containing compounds suggest that the *cisoid* conformations required for the interaction with the protein are energetically more favorable than the *transoid* (Fig. 114). The introduction of substituents on the sulfonamide nitrogen augments the energetic difference between conformations, thus favoring the interacting pose. Moreover, the presence of a sulfonamide could improve the aqueous solubility since its oxygen atoms are weak hydrogen bond acceptors,[553] and the NH group is a hydrogen bond donor.[554]

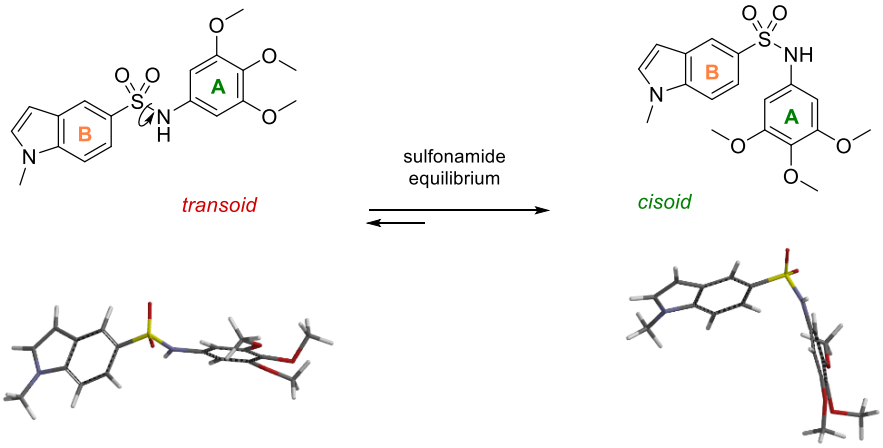

Figure 114. Conformational equilibrium of compound **80** regarding the sulfonamide bond. The *transoid* conformation shows an extended disposition of the aromatic rings. The equilibrium is displaced towards *cisoid* conformations, which are the ones interacting at the colchicine domain.

The introduction of tetrazole rings in replacement of the olefin locks the two aromatic rings into a *cisoid* disposition, adopting a similar pose to that of sulfonamides (Fig. 115). This conformation is favorable for the interaction with tubulin. The amide precursors in the synthetic route of tetrazoles are preferentially *transoid* but are required to adopt a *cisoid* disposition to bind at the colchicine domain. The energetic penalty associated with this rotation may in part explain the reduced activity against cell proliferation displayed by amide derivatives versus their tetrazole-containing counterparts.

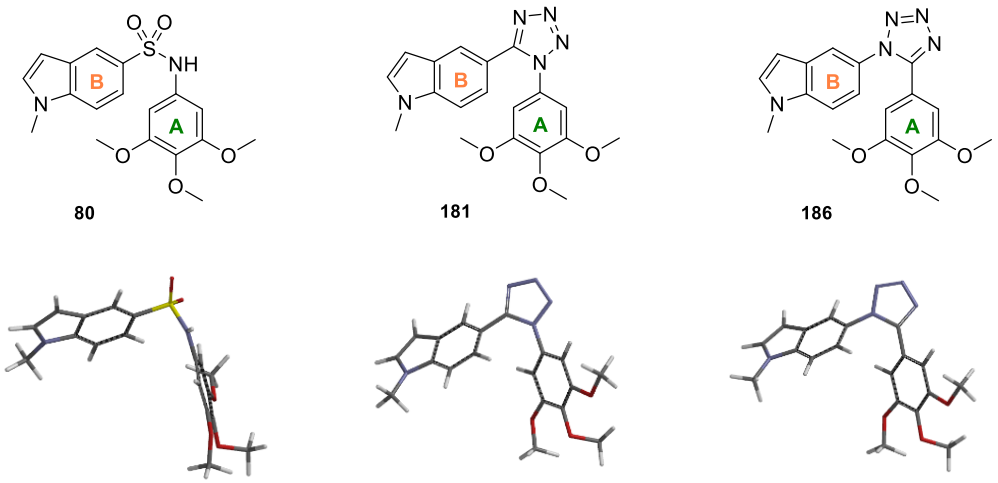

Figure 115. Equilibrium conformer of compounds **80**, **181**, and **186**. The sulfonamide bridge preferentially adopts a *cisoid* conformation. The inclusion of the bridge in a tetrazole cycle blocks the aromatic rings into a *cisoid* disposition.

The replacement of the planar olefin bridge by these groups additionally carries changes in geometry and volume of the bridge region (Fig. 116). The amides are the most similar groups to olefins in terms of volume and share the trigonal planar geometry. The orientation of the amide bridge, where the carbonyl is bound to the B ring (A1) or the A ring (A2), is critical for the activity (Fig. 117). Assuming that the indole ring binds to zone 1 and the benzene to zone 2, the carbonyl is exposed towards the solvent in amides A1 while the NH group unfavorably points to a hydrophobic region. The reversal of the amide orientation turns the inactive compound **171** (A1) to the potent ligand **174** (A2), whose NH group contacts the solvent. The methylation of the amide nitrogen increases the size and preferentially predisposes the aromatic rings into a *cisoid* disposition (Fig. 116). However, it does not improve the cytotoxic potency of *N*-indole-amide **175** versus **174** (Fig. 117), indicating that masking the NH group at position 5 of the indole ring (A2) that points towards the solvent is unfavorable for the antitumor activity.

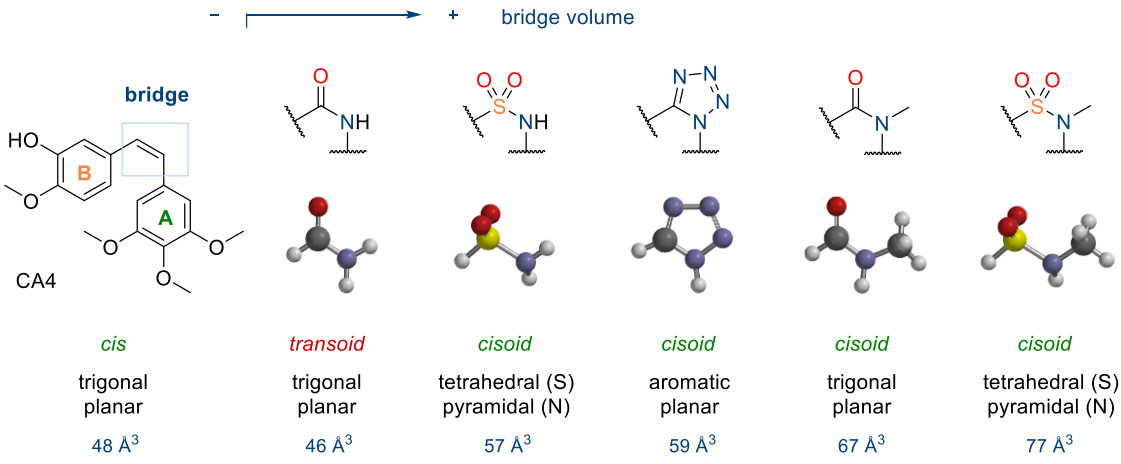

Figure 116. Replacement of the olefin bridge of CA4 by different groups. The *cis* olefin adopts a trigonal planar geometry and isomerizes to the thermodynamically more stable *trans* olefin. The amide group has a similar geometry, but preferentially adopts a *transoid* disposition unless methylated. The introduction of planar tetrazole rings forces a *cisoid* disposition of the aromatic rings. Sulfonamides have a different geometry and preferentially adopt *cisoid* dispositions, even more favorable when the sulfonamide is substituted. The volume of each group is indicated in **blue**.

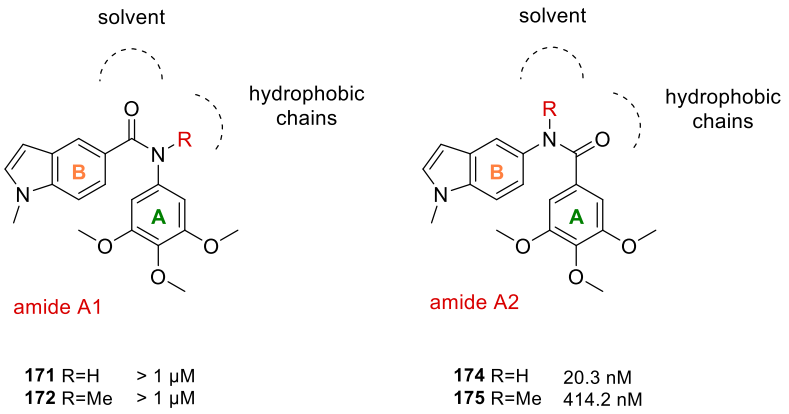

171 R=H > 1 μM
172 R=Me > 1 μM

174 R=H 20.3 nM
175 R=Me 414.2 nM

Figure 117. Two possible amide orientations. Amides A1 with the carbonyl conjugated with the B ring, whose NH is close to a hydrophobic region. Amides A2 with the carbonyl conjugated with the A ring, whose NH contacts the solvent. The cytotoxic activity of each compound is indicated as the IC_{50} value against HeLa cells.

Tetrazoles are slightly bulkier than sulfonamides and are entirely planar due to the aromaticity (Fig. 116). These features are not affected by the orientation of the tetrazole ring. Even so, there are differences in potency between tetrazoles with the nitrogen bound to the A ring (T1) or the B ring (T2) (Fig. 118). There are at least two components that may contribute to the enhanced activity of T1 over T2 compounds. Computational studies suggest that the highest electron density in tetrazoles T1 is preferentially located on the tetrazole region that is exposed to the solvent, and unfavorably towards the hydrophobic side chains in T2 tetrazoles (Fig. 118). In addition, the indole ring is forced to rotate with respect to the tetrazole plane so that the trimethoxybenzene (A ring) can interact in zone 2. This rotation is less unfavorable when the nitrogen in the bridge is next to the trimethoxybenzene ring (T1) than the opposite case (T2), becoming more relevant in the presence of extended substituents on the indole ring.

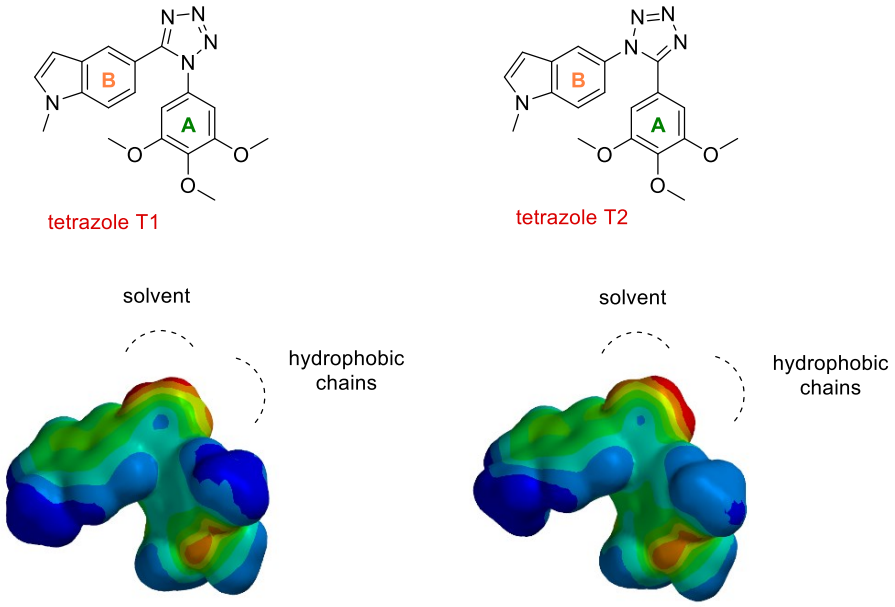

Figure 118. Chemical structures of tetrazole derivatives **181** (tetrazole T1) and **186** (tetrazole T2) and their electrostatic potential maps underneath. The lowest electrostatic potential energy is indicated in **red** (electron-rich region) and the highest in **blue** (electron-poor region).

The presence of a sulfonamide implies a different geometry since the sulfonamide sulfur is tetrahedral, and the nitrogen shows pyramidal geometry (Fig. 116), with a slightly different dihedral angle in substituted sulfonamides. Similar to amide derivatives (Fig. 117), the interaction at the colchicine domain places the sulfone in position 5 of the indole ring exposed towards the solvent, and the NH group in a hydrophobic region. According to this, a reversed orientation of the sulfonamide with the NH contacting the solvent might have a positive effect on the potency. In an attempt to obtain a series of compounds with that orientation, we introduced a sulfonyl chloride on 1,2,3-trimethoxybenzene to form the corresponding sulfonamide. The reaction yields 2,3,4-trimethoxybenzene sulfonyl chloride instead of 3,4,5-trimethoxybenzene sulfonyl chloride. The activity reduction of the resulting sulfonamide **99** could probably be due to the altered substitution pattern of the A ring, similar to what is usually observed for other bridges.[198,499,505,554] Even so, the 2,3,4-trimethoxyphenyl arrangement is present in compounds such as colchicine or MTC and, in some cases, yields novel potent ligands.[555]

The methylation of the sulfonamide nitrogen is optimal for the activity regardless of the A ring, with akin antitumor potencies to their tetrazole counterparts. This methylation further displaces the conformational equilibrium towards the *cisoid* disposition of the aromatic rings and masks the unfavorable exposure of the NH group towards the hydrophobic region, wide enough to harbor a methyl group. In general terms, bulkier substituents also favor the interacting conformation but are too big for this region. The larger the substituent, the weaker the potency. The ethyl group is followed in potency by acetonitrile substituents, benzyl, and ethyl acetate groups.

Regarding the A ring, the 3,4,5-trimethoxybenzene is a common moiety present in many colchicine site ligands despite its high volume and hydrophobicity.[193] The preferred conformation of this group places the two lateral methoxy groups in the benzene plane with the methyl carbons in the opposite direction with respect to the central methoxy group (Fig. 119). The steric hindrance with the *ortho* methoxy groups forces the one in the middle to protrude out of the ring plane. This conformation results in a wider than tall moiety with 7.2 Å distance in the 3-5 direction. The replacement of the olefin bridge by bulkier sulfonamide and tetrazole groups might affect the overall disposition of the ligands in the colchicine domain. To partially compensate for this increase in size, we have explored different alternatives as A ring, having in common the loss of the central methoxy group that relieves the steric restriction towards the lateral methoxy groups. The removal of the central methoxy may have an additional advantage since it is prone to suffer phase I metabolism by O-demethylation in CA4, leading to the isomerization and therefore inactivation of the *cis* olefin.[195]

The 3,5-dimethoxyphenyl moiety lacking the central methoxy group shows higher adaptability to the spatial requirements of the interaction pocket. The two methoxy groups are placed in the benzene plane with four possible orientations: the two of them pointing towards the sulfonamide (upwards), opposing the sulfonamide (downwards), or each one in a different direction (upwards-downwards or vice versa) (Fig. 119). This diversity results in an average slight reduction in size in the 3-5 direction (less wide) compared to the classical 3,4,5-trimethoxyphenyl, with methoxy carbon to methoxy carbon distances of 5.0-7.2 Å (Fig. 119). The 3,5-dimethoxyphenyl group is also shorter in the 1-4 direction, given the removal of the central methoxy group.

The 2,5-dimethoxy substitution pattern implies an important lateral and vertical size reduction. The angle of the 2,5-dimethoxyphenyl plane with regard to that of the indole ring is slightly different depending on whether the sulfonamide is substituted or not. When free, the NH group can establish an intramolecular hydrogen bond with the oxygen of the 2-methoxy group. By contrast, the steric clashes upon substitution

of the sulfonamide nitrogen force the rotation of the 2,5-dimethoxyphenyl ring. Regardless of the substitution status of the sulfonamide, the least energetic conformations place the 2-methoxy carbon opposing the nitrogen due to steric hindrance and the 5-methoxy group in the benzene plane with two possible methyl carbon orientations (Fig. 119). The introduction of a bromine atom at position 4, roughly as big as a methoxy group, restores the vertical size of the moiety, similar to that of 3,4,5-trimethoxyphenyl. The steric hindrance of the bromine to the *o*-methoxy group restrains the methyl carbon in the 3,5 direction, slightly increasing the lateral size of this group with respect to 2,5-dimethoxyphenyl (Fig. 119).

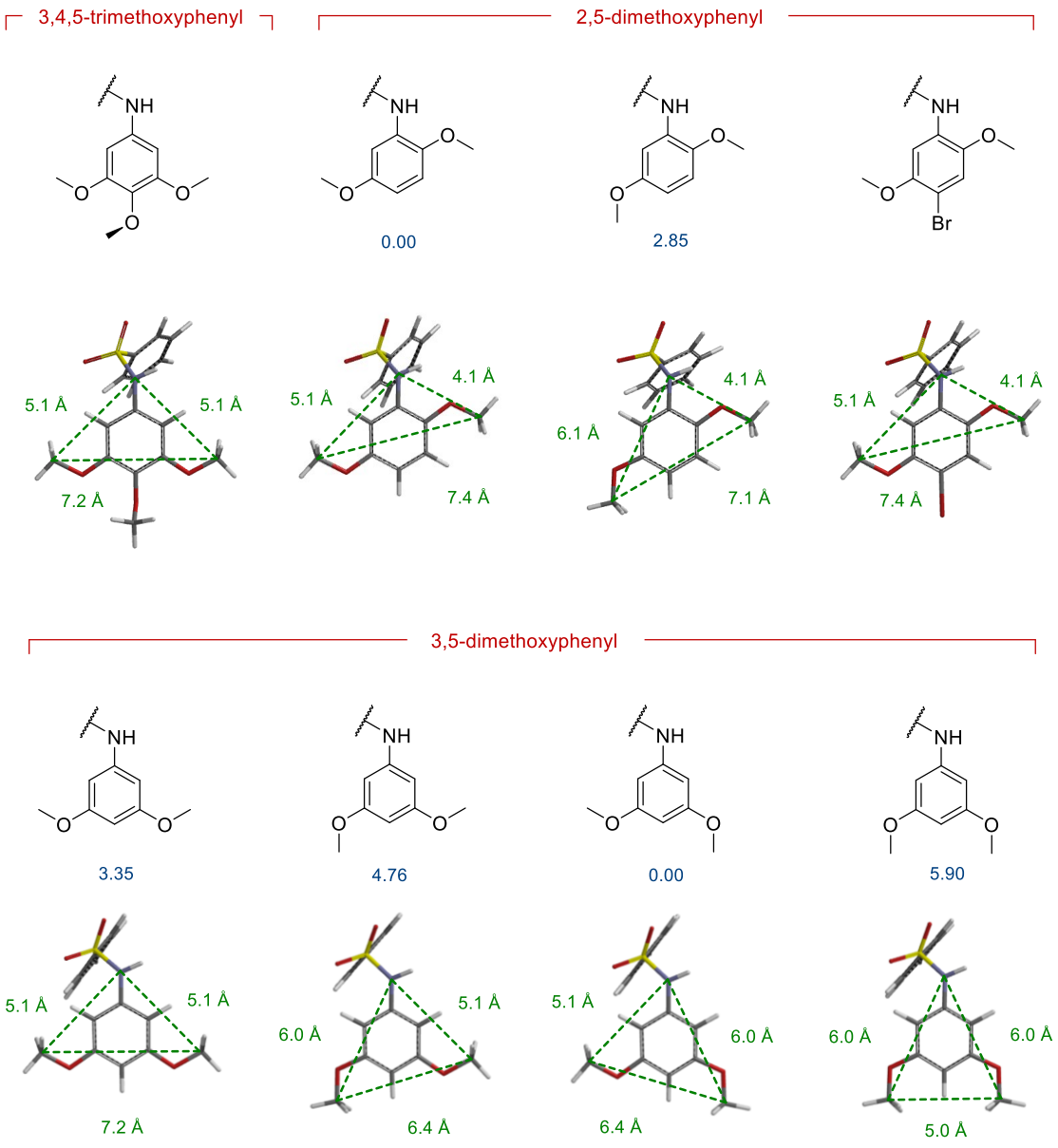

Figure 119. Geometries of the different conformers for *N*-(3,4,5-trimethoxyphenyl), *N*-(3,5-dimethoxyphenyl), and *N*-(2,5-trimethoxyphenyl) benzenesulfonamides. The 2D representations on top indicate the orientations of the methoxy carbons in the same dispositions as the 3D conformers underneath. The triangles represent the dimensions of the A ring, with the distances between atoms in **green**. The relative energies (kJ/mol) in apolar media (vacuum) between conformers are indicated in **blue**, according to DFT calculations.

Compounds with a 3,4,5-trimethoxyphenyl ring show the highest potencies among sulfonamides, followed by 3,5-dimethoxyphenyl derivatives, which in turn display higher activity than those with a 2,5-dimethoxyphenyl group. The increase in the bridge volume by the substitution of the sulfonamide nitrogen or the conversion of amide into tetrazole directs the A ring deeper into zone 2, which may compromise the interaction with the protein. Alkylation of sulfonamides with a 3,5-dimethoxyphenyl group (A ring) leads to a remarkable potency improvement, suggesting that the removal of the central methoxy group compensates for the increased size of the bridge. The bromination of 3,5-dimethoxyphenyl ring in tetrazoles **144** and **150** leads to the loss of cytotoxic activity, possibly due to the altered conformation of the brominated products (**146**, **147**, and **152**). Conformational analyses predict that the planes of the B and A rings in the least energetic conformations of non-brominated compounds are respectively tilted around 30° and 45° angles compared to the tetrazole plane. Dibromination at positions 2 and 6 of the A ring has two main consequences: it directs the *ortho* methoxy groups to the opposite direction of the bromine due to steric hindrance (Fig. 120), and forces the A ring to rotate up to 90° with respect to the tetrazole plane. The methyl carbon of the 3-methoxy group protrudes out of the benzene plane when flanked by bromines at positions 2 and 4 (Fig. 120).

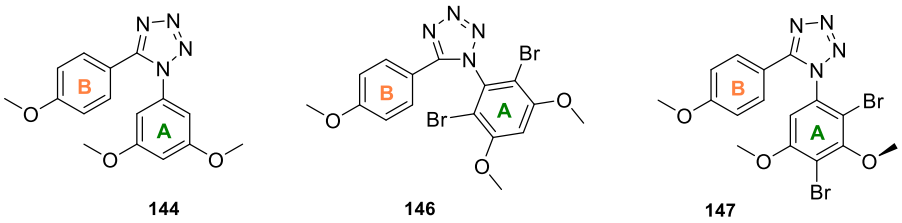

Figure 120. Chemical structures of **144**, **146**, and **147** (T1). The methoxy carbons in 2D representations are depicted in the same disposition as the least energetic conformers. The methoxy carbons in tetrazoles **150** and **152** (T2) are similarly placed as those in **144** and **146**, respectively.

The volume reduction of replacing a 3,4,5-trimethoxy with a 2,5-dimethoxyphenyl group leads to a notable decrease in potency. The introduction of bromine at position 4 mimicking the central methoxy group slightly restores the cytotoxic activity. Our results regarding antiproliferative activities indicate that the presence of the bromine at position 4 appears to be more efficient than recovering the 3-methoxy group.

To avoid phase II metabolic transformation of the hydroxyl group of CA4, we have removed the phenolic ring, replaced by benzene or *N*-methyl-indol-5-yl. The benzene ring is smaller than the indole group, whose size increases when introducing substituents at position 3. The substituents on the different B rings are conjugated and therefore located in the same plane as the aromatic ring. The methyl carbon of *p*-methoxyphenyl, which is the smallest moiety in size, shows two possible orientations. The dimethylamino group is slightly bulkier than the methoxy group (Fig. 121), and its stronger electron-donating character implies a higher conjugation with the benzene ring. The dimethylaminophenyl resembles an open indole, with the dimethylamino mimicking the pyrrole ring in hydrophobicity, but lacking the aromatic character. This high degree of similarity with the highly potent indole-based ligands is possibly related to the increased cytotoxic activity compared to the *p*-methoxy group (**156** versus **144**), although the best results were obtained for compounds with unsubstituted indole rings (e.g. **166**). The replacement of the phenolic ring by the lipophilic *N*-methyl-indol-5-yl group endows colchicine site ligands with high potency but results in poor physicochemical properties that need to be counteracted by the introduction of polar groups in other parts of the scaffold.[556]

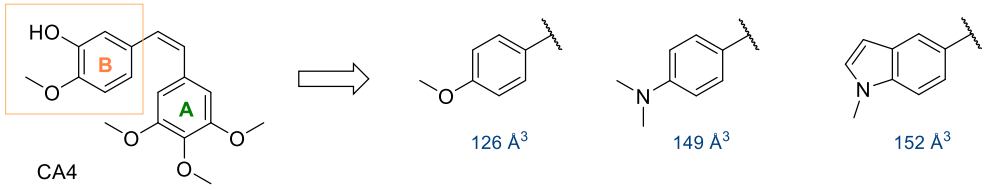

Figure 121. Replacement of the phenolic B ring of CA4 that interacts in zone 1 by different groups: *p*-methoxyphenyl, *p*-dimethylaminophenyl, *N*-methyl-indol-5-yl. The volume of each group is indicated in **blue**.

The introduction of substituents at position 3 of the indole pursues two goals, endowing the compounds with higher aqueous solubility to compensate for the removal of the hydroxyl group, and establishing potential additional interactions with the side chains in zone 1. These substitutions that greatly improve the antiproliferative potencies of indole combretastatins[499] are detrimental in indole sulfonamides, similar to the decrease in cytotoxic potency in indole phenstatins and isocombretastatins.[505] The subtle changes in the relative disposition of the aromatic rings by the different bridges translate into relevant changes in the orientation of substituents at indole 3-position. Because of that, the impact on the activity is highly dependent on each chemical context.

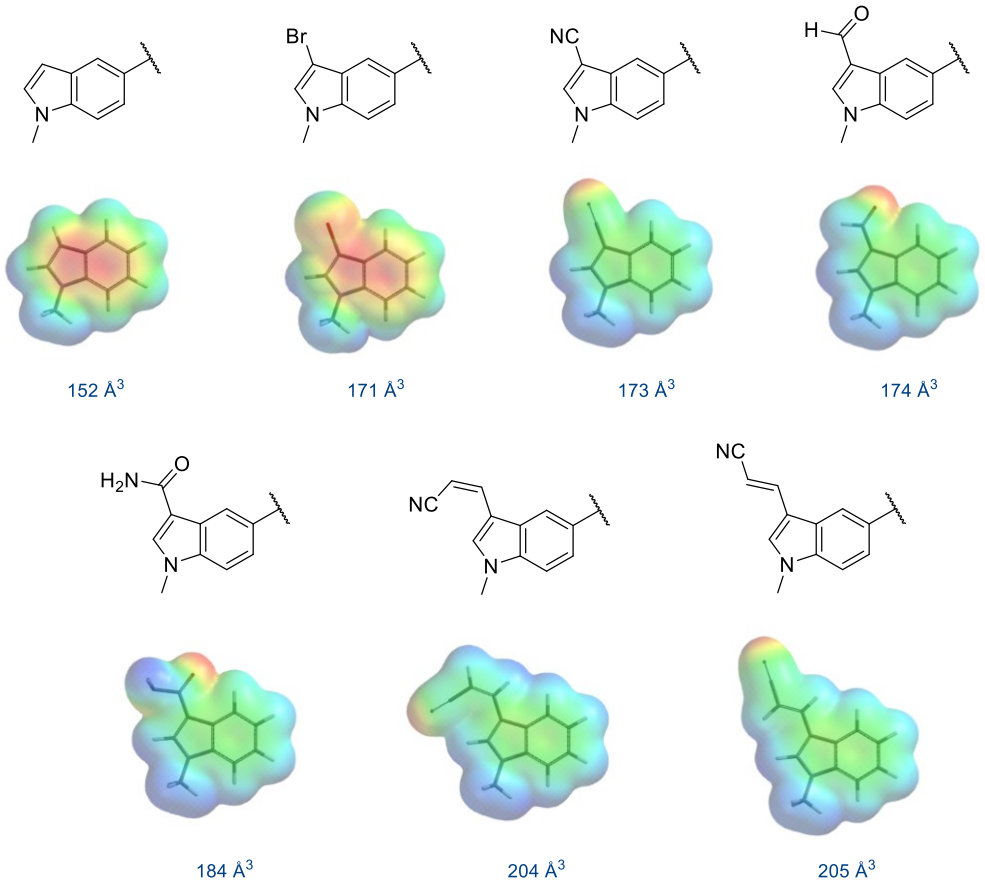

Figure 122. Substitutions at the indole 3-position. 2D chemical structures with their 3D electrostatic potential maps underneath. The lowest electrostatic potential energy is indicated in **red** (electron-rich region) and the highest in **blue** (electron-poor region).

Besides entailing changes in volume, the substituents at the indole 3-position subtract electron density from the aromatic ring. The introduction of bromine, carbonitrile, or aldehyde groups leads to a similar spatial occupation in terms of volume, but they show differences in electronic distribution (Fig. 122). In general terms, compounds with bromine and carbonitrile groups have proven more potent than formyl derivatives. Additionally, aldehydes have two possible orientations, and freezing one of them for the interaction with the protein leads to an entropy loss. The same occurs in amides, which are bulkier than aldehydes. Although *E* and *Z* propenenitriles have similar volumes, the nitrile group is placed in different directions, influencing the interaction with the protein. Indeed, the cytotoxic activity of *E* isomers is slightly higher than that of *Z* isomers.

Mechanism of action of the compounds: tubulin is the biological target

We have demonstrated in this work that an *N*-methyl-indol-5-yl moiety combined with a polymethoxylated ring linked by sulfonamide or tetrazole groups are suitable scaffolds for colchicine site ligands. This combination yields potent cytotoxic compounds with IC_{50} values in the nanomolar or submicromolar range against several human tumor and non-tumorigenic cell lines that also inhibit the anchorage-independent growth of HeLa cells. Drug resistance to tubulin binding drugs (e.g. paclitaxel and vinca alkaloids) is often ascribed to the unspecific pumping of the drugs out of the cell by MDR transporters.[96,115] The evaluation of the antiproliferative profile of the compounds in the absence of MDR-mediated transport by pharmacological inhibition has shown that there are hardly any changes in the IC_{50} values compared to those obtained without inhibition of MDR transporters. Only a few compounds show around two-fold increased potency in the presence of verapamil and elacridar. The activity of ethyl sulfonamide **82**, however, is notably restored up to 7-11 times when blocking MDR-mediated transport. The few candidates to be substrates of P-gp have in common the presence of bulky or lipophilic groups. This is in agreement with the already reported fact that these transporters, among them P-gp, preferentially export big-sized highly lipophilic compounds with several aromatic rings and no net charge at neutral pH.[557]

The evaluation of the cell cycle distribution upon treatment with the compounds has evidenced a remarkable arrest in G_2/M in all the tested cell lines, indicative of an antimitotic mechanism of action. The increased detection of mitotic phosphoproteins by immunoblotting has further confirmed the blockage in mitosis. Drug-induced effects can also be detected under microscope by the rounding-up of cells as they enter mitosis. Cells detach from the culture surface, adopting a rounded morphology for the division stage, retrieving the flattish and extended cellular shape when adhered. The arrest in mitosis leads to the sustained presence of refringent rounded cells suspended in the culture media. Upon treatment, the accumulation of cells in G_2/M evolves at a similar pace irrespective of the compound. In HeLa cells, the effect begins approximately 8 h after adding the treatments at the expense of a decrease in the G_0/G_1 population, reaching the maximum G_2/M percentage after 24 h. This pace is cell type-specific due to the different proliferation rates. In the particular case of compound **104**, HeLa cells experience an initial arrest in G_2/M, with a maximum percentage after 15-h incubation. However, this percentage decreases at the expense of a slight increase in the number of cells in G_0/G_1 after 24 h, suggesting that a small population of cells can bypass the arrest and reenter G_0/G_1 after effective cytokinesis. In line with this, HEK-293 cells show analogous behavior upon treatment with **104**.

The sustained arrest of HeLa cells eventually ends up in cell death with a reduced MPM-2 signal after 48 h, even though the DNA profiles show the majority of the cells still standing in G_2/M. In light of the antimitotic effect, it is not surprising that the compounds exhibit similar inhibitory activity against cell growth in non-tumorigenic and primary cells compared to the tumor cell lines we tested. The concentrations of compounds required to induce G_2/M arrest correlate with the IC_{50} values against cell proliferation, suggesting that the inhibitory effect of cell growth is due to the mitotic arrest. Compounds with IC_{50} values against HeLa cell proliferation around 10^{-7} M induce mitotic arrest at 1 μM, those with IC_{50} values around 10^{-8} M exert the accumulation of cells in G_2/M at 100 nM, and the most potent compounds with IC_{50} values around 10^{-9} M show effect on the cell cycle distribution at 10 nM.

The indirect immunofluorescence experiments in HeLa cells have revealed that the antimitotic activity occurs with disruption of the microtubule network. Incubations with the drugs for 24 h induce a non-defined dispersed location of α-tubulin throughout the cytosol, as opposed to the perfectly organized tubulin cytoskeleton in filamentous fibers in untreated cells. This qualitative feature is characteristic of a microtubule destabilizing effect, different from the action of MSAs such as paclitaxel that typically induce the formation of microtubule bundles.[530] Consistent with that finding, subsequent biochemical studies have shown that the compounds inhibit tubulin polymerization *in vitro* in a dose-dependent manner with potencies comparable to that of CA4 (IC_{50} = 3 μM) in the case of compounds **81** and **82** (IC_{50} = 2.1 and 2.2 μM, respectively). By contrast, MSAs typically induce higher tubulin polymerization percentages than in the absence of compounds.

The differences between IC_{50} values in the proliferation assay and the tubulin polymerization assay are fairly apparent. However, it should be taken into account that the latter monitors the effect on the microtubule mass rather than alterations on microtubule dynamics. Therefore, the polymerization assay measures the concentration of compound required to reduce the mass polymer by 50% as a proxy to easily compare the potencies of different ligands relative to their antitubulin activity. In an *in vitro* cellular model, a subtle interference in microtubule dynamics achieved at much lower concentrations is sufficient to cause the malfunctioning of the spindle and arrest the cells in mitosis (**81** shows IC_{50} values of 2.4 nM against HeLa cell proliferation and 2.1 μM against tubulin polymerization).

We have proven by MTC displacement the binding to the colchicine domain, thus demonstrating that the biological target is indeed tubulin. This interaction is presumably causing the inhibitory effect on tubulin polymerization. The decay in fluorescence intensity of the MTC-tubulin complex when adding increasing concentrations of compounds indicates the competition for binding to the colchicine domain. Even though we only tested some representative ligands in the competition assay, it seems reasonable to assume that the cytotoxic effect of compounds that have proven antimitotic activity is caused by the binding to the colchicine domain regardless of the structural variations on the scaffold. Two of the lead compounds, **81** and **104**, interact with tubulin with binding constants (K_b = 1.3 and $1.1 \cdot 10^7$ M^{-1} at 25 °C) similar to that of colchicine (K_b = $1.2 \cdot 10^7$ M^{-1} at 37 °C).[537] These values should be taken with caution because of the affinity difference separating **81** and **104** from MTC (K_b = $4.7 \cdot 10^5$ M^{-1}).[534] Using MTC as a probe is not the optimal strategy to calculate the binding constants of those two compounds accurately. It rather requires a reference ligand with a higher affinity for the colchicine domain than MTC. The results obtained in the evaluation of tetrazole **166** do not allow us to determine the binding constant due to its insolubilization. In light of the dose-fluorescence curves, this compound indeed interacts with the colchicine domain, presumably stronger than sulfonamide derivatives.

Tubulin binding drugs have proven to display relevant antiangiogenic and vascular disrupting properties, primarily by jeopardizing endothelial cells.[558] Regardless of their stabilizing or destabilizing effect, TBDs show antiproliferative activity against endothelial cells, they compromise their migration and inhibit the formation of tube-like structures. Altogether, these activities have been associated to an antiangiogenic profile.[558] Moreover, MDAs (e.g. CA4, ABT-751, or vinca alkaloids) induce morphological changes in the endothelial cells that cover the inner lumen of tumor-associated vessels, leading to a rapid vascular occlusion and collapse *in vivo*.[472] These properties are being exploited in clinical trials by combining antivascular drugs that cause the necrosis of the tumor core with cytotoxic drugs that challenge the survival of the outer rim of cells in the tumor periphery. This combination allows to decrease the doses and therefore attenuate the side effects of chemotherapy.

We have shown that the lead compounds inhibit the formation of capillary-like structures in murine endothelial 3B-11 cells in a dose-dependent manner. We are fully aware that this assay simulates angiogenesis conditions, meaning that these data are taken as a preliminary evaluation of the antivascular profile of the drugs. The ligands should be added once the vascular network is already formed to ascertain whether the compounds display vascular disrupting activity. The potency observed in tube-formation assays matches the IC_{50} values against 3B-11 proliferation, suggesting that the inhibition of angiogenesis is presumably due to the effect on tubulin. The observed inhibitory effect is achieved at doses that cause G_2/M arrest in HeLa cells and subsequent cell death. We have not evaluated the effect on the cell cycle distribution in 3B-11 cells, but given the similar IC_{50} values irrespective of the cell line, we could assume that those concentrations will arrest 3B-11 cells in mitosis. However, it has been hypothesized that the actions on endothelial cells *in vitro* occur by perturbing microtubule dynamics at low concentrations that neither interfere with microtubule morphology nor induce mitotic arrest.[558] The hypothetical arrest of 3B-11 cells will not necessarily lead to cell death, considering the scarce apoptosis we observed in non-tumorigenic cells upon treatment with the compounds. Based on the findings in the present work, the 6-h span in the angiogenesis experiment is likely not enough for the cells to undergo cell demise.

Contribution of apoptosis and necrosis to the overall cell demise

In previous studies, TBDs have shown to induce apoptotic cell death in solid and hematological tumors as a consequence of a sustained mitotic arrest, although the precise molecular mechanisms that link these two processes are poorly understood. In line with this, our work has revealed that apoptosis is the major cell death routine that accounts for the cell demise in HeLa upon treatment with the lead compounds. Time-lapse videomicroscopy experiments recording the evolution of cell morphology after treatment have shown an apoptotic phenotype, evidenced by membrane blebbing, which is one of the morphological hallmarks of apoptosis. Cell cycle analyses in HeLa cells have shown a time-dependent increase in the $SubG_0/G_1$ population (hypodiploid cells) upon treatment with the compounds, indicating an apoptotic component in cell death. The ethanol used in this assay to fix the cells creates pores in the plasma membrane allowing PI to penetrate and label the genetic material. At the same time, the small internucleosomal DNA fragments leak outside apoptotic cells resulting in lower fluorescence intensity ($SubG_0/G_1$). It is important to emphasize that although the percentage of cells in the $SubG_0/G_1$ population correlates with the extent of apoptosis, it does not necessarily equate the number of apoptotic cells. First, because apoptosis is initiated before DNA fragmentation occurs, and second, because DNA is gradually fragmented by nucleases, implying that cells dying while in G_2/M will progressively transition towards the $SubG_0/G_1$ peak, and therefore might be wrongly considered as either S or G_0/G_1 cells in that process.

In contrast to the rapid apoptosis induced by staurosporine, used as a positive control, DNA fragmentation is delayed with respect to the induction of mitotic arrest observed upon treatment with the ligands. Apoptosis increases over time, mainly from 24 h after treatment onwards, at the expense of a reduction in the G_2/M population, indicating that the mitotic arrest occurs long before the induction of apoptosis. We have validated this finding by incubation with the caspase inhibitor Z-VAD-fmk, which abrogates DNA fragmentation, indicating that this apoptotic feature observed after treatment is caspase-dependent. However, it does not affect the antimitotic effect and morphological changes. The inhibition of the apoptotic pathway elicited by Z-VAD-fmk leads to a higher extent of the mitotic arrest, assessed by cell cycle analysis and the increased signal coming from mitotic phosphoproteins.

The apoptotic response observed after treatment courses with a loss of plasma membrane integrity and occurs to a greater extent than the DNA fragmentation at the same time-point. This suggests that the permeabilization of the membrane is an early event. Even though the increase in the $SubG_0/G_1$ peak and the percentage of PI-positive cells follow a similar pace irrespective of the ligands, treatment with compound **104** causes membrane permeabilization in a lesser extent than the other five compounds under equal DNA fragmentation. The loss of plasma membrane integrity is typically a necrotic cellular feature, but there is no sign of necrotic cells in time-lapse experiments. Double staining experiments with Annexin V-FITC and PI have pointed out that this phenomenon is necrosis-independent. These experiments have also confirmed the apoptotic cell death due to the appearance of Annexin V single positive cells corresponding to those that expose PtdSer at the outer leaflet of the plasma membrane (eat-me signal), and Annexin V-PI double positive cells as a consequence of advanced stages of apoptosis. This double-positive population may correspond to necrotic cells with a high degree of plasma membrane permeabilization that might allow proteins as big as Annexin V to enter the cytosol labeling the PtdSer at the inner leaflet. However, we have discarded this possibility. If that happened, we should have detected PI single positive cells at early incubation periods with the drugs, later becoming a double positive population, and it was not the case. In fact, the combination of Z-VAD-fmk and the compounds prevents PtdSer exposure (Annexin V single positive cells) and also abrogates membrane permeabilization in Annexin V-PI and PI uptake experiments, indicating that the loss of membrane integrity is a consequence of apoptosis, and can be considered as late apoptosis or necrosis secondary to apoptosis.

Consistent with the aforementioned finding, there is a coordinated time-dependent response upon treatment regarding the cleavage of caspases 9 and 3, and PARP cleavage, a major caspase substrate. The appearance of cleaved bands for these proteins mainly occurs after 32 and 48-h treatments, parallel with the increase in DNA fragmentation found by cell cycle analysis. The increase in cytochrome c levels in the cytosolic fraction and the activation of the initiator caspase 9 highlight the role of the mitochondria in the apoptotic response. These events could arise as an amplification loop of the extrinsic pathway mediated by caspases 8 or 10 or directly via the intrinsic pathway. Z-VAD-fmk completely blocks the cleavage of PARP due to the inhibitory effect on caspase 3 activation. The 17 kDa and 19 kDa fragments of active caspase 3 after 48-h treatments are not observed in the presence of Z-VAD-fmk. However, we have detected an upper cleaved form of caspase 3 of around 20 kDa, which might be an incomplete cleavage product. This fragment is catalytically inactive because it does not cleave PARP. We have found that Z-VAD-fmk upregulates the cleavage of caspase 9, accompanied by reduced levels of the procaspase form. This effect has been previously described in etoposide-treated embryonic fibroblasts.[540] The fact that Z-VAD-fmk only enhances the activation of caspase 9 when its cleavage has already been triggered by the compounds, hints that it could serve as a compensatory mechanism to counteract the pharmacological inhibition of caspase 3 cleavage in the presence of apoptotic stimuli as TBDs.

Taken altogether, these data suggest that HeLa cells undergo a caspase-dependent apoptotic death following the mitotic arrest. Kinases Akt, JNK, and Erk1/2, which are important regulators of cell survival and proliferation, do not appear to participate in the response to these drugs. The pharmacological inhibition of effector caspases translates into an exacerbated reduction in DNA fragmentation by cell cycle analysis, milder in the case of compound **104**, and abrogates PtdSer flipping to the cell surface. The absence of PI single positive cells at early incubation periods and the fact that inhibiting apoptosis prevents membrane damage, put in evidence that necrosis, if any, is a marginal cell death response in this instance. This observation can be extended to necroptosis since the incubation with the RIPK1 inhibitor necrostatin-1 combined with the lead compounds has no impact on the extent of apoptosis evaluated by the $SubG_0/G_1$ population and PARP cleavage. However, the combination with necrostatin-1 increases the rate of membrane permeabilization, presumably due to the treatment itself, since this effect is also observed in HeLa cells treated with necrostatin-1 alone compared to untreated samples. Either way, these findings indicate that necroptosis does not account for the overall cell demise either.

It has been widely assumed that tubulin binding drugs induce cell death in treated cells as a consequence of the mitotic arrest. Nevertheless, prolonging the time that cells spend in mitosis by pharmacological induction does not appear to be sufficient for an efficient killing effect.[401] Several outcomes may result from the treatment with spindle poisons. Cells could bypass the arrest by exiting mitosis during an active spindle assembly checkpoint, either by improperly dividing the DNA content in daughter cells or by endocycling, repeatedly replicating the DNA without subsequent division (slippage).[559] Cell death can also take place in different instances like mitosis, interphase, or interphase after one or more mitotic cycles.[411] The sensitivity to this type of drugs greatly differs between different cancers.[560] We have observed this distinct behavior by comparing the drug-induced cell death in different cell lines. According to our experiments, akin antiproliferative activities do not necessarily translate into cell death, given the exacerbated differences in the apoptosis extent between cell lines whose sensitivities in the proliferation assay are somewhat similar, indicating that different cell lines are also differently prone to die.

We have observed a different behavior of the cell lines in terms of the percentage in the $SubG_0/G_1$ region and PI uptake after treatment with the lead compounds. All of them cause a prolonged mitotic arrest by microtubule disruption, assessed by cell cycle analysis and indirect immunofluorescence (in HeLa, HEK-293, and HPNE cell lines). As mentioned above, upon treatment with compound **104**, HeLa cells undergo a strong mitotic arrest after 15-h incubation precluding the accomplishment of accurate mitosis. Even so, it should be noted that part of the G_2/M population successfully exits mitosis and reenters G_0/G_1 phase with cell division, which does not occur with the other ligands. Prolonging the time cells spend in mitosis does not lead to significant apoptosis in the case of non-tumorigenic cell lines HEK-293, HPNE, BHK, or L929, or at least show higher resistance to apoptosis than HeLa cells. In fact, HPNE cells can evade cell death after 7 days of treatment, with DNA fragmentation as low as 2.9-8.3%, suggesting that the abrogation of the microtubule network is not sufficient for the cell to die. The resistance of HPNE to drug-induced cell death is related to the antimitotic mechanism of action (the effect is similar upon treatment with colchicine, nocodazole, paclitaxel, and vincristine) since the protein kinase inhibitor staurosporine induces 34.9% DNA fragmentation in HPNE cells after 72 h. The human tumor cell lines AGS, SNU-1, and MIA PaCa-2 exhibit an increase in DNA fragmentation over time, together with loss of plasma membrane integrity upon treatment with the lead compounds. U2OS and Huh-7 cell lines are less sensitive to cell death after a sustained mitotic arrest. The response of Huh-7 to treatment is more similar to non-tumorigenic cells than to tumor cells.

A possible explanation includes endocycling in the cell lines that do not undergo significant apoptosis. We have observed the appearance of a considerable amount of cells that fluoresce brighter than those in G_2/M by cell cycle analysis, a reason why we suspect that cells that do not undergo apoptosis after a sustained arrest may have exited mitosis after doubling their genetic material without cytokinesis. In any case, whether this hypothesis explains our results will have to be explored in the future.

Role of autophagy in response to treatment

Microtubules have been shown to participate in autophagosome formation and the trafficking thereof towards lysosomes in the perinuclear region, but not in the fusion step.[561] The disassembly of microtubules impedes the colocalization of autophagosomes and lysosomes that relies on dynein-mediated transport.[544] However, there is some controversy about the effect of tubulin binding drugs in the autophagy process. Paclitaxel and nocodazole block autophagy by preventing autophagosome formation upon aminoacid starvation.[562] Contrarily, the formation of autophagosomes is enhanced upon treatment with vinca alkaloids,[563] which also inhibit autophagy-dependent protein degradation after serum deprivation.[564] In addition, the colchicine site ligand ABT-751 has recently shown to induce early autophagy in Huh-7 and Hep-3B cells.[565,566]

The most widely monitored protein within the autophagy pathway is LC3-II, whose levels correlate with the number of autophagosomes. The time-course measurement of LC3 upon treatment with the lead compounds reveals blurry results without a clear tendency. The levels of LC3-II in a static time-point offer little information about the autophagic flux since an increased number of autophagosomes does not necessarily imply increased autophagy. The number of autophagic vesicles is a function of the balance between formation and degradation rates, and therefore a rise in LC3-II levels could also respond to a defect in autophagosome turnover. Low levels of LC3-II could be related to an intense autophagic flux with rapid degradation. Moreover, upon autophagy stimuli, there may be an enhanced conversion of LC3-I into LC3-II, or a decrease in LC3-II relative to LC3-I if the lysosomal degradation is very rapid. The changes in LC3-II levels are highly dependent on the cellular context and the cell line. Given the high dynamicity of the process, the occurrence of an autophagy response could be better demonstrated by studying the autophagic flux, which cannot be addressed by measuring LC3 levels on their own.[541] Advantageously, this autophagic flux includes the whole dynamic process from the formation of autophagosomes to the degradation of their cargoes following fusion with lysosomes.

The autophagic flux is usually deduced from LC3-II turnover in the absence of lysosomal degradation. Inhibiting the effective lysosomal degradation in HeLa cells with bafilomycin A1 or chloroquine results in the accumulation of autophagosomes, indicating a basal autophagic flux, assessed by the increased levels of LC3-II in Western blotting experiments and puncta formation by immunofluorescence. The slight increase of LC3-II upon treatment with the lead compounds, together with the additive effect when combined with bafilomycin A1, relates to an enhanced autophagic flux. An important caveat of this assay is that it monitors autophagic carrier flux to the stage of reaching the lysosome, which might occur in the absence of actual cargo flux.[567] Thus, these results do not imply that the detected induction of autophagic flux includes fusion with lysosomes and degradation of sequestered cargoes. Given the dismantling of the microtubule network upon treatment, which has been reported to prevent the colocalization of autophagosomes and lysosomes, we cannot rule out that the additive effect in LC3-II is the result of enhanced synthesis of autophagic membranes as a compensatory mechanism to counterbalance a defective degradation of substrates. The most straightforward explanation to our findings would probably

be the lack of autophagosome trafficking to the lysosomes in the absence of microtubules and subsequent accumulation of autophagic membranes, pending further investigation in the future. In any case, it would be worth evaluating the short-term effects of the compounds on the autophagic flux, when the microtubule network is not completely disabled.

The pharmacological inhibition of autophagy with bafilomycin A1 reduces the viability in HeLa cells with an increase in DNA degradation, which is not surprising given the cytoprotective role of autophagy. The apoptotic response driven by compounds **104** and **123** is diminished when combined with bafilomycin A1, assessed by cell cycle analysis, AnV-PI staining, and PARP cleavage. The negative effect of bafilomycin A1 alone on cell viability might mask a positive effect it might have in combination with the other ligands. In that case, the inhibition of autophagy would increase cell viability if autophagy contributed to cell death in response to the lead compounds. Such instance will not be considered as autophagic cell death (type II) since the NCCD excludes from the definition such cases when autophagy manipulation impacts other forms of regulated cell death. The apoptosis rate upon treatment with **181** and **186** is, by contrast, enhanced in the absence of autophagy. These disparate results raise some doubts about the role of autophagy in the overall cell demise. Nevertheless, the combination with chloroquine does not induce any changes in the extent of DNA fragmentation and membrane permeabilization compared to the treatments alone. Chloroquine also blocks autophagy, triggering higher levels of LC3-II, by increasing the lysosomal pH and decreasing the fusion between autophagosomes and lysosomes.[546,547]

Since the two drugs display a similar mechanism of autophagy inhibition, we can conclude that the differences observed in HeLa cells with the combination of bafilomycin A1 and the ligands compared to the ligands alone are not related to autophagy blockage. Autophagy thus hardly contributes to the overall cell death induced by the lead compounds. Instead, these differences are presumably caused by the long-term treatment with bafilomycin A1, which is recommended for relatively short incubations to avoid non-specific or secondary effects.[568] It should be indicated that we have carried out long incubations to evaluate the impact on apoptosis when it has already been prompted because, as already discussed, cell death occurs after the mitotic arrest.

Drug-induced mitochondrial changes

We have demonstrated that apoptotic cell death is a consequence of the mitotic arrest because the pharmacological inhibition of caspases prevents apoptosis but not the accumulation of cells in G_2/M. There is a rather long lag between the two processes. However, the link between the prolonged arrest and the onset of apoptosis remains unclear. It has been hypothesized that there is a separate pathway controlling the induction of apoptosis during mitotic arrest and that mitochondria-related proteins may play a role in this connection.[411] Mitochondria play a central role in regulating cell death at several levels, such as ATP synthesis, maintenance of $\Delta\Psi_m$, or production of ROS.[569–571] We have shown by immunoblotting the release of cytochrome c to the cytosol after treatment at the onset of cell demise that results in the activation of initiator caspase 9. Flow cytometry experiments have also indicated alterations in mitochondrial transmembrane potential ($\Delta\Psi_m$) and intracellular ROS levels. Our results support that mitochondria are implicated in the drug-induced apoptosis.

We have observed a slight increase in the levels of intracellular ROS after 15-h treatments, which may contribute to mitochondrial damage and imbalance the intracellular redox status. DHE detects superoxide anion, which is the most abundant ROS that can react with other radicals or undergo dismutation to H_2O_2.

At physiological levels, ROS produced in the respiratory chain are involved in hypoxia adaptation, but high levels can induce apoptosis and autophagy due to the opening of mitochondrial pores and the oxidation of Atg4, respectively.[572] The increased production of ROS in HeLa cells is thus an early event and precedes the later alteration in the mitochondrial transmembrane potential that begins to be detectable from 24 h onwards. This is in line with previous reports describing that the enrichment in ROS is upstream of mitochondrial membrane permeabilization and cytochrome c release.[573]

The incubation with the lead compounds for 48 h results in two populations of live cells regarding the fluorescence signal of $DiOC_6[3]$ probe. There is a population allegedly hyperpolarized, and a second population less bright (depolarized) than untreated cells. The biological significance of the hyperpolarization in this model is not clear. Even so, long-lasting changes in mitochondrial transmembrane potential ($\Delta\Psi_m$), either augmented or diminished, may lead to cell death. MOMP driven by the imbalance between prosurvival and proapoptotic Bcl-2 proteins is usually associated with the dissipation of the mitochondrial transmembrane potential and leads to the subsequent release of cytochrome c.[574] This phenomenon has been described as an early and irreversible step in apoptotic cell death that precedes the activation of caspases and nucleases. The alteration of the mitochondrial permeability impairs oxidative phosphorylation, ATP synthesis, and compromises the transmembrane potential.[549] The timing of $\Delta\Psi_m$ loss depends on the cell system and the apoptotic stimuli. It has also been described in most apoptotic models as an early event, but in some others, as a consequence of the apoptotic pathway. In treated HeLa cells, the depletion in $\Delta\Psi_m$ concurs with the increase in the apoptotic response, including PtdSer exposure, DNA degradation, and PARP cleavage. However, our results have revealed the release of cytochrome c and caspase 9 cleavage at time-points with no detectable changes in $\Delta\Psi_m$. A plausible explanation to these findings includes the sensitivity of $DiOC_6[3]$ as a fluorescence probe that can be validated by using different dyes (e.g. JC-1). The fluorochromes used to monitor $\Delta\Psi_m$ show different degrees of sensitivity and discrimination of mitochondrial changes.[575] The most straightforward theory is that mitochondrial depolarization in HeLa cells indeed occurs after apoptosome activation. Consistent with this, previous studies have demonstrated that the loss of $\Delta\Psi_m$ is not required for the release of cytochrome c.[549]

We have detected mitochondrial depolarization when the plasma membrane is already compromised, which is a caspase-dependent process according to our experiments. The plasma membrane permeabilization occurs early upon treatment, even though the caspase 3 cleavage observed by immunoblotting is boosted after 32-h treatments. This seems to suggest that low levels of active caspase 3 before its enhanced activation may lead to plasma membrane damage, in which case the loss of mitochondrial integrity is detected after caspase cleavage. This supports the idea that the dissipation of the mitochondrial transmembrane potential occurs after MOMP and cytochrome c release. In any case, without evaluating the status of the mitochondrial transmembrane potential in the absence of caspase activity (e.g. pharmacological inhibition with Z-VAD-fmk), we cannot conclude that the loss of $\Delta\Psi_m$ is directly induced downstream of caspases, or a delayed effect of previous mitochondrial alterations (i.e. formation of leaking channels to release cytochrome c).

The expression levels of prosurvival proteins from the Bcl-2 family have shown a transient initial upregulation upon treatment of Bcl-xL, Mcl-1, and phospho-Bcl-2 with a decay over time, earlier in the case of Mcl-1 than the other two. These findings suggest that the three of them fulfill a protective role induced in response to microtubule alterations. The expression of Mcl-1 has been reported to be transiently increased at critical periods, as it is the case of the mitotic arrest upon treatment with TBDs.

In fact, Mcl-1 has been described to couple the timing of mitosis to the induction of apoptosis.[433] High levels of Mcl-1 empower cells to better inhibit apoptosis in the face of damaging insults that otherwise will cause immediate cell death.[576] Since the upregulation of Mcl-1 is transient, apoptosis is induced if the errors cannot be solved during that period.[433] In this regard, the temporary upregulation of Mcl-1 after 9-h treatments is probably the reflection of a survival feedback. After the immediate induction, we have observed a progressive decrease in Mcl-1, presumably as its degradation occurs. This agrees with the fact that it is phosphorylated during an active spindle assembly checkpoint, a signal for its subsequent ubiquitination and eventual degradation.[411] The decay in Mcl-1 levels, a prosurvival protein, thus translates into a proapoptotic cue. The parallel analysis of Mcl-1 and PARP by immunoblotting has revealed the time-dependent coupling of Mcl-1 reduction and PARP cleavage, suggesting that the drop in Mcl-1 may ease or contribute to the onset of apoptosis in response to the lead compounds. The time-course of Bcl-xL levels shows a similar trend, with a progressive drug-induced upregulation compatible with a protective role. Bcl-2, unlike Mcl-1 and Bcl-xL, remains constant upon treatment, although its phosphorylation is dramatically induced. The role of Bcl-2 phosphorylation in relation to the apoptotic rate has been challenged. Our results suggest that the initial induction of Bcl-2 phosphorylation may respond to a prosurvival role, in line with previous studies.[440–443] The expression of Bcl-xL and P-Bcl-2 is eventually reduced, mainly after 48-h treatments, concurrently with rather advanced apoptosis, when PARP has already been cleaved.

Many tumors show abnormal expression of apoptosis-related proteins, such as overexpression of members of the Bcl-2 family (e.g. Bcl-2, Bcl-xL, and Mcl-1).[577,578] The overexpression of Bcl-2 and Bcl-xL by gene transfer in HeLa cells partly protects them from apoptosis induced by the lead compounds, especially Bcl-2, but does not affect the cell cycle arrest in G_2/M and the disorganization of the microtubule network observed by immunofluorescence. The reduced apoptotic response is also observed by the little PARP cleavage after 48-h incubations with the drugs, in contrast to the intensity of the cleaved PARP band in WT cells. Even though these proteins serve a protective role, the lead compounds induce apoptosis in HeLa cells overexpressing Bcl-2 and Bcl-xL, but to a lesser extent compared to wild type cells. The Hill slope of the increasing apoptosis in transfected cells over time is less pronounced than wild type cells, but the extent of membrane permeabilization reaches similar levels after 72-h treatments, indicating that the prosurvival role of Bcl-2 and Bcl-xL introduces a delay of approximately one day in apoptosis induction rather than an overall reduction. The apoptotic response triggered as a consequence of the sustained mitotic arrest is lower in the case of Bcl-2 transfected cells than those overexpressing Bcl-xL.

In consideration of the time-course results, the partial protection of Bcl-2 and Bcl-xL to apoptosis is due to a delay rather than an abrogating effect. However, we cannot rule out that the combined overexpression of multiple antiapoptotic proteins may have a total protective effect. According to immunoblotting experiments in HeLa cells, apoptosis is triggered even though Bcl-2 and Bcl-xL are still upregulated. By contrast, PARP is progressively cleaved as Mcl-1 drops. This seems to indicate that the overexpression of Mcl-1 may prevent apoptosis in our model, if not completely, to a greater extent than Bcl-2 and Bcl-xL. It should be noted that the cytoprotective effect of Bcl-2 and Bcl-xL overexpression is complete in the case of HEL cells challenged with MTC, which remain arrested in G_2/M for long periods without undergoing apoptosis.[425] We first thought that the partial effect of Bcl-2 and Bcl-xL in HeLa cells might be related to differential expression between cells. However, this theory has been refuted by the presence of a homogeneous population of cells in flow cytometry experiments.

Drug withdrawal results in mitotic exit related to the incubation period

We have proven that the mitotic arrest induced by the lead compounds, rather than irreversible, can be alleviated after withdrawing the drugs from the culture media, assessed by cell cycle analysis and the decrease in MPM-2 signal by immunoblotting. This reversible response is highly dependent on the previous incubation period. The longer the treatment, the less likely it is for cells to get back to a normal cell cycle distribution. This is consistent with previous studies showing a time-dependent reversion of MTC-induced effects on the microtubule network and cell cycle arrest in HL-60 cells shortly after drug removal.[425] However, colchicine behaves as an irreversible agent. We hypothesized that this time-dependency would rely on the extent of apoptosis observed at each time-point. The irreversible commitment of DNA breakdown depends on the initial incubation with the drugs. Nevertheless, the mitotic arrest observed in HEK-293 and HPNE cells at time-points (48 h and 7 days, respectively) with hardly any DNA fragmentation is irreversible. By contrast, HeLa cells do recover from drug-induced responses coursing with similar $SubG_0/G_1$ values (15-24 h). This is a clear indicator that the percentage of apoptotic cells at the moment of rescue does not correlate to the successful exit from mitosis.

There is a lag time between the complete abrogation of the microtubule network and the irreversible induction of apoptosis, during which microtubules can re-polymerize recovering a normal cell cycle distribution. The length of this period, which differs between cell lines, could reflect the balance between prosurvival and proapoptotic cues. Regarding HeLa cells, the antimitotic effect cannot be reversed when apoptosis has already been triggered (i.e. 48 h after treatment), except in the case of compound **104**. The time spanning the mitotic arrest and the irreversible apoptotic commitment has been described to depend on the drug concentration,[425] which could explain the distinct behavior of HeLa cells in response to **104**. The other five lead compounds show partial accumulation in G_2/M at one order of magnitude lower concentration than the working one, but **104** does not. Altogether, our data point out that whether the initial percentages of the cell cycle phases can be restored depends on how prolonged the mitotic arrest has been. Cell fate after drug removal is thereby dictated by events that connect microtubule deprivation to the eventual outcome, whether it is apoptosis induction or slippage.

HeLa cells completely recover from the mitotic arrest elicited after 15-h incubation with the lead compounds. This restoring process in the normal cell cycle distribution begins early after rescue (around 6 h), and is roughly complete after 48 h without affecting the overall viability. We have proven using indirect immunofluorescence that the microtubule network re-polymerizes before the full recovery of the cell cycle distribution. At the same time, the rounded morphology of arrested cells is also reverted, getting attached to the culture surface. We have shown that the exit from mitosis depends on the synthesis of proteins, evidenced by the deficient recovery to normal G_2/M percentages in the presence of the protein synthesis inhibitor cycloheximide. However, there is an initial slight reduction in the G_2/M peak 3 h after removing the drugs in the presence and the absence of CHX. This may suggest that the alleviation of the mitotic arrest is only partly dependent on the synthesis of proteins. This finding would also be explained if microtubule re-polymerization starts right after the rescue, earlier than CHX inhibits protein synthesis. Immunoblotting experiments have revealed that the full recovery of HeLa cells previously treated for 15 h is associated with a remarkable alteration in P-Bcl-2 levels. As already mentioned, there is a transient upregulation of P-Bcl-2 after treatment with a decay right after removing the drugs. This backs up the protective role of P-Bcl-2. Its time-dependent decrease after rescue occurs in parallel with that of mitotic burden (i.e. MPM-2 signal).

Conversely, the removal of the compounds after 24-h incubation in HeLa cells only results in a partial recovery of the baseline status. The mitotic arrest is alleviated, but Annexin V-PI experiments have indicated reduced viability after rescue, correlating with enhanced DNA fragmentation. Even so, $SubG_0/G_1$ percentages follow a decreasing tendency over time. This seems to suggest that, while part of the cell population cannot recover since apoptosis has already been triggered, another population of cells skips the arrest by re-building the microtubule cytoskeleton and evades cell death. After 48-h treatments, the processes linking the mitotic arrest and the onset of apoptosis are presumably so advanced that cells cannot recover from mitotic arrest when washing out the ligand. After drug removal, there is increasing DNA fragmentation and a higher percentage of AnV^+/PI^+ double positive cells, indicating advanced stages of apoptosis. Surprisingly, the effect of compound **104** in HeLa cells is reversible even after 48-h treatment. It has been described that the eventual fate of cells challenged with antimitotic drugs may differ between cell lines and compounds.[411] Indeed, our results in tumor versus non-tumorigenic cell lines support that theory. A possible explanation for the differences between **104** and the other lead compounds is that cells are more prone to exit mitosis upon treatment with **104**. The partial increase of the G_0/G_1 population after a complete mitotic arrest in HeLa and HEK-293 cells treated with **104** backs up this hypothesis. Another potential explanation is the lesser extent of membrane permeabilization induced by **104** compared to the other compounds, because the loss of membrane integrity is widely considered a point of no return from which cells can be deemed non-viable.[579]

According to our experiments, 48 h is the span required so that HeLa cells previously treated for 15 h can restore the normal cell cycle distribution. At that point, the cells have reconstructed the cytoskeleton and exhibit normal morphology. Despite the absence of DNA fragmentation, we have detected a higher percentage of PI-positive cells after rescue compared to untreated samples, suggesting that the plasma membrane is compromised at least in a small population of cells. This could be related to the sensitization of HeLa cells when challenged with the same drugs in a second cycle of treatment. The mitochondrial alterations observed after rescue might also contribute to this higher susceptibility.

The analysis of the transmembrane potential ($\Delta\Psi_m$) in HeLa cells has shown a hyperpolarized status of the mitochondria after removing the drugs, with minor changes in ROS levels. Drug removal after 48-h incubations results in $DiOC_6[3]$ histogram displacement towards higher fluorescence intensities with the disappearance of the depolarized population found after treatment. This observation may indicate advanced stages of apoptosis, as evidenced by the increase in AnV^+/PI^+ double positive cells. Depolarized viable cells detected after 48-h treatments would get permeabilized and shift towards the ungated region. However, we cannot be sure whether the higher fluorescence of $DiOC_6[3]$ is indicative of a hyperpolarization status of the mitochondria or, by contrast, it is an artefact that arises from differences in dye uptake given the dramatic decrease in the number of cells compared to control conditions. This will have to be further explored in the future. The use of the uncoupling compound CCCP as a positive control for mitochondrial depolarization validates the procedure. In order to understand the significance of an increased $DiOC_6[3]$ signal, the drugs should be combined with CCCP to corroborate that the staining profiles after this co-treatment equals that of untreated cells in the presence of CCCP. Either way, the alleged hyperpolarization resulting from drug removal is not related to self-protection since adding the treatments again at that point induces increased apoptosis compared to cells that have not been previously exposed to the treatments.

Chapter 6

CONCLUSIONS

In this Ph.D. thesis, we have obtained novel antimitotic compounds as promising pharmacological agents in cancer therapy. The investigated compounds have been designed to interact with the colchicine domain in β-tubulin, which is usually divided into three consecutive zones based on the binding modes of ligands in X-ray structures. According to the initial approach discussed in "Objectives", we have synthesized compounds aimed to bind to zones 1-2, 2-3, or 1-2-3 of the colchicine domain. We have then conducted the *in vitro* biological evaluation and the study of the mechanism of action of some representative ligands as antitumor drugs. Based on our results, this work allows us to state the following conclusions:

i. The synthetic procedures used in this work are adequate to prepare the proposed compounds, which have been obtained in good yields in most cases.

ii. A 1,3-substitution pattern of the central A ring in three-ring sulfonamides based on ABT-751 with large linkers between A-C rings does not lead to active compounds in *in vitro* cell proliferation assays.

iii. The replacement of the *trans* olefin in MI-181 by amides, methylamines, ureas, or carbamates implies losing the antiproliferative activity, except in the case of ethylurea **270**. Hybrid compounds with polymethoxylated benzenes (A ring) like CA4 and pyridines (C ring) like MI-181 linked by amide groups do not display *in vitro* cytotoxic activity.

iv. The combination of *N*-methyl-indol-5-yl (B ring) with polymethoxylated benzenes (A ring) connected by sulfonamide or tetrazole groups (bridge) yields potent cytotoxic compounds. These compounds display IC_{50} values in the nanomolar or submicromolar range in different tumor and non-tumorigenic cell lines and primary cells. In most cases, their antiproliferative activity is not influenced by the pharmacological inhibition of P-gp, suggesting that they may overcome the multidrug-resistance phenotype *in vivo*. The upcoming conclusions refer to this family of compounds.

v. In sulfonamides, the position of methoxy groups on the A ring is crucial for the resulting biological activity. The classical 3,4,5-trimethoxyphenyl group leads to the most potent compounds, followed by 3,5-dimethoxyphenyl ligands, which in turn display higher cytotoxic activity than those with a 2,5-dimethoxyphenyl group. The bromination of 2,5-dimethoxyphenyl at position 4 improves the potency. The 2,3,4-trimethoxy substitution pattern, together with a reversed orientation of the sulfonamide, does not provide active compounds. The A ring is not that critical in tetrazoles.

vi. The methylation of the sulfonamide nitrogen increases the potency, yielding the most potent sulfonamides in each series regarding the A ring, although the introduction of bulkier substituents leads to lower potency. The potencies of methylated sulfonamides are comparable to tetrazoles with the same nitrogen position on the bridge. Tetrazoles are, in turn, strikingly more potent than their amide counterparts.

vii. Substitutions at the indole 3-position are detrimental for the activity. In tetrazoles, we have also evaluated benzenes as B rings besides *N*-methylindole. Phenyl rings substituted at position 4, although less potent than indoles, yield compounds with submicromolar potencies, better in the case of dimethylamino than methoxy derivatives.

viii. The biological target of the compounds is tubulin. They act as destabilizing agents by binding to the colchicine domain in α,β-tubulin with high-affinity binding constants. This leads to microtubule disruption, inducing antimitotic and antivascular activities. The antitumor activity of the compounds is the result of the antimitotic mechanism, causing *in vitro* antiproliferative effects with similar potencies between cell lines.

ix. The lead compounds induce caspase-dependent apoptotic cell death in HeLa cells after a sustained mitotic arrest with rapid permeabilization of the plasma membrane. Despite the similar antiproliferative potencies of the compounds against different cell lines, the extent of cell death is highly dependent on each cell type. In general terms, the non-tumorigenic cell lines that have been tested show higher resistance to apoptosis than tumor cell lines.

x. There is a reversible lag phase between microtubule disruption and the irreversible commitment of apoptosis that varies between cell lines. The mitotic arrest can be alleviated in drug-free media by re-polymerization of the tubulin cytoskeleton, which depends on protein synthesis. Although the initial percentages of cell cycle phases can be completely restored, HeLa cells become more sensitive to an additional treatment cycle.

xi. Mitochondria are involved in drug-induced apoptosis, with dissipation of $\Delta\Psi_m$ that occurs after the increase in ROS production and cytochrome c release. Some proteins of the Bcl-2 family, namely Mcl-1, Bcl-xL, and P-Bcl-2, show transient upregulation early upon treatment serving a protective role. Moreover, the overexpression of Bcl-xL and Bcl-2 in HeLa cells by gene transfer delays the onset of apoptosis but does not completely prevent the induction of cell death.

xii. The autophagic flux is increased in HeLa cells upon treatment with the lead compounds, but autophagy does not appear to display a relevant role in cell demise.

Our work has yielded novel indole-based compounds as promising drug candidates for cancer chemotherapy. These compounds exhibit optimized properties with potencies similar to that of CA4 – one of the most advanced colchicine site ligands in clinical trials – or even higher in some cases, and are not susceptible to MDR-mediated transport. The study of their mechanism of action contributes to further unraveling the molecular processes, both reversible or irreversible, that are involved in the transition from microtubule depolymerization to cell death. This work provides input for future research regarding the determinants that dictate different cell fates in distinct cell lines.

Chapter 7

MATERIALS and METHODS

GENERAL CHEMICAL TECHNIQUES

Equipment and instrumentation

Melting points were measured on a Buchi 510 apparatus, an LLG MPM-HV2 apparatus, or an Electrothermal ET0001 digital melting point apparatus and are uncorrected. 1D- and 2D-NMR spectra were acquired in $CDCl_3$ unless otherwise indicated, on a Varian Mercury Spectrometer operating at 400/100 MHz for $^{1}H/^{13}C$, respectively. Chemical shift values (δ) are expressed in ppm downfield from tetramethylsilane, and coupling constants (*J*) are given in Hz. The multiplicity (s: singlet, d: doublet, t: triplet, q: quartet, m: multiplet, dd: doublet of doublets, td: triplet of doublets, bs: broad singlet, bd: broad doublet, bt: broad triplet) and signal assignment are shown for each compound. The indicated assignments are based on the splitting patterns, coupling constants, and chemical shifts. A Nicolet Impact 410 Spectrophotometer was used for IR spectra in KBr disk or film on NaCl, and absorption frequencies are expressed in cm^{-1}. A hybrid QSTAR XL quadrupole/time of flight spectrometer was used for HRMS analyses. GC-MS spectra were performed using a Hewlett-Packard 5890 series II mass detector. Irradiation experiments were conducted using a Monowave 300 (Anton Paar) microwave synthesis reactor functioning at 850 W and 600 rpm.

Chromatographic techniques

Chemical reactions were monitored by thin layer chromatography (TLC) using pre-coated silica gel polyester plates (0.25 mm thickness) with UV fluorescence indicator 254 (Polychrom SI F_{254}). In addition, a solution of 10% sulfuric acid or 10% phosphomolybdic acid in ethanol was sprayed, and the plate was heated at 100 °C for a few minutes. Column purifications were carried out using silica gel columns by flash chromatography (Kieselgel 40, 0.040-0.063 mm; Merck), and 1.0 mm thickness silica gel plates were used for preparative TLC purifications (PLC Kieselgel 60 F_{254}; concentration zone 20 x 4 cm), then eluted with EtOAc.

Organic solvent processing

All the solvents (Carlo Erba Reagents) and reagents (Sigma-Aldrich) were used as purchased from commercial suppliers without further purification. The solvents (CH_2Cl_2, EtOAc, DMF, ACN, methanol, ethanol, toluene, MTBE) were stored over molecular sieves except for THF, which was freshly refluxed with sodium/benzophenone right before use, and hexane, dried by distillation and stored over $CaCl_2$.

GENERAL SYNTHETIC METHODS

Method A: Amide bond formation

A. Method A1: Using a coupling agent

The carboxylic acid (1.0-2.3 eq) together with *p*-DMAP (0.3-1.4 eq) and a coupling agent (1.3-2.3 eq of EDC·HCl or 1.1-2.8 eq of DCI) was heated in refluxing CH_2Cl_2 for 1-3 h prior to the addition of the amine dissolved in CH_2Cl_2 (the addition was carried out at room temperature). This mixture was stirred under reflux and N_2 atmosphere for 6 h-9 days and poured into cold water, washed with 1-2N HCl, 5% $NaHCO_3$, and saturated NaCl. The organic layer was dried over anhydrous Na_2SO_4, filtered, and evaporated under vacuum. Alternatively, the reaction can be carried out all-in-one by irradiation in a microwave reactor at 100-130 °C for 3 min to 2 h.

B. Method A2: Via preparation of acyl chlorides

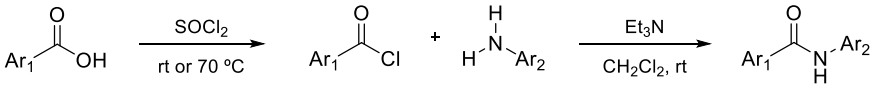

An excess of $SOCl_2$ (0.3-2 mL) was carefully added into a sealed tube containing the carboxylic acid. Depending on the acid used, the mixture was kept under agitation at room temperature, and alternatively, heated at 70 °C. The reaction progress was easily followed by color changes (Table 29). The remaining $SOCl_2$ was rotary eliminated, and the acyl chloride dissolved in a few mL of CH_2Cl_2 was added drop by drop into a solution of the corresponding amine (0.7-1.5 eq) in CH_2Cl_2 or ACN with triethylamine (0.1-10 mL) at room temperature and N_2 atmosphere. After 30 min to 5 days, it was poured into cold water and washed with 5% $NaHCO_3$ and brine until neutrality. If ACN was used, the solvent was evaporated and the residue re-dissolved in CH_2Cl_2 before the L-L extraction. The organic layer was dried over anhydrous Na_2SO_4, filtered, and concentrated to dryness.

Carboxylic acid	Temperature	Time period	Initial aspect	Final aspect
4-nitrobenzoic	70 °C	48-72 h	white suspension	translucent solution
4-nitrophenylacetic	70 °C	4-15 h	white suspension	translucent solution
2,3,4-trimethoxybenzoic	rt	4-24 h	yellow solution	dark red solution
2,3-dimethoxybenzoic	rt	15-72 h	orange solution	purple solution
2,4-dimethoxybenzoic	rt	5-7 h	yellow solution	ocher/purple solution
picolinic	rt	24 h	green solution	purple solution
nicotinic	rt	4 days	white suspension	translucent solution
isonicotinic	rt	21-48 h	white suspension	translucent solution

Table 29. Preparation of acyl chlorides. Color and aspect transitions can be followed to determine the formation of the product, since TLC cannot properly detect the conversion of the carboxylic acid into its acyl chloride in $SOCl_2$.

Method B: Reduction of nitro groups via catalytic hydrogenation

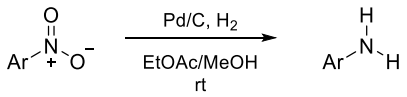

Palladium on activated charcoal approximately 10% in weight respect to the reagent was slowly added to a mixture of EtOAc (or alternatively CH_2Cl_2) and methanol, and the nitro derivative dissolved in EtOAc (or CH_2Cl_2) was poured into the previous suspension. The reaction was vigorously stirred under hydrogen atmosphere at room temperature for 14 h-6 days, then filtered through celite and evaporated under vacuum.

Method C: Modification of the sulfonamide nitrogen

A. Method C1: Alkylation with KOH in ACN

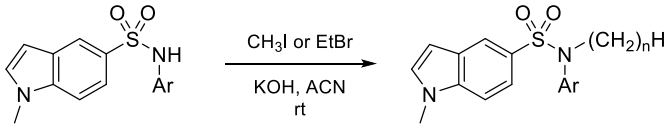

The sulfonamide derivative was mixed with ground KOH in excess in acetonitrile and stirred for 30 min. Then, 2.0-2.8 eq of methyl iodide or 2.0-4.0 eq of ethyl bromide were added to the previous suspension and kept under agitation at room temperature under N_2 atmosphere for 3 h to 8 days. KOH was filtered off, and the filtrate was evaporated, dissolved in CH_2Cl_2, and washed with brine until neutrality. The organic layer was dried over anhydrous Na_2SO_4, filtered, and concentrated to dryness.

B. Method C2: Alkylation with K_2CO_3 in DMF

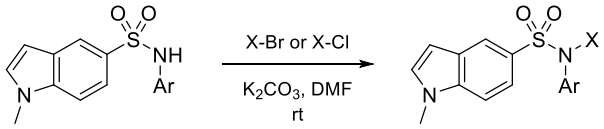

The halogen derivative (2.0-2.4 eq of ethyl bromoacetate, 2.0-8.6 eq of chloroacetonitrile, 2.0-2.2 eq of benzyl chloride or 2.3 eq of 4-fluorobenzyl chloride) was slowly added to a solution of the sulfonamide in 1 mL of sieve-dried DMF in the presence of excess K_2CO_3. The reaction was stirred for 3 h to 10 days at room temperature and N_2 atmosphere, and then filtered and evaporated. The residue was dissolved in CH_2Cl_2, washed with saturated NaCl, dried over anhydrous Na_2SO_4, and evaporated under vacuum after filtration.

Method D: Vilsmeier-Haack reaction

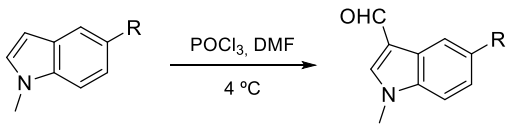

$POCl_3$ (6.0-7.2 mmol per mmol of the indolic compound) was carefully added to sieve-dried DMF (0.5-2 mL) at 4 °C and stirred for half an hour under N_2 atmosphere. The mixture was subsequently added drop

by drop into a solution of the indole derivative in ice-cooled DMF (0.5-8 mL) and progressively warmed to room temperature. After between 5 min to 2 h under agitation, the reaction was poured into iced water with sodium acetate and kept at 4 °C at least overnight until precipitation. The resulting powder was filtered off to obtain the aldehyde derivative.[518]

Method E: Preparation of carbonitriles via oximes

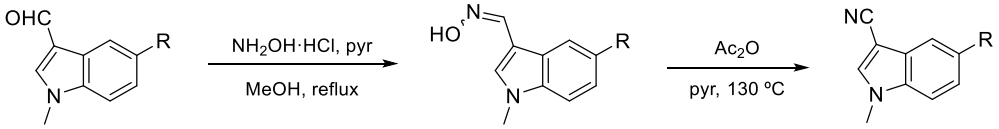

A solution of the aldehyde with 10 eq of $NH_2OH{\cdot}HCl$ and 4 drops of pyridine was heated in refluxing methanol for 12-48 h. Once tempered, methanol was evaporated and CH_2Cl_2 was added and washed with brine until neutral pH. The organic layer was dried over anhydrous Na_2SO_4, filtered, and rotary evaporated to obtain a mixture of both oximes (*E*+*Z*).[504] The mixture was dissolved in pyridine with acetic anhydride in excess (0.5-1 mL) and heated at 130 °C under N_2 atmosphere for 30-96 h.[499] The reaction was quenched by pouring onto ice and extracted with CH_2Cl_2, washed with 1-2N HCl, 5% $NaHCO_3$ (or Na_2CO_3), and saturated NaCl. Then, the organic layer was dried over anhydrous Na_2SO_4, filtered, and evaporated.

Method F: Formation of tetrazole rings

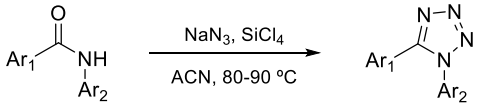

The amide and sodium azide (8.0-8.5 mmol per mmol of amide) were mixed in a sealed tube and suspended in the minimum volume of acetonitrile needed to cover the powder (2-3 mL). Silicon tetrachloride (8.2-9.0 eq) was subsequently added drop by drop, and the resulting suspension was stirred at 80-90 °C for 3-6 days, then cooled down in ice bath.[520] The reaction was quenched by dilution with CH_2Cl_2 and 5% $NaHCO_3$, and vigorously stirred for 0.5-1.5 h before extraction. The aqueous layer was extracted with EtOAc, and the organic solvents were washed with brine until neutrality, then dried over anhydrous Na_2SO_4, filtered, and rotary evaporated. For amide quantities larger than 300 mg, conventional reflux (20 mL of ACN) is preferred to the sealed system.

SYNTHESIS OF PRECURSORS

Synthesis of 1-(indolin-1-yl)ethan-1-one (1)

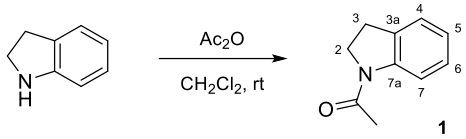

A mixture of acetic anhydride (606 µL, 6.41 mmol) and indoline (600 µL, 5.35 mmol) in 5 mL of CH_2Cl_2 was stirred at room temperature for 15 min, then poured into iced water and washed with 5% $NaHCO_3$ and brine. The organic layer was dried over anhydrous Na_2SO_4, filtered, and rotary concentrated yielding 814 mg (5.06 mmol, 94%) of **1**.

*1-(Indolin-1-yl)ethan-1-one (**1**).* White solid. **^{1}H-NMR** (400 MHz, $CDCl_3$): δ (*E*) 2.37 (3H, s, Ac); 3.00 (2H, t, *J* = 8.4 Hz, H3); 4.08 (2H, t, *J* = 8.4 Hz, H2); 6.94 (1H, t, *J* = 8.0 Hz, H6); 7.10-7.15 (2H, m, H4 and H5); 8.14 (1H, d, *J* = 8.0 Hz, H7). (*Z*) 2.16 (3H, s, Ac); 3.14 (2H, t, *J* = 8.4 Hz, H3); 3.98 (2H, t, *J* = 8.4 Hz, H2); 6.94 (1H, t, *J* = 8.0 Hz, H6); 7.10-7.15 (2H, m, H4 and H5); 8.14 (1H, d, *J* = 8.0 Hz, H7). **^{13}C-NMR** (100 MHz, $CDCl_3$): δ 24.1 (CH_3, Ac); 27.8 (CH_2, C3); 48.6 (CH_2, C2); 116.7 (CH, C7); 123.4 (CH, C4); 124.5 (CH, C6); 127.3 (CH, C5); 131.2 (C, C3a); 142.8 (C, C7a); 168.6 (C, CO). **GC-MS** ($C_{10}H_{11}NO^+$): 161 (M^+).

Synthesis of indoline-1-carbaldehyde (2) [210]

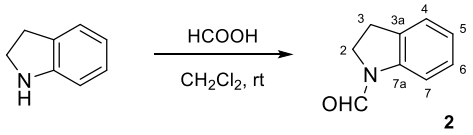

Formic acid (4.5 mL, 100 mmol) was added dropwise to a solution of indoline (10 mL, 88 mmol) in 50 mL of CH_2Cl_2. The reaction was stirred at room temperature under N_2 atmosphere for 22 h, poured onto ice, and washed with 5% $NaHCO_3$ and brine. The organic layer was dried over anhydrous Na_2SO_4, filtered, and evaporated under vacuum to obtain 12.588 g (85.63 mmol, 97%) of **2** as a yellow oil.

*Indoline-1-carbaldehyde (**2**).* Yellow oil. **^{1}H-NMR** (400 MHz, CD_3OD): δ (*E*) 3.16 (2H, t, *J* = 8.4 Hz, H3); 4.00 (2H, t, *J* = 8.4 Hz, H2); 7.06 (1H, td, *J* = 2.4, 8.0 and 8.4 Hz, H5); 7.18 (1H, td, *J* = 2.8, 8.0 and 8.4 Hz, H6); 7.27 (1H, dd, *J* = 2.8 and 8.0 Hz, H4); 7.33 (1H, dd, *J* = 2.4 and 8.0 Hz, H7); 8.95 (1H, s, CHO). (*Z*) 3.18 (2H, t, *J* = 8.4 Hz, H3); 4.15 (2H, t, *J* = 8.4 Hz, H2); 7.06 (1H, td, *J* = 2.4, 8.0 and 8.4 Hz, H5); 7.18 (1H, td, *J* = 2.8, 8.0 and 8.4 Hz, H6); 7.27 (1H, dd, *J* = 2.8 and 8.0 Hz, H4); 7.95 (1H, dd, *J* = 2.4 and 8.0 Hz, H7); 8.46 (1H, s, CHO). **^{13}C-NMR** (100 MHz, $CDCl_3$): δ (*E*) 26.8 (CH_2, C3); 44.3 (CH_2, C2); 109.2 (CH, C7); 123.8 (CH, C4); 125.7 (CH, C6); 127.2 (CH, C5); 131.7 (C, C3a); 140.8 (C, C7a); 157.3 (CH, CHO). (*Z*) 27.4 (CH_2, C3); 46.6 (CH_2, C2); 116.1 (CH, C7); 124.2 (CH, C4); 124.6 (CH, C6); 127.2 (CH, C5); 132.0 (C, C3a); 141.0 (C, C7a); 159.2 (CH, CHO). **GC-MS** ($C_9H_9NO^+$): 147 (M^+).

Synthesis of indoline-5-sulfonyl chloride (3)

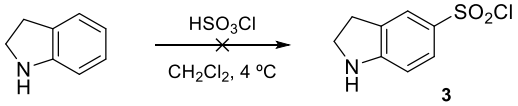

Chlorosulfonic acid (66 µL, 0.99 mmol) was added to a solution of indoline (100 µL, 0.89 mmol) in 5 mL of CH_2Cl_2 at 4 °C, keeping the low temperature and N_2 atmosphere for 6 h. The reaction was subsequently poured onto ice and diluted with CH_2Cl_2, then washed with brine until neutral pH. The organic layer was dried over anhydrous Na_2SO_4, filtered, and evaporated (48 mg). The signals corresponding to compound **3** are not observed.

Synthesis of 1-acetylindoline-5-sulfonyl chloride (4)

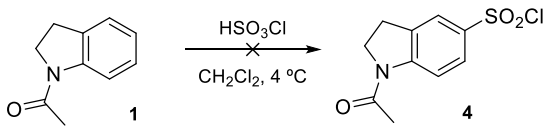

Chlorosulfonic acid (95 µL, 1.42 mmol) was carefully added to a solution of 1-(indolin-1-yl)ethan-1-one (**1**, 207 mg, 1.29 mmol) in 5 mL of CH_2Cl_2 at 4 °C. An insoluble resin-like mass was formed while stirring, although no reaction progress was observed by TLC.

Synthesis of 1-formylindoline-5-sulfonyl chloride (5) [210]

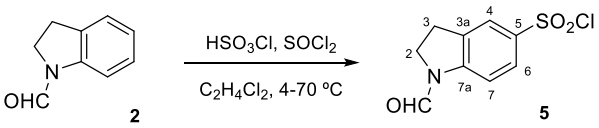

Drop by drop, chlorosulfonic acid (8726 µL, 130.31 mmol) was added to a 4 °C solution of indoline-1-carbaldehyde (**2**, 9577 mg, 65.15 mmol) in 100 mL of 1,2-dichloroethane. Once mixed, the reaction was heated and $SOCl_2$ (9452 µL, 130.30 mmol) was slowly added when it reached 70 °C.[210] After 5 hours under N_2 atmosphere, it was cooled down to 4 °C and, while vigorously stirring, the solution was diluted with 500 mL of water and 500 mL of heptane until precipitation occurred 3 h later. The suspension was filtered off, washing the solid with water and heptane to provide sulfonyl chloride **5** (15.8 g, 64.36 mmol, 99%).

*1-Formylindoline-5-sulfonyl chloride (**5**).* Yellow powder. **IR** (KBr): 1678, 1494, 1360, 1180 cm^{-1}. **^{1}H-NMR** (400 MHz, $CDCl_3$): δ (*E*) 3.27 (2H, t, *J* = 8.8 Hz, H3); 4.17 (2H, t, *J* = 8.8 Hz, H2); 7.30 (1H, d, *J* = 8.0 Hz, H7); 7.89 (2H, m, H4 and H6); 9.04 (1H, s, CHO). (*Z*) 3.32 (2H, t, *J* = 8.4 Hz, H3); 4.26 (2H, t, *J* = 8.4 Hz, H2); 7.89 (2H, m, H4 and H6); 8.25 (1H, d, *J* = 8.4 Hz, H7); 8.58 (1H, s, CHO). **^{13}C-NMR** (100 MHz, $CDCl_3$): δ (*E*) 26.6 (CH_2, C3); 45.5 (CH_2, C2); 109.3 (CH, C7); 125.2 (CH, C6); 128.4 (CH, C4); 133.8 (C, C3a); 139.2 (C, C5); 147.3 (C, C7a); 157.7 (CH, CHO). (*Z*) 27.3 (CH_2, C3); 47.4 (CH_2, C2); 116.4 (CH, C7); 123.9 (CH, C6); 128.4 (CH, C4); 133.8 (C, C3a); 139.2 (C, C5); 147.1 (C, C7a); 160.1 (CH, CHO).

Synthesis of 2,3,4-trimethoxybenzenesulfonyl chloride (6)

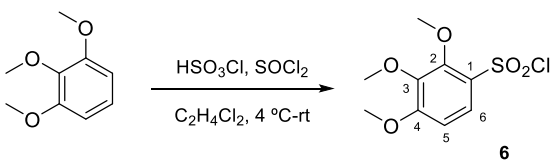

Chlorosulfonic acid (445 µL, 6.65 mmol) was carefully added dropwise to a solution of 1,2,3-trimethoxybenzene (1065 mg, 6.33 mmol) in ice-cooled 1,2-dichloroethane (25 mL) under N_2. Half an hour later, thionyl chloride was slowly added (919 µL, 12.67 mmol) and progressively warmed to room

temperature. After one hour and a half, the reaction was evaporated under vacuum yielding an oily crude (1596 mg, <95%) that contained compound **6** with minor impurities. The unpurified product was used as such in the next step.

*2,3,4-Trimethoxybenzenesulfonyl chloride (**6**).* Brown oil. **^{1}H-NMR** (400 MHz, $CDCl_3$): δ 3.91 (3H, s, 3-OCH_3); 3.96 (3H, s, 4-OCH_3); 4.14 (3H, s, 2-OCH_3); 6.74 (1H, d, *J* = 9.2 Hz, H5); 7.68 (1H, d, *J* = 9.2 Hz, H6). **^{13}C-NMR** (100 MHz, $CDCl_3$): δ 57.9 (CH_3, 4-OCH_3); 62.4 (CH_3, 3-OCH_3); 63.3 (CH_3, 2-OCH_3); 107.5 (CH, C5); 126.4 (CH, C6); 130.9 (C, C1); 144.3 (C, C3); 153.6 (C, C2); 161.7 (C, C4). **GC-MS** ($C_9H_{11}ClO_5S^+$): 266 (M^+).

Synthesis of 5-nitroindoline (7)

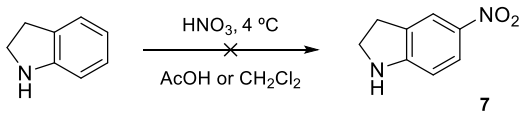

Procedure 1: 65% HNO_3 (68 µL, 0.98 mmol) was carefully added to a solution of indoline (100 µL, 0.89 mmol) in 5 mL of CH_2Cl_2 at 4 °C. After 20 h, anhydrous Na_2SO_4 and Na_2CO_3 1:1 were added to the reaction, which was subsequently filtered and rotary evaporated, obtaining 83 mg (0.70 mmol) of indoline.

Procedure 2: 65% HNO_3 (68 µL, 0.98 mmol) was added to a solution of indoline (100 µL, 0.89 mmol) in 2 mL of acetic acid at 4 °C. After 20 h, the reaction mixture was poured onto ice, diluted with CH_2Cl_2, and washed with 5% $NaHCO_3$ and saturated NaCl. The organic layer was dried over anhydrous Na_2SO_4, filtered, and concentrated to dryness, recovering 68 mg (0.57 mmol) of indoline.

Preparation of compound 8 and 9

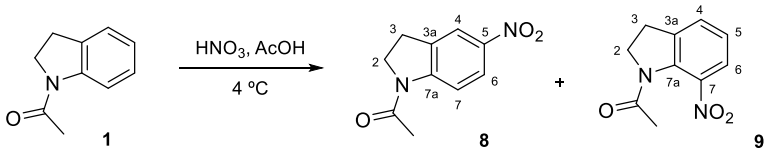

65% HNO_3 (144 µL, 2.08 mmol) was added to a solution of **1** (305 mg, 1.89 mmol) in 2 mL of acetic acid at 4 °C. After 9 h, the reaction mixture was poured onto ice, diluted with CH_2Cl_2, and washed with 5% $NaHCO_3$ and brine until neutrality. The organic layer was dried over anhydrous Na_2SO_4, filtered, and evaporated, obtaining a mixture of **8** (280 mg, 1.36 mmol, 72%) and **9** (46 mg, 0.22 mmol, 12%) as a white solid.

*1-(5-Nitroindolin-1-yl)ethan-1-one (**8**).* Non-isolated product. **^{1}H-NMR** (400 MHz, $CDCl_3$): δ 2.28 (3H, s, Ac); 3.29 (2H, t, *J* = 8.0 Hz, H3); 4.19 (2H, t, *J* = 8.0 Hz, H2); 8.04 (1H, bs, H4); 8.13 (1H, dd, *J* = 2.4 and 8.8 Hz, H6); 8.29 (1H, bd, *J* = 8.8 Hz, H7).

*1-(7-Nitroindolin-1-yl)ethan-1-one (**9**).* Non-isolated product. **^{1}H-NMR** (400 MHz, $CDCl_3$): δ 2.34 (3H, s, Ac); 3.22 (2H, t, *J* = 8.0 Hz, H3); 4.23 (2H, t, *J* = 8.0 Hz, H2); 7.14 (1H, t, *J* = 8.0 Hz, H5); 7.41 (1H, dd, *J* = 1.2 and 8.0 Hz, H4); 7.64 (1H, dd, *J* = 1.2 and 8.0 Hz, H6).

Synthesis of 5-nitroindoline-1-carbaldehyde (10)

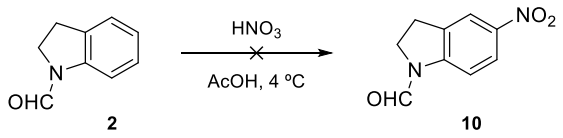

65% HNO_3 (5 mL, 72 mmol) was added drop by drop to a solution of indoline-1-carbaldehyde (**2**, 9665 mg, 65.75 mmol) in 10 mL of acetic acid at 4 °C. After 5 days, the reaction was poured onto ice, diluted with CH_2Cl_2, and washed with 5% $NaHCO_3$ and brine. The organic layer was dried over anhydrous Na_2SO_4, filtered, and evaporated, yielding 1415 mg of a complex mixture.

Synthesis of 1-(5-nitro-1H-indol-1-yl)ethan-1-one (11)

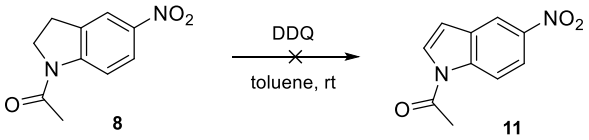

DDQ (282 mg, 1.24 mmol) was added to a solution of 177 mg (0.86 mmol) of a 6:1 mixture of **8** and **9** in 25 mL of toluene with 1 mL of CH_2Cl_2.[580] It was stirred at room temperature for 2 h, then heated under reflux for 3 days. Additional DDQ (116 mg, 0.51 mmol) was added to the reaction stirring for 4 days more before evaporating to dryness. Product **11** was not obtained. A similar result was obtained with DDQ in dioxane at room temperature.

Synthesis of 1-methyl-5-nitro-1H-indole (12)

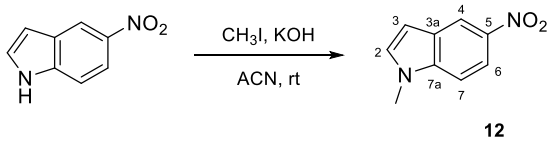

Methylation of 5-nitro-1*H*-indole was carried out as described for sulfonamides in general procedure **C1**. The indole derivative (255 mg, 1.57 mmol) in 25 mL of ACN with ground KOH in excess was treated with methyl iodide (196 µL, 3.15 mmol). After one day, the desired product **12** (274 mg, 1.56 mmol, 99%) was obtained and crystallized in CH_2Cl_2/Hex (149 mg, 0.85 mmol, 54%).

*1-Methyl-5-nitro-1H-indole (**12**).* Yellow crystals. **Mp** (CH_2Cl_2/Hex): 169.2-170.4 °C. **IR** (KBr): 1520, 1328, 743 cm^{-1}. **^{1}H-NMR** (400 MHz, $CDCl_3$): δ 3.86 (3H, s, NCH_3); 6.67 (1H, d, *J* = 3.6 Hz, H3); 7.21 (1H, d, *J* = 3.6 Hz, H2); 7.34 (1H, d, *J* = 8.8 Hz, H7); 8.13 (1H, dd, *J* = 2.4 and 8.8 Hz, H6); 8.59 (1H, d, *J* = 2.4 Hz, H4). **^{13}C-NMR** (100 MHz, $CDCl_3$): δ 33.3 (CH_3, NCH_3); 103.8 (CH, C3); 109.1 (CH, C7); 117.2 (CH, C6); 118.1 (CH, C2); 127.6 (C, C3a); 132.1 (CH, C4); 139.4 (C, C5); 141.5 (C, C7a). **GC-MS** ($C_9H_8N_2O_2^+$): 176 (M^+).

Synthesis of 1-methyl-1H-indol-5-amine (13)

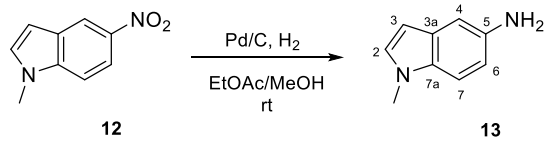

Following methodology **B**, 1-methyl-5-nitro-1*H*-indole (**12**, 1190 mg, 6.76 mmol) was reduced in the presence of Pd/C in EtOAc/methanol (100 mL) under hydrogen atmosphere providing **13** (980 mg, 6.71 mmol, 99%) after 14 h.

*1-Methyl-1H-indol-5-amine (**13**).* Red crystals. **Mp** (ether): 110-112 °C. **IR** (KBr): 3407, 3335, 1498, 727 cm^{-1}. **^{1}H-NMR** (400 MHz, $CDCl_3$): δ 3.73 (3H, s, NCH_3); 6.28 (1H, d, *J* = 3.2 Hz, H3); 6.69 (1H, dd, *J* = 2.0 and 8.4 Hz, H6); 6.92 (1H, d, *J* = 2.0 Hz, H4); 6.96 (1H, d, *J* = 3.2 Hz, H2); 7.12 (1H, d, *J* = 8.4 Hz, H7). **^{13}C-NMR** (100 MHz, $CDCl_3$): δ 33.9 (CH_3, NCH_3); 99.5 (CH, C3); 105.8 (CH, C4); 109.7 (CH, C6); 112.6 (CH, C7); 129.2 (CH, C2); 129.4 (C, C7a); 131.9 (C, C3a); 139.4 (C, C5). **GC- MS** ($C_9H_{10}N_2^+$): 146 (M^+).

Synthesis of 1-methyl-5-nitro-1H-indole-3-carbaldehyde (14)

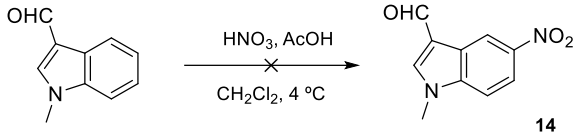

14

65% HNO_3 (60 µL, 0.87 mmol) was added to a solution of 1-methyl-1*H*-indole-3-carbaldehyde (114 mg, 0.72 mmol) in 5 mL of CH_2Cl_2 with 60 µL (1.05 mmol) of acetic acid at 4 °C. No reaction progress was observed.

Synthesis of 5-nitro-1H-indole-3-carbaldehyde (15)

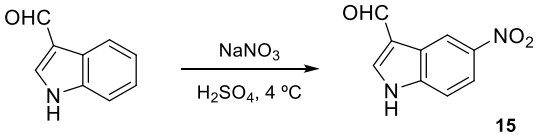

15

Procedure 1: 65% HNO_3 (90 µL, 1.30 mmol) was added to a cold solution of 1*H*-indole-3-carbaldehyde (142 mg, 0.98 mmol) in 5 mL of CH_2Cl_2. After 30 min, the resulting precipitate was filtered off, obtaining 78 mg (0.54 mmol) of the starting material.

Procedure 2: A solution of $NaNO_3$ (84 mg, 0.99 mmol) in 5 mL of H_2SO_4 was added drop by drop to 1*H*-indole-3-carbaldehyde (109 mg, 0.75 mmol) in 5 mL of H_2SO_4 at 4 °C.[581] After one and a half hours under N_2, it was poured onto ice, neutralized to pH 7, and extracted with CH_2Cl_2. Once dried over anhydrous Na_2SO_4, the organic layer was filtered and evaporated, obtaining 20 mg of a 1:1 mixture of 1*H*-indole-3-carbaldehyde and another indole-3-carbaldehyde derivative, putatively corresponding to **15**.

Preparation of compound 16 and 17

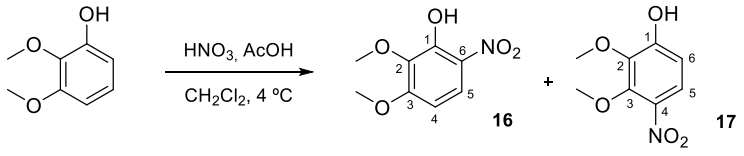

16 **17**

2,3-Dimethoxyphenol (5 mL, 38 mmol) was dissolved in 5 mL of CH_2Cl_2 with 500 µL of acetic acid at 4 °C. Then, nitric acid (2861 µL, 41.32 mmol) was added dropwise and the reaction was stirred for 72 h. It was subsequently poured onto ice, diluted with CH_2Cl_2, and washed with brine until neutral pH. The organic

layer was dried over anhydrous Na_2SO_4, filtered, and evaporated under vacuum, obtaining 5918 mg (29.74 mmol, 79%) of a 6:4 mixture of **16** and **17**.

*2,3-Dimethoxy-6-nitrophenol (**16**).* Non-isolated compound. **^{1}H-NMR** (400 MHz, $CDCl_3$): δ 3.92 (3H, s, 2-OCH_3); 3.98 (3H, s, 3-OCH_3); 6.58 (1H, d, *J* = 9.6 Hz, H4); 7.93 (1H, d, *J* = 9.6 Hz, H5); 10.81 (1H, bs, OH).

*2,3-Dimethoxy-4-nitrophenol (**17**).* Non-isolated compound. **^{1}H-NMR** (400 MHz, $CDCl_3$): δ 3.92 (3H, s, 2-OCH_3); 4.02 (3H, s, 3-OCH_3); 6.77 (1H, d, *J* = 9.2 Hz, H6); 7.67 (1H, d, *J* = 9.2 Hz, H5).

Synthesis of 1,2,3-trimethoxy-4-nitrobenzene (18)

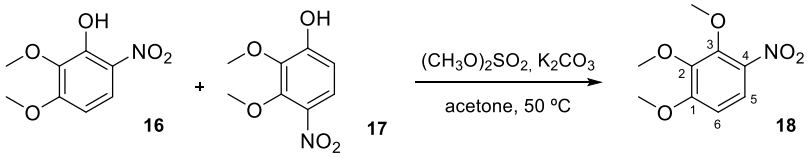

A mixture of **16** and **17** (78 mg, 0.39 mmol) was dissolved in 5 mL of acetone with 542 mg (3.92 mmol) of K_2CO_3. Then, dimethyl sulfate (284 µL, 3.00 mmol) was slowly added to the reaction and heated at 50 °C under N_2 atmosphere for 21 h.[582] Once filtered, it was concentrated to dryness, re-dissolved in CH_2Cl_2, and washed with saturated NaCl. The organic layer was dried over anhydrous Na_2SO_4, filtered, and evaporated, providing 45 mg (0.21 mmol, 54%) of **18**.

*1,2,3-Trimethoxy-4-nitrobenzene (**18**).* Brown oil. **^{1}H-NMR** (400 MHz, $CDCl_3$): δ 3.94 (3H, s, 2-OCH_3); 3.96 (3H, s, 1-OCH_3); 4.01 (3H, s, 3-OCH_3); 6.70 (1H, d, *J* = 9.2 Hz, H6); 7.69 (1H, d, *J* = 9.2 Hz, H5). **GC-MS** ($C_9H_{11}NO_5^+$): 213 (M^+).

Synthesis of 1,2,3-trimethoxy-5-nitrobenzene (19)

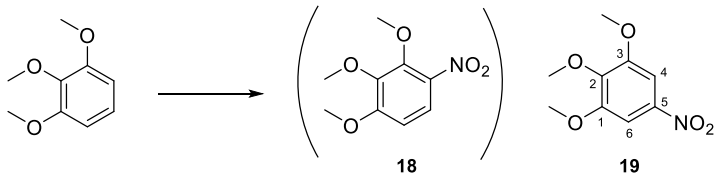

Procedure 1: KNO_3 (32 mg, 0.32 mmol) and catalytic tetrabutylammonium hydrogen sulfate were added to a solution of 1,2,3-trimethozybenzene (44 mg, 0.26 mmol) in 1 mL of acetonitrile at 4 °C. After 48 h under N_2, the reaction was heated under reflux for 6 days. No reaction progress was observed by ^{1}H-NMR. $ZnCl_2$ and KNO_3 were added to the crude residue in 3 mL of acetonitrile and stirred at room temperature, yielding the starting material after 4 days (40 mg, 0.24 mmol).

Procedure 2: 65% HNO_3 (20 µL, 0.29 mmol) was added to a solution of 1,2,3-trimethozybenzene (40 mg, 0.24 mmol) in 0.5 mL of acetic acid in ice bath. After 30 min, the reaction was poured onto ice, diluted with CH_2Cl_2, and washed with 5% $NaHCO_3$ and brine. The organic layer was dried over anhydrous Na_2SO_4, filtered, and evaporated, yielding 32 mg (0.15 mmol, 64%) of 1,2,3-trimethoxy-5-nitrobenzene (**19**).

Procedure 3: *Tert*-butyl nitrite (90%, 110 µL, 0.83 mmol) was added to 1,2,3-trimethoxybenzene (142 mg, 0.84 mmol) in 3 mL of refluxing acetonitrile. After 4 days, the reaction was filtered and evaporated under vacuum, obtaining 150 mg of a 2:1 mixture of **19** and 1,2,3-trimethoxybenzene.

*1,2,3-Trimethoxy-5-nitrobenzene (**19**).* Non-isolated product. **^{1}H-NMR** (400 MHz, $CDCl_3$): δ 3.85 (3H, s, OCH_3); 3.94 (6H, s, OCH_3); 7.52 (2H, s, H4 and H6).

Synthesis of 1-bromo-3,4,5-trimethoxy-2-nitrobenzene (20)

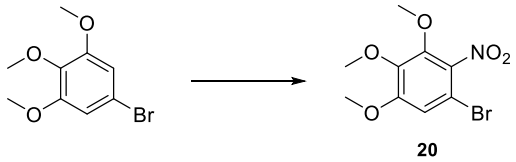

20

Procedure 1: 5-Bromo-1,2,3-trimethoxybenzene (168 mg, 0.68 mmol) was dissolved in 700 µL of acetic acid and cooled to 4 °C. 65% HNO_3 (56 µL, 0.81 mmol) was carefully added to that solution, which turned from yellow to red right after the addition. After 4 h, it was diluted with CH_2Cl_2, poured into iced water, and washed with 5% $NaHCO_3$ and brine. The organic layer was dried over anhydrous Na_2SO_4, filtered, and evaporated, yielding 142 mg of a complex mixture.

Procedure 2: HNO_3 (65%, 70 µL, 1.01 mmol) was added to a solution of the bromo derivative (138 mg, 0.56 mmol) in 2 mL of cold CH_2Cl_2. After 6 h, the reaction mixture was poured onto ice and washed with 5% $NaHCO_3$ and brine. The organic layer was dried over anhydrous Na_2SO_4, filtered, and concentrated to dryness, giving 99 mg of a complex mixture.

Procedure 3: 65% HNO_3 (53 µL, 0.77 mmol) was added to 5-bromo-1,2,3-trimethoxybenzene (158 mg, 0.64 mmol) in 1 mL of acetonitrile in ice bath, and stirred for 24 h, yielding a complex mixture.

Procedure 4: Montmorillonite K-10 (540 mg), bismuth subnitrate (411 mg, 0.28 mmol), and 5-bromo-1,2,3-trimethoxybenzene (219 mg, 0.89 mmol) were suspended in 20 mL of THF and stirred under vacuum for 6 h.[583] No reaction progress was observed. A similar result was obtained by irradiation in a microwave oven at 90 °C for 3 min.

Procedure 5: *Tert*-butyl nitrite (90%, 616 µL, 4.66 mmol) was added to a solution of 5-bromo-1,2,3-trimethoxybenzene (685 mg, 2.77 mmol) in 5 mL of acetonitrile and heated under reflux for 2 days, giving a mixture of compounds.

Synthesis of 2,3,4-trimethoxyaniline (21)

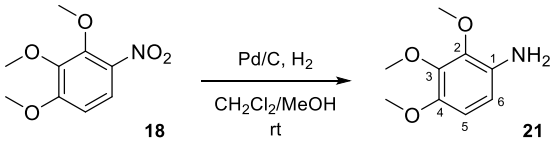

18 **21**

Following general method **B**, nitro derivative **18** (407 mg, 1.91 mmol) was stirred under H_2 with Pd/C in excess in 25 mL of CH_2Cl_2/MeOH for 3 days, providing 317 mg (1.73 mmol, 91%) of **21**.

*2,3,4-Trimethoxyaniline (**21**).* Black oil. **^{1}H-NMR** (400 MHz, $CDCl_3$): δ 3.74 (3H, s, 3-OCH_3); 3.78 (3H, s, 4-OCH_3); 3.88 (3H, s, 2-OCH_3); 6.43 (1H, d, *J* = 8.8 Hz, H5); 6.52 (1H, d, *J* = 8.8 Hz, H6). **GC-MS** ($C_9H_{13}NO_3^+$): 183 (M^+).

Synthesis of 1,4-dimethoxy-2-nitrobenzene (22)

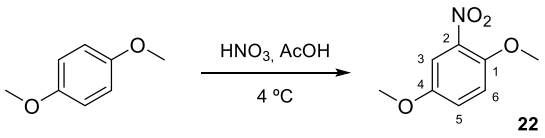

Nitric acid (1193 µL, 17.23 mmol) was carefully added drop by drop to a solution of 1,4-dimethoxybenzene (2164 mg, 15.66 mmol) in 15 mL of acetic acid at 4 °C. It was stirred for half an hour, quenched by pouring the mixture onto ice, extracted with EtOAc, and washed with 5% $NaHCO_3$ and brine. The organic layer was dried over anhydrous Na_2SO_4, filtered, and evaporated under vacuum giving 1,4-dimethoxy-2-nitrobenzene (**22**, 2730 mg, 14.92 mmol, 95%). Crystallization in CH_2Cl_2/Hex gave 2020 mg (11.04 mmol, 70%) of **22**.

*1,4-Dimethoxy-2-nitrobenzene (**22**).* Yellow crystals. **Mp** (CH_2Cl_2/Hex): 71.8-72.5 °C. **IR** (KBr): 1528, 1355 cm^{-1}. **^{1}H-NMR** (400 MHz, $CDCl_3$): δ 3.82 (3H, s, 4-OCH_3); 3.92 (3H, s, 1-OCH_3); 7.03 (1H, d, *J* = 8.8 Hz, H6); 7.11 (1H, dd, *J* = 3.2 and 8.8 Hz, H5); 7.40 (1H, d, *J* = 3.2 Hz, H3). **^{13}C-NMR** (100 MHz, $CDCl_3$): δ 56.0 (CH_3, 1-OCH_3); 57.0 (CH_3, 4-OCH_3); 109.9 (CH, C3); 115.0 (CH, C6); 120.9 (CH, C5); 139.4 (C, C2); 147.3 (C, C1); 152.8 (C, C4). **GC-MS** ($C_8H_9NO_4^+$): 183 (M^+).

Synthesis of 2,5-dimethoxyaniline (23)

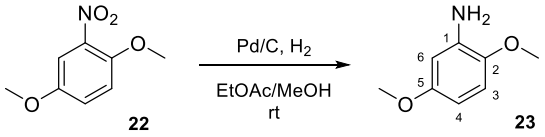

As described in procedure **B**, nitro derivative **22** (9523 mg, 52.04 mmol) mixed with Pd/C in EtOAc/methanol (250 mL) under H_2 atmosphere provided 2,5-dimethoxyaniline (**23**, 7710 mg, 50.04 mmol, 97%) after 6 days. Crystallization in CH_2Cl_2 gave 6802 mg (44.46 mmol, 85%) of **23**.

*2,5-Dimethoxyaniline (**23**).* Brilliant black crystals. **Mp** (CH_2Cl_2): 73.8-75.0 °C. **IR** (KBr): 3459, 3368, 1519, 1227 cm^{-1}. **^{1}H-NMR** (400 MHz, $CDCl_3$): δ 3.72 (3H, s, 5-OCH_3); 3.80 (3H, s, 2-OCH_3); 6.24 (1H, dd, *J* = 2.8 and 8.8 Hz, H4); 6.33 (1H, d, *J* = 2.8 Hz, H6); 6.69 (1H, d, *J* = 8.8 Hz, H3). **^{13}C-NMR** (100 MHz, $CDCl_3$): δ 54.5 (CH_3, 2-OCH_3); 55.1 (CH_3, 5-OCH_3); 100.9 (CH, C3); 101.0 (CH, C5); 110.3 (CH, C6); 136.2 (C, C2); 140.9 (C, C1); 153.4 (C, C4). **GC-MS** ($C_8H_{11}NO_2^+$): 153 (M^+).

Synthesis of 4-bromo-2,5-dimethoxyaniline (24)

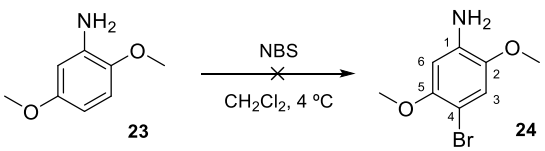

N-bromosuccinimide (898 mg, 5.04 mmol) was added to a solution of 2,5-dimethoxyaniline (**23**, 702 mg, 4.59 mmol) in 50 mL of CH_2Cl_2 at 4 °C and stirred under N_2 for 7 h. Concentration under vacuum resulted in product decomposition.

Synthesis of 2-bromo-1,4-dimethoxybenzene (25)

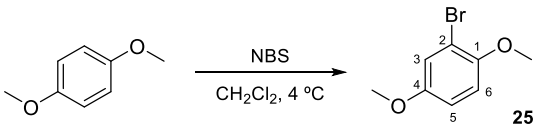

Procedure 1*: N*-bromosuccinimide (160 mg, 0.90 mmol) and 1,4-dimethoxybenzene (110 mg, 0.80 mmol) in 10 mL of CH_2Cl_2 at 4 °C were stirred under N_2 atmosphere for 5 days. No reaction progress was observed by ^{1}H-NMR.

Procedure 2*:* A mixture of 1,4-dimethoxybenzene (132 mg, 0.96 mmol) and *N*-bromosuccinimide (195 mg, 1.10 mmol) in 5 mL of CH_2Cl_2 was stirred at 4 °C in the presence of $FeCl_3$ in excess for 48 h. Concentration under vacuum gave compound **25** with succinimide.

*2-Bromo-1,4-dimethoxybenzene (**25**).* Non-isolated product. **^{1}H-NMR** (400 MHz, $CDCl_3$): δ 3.74 (3H, s, 4-OCH_3); 3.82 (3H, s, 1-OCH_3); 6.81 (2H, m, H5 and H6); 7.10 (1H, d, *J* = 2.4 Hz, H3).

Synthesis of methyl 4-ureidobenzoate (26)

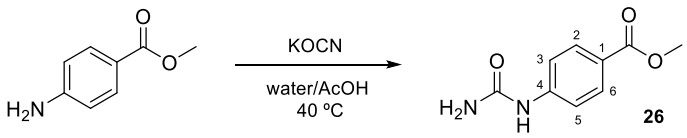

Potassium cyanate (1083 mg, 13.35 mmol) was slowly added to a solution of methyl 4-aminobenzoate (994 mg, 6.58 mmol) in 30 mL of a 1:1 mixture of water and acetic acid. The reaction was heated at 40 °C under N_2 atmosphere for 24 h. It was poured into water with ice and kept at 4 °C overnight, yielding 1021 mg (5.26 mmol, 80%) of compound **26**.

*Methyl 4-ureidobenzoate (**26**).* White crystals. **Mp** (H_2O): 187.3 °C. **IR** (KBr): 3462, 3347, 3263, 1713, 1668, 1587, 1268 cm^{-1}. **^{1}H-NMR** (400 MHz, acetone-D6): δ 3.83 (3H, s, OCH_3); 5.84 (2H, bs, NH_2); 7.60 (2H, d, *J* = 7.8 Hz, H3 and H5); 7.87 (2H, d, *J* = 7.8 Hz, H2 and H6); 8.66 (1H, bs, NH). **^{13}C-NMR** (100 MHz, acetone-D6): δ 51.1 (CH_3, OCH_3); 117.2 (2) (CH, C3 and C5); 122.9 (C, C1); 130.4 (2) (CH, C2 and C6); 145.1 (C, C4); 155.9 (C, urea); 166.2 (C, ester). **HRMS** ($C_9H_{10}N_2NaO_3^+$): calculated 217.0584 ($M+Na^+$), found 217.0584.

Synthesis of 4-ureidobenzoic acid (27)

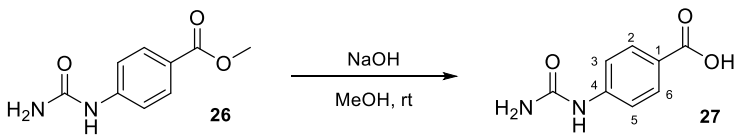

Excess powdered NaOH was added to **26** (580 mg, 2.99 mmol) dissolved in 12 mL of methanol and heated for 30 min. Then, 2N HCl was added and extracted with EtOAc. The organic layer was dried over anhydrous Na_2SO_4, filtered, and evaporated to obtain a mixture of **26** and **27** (400 mg, 2.22 mmol, 74%). The product was used without purification for the next reaction.

*4-Ureidobenzoic acid (**27**).* Non-isolated product. **^{1}H-NMR** (400 MHz, CD_3OD): δ 6.79 (2H, d, *J* = 7.2 Hz, H3 and H5); 8.07 (2H, d, *J* = 7.2 Hz, H2 and H6).

Synthesis of methyl 4-acetamidobenzoate (28)

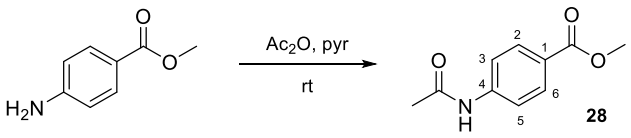

A solution of methyl 4-aminobenzoate (1333 mg, 8.83 mmol) in 1 mL of acetic anhydride and 1.5 mL of pyridine was stirred at room temperature for 4 h, yielding a white solid. It was diluted with EtOAc and washed with 2 N HCl, 5% $NaHCO_3$, and brine. The organic layer was dried over anhydrous Na_2SO_4, filtered, and evaporated to obtain the acetylated product **28** (1539 mg, 7.97 mmol, 90%). Crystallization in CH_2Cl_2/Hex gave 1160 mg (6.01 mmol, 68%) of **28**.

*Methyl 4-acetamidobenzoate (**28**)*. White crystals. **Mp** (CH_2Cl_2/Hex): 128.7 °C. **IR** (KBr): 3361, 1702, 1690, 1597, 1252 cm^{-1}. **^{1}H-NMR** (400 MHz, $CDCl_3$): δ 2.20 (3H, s, Ac); 3.83 (3H, s, OCH_3); 7.62 (2H, d, *J* = 7.6 Hz, H3 and H5); 7.90 (2H, d, *J* = 7.6 Hz, H2 and H6); 9.15 (1H, bs, NH). **^{13}C-NMR** (100 MHz, CD_3OD): δ 24.5 (CH_3, Ac); 52.1 (CH_3, OCH_3); 119.0 (2) (CH, C3 and C5); 125.1 (C, C1); 130.6 (2) (CH, C2 and C6); 142.7 (C, C4); 166.9 (C, ester); 169.8 (C, amide). **HRMS** ($C_{10}H_{11}NNaO_3^+$): calculated 216.0631 ($M+Na^+$), found 216.0632.

Synthesis of 4-acetamidobenzoic acid (29)

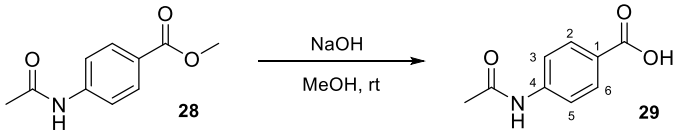

An excess of powdered NaOH in water was added to a solution of methyl ester **28** (753 mg, 3.90 mmol) in 20 mL of methanol. The reaction was stirred at room temperature for 3 h, and after adding EtOAc, it was washed with 2N HCl and brine. The organic layer was dried over anhydrous Na_2SO_4, filtered, and evaporated, yielding 414 mg (2.31 mmol, 59%) of **29**.

*4-Acetamidobenzoic acid (**29**).* White solid. **IR** (KBr): 3306, 1670, 1521, 1295 cm^{-1}. **^{1}H-NMR** (400 MHz, CD_3OD): δ 2.14 (3H, s, Ac); 7.66 (2H, d, *J* = 8.4 Hz, H3 and H5); 7.96 (2H, d, *J* = 8.4 Hz, H2 and H6). **^{13}C-NMR** (100 MHz, DMSO-d6): δ 29.3 (CH_3, Ac); 123.4 (2) (CH, C3 and C5); 130.1 (C, C1); 135.6 (2) (CH, C2 and C6); 148.5 (C, C4); 172.2 (C, amide); 174.2 (C, acid).

Synthesis of 1-methyl-1H-indole-5-carbaldehyde (30)

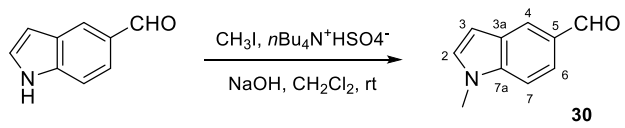

Methyl iodide (2012 µL, 32.32 mmol) was slowly added after 1 h into the mixture of 1*H*-indole-5-carbaldehyde (1580 mg, 10.67 mmol), ground NaOH in excess and catalytic tetrabutylammonium hydrogen sulfate in 150 mL of CH_2Cl_2. The reaction was stirred for 48 h under N_2 atmosphere at room temperature and subsequently washed with 5% $NaHCO_3$ and brine until neutral pH. The organic layer was dried over anhydrous Na_2SO_4, filtered, and evaporated to dryness (1677 mg). Crystallization in CH_2Cl_2/Hex gave compound **30** (1607 mg, 10.11 mmol, 93%).

*1-Methyl-1H-indole-5-carbaldehyde (**30**).* Orange crystals. **Mp** (CH_2Cl_2/Hex): 82-83 °C. **IR** (KBr): 1678, 1605, 1341, 1301 cm^{-1}. **^{1}H-NMR** (400 MHz, $CDCl_3$): δ 3.79 (3H, s, NCH_3); 6.60 (1H, d, *J* = 3.2 Hz, H3); 7.10 (1H, d, *J* = 3.2 Hz, H2); 7.35 (1H, d, *J* = 8.8 Hz, H7); 7.34 (1H, dd, *J* = 1.6 and 8.8 Hz, H6); 8.09 (1H, d, *J* = 1.6 Hz, H4); 9.98 (1H, s, CHO). **^{13}C-NMR** (100 MHz, $CDCl_3$): δ 39.9 (CH_3, NCH_3); 103.8 (CH, C3); 110.6 (CH, C6); 122.5 (CH, C4); 127.3 (CH, C7); 129.0 (CH, C2); 130.0 (C, C3a); 131.9 (C, C5); 140.7 (C, C7a); 193.5 (CH, CHO).

Synthesis of 1-methyl-1H-indole-5-carboxylic acid (31)

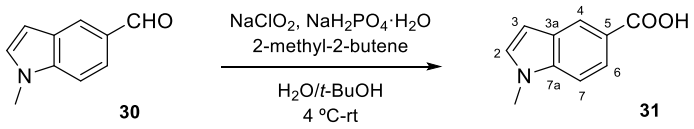

1-Methyl-1*H*-indole-5-carbaldehyde (**30**, 433 mg, 2.72 mmol) dissolved in 64 mL of *tert*-butanol and 30 mL of 2-methyl-2-butene was added to a mixture of $NaClO_2$ (4967 mg, 54.92 mmol) and NaH_2PO_4 monohydrate (5022 mg, 36.39 mmol) in 40 mL of water at 4 °C.[519] Once the addition was completed, the reaction was warmed to room temperature and stirred under N_2 for 24 h. It was subsequently extracted with CH_2Cl_2 and washed with brine. The organic layer was dried over anhydrous Na_2SO_4, filtered, and evaporated under vacuum obtaining 435 mg. Carboxylic acid **31** was purified by silica gel column chromatography with EtOAc/toluene 4:6 (363 mg, 2.07 mmol, 76%).

*1-Methyl-1H-indole-5-carboxylic acid (**31**).* White solid. **IR** (KBr): 1674, 1611, 1571, 1145 cm^{-1}. **^{1}H-NMR** (400 MHz, $CDCl_3$): δ 3.84 (3H, s, NCH_3); 6.62 (1H, d, *J* = 3.2 Hz, H3); 7.13 (1H, d, *J* = 3.2 Hz, H2); 7.36 (1H, d, *J* = 9.2 Hz, H7); 8.00 (1H, dd, *J* = 1.6 and 8.8 Hz, H6); 8.49 (1H, d, *J* = 1.6 Hz, H4). **^{13}C-NMR** (100 MHz, $CDCl_3$/CD_3OD): δ 32.7 (CH_3, NCH_3); 102.4 (CH, C3); 108.7 (CH, C6); 121.6 (C, C3a); 122.9 (CH, C4); 124.0 (CH, C7); 126.6 (C, C5); 127.9 (CH, C2); 139.1 (C, C7a); 170.4 (C, COOH).

Synthesis of N,N-dimethyl-4-nitroaniline (32)

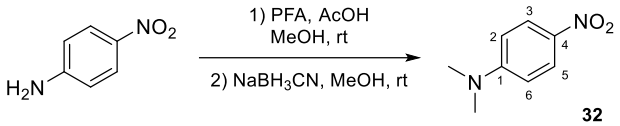

4-Nitroaniline (530 mg, 3.84 mmol) was added to a mixture of acetic acid (1 mL) and paraformaldehyde (1160 mg, 38.67 mmol) in 50 mL of methanol, and stirred for one and a half hours at room temperature under N_2. Afterward, $NaBH_3CN$ (518 mg, 8.12 mmol) was added to the reaction mixture, keeping the agitation for 1 week. It was then evaporated under vacuum, re-dissolved in CH_2Cl_2, and poured into iced water. Once washed with 2N HCl and brine, the organic layer was dried over anhydrous Na_2SO_4, filtered, and evaporated, giving alkylated derivative **32** (548 mg, 3.30 mmol, 86%). Crystallization in MeOH yielded 225 mg (1.36 mmol, 35%) of **32**.

*N,N-dimethyl-4-nitroaniline (**32**).* Yellow needles. **Mp** (MeOH): 165 °C. **^{1}H-NMR** (400 MHz, $CDCl_3$): δ 3.11 (6H, s, NCH_3); 6.60 (2H, d, *J* = 9.2 Hz, H2 and H6); 8.12 (2H, d, *J* = 9.2 Hz, H3 and H5).

Synthesis of N^1,N^1-dimethylbenzene-1,4-diamine (33)

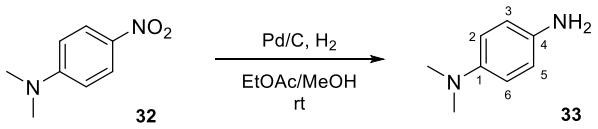

Following method **B**, nitro derivative **32** (479 mg, 2.89 mmol) was converted into **33** in the presence of Pd/C and H_2 atmosphere in 100 mL of EtOAc/MeOH, giving 369 mg of **33** (2.71 mmol, 94%) as a black solid after 24 h.

*N^1,N^1-dimethylbenzene-1,4-diamine (**33**).* Non-isolated compound. **^{1}H-NMR** (400 MHz, $CDCl_3$): δ 2.66 (6H, s, NCH_3); 3.18 (2H, bs, NH_2); 6.51 (4H, m).

Synthesis of 4-bromo-6-methylbenzo[d]thiazol-2-amine (34)

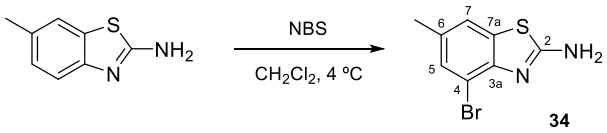

N-bromosuccinimide (3829 mg, 21.51 mmol) was slowly added to a solution of 6-methylbenzo[d]thiazol-2-amine (3212 mg, 19.56 mmol) in 125 mL of CH_2Cl_2 in ice. The reaction mixture was kept at 4 °C under agitation and N_2 atmosphere for 4 h. After rotary removing the solvent, the crude residue was filtered through silica (0.063-0.200 mm), eluting with CH_2Cl_2, EtOAc and MeOH, sequentially. The EtOAc-derived fraction was purified by crystallization in EtOAc, yielding bromo derivative **34** (1373 mg, 5.67 mmol, 29%).

*4-Bromo-6-methylbenzo[d]thiazol-2-amine (**34**).* Brown prisms. **Mp** (EtOAc): 211-212 °C. **^{1}H-NMR** (400 MHz, $CDCl_3$): δ 2.37 (3H, s, CH_3); 5.82 (2H, bs, NH); 7.32 (2H, bs, H5 and H7). **^{13}C-NMR** (100 MHz, DMSO-D6): δ 20.7 (CH_3); 110.3 (C, C4); 120.9 (CH, C7); 129.7 (CH, C5); 131.9 (C, C7a); 132.0 (C, C6); 149.0 (C, C3a); 166.7 (C, C2). **GC-MS** ($C_8H_7BrN_2S^+$): 242 (M^+).

SYNTHESIS OF SULFONAMIDES AND RELATED COMPOUNDS

Preparation of compounds 35 and 36

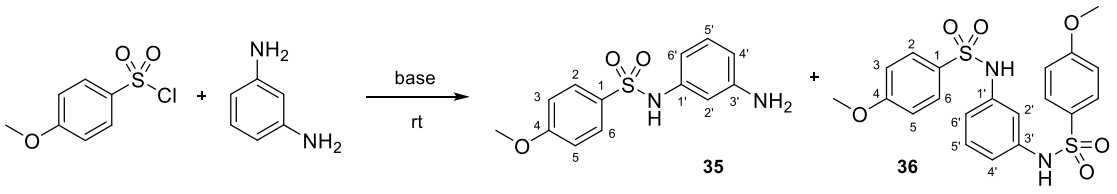

Procedure 1: 4-Methoxybenzenesulfonyl chloride (97 mg, 0.47 mmol) was added to a solution of *m*-phenylenediamine (70 mg, 0.65 mmol) in 25 mL of CH_2Cl_2 with a few drops of pyridine. The reaction was stirred at room temperature under N_2 atmosphere for 24 h. The resulting precipitate (*m*-phenylenediamine) was removed by filtration, and the organic layer was evaporated to obtain 120 mg of crude containing a 1:1 mixture of **35** (40 mg, 0.14 mmol, 31%) and **36** (70 mg, 0.16 mmol, 67%).

Procedure 2: The sulfonyl chloride (3072 mg, 14.87 mmol) was added to *m*-phenylenediamine (3203 mg, 29.62 mmol) dissolved in 50 mL of CH_2Cl_2 with 4 mL of triethylamine. After stirring for 16 h at room temperature under N_2 atmosphere, the reaction was poured onto ice and washed with saturated NaCl. The organic layer was dried over anhydrous Na_2SO_4, filtered and evaporated (4428 mg). Successive crystallizations in methanol provided compounds **35** (3336 mg, 12.00 mmol, 81%) and **36** (250 mg, 0.56 mmol, 7%).

Procedure 3: A solution of *m*-phenylenediamine (2748 mg, 25.41 mmol) and 4-methoxybenzenesulfonyl chloride (3143 mg, 15.21 mmol) in 50 mL of methanol with 4 mL of triethylamine was stirred at room temperature under N_2 atmosphere for 24 h. The reaction mixture was evaporated, re-dissolved in EtOAc, and washed with brine until neutrality. The organic layer was dried over anhydrous Na_2SO_4, filtered, and evaporated (4951 mg). Crystallization in methanol gave **35** (3212 mg, 11.55 mmol, 76%) and **36** (350 mg, 0.78 mmol, 10%).

*N-(3-aminophenyl)-4-methoxybenzenesulfonamide (**35**).* White crystals. **Mp** (MeOH): 122.0 °C. **IR** (KBr): 3393, 3341, 3245, 1594, 1496, 1312, 1262, 1148 cm^{-1}. **^{1}H-NMR** (400 MHz, $CDCl_3$): δ 3.67 (2H, bs, NH_2); 3.83 (3H, s, OCH_3); 6.30 (1H, bs, NH); 6.33 (1H, dd, *J* = 2.2 and 8.0 Hz, H6'); 6.42 (1H, dd, *J* = 2.2 and 8.0 Hz, H4'); 6.50 (1H, t, *J* = 2.2 Hz, H2'); 6.89 (2H, d, *J* = 8.4 Hz, H3 and H5); 6.97 (1H, t, *J* = 8.0 Hz, H5'); 7.71 (2H, d, *J* = 8.4 Hz, H2 and H6). **^{13}C-NMR** (100 MHz, CD_3OD): δ 54.8 (CH_3, OCH_3); 107.5 (CH, C2'); 110.3 (CH, C4'); 111.5 (CH, C6'); 113.7 (2) (CH, C3 and C5); 129.0 (2) (CH, C2 and C6); 129.3 (CH, C5'); 131.0 (C, C1); 138.4 (C, C1'); 148.2 (C, C3'); 163.0 (C, C4). **HRMS** ($C_{13}H_{15}N_2O_3S^+$): calculated 279.0798 ($M+H^+$), found 279.0805.

*N,N'-(1,3-phenylene)bis(4-methoxybenzenesulfonamide) (**36**).* Non-isolated compound. **^{1}H-NMR** (400 MHz, $CDCl_3$): δ 3.82 (6H, s, OCH_3 [bis]); 6.72 (2H, dd, *J* = 2.0 and 8.0 Hz, H4' and H6'); 6.87 (4H, d, *J* = 8.4 Hz, H3 and H5 [bis]); 6.92 (1H, t, *J* = 2.0 Hz, H2'); 7.06 (1H, t, *J* = 8.0 Hz, H5'); 7.66 (4H, d, *J* = 8.4 Hz, H2 and H6 [bis]). **^{13}C-NMR** (100 MHz, CD_3OD): δ 54.9 (2) (CH_3, OCH_3 [bis]); 111.6 (CH, C2'); 113.8 (4) (CH, C3 and C5 [bis]); 115.9 (2) (CH, C4' and C6'); 129.1 (4) (CH, C2 and C6 [bis]); 129.6 (CH, C5'); 130.6 (2) (C, C1 [bis]); 138.6 (2) (C, C1' and C3'); 163.1 (2) (C, C4 [bis]).

Synthesis of N-(3-aminophenyl)-4-methoxy-N-methylbenzenesulfonamide (37)

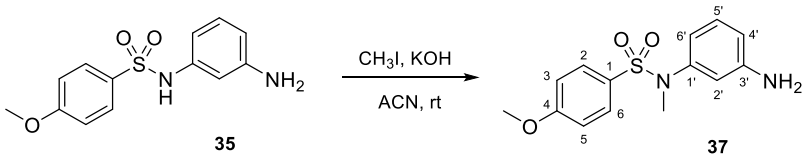

35 37

Following general procedure **C1**, sulfonamide **35** (169 mg, 0.61 mmol) dissolved in 25 mL of ACN was stirred for 30 min at room temperature with 2 ground lentils of KOH; methyl iodide (80 µL, 1.28 mmol) was then added dropwise. After 3 days, the suspension was filtered off and the solvent was rotary evaporated. EtOAc was added and washed with 5% $NaHCO_3$ and brine. The organic layer was dried over anhydrous Na_2SO_4, filtered, and evaporated under vacuum giving 143 mg. Crystallization in CH_2Cl_2/Hex provided 84 mg (0.22 mmol, 47%) of **37**.

*N-(3-aminophenyl)-4-methoxy-N-methylbenzenesulfonamide (**37**).* Silver crystals. **^{1}H-NMR** (400 MHz, $CDCl_3$): δ 3.11 (3H, s, NCH_3); 3.68 (2H, bs, NH_2); 3.86 (3H, s, OCH_3); 6.34 (1H, dd, *J* = 2.0 and 8.4 Hz, H6'); 6.56 (2H, m, H2' and H4'); 6.91 (2H, d, *J* = 8.8 Hz, H3 and H5); 7.02 (1H, t, *J* = 8.4 Hz, H5'); 7.51 (2H, d, *J* = 8.8 Hz, H2 and H6). **HRMS** ($C_{14}H_{16}N_2NaO_3S^+$): calculated 315.0774 ($M+Na^+$), found 315.0775.

Preparation of compounds 38-41

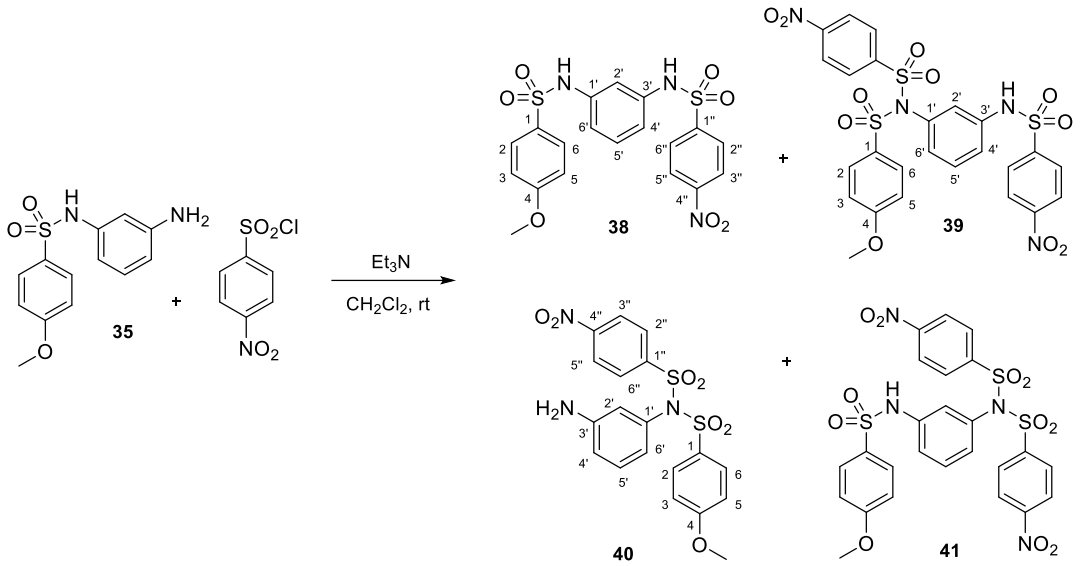

p-Nitrobenzenesulfonyl chloride (322 mg, 1.45 mmol) was added to a solution of **35** (197 mg, 0.71 mmol) with 0.2 mL of triethylamine in 12 mL of CH_2Cl_2, turning yellow over the time. The reaction was stirred for 17 h at room temperature under N_2, then poured into cold water and washed with brine. The organic layer was dried over anhydrous Na_2SO_4, filtered, and evaporated providing a yellow solid (338 mg) containing compounds **38**-**41**. Precipitation in CH_2Cl_2/MeOH followed by crystallization in acetone gave 50 mg (0.08 mmol, 11%) of **39**. Column chromatography with the mother liquors in CH_2Cl_2/MeOH yielded 26 mg (0.06 mmol, 8%) of **40**. An additional fraction of 149 mg was subjected to preparative TLC with CH_2Cl_2/MeOH giving 77 mg (0.17 mmol, 24%) of **38**. Global yields: **38** (127 mg, 0.27 mmol, 39%), **39** (58 mg, 0.09 mmol, 13%), **40** (86 mg, 0.19 mmol, 26%) and **41** (25 mg, 0.04 mmol, 5%).

*4-Methoxy-N-(3-((4-nitrophenyl)sulfonamido)phenyl)benzenesulfonamide (**38**).* Brown crystals. **Mp** (CH_2Cl_2): 75.6 °C. **IR** (KBr): 3272, 1596, 1497, 1312, 1263, 1148 cm^{-1}. **^{1}H-NMR** (400 MHz, $CDCl_3$): δ 3.82 (3H, s, OCH_3); 6.79 (2H, m, H4' and H6'); 6.87 (2H, d, *J* = 8.8 Hz, H3 and H5); 7.02 (1H, t, *J* = 2.0 Hz, H2'); 7.09 (1H, t, *J* = 8.0 Hz, H5'); 7.21 (1H, bs, NH); 7.35 (1H, bs, NH); 7.70 (2H, d, *J* = 8.8 Hz, H2 and H6); 7.90 (2H, d, *J* = 8.8 Hz, H2'' and H6''); 8.20 (2H, d, *J* = 8.8 Hz, H3'' and H5''). **^{13}C-NMR** (100 MHz, acetone-d6): δ 56.6 (CH_3, OCH_3); 113.4 (CH, C2'); 115.5 (2) (CH, C3 and C5); 117.6 (CH, C4'); 117.9 (CH, C6'); 125.7 (2) (CH, C3'' and C5''); 130.0 (2) (CH, C2 and C6); 130.6 (2) (CH, C2'' and C6''); 131.4 (CH, C5'); 132.6 (C, C1); 139.2 (C, C1'); 140.5 (C, C3'); 146.4 (C, C1''); 151.7 (C, C4''); 164.5 (C, C4). **HRMS** ($C_{19}H_{17}N_3NaO_7S_2^+$): calculated 486.0400 ($M+Na^+$), found 486.0406.

*4-Methoxy-N-(3-((4-nitrophenyl)sulfonamido)phenyl)-N-((4-nitrophenyl)sulfonyl)benzenesulfonamide (**39**).* White crystals. **^{1}H-NMR** (400 MHz, $CDCl_3$): δ 3.92 (3H, s, OCH_3); 6.68 (1H, t, *J* = 2.0 Hz, H2'); 7.03 (2H, d, *J* = 8.4 Hz, H3 and H5); 7.27 (1H, m, H4'); 7.33 (1H, dd, *J* = 2.0 and 8.0 Hz, H6'); 7.55 (1H, t, *J* = 8.0 Hz, H5'); 7.82 (2H, d, *J* = 8.4 Hz, H2 and H6); 8.09 (2H, d, *J* = 8.8 Hz, $PhNO_2$); 8.11 (2H, d, *J* = 8.8 Hz, $PhNO_2$); 8.39 (2H, d, *J* = 8.8 Hz, $PhNO_2$); 8.42 (2H, d, *J* = 8.8 Hz, $PhNO_2$).

*N-(3-aminophenyl)-4-methoxy-N-((4-nitrophenyl)sulfonyl)benzenesulfonamide (**40**).* **^{1}H-NMR** (400 MHz, $CDCl_3$): δ 3.84 (3H, s, OCH_3); 6.77 (2H, d, *J* = 8.0 Hz, H4' and H6'); 6.89 (2H, d, *J* = 8.4 Hz, H3 and H5); 7.02 (1H, bs, H2'); 7.10 (1H, t, *J* = 8.0 Hz, H5'); 7.69 (2H, d, *J* = 8.4 Hz, H2 and H6); 7.90 (2H, d, *J* = 8.4 Hz, H2''

and H6''); 8.23 (2H, d, *J* = 8.4 Hz, H3'' and H5''). **HRMS** ($C_{19}H_{17}N_3NaO_7S_2^+$): calculated 486.0400 ($M+Na^+$), found 486.0395.

*N-(3-((4-methoxyphenyl)sulfonamido)phenyl)-4-nitro-N-((4-nitrophenyl)sulfonyl)benzenesulfonamide (**41**).* Non-isolated compound.

Synthesis of 4-(dimethylamino)-N-(3-((4-methoxyphenyl)sulfonamido)phenyl)benzenesulfonamide (42)

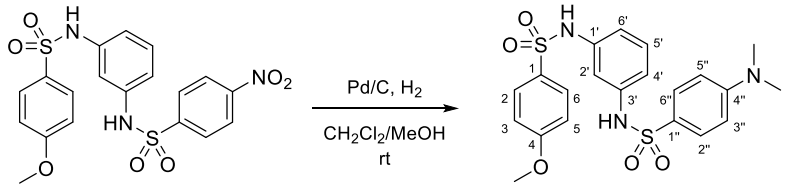

38 42

As detailed in method **B**, compound **38** (50 mg, 0.11 mmol) was added to a suspension of Pd/C in 12 mL of CH_2Cl_2/MeOH. The reaction was vigorously stirred for 4 days under H_2 atmosphere at room temperature giving 48 mg. Preparative TLC using Hex/EtOAc 1:1 as eluent provided 16 mg (0.03 mmol, 32%) of **42**.

*4-(Dimethylamino)-N-(3-((4-methoxyphenyl)sulfonamido)phenyl)benzenesulfonamide (**42**).* **IR** (KBr): 3255, 1597, 1498, 1311, 1262, 1148 cm^{-1}. **^{1}H-NMR** (400 MHz, CD_3OD): δ 2.98 (6H, s, NCH_3); 3.80 (3H, s, OCH_3); 6.63 (2H, m, H4' and H6'); 6.63 (2H, d, *J* = 8.8 Hz, H3'' and H5''); 6.90 (2H, d, *J* = 8.8 Hz, H3 and H5); 6.96 (1H, t, *J* = 8.0 Hz, H5'); 7.14 (1H, t, *J* = 2.4 Hz, H2'); 7.49 (2H, d, *J* = 8.8 Hz, H2'' and H6''); 7.60 (2H, d, *J* = 8.8 Hz, H2 and H6). **^{13}C-NMR** (100 MHz, CD_3OD): δ 38.7 (2) (CH_3, NCH_3); 54.7 (CH_3, OCH_3); 110.4 (2) (CH, C3'' and C5''); 112.0 (CH, C2'); 113.6 (2) (CH, C3 and C5); 115.7 (2) (CH, C4' and C6'); 124.3 (C, C1''); 128.6 (2) (CH, C2'' and C6''); 129.0 (2) (CH, C2 and C6); 129.2 (CH, C5'); 131.0 (C, C1); 138.7 (C, C1'); 139.1 (C, C3'); 153.1 (C, C4''); 163.0 (C, C4). **HRMS** ($C_{21}H_{23}N_3NaO_5S_2^+$): calculated 484.0971 ($M+Na^+$), found 484.0965.

Preparation of compounds 43-46

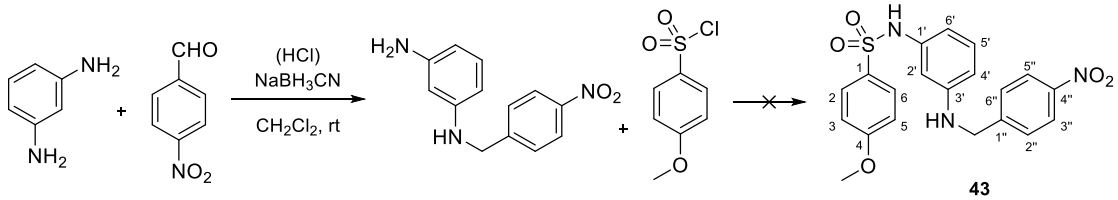

43

Procedure 1: *p*-Nitrobenzaldehyde (206 mg, 1.36 mmol) was added to *m*-phenylenediamine (295 mg, 2.73 mmol) in 25 mL of CH_2Cl_2 at room temperature under N_2 atmosphere. 3 h later, $NaBH_3CN$ (88 mg, 1.40 mmol) was added, stirring the mixture for 24 h. The reaction was washed with brine, dried over anhydrous Na_2SO_4, filtered, and evaporated, obtaining 255 mg of a mixture of *m*-phenylenediamine, the product of the reductive amination and both *E+Z* imines.

Procedure 2: Two drops of 2N HCl and 210 mg (1.39 mmol) of the aldehyde derivative were added to a solution of *m*-phenylenediamine (296 mg, 2.74 mmol) in 25 mL of CH_2Cl_2 at room temperature. $NaBH_3CN$ (80 mg, 1.27 mmol) was added after 30 min and stired for 24 h. The reaction was poured into cold water

and washed with brine. The organic layer was dried over anhydrous Na_2SO_4, filtered, and evaporated, yielding 169 mg of a mixture of the product of the reductive amination and both *E*+*Z* imines.

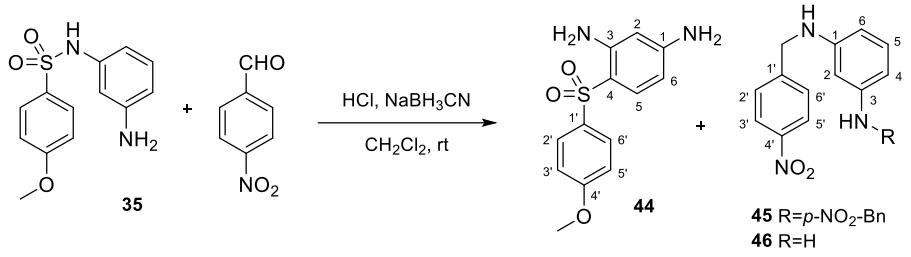

Procedure 3: A few drops of 2N HCl were added to a solution of **35** (196 mg, 0.71 mmol) and *p*-nitrobenzaldehyde (129 mg, 0.85 mmol) in 25 mL of CH_2Cl_2. After 3 h under N_2 at room temperature, $NaBH_3CN$ (112 mg, 1.78 mmol) was added and the reaction was stirred for 4 days. It was poured into cold water and the organic layer was washed with brine, dried over anhydrous Na_2SO_4, filtered, and evaporated obtaining 321 mg. Column chromatography using Hex/EtOAc 6:4 as eluent yielded compounds **44** (23 mg, 0.08 mmol, 12%), **45** (120 mg, 0.32 mmol, 75%), and **46** (21 mg, 0.09 mmol, 12%).

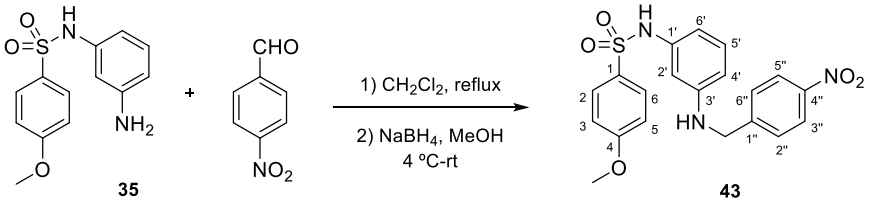

Procedure 4: A solution of **35** (970 mg, 3.49 mmol) and *p*-nitrobenzaldehyde (1008 mg, 6.68 mmol) in 50 mL of CH_2Cl_2 was heated under reflux and N_2 atmosphere for 90 h. The solvent was rotary evaporated, methanol was added and cooled to 4 °C. $NaBH_4$ (503 mg, 13.3 mmol) was progressively added to the mixture, and after 48 h, it was poured into cold water and kept at 4 °C. The resulting precipitate was dissolved in CH_2Cl_2, dried over anhydrous Na_2SO_4, filtered, and evaporated, yielding 497 mg (1.20 mmol, 35%) of **43**. The aqueous layer was extracted with EtOAc, providing 1443 mg of a mixture of **43** (900 mg, 2.18 mmol, 62%) and (4-nitrophenyl)methanol. Global yield: 1397 mg, 3.38 mmol, 97%.

*4-Methoxy-N-(3-((4-nitrobenzyl)amino)phenyl)benzenesulfonamide (**43**).* Yellow oil. **^{1}H-NMR** (400 MHz, $CDCl_3$): δ 3.82 (3H, s, OCH_3); 4.30 (2H, bs, NH); 4.42 (2H, s, CH_2); 6.27 (1H, dd, *J* = 2.2 and 8.0 Hz, H6'); 6.31 (1H, dd, *J* = 2.2 and 8.0 Hz, H4'); 6.41 (1H, t, *J* = 2.2 Hz, H2'); 6.84 (2H, d, *J* = 8.8 Hz, H3 and H5); 6.98 (1H, t, *J* = 8.0 Hz, H5'); 7.48 (2H, d, *J* = 8.4 Hz, H2'' and H6''); 7.60 (2H, d, *J* = 8.8 Hz, H2 and H6); 8.18 (2H, d, *J* = 8.4 Hz, H3'' and H5''). **^{13}C-NMR** (100 MHz, CD_3OD): δ 46.3 (CH_2); 54.8 (CH_3, OCH_3); 104.1 (CH, C2'); 109.1 (CH, C4'); 109.4 (CH, C6'); 113.6 (2) (CH, C3 and C5); 123.1 (2) (CH, C3'' and C5''); 127.6 (2) (CH, C2 and C6); 128.9 (2) (CH, C2'' and C6''); 129.5 (CH, C5'); 130.9 (C, C1); 138.6 (C, C1'); 146.7 (C, C4''); 148.2 (C, C1''); 148.8 (C, C3'); 162.9 (C, C4). **HRMS** ($C_{20}H_{19}N_3NaO_5S^+$): calculated 436.0938 ($M+Na^+$), found 436.0916.

*4-((4-Methoxyphenyl)sulfonyl)benzene-1,3-diamine (**44**).* Non-isolated compound. **^{1}H-NMR** (400 MHz, $CDCl_3$): δ 3.82 (3H, s, OCH_3); 6.01 (1H, d, *J* = 2.4 Hz, H2); 6.09 (1H, dd, *J* = 2.4 and 8.4 Hz, H6); 6.75 (1H, d, *J* = 8.4 Hz, H5); 7.27 (2H, d, *J* = 8.8 Hz, H3' and H5'); 8.06 (2H, d, *J* = 8.8 Hz, H2' and H6').

*N^1,N^3-bis(4-nitrobenzyl)benzene-1,3-diamine (**45**).* Brown solid. **^{1}H-NMR** (400 MHz, $CDCl_3$): δ 4.39 (4H, s, CH_2 [bis]); 5.74 (1H, t, *J* = 2.0 Hz, H2); 6.01 (2H, dd, *J* = 2.0 and 8.0 Hz, H4 and H6); 6.96 (1H, t, *J* = 8.0 Hz,

H5); 7.48 (4H, d, *J* = 8.8 Hz, H2' and H6' [bis]); 8.16 (4H, d, *J* = 8.8 Hz, H3' and H5' [bis]). **^{13}C-NMR** (100 MHz, $CDCl_3$): δ 47.5 (2) (CH_2 [bis]); 97.2 (CH, C2); 103.5 (2) (CH, C4 and C6); 123.8 (4) (CH, C3' and C5' [bis]); 127.6 (4) (CH, C2' and C6' [bis]); 130.3 (CH, C5); 147.1 (2) (C, C4' [bis]); 147.6 (2) (C, C1' [bis]); 148.6 (2) (C, C1 and C3). **HRMS** ($C_{20}H_{18}N_4NaO_4^+$): calculated 401.1220 ($M+Na^+$), found 401.1235.

*N^1-(4-nitrobenzyl)benzene-1,3-diamine (**46**).* Brown solid. **^{1}H-NMR** (400 MHz, $CDCl_3$): δ 4.44 (2H, s, CH_2); 5.90 (1H, t, *J* = 2.0 Hz, H2); 6.03 (1H, dd, *J* = 2.0 and 8.0 Hz, H6); 6.11 (1H, dd, *J* = 2.0 and 8.0 Hz, H4); 6.95 (1H, t, *J* = 8.0 Hz, H5); 7.52 (2H, d, *J* = 8.8 Hz, H2' and H6'); 8.19 (2H, d; *J* = 8.8 Hz, H3' and H5'). **^{13}C-NMR** (100 MHz, $CDCl_3$): δ 47.5 (CH_2); 99.4 (CH, C2); 103.9 (CH, C4); 105.6 (CH, C6); 123.9 (2) (CH, C3' and C5'); 127.6 (2) (CH, C2' and C6'); 130.3 (CH, C5); 147.1 (C, C4'); 147.5 (C, C1'); 147.7 (C, C3); 148.5 (C, C1). **HRMS** ($C_{13}H_{14}N_3O_2^+$): calculated 244.1081 ($M+H^+$), found 244.1083.

Synthesis of N-(3-((4-aminobenzyl)amino)phenyl)-4-methoxybenzenesulfonamide (47)

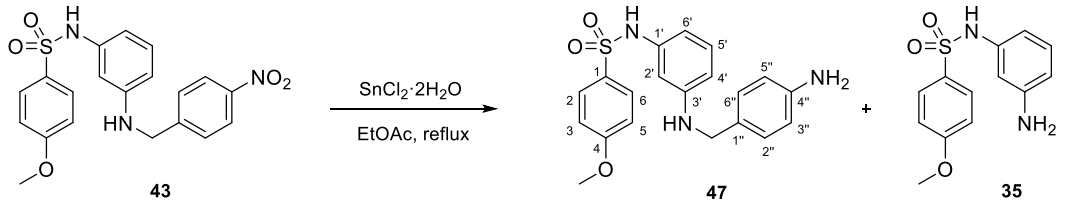

$SnCl_2·2H_2O$ (847 mg, 3.75 mmol) was added to a solution of **43** (139 mg, 0.34 mmol) in 25 mL of EtOAc and heated under reflux for 18 h under N_2 atmosphere.[515] The reaction was repeatedly washed with 5% $NaHCO_3$, dried over anhydrous Na_2SO_4, filtered, and evaporated under vacuum. The resulting residue had a mixture of compound **35** (38 mg, 0.14 mmol, 41%) and **47** (59 mg, 0.15 mmol, 46%), the latter, purified by precipitation in $MeOH/CH_2Cl_2$ (9 mg, 0.02 mmol, 7%).

*N-(3-((4-aminobenzyl)amino)phenyl)-4-methoxybenzenesulfonamide (**47**).* **^{1}H-NMR** (400 MHz, CD_3OD): δ 3.43 (2H, s, CH_2); 3.85 (3H, s, OCH_3); 6.44 (1H, dd, *J* = 2.4 and 8.4 Hz, H6'); 6.63 (7H, m); 6.96 (2H, d, *J* = 8.8 Hz, H3 and H5); 7.56 (2H, d, *J* = 8.8 Hz, H2 and H6). **HRMS** ($C_{20}H_{21}N_3NaO_3S^+$): calculated 406.1196 ($M+Na^+$), found 406.1188.

Preparation of compounds 49 and 50

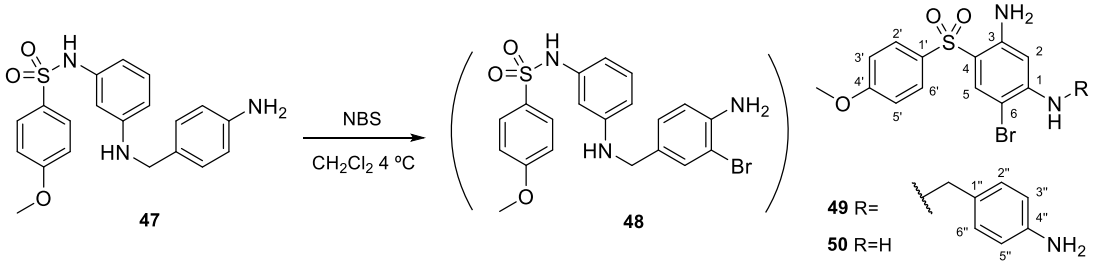

N-bromosuccinimide (83 mg, 0.47 mmol) was added to a solution of **47** (169 mg, 0.44 mmol) in 25 mL CH_2Cl_2 at 4 °C under N_2 atmosphere. The solvent was evaporated after 2 h. Column chromatography using Hex/EtOAc 1:1 as eluent yielded **49** (57 mg, 0.12 mmol, 28%) and **50** (22 mg, 0.06 mmol, 14%).

*N^1-(4-aminobenzyl)-6-bromo-4-((4-methoxyphenyl)sulfonyl)benzene-1,3-diamine (**49**).* Non-isolated product. **^{1}H-NMR** (400 MHz, $CDCl_3$): δ 3.30 (2H, s, CH_2); 3.85 (3H, s, OCH_3); 4.06 (2H, bs, NH_2); 6.18 (1H, bs, NH); 6.59 (2H, d, *J* = 8.4 Hz, H3'' and H5''); 6.73 (2H, d, *J* = 8.4 Hz, H2'' and H6''); 6.88 (2H, d, *J* = 8.8 Hz,

H3' and H5'); 6.95 (1H, s, H2); 7.11 (1H, s, H5); 7.52 (2H, d, *J* = 8.8 Hz, H2' and H6'). **HRMS** ($C_{20}H_{20}BrN_3NaO_3S^+$): calculated 484.0301 ($M+Na^+$), found 484.0295.

*4-Bromo-6-((4-methoxyphenyl)sulfonyl)benzene-1,3-diamine (**50**).* **^{1}H-NMR** (400 MHz, $CDCl_3$): δ 3.84 (3H, s, OCH_3); 4.20 (2H, bs, NH_2); 6.78 (1H, bs, NH); 6.90 (2H, d, *J* = 8.8 Hz, H3' and H5'); 7.13 (1H, s, H2); 7.40 (1H, s, H5); 7.69 (2H, d, *J* = 8.8 Hz, H2' and H6').

Synthesis of 4-methoxy-N-(3-((4-ureidobenzyl)amino)phenyl)benzenesulfonamide (51)

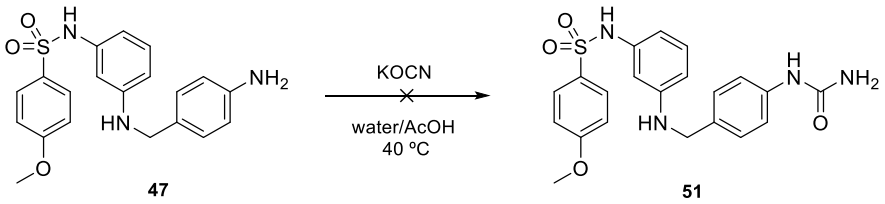

47 51

Potassium cyanate (106 mg, 1.31 mmol) was slowly added to a solution of **47** (266 mg, 0.69 mmol) in 10 mL of water and 10 mL of acetic acid. The reaction was heated at 40 °C under N_2 atmosphere for 2 h, poured into cold water and kept at 4 °C until a yellow precipitate appeared. The solvent mixture was extracted with EtOAc, dried over anhydrous Na_2SO_4, filtered, and evaporated, giving 209 mg of a complex mixture.

Synthesis of N-(3-((4-guanidinobenzyl)amino)phenyl)-4-methoxybenzenesulfonamide (52)

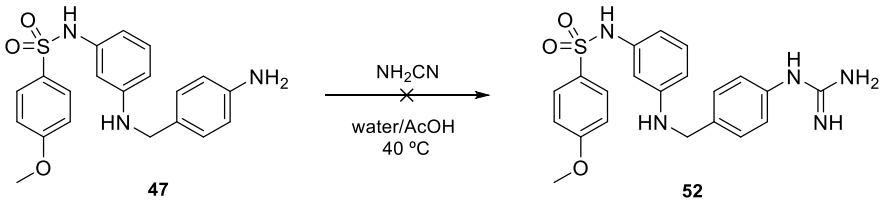

47 52

A mixture of **47** (170 mg, 0.44 mmol) and 50% cyanamide in water (350 µL, 4.50 mmol) in 10 mL of water and 10 mL of acetic acid was heated at 40 °C and N_2 atmosphere for 24 h. Then, the temperature was progressively increased to 80 °C and kept 24 h more. The reaction was poured into cold water, basified with Na_2CO_3 and kept at 4 °C. The resulting precipitate (23 mg) was filtered off and the solvent extracted with EtOAc, dried over anhydrous Na_2SO_4, filtered, and evaporated, obtaining 192 mg of a complex mixture. (192 mg).

Synthesis of N-(4-(((3-((4-methoxyphenyl)sulfonamido)phenyl)amino)methyl)phenyl)acetamide (53)

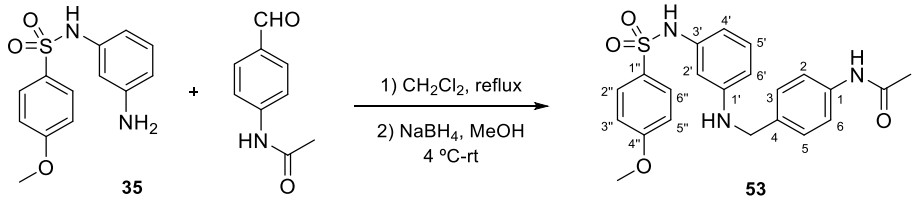

35 53

N-(4-formylphenyl)acetamide (483 mg, 2.96 mmol) was added to 320 mg (1.15 mmol) of compound **35** in 25 mL of refluxing CH_2Cl_2, and kept under N_2 atmosphere for 19 h. After evaporation, the residue was dissolved in methanol, cooled down to 4 °C, and $NaBH_4$ (112 mg, 2.96 mmol) was added to the solution.

The reaction was warmed to room temperature and after 24 h, it was poured onto ice and extracted with EtOAc. The organic layer was dried over anhydrous Na_2SO_4, filtered, and evaporated under vacuum obtaning 605 mg. Column chromatography using Hex/EtOAc 1:1 as eluent gave 213 mg (0.50 mmol, 44%) of **53**.

*N-(4-(((3-((4-methoxyphenyl)sulfonamido)phenyl)amino)methyl)phenyl)acetamide (**53**).* Yellow solid. **IR** (KBr): 3360, 3255, 3120, 1668, 1597, 1514, 1317, 1261, 1148 cm^{-1}. **^{1}H-NMR** (400 MHz, $CDCl_3$): δ 2.20 (3H, s, Ac); 3.82 (3H, s, OCH_3); 4.21 (2H, s, CH_2); 6.26 (1H, dd, *J* = 2.2 and 8.8 Hz, H4'); 6.34 (1H, dd, *J* = 2.2 and 8.8 Hz, H6'); 6.41 (1H, t, *J* = 2.2 Hz, H2'); 6.43 (1H, bs, NH); 6.86 (2H, d, *J* = 8.4 Hz, H3'' and H5''); 6.96 (1H, t, *J* = 8.8 Hz, H5'); 7.26 (2H, d, *J* = 8.4 Hz, H3 and H5); 7.46 (2H, d, *J* = 8.4 Hz, H2 and H6); 7.62 (2H, d, *J* = 8.4 Hz, H2'' and H6''). **^{13}C-NMR** (100 MHz, CD_3OD): δ 22.6 (CH_3, Ac); 46.6 (CH_2); 54.8 (CH_3, OCH_3); 104.4 (CH, C2'); 108.9 (CH, C6'); 109.6 (CH, C4'); 113.7 (2) (CH, C3'' and C5''); 119.8 (2) (CH, C2 and C6); 127.3 (2) (CH, C2'' and C6''); 129.0 (2) (CH, C3 and C5); 129.2 (CH, C5'); 130.9 (C, C1''); 135.7 (C, C4); 137.1 (C, C1); 138.5 (C, C3'); 149.3 (C, C1'); 162.9 (C, C4''); 170.2 (C, CO). **HRMS** ($C_{22}H_{24}N_3O_4S^+$): calculated 426.1482 ($M+H^+$), found 426.1482.

Synthesis of N-(3-((4-methoxyphenyl)sulfonamido)phenyl)-4-nitrobenzamide (54)

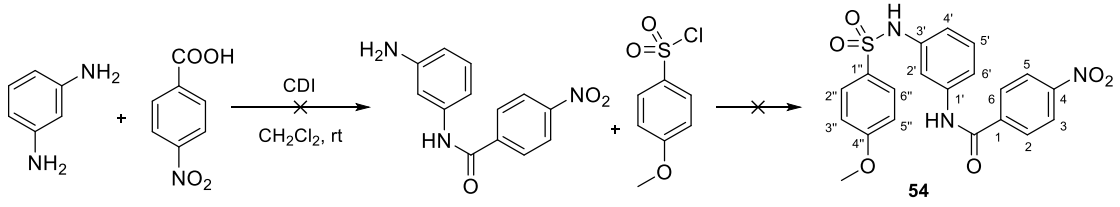

Procedure 1: A solution of *p*-nitrobenzoic acid (225 mg, 1.35 mmol) and CDI (231 mg, 1.43 mmol) in 12 mL of CH_2Cl_2 was stirred at room temperature, and 2 h later, *m*-phenylenediamine (292 mg, 2.78 mmol) was added. After 18 h under N_2 atmosphere, the reaction was poured into 5% $NaHCO_3$ and washed with brine. The organic layer was dried over anhydrous Na_2SO_4, filtered, and evaporated, recovering 138 mg (1.28 mmol) of *m*-phenylenediamine.

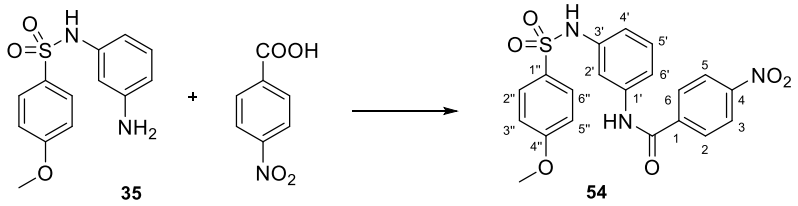

Procedure 2: Following method **A1**, sulfonamide **35** (262 mg, 0.94 mmol) was added to a solution of *p*-nitrobenzoic acid (365 mg, 2.18 mmol), *p*-DMAP (55 mg, 0.45 mmol) and DCI (534 mg, 2.59 mmol) in 50 mL of CH_2Cl_2 that had been previously stirred for 1 h at room temperature. After 72 h under N_2 atmosphere, the reaction was poured into cold water and washed with brine until neutrality. The organic layer was dried over anhydrous Na_2SO_4, filtered, and evaporated under vacuum, yielding 713 mg of a complex mixture.

Procedure 3: As described in method **A1**, a mixture of *p*-nitrobenzoic acid (375 mg, 2.24 mmol), *p*-DMAP (143 mg, 1.17 mmol), and EDC hydrochloride (485 mg, 2.53 mmol) in 50 mL of CH_2Cl_2 was stirred for 30 min before adding 312 mg (1.12 mmol) of compound **35**. The reaction was stirred at room temperature under N_2 atmosphere for 18 h, poured into cold water and washed with saturated NaCl. The organic layer

was dried over anhydrous Na_2SO_4, filtered, and evaporated (736 mg). Precipitation in CH_2Cl_2 provided compound **54** as a white solid (301 mg, 0.70 mmol, 63%).

Procedure 4: Via general procedure **A1**, the mixture of *p*-nitrobenzoic acid (90 mg, 0.53 mmol), EDC hydrochloride (142 mg, 0.74 mmol), *p*-DMAP (66 mg, 0.54 mmol), and compound **35** (99 mg, 0.36 mmol) in 6 mL of CH_2Cl_2 was irradiated in a microwave oven at 130 °C for 3 min. Afterward, it was washed with brine and the organic layer was dried over anhydrous Na_2SO_4, filtered, and evaporated (186 mg). Precipitation in CH_2Cl_2 followed by crystallization in methanol gave 48 mg (0.11 mmol, 32%) of **54**.

Procedure 5: As detailed in method **A2**, $SOCl_2$ (0.5 mL) was carefully added into a sealed tube with the carboxylic acid (120 mg, 0.72 mmol) and heated at 70 °C for 48 h. The acyl chloride was added dropwise to a solution of sulfonamide **35** (151 mg, 0.54 mmol) in CH_2Cl_2 with a few drops of DMF. The solution was stirred for 4 days at room temperature and N_2 atmosphere, turning yellowish-green. It was then poured into cold water, washed with brine, dried over anhydrous Na_2SO_4, filtered, and evaporated (196 mg). Crystallization in methanol gave 83 mg (0.19 mmol, 36%) of **54**.

*N-(3-((4-methoxyphenyl)sulfonamido)phenyl)-4-nitrobenzamide (**54**).* Yellow crystals. **Mp** (MeOH): 220.2 °C. **IR** (KBr): 3335, 3178, 1662, 1598, 1497, 1300, 1259, 1148 cm^{-1}. **^{1}H-NMR** (400 MHz, CD_3OD): δ 3.81 (3H, s, OCH_3); 6.87 (1H, dd, *J* = 2.0 and 8.0 Hz, H4'); 6.98 (2H, d, *J* = 8.8 Hz, H3'' and H5''); 7.19 (1H, t, *J* = 8.0 Hz, H5'); 7.35 (1H, dd, *J* = 2.0 and 8.0 Hz, H6'); 7.69 (1H, t, *J* = 2.0 Hz, H2'); 7.75 (2H, d, *J* = 8.8 Hz, H2'' and H6''); 8.09 (2H, d, *J* = 8.8 Hz, H2 and H6); 8.35 (2H, d, *J* = 8.8 Hz, H3 and H5). **^{13}C-NMR** (100 MHz, acetone-d6): δ 55.2 (CH_3, OCH_3); 111.8 (CH, C2'); 114.1 (CH, C3'' and C5''); 115.8 (2) (CH, C4' and C6'); 123.5 (2) (CH, C3 and C5); 129.0 (2) (CH, C2'' and C6''); 129.3 (2) (CH, C2 and C6); 131.5 (CH, C5'); 138.7 (2) (C, C1' and C3'); 139.6 (C, C1''); 140.9 (C, C1); 149.7 (C, C4); 163.0 (C, C4''); 163.2 (C, CO). **HRMS** ($C_{20}H_{17}N_3NaO_6S^+$): calculated 450.0730 ($M+Na^+$), found 450.0727.

Synthesis of 4-amino-N-(3-((4-methoxyphenyl)sulfonamido)phenyl)benzamide (55)

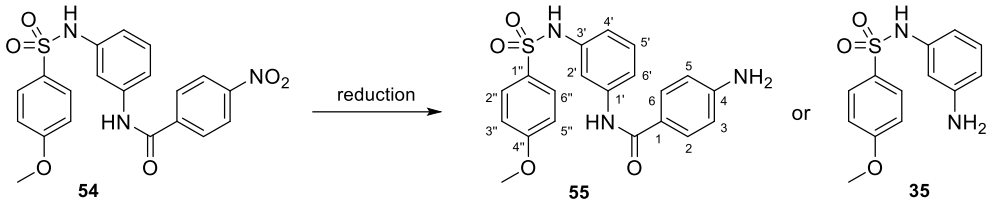

Procedure 1: Following general procedure **B**, nitro derivative **54** (47 mg, 0.11 mmol) was added to a suspension of Pd/C in 25 mL of CH_2Cl_2/MeOH. It was vigorously stirred under H_2 atmosphere at room temperature for 24 h, then filtered through celite, and evaporated (56 mg). Preparative TLC using CH_2Cl_2/EtOAc 1:1 as eluent gave 11 mg (0.03 mmol, 26%) of **55**.

Procedure 2: Compound **54** (106 mg, 0.25 mmol) was dissolved in a mixture of AcOH (6 mL), EtOH (6 mL), and water (3 mL) with a drop of 2N HCl. Metallic iron (138 mg, 2.51 mmol) was added to the previous solution, which was heated under reflux for 30 min, turning yellow.[514] Once filtered through celite, CH_2Cl_2 was added and washed with 5% Na_2CO_3 and brine. The organic layer was dried over anhydrous Na_2SO_4, filtered, and evaporated, yielding 41 mg (0.15 mmol, 59%) of **35**.

Procedure 3: Compound **54** (316 mg, 0.74 mmol) was reduced in the presence of $SnCl_2 \cdot 2H_2O$ (2051 mg, 9.09 mmol) in 25 mL of EtOAc.[515] The reaction was stirred under N_2 atmosphere at room temperature for

12 h and refluxed for 9 h. Anhydrous Na_2CO_3 was added, and once filtered, the solution was repeatedly washed with 5% $NaHCO_3$. The organic layer was dried over anhydrous Na_2SO_4, filtered, and evaporated to obtain 230 mg (0.58 mmol, 78%) of **55**.

Procedure 4: A mixture of **54** (22 mg, 0.05 mmol) and 147 mg (0.65 mmol) of $SnCl_2 \cdot 2H_2O$ in 6 mL of EtOAc was irratiated in a microwave oven at 120 °C for 15 min. After adding anhydrous Na_2CO_3, it was filtered and evaporated to dryness, obtaining a mixture of product **55** and stannous dichloride.

*4-Amino-N-(3-((4-methoxyphenyl)sulfonamido)phenyl)benzamide (**55**).* Yellow oil. **IR** (film): 3458, 3376, 3233, 1702, 1601, 1497, 1301, 1261, 1152 cm^{-1}. **^{1}H-NMR** (400 MHz, CD_3OD): δ 3.80 (3H, s, OCH_3); 6.69 (2H, d, *J* = 8.4 Hz, H3 and H5); 6.82 (1H, dd, *J* = 1.8 and 8.0 Hz, H4'); 6.97 (2H, d, *J* = 8.4 Hz, H3'' and H5''); 7.14 (1H, t, *J* = 8.0 Hz, H5'); 7.28 (1H, dd, *J* = 1.8 and 8.0 Hz, H6'); 7.61 (1H, t, *J* = 1.8 Hz, H2'); 7.69 (2H, d, *J* = 8.4 Hz, H2 and H6); 7.75 (2H, d, *J* = 8.4 Hz, H2'' and H6''). **^{13}C-NMR** (100 MHz, CD_3OD): δ 54.7 (CH_3, OCH_3); 113.1 (CH, C2'); 113.2 (2) (CH, C3'' and C5''); 113.7 (2) (CH, C3 and C5); 115.8 (CH, C6'); 116.0 (CH, C4'); 116.6 (CH, C5'); 121.9 (C, C1); 128.8 (2) (CH, C2'' and C6''); 129.1 (2) (CH, C2 and C6); 131.1 (C, C1''); 138.2 (C, C3'); 139.7 (C, C1'); 152.2 (C, C4); 163.1 (C, C4''); 167.6 (C, CO). **HRMS** ($C_{20}H_{19}N_3NaO_4S^+$): calculated 420.0988 ($M+Na^+$), found 420.0978.

Synthesis of 4-amino-3-bromo-N-(3-((4-methoxyphenyl)sulfonamido)phenyl)benzamide (56)

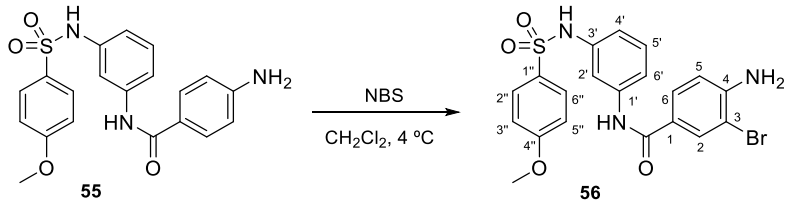

A solution of **55** (83 mg, 0.21 mmol) in 25 mL of CH_2Cl_2 was cooled at 4 °C, and *N*-bromosuccinimide (41 mg, 0.23 mmol) was added and stirred for 1 h under N_2. After rotary evaporation, preparative TLC using Hex/EtOAc 4:6 as eluent yielded 49 mg (0.10 mmol, 49%) of bromo derivative **56**.

*4-Amino-3-bromo-N-(3-((4-methoxyphenyl)sulfonamido)phenyl)benzamide (**56**).* Yellow solid. **IR** (KBr): 3466, 3370, 1701, 1596, 1498, 1300, 1260, 1148 cm^{-1}. **^{1}H-NMR** (400 MHz, CD_3OD): δ 3.77 (3H, s, OCH_3); 6.81 (1H, d, *J* = 8.4 Hz, H5); 6.82 (1H, dd, *J* = 2.4 and 8.0 Hz, H4'); 6.94 (2H, d, *J* = 8.8 Hz, H3'' and H5''); 7.13 (1H, t, *J* = 8.0 Hz, H5'); 7.27 (1H, dd, *J* = 2.4 and 8.0 Hz, H6'); 7.61 (1H, t, *J* = 2.4 Hz, H2'); 7.66 (1H, dd, *J* = 2.4 and 8.4 Hz, H6); 7.74 (2H, d, *J* = 8.8 Hz, H2'' and H6''); 7.99 (1H, d, *J* = 2.4 Hz, H2). **^{13}C-NMR** (100 MHz, CD_3OD): δ 54.7 (CH_3, OCH_3); 106.8 (CH, C2'); 113.2 (CH, C6'); 113.7 (2) (CH, C3'' and C5''); 113.9 (CH, C4'); 116.0 (C, C3); 116.4 (CH, C5); 123.2 (C, C1); 127.9 (CH, C6); 128.8 (CH, C5'); 129.0 (2) (CH, C2'' and C6''); 131.3 (C, C1''); 132.2 (CH, C2); 138.8 (C, C3'); 139.4 (C, C1'); 149.1 (C, C4); 163.0 (C, C4''); 166.0 (C, CO). **HRMS** ($C_{20}H_{18}BrN_3NaO_4S^+$): calculated 498.0094 ($M+Na^+$), found 498.0092.

Synthesis of N-(3-((4-methoxyphenyl)sulfonamido)phenyl)-4-ureidobenzamide (57)

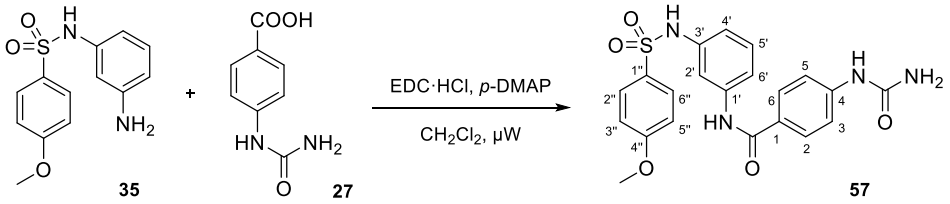

35 27 57

According to method **A1**, the mixture of **35** (475 mg, 1.71 mmol), **27** (400 mg, 2.22 mmol), EDC hydrochloride (699 mg, 3.65 mmol) and *p*-DMAP (284 mg, 2.33 mmol) was dissolved in 20 mL of CH_2Cl_2 and irradiated in a microwave oven at 130 °C for 3 min. The residue (1413 mg) was dissolved in EtOAc, appearing a jelly solid (1152 mg), subjected to column chromatography using CH_2Cl_2/MeOH 9:1 to give **57** (101 mg, 0.23 mmol, 13%). Crystallization in THF/H_2O gave 60 mg (0.14 mmol, 8%) of **57**.

*N-(3-((4-methoxyphenyl)sulfonamido)phenyl)-4-ureidobenzamide (**57**).* White crystals. **Mp** (THF/H_2O): 260.9 °C. **IR** (KBr): 3449, 3365, 3351, 1683, 1656, 1589, 1261, 1146 cm^{-1}. **^{1}H-NMR** (400 MHz, DMSO-D6): δ 3.82 (3H, s, OCH_3); 5.98 (1H, bs, NH); 6.75 (1H, bd, *J* = 8.0 Hz, H4'); 7.02 (2H, d, *J* = 8.8 Hz, H3'' and H5''); 7.11 (1H, t, *J* = 8.0 Hz, H5'); 7.36 (1H, bd, *J* = 8.0 Hz, H6'); 7.48 (2H, d, *J* = 8.8 Hz, H2 and H6); 7.65 (1H, t, *J* = 2.0 Hz, H2'); 7.71 (2H, d, *J* = 8.8 Hz, H2'' and H6''); 7.79 (2H, d, *J* = 8.8 Hz, H3 and H5); 8.87 (1H, bs, NH); 10.02 (1H, bs, NH). **^{13}C-NMR** (100 MHz, DMSO-d6): δ 56.0 (CH_3, OCH_3); 112.0 (CH, C2'); 114.8 (2) (CH, C3'' and C5''); 115.1 (CH, C6'); 116.2 (CH, C4'); 117.0 (2) (CH, C3 and C5); 127.3 (C, C1); 129.2 (2) (CH, C2'' and C6''); 129.4 (2) (CH, C2 and C6); 129.5 (CH, C5'); 131.6 (C, C1''); 138.7 (C, C3'); 140.5 (C, C1'); 144.3 (C, C4); 156.2 (C, urea); 162.8 (C, C4''); 165.5 (C, amide). **HRMS** ($C_{21}H_{20}N_4NaO_5S^+$): calculated 463.1047 ($M+Na^+$), found 463.1040.

Synthesis of N-(3-((4-methoxyphenyl)sulfonamido)phenyl)-2-(4-nitrophenyl)acetamide (58)

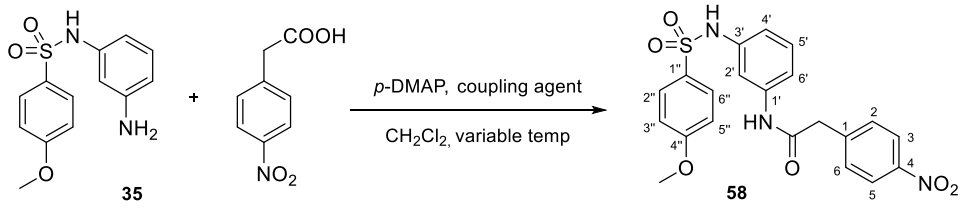

35 58

Procedure 1: According to general method **A1**, a mixture of 2-(4-nitrophenyl)acetic acid (314 mg, 1.73 mmol), *p*-DMAP (121 mg, 0.99 mmol), and EDC hydrochloride (341 mg, 1.78 mmol) was stirred in 25 mL of CH_2Cl_2 at room temperature under N_2 atmosphere for 2 h before adding compound **35** (300 mg, 1.08 mmol). 72 h later, the reaction was poured into cold water and washed with brine, obtaining 681 mg of a complex mixture.

Procedure 2: 2-(4-nitrophenyl)acetic acid (652 mg, 3.45 mmol) in 25 mL of CH_2Cl_2 with 738 mg (3.58 mmol) of DCI and 280 mg (2.30 mmol) of *p*-DMAP was stirred for 30 min at room temperature and N_2 atmosphere. Compound **35** (464 mg, 1.67 mmol) was added and the mixture was heated under reflux with 2 mL of THF. After 24 h, it was poured onto ice and washed with brine. The organic layer was dried over anhydrous Na_2SO_4, filtered, and evaporated, obtaining 1768 mg. Two column chromatographies with CH_2Cl_2/EtOAc (95:5) and then CH_2Cl_2/methanol (97:3) gave 420 mg of a 2:1 mixture of **58** and **35**. Precipitation in CH_2Cl_2 yielded 60 mg (0.14 mmol, 8%) of **58**. Global yield: 282 mg, 0.64 mmol, 38%.

Procedure 3: Following method **A1**, a mixture of **35** (486 mg, 1.75 mmol), 2-(4-nitrophenyl)acetic acid (492 mg, 2.72 mmol), *p*-DMAP (215 mg, 1.76 mmol), and EDC hydrochloride (672 mg, 3.51 mmol) in 20 mL of CH_2Cl_2 was irradiated in a microwave oven for 3 min at 130 °C, to obtain 1998 mg. Crystallization in MeOH gave 320 mg (0.73 mmol, 42%) of **58** and the mother liquors precipited in CH_2Cl_2, yielding 212 mg (0.48 mmol, 27%) of **58**. Global yield: 532 mg, 1.21 mmol, 69%.

*N-(3-((4-methoxyphenyl)sulfonamido)phenyl)-2-(4-nitrophenyl)acetamide (**58**).* Orange crystals. **Mp** (MeOH): 184.8 °C. **IR** (KBr): 3240, 1653, 1596, 1497, 1268, 1148 cm^{-1}. **^{1}H-NMR** (400 MHz, CD_3OD): δ 3.69 (2H, s, CH_2); 3.79 (3H, s, OCH_3); 6.79 (1H, dd, *J* = 2.0 and 8.0 Hz, H4'); 6.93 (2H, d, *J* = 8.8 Hz, H3'' and H5''); 7.12 (1H, t, *J* = 8.0 Hz, H5'); 7.20 (1H, dd, *J* = 2.0 and 8.0 Hz, H6'); 7.47 (1H, t, *J* = 2.0 Hz, H2'); 7.56 (2H, d, *J* = 8.8 Hz, H2 and H6); 7.69 (2H, d, *J* = 8.8 Hz, H2'' and H6''); 8.19 (2H, d, *J* = 8.8 Hz, H3 and H5). **^{13}C-NMR** (100 MHz, acetone-d6): δ 43.1 (CH_2); 55.2 (CH_3, OCH_3); 110.9 (CH, C2'); 113.9 (CH, C6'); 114.0 (2) (CH, C3'' and C5''); 114.9 (CH, C4'); 115.1 (CH, C5'); 123.3 (2) (CH, C3 and C5); 129.2 (2) (CH, C2'' and C6''); 130.6 (2) (CH, C2 and C6); 131.5 (C, C1''); 138.6 (C, C3'); 139.8 (C, C1'); 143.6 (C, C1); 146.9 (C, C4); 163.0 (C, C4''); 167.9 (C, CO). **HRMS** ($C_{21}H_{19}N_3NaO_6S^+$): calculated 464.0887 ($M+Na^+$), found 464.0878.

Synthesis of 2-(4-aminophenyl)-N-(3-((4-methoxyphenyl)sulfonamido)phenyl)acetamide (59)

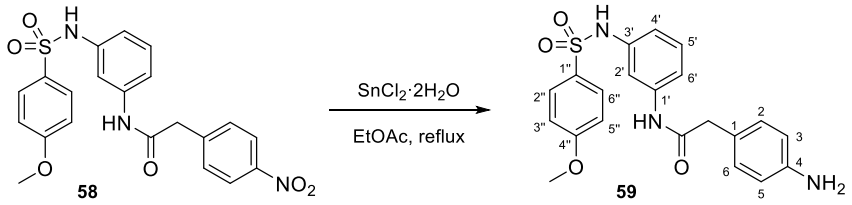

Procedure 1: Following method **B**, a solution of **58** (92 mg, 0.21 mmol) in 50 mL of CH_2Cl_2/MeOH with Pd/C was vigorously stirred for 72 h under H_2 atmosphere. The suspension was filtered through celite leading to a green crude (88 mg) with complex spectra.

Procedure 2: $SnCl_2{\cdot}2H_2O$ (1188 mg, 5.27 mmol) was added to a solution of compound **58** (232 mg, 0.53 mmol) in EtOAc (25 mL) and heated under reflux for 10 h.[515] It was repeatedly washed with 5% $NaHCO_3$ and the organic layer was dried over anhydrous Na_2SO_4, filtered, and evaporated, obtaining 187 mg. Crystallization in CH_2Cl_2 gave 167 mg (0.41 mmol, 77%) of amine **59**.

*2-(4-Aminophenyl)-N-(3-((4-methoxyphenyl)sulfonamido)phenyl)acetamide (**59**).* White crystals. **Mp** (CH_2Cl_2): 89.0 °C. **IR** (KBr): 3436, 3368, 3250, 3135, 1660, 1597, 1497, 1329, 1262, 1141 cm^{-1}. **^{1}H-NMR** (400 MHz, CD_3OD): δ 3.49 (2H, s, CH_2); 3.80 (3H, s, OCH_3); 6.70 (2H, d, *J* = 8.8 Hz, H3 and H5); 6.78 (1H, dd, *J* = 2.0 and 8.0 Hz, H4'); 6.95 (2H, d, *J* = 8.8 Hz, H3'' and H5''); 7.07 (2H, d, *J* = 8.8 Hz, H2 and H6); 7.10 (1H, t, *J* = 8.0 Hz, H5'); 7.19 (1H, dd, *J* = 2.0 and 8.0 Hz, H6'); 7.46 (1H, t, *J* = 2.0 Hz, H2'); 7.70 (2H, d, *J* = 8.8 Hz, H2'' and H6''). **^{13}C-NMR** (100 MHz, acetone-d6): δ 43.2 (CH_2); 55.2 (CH_3, OCH_3); 110.9 (CH, C2'); 114.0 (2) (CH, C3'' and C5''); 114.4 (2) (CH, C3 and C5); 114.5 (CH, C6'); 114.9 (CH, C4'); 119.6 (CH, C5'); 123.6 (C, C1); 129.3 (2) (CH, C2'' and C6''); 129.8 (2) (CH, C2 and C6); 131.4 (C, C1''); 138.6 (C, C3'); 140.2 (C, C1'); 147.2 (C, C4); 163.0 (C, C4''); 170.3 (C, CO). **HRMS** ($C_{21}H_{22}N_3O_4S^+$): calculated 412.1326 ($M+H^+$), found 412.1323.

Synthesis of 2-(4-(3-benzylureido)phenyl)-N-(3-((4-methoxyphenyl)sulfonamido)phenyl)acetamide (60)

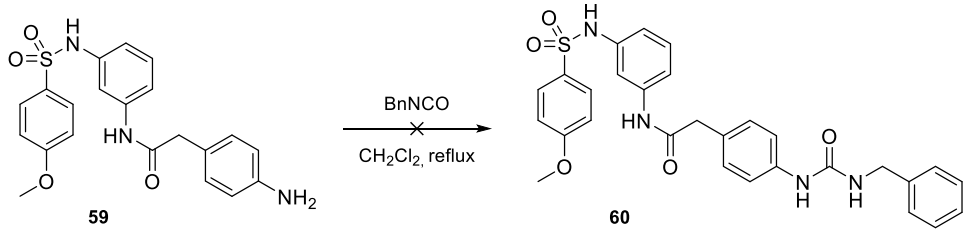

Benzyl isocyanate (37 µL, 0.30 mmol) was added to a solution of **59** (112 mg, 0.27 mmol) in 25 mL of CH_2Cl_2. The reaction was heated under reflux and N_2 atmosphere for 24 h, turning from yellow to orange. The solvent was evaporated and preparative TLC using CH_2Cl_2/MeOH 9:1 as eluent gave 133 mg of a solid with complex spectra.

Synthesis of 2,6-dihydroxy-N-(3-((4-methoxyphenyl)sulfonamido)phenyl)isonicotinamide (61)

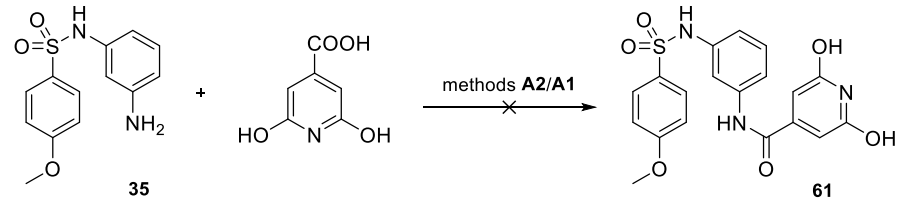

Procedure 1: Via procedure **A2**, $SOCl_2$ (300 µL) was added to 106 mg (0.68 mmol) of citrazinic acid and heated at 70 °C for 5 days. The acyl chloride was then added drop by drop to a solution of **35** (190 mg, 0.68 mmol) in 25 mL of CH_2Cl_2 together with 100 µL of triethylamine and stirred under N_2 at room temperature. No progress was observed by TLC. A similar result was obtained when heating under reflux.

Procedure 2: $SOCl_2$ (300 µL) was added to a solution of citrazinic acid (115 mg, 0.74 mmol) in 50 mL of DMF in ice bath, then warmed to room temperature after the addition. 2 h later, the excess of $SOCl_2$ was rotary removed, and compound **35** (215 mg, 0.77 mmol) in DMF was slowly added to the previous solution. No progress was observed by TLC even in the presence of Et_3N or when heating at 100 °C.

Procedure 3: Following general method **A1**, the mixture of citrazinic acid (132 mg, 0.85 mmol), sulfonamide **35** (172 mg, 0.62 mmol), DCI (160 mg, 0.78 mmol), and *p*-DMAP (40 mg, 0.33 mmol) was heated at 100 °C in 10 mL of DMF. No progress was observed by TLC.

Preparation of compounds 62 and 63

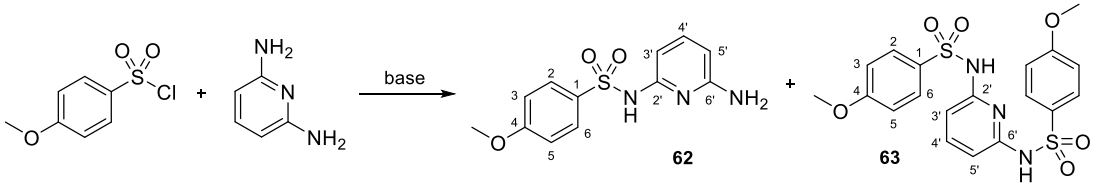

Procedure 1: 4-Methoxybenzenesulfonyl chloride (101 mg, 0.49 mmol) was added to a solution of pyridine-2,6-diamine (65 mg, 0.60 mmol) together with 2 drops of pyridine in 10 mL of CH_2Cl_2. Pyridine-2,6-diamine (47 mg, 0.43 mmol) precipitated after 4 h stirring at room temperature under N_2 atmosphere.

Procedure 2: Pyridine-2,6-diamine (65 mg, 0.60 mmol) and 4-methoxybenzenesulfonyl chloride (102 mg, 0.49 mmol) were dissolved in 10 mL of methanol in presence of triethylamine (0.2 mL) at room temperature. No reaction was observed after 3 days even when heating.

Procedure 3: The sulfonyl chloride (3085 mg, 14.93 mmol) was added to pyridine-2,6-diamine (3895 mg, 35.73 mmol) dissolved in 125 mL of CH_2Cl_2 with 4 mL of triethylamine. The mixture was heated under reflux and N_2 atmosphere for 24 h, then poured into cold water. 2N HCl was added until neutrality and the organic layer was washed with brine, dried over anhydrous Na_2SO_4, filtered, and rotary evaporated, obtaining 4313 mg of **62** and disulfonamide **63**. The two products were individually purified by crystallization. Global yields: **62** (3233 mg, 11.59 mmol, 78%) and **63** (492 mg, 1.10 mmol, 15%).

*N-(6-aminopyridin-2-yl)-4-methoxybenzenesulfonamide (**62**)*. White crystals. **Mp** (MeOH/EtOAc): 163.6-164.2 °C. **IR** (KBr): 3373, 3321, 3186, 1605, 1498, 1374, 1263, 1128 cm^{-1}. **^{1}H-NMR** (400 MHz, $CDCl_3$): δ 3.84 (3H, s, OCH_3); 5.57 (2H, bs, NH_2); 5.99 (1H, d, *J* = 8.0 Hz, H5'); 6.67 (1H, d, *J* = 8.0 Hz, H3'); 6.91 (2H, d, *J* = 8.8 Hz, H3 and H5); 7.34 (1H, t, *J* = 8.0 Hz, H4'); 7.83 (2H, d, *J* = 8.8 Hz, H2 and H6); 11.24 (1H, bs, NH). **^{13}C-NMR** (100 MHz, $CDCl_3$): δ 55.5 (CH_3, OCH_3); 100.3 (CH, C5'); 101.6 (CH, C3'); 114.0 (2) (CH, C3 and C5); 128.9 (2) (CH, C2 and C6); 133.6 (C, C1); 143.0 (CH, C4'); 152.8 (C, C2'); 154.5 (C, C6'); 162.3 (C, C4). **HRMS** ($C_{12}H_{13}N_3NaO_3S^+$): calculated 302.0570 ($M+Na^+$), found 302.0570.

*N,N'-(pyridine-2,6-diyl)bis(4-methoxybenzenesulfonamide) (**63**).* White crystals. **Mp** (EtOAc): 163.0-163.5 °C. **IR** (KBr): 3190, 1595, 1498, 1263, 1157 cm^{-1}. **^{1}H-NMR** (400 MHz, $CDCl_3$): δ 3.83 (6H, s, OCH_3 [bis]); 6.88 (4H, d, *J* = 8.8 Hz, H3 and H5 [bis]); 7.05 (2H, d, *J* = 8.4 Hz, H3' and H5'); 7.56 (1H, t, *J* = 8.4 Hz, H4'); 7.74 (4H, d, *J* = 8.8 Hz, H2 and H6 [bis]); 8.68 (2H, bs, NH). **^{13}C-NMR** (100 MHz, $CDCl_3$): δ 55.6 (2) (CH_3, OCH_3 [bis]); 108.7 (2) (CH, C3' and C5'); 114.3 (4) (CH, C3 and C5 [bis]); 129.4 (4) (CH, C2 and C6 [bis]); 130.5 (2) (C, C1 [bis]); 141.2 (CH, C4'); 149.8 (2) (C, C2' and C6'); 163.4 (2) (C, C4 [bis]).

Synthesis of N-(6-aminopyridin-2-yl)-4-methoxy-N-methylbenzenesulfonamide (64)

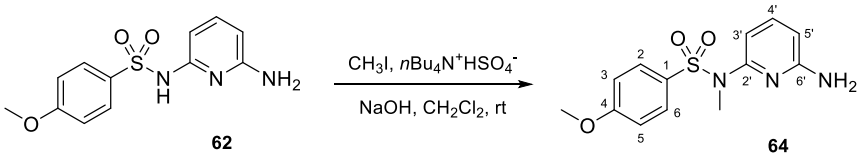

Sulfonamide **62** (234 mg, 0.84 mmol) in 25 mL CH_2Cl_2 was stirred with excess ground NaOH, catalytic tetrabutylammonium hydrogen sulfate, and methyl iodide (100 µL, 1.61 mmol) under N_2 atmosphere for 3 days. NaOH was filtered off and the remaining solution was poured into cold water and repeatedly washed with brine until neutrality, dried over anhydrous Na_2SO_4, filtered, and evaporated. The residue (228 mg) was purified by preparative TLC (CH_2Cl_2/MeOH 98:2) yielding 78 mg (0.27 mmol, 32%) of **64**.

*N-(6-aminopyridin-2-yl)-4-methoxy-N-methylbenzenesulfonamide (**64**).* Yellow oil. **IR** (film): 3480, 3379, 1620, 1595, 1461, 1159 cm^{-1}. **^{1}H-NMR** (400 MHz, $CDCl_3$): δ 3.20 (3H, s, NCH_3); 3.84 (3H, s, OCH_3); 4.24 (2H, bs, NH_2); 6.27 (1H, d, *J* = 8.0 Hz, H5'); 6.90 (2H, d, *J* = 8.8 Hz, H3 and H5); 6.96 (1H, d, *J* = 8.0 Hz, H3'); 7.41 (1H, t, *J* = 8.0 Hz, H4'); 7.59 (2H, d, *J* = 8.8 Hz, H2 and H6). **^{13}C-NMR** (100 MHz, $CDCl_3$): δ 35.8 (CH_3, NCH_3); 55.9 (CH_3, OCH_3); 105.6 (CH, C5'); 109.7 (CH, C3'); 114.3 (2) (CH, C3 and C5); 129.8 (C, C1); 130.1 (2) (CH, C2 and C6); 139.5 (CH, C4'); 152.6 (C, C6'); 157.7 (C, C2'); 163.3 (C, C4). **HRMS** ($C_{13}H_{15}N_3NaO_3S^+$): calculated 316.0727 ($M+Na^+$), found 316.0724.

Synthesis of 4-methoxy-N-(6-((4-nitrophenyl)sulfonamido)pyridin-2-yl)benzenesulfonamide (65)

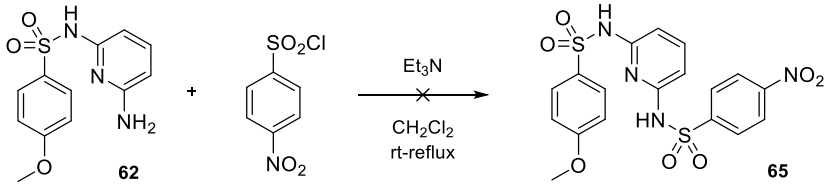

4-Nitrobenzenesulfonyl chloride (727 mg, 3.28 mmol) was progressively added to a solution of **62** (416 mg, 1.49 mmol) with 500 µL of triethylamine in CH_2Cl_2 (50 mL). The reaction was stirred at room temperature under N_2 atmosphere for 4 days, then heated under reflux for two weeks. It was poured into iced water and washed with brine. The organic layer was dried over anhydrous Na_2SO_4, filtered, and evaporated, yielding 729 mg of a complex mixture.

Synthesis of 4-methoxy-N-(6-((3-nitrobenzyl)amino)pyridin-2-yl)benzenesulfonamide (67)

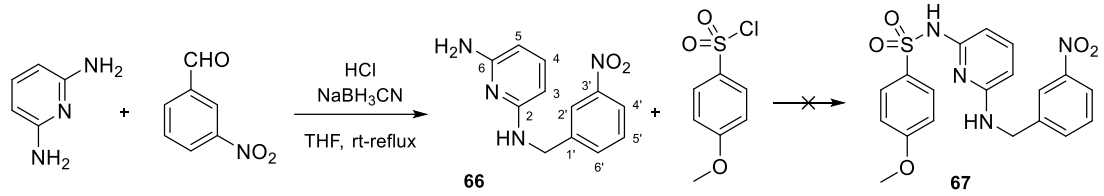

3-Nitrobenzaldehyde (141 mg, 0.93 mmol) was dissolved in 15 mL of THF, adding then 105 mg (0.96 mmol) of 2,6-diaminopyridine, 106 mg (1.69 mmol) of $NaBH_3CN$ and one drop of HCl. The reaction mixture was stirred for 30 h under N_2 atmosphere at room temperature, then heated under reflux for 18 h. It was subsequently poured into cold water and extracted with CH_2Cl_2. The organic layer was dried over anhydrous Na_2SO_4, filtered, and evaporated. Once gently washed with hexane, compound **66** was obtained as a brown oil (145 mg, 0.59 mmol, 64%). For the second step, 4-methoxybenzenesulfonyl chloride (70 mg, 0.34 mmol) was added to a solution of **66** (75 mg, 0.31 mmol) and 56 µL of triethylamine in 15 mL of refluxing CH_2Cl_2. After 48 h under N_2, it was poured into iced water and washed with saturated NaCl. The organic layer was dried over anhydrous Na_2SO_4, filtered and evaporated, yielding 66 mg of a complex mixture.

*N^2-(3-nitrobenzyl)pyridine-2,6-diamine (**66**).* Brown oil. **IR** (film): 3473, 3381, 1614, 1526, 1351 cm^{-1}. **^{1}H-NMR** (400 MHz, $CDCl_3$): δ 4.82 (2H, s, CH_2); 5.86 (2H, d, *J* = 7.6 Hz, H3 and H5); 7.21 (1H, t, *J* = 7.6 Hz, H4); 7.52 (1H, t, *J* = 8.0 Hz, H5'); 7.70 (1H, bd, *J* = 8.0 Hz, H6'); 8.13 (1H, dd, *J* = 1.2 and 8.0 Hz, H4'); 8.24 (1H, bs, H2').

Synthesis of 4-methoxy-N-(6-((4-nitrobenzyl)amino)pyridin-2-yl)benzenesulfonamide (68)

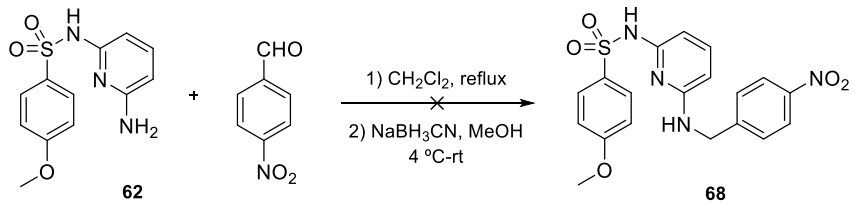

Procedure 1: A mixture of sulfonamide **62** (202 mg, 0.72 mmol), 4-nitrobenzaldehyde (227 mg, 1.50 mmol), and a drop of 2N HCl in 25 mL of CH_2Cl_2 was heated under reflux for 48 h. The solvent was rotary evaporated, adding then methanol, $NaBH_3CN$ (99 mg, 1.58 mmol), and one drop of 2N HCl. No reaction was observed after 3 days at room temperature under N_2.

Procedure 2: A mixture of **62** (314 mg, 1.13 mmol), progressively added 4-nitrobenzaldehyde (773 mg, 5.12 mmol) and a drop of 2N HCl in 50 mL of dry THF was stirred at room temperature under N_2 for 9 days, then evaporated and dissolved in methanol. $NaBH_3CN$ (292 mg, 4.65 mmol) was progressively added, and after 5 days, the reaction was evaporated, dissolved in CH_2Cl_2, and washed with brine. The organic layer was dried over anhydrous Na_2SO_4, filtered, and concentrated to dryness (514 mg). Compound **68** was not obtained.

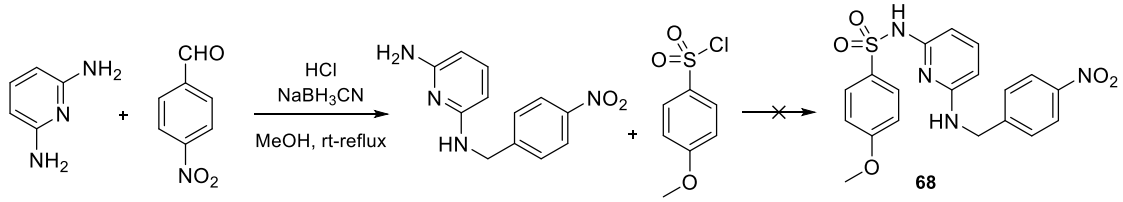

Procedure 3: 2,6-Diaminopyridine (100 mg, 0.92 mmol) was mixed with 4-nitrobenzaldehyde (275 mg, 1.82 mmol), $NaBH_3CN$ (112 mg, 1.78 mmol) in 15 mL of methanol with a few drops of 2N HCl. The resulting greenish-brown solution was stirred for 72 h under N_2 at room temperature. Then, more $NaBH_3CN$ (112 mg, 1.78 mmol) was added to the reaction and heated under reflux for 21 h, obtaining 432 mg of a complex mixture.

Synthesis of N-(4-(((6-((4-methoxyphenyl)sulfonamido)pyridin-2-yl)amino)methyl)phenyl)acetamide (69)

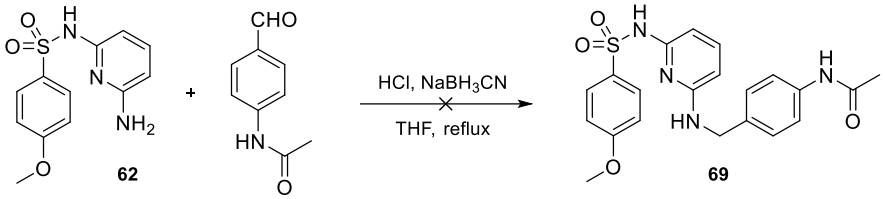

A mixture of **62** (197 mg, 0.71 mmol), *N*-(4-formylphenyl)acetamide (385 mg, 2.36 mmol), $NaBH_3CN$ (288 mg, 4.58 mmol), and a drop of HCl was heated in 20 mL of refluxing THF for 4 days under N_2 atmosphere. The reaction was then poured into iced water and extracted with CH_2Cl_2 at pH 7. EtOAc was added and the solvent partially evaporated. Both organic layers were dried over anhydrous Na_2SO_4, filtered, and evaporated, obtaining 427 mg of a complex mixture.

Preparation of compounds 70 and 71

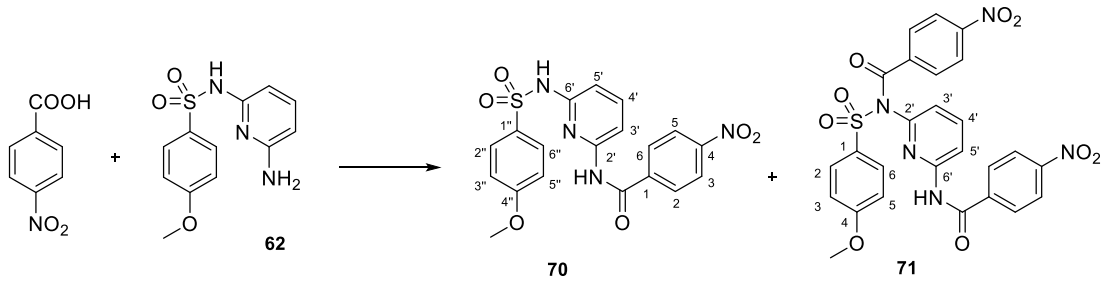

Procedure 1: Following general procedure **A1**, the mixture of **62** (257 mg, 0.92 mmol), 4-nitrobenzoic acid (187 mg, 1.12 mmol), EDC hydrochloride (238 mg, 1.24 mmol), and *p*-DMAP (58 mg, 0.48 mmol) was dissolved in 10 mL of CH_2Cl_2 and irradiated in a microwave oven at 130 °C for 6 min. It was then washed with 2N HCl, 5% $NaHCO_3$, and brine until neutral pH to provide 70 mg. Crystallization in CH_2Cl_2/Hex gave yellow crystals (**70**, 28 mg, 0.07 mmol, 7%) and white crystals (**62**, 3 mg, 0.01 mmol).

Procedure 2: $SOCl_2$ (104 µL, 1.43 mmol) was carefully added to the carboxylic acid (127 mg, 0.76 mmol) in 3 mL of toluene and heated under reflux for 4 h under N_2,[584] resulting in the precipitation of the carboxylic acid (116 mg, 0.69 mmol).

Procedure 3: The acid (116 mg, 0.69 mmol) was added to 200 µL (2.76 mmol) of $SOCl_2$ in ice bath and stirred for 7 h under N_2 atmosphere. After rotary evaporation, the crude was dissolved in CH_2Cl_2 (3 mL) and amine **62** (99 mg, 0.35 mmol) was added to that solution and stirred for 24 h at room temperature. The solvent was removed and the residue dissolved in 5 mL of toluene at 4 °C with a few drops of dry DMF and 100 µL (1.38 mmol) of $SOCl_2$. After the addition, the reaction was warmed to room temperature and stirred for 24 h. No reaction progress was observed.

Procedure 4: $SOCl_2$ (87 µL, 1.20 mmol) was added to a light yellow solution of the carboxylic acid (107 mg, 0.64 mmol) in 5 mL of dry DMF at 4 °C, then warmed to room temperature. $SOCl_2$ was selectively removed under vacuum after 3 h, and then, 100 mg (0.36 mmol) of **62** and anhydrous Na_2CO_3 in excess were added to the previous solution. After 72 h under N_2 atmosphere, the suspension was filtered and 5% $NaHCO_3$ and EtOAc were added. The organic layer was dried over anhydrous Na_2SO_4, filtered, and evaporated, obtaining 53 mg of a complex mixture.

Procedure 5: $SOCl_2$ (200 µL, 2.76 mmol) was added to the carboxylic acid (122 mg, 0.73 mmol) and heated under reflux for 24 h. Once evaporated, the residue was dissolved in 5 mL of CH_2Cl_2 and amine **62** (102 mg, 0.37 mmol) with Cs_2CO_3 (200 mg) were added, turning intense yellow. The reaction was stirred for 24 h under N_2 at room temperature, then filtered and evaporated under vacuum obtaining 95 mg of a complex mixture. The precipitate was washed with THF and hexane, providing 147 mg. Column chromatography using EtOAc gave 51 mg (0.12 mmol, 27%) of **70**.

Procedure 6: The mixture of $SOCl_2$ (400 µL) and 4-nitrobenzoic acid (122 mg, 0.73 mmol) was heated in a sealed tube at 70 °C. After 72 h, the reaction was rotary evaporated, the residue was dissolved in CH_2Cl_2 and added dropwise to a solution of 129 mg (0.46 mmol) of **62** in 10 mL of CH_2Cl_2. It was stirred for 6 h at room temperature under N_2, adding first 100 mg (0.94 mmol) of Na_2CO_3, then 256 mg (0.78 mmol) of Cs_2CO_3. Once added, the yellow reaction turned darker. After 15 h, it was filtered off, and the solid was

repeatedly washed with EtOAc obtaining 271 mg of a mixture of **70**, rests of the acid and another unidentified set of products.

Procedure 7: 499 mg (2.99 mmol) of the carboxylic acid were heated at 70 °C with 800 µL of $SOCl_2$ for 48 h. Once evaporated, the acyl chloride was dissolved in CH_2Cl_2 and added to a solution of **62** (426 mg, 1.53 mmol) in 50 mL of CH_2Cl_2 with 3 mL of DMF. The reaction mixture was stirred for 4 days under N_2 at room temperature, then heated under reflux for 24 h with no observed reaction.

Procedure 8: Following method **A2**, $SOCl_2$ (800 µL) was added to the carboxylic acid (574 mg, 3.43 mmol) and heated in a sealed tube at 70 °C for 21 h. The evaporated residue was dissolved in CH_2Cl_2 and added drop by drop to a solution of **62** (305 mg, 1.09 mmol) and 200 µL of triethylamine in 50 mL of CH_2Cl_2. The reaction mixture was stirred under N_2 at room temperature for 72 h, then poured into iced water and washed with brine to obtain 757 mg of a complex mixture. Crystallization in MeOH/acetone gave 302 mg (0.52 mmol, 48%) of **71**.

Procedure 9: As described in procedure **A2**, the acyl chloride of 4-nitrobenzoic acid (509 mg, 3.05 mmol) was prepared by treatment with $SOCl_2$ (800 µL) in a sealed tube at 70 °C for 15 h. It was added dropwise to a solution of **62** (861 mg, 3.08 mmol) and 0.5 mL of triethylamine in 50 mL of CH_2Cl_2. After 6 days, the resulting precipitate (408 mg) was filtered off and purified by column chromatography in Hex/EtOAc 4:6 to provide **70** (208 mg, 0.49 mmol, 16%) as a white solid.

*N-(6-((4-methoxyphenyl)sulfonamido)pyridin-2-yl)-4-nitrobenzamide (**70**).* White solid. **IR** (KBr): 3309, 1683, 1598, 1453, 1285, 1147 cm^{-1}. **^{1}H-NMR** (400 MHz, DMSO-D6): δ 3.77 (3H, s, OCH_3); 6.80 (1H, d, *J* = 8.0 Hz, H5'); 7.05 (2H, d, *J* = 8.8 Hz, H3'' and H5''); 7.69 (2H, m, H3' and H4'); 7.94 (2H, d, *J* = 8.8 Hz, H2'' and H6''); 8.11 (2H, d, *J* = 8.8 Hz, H2 and H6); 8.33 (2H, d, *J* = 8.8 Hz, H3 and H5). **^{13}C-NMR** (100 MHz, DMSO-D6): 56.0 (CH_3, OCH_3); 108.9 (CH); 114.5 (2) (CH); 123.9 (2) (CH); 129.9 (2) (CH); 140.8 (C); 149.6 (C); 162.8 (C). The rest of the signals are not observed. **HRMS** ($C_{19}H_{16}N_4NaO_6S^+$): calculated 451.0683 ($M+Na^+$), found 451.0674.

*N-((4-methoxyphenyl)sulfonyl)-4-nitro-N-(6-(4-nitrobenzamido)pyridin-2-yl)benzamide (**71**).* White crystals. **IR** (KBr): 3326, 1682, 1576, 1521, 1262, 1165 cm^{-1}. **^{1}H-NMR** (400 MHz, acetone-D6): δ 3.95 (3H, s, OCH_3); 7.17 (2H, d, *J* = 8.8 Hz, H3 and H5); 7.62 (1H, d, *J* = 8.0 Hz, H5'); 7.74 (2H, d, *J* = 8.8 Hz, H2 and H6); 7.97 (2H, d, *J* = 8.8 Hz, $PhNO_2$); 8.03 (1H, t, *J* = 8.0 Hz, H4'); 8.12 (2H, d, *J* = 8.8 Hz, $PhNO_2$); 8.17 (2H, d, *J* = 8.8 Hz, $PhNO_2$); 8.33 (3H, m, H3' and $PhNO_2$); 10.22 (1H, bs, NH). **HRMS** ($C_{26}H_{20}N_5O_9S^+$): calculated 578.0976 ($M+H^+$), found 578.0992.

Synthesis of 4-amino-N-(6-((4-methoxyphenyl)sulfonamido)pyridin-2-yl)benzamide (72)

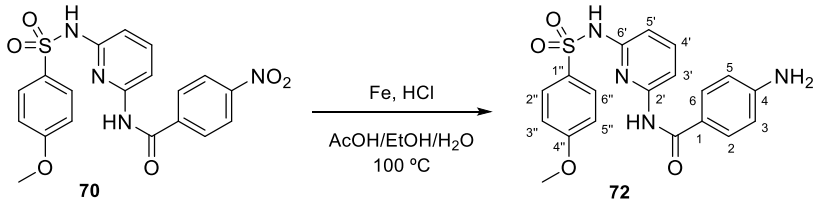

70 72

Metallic iron (128 mg, 2.29 mmol) and a few drops of 2N HCl were added to compound **70** (107 mg, 0.25 mmol) dissolved in 25 mL of acetic acid, ethanol, and water (2:2:1).[514] The reaction was heated at 100 °C for 15 h under N_2, turning first yellow, then darker over time. Once filtered through celite, 4% NaOH was

added and extracted with CH_2Cl_2, then washed with brine. The organic layer was dried over anhydrous Na_2SO_4, and the supernatant was filtered through silica (0.063-0.200 mm), eluting with EtOAc. Product **72** (48 mg, 0.12 mmol, 48%) was obtained as a yellow solid.

*4-Amino-N-(6-((4-methoxyphenyl)sulfonamido)pyridin-2-yl)benzamide (**72**).* Yellow solid. **IR** (KBr): 3473, 3369, 3233, 1660, 1600, 1440, 1154 cm^{-1}. **^{1}H-NMR** (400 MHz, $CDCl_3$): δ 3.81 (3H, s, OCH_3); 6.64 (2H, d, *J* = 8.4 Hz, H3 and H5); 6.89 (2H, d, *J* = 9.2 Hz, H3'' and H5''); 7.07 (1H, d, *J* = 8.4 Hz, H5'); 7.66 (1H, t, *J* = 8.4 Hz, H4'); 7.69 (2H, d, *J* = 8.4 Hz, H2 and H6); 7.77 (2H, d, *J* = 9.2 Hz, H2'' and H6''); 7.99 (1H, d, *J* = 8.4 Hz, H3'); 8.53 (1H, bs, NH). **^{13}C-NMR** (100 MHz, $CDCl_3$): δ 55.6 (CH_3, OCH_3); 108.4 (CH, C3'); 110.8 (CH, C5'); 114.0 (2) (CH, C3 and C5); 114.1 (2) (CH, C3'' and C5''); 122.7 (C, C1); 129.2 (2) (CH, C2'' and C6''); 129.5 (2) (CH, C2 and C6); 130.6 (C, C1''); 140.9 (CH, C4'); 149.1 (C, C6'); 150.5 (C, C4); 150.9 (C, C2'); 163.3 (C, C4''); 165.7 (C, CO). **HRMS** ($C_{19}H_{18}N_4NaO_4S^+$): calculated 421.0941 (M+Na^+), found 421.0948.

Synthesis of 4-acetamido-N-(6-((4-methoxyphenyl)sulfonamido)pyridin-2-yl)benzamide (73)

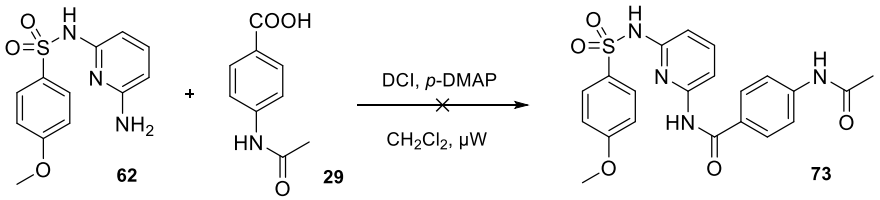

Following method **A1**, the mixture of **62** (113 mg, 0.41 mmol), **29** (100 mg, 0.56 mmol), DCI (194 mg, 0.94 mmol), and *p*-DMAP (55 mg, 0.45 mmol) was dissolved in 3 mL of CH_2Cl_2 and irradiated in a microwave oven at 130 °C for 6 minutes. The reaction was then poured into iced water and washed with 5% $NaHCO_3$, 2N HCl, and brine, obtaining 128 mg of a complex mixture.

Synthesis of N-(6-((4-methoxy-N-methylphenyl)sulfonamido)pyridin-2-yl)-4-nitrobenzamide (74)

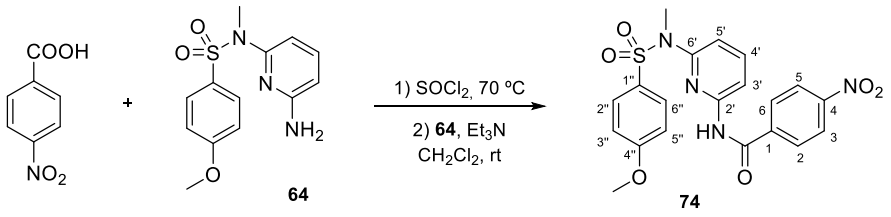

Following general procedure **A2**, $SOCl_2$ (1 mL) was added into a sealed tube with 537 mg (3.21 mmol) of 4-nitrobenzoic acid and stirred for 72 h at 70 °C. The acyl chloride dissolved in CH_2Cl_2 was slowly added to a solution of **64** (330 mg, 1.13 mmol) in 50 mL of CH_2Cl_2 with 0.4 mL of triethylamine and stirred at room temperature for 5 days, then poured into cold water and washed with 2N HCl, 5% $NaHCO_3$, and brine, providing 537 mg. Crystallization in methanol gave 149 mg (0.34 mmol, 30%) of **74**.

*N-(6-((4-methoxy-N-methylphenyl)sulfonamido)pyridin-2-yl)-4-nitrobenzamide (**74**).* Brown crystals. **Mp** (MeOH): 134-135 °C. **IR** (KBr): 3397, 1677, 1595, 1497, 1308, 1156 cm^{-1}. **^{1}H-NMR** (400 MHz, $CDCl_3$): δ 3.25 (3H, s, NCH_3); 3.83 (3H, s, OCH_3); 6.90 (2H, d, *J* = 9.2 Hz, H3'' and H5''); 7.50 (1H, d, *J* = 8.0 Hz, H5'); 7.56 (2H, d. *J* = 9.2 Hz, H2'' and H6''); 7.77 (1H, t, *J* = 8.0 Hz, H4'); 8.04 (2H, d, *J* = 8.8 Hz, H2 and H6); 8.11 (1H, d, *J* = 8.0 Hz, H3'); 8.24 (1H, bs, NH); 8.33 (2H, d, *J* = 8.8 Hz, H3 and H5). **^{13}C-NMR** (100 MHz, $CDCl_3$): δ 35.3 (CH_3, NCH_3); 55.6 (CH_3, OCH_3); 110.5 (CH, C3'); 114.2 (2) (CH, C3'' and C5''); 115.6 (CH, C5'); 123.5 (2) (CH, C3 and C5); 128.5 (2) (CH, C2'' and C6''); 129.1 (C, C1''); 129.5 (2) (CH, C2 and C6); 139.6 (C, C1); 140.2 (CH,

C4'); 149.1 (C, C2'); 149.9 (C, C4); 152.1 (C, C6'); 163.2 (C, C4''); 163.5 (C, CO). **HRMS** ($C_{20}H_{19}N_4O_6S^+$): calculated 443.1020 ($M+H^+$), found 443.1030.

Synthesis of N-(6-((4-methoxyphenyl)sulfonamido)pyridin-2-yl)-2-(4-nitrophenyl)acetamide (75)

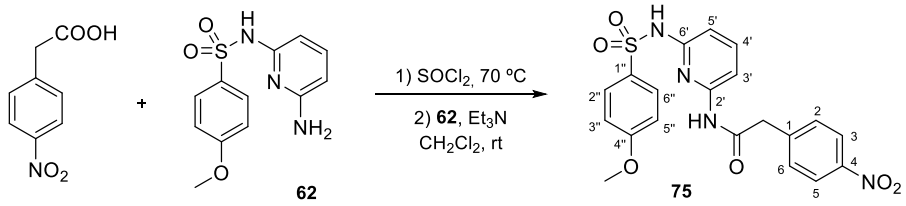

Following method **A2**, 2-(4-nitrophenyl)acetyl chloride was formed by adding 0.6 mL of $SOCl_2$ into a sealed tube with 299 mg (1.65 mmol) of the carboxylic acid, heating at 70 °C for 15 h. The acyl chloride dissolved in CH_2Cl_2 was added dropwise to a solution of **62** (450 mg, 1.61 mmol) in 50 mL of CH_2Cl_2 with 0.5 mL of triethylamine. After 7 hours at room temperature under N_2, the ocher solution was poured into cold water and washed with brine until neutral pH, obtaining 563 mg. Column chromatography using Hex/EtOAc 3:7 as eluent yielded 257 mg (0.58 mmol, 36%) of **75**.

*N-(6-((4-methoxyphenyl)sulfonamido)pyridin-2-yl)-2-(4-nitrophenyl)acetamide (**75**).* White solid. **IR** (KBr): 3309, 3112, 1701, 1586, 1519, 1447, 1346, 1153 cm^{-1}. **^{1}H-NMR** (400 MHz, $CDCl_3$): δ 3.82 (2H, s, CH_2); 3.87 (3H, s, OCH_3); 6.91 (2H, d, *J* = 9.2 Hz, H3'' and H5''); 7.19 (1H, d, *J* = 8.4 Hz, H5'); 7.51 (2H, d, *J* = 8.4 Hz, H2 and H6); 7.69 (2H, d, *J* = 9.2 Hz, H2'' and H6''); 7.69 (1H, t, *J* = 8.4 Hz, H4'); 7.97 (1H, d, *J* = 8.4 Hz, H3'); 8.16 (2H, d, *J* = 8.4 Hz, H3 and H5). **^{13}C-NMR** (100 MHz, $CDCl_3$): δ 43.7 (CH_2); 55.8 (CH_3, OCH_3); 110.0 (CH, C3'); 111.0 (CH, C5'); 114.6 (2) (CH, C3'' and C5''); 123.7 (2) (CH, C3 and C5); 129.2 (2) (C2'' and C6''); 129.9 (C, C1''); 130.3 (2) (CH, C2 and C6); 141.5 (CH, C4'); 141.8 (C, C1); 147.1 (C, C4); 148.7 (C, C6'); 150.7 (C, C2'); 163.7 (C, C4''); 168.7 (C, CO). **HRMS** ($C_{20}H_{18}N_4NaO_6S^+$): calculated 465.0839 ($M+Na^+$), found 465.0861.

Synthesis of N-(6-((4-methoxy-N-methylphenyl)sulfonamido)pyridin-2-yl)-2-(4-nitrophenyl)acetamide (76)

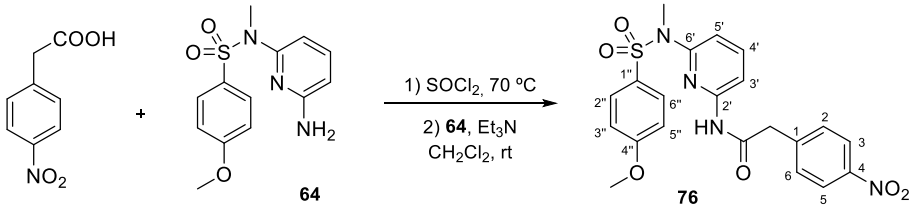

Following method **A2**, $SOCl_2$ (0.6 mL) was added to the carboxylic acid (297 mg, 1.64 mmol) in a sealed tube and heated at 70 °C for 4 h. Once rotary evaporated, the acyl chloride in CH_2Cl_2 was added dropwise to compound **64** (264 mg, 0.90 mmol) in 25 mL of CH_2Cl_2 with 0.2 mL of triethylamine. The reaction mixture was stirred for 30 min at room temperature under N_2, then treated as described to obtain 481 mg. Column chromatography using CH_2Cl_2 gave 134 mg (0.29 mmol, 33%) of **76**.

*N-(6-((4-methoxy-N-methylphenyl)sulfonamido)pyridin-2-yl)-2-(4-nitrophenyl)acetamide (**76**).* Orange oil. **IR** (film): 3337, 1694, 1596, 1520, 1448, 1346, 1156 cm^{-1}. **^{1}H-NMR** (400 MHz, $CDCl_3$): δ 3.19 (3H, s, NCH_3); 3.82 (2H, s, CH_2); 3.83 (3H, s, OCH_3); 6.87 (2H, d, *J* = 9.2 Hz, H3'' and H5''); 7.38 (1H, d, *J* = 8.0 Hz, H5'); 7.48 (2H, d, *J* = 8.4 Hz, H2 and H6); 7.53 (2H, d, *J* = 9.2 Hz, H2'' and H6''); 7.66 (1H, t, *J* = 8.0 Hz, H4'); 7.78 (1H, bs, NH); 7.91 (1H, d, *J* = 8.0 Hz, H3'); 8.19 (2H, d, *J* = 8.4 Hz, H3 and H5). **^{13}C-NMR** (100 MHz, $CDCl_3$): δ 33.8

(CH_3, NCH_3); 43.4 (CH_2); 55.2 (CH_3, OCH_3); 109.8 (CH, C3'); 113.7 (2) (CH, C3'' and C5''); 114.6 (CH, C5'); 123.4 (2) (CH, C3 and C5); 128.6 (C, C1''); 129.1 (2) (CH, C2'' and C6''); 129.9 (2) (CH, C2 and C6); 139.6 (CH, C4'); 141.1 (C, C1); 146.8 (C, C4); 148.8 (C, C2'); 151.4 (C, C6'); 162.8 (C, C4''); 167.4 (C, CO). **HRMS** ($C_{21}H_{20}N_4NaO_6S^+$): calculated 479.0996 ($M+Na^+$), found 479.0994.

Synthesis of N-(6-((4-methoxyphenyl)sulfonamido)pyridin-2-yl)-1H-benzo[d]imidazole-5-carboxamide (77)

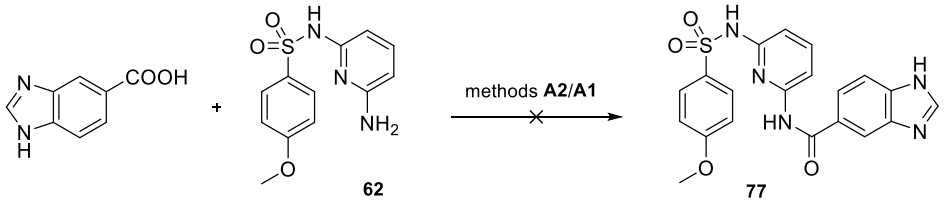

Procedure 1: As described in method **A2**, $SOCl_2$ (1.5 mL) was mixed with 1*H*-benzo[d]imidazole-5-carboxylic acid (287 mg, 1.83 mmol) and heated at 70 °C. One week later, the acyl chloride was added drop by drop to a solution of **62** (505 mg, 1.81 mmol) with 5 mL of triethylamine in 50 mL of CH_2Cl_2. The reaction mixture was stirred at room temperature for 24 h, then poured into cold water and washed with brine. The organic layer was dried over anhydrous Na_2SO_4, filtered, and evaporated, obtaining **62** (396 mg, 1.42 mmol).

Procedure 2: Following general method **A1**, the mixture of 1*H*-benzo[d]imidazole-5-carboxylic acid (103 mg, 0.64 mmol), **62** (147 mg, 0.53 mmol), EDC hydrochloride (207 mg, 1.08 mmol), and *p*-DMAP (43 mg, 0.35 mmol) in 50 mL of refluxing CH_2Cl_2 was stirred under N_2. No progress was observed.

Synthesis of 1-formyl-N-(3,4,5-trimethoxyphenyl)indoline-5-sulfonamide (78) [210]

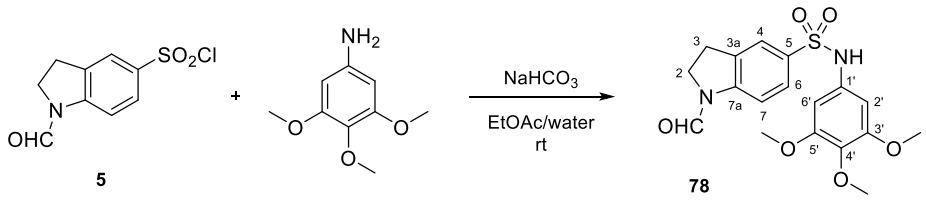

Reagents **5** (408 mg, 1.66 mmol) and 3,4,5-trimethoxyaniline (276 mg, 1.51 mmol) were mixed in 50 mL of 1:1 EtOAc/water with 195 mg (2.32 mmol) of $NaHCO_3$, and stirred for 4 h at room temperature under N_2.[210] MTBE (25 mL) was added, stirred for 1.5 h, and kept overnight at 4 °C. The precipitate was filtered and washed with water and MTBE giving **78** (334 mg, 0.85 mmol, 56%). The organic layers were dried over anhydrous Na_2SO_4, filtered, and evaporated, obtaining compound **78** (159 mg, 0.41 mmol, 27**%**). Global yield: 493 mg, 1.26 mmol, 83%.

*1-Formyl-N-(3,4,5-trimethoxyphenyl)indoline-5-sulfonamide (**78**).* White powder. **IR** (KBr): 3273, 1683, 1603, 1486, 1130 cm^{-1}. **^{1}H-NMR** (400 MHz, $CDCl_3$): δ (*E*) 3.16 (2H, t, *J* = 8.8 Hz, H3); 3.77 (6H, s, OCH_3); 3.78 (3H, s, OCH_3); 4.11 (2H, t, *J* = 8.8 Hz, H2); 6.31 (2H, s, H2' and H6'); 6.41 (1H, bs, NH); 7.17 (1H, d, *J* = 8.8 Hz, H7); 7.62 (2H, m, H4 and H6); 8.96 (1H, s, CHO). (*Z*) 3.20 (2H, t, *J* = 8.8 Hz, H3); 3.76 (6H, s, OCH_3); 3.78 (3H, s, OCH_3); 4.18 (2H, t, *J* = 8.8 Hz, H2); 6.30 (2H, s, H2' and H6'); 6.42 (1H, bs, NH); 7.56 (1H, d, *J* = 1.6 Hz, H4); 7.68 (1H, dd, *J* = 1.6 and 8.0 Hz, H6); 8.13 (1H, d, *J* = 8.0 Hz, H7); 8.54 (1H, s, CHO). **^{13}C-NMR** (100 MHz, $CDCl_3$): δ (*E*) 26.7 (CH_2, C3); 45.2 (CH_2, C2); 56.1 (2) (CH_3, OCH_3); 60.9 (CH_3, OCH_3); 99.4 (2) (CH, C2'

and C6'); 109.1 (CH, C7); 125.3 (CH, C4); 128.1 (CH, C6); 132.5 (C, C1'); 133.0 (C, C3a); 134.2 (C, C5); 135.7 (C, C4'); 145.2 (C, C7a); 153.5 (2) (C, C3' and C5'); 157.9 (CH, CHO). (*Z*) 27.3 (CH_2, C3); 47.2 (CH_2, C2); 56.1 (2) (CH_3, OCH_3); 60.9 (CH_3, OCH_3); 99.4 (2) (CH, C2' and C6'); 116.2 (CH, C7); 124.3 (CH, C4); 127.9 (CH, C6); 132.5 (C, C1'); 133.0 (C, C3a); 134.3 (C, C5); 135.6 (C, C4'); 145.1 (C, C7a); 153.5 (2) (C, C3' and C5'); 160.0 (CH, CHO).

Synthesis of 1-methyl-N-(3,4,5-trimethoxyphenyl)indoline-5-sulfonamide (79) [210]

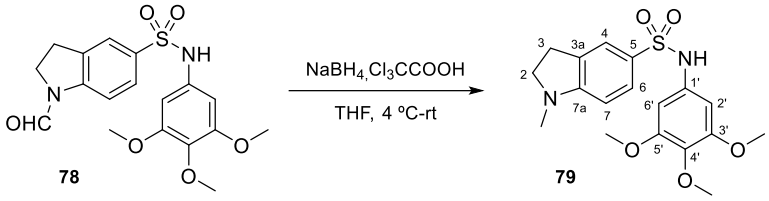

$NaBH_4$ (1477 mg, 38.46 mmol) was carefully added to a solution of sulfonamide **78** (5026 mg, 12.82 mmol) in 125 mL of dry THF at 4 °C under N_2 atmosphere, and subsequently, trichloroacetic acid (6282 mmol, 38.45 mmol) was slowly added to the reaction mixture and progressively warmed to room temperature. After 72 h, it was three-fold diluted with water and vigorously stirred for 1 h at 4 °C until precipitation occurred.[210] The suspension was filtered, washed with water and MTBE, yielding compound **79** (3180 mg, 8.41 mmol, 65%). EtOAc was added to the mother liquors and partially evaporated. The organic layer was washed with brine and dried over anhydrous Na_2SO_4, filtered, and evaporated obtaining **79** (1146 mg, 3.03 mmol, 24%). Global yield: 4326 mg, 11.44 mmol, 89%.

*1-Methyl-N-(3,4,5-trimethoxyphenyl)indoline-5-sulfonamide (**79**).* White powder. **IR** (KBr): 3285, 1601, 1320, 1131, 619 cm^{-1}. **^{1}H-NMR** (400 MHz, $CDCl_3$): δ 2.79 (3H, s, NCH_3); 2.94 (2H, t, *J* = 8.4 Hz, H3); 3.46 (2H, t, *J* = 8.4 Hz, H2); 3.74 (6H, s, OCH_3); 3.76 (3H, s, OCH_3); 6.27 (1H, d, *J* = 8.4 Hz, H7); 6.31 (2H, s, H2' and H6'); 6.71 (1H, bs, NH); 7.37 (1H, d, *J* = 2.0 Hz, H4); 7.51 (1H, dd, *J* = 2.0 and 8.4 Hz, H6). **^{13}C-NMR** (100 MHz, $CDCl_3$): δ 27.6 (CH_2, C3); 34.2 (CH_3, NCH_3); 54.9 (CH_2, C2); 56.1 (2) (CH_3, OCH_3); 60.9 (CH_3, OCH_3); 98.8 (2) (CH, C2' and C6'); 104.3 (CH, C7); 123.3 (CH, C4); 125.0 (C, C3a); 129.2 (CH, C6); 130.2 (C, C5); 133.3 (C, C4'); 135.0 (C, C1'); 153.3 (2) (C, C3' and C5'); 156.6 (C, C7a).

Synthesis of 1-methyl-N-(3,4,5-trimethoxyphenyl)-1H-indole-5-sulfonamide (80) [210]

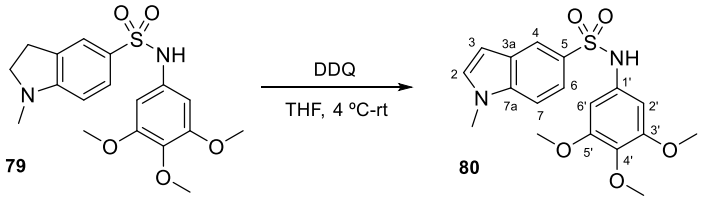

DDQ (2776 mg, 12.22 mmol) was added to compound **79** (4168 mg, 11.03 mmol) dissolved in 50 mL of dry THF at 4 °C, and kept under N_2 atmosphere for 4 h, then warmed to room temperature.[210] The resulting suspension was filtered off 14 h later and the solid was washed with MTBE, yielding the indole derivative **80** (2917 mg, 7.76 mmol, 70%).

*1-Methyl-N-(3,4,5-trimethoxyphenyl)-1H-indole-5-sulfonamide (**80**).* White powder. **IR** (KBr): 3251, 1598, 1468, 1129, 702 cm^{-1}. **^{1}H-NMR** (400 MHz, $CDCl_3$): δ 3.70 (6H, s, OCH_3); 3.74 (3H, s, OCH_3); 3.82 (3H, s, NCH_3); 6.28 (2H, s, H2' and H6'); 6.37 (1H, bs, NH); 6.56 (1H, d, *J* = 3.2 Hz; H3); 7.16 (1H, d, *J* = 3.2 Hz; H2);

7.33 (1H, d, *J* = 8.8 Hz, H7); 7.60 (1H, dd, *J* = 1.6 and 8.8 Hz, H6); 8.12 (1H, d, *J* = 1.6 Hz, H4). **^{13}C-NMR** (100 MHz, $CDCl_3$): δ 33.1 (CH_3, NCH_3); 56.0 (2) (CH_3, OCH_3); 60.9 (CH_3, OCH_3); 99.3 (2) (CH, C2' and C6'); 102.7 (CH, C3); 109.6 (CH, C7); 120.2 (CH, C4); 121.9 (CH, C6); 127.7 (C, C3a); 129.4 (C, C4'); 131.2 (CH, C2); 133.0 (C, C1'); 135.3 (C, C5); 138.4 (C, C7a); 153.3 (2) (C, C3' and C5'). **HRMS** ($C_{18}H_{20}N_2NaO_5S^+$): calculated 399.0985 ($M+Na^+$), found 399.0974.

Synthesis of N,1-dimethyl-N-(3,4,5-trimethoxyphenyl)-1H-indole-5-sulfonamide (81) [210]

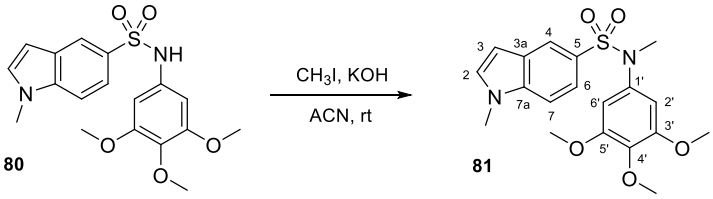

As described in procedure **C1**, 141 mg (0.38 mmol) of **80** in 50 mL of ACN with ground KOH in excess was stirred for 30 min before adding methyl iodide (50 µL, 0.80 mmol). After 19 h, the crude residue (**81**, 133 mg, 0.34 mmol, 91%) was purified by column chromatography using toluene/EtOAc 6:4 (**81**, 107 mg, 0.27 mmol, 73%).

*N,1-dimethyl-N-(3,4,5-trimethoxyphenyl)-1H-indole-5-sulfonamide (**81**).* Yellow solid. **IR** (KBr): 1594, 1498, 1345, 1157, 644 cm^{-1}. **^{1}H-NMR** (400 MHz, $CDCl_3$): δ 3.12 (3H, s, SO_2NCH_3); 3.67 (6H, s, OCH_3); 3.84 (3H, s, OCH_3); 3.85 (3H, s, 1-NCH_3); 6.28 (2H, s, H2' and H6'); 6.52 (1H, d, *J* = 3.2 Hz, H3); 7.18 (1H, d, *J* = 3.2 Hz, H2); 7.35 (1H, d, *J* = 8.4 Hz, H7); 7.44 (1H, dd, *J* = 2.0 and 8.4 Hz, H6); 7.97 (1H, d, *J* = 2.0 Hz, H4). **^{13}C-NMR** (100 MHz, $CDCl_3$): δ 33.1 (CH_3, 1-NCH_3); 38.5 (CH_3, SO_2NCH_3); 56.1 (2) (CH_3, OCH_3); 60.9 (CH_3, OCH_3); 102.6 (CH, C3); 104.7 (2) (CH, C2' and C6'); 109.1 (CH, C7); 121.0 (CH, C4); 122.4 (CH, C6); 126.9 (C, C4'); 127.6 (C, C3a); 131.2 (CH, C2); 137.3 (C, C5); 137.8 (C, C1'); 138.4 (C, C7a); 152.8 (2) (C, C3' and C5'). **HRMS** ($C_{19}H_{22}N_2NaO_5S^+$): calculated 413.1142 ($M+Na^+$), found 413.1138.

Synthesis of N-ethyl-1-methyl-N-(3,4,5-trimethoxyphenyl)-1H-indole-5-sulfonamide (82) [210]

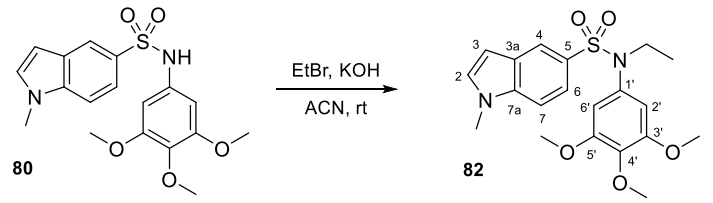

Following method **C1**, a mixture of powdered KOH, sulfonamide **80** (188 mg, 0.50 mmol), and ethyl bromide (75 µL, 1.00 mmol) in 50 mL of ACN reacted over 72 h, giving 169 mg (0.42 mmol, 84%) of compound **82**. Crystallization in CH_2Cl_2/Hex gave 66 mg (0.16 mmol, 33%) of **82** as yellow crystals.

*N-ethyl-1-methyl-N-(3,4,5-trimethoxyphenyl)-1H-indole-5-sulfonamide (**82**).* Yellow crystals. **Mp** (CH_2Cl_2/Hex): 175.9-176.3 °C. **IR** (KBr): 1595, 1331, 1124, 644 cm^{-1}. **^{1}H-NMR** (400 MHz, $CDCl_3$): δ 1.07 (3H, t, *J* = 7.2 Hz, Et); 3.53 (2H, q, *J* = 7.2 Hz, Et); 3.64 (6H, s, OCH_3); 3.84 (6H, s, OCH_3 and NCH_3); 6.22 (2H, s, H2' and H6'); 6.57 (1H, d, *J* = 3.2 Hz, H3); 7.17 (1H, d, *J* = 3.2 Hz, H2); 7.35 (1H, d, *J* = 8.4 Hz, H7); 7.51 (1H, dd, *J* = 1.6 and 8.4 Hz, H6); 7.99 (1H, d, *J* = 1.6 Hz, H4). **^{13}C-NMR** (100 MHz, $CDCl_3$): δ 14.1 (CH_3, Et); 33.1 (CH_3, NCH_3); 45.7 (CH_2, Et); 56.0 (2) (CH_3, OCH_3); 60.9 (CH_3, OCH_3); 102.5 (CH, C3); 106.6 (2) (CH, C2' and C6'); 109.1 (CH, C7); 120.8 (CH, C4); 122.2 (CH, C6); 127.6 (C, C4'); 128.6 (C, C3a); 131.2 (CH, C2); 135.0 (C,

C5); 137.6 (C, C1'); 138.3 (C, C7a); 152.9 (2) (C, C3' and C5'). **HRMS** ($C_{20}H_{25}N_2O_5S^+$): calculated 405.1479 ($M+H^+$), found 405.1481.

Synthesis of ethyl ((1-methyl-1H-indol-5-yl)sulfonyl)(3,4,5-trimethoxyphenyl)carbamate (83)

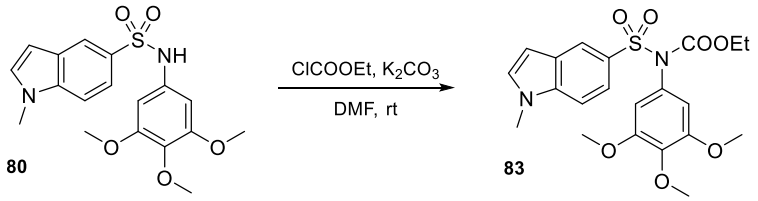

Compound **80** (80 mg, 0.21 mmol) in 1 mL of dry DMF with excess K_2CO_3 was mixed with ethyl chloroformate (41 µL, 0.43 mmol) and stirred for 8 h at room temperature under N_2 atmosphere. The solvent was rotary evaporated, and CH_2Cl_2 was added, washed with brine and the organic layer dried over anhydrous Na_2SO_4, filtered, and concentrated to dryness yielding 84 mg of **80** as the major product with a very minor impurity of **83**.

Synthesis of ethyl N-((1-methyl-1H-indol-5-yl)sulfonyl)-N-(3,4,5-trimethoxyphenyl)glycinate (84)

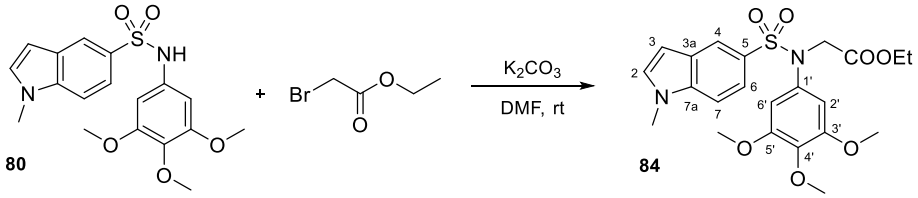

As detailed in procedure **C2**, ethyl bromoacetate (107 µL, 0.97 mmol) was added to a solution of **80** (182 mg, 0.48 mmol) with excess K_2CO_3 in dry DMF (1 mL) and stirred at room temperature for three days, providing compound **84** (204 mg, 0.44 mmol, 91%). Crystallization in methanol gave 68 mg (0.15 mmol, 30%) of **84**.

*Ethyl N-((1-methyl-1H-indol-5-yl)sulfonyl)-N-(3,4,5-trimethoxyphenyl)glycinate (**84**).* Yellow crystals. **Mp** (MeOH): 124.5-125.8 °C. **IR** (KBr): 1750, 1503, 1334, 641 cm^{-1}. **^{1}H-NMR** (400 MHz, $CDCl_3$): δ 1.22 (3H, t, *J* = 7.2 Hz, Et); 3.48 (6H, s, OCH_3); 3.81 (3H, s, OCH_3); 3.84 (3H, s, NCH_3); 4.15 (2H, q, *J* = 7.2 Hz, Et); 4.36 (2H, s, CH_2); 6.39 (2H, s, H2' and H6'); 6.56 (1H, d, *J* = 3.2 Hz, H3); 7.17 (1H, d, *J* = 3.2 Hz, H2); 7.35 (1H, d, *J* = 8.8 Hz, H7); 7.57 (1H, dd, *J* = 1.6 and 8.8 Hz, H6); 8.03 (1H, d, *J* = 1.6 Hz, H4). **^{13}C-NMR** (100 MHz, $CDCl_3$): δ 14.1 (CH_3, Et); 33.1 (CH_3, NCH_3); 52.9 (CH_2); 55.9 (2) (CH_3, OCH_3); 60.7 (CH_2, Et); 61.3 (CH_3, OCH_3); 102.5 (CH, C3); 106.4 (2) (CH, C2' and C5'); 109.2 (CH, C7); 120.6 (CH, C4); 122.2 (CH, C6); 127.5 (C, C4'); 129.0 (C, C3a); 131.3 (CH, C2); 135.8 (C, C5); 137.7 (C, C1'); 138.3 (C, C7a); 152.9 (2) (C, C3' and C5'); 168.9 (C, CO). **HRMS** ($C_{22}H_{27}N_2O_7S^+$): calculated 463.1533 ($M+H^+$), found 463.1522.

Synthesis of N-((1-methyl-1H-indol-5-yl)sulfonyl)-N-(3,4,5-trimethoxyphenyl)glycine (85)

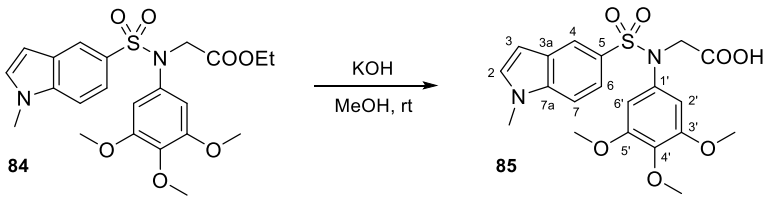

Compound **84** (130 mg, 0.28 mmol) in methanol (5 mL) with excess KOH was vigorously stirred for half an hour, and subsequently evaporated to be dissolved in CH_2Cl_2 and washed repeatedly with brine. The organic layer was dried over anhydrous Na_2SO_4, filtered, and evaporated, yielding **85** (83 mg, 0.19 mmol, 68%). Flash chromatography (CH_2Cl_2/methanol 9:1) gave 29 mg (0.07 mmol, 24%) of **85**.

*N-((1-methyl-1H-indol-5-yl)sulfonyl)-N-(3,4,5-trimethoxyphenyl)glycine (**85**).* White solid. **IR** (KBr): 2943, 1731, 1589, 1129, 649 cm^{-1}. **^{1}H-NMR** (400 MHz, $CDCl_3$): δ 3.58 (6H, s, OCH_3); 3.77 (3H, s, OCH_3); 3.80 (3H, s, NCH_3); 4.34 (2H, s, CH_2); 6.35 (2H, s, H2' and H6'); 6.53 (1H, d, *J* = 3.2 Hz, H3); 7.14 (1H, d, *J* = 3.2 Hz, H2); 7.32 (1H, d, *J* = 8.8 Hz, H7); 7.53 (1H, dd, *J* = 2.0 and 8.8 Hz, H6); 8.00 (1H, d, *J* = 2.0 Hz, H4). **^{13}C-NMR** (100 MHz, $CDCl_3$): δ 33.2 (CH_3, NCH_3); 53.4 (CH_2); 56.0 (2) (CH_3, OCH_3); 60.8 (CH_3, OCH_3); 102.7 (CH, C3); 106.3 (2) (CH, C2' and C6'); 109.4 (CH, C7); 120.8 (CH, C4); 122.4 (CH, C6); 127.6 (C, C4'); 128.7 (C, C3a); 131.2 (CH, C2); 135.9 (C, C5); 137.7 (C, C1'); 138.4 (C, C7a); 153.0 (2) (C, C3' and C5'); 173.0 (C, CO). **HRMS** ($C_{20}H_{22}N_2NaO_7S^+$): calculated 457.1040 ($M+Na^+$), found 457.1035.

Synthesis of N-(cyanomethyl)-1-methyl-N-(3,4,5-trimethoxyphenyl)-1H-indole-5-sulfonamide (86)

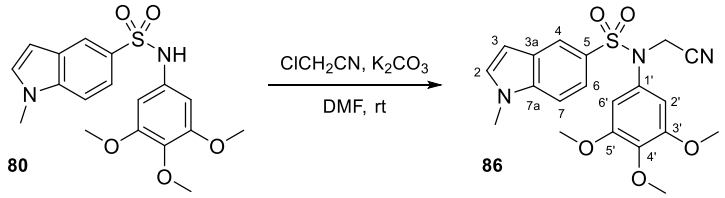

Following method **C2**, chloroacetonitrile (20 µL, 0.32 mmol) was added to a solution of **80** (48 mg, 0.13 mmol) in dry DMF (1 mL) with K_2CO_3 in excess and stirred for 3 h obtaining compound **86** (41 mg, 0.10 mmol, 70%). Crystallization in CH_2Cl_2/Hex gave 22 mg (0.05 mmol, 42%) of **86**.

*N-(cyanomethyl)-1-methyl-N-(3,4,5-trimethoxyphenyl)-1H-indole-5-sulfonamide (**86**).* White crystals. **Mp** (CH_2Cl_2/Hex): 140.2-141.0 °C. **IR** (KBr): 1594, 1342, 1125, 642 cm^{-1}. **^{1}H-NMR** (400 MHz, $CDCl_3$): δ 3.63 (6H, s, OCH_3); 3.84 (3H, s, OCH_3); 3.86 (3H, s, NCH_3); 4.56 (2H, s, CH_2); 6.36 (2H, s, H2' and H6'); 6.60 (1H, d, *J* = 3.2 Hz, H3); 7.20 (1H, d, *J* = 3.2 Hz, H2); 7.41 (1H, d, *J* = 8.8 Hz, H7); 7.59 (1H, dd, *J* = 2.0 and 8.8 Hz, H6); 8.03 (1H, d, *J* = 2.0 Hz, H4). **^{13}C-NMR** (100 MHz, $CDCl_3$): δ 33.2 (CH_3, NCH_3); 39.8 (CH_2); 56.0 (2) (CH_3, OCH_3); 60.9 (CH_3, OCH_3); 102.9 (CH, C3); 106.0 (2) (CH, C2' and C6'); 109.6 (CH, C7); 115.2 (C, CN); 120.8 (CH, C4); 122.8 (CH, C6); 127.5 (C, C4'); 127.7 (C, C3a); 131.6 (CH, C2); 134.2 (C, C5); 138.5 (C, C1'); 138.7 (C, C7a); 153.4 (2) (C, C3' and C5'). **HRMS** ($C_{20}H_{22}N_3O_5S^+$): calculated 416.1275 ($M+H^+$), found 416.1266.

Synthesis of 3-bromo-1-methyl-N-(3,4,5-trimethoxyphenyl)-1H-indole-5-sulfonamide (87)

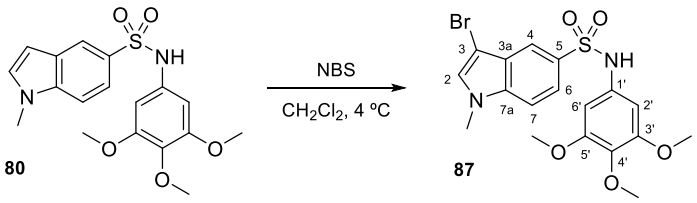

A solution of **80** (260 mg, 0.69 mmol) in CH_2Cl_2 (15 mL) was cooled in ice bath and then *N*-bromosuccinimide (142 mg, 0.80 mmol) was added and stirred for 3 h under nitrogen atmosphere until white crystals appeared. Compound **87** (192 mg, 0.42 mmol, 61%) was obtained after filtration.

*3-Bromo-1-methyl-N-(3,4,5-trimethoxyphenyl)-1H-indole-5-sulfonamide (**87**).* White crystals. **Mp** (CH_2Cl_2): 236.9-237.2 °C. **IR** (KBr): 3247, 1604, 1329, 1127, 1010 cm^{-1}. **^{1}H-NMR** (400 MHz, $CDCl_3$): δ 3.71 (6H, s, OCH_3); 3.74 (3H, s, OCH_3); 3.79 (3H, s, NCH_3); 6.29 (2H, s, H2' and H6'); 6.39 (1H, bs, NH); 7.18 (1H, s, H2); 7.31 (1H, d, *J* = 8.8 Hz, H7); 7.61 (1H, dd, *J* = 1.6 and 8.8 Hz, H6); 8.09 (1H, d, *J* = 1.6 Hz, H4). **^{13}C-NMR** (100 MHz, DMSO-D6): δ 33.5 (CH_3, NCH_3); 56.1 (2) (CH_3, OCH_3); 60.5 (CH_3, OCH_3); 89.2 (C, C3); 97.9 (2) (CH, C2' and C6'); 111.8 (CH, C7); 119.1 (CH, C4); 120.8 (CH, C6); 126.1 (C, C5); 131.3 (C, C3a); 131.9 (CH, C2); 134.3 (C, C4'); 134.5 (C, C1'); 138.0 (C, C7a); 153.4 (2) (C, C3' and C5'). **HRMS** ($C_{18}H_{19}BrN_2NaO_5S^+$): calculated 477.0090 ($M+Na^+$), found 477.0091.

Synthesis of 3-bromo-N-ethyl-1-methyl-N-(3,4,5-trimethoxyphenyl)-1H-indole-5-sulfonamide (88)

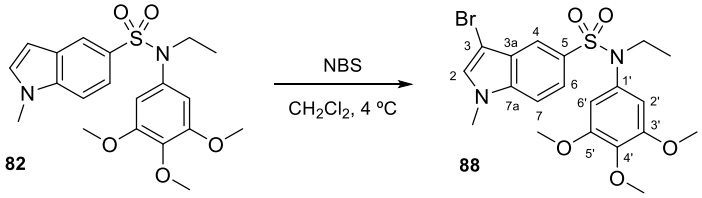

N-bromosuccinimide (52 mg, 0.29 mmol) was added to a pre-cooled solution of **82** (100 mg, 0.25 mmol) in CH_2Cl_2 (5 mL) and stirred under N_2 for one hour. The mixture was evaporated and the product was crystallized in methanol/CH_2Cl_2 (**88**, 40 mg, 0.08 mmol, 33%). Global yield 78%.

*3-Bromo-N-ethyl-1-methyl-N-(3,4,5-trimethoxyphenyl)-1H-indole-5-sulfonamide (**88**).* Yellow crystals. **Mp** (methanol/CH_2Cl_2): 155.7-156.2 °C. **IR** (KBr): 1594, 1234, 1128, 647 cm^{-1}. **^{1}H-NMR** (400 MHz, $CDCl_3$): δ 1.09 (3H, t, *J* = 7.2 Hz, Et); 3.53 (2H, q, *J* = 7.2 Hz, Et); 3.68 (6H, s, OCH_3); 3.84 (3H, s, OCH_3); 3.86 (3H, s, NCH_3); 6.24 (2H, s, H2' and H6'); 7.21 (1H, s, H2); 7.35 (1H, d, *J* = 8.8 Hz, H7); 7.56 (1H, dd, *J* = 1.6 and 8.8 Hz, H6); 7.94 (1H, d, *J* = 1.6 Hz, H4). **^{13}C-NMR** (100 MHz, $CDCl_3$): δ 14.1 (CH_3, Et); 33.4 (CH_3, NCH_3); 47.8 (CH_2, Et); 56.1 (2) (CH_3, OCH_3); 60.9 (CH_3, NCH_3); 91.0 (C, C3); 106.5 (2) (CH, C2' and C6'); 109.5 (CH, C7); 120.8 (CH, C4); 122.1 (CH, C6); 126.8 (C, C5); 130.0 (C, C4'); 130.1 (CH, C2); 134.8 (C, C3a); 137.8 (C, C1'); 137.9 (C, C7a); 153.0 (2) (C, C3' and C5'). **HRMS** ($C_{20}H_{23}BrN_2NaO_5S^+$): calculated 505.0403 ($M+Na^+$), found 505.0403.

Synthesis of 3-formyl-1-methyl-N-(3,4,5-trimethoxyphenyl)-1H-indole-5-sulfonamide (89)

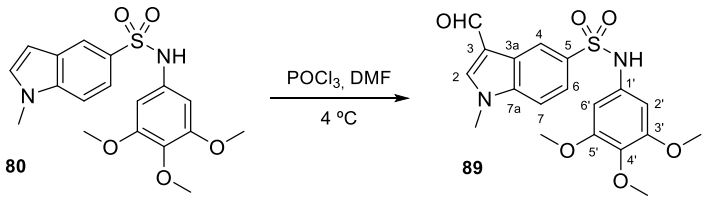

Via Vilsmeier-Haack reaction (method **D**), $POCl_3$ (860 µL, 9.39 mmol) was added to 2 mL of dry DMF in ice and stirred for half an hour under N_2, followed by the addition of **80** (589 mg, 1.54 mmol) in dry DMF (3 mL). One hour later, the mixture was poured into water/sodium acetate and kept at 4 °C for three days. The suspension was filtered off to obtain **89** (602 mg, 1.49 mmol, 95%).

*3-Formyl-1-methyl-N-(3,4,5-trimethoxyphenyl)-1H-indole-5-sulfonamide (**89**).* Yellow crystals. **Mp** (MeOH/acetone): 237.9-238.3 °C. **IR** (KBr): 3143, 1644, 1495, 1329, 1126 cm^{-1}. **^{1}H-NMR** (400 MHz, $CDCl_3$): δ 3.73 (9H, s, OCH_3); 3.90 (3H, s, NCH_3); 6.34 (2H, s, H2' and H6'); 6.57 (1H, bs, NH); 7.38 (1H, d, *J* = 8.8 Hz, H7); 7.73 (1H, dd, *J* = 2.0 and 8.8 Hz, H6); 7.79 (1H, s, H2); 8.88 (1H, d, *J* = 2.0 Hz, H4); 10.00 (1H, s, CHO). **^{13}C-NMR** (100 MHz, $CDCl_3$): δ 34.0 (CH_3, NCH_3); 56.1 (2) (CH_3, OCH_3); 60.9 (CH_3, OCH_3); 90.1 (2) (CH, C2' and C6'); 110.3 (CH, C7); 118.7 (C, C3); 122.7 (CH, C4); 123.1 (CH, C6); 124.8 (C, C3a); 132.5 (C, C5); 133.3 (C, C4'); 135.5 (C, C1'); 139.5 (C, C7a); 140.7 (CH, C2); 153.5 (2) (C, C3' and C5'); 184.0 (CH, CHO). **HRMS** ($C_{19}H_{20}N_2NaO_6S^+$): calculated 427.0934 ($M+Na^+$), found 427.0935.

Preparation of compounds 90-92

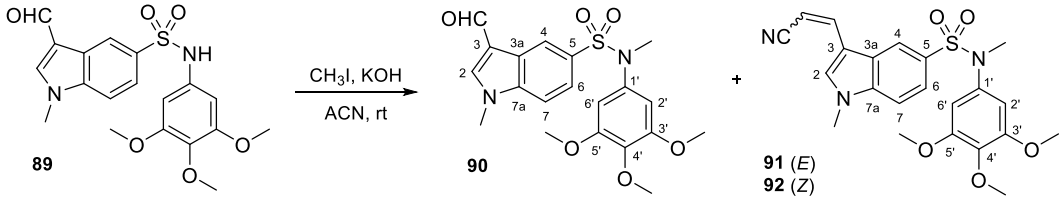

Procedure 1: As explained in procedure **C1**, methyl iodide (45 µL, 0.72 mmol) was added to a solution of **89** (138 mg, 0.34 mmol) in ACN (50 mL) with powdered KOH in excess, previously stirred for half an hour. 24 h later, more KOH and methyl iodide were added (55 µL, 0.88 mmol) and after 6 days, it was evaporated under vacuum, re-dissolved in CH_2Cl_2 and washed with brine. The organic layer was dried over anhydrous Na_2SO_4, filtered, and evaporated (119 mg). Preparative TLC (toluene/EtOAc 3:7) gave **90** (40 mg, 0.10 mmol, 28%), **91** (50 mg, 0.11 mmol, 33%), and **92** (14 mg, 0.03 mmol, 9%).

Procedure 2: Following procedure **C1**, compound **89** (609 mg, 1.51 mmol) was dissolved in 150 mL of ACN and stirred in the presence of KOH in excess for 30 min. Then, methyl iodide (188 µL, 3.02 mmol) was added to the previous suspension. After 2 days, the reaction was quenched, obtaining 576 mg (1.38 mmol, 91%) of derivative **90** as a single product.

*3-Formyl-N,1-dimethyl-N-(3,4,5-trimethoxyphenyl)-1H-indole-5-sulfonamide (**90**).* White solid. **IR** (KBr): 1660, 1329, 1125, 651 cm^{-1}. **^{1}H-NMR** (400 MHz, $CDCl_3$): δ 3.16 (3H, s, SO_2NCH_3); 3.69 (6H, s, OCH_3); 3.83 (3H, s, OCH_3); 3.92 (3H, s, 1-NCH_3); 6.31 (2H, s, H2' and H6'); 7.36 (1H, d, *J* = 8.4 Hz, H7); 7.50 (1H, dd, *J* = 1.6 and 8.4 Hz, H6); 7.80 (1H, s, H2); 8.68 (1H, d, *J* = 1.6 Hz, H4); 10.00 (1H, s, CHO). **^{13}C-NMR** (100 MHz, $CDCl_3$): δ 34.0 (CH_3, 1-NCH_3); 38.6 (CH_3, SO_2NCH_3); 56.2 (2) (CH_3, OCH_3); 60.9 (CH_3, OCH_3); 104.6 (2) (CH,

C2' and C6'); 110.0 (CH, C7); 118.4 (C, C3); 122.6 (CH, C4); 123.4 (CH, C6); 124.4 (C, C3a); 131.0 (C, C5); 137.4 (C, C4'); 139.4 (C, C1'); 140.9 (C, C7a); 141.0 (CH, C2); 153.0 (2) (C, C3' and C5'); 184.0 (CH, CHO). **HRMS** ($C_{20}H_{22}N_2NaO_6S^+$): calculated 441.1091 (M+Na^+), found 441.1084.

*(E)-3-(2-cyanovinyl)-N,1-dimethyl-N-(3,4,5-trimethoxyphenyl)-1H-indole-5-sulfonamide (**91**).* Yellow solid. **IR** (KBr): 2203, 1595, 1334, 1126 cm^{-1}. **^{1}H-NMR** (400 MHz, $CDCl_3$): δ 3.14 (3H, s, SO_2NCH_3); 3.69 (6H, s, OCH_3); 3.85 (3H, s, OCH_3); 3.88 (3H, s, 1-NCH_3); 5.67 (1H, d, *J* = 16.4 Hz, olefin); 6.29 (2H, s, H2' and H6'); 7.40 (1H, d, *J* = 8.4 Hz, H7); 7.46 (1H, s, H2); 7.47 (1H, d, *J* = 16.4 Hz, olefin); 7.53 (1H, dd, *J* = 1.6 and 8.4 Hz, H6); 8.04 (1H, d, *J* = 1.6 Hz, H4). **^{13}C-NMR** (100 MHz, $CDCl_3$): δ 33.3 (CH_3, 1-NCH_3); 38.1 (CH_3, SO_2NCH_3); 55.7 (2) (CH_3, OCH_3); 60.5 (CH_3, OCH_3); 91.4 (CH, olefin); 104.3 (2) (CH, C2' and C6'); 109.9 (CH, C7); 112.2 (C, C3); 118.7 (C, CN); 120.5 (CH, C4); 122.2 (CH, C6); 124.2 (C, C3a); 129.0 (C, C5); 134.1 (CH, C2); 136.9 (C, C4'); 137.1 (C, C1'); 139.2 (C, C7a); 141.6 (CH, olefin); 152.6 (2) (C, C3' and C5'). **HRMS** ($C_{22}H_{23}N_3NaO_5S^+$): calculated 464.1251 (M+Na^+), found 464.1250.

*(Z)-3-(2-cyanovinyl)-N,1-dimethyl-N-(3,4,5-trimethoxyphenyl)-1H-indole-5-sulfonamide (**92**).* Yellow solid. **IR** (KBr): 2208, 1594, 1335, 1126 cm^{-1}. **^{1}H-NMR** (400 MHz, $CDCl_3$): δ 3.13 (3H, s, SO_2NCH_3); 3.67 (6H, s, OCH_3); 3.82 (3H, s, OCH_3); 3.92 (3H, s, 1-NCH_3); 5.26 (1H, d, *J* = 11.6 Hz, olefin); 6.27 (2H, s, H2' and H6'); 7.33 (1H, d, *J* = 11.6 Hz, olefin); 7.41 (1H, d, *J* = 8.8 Hz, H7); 7.52 (1H, dd, *J* = 1.6 and 8.8 Hz, H6); 7.99 (1H, d, *J* = 1.6 Hz, H4); 8.31 (1H, s, H2). **^{13}C-NMR** (100 MHz, $CDCl_3$): δ 33.7 (CH_3, 1-NCH_3); 38.5 (CH_3, SO_2NCH_3); 56.1 (2) (CH_3, OCH_3); 61.0 (CH_3, OCH_3); 89.9 (CH, olefin); 104.7 (2) (CH, C2' and C6'); 110.0 (CH, C7); 111.8 (C, C3); 119.1 (C, CN); 119.6 (CH, C4); 121.0 (CH, C6); 122.4 (C, C3a); 126.8 (C, C5); 129.0 (CH, C2); 132.6 (C, C4'); 137.4 (C, C1'); 138.1 (C, C7a); 138.5 (CH, olefin); 152.9 (2) (C, C3' and C5'). **HRMS** ($C_{22}H_{23}N_3NaO_5S^+$): calculated 464.1251 (M+Na^+), found 464.1239.

Preparation of compounds 93-95

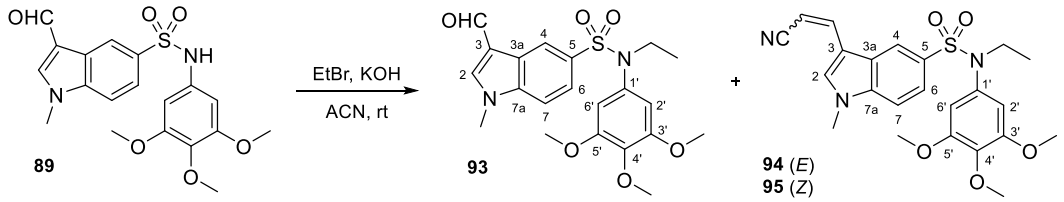

Following method **C1**, compound **89** (118 mg, 0.29 mmol) in ACN (50 mL) with ground KOH in excess was stirred for half an hour, followed by the addition of ethyl bromide (50 µL, 0.67 mmol). The reaction was stirred for 6 days under N_2, evaporated under vacuum, dissolved in CH_2Cl_2, and washed with brine until neutrality. The organic layer was dried over anhydrous Na_2SO_4, filtered, and evaporated (100 mg). Preparative TLC (toluene/EtOAc 25:75) provided **93** (14 mg, 0.03 mmol, 11%), **94** (50 mg, 0.11 mmol, 38%), and **95** (12 mg, 0.03 mmol, 9%).

*N-Ethyl-3-formyl-1-methyl-N-(3,4,5-trimethoxyphenyl)-1H-indole-5-sulfonamide (**93**).* Yellow solid. **IR** (KBr): 1662, 1334, 1124, 653 cm^{-1}. **^{1}H-NMR** (400 MHz, $CDCl_3$): δ 1.09 (3H, t, *J* = 7.2 Hz, Et); 3.58 (2H, q, *J* = 7.2 Hz, Et); 3.68 (6H, s, OCH_3); 3.82 (3H, s, OCH_3); 3.91 (3H, s, NCH_3); 6.27 (2H, s, H2' and H6'); 7.38 (1H, d, *J* = 8.4 Hz, H7); 7.60 (1H, dd, *J* = 2.0 and 8.4 Hz, H6); 7.80 (1H, s, H2); 8.72 (1H, d, *J* = 2.0 Hz, H4); 10.01 (1H, s, CHO). **^{13}C-NMR** (100 MHz, $CDCl_3$): δ 13.8 (CH_3, Et); 33.8 (CH_3, NCH_3); 45.7 (CH_2, Et); 55.9 (2) (CH_3, OCH_3); 60.6 (CH_3, OCH_3); 106.3 (2) (CH, C2' and C6'); 109.6 (CH, C7); 118.4 (C, C3); 122.2 (CH, C4); 123.4 (CH, C6); 124.4 (C, C3a); 132.9 (C, C4'); 134.4 (C, C5); 137.5 (C, C1'); 139.1 (C, C7a); 140.3 (CH, C2); 152.8 (2) (C, C3' and C5'); 183.7 (CH, CHO). **HRMS** ($C_{21}H_{24}N_2NaO_6S^+$): calculated 455.1247 (M+Na^+), found 455.1210.

*(E)-3-(2-cyanovinyl)-N-ethyl-1-methyl-N-(3,4,5-trimethoxyphenyl)-1H-indole-5-sulfonamide (**94**).* Yellow solid. **IR** (KBr): 2207, 1619, 1592, 1125, 647 cm^{-1}. **^{1}H-NMR** (400 MHz, $CDCl_3$): δ 1.09 (3H, t, *J* = 7.2 Hz, Et); 3.53 (2H, q, *J* = 7.2 Hz, Et); 3.64 (6H, s, OCH_3); 3.85 (3H, s, OCH_3); 3.92 (3H, s, NCH_3); 5.66 (1H, d, *J* = 16.8 Hz, olefin); 6.22 (2H, s, H2' and H6'); 7.40 (1H, d, *J* = 8.8 Hz, H7); 7.44 (1H, d, *J* = 16.8 Hz, olefin); 7.45 (1H, s, H2); 7.59 (1H, dd, *J* = 1.6 and 8.8 Hz, H6); 8.04 (1H, d, *J* = 1.6 Hz, H4). **^{13}C-NMR** (100 MHz, $CDCl_3$): δ 14.1 (CH_3, Et); 33.6 (CH_3, NCH_3); 45.8 (CH_2, Et); 56.1 (2) (CH_3, OCH_3); 61.0 (CH_3, OCH_3); 91.9 (CH, olefin); 106.6 (2) (CH, C2' and C6'); 110.3 (CH, C7); 112.7 (C, C3); 119.0 (C, CN); 120.7 (CH, C4); 122.5 (CH, C6); 124.6 (C, C5); 131.4 (C, C3a); 134.4 (CH, C2); 134.5 (C, C4'); 137.9 (C, C1'); 139.5 (C, C7a); 142.0 (CH, olefin); 153.1 (2) (C, C3' and C5'). **HRMS** ($C_{23}H_{25}N_3NaO_5S^+$): calculated 478.1407 ($M+Na^+$), found 478.1405.

*(Z)-3-(2-cyanovinyl)-N-ethyl-1-methyl-N-(3,4,5-trimethoxyphenyl)-1H-indole-5-sulfonamide (**95**).* Yellow solid. **IR** (KBr): 2204, 1596, 1329, 1125, 652 cm^{-1}. **^{1}H-NMR** (400 MHz, $CDCl_3$): δ 1.09 (3H, t, *J* = 7.2 Hz, Et); 3.54 (2H, q, *J* = 7.2 Hz, Et); 3.64 (6H, s, OCH_3); 3.83 (3H, s, OCH_3); 3.92 (3H, s, NCH_3); 5.26 (1H, d, *J* = 12.0 Hz, olefin); 6.21 (2H, s, H2' and H6'); 7.34 (1H, d, *J* = 12.0 Hz, olefin); 7.42 (1H, d, *J* = 8.8 Hz, H7); 7.59 (1H, dd, *J* = 1.6 and 8.8 Hz, H6); 8.01 (1H, d, *J* = 1.6 Hz, H4); 8.31 (1H, s, H2). **^{13}C-NMR** (100 MHz, $CDCl_3$): δ 14.1 (CH_3, Et); 33.9 (CH_3, NCH_3); 45.8 (CH_2, Et); 56.1 (2) (CH_3, OCH_3); 61.0 (CH_3, OCH_3); 89.8 (CH, olefin); 106.6 (2) (CH, C2' and C6'); 110.1 (CH, C7); 111.8 (C, C3); 119.2 (C, CN); 119.4 (CH, C4); 122.3 (CH, C6); 126.8 (C, C5); 130.9 (C, C3a); 132.5 (CH, C2); 134.6 (C, C4'); 137.8 (C, C1'); 138.0 (C, C7a); 138.5 (CH, olefin); 153.1 (2) (C, C3' and C5'). **HRMS** ($C_{23}H_{25}N_3NaO_5S^+$): calculated 478.1407 ($M+Na^+$), found 478.1406.

Synthesis of 3-cyano-1-methyl-N-(3,4,5-trimethoxyphenyl)-1H-indole-5-sulfonamide (96)

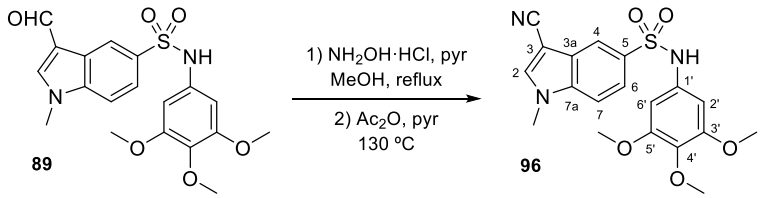

Following procedure **E**, a mixture of **89** (515 mg, 1.27 mmol), $NH_2OH{\cdot}HCl$ (902 mg, 13.0 mmol) and a few drops of pyridine in methanol (50 mL) was heated under reflux for 12 h yielding (*E*/*Z*)-3-((hydroxyimino)methyl)-1-methyl-*N*-(3,4,5-trimethoxyphenyl)-1*H*-indole-5-sulfonamide. The oximes were heated at 130 °C in pyridine (50 mL) with acetic anhydride (1 mL) and stirred for 72 h, yielding 574 mg of a complex mixture. Crystallization in methanol/acetone gave 74 mg (0.18 mmol, 14%) of **96**. Global yield 28%.

*3-Cyano-1-methyl-N-(3,4,5-trimethoxyphenyl)-1H-indole-5-sulfonamide (**96**).* White crystals. **Mp** (MeOH/acetone): 236.0-237.4 °C. **IR** (KBr): 3232, 2231, 1600, 1331, 1126 cm^{-1}. **^{1}H-NMR** (400 MHz, $CDCl_3$): δ 3.73 (6H, s, OCH_3); 3.76 (3H, s, OCH_3); 3.93 (3H, s, NCH_3); 6.32 (2H, s, H2' and H6'); 6.56 (1H, bs, NH); 7.43 (1H, d, *J* = 8.8 Hz, H7); 7.69 (1H, s, H2); 7.72 (1H, dd, *J* = 1.6 and 8.8 Hz, H6); 8.32 (1H, d, *J* = 1.6 Hz, H4). **^{13}C-NMR** (100 MHz, $CDCl_3$): δ 34.0 (CH_3, NCH_3); 56.2 (2) (CH_3, OCH_3); 60.9 (CH_3, OCH_3); 87.5 (C, C3); 99.4 (2) (CH, C2' and C6'); 111.0 (CH, C7); 114.3 (C, CN); 120.5 (CH, C4); 122.7 (CH, C6); 127.2 (C, C5); 132.2 (C, C3a); 133.0 (C, C4'); 135.8 (C, C1'); 137.7 (CH, C2); 137.8 (C, C7a); 153.5 (2) (C, C3' and C5'). **HRMS** ($C_{19}H_{19}N_3NaO_5S^+$): calculated 424.0938 ($M+Na^+$), found 424.0940.

Synthesis of 3-cyano-N,1-dimethyl-N-(3,4,5-trimethoxyphenyl)-1H-indole-5-sulfonamide (97)

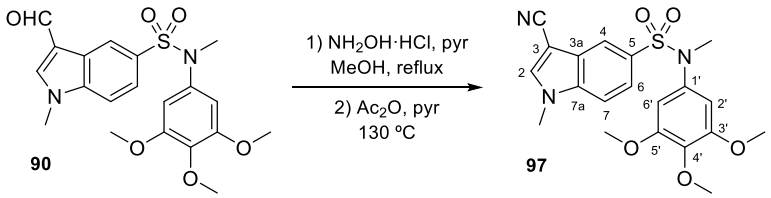

As described in method **E**, a solution of **90** (576 mg, 1.38 mmol) and $NH_2OH{\cdot}HCl$ (977 mg, 14.06 mmol) in methanol (25 mL) with a few drops of pyridine was heated under reflux for 24 h. The resulting mixture of oximes was heated at 130 °C in pyridine (50 mL) with acetic anhydride (0.5 mL) providing 380 mg after three days. Crystallization in CH_2Cl_2/Hex gave 289 mg (0.70 mmol, 51%) of **97**. Global yield 63%.

*3-Cyano-N,1-dimethyl-N-(3,4,5-trimethoxyphenyl)-1H-indole-5-sulfonamide (**97**).* Light brown crystals. **Mp** (CH_2Cl_2/Hex): 182.3-182.8 °C. **IR** (KBr): 2225, 1595, 1334, 1126, 654 cm^{-1}. **^{1}H-NMR** (400 MHz, $CDCl_3$): δ 3.16 (3H, s, SO_2NCH_3); 3.70 (6H, s, OCH_3); 3.84 (3H, s, OCH_3); 3.92 (3H, s, 1-NCH_3); 6.30 (2H, s, H2' and H6'); 7.43 (1H, d, *J* = 8.8 Hz, H7); 7.52 (1H, dd, *J* = 1.6 and 8.8 Hz, H6); 7.72 (1H, s, H2); 8.18 (1H, d, *J* = 1.6 Hz, H4). **^{13}C-NMR** (100 MHz, $CDCl_3$): δ 34.1 (CH_3, 1- NCH_3); 38.6 (CH_3, SO_2NCH_3); 56.2 (2) (CH_3, OCH_3); 60.9 (CH_3, OCH_3); 86.8 (C, C3); 104.6 (2) (CH, C2' and C6'); 110.8 (CH, C7); 114.5 (C, CN); 120.5 (CH, C4); 123.1 (CH, C6); 126.9 (C, C5); 130.3 (C, C4'); 137.2 (C, C3a); 137.5 (C, C1'); 137.7 (C, C7a); 138.2 (CH, C2); 153.0 (2) (C, C3' and C5'). **HRMS** ($C_{20}H_{21}N_3NaO_5S^+$): calculated 464.1094 ($M+Na^+$), found 464.1097.

Synthesis of 1-formyl-N-(2,3,4-trimethoxyphenyl)indoline-5-sulfonamide (98)

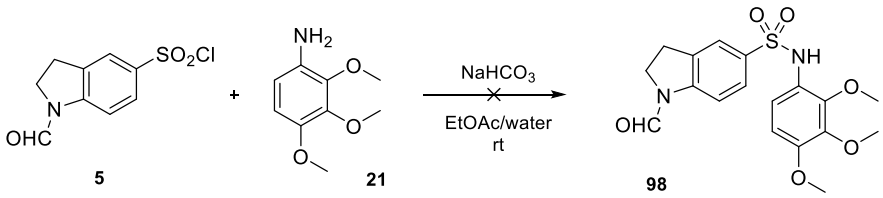

A mixture of **5** (326 mg, 1.33 mmol) and **21** (231 mg, 1.26 mmol) with 180 mg (2.14 mmol) of $NaHCO_3$ dissolved in 50 mL of EtOAc/water (1:1) was stirred for 4 h under N_2 atmosphere at room temperature. No transformation was observed.

Synthesis of 2,3,4-trimethoxy-N-(1-methyl-1H-indol-5-yl)benzenesulfonamide (99)

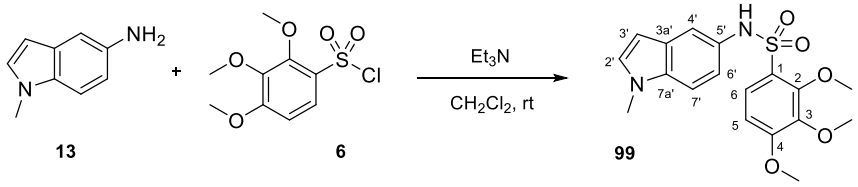

Excess sulfonyl chloride **6** was progressively added to a solution of **13** (170 mg, 1.16 mmol) in CH_2Cl_2 (25 mL) with a few drops of triethylamine under N_2. After 24 h, the reaction was poured onto ice and washed with brine. The organic layer was dried over anhydrous Na_2SO_4, filtered, and evaporated (325 mg). Silica gel flash chromatography (CH_2Cl_2) afforded 206 mg (0.55 mmol, 47%) of **99**.

*2,3,4-Trimethoxy-N-(1-methyl-1H-indol-5-yl)benzenesulfonamide (**99**).* Pink solid. **IR** (KBr): 3278, 2942, 1583, 1090 cm^{-1}. **^{1}H-NMR** (400 MHz, $CDCl_3$): δ 3.69 (3H, s, NCH_3); 3.81 (3H, s, 2-OCH_3*); 3.91 (3H, s, 3-OCH_3); 4.15 (3H, s, 4-OCH_3*); 6.34 (1H, d, *J* = 3.2 Hz, H3'); 6.51 (1H, d, *J* = 8.8 Hz, H5); 6.88 (1H, bs, NH); 6.99 (1H, d, *J* = 3.2 Hz, H2'); 7.00 (1H, dd, *J* = 2.0 and 8.8 Hz, H6'); 7.11 (1H, d, *J* = 8.8 Hz, H7'); 7.33 (1H, d, *J* = 2.0 Hz, H4'); 7.34 (1H, d, *J* = 8.8 Hz, H6). **^{13}C-NMR** (100 MHz, $CDCl_3$): δ 32.9 (CH_3, NCH_3); 56.1 (CH_3, 2-OCH_3*); 61.0 (CH_3, 3-OCH_3); 62.2 (CH_3, 4-OCH_3*); 100.9 (CH, C3'); 106.5 (CH, C5); 109.5 (CH, C7'); 115.9 (CH, C4'); 118.4 (CH, C6'); 124.3 (C, C1); 125.5 (CH, C6); 128.4 (C, C3a'); 128.6 (C, C5'); 129.8 (CH, C2'); 135.1 (C, C7a'); 142.4 (C, C3); 150.7 (C, C4*); 157.8 (C, C2*). *Interchangeable signals. **HRMS** ($C_{18}H_{20}N_2NaO_5S^+$): calculated 399.0985 ($M+Na^+$), found 399.0971.

Synthesis of 2,3,4-trimethoxy-N-methyl-N-(1-methyl-1H-indol-5-yl)benzenesulfonamide (100)

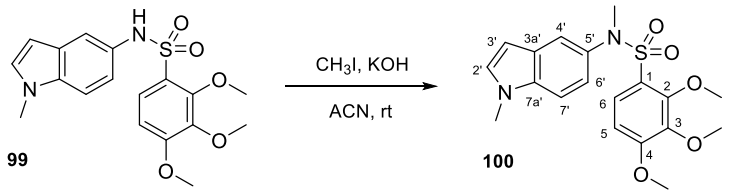

Methylation of compound **99** was carried out following method **C1**: methyl iodide (30 µL, 0.48 mmol) was added to **99** (90 mg, 0.24 mmol) in 5 mL of ACN with ground KOH and stirred for 3 h to give **100** (90 mg, 0.28 mmol, 97%). Flash chromatography in CH_2Cl_2 yielded 80 mg (0.21 mmol, 86%) of **99** as an oil.

*2,3,4-Trimethoxy-N-methyl-N-(1-methyl-1H-indol-5-yl)benzenesulfonamide (**100**).* Orange oil. **IR** (film): 2942, 1582, 1488, 1092 cm^{-1}. **^{1}H-NMR** (400 MHz, $CDCl_3$): δ 3.44 (3H, s, NCH_3SO_2); 3.72 (3H, s, 1'-NCH_3); 3.84 (3H, s, 2-OCH_3*); 3.92 (3H, s, 3-OCH_3); 4.03 (3H, s, 4-OCH_3*); 6.36 (1H, d, *J* = 3.2 Hz, H3'); 6.50 (1H, d, *J* = 8.8 Hz, H5); 7.01 (1H, d, *J* = 3.2 Hz, H2'); 7.04 (1H, dd, *J* = 2.0 and 8.8 Hz, H6'); 7.16 (1H, d, *J* = 8.8 Hz, H7'); 7.30 (1H, d, *J* = 8.8 Hz, H6); 7.40 (1H, d, *J* = 2.0 Hz, H4'). **^{13}C-NMR** (100 MHz, $CDCl_3$): δ 32.7 (CH_3, 1'-NCH_3); 40.1 (CH_3, NCH_3SO_2); 55.8 (CH_3, 2-OCH_3*); 60.7 (CH_3, 3-OCH_3); 61.4 (CH_3, 4-OCH_3*); 101.0 (CH, C3'); 105.9 (CH, C5); 109.2 (CH, C7'); 119.8 (CH, C4'); 121.1 (CH, C6'); 125.1 (C, C1); 126.3 (CH, C6); 128.2 (C, C3a'); 129.6 (CH, C2'); 133.1 (C, C5'); 135.3 (C, C7a'); 142.4 (C, C3); 151.5 (C, C4*); 157.2 (C, C2*). *Interchangeable signals. **HRMS** ($C_{19}H_{22}N_2NaO_5S^+$): calculated 413.1142 ($M+Na^+$), found 413.1148.

Synthesis of N-(3,5-dimethoxyphenyl)-1-formylindoline-5-sulfonamide (101)

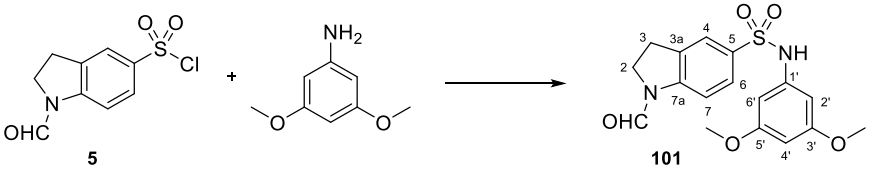

Procedure 1: The mixture of **5** (1490 mg, 6.07 mmol) and 3,5-dimethoxyaniline (837 mg, 5.47 mmol) was dissolved in 50 mL of EtOAc/water 1:1 in the presence of 715 mg (8.51 mmol) of $NaHCO_3$. After 14 h at room temperature under N_2, the reaction mixture was diluted with 25 mL of MTBE and vigorously stirred for 3 h.[210] The resulting precipitate was filtered off, washed with water and MTBE yielding 970 mg (2.68 mmol, 49%) of **101** as a white solid. The organic layer was washed with 2N HCl and brine, dried over anhydrous Na_2SO_4, filtered, and evaporated, providing 596 mg of a solid (**101** and **5**). Global yield: 1525 mg, 4.21 mmol, 77%.

Procedure 2: A solution of 1-formylindoline-5-sulfonyl chloride (**5**, 1952 mg, 7.95 mmol) and 3,5-dimethoxyaniline (1215 mg, 7.94 mmol) in CH_2Cl_2 (50 mL) with pyridine (1 mL) was stirred at room temperature for 14 h in N_2, and additional sulfonyl chloride was subsequently added (329 mg, 1.34 mmol). After 5 h, it was poured onto ice and washed with 2N HCl and brine until neutrality. The organic layer was dried over anhydrous Na_2SO_4, filtered, and evaporated to obtain **101** (2609 mg, 7.21 mmol, 91%).

*N-(3,5-dimethoxyphenyl)-1-formylindoline-5-sulfonamide (**101**).* White solid. **IR** (KBr): 3202, 2957, 1660, 1584, 1328, 1145, 711 cm^{-1}. **^{1}H-NMR** (400 MHz, $CDCl_3$): δ (*E*) 3.16 (2H, t, *J* = 8.8 Hz, H3); 3.72 (6H, s, OCH_3); 4.10 (2H, t, *J* = 8.8 Hz, H2); 6.19 (1H, t, *J* = 2.4 Hz, H4'); 6.26 (2H, d, *J* = 2.4 Hz, H2' and H6'); 6.73 (1H, bs, NH); 7.17 (1H, d, *J* = 8.8 Hz, H7); 7.67 (2H, m, H4 and H6); 8.95 (1H, s, CHO). (*Z*) 3.19 (2H, t, *J* = 8.8 Hz, H3); 3.72 (6H, s, OCH_3); 4.18 (2H, t, *J* = 8.8 Hz, H2); 6.19 (1H, t, *J* = 2.4 Hz, H4'); 6.26 (2H, d, *J* = 2.4 Hz, H2' and H6'); 6.73 (1H, bs, NH); 7.67 (2H, m, H4 and H6); 8.10 (1H, d, *J* = 8.8 Hz, H7); 8.53 (1H, s, CHO). **^{13}C-NMR** (100 MHz, acetone-D6): δ (*E*) 26.4 (CH_2, C3); 44.8 (CH_2, C2); 55.7 (2) (CH_3, OCH_3); 95.6 (CH, C4'); 98.1 (2) (CH, C2' and C6'); 109.3 (CH, C7); 124.9 (CH, C4); 127.7 (CH, C6); 133.3 (C, C5); 134.5 (C, C3a); 139.8 (C, C1'); 145.7 (C, C7a); 158.1 (CH, CHO); 161.4 (2) (C, C3' and C5'). (*Z*) 27.0 (CH_2, C3); 47.0 (CH_2, C2); 55.7 (2) (CH_3, OCH_3); 95.6 (CH, C4'); 98.1 (2) (CH, C2' and C6'); 115.2 (CH, C7); 124.1 (CH, C4); 127.5 (CH, C6); 133.9 (C, C5); 134.7 (C, C3a); 139.7 (C, C1'); 145.4 (C, C7a); 160.4 (CH, CHO); 161.4 (2) (C, C3' and C5').

Synthesis of N-(3,5-dimethoxyphenyl)-1-methylindoline-5-sulfonamide (102)

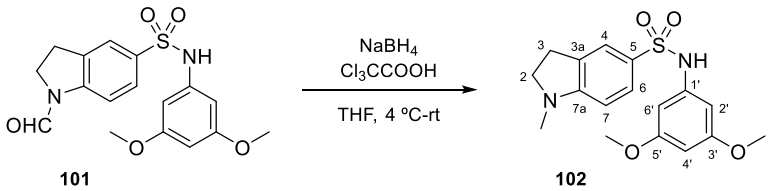

$NaBH_4$ (438 mg, 11.58 mmol) and trichloroacetic acid (1857 mg, 11.36 mmol) were added to a solution of 2702 mg (7.46 mmol) of **101** in 100 mL of dry THF at 4 °C. The reaction was warmed to room temperature and after 4 h under N_2 atmosphere, it was diluted with 300 mL of water and vigorously stirred until precipitation.[210] The suspension was filtered and the solid washed with water and MTBE, yielding 2282 mg (6.56 mmol, 88%) of **102**.

*N-(3,5-dimethoxyphenyl)-1-methylindoline-5-sulfonamide (**102**).* White powder. **IR** (KBr): 3241, 2838, 1601, 1306, 1134 cm^{-1}. **^{1}H-NMR** (400 MHz, $CDCl_3$): δ 2.79 (3H, s, NCH_3); 2.95 (2H, t, *J* = 8.4 Hz, H3); 3.47 (2H, t, *J* = 8.4 Hz, H2); 3.71 (6H, s, OCH_3); 6.15 (1H, t, *J* = 2.4 Hz, H4'); 6.24 (2H, d, *J* = 2.4 Hz, H2' and H6'); 6.27 (1H, d, *J* = 8.0 Hz, H7); 6.56 (1H, bs, NH); 7.39 (1H, d, *J* = 2.0 Hz, H4); 7.55 (1H, dd, *J* = 2.0 and 8.0 Hz, H6). **^{13}C-NMR** (100 MHz, $CDCl_3$): δ 27.7 (CH_2, C3); 34.2 (CH_3, NCH_3); 55.0 (CH_2, C2); 55.4 (2) (CH_3, OCH_3); 96.5 (CH, C4'); 98.3 (2) (CH, C2' and C6'); 104.4 (CH, C7); 123.2 (CH, C4); 125.1 (C, C3a); 129.3 (CH, C6); 130.3 (C, C5); 139.2 (C, C1'); 156.6 (C, C7a); 161.1 (2) (C, C3' and C5').

Synthesis of N-(3,5-dimethoxyphenyl)-1-methyl-1H-indole-5-sulfonamide (103)

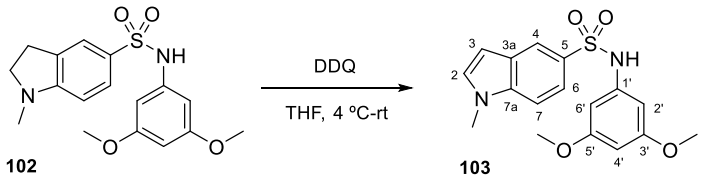

DDQ (1274 mg, 5.61 mmol) was added to compound **102** (1851 mg, 5.32 mmol) dissolved in 50 mL of dry THF at 4 °C. After the addition, it was warmed to room temperature and stirred for 24 h under N_2. The reaction mixture was concentrated until around 25 mL final volume, diluted once with MTBE and stirred at 4 °C.[210] The following day, it was filtered off and the precipitate washed with MTBE, yielding 1440 mg (4.16 mmol, 78%) of **103**.

*N-(3,5-dimethoxyphenyl)-1-methyl-1H-indole-5-sulfonamide (**103**).* Brown crystals. **Mp** (ACN/MTBE): 186-187 °C. **IR** (KBr): 3241, 2948, 1598, 1312, 1140, 726 cm^{-1}. **^{1}H-NMR** (400 MHz, $CDCl_3$): δ 3.69 (6H, s, OCH_3); 3.81 (3H, s, NCH_3); 6.14 (1H, t, *J* = 2.0 Hz, H4'); 6.24 (2H, d, *J* = 2.0 Hz, H2' and H6'); 6.43 (1H, bs, NH); 6.57 (1H, d, *J* = 3.2 Hz, H3); 7.15 (1H, d, *J* = 3.2 Hz, H2); 7.33 (1H, d, *J* = 8.4 Hz, H7); 7.63 (1H, dd, *J* = 2.0 and 8.4 Hz, H6); 8.17 (1H, d, *J* = 2.0 Hz, H4). **^{13}C-NMR** (100 MHz, $CDCl_3$): δ 32.8 (CH_3, NCH_3); 55.0 (2) (CH_3, OCH_3); 96.4 (CH, C4'); 98.3 (2) (CH, C2' and C6'); 102.5 (CH, C3); 109.4 (CH, C7); 119.8 (CH, C6); 121.6 (CH, C4); 127.4 (C, C3a); 129.1 (C, C5); 130.8 (CH, C2); 138.1 (C, C7a); 138.6 (C, C1'); 160.7 (2) (C, C3' and C5'). **HRMS** ($C_{17}H_{18}N_2NaO_4S^+$): calculated 369.0879 ($M+Na^+$), found 369.0878.

Synthesis of N-(3,5-dimethoxyphenyl)-N,1-dimethyl-1H-indole-5-sulfonamide (104)

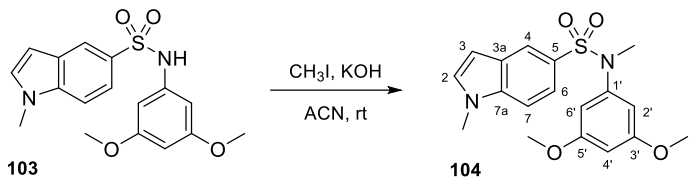

Following procedure **C1**, a mixture of **103** (399 mg, 1.15 mmol) in ACN (25 mL) with excess powdered KOH and methyl iodide (143 µL, 2.30 mmol) gave 378 mg (1.05 mmol, 91%) of **104** after 19 h. Flash chromatography using toluene/EtOAc 9:1 as eluent provided (355 mg, 0.99 mmol, 86%) of **104**.

*N-(3,5-dimethoxyphenyl)-N,1-dimethyl-1H-indole-5-sulfonamide (**104**).* White solid. **IR** (KBr): 2836, 1609, 1330, 1156, 642 cm^{-1}. **^{1}H-NMR** (400 MHz, $CDCl_3$): δ 3.11 (3H, s, SO_2NCH_3); 3.69 (6H, s, OCH_3); 3.82 (3H, s, 1-NCH_3); 6.27 (2H, d, *J* = 2.0 Hz, H2' and H6'); 6.34 (1H, t, *J* = 2.0 Hz, H4'); 6.56 (1H, d, *J* = 3.2 Hz, H3); 7.15 (1H, d, *J* = 3.2 Hz, H2); 7.31 (1H, d, *J* = 8.4 Hz, H7); 7.39 (1H, dd, *J* = 1.6 and 8.4 Hz, H6); 7.97 (1H, d, *J* = 1.6 Hz, H4). **^{13}C-NMR** (100 MHz, $CDCl_3$): δ 33.0 (CH_3, 1-NCH_3); 38.2 (CH_3, SO_2NCH_3); 55.3 (2) (CH_3, OCH_3); 99.3 (CH, C4'); 102.5 (CH, C3); 104.9 (2) (CH, C2' and C6'); 109.3 (CH, C7); 120.7 (CH, C6); 122.1 (CH, C4); 126.8 (C, C3a); 127.5 (C, C5); 131.3 (CH, C2); 138.4 (C, C7a); 143.9 (C, C1'); 160.5 (2) (C, C3' and C5'). **HRMS** ($C_{18}H_{20}N_2NaO_4S^+$): calculated 383.1036 ($M+Na^+$), found 383.1026.

Synthesis of N-(3,5-dimethoxyphenyl)-N-ethyl-1-methyl-1H-indole-5-sulfonamide (105)

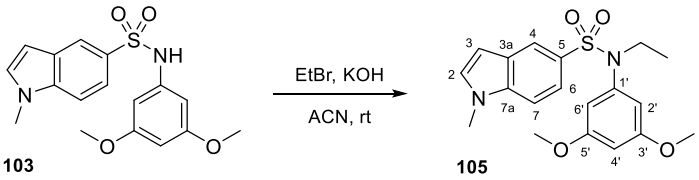

As described in method **C1**, ethyl bromide (67 µL, 0.90 mmol) was added to a solution of **103** (156 mg, 0.45 mmol) in ACN (15 mL) with excess KOH in powder. The reaction was stirred for 8 days yielding **105** (134 mg, 0.36 mmol, 79%). Crystallization in methanol gave 73 mg (0.20 mmol, 43%) of **105**.

*N-(3,5-dimethoxyphenyl)-N-ethyl-1-methyl-1H-indole-5-sulfonamide (**105**).* Yellow crystals. **Mp** (MeOH): 119-120 °C. **IR** (KBr): 2968, 1608, 1335, 1159, 643 cm^{-1}. **^{1}H-NMR** (400 MHz, $CDCl_3$): δ 1.06 (3H, t, *J* = 7.2 Hz, CH_3); 3.54 (2H, q, *J* = 7.2 Hz, CH_2); 3.68 (6H, s, OCH_3); 3.84 (3H, s, NCH_3); 6.21 (2H, d, *J* = 2.4 Hz, H2' and H6'); 6.38 (1H, t, *J* = 2.4 Hz, H4'); 6.57 (1H, d, *J* = 3.2 Hz, H3); 7.16 (1H, d, *J* = 3.2 Hz, H2); 7.33 (1H, d, *J* = 8.8 Hz, H7); 7.48 (1H, dd, *J* = 2.0 and 8.8 Hz, H6); 8.01 (1H, d, *J* = 2.0 Hz, H4). **^{13}C-NMR** (100 MHz, $CDCl_3$): δ 14.0 (CH_3, Et); 33.1 (CH_3, NCH_3); 45.5 (CH_2); 55.4 (2) (CH_3, OCH_3); 100.2 (CH, C4'); 102.7 (CH, C3); 107.2 (2) (CH, C2' and C6'); 109.1 (CH, C7); 120.8 (CH, C6); 122.1 (CH, C4); 127.6 (C, C3a); 129.0 (C, C5); 131.0 (CH, C2); 138.3 (C, C7a); 141.2 (C, C1'); 160.5 (2) (C, C3' and C5'). **HRMS** ($C_{19}H_{22}N_2NaO_4S^+$): calculated 397.1192 ($M+Na^+$), found 397.1182.

Synthesis of ethyl N-(3,5-dimethoxyphenyl)-N-((1-methyl-1H-indol-5-yl)sulfonyl)glycinate (106)

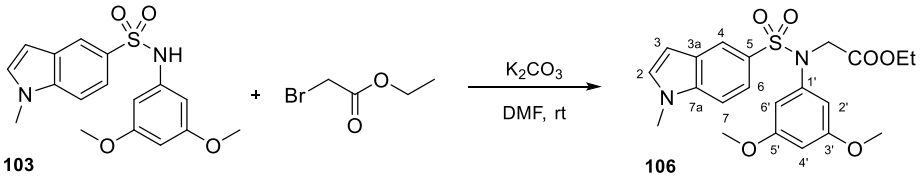

As described in method **C2**, ethyl bromoacetate (68 µL, 0.61 mmol) was added to **103** (107 mg, 0.31 mmol) in dry DMF (1 mL) with excess K_2CO_3, and the suspension was stirred for one week giving **106** (126 mg, 0.29 mmol, 94%). Crystallization in methanol/CH_2Cl_2 gave 89 mg (0.21 mmol, 66%) of **106**.

*Ethyl N-(3,5-dimethoxyphenyl)-N-((1-methyl-1H-indol-5-yl)sulfonyl)glycinate (**106**).* Yellow crystals. **Mp** (MeOH/CH_2Cl_2): 111-112 °C. **IR** (KBr): 1748, 1607, 1326, 1150, 640 cm^{-1}. **^{1}H-NMR** (400 MHz, $CDCl_3$): δ 1.21 (3H, t, *J* = 7.2 Hz, CH_3); 3.65 (6H, s, OCH_3); 3.83 (3H, s, NCH_3); 4.14 (2H, q, *J* = 7.2 Hz, CH_2); 4.36 (2H, s, CH_2); 6.33 (1H, t, *J* = 2.4 Hz, H4'); 6.35 (2H, d, *J* = 2.4 Hz, H2' and H6'); 6.56 (1H, d, *J* = 3.2 Hz, H3); 7.15 (1H, d, *J* = 3.2 Hz, H2); 7.33 (1H, d, *J* = 8.8 Hz, H7); 7.55 (1H, dd, *J* = 2.0 and 8.8 Hz, H6); 8.06 (1H, d, *J* = 2.0 Hz, H4). **^{13}C-NMR** (100 MHz, $CDCl_3$): δ 13.2 (CH_3, Et); 32.2 (CH_3, NCH_3); 51.8 (CH_2, Et); 54.5 (2) (CH_3, OCH_3); 60.5 (CH_2); 99.5 (CH, C4'); 101.9 (CH, C3); 105.5 (2) (CH, C2' and C6'); 108.4 (CH, C7); 120.0 (CH, C6); 121.4 (CH, C4); 126.7 (C, C3a); 128.4 (C, C5); 130.2 (CH, C2); 137.6 (C, C7a); 141.2 (C, C1'); 159.7 (2) (C, C3' and C5'); 168.0 (C, CO). **HRMS** ($C_{21}H_{24}N_2NaO_6S^+$): calculated 455.1247 ($M+Na^+$), found 455.1246.

Synthesis of N-(cyanomethyl)-N-(3,5-dimethoxyphenyl)-1-methyl-1H-indole-5-sulfonamide (107)

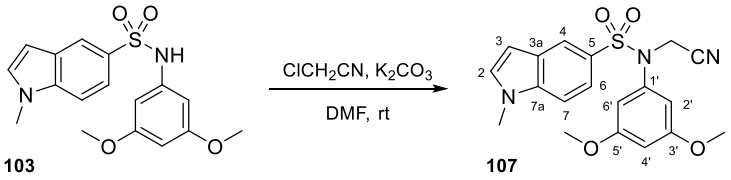

Chloroacetonitrile (35 µL, 0.55 mmol) was added to **103** (94 mg, 0.27 mmol) in dry DMF (1 mL) with K_2CO_3 as indicated in method **C2**. Compound **107** (87 mg, 0.23 mmol, 84%) was obtained after 15 h. It was then crystallized in methanol/CH_2Cl_2 (67 mg, 0.17 mmol, 64%).

*N-(cyanomethyl)-N-(3,5-dimethoxyphenyl)-1-methyl-1H-indole-5-sulfonamide (**107**).* Brown crystals. **Mp** (MeOH/CH_2Cl_2): 128-129 °C. **IR** (KBr): 1607, 1342, 1154, 645 cm^{-1}. **^{1}H-NMR** (400 MHz, $CDCl_3$): δ 3.67 (6H, s, OCH_3); 3.85 (3H, s, NCH_3); 4.54 (2H, s, CH_2); 6.33 (2H, d, *J* = 2.4 Hz, H2' and H6'); 6.42 (1H, t, *J* = 2.4 Hz, H4'); 6.59 (1H, d, *J* = 3.2 Hz, H3); 7.18 (1H, d, *J* = 3.2 Hz, H2); 7.39 (1H, d, *J* = 8.8 Hz, H7); 7.55 (1H, dd, *J* =

1.6 and 8.8 Hz, H6); 8.05 (1H, d, *J* = 1.6 Hz, H4). **^{13}C-NMR** (100 MHz, $CDCl_3$): δ 33.2 (CH_3, NCH_3); 39.5 (CH_2); 55.4 (2) (CH_3, OCH_3); 101.3 (CH, C4'); 102.9 (CH, C3); 106.2 (2) (CH, C2' and C6'); 109.6 (CH, C7); 115.1 (C, CN); 120.7 (CH, C6); 122.6 (CH, C4); 127.6 (C, C3a); 127.8 (C, C5); 131.5 (CH, C2); 138.8 (C, C7a); 140.5 (C, C1'); 161.0 (2) (C, C3' and C5'). **HRMS** ($C_{19}H_{19}N_3NaO_4S^+$): calculated 408.0988 (M+Na^+), found 408.0977.

Synthesis of N-(2-cyanoethyl)-N-(3,5-dimethoxyphenyl)-1-methyl-1H-indole-5-sulfonamide (108)

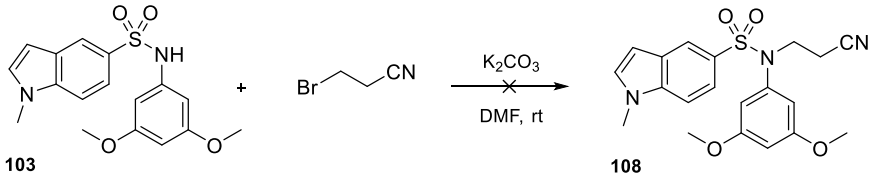

A mixture of **103** (74 mg, 0.21 mmol) and K_2CO_3 in excess in 1 mL of dry DMF was stirred for 1 h at room temperature prior to the addition of 3-bromopropanenitrile (36 µL, 0.43 mmol). 4 days later, the solvent was evaporated, CH_2Cl_2 was added, washed with brine, dried over anhydrous Na_2SO_4, filtered, and concentrated to dryness. The starting material was recovered (63 mg, 0.18 mmol).

Synthesis of N-benzyl-N-(3,5-dimethoxyphenyl)-1-methyl-1H-indole-5-sulfonamide (109)

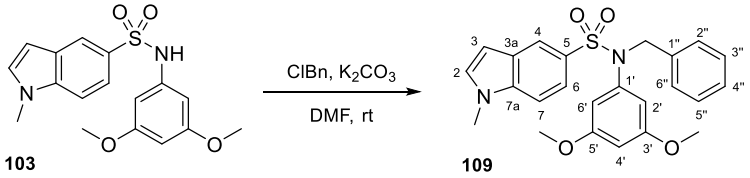

Following procedure **C2**, reaction between **103** (336 mg, 0.97 mmol) and benzyl chloride (224 µL, 1.95 mmol) in dry DMF (1 mL) with excess K_2CO_3 led to **109** (338 mg, 0.78 mmol, 80%) after four days. Crystallization in methanol/CH_2Cl_2 gave 218 mg (0.50 mmol, 52%) of **109**.

N-benzyl-N-(3,5-dimethoxyphenyl)-1-methyl-1H-indole-5-sulfonamide ***(109)***. Yellow crystals. **Mp** (MeOH/CH_2Cl_2): 124-125 °C. **IR** (KBr): 1595, 1332, 1152, 642 cm^{-1}. **^{1}H-NMR** (400 MHz, $CDCl_3$): δ 3.59 (6H, s, OCH_3); 3.86 (3H, s, NCH_3); 4.67 (2H, s, CH_2); 6.14 (2H, d, *J* = 2.0 Hz, H2' and H6'); 6.27 (1H, t, *J* = 2.0 Hz, H4'); 6.59 (1H, d, *J* = 2.8 Hz, H3); 7.18 (1H, d, *J* = 2.8 Hz, H2); 7.21 (5H, m, Ph); 7.37 (1H, d, *J* = 8.8 Hz, H7); 7.53 (1H, dd, *J* = 1.6 and 8.8 Hz, H6); 8.07 (1H, d, *J* = 1.6 Hz, H4). **^{13}C-NMR** (100 MHz, $CDCl_3$): δ 33.1 (CH_3, NCH_3); 54.7 (CH_2); 55.3 (2) (CH_3, OCH_3); 100.1 (CH, C4'); 102.8 (CH, C3); 107.2 (2) (CH, C2' and C6'); 109.3 (CH, C7); 120.8 (CH, C6); 122.2 (CH, C4); 127.4 (CH, C4''); 127.7 (C, C3a); 128.3 (2) (CH, C2'' and C6''); 128.5 (2) (CH, C3'' and C5''); 129.2 (C, C5); 131.1 (CH, C2); 136.3 (C, C7a); 138.4 (C, C1'); 141.3 (C, C1''); 160.4 (2) (C, C3' and C5'). **HRMS** ($C_{24}H_{24}N_2NaO_4S^+$): calculated 459.1349 (M+Na^+), found 459.1337.

Synthesis of N-(3,5-dimethoxyphenyl)-N-(4-fluorobenzyl)-1-methyl-1H-indole-5-sulfonamide (110)

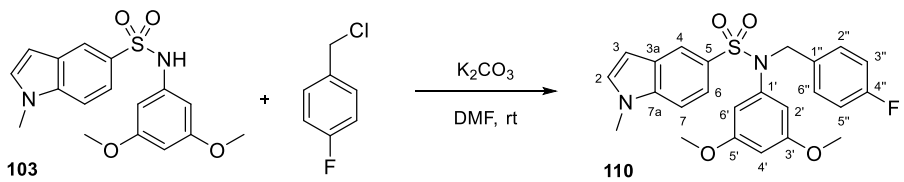

As indicated in method **C2**, 4-fluorobenzyl chloride (71 µL, 0.58 mmol) was added to a solution of **103** (85 mg, 0.25 mmol) in dry DMF (1 mL) with excess K_2CO_3 and stirred for two days yielding 100 mg. Preparative TLC using EtOAc/Hex (8:2) as eluent gave 94 mg (0.21 mmol, 85%) of **110**.

*N-(3,5-dimethoxyphenyl)-N-(4-fluorobenzyl)-1-methyl-1H-indole-5-sulfonamide (**110**).* Yellow solid. **IR** (KBr): 1607, 1150, 1060, 645 cm^{-1}. **^{1}H-NMR** (400 MHz, $CDCl_3$): δ 3.60 (6H, s, OCH_3); 3.84 (3H, s, NCH_3); 4.63 (2H, s, CH_2); 6.12 (2H, d, *J* = 2.4 Hz, H2' and H6'); 6.29 (1H, t, *J* = 2.4 Hz, H4'); 6.59 (1H, d, *J* = 3.2 Hz, H3); 6.90 (2H, t, *J* = 8.4 Hz, H3'' and H5''); 7.20 (1H, d, *J* = 3.2 Hz, H2); 7.22 (2H, dd, *J* = 5.2 and 8.4 Hz, H2'' and H6''); 7.36 (1H, d, *J* = 8.8 Hz, H7); 7.51 (1H, dd, *J* = 1.6 and 8.8 Hz, H6); 8.06 (1H, d, *J* = 1.6 Hz, H4). **^{13}C-NMR** (100 MHz, $CDCl_3$): δ 33.1 (CH_3, NCH_3); 54.0 (CH_2); 55.3 (2) (CH_3, OCH_3); 100.1 (CH, C4'); 102.7 (CH, C3); 107.2 (2) (CH, C2' and C6'); 109.4 (CH, C7); 115.2 (2) (CH, d, *J* = 21.4 Hz, C3'' and C5''); 120.7 (CH, C6); 122.1 (CH, C4); 127.7 (C, C3a); 129.0 (C, C5); 130.2 (2) (CH, d, *J* = 8.0 Hz, C2'' and C6''); 131.2 (CH, C2); 132.1 (C, C1''); 138.4 (C, C7a); 141.1 (C, C1'); 160.4 (2) (C, C3' and C5'); 162.2 (C, d, *J* = 244.4 Hz, C4''). **HRMS** ($C_{24}H_{24}FN_2O_4S^+$): calculated 455.1435 ($M+H^+$), found 455.1418.

Synthesis of N-(3,5-dimethoxyphenyl)-1-methyl-N-(4-nitrobenzyl)-1H-indole-5-sulfonamide (111)

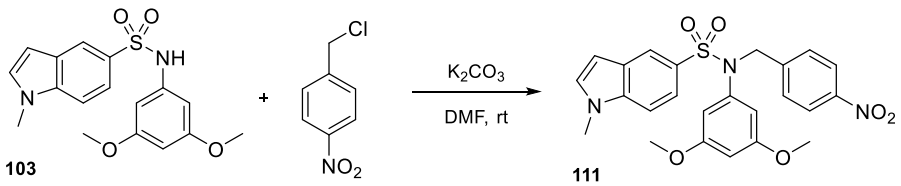

1-(Chloromethyl)-4-nitrobenzene (92 mg, 0.54 mmol) was added to compound **103** (88 mg, 0.25 mmol) in 1 mL of dry DMF with excess K_2CO_3. The mixture was stirred under N_2 at room temperature for one week, evaporated, dissolved in CH_2Cl_2, and washed with brine. The organic layer was dried over anhydrous Na_2SO_4, filtered, and rotary evaporated (124 mg). Preparative TLC (toluene/EtOAc 8:2) gave 98 mg of a complex mixture.

Synthesis of 5-(N-(3,5-dimethoxyphenyl)sulfamoyl)-1-methyl-1H-indole-3-carboxamide (112)

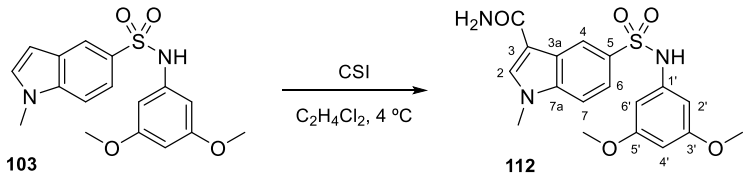

CSI (47 µL, 0.53 mmol) was added dropwise to **103** (123 mg, 0.36 mmol) in 1,2-dichloroethane (15 mL) at 4 °C, and warmed to room temperature under N_2.[517] After 24 h, the reaction mixture was rotary evaporated. Crystallization in methanol yielded amide **112** (80 mg, 0.21 mmol, 58%).

*5-(N-(3,5-dimethoxyphenyl)sulfamoyl)-1-methyl-1H-indole-3-carboxamide (**112**).* Red crystals. **Mp** (MeOH): 229-231 °C. **IR** (KBr): 3381, 1641, 1609, 1322, 1145, 657 cm^{-1}. **^{1}H-NMR** (400 MHz, DMSO-D6): δ 3.58 (6H, s, OCH_3); 3.80 (3H, s, NCH_3); 6.04 (1H, bs, H4'); 6.25 (2H, bs, H2' and H6'); 7.59 (2H, m, H6 and H7); 8.09 (1H, s, H2); 8.71 (1H, bs, H4); 10.20 (1H, bs, NH). **^{13}C-NMR** (100 MHz, DMSO-D6): δ 33.7 (CH_3, NCH_3); 55.5 (2) (CH_3, OCH_3); 95.3 (CH, C4'); 97.6 (2) (CH, C2' and C6'); 111.0 (C, C3); 111.5 (CH, C7); 120.6 (CH, C6); 122.1 (CH, C4); 126.4 (C, C3a); 132.0 (C, C5); 134.8 (CH, C2); 138.7 (C, C1'); 140.4 (C, C7a); 161.0 (2) (C, C3' and C5'); 165.9 (C, CO). **HRMS** ($C_{18}H_{19}N_3NaO_5S^+$): calculated 412.0938 ($M+Na^+$), found 412.0943.

Synthesis of 5-(N-(3,5-dimethoxyphenyl)-N-methylsulfamoyl)-1-methyl-1H-indole-3-carboxamide (113)

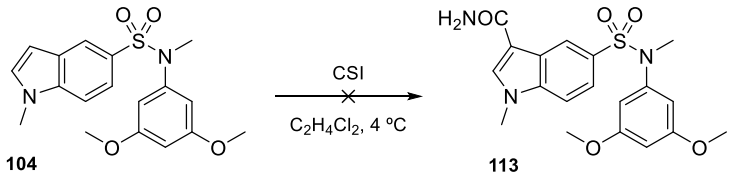

CSI (24 µL, 0.28 mmol) was added to a solution of **104** (66 mg, 0.18 mmol) in 15 mL of 1,2-dichloroethane at 4 °C.[517] The reaction was stirred under N_2 atmosphere for 3 h, then poured onto ice and washed with brine. The organic layer was dried over anhydrous Na_2SO_4, filtered, and evaporated, obtaining 41 mg of **104** and another unidentified product.

Synthesis of N-(3,5-dimethoxyphenyl)-3-formyl-1-methyl-1H-indole-5-sulfonamide (114)

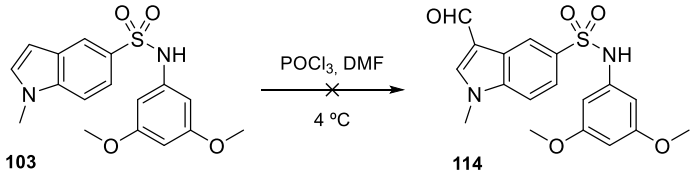

As described in general procedure **D**, the mixture of $POCl_3$ (238 µL, 2.60 mmol) and 0.4 mL of dry DMF was stirred at 4 °C under N_2 for one hour, then added dropwise to a cold solution of compound **103** (152 mg, 0.44 mmol) dissolved in 1 mL of dry DMF. 3 h later, the reaction mixture was poured into cold water with sodium acetate and kept overnight at 4 °C. Precipitation did not occur and nothing was recovered when extracted with organic solvents.

Synthesis of N-(3,5-dimethoxyphenyl)-3-formyl-N,1-dimethyl-1H-indole-5-sulfonamide (115)

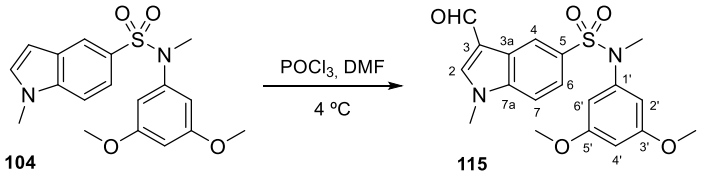

Following procedure **D**, $POCl_3$ (476 µL, 5.20 mmol) in dry DMF (0.5 mL) at 4 °C was stirred for 30 min and poured into a solution of indole **104** (312 mg, 0.87 mmol) in 0.5 mL of cold DMF, processed as described after 1 h. The resulting powder was filtered off to obtain **115** (276 mg, 0.71 mmol, 82%), then crystallized in MeOH/CH_2Cl_2 (195 mg, 0.50 mmol, 58%).

*N-(3,5-dimethoxyphenyl)-3-formyl-N,1-dimethyl-1H-indole-5-sulfonamide (**115**).* Yellow crystals. **Mp** (methanol/CH_2Cl_2): 194-195 °C. **IR** (KBr): 1663, 1610, 1333, 1157, 634 cm^{-1}. **^{1}H-NMR** (400 MHz, $CDCl_3$): δ 3.16 (3H, s, SO_2NCH_3); 3.71 (6H, s, OCH_3); 3.92 (3H, s, 1-NCH_3); 6.27 (2H, d, *J* = 2.0 Hz, H2' and H6'); 6.35 (1H, t, *J* = 2.0 Hz, H4'); 7.35 (1H, d, *J* = 8.4 Hz, H7); 7.46 (1H, dd, *J* = 2.0 and 8.4 Hz, H6); 7.79 (1H, s, H2); 8.67 (1H, d, *J* = 2.0 Hz, H4), 10.00 (1H, s, CHO). **^{13}C-NMR** (100 MHz, $CDCl_3$): δ 34.0 (CH_3, 1-NCH_3); 38.3 (CH_3, SO_2NCH_3); 55.4 (2) (CH_3, OCH_3); 99.4 (CH, C4'); 104.9 (2) (CH, C2' and C6'); 110.0 (CH, C7); 118.5 (C, C3); 122.6 (CH, C6); 123.3 (CH, C4); 124.5 (C, C3a); 131.0 (C, C5); 139.5 (C, C7a); 140.5 (CH, C2); 143.5 (C, C1'); 160.6 (2) (C, C3' and C5'); 184.0 (CH, CHO). **HRMS** ($C_{19}H_{20}N_2NaO_5S^+$): calculated 411.0985 ($M+Na^+$), found 411.0977.

Synthesis of N-benzyl-N-(3,5-dimethoxyphenyl)-3-formyl-1-methyl-1H-indole-5-sulfonamide (116)

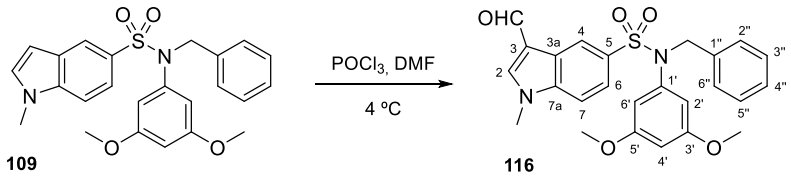

Following Vilsmeier-Haack procedure (method **D**), a mixture of $POCl_3$ (500 µL, 5.46) and dry DMF (0.5 mL) at 4 °C was stirred for half an hour under N_2, and subsequently added dropwise to a solution of **109** (353 mg, 0.81 mmol) in ice-cold DMF (0.5 mL) and stirred for 1 h. The powder was filtered off to obtain **116** (362 mg, 0.78 mmol, 97%). Crystallization in $MeOH/CH_2Cl_2$ gave 222 mg (0.48 mmol, 59%) of **116**.

*N-benzyl-N-(3,5-dimethoxyphenyl)-3-formyl-1-methyl-1H-indole-5-sulfonamide (**116**).* Yellow crystals. **Mp** ($MeOH/CH_2Cl_2$): 162-163 °C. **IR** (KBr): 1662, 1605, 1330, 1163, 697 cm^{-1}. **^{1}H-NMR** (400 MHz, $CDCl_3$): δ 3.61 (6H, s, OCH_3); 3.94 (3H, s, NCH_3); 4.72 (2H, s, CH_2); 6.14 (2H, d, *J* = 2.4 Hz, H2' and H6'); 6.27 (1H, t, *J* = 2.4 Hz, H4'); 7.22 (5H, m, Ph); 7.40 (1H, d, *J* = 8.8 Hz, H7); 7.61 (1H, dd, *J* = 2.0 and 8.8 Hz, H6); 7.82 (1H, s, H2); 8.77 (1H, d, *J* = 2.0 Hz, H4); 10.02 (1H, s, CHO). **^{13}C-NMR** (100 MHz, $CDCl_3$): δ 34.0 (CH_3, NCH_3); 54.9 (CH_2); 55.3 (2) (CH_3, OCH_3); 100.1 (CH, C4'); 107.2 (2) (CH, C2' and C6'); 110.1 (CH, C7); 118.7 (C, C3); 122.4 (CH, C6); 123.4 (CH, C4); 124.8 (C, C3a); 127.5 (CH, C4''); 128.3 (2) (CH, C2'' and C6''); 128.5 (2) (CH, C3'' and C5''); 133.3 (C, C5); 136.1 (C, C7a); 139.5 (C, C1'); 140.3 (CH, C2); 140.9 (C, C1''); 160.4 (2) (C, C3' and C5'); 183.9 (CH, CHO). **HRMS** ($C_{25}H_{24}N_2NaO_5S^+$): calculated 487.1298 ($M+Na^+$), found 487.1297.

Synthesis of 3-cyano-N-(3,5-dimethoxyphenyl)-N,1-dimethyl-1H-indole-5-sulfonamide (117)

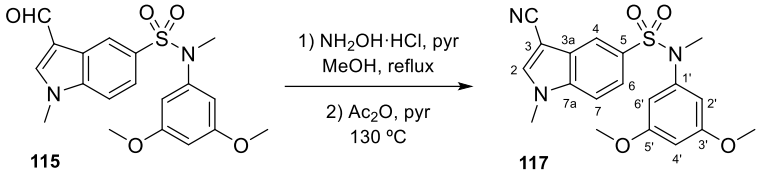

As detailed in method **E**, a mixture of **115** (185 mg, 0.48 mmol) and $NH_2OH{\cdot}HCl$ (339 mg, 4.88 mmol) in 25 mL of methanol with a few drops of pyridine was heated under reflux for 15 h. The resulting oximes were heated at 130 °C in pyridine (25 mL) with acetic anhydride (1 mL) for 4 days, yielding 167 mg. Crystallization ($MeOH/CH_2Cl_2$) followed by preparative thin layer chromatography (EtOAc/Hex 85:15) gave 44 mg (0.11 mmol, 24%) of **117**.

*3-Cyano-N-(3,5-dimethoxyphenyl)-N,1-dimethyl-1H-indole-5-sulfonamide (**117**).* Brown crystals. **Mp** ($MeOH/CH_2Cl_2$): 163-164 °C. **IR** (KBr): 2221, 1607, 1335, 1204, 657 cm^{-1}. **^{1}H-NMR** (400 MHz, $CDCl_3$): δ 3.14 (3H, s, SO_2NCH_3); 3.72 (6H, s, OCH_3); 3.90 (3H, s, 1-NCH_3); 6.24 (2H, d, *J* = 2.4 Hz, H2' and H6'); 6.36 (1H, t, *J* = 2.4 Hz, H4'); 7.40 (1H, d, *J* = 8.8 Hz, H7); 7.47 (1H, dd, *J* = 1.6 and 8.8 Hz, H6); 7.69 (1H, s, H2); 8.10 (1H, d, *J* = 1.6 Hz, H4). **^{13}C-NMR** (100 MHz, $CDCl_3$): δ 34.0 (CH_3, 1-NCH_3); 38.3 (CH_3, SO_2NCH_3); 55.5 (2) (CH_3, OCH_3); 87.3 (C, C3); 99.4 (CH, C4'); 105.0 (2) (CH, C2' and C6'); 110.7 (CH, C7); 114.5 (C, CN); 120.6 (CH, C6); 123.1 (CH, C4); 126.9 (C, C5); 130.5 (C, C3a); 137.7 (C, C7a); 137.8 (CH, C2); 143.3 (C, C1'); 160.6 (2) (C, C3' and C5'). **HRMS** ($C_{19}H_{19}N_3NaO_4S^+$): calculated 408.0988 ($M+Na^+$), found 408.0984.

Synthesis of N-benzyl-3-cyano-N-(3,5-dimethoxyphenyl)-1-methyl-1H-indole-5-sulfonamide (118)

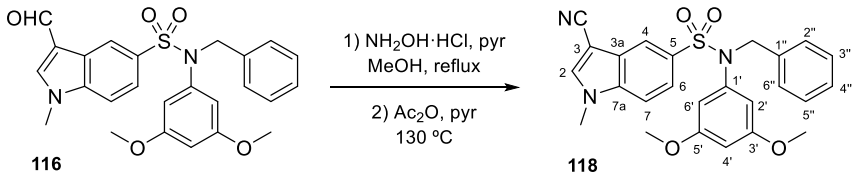

A solution of compound **116** (316 mg, 0.68 mmol) with $NH_2OH{\cdot}HCl$ (490 mg, 7.05 mmol) in methanol (25 mL) with a few drops of pyridine was heated under reflux for 24 h, according to method **E**. The resulting mixture of oximes was heated at 130 °C in pyridine (25 mL) with acetic anhydride (1 mL) for 3 days, giving 179 mg. Crystallization in CH_2Cl_2/Hex yielded compound **118** (86 mg, 0.19 mmol, 27%).

*N-benzyl-3-cyano-N-(3,5-dimethoxyphenyl)-1-methyl-1H-indole-5-sulfonamide (**118**).* Brown crystals. **Mp** (CH_2Cl_2/Hex): 191-193 °C. **IR** (KBr): 2223, 1601, 1165, 656 cm^{-1}. **^{1}H-NMR** (400 MHz, $CDCl_3$): δ 3.63 (6H, s, OCH_3); 3.93 (3H, s, NCH_3); 4.71 (2H, s, CH_2); 6.12 (2H, d, *J* = 2.4 Hz, H2' and H6'); 6.30 (1H, t, *J* = 2.4 Hz, H4'); 7.25 (5H, m, Ph); 7.46 (1H, d, *J* = 8.8 Hz, H7); 7.64 (1H, dd, *J* = 1.6 and 8.8 Hz, H6); 7.71 (1H, s, H2); 8.21 (1H, d, *J* = 1.6 Hz, H4). **^{13}C-NMR** (100 MHz, $CDCl_3$): δ 34.0 (CH_3, NCH_3); 54.9 (CH_2); 55.3 (2) (CH_3, OCH_3); 87.4 (C, C3); 100.0 (CH, C4'); 107.2 (2) (CH, C2' and C6'); 110.8 (CH, C7); 114.5 (C, CN); 120.5 (CH, C6); 123.1 (CH, C4); 127.0 (C, C5); 127.7 (CH, C4''); 128.3 (2) (CH, C2'' and C6''); 128.5 (2) (CH, C3'' and C5''); 132.7 (C, C3a); 135.9 (C, C7a); 137.6 (C, C1'); 137.7 (CH, C2); 140.8 (C, C1''); 160.5 (2) (C, C3' and C5'). **HRMS** ($C_{25}H_{23}N_3NaO_4S^+$): calculated 484.1301 (M+Na^+), found 484.1286.

Synthesis of 3-cyano-N-(3,5-dimethoxyphenyl)-1-methyl-1H-indole-5-sulfonamide (119)

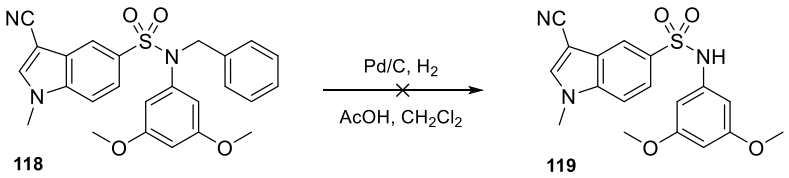

Benzyl derivative **118** (54 mg, 0.12 mmol) was added to a suspension of Pd/C in CH_2Cl_2 with 2 mL of acetic acid, and vigorously stirred under N_2 atmosphere for 24 h. The mixture was filtered through celite and washed with brine but the starting material was recovered as the major product (48 mg).

Synthesis of N-(2,5-dimethoxyphenyl)-1-formylindoline-5-sulfonamide (120)

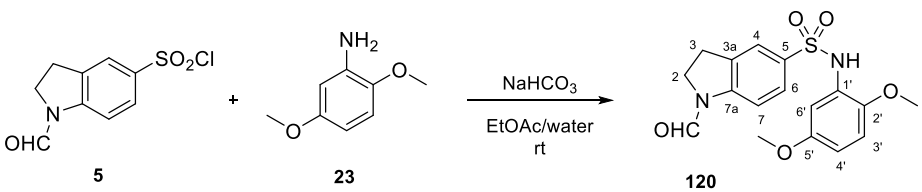

$NaHCO_3$ (1427 mg, 16.99 mmol) was added to a solution of 1-formylindoline-5-sulfonyl chloride (**5**, 2964 mg, 12.07 mmol) and 2,5-dimethoxyaniline (**23**, 1756 mg, 11.48 mmol) in 50 mL of EtOAc/water (1:1) and stirred for 6 h under N_2 at room temperature.[210] MTBE (25 mL) was added and stirred at 4 °C until precipitation, and then, the solid was filtered off and washed with water and MTBE (**120**, 2277 mg, 6.29

mmol, 52%). The organic layer was dried over anhydrous Na_2SO_4, filtered, and evaporated (1175 mg, 3.25 mmol, 27%). Global yield: 3452 mg, 9.54 mmol, 79%.

*N-(2,5-dimethoxyphenyl)-1-formylindoline-5-sulfonamide (**120**).* White powder. **IR** (KBr): 3228, 1672, 1496, 1325 cm^{-1}. **^{1}H-NMR** (400 MHz, $CDCl_3$): δ (*E*) 3.14 (2H, t, *J* = 8.4 Hz, H3); 3.66 (3H, s, 2'-OCH_3); 3.75 (3H, s, 5'-OCH_3); 4.08 (2H, t, *J* = 8.4 Hz, H2); 6.55 (1H, dd, *J* = 3.2 and 8.8 Hz, H4'); 6.68 (1H, d, *J* = 8.8 Hz, H3'); 7.04 (1H, bs, NH); 7.13 (2H, m, H7 and H6'); 7.65 (2H, m, H4 and H6); 8.93 (1H, s, CHO). (*Z*) 3.19 (2H, t, *J* = 8.8 Hz, H3); 3.65 (3H, s, 2'-OCH_3); 3.74 (3H, s, 5'-OCH_3); 4.16 (2H, t, *J* = 8.8 Hz, H2); 6.53 (1H, dd, *J* = 3.2 and 8.8 Hz, H4'); 6.66 (1H, d, *J* = 8.8 Hz, H3'); 7.04 (1H, bs, NH); 7.13 (1H, m, H6'); 7.65 (2H, m, H4 and H6); 8.07 (1H, d, *J* = 8.0 Hz, H7); 8.51 (1H, s, CHO). **^{13}C-NMR** (100 MHz, $CDCl_3$): δ (*E*) 26.7 (CH_2, C3); 45.2 (CH_2, C2); 55.8 (CH_3, 5'-OCH_3); 56.2 (CH_3, 2'-OCH_3); 106.9 (CH, C6'); 108.9 (CH, C7); 109.5 (CH, C4'); 111.4 (CH, C3'); 128.0 (CH, C6); 125.3 (CH, C4); 126.6 (C, C1'); 132.8 (C, C3a); 134.5 (C, C5); 143.4 (C, C2'); 145.2 (C, C7a); 153.9 (C, C5'); 157.6 (CH, CHO). (*Z*) 27.2 (CH_2, C3); 47.2 (CH_2, C2); 55.8 (CH_3, 5'-OCH_3); 56.2 (CH_3, 2'-OCH_3); 106.9 (CH, C6'); 109.5 (CH, C4'); 111.4 (CH, C3'); 116.1 (CH, C7); 125.3 (CH, C4); 126.6 (C, C1'); 128.0 (CH, C6); 132.8 (C, C3a); 134.5 (C, C5); 143.4 (C, C2'); 145.2 (C, C7a); 153.9 (C, C5'); 159.8 (CH, CHO). **GC-MS** ($C_{17}H_{18}N_2O_2S^+$): 362 (M^+).

Synthesis of N-(2,5-dimethoxyphenyl)-1-methylindoline-5-sulfonamide (121)

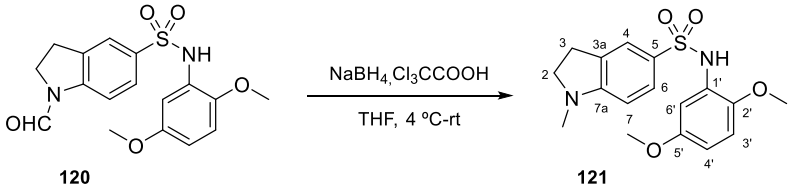

$NaBH_4$ (770 mg, 20.37 mmol) was carefully added to a solution of the sulfonamide **120** (4676 mg, 12.92 mmol) in 125 mL of dry THF at 4 °C, and subsequently, trichloroacetic acid (3199 mg, 19.58 mmol) was slowly added to the reaction mixture and progressively warmed to room temperature. After 4 h under N_2, it was three-fold diluted with water and vigorously stirred for 24 h at 4 °C until precipitation.[210] The solid was filtered off, washed with water and MTBE, obtaining compound **121** (4100 mg, 11.78 mmol, 91%).

*N-(2,5-dimethoxyphenyl)-1-methylindoline-5-sulfonamide (**121**).* White powder. **IR** (KBr): 3283, 1602, 1513, 1322 cm^{-1}. **^{1}H-NMR** (400 MHz, $CDCl_3$): δ 2.78 (3H, s, NCH_3); 2.93 (2H, t, *J* = 8.4 Hz, H3); 3.44 (2H, t, *J* = 8.4 Hz, H2); 3.66 (3H, s, 2'-OCH_3); 3.73 (3H, s, 5'-OCH_3); 6.25 (1H, d, *J* = 8.8 Hz, H3'); 6.49 (1H, dd, *J* = 2.8 and 8.8 Hz, H4'); 6.66 (1H, d, *J* = 9.2 Hz, H7); 7.01 (1H, bs, NH); 7.11 (1H, d, *J* = 2.8 Hz, H6'); 7.39 (1H, d, *J* = 2.0 Hz, H4); 7.54 (1H, dd, *J* = 2.0 and 8.0 Hz, H6). **^{13}C-NMR** (100 MHz, $CDCl_3$): δ 25.5 (CH_2, C3); 32.1 (CH_3, NCH_3); 52.8 (CH_2, C2); 53.6 (CH_3, 5'-OCH_3); 54.3 (CH_3, 2'-OCH_3); 102.2 (CH, C6'); 104.0 (CH, C4'); 106.6 (CH, C3'); 109.3 (CH, C7); 121.0 (CH, C4); 123.3 (C, C3a); 125.5 (C, C5); 127.0 (CH, C6); 128.0 (C, C1'); 141.0 (C, C2'); 151.8 (C, C5'); 154.5 (C, C7a). **GC-MS** ($C_{17}H_{20}N_2O_4S^+$): 348 (M^+).

Synthesis of N-(2,5-dimethoxyphenyl)-1-methyl-1H-indole-5-sulfonamide (122)

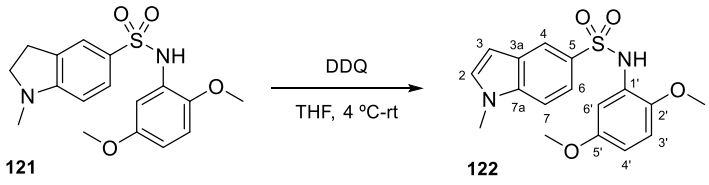

DDQ (967 mg, 4.26 mmol) was added to a solution of the sulfonamide **121** (1402 mg, 4.03 mmol) in dry THF (50 mL) at 4 °C and warmed to room temperature. 24 h later, the reaction mixture was concentrated in half the volume, diluted with MTBE (25 mL) and stirred at 4 °C until precipitation.[210] The solid was filtered off and washed with MTBE, obtaining 1005 mg (2.90 mmol, 72%) of indole derivative **122**. Crystallization in ACN/MTBE gave 801 mg (2.32 mmol, 57%) of **122**.

*N-(2,5-dimethoxyphenyl)-1-methyl-1H-indole-5-sulfonamide (**122**).* Purple crystals. **Mp** (ACN/MTBE): 153.8-154.8 °C. **IR** (KBr): 3258, 1510, 1122, 636 cm^{-1}. **^{1}H-NMR** (400 MHz, $CDCl_3$): δ 3.58 (3H, s, NCH_3); 3.72 (3H, s, 2'-OCH_3); 3.78 (3H, s, 5'-OCH_3); 6.46 (1H, dd, *J* = 2.8 and 8.8 Hz, H4'); 6.55 (1H, d, 3.2 Hz, H3); 6.60 (1H, d, *J* = 8.8 Hz, H3'); 7.12 (1H, bs, NH); 7.13 (1H, d, *J* = 2.8 Hz, H6'); 7.18 (1H, d, *J* = 3.2 Hz, H2); 7.29 (1H, d, *J* = 8.8 Hz, H7); 7.63 (1H, dd, *J* = 1.6 and 8.8 Hz, H6); 8.16 (1H, d, *J* = 1.6 Hz, H4). **^{13}C-NMR** (100 MHz, $CDCl_3$): δ 33.0 (CH_3, NCH_3); 55.7 (CH_3, 5'-OCH_3); 56.3 (CH_3, 2'-OCH_3); 102.7 (CH, C6'); 106.3 (CH, C3); 109.0 (CH, C4'); 109.4 (CH, C3'); 111.5 (CH, C7); 120.1 (CH, C4); 121.8 (CH, C6); 127.3 (C, C3a); 127.6 (C, C1'); 129.7 (C, C5); 131.1 (CH, C2); 138.4 (C, C2'); 143.2 (C, C7a); 153.9 (C, C5'). **HRMS** ($C_{17}H_{18}N_2NaO_4S^+$): calculated 369.0879 ($M+Na^+$), found 369.0868.

Synthesis of N-(2,5-dimethoxyphenyl)-N,1-dimethyl-1H-indole-5-sulfonamide (123)

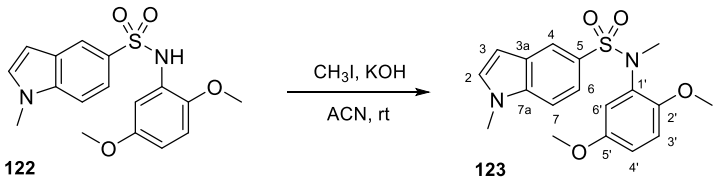

122 123

Following procedure **C1**, compound **122** (157 mg, 0.45 mmol) in ACN (50 mL) with ground KOH in excess was stirred for half an hour, followed by the addition of methyl iodide (60 µL, 0.96 mmol). After 24 h, **123** (153 mg, 0.43 mmol, 94%) was obtained and later purified by silica gel flash chromatography (toluene/EtOAc 6:4): 136 mg (**123**, 0.38 mmol, 83%).

*N-(2,5-dimethoxyphenyl)-N,1-dimethyl-1H-indole-5-sulfonamide (**123**).* Yellow solid. **IR** (KBr): 1505, 1328, 1216, 640 cm^{-1}. **^{1}H-NMR** (400 MHz, $CDCl_3$): δ 3.18 (3H, s, SO_2NCH_3); 3.32 (3H, s, 1-NCH_3); 3.71 (3H, s, 2'-OCH_3); 3.83 (3H, s, 5'-OCH_3); 6.56 (1H, d, *J* = 3.6 Hz, H3); 6.71 (1H, d, *J* = 8.4 Hz, H3'); 6.81 (1H, dd, *J* = 2.8 and 8.4 Hz, H4'); 6.83 (1H, d, *J* = 2.8 Hz, H6'); 7.15 (1H, d, *J* = 3.6 Hz, H2); 7.34 (1H, d, *J* = 8.4 Hz, H7); 7.57 (1H, dd, *J* = 1.6 and 8.4 Hz, H6); 8.05 (1H, d, *J* = 1.6 Hz, H4). **^{13}C-NMR** (100 MHz, $CDCl_3$): δ 33.1 (CH_3, 1-NCH_3); 37.9 (CH_3, SO_2NCH_3); 55.6 (CH_3, 5'-OCH_3); 55.8 (CH_3, 2'-OCH_3); 102.5 (CH, C6'); 108.9 (CH, C3); 112.6 (CH, C4'); 114.6 (CH, C3'); 116.7 (CH, C7); 120.9 (CH, C4); 121.9 (CH, C6); 127.6 (C, C3a); 129.9 (C, C5); 130.2 (C, C2'); 130.8 (CH, C2); 138.2 (C, C1'); 150.9 (C, C7a); 153.1 (C, C5'). **HRMS** ($C_{18}H_{20}N_2NaO_4S^+$): calculated 383.1036 ($M+Na^+$), found 383.1039.

Synthesis of N-(2,5-dimethoxyphenyl)-N-ethyl-1-methyl-1H-indole-5-sulfonamide (124)

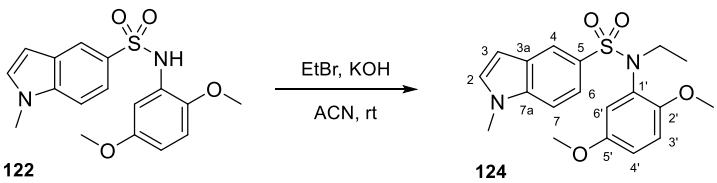

122 124

As described in method **C1**, the mixture of **122** (205 mg, 0.59 mmol) and ground KOH in excess in 25 mL of ACN was stirred at room temperature for 1 h prior to the addition of ethyl bromide (176 µL, 2.36 mmol). The reaction was kept under N_2 for 5 days, evaporated, and the residue was dissolved in CH_2Cl_2 and washed with brine, providing 176 mg. Crystallization in CH_2Cl_2/Hex gave 39 mg (0.11 mmol) of **122** and preparative TLC (CH_2Cl_2/MeOH 98:2) with the mother liquors (118 mg) gave a 10:1 mixture of **124** (107 mg, 0.29 mmol, 48%) and **122** (11 mg, 0.03 mmol).

*N-(2,5-dimethoxyphenyl)-N-ethyl-1-methyl-1H-indole-5-sulfonamide (**124**).* Non-isolated product. **^{1}H-NMR** (400 MHz, $CDCl_3$): δ 1.03 (3H, t, *J* = 7.2 Hz, Et); 3.30 (3H, s, NCH_3); 3.61 (2H, q, *J* = 7.2 Hz, Et); 3.72 (3H, s, 2'-OCH_3); 3.82 (3H, s, 5'-OCH_3); 6.54 (1H, d, *J* = 2.4 Hz, H6'); 6.71 (1H, d, *J* = 8.8 Hz, H3'); 6.80 (1H, dd, *J* = 2.4 and 8.8 Hz, H4'); 6.83 (1H, d, *J* = 3.2 Hz, H3); 7.13 (1H, d, *J* = 3.2 Hz, H2); 7.31 (1H, d, *J* = 8.8 Hz, H7); 7.58 (1H, dd, *J* = 1.6 and 8.8 Hz, H6); 8.04 (1H, d, *J* = 1.6 Hz, H4).

Synthesis of ethyl N-(2,5-dimethoxyphenyl)-N-((1-methyl-1H-indol-5-yl)sulfonyl)glycinate (125)

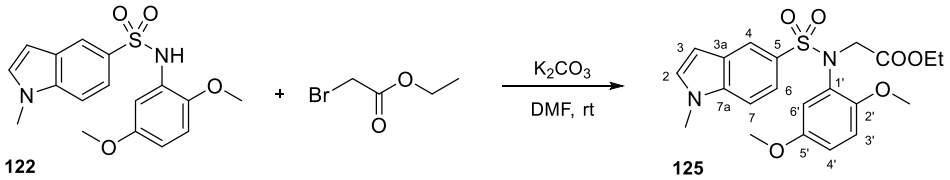

Following method **C2**, ethyl bromoacetate (146 µL, 1.32 mmol) was slowly added to a solution of **122** (189 mg, 0.55 mmol) in dry DMF (1 mL) with K_2CO_3, obtaining 196 mg after ten days. Crystallization in methanol yielded **125** (136 mg, 0.33 mmol, 60%).

*Ethyl N-(2,5-dimethoxyphenyl)-N-((1-methyl-1H-indol-5-yl)sulfonyl)glycinate (**125**).* Orange crystals. **Mp** (MeOH): 116-117 °C. **IR** (KBr): 1749, 1503, 1336, 644 cm^{-1}. **^{1}H-NMR** (400 MHz, $CDCl_3$): δ 1.22 (3H, d, *J* = 7.2 Hz, Et); 3.22 (3H, s, NCH_3); 3.71 (3H, s, 2'-OCH_3); 3.82 (3H, s, 5'-OCH_3); 4.13 (2H, q, *J* = 7.2 Hz, Et); 4.42 (2H, s, CH_2); 6.54 (1H, d, *J* = 3.2 Hz, H3); 6.64 (1H, d, *J* = 8.8 Hz, H3'); 6.80 (1H, dd, *J* = 3.2 and 8.8 Hz, H4'); 7.12 (1H, d, *J* = 3.2 Hz, H6'); 7.13 (1H, d, *J* = 3.2 Hz, H2); 7.31 (1H, d, *J* = 8.4 Hz, H7); 7.55 (1H, dd, *J* = 2.0 and 8.4 Hz, H6); 8.00 (1H, d, *J* = 2.0 Hz, H4). **^{13}C-NMR** (100 MHz, $CDCl_3$): δ 14.1 (CH_3, Et); 33.1 (CH_3, NCH_3); 51.2 (CH_2); 55.4 (CH_3, 5'-OCH_3); 55.7 (CH_3, 2'-OCH_3); 61.1 (CH_2, Et); 102.6 (CH, C6'); 108.8 (CH, C3); 112.1 (CH, C4'); 115.4 (CH, C3'); 118.7 (CH, C7); 120.7 (CH, C4); 121.8 (CH, C6); 127.5 (C, C3a); 127.7 (C, C5); 130.8 (CH, C2); 130.9 (C, C2'); 138.3 (C, C1'); 150.2 (C, C7a); 153.0 (C, C5'); 169.6 (C, CO). **HRMS** ($C_{21}H_{24}N_2NaO_6S^+$): calculated 455.1247 ($M+Na^+$), found 455.1232.

Synthesis of N-(cyanomethyl)-N-(2,5-dimethoxyphenyl)-1-methyl-1H-indole-5-sulfonamide (126)

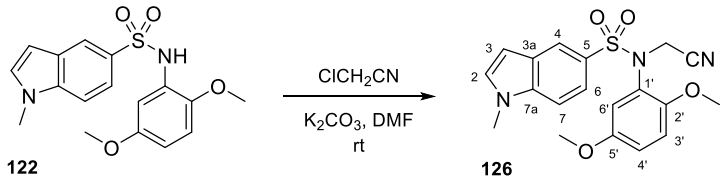

As described in general procedure **C2**, chloroacetonitrile (224 µL, 3.54 mmol) was added to compound **122** (142 mg, 0.41 mmol) in dry DMF (1 mL) with excess K_2CO_3 and stirred for five days, providing 143 mg. Crystallization in CH_2Cl_2/Hex gave 75 mg (0.19 mmol, 47%) of **126**.

*N-(cyanomethyl)-N-(2,5-dimethoxyphenyl)-1-methyl-1H-indole-5-sulfonamide (**126**).* Yellow crystals. **Mp** (CH_2Cl_2/Hex): 150.0-150.4 °C. **IR** (KBr): 1502, 1325, 1145 cm^{-1}. **^{1}H-NMR** (400 MHz, $CDCl_3$): δ 3.29 (3H, s, NCH_3); 3.70 (3H, s, 2'-OCH_3); 3.84 (3H, s, 5'-OCH_3); 4.59 (2H, s, CH_2); 6.57 (1H, d, *J* = 3.2 Hz, H3); 6.71 (1H, d, *J* = 9.2 Hz, H3'); 6.87 (1H, dd, *J* = 3.2 and 9.2 Hz, H4'); 6.91 (1H, d, *J* = 3.2 Hz, H6'); 7.17 (1H, d, *J* = 3.2 Hz, H2); 7.36 (1H, d, *J* = 9.2 Hz, H7); 7.56 (1H, dd, *J* = 2.0 and 9.2 Hz, H6); 8.01 (1H, d, *J* = 2.0 Hz, H4). **^{13}C-NMR** (100 MHz, $CDCl_3$): δ 33.2 (CH_3, NCH_3); 38.4 (CH_2); 55.5 (CH_3, 5'-OCH_3); 55.8 (CH_3, 2'-OCH_3); 102.8 (CH, C6'); 109.3 (CH, C3); 112.6 (CH, C4'); 115.6 (C, CN); 116.3 (CH, C3'); 117.4 (CH, C7); 120.6 (CH, C4); 122.1 (CH, C6); 126.2 (C, C3a); 127.7 (C, C5); 129.3 (C, C2'); 131.2 (CH, C2); 138.6 (C, C1'); 150.3 (C, C7a); 153.4 (C, C5'). **HRMS** ($C_{19}H_{20}N_3O_4S^+$): calculated 386.1169 ($M+H^+$), found 386.1170.

Synthesis of N-benzyl-N-(2,5-dimethoxyphenyl)-1-methyl-1H-indole-5-sulfonamide (127)

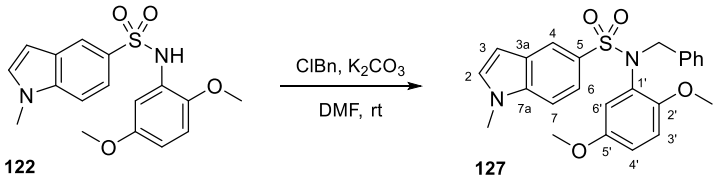

Following method **C2**, a solution of **122** (195 mg, 0.56 mmol) and benzyl chloride (130 µL, 1.23 mmol) in dry DMF (1 mL) with excess K_2CO_3 was stirred for ten days, obtaining 205 mg. Silica gel flash chromatography with toluene/EtOAc 9:1 as eluent yielded **127** (153 mg, 0.35 mmol, 62%).

*N-benzyl-N-(2,5-dimethoxyphenyl)-1-methyl-1H-indole-5-sulfonamide (**127**).* White solid. **IR** (KBr): 1503, 1333, 1149, 642 cm^{-1}. **^{1}H-NMR** (400 MHz, $CDCl_3$): δ 3.20 (3H, s, 2'-OCH_3); 3.60 (3H, s, 5'-OCH_3); 3.83 (3H, s, NCH_3); 4.76 (2H, s, CH_2); 6.55 (1H, d, *J* = 3.2 Hz, H3); 6.61 (1H, d, *J* = 8.8 Hz, H3'); 6.64 (1H, d, *J* = 3.2 Hz, H6'); 6.72 (1H, dd, *J* = 3.2 and 8.8 Hz, H4'); 7.15 (1H, d, *J* = 3.2 Hz, H2); 7.21 (5H, m, Ph); 7.34 (1H, d, *J* = 8.8 Hz, H7); 7.61 (1H, dd, *J* = 1.6 and 8.8 Hz, H6); 8.06 (1H, d, *J* = 1.6 Hz, H4). **^{13}C-NMR** (100 MHz, $CDCl_3$): δ 33.1 (CH_3, NCH_3); 53.6 (CH_2); 55.4 (CH_3, 2'-OCH_3); 55.7 (CH_3, 5'-OCH_3); 102.5 (CH, C3); 109.0 (CH, C7); 112.2 (CH, C3'); 114.7 (CH, C4'); 118.9 (CH, C6'); 120.8 (CH, C6); 121.8 (CH, C4); 127.3 (CH, Ph); 127.5 (C, C3a); 127.6 (C, C5); 128.1 (2) (CH, Ph); 128.7 (2) (CH, Ph); 131.0 (CH, C2); 137.1 (C, C3a); 138.3 (C, C1'); 151.1 (C, C2'); 152.9 (C, C5'). Quaternary carbon (C7a) not observed. **HRMS** ($C_{24}H_{24}N_3NaO_4S^+$): calculated 459.1349 ($M+Na^+$), found 459.1339.

Synthesis of 3-bromo-N-(4-bromo-2,5-dimethoxyphenyl)-1-methyl-1H-indole-5-sulfonamide (128)

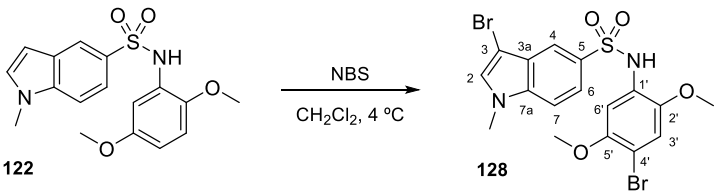

N-bromosuccinimide (132 mg, 0.74 mmol) was added to a solution of **122** (117 mg, 0.34 mmol) in ice-cold CH_2Cl_2 (3 mL), stirred for 15 min under N_2 and washed with 5% $NaHCO_3$ and brine. The organic layer was dried over anhydrous Na_2SO_4, filtered, and evaporated (165 mg). Crystallization in methanol/CH_2Cl_2 gave 85 mg (0.17 mmol, 50%) of **128**.

*3-Bromo-N-(4-bromo-2,5-dimethoxyphenyl)-1-methyl-1H-indole-5-sulfonamide (**128**).* White crystals. **Mp** (MeOH/CH_2Cl_2): 174.5-175.1 °C. **IR** (KBr): 3269, 1501, 1326, 1139, 672 cm^{-1}. **^{1}H-NMR** (400 MHz, $CDCl_3$): δ

3.69 (3H, s, NCH_3); 3.79 (3H, s, 2'-OCH_3); 3.86 (3H, s, 5'-OCH_3); 6.86 (1H, s, H6'); 7.10 (1H, bs, NH); 7.18 (1H, s, H2); 7.25 (1H, s, H3'); 7.30 (1H, d, *J* = 8.4 Hz, H7); 7.62 (1H, dd, *J* = 1.6 and 8.4 Hz, H6); 8.12 (1H, d, *J* = 1.6 Hz, H4). **^{13}C-NMR** (100 MHz, $CDCl_3$): δ 33.1 (CH_3, NCH_3); 56.2 (CH_3, 5'-OCH_3); 56.6 (CH_3, 2'-OCH_3); 90.7 (C, C3); 104.7 (CH, C6'); 105.3 (C, C4'); 109.8 (CH, C7); 115.5 (CH, C3'); 120.3 (CH, C4); 120.7 (CH, C6); 125.9 (C, C5); 126.4 (C, C3a); 129.8 (CH, C2); 129.9 (C, C1'); 137.8 (C, C7a); 143.0 (C, C2'); 149.9 (C, C5'). **HRMS** ($C_{17}H_{16}Br_2N_2NaO_4S^+$): calculated 524.9090 ($M+Na^+$), found 524.9099.

Synthesis of 3-bromo-N-(4-bromo-2,5-dimethoxyphenyl)-N,1-dimethyl-1H-indole-5-sulfonamide (129)

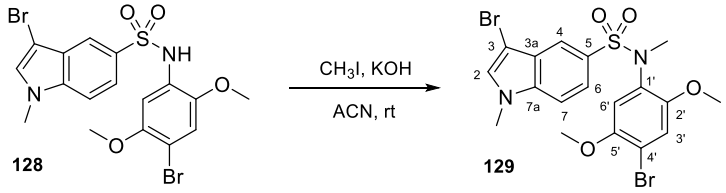

Following general procedure **C1**, methyl iodide (26 µL, 0.42 mmol) was added to a solution of **128** (104 mg, 0.21 mmol) in ACN (10 mL) with ground KOH in excess, previously stirred for half an hour. The reaction provided 98 mg after three days. Crystallization in methanol/CH_2Cl_2 yielded **129** (52 mg, 0.10 mmol, 49%).

*3-Bromo-N-(4-bromo-2,5-dimethoxyphenyl)-N,1-dimethyl-1H-indole-5-sulfonamide (**129**).* Yellow crystals. **Mp** (MeOH/CH_2Cl_2): 124.0-125.2 °C. **IR** (KBr): 1495, 1338, 1217, 697 cm^{-1}. **^{1}H-NMR** (400 MHz, $CDCl_3$): δ 3.17 (3H, s, SO_2NCH_3); 3.30 (3H, s, 1-NCH_3); 3.82 (3H, s, 2'-OCH_3); 3.83 (3H, s, 5'-OCH_3); 6.92 (1H, s, H6'); 6.98 (1H, s, H2); 7.20 (1H, s, H3'); 7.34 (1H, d, *J* = 8.8 Hz, H7); 7.60 (1H, dd, *J* = 1.6 and 8.8 Hz, H6); 8.00 (1H, d, *J* = 1.6, H4). **^{13}C-NMR** (100 MHz, $CDCl_3$): δ 33.4 (CH_3, 1-NCH_3); 37.7 (CH_3, SO_2NCH_3); 55.7 (CH_3, 5'-OCH_3); 56.9 (CH_3, 2'-OCH_3); 90.8 (C, C3); 109.4 (CH, C6'); 111.4 (C, C4'); 115.6 (CH, C7); 116.8 (CH, C3'); 120.4 (CH, C4); 121.9 (CH, C6); 126.7 (C, C3a); 129.0 (C, C5); 129.9 (CH, C2); 130.9 (C, C2'); 137.9 (C, C1'); 149.7 (C, C7a); 150.7 (C, C5'). **HRMS** ($C_{18}H_{18}Br_2N_2NaO_4S^+$): calculated 538.9246 ($M+Na^+$), found 538.9249.

Preparation of compounds 130 and 131

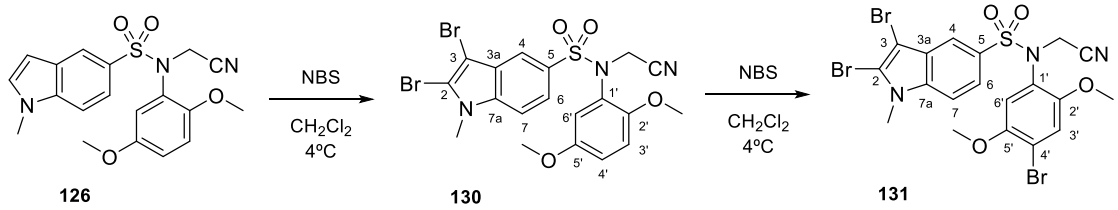

N-bromosuccinimide (72 mg, 0.40 mmol) was added to a cold solution of **126** (75 mg, 0.19 mmol) in 5 mL of CH_2Cl_2. The reaction was stirred for 3 h before the solvent was removed, obtaining **130** with a minor impurity. The residue was dissolved in CH_2Cl_2 and more NBS (287 mg, 1.61 mmol) was added and stirred during 72 h, to obtain compound **131**.

*2,3-Dibromo-N-(cyanomethyl)-N-(2,5-dimethoxyphenyl)-1-methyl-1H-indole-5-sulfonamide (**130**).* Non-isolated product. **^{1}H-NMR** (400 MHz, $CDCl_3$): δ 3.34 (3H, s, NCH_3); 3.74 (3H, 2'-OCH_3); 3.84 (3H, s, 5'-OCH_3); 4.56 (2H, s, CH_2); 6.72 (1H, d, *J* = 8.8 Hz, H3'); 6.88 (1H, dd, *J* = 2.8 and 8.8 Hz, H4'); 6.94 (1H, d, *J* = 2.8 Hz, H6'); 7.34 (1H, d, *J* = 8.8 Hz, H7); 7.59 (1H, dd, *J* = 2.4 and 8.8 Hz, H6); 7.90 (1H, d, *J* = 2.4 Hz, H4).

*2,3-Dibromo-N-(4-bromo-2,5-dimethoxyphenyl)-N-(cyanomethyl)-1-methyl-1H-indole-5-sulfonamide (**131**).* Non-isolated product. **^{1}H-NMR** (400 MHz, $CDCl_3$): δ 3.30 (3H, s, NCH_3); 3.42 (3H, s, 2'-OCH_3); 3.88 (3H, s, 5'-OCH_3); 4.54 (2H, s, CH_2); 6.90 (1H, d, *J* = 8.4 Hz, H7); 7.01 (1H, s, H6'); 7.04 (1H, s, H3'); 7.73 (1H, dd, *J* = 1.6 and 8.4 Hz, H6); 7.79 (1H, d, *J* = 1.6 Hz, H4).

Synthesis of N-(2,5-dimethoxyphenyl)-3-formyl-1-methyl-1H-indole-5-sulfonamide (132)

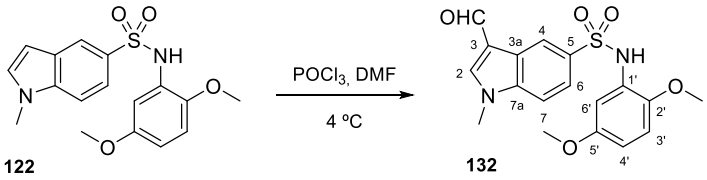

The reaction was carried out following Vilsmeier-Haack procedure (method **D**). A mixture of $POCl_3$ (1019 µL, 11.10 mmol) and dry DMF (2 mL) at 4 °C was stirred for half an hour, and **122** (642 mg, 1.86 mmol) in dry DMF (8 mL) was added dropwise and stirred for five minutes. The resulting precipitate was filtered off obtaining **132** (667 mg, 1.78 mmol, 96%).

*N-(2,5-dimethoxyphenyl)-3-formyl-1-methyl-1H-indole-5-sulfonamide (**132**).* Brown solid. **IR** (KBr): 3104, 1644, 1509, 1168 cm^{-1}. **^{1}H-NMR** (400 MHz, $CDCl_3$): δ 3.64 (3H, s, NCH_3); 3.75 (3H, s, 2'-OCH_3); 3.87 (3H, s, 5'-OCH_3); 6.47 (1H, dd, *J* = 3.2 and 8.8 Hz, H4'); 6.61 (1H, d, *J* = 8.8 Hz, H3'); 7.19 (1H, d, *J* = 3.2 Hz, H6'); 7.20 (1H, bs, NH); 7.34 (1H, d, *J* = 8.4 Hz, H7); 7.73 (1H, s, H2); 7.79 (1H, dd, *J* = 1.6 and 8.4 Hz, H6); 8.84 (1H, d, *J* = 1.6 Hz, H4); 9.97 (1H, s, CHO). **^{13}C-NMR** (100 MHz, acetone-D6): δ 33.2 (CH_3, NCH_3); 54.9 (CH_3, 5'-OCH_3); 55.8 (CH_3, 2'-OCH_3); 107.2 (CH, C6'); 109.0 (CH, C4'); 110.9 (CH, C3'); 112.0 (CH, C7); 118.3 (C, C3); 121.8 (CH, C4); 122.2 (CH, C6); 124.3 (C, C3a); 127.4 (C, C5); 134.0 (C, C1'); 139.8 (C, C2'); 142.6 (CH, C2); 144.1 (C, C7a); 153.8 (C, C5'); 184.0 (CH, CHO). **HRMS** ($C_{18}H_{18}N_2NaO_5S^+$): calculated 397.0829 ($M+Na^+$), found 397.0827.

Synthesis of N-(2,5-dimethoxyphenyl)-3-formyl-N,1-dimethyl-1H-indole-5-sulfonamide (133)

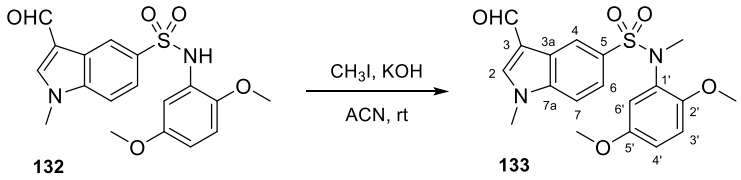

As described in method **C1**, the mixture of compound **132** (453 mg, 1.21 mmol) and methyl iodide (150 µL, 2.41 mmol) in 125 mL of ACN with powdered KOH gave **133** (419 mg, 1.08 mmol, 89%) after 24 h. It was then crystallized in CH_2Cl_2/Hex (267 mg, 0.67 mmol, 57%).

*N-(2,5-dimethoxyphenyl)-3-formyl-N,1-dimethyl-1H-indole-5-sulfonamide (**133**).* Yellow crystals. **Mp** (CH_2Cl_2/Hex): 169.2-170.3 °C. **IR** (KBr): 1661, 1508, 1329, 1041 cm^{-1}. **^{1}H-NMR** (400 MHz, $CDCl_3$): δ 3.19 (3H, s, SO_2NCH_3); 3.66 (3H, s, 1-NCH_3); 3.74 (3H, s, 2'-OCH_3); 3.92 (3H, s, 5'-OCH_3); 6.72 (1H, d, *J* = 8.8 Hz, H3'); 6.82 (1H, dd, *J* = 2.8 and 8.8 Hz, H4'); 6.87 (1H, d, *J* = 2.8 Hz, H6'); 7.37 (1H, d, *J* = 8.8 Hz, H7); 7.71 (1H, dd, *J* = 2.0 and 8.8 Hz, H6); 7.72 (1H, s, H2); 8.74 (1H, d, *J* = 2.0 Hz, H4); 10.01 (1H, s, CHO). **^{13}C-NMR** (100 MHz, $CDCl_3$): δ 33.9 (CH_3, 1-NCH_3); 37.8 (CH_3, SO_2NCH_3); 55.4 (CH_3, 5'-OCH_3); 55.8 (CH_3, 2'-OCH_3); 109.7 (CH, C6'); 112.5 (CH, C4'); 114.6 (CH, C3'); 116.9 (CH, C7); 118.3 (C, C3); 122.2 (CH, C4); 123.3 (CH, C6); 124.3 (C,

C3a); 129.8 (C, C5); 133.7 (C, C2'); 139.3 (C, C1'); 140.9 (CH, C2); 150.7 (C, C7a); 153.2 (C, C5'); 184.1 (CH, CHO). **HRMS** ($C_{19}H_{20}N_2NaO_5S^+$): calculated 411.0985 ($M+Na^+$), found 411.0982.

Synthesis of N-(4-bromo-2,5-dimethoxyphenyl)-3-formyl-N,1-dimethyl-1H-indole-5-sulfonamide (134)

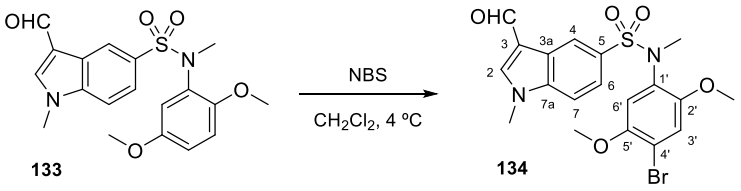

N-bromosuccinimide (27 mg, 0.15 mmol) was added to a solution of **133** (46 mg, 0.12 mmol) in CH_2Cl_2 (3 mL) at 4 °C, stirred for 24 h under N_2 and evaporated. After preparative TLC (EtOAc/Hex 85:15) the residue was dissolved in CH_2Cl_2, washed with 5% $NaHCO_3$ and saturated NaCl. The organic layer was dried over anhydrous Na_2SO_4, filtered, and evaporated (44 mg). Crystallization in CH_2Cl_2/Hex gave 19 mg (0.04 mmol, 35%) of **134**.

*N-(4-bromo-2,5-dimethoxyphenyl)-3-formyl-N,1-dimethyl-1H-indole-5-sulfonamide (**134**).* Yellow crystals. **Mp** (CH_2Cl_2/Hex): 212-213 °C. **IR** (KBr): 1659, 1503, 1337, 1216 cm^{-1}. **^{1}H-NMR** (400 MHz, $CDCl_3$): δ 3.18 (3H, s, SO_2NCH_3); 3.32 (3H, s, 1-NCH_3); 3.82 (3H, s, 2'-OCH_3); 3.92 (3H, s, 5'-OCH_3); 6.94 (1H, s, H6'); 6.97 (1H, s, H3'); 7.37 (1H, d, *J* = 8.4 Hz, H7); 7.67 (1H, dd, *J* = 1.6 and 8.4 Hz, H6); 7.79 (1H, s, H2); 8.76 (1H, d, *J* = 1.6 Hz, H4); 10.01 (1H, s, CHO). **^{13}C-NMR** (100 MHz, $CDCl_3$): δ 34.0 (CH_3, 1-NCH_3); 37.7 (CH_3, SO_2NCH_3); 55.6 (CH_3, 5'-OCH_3); 56.9 (CH_3, 2'-OCH_3); 109.7 (CH, C6'); 111.6 (C, C4'); 115.7 (CH, C7); 116.8 (CH, C3'); 118.5 (C, C3); 122.4 (CH, C4); 123.5 (CH, C6); 124.5 (C, C3a); 128.9 (C, C5); 133.8 (C, C2'); 139.4 (C, C1'); 140.6 (CH, C2); 149.7 (C, C7a); 150.8 (C, C5'); 184.0 (CH, CHO). **HRMS** ($C_{19}H_{19}BrN_2NaO_5S^+$): calculated 489.0090 ($M+Na^+$), found 489.0098.

Synthesis of N-(4-bromo-2,5-dimethoxyphenyl)-3-formyl-1-methyl-1H-indole-5-sulfonamide (135)

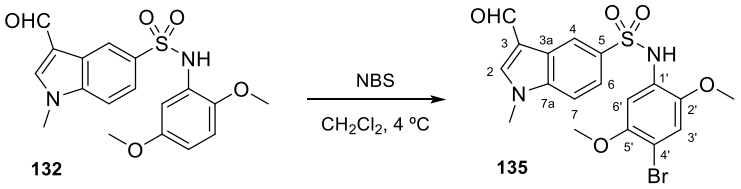

Aldehyde **132** (245 mg, 0.66 mmol) in CH_2Cl_2/ACN (25 mL) was cooled to 4 °C and *N*-bromosuccinimide (123 mg, 0.72 mmol) was added and stirred under N_2. Half an hour later, the reaction was washed with 5% $NaHCO_3$ and brine. The organic layer was dried over anhydrous Na_2SO_4, filtered, and evaporated, obtaining 202 mg (0.45 mmol, 68%) of **135**. Crystallization in methanol/acetone yielded 47 mg (0.10 mmol, 16%) of **135**.

*N-(4-bromo-2,5-dimethoxyphenyl)-3-formyl-1-methyl-1H-indole-5-sulfonamide (**135**).* Light brown crystals. **Mp** (MeOH/acetone): 224.0-224.7 °C. **IR** (KBr): 3105, 1648, 1330, 1169, 723 cm^{-1}. **^{1}H-NMR** (400 MHz, $CDCl_3$): δ 3.61 (3H, s, NCH_3); 3.84 (3H, s, 2'-OCH_3); 3.86 (3H, s, 5'-OCH_3); 6.82 (1H, s, H6'); 7.13 (1H, bs, NH); 7.24 (1H, s, H3'); 7.33 (1H, d, *J* = 8.4 Hz, H7); 7.72 (1H, dd, *J* = 2.0 and 8.4 Hz, H6); 7.74 (1H, s, H2); 8.84 (1H, d, *J* = 2.0 Hz, H4); 9.96 (1H, s, CHO). **^{13}C-NMR** (100 MHz, $CDCl_3$): δ 34.0 (CH_3, NCH_3); 56.4 (CH_3, 5'-OCH_3); 56.9 (CH_3, 2'-OCH_3); 104.7 (CH, C6'); 105.5 (C, C4'); 110.3 (CH, C7); 115.7 (CH, C3'); 118.7 (C, C3); 122.7 (CH, C4); 122.8 (CH, C6); 124.6 (C, C3a); 126.2 (C, C5); 133.1 (C, C1'); 139.6 (C, C7a); 140.6 (CH, C2);

143.1 (C, C2'); 150.3 (C, C5'); 183.9 (CH, CHO). **HRMS** ($C_{18}H_{17}BrN_2NaO_5S^+$): calculated 474.9934 ($M+Na^+$), found 474.9936.

Synthesis of N-(4-bromo-2,5-dimethoxyphenyl)-3-cyano-1-methyl-1H-indole-5-sulfonamide (136)

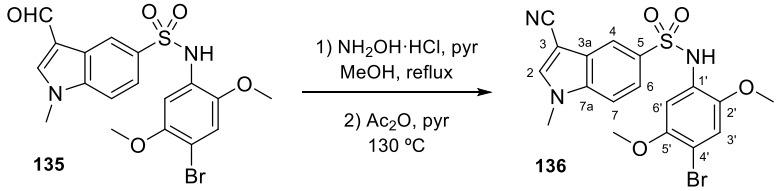

Following the two-step reaction described in method **E**, compound **135** (150 mg, 0.33 mmol) and $NH_2OH{\cdot}HCl$ (231 mg, 3.32 mmol) were dissolved in methanol (50 mL) with a few drops of pyridine and heated under reflux for two days yielding a mixture of (*E/Z*)-*N*-(4-bromo-2,5-dimethoxyphenyl)-3-((hydroxyimino)methyl)-1-methyl-1*H*-indole-5-sulfonamide. The oximes were dissolved in pyridine (25 mL) with acetic anhydride (0.5 mL) and heated at 130 °C for 4 days, obtaining 84 mg. Crystallization in methanol/acetone gave 28 mg (0.06 mmol, 19%) of **136**.

*N-(4-bromo-2,5-dimethoxyphenyl)-3-cyano-1-methyl-1H-indole-5-sulfonamide (**136**).* Brown crystals. **Mp** (MeOH/acetone): 247.2-247.7 °C. **IR** (KBr): 3220, 3109, 2221, 1498, 1331, 1160, 690 cm^{-1}. **^{1}H-NMR** (400 MHz, $CDCl_3$): δ 3.65 (3H, s, NCH_3); 3.86 (3H, s, 2'-OCH_3); 3.88 (3H, s, 5'-OCH_3); 6.88 (1H, s, H6'); 7.12 (1H, bs, NH); 7.25 (1H, s, H2); 7.40 (1H, d, *J* = 8.8 Hz, H7); 7.68 (1H, s, H3'); 7.72 (1H, dd, *J* = 1.6 and 8.8 Hz, H6); 8.32 (1H, d, *J* = 1.6 Hz, H4). **^{13}C-NMR** (100 MHz, $CDCl_3$): δ 33.7 (CH_3, NCH_3); 56.2 (CH_3, 5'-OCH_3); 56.7 (CH_3, 2'-OCH_3); 87.4 (C, C3); 105.0 (CH, C6'); 105.9 (C, C4'); 110.7 (CH, C7); 113.9 (C, CN); 115.3 (CH, C3'); 120.2 (CH, C4); 122.2 (CH, C6); 125.5 (C, C5); 126.8 (C, C3a); 132.6 (C, C1'); 137.4 (CH, C2); 137.5 (C, C2'); 143.1 (C, C7a); 150.1 (C, C5'). **HRMS** ($C_{18}H_{16}BrN_3NaO_4S^+$): calculated 471.9937 ($M+Na^+$), found 471.9943.

Preparation of compounds 137 and 138

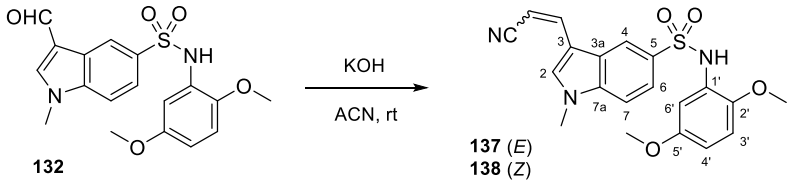

A solution of **132** (132 mg, 0.35 mmol) in ACN (25 mL) with ground KOH in excess was stirred for one week. It was then evaporated, re-dissolved in CH_2Cl_2, and washed with brine. The organic layer was dried over anhydrous Na_2SO_4, filtered, and concentrated to dryness yielding 67 mg of a 2:1 mixture of compounds **137**/**138**, which were separated by preparative TLC using EtOAc/toluene 8:2 as eluent, obtaining **137** (28 mg, 0.07 mmol, 20%) and **138** (14 mg, 0.04 mmol, 10%).

*(E)-3-(2-cyanovinyl)-N-(2,5-dimethoxyphenyl)-1-methyl-1H-indole-5-sulfonamide (**137**).* White solid. **IR** (KBr): 3242, 2210, 1618, 1509, 1169, 644 cm^{-1}. **^{1}H-NMR** (400 MHz, $CDCl_3$): δ 3.52 (3H, s, NCH_3); 3.69 (3H, s, 2'-OCH_3); 3.76 (3H, s, 5'-OCH_3); 5.60 (1H, d, *J* = 16.4 Hz, olefin); 6.45 (1H, dd, *J* = 3.2 and 8.8 Hz, H4'); 6.56 (1H, d, *J* = 8.8 Hz, H3'); 7.06 (1H, bs, NH); 7.17 (1H, d, *J* = 3.2 Hz, H6'); 7.29 (1H, d, *J* = 8.8 Hz, H7); 7.32 (1H, s, H2); 7.41 (1H, d, *J* = 16.4 Hz, olefin); 7.70 (1H, dd, *J* = 1.6 and 8.8 Hz, H6); 8.11 (1H, d, *J* = 1.6 Hz, H4). **^{13}C-NMR** (100 MHz, $CDCl_3$): δ 33.5 (CH_3, NCH_3); 55.7 (CH_3, 5'-OCH_3); 56.2 (CH_3, 2'-OCH_3); 91.9 (CH, C6'); 107.1 (CH, C4'); 109.3 (CH, olefin); 110.5 (CH, C3'); 111.4 (CH, C7); 112.8 (C, CN); 119.2 (C, C3); 120.2

(CH, C4); 121.9 (CH, C6); 124.6 (C, C3a); 126.9 (C, C5); 132.3 (CH, C2); 134.4 (C, C1'); 139.7 (CH, olefin); 142.0 (C, C2'); 143.4 (C, C7a); 153.9 (C, C5'). **HRMS** ($C_{20}H_{19}N_3NaO_4S^+$): calculated 420.0988 ($M+H^+$), found 420.0997.

*(Z)-3-(2-cyanovinyl)-N-(2,5-dimethoxyphenyl)-1-methyl-1H-indole-5-sulfonamide (**138**).* Yellow solid. **IR** (KBr): 3249, 2207, 1508, 1167, 646 cm^{-1}. **^{1}H-NMR** (400 MHz, $CDCl_3$): δ 3.57 (3H, s, NCH_3); 3.73 (3H, s, 2'-OCH_3); 3.88 (3H, s, 5'-OCH_3); 5.27 (1H, d, *J* = 12.0 Hz, olefin); 6.50 (1H, dd, *J* = 2.8 and 9.2 Hz, H4'); 6.61 (1H, d, *J* = 9.2 Hz, H3'); 7.11 (1H, bs, NH); 7.17 (1H, d, *J* = 2.8 Hz, H6'); 7.35 (1H, d, *J* = 12.0 Hz, olefin); 7.36 (1H, d, *J* = 8.8 Hz, H7); 7.70 (1H, dd, *J* = 1.6 and 8.8 Hz, H6); 8.19 (1H, d, *J* = 1.6 Hz, H4); 8.28 (1H, s, H2). **^{13}C-NMR** (100 MHz, $CDCl_3$): δ 31.6 (CH_3, NCH_3); 53.6 (CH_3, 5'-OCH_3); 54.0 (CH_3, 2'-OCH_3); 87.4 (CH, C6'); 104.7 (CH, C4'); 107.2 (CH, olefin); 108.1 (CH, C3'); 109.2 (CH, C7); 109.7 (C, CN); 116.7 (CH, C4); 117.0 (C, C3); 119.3 (CH, C6); 124.7 (C, C3a); 129.6 (C, C5); 130.4 (CH, C2); 136.0 (CH, olefin); 136.4 (C, C1'); 141.2 (C, C2'); 151.7 (C, C5'). Quaternary carbon (C7a) not observed. HRMS ($C_{20}H_{19}N_3NaO_4S^+$): calculated 420.0988 ($M+H^+$), found 420.0985.

Preparation of compounds 139 and 140

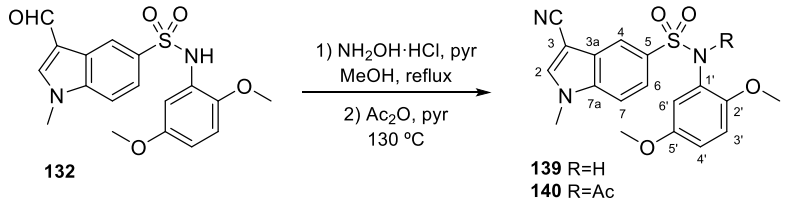

Preparation of compounds **139** and **140** was accomplished following the two-step method **E**. A solution of $NH_2OH{\cdot}HCl$ (270 mg, 3.89 mmol) and **132** (140 mg, 0.37 mmol) in refluxing methanol (25 mL) with a few drops of pyridine was stirred for 24 h. The oximes were then heated at 130 °C in pyridine (25 mL) with acetic anhydride in excess (0.5 mL), obtaining 95 mg after 30 h. Preparative TLC with CH_2Cl_2/methanol 99:1 as eluent gave **139** (29 mg, 0.08 mmol, 28%) and **140** (32 mg, 0.07 mmol, 27%).

*3-Cyano-N-(2,5-dimethoxyphenyl)-1-methyl-1H-indole-5-sulfonamide (**139**).* White solid. **IR** (KBr): 3217, 3108, 2220, 1510, 1331, 1159, 688 cm^{-1}. **^{1}H-NMR** (400 MHz, $CDCl_3$): δ 3.64 (3H, s, NCH_3); 3.74 (3H, s, 2'-OCH_3); 3.86 (3H, s, 5'-OCH_3); 6.50 (1H, dd, *J* = 2.8 and 9.2 Hz, H4'); 6.62 (1H, d, *J* = 9.2 Hz, H3'); 7.16 (1H, bs, NH); 7.17 (1H, d, *J* = 2.8 Hz, H6'); 7.39 (1H, d, *J* = 8.8 Hz, H7); 7.64 (1H, s, H2); 7.77 (1H, dd, *J* = 1.6 and 8.8 Hz, H6); 8.29 (1H, d, *J* = 1.6 Hz, H4). **^{13}C-NMR** (100 MHz, $CDCl_3$): δ 34.0 (CH_3, NCH_3); 55.8 (CH_3, 5'-OCH_3); 56.2 (CH_3, 2'-OCH_3); 87.5 (C, C3); 106.6 (CH, C6'); 109.7 (CH, C4'); 110.8 (CH, C3'); 111.4 (CH, C7); 114.3 (C, CN); 120.3 (CH, C4); 122.6 (CH, C6); 126.6 (C, C5); 127.0 (C, C3a); 133.2 (C, C1'); 137.6 (CH, C2); 137.7 (C, C7a); 143.2 (C, C2'); 153.9 (C, C5'). **HRMS** ($C_{18}H_{17}N_3NaO_4S^+$): calculated 394.0832 ($M+Na^+$), found 394.0837.

*N-((3-cyano-1-methyl-1H-indol-5-yl)sulfonyl)-N-(2,5-dimethoxyphenyl)acetamide (**140**).* White solid. **IR** (KBr): 2219, 1703, 1508, 1356, 1148 cm^{-1}. **^{1}H-NMR** (400 MHz, $CDCl_3$): δ 1.82 (3H, s, Ac); 3.83 (3H, s, NCH_3); 3.84 (3H, s, 2'-OCH_3); 3.92 (3H, s, 5'-OCH_3); 7.01 (3H, m, H3', H4' and H6'); 7.52 (1H, d, *J* = 9.2 Hz, H7); 7.71 (1H, s, H2); 8.22 (1H, dd, *J* = 1.6 and 9.2 Hz, H6); 8.51 (1H, d, *J* = 1.6 Hz, H4). **^{13}C-NMR** (100 MHz, $CDCl_3$): δ 23.9 (CH_3, Ac); 34.0 (CH_3, NCH_3); 55.7 (CH_3, 5'-OCH_3); 55.9 (CH_3, 2'-OCH_3); 87.6 (C, C3); 109.9 (CH, C6'); 112.6 (CH, C3'); 114.5 (C, CN); 117.0 (CH, C4'); 117.4 (CH, C7); 122.1 (CH, C4); 125.3 (C, C5); 125.7 (CH, C6); 126.9 (C, C3a); 133.7 (C, C1'); 137.6 (CH, C2); 138.3 (C, C7a); 150.0 (C, C2'); 153.7 (C, C5'); 170.4 (C, CO). **HRMS** ($C_{20}H_{19}N_3NaO_5S^+$): calculated 436.0938 ($M+Na^+$), found 436.0943.

SYNTHESIS OF TETRAZOLES AND AMIDE PRECURSORS

Synthesis of N-(3,5-dimethoxyphenyl)-4-methoxybenzamide (141)

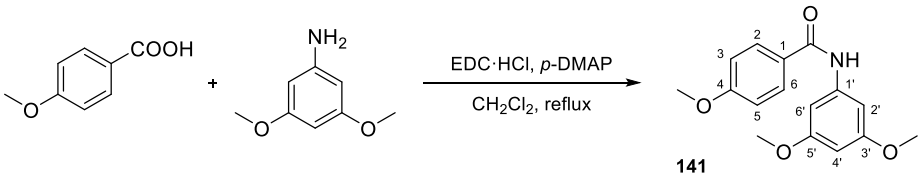

Following procedure **A1**, 3,5-dimethoxyaniline (353 mg, 2.31 mmol) was added to a solution of 4-methoxybenzoic acid (444 mg, 2.92 mmol) mixed with EDC·HCl (845 mg, 4.41 mmol), and *p*-DMAP (187 mg, 1.53 mmol) in 50 mL of refluxing CH_2Cl_2. After 16 h, 551 mg (1.92 mmol, 83%) of **141** were obtained and crystallized in CH_2Cl_2/Hex yielding amide **141** (386 mg, 1.34 mmol, 56%) as white crystals.

*N-(3,5-dimethoxyphenyl)-4-methoxybenzamide (**141**).* White crystals. **Mp** (CH_2Cl_2/Hex): 119.4-120.0 °C. **IR** (KBr): 3311, 1643, 1604, 1454, 1258, 1154 cm^{-1}. **^{1}H-NMR** (400 MHz, $CDCl_3$): δ 3.80 (6H, s, OCH_3); 3.87 (3H, s, OCH_3); 6.26 (1H, t, *J* = 2.0 Hz, H4'); 6.88 (2H, d, *J* = 2.0 Hz, H2' and H6'); 6.97 (2H, d, *J* = 8.8 Hz, H3 and H5); 7.70 (1H, bs, NH); 7.82 (2H, d, *J* = 8.8 Hz, H2 and H6). **^{13}C-NMR** (100 MHz, $CDCl_3$): δ 55.2 (2) (CH_3, OCH_3); 55.3 (CH_3, OCH_3); 96.9 (CH, C4'); 98.9 (2) (CH, C2' and C6'); 113.7 (2) (CH, C3 and C5); 126.9 (C, C1); 129.1 (2) (CH, C2 and C6); 140.3 (C, C1'); 160.9 (2) (C, C3' and C5'); 162.3 (C, C4); 166.0 (C, CO). **HRMS** ($C_{16}H_{17}NNaO_4^+$): calculated 310.1050 ($M+Na^+$), found 310.1053.

Preparation of compounds 142 and 143

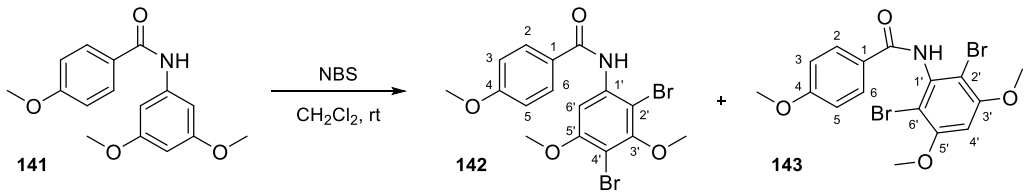

N-bromosuccinimide (455 mg, 2.56 mmol) was added to a solution of **141** (166 mg, 0.58 mmol) in 5 mL of CH_2Cl_2 and stirred for 48 h. Silica gel chromatography using EtOAc/Hex 4:6 as eluent yielded **142** (141 mg, 0.32 mmol, 55%) and **143** (44 mg, 0.10 mmol, 17%), that were crystallized in MeOH/CH_2Cl_2 and CH_2Cl_2/Hex, respectively.

*N-(2,4-dibromo-3,5-dimethoxyphenyl)-4-methoxybenzamide (**142**)*. White crystals. **Mp** (CH_2Cl_2/Hex): 162-163 °C. **IR** (KBr): 3420, 1682, 1607, 1519, 1393, 1247, 1181 cm^{-1}. **^{1}H-NMR** (400 MHz, $CDCl_3$): δ 3.89 (3H, s, 4-OCH_3); 3.90 (3H, 3'-OCH_3); 3.96 (3H, s, 5'OCH_3); 7.02 (2H, d, *J* = 8.8 Hz, H3 and H5); 7.90 (2H, d, *J* = 8.8 Hz, H2 and H6); 8.28 (1H, s, H6'); 8.55 (1H, bs, NH). **^{13}C-NMR** (100 MHz, $CDCl_3$): δ 55.5 (CH_3, 5'-OCH_3); 56.7 (CH_3, 4-OCH_3); 60.6 (CH_3, 3'-OCH_3); 100.3 (C, C4'); 100.6 (CH, C6'); 101.8 (C, C2'); 114.3 (2) (CH, C3 and C5); 126.4 (C, C1); 129.0 (2) (CH, C2 and C6); 136.5 (C, C1'); 154.7 (C, C5'); 156.7 (C, C3'); 163.0 (C, C4); 164.9 (C, CO). **HRMS** ($C_{16}H_{15}Br_2NNaO_4^+$): calculated 465.9260 ($M+Na^+$), found 465.9251.

*N-(2,6-dibromo-3,5-dimethoxyphenyl)-4-methoxybenzamide (**143**).* White crystals. **Mp** (MeOH/CH_2Cl_2): 246-247 °C. **IR** (KBr): 3330, 1645, 1605, 1484, 1349, 1252, 1179 cm^{-1}. **^{1}H-NMR** (400 MHz, $CDCl_3$): δ 3.88 (3H, s, OCH_3); 3.94 (6H, s, OCH_3); 6.52 (1H, s, H4'); 6.98 (2H, d, *J* = 9.2 Hz, H3 and H5); 7.54 (1H, bs, NH); 7.94 (2H, d, *J* = 9.2 Hz, H2 and H6). **^{13}C-NMR** (100 MHz, $CDCl_3$): δ 55.5 (CH_3, OCH_3); 56.7 (2) (CH_3, OCH_3);

96.0 (CH, C4'); 104.1 (2) (C, C2' and C6'); 113.9 (2) (CH, C3 and C5); 126.0 (C, C1); 129.5 (2) (CH, C2 and C6); 136.4 (C, C1'); 156.4 (2) (C, C3' and C5'); 162.8 (C, C4); 177.2 (C, CO). **HRMS** ($C_{16}H_{15}Br_2NNaO_4^+$): calculated 465.9260 ($M+Na^+$), found 465.9245.

Synthesis of 1-(3,5-dimethoxyphenyl)-5-(4-methoxyphenyl)-1H-tetrazole (144)

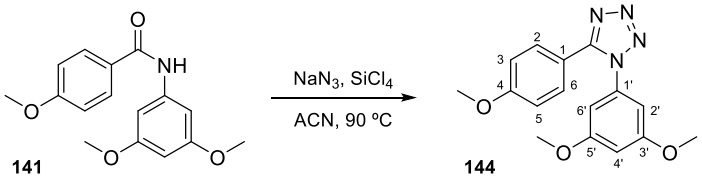

According to procedure **F**, $SiCl_4$ (900 µL, 7.86 mmol) was slowly added to a suspension of amide **141** (270 mg, 0.94 mmol) and sodium azide (499 mg, 7.68 mmol) in 3 mL of ACN in a sealed tube. The mixture was heated at 90 °C for 3 days and once quenched, a white solid corresponding to the tetrazole derivative **144** (229 mg, 0.73 mmol, 78%) was obtained and purified by crystallization in $MeOH/CH_2Cl_2$ (143 mg, 0.46 mmol, 49%).

*1-(3,5-Dimethoxyphenyl)-5-(4-methoxyphenyl)-1H-tetrazole (**144**).* Transparent crystals. **Mp** ($MeOH/CH_2Cl_2$): 150.5-150.7 °C. **IR** (KBr): 1613, 1476, 1261, 1157, 842 cm^{-1}. **^{1}H-NMR** (400 MHz, $CDCl_3$): δ 3.78 (6H, s, OCH_3); 3.84 (3H, s, OCH_3); 6.52 (2H, d, *J* = 2.4 Hz, H2' and H6'); 6.60 (1H, t, *J* = 2.4 Hz, H4'); 6.92 (2H, d, *J* = 9.2 Hz, H3 and H5); 7.57 (2H, d, *J* = 9.2 Hz, H2 and H6). **^{13}C-NMR** (100 MHz, $CDCl_3$): δ 54.6 (CH_3, OCH_3); 54.9 (2) (CH_3, OCH_3); 101.4 (CH, C4'); 103.0 (2) (CH, C2' and C6'); 113.6 (2) (CH, C3 and C5); 114.7 (C, C1); 129.6 (2) (CH, C2 and C6); 135.3 (C, C1'); 152.5 (C, C4); 160.6 (2) (C, C3' and C5'); 161.0 (C, tetrazole). **HRMS** ($C_{16}H_{16}N_4NaO_3^+$): calculated 335.1115 ($M+Na^+$), found 335.1125.

Synthesis of 1-(2-bromo-3,5-dimethoxyphenyl)-5-(4-methoxyphenyl)-1H-tetrazole (145)

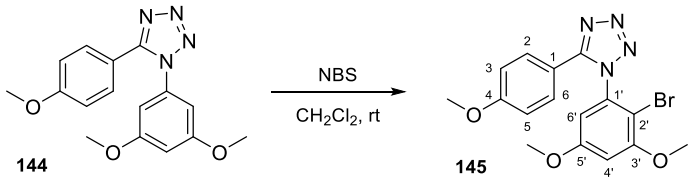

N-bromosuccinimide (44 mg, 0.25 mmol) was added to **144** (22 mg, 0.07 mmol) in 2 mL of CH_2Cl_2 at room temperature. The solution was concentrated under vacuum after 24 h, obtaining **145** by preparative TLC using EtOAc/Hex 1:1 as eluent, with rests of succinimide. Global yield: 22 mg, 0.06 mmol, 78%.

*1-(2-Bromo-3,5-dimethoxyphenyl)-5-(4-methoxyphenyl)-1H-tetrazole (**145**).* Non-isolated product. **^{1}H-NMR** (400 MHz, $CDCl_3$): δ 3.82 (3H, s, 4-OCH_3); 3.83 (3H, s, 5'-OCH_3); 3.94 (3H, s, 3'-OCH_3); 6.63 (1H, d, *J* = 2.8 Hz, H4'); 6.69 (1H, d, *J* = 2.8 Hz, H6'); 6.88 (2H, d, *J* = 8.8 Hz, H3 and H5); 7.56 (2H, d, *J* = 8.8 Hz, H2 and H6). **^{13}C-NMR** (100 MHz, $CDCl_3$): δ 55.4 (CH_3, 4-OCH_3); 56.0 (CH_3, 5'-OCH_3); 56.7 (CH_3, 3'-OCH_3); 101.9 (CH, C4'); 102.6 (C, C2'); 105.1(CH, C6'); 114.5 (2) (CH, C3 and C5); 115.7 (C, C1); 129.8 (2) (CH, C2 and C6); 135.8 (C, C1'); 153.9 (C, C3'); 158.0 (C, C5'); 160.4 (C, C4); 161.9 (C, tetrazole).

Synthesis of 1-(2,6-dibromo-3,5-dimethoxyphenyl)-5-(4-methoxyphenyl)-1H-tetrazole (146)

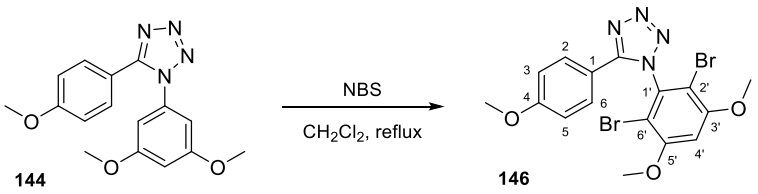

N-bromosuccinimide (43 mg, 0.24 mmol) was added to a solution of **144** (22 mg, 0.07 mmol) in 5 mL of refluxing CH_2Cl_2 and stirred for 24 h. Once rotary evaporated, crystallization in MeOH gave 30 mg (0.06 mmol, 91%) of compound **146**.

*1-(2,6-Dibromo-3,5-dimethoxyphenyl)-5-(4-methoxyphenyl)-1H-tetrazole (**146**).* White crystals. **Mp** (MeOH/CH_2Cl_2): 214-216 °C. **IR** (KBr): 1614, 1598, 1478, 1257 cm^{-1}. **^{1}H-NMR** (400 MHz, $CDCl_3$): δ 3.81 (3H, s, OCH_3); 4.00 (6H, s, OCH_3); 6.71 (1H, s, H4'); 6.88 (2H, d, *J* = 8.8 Hz, H3 and H5); 7.56 (2H, d, *J* = 8.8 Hz, H2 and H6). **^{13}C-NMR** (100 MHz, $CDCl_3$): δ 55.4 (CH_3, OCH_3); 56.9 (2) (CH_3, OCH_3); 98.5 (CH, C4'); 103.6 (2) (C, C2' and C6'); 114.6 (2) (CH, C3 and C5); 115.5 (C, C1); 129.6 (2) (CH, C2 and C6); 135.0 (C, C1'); 154.0 (C, C4); 157.0 (2) (C, C3' and C5'); 162.0 (C, tetrazole). **HRMS** ($C_{16}H_{14}Br_2N_4NaO_3^+$): calculated 490.9325 ($M+Na^+$), found 490.9332.

Synthesis of 1-(2,4-dibromo-3,5-dimethoxyphenyl)-5-(4-methoxyphenyl)-1H-tetrazole (147)

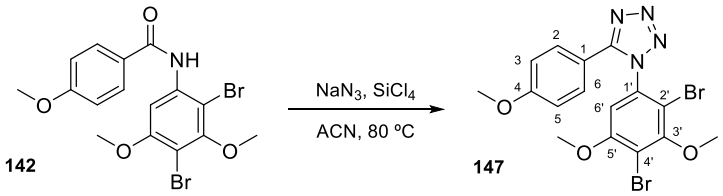

As described in method **F**, $SiCl_4$ (200 µL, 1.75 mmol) was slowly added into a sealed tube containing a mixture of **142** (95 mg, 0.21 mmol) and sodium azide (116 mg, 1.78 mmol) suspended in 2 mL of ACN. The reaction was heated at 80 °C for 5 days, turning white over the time, and gave tetrazole **147** (98 mg, 0.21 mmol, 98%). Preparative TLC with EtOAc/Hex 4:6 as eluent yielded the product (80 mg, 0.17 mmol, 80%) as a white solid.

*1-(2,4-Dibromo-3,5-dimethoxyphenyl)-5-(4-methoxyphenyl)-1H-tetrazole (**147**).* White solid. **IR** (film): 1611, 1578, 1454, 1241, 1105 cm^{-1}. **^{1}H-NMR** (400 MHz, $CDCl_3$): δ 3.75 (3H, s, 4-OCH_3); 3.84 (3H, s, 3'-OCH_3); 3.85 (3H, s, 5'-OCH_3); 6.79 (1H, s, H6'); 6.83 (2H, d, *J* = 8.8 Hz, H3 and H5); 7.47 (2H, d, *J* = 8.8 Hz, H2 and H6). **^{13}C-NMR** (100 MHz, $CDCl_3$): δ 55.4 (CH_3, 4-OCH_3); 57.2 (CH_3, 5'-OCH_3); 60.9 (CH_3, 3'-OCH_3); 107.9 (CH, C6'); 108.9 (C, C2'); 111.6 (C, C4'); 114.6 (2) (CH, C3 and C5); 115.3 (C, C1); 129.7 (2) (CH, C2 and C6); 134.4 (C, C1'); 153.9 (C, C5'); 156.7 (C, C3'); 157.2 (C, C4); 162.1 (C, tetrazole). **HRMS** ($C_{16}H_{14}Br_2N_4NaO_3^+$): calculated 490.9325 ($M+Na^+$), found 490.9314.

Synthesis of 3,5-dimethoxy-N-(4-methoxyphenyl)benzamide (148)

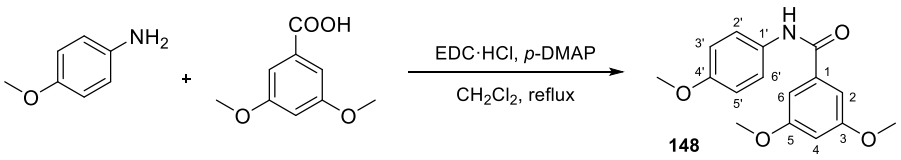

Following method **A1**, the carboxylic acid (426 mg, 2.34 mmol) dissolved in 50 mL of CH_2Cl_2 was mixed with *p*-DMAP (150 mg, 1.23 mmol) and EDC·HCl (673 mg, 3.51 mmol) and heated under reflux. 4-Methoxyaniline (289 mg, 2.35 mmol) was then added to the reaction, giving a brown oily residue (**148**, 520 mg, 1.81 mmol, 77%) after 14 h. Crystallization in acetone yielded 360 mg (1.25 mmol, 54%) of **148** as white crystals.

*3,5-Dimethoxy-N-(4-methoxyphenyl)benzamide (**148**).* White crystals. **Mp** (acetone): 96.9-98.3 °C. **IR** (KBr): 3282, 1648, 1541, 1508, 1245, 1154 cm^{-1}. **^{1}H-NMR** (400 MHz, $CDCl_3$): δ 3.81 (3H, s, OCH_3); 3.84 (6H, s, OCH_3); 6.60 (1H, t, *J* = 2.0 Hz, H4); 6.90 (2H, d, *J* = 8.8 Hz, H3' and H5'); 6.96 (2H, d, *J* = 2.0 Hz, H2 and H6); 7.52 (2H, d, *J* = 8.8 Hz, H2' and H6'); 7.67 (1H, bs, NH). **^{13}C-NMR** (100 MHz, $CDCl_3$): δ 55.2 (2) (CH_3); 55.3 (CH_3); 103.7 (CH, C4); 105.1 (2) (CH, C2 and C6); 113.9 (2) (CH, C3' and C5'); 122.7 (2) (CH, C2' and C6'); 131.2 (C, C1'); 137.0 (C, C1); 156.4 (C, C4'); 160.7 (2) (C, C3 and C5); 166.3 (C, CO). **HRMS** ($C_{16}H_{17}NNaO_4^+$): calculated 310.1050 ($M+Na^+$), found 310.1046.

Synthesis of 2,6-dibromo-3,5-dimethoxy-N-(4-methoxyphenyl)benzamide (149)

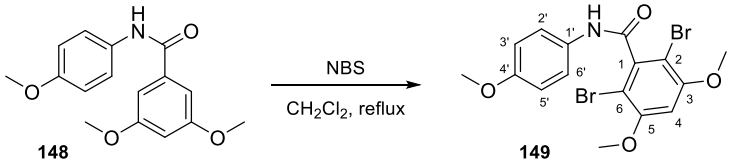

N-bromosuccinimide (152 mg, 0.85 mmol) was added to a solution of **148** (116 mg, 0.40 mmol) in 3 mL of CH_2Cl_2 and heated for 5 min until precipitation occurred. The solid was filtered off and crystallized in MeOH/acetone obtaining **149** with minor impurities. Global yield: 125 mg, 0.34 mmol, 84%.

*2,6-Dibromo-3,5-dimethoxy-N-(4-methoxyphenyl)benzamide (**149**).* Non-isolated product. **^{1}H-NMR** (400 MHz, $CDCl_3$): δ 3.82 (3H, s, OCH_3); 3.94 (6H, s, OCH_3); 6.53 (1H, s, H4); 6.92 (2H, d, *J* = 8.4 Hz, H3' and H5'); 7.55 (2H, d, *J* = 8.4 Hz, H2' and H6'). **^{13}C-NMR** (100 MHz, $CDCl_3$): δ 55.5 (CH_3, OCH_3); 56.8 (2) (CH_3, OCH_3); 97.5 (CH, C4); 100.7 (2) (C, C2 and C6); 114.3 (2) (CH, C3' and C5'); 122.4 (2) (CH, C2' and C6'); 130.2 (C, C1'); 141.2 (C, C1); 156.4 (2) (C, C3 and C5); 157.1 (C, C4'); 164.1 (C, CO).

Synthesis of 5-(3,5-dimethoxyphenyl)-1-(4-methoxyphenyl)-1H-tetrazole (150)

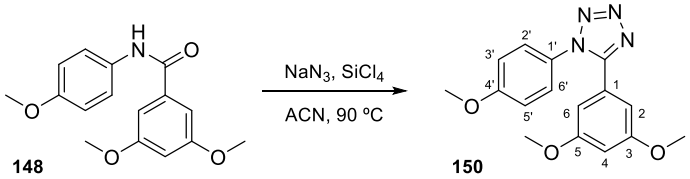

Amide **148** (302 mg, 1.05 mmol) and sodium azide (547 mg, 8.41 mmol) were suspended in 2 mL of ACN in a sealed tube. Following procedure **F**, $SiCl_4$ (1 mL, 8.73 mmol) was added dropwise to that mixture,

heated at 90 °C for 3 days yielding compound **150** (308 mg, 0.99 mmol, 94 %). Crystallization in CH_2Cl_2/Hex gave 156 mg (0.50 mmol, 48%) of **150**.

*5-(3,5-Dimethoxyphenyl)-1-(4-methoxyphenyl)-1H-tetrazole (**150**).* Translucent crystals. **Mp** (CH_2Cl_2/Hex): 116-117 °C. **IR** (KBr): 1602, 1511, 1253, 1156, 842 cm^{-1}. **^{1}H-NMR** (400 MHz, $CDCl_3$): δ 3.71 (6H, s, OCH_3); 3.88 (3H, s, OCH_3); 6.55 (1H, t, *J* = 2.0 Hz, H4); 6.70 (2H, d, *J* = 2.0 Hz, H2 and H6); 7.02 (2H, d, *J* = 8.4 Hz, H3' and H5'); 7.33 (2H, d, *J* = 8.4 Hz, H2' and H6'). **^{13}C-NMR** (100 MHz, $CDCl_3$): δ 54.9 (2) (CH_3, OCH_3); 55.2 (CH_3, OCH_3); 103.0 (CH, C4); 106.0 (2) (CH, C2 and C6); 114.4 (2) (CH, C3' and C5'); 124.6 (C, C1'); 126.3 (2) (CH, C2' and C6'); 126.7 (C, C1); 152.9 (C, C4'); 160.4 (2) (C, C3 and C5). Quaternary carbon (tetrazole) not observed. **HRMS** ($C_{16}H_{16}N_4NaO_3^+$): calculated 335.1115 ($M+Na^+$), found 335.1123.

Preparation of compounds 151 and 152

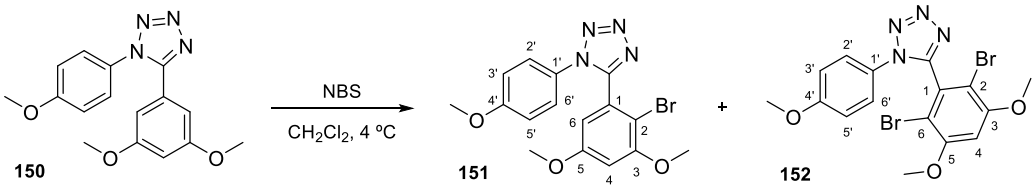

N-bromosuccinimide (261 mg, 1.47 mmol) was progressively added to a solution of **150** (120 mg, 0.38 mmol) in 5 mL of cold CH_2Cl_2, and stirred under N_2 atmosphere for 3 days, washed with brine, dried over anhydrous Na_2SO_4, filtered, and evaporated (**151** with NBS and succinimide). Preparative TLC (EtOAc/Hex 1:1) and crystallization in MeOH/CH_2Cl_2 gave **152** in both cases. Global yield: **152**, 109 mg, 0.23 mmol, 61%.

*5-(2-Bromo-3,5-dimethoxyphenyl)-1-(4-methoxyphenyl)-1H-tetrazole (**151**).* Non-isolated product. **^{1}H-NMR** (400 MHz, $CDCl_3$): δ 3.80 (3H, s, 4'-OCH_3); 3.81 (3H, s, 5-OCH_3); 3.87 (3H, s, 3-OCH_3); 6.60 (2H, s, H4 and H6); 6.88 (2H, d, *J* = 8.4 Hz, H3' and H5'); 7.27 (2H, d, *J* = 8.4 Hz, H2' and H6').

*5-(2,6-Dibromo-3,5-dimethoxyphenyl)-1-(4-methoxyphenyl)-1H-tetrazole (**152**).* Transparent crystals. **Mp** (MeOH/CH_2Cl_2): 229-231 °C. **IR** (KBr): 1607, 1575, 1513, 1431, 1257, 1223 cm^{-1}. **^{1}H-NMR** (400 MHz, $CDCl_3$): δ 3.80 (3H, s, OCH_3); 3.93 (6H, s, OCH_3); 6.62 (1H, s, H4); 6.88 (2H, d, *J* = 9.2 Hz, H3' and H5'); 7.36 (2H, d, *J* = 9.2 Hz, H2' and H6'). **^{13}C-NMR** (100 MHz, $CDCl_3$): δ 55.5 (CH_3, OCH_3); 56.8 (2) (CH_3, OCH_3); 98.9 (CH, C4); 104.7 (2) (C, C2 and C6); 114.6 (2) (CH, C3' and C5'); 125.4 (2) (CH, C2' and C6'); 126.5 (C, C1'); 129.3 (C, C1); 152.9 (C, C4'); 156.5 (2) (C, C3 and C5); 160.7 (C, tetrazole). **HRMS** ($C_{16}H_{14}Br_2N_4NaO_3^+$): calculated 490.9325 ($M+Na^+$), found 490.9325.

Synthesis of N-(3,5-dimethoxyphenyl)-4-nitrobenzamide (153)

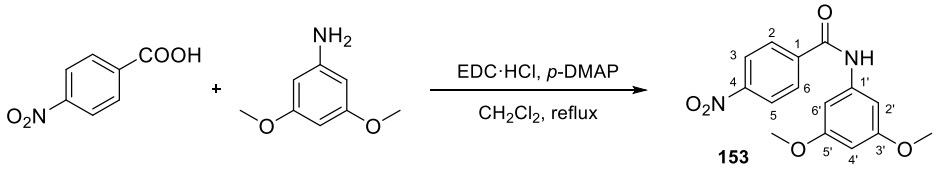

Following procedure **A1**, a solution of 4-nitrobenzoic acid (733 mg, 4.39 mmol), EDC hydrochloride (974 mg, 5.08 mmol), and *p*-DMAP (140 mg, 1.15 mmol) in 50 mL of CH_2Cl_2 was heated under reflux and N_2 atmosphere for 1 h. Subsequently, 3,5-dimethoxyaniline (345 mg, 2.25 mmol) was added and stirred for

3 days, turning yellow over time, obtaining 615 mg. Crystallization in CH_2Cl_2/acetone yielded compound **153** (357 mg, 1.18 mmol, 52%).

*N-(3,5-dimethoxyphenyl)-4-nitrobenzamide (**153**).* Yellow crystals. **Mp** (CH_2Cl_2/acetone): 212-213 °C. **IR** (KBr): 3270, 1652, 1599, 1517, 1290, 1155 cm^{-1}. **^{1}H-NMR** (400 MHz, $CDCl_3$): δ 3.82 (6H, s, OCH_3); 6.32 (1H, t, *J* = 2.4 Hz, H4'); 6.88 (2H, d, *J* = 2.4 Hz, H2' and H6'); 7.76 (1H, bs, NH); 8.03 (2H, d, *J* = 8.8 Hz, H2 and H6); 8.35 (2H, d, *J* = 8.8 Hz, H3 and H5). **^{13}C-NMR** (100 MHz, DMSO-D6): δ 55.6 (2) (CH_3, OCH_3); 96.6 (CH, C4'); 99.1 (2) (CH, C2' and C6'); 124.0 (2) (CH, C3 and C5); 129.6 (2) (CH, C2 and C6); 140.8 (C, C1); 141.0 (C, C1'); 149.6 (C, C4); 160.9 (2) (C, C3' and C5'); 164.4 (C, CO). **HRMS** ($C_{15}H_{14}N_2NaO_5^+$): calculated 325.0795 ($M+Na^+$), found 325.0797.

Synthesis of 4-amino-N-(3,5-dimethoxyphenyl)benzamide (154)

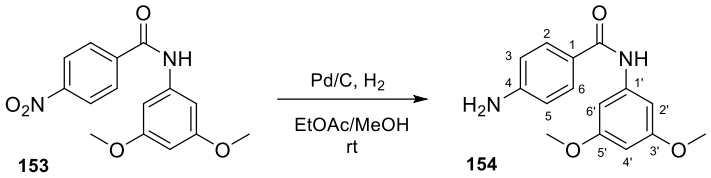

Nitro derivative **153** (260 mg, 0.86 mmol) was reduced via catalytic hydrogenation (method **B**). It was poured into a suspension of Pd/C in 50 mL of EtOAc/MeOH, and vigorously stirred at room temperature under H_2 atmosphere for 24 h, providing 187 mg. Column chromatography in toluene/EtOAc 6:4 followed by crystallization in CH_2Cl_2/Hex gave 112 mg (0.41 mmol, 48%) of aniline **154**.

*4-Amino-N-(3,5-dimethoxyphenyl)benzamide (**154**).* White crystals. **Mp** (CH_2Cl_2/Hex): 159-160 °C. **IR** (KBr): 3406, 3295, 1642, 1607, 1416, 1206, 1153 cm^{-1}. **^{1}H-NMR** (400 MHz, $CDCl_3$): δ 3.81 (6H, s, OCH_3); 4.04 (2H, bs, NH_2); 6.25 (1H, t, *J* = 2.4 Hz, H4'); 6.70 (2H, d, *J* = 8.8 Hz, H3 and H5); 6.88 (2H, d, *J* = 2.4 Hz, H2' and H6'); 7.66 (1H, bs, NH); 7.69 (2H, d, *J* = 8.8 Hz, H2 and H6). **^{13}C-NMR** (100 MHz, $CDCl_3$): δ 55.4 (2) (CH_3, OCH_3); 96.7 (CH, C4'); 98.1 (2) (CH, C2' and C6'); 114.2 (2) (CH, C3 and C5); 124.2 (C, C1); 128.8 (2) (CH, C2 and C6); 140.1 (C, C1'); 150.0 (C, C4); 161.1 (2) (C, C3' and C5'); 165.4 (C, CO). **HRMS** ($C_{15}H_{16}N_2NaO_3^+$): calculated 295.1053 ($M+Na^+$), found 295.1052.

Synthesis of N-(3,5-dimethoxyphenyl)-4-(dimethylamino)benzamide (155)

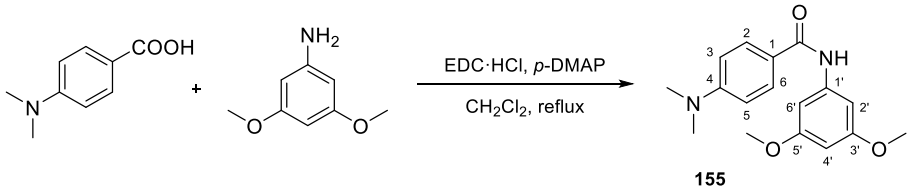

Via **A1** methodology, a mixture of 4-(dimethylamino)benzoic acid (450 mg, 2.72 mmol), EDC·HCl (798 mg, 4.16 mmol), and *p*-DMAP (180 mg, 1.48 mmol) was heated in refluxing CH_2Cl_2 (50 mL). Then, the aniline (375 mg, 2.45 mmol) was added and stirred for one week giving 553 mg (1.84 mmol, 75%) of **155**, which was crystallized in CH_2Cl_2/Hex (468 mg, 1.56 mmol, 64%).

*N-(3,5-dimethoxyphenyl)-4-(dimethylamino)benzamide (**155**).* White crystals. **Mp** (CH_2Cl_2/Hex): 57 °C. **IR** (KBr): 3296, 1640, 1605, 1523, 1285, 1203 cm^{-1}. **^{1}H-NMR** (400 MHz, $CDCl_3$): δ 2.81 (6H, s, NCH_3); 3.57 (6H, s, OCH_3); 6.01 (1H, t, *J* = 2.0 Hz, H4'); 6.48 (2H, d, *J* = 8.8 Hz, H3 and H5); 6.67 (2H, d, *J* = 2.0 Hz, H2' and

H6'); 7.44 (1H, bs, NH); 7.53 (2H, d, *J* = 8.8 Hz, H2 and H6). **^{13}C-NMR** (100 MHz, $CDCl_3$): δ 40.0 (2) (CH_3, NCH_3); 55.2 (2) (CH_3, OCH_3); 96.4 (CH, C4'); 98.0 (2) (CH, C2' and C6'); 111.0 (2) (CH, C3 and C5); 121.1 (C, C1); 128.5 (2) (CH, C2 and C6); 140.3 (C, C1'); 152.4 (C, C4); 160.8 (2) (C, C3' and C5'); 165.6 (C, CO). **HRMS** ($C_{17}H_{20}N_2NaO_3^+$): calculated 323.1366 ($M+Na^+$), found 323.1361.

Synthesis of 4-(1-(3,5-dimethoxyphenyl)-1H-tetrazol-5-yl)-N,N-dimethylaniline (156)

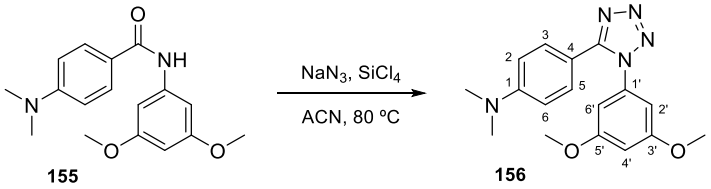

155 156

Following general method **F**, a mixture of **155** (288 mg, 0.96 mmol), NaN_3 (501 mg, 7.71 mmol) and $SiCl_4$ (1 mL, 8.73 mmol) in 3 mL of ACN was heated in a sealed tube at 80 °C for 4 days, obtaining 244 mg (0.75 mmol, 78%) of **156**. Crystallization in CH_2Cl_2/Hex gave 74 mg (0.23 mmol, 24%) of **156**.

*4-(1-(3,5-Dimethoxyphenyl)-1H-tetrazol-5-yl)-N,N-dimethylaniline (**156**).* Grey crystals. **Mp** (CH_2Cl_2/Hex/acetone): 172-175 °C. **IR** (KBr): 1610, 1490, 1205, 1161 cm^{-1}. **^{1}H-NMR** (400 MHz, $CDCl_3$): δ 2.92 (6H, s, NCH_3); 3.70 (6H, s, OCH_3); 6.47 (2H, d, *J* = 1.6 Hz, H2' and H6'); 6.51 (1H, t, *J* = 1.6 Hz, H4'); 6.55 (2H, d, *J* = 8.8 Hz, H2 and H6); 7.41 (2H, d, *J* = 8.8 Hz, H3 and H5). **^{13}C-NMR** (100 MHz, $CDCl_3$): δ 40.0 (2) (CH_3, NCH_3); 55.7 (2) (CH_3, OCH_3); 102.2 (CH, C4'); 104.0 (2) (CH, C2' and C6'); 109.8 (C, C4); 111.5 (2) (CH, C2 and C6); 129.9 (2) (CH, C3 and C5); 136.6 (C, C1'); 151.9 (C, C1); 153.8 (C, tetrazole); 161.4 (2) (C, C3' and C5'). **HRMS** ($C_{17}H_{19}N_5NaO_2^+$): calculated 348.1431 ($M+Na^+$), found 348.1429.

Synthesis of 3,5-dimethoxy-N-(4-nitrophenyl)benzamide (157)

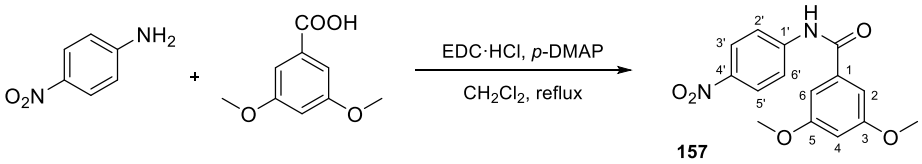

157

Following **A1**, the mixture of 3,5-dimethoxybenzoic acid (450 mg, 2.47 mmol) with EDC hydrochloride (558 mg, 2.91 mmol) and *p*-DMAP (128 mg, 1.05 mmol) was dissolved in 50 mL of CH_2Cl_2 and heated under reflux and N_2 atmosphere for 1 h prior to the addition of the aniline (264 mg, 1.91 mmol). After 9 days, the residue (**157**, 560 mg, 1.85 mmol, 97%) was crystallized in MeOH, giving 313 mg (1.04 mmol, 54%) of **157**.

*3,5-Dimethoxy-N-(4-nitrophenyl)benzamide (**157**).* White crystals. **Mp** (MeOH): 178-179 °C. **IR** (KBr): 3305, 1655, 1595, 1483, 1348, 1157 cm^{-1}. **^{1}H-NMR** (400 MHz, $CDCl_3$): δ 3.86 (6H, s, OCH_3); 6.65 (1H, t, *J* = 2.4 Hz, H4); 6.97 (2H, d, *J* = 2.4 Hz, H2 and H6); 7.83 (2H, d, *J* = 8.8 Hz, H2' and H6'); 8.01 (1H, bs, NH); 8.27 (2H, d, *J* = 8.8 Hz, H3' and H5'). **^{13}C-NMR** (100 MHz, $CDCl_3$): δ 55.6 (2) (CH_3, OCH_3); 104.2 (CH, C4); 105.1 (2) (CH, C2 and C6); 119.4 (2) (CH, C2' and C6'); 125.1 (2) (CH, C3' and C5'); 136.1 (C, C1); 143.6 (C, C1'); 143.7 (C, C4'); 161.2 (2) (C, C3 and C5); 165.7 (C, CO). **HRMS** ($C_{15}H_{14}N_2NaO_5^+$): calculated 325.0795 ($M+Na^+$), found 325.0789.

Synthesis of N-(4-aminophenyl)-3,5-dimethoxybenzamide (158)

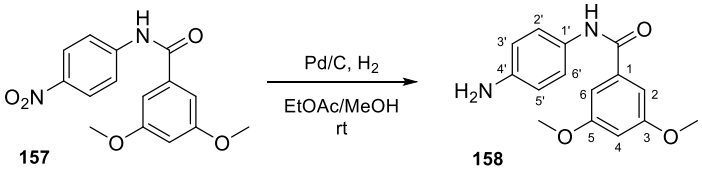

Nitro derivative **157** (498 mg, 1.65 mmol) in EtOAc was added to a suspension of Pd/C in 100 mL of EtOAc/MeOH. According to method **B**, it was vigorously stirred under H_2 atmosphere for 3 days, yielding compound **158** (445 mg, 1.64 mmol, 99%), then crystallized in MeOH (141 mg, 0.52 mmol, 31%).

*N-(4-aminophenyl)-3,5-dimethoxybenzamide (**158**).* Pinkish-orange crystals. **Mp** (MeOH): 161-162 °C. **IR** (KBr): 3291, 1643, 1594, 1514, 1349, 1208, 1156 cm^{-1}. **^{1}H-NMR** (400 MHz, $CDCl_3$): δ 3.64 (2H, bs, NH_2); 3.84 (6H, s, OCH_3); 6.59 (1H, t, *J* = 2.4 Hz, H4); 6.69 (2H, d, *J* = 8.4 Hz, H3' and H5'); 6.95 (2H, d, *J* = 2.4 Hz, H2 and H6); 7.39 (2H, d, *J* = 8.4 Hz, H2' and H6'); 7.60 (1H, bs, NH). **^{13}C-NMR** (100 MHz, $CDCl_3$): δ 55.6 (2) (CH_3, OCH_3); 103.6 (CH, C4); 104.9 (2) (CH, C2 and C6); 115.4 (2) (CH, C3' and C5'); 122.2 (2) (CH, C2' and C6'); 129.2 (C, C1'); 137.5 (C, C1); 143.5 (C, C4'); 160.9 (2) (C, C3 and C5); 165.4 (C, CO). **HRMS** ($C_{15}H_{16}N_2NaO_3^+$): calculated 295.1053 ($M+Na^+$), found 295.1047.

Synthesis of N-(4-(dimethylamino)phenyl)-3,5-dimethoxybenzamide (159)

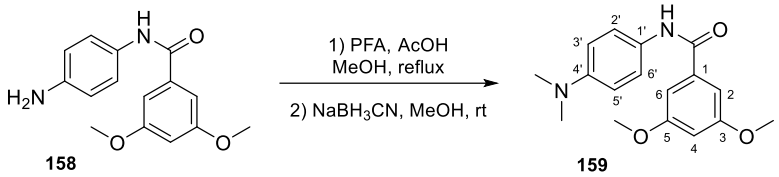

Amide **158** (352 mg, 1.29 mmol) dissolved in a few milliliters of methanol was added to a mixture of acetic acid (1 mL) and paraformaldehyde (388 mg, 12.93 mmol) in 50 mL of methanol, and subsequently heated under reflux for 12 h under N_2 atmosphere. The reaction was warmed to room temperature and $NaBH_3CN$ (165 mg, 2.59 mmol) was added and stirred under N_2 for 12 h. The solvent was rotary eliminated and the residue dissolved in CH_2Cl_2 was washed with 2N HCl. The acidic aqueous layer was neutralized and extracted with CH_2Cl_2, and both organic layers were washed with brine, dried over anhydrous Na_2SO_4, filtered, and evaporated (140 mg). Preparative TLC using Hex/EtOAc (4:6) as eluent gave 10 mg (0.03 mmol, 3%) of **159**. Global yield: 130 mg, 0.43 mmol, 34%.

*N-(4-(dimethylamino)phenyl)-3,5-dimethoxybenzamide (**159**).* Green solid. **IR** (KBr): 3292, 1641, 1592, 1327, 1157 cm^{-1}. **^{1}H-NMR** (400 MHz, $CDCl_3$): δ 2.94 (6H, s, NCH_3); 3.83 (6H, s, OCH_3); 6.59 (1H, t, *J* = 2.0 Hz, H4); 6.73 (2H, d, *J* = 8.8 Hz, H3' and H5'); 6.98 (2H, d, *J* = 2.0 Hz, H2 and H6); 7.47 (2H, d, *J* = 8.8 Hz, H2' and H6'); 7.67 (1H, bs, NH). **^{13}C-NMR** (100 MHz, $CDCl_3$): δ 40.9 (2) (CH_3, NCH_3); 55.6 (2) (CH_3, OCH_3); 103.5 (CH, C4); 104.9 (2) (CH, C2 and C6); 113.1 (2) (CH, C3' and C5'); 121.9 (2) (CH, C2' and C6'); 127.7 (C, C1'); 137.6 (C, C1); 148.1 (C, C4'); 160.9 (2) (C, C3 and C5); 165.2 (C, CO). **HRMS** ($C_{17}H_{20}N_2NaO_3^+$): calculated 323.1366 ($M+Na^+$), found 323.1378.

Synthesis of 2,5-dichloro-N-(4-methoxyphenyl)benzamide (160)

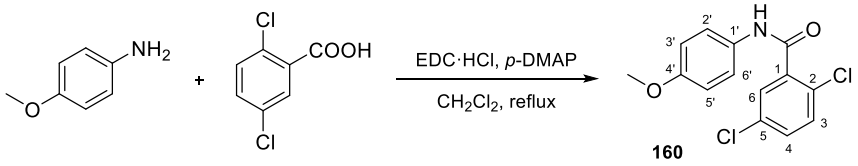

Following method **A1**, the reaction between *p*-anisidine (312 mg, 2.54 mmol) and 2,5-dichlorobenzoic acid (501 mg, 2.54 mmol) in the presence of EDC hydrochloride (748 mg, 3.90 mmol) and *p*-DMAP (163 mg, 1.34 mmol) in 50 mL of refluxing CH_2Cl_2 gave 290 mg after 24 h under N_2 atmosphere. Column chromatography with EtOAc/Hex 2:8 yielded 165 mg (0.56 mmol, 22%) of **160**.

*2,5-Dichloro-N-(4-methoxyphenyl)benzamide (**160**).* White solid. **^{1}H-NMR** (400 MHz, $CDCl_3$): δ 3.82 (3H, s, OCH_3); 6.90 (2H, d, *J* = 9.2 Hz, H3' and H5'); 7.36 (2H, bs, H3 and H4); 7.52 (2H, d, *J* = 9.2 Hz, H2' and H6'); 7.72 (1H, bs, H6); 7.85 (1H, bs, NH). **^{13}C-NMR** (100 MHz, $CDCl_3$): δ 55.5 (CH_3, OCH_3); 114.2 (2) (CH, C3' and C5'); 122.2 (2) (CH, C2' and C6'); 129.0 (C, C1'); 129.9 (CH, C6); 130.4 (C, C5); 131.3 (CH, C4); 131.4 (CH, C3); 133.2 (C, C2); 136.6 (C, C1); 156.9 (C, C4'); 163.2 (C, CO). **HRMS** ($C_{14}H_{11}Cl_2NNaO_2^+$): calculated 318.0059 ($M+Na^+$), found 318.0049.

Synthesis of 2,5-dichloro-N-(4-nitrophenyl)benzamide (161)

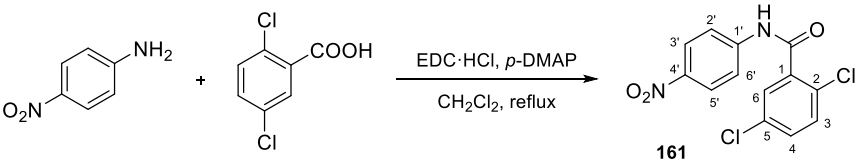

The synthesis of amide **161** was accomplished following method **A1**: a mixture of 4-nitroaniline (580 mg, 4.20 mmol), 2,5-dichlorobenzoic acid (931 mg, 4.73 mmol), EDC hydrochloride (1402 mg, 7.31 mmol), and *p*-DMAP (301 mg, 2.47 mmol) was heated under reflux in 50 mL of CH_2Cl_2 and N_2 atmosphere for 30 h to obtain 1354 mg. Crystallization in CH_2/Cl_2/Hex gave 591 mg (1.90 mmol, 45%) of **161**.

*2,5-Dichloro-N-(4-nitrophenyl)benzamide (**161**).* Yellow crystals. **Mp** (CH_2Cl_2/Hex): 172-173 °C. **IR** (KBr): 3375, 1706, 1611, 1537, 1331, 1227, 1103 cm^{-1}. **^{1}H-NMR** (400 MHz, $CDCl_3$): δ 7.42 (2H, bs, H3 and H4); 7.77 (1H, bs, H6); 7.82 (2H, d, *J* = 9.2 Hz, H2' and H6'); 8.23 (1H, bs, NH); 8.26 (2H, d, *J* = 9.2 Hz, H3' and H5'). **^{13}C-NMR** (100 MHz, $CDCl_3$): δ 119.7 (2) (CH, C2' and C6'); 125.1 (2) (CH, C3' and C5'); 129.0 (C, C5); 130.1 (CH, C6); 131.7 (CH, C4); 132.2 (CH, C3); 133.6 (C, C2); 135.4 (C, C1); 143.1 (C, C4'); 144.0 (C, C1'); 163.6 (C, CO). **HRMS** ($C_{13}H_8Cl_2N_2NaO_3^+$): calculated 332.9804 ($M+Na^+$), found 332.9808.

Synthesis of N-(3,5-dimethoxyphenyl)-1-methyl-1H-indole-5-carboxamide (162)

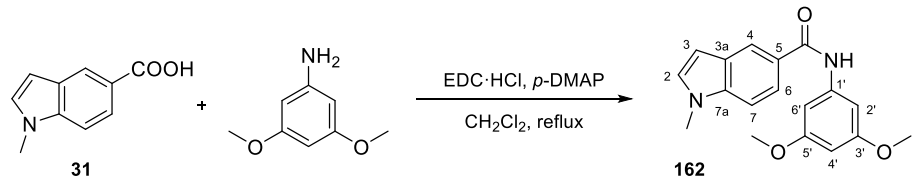

As described in method **A1**, the mixture of carboxylic acid **31** (300 mg, 1.71 mmol), 3,5-dimethoxyaniline (218 mg, 1.42 mmol), EDC·HCl (425 mg, 2.22 mmol), and *p*-DMAP (95 mg, 0.78 mmol) was heated in 50 mL of refluxing CH_2Cl_2 for 6 h under N_2, providing 383 mg of residue, which contained amide **162** with impurities.

*N-(3,5-dimethoxyphenyl)-1-methyl-1H-indole-5-carboxamide (**162**).* Non-isolated product. **^{1}H-NMR** (400 MHz, $CDCl_3$): δ 3.82 (6H, s, OCH_3); 3.84 (3H, s, NCH_3); 6.26 (1H, t, *J* = 2.0 Hz, H4'); 6.59 (1H, d, *J* = 3.2 Hz, H3); 6.94 (2H, d, *J* = 2.0 Hz, H2' and H6'); 7.14 (1H, d, *J* = 3.2 Hz, H2); 7.39 (1H, d, *J* = 8.4 Hz, H7); 7.75 (1H, dd, *J* = 1.6 and 8.4 Hz, H6); 7.85 (1H, bs, NH); 8.15 (1H, d, *J* = 1.6 Hz, H4).

Synthesis of 3,5-dimethoxy-N-(1-methyl-1H-indol-5-yl)benzamide (163)

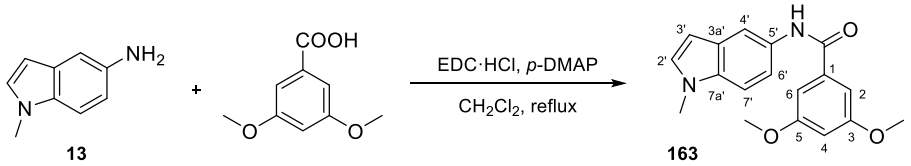

Following conditions **A1**, amine **13** (1471 mg, 10.08 mmol) was added to a mixture of 3,5-dimethoxybenzoic acid (2005 mg, 11.02 mmol), EDC·HCl (2475 mg, 12.91 mmol), and *p*-DMAP (332 mg, 2.72 mmol) in refluxing CH_2Cl_2 (50 mL) and stirred for 4 days. We obtained 2681 mg (8.65 mmol, 86%) of amide **163**, purified by crystallization in acetone (1211 mg, 3.91 mmol, 39%).

*3,5-Dimethoxy-N-(1-methyl-1H-indol-5-yl)benzamide (**163**).* White crystals. **Mp** (acetone): 150.1-150.9 °C. **IR** (KBr): 3285, 1640, 1590, 1492, 1202, 1155 cm^{-1}. **^{1}H-NMR** (400 MHz, $CDCl_3$): δ 3.79 (3H, s, NCH_3); 3.85 (6H, s, OCH_3); 6.47 (1H, d, *J* = 2.8 Hz, H3'); 6.61 (1H, t, *J* = 2.4 Hz, H4); 7.01 (2H, d, *J* = 2.4 Hz, H2 and H6); 7.06 (1H, d, *J* = 2.8 Hz, H2'); 7.29 (1H, d, *J* = 8.4 Hz, H7'); 7.37 (1H, dd, *J* = 2.0 and 8.4 Hz, H6'); 7.80 (1H, bs, NH); 7.93 (1H, d, *J* = 2.0 Hz, H4'). **^{13}C-NMR** (100 MHz, $CDCl_3$): δ 33.9 (CH_3, NCH_3); 55.5 (2) (CH_3, OCH_3); 101.1 (CH, C3'); 103.6 (CH, C4); 105.0 (2) (CH, C2 and C6); 109.3 (CH, C7'); 113.2 (CH, C4'); 116.2 (CH, C6'); 128.5 (C, C3a'); 129.7 (CH, C2'); 130.2 (C, C5'); 134.4 (C, C1); 137.7 (C, C7a'); 160.9 (2) (C, C3 and C5); 165.7 (C, CO). **HRMS** ($C_{18}H_{19}N_2O_3^+$): calculated 311.1390 ($M+H^+$), found 311.1394.

Synthesis of N-(3-bromo-1-methyl-1H-indol-5-yl)-3,5-dimethoxybenzamide (164)

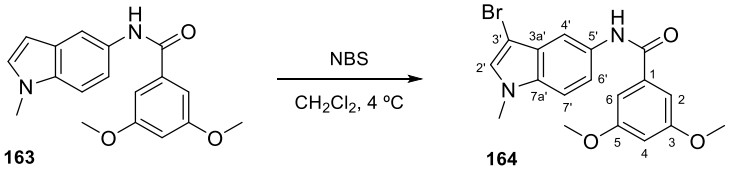

N-bromosuccinimide (128 mg, 0.72 mmol) was slowly added to a solution of **163** (210 mg, 0.68 mmol) in 10 mL of CH_2Cl_2 at 4 °C. The reaction was stirred under N_2 atmosphere for 3 h and washed with brine until neutrality. The organic layer was dried over anhydrous Na_2SO_4, filtered, and the evaporated residue that contained bromo derivative **164** (238 mg, 0.61 mmol, 90%) was purified by crystallization in acetone (63 mg, 0.16 mmol, 24%).

*N-(3-bromo-1-methyl-1H-indol-5-yl)-3,5-dimethoxybenzamide (**164**).* Light brown crystals. **Mp** (acetone): 230-233 °C. **IR** (KBr): 3299, 1642, 1593, 1531, 1349, 1205, 1153 cm^{-1}. **^{1}H-NMR** (400 MHz, $CDCl_3$): δ 3.79 (3H, s, NCH_3); 3.86 (6H, s, OCH_3); 6.62 (1H, t, *J* = 2.0 Hz, H4); 7.02 (2H, d, *J* = 2.0 Hz, H2 and H6); 7.09 (1H,

s, H2'); 7.30 (1H, d, *J* = 8.8 Hz, H7'); 7.54 (1H, dd, *J* = 2.0 and 8.8 Hz, H6'); 7.79 (1H, d, *J* = 2.0 Hz, H4'); 7.87 (1H, bs, NH). **^{13}C-NMR** (100 MHz, $CDCl_3$): δ 33.2 (CH_3, NCH_3); 55.6 (2) (CH_3, OCH_3); 89.3 (C, C3'); 103.7 (CH, C4); 104.9 (2) (CH, C2 and C6); 109.9 (CH, C7'); 111.2 (CH, C4'); 117.1 (CH, C6'); 127.4 (C, C3a'); 128.6 (CH, C2'); 131.0 (C, C5'); 133.9 (C, C1); 137.5 (C, C7a'); 161.0 (2) (C, C3 and C5); 165.5 (C, CO). **HRMS** ($C_{18}H_{17}BrN_2NaO_3^+$): calculated 411.0315 ($M+Na^+$), found 411.0319.

Synthesis of N-(2,3-dibromo-1-methyl-1H-indol-5-yl)-3,5-dimethoxybenzamide (165)

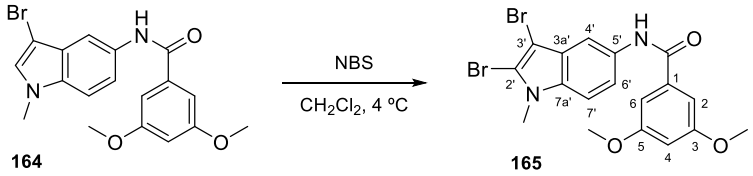

Monobromo derivative **164** (161 mg, 0.41 mmol) was dissolved in CH_2Cl_2 (50 mL) and cooled at 4 °C before adding *N*-bromosuccinimide (79 mg, 0.44 mmol). After 4 days stirring under N_2 atmosphere, the mixture was washed with brine and the organic solvent dried over anhydrous Na_2SO_4, filtered, and concentrated to dryness (218 mg). Silica gel chromatography with EtOAc/Hex 3:7, followed by crystallization in the same solvent mixture gave 180 mg (0.38 mmol, 93%) of **165** as white needles.

*N-(2,3-dibromo-1-methyl-1H-indol-5-yl)-3,5-dimethoxybenzamide (**165**).* White crystals. **Mp** (EtOAc/Hex): 200-201 °C. **IR** (KBr): 3191, 1634, 1600, 1476, 1329, 1155 cm^{-1}. **^{1}H-NMR** (200 MHz, $CDCl_3$): δ 3.78 (3H, s, NCH_3); 3.85 (6H, s, OCH_3); 6.61 (1H, t, *J* = 2.4 Hz, H4); 7.01 (2H, d, *J* = 2.4 Hz, H2 and H6); 7.24 (1H, d, *J* = 8.8 Hz, H7'); 7.48 (1H, dd, *J* = 2.0 and 8.8 Hz, H6'); 7.75 (1H, d, *J* = 2.0 Hz, H4'); 7.92 (1H, bs, NH). **^{13}C-NMR** (100 MHz, $CDCl_3$): δ 32.5 (CH_3, NCH_3); 55.6 (2) (CH_3, OCH_3); 92.6 (C, C3'); 103.8 (CH, C4); 104.9 (2) (CH, C2 and C6); 110.0 (CH, C7'); 110.7 (CH, C4'); 115.7 (C, C2'); 117.2 (CH, C6'); 127.0 (C, C3a'); 131.6 (C, C5'); 133.8 (C, C1); 137.3 (C, C7a'); 161.0 (2) (C, C3 and C5); 165.5 (C, CO). **HRMS** ($C_{18}H_{16}Br_2N_2NaO_3^+$): calculated 488.9420 ($M+Na^+$), found 488.9427.

Synthesis of 5-(5-(3,5-dimethoxyphenyl)-1H-tetrazol-1-yl)-1-methyl-1H-indole (166)

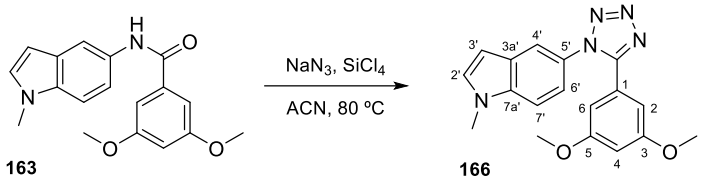

As detailed in method **F**, amide **163** (427 mg, 1.38 mmol) and sodium azide (749 mg, 11.52 mmol) were dissolved in 20 mL of ACN, and subsequently, $SiCl_4$ (1.3 mL, 11.35 mmol) was carefully added dropwise. The reaction was heated at 80 °C for 6 days under N_2 atmosphere and treated as previously described, yielding tetrazole **166** (444 mg, 1.33 mmol, 96%). Crystallization in $MeOH/CH_2Cl_2$ gave 328 mg (0.98 mmol, 71%) of **166**.

*5-(5-(3,5-Dimethoxyphenyl)-1H-tetrazol-1-yl)-1-methyl-1H-indole (**166**).* Dark green crystals. **Mp** ($MeOH/CH_2Cl_2$): 170-171 °C. **IR** (KBr): 1605, 1434, 1195, 1161, 841 cm^{-1}. **^{1}H-NMR** (400 MHz, $CDCl_3$): δ 3.64 (6H, s, OCH_3); 3.87 (3H, s, NCH_3); 6.50 (1H, t, *J* = 2.4 Hz, H4); 6.55 (1H, d, *J* = 3.2 Hz, H3'); 6.73 (2H, d, *J* = 2.4 Hz, H2 and H6); 7.17 (1H, dd, *J* = 2.0 and 8.8 Hz, H6'); 7.19 (1H, d, *J* = 3.2 Hz, H2'); 7.41 (1H, d, *J* = 9.2 Hz, H7'); 7.66 (1H, d, *J* = 2.0 Hz, H4'). **^{13}C-NMR** (100 MHz, $CDCl_3$): δ 33.2 (CH_3, NCH_3); 55.4 (2) (CH_3, OCH_3);

101.2 (CH, C4); 103.5 (CH, C3'); 106.8 (2) (CH, C2 and C6); 110.1 (CH, C7'); 118.4 (CH, C6'); 118.8 (CH, C4'); 125.5 (C, C5'); 126.7 (C, C3a'); 128.5 (C, C1); 131.3 (CH, C2'); 136.9 (C, C7a'); 153.7 (C, tetrazole); 160.8 (2) (C, C3 and C5). **HRMS** ($C_{18}H_{17}N_5NaO_2^+$): calculated 358.1274 ($M+Na^+$), found 358.1267.

Synthesis of 3-bromo-5-(5-(3,5-dimethoxyphenyl)-1H-tetrazol-1-yl)-1-methyl-1H-indole (167)

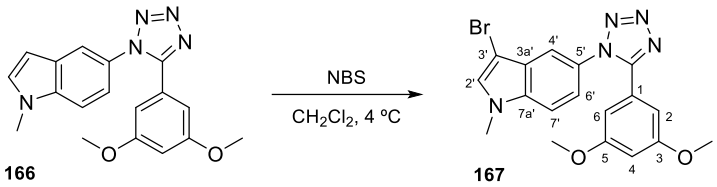

N-bromosuccinimide (62 mg, 0.35 mmol) was added to a solution of tetrazole derivative **166** (105 mg, 0.31 mmol) in 5 mL of CH_2Cl_2 at 4 °C. The reaction was stirred under N_2 atmosphere for 16 h and evaporated. Crystallization in CH_2Cl_2 gave 12 mg of succinimide, and the mother liquors (140 mg) were subjected to preparative TLC (EtOAc/toluene 4:6) yielding 98 mg (0.24 mmol, 76%) of bromo derivative **167**, then crystallized in MeOH/CH_2Cl_2 (74 mg, 0.18 mmol, 57%).

*3-Bromo-5-(5-(3,5-dimethoxyphenyl)-1H-tetrazol-1-yl)-1-methyl-1H-indole (**167**).* Yellow crystals. **Mp** (MeOH/CH_2Cl_2): 156-157 °C. **IR** (KBr): 1617, 1594, 1498, 1318, 1206, 1167 cm^{-1}. **^{1}H-NMR** (400 MHz, $CDCl_3$): δ 3.67 (6H, s, OCH_3); 3.86 (3H, s, NCH_3); 6.52 (1H, t, *J* = 2.4 Hz, H4); 6.72 (2H, d, *J* = 2.4 Hz, H2 and H6); 7.18 (1H, dd, *J* = 2.0 and 8.8 Hz, H6'); 7.23 (1H, s, H2'); 7.46 (1H, d, *J* = 8.8 Hz, H7'); 7.68 (1H, d, *J* = 2.0 Hz, H4'). **^{13}C-NMR** (100 MHz, $CDCl_3$): δ 34.1 (CH_3, NCH_3); 56.1 (2) (CH_3, OCH_3); 90.7 (C, C3'); 104.1 (CH, C4); 107.5 (2) (CH, C2 and C6); 111.4 (CH, C7'); 117.7 (CH, C6'); 120.6 (CH, C4'); 125.9 (C, C5'); 128.1 (C, C3a'); 128.2 (C, C1); 131.0 (CH, C2'); 137.1 (C, C7a'); 154.4 (C, tetrazole); 161.5 (2) (C, C3 and C5). **HRMS** ($C_{18}H_{16}BrN_5NaO_2^+$): calculated 436.0380 ($M+Na^+$), found 436.0380.

Synthesis of 2,3-dibromo-5-(5-(2-bromo-3,5-dimethoxyphenyl)-1H-tetrazol-1-yl)-1-methyl-1H-indole (168)

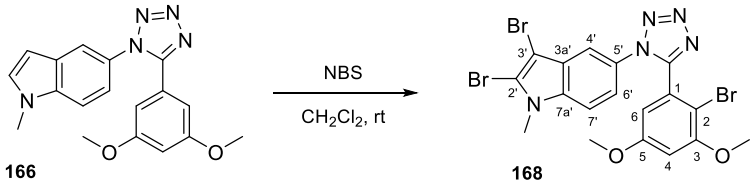

N-bromosuccinimide (115 mg, 0.65 mmol) was added to a solution of **166** (66 mg, 0.20 mmol) in 2 mL of CH_2Cl_2 and stirred for 5 h. After evaporating the solvent, the crude residue was crystallized in MeOH/CH_2Cl_2 to obtain tribromo derivative **168** (57 mg, 0.10 mmol, 51%).

*2,3-Dibromo-5-(5-(2-bromo-3,5-dimethoxyphenyl)-1H-tetrazol-1-yl)-1-methyl-1H-indole (**168**)*. Brown crystals. **Mp** (MeOH/CH_2Cl_2): 229-230 °C. **IR** (KBr): 1584, 1482, 1318, 1217, 1088 cm^{-1}. **^{1}H-NMR** (400 MHz, $CDCl_3$): δ 3.81 (3H, s, NCH_3); 3.82 (3H, s, 5-OCH_3); 3.84 (3H, s, 3-OCH_3); 6.59 (1H, d, *J* = 2.4 Hz, H4); 6.66 (1H, d, *J* = 2.4 Hz, H6); 7.21 (1H, dd, *J* = 2.0; 8.8 Hz, H6'); 7.29 (1H, d, *J* = 8.8 Hz, H7'); 7.51 (1H, d, *J* = 2.0 Hz, H4'). **^{13}C-NMR** (100 MHz, $CDCl_3$): δ 32.7 (CH_3, NCH_3); 55.9 (CH_3, 3-OCH_3); 56.4 (CH_3, 5-OCH_3); 93.4 (C, C3'); 102.2 (CH, C4); 104.1 (C, C2); 107.6 (CH, C6); 110.6 (CH, C7'); 114.7 (CH, C6'); 117.5 (C, C2'); 118.6 (CH, C4'); 126.9 (C, C5'); 127.8 (C, C3a'); 128.0 (C, C1); 136.2 (C, C7a'); 153.4 (C, tetrazole); 157.3 (C, C3); 160.1 (C, C5). **HRMS** ($C_{18}H_{14}Br_3N_5NaO_2^+$): calculated 591.8590 ($M+Na^+$), found 591.8615.

Synthesis of 5-(5-(3,5-dimethoxyphenyl)-1H-tetrazol-1-yl)-1-methyl-1H-indole-3-carbaldehyde (169)

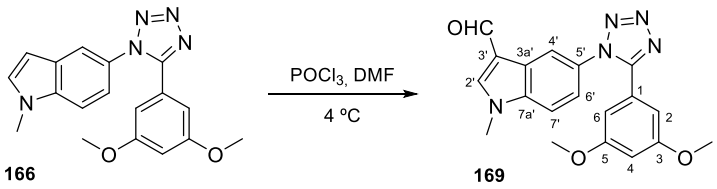

Compound **169** was synthesized by Vilsmeier-Haack reaction (method **D**). A mixture of $POCl_3$ (656 µL, 7.17 mmol) in 0.8 mL of dry DMF at 4 °C was stirred for 30 min and poured into a solution of indole derivative **166** (335 mg, 1.00 mmol) in 4 mL of dry DMF in ice bath and stirred for 2 h. The precipitate was filtered (**169**, 272 mg, 0.75 mmol, 75%) and crystallized in MeOH/CH_2Cl_2 (181 mg, 0.50 mmol, 50%).

*5-(5-(3,5-Dimethoxyphenyl)-1H-tetrazol-1-yl)-1-methyl-1H-indole-3-carbaldehyde (**169**).* White crystals. **Mp** (MeOH/CH_2Cl_2): 200-201 °C. **IR** (KBr): 1656, 1599, 1491, 1369, 1206, 1161 cm^{-1}. **^{1}H-NMR** (400 MHz, $CDCl_3$): δ 3.67 (6H, s, OCH_3); 3.97 (3H, s, NCH_3); 6.50 (1H, t, *J* = 2.4 Hz, H4); 6.70 (2H, d, *J* = 2.4 Hz, H2 and H6); 7.32 (1H, dd, *J* = 2.0 and 8.4 Hz, H6'); 7.46 (1H, d, *J* = 8.4 Hz, H7'); 7.83 (1H, s, H2'); 8.42 (1H, d, *J* = 2.0 Hz, H4'); 9.98 (1H, s, CHO). **^{13}C-NMR** (100 MHz, $CDCl_3$): δ 34.1 (CH_3, NCH_3); 55.5 (2) (CH_3, OCH_3); 103.4 (CH, C4); 107.0 (2) (CH, C2 and C6); 111.1 (CH, C7'); 118.3 (C, C3'); 119.8 (CH, C6'); 121.4 (CH, C4'); 125.1 (C, C5'); 125.5 (C, C3a'); 129.8 (C, C1); 138.0 (C, C7a'); 140.8 (CH, C2'); 153.8 (C, tetrazole); 160.9 (2) (C, C3 and C5); 184.1 (CH, CHO). **HRMS** ($C_{19}H_{17}N_5NaO_3^+$): calculated 386.1224 ($M+Na^+$), found 386.1223.

Synthesis of 5-(5-(3,5-Dimethoxyphenyl)-1H-tetrazol-1-yl)-1-methyl-1H-indole-3-carbonitrile (170)

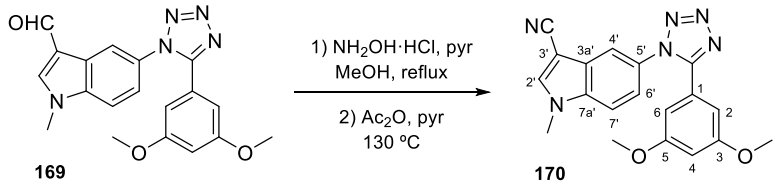

Following the two-step procedure **E**, a solution of aldehyde **169** (173 mg, 0.48 mmol) and $NH_2OH{\cdot}HCl$ (333 mg, 4.79 mmol) was heated under reflux in 25 mL of MeOH with a few drops of pyridine for 2 days. The mixture of oximes was heated at 130 °C in 25 mL of pyridine and 1 mL of acetic anhydride under N_2 atmosphere for 72 h, then processed as described to obtain 66 mg. Preparative TLC using EtOAc/toluene 1:1 as eluent yielded **170** (31 mg, 0.09 mmol, 18%).

*5-(5-(3,5-Dimethoxyphenyl)-1H-tetrazol-1-yl)-1-methyl-1H-indole-3-carbonitrile (**170**).* Yellow solid. **IR** (KBr): 2219, 1599, 1457, 1211, 1163, 1067 cm^{-1}. **^{1}H-NMR** (400 MHz, $CDCl_3$): δ 3.67 (6H, s, OCH_3); 3.95 (3H, s, NCH_3); 6.52 (1H, t, *J* = 2.0 Hz, H4); 6.55 (2H, d, *J* = 2.0 Hz, H2 and H6); 7.31 (1H, dd, *J* = 2.0 and 8.8 Hz, H6'); 7.52 (1H, d, *J* = 8.8 Hz, H7'); 7.73 (1H, s, H2'); 7.81 (1H, d, *J* = 2.0 Hz, H4'). **^{13}C-NMR** (100 MHz, $CDCl_3$): δ 34.1 (CH_3, NCH_3); 55.5 (2) (CH_3, OCH_3); 86.8 (C, C3'); 103.3 (CH, C4); 107.0 (2) (CH, C2 and C6); 111.8 (CH, C7'); 114.5 (C, CN); 117.3 (CH, C6'); 121.3 (CH, C4'); 124.9 (C, C5'); 127.9 (C, C3a'); 129.2 (C, C1); 136.2 (C, C7a'); 137.9 (CH, C2'); 153.8 (C, tetrazole); 161.0 (2) (C, C3 and C5). **HRMS** ($C_{19}H_{17}N_6O_2^+$): calculated 361.1408 ($M+H^+$), found 361.1403.

Preparation of compounds 171-190

Compounds **171-190** were synthesized by Sara del Mazo as part of her Master's thesis, and Dr. Pilar Puebla at the Department of Pharmaceutical Sciences (University of Salamanca). Synthetic procedures and characterization of the compounds are available in the thesis entitled "New antimitotic compounds based on natural products" defended in July 2017.[521]

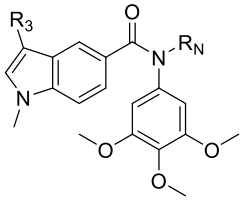

171 R_3=H; R_N=H
172 R_3=H; R_N=Me
173 R_3=CHO; R_N=H

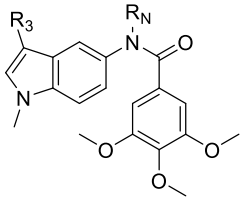

174 R_3=H; R_N=H
175 R_3=H; R_N=Me
176 R_3=CHO; R_N=H
177 R_3=CN; R_N=H

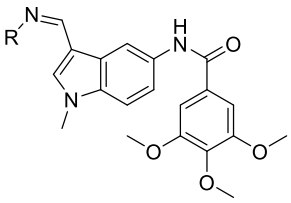

178 R=NMe_2
179 R=NHPh
180 R=NH-imidazol-2-yl

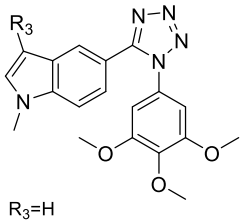

181 R_3=H
182 R_3=Cl
183 R_3=CHO
184 R_3=CN
185 R=$CHNNMe_2$

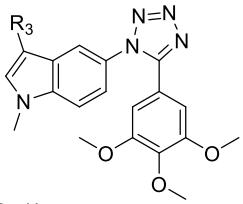

186 R_3=H
187 R_3=$CONH_2$
188 R_3=CHO
189 R_3=CN

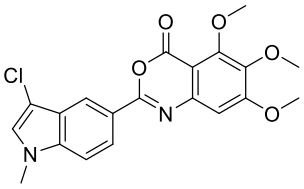

190

SYNTHESIS OF AMIDES, UREAS, AND CARBAMATES

Synthesis of N-(2-aminophenyl)-2,3,4-trimethoxybenzamide (191)

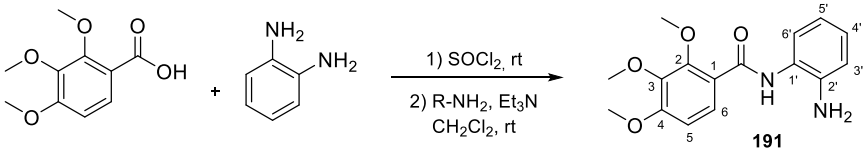

191

Following method **A2**, $SOCl_2$ (0.6 mL) was added dropwise into a sealed tube containing 294 mg (1.39 mmol) of 2,3,4-trimethoxybenzoic acid. After 4 h at room temperature, the acyl chloride was poured drop by drop dissolved in CH_2Cl_2 to a mixture of the amine (283 mg, 1.37 mmol) and triethylamine (100 µL) in 25 mL of CH_2Cl_2, obtaining 266 mg after 3 days. Crystallization in EtOH gave amide **191**. Global yield: 205 mg, 0.68 mmol, 49%.

*N-(2-aminophenyl)-2,3,4-trimethoxybenzamide (**191**).* Yellowish-brown crystals. **Mp** (EtOH): 104.3-105.5 °C. **IR** (KBr): 3366, 3311, 1663, 1535, 1455, 1280, 1092 cm^{-1}. **^{1}H-NMR** (400 MHz, $CDCl_3$): δ 3.88 (3H, s, 4-OCH_3); 3.91 (3H, s, 3-OCH_3); 4.08 (3H, s, 2-OCH_3); 6.80 (1H, d, *J* = 8.8 Hz, H5); 6.81 (1H, td, *J* = 1.6, 7.6 and 8.0 Hz, H5'); 6.84 (1H, dd, *J* = 1.6 and 7.2 Hz, H3'); 7.04 (1H, td, *J* = 1.6, 7.2 and 8.0 Hz, H4'); 7.37 (1H, dd, *J* = 1.6 and 7.6 Hz, H6'); 7.99 (1H, d, *J* = 8.8 Hz, H6); 9.77 (1H, bs, NH). **^{13}C-NMR** (100 MHz, $CDCl_3$): δ 56.0 (CH_3, 4-OCH_3); 61.0 (CH_3, 3-OCH_3); 61.8 (CH_3, 2-OCH_3); 107.6 (CH, C5); 118.1 (CH, C3'); 118.4 (C, C1); 119.5

(CH, C5'); 125.0 (CH, C6); 126.7 (CH, C4'); 127.1 (CH, C6'); 140.4 (C, C3); 141.7 (C, C2'); 152.4 (C, C2); 156.9 (C, C4); 163.1 (C, CO). Quaternary carbon (C1') not observed. **HRMS** ($C_{16}H_{19}N_2O_4^+$): calculated 303.1339 ($M+H^+$), found 303.1336.

Synthesis of N-(2-acetamidophenyl)-2,3,4-trimethoxybenzamide (192)

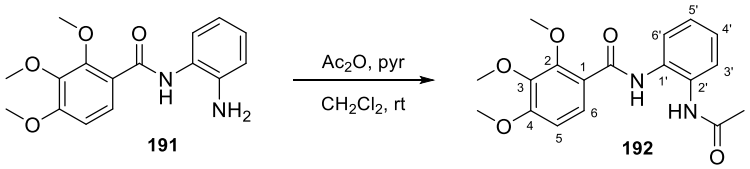

Acetic anhydride (90 µL, 0.95 mmol) was added to a solution of **191** (237 mg, 0.78 mmol) in 3 mL of CH_2Cl_2 with 1 mL of pyridine and stirred at room temperature under N_2 for 36 h, adding then 90 µL (0.95 mmol) of acetic anhydride. Three days later, the reaction mixture was poured into cold water and washed with 2N HCl, 5% $NaHCO_3$ and brine. The organic layer was dried over anhydrous Na_2SO_4, filtered, and evaporated to dryness (89 mg). Preparative TLC in EtOAc/CH_2Cl_2 1:1 gave 44 mg (0.13 mmol, 16%) of **192**.

*N-(2-acetamidophenyl)-2,3,4-trimethoxybenzamide (**192**).* Yellow oil. **^{1}H-NMR** (400 MHz, $CDCl_3$): δ 2.14 (3H, s, Ac); 3.90 (3H, s, 4-OCH_3); 3.94 (3H, s, 3-OCH_3); 4.09 (3H, s, 2-OCH_3); 6.83 (1H, d, *J* = 8.8 Hz, H5); 7.18 (1H, td, *J* = 1.2, 7.2 and 8.0 Hz, H5'); 7.29 (2H, m, H3' and H4'); 7.78 (1H, bd, *J* = 8.0 Hz, H6'); 7.99 (1H, d, *J* = 8.8 Hz, H6); 8.67 (1H, bs, NH, Ac); 10.06 (1H, bs, NH). **^{13}C-NMR** (100 MHz, $CDCl_3$): δ 23.9 (CH_3, Ac); 56.1 (CH_3, 4-OCH_3); 60.9 (CH_3, 3-OCH_3); 62.0 (CH_3, 2-OCH_3); 107.6 (CH, C5); 117.9 (C, C1); 124.5 (CH, C6); 125.9 (CH, C3'*); 126.1 (CH, C5'*); 126.2 (CH, C4'); 127.0 (CH, C6'); 130.6 (C, C2'); 130.9 (C, C1'); 141.7 (C, C3); 152.6 (C, C2); 157.2 (C, C4); 164.0 (C, CO); 169.3 (C, CO, Ac). *Interchangeable signals.

Preparation of compounds 193 and 194

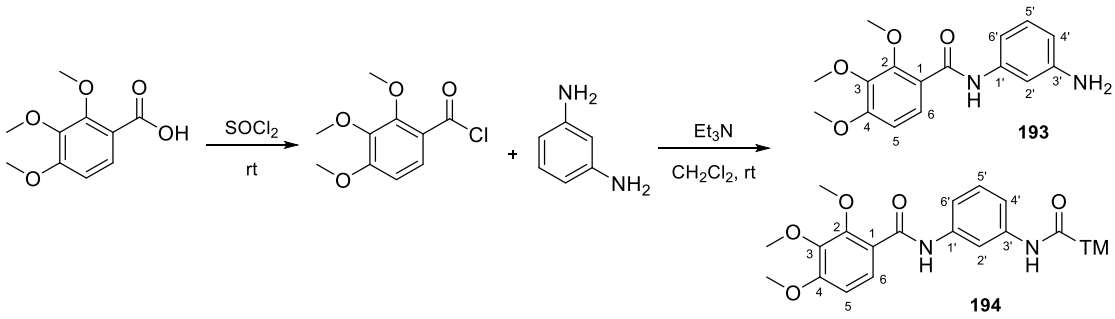

Following procedure **A2**, 2,3,4-trimethoxybenzoic acid (910 mg, 4.29 mmol) was converted into the acyl chloride in 24 h by treatment with $SOCl_2$ (1.2 mL). It was subsequently poured into a solution of *m*-phenylenediamine (685 mg, 6.34 mmol) in 125 mL of CH_2Cl_2 with 0.5 mL of triethylamine. The reaction turned yellow. After 15 h, it was washed with 1N HCl, 5% $NaHCO_3$, and brine, obtaining 606 mg of a 2:1 mixture of **193** and **194**. Crystallization in MeOH gave 99 mg (0.20 mmol, 9%) of **194**. Global yields: **193** (340 mg, 1.13 mmol, 26%) and **194** (238 mg, 0.48 mmol, 22%).

*N-(3-aminophenyl)-2,3,4-trimethoxybenzamide (**193**).* Non-isolated product. **^{1}H-NMR** (400 MHz, $CDCl_3$): δ 3.92 (3H, s, 4-OCH_3); 3.94 (3H, s, 3-OCH_3); 4.04 (3H, s, 2-OCH_3); 6.46 (1H, bd, *J* = 8.0 Hz, H4'); 6.84 (2H, m, H5 and H6'); 7.11 (1H, t, *J* = 8.0 Hz, H5'); 7.38 (1H, bs, H2'); 7.97 (1H, d, *J* = 9.2 Hz, H6); 9.89 (1H, bs, NH).

*N,N'-(1,3-phenylene)bis(2,3,4-trimethoxybenzamide) (**194**).* Grey crystals. **Mp** (MeOH): 150.2-151.1 °C. **IR** (KBr): 3339, 3291, 1667, 1596, 1489, 1284, 1089 cm^{-1}. **^{1}H-NMR** (400 MHz, $CDCl_3$): δ 3.87 (6H, s, 4-OCH_3 [bis]); 3.90 (6H, s, 3-OCH_3 [bis]); 4.05 (6H, s, 2-OCH_3 [bis]); 6.80 (2H, d, *J* = 8.8 Hz, H5 [bis]); 7.32 (1H, t, *J* = 8.0 Hz, H5'); 7.47 (2H, dd, *J* = 2.0 and 8.0 Hz, H4' and H6'); 7.96 (2H, d, *J* = 8.8 Hz, H6 [bis]); 8.11 (1H, t, *J* = 2.0 Hz, H2'); 10.00 (2H, bs, NH). **^{1}H-NMR** (100 MHz, $CDCl_3$): δ 56.1 (6H, s, 4-OCH_3 [bis]); 61.1 (6H, s, 3-OCH_3 [bis]); 62.0 (6H, s, 2-OCH_3 [bis]); 107.8 (2) (CH, C5 [bis]); 111.7 (CH, C2'); 115.7 (2) (CH, C4' and C6'); 118.9 (2) (C, C1 [bis]); 126.9 (2) (CH, C6 [bis]); 129.5 (CH, C5'); 139.1 (2) (C, C1' and C3'); 141.7 (2) (C, C3 [bis]); 152.2 (2) (C, C2 [bis]); 156.8 (2) (C, C4 [bis]); 162.9 (2) (C, CO [bis]). **HRMS** ($C_{26}H_{29}N_2O_8^+$): calculated 497.1918 ($M+H^+$), found 497.1918.

Synthesis of N-(4-aminophenyl)-2,3,4-trimethoxybenzamide (195)

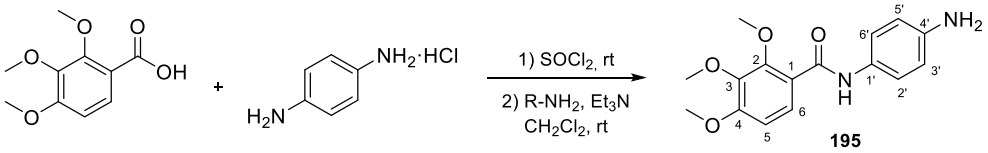

Following general methodology **A2**, the 9-h reaction at room temperature between $SOCl_2$ (1.5 mL) and 2,3,4-trimethoxybenzoic acid (1335 mg, 6.29 mmol) gave the acyl chloride. It was added to a solution of *p*-phenylenediamine hydrochloride (1726 mg, 9.53 mmol) in CH_2Cl_2 (125 mL) with triethylamine (10 mL), providing 1189 mg after 14 h. Flash chromatography with CH_2Cl_2/MeOH 98:2 gave 1034 mg (3.42 mmol, 54%) of **195**. It crystallized into dark red crystals in MeOH.

*N-(4-aminophenyl)-2,3,4-trimethoxybenzamide (**195**).* Dark red crystals. **^{1}H-NMR** (400 MHz, $CDCl_3$): δ 3.61 (2H, bs, NH_2); 3.90 (3H, s, 4-OCH_3); 3.92 (3H, s, 3-OCH_3); 4.04 (3H, s, 2-OCH_3); 6.70 (2H, d, *J* = 8.8 Hz, H3' and H5'); 6.81 (1H, d, *J* = 8.8 Hz, H5); 7.46 (2H, d, *J* = 8.8 Hz, H2' and H6'); 7.97 (1H, d, *J* = 8.8 Hz, H6); 9.76 (1H, bs, NH).

Synthesis of 2,3,4-trimethoxy-N-(4-(methylamino)phenyl)benzamide (196)

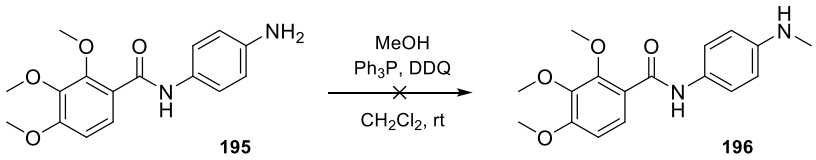

Compound **195** (338 mg, 1.12 mmol) was dissolved in 10 mL of CH_2Cl_2 with 302 mg (1.33 mmol) of DDQ and 330 mg (1.26 mmol) of triphenylphosphine.[522] Methanol (80 µL, 1.98 mmol) was added and stirred at room temperature under N_2. No progress was observed.

Synthesis of N-(4-acetamidophenyl)-2,3,4-trimethoxybenzamide (197)

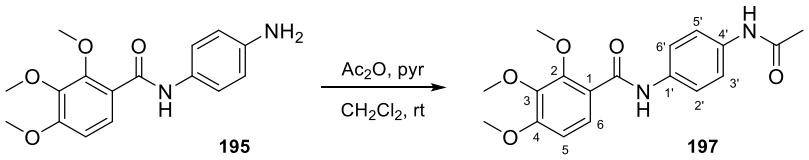

The mixture of acetic anhydride (120 µL, 1.27 mmol) and **195** (300 mg, 0.99 mmol) in 1 mL of pyridine and 2 mL of CH_2Cl_2 was stirred under N_2 at room temperature. Three hours later, it was poured into iced water, washed with 2N HCl, 5% $NaHCO_3$, and brine. The organic layer was dried over anhydrous Na_2SO_4, filtered, and evaporated (319 mg). Crystallization in MeOH or EtOH gave **197**. Global yield: 247 mg, 0.72 mmol, 72%.

*N-(4-acetamidophenyl)-2,3,4-trimethoxybenzamide (**197**).* Light brown crystals. **Mp** (EtOH): 176-177 °C. **^{1}H-NMR** (400 MHz, $CDCl_3$): δ 2.18 (3H, s, Ac); 3.91 (3H, s, 4-OCH_3); 3.94 (3H, s, 3-OCH_3); 4.07 (3H, s, 2-OCH_3); 6.83 (1H, d, *J* = 9.2 Hz, H5); 7.25 (1H, bs, NH); 7.49 (2H, d, *J* = 8.4 Hz, H2' and H6'); 7.64 (2H, d, *J* = 8.4 Hz, H3' and H5'); 7.98 (1H, d, *J* = 9.2 Hz, H6); 9.97 (1H, bs, NH). **^{13}C-NMR** (100 MHz, $CDCl_3$): δ 24.3 (CH_3, Ac); 56.1 (CH_3, 4-OCH_3); 61.0 (CH_3, 3-OCH_3); 62.0 (CH_3, 2-OCH_3); 107.8 (CH, C5); 118.7 (C, C1); 120.8 (2) (CH, C3' and C5'); 121.0 (2) (CH, C2' and C6'); 126.8 (CH, C6); 134.1 (C, C1'); 134.6 (C, C4'); 141.8 (C, C3); 152.2 (C, C2); 156.8 (C, C4); 162.9 (C, CO); 168.8 (C, CO, Ac). **HRMS** ($C_{18}H_{21}N_2O_5^+$): calculated 345.1445 ($M+H^+$), found 345.1450.

Synthesis of 2,3,4-trimethoxy-N-(4-(3-phenylureido)phenyl)benzamide (198)

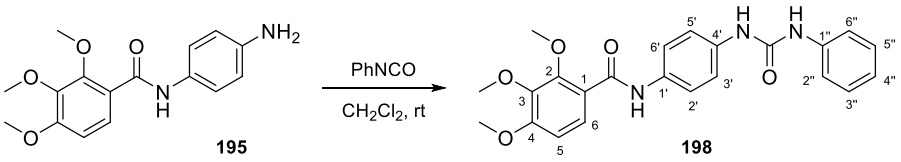

Phenyl isocyanate (110 µL, 1.01 mmol) was added to a solution of **195** (200 mg, 0.66 mmol) in 5 mL of CH_2Cl_2 at room temperature and stirred under N_2. A precipitate of **198** (111 mg, 0.26 mmol, 40%) was filtered after 5.5 h. The mother liquors were crystallized in MeOH/CH_2Cl_2 giving 87 mg (0.21 mmol, 31%) of **198**. Global yield: 198 mg, 0.47 mmol, 71%.

*2,3,4-Trimethoxy-N-(4-(3-phenylureido)phenyl)benzamide (**198**).* White crystals. **Mp** (MeOH/CH_2Cl_2): 196.5-197.0 °C. **IR** (KBr): 3313, 1656, 1641, 1599, 1490, 1288, 1090 cm^{-1}. **^{1}H-NMR** (400 MHz, $CDCl_3$): δ 3.90 (3H, s, 4-OCH_3); 3.94 (3H, s, 3-OCH_3); 4.06 (3H, s, 2-OCH_3); 6.80 (1H, d, *J* = 8.8 Hz, H5); 6.99 (1H, bt, *J* = 7.6 Hz, H4''); 7.13 (2H, d, *J* = 8.8 Hz, H3' and H5'); 7.22 (2H, bt, *J* = 8.0 Hz, H3'' and H5''); 7.33 (2H, bd, *J* = 8.0 Hz, H2'' and H6''); 7.37 (2H, *J* = 8.8 Hz, H2' and H6'); 7.87 (1H, bs, NH); 7.95 (1H, d, *J* = 8.8 Hz, H6); 8.08 (1H, bs, NH); 9.94 (1H, bs, NH). **^{13}C-NMR** (100 MHz, $CDCl_3$): δ 56.2 (CH_3, 4-OCH_3); 61.1 (CH_3, 3-OCH_3); 62.0 (CH_3, 2-OCH_3); 107.8 (CH, C5); 118.2 (C, C1); 119.7 (2) (CH, C3' and C5'); 121.6 (2) (CH, C2' and C6'); 122.6 (2) (CH, C2'' and C6''); 122.8 (CH, C4''); 126.7 (CH, C6); 128.9 (2) (CH, C3'' and C5''); 132.5 (C, C1'); 135.9 (C, C4'); 139.0 (C, C1''); 141.9 (C, C3); 152.5 (C, C2); 153.8 (C, urea); 157.2 (C, C4); 164.0 (C, amide). **HRMS** ($C_{23}H_{24}N_3O_5^+$): calculated 422.1710 ($M+H^+$), found 422.1713.

Synthesis of 2,3,4-trimethoxy-N-(naphthalen-1-yl)benzamide (199)

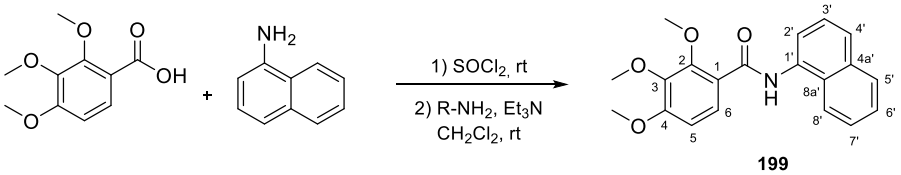

According to **A2**, $SOCl_2$ (600 µL) and 2,3,4-trimethoxybenzoic acid (255 mg, 1.20 mmol) reacted over 24 h to provide the acyl chloride, which was subsequently added to a solution of α-naphthylamine (142 mg,

1.00 mmol) and 200 µL of triethylamine in 25 mL of CH_2Cl_2. After 6 h, the reaction mixture was processed, giving 422 mg. Crystallization in MeOH yielded 286 mg (0.85 mmol, 85%) of **199**.

*2,3,4-Trimethoxy-N-(naphthalen-1-yl)benzamide (**199**).* Violet crystals. **Mp** (MeOH): 76.2-77.0 °C. **IR** (KBr): 3331, 1675, 1548, 1492, 1284, 1092 cm^{-1}. **^{1}H-NMR** (400 MHz, $CDCl_3$): δ 3.96 (3H, s, 4-OCH_3); 3.98 (3H, s, 3-OCH_3); 4.17 (3H, s, 2-OCH_3); 6.87 (1H, d, *J* = 8.8 Hz, H5); 7.50-7.60 (3H, m, H3', H6' and H7'); 7.68 (1H, bd, *J* = 8.4 Hz, H4'); 7.90 (1H, bd, *J* = 8.8 Hz, H5'); 8.02 (1H, bd, *J* = 8.8 Hz, H8'); 8.08 (1H, d, *J* = 8.8 Hz, H6); 8.44 (1H, bd, *J* = 8.0 Hz, H2'); 10.58 (1H, bs, NH). **^{13}C-NMR** (100 MHz, $CDCl_3$): δ 56.1 (CH_3, 4-OCH_3); 61.1 (CH_3, 3-OCH_3); 62.3 (CH_3, 2-OCH_3); 107.9 (CH, C5); 119.0 (CH, C2'); 120.2 (CH, C8'); 124.6 (CH, C4'); 125.8-126.2 (3) (CH, C3', C6' and C7'); 127.2 (CH, C6); 128.9 (CH, C5'); 133.4 (C, C4a'*); 134.1 (C, C1'*); 141.7 (C, C3); 152.3 (C, C2); 156.9 (C, C4); 163.2 (C, CO). Quaternary carbons (C1 and C8a') not observed. *Interchangeable signals. **HRMS** ($C_{20}H_{19}NNaO_4^+$): calculated 360.1206 (M+Na^+), found 306.1205.

Synthesis of 2,3,4-trimethoxy-N-(pyridin-2-yl)benzamide (200)

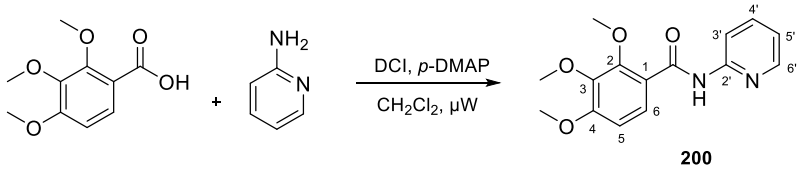

As described in procedure **A1**, reaction between 2,3,4-trimethoxybenzoic acid (229 mg, 1.08 mmol) and 2-aminopyridine (89 mg, 0.95 mmol) in the presence of DCI (203 mg, 0.99 mmol) and *p*-DMAP (117 mg, 0.96 mmol) in 20 mL of CH_2Cl_2 was conducted by irradiation in a microwave oven at 130 °C for 2 h. Crystallization in MeOH gave 147 mg (0.51 mmol, 54%) of **200**.

*2,3,4-Trimethoxy-N-(pyridin-2-yl)benzamide (**200**).* White needles. **Mp** (MeOH): 125-126 °C. **IR** (KBr): 3326, 1674, 1575, 1435, 1088 cm^{-1}. **^{1}H-NMR** (400 MHz, $CDCl_3$): δ 3.90 (3H, s, 4-OCH_3); 3.94 (3H, s, 3-OCH_3); 4.11 (3H, s, 2-OCH_3); 6.83 (1H, d, *J* = 8.8 Hz, H5); 7.04 (1H, dd, *J* = 5.2 and 8.0 Hz, H5'); 7.72 (1H, td, *J* = 2.0 and 8.0 Hz, H4'); 7.99 (1H, d, *J* = 8.8 Hz, H6); 8.33 (1H, bd, *J* = 5.2 Hz, H6'); 8.40 (1H, d, *J* = 8.0 Hz, H3'); 10.53 (1H, bs, NH). **^{13}C-NMR** (100 MHz, DMSO-D6): δ 56.6 (CH_3, 4-OCH_3); 61.0 (CH_3, 3-OCH_3); 62.4 (CH_3, 2-OCH_3); 108.7 (CH, C5); 114.1 (CH, C3'); 119.2 (C, C1); 120.2 (CH, C5'); 126.2 (CH, C6); 138.9 (CH, C4'); 141.9 (C, C3); 148.7 (CH, C6'); 152.0 (C, C2'); 152.3 (C, C2); 157.1 (C, C4); 163.3 (C, CO). **HRMS** ($C_{15}H_{16}N_2NaO_4^+$): calculated 311.1003 (M+Na^+), found 311.1004.

Synthesis of 2,3,4-trimethoxy-N-(pyridin-2-yl)-N-(2,3,4-trimethoxybenzoyl)benzamide (201)

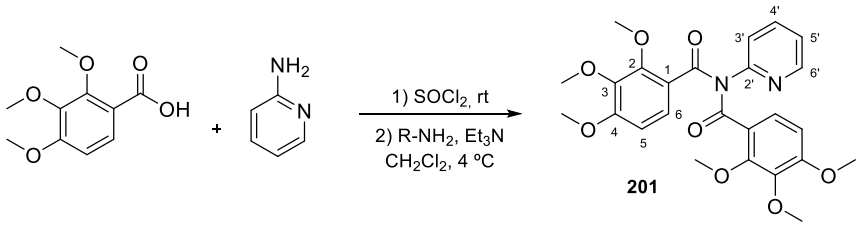

Following method **A2**, the acyl chloride formed after 6 h between $SOCl_2$ (300 µL) and 2,3,4-trimethoxybenzoic acid (272 mg, 1.28 mmol) was added dropwise to a solution of 2-aminopyridine (185 mg, 1.97 mmol) in 5 mL of CH_2Cl_2 at 4 °C, turning yellow and giving 275 mg after 16 h. Crystallization in MeOH yielded 116 mg (0.24 mmol, 38%) of **201**. Global yield: 175 mg, 0.36 mmol, 57%.

*2,3,4-Trimethoxy-N-(pyridin-2-yl)-N-(2,3,4-trimethoxybenzoyl)benzamide (**201**).* Translucent crystals. **Mp** (MeOH): 127-128 °C. **IR** (KBr): 1693, 1659, 1588, 1464, 1277, 1096 cm^{-1}. **^{1}H-NMR** (400 MHz, $CDCl_3$): δ 3.74 (6H, s, 4-OCH_3 [bis]); 3.82 (6H, s, 3-OCH_3 [bis]); 3.97 (6H, s, 2-OCH_3 [bis]); 6.55 (2H, d, *J* = 8.8 Hz, H5 [bis]); 7.20 (1H, dd, *J* = 4.8 and 7.6 Hz, H5'); 7.33 (3H, m, H6 [bis] and H3'); 7.74 (1H, bt, 7.6 Hz, H4'); 8.50 (1H, bd, *J* = 4.8 Hz, H6'). **^{13}C-NMR** (100 MHz, $CDCl_3$): δ 56.0 (2) (CH_3, 4-OCH_3 [bis]); 60.8 (2) (CH_3, 3-OCH_3 [bis]); 62.1 (2) (CH_3, 2-OCH_3 [bis]); 106.7 (2) (CH, C5 [bis]); 122.5 (CH, C5'); 123.0 (CH, C3'); 123.5 (2) (C, C1 [bis]); 125.6 (2) (CH, C6 [bis]); 137.9 (CH, C4'); 141.5 (2) (C, C3) [bis]); 149.3 (CH, C6'); 152.2 (C, C2'); 153.7 (2) (C, C2 [bis]); 156.3 (2) (C, C4 [bis]); 170.0 (2) (C, CO [bis]). **HRMS** ($C_{25}H_{26}N_2NaO_8^+$): calculated 505.1581 ($M+Na^+$), found 505.1584.

Synthesis of 2,3,4-trimethoxy-N-(4-methylpyridin-2-yl)benzamide (202)

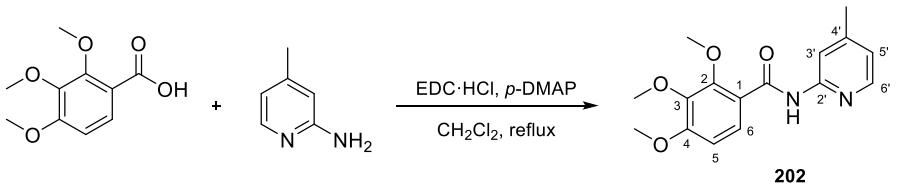

Following procedure **A1**, a solution of 2,3,4-trimethoxybenzoic acid (259 mg, 1.22 mmol), EDC·HCl (316 mg, 1.64 mmol), and *p*-DMAP (75 mg, 0.61 mmol) in 25 mL of CH_2Cl_2 was heated under reflux and mixed with 4-methylpyridin-2-amine (127 mg, 1.17 mmol). It was processed after three days, providing 225 mg. Crystallization in MeOH gave 116 mg (0.38 mmol, 33%) of **202**. Global yield: 196 mg, 0.65 mmol, 55%.

*2,3,4-Trimethoxy-N-(4-methylpyridin-2-yl)benzamide (**202**).* White crystals. **Mp** (MeOH): 132-133 °C. **IR** (KBr): 3321, 1677, 1534, 1412, 1294, 1091 cm^{-1}. **^{1}H-NMR** (400 MHz, $CDCl_3$): δ 2.93 (3H, s, 4'-CH_3); 3.90 (3H, s, 4-OCH_3); 3.94 (3H, s, 3-OCH_3); 4.10 (3H, s, 2-OCH_3); 6.83 (1H, d, *J* = 9.2 Hz, H5); 6.87 (1H, dd, *J* = 1.2 and 4.8 Hz, H5'); 7.98 (1H, d, *J* = 9.2 Hz, H6); 8.18 (1H, d, *J* = 4.8 Hz, H6'); 8.26 (1H, d, *J* = 1.2 Hz, H3'); 10.48 (1H, bs, NH). **^{13}C-NMR** (100 MHz, $CDCl_3$): δ 21.4 (CH_3, Me); 56.1 (CH_3, 4-OCH_3); 61.0 (CH_3, 3-OCH_3); 62.0 (CH_3, 2-OCH_3); 107.7 (CH, C5); 115.1 (CH, C3'); 118.6 (C, C1); 120.7 (CH, C5'); 127.0 (CH, C6); 141.8 (C, C3); 147.5 (CH, C6'); 149.7 (C, C4'); 152.0 (C, C2'); 152.7 (C, C2); 157.7 (C, C4); 163.1 (C, CO). **HRMS** ($C_{16}H_{19}N_2O_4^+$): calculated 303.1339 ($M+H^+$), found 303.1332.

Synthesis of 2,3,4-trimethoxy-N-methyl-N-(4-methylpyridin-2-yl)benzamide (203)

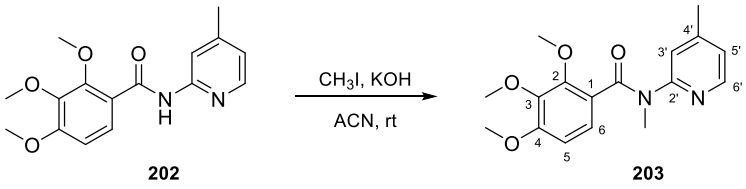

Methylation of **202** was carried following method **C1**. A mixture of **202** (109 mg, 0.36 mmol), excess powdered KOH and methyl iodide (50 µL, 0.80 mmol) gave 119 mg after 6 days at room temperature. Preparative TLC with EtOAc as eluent yielded 43 mg (0.14 mmol, 38%) of **203**.

*2,3,4-Trimethoxy-N-methyl-N-(4-methylpyridin-2-yl)benzamide (**203**).* Non-isolated product. **^{1}H-NMR** (400 MHz, $CDCl_3$): δ 2.14 (3H, s, 4'-CH_3); 3.47 (3H, s, NCH_3); 3.72 (3H, s, 4-OCH_3); 3.82 (3H, s, 3-OCH_3); 3.86 (3H, s, 2-OCH_3); 6.52 (1H, d, *J* = 8.4 Hz, H5); 6.80 (1H, d, *J* = 4.8 Hz, H5'); 6.87 (2H, m, H6 and H3'); 8.21 (1H, d, *J* = 4.8 Hz, H6'). **^{13}C-NMR** (100 MHz, $CDCl_3$): δ 20.8 (CH_3, 4'-Me); 35.3 (CH_3, NCH_3); 56.0 (CH_3, 4-OCH_3);

60.9 (CH_3, 3-OCH_3); 61.6 (CH_3, 2-OCH_3); 107.0 (CH, C5); 121.1 (CH, C3'); 121.9 (CH, C5'); 123.4 (CH, C6); 124.4 (C, C1); 141.8 (C, C3); 147.8 (CH, C6'); 148.5 (C, C4'); 150.6 (C, C2'); 154.7 (C, C2); 155.9 (C, C4); 168.9 (C, CO).

Synthesis of N-(4-bromopyridin-2-yl)-2,3,4-trimethoxybenzamide (204)

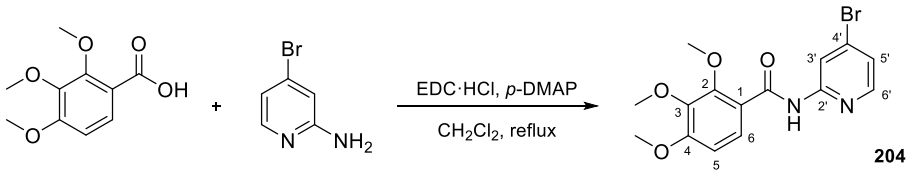

As detailed in method **A1**, 2,3,4-trimethoxybenzoic acid (220 mg, 1.04 mmol) and 4-bromopyridin-2-amine (175 mg, 1.01 mmol) in the presence of EDC hydrochloride (303 mg, 1.58 mmol) and *p*-DMAP (60 mg, 0.49 mmol) in refluxing CH_2Cl_2 (50 mL) provided 314 mg after 48 h. Crystallization in MeOH gave 271 mg (0.74 mmol, 73%) of **204**.

*N-(4-bromopyridin-2-yl)-2,3,4-trimethoxybenzamide (**204**).* White crystals. **Mp** (MeOH): 175.2-176.4 °C. **IR** (KBr): 3307, 1681, 1600, 1558, 1397, 1292, 1089 cm^{-1}. **^{1}H-NMR** (400 MHz, $CDCl_3$): δ 3.89 (3H, s, 4-OCH_3); 3.93 (3H, s, 3-OCH_3); 4.10 (3H, s, 2-OCH_3); 6.83 (1H, d, *J* = 8.8 Hz, H5); 7.20 (1H, dd, *J* = 1.6 and 5.6 Hz, H5'); 7.97 (1H, d, *J* = 8.8 Hz, H6); 8.13 (1H, d, *J* = 5.6 Hz, H6'); 8.68 (1H, d, *J* = 1.6 Hz, H3'); 10.60 (1H, bs, NH). **^{13}C-NMR** (100 MHz, $CDCl_3$): δ 56.1 (CH_3, 4-OCH_3); 61.0 (CH_3, 3-OCH_3); 62.1 (CH_3, 2-OCH_3); 107.8 (CH, C5); 117.7 (CH, C3'); 118.0 (C, C1); 122.8 (CH, C5'); 127.1 (CH, C6); 134.5 (C, C4'); 141.8 (C, C3); 148.3 (CH, C6'); 152.6 (C, C2'); 152.7 (C, C2); 157.5 (C, C4); 163.2 (C, CO). **HRMS** ($C_{15}H_{16}BrN_2O_4^+$): calculated 367.0288 ($M+H^+$), found 367.0286.

Synthesis of N-(4-aminopyridin-2-yl)-2,3,4-trimethoxybenzamide (205)

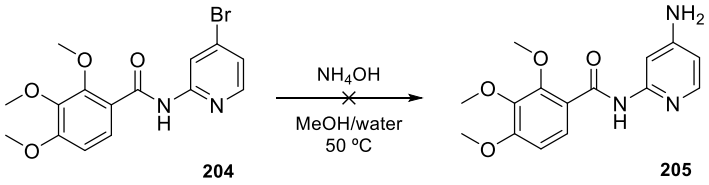

A solution of **204** (55 mg, 0.15 mmol) and 1 mL 30% NH_4OH in 6 mL of MeOH/water 5:1 was heated in a sealed tube at 50 °C for 14 days. The resulting precipitate was filtered off, obtaining 28 mg (0.08 mmol) of the starting material.

Synthesis of N-(5-bromopyridin-2-yl)-2,3,4-trimethoxybenzamide (206)

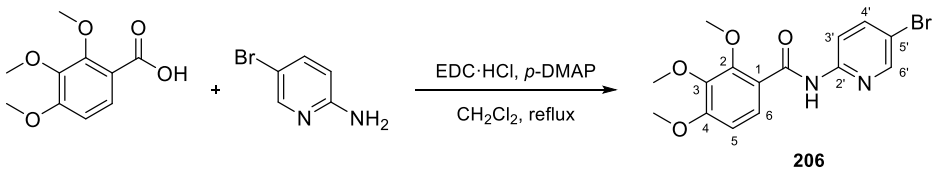

Amide **206** was obtained by general method **A1**. 2,3,4-Trimethoxybenzoic acid (420 mg, 2.00 mmol), 5-bromopyridin-2-amine (251 mg, 1.45 mmol), *p*-DMAP (103 mg, 0.84 mmol), and EDC hydrochloride (559

mg, 2.92 mmol) were heated in 25 mL of refluxing CH_2Cl_2 for 1 week, obtaining 377 mg. Crystallization in MeOH/CH_2Cl_2 yielded 235 mg (0.64 mmol, 44%) of **206**.

*N-(5-bromopyridin-2-yl)-2,3,4-trimethoxybenzamide (**206**).* White crystals. **Mp** (MeOH/CH_2Cl_2): 179.2-180.7 °C. **IR** (KBr): 3233, 1670, 1599, 1492, 1293, 1093 cm^{-1}. **^{1}H-NMR** (400 MHz, $CDCl_3$): δ 3.90 (3H, s, 4-OCH_3); 3.94 (3H, s, 3-OCH_3); 4.10 (3H, s, 2-OCH_3); 6.83 (1H, d, *J* = 9.2 Hz, H5); 7.82 (1H, dd, *J* = 2.0 and 8.8 Hz, H4'); 7.97 (1H, d, *J* = 9.2 Hz, H6); 8.36 (2H, m, H3' and H6'); 10.59 (1H, bs, NH). **^{13}C-NMR** (100 MHz, $CDCl_3$): δ 56.1 (CH_3, 4-OCH_3); 60.0 (CH_3, 3-OCH_3); 62.0 (CH_3, 2-OCH_3); 107.7 (CH, C5); 114.3 (C, C5'); 115.7 (CH, C3'); 118.1 (C, C1); 127.1 (CH, C6); 140.5 (CH, C4'); 141.8 (C, C3); 148.9 (CH, C6'); 150.7 (C, C2'); 152.7 (C, C2); 157.4 (C, C4); 163.1 (C, CO). **HRMS** ($C_{15}H_{16}BrN_2O_4^+$): calculated 367.0288 ($M+H^+$), found 367.0285.

Preparation of compounds 207 and 208

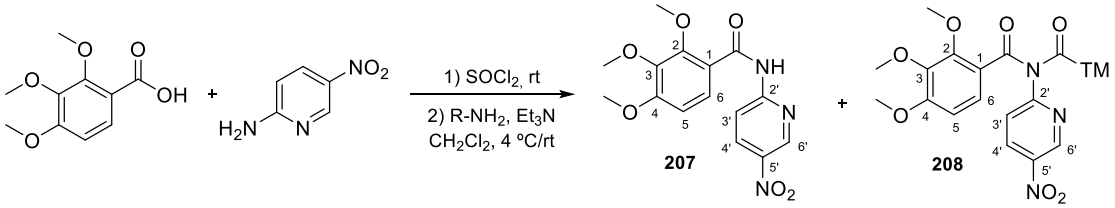

Procedure 1: 2,3,4-Trimethoxybenzoic acid 213 mg (1.00 mmol) was heated for 20 h with $SOCl_2$ (method **A2**). The acyl chloride was added to a yellow solution of the amine (120 mg, 0.86 mmol) with 200 µL of triethylamine in 25 mL of ACN and stirred for 24 h, turning orange, and gave 167 mg. Preparative TLC using EtOAc/Hex 7:3 as eluent gave **207** (40 mg, 0.12 mmol, 14%) and crystallization in EtOAc yielded **208** (60 mg, 0.11 mmol, 23%). Similar results were obtained when the reaction was conducted at 4 °C: **207** (14%) and **208** (32%).

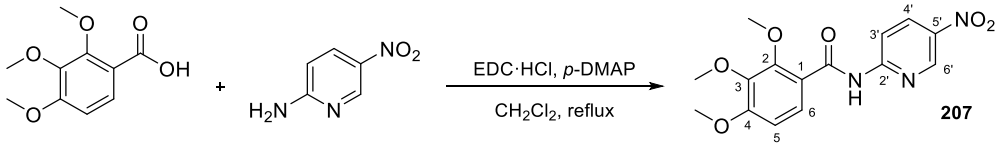

Procedure 2: Following method **A1**, 5-nitropyridin-2-amine (321 mg, 2.31 mmol), 2,3,4-trimethoxybenzoic acid (726 mg, 3.42 mmol), EDC hydrochloride (1030 mg, 5.37 mmol), and *p*-DMAP (185 mg, 1.52 mmol) in 100 mL of refluxing CH_2Cl_2 gave 597 mg after 1 week. Crystallization in MeOH/CH_2Cl_2 yielded 447 mg (1.34 mmol, 58%) of **207**.

*2,3,4-Trimethoxy-N-(5-nitropyridin-2-yl)benzamide (**207**).* Orange crystals. **Mp** (MeOH/CH_2Cl_2): 198.6-199.6 °C. **IR** (KBr): 3283, 1692, 1598, 1515, 1314, 1279, 1093 cm^{-1}. **^{1}H-NMR** (400 MHz, $CDCl_3$): δ 3.86 (3H, s, 4-OCH_3); 3.89 (3H, s, 3-OCH_3); 4.08 (3H, s, 2-OCH_3); 6.79 (1H, d, *J* = 8.8 Hz, H5); 7.93 (1H, d, *J* = 8.8 Hz, H6); 8.45 (1H, dd, *J* = 2.8 and 9.2 Hz, H4'); 8.53 (1H, d, *J* = 9.2 Hz, H3'); 9.12 (1H, d, *J* = 2.8 Hz, H6'); 10.94 (1H, bs, NH). **^{13}C-NMR** (100 MHz, $CDCl_3$): δ 56.2 (CH_3, 4-OCH_3); 61.0 (CH_3, 3-OCH_3); 62.2 (CH_3, 2-OCH_3); 107.9 (CH, C5); 113.3 (CH, C3'); 117.3 (C, C1); 127.4 (CH, C6); 133.8 (CH, C4'); 140.2 (C, C5'); 141.8 (C, C3); 144.9 (CH, C6'); 152.8 (C, C2); 156.1 (C, C2'); 157.9 (C, C4); 163.3 (C, CO). **HRMS** ($C_{15}H_{13}N_3O_6^+$): calculated 334.1034 ($M+H^+$), found 334.1030.

*2,3,4-Trimethoxy-N-(5-nitropyridin-2-yl)-N-(2,3,4-trimethoxybenzoyl)benzamide (**208**).* Brown crystals. **Mp** (EtOAc): 189-191 °C. **IR** (KBr): 1692, 1661, 1594, 1337, 1297, 1091 cm^{-1}. **^{1}H-NMR** (400 MHz, $CDCl_3$): δ

3.67 (6H, s, 4-OCH_3 [bis]); 3.78 (6H, s, 3-OCH_3 [bis]); 3.89 (6H, s, 2-OCH_3 [bis]); 6.51 (2H, d, *J* = 8.4 Hz, H5 [bis]); 7.25 (2H, d, *J* = 8.4 Hz, H6 [bis]); 7.48 (1H, d, *J* = 8.8 Hz, H3'); 8.45 (1H, dd, *J* = 2.8 and 8.8 Hz, H4'); 9.20 (1H, d, *J* = 2.8 Hz, H6'). **^{13}C-NMR** (100 MHz, $CDCl_3$): δ 56.1 (2) (CH_3, 4-OCH_3 [bis]); 60.8 (2) (CH_3, 3-OCH_3 [bis]); 62.1 (2) (CH_3, 2-OCH_3 [bis]); 106.9 (2) (CH, C5 [bis]); 122.2 (CH, C3'); 122.4 (2) (C, C1 [bis]); 126.0 (2) (CH, C6 [bis]); 132.9 (CH, C4'); 141.6 (C, C5'); 142.2 (2) (C, C3 [bis]); 144.8 (CH, C6'); 152.4 (2) (C, C2 [bis]); 157.0 (2) (C, C4 [bis]); 158.4 (C, C2'); 169.4 (2) (C, CO [bis]). **HRMS** ($C_{25}H_{25}N_3NaO_{10}^+$): calculated 505.1432 ($M+Na^+$), found 505.1440.

Preparation of compounds 209 and 210

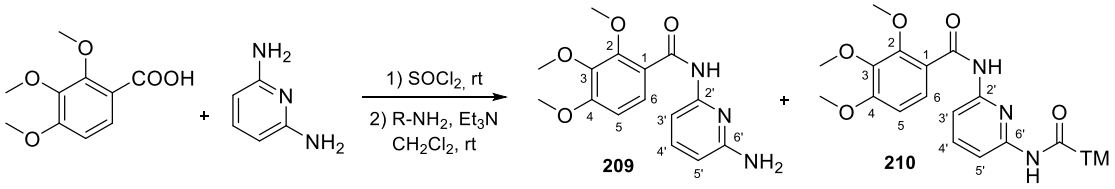

Following procedure **A2**, $SOCl_2$ (1 mL) and 2,3,4-trimethoxybenzoic acid (1529 mg, 7.20 mmol) gave the acyl chloride after 6 h, which was added to a solution of 2,6-diaminopyridine (969 mg, 8.88 mmol) in 50 mL of CH_2Cl_2 with 5 mL of triethylamine, to obtain 2212 mg after 5 h. Compounds **209** and **210** were separated by silica gel flash chromatography with EtOAc/Hex 8:2, followed by crystallization. Global yields: **209** (1613 mg, 5.32 mmol, 74%) and **210** (122 mg, 0.25 mmol, 7%).

*N-(6-aminopyridin-2-yl)-2,3,4-trimethoxybenzamide (**209**).* White crystals. **Mp** (CH_2Cl_2/Hex): 168.5-168.7 °C. **IR** (KBr): 3462, 3353, 1654, 1547, 1455, 1288, 1098 cm^{-1}. **^{1}H-NMR** (400 MHz, $CDCl_3$): δ 3.90 (3H, s, 4-OCH_3); 3.93 (3H, s, 3-OCH_3); 4.08 (3H, s, 2-OCH_3); 4.40 (2H, bs, NH_2); 6.27 (1H, d, *J* = 8.0 Hz, H5'); 6.82 (1H, d, *J* = 8.8 Hz, H5); 7.48 (1H, t, *J* = 8.0 Hz, H4'); 7.74 (1H, d, *J* = 8.0 Hz, H3'); 7.97 (1H, d, *J* = 8.8 Hz, H6); 10.20 (1H, bs, NH). **^{13}C-NMR** (100 MHz, $CDCl_3$): δ 56.1 (CH_3, 4-OCH_3); 61.0 (CH_3, 3-OCH_3); 62.0 (CH_3, 2-OCH_3); 104.0 (CH, C5'); 104.2 (CH, C3'); 107.6 (CH, C5); 118.8 (C, C1); 127.0 (CH, C6); 139.4 (CH, C4'); 141.8 (C, C3); 150.4 (C, C2'); 152.6 (C, C2); 157.0 (C, C6'); 157.2 (C, C4); 162.8 (C, CO). **HRMS** ($C_{15}H_{18}N_3O_4^+$): calculated 304.1292 ($M+H^+$), found 304.1286.

*N-(6-aminopyridin-2-yl)-2,3,4-trimethoxy-N-(2,3,4-trimethoxybenzoyl)benzamide (**210**).* White crystals. **Mp** (acetone/H_2O): 201.8-202.0 °C. **IR** (KBr): 3461, 3351, 1669, 1585, 1451, 1286, 1093 cm^{-1}. **^{1}H-NMR** (400 MHz, $CDCl_3$): δ 3.90 (6H, s, 4-OCH_3 [bis]); 3.93 (6H, s, 3-OCH_3 [bis]); 4.11 (6H, s, 2-OCH_3 [bis]); 6.84 (2H, d, *J* = 8.8 Hz, H5 [bis]); 7.77 (1H, t, *J* = 8.0 Hz, H4'); 7.99 (2H, d, *J* = 8.8 Hz, H6 [bis]); 8.12 (2H, d, *J* = 8.0 Hz, H3' and H5'). **^{13}C-NMR** (100 MHz, $CDCl_3$): δ 56.1 (2) (CH_3, 4-OCH_3 [bis]); 61.0 (2) (CH_3, 3-OCH_3 [bis]); 62.0 (2) (CH_3, 2-OCH_3 [bis]); 107.7 (2) (CH, C3' and C5'); 110.0 (2) (CH, C5 [bis]); 118.5 (2) (C, C1 [bis]); 127.0 (2) (CH, C6 [bis]); 140.4 (CH, C4'); 141.7 (2) (C, C3 [bis]); 150.3 (2) (C, C2' and C6'); 152.5 (2) (C, C2 [bis]); 157.1 (2) (C, C4 [bis]); 162.9 (2) (C, CO [bis]). **HRMS** ($C_{25}H_{27}N_3NaO_8^+$): calculated 520.1690 ($M+Na^+$), found 520.1691.

Preparation of compounds 211 and 212

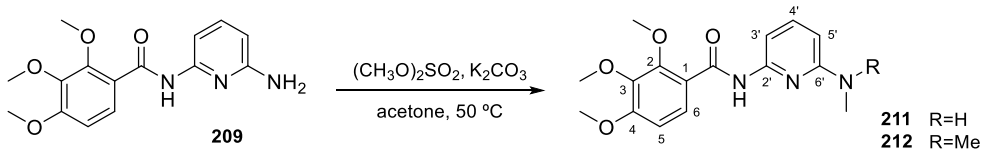

Compound **209** (475 mg, 1.57 mmol) was dissolved in 50 mL of acetone together with 2187 mg (15.82 mmol) of K_2CO_3 and subsequently, dimethyl sulfate (1113 µL, 11.76 mmol) was slowly added drop by drop.[582] The reaction mixture was heated at 50 °C and kept under N_2 for 1 week. It was filtered, evaporated, dissolved in CH_2Cl_2 and washed with brine. The organic layer was dried over anhydrous Na_2SO_4, filtered, and concentrated to dryness to obtain 336 mg of **211**, **212** and **209.** Crystallization in MeOH gave 88 mg (0.27 mmol, 17%) of **212**. Global yields: **211** (140 mg, 0.44 mmol, 28%) and **212** (150 mg, 0.45 mmol, 29%).

*2,3,4-Trimethoxy-N-(6-(methylamino)pyridin-2-yl)benzamide (**211**).* Non-isolated product. **^{1}H-NMR** (400 MHz, $CDCl_3$): δ 2.91 (3H, s, NCH_3); 3.91 (3H, s, 4-OCH_3); 3.93 (3H, s, 3-OCH_3); 4.07 (3H, 2-OCH_3); 6.16 (1H, d, *J* = 8.0 Hz, H5'); 6.82 (1H, d, *J* = 8.8 Hz, H5); 7.50 (1H, t, *J* = 8.0 Hz, H4'); 7.65 (1H, d, *J* = 8.0 Hz, H3'); 7.97 (1H, d, *J* = 8.8 Hz, H6); 10.20 (1H, bs, NH).

*N-(6-(dimethylamino)pyridin-2-yl)-2,3,4-trimethoxybenzamide (**212**).* Light brown crystals. **Mp** (MeOH): 90-91 °C. **IR** (KBr): 3358, 1681, 1597, 1491, 1292, 1090 cm^{-1}. **^{1}H-NMR** (400 MHz, $CDCl_3$): δ 3.07 (6H, s, NCH_3); 3.91 (3H, s, 4-OCH_3); 3.93 (3H, s, 3-OCH_3); 4.07 (3H, 2-OCH_3); 6.29 (1H, d, *J* = 8.0 Hz, H5'); 6.84 (1H, d, *J* = 8.8 Hz, H5); 7.50 (1H, t, *J* = 8.0 Hz, H4'); 7.60 (1H, d, *J* = 8.0 Hz, H3'); 7.98 (1H, d, *J* = 8.8 Hz, H6); 10.27 (1H, bs, NH). **^{13}C-NMR** (100 MHz, $CDCl_3$): δ 37.8 (2) (CH_3, NCH_3); 56.1 (CH_3, 4-OCH_3); 61.0 (CH_3, 3-OCH_3); 61.9 (CH_3, 2-OCH_3); 101.5 (2) (CH, C3' and C5'); 107.7 (CH, C5); 119.1 (C, C1); 127.0 (CH, C6); 139.3 (CH, C4'); 141.8 (C, C3); 150.1 (C, C2'); 152.5 (C, C2); 156.8 (C, C6'); 158.2 (C, C4); 162.7 (C, CO). **HRMS** ($C_{17}H_{22}N_3O_4^+$): calculated 332.1605 ($M+H^+$), found 332.1609.

Synthesis of 2,3,4-trimethoxy-N-(6-(N-(methylsulfonyl)methylsulfonamido)pyridin-2-yl)benzamide (213)

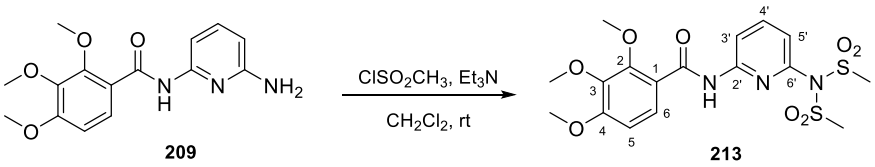

Mesyl chloride (60 µL, 0.78 mmol) was added to a solution of compound **209** (150 mg, 0.50 mmol) with 200 µL of triethylamine in 5 mL of CH_2Cl_2 at room temperature. Additional mesyl chloride (30 µL, 0.39 mmol) was added after 72 h under N_2, and the reaction mixture was poured into cold water 5 h later, and washed with brine until neutral pH. The organic layer was dried over anhydrous Na_2SO_4, filtered, and evaporated (220 mg). Precipitation in MeOH yielded 164 mg (0.36 mmol, 72%) of **213**.

*2,3,4-Trimethoxy-N-(6-(N-(methylsulfonyl)methylsulfonamido)pyridin-2-yl)benzamide (**213**).* White powder. **IR** (KBr): 3288, 1678, 1598, 1363, 1260, 1095 cm^{-1}. **^{1}H-NMR** (400 MHz, $CDCl_3$): δ 3.75 (6H, s, SCH_3); 3.90 (3H, s, 4-OCH_3); 3.93 (3H, s, 3-OCH_3); 4.07 (3H, s, 2-OCH_3); 6.83 (1H, d, *J* = 8.8 Hz, H5); 7.07 (1H, d, *J* = 8.0 Hz, H3'); 7.87 (1H, t, *J* = 8.0 Hz, H4'); 7.96 (1H, d, *J* = 8.8 Hz, H6); 8.52 (1H, d, *J* = 8.0 Hz, H5'); 10.59 (1H,

bs, NH). **^{13}C-NMR** (100 MHz, $CDCl_3$): δ 43.9 (2) (CH_3, SCH_3); 56.1 (CH_3, 4-OCH_3); 61.1 (CH_3, 3-OCH_3); 62.1 (CH_3, 2-OCH_3); 107.9 (CH, C5); 115.9 (CH, C5'); 117.9 (C, C1); 120.3 (CH, C3'); 127.2 (CH, C6); 141.3 (CH, C4'); 141.8 (C, C3); 146.1 (C, C6'); 151.9 (C, C2'); 152.5 (C, C2); 157.5 (C, C4); 163.1 (C, CO). **HRMS** ($C_{17}H_{21}N_3NaO_8S_2^+$): calculated 482.0662 ($M+Na^+$), found 482.0660.

Synthesis of N-(6-acetamidopyridin-2-yl)-2,3,4-trimethoxybenzamide (214)

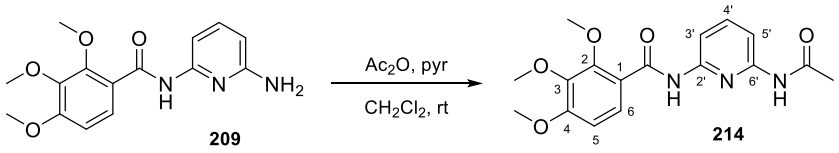

A mixture of acetic anhydride (1 mL), pyridine (1 mL), and **209** (186 mg, 0.61 mmol) in 5 mL of CH_2Cl_2 was stirred for 3 days under N_2 atmosphere at room temperature. The reaction was diluted with CH_2Cl_2 and poured into cold water, washed with 5% $NaHCO_3$ and brine until neutrality. The organic layer was dried over anhydrous Na_2SO_4, filtered, and rotary evaporated (203 mg). Precipitation in MeOH provided **214** (193 mg, 0.56 mmol, 91%).

*N-(6-acetamidopyridin-2-yl)-2,3,4-trimethoxybenzamide (**214**).* White powder. **IR** (KBr): 3320, 1677, 1587, 1491, 1287, 1097 cm^{-1}. **^{1}H-NMR** (400 MHz, CD_3OD): δ 2.16 (3H, s, Ac); 3.88 (3H, s, 4-OCH_3); 3.93 (3H, s, 3-OCH_3); 4.07 (3H, s, 2-OCH_3); 6.97 (1H, d, *J* = 8.4 Hz, H5); 7.76 (1H, t, *J* = 8.0 Hz, H4'); 7.84 (2H, d, *J* = 8.0 Hz, H3' and H5'); 7.98 (1H, d, *J* = 8.4 Hz, H6). **^{13}C-NMR** (100 MHz, $CDCl_3$): δ 24.5 (CH_3, Ac); 56.1 (CH_3, 4-OCH_3); 61.0 (CH_3, 3-OCH_3); 62.0 (CH_3, 2-OCH_3); 107.7 (CH, C5); 109.3 (CH, C5'); 110.0 (CH, C3'); 118.1 (C, C1); 127.0 (CH, C6); 140.7 (CH, C4'); 141.6 (C, C3); 149.8 (C, C6'); 150.0 (C, C2'); 152.4 (C, C2); 157.2 (C, C4); 162.8 (C, CO). Quaternary carbon (CO, Ac) not observed. **HRMS** ($C_{17}H_{19}N_3NaO_5^+$): calculated 368.1217 ($M+Na^+$), found 368.1221.

Synthesis of 2,3,4-trimethoxy-N-(6-(2,2,2-trifluoroacetamido)pyridin-2-yl)benzamide (215)

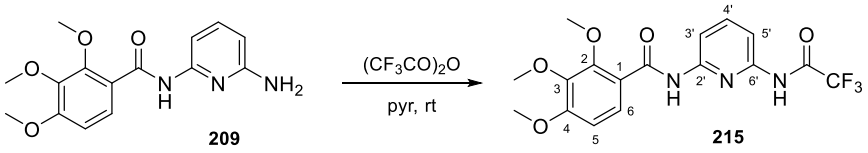

Trifluoroacetic anhydride (161 µL, 1.15 mmol) was carefully added to a solution of amide **209** (291 mg, 0.96 mmol) in 1 mL of pyridine and stirred under N_2 atmosphere for 24 h. More anhydride (161 µL, 1.15 mmol) was added to the reaction mixture and stirred for 12 h. It was diluted with CH_2Cl_2 and washed with 5% $NaHCO_3$, 2N HCl, and brine until neutrality. The organic layer was dried over anhydrous Na_2SO_4, filtered, and concentrated to dryness (371 mg). **215** underwent fragmentation in silica following column chromatography with EtOAc/Hex 1:1 as eluent.

Synthesis of 2,3,4-trimethoxy-N-(6-propionamidopyridin-2-yl)benzamide (216)

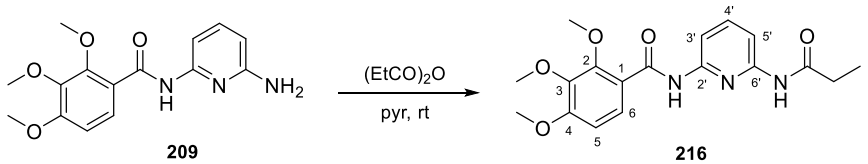

Propionic anhydride (200 µL, 1.51 mmol) was added to a solution of **209** (212 mg, 0.70 mmol) in 1 mL of pyridine and stirred for 4 h at room temperature under N_2. CH_2Cl_2 was added and poured into cold water and washed with 5% $NaHCO_3$, 2N HCl, and brine. The organic layer was dried over anhydrous Na_2SO_4, filtered, and concentrated to dryness (252 mg). Crystallization in MeOH yielded 161 mg (0.45 mmol, 64%) of **216**.

*2,3,4-Trimethoxy-N-(6-propionamidopyridin-2-yl)benzamide (**216**).* White crystals. **Mp** (MeOH): 180-181 °C. **IR** (KBr): 3535, 3459, 3287, 1705, 1646, 1586, 1458, 1289, 1094 cm^{-1}. **^{1}H-NMR** (400 MHz, $CDCl_3$): δ 1.23 (3H, t, *J* = 7.2 Hz, Et); 2.41 (2H, q, *J* = 7.2 Hz, Et); 3.87 (3H, s, 4-OCH_3); 3.91 (3H, s, 3-OCH_3); 4.04 (3H, s, 2-OCH_3); 6.81 (1H, d, *J* = 8.8 Hz, H5); 7.72 (1H, t, *J* = 8.0 Hz, H4'); 7.91 (1H, bd, *J* = 8.0 Hz, H3'); 7.98 (1H, d, *J* = 8.8 Hz, H6); 8.08 (1H, bd, *J* = 8.0 Hz, H5'); 10.32 (1H, bs, NH). **^{13}C-NMR** (100 MHz, $CDCl_3$): δ 9.4 (CH_3, Et); 30.8 (CH_2, Et); 56.1 (CH_3, 4-OCH_3); 61.0 (CH_3, 3-OCH_3); 62.1 (CH_3, 2-OCH_3); 107.8 (CH, C5); 109.3 (CH, C5'); 110.1 (CH, C3'); 118.3 (C, C1); 127.1 (CH, C6); 140.7 (CH, C4'); 141.8 (C, C3); 149.7 (C, C6'); 150.1 (C, C2'); 152.5 (C, C2); 157.2 (C, C4); 162.9 (C, CO); 172.3 (C, CO). **HRMS** ($C_{18}H_{21}N_3NaO_5^+$): calculated 382.1373 ($M+Na^+$), found 382.1376.

Synthesis of N-(6-benzamidopyridin-2-yl)-2,3,4-trimethoxybenzamide (217)

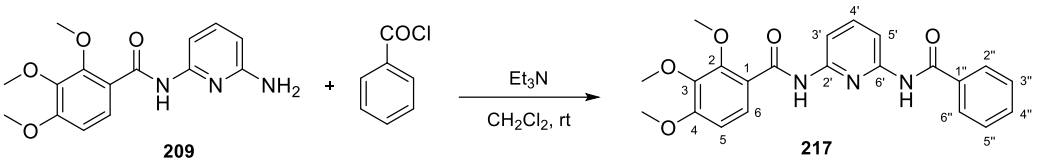

Benzoyl chloride (80 µL, 0.69 mmol) was added to a solution of **209** (132 mg, 0.44 mmol) with 100 µL of triethylamine in CH_2Cl_2 (5 mL). The reaction was stirred for 24 h at room temperature under N_2 atmosphere, poured into cold water, and washed with brine until neutrality. The organic layer was dried over anhydrous Na_2SO_4, filtered, and evaporated to dryness (207 mg). Flash chromatography using a gradient of EtOAc/Hex (from 3:7 to 1:1) followed by crystallization in MeOH gave **217** (174 mg, 0.43 mmol, 98%).

*N-(6-benzamidopyridin-2-yl)-2,3,4-trimethoxybenzamide (**217**).* White crystals. **Mp** (MeOH): 150-151 °C. **IR** (KBr): 3430, 3337, 1684, 1584, 1453, 1285, 1093 cm^{-1}. **^{1}H-NMR** (400 MHz, $CDCl_3$): δ 3.84 (3H, s, 4-OCH_3); 3.85 (3H, s, 3-OCH_3); 4.00 (3H, s, 2-OCH_3); 6.74 (1H, d, *J* = 8.8 Hz, H5); 7.45 (2H, bd, *J* = 8.0 Hz, H3'' and H5''); 7.57 (1H, bt, *J* = 8.0 Hz, H4''); 7.74 (1H, t, *J* = 8.0 Hz, H4'); 7.84 (2H, dd, *J* = 1.6 and 8.8 Hz, H2'' and H6''); 7.90 (1H, d, *J* = 8.8 Hz, H6); 8.06 (1H, d, *J* = 8.0 Hz, H3'*); 8.09 (1H, d, *J* = 8.0 Hz, H5'*); 8.70 (1H, bs, NH); 10.28 (1H, bs, NH). *Interchangeable signals. **^{13}C-NMR** (100 MHz, $CDCl_3$): δ 56.1 (CH_3, 4-OCH_3); 61.0 (CH_3, 3-OCH_3); 62.0 (CH_3, 2-OCH_3); 107.7 (CH, C5); 109.5 (CH, C5'); 110.4 (CH, C3'); 118.2 (C, C1); 127.0 (CH, C6); 127.2 (2) (CH, C2'' and C6''); 128.7 (2) (CH, C3'' and C5''); 132.1 (CH, C4''); 134.2 (C, C1''); 140.7 (CH, C4'); 141.7 (C, C3); 149.9 (C, C6'); 150.3 (C, C2'); 152.5 (C, C2); 157.2 (C, C4); 162.9 (C, CO); 165.7 (C, CO). **HRMS** ($C_{22}H_{21}N_3NaO_5^+$): calculated 430.1374 ($M+Na^+$), found 430.1357.

Synthesis of 2,3,4-trimethoxy-N-(6-(2-phenylacetamido)pyridin-2-yl)benzamide (218)

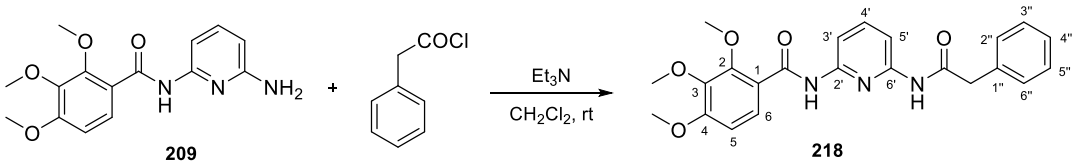

2-Phenylacetyl chloride (122 µL, 0.92 mmol) was added to a solution of **209** (182 mg, 0.60 mmol) and triethylamine (200 µL) in 5 mL of CH_2Cl_2. The reaction mixture was stirred for 30 h at room temperature and N_2 atmosphere, poured into cold water, and washed with 5% $NaHCO_3$ and brine. The organic layer was dried over anhydrous Na_2SO_4, filtered, and concentrated under vacuum to obtain 310 mg. Crystallization in MeOH gave 203 mg (0.48 mmol, 80%) of **218**.

*2,3,4-Trimethoxy-N-(6-(2-phenylacetamido)pyridin-2-yl)benzamide (**218**).* White crystals. **Mp** (MeOH): 111.5-113.0 °C. **IR** (KBr): 3325, 3303, 1676, 1582, 1453, 1285, 1094 cm^{-1}. **^{1}H-NMR** (400 MHz, $CDCl_3$): δ 3.49 (2H, s, CH_2); 3.90 (3H, s, 4-OCH_3); 3.93 (3H, s, 3-OCH_3); 4.03 (3H, s, 2-OCH_3); 6.82 (1H, d, *J* = 8.8 Hz, H5); 7.35-7.41 (5H, m, Ph); 7.59 (1H, bs, NH); 7.72 (1H, t, *J* = 7.6 Hz, H4'); 7.92 (1H, d, *J* = 7.6 Hz, H3'); 7.96 (1H, d, *J* = 8.8 Hz, H6); 8.08 (1H, d, *J* = 7.6 Hz, H5'); 10.22 (1H, bs, NH). **^{13}C-NMR** (100 MHz, $CDCl_3$): δ 44.9 (CH_2); 56.1 (CH_3, 4-OCH_3); 61.0 (CH_3, 3-OCH_3); 62.0 (CH_3, 2-OCH_3); 107.8 (CH, C5); 109.3 (CH, C5'); 110.4 (CH, C3'); 118.3 (C, C1); 127.1 (CH, C6); 127.6 (CH, C4''); 129.1 (2) (CH, C3'' and C5''); 129.5 (2) (CH, C2'' and C6''); 134.0 (C, C1''); 140.7 (CH, C4'); 141.7 (C, C3); 149.4 (C, C6'); 150.1 (C, C2'); 152.5 (C, C2); 157.2 (C, C4); 162.9 (C, CO); 169.3 (C, CO). **HRMS** ($C_{23}H_{23}N_3NaO_5^+$): calculated 444.1530 ($M+Na^+$), found 444.1525.

Synthesis of 2,3,4-trimethoxy-N-(6-ureidopyridin-2-yl)benzamide (219)

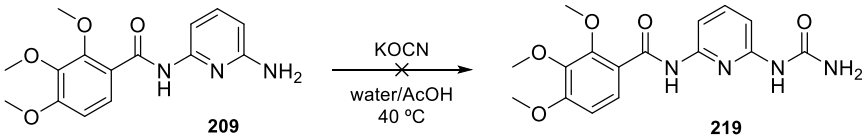

Potassium cyanate (85 mg, 1.00 mmol) was carefully added to a solution of **209** (146 mg, 0.48 mmol) in 20 mL of water/acetic acid 1:1 at room temperature. The reaction was heated at 40 °C for 4 h under N_2 atmosphere. The mixture was extracted at basic pH with EtOAc, washed with brine until neutrality, dried over anhydrous Na_2SO_4, filtered, and evaporated to provide 142 mg (142 mg, 0.47 mmol, 97%) of **209**.

Synthesis of N-(6-(3-ethylureido)pyridin-2-yl)-2,3,4-trimethoxybenzamide (220)

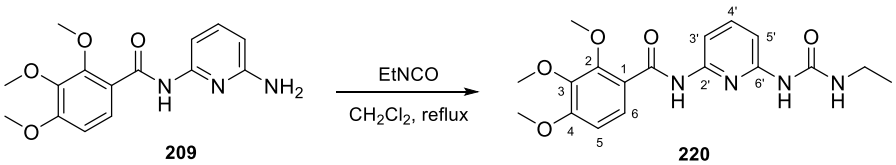

Ethyl isocyanate (205 µL, 2.54 mmol) was added to a solution of **209** (265 mg, 0.87 mmol) in 5 mL of CH_2Cl_2. The reaction was heated under reflux and N_2 atmosphere for 4 days. The resulting crystals were filtered off, obtaining compound **220** (139 mg, 0.37 mmol, 43%).

*N-(6-(3-ethylureido)pyridin-2-yl)-2,3,4-trimethoxybenzamide (**220**).* White crystals. **Mp** (CH_2Cl_2): 219-220 °C. **IR** (KBr): 3333, 3257, 3121, 1700, 1679, 1591, 1449, 1268, 1093 cm^{-1}. **^{1}H-NMR** (400 MHz, $CDCl_3$): δ 1.33 (3H, t, *J* = 7.2 Hz, Et); 3.47 (2H, q, *J* = 7.2 Hz, Et); 3.91 (4H, s, 3-OCH_3); 3.94 (3H, s, 3-OCH_3); 4.09 (3H, s, 2-OCH_3); 6.54 (1H, d, *J* = 7.6 Hz, H3'); 6.85 (1H, d, *J* = 8.8 Hz, H5); 7.61 (1H, t, *J* = 7.6 Hz, H4'); 7.83 (1H, d, *J* = 7.6 Hz, H5'); 7.99 (1H, d, *J* = 8.8 Hz, H6); 8.26 (1H, bs, NH); 9.03 (1H, bs, NH); 10.40 (1H, bs, NH). **^{13}C-NMR** (100 MHz, $CDCl_3$): δ 16.2 (CH_3, Et); 35.6 (CH_2, Et); 57.0 (CH_3, 4-OCH_3); 61.9 (CH_3, 3-OCH_3); 63.0 (CH_3, 2-OCH_3); 107.3 (CH, C5); 107.9 (CH, C5'); 108.8 (CH, C3'); 119.1 (C, C1); 128.0 (CH, C6); 141.4 (CH, C3); 142.6 (C, C4'); 149.7 (C, C2'); 152.8 (C, C2); 153.3 (C, C6'); 156.5 (C, urea); 158.1 (C, C4); 163.5 (C, amide). **HRMS** ($C_{18}H_{22}N_4NaO_5^+$): calculated 397.1482 ($M+Na^+$), found 397.1488.

Synthesis of 2,3,4-trimethoxy-N-(6-(3-phenylureido)pyridin-2-yl)benzamide (221)

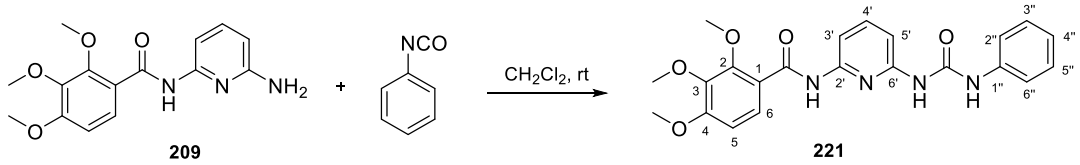

Phenyl isocyanate (75 µL, 0.68 mmol) and **209** (137 mg, 0.45 mmol) in 5 mL of CH_2Cl_2 reacted over 2 days at room temperature under N_2, giving **221** as white crystals in the reaction medium (170 mg, 0.40 mmol, 89%).

*2,3,4-Trimethoxy-N-(6-(3-phenylureido)pyridin-2-yl)benzamide (**221**).* White crystals. **Mp** (CH_2Cl_2): 217.5-218-5 °C. **IR** (KBr): 3327, 3205, 3055, 1697, 1597, 1449, 1239, 1087 cm^{-1}. **^{1}H-NMR** (400 MHz, $CDCl_3$): δ 3.96 (3H, s, 4-OCH_3); 3.98 (3H, s, 3-OCH_3); 4.07 (3H, s, 2-OCH_3); 6.53 (1H, d, *J* = 8.0 Hz, H3'); 6.87 (1H, d, *J* = 9.2 Hz, H5); 7.13 (1H, bt, *J* = 8.0 Hz, H4''); 7.38 (2H, bt, *J* = 8.0 Hz, H3'' and H5''); 7.62 (1H, bs, NH); 7.72 (3H, m, H4', H3'' and H5''); 7.96 (1H, d, *J* = 8.0 Hz, H5'); 8.01 (1H, d, *J* = 9.2 Hz, H6); 10.61 (1H, bs, NH); 11.61 (1H, bs, NH). **^{13}C-NMR** (100 MHz, $CDCl_3$): 56.2 (CH_3, 4-OCH_3); 60.9 (CH_3. 3-OCH_3); 62.3 (CH_3, 2-OCH_3); 106.7 (CH, C5'); 107.0 (CH, C3'); 108.1 (CH, C5); 118.2 (C, C1); 119.7 (2) (CH, C2'' and C6''); 123.4 (CH, C4''); 127.2 (CH, C6); 129.0 (2) (CH, C3'' and C5''); 138.6 (C, C1''); 141.1 (CH, C4'); 149.0 (C, C2'); 151.1 (C, urea); 152.4 (C, C6'); 152.6 (C, C2); 157.4 (C, C4); 162.7 (C, amide). Quaternary carbon (C3) not observed. **HRMS** ($C_{22}H_{22}N_4NaO_5^+$): calculated 445.1483 ($M+Na^+$), found 445.1480.

Synthesis of ethyl (6-(2,3,4-trimethoxybenzamido)pyridin-2-yl)carbamate (222)

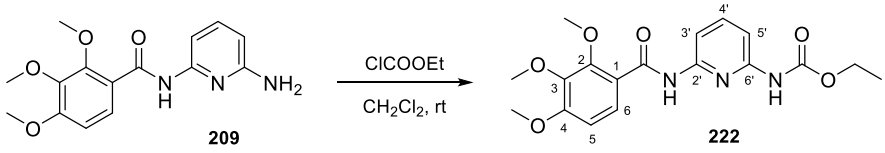

Ethyl chloroformate (90 µL, 0.91 mmol) was added to a yellow solution of compound **209** (179 mg, 0.59 mmol) in 10 mL of CH_2Cl_2, which turned red over time. The reaction was stirred for 18 h at room temperature under N_2, and the resulting precipitate was filtered off to obtain the starting material **209** (51 mg, 0.17 mmol). Preparative TLC with the mother liquors (143 mg) using EtOAc/Hex 1:1 yielded 53 mg (0.14 mmol, 24%) of **222**.

*Ethyl (6-(2,3,4-trimethoxybenzamido)pyridin-2-yl)carbamate (**222**).* White solid. **IR** (KBr): 3350, 3296, 1732, 1667, 1586, 1450, 1219, 1096 cm^{-1}. **^{1}H-NMR** (400 MHz, $CDCl_3$): δ 1.23 (3H, t, *J* = 7.2 Hz, Et); 3.86 (3H,

s, 4-OCH_3); 3.90 (3H, s, 3-OCH_3); 4.00 (3H, s, 2-OCH_3); 4.18 (2H, q, *J* = 7.2 Hz, Et); 6.78 (1H, d, *J* = 8.8 Hz, H5); 7.68 (2H, m, H4' and H5'); 7.77 (1H, bs, NH); 7.94 (1H, d, *J* = 8.8 Hz, H6); 8.03 (1H, d, *J* = 8.0 Hz, H3'); 10.22 (1H, bs, NH). **^{13}C-NMR** (100 MHz, $CDCl_3$): δ 14.4 (CH_3, Et); 56.1 (CH_3, 4-OCH_3); 61.0 (CH_3, 3-OCH_3); 61.4 (CH_2, Et); 62.0 (CH_3, 2-OCH_3); 107.5 (CH, C5); 107.7 (CH, C5'); 109.1 (CH, C3'); 118.4 (C, C1); 127.0 (CH, C6); 140.7 (CH, C4'); 141.7 (C, C3); 150.0 (C, C6'); 150.2 (C, C2'); 152.5 (C, C2); 153.1 (C, carbamate); 157.2 (C, C4); 162.9 (C, amide). **HRMS** ($C_{18}H_{21}N_3NaO_6^+$): calculated 398.1323 (M+Na^+), found 398.1325.

Synthesis of 2,3,4-trimethoxy-N-(pyridin-3-yl)benzamide (223)

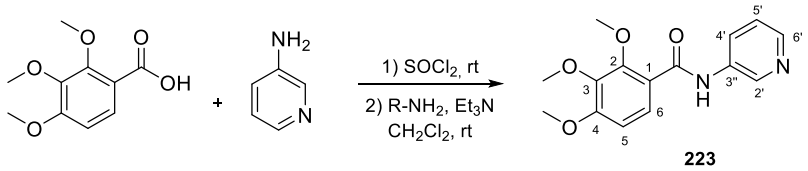

As described in procedure **A2**, $SOCl_2$ (300 µL) and 208 mg (0.98 mmol) of 2,3,4-trimethoxybenzoic acid gave the corresponding acyl chloride after 6 h. It was added to a solution of 3-aminopyridine (79 mg, 0.84 mmol) with 100 µL of triethylamine in 5 mL of CH_2Cl_2, obtaining 222 mg after 1 h. Crystallization in MeOH gave 156 mg (0.54 mmol, 64%) of amide **223**.

*2,3,4-Trimethoxy-N-(pyridin-3-yl)benzamide (**223**).* Yellow crystals. **Mp** (MeOH): 117.8-118.1 °C. **IR** (KBr): 3308, 1675, 1538, 1482, 1285, 1088 cm^{-1}. **^{1}H-NMR** (400 MHz, $CDCl_3$): δ 3.92 (3H, s, 4-OCH_3); 3.94 (3H, s, 3-OCH_3); 4.10 (3H, s, 2-OCH_3); 6.84 (1H, d, *J* = 8.8 Hz, H5); 7.31 (1H, dd, *J* = 5.6 and 8.0 Hz, H5'); 7.99 (1H, d, *J* = 8.8 Hz, H6); 8.37 (2H, m, H4' and H6'); 8.65 (1H, d, *J* = 2.0 Hz, H2'); 10.08 (1H, bs, NH). **^{13}C-NMR** (100 MHz, $CDCl_3$): δ 56.0 (CH_3, 4-OCH_3); 60.9 (CH_3, 3-OCH_3); 61.9 (CH_3, 2-OCH_3); 107.8 (CH, C5); 118.0 (C, C1); 123.7 (CH, C5'); 126.8 (CH, C6); 127.2 (CH, C2'); 135.3 (C, C3'); 141.2 (CH, C6'); 141.6 (C, C3); 144.7 (CH, C4'); 152.1 (C, C2); 157.1 (C, C4); 163.2 (C, CO). **HRMS** ($C_{15}H_{16}N_2NaO_4^+$): calculated 311.1003 (M+Na^+), found 311.0999.

Synthesis of 2,3,4-trimethoxy-N-methyl-N-(pyridin-3-yl)benzamide (224)

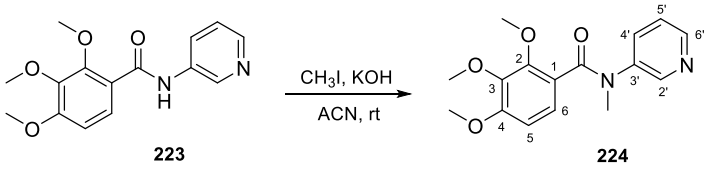

Following method **C1**, an excess of powdered KOH was added to a solution of **223** (202 mg, 0.70 mmol) in 25 mL of ACN, stirred for 1 h at room temperature. Methyl iodide (130 µL, 2.09 mmol) was added and 24 h later, the reaction was processed obtaining 190 mg. Column chromatography using EtOAc as eluent gave 115 mg (0.38 mmol, 55%) of **224**. A similar result was obtained using NaOH and tetrabutylammonium hydrogen sulfate in CH_2Cl_2.

*2,3,4-Trimethoxy-N-methyl-N-(pyridin-3-yl)benzamide (**224**).* Orange oil. **IR** (film): 1648, 1597, 1465, 1297, 1090 cm^{-1}. **^{1}H-NMR** (400 MHz, $CDCl_3$): δ 3.39 (3H, s, NCH_3); 3.56 (3H, s, 4-OCH_3); 3.76 (3H, s, 3-OCH_3); 3.80 (3H, s, 2-OCH_3); 6.50 (1H, bs, H5); 6.86 (1H, bs, H6); 7.09 (1H, bs, H5'); 7.39 (1H, bs, H4'); 8.27 (2H, bs, H2' and H6'). **^{13}C-NMR** (100 MHz, $CDCl_3$): δ 37.4 (CH_3, NCH_3); 55.9 (CH_3, 4-OCH_3); 60.8 (CH_3, 3-OCH_3); 61.6 (CH_3, 2-OCH_3); 107.2 (CH, C5); 123.1 (CH, C6); 123.5 (C, C1); 133.8 (CH, C4'); 140.5 (C, C3'); 141.7 (C, C3); 147.2

(CH, C6'); 147.9 (CH, C2'); 149.8 (C, C2); 154.8 (C, C4); 168.8 (C, CO). Tertiary carbon (C5') not observed. **HRMS** ($C_{16}H_{19}N_2O_4^+$): calculated 303.1339 ($M+H^+$), found 303.1336.

Synthesis of N-(2-aminopyridin-3-yl)-2,3,4-trimethoxybenzamide (225)

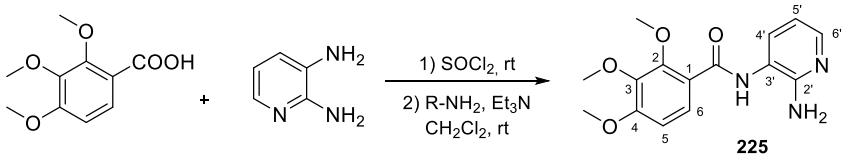

Following general method **A2**, 8-h reaction between $SOCl_2$ (500 µL) and 2,3,4-trimethoxybenzoic acid (263 mg, 1.24 mmol) gave the acyl chloride, which was subsequently added drop by drop to a solution of 2,3-diaminopyridine (113 mg, 1.04 mmol) together with 200 µL of triethylamine in 25 mL of CH_2Cl_2. Three and a half hours later, the reaction was processed obtaining 287 mg. Crystallization in MeOH yielded 177 mg (0.58 mmol, 56%) of **225**.

*N-(2-aminopyridin-3-yl)-2,3,4-trimethoxybenzamide (**225**).* Brown crystals. **Mp** (MeOH): 138.7-139.3 °C. **IR** (KBr): 3315, 3137, 1651, 1594, 1450, 1273, 1093 cm^{-1}. **^{1}H-NMR** (400 MHz, $CDCl_3$): δ 3.88 (3H, s, 4-OCH_3); 3.92 (3H, s, 3-OCH_3); 4.08 (3H, s, 2-OCH_3); 4.72 (2H, bs, NH_2); 6.76 (1H, dd, *J* = 5.2 and 8.0 Hz, H5'); 6.80 (1H, d, *J* = 8.8 Hz, H5); 7.76 (1H, dd, *J* = 1.6 and 8.0 Hz, H4'); 7.96 (1H, dd, *J* = 1.6 and 5.2 Hz, H6'); 7.97 (1H, d, *J* = 8.8 Hz, H6); 9.70 (1H, bs, NH). **^{13}C-NMR** (100 MHz, $CDCl_3$): δ 55.1 (CH_3, 4-OCH_3); 61.0 (CH_3, 3-OCH_3); 62.0 (CH_3, 2-OCH_2); 107.7 (CH, C5); 115.0 (CH, C5'); 117.9 (C, C1); 120.1 (C, C3'); 127.1 (CH, C6); 132.0 (CH, C4'); 141.6 (C, C3); 144.8 (CH, C6'); 152.3 (C, C2'); 152.7 (C, C2); 157.2 (C, C4); 163.3 (C, CO). **HRMS** ($C_{15}H_{17}N_3NaO_4^+$): calculated 326.1111 ($M+Na^+$), found 326.1108.

Synthesis of 2,3,4-trimethoxy-N-(6-methoxypyridin-3-yl)benzamide (226)

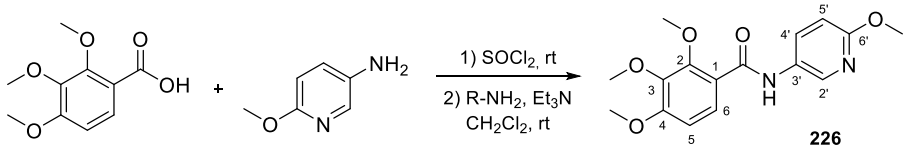

As indicated in procedure **A2**, the acyl chloride formed by a 12-h reaction between $SOCl_2$ (500 µL) and the carboxylic acid (277 mg, 1.31 mmol) was added to 6-methoxypyridin-3-amine (139 mg, 1.12 mmol) and 100 µL of triethylamine in 5 mL of CH_2Cl_2. The reaction mixture was kept under N_2 atmosphere for 1 h obtaining 360 mg. Silica gel flash chromatography with EtOAc/Hex 4:6 yielded 242 mg (0.76 mmol, 68%) of **226** as a white solid.

*2,3,4-Trimethoxy-N-(6-methoxypyridin-3-yl)benzamide (**226**).* White solid. **IR** (KBr): 3333, 1662, 1590, 1464, 1380, 1087 cm^{-1}. **^{1}H-NMR** (400 MHz, $CDCl_3$): δ 3.84 (3H, s, 6'-OCH_3); 3.86 (6H, s, 4- and 3-OCH_3); 4.01 (3H, s, 2-OCH_3); 6.70 (1H, d, *J* = 8.4 Hz, H5'); 6.76 (1H, d, *J* = 9.2 Hz, H5); 7.90 (1H, d, *J* = 9.2 Hz, H6); 8.03 (1H, dd, *J* = 2.8 and 8.4 Hz, H4'); 8.25 (1H, d, *J* = 2.8 Hz, H2'); 9.81 (1H, bs, NH). **^{13}C-NMR** (100 MHz, $CDCl_3$): δ 53.5 (CH_3, 6'-OCH_3); 56.0 (CH_3, 4-OCH_3); 61.0 (CH_3, 3-OCH_3); 61.9 (CH_3, 2-OCH_3); 107.8 (CH, C5); 110.5 (CH, C5'); 118.4 (C, C1); 126.8 (CH, C6); 129.3 (C, C3'); 132.2 (CH, C4'); 138.4 (CH, C2'); 141.7 (C, C3); 152.1 (C, C2); 156.9 (C, C4); 160.8 (C, C6'); 163.0 (C, CO). **HRMS** ($C_{16}H_{18}N_2NaO_5^+$): calculated 341.1108 ($M+Na^+$), found 341.1112.

Synthesis of 2,3,4-trimethoxy-N-(6-methoxypyridin-3-yl)-N-methylbenzamide (227)

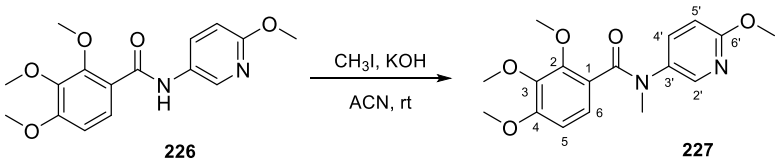

226 **227**

Following method **C1**, powdered KOH in excess was added to a solution of **226** (109 mg, 0.34 mmol) in 5 mL of ACN, and stirred for 30 min before adding methyl iodide (50 µL, 0.80 mmol). After 24 h, the reaction was processed as described obtaining 58 mg. Preparative TLC using EtOAc gave the oily product **227** (48 mg, 0.14 mmol, 42%).

*2,3,4-Trimethoxy-N-(6-methoxypyridin-3-yl)-N-methylbenzamide (**227**).* Transparent oil. **IR** (film): 1638, 1600, 1465, 1316, 1098 cm^{-1}. **^{1}H-NMR** (400 MHz, $CDCl_3$): δ 3.40 (3H, s, NCH_3); 3.62 (3H, s, 6'-CH_3); 3.76 (3H, s, 4-CH_3); 3.80 (3H, s, 3-CH_3); 3.83 (3H, s, 2-CH_3); 6.51 (2H, m, H5 and H5'); 6.82 (1H, bd, *J* = 8.4 Hz, H4'*); 7.29 (1H, bd, *J* = 8.4 Hz, H6*); 7.83 (1H, bs, H2'). *Interchangeable signals. **^{13}C-NMR** (100 MHz, $CDCl_3$): δ 37.4 (CH_3, NCH_3); 53.6 (CH_3, 6'-OCH_3); 55.9 (CH_3, 4-OCH_3); 60.8 (CH_3, 3-OCH_3); 61.6 (CH_3, 2-OCH_3); 107.1 (CH, C5); 110.4 (CH, C5'); 122.8 (CH, C6); 124.1 (C, C1); 134.4 (C, C3'); 137.3 (CH, C4'); 141.6 (C, C3); 145.1 (CH, C2'); 149.7 (C, C2); 154.4 (C, C4); 162.1 (C, C6'); 169.0 (C, CO). **HRMS** ($C_{17}H_{21}N_2O_5^+$): calculated 333.1445 ($M+H^+$), found 333.1448.

Synthesis of N-(6-aminopyridin-3-yl)-2,3,4-trimethoxybenzamide (228)

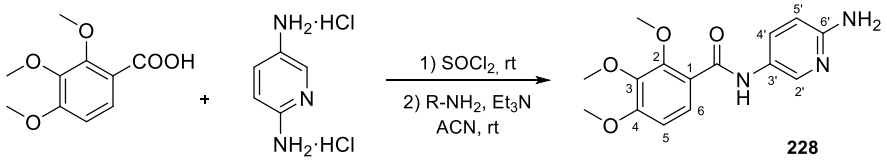

228

Following method **A2**, the acyl chloride formed after a 19-h reaction between $SOCl_2$ (700 µL) and 2,3,4-trimethoxybenzoic acid (685 mg, 3.23 mmol) was added to pyridine-2,5-diamine dihydrochloride (855 mg, 4.70 mmol) dissolved in 125 mL of ACN and stirred for 4 days in the presence triethylamine (10 mL). The residue (791 mg) was crystallized in ethanol, giving 670 mg (2.21 mmol, 69%) of **228**.

*N-(6-aminopyridin-3-yl)-2,3,4-trimethoxybenzamide (**228**).* Brown crystals. **Mp** (EtOH): 177.6-178.3 °C. **IR** (KBr): 3416, 3326, 1648, 1496, 1286, 1092 cm^{-1}. **^{1}H-NMR** (400 MHz, $CDCl_3$): δ 3.88 (3H, s, 4-OCH_3); 3.92 (3H, s, 3-OCH_3); 4.06 (3H, s, 2-OCH_3); 4.38 (2H, bs, NH_2); 6.55 (1H, d, *J* = 8.4 Hz, H5'); 6.82 (1H, d, *J* = 8.8 Hz, H5); 7.96 (1H, d, *J* = 8.8 Hz, H6); 8.00 (1H, dd, *J* = 2.4 and 8.4 Hz, H4'); 8.17 (1H, d, *J* = 2.4 Hz, H2'); 9.77 (1H, bs, NH). **^{13}C-NMR** (100 MHz, $CDCl_3$): δ 55.1 (CH_3, 4-OCH_3); 61.0 (CH_3, 3-OCH_3); 61.9 (CH_3, 2-OCH_3); 107.8 (CH, C5); 108.5 (CH, C5'); 118.5 (C, C1); 126.9 (CH, C6); 131.7 (CH, C4'); 140.2 (CH, C2'); 141.7 (C, C3); 152.1 (C, C2); 155.3 (C, C3'); 156.8 (C, C4); 163.0 (C, CO). Quaternary carbon (C6') not observed. **HRMS** ($C_{15}H_{18}N_3O_4^+$): calculated 304.1292 ($M+H^+$), found 304.1293.

Synthesis of N-(6-acetamidopyridin-3-yl)-2,3,4-trimethoxybenzamide (229)

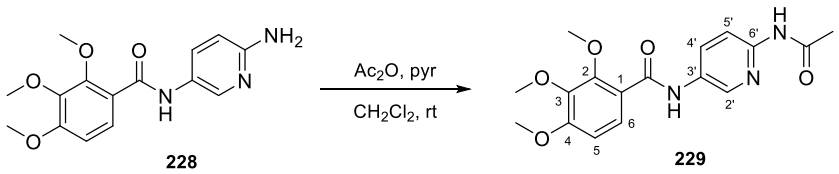

Acetic anhydride (90 µL, 0.95 mmol) was added to a solution of **228** in 5 mL of CH_2Cl_2 with pyridine (2 mL) and stirred for 24 h at room temperature under N_2 atmosphere. It was poured into cold water and washed with 5% $NaHCO_3$, 2N HCl, and saturated NaCl. The organic layer was dried over anhydrous Na_2SO_4, filtered, and concentrated under vacuum (116 mg). Crystallization in ethanol yielded **229** (39 mg, 0.11 mmol, 14%).

*N-(6-acetamidopyridin-3-yl)-2,3,4-trimethoxybenzamide (**229**).* Pinkish-red crystals. **Mp** (EtOH): 219-221 °C. **IR** (KBr): 3289, 3129, 1698, 1665, 1539, 1253, 1083 cm^{-1}. **^{1}H-NMR** (400 MHz, $CDCl_3$): δ 2.24 (3H, s, Ac); 3.91 (3H, s, 4-OCH_3); 3.94 (3H, s, 3-OCH_3); 4.08 (3H, s, 2-OCH_3); 6.83 (1H, d, *J* = 8.8 Hz, H5); 7.97 (1H, d, *J* = 8.8 Hz, H6); 8.05 (1H, dd, *J* = 2.4 and 9.2 Hz, H4'); 8.26 (1H, d, *J* = 9.2 Hz, H5'); 8.69 (1H, d, *J* = 2.4 Hz, H2'); 8.94 (1H, bs, NH); 10.04 (1H, bs, NH). **^{13}C-NMR** (100 MHz, $CDCl_3$): δ 24.7 (CH_3, Ac); 56.1 (CH_3, 4-OCH_3); 61.1 (CH_3, 3-OCH_3); 62.1 (CH_3, 2-OCH_3); 107.9 (CH, C5); 114.4 (CH, C5'); 117.9 (C, C1); 127.1 (CH, C6); 131.1 (CH, C4'); 131.8 (C, C6'); 137.8 (CH, C2'); 141.7 (C, C3); 147.2 (C, C3'); 152.2 (C, C2); 157.2 (C, C4); 163.0 (C, CO); 168.9 (C, CO). **HRMS** ($C_{17}H_{20}N_3O_5^+$): calculated 346.1397 ($M+H^+$), found 346.1398.

Synthesis of 2,3,4-trimethoxy-N-(6-propionamidopyridin-3-yl)benzamide (230)

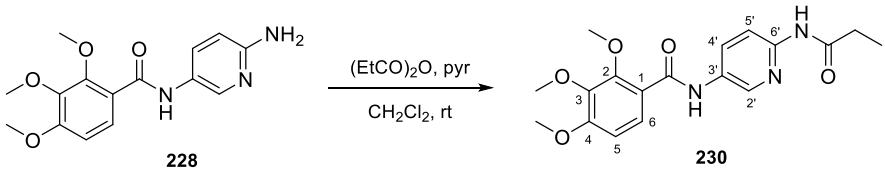

Propionic anhydride (100 µL, 0.75 mmol) was added to compound **228** (180 mg, 0.59 mmol) dissolved in 1 mL of pyridine and 3 mL of CH_2Cl_2. The solution was stirred for 34 h at room temperature under N_2 atmosphere, poured into cold water and washed with 5% $NaHCO_3$, 2N HCl, and brine until neutral pH. The organic solvent was dried over anhydrous Na_2SO_4, filtered, and evaporated to obtain 130 mg. Crystallization in MeOH gave 54 mg (0.15 mmol, 25%) of **230**.

*2,3,4-Trimethoxy-N-(6-propionamidopyridin-3-yl)benzamide (**230**).* White crystals. **Mp** (MeOH): 161.7-162.5 °C. **IR** (KBr): 3296, 3255, 1687, 1675, 1554, 1386, 1284, 1091 cm^{-1}. **^{1}H-NMR** (400 MHz, $CDCl_3$): δ 1.23 (3H, t, *J* = 7.6 Hz, Et); 2.48 (2H, q, *J* = 7.6 Hz, Et); 3.89 (3H, s, 4-OCH_3); 3.92 (3H, s, 3-OCH_3); 4.08 (3H, s, 2-OCH_3); 6.81 (1H, d, *J* = 9.2 Hz, H5); 7.94 (1H, d, *J* = 9.2 Hz, H6); 8.05 (1H, dd, *J* = 2.4 and 8.8 Hz, H4'); 8.29 (1H, d, *J* = 8.8 Hz, H5'); 8.71 (1H, d, *J* = 2.0 Hz, H2'); 9.17 (1H, bs, NH); 10.05 (1H, bs, NH). **^{13}C-NMR** (100 MHz, $CDCl_3$): δ 9.3 (CH_3, Et); 30.7 (CH_2, Et); 56.1 (CH_3, 4-OCH_3); 61.0 (CH_3, 3-OCH_3); 62.1 (CH_3, 2-OCH_3); 107.9 (CH, C5); 114.6 (CH, C5'); 117.9 (C, C1); 127.1 (CH, C6); 131.5 (C, C6'); 131.7 (CH, C4'); 137.1 (CH, C2'); 141.7 (C, C3); 147.1 (C, C3'); 152.2 (C, C2); 157.3 (C, C4); 163.1 (C, CO); 172.9 (C, CO). **HRMS** ($C_{18}H_{21}N_3NaO_5^+$): calculated 382.1373 ($M+Na^+$), found 382.1371.

Synthesis of N-(6-(N-benzoylbenzamido)pyridin-3-yl)-2,3,4-trimethoxybenzamide (231)

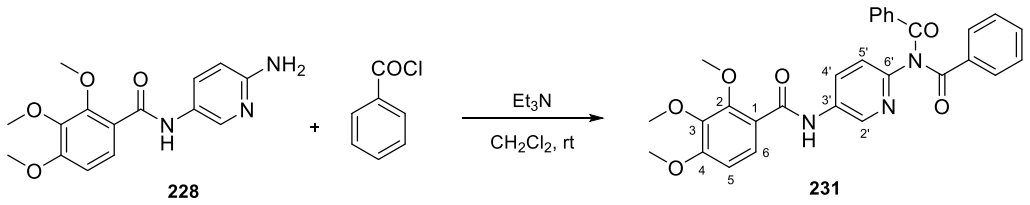

Benzoyl chloride (180 µL, 1.55 mmol) was slowly added to a solution of **228** (208 mg, 0.69 mmol) and 100 µL of triethylamine in 5 mL of CH_2Cl_2. The reaction was poured into cold water after 2 days at room temperature and N_2 atmosphere. It was then washed with brine and the organic solvent was dried over anhydrous Na_2SO_4, filtered, and evaporated (360 mg). Crystallization in MeOH yielded 220 mg (0.43 mmol, 63%) of **231**.

*N-(6-(N-benzoylbenzamido)pyridin-3-yl)-2,3,4-trimethoxybenzamide (**231**).* Brown crystals. **Mp** (MeOH): 175-177 °C. **IR** (KBr): 3298, 1702, 1689, 1667, 1526, 1240, 1092 cm^{-1}. **^{1}H-NMR** (400 MHz, $CDCl_3$): δ 3.90 (3H, s, 4-OCH_3); 3.94 (3H, s, 3-OCH_3); 4.06 (3H, s, 2-OCH_3); 6.83 (1H, d, *J* = 8.8 Hz, H5); 7.27 (1H, d, *J* = 8.8 Hz, H5'); 7.36 (4H, bt, *J* = 8.0 Hz, Ph); 7.46 (2H, bt, *J* = 8.0 Hz, Ph); 7.79 (4H, bd, *J* = 8.0 Hz, Ph); 7.95 (1H, d, *J* = 8.8 Hz, H6); 8.42 (1H, dd, *J* = 2.0 and 8.8 Hz, H4'); 8.44 (1H, d, *J* = 2.0 Hz, H2'); 10.1 (1H, bs, NH). **^{13}C-NMR** (100 MHz, $CDCl_3$): δ 56.1 (CH_3, 4-OCH_3); 61.0 (CH_3, 3-OCH_3); 62.0 (CH_3, 2-OCH_3); 108.0 (CH, C5); 117.6 (C, C1); 122.3 (CH, C4'); 127.0 (CH, C6); 128.6 (4) (CH, Ph); 129.3 (4) (CH, Ph); 132.5 (2) (CH, Ph); 134.2 (C, C6'); 134.6 (2) (C, Ph); 140.3 (CH, C2'); 141.7 (C, C3); 148.7 (C, C3'); 152.2 (C, C2); 157.3 (C, C4); 163.2 (C, CO); 173.1 (2) (C, CO). Tertiary carbon (C5') not observed. **HRMS** ($C_{29}H_{26}N_3O_6^+$): calculated 512.1816 ($M+H^+$), found 512.1818.

Synthesis of N-(6-(3-ethylureido)pyridin-3-yl)-2,3,4-trimethoxybenzamide (232)

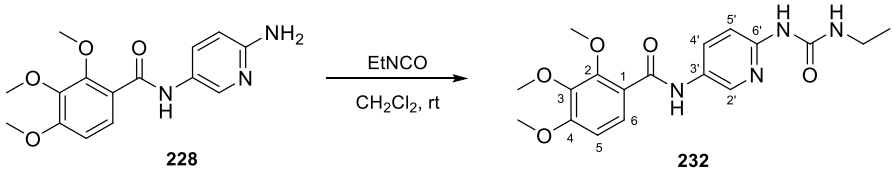

Ethyl isocyanate (204 µL, 2.54 mmol) was added to a solution of compound **228** (258 mg, 0.85 mmol) in 5 mL of CH_2Cl_2. The reaction was heated under reflux and N_2 atmosphere for 5 days, then poured into cold water and washed with brine. The organic layer was dried over anhydrous Na_2SO_4, filtered, and evaporated, to obtain 237 mg. Crystallization in MeOH/CH_2Cl_2 gave derivative **232** (175 mg, 0.47 mmol, 55%).

*N-(6-(3-ethylureido)pyridin-3-yl)-2,3,4-trimethoxybenzamide (**232**).* Salmon crystals. **Mp** (MeOH/CH_2Cl_2): 202.0-202.5 °C. **IR** (KBr): 3304, 3202, 3092, 1685, 1663, 1561, 1493, 1376, 1092 cm^{-1}. **^{1}H-NMR** (400 MHz, $CDCl_3$): δ 1.25 (3H, t, *J* = 7.2 Hz, Et); 3.42 (2H, q, *J* = 7.2 Hz, Et); 3.91 (3H, s, 4-OCH_3); 3.93 (3H, s, 3-OCH_3); 4.08 (3H, s, 2-OCH_3); 6.83 (1H, d, *J* = 8.8 Hz, H5); 6.90 (1H, d, *J* = 8.8 Hz, H5'); 7.97 (1H, d, *J* = 8.8 Hz, H6); 7.99 (1H, dd, *J* = 2.4 and 8.8 Hz, H4'); 8.48 (1H, d, *J* = 2.4 Hz, H2'); 8.74 (1H, bs, NH); 9.14 (1H, bs, NH); 9.90 (1H, bs, NH). **^{13}C-NMR** (100 MHz, $CDCl_3$): δ 14.9 (CH_3, Et); 34.2 (CH_2, Et); 55.7 (CH_3, 4-OCH_3); 60.6 (CH_3, 3-OCH_3); 61.6 (CH_3, 2-OCH_3); 107.4 (CH, C5); 111.5 (CH, C5'); 117.8 (C, C1); 126.6 (CH, C6); 128.8 (C, C6');

130.8 (CH, C4'); 137.4 (CH, C2'); 141.2 (C, C3); 149.4 (C, C3'); 151.7 (C, C2); 155.6 (C, urea); 156.6 (C, C4); 162.5 (C, amide). **HRMS** ($C_{18}H_{23}N_4O_5^+$): calculated 375.1663 ($M+H^+$), found 375.1664.

Synthesis of 2,3,4-trimethoxy-N-(6-(3-phenylureido)pyridin-3-yl)benzamide (233)

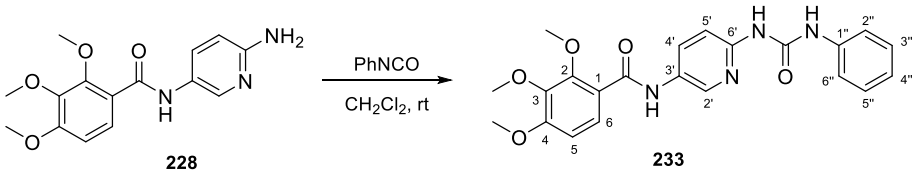

228 233

Phenyl isocyanate (105 µL, 0.95 mmol) was added to a solution of **228** (191 mg, 0.63 mmol) in 5 mL of CH_2Cl_2. The reaction was stirred for 24 h under N_2 atmosphere at room temperature. The resulting precipitate was filtered off, followed by crystallization in MeOH to provide compound **233** (133 mg, 0.32 mmol, 50%).

*2,3,4-Trimethoxy-N-(6-(3-phenylureido)pyridin-3-yl)benzamide (**233**).* Pinkish-red crystals. **Mp** (MeOH): 197.9-198.6 °C. **IR** (KBr): 3321, 3077, 3027, 1696, 1595, 1495, 1376, 1287, 1091 cm^{-1}. **^{1}H-NMR** (400 MHz, $CDCl_3$): δ 3.92 (3H, s, 4-OCH_3); 3.94 (3H, s, 3-OCH_3); 4.10 (3H, s, 2-OCH_3); 6.84 (1H, d, *J* = 8.8 Hz, H5); 7.05 (1H, d, *J* = 8.8 Hz, H5'); 7.09 (1H, bt, *J* = 8.0 Hz, H4''); 7.36 (2H, bt, *J* = 8.0 Hz, H3'' and H5''); 7.63 (2H, bd, *J* = 8.0 Hz, H2'' and H6''); 7.99 (1H, d, *J* = 8.8 Hz, H6); 8.05 (1H, dd, *J* = 2.4 and 8.8 Hz, H4'); 8.62 (1H, d, *J* = 2.4 Hz, H2'); 9.36 (1H, bs, NH); 9.97 (1H, bs, NH); 11.62 (1H, bs, NH). **^{13}C-NMR** (100 MHz, $CDCl_3$): δ 56.1 (CH_3, 4-OCH_3); 61.1 (CH_3, 3-OCH_3); 62.0 (CH_3, 2-OCH_3); 107.9 (CH, C5); 112.4 (CH, C5'); 118.1 (C, C1); 120.2 (2) (CH, C2'' and C6''); 123.4 (C, C6'); 127.0 (CH, C6); 129.0 (2) (CH, C3'' and C5''); 129.8 (CH, C4''); 131.5 (CH, C4'); 137.7 (CH, C2'); 138.6 (C, C1''); 141.7 (C, C3); 149.4 (C, C3'); 152.2 (C, C2); 153.8 (C, urea); 157.1 (C, C4); 163.1 (C, amide). **HRMS** ($C_{22}H_{23}N_4O_5^+$): calculated 423.1663 ($M+H^+$), found 423.1664.

Synthesis of N-(6-(3-benzylureido)pyridin-3-yl)-2,3,4-trimethoxybenzamide (234)

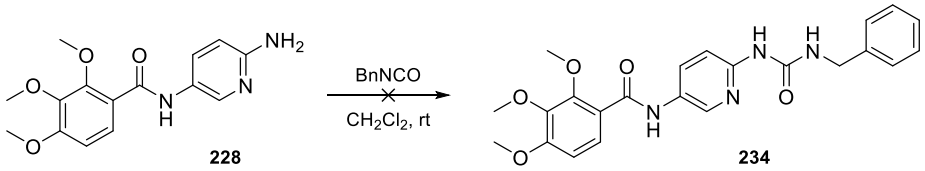

228 234

Benzyl isocyanate (100 µL, 0.81 mmol) was added to a solution of **228** (150 mg, 0.50 mmol) in 5 mL of CH_2Cl_2. It was stirred under N_2 for one week, and more benzyl isocyanate (60 µL, 0.49 mmol) was added to the reaction mixture. 24 h later, the solution was poured into iced water and washed with saturated NaCl. The organic layer was dried over anhydrous Na_2SO_4, filtered, and evaporated, obtaining 205 mg of a complex mixture.

Synthesis of ethyl (5-(2,3,4-trimethoxybenzamido)pyridin-2-yl)carbamate (235)

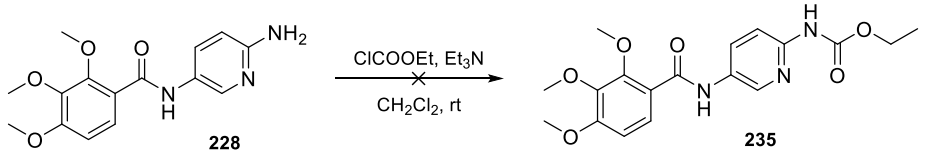

228 235

Ethyl chloroformate (80 µL, 0.84 mmol) was added to a solution of **228** (163 mg, 0.54 mmol) and 100 µL of triethylamine in 5 mL of CH_2Cl_2. The reaction was stirred for 4 days under N_2 atmosphere at room temperature, adding additional ethyl chloroformate (50 µL, 0.52 mmol). After 24 h, it was poured into cold water and washed with brine. The organic layer was dried over anhydrous Na_2SO_4, filtered, and evaporated to dryness, obtaining 183 mg of a complex mixture.

Synthesis of N-(3-aminopyridin-4-yl)-2,3,4-trimethoxybenzamide (236)

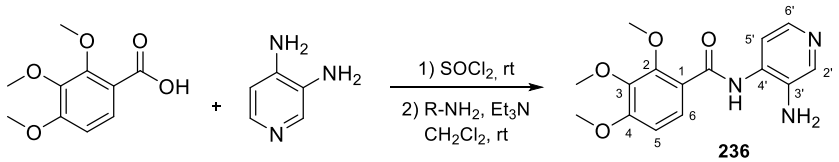

Following method **A2**, $SOCl_2$ (1 mL) reacted with the carboxylic acid (1056 mg, 5.00 mmol) over 24 h. The acyl chloride was added to a solution of 3,4-diaminopyridine (508 mg, 4.66 mmol) with 1 mL of triethylamine in 50 mL of CH_2Cl_2 and stirred for 16 h, obtaining 1315 mg. Crystallization in MeOH gave 1111 mg (3.67 mmol, 79%) of amide **236**.

*N-(3-aminopyridin-4-yl)-2,3,4-trimethoxybenzamide (**236**).* Yellow crystals. **Mp** (MeOH): 154.6-155.1 °C. **IR** (KBr): 3379, 3309, 1670, 1588, 1519, 1291, 1088 cm^{-1}. **^{1}H-NMR** (400 MHz, $CDCl_3$): δ 3.76 (2H, bs, NH_2); 3.86 (3H, s, 3-OCH_3); 3.89 (3H, s, 4-OCH_3); 4.08 (3H, s, 2-OCH_3); 6.77 (1H, d, *J* = 9.2 Hz, H5); 7.75 (1H, d, *J* = 5.2 Hz, H5'); 7.93 (1H, d, *J* = 9.2 Hz, H6); 8.05 (1H, d, *J* = 5.2 Hz, H6'); 8.14 (1H, s, H2'); 10.21 (1H, bs, NH). **^{13}C-NMR** (100 MHz, $CDCl_3$): δ 56.1 (CH_3, 4-OCH_3); 61.0 (CH_3, 3-OCH_3); 62.1 (CH_3, 2-OCH_3); 107.8 (CH, C5); 116.1 (CH, C5'); 117.7 (C, C1); 127.2 (CH, C6); 133.6 (C, C3'); 133.8 (C, C4'); 140.6 (CH, C6'); 141.6 (C, C3); 142.3 (CH, C2'); 152.3 (C, C2); 157.3 (C, C4); 163.1 (C, CO). **HRMS** ($C_{15}H_{18}N_3O_4^+$): calculated 304.1292 ($M+H^+$), found 304.1283.

Synthesis of N-(3-acetamidopyridin-4-yl)-2,3,4-trimethoxybenzamide (237)

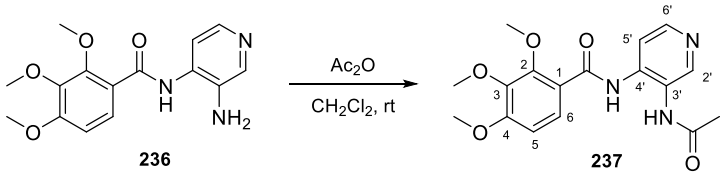

Acetic anhydride (90 µL, 0.95 mmol) was added to a solution of **236** (237 mg, 0.78 mmol) in 5 mL of CH_2Cl_2, and stirred for 5 days under N_2 at room temperature. It was poured into cold water and washed with 5% $NaHCO_3$ and saturated NaCl until neutral pH. The organic layer was dried over anhydrous Na_2SO_4, filtered, and evaporated under vacuum yielding 230 mg. Crystallization in MeOH/CH_2Cl_2 gave 144 mg (0.42 mmol, 54%) of **237**.

*N-(3-acetamidopyridin-4-yl)-2,3,4-trimethoxybenzamide (**237**).* White crystals. **Mp** (MeOH/CH_2Cl_2): 177.6-180.5 °C. **IR** (KBr): 3278, 3139, 1688, 1583, 1511, 1275, 1088 cm^{-1}. **^{1}H-NMR** (400 MHz, DMSO-D6): δ 2.15 (3H, s, Ac); 3.80 (3H, s, 3-OCH_3); 3.87 (3H, s, 4-OCH_3); 3.96 (3H, s, 2-OCH_3); 7.01 (1H, d, *J* = 8.8 Hz, H5); 7.76 (1H, d, *J* = 8.8 Hz, H6); 8.31 (1H, d, *J* = 6.0 Hz, H5'); 8.35 (1H, s, H2'); 8.38 (1H, d, *J* = 6.0 Hz, H6'); 9.89 (1H, bs, NH); 10.24 (1H, bs, NH). **^{13}C-NMR** (100 MHz, $CDCl_3$): δ 23.4 (CH_3, Ac); 56.2 (CH_3, 4-OCH_3); 61.0 (CH_3, 3-OCH_3); 62.4 (CH_3, 2-OCH_3); 107.8 (CH, C5); 116.4 (CH, C5'); 117.6 (C, C1); 124.3 (C, C3'); 127.2 (CH, C6);

141.0 (C, C4'); 141.6 (C, C3); 147.9 (CH, C6'); 148.0 (CH, C2'); 152.6 (C, C2); 157.6 (C, C4); 163.9 (C, CO); 170.3 (C, CO). **HRMS** ($C_{17}H_{20}N_3O_5^+$): calculated 346.1397 ($M+H^+$), found 346.1406.

Synthesis of N-(3-benzamidopyridin-4-yl)-2,3,4-trimethoxybenzamide (238)

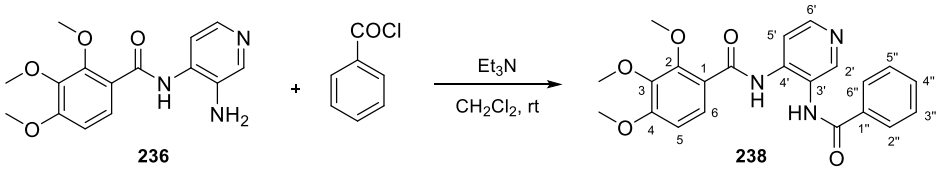

Benzoyl chloride (124 µL, 1.07 mmol) was added to a solution of amide **236** (214 mg, 0.71 mmol) with 100 µL of triethylamine in CH_2Cl_2 (5 mL) at room temperature. The reaction mixture was kept under N_2 for 48 h, poured into iced water, and washed with saturated NaCl. Then, the organic solvent was dried over anhydrous Na_2SO_4, filtered, and evaporated, obtaining 372 mg. Crystallization in methanol gave 32 mg (<11%) of **238** with very minor impurities.

*N-(3-benzamidopyridin-4-yl)-2,3,4-trimethoxybenzamide (**238**).* Non-isolated product. **^{1}H-NMR** (400 MHz, $CDCl_3$): δ 3.76 (3H, s, 3-OCH_3); 3.82 (3H, s, 4-OCH_3); 3.84 (3H, s, 2-OCH_3); 6.75 (1H, d, *J* = 9.2 Hz, H5); 7.45 (2H, bt, *J* = 8.0 Hz, H3'' and H5''); 7.52 (1H, bt, *J* = 8.0 Hz, H4''); 7.89 (1H, overlapped signal, H5'); 7.91 (1H, d, *J* = 9.2 Hz, H6); 8.03 (2H, bd, *J* = 8.0 Hz, H2'' and H6''); 8.34 (1H, d, *J* = 5.6 Hz, H6'); 8.85 (1H, s, H2'); 9.46 (1H, bs, NH); 10.48 (1H, bs, NH).

Synthesis of N-(3-(3-ethylureido)pyridin-4-yl)-2,3,4-trimethoxybenzamide (239)

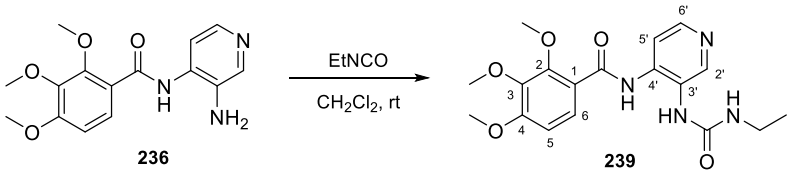

Ethyl isocyanate (100 µL, 1.24 mmol) was added to a solution of amide **236** (240 mg, 0.79 mmol) in 5 mL of CH_2Cl_2. The reaction mixture was stirred under N_2 atmosphere at room temperature for 1 week, turning into a suspension. The resulting precipitate was filtered off to obtain **239**, purified by crystallization in MeOH. Global yield: 175 mg, 0.47 mmol, 59%.

*N-(3-(3-ethylureido)pyridin-4-yl)-2,3,4-trimethoxybenzamide (**239**).* White needles. **Mp** (MeOH): 183 °C. **IR** (KBr): 3315, 3261, 1675, 1635, 1584, 1457, 1289, 1094 cm^{-1}. **^{1}H-NMR** (400 MHz, $CDCl_3$): δ 1.11 (3H, t, *J* = 7.2 Hz, Et); 3.27 (2H, q, *J* = 7.2 Hz, Et); 3.87 (3H, s, 3-OCH_3); 3.94 (3H, s, 4-OCH_3); 4.13 (3H, s, 2-OCH_3); 4.96 (1H, bs, NHEt); 6.82 (1H, d, *J* = 9.2 Hz, H5); 6.83 (1H, bs, NH); 7.97 (1H, d, *J* = 9.2 Hz, H6); 8.41 (1H, d, *J* = 5.2 Hz, H5'); 8.45 (1H, d, *J* = 5.2 Hz, H6'); 8.49 (1H, s, H2'); 10.91 (1H, bs, NH, amide). **^{13}C-NMR** (100 MHz, DMSO-D6): δ 15.8 (CH_3, Et); 34.8 (CH_2, Et); 56.6 (CH_3, 4-OCH_3); 61.0 (CH_3, 3-OCH_3); 62.5 (CH_3, 2-OCH_3); 108.7 (CH, C5); 115.3 (CH, C5'); 118.5 (C, C1); 125.7 (C, C3'); 126.8 (CH, C6); 141.7 (C, C4'); 141.8 (C, C3); 147.5 (CH, C6'); 148.5 (CH, C2'); 152.5 (C, C2); 156.7 (C, urea); 157.5 (C, C4); 163.3 (C, amide). **HRMS** ($C_{18}H_{23}N_4O_5^+$): calculated 375.1663 ($M+H^+$), found 375.1664.

Synthesis of 2,3,4-trimethoxy-N-(3-(3-phenylureido)pyridin-4-yl)benzamide (240)

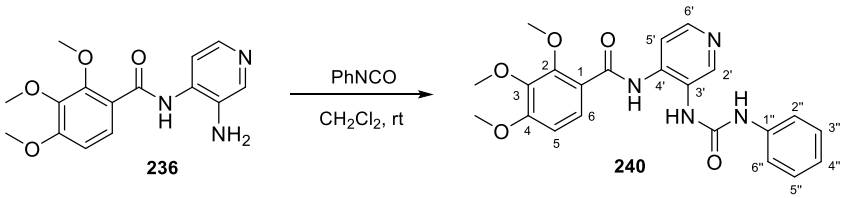

A mixture of compound **236** (91 mg, 0.30 mmol) and phenyl isocyanate (50 µL, 0.45 mmol) in 5 mL of CH_2Cl_2 was stirred for 4 h under N_2 atmosphere at room temperature, resulting in *in situ* crystallization. The suspension was filtered off, obtaining 96 mg (0.23 mmol, 76%) of **240**.

*2,3,4-Trimethoxy-N-(3-(3-phenylureido)pyridin-4-yl)benzamide (**240**).* White crystals. **Mp** (CH_2Cl_2): 196 °C. **IR** (KBr): 3324, 3274, 3235, 1676, 1629, 1585, 1490, 1289, 1093 cm^{-1}. **^{1}H-NMR** (400 MHz, $CDCl_3$): δ 3.77 (3H, s, 3-OCH_3); 3.91 (3H, s, 4-OCH_3); 4.01 (3H, s, 2-OCH_3); 6.76 (1H, d, *J* = 9.2 Hz, H5); 7.04 (1H, bt, *J* = 8.0 Hz, H4''); 7.23 (2H, bt, *J* = 8.0 Hz, H3'' and H5''); 7.32 (2H, bd, *J* = 8.0 Hz, H2'' and H6''); 7.51 (1H, bs, NH); 7.61 (1H, bs, NH); 7.88 (1H, d, *J* = 9.2 Hz, H6); 8.20 (1H, d, *J* = 5.6 Hz, H5'); 8.32 (1H, d, *J* = 5.6 Hz, H6'); 8.42 (1H, s, H2'); 10.69 (1H, bs, NH). **^{13}C-NMR** (100 MHz, DMSO-D6): 56.6 (CH_3, 4-OCH_3); 60.8 (CH_3, 3-OCH_3); 62.5 (CH_3, 2-OCH_3); 108.8 (CH, C5); 115.4 (CH, C5'); 118.4 (C, C1); 119.1 (2) (CH, C2'' and C6''); 122.6 (CH, C4''); 124.9 (C, C3'); 126.8 (CH, C6); 129.2 (2) (CH, C3'' and C5''); 140.0 (C, C1''); 141.7 (C, C3); 142.0 (C, C4'); 148.1 (CH, C6'); 149.0 (CH, C2'); 152.5 (C, C2); 154.4 (C, urea); 157.5 (C, C4); 163.4 (C, amide). **HRMS** ($C_{22}H_{23}N_4O_5^+$): calculated 423.1663 ($M+H^+$), found 423.1658.

Synthesis of 2,3,4-trimethoxy-N-(pyridin-4-yl)benzamide (241)

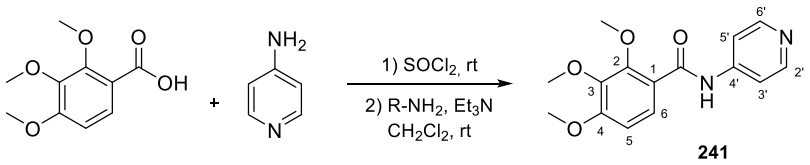

Following method **A2**, $SOCl_2$ (300 µL) reacted with 193 mg (0.91 mmol) of 2,3,4-trimethoxybenzoic acid over 6 h. The acyl chloride was subsequently added to a solution of 4-aminopyridine (78 mg, 0.83 mmol) and 0.5 mL of triethylamine in 25 mL of CH_2Cl_2. After 15 h, the residue (**241**, 202 mg, 0.70 mmol, 85%) was crystallized in MeOH (**241**, 30 mg, 0.10 mmol, 13%).

*2,3,4-Trimethoxy-N-(pyridin-4-yl)benzamide (**241**).* White crystals. **Mp** (MeOH): 132.4-132.7 °C. **IR** (KBr): 3315, 1672, 1584, 1490, 1285, 1089 cm^{-1}. **^{1}H-NMR** (400 MHz, $CDCl_3$): δ 3.91 (3H, s, 4-OCH_3); 3.94 (3H, s, 3-OCH_3); 4.09 (3H, s, 2-OCH_3); 6.85 (1H, d, *J* = 8.8 Hz, H5); 7.61 (2H, d, *J* = 6.0 Hz, H3' and H5'); 7.98 (1H, d, *J* = 8.8 Hz, H6); 8.53 (2H, d, *J* = 6.0 Hz, H2' and H6'); 10.17 (1H, bs, NH). **^{13}C-NMR** (100 MHz, $CDCl_3$): δ 56.1 (CH_3, 4-OCH_3); 61.0 (CH_3, 3-OCH_3); 62.1 (CH_3, 2-OCH_3); 107.9 (CH, C5); 114.0 (2) (CH, C3' and C5'); 117.9 (C, C1); 127.1 (CH, C6); 141.6 (C, C3); 145.4 (C, C4'); 150.5 (2) (CH, C2' and C6'); 152.2 (C, C2); 157.4 (C, C4); 163.5 (C, CO). **HRMS** ($C_{15}H_{16}N_2NaO_4^+$): calculated 311.1003 ($M+Na^+$), found 311.1003.

Synthesis of 2,3,4-trimethoxy-N-methyl-N-(pyridin-4-yl)benzamide (242)

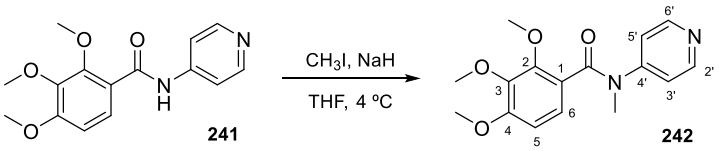

Procedure 1: A mixture of **241** (148 mg, 0.51 mmol), excess powdered NaOH, catalytic tetrabutylammonium hydrogen sulfate, and methyl iodide (57 µL, 0.92 mmol) in 5 mL of CH_2Cl_2 was stirred for 48 h at room temperature under N_2. It was filtered and washed with 2N HCl, 5% $NaHCO_3$, and brine. The organic layer was dried over anhydrous Na_2SO_4, filtered, and evaporated (43 mg), but the signals corresponding to **242** were not observed in ^{1}H-NMR spectra.

Procedure 2: Amide **241** (177 mg, 0.61 mmol) was dissolved in dry THF and cooled to 4 °C before adding 55 mg (1.38 mmol) of 60% NaH. The mixture was stirred at 4 °C under N_2 atmosphere, and after 1 h, methyl iodide (57 µL, 0.92 mmol) was added. The reaction was poured into water 72 h later, EtOAc was added and partially evaporated. The organic solvent was washed with brine until neutrality and dried over anhydrous Na_2SO_4, filtered, and concentrated to dryness, obtaining 94 mg. Preparative TLC using EtOAc/MeOH 85:15 gave 70 mg (0.23 mmol, 38%) of **242**.

*2,3,4-Trimethoxy-N-methyl-N-(pyridin-4-yl)benzamide (**242**).* Yellow oil. **IR** (film): 1653, 1559, 1506, 1418, 1362, 1097 cm^{-1}. **^{1}H-NMR** (400 MHz, $CDCl_3$): δ 3.44 (3H, s, NCH_3); 3.67 (3H, s, 4-OCH_3); 3.77 (3H, s, 3-OCH_3); 3.80 (3H, s, 2-OCH_3); 6.56 (1H, d, *J* = 8.8 Hz, H5); 6.91 (1H, d, *J* = 8.8 Hz, H6); 7.02 (2H, bs, H3' and H5'); 8.42 (2H, bs, H2' and H6'). **^{13}C-NMR** (100 MHz, $CDCl_3$): δ 36.5 (CH_3, NCH_3); 56.0 (CH_3, 4-OCH_3); 60.9 (CH_3, 3-OCH_3); 61.5 (CH_3, 2-OCH_3); 107.2 (CH, C5); 119.7 (2) (CH, C3' and C5'); 123.3 (CH, C6); 141.8 (C, C3); 149.9 (2) (CH, C2' and C6'); 150.4 (C, C2); 151.4 (C, C4'); 155.3 (C, C4); 168.6 (C, CO). Quaternary carbon (C1) not observed. **HRMS** ($C_{16}H_{19}N_2O_4^+$): calculated 303.1339 (M+H$^+$), found 303.1338.

Synthesis of 2,3,4-trimethoxy-N-(pyrimidin-2-yl)benzamide (243)

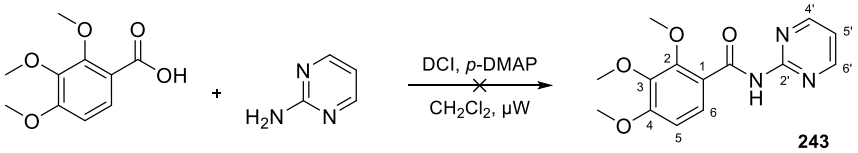

Following general procedure **A1**, the mixture of 2,3,4-trimethoxybenzoic acid (305 mg, 1.44 mmol), 2-aminopyrimidine (120 mg, 1.26 mmol), *p*-DMAP (196 mg, 1.61 mmol), and DCI (591 mg, 2.87 mmol) was dissolved in 10 mL of CH_2Cl_2 and irradiated in a microwave oven for 2 h at 100 °C, obtaining 726 mg of a complex mixture.

Preparation of compounds 244 and 245

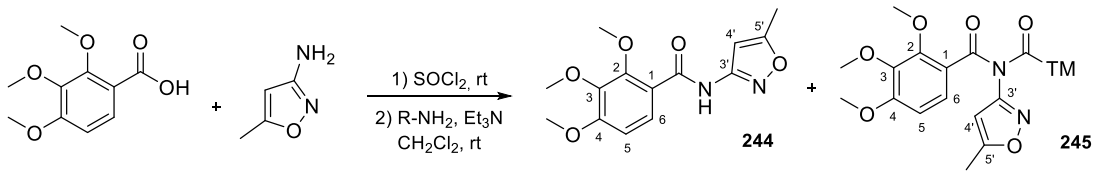

Following general method **A2**, the acyl chloride of 2,3,4-trimethoxybenzoic acid (194 mg, 0.91 mmol) was obtained after 6 h by reaction with 0.5 mL of $SOCl_2$. It was carefully added to a solution of 5-methylisoxazol-3-amine (80 mg, 0.82 mmol) in 12 mL of CH_2Cl_2 with 0.5 mL of Et_3N. The reaction was stirred for 5 h at room temperature providing 209 mg. Crystallization in EtOAc gave 35 mg (0.12 mmol, 15%) of **244** and 28 mg (0.06 mmol, 13%) of **245**. Global yields: **244** (71 mg, 0.24 mmol, 30%) and **245** (108 mg, 0.22 mmol, 49%).

*2,3,4-Trimethoxy-N-(5-methylisoxazol-3-yl)benzamide (**244**).* White crystals. **Mp** (EtOAc): 155-156 °C. **IR** (KBr): 3322, 1684, 1595, 1425, 1289, 1091 cm^{-1}. **^{1}H-NMR** (400 MHz, $CDCl_3$): δ 2.43 (3H, s, CH_3); 3.89 (3H, s, 4-OCH_3); 3.94 (3H, s, 3-OCH_3); 4.08 (3H, s, 2-OCH_3); 6.82 (1H, d, *J* = 8.8 Hz, H5); 6.83 (1H, s, H4'); 7.96 (1H, d, *J* = 8.8 Hz, H6); 10.43 (1H, bs, NH). **^{13}C-NMR** (100 MHz, $CDCl_3$): δ 12.7 (CH_3, Me); 56.1 (CH_3, 4-OCH_3); 61.0 (CH_3, 3-OCH_3); 62.0 (CH_3, 2-OCH_3); 97.0 (CH, C4'); 107.8 (CH, C5); 117.4 (C, C1); 127.2 (CH, C6); 141.7 (C, C3); 152.7 (C, C2); 157.6 (C, C4); 158.4 (C, C3'); 162.6 (C, CO); 169.7 (C, C5'). **HRMS** ($C_{14}H_{16}N_2NaO_5^+$): calculated 315.0951 ($M+Na^+$), found 315.0929.

*2,3,4-Trimethoxy-N-(5-methylisoxazol-3-yl)-N-(2,3,4-trimethoxybenzoyl)benzamide (**245**).* White crystals. **Mp** (EtOAc): 144.0-144.8 °C. **^{1}H-NMR** (400 MHz, $CDCl_3$): δ 2.43 (3H, s, CH_3); 3.73 (6H, s, 4-OCH_3 [bis]); 3.82 (6H, s, 3-OCH_3 [bis]); 3.92 (6H, s, 2-OCH_3 [bis]); 6.10 (1H, s, H4'); 6.56 (2H, d, *J* = 8.8 Hz, H5 [bis]); 7.30 (2H, d, *J* = 8.8 Hz, H6 [bis]). **^{13}C-NMR** (100 MHz, $CDCl_3$): δ 12.9 (CH_3, Me); 56.1 (2) (CH_3, 4-OCH_3 [bis]); 60.8 (2) (CH_3, 3-OCH_3 [bis]); 62.0 (2) (CH_3, 2-OCH_3 [bis]); 100.8 (CH, C4'); 106.9 (2) (CH, C5 [bis]); 122.2 (2) (C, C1 [bis]); 125.9 (2) (CH, C6 [bis]); 141.4 (2) (C, C3 [bis]); 152.2 (2) (C, C2 [bis]); 156.7 (2) (C, C4 [bis]); 159.9 (C, C3'); 168.5 (2) (C, CO) [bis]); 170.8 (C, C5'). **HRMS** ($C_{24}H_{26}N_2NaO_9^+$): calculated 509.1531 ($M+Na^+$), found 509.1522.

Synthesis of 2,3,4-trimethoxy-N-(thiazol-2-yl)benzamide (246)

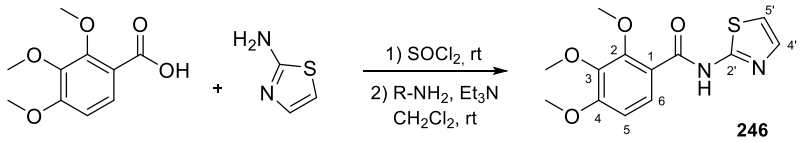

246

Following method **A2**, a mixture of 0.5 mL of $SOCl_2$ and 2,3,4-trimethoxybenzoic acid (309 mg, 1.46 mmol) was stirred for 6 h, and the resulting acyl chloride was added drop by drop to a solution of thiazol-2-amine (117 mg, 1.17 mmol) and triethylamine (0.5 mL) in 25 mL of CH_2Cl_2. The reaction was stirred for 2 days at room temperature under N_2 atmosphere giving 302 mg. Crystallization in MeOH yielded 247 mg (0.84 mmol, 72%) of **246**.

*2,3,4-Trimethoxy-N-(thiazol-2-yl)benzamide (**246**).* Yellowish-brown crystals. **Mp** (MeOH): 160.0-160.5 °C. **IR** (KBr): 3311, 1660, 1534, 1463, 1290, 1090 cm^{-1}. **^{1}H-NMR** (400 MHz, $CDCl_3$): δ 3.90 (3H, s, 4-OCH_3); 3.94 (3H, s, 3-OCH_3); 4.13 (3H, s, 2-OCH_3); 6.84 (1H, d, *J* = 9.2 Hz, H5); 7.00 (1H, d, *J* = 3.6 Hz, H5'); 7.50 (1H, d, *J* = 3.6 Hz, H4'); 8.02 (1H, d, *J* = 9.2 Hz, H6); 11.25 (1H, bs, NH). **^{13}C-NMR** (100 MHz, $CDCl_3$): δ 56.2 (CH_3, 4-OCH_3); 61.0 (CH_3, 3-OCH_3); 62.1 (CH_3, OCH_3); 107.9 (CH, C5); 113.7 (CH, C5'); 116.2 (C, C1); 127.3 (CH, C6); 137.8 (CH, C4'); 141.7 (C, C3); 152.7 (C, C2); 157.8 (C, C4); 158.3 (C, C2'); 162.1 (C, CO). **HRMS** ($C_{13}H_{14}N_2NaO_4S^+$): calculated 317.0566 ($M+Na^+$), found 317.0561.

Synthesis of 2,3,4-trimethoxy-N-(6-methylbenzo[d]thiazol-2-yl)benzamide (247)

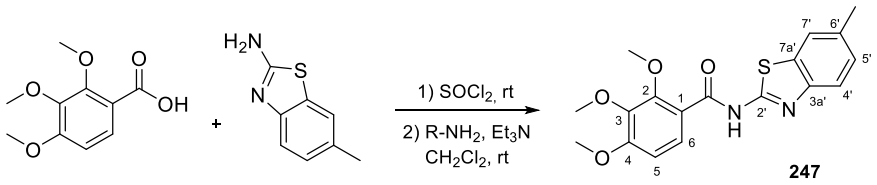

247

Following general method **A2**, $SOCl_2$ (0.5 mL) was added to the carboxylic acid (235 mg, 1.11 mmol) and stirred for 6 h at room temperature. Then, the acyl chloride was added dropwise to a solution of 6-methylbenzo[d]thiazol-2-amine (148 mg, 0.90 mmol) and 100 µL of triethylamine in 5 mL of CH_2Cl_2. The reaction was kept for 72 h at room temperature to obtain 362 mg. Crystallization in $MeOH/CH_2Cl_2$ yielded 226 mg (0.63 mmol, 70%) of **247**.

*2,3,4-Trimethoxy-N-(6-methylbenzo[d]thiazol-2-yl)benzamide (**247**).* White crystals. **Mp** ($MeOH/CH_2Cl_2$): 208.1-208.9 °C. **IR** (KBr): 3315, 1672, 1597, 1536, 1273, 1093 cm^{-1}. **^{1}H-NMR** (400 MHz, $CDCl_3$): δ 2.47 (3H, s, CH_3); 3.90 (3H, s, 4-OCH_3); 3.94 (3H, s, 3-OCH_3); 4.16 (3H, s, 2-OCH_3); 6.84 (1H, d, *J* = 8.8 Hz, H5); 7.25 (1H, dd, *J* = 2.0 and 8.4 Hz, H5'); 7.63 (1H, d, *J* = 2.0 Hz, H7'); 7.69 (1H, d, *J* = 8.4 Hz, H4'); 8.03 (1H, d, *J* = 8.8 Hz, H6); 11.28 (1H, bs, NH). **^{13}C-NMR** (100 MHz, $CDCl_3$): δ 21.4 (CH_3, Me); 56.2 (CH_3, 4-OCH_3); 61.0 (CH_3, 3-OCH_3); 62.2 (CH_3, 2-OCH_3); 107.9 (CH, C5); 116.2 (C, C1); 120.5 (CH, C4'); 121.1 (CH, C7'); 127.4 (CH, C6); 127.6 (CH, C5'); 132.6 (C, C7a); 133.7 (C, C6'); 141.7 (C, C3); 146.8 (C, C3a); 152.9 (C, C2); 157.2 (C, C4); 158.1 (C, C2'); 162.7 (C, CO). **HRMS** ($C_{18}H_{19}N_2O_4S^+$): calculated 359.1060 ($M+H^+$), found 359.1062.

Synthesis of 2,3-dimethoxy-N-(pyridin-3-yl)benzamide (248)

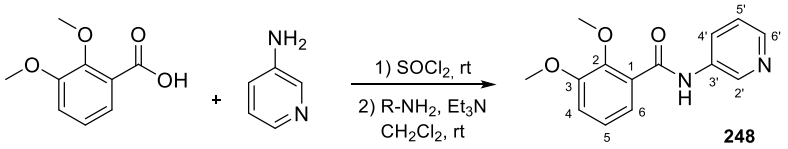

248

The acyl chloride was formed via method **A2** by reaction between $SOCl_2$ (800 µL) and 2,3-dimethoxybenzoic acid (224 mg, 1.23 mmol) for 15 h. It was added to a solution of 3-aminopyridine (93 mg, 1.00 mmol) in 25 mL of CH_2Cl_2 with 200 µL of triethylamine. The reaction mixture was stirred for 15 h, turning from yellow to orange over the time, giving 229 mg. Column chromatography with EtOAc/Hex 7:3 yielded 155 mg (0.60 mmol, 61%) of **248** as a white solid.

*2,3-Dimethoxy-N-(pyridin-3-yl)benzamide (**248**).* White solid. **IR** (KBr): 3286, 1681, 1588, 1425, 1265, 1061 cm^{-1}. **^{1}H-NMR** (400 MHz, $CDCl_3$): δ 3.82 (3H, s, 3-OCH_3); 3.91 (3H, s, 2-OCH_3); 7.01 (1H, dd, *J* = 2.0 and 8.0 Hz, H4); 7.09 (1H, t, *J* = 8.0 Hz, H5); 7.20 (1H, dd, *J* = 4.8 and 8.4 Hz. H5'); 7.64 (1H, dd, *J* = 2.0 and 8.0 Hz, H6); 8.24 (2H, m, H4' and H6'); 8.60 (1H, d, *J* = 2.8 Hz, H2'); 10.07 (1H, bs, NH). **^{13}C-NMR** (100 MHz, $CDCl_3$): δ 54.7 (CH_3, 3-OCH_3); 60.3 (CH_3, 2-OCH_3); 114.7 (CH, C4); 121.3 (CH, C6); 122.3 (CH, C5); 123.4 (CH, C5'); 124.7 (C, C1); 125.9 (CH, C2'); 138.8 (C, C3'); 140.1 (CH, C6'); 143.7 (CH, C4'); 145.8 (C, C2); 151.2 (C, C3); 162.2 (C, CO). **HRMS** ($C_{14}H_{14}N_2NaO_3^+$): calculated 281.0897 ($M+Na^+$), found 281.0896.

Synthesis of 2,3-dimethoxy-N-(pyridin-4-yl)benzamide (249)

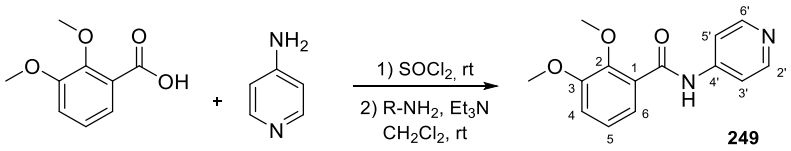

As detailed in method **A2**, the mixture of $SOCl_2$ (0.6 mL) and 2,3-dimethoxybenzoic acid (254 mg, 1.40 mmol) was stirred at room temperature for 3 days, giving the corresponding acyl chloride, which was then added dropwise to a solution of 4-aminopyridine (106 mg, 1.13 mmol) and triethylamine (1 mL) in 50 mL of CH_2Cl_2. Two hours later, the reaction was treated as described, obtaining 247 mg. Column chromatography using EtOAc provided 194 mg (0.74 mmol, 67%) of **249**, then crystallized in CH_2Cl_2/Hex (68 mg, 0.26 mmol, 23%).

*2,3-Dimethoxy-N-(pyridin-4-yl)benzamide (**249**).* Purple crystals. **Mp** (CH_2Cl_2/Hex): 104.2-105.1 °C. **IR** (KBr): 3305, 1693, 1581, 1513, 1260, 1052 cm^{-1}. **^{1}H-NMR** (400 MHz, $CDCl_3$): δ 3.94 (3H, s, 3-OCH_3); 4.02 (3H, s, 2-OCH_3); 7.14 (1H, dd, *J* = 1.6 and 8.0 Hz, H4); 7.23 (1H, t, *J* = 8.0 Hz, H5); 7.65 (2H, d, *J* = 6.4 Hz, H3' and H5'); 7.76 (1H, dd, *J* = 1.6 and 8.0 Hz, H6); 8.54 (2H, d, *J* = 6.4 Hz, H2' and H6'); 10.28 (1H, bs, NH). **^{13}C-NMR** (100 MHz, $CDCl_3$): δ 56.1 (CH_3, 3-OCH_3); 61.7 (CH_3, 2-OCH_3); 114.0 (2) (CH, C3' and C5'); 116.3 (CH, C4); 122.6 (CH, C6); 124.8 (CH, C5); 126.0 (C, C1); 145.3 (C, C2); 147.2 (C, C3); 150.5 (2) (CH, C2' and C6'); 152.5 (C, C4'); 163.8 (C, CO). **HRMS** ($C_{14}H_{14}N_2NaO_3^+$): calculated 281.0897 ($M+Na^+$), found 281.0892.

Synthesis of N-(3,4-dimethoxyphenyl)picolinamide (250)

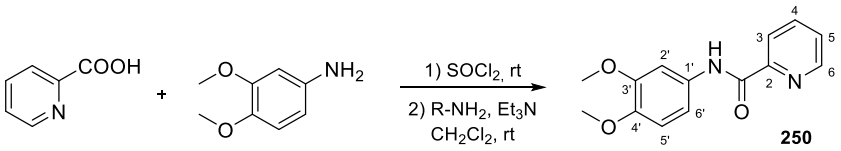

As explained in method **A2**, $SOCl_2$ (2 mL) reacted with picolinic acid (429 mg, 3.48 mmol) over 24 h to provide the acyl chloride. It was added to a solution of 4-aminoveratrole (473 mg, 3.09 mmol) and 2 mL of triethylamine in 50 mL of CH_2Cl_2 and kept for 8 h at room temperature, to obtain 799 mg. Column chromatography with EtOAc/Hex 1:1 provided 512 mg (1.98 mmol, 64%) of **250**, which was crystallized in MeOH (176 mg, 0.68 mmol, 22%).

*N-(3,4-dimethoxyphenyl)picolinamide (**250**).* Pinkish brown crystals. **Mp** (MeOH): 89-90 °C. **^{1}H-NMR** (400 MHz, $CDCl_3$): δ 3.89 (3H, s, 3'-OCH_3); 3.94 (3H, s, 4'-OCH_3); 6.87 (1H, d, *J* = 8.8 Hz, H5'); 7.15 (1H, dd, *J* = 2.4 and 8.8 Hz, H6'); 7.48 (1H, ddd, *J* = 1.2, 4.8 and 8.0 Hz, H5); 7.63 (1H, d, *J* = 2.4 Hz, H2'); 7.91 (1H, td, *J* = 1.2 and 8.0 Hz, H4); 8.29 (1H, bd, *J* = 8.0 Hz, H3); 8.61 (1H, bd, *J* = 4.8 Hz, H6); 9.95 (1H, bs, NH). **^{13}C-NMR** (100 MHz, $CDCl_3$): δ 55.9 (CH_3, OCH_3); 56.1 (CH_3, OCH_3); 104.3 (CH, C2'); 111.4 (CH, C5'); 111.5 (CH, C6'); 122.2 (CH, C3); 126.3 (CH, C5); 131.5 (C, C1'); 137.7 (CH, C4); 145.8 (C, C4'); 147.9 (CH, C6); 149.1 (C, C3'); 149.9 (C, C2); 161.7 (C, CO). **HRMS** ($C_{14}H_{14}N_2NaO_3^+$): calculated 281.0897 ($M+Na^+$), found 281.0908.

Synthesis of N-(3,4-dimethoxyphenyl)nicotinamide (251)

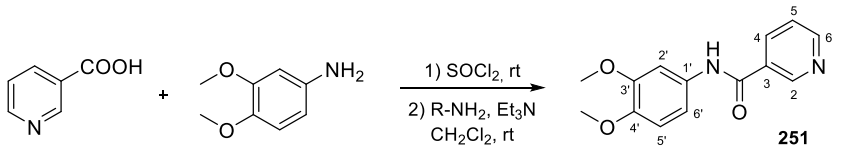

Following method **A2**, the acyl chloride formed after 4 days at room temperature between $SOCl_2$ (1 mL) and nicotinic acid (353 mg, 2.89 mmol) was added drop by drop into a solution of 4-aminoveratrole (381 mg, 2.49 mmol) and 500 µL of triethylamine in 50 mL of CH_2Cl_2. One hour and a half later, the reaction was processed, providing 530 mg (2.05 mmol, 83%) of **251**. Crystallization in MeOH gave 223 mg (0.86 mmol, 35%) of **251** as grey crystals.

*N-(3,4-dimethoxyphenyl)nicotinamide (**251**).* Grey crystals. **Mp** (MeOH): 150.9-151.9 °C. **IR** (KBr): 3271, 1650, 1606, 1510, 1236, 1025 cm^{-1}. **^{1}H-NMR** (400 MHz, $CDCl_3$): δ 3.88 (3H, s, 3'-OCH_3); 3.90 (3H, s, 4'-OCH_3); 6.85 (1H, d, *J* = 8.4 Hz, H5'); 7.03 (1H, dd, *J* = 1.6 and 8.4 Hz, H6'); 7.42-7.45 (2H, m, H2' and H5); 8.05 (1H, bs, NH); 8.21 (1H, bd, *J* = 7.6 Hz, H4); 8.75 (1H, bd, *J* = 5.4 Hz, H6); 9.10 (1H, bs, H2). **^{13}C-NMR** (100 MHz, $CDCl_3$): δ 55.7 (CH_3, OCH_3); 56.1 (CH_3, OCH_3); 105.5 (CH, C2'); 111.2 (CH, C5'); 112.8 (CH, C6'); 123.6 (CH, C5); 130.8 (C, C3); 131.2 (C, C1'); 135.4 (CH, C4); 146.2 (C, C4'); 148.0 (CH, C6); 148.9 (C, C3'); 152.1 (CH, C2); 164.0 (C, CO). **HRMS** ($C_{14}H_{14}N_2NaO_3^+$): calculated 281.0897 ($M+Na^+$), found 281.0909.

Synthesis of N-(3,4-dimethoxyphenyl)-N-methylnicotinamide (252)

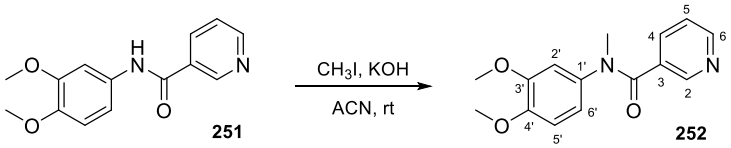

Following method **C1**, methyl iodide was added to a solution of **251** (352 mg, 1.36 mmol) with excess KOH in powder in 25 mL of ACN. The reaction was stirred for 72 h at room temperature to obtain 269 mg. Column chromatography with EtOAc gave 181 mg (0.63 mmol, 46%) of **252**.

*N-(3,4-dimethoxyphenyl)-N-methylnicotinamide (**252**).* Brown solid. **IR** (KBr): 1625, 1597, 1513, 1413, 1252, 1024 cm^{-1}. **^{1}H-NMR** (400 MHz, $CDCl_3$): δ 3.46 (3H, s, NCH_3); 3.71 (3H, s, 3'-OCH_3); 3.80 (3H, s, 4'-OCH_3); 6.53 (1H, bs, H2'); 6.58 (1H, bd, *J* = 8.4 Hz, H6'); 6.68 (1H, bd, *J* = 8.4 Hz, H5'); 7.12 (1H, m, H5); 7.62 (1H, bd, *J* = 6.8 Hz, H4); 8.44 (1H, bd, *J* = 4.8 Hz, H6); 8.51 (1H, bs, H2). **^{13}C-NMR** (100 MHz, $CDCl_3$): δ 38.4 (CH_3, NCH_3); 55.7 (CH_3, OCH_3); 56.0 (CH_3, OCH_3); 110.4 (CH, C2'); 111.1 (CH, C5'); 119.3 (CH, C6'); 122.6 (CH, C5); 131.9 (C, C3); 135.7 (CH, C4); 136.9 (C, C1'); 147.9 (C, C4'); 149.3 (CH, C6); 150.1 (CH, C2); 168.0 (C, CO). Quaternary carbon (C3') not observed. **HRMS** ($C_{15}H_{16}N_2NaO_3^+$): calculated 295.1053 ($M+Na^+$), found 295.1066.

Synthesis of N-(3,4-dimethoxyphenyl)isonicotinamide (253)

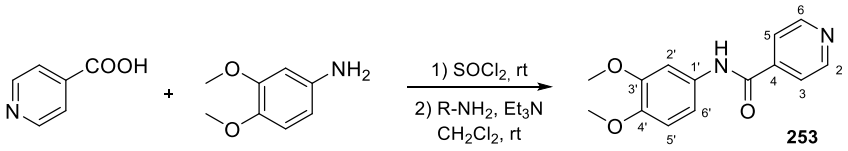

As described in method **A2**, $SOCl_2$ (1 mL) converted isonicotinic acid (360 mg, 2.92 mmol) into its acyl chloride after 21 h at room temperature. It was subsequently added dropwise to a mixture of 4-aminoveratrole (360 mg, 2.35 mmol) and triethylamine (1 mL) in 50 mL of CH_2Cl_2. After 10 h, the reaction was treated as described obtaining 532 mg (2.06 mmol, 88%) of **253**. Crystallization in MeOH gave 310 mg (**253**, 1.20 mmol, 51%).

*N-(3,4-dimethoxyphenyl)isonicotinamide (**253**).* Brown crystals. **Mp** (MeOH): 144.7-145.4 °C. **IR** (KBr): 3253, 1671, 1610, 1513, 1404, 1234, 1028 cm^{-1}. **^{1}H-NMR** (400 MHz, $CDCl_3$): δ 3.88 (6H, s, OCH_3); 6.84 (1H, d, *J* = 8.8 Hz, H5'); 7.02 (1H, dd, *J* = 2.4 and 8.8 Hz, H6'); 7.43 (1H, d, *J* = 2.4 Hz, H2'); 7.71 (2H, d, *J* = 5.6 Hz, H3 and H5); 8.13 (1H, bs, NH); 8.75 (2H, d, *J* = 5.6 Hz, H2 and H6). **^{13}C-NMR** (100 MHz, $CDCl_3$): δ 56.0 (2) (CH_3, OCH_3); 105.4 (CH, C2'); 111.2 (CH, C5'); 112.8 (CH, C6'); 121.0 (2) (CH, C3 and C5); 130.9 (C, C1'); 142.2 (C, C4); 146.4 (C, C4'); 149.0 (C, C3'); 150.4 (2) (CH, C2 and C6); 163.8 (C, CO). **HRMS** ($C_{14}H_{14}N_2NaO_3^+$): calculated 281.0897 ($M+Na^+$), found 281.0907.

Synthesis of N-(3,4-dimethoxyphenyl)-N-methylisonicotinamide (254)

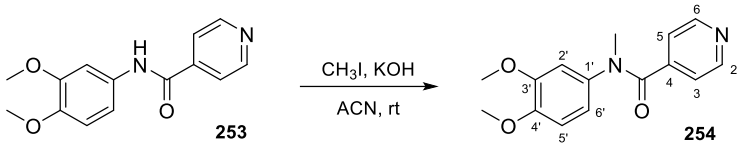

Methylation of **253** was conducted via method **C1**: methyl iodide was added to the amide derivative (**253**, 211 mg, 0.82 mmol) with ground KOH in excess in 25 mL of ACN. The reaction mixture was stirred for 72 h under N_2 at room temperature, obtaining 204 mg. Column chromatography using EtOAc provided 152 mg (0.56 mmol, 68%) of **254**.

*N-(3,4-dimethoxyphenyl)-N-methylisonicotinamide (**254**).* Brown solid. **IR** (KBr): 1635, 1585, 1513, 1250, 1023 cm^{-1}. **^{1}H-NMR** (400 MHz, $CDCl_3$): δ 3.40 (3H, s, NCH_3); 3.67 (3H, s, 3'-OCH_3); 6.76 (3H, s, 4'-OCH_3); 6.49 (2H, m, H2' and H6'); 6.61 (1H, bd, *J* = 8.0 Hz, H5'); 7.08 (2H, bd, *J* = 4.8 Hz, H3 and H5); 8.40 (2H, bd, *J* = 4.8 Hz, H2 and H6). **^{13}C-NMR** (100 MHz, $CDCl_3$): δ 38.3 (CH_3, NCH_3); 55.9 (2) (CH_3, OCH_3); 110.3 (CH, C2'); 111.0 (CH, C5'); 119.4 (CH, C6'); 122.3 (2) (CH, C3 and C5); 136.5 (C, C1'); 143.8 (C, C4); 148.1 (C, C4'); 149.3 (C, C3'); 149.6 (2) (CH, C2 and C6); 168.2 (C, CO). **HRMS** ($C_{15}H_{16}N_2NaO_3^+$): calculated 295.1053 ($M+Na^+$), found 295.1061.

Synthesis of 1-(3,4-dimethoxyphenyl)-3-ethylurea (255)

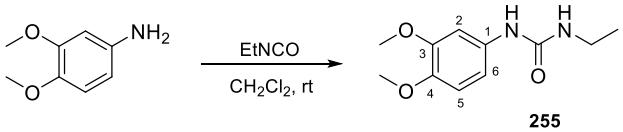

A mixture of ethyl isocyanate (228 µL, 2.88 mmol) and 4-aminoveratrole (294 mg, 1.92 mmol) in 15 mL of CH_2Cl_2 was kept for 24 h at room temperature and N_2, then poured into cold water and washed with brine until neutrality. The organic layer was dried over anhydrous Na_2SO_4, filtered, and rotary evaporated, providing 362 mg (1.62 mmol, 84%) of **255**. It was then crystallized in MeOH (56 mg, 0.25 mmol, 13%).

*1-(3,4-Dimethoxyphenyl)-3-ethylurea (**255**).* Pink crystals. **Mp** (MeOH): 127.7-128.5 °C. **IR** (KBr): 3321, 1644, 1609, 1519, 1237, 1024 cm^{-1}. **^{1}H-NMR** (400 MHz, $CDCl_3$): δ 1.13 (3H, t, *J* = 7.2 Hz, Et); 3.28 (2H, q, *J*

= 7.2 Hz, Et); 3.87 (6H, s, OCH_3); 4.63 (1H, bs, NH); 6.14 (1H, bs, NH); 6.72 (1H, dd, *J* = 2.4 and 8.4 Hz, H6); 6.81 (1H, d, *J* = 8.4 Hz, H5); 6.96 (1H, d, *J* = 2.4 Hz, H2). **^{13}C-NMR** (100 MHz, $CDCl_3$): δ 15.6 (CH_3, Et); 35.0 (CH_2, Et); 55.8 (CH_3, OCH_3); 56.3 (CH_3, OCH_3); 105.4 (CH, C2); 111.8 (CH, C5); 112.3 (CH, C6); 133.1 (C, C1); 145.0 (C, C4); 149.2 (C, C3); 157.3 (C, CO). **HRMS** ($C_{11}H_{16}N_2NaO_3^+$): calculated 247.1053 ($M+Na^+$), found 247.1058.

Synthesis of 1-(2-bromo-4,5-dimethoxyphenyl)-3-ethylurea (256)

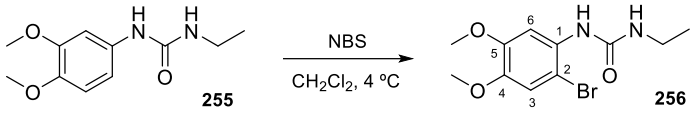

255 256

N-bromosuccinimide (127 mg, 0.71 mmol) was added to a solution of **255** (146 mg, 0.65 mmol) in 5 mL of CH_2Cl_2 at 4 °C, which turned from brown to purple after the addition. After 15 h under N_2 atmosphere the reaction was concentrated to dryness. Crystallization in MeOH followed by column chromatography with CH_2Cl_2/EtOAc 85:15 gave compound **256** with succinimide. Global yield: 182 mg, 0.60 mmol, 92%.

*1-(2-Bromo-4,5-dimethoxyphenyl)-3-ethylurea (**256**).* Non-isolated product. **^{1}H-NMR** (400 MHz, $CDCl_3$): δ 1.19 (3H, t, *J* = 7.2 Hz, Et); 3.31 (2H, q, *J* = 7.2 Hz, Et); 3.84 (3H, s, 5-OCH_3); 3.87 (3H, s, 4-OCH_3); 6.59 (1H, bs, NH); 6.97 (1H, s, H6); 7.63 (1H, s, H3). **HRMS** ($C_{11}H_{15}BrN_2NaO_3^+$): calculated 327.0158 ($M+Na^+$), found 327.0151.

Synthesis of 1-(3,4-dimethoxyphenyl)-3-phenylurea (257)

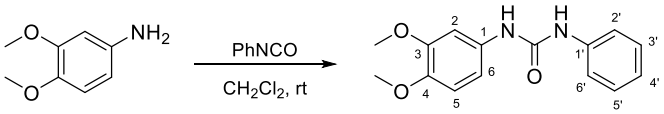

257

Phenyl isocyanate (254 µL, 2.33 mmol) was added to a solution of 4-aminoveratrole (239 mg, 1.56 mmol) in 15 mL of CH_2Cl_2 and stirred for 24 h under N_2 atmosphere at room temperature, turning into a pinkish-brown suspension. The resulting crystals were filtered off to obtain urea derivative **257** (387 mg, 1.42 mmol, 91%).

*1-(3,4-Dimethoxyphenyl)-3-phenylurea (**257**).* White crystals. **Mp** (CH_2Cl_2): 180.0-180.3 °C. **IR** (KBr): 3293, 1628, 1562, 1517, 1233, 1134, 1027 cm^{-1}. **^{1}H-NMR** (400 MHz, $CDCl_3$): δ 3.85 (3H, s, 3-OCH_3); 3.86 (3H, s, 4-OCH_3); 6.61 (1H, bs, NH); 6.73 (1H, bs, NH); 6.76 (1H, dd, *J* = 2.4 and 8.4 Hz, H6); 6.81 (1H, d, *J* = 8.4 Hz, H5); 7.02 (1H, d, *J* = 2.4 Hz, H2); 7.09 (1H, dt, *J* = 1.6 and 8.8 Hz, H4'); 7.28-7.34 (4H, m, H2', H3', H5' and H6'). **^{13}C-NMR** (100 MHz, DMSO-D6): δ 55.8 (CH_3, OCH_3); 56.2 (CH_3, OCH_3); 104.4 (CH, C2); 110.7 (CH, C5); 112.9 (CH, C6); 118.6 (2) (CH, C2' and C6'); 122.1 (CH, C4'); 129.2 (2) (CH, C3' and C5'); 133.8 (C, C1); 140.3 (C, C1'); 144.5 (C, C4); 149.3 (C, C3); 153.2 (C, CO). **HRMS** ($C_{15}H_{16}N_2NaO_3^+$): calculated 295.1053 ($M+Na^+$), found 295.1065.

Synthesis of 1-benzyl-3-(3,4-dimethoxyphenyl)urea (258)

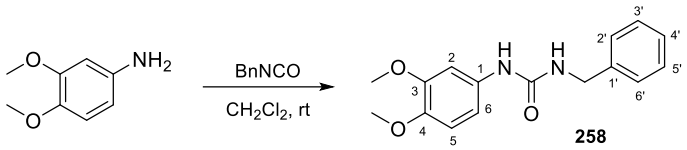

A mixture of 4-aminoveratrole (262 mg, 1.71 mmol) and benzyl isocyanate (317 µL, 2.57 mmol) in 15 mL of CH_2Cl_2 was kept for 24 h at room temperature under N_2, turning purple. The resulting crystals were filtered off, obtaining 410 mg (1.43 mmol, 84%) of **258**.

*1-Benzyl-3-(3,4-dimethoxyphenyl)urea (**258**).* White crystals. **Mp** (CH_2Cl_2): 155-156 °C. **IR** (KBr): 3308, 1632, 1570, 1516, 1234, 1028 cm^{-1}. **^{1}H-NMR** (400 MHz, $CDCl_3$): δ 3.83 (3H, s, 3-OCH_3); 3.85 (3H, s, 4-OCH_3); 4.43 (2H, s, CH_2); 6.27 (1H, bs, NH); 6.71 (1H, dd, *J* = 2.4 and 8.8 Hz, H6); 6.78 (1H, d, *J* = 8.8 Hz, H5); 6.94 (1H, d, *J* = 2.4 Hz, H2); 7.26-7.34 (5H, m, Ph). **^{13}C-NMR** (100 MHz, $CDCl_3$): δ 45.3 (CH_2); 57.0 (CH_3, OCH_3); 57.5 (CH_3, OCH_3); 107.4 (CH, C2); 113.0 (CH, C5); 114.5 (CH, C6); 128.5 (CH, C4'); 128.9 (2) (CH, C2' and C6'); 130.0 (2) (CH, C3' and C5'); 133.6 (C, C1); 140.6 (C, C1'); 146.8 (C, C4); 150.6 (C, C3); 158.4 (C, CO). **HRMS** ($C_{16}H_{18}N_2NaO_3^+$): calculated 309.1210 ($M+Na^+$), found 309.1209.

Synthesis of 1-benzyl-3-(2-bromo-4,5-dimethoxyphenyl)urea (259)

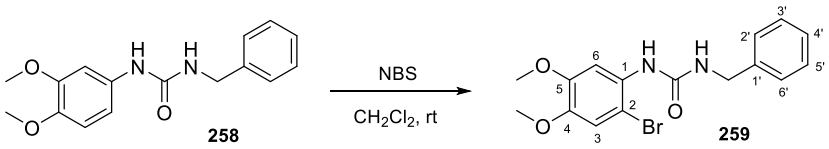

N-bromosuccinimide (102 mg, 0.57 mmol) was added to a solution of **258** (140 mg, 0.49 mmol) in 5 mL of CH_2Cl_2 at room temperature. The reaction was stirred for 30 min under N_2 atmosphere, turning pinkish-violet. The evaporated residue (264 mg) was crystallized in MeOH, providing compound **259** (166 mg, 0.45 mmol, 93%).

*1-Benzyl-3-(2-bromo-4,5-dimethoxyphenyl)urea (**259**).* White crystals. **Mp** (MeOH): 178.7-179.8 °C. **IR** (KBr): 3326, 3255, 1635, 1510, 1207, 1038 cm^{-1}. **^{1}H-NMR** (400 MHz, $CDCl_3$): δ 3.84 (3H, s, 5-OCH_3); 3.86 (3H, s, 4-OCH_3); 4.47 (2H, d, *J* = 5.6 Hz, CH_2); 4.94 (1H, bs, NH); 6.41 (1H, bs, NH); 6.96 (1H, s, H6); 7.27-7.35 (5H, m, Ph); 7.67 (1H, s, H3). **^{13}C-NMR** (100 MHz, $CDCl_3$): δ 44.3 (CH_2); 56.0 (CH_3, OCH_3); 56.3 (CH_3, OCH_3); 104.6 (CH, C6); 106.9 (C, C2); 114.7 (CH, C3); 127.4 (CH, C4'); 127.5 (2) (CH, C2' and C6'); 128.7 (2) (CH, C3' and C5'); 130.0 (C, C1); 138.6 (C, C1'); 145.7 (C, C4); 148.6 (C, C5); 155.6 (C, CO). **HRMS** ($C_{16}H_{18}BrN_2O_3^+$): calculated 365.0495 ($M+H^+$), found 365.0500.

Synthesis of 1-benzyl-3-(2,6-dibromo-3,4-dimethoxyphenyl)urea (260)

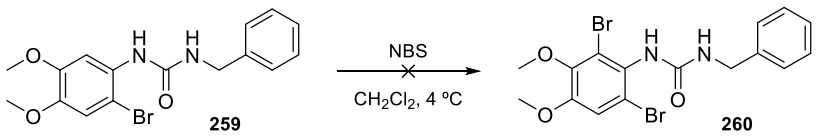

N-bromosuccinimide (62 mg, 0.35 mmol) was added to a solution of **259** (113 mg, 0.31 mmol) in 5 mL of CH_2Cl_2 at 4 °C. The reaction mixture was stirred under N_2 for 24 h. It was then evaporated under vacuum obtaining 172 mg of a complex mixture.

Synthesis of 2,4-dimethoxy-N-(pyridin-2-yl)benzamide (261)

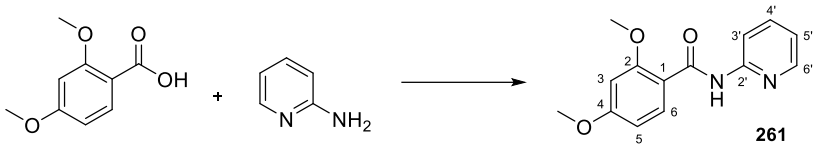

Procedure 1: Following method **A2**, $SOCl_2$ (400 µL) added to the carboxylic acid (359 mg, 1.97 mmol) gave the corresponding acyl chloride after 6 h. It was subsequently poured drop by drop into a solution of 2-aminopyridine (164 mg, 1.74 mmol) and 100 µL of triethylamine in 5 mL of CH_2Cl_2. The reaction mixture was kept for 15 h under N_2 atmosphere and processed, obtaining 395 mg of a complex mixture.

Procedure 2: As described in method **A1**, the mixture of 2,4-dimethoxybenzoic acid (288 mg, 1.58 mmol), 2-aminopyridine (123 mg, 1.31 mmol), DCI (631 mg, 3.06 mmol), and *p*-DMAP (197 mg, 1.61 mmol) in 10 mL of CH_2Cl_2 was irradiated in a microwave oven at 100 °C for 30 min, obtaining 387 mg. Column chromatography using EtOAc/Hex 1:1 as eluent, followed by crystallization in MeOH gave 65 mg (0.25 mmol, 19%) of **261**.

*2,4-Dimethoxy-N-(pyridin-2-yl)benzamide (**261**).* White crystals. **Mp** (MeOH): 157-158 °C. **IR** (KBr): 3340, 1663, 1534, 1424, 1284, 1166 cm^{-1}. **^{1}H-NMR** (400 MHz, $CDCl_3$): δ 3.85 (3H, s, 4-OCH_3); 4.04 (3H, s, 2-OCH_3); 6.52 (1H, d, *J* = 2.0 Hz, H3); 6.63 (1H, dd, *J* = 2.0 and 8.8 Hz, H5); 7.01 (1H, dd, *J* = 5.2 and 8.0 Hz, H5'); 7.70 (1H, td, *J* = 1.2 and 8.0 Hz, H4'); 8.23 (1H, d, *J* = 8.8 Hz, H6); 8.30 (1H, dd, *J* = 1.2 and 5.2 Hz, H6'); 8.41 (1H, bd, *J* = 8.0 Hz, H3'); 10.25 (1H, bs, NH). **^{13}C-NMR** (100 MHz, $CDCl_3$): δ 55.6 (CH_3, 2-OCH_3); 56.2 (CH_3, 4-OCH_3); 98.6 (CH, C3); 105.7 (CH, C5); 114.3 (C, C1); 114.7 (CH, C3'); 119.4 (CH, C5'); 134.2 (CH, C6); 138.2 (CH, C4'); 147.9 (CH, C6'); 152.2 (C, C2); 158.9 (C, C2'); 163.4 (C, C4); 164.1 (C, CO). **HRMS** ($C_{14}H_{15}N_2O_3^+$): calculated 259.1077 ($M+H^+$), found 259.1080.

Synthesis of 2,4-dimethoxy-N-(pyridin-3-yl)benzamide (262)

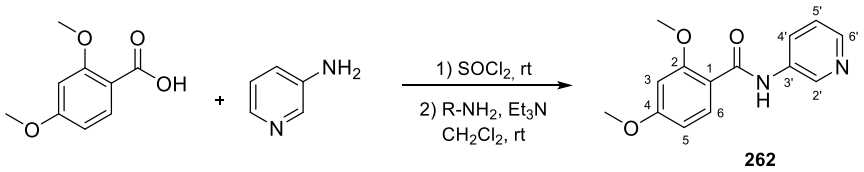

According to general method **A2**, the mixture of $SOCl_2$ (400 µL) and 2,4-dimethoxybenzoic acid (317 mg, 1.74 mmol) provided the acyl chloride after 5 h. It was then added drop by drop into a solution of 3-aminopyridine (152 mg, 1.61 mmol) and 100 µL of triethylamine in 12 mL of CH_2Cl_2, turning orange, obtaining 362 mg after 14 h. Column chromatography using EtOAc/Hex (2:8) as eluent, followed by crystallization in MeOH gave 125 mg (0.48 mmol, 30%) of **262**.

*2,4-Dimethoxy-N-(pyridin-3-yl)benzamide (**262**).* White crystals. **Mp** (MeOH): 121-123 °C. **IR** (KBr): 3336, 1669, 1540, 1421, 1257, 1094 cm^{-1}. **^{1}H-NMR** (400 MHz, $CDCl_3$): δ 3.85 (3H, s, 4-OCH_3); 4.02 (3H, s, 2-OCH_3); 6.52 (1H, d, *J* = 2.4 Hz, H3); 6.64 (1H, dd, *J* = 2.4 and 8.8 Hz, H5); 7.27 (1H, dd, *J* = 4.8 and 8.0 Hz, H5'); 8.22

(1H, d, *J* = 8.8 Hz, H6); 8.33 (2H, m, H4' and H6'); 8.61 (1H, d, *J* = 2.8 Hz, H2'); 9.75 (1H, bs, NH). **^{13}C-NMR** (100 MHz, $CDCl_3$): δ 55.6 (CH_3, 2-OCH_3); 56.3 (CH_3, 4-OCH_3); 98.8 (CH, C3); 105.9 (CH, C5); 114.0 (C, C1); 123.7 (CH, C5'); 127.5 (CH, C6); 134.2 (CH, C2'); 135.4 (C, C3'); 141.6 (CH, C6'); 144.9 (CH, C4'); 158.6 (C, C2); 163.6 (C, C4); 164.1 (C, CO). **HRMS** ($C_{14}H_{15}N_2O_3^+$): calculated 259.1077 ($M+H^+$), found 259.1080.

Synthesis of 2,4-dimethoxy-N-(pyridin-4-yl)benzamide (263)

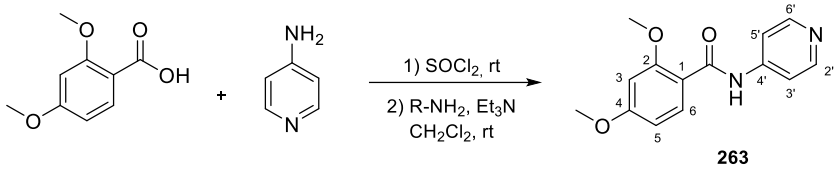

Following procedure **A2**, $SOCl_2$ (0.4 mL) reacted with 325 mg (1.78 mmol) of 2,4-dimethoxybenzoic acid over 7 h at room temperature. The acyl chloride was slowly added to a solution of 4-aminopyridine (154 mg, 1.64 mmol) and triethylamine (100 µL) in 5 mL of CH_2Cl_2. It was processed after 24 h, obtaining 325 mg (1.26 mmol, 77%) of **263**. Crystallization in ethanol gave 180 mg of amide **263** (0.70 mmol, 43%).

*2,4-Dimethoxy-N-(pyridin-4-yl)benzamide (**263**).* White crystals. **Mp** (EtOH): 152-153 °C. **IR** (KBr): 3344, 1666, 1584, 1419, 1265, 1167 cm^{-1}. **^{1}H-NMR** (400 MHz, $CDCl_3$): δ 3.89 (3H, s, 4-OCH_3); 4.06 (3H, s, 2-OCH_3); 6.54 (1H, d, *J* = 2.0 Hz, H3); 6.67 (1H, dd, *J* = 2.0 and 8.8 Hz, H5); 7.59 (2H, d, *J* = 6.0 Hz, H3' and H5'); 8.24 (1H, d, *J* = 8.8 Hz, H6); 8.51 (2H, d, *J* = 6.0 Hz, H2' and H6'); 9.87 (1H, bs, NH). **^{13}C-NMR** (100 MHz, $CDCl_3$): δ 55.4 (CH_3, 2-OCH_3); 56.1 (CH_3, 4-OCH_3); 98.3 (CH, C3); 105.8 (CH, C5); 113.4 (C, C1); 113.9 (2) (CH, C3' and C5'); 133.9 (CH, C6); 145.3 (C, C2); 150.3 (2) (CH, C2' and C6'); 158.4 (C, C4'); 163.6 (C, CO); 164.1 (C, C4). **HRMS** ($C_{14}H_{15}N_2O_3^+$): calculated 259.1077 ($M+H^+$), found 259.1068.

Synthesis of 2,4-dimethoxy-N-methyl-N-(pyridin-4-yl)benzamide (264)

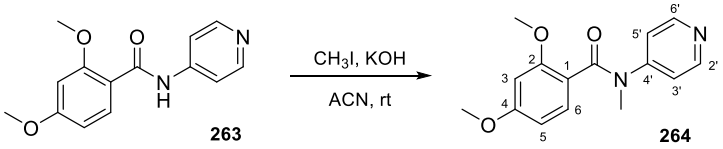

Following method **C1**, methyl iodide (70 µL, 1.12 mmol) was added to a mixture of **263** (127 mg, 0.49 mmol) with ground KOH in excess in 5 mL of ACN, that had been previously stirred for 30 min. The suspension was stirred for 3 days at room temperature under N_2, obtaining 68 mg (0.25 mmol, 51%) of **264**. Preparative TLC using EtOAc gave 12 mg (0.04 mmol, 9%) of **264**.

*2,4-Dimethoxy-N-methyl-N-(pyridin-4-yl)benzamide (**264**).* Yellow oil. **^{1}H-NMR** (400 MHz, $CDCl_3$): δ 3.40 (3H, s, NCH_3); 3.42 (3H, s, 4-OCH_3); 3.71 (3H, s, 2-OCH_3); 6.14 (1H, d, *J* = 2.0 Hz, H3); 6.39 (1H, dd, *J* = 2.0 and 8.4 Hz, H5); 6.89 (2H, d, *J* = 5.6 Hz, H3' and H5'); 7.22 (1H, d, *J* = 8.4 Hz, H6); 8.33 (2H, d, *J* = 5.6 Hz, H2' and H6'). **^{13}C-NMR** (100 MHz, $CDCl_3$): δ 36.4 (CH_3, NCH_3); 55.0 (CH_3, 2-OCH_3); 55.4 (CH_3, 4-OCH_3); 98.2 (CH, C3); 105.0 (2) (CH, C3' and C5'); 118.1 (C, C1); 119.4 (CH, C5); 130.7 (CH, C6); 150.0 (2) (CH, C2' and C6'); 151.8 (C, C2); 156.8 (C, C4'); 162.6 (C, C4); 168.8 (C, CO). **HRMS** ($C_{15}H_{16}N_2NaO_3^+$): calculated 295.1053 ($M+Na^+$), found 295.1048.

Synthesis of 1-(2,5-dimethoxyphenyl)-3-ethylurea (265)

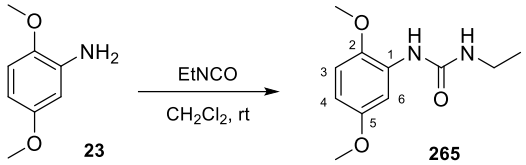

Ethyl isocyanate (191 µL, 2.41 mmol) was added to a solution of aniline **23** (246 mg, 1.61 mmol) in 5 mL of CH_2Cl_2, and stirred for 1 week at room temperature under N_2. The reaction mixture was then poured into cold water and washed with brine until neutral pH. The organic layer was dried over anhydrous Na_2SO_4, filtered, and rotary evaporated (280 mg). Column chromatography using CH_2Cl_2/EtOAc 9:1 yielded 254 mg (1.13 mmol, 71%) of **265**.

*1-(2,5-Dimethoxyphenyl)-3-ethylurea (**265**).* White solid. **IR** (KBr): 3326, 3087, 1693, 1643, 1461, 1281, 1025 cm^{-1}. **^{1}H-NMR** (400 MHz, $CDCl_3$): δ 1.09 (1H, t, *J* = 7.2 Hz, Et); 3.25 (2H, q, *J* = 7.2 Hz, Et); 3.67 (6H, s, OCH_3); 6.14 (1H, bs, NH); 6.41 (1H, dd, *J* = 3.2 and 9.2 Hz, H4); 6.68 (1H, d, *J* = 9.2 Hz, H3); 7.61 (1H, bs, NH); 7.84 (1H, d, *J* = 3.2 Hz, H6). **^{13}C-NMR** (100 MHz, $CDCl_3$): δ 16.5 (CH_3, Et); 36.2 (CH_2, Et); 56.8 (CH_3, OCH_3); 57.4 (CH_3, OCH_3); 106.8 (CH, C6); 107.8 (CH, C3); 112.2 (CH, C4); 131.2 (C, C1); 143.7 (C, C2); 155.2 (C, C5); 157.5 (C, CO). **HRMS** ($C_{11}H_{16}N_2NaO_3^+$): calculated 247.1053 ($M+Na^+$), found 247.1058.

Synthesis of 1-(2,5-dimethoxyphenyl)-3-phenylurea (266)

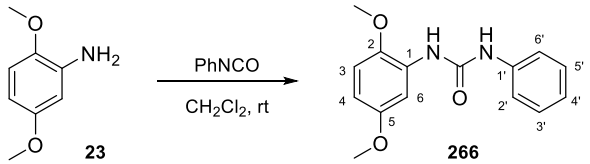

Phenyl isocyanate (221 µL, 2.03 mmol) was added to **23** (207 mg, 1.35 mmol) in 5 mL of CH_2Cl_2 and stirred for 24 h at room temperature under N_2. The reaction was poured into cold water, washed with brine until neutral pH, and the organic layer was dried over anhydrous Na_2SO_4, filtered and evaporated (282 mg). Column chromatography with CH_2Cl_2/EtOAc 95:5 yielded 182 mg (0.67 mmol, 49%) of **266**.

*1-(2,5-Dimethoxyphenyl)-3-phenylurea (**266**).* Light brown solid. **IR** (KBr): 3353, 3317, 1652, 1597, 1499, 1237 cm^{-1}. **^{1}H-NMR** (400 MHz, $CDCl_3$): δ 3.70 (3H, s, 5-OCH_3); 3.71 (3H, s, 2-OCH_3); 6.50 (1H, dd, *J* = 2.8 and 9.2 Hz, H4); 6.74 (1H, d, *J* = 9.2 Hz, H3); 7.05 (1H, bt, *J* = 7.2 Hz, H4'); 7.25 (2H, bt, *J* = 7.6 Hz, H3' and H5'); 7.35 (2H, bd, *J* = 7.6 Hz, H2' and H6'); 7.72 (1H, bs, NH); 7.78 (1H, bs, NH); 7.88 (1H, d, *J* = 2.8 Hz, H6). **^{13}C-NMR** (100 MHz, $CDCl_3$): δ 55.6 (CH_3, OCH_3); 56.4 (CH_3, OCH_3); 105.9 (CH, C6); 107.7 (CH, C3); 111.3 (CH, C4); 120.8 (2) (CH, C2' and C6'); 123.8 (CH, C4'); 129.0 (C, C1); 129.1 (2) (CH, C3' and C5'); 138.3 (C, C1'); 142.6 (C, C2); 153.5 (C, CO); 154.0 (C, C5). **HRMS** ($C_{15}H_{16}N_2NaO_3^+$): calculated 295.1053 ($M+Na^+$), found 295.1065.

Synthesis of 1-benzyl-3-(2,5-dimethoxyphenyl)urea (267)

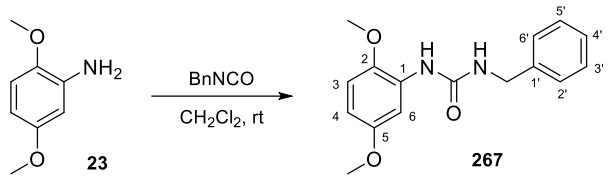

Benzyl isocyanate (231 µL, 1.87 mmol) was added to a solution of amine **23** (191 mg, 1.25 mmol) in 5 mL of CH_2Cl_2. The mixture was stirred for 1 week at room temperature under N_2, poured into iced water, and washed with brine until neutrality. The organic layer was dried over anhydrous Na_2SO_4, filtered, and concentrated to dryness to obtain 368 mg. Column chromatography with CH_2Cl_2/EtOAc 95:5 gave 204 mg (0.71 mmol, 57%) of **267**.

*1-Benzyl-3-(2,5-dimethoxyphenyl)urea (**267**).* White solid. **IR** (KBr): 3347, 3316, 1645, 1540, 1217, 1043 cm^{-1}. **^{1}H-NMR** (400 MHz, $CDCl_3$): δ 3.61 (3H, s, 5-OCH_3); 3.64 (3H, s, 2-OCH_3); 4.29 (2H, d, *J* = 5.2 Hz, CH_2); 6.45 (1H, dd, *J* = 2.8 and 8.8 Hz, H4); 6.56 (1H, bs, NH); 6.68 (1H, d, *J* = 8.8 Hz, H3); 7.16-7.20 (5H, m, Ph); 7.78 (1H, bs, NH); 7.87 (1H, d, *J* = 2.8 Hz, H6). **^{13}C-NMR** (100 MHz, $CDCl_3$): δ 43.9 (CH_2); 55.5 (CH_3, OCH_3); 56.0 (CH_3, OCH_3); 105.5 (CH, C6); 106.8 (CH, C3); 110.9 (CH, C4); 127.0 (CH, C4'); 127.2 (2) (CH, C2' and C6'); 128.4 (2) (CH, C3' and C5'); 129.7 (C, C1); 139.2 (C, C1'); 142.4 (C, C2); 153.9 (C, C5); 156.2 (C, CO). **HRMS** ($C_{16}H_{18}N_2NaO_3^+$): calculated 309.1210 ($M+Na^+$), found 309.1207.

Synthesis of phenyl (2,5-dimethoxyphenyl)carbamate (268)

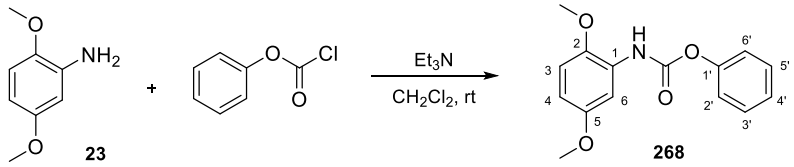

Phenyl chloroformate (256 µL, 2.04 mmol) was added to a solution of **23** (208 mg, 1.36 mmol) and 100 µL of triethylamine in 5 mL of CH_2Cl_2. After 24 h under N_2 atmosphere at room temperature, it was poured into cold water and washed with brine. The organic solvent was dried over anhydrous Na_2SO_4, filtered, and concentrated to dryness obtaining 393 mg. Column chromatography using toluene/CH_2Cl_2 6:4 yielded 202 mg (0.74 mmol, 54%) of **268** as a yellow solid.

*Phenyl (2,5-dimethoxyphenyl)carbamate (**268**).* Yellow solid. **IR** (KBr): 3391, 1750, 1535, 1476, 1230, 1158 cm^{-1}. **^{1}H-NMR** (400 MHz, $CDCl_3$): δ 3.78 (3H, s, 5-OCH_3); 3.85 (3H, s, 2-OCH_3); 6.59 (1H, dd, *J* = 2.8 and 8.8 Hz, H4); 6.82 (1H, d, *J* = 8.8 Hz, H3); 7.21-7.28 (3H, m, H2', H6' and H4'); 7.40 (2H, t, *J* = 8.4 Hz, H3' and H5'); 7.68 (1H, bs, H6); 7.90 (1H, bs, NH). **^{13}C-NMR** (100 MHz, $CDCl_3$): δ 55.7 (CH_3, OCH_3); 56.3 (CH_3, OCH_3); 104.5 (CH, C6); 108.2 (CH, C3); 111.0 (CH, C4); 121.8 (2) (CH, C2' and C6'); 125.7 (C, C4'); 127.8 (C, C1); 129.5 (2) (CH, C3' and C5'); 142.0 (C, C2); 150.6 (C, CO); 151.5 (C, C1'); 154.1 (C, C5). **HRMS** ($C_{15}H_{15}NNaO_4^+$): calculated 296.0893 ($M+Na^+$), found 296.0907.

PREPARATION OF BENZOTHIAZOLE-BASED DERIVATIVES

Synthesis of 1-ethyl-3-(6-methylbenzo[d]thiazol-2-yl)urea (269)

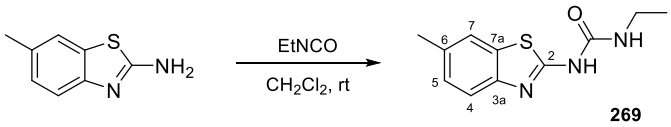

Ethyl isocyanate (208 µL, 2.63 mmol) was added to a solution of 6-methylbenzo[d]thiazol-2-amine (288 mg, 1.75 mmol) in 20 mL of CH_2Cl_2 at room temperature. The mixture was stirred for 24 h under N_2 atmosphere, resulting in *in situ* crystallization of **269** (205 mg, 0.87 mmol, 50%).

*1-Ethyl-3-(6-methylbenzo[d]thiazol-2-yl)urea (**269**).* White crystals. **Mp** (CH_2Cl_2): 312-313 °C. **IR** (KBr): 3325, 1709, 1549, 1468, 1275 cm^{-1}. **^{1}H-NMR** (400 MHz, $CDCl_3$): δ 1.26 (3H, t, *J* = 7.2 Hz, Et); 2.44 (3H, s, Me); 3.42 (2H, q, *J* = 7.2 Hz, Et); 7.20 (1H, dd, *J* = 1.2 and 8.4 Hz, H5); 7.52 (1H, bs, H7); 7.61 (1H, d, *J* = 8.4 Hz, H4). **^{13}C-NMR** (100 MHz, DMSO-D6): δ 15.6 (CH_3, Et); 21.3 (CH_3, Me); 34.7 (CH_2, Et); 119.6 (CH, C4); 121.4 (CH, C7); 127.4 (CH, C5); 131.9 (C, C7a); 132.3 (C, C6); 141.4 (C, C3a); 154.2 (C, CO); 156.5 (C, C2). **HRMS** ($C_{11}H_{13}N_3NaOS^+$): calculated 258.0672 ($M+Na^+$), found 258.0671.

Synthesis of 1-(4-bromo-6-methylbenzo[d]thiazol-2-yl)-3-ethylurea (270)

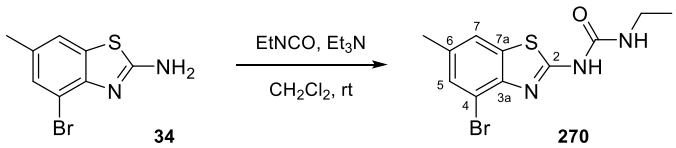

A mixture of ethyl isocyanate (90 µL, 1.14 mmol) and bromoderivative **34** (181 mg, 0.74 mmol) in 25 mL of CH_2Cl_2 and 1 mL of triethylamine was stirred for 1 week at room temperature under N_2 atmosphere. The reaction was poured into cold water and washed with brine until neutral pH. The organic layer was dried over anhydrous Na_2SO_4, filtered and rotary evaporated (266 mg). Crystallization in MeOH gave 147 mg (0.47 mmol, 63%) of **270**.

*1-(4-Bromo-6-methylbenzo[d]thiazol-2-yl)-3-ethylurea (**270**).* Brown crystals. **Mp** (MeOH): 279-280 °C. **IR** (KBr): 3367, 3111, 1704, 1682, 1563, 1442, 1259 cm^{-1}. **^{1}H-NMR** (400 MHz, DMSO-D6): δ 1.05 (3H, t, *J* = 6.8 Hz, Et); 2.33 (3H, s, CH_3); 3.16 (2H, q, *J* = 6.8 Hz, Et); 6.52 (1H, bs, NH); 7.38 (1H, s, H5); 7.64 (1H, s, H7); 11.16 (1H, bs, NH). **^{13}C-NMR** (100 MHz, DMSO-D6): δ 15.6 (CH_3, Et); 20.9 (CH_3, Me); 34.8 (CH_2, Et); 112.6 (C, C4); 121.2 (CH, C7); 130.2 (CH, C5); 132.9 (C, C7a); 134.1 (C, C6); 145.7 (C, C3a); 154.0 (C, CO); 160.2 (C, C2). **HRMS** ($C_{11}H_{12}BrN_3NaOS^+$): calculated 335.9777 ($M+Na^+$), found 335.9791.

Synthesis of 1-(6-methylbenzo[d]thiazol-2-yl)-3-phenylurea (271)

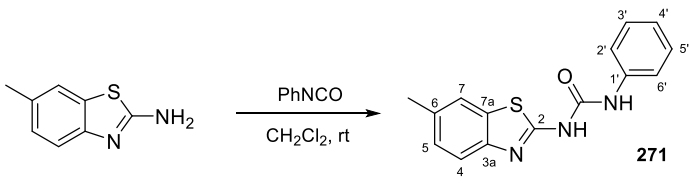

Phenyl isocyanate (258 µL, 2.37 mmol) was added to 6-methylbenzo[d]thiazol-2-amine (260 mg, 1.58 mmol) dissolved in 10 mL of CH_2Cl_2. After 5 h under N_2 at room temperature, **271** crystallized *in situ.* It was filtered off to obtain 365 mg (**271**, 1.29 mmol, 81%) as white crystals.

*1-(6-Methylbenzo[d]thiazol-2-yl)-3-phenylurea (**271**).* White crystals. **Mp** (CH_2Cl_2): 327-329 °C. **IR** (KBr): 3206, 1726, 1692, 1542, 1291 cm^{-1}. **^{1}H-NMR** (400 MHz, $CDCl_3$): δ 2.45 (3H, s, CH_3); 7.13 (1H, bt, *J* = 7.6 Hz, H4'); 7.23 (1H, dd, *J* = 1.2 and 8.0 Hz, H5); 7.34 (2H, t, *J* = 7.6 Hz, H3' and H5'); 7.52 (2H, t, *J* = 7.6 Hz, H2' and H6'); 7.54 (1H, bs, H7); 7.62 (1H, d, *J* = 8.0 Hz, H4). **^{13}C-NMR** (100 MHz, DMSO-D6): δ 21.3 (CH_3); 119.2 (2) (CH, C2' and C6'); 119.4 (CH, C4); 121.6 (CH, C7); 123.4 (CH, C4'); 127.6 (CH, C5); 129.4 (2) (CH, C3' and C5'); 131.7 (C, C7a); 132.7 (C, C6); 139.0 (C, C1'); 146.3 (C, C3a); 152.6 (C, CO); 159.4 (C, C2). **HRMS** ($C_{15}H_{13}N_3NaOS^+$): calculated 306.0672 ($M+Na^+$), found 306.0676.

Synthesis of 1-(6-methylbenzo[d]thiazol-2-yl)-3-phenylimidazolidin-2-one (272)

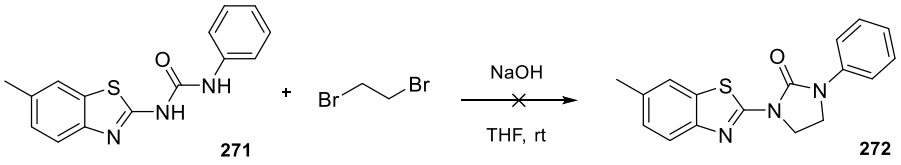

A solution of amide **271** (284 mg, 1.00 mmol) in 20 mL of THF and a few drops of 4% NaOH was added dropwise to 1,2-dibromoethane (104 µL, 1.21 mmol) in 80 mL of THF, and stirred for 4 days at room temperature under N_2. The reaction was concentrated under vacuum giving a complex mixture. A similar result was obtained with 60% NaH in dry THF at 4 °C.

Synthesis of 1,3-dimethyl-1-(6-methylbenzo[d]thiazol-2-yl)-3-phenylurea (273)

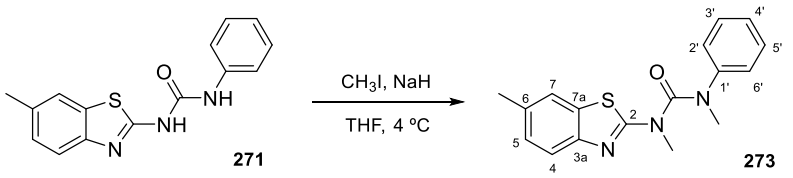

60% NaH (223 mg, 9.29 mmol) was carefully added to a pre-cooled solution of **271** (309 mg, 1.09 mmol) in 25 mL of dry THF, and methyl iodide (136 µL, 2.18 mmol) was subsequently added. After 4 days under N_2, methyl iodide (150 µL, 2.41 mmol) was added, and 6 days later, the reaction was poured into cold water, EtOAc was added and partially evaporated. The organic layer was washed with brine until neutral pH, dried over anhydrous Na_2SO_4, filtered, and concentrated to dryness (352 mg). Crystallization in MeOH/CH_2Cl_2 yielded 120 mg (0.39 mmol, 35%) of **273**.

*1,3-Dimethyl-1-(6-methylbenzo[d]thiazol-2-yl)-3-phenylurea (**273**).* White crystals. **Mp** (MeOH/CH_2Cl_2): 170.3-170.4 °C. **IR** (KBr): 1613, 1590, 1532, 1490, 1362 cm^{-1}. **^{1}H-NMR** (400 MHz, $CDCl_3$): δ 2.40 (3H, s, CH_3); 3.51 (6H, bs, NCH_3); 7.04 (1H, bd, *J* = 8.0 Hz, H5); 7.15 (1H, bd, *J* = 8.0 Hz, H4); 7.20 (1H, m, H4'); 7.37 (5H, m, H2', H3', H5', H6' and H7). **^{13}C-NMR** (100 MHz, $CDCl_3$): δ 21.0 (CH_3, Me); 31.5 (CH_3, NCH_3); 37.5 (CH_3, NCH_3); 110.1 (CH, C4); 112.6 (CH, C7); 125.3 (CH, C5); 126.3 (2) (CH, C2' and C6'); 126.6 (C, C7a); 127.2 (2) (CH, C3' and C5'); 128.4 (CH, C4'); 132.8 (C, C6); 135.7 (C, C1'); 144.9 (C, C3a); 162.0 (C, CO); 166.1 (C, C2). **HRMS** ($C_{17}H_{18}N_3OS^+$): calculated 312.1165 ($M+H^+$), found 312.1171.

Synthesis of 1-(4-bromo-6-methylbenzo[d]thiazol-2-yl)-3-phenylurea (274)

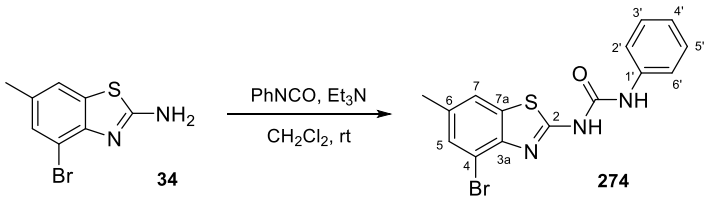

Phenyl isocyanate (90 µL, 0.83 mmol) was added to a solution of **34** (126 mg, 0.52 mmol) and 1 mL of triethylamine in CH_2Cl_2 (25 mL). The reaction was stirred for 5 days at room temperature under N_2 and subsequently poured into cold water and washed with brine. The organic layer was dried over anhydrous Na_2SO_4, filtered, and evaporated to dryness obtaining 336 mg. Crystallization in MeOH gave 24 mg of impure **274**.

*1-(4-Bromo-6-methylbenzo[d]thiazol-2-yl)-3-phenylurea (**274**).* Non-isolated product. **^{1}H-NMR** (400 MHz, $CDCl_3$): δ 2.39 (3H, s, CH_3); 7.09 (1H, bd, *J* = 8.0 Hz, H4'); 7.31 (2H, bd, *J* = 8.0 Hz, H3' and H5'); 7.38 (1H, bs, H5); 7.42 (1H, bs, H7); 7.55 (2H, bd, *J* = 7.6 Hz, H2' and H6').

Synthesis of 1-benzyl-3-(6-methylbenzo[d]thiazol-2-yl)urea (275)

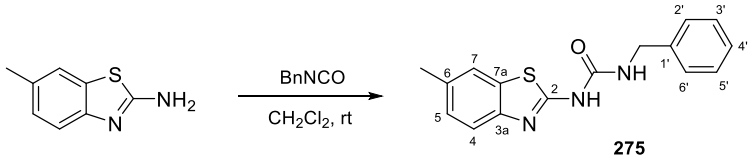

Benzyl isocyanate (314 µL, 2.54 mmol) was added to 6-methylbenzo[d]thiazol-2-amine (278 mg, 1.69 mmol) dissolved in 20 mL of CH_2Cl_2. The mixture was stirred for 5 h at room temperature under N_2 until precipitation. The resulting white crystals were filtered, obtaining **275** (463 mg, 1.56 mmol, 92%).

*1-Benzyl-3-(6-methylbenzo[d]thiazol-2-yl)urea (**275**).* White crystals. **Mp** (CH_2Cl_2): 283.4-285.7 °C. **IR** (KBr): 3344, 1708, 1537, 1275 cm^{-1}. **^{1}H-NMR** (400 MHz, $CDCl_3$): δ 2.44 (3H, s, CH_3); 4.54 (2H, d, *J* = 5.6 Hz, CH_2); 7.17 (1H, dd, *J* = 1.2 and 8.0 Hz, H5); 7.26-7.33 (5H, m, Ph); 7.51 (1H, bs, H7); 7.57 (1H, d, *J* = 8.0 Hz, H4). **^{13}C-NMR** (100 MHz, DMSO-D6): δ 21.3 (CH_3); 43.4 (CH_2); 119.7 (CH, C4); 121.5 (CH, C7); 127.4 (CH, C5); 127.5 (CH, C4'); 127.6 (2) (CH, C2' and C6'); 128.9 (2) (CH, C3' and C5'); 131.9 (C, C7a); 132.5 (C, C6); 139.8 (C, C1'); 147.4 (C, C3a); 154.4 (C, CO); 159.4 (C, C2). **HRMS** ($C_{16}H_{15}N_3NaOS^+$): calculated 320.0828 ($M+Na^+$), found 320.0834.

Synthesis of 1-benzyl-3-(4-bromo-6-methylbenzo[d]thiazol-2-yl)urea (276)

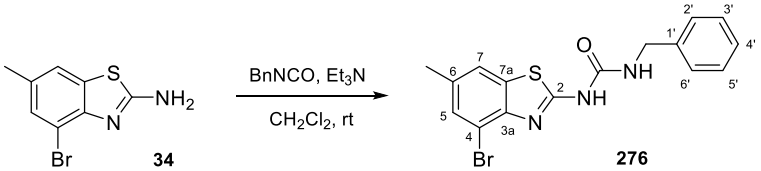

A solution of **34** (125 mg, 0.51 mmol) and benzyl isocyanate (100 µL, 0.81 mmol) in 15 mL of CH_2Cl_2 and 1 mL of triethylamine was stirred for 3 days at room temperature under N_2. It was poured into cold water

and washed with brine. The organic layer was dried over anhydrous Na_2SO_4, filtered, and rotary evaporated to obtain 354 mg. Crystallization in MeOH yielded 124 mg (0.33 mmol, 65%) of **276**.

*1-Benzyl-3-(4-bromo-6-methylbenzo[d]thiazol-2-yl)urea (**276**).* White crystals. **Mp** (MeOH): 204 °C. **^{1}H-NMR** (400 MHz, DMSO-D6): δ 2.34 (3H, s, CH_3); 4.35 (2H, d, *J* = 6.0 Hz, CH_2); 7.04 (1H, bs, NH); 7.24-7.35 (5H, m, Ph); 7.41 (1H, s, H5); 7.67 (1H, s, H7); 11.29 (1H, bs, NH). **^{13}C-NMR** (100 MHz, DMSO-D6): δ 20.9 (CH_3); 43.4 (CH_2); 112.6 (C, C4); 121.2 (CH, C7); 127.4 (CH, C4'); 127.6 (2) CH, C2' and C6'); 128.9 (2) (CH, C3' and C5'); 130.3 (CH, C5); 132.9 (C, C7a); 134.2 (C, C6); 139.8 (C, C1'); 145.7 (C, C3a); 154.2 (C, CO); 160.2 (C, C2). **HRMS** ($C_{16}H_{15}BrN_3OS^+$): calculated 376.0114 ($M+H^+$), found 376.0122.

Synthesis of ethyl (6-methylbenzo[d]thiazol-2-yl)carbamate (277)

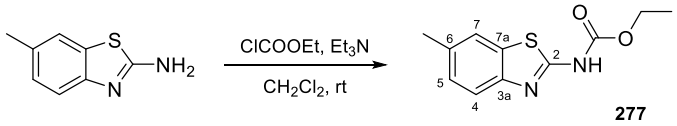

Ethyl chloroformate (226 µL, 2.36 mmol) was added to a solution of 6-methylbenzo[d]thiazol-2-amine (259 mg, 1.58 mmol) together with 100 µL of triethylamine in 10 mL of CH_2Cl_2. The mixture was stirred for 20 h at room temperature under N_2 atmosphere and the crystals were filtered providing 300 mg (1.27 mmol, 81%) of carbamate **277**.

*Ethyl (6-methylbenzo[d]thiazol-2-yl)carbamate (**277**).* Tiny white crystals. **Mp** (CH_2Cl_2): 252.8-254.0 °C. **^{1}H-NMR** (400 MHz, $CDCl_3$): δ 1.41 (3H, t, *J* = 7.2 Hz, Et); 2.45 (3H, s, CH_3); 4.39 (2H, q, *J* = 7.2 Hz, Et); 7.22 (1H, dd, *J* = 1.6 and 8.0 Hz, H5); 7.59 (1H, bs, H7); 7.80 (1H, d, *J* = 8.0 Hz. H4). **^{13}C-NMR** (100 MHz, DMSO-D6): δ 14.7 (CH_3, Et); 21.4 (CH_3, Me); 62.3 (CH_2, Et); 120.3 (CH, C4); 121.6 (CH, C7); 127.7 (CH, C5); 132.0 (C, C7a); 133.1 (C, C6); 147.6 (C, C3a); 154.4 (C, CO); 159.2 (C, C2). **HRMS** ($C_{11}H_{12}N_2NaO_2S^+$): calculated 259.0512 ($M+Na^+$), found 259.0517.

Synthesis of ethyl (4-bromo-6-methylbenzo[d]thiazol-2-yl)carbamate (278)

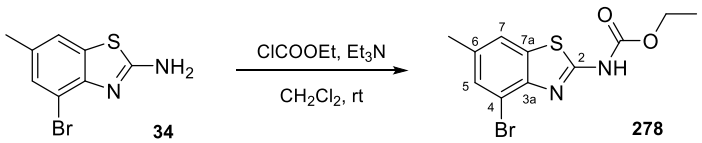

A mixture of **34** (101 mg, 0.42 mmol), ethyl chloroformate (60 µL, 0.63 mmol), and 1 mL of triethylamine in 25 mL of CH_2Cl_2 was stirred for 24 h at room temperature under N_2 atmosphere. The reaction was poured into cold water and washed with brine until neutrality. Once dried over anhydrous Na_2SO_4, the organic layer was filtered and concentrated to dryness, obtaining 150 mg. Crystallization in MeOH yielded 103 mg (0.33 mmol, 79%) of carbamate **278**.

*Ethyl (4-bromo-6-methylbenzo[d]thiazol-2-yl)carbamate (**278**).* White crystals. **Mp** (MeOH): 177-178 °C. **^{1}H-NMR** (400 MHz, $CDCl_3$): δ 1.37 (3H, t, *J* = 7.2 Hz, Et); 2.44 (3H, s, CH_3); 4.33 (2H, q, *J* = 7.2 Hz, Et); 7.44 (1H, s, H5); 7.51 (1H, s, H7); 8.50 (1H, bs, NH). **^{13}C-NMR** (100 MHz, DMSO-D6): δ 14.3 (CH_3, Et); 21.2 (CH_3, Me); 62.9 (CH_2, Et); 113.6 (C, C4); 120.3 (CH, C7); 130.7 (CH, C5); 132.8 (C, C7a); 134.9 (C, C6); 145.3 (C, C3a); 153.2 (C, CO); 159.4 (C, C2). **HRMS** ($C_{11}H_{12}BrN_2O_2S^+$): calculated 314.9797 ($M+H^+$), found 314.9790.

Synthesis of phenyl (6-methylbenzo[d]thiazol-2-yl)carbamate (279)

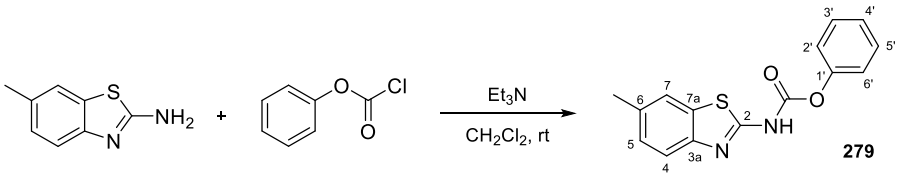

6-Methylbenzo[d]thiazol-2-amine (301 mg, 1.83 mmol) was dissolved in 20 mL of CH_2Cl_2 with 100 µL of triethylamine, and phenyl chloroformate (345 µL, 2.75 mmol) was added dropwise. The reaction was stirred for 22 h at room temperature under N_2. The resulting crystals were filtered off, obtaining 414 mg (1.46 mmol, 80%) of **279**, re-crystallized in MeOH (**279**, 304 mg, 1.07 mmol, 58%).

*Phenyl (6-methylbenzo[d]thiazol-2-yl)carbamate (**279**).* White crystals. **Mp** (MeOH): 251-253 °C. **IR** (KBr): 3074, 1739, 1613, 1580, 1277, 1188 cm^{-1}. **^{1}H-NMR** (400 MHz, $CDCl_3$): δ 2.46 (3H, s, CH_3); 7.22 (1H, bd, *J* = 8.4 Hz, H5); 7.26-7.33 (3H, m, H2', H4' and H6'); 7.44 (2H, t, *J* = 8.0 Hz, H3' and H5'); 7.61 (1H, bs, H7); 7.80 (1H, d, *J* = 8.4 Hz, H4). **^{13}C-NMR** (100 MHz, DMSO-D6): δ 21.4 (CH_3); 120.3 (CH, C4); 121.8 (CH, C7); 122.3 (2) (CH, C2' and C6'); 126.6 (CH, C4'); 127.9 (CH, C5); 130.1 (2) (CH, C3' and C5'); 132.0 (C, C7a); 133.4 (C, C6); 147.2 (C, C3a); 150.5 (C, C1'); 153.3 (C, CO); 159.3 (C, C2). **HRMS** ($C_{15}H_{12}N_2NaO_2S^+$): calculated 307.0512 ($M+Na^+$), found 307.0519.

Synthesis of phenyl (4-bromo-6-methyl-N-phenoxycarbonylbenzo[d]thiazol-2-yl)carbamate (280)

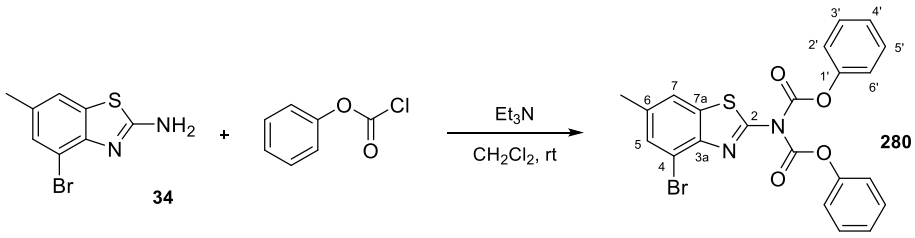

Benzothiazole derivative **34** (136 mg, 0.56 mmol) reacted with phenyl chloroformate (110 µL, 0.88 mmol) in 15 mL of CH_2Cl_2 with 2 mL of triethylamine. After 5 h at room temperature under N_2, it was poured into cold water and washed with saturated NaCl. The organic layer was dried over anhydrous Na_2SO_4, filtered, and evaporated, obtaining 412 mg of a complex mixture. Crystallization in MeOH yielded 47 mg (0.10 mmol, 22%) of **280**.

*Phenyl (4-bromo-6-methyl-N-phenoxycarbonylbenzo[d]thiazol-2-yl)carbamate (**280**).* White crystals. **Mp** (MeOH): 100 °C. **^{1}H-NMR** (400 MHz, $CDCl_3$): δ 2.48 (3H, s, CH_3); 7.29-7.33 (6H, m, H2', H4' and H6' [bis]); 7.43 (4H, t, *J* = 8.8 Hz, H3' and H5' [bis]); 7.54 (1H, bs, H5); 7.59 (1H, bs, H7). **^{13}C-NMR** (100 MHz, $CDCl_3$): δ 21.3 (CH_3); 116.0 (C, C4); 120.5 (CH, C7); 121.1 (4) (CH, C2' and C6' [bis]); 126.9 (2) (CH, C4' [bis]); 129.6 (4) (CH, C3' and C5' [bis]); 131.4 (CH, C5); 135.3 (C, C7a); 137.0 (C, C6); 145.8 (C, C3a); 149.3 (C, C1' [bis]); 150.3 (C, CO [bis]); 156.4 (C, C2). **HRMS** ($C_{22}H_{15}BrN_2NaO_4S^+$): calculated 504.9828 ($M+Na^+$), found 504.9824.

Synthesis of benzyl (6-methylbenzo[d]thiazol-2-yl)carbamate (281)

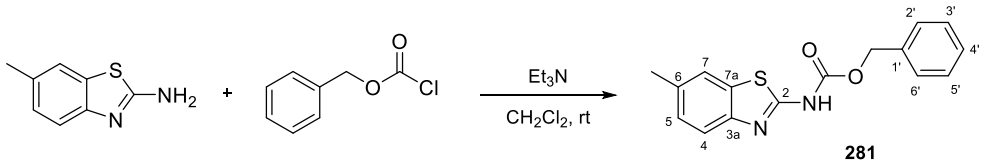

Benzyl chloroformate (217 µL, 2.21 mmol) was added to a solution of 6-methylbenzo[d]thiazol-2-amine (241 mg, 1.47 mmol) in 20 mL of CH_2Cl_2 with 100 µL of triethylamine, and stirred for 23 h at room temperature under N_2 atmosphere. The resulting crystals were filtered, yielding 58 mg (0.19 mmol, 13%) of **281**.

*Benzyl (6-methylbenzo[d]thiazol-2-yl)carbamate (**281**).* White crystals. **Mp** (CH_2Cl_2): 254-255 °C. **^{1}H-NMR** (400 MHz, $CDCl_3$): δ 2.43 (3H, s, CH_3); 5.33 (2H, s, CH_2); 6.97 (1H, bd, *J* = 8.0 Hz, H5); 7.38-7.44 (5H, m, Ph); 7.55 (1H, bs, H7); 7.59 (1H, d, *J* = 8.0 Hz, H4). **^{13}C-NMR** (100 MHz, DMSO-D6): δ 21.4 (CH_3); 67.6 (CH_2); 120.3 (CH, C4); 121.7 (CH, C7); 127.8 (CH, C5); 128.7 (CH, C4'); 128.8 (2) (CH, C2' and C6'); 129.0 (2) (CH, C3' and C5'); 132.0 (C, C7a); 133.1 (C, C6); 136.2 (C, C1'); 147.6 (C, C3a); 154.3 (C, CO); 159.1 (C, C2). **HRMS** ($C_{16}H_{15}N_2O_2S^+$): calculated 299.0849 ($M+H^+$), found 299.0859.

Synthesis of benzyl (4-bromo-6-methylbenzo[d]thiazol-2-yl)carbamate (282)

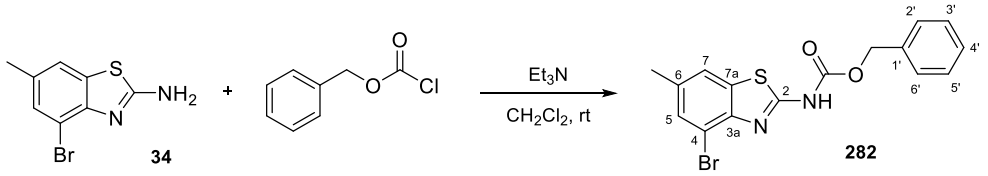

A mixture of benzyl chloroformate (100 µL, 1.02 mmol), **34** (149 mg, 0.61 mmol), and 1 mL of triethylamine in 25 mL of CH_2Cl_2 was stirred for 21 h at room temperature under N_2. It was then concentrated to dryness obtaining 350 mg of a complex mixture.

Synthesis of N-(6-methylbenzo[d]thiazol-2-yl)benzamide (283)

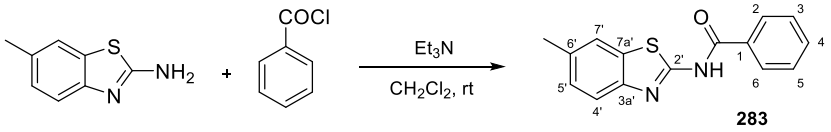

Benzoyl chloride (275 µL, 2.37 mmol) was added to a solution of 6-methylbenzo[d]thiazol-2-amine (259 mg, 1.58 mmol) and 100 µL of triethylamine in 10 mL of CH_2Cl_2. The reaction mixture was stirred for 5 days at room temperature, then poured into iced water and washed with brine until neutral pH. The organic layer was dried over anhydrous Na_2SO_4, filtered, and evaporated under vacuum to obtain 426 mg. Crystallization in MeOH/CH_2Cl_2 gave amide **283** (312 mg, 1.16 mmol, 74%).

*N-(6-methylbenzo[d]thiazol-2-yl)benzamide (**283**).* Pinkish white crystals. **Mp** (MeOH/CH_2Cl_2): 222-224 °C. **IR** (KBr): 3058, 1676, 1604, 1551, 1467, 1300 cm^{-1}. **^{1}H-NMR** (400 MHz, $CDCl_3$): δ 2.48 (3H, s, CH_3); 7.20 (1H, bd, *J* = 8.0 Hz, H5'); 7.43 (1H, bt, *J* = 8.0 Hz, H4); 7.50 (2H, bt, *J* = 8.0 Hz, H3 and H5); 7.59-7.65 (2H, m, H4' and H7'); 8.03 (2H, bd, *J* = 8.0 Hz, H2 and H6). **^{13}C-NMR** (100 MHz, DMSO-D6): δ 21.4 (CH_3); 120.4 (CH,

C4'); 121.7 (CH, C7'); 127.9 (CH, C5'); 128.7 (2) (CH, C2 and C6); 129.1 (2) (CH, C3 and C5); 132.1 (C, C7a'); 132.4 (C, C1); 133.2 (C, C6'); 133.6 (CH, C4); 146.7 (C, C3a'); 158.5 (C, C2'); 166.3 (C, CO). **HRMS** ($C_{15}H_{12}N_2NaO_2S^+$): calculated 291.0563 ($M+Na^+$), found 291.0568.

Synthesis of N-(4-bromo-6-methylbenzo[d]thiazol-2-yl)benzamide (284)

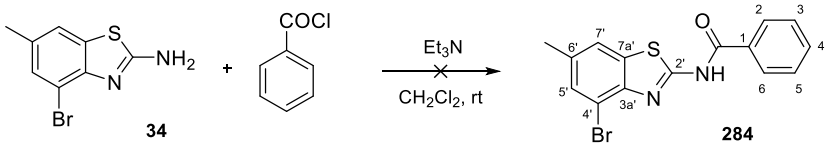

A solution containing 4-bromo-6-methylbenzo[d]thiazol-2-amine (**34**, 135 mg, 0.56 mmol), benzoyl chloride (100 µL, 0.86 mmol), and 1 mL of triethylamine in CH_2Cl_2 (25 mL) was stirred for 24 h under N_2 atmosphere at room temperature. It was subsequently poured into iced water and washed with brine until neutral pH. The organic layer was dried over anhydrous Na_2SO_4, filtered, and evaporated under vacuum, obtaining 296 mg of a complex mixture.

Synthesis of N-(6-methylbenzo[d]thiazol-2-yl)-2-phenylacetamide (285)

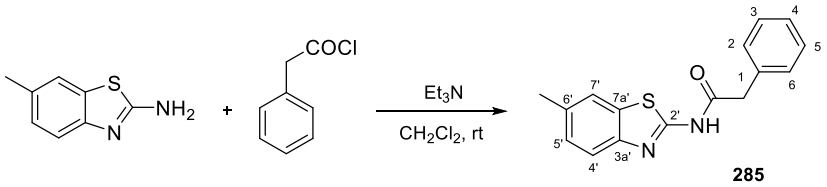

A mixture of 2-phenylacetyl chloride (285 µL, 2.16 mmol) and 6-methylbenzo[d]thiazol-2-amine (236 mg, 1.44 mmol) with 100 µL of triethylamine in 10 mL of CH_2Cl_2, reacted over 5 days under N_2 atmosphere at room temperature. It was then poured into iced water and washed with brine until neutrality. The organic layer was dried over anhydrous Na_2SO_4, filtered and evaporated to obtain 533 mg. Crystallization in MeOH/CH_2Cl_2 yielded 292 mg (1.04 mmol, 72%) of **285**.

*N-(6-methylbenzo[d]thiazol-2-yl)-2-phenylacetamide (**285**).* White crystals. **Mp** (MeOH/CH_2Cl_2): 190-191 °C. **IR** (KBr): 3127, 1697, 1534, 1454, 1263 cm^{-1}. **^{1}H-NMR** (400 MHz, $CDCl_3$): δ 2.46 (3H, s, CH_3); 3.87 (2H, s, CH_2); 7.24 (1H, m, H5'); 7.30-7.41 (5H, m, Ph); 7.59 (2H, m, *J* = H4' and H7'). **^{13}C-NMR** (100 MHz, $CDCl_3$): δ 21.5 (CH_3); 43.4 (CH_2); 120.1 (CH, C4'); 121.3 (CH, C7'); 127.9 (CH, C5'); 128.0 (CH, C4); 129.2 (2) (CH, C3 and C5); 129.4 (2) (CH, C2 and C6); 132.1 (C, C7a'); 132.8 (C, C6'); 134.2 (C, C1); 145.6 (C, C3a'); 158.0 (C, C2'); 169.4 (C, CO). **HRMS** ($C_{16}H_{14}N_2NaOS^+$): calculated 305.0719 ($M+Na^+$), found 305.0719.

Synthesis of N-(4-bromo-6-methylbenzo[d]thiazol-2-yl)-2-phenylacetamide (286)

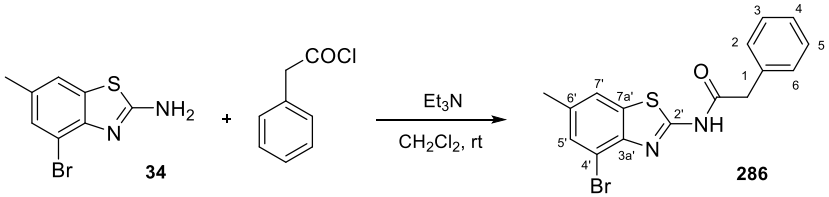

The mixture of 2-phenylacetyl chloride (119 µL, 0.90 mmol), 4-bromo-6-methylbenzo[d]thiazol-2-amine (**34**, 146 mg, 0.60 mmol) and 1 mL of triethylamine in 25 mL of CH_2Cl_2 was stirred for 23 h at room

temperature under N_2. Once poured into cold water and washed with brine, the organic layer was dried over anhydrous Na_2SO_4, filtered, and rotary evaporated (376 mg). Crystallization in $MeOH/CH_2Cl_2$ yielded 122 mg (0.34 mmol, 57%) of **286**.

*N-(4-bromo-6-methylbenzo[d]thiazol-2-yl)-2-phenylacetamide (**286**).* Yellowish-orange crystals. **Mp** ($MeOH/CH_2Cl_2$): 234-236 °C. **IR** (KBr): 3142, 1651, 1599, 1328, 1266 cm^{-1}. **^{1}H-NMR** (400 MHz, $CDCl_3$): δ 2.43 (3H, s, CH_3); 3.85 (2H, s, CH_2); 7.26 (2H, m, H3 and H5); 7.36 (3H, m, H2, H4 and H6); 7.44 (1H, bs, H5'); 7.53 (1H, bs, H7'); 9.08 (1H, bs, NH). **^{13}C-NMR** (100 MHz, $CDCl_3$): δ 21.1 (CH_3); 43.8 (CH_2); 113.7 (C, C4'); 120.5 (CH, C7'); 128.0 (CH, C4); 129.2 (2) (CH, C3 and C5); 129.4 (2) (CH, C2 and C6); 130.9 (CH, C5'); 132.5 (C, C7a'); 133.0 (C, C6'); 135.4 (C, C1); 144.5 (C, C3a'); 157.8 (C, C2'); 169.7 (C, CO). **HRMS** ($C_{16}H_{14}BrN_2OS^+$): calculated 361.0005 ($M+H^+$), found 361.0000.

Synthesis of N-(6-methylbenzo[d]thiazol-2-yl)picolinamide (287)

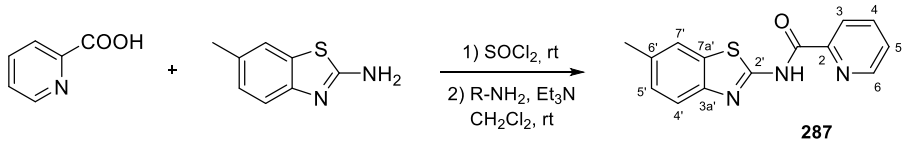

Following general method **A2**, picolinic acid (323 mg, 2.62 mmol) was converted to its acyl chloride when treated with $SOCl_2$ (2 mL) for 24 h at room temperature. It was added dropwise to 6-methylbenzo[d]thiazol-2-amine (356 mg, 2.17 mmol) dissolved in 50 mL of CH_2Cl_2 with 0.5 mL of triethylamine. After 3 h, the reaction mixture was treated obtaining 599 mg. Crystallization in $MeOH/CH_2Cl_2$ yielded 458 mg (1.70 mmol, 79%) of **287**.

*N-(6-methylbenzo[d]thiazol-2-yl)picolinamide (**287**).* White crystals. **Mp** ($MeOH/CH_2Cl_2$): 182-183 °C. **IR** (KBr): 3350, 1693, 1558, 1459, 1264 cm^{-1}. **^{1}H-NMR** (400 MHz, $CDCl_3$): δ 2.49 (3H, s, CH_3); 7.28 (1H, dd, *J* = 1.6 and 8.4 Hz, H5'); 7.56 (1H, ddd, *J* = 1.2, 4.8 and 8.0 Hz, H5); 7.66 (1H, d, *J* = 1.6 Hz, H7'); 7.73 (1H, d, *J* = 8.4 Hz, H4'); 7.95 (1H, td, *J* = 1.6 and 8.0 Hz, H4); 8.31 (1H, dd, *J* = 1.2 and 8.0 Hz, H3); 8.68 (1H, bd, *J* = 4.8 Hz, H6); 11.29 (1H, bs, NH). **^{13}C-NMR** (100 MHz, $CDCl_3$): δ 21.5 (CH_3); 120.8 (CH, C4'); 121.2 (CH, C7'); 122.9 (CH, C3); 127.4 (CH, C5'); 127.7 (CH, C5); 132.5 (C, C7a'); 134.0 (C, C6'); 137.7 (CH, C4); 146.8 (C, C3a'); 147.6 (C, C2); 148.6 (CH, C6); 156.5 (C, C2'); 162.4 (C, CO). **HRMS** ($C_{14}H_{11}N_3NaOS^+$): calculated 292.0515 ($M+Na^+$), found 292.0520.

Synthesis of N-(4-bromo-6-methylbenzo[d]thiazol-2-yl)picolinamide (288)

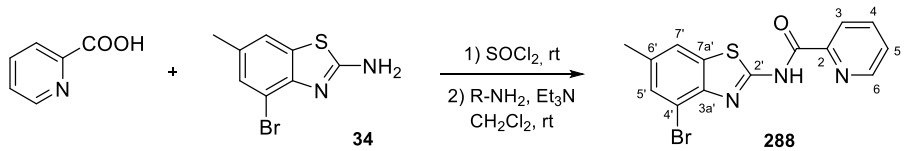

Following procedure **A2**, the acyl chloride formed after 24 h at room temperature between picolinic acid (112 mg, 0.91 mmol) and $SOCl_2$ (1 mL) was added to a solution of **34** (163 mg, 0.67 mmol) in 50 mL of CH_2Cl_2 with 2 mL of triethylamine. The reaction was treated after 28 h, obtaining 201 mg. Crystallization in $MeOH/CH_2Cl_2$ yielded amide **288** (38 mg, 0.11 mmol, 16%).

*N-(4-bromo-6-methylbenzo[d]thiazol-2-yl)picolinamide (**288**).* White crystals. **Mp** ($MeOH/CH_2Cl_2$): 239-241 °C. **IR** (KBr): 3299, 1689, 1532, 1425, 1260, 1079 cm^{-1}. **^{1}H-NMR** (400 MHz, $CDCl_3$): δ 2.46 (3H, s, CH_3);

7.50 (1H, bs, H5'); 7.57 (1H, dd, *J* = 4.8 and 8.0 Hz, H5); 7.59 (1H, bs, H7'); 7.96 (1H, td, *J* = 1.6 and 8.0 Hz, H4); 8.31 (1H, d, *J* = 8.0 Hz, H3); 8.67 (1H, bd, *J* = 4.8 Hz, H6); 11.43 (1H, bs, NH). **^{13}C-NMR** (100 MHz, $CDCl_3$): δ 21.2 (CH_3); 114.1 (C, C4'); 120.6 (CH, C7'); 123.0 (CH, C3); 127.6 (CH, C5); 130.9 (CH, C5'); 133.2 (C, C7a'); 135.4 (C, C6'); 137.8 (CH, C4); 145.2 (C, C3a'); 147.4 (C, C2); 148.7 (CH, C6); 157.0 (C, C2'); 162.7 (C, CO). **HRMS** ($C_{14}H_{11}BrN_3OS^+$): calculated 347.9801 ($M+H^+$), found 347.9812.

Synthesis of N-(6-methylbenzo[d]thiazol-2-yl)nicotinamide (289)

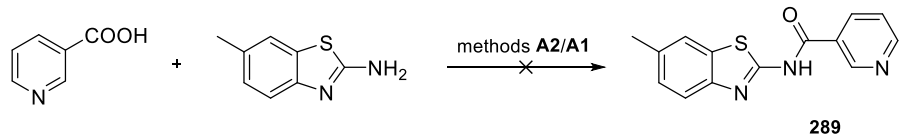

289

Procedure 1: Following method **A2**, the acyl chloride formed at room temperature after 2 weeks between $SOCl_2$ (1 mL) and nicotinic acid (289 mg, 2.35 mmol) was added to a solution of 6-methylbenzo[d]thiazol-2-amine (314 mg, 1.92 mmol) and 500 µL of triethylamine in 50 mL of CH_2Cl_2 and stirred for 22 h. The reaction gave 480 mg of a complex mixture.

Procedure 2: Following method **A1**, the mixture of nicotinic acid (290 mg, 2.36 mmol), EDC hydrochloride (679 mg, 3.54 mmol), *p*-DMAP (154 mg, 1.26 mmol), and the amine (392 mg, 2.39 mmol) was heated under reflux in 50 mL of CH_2Cl_2. It was treated after 3 weeks providing 64 mg. Product **289** was not obtained.

Synthesis of 6-methyl-N-(pyridin-2-ylmethyl)benzo[d]thiazol-2-amine (290)

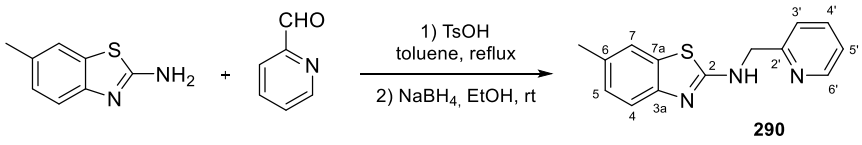

290

Procedure 1: A mixture of 6-methylbenzo[d]thiazol-2-amine (202 mg, 1.23 mmol) and the aldehyde (145 mg, 1.36 mmol) was heated under reflux in 25 mL of CH_2Cl_2 with a few drops of HCl. After 7 days, the solvent was evaporated, the residue was re-dissolved in MeOH and $NaBH_4$ (147 mg, 3.89 mmol) was added. The reaction was stirred at room temperature for 3 days, evaporated, re-dissolved in EtOAc, and washed with brine. The organic layer was dried over anhydrous Na_2SO_4, filtered, and evaporated, obtaining 287 mg of a complex mixture.

Procedure 2: An excess of *p*-toluenesulfonic acid was added to a solution of 6-methylbenzo[d]thiazol-2-amine (477 mg, 2.91 mmol) and picolinaldehyde (343 mg, 3.21 mmol) in 50 mL of toluene, and heated under reflux for 24 h. The solvent was evaporated, ethanol (50 mL) and $NaBH_4$ (552 mg, 14.59 mmol) were added and stirred for 5 days at room temperature under N_2, then evaporated and re-dissolved in CH_2Cl_2. After pouring the mixture into cold water, it was washed with brine until neutrality, and the organic layer was dried over anhydrous Na_2SO_4, filtered, and evaporated to dryness (770 mg). Flash chromatography using CH_2Cl_2/EtOAc 1:1, followed by crystallization in CH_2Cl_2/Hex yielded 143 mg (0.56 mmol, 19%) of **290**.

*6-Methyl-N-(pyridin-2-ylmethyl)benzo[d]thiazol-2-amine (**290**).* Yellow crystals. **Mp** (CH_2Cl_2/Hex): 148.0-148.7 °C. **IR** (KBr): 3221, 3016, 1577, 1560, 1465, 1197, 803 cm^{-1}. **^{1}H-NMR** (400 MHz, $CDCl_3$): δ 2.40 (3H, s, CH_3); 4.81 (2H, s, CH_2); 7.13 (1H, bd, *J* = 8.4 Hz, H5); 7.24 (1H, m, H5'); 7.38 (2H, m, H7 and H3'); 7.48 (1H,

d, *J* = 8.4 Hz, H4); 7.70 (1H, td, *J* = 1.6 and 8.0 Hz, H4'); 8.58 (1H, bd, *J* = 4.4 Hz, H6'). **^{13}C-NMR** (100 MHz, $CDCl_3$): δ 20.2 (CH_3); 48.3 (CH_2); 117.5 (CH, C4); 119.8 (CH, C5'); 120.8 (CH, C3'); 121.5 (CH, C7); 126.0 (CH, C5); 129.7 (C, C7a); 130.3 (C, C6); 135.8 (CH, C4'); 148.0 (CH, C6'); 149.2 (C, C3a); 155.1 (C, C2'); 165.2 (C, C2). **HRMS** ($C_{14}H_{13}N_3NaS^+$): calculated 278.0722 ($M+Na^+$), found 278.0726.

Synthesis of 6-methyl-N-(pyridin-3-ylmethyl)benzo[d]thiazol-2-amine (291)

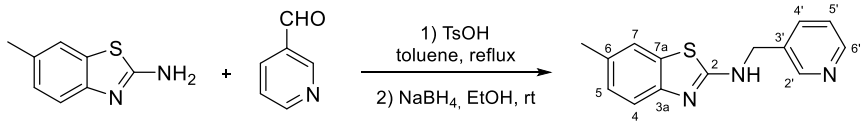

291

A solution of 6-methylbenzo[d]thiazol-2-amine (225 mg, 1.37 mmol), nicotinaldehyde (160 mg, 1.50 mmol) and *p*-toluenesulfonic acid in excess in 20 mL of toluene was heated under reflux for 4 h. It was evaporated, re-dissolved in 20 mL of ethanol, and $NaBH_4$ (265 mg, 7.01 mmol) was carefully added and stirred at room temperature for 30 min. The solvent was removed under vacuum and the resulting residue was dissolved in CH_2Cl_2 and washed with brine until neutrality. The organic layer was dried over anhydrous Na_2SO_4, filtered, and evaporated (293 mg). Column chromatography using EtOAc/CH_2Cl_2 4:6 (1st) and methanol (2nd) yielded 92 mg (0.36 mmol, 26%) of **291** as a white solid.

*6-Methyl-N-(pyridin-3-ylmethyl)benzo[d]thiazol-2-amine (**291**).* White solid. **IR** (KBr): 3090, 1619, 1589, 1468, 1356, 824 cm^{-1}. **^{1}H-NMR** (400 MHz, $CDCl_3$): δ 2.33 (3H, s, CH_3); 4.59 (2H, s, CH_2); 7.03 (1H, bd, *J* = 8.0 Hz, H5); 7.18 (1H, dd, *J* = 4.8 and 8.0 Hz, H5'); 7.24 (1H, d, *J* = 8.0 Hz, H4); 7.30 (1H, bs, H7); 7.68 (1H, bd, *J* = 8.0 Hz, H4'); 8.45 (1H, bd, *J* = 4.8 Hz, H6'); 8.56 (1H, bs, H2'). **^{13}C-NMR** (100 MHz, $CDCl_3$): δ 21.2 (CH_3); 46.5 (CH_2); 118.3 (CH, C4); 120.9 (CH, C7); 123.6 (CH, C5'); 127.2 (CH, C5); 130.3 (C, C7a); 131.5 (C, C6); 133.6 (C, C3'); 135.5 (CH, C4'); 148.9 (CH, C6'); 149.0 (CH, C2'); 149.8 (C, C3a); 166.8 (C, C2). **HRMS** ($C_{14}H_{14}N_3S^+$): calculated 256.0903 ($M+H^+$), found 256.0907.

Preparation of compounds 292 and 293

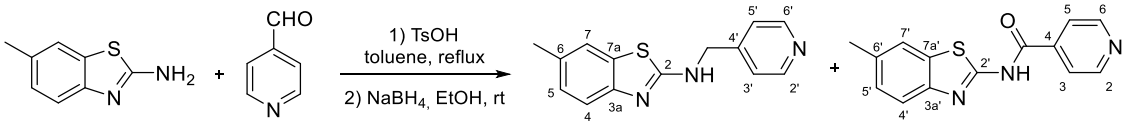

292 **293**

Procedure 1: An excess of *p*-toluenesulfonic acid was added to a solution of the benzothiazole (196 mg, 1.19 mmol) and isonicotinaldehyde (249 mg, 2.32 mmol) and heated under N_2 in 20 mL of refluxing toluene, turning orange over the time. After 2 days, the reaction was warmed to room temperature and evaporated under vacuum. The residue was re-dissolved in 20 mL of ethanol and $NaBH_4$ (226 mg, 5.97 mmol) was carefully added and stirred at room temperature for 5 h. The red-colored solution was evaporated to dryness, dissolved in CH_2Cl_2 and washed with brine until neutrality. The organic layer was dried over anhydrous Na_2SO_4, filtered, and rotary evaporated (254 mg). Silica gel flash chromatography with EtOAc/CH_2Cl_2 8:2 as eluent gave two fractions: 25 mg (0.10 mmol, 9%) of **292** and 30 mg (0.11 mmol, 9%) of **293**.

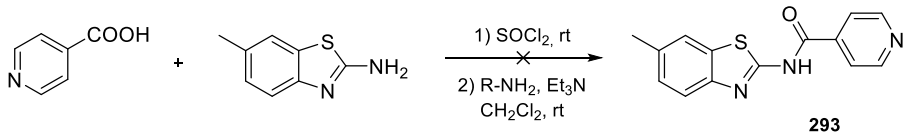

293

Procedure 2: According to method **A2**, $SOCl_2$ (1 mL) was added to 322 mg (2.62 mmol) of isonicotinic acid and stirred for 48 h at room temperature. It was then added dropwise to a solution of the amine (348 mg, 2.12 mmol) and 500 µL of triethylamine. The reaction was treated after 30 min obtaining 53 mg (0.32 mmol, 15%) of 6-methylbenzo[d]thiazol-2-amine.

*6-Methyl-N-(pyridin-4-ylmethyl)benzo[d]thiazol-2-amine (**292**).* Yellow solid. **^{1}H-NMR** (400 MHz, $CDCl_3$): δ 2.38 (3H, s, CH_3); 4.68 (2H, s, CH_2); 7.09 (1H, bs, *J* = 7.6 Hz, H5); 7.32 (2H, d, *J* = 6.4 Hz, H3' and H5'); 7.36 (2H, m, H4 and H7); 8.55 (2H, d, *J* = 6.4 Hz, H2' and H6'). **^{13}C-NMR** (100 MHz, $CDCl_3$): δ 21.2 (CH_3); 47.8 (CH_2); 118.4 (CH, C4); 121.0 (CH, C7); 122.2 (2) (CH, C3' and C5'); 127.3 (CH, C5); 130.3 (C, C7a); 131.8 (C, C6); 147.4 (C, C4'); 149.6 (C, C3a); 149.8 (2) (CH, C2' and C6'); 166.9 (C, C2). **HRMS** ($C_{14}H_{14}N_3S^+$): calculated 256.0903 ($M+H^+$), found 256.0914.

*N-(6-methylbenzo[d]thiazol-2-yl)isonicotinamide (**293**).* Yellow crystals. **Mp** (MeOH/acetone): 273.2-274.5 °C. **^{1}H-NMR** (400 MHz, $CDCl_3$): δ 2.48 (3H, s, CH_3); 7.20 (1H, bd, *J* = 8.4 Hz, H5'); 7.37 (1H, bd, *J* = 8.4 Hz, H4'); 7.66 (1H, bs, H7'); 7.81 (2H, d, *J* = 6.0 Hz, H3 and H5); 8.79 (2H, d, *J* = 6.0 Hz, H2 and H6). **^{13}C-NMR** (100 MHz, DMSO-D6): δ 21.4 (CH_3, Me); 120.2 (CH, C4'); 121.8 (CH, C7'); 122.2 (2) (CH, C3 and C5); 128.1 (CH, C5'); 131.9 (C, C7a'); 133.8 (C, C6'); 139.8 (C, C4); 150.8 (2) (CH, C2 and C6). Quaternary carbons (C2', C3a' and amide) not observed. **HRMS** ($C_{14}H_{12}N_3OS^+$): calculated 270.0696 ($M+H^+$), found 270.0714.

BIOLOGY MATERIALS AND METHODS

Cell lines and culture conditions

Cell lines listed below (Table 30) were purchased from ATCC, except for mouse fibroblasts, which were primary cells isolated as described in the next section. Cells were cultured at 37 °C in sub-confluent conditions under 95% humidified atmosphere and 5% CO_2 in Dulbecco's Modified Eagle Medium (DMEM), RPMI 1640, or DMEM F-12 Nutrient Mixture 1:1 (DMEM/F12) media (Gibco). Each media was supplemented with 10% heat-inactivated Fetal Bovine Serum (FBS, Sigma-Aldrich), 2 mM L-glutamine, 100 units/mL penicillin, 100 µg/mL streptomycin (Gibco), and 12.5 µg/mL ciprofloxacin (Sigma-Aldrich). The inactivation of FBS was carried out by heating at 56 °C for 45 min. Culture medium was replaced every 2-4 days, and cells were washed with Na^+/K^+ PBS and passaged at 80-90% confluency by incubating with 0.05% Trypsin-EDTA (Gibco) in case of adherent cells at 37 °C for 5 min. Trypsin was neutralized with at least twice the volume of complete media, and cells were centrifuged at 1200 rpm for 7 min, then seeded at the desired dilution in each case. Cells were counted in a Neubauer chamber using 0.4% Trypan Blue solution (Sigma-Aldrich) as an exclusion staining to count living cells selectively.

Cell line	Species	Disease	Tissue	Morphology	Media
HeLa	human	cervix adenocarcinoma	cervix	epithelial	DMEM
HT-29	human	colorectal adenocarcinoma	colon	epithelial	RPMI
AGS	human	gastric adenocarcinoma	stomach	epithelial	DMEM/F12
SNU-1	human	gastric adenocarcinoma	stomach	epithelial	RPMI
MIA PaCa-2	human	pancreatic carcinoma	pancreas	epithelial	DMEM
Huh-7	human	hepatocellular carcinoma	liver	epithelial	DMEM
U2OS	human	osteosarcoma	bone	epithelial	DMEM
HL-60	human	acute myeloid leukemia	peripheral blood	myeloblastic	RPMI
RPMI-8226	human	multiple myeloma	peripheral blood	lymphoblast	RPMI
U266	human	multiple myeloma	peripheral blood	lymphoblast	RPMI
HEK-293	human	non-tumorigenic	embryonic kidney	epithelial	DMEM
HPNE	human	non-tumorigenic	pancreas duct	epithelial-like	DMEM
BHK	hamster	non-tumorigenic	kidney	fibroblast	DMEM
L929	mouse	non-tumorigenic	connective tissue	fibroblast	RPMI
3B-11	mouse	non-tumorigenic	vascular epithelium	epithelial	DMEM
Fibroblasts	mouse	non-tumorigenic	dermis	fibroblast	DMEM

Table 30. Summary of the cell lines used for the upcoming experiments mentioned below, together with the origin and culture characteristics. All the cell lines are adherent except for HL-60, RPMI-8226, and U266, which grow in suspension. SNU-1 cells exhibit mixed behavior and can be categorized as semi-adherent.

Cell cryopreservation

For long-term storage, cells were kept in liquid nitrogen, frozen down at the exponential growth stage. Cells were detached from the culture plate surface if adherent, centrifuged at 1200 rpm for 7 min, washed with complete media, and centrifuged again. The pellet was re-suspended in warmed 10% DMSO in FBS at a final concentration of 2-3 million cells/mL. Cryotubes were kept at -20 °C, during a few hours up to overnight, then moved in dry ice to -80 °C, and the next day to liquid nitrogen tanks at -196 °C. In order to bring cells up from liquid nitrogen, the vials were thawed in a 37 °C water bath and the content poured into 9 mL of media and centrifuged at 1000 rpm for 4 min. The pellet was re-suspended in new complete media and seeded into T25 culture flasks.

Fibroblasts isolation

Primary fibroblasts were isolated from wild type C57Bl/6 mice pups at 1-4 days of age, as described in the literature.[585] This technique was conducted while at Dr. Katie DeCicco-Skinner's laboratory at the American University (Washington, DC, USA) during a short-term stay. All mice were bred and maintained at The American University animal facility under NIH guidelines and an approved IACUC protocol.

Newborn mice were euthanized by deep CO_2 narcosis for 20 min, followed by 35 min in ice. The animals were gently washed with povidone iodine and 70% ethanol before the skinning process. Epidermis and dermis layers were separated after an overnight incubation at 4 °C in 0.25% EDTA-free Trypsin (Gibco). The dermal tissue was digested with 0.35% Collagenase II (Gibco) in DMEM in a shaking incubator at 125 rpm and 37 °C for 30 min. The digestion was completed by incubation under the same conditions with 12.5 µL of DNase I (20.000 units/mL, Worthington) per skin for 5 min. The digested tissue was filtered through a 100 µm strainer, and fibroblasts were isolated after several sequential centrifugations (Fig. 123). Cells can be stored in liquid N_2, or the experiments could be subsequently carried out right after isolation.

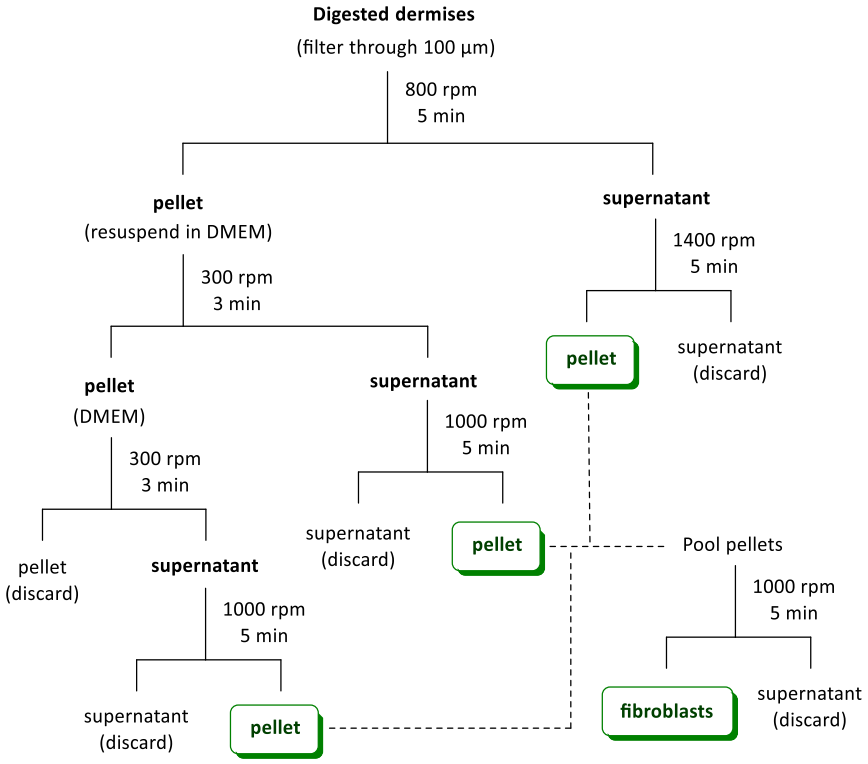

Figure 123. Sequential centrifugation steps to isolate primary fibroblasts from newborn mice digested dermises.

HeLa cells transfection with Bcl-xL and Bcl-2

HeLa cells overexpressing Bcl-xL or Bcl-2 proteins were stably generated by Dr. Consuelo Gajate in our laboratory. Cells were transfected by electroporation with the SFFV-Neo expression vector containing the human *bcl-xL* or *bcl-2* open reading frame driven by the long terminal repeat of the spleen focus-forming virus (pSFFV-*bcl-xL* or pSFFV-*bcl-2*).[586] Transfection was also performed with the empty SFFV-Neo plasmid, serving as a control. Around $4 \cdot 10^7$ cells were subjected to electroporation at 500 V, 1700 µF, and 72 Ω in a BTX electro cell manipulator 600 and selected by growth in complete DMEM additionally supplemented

with 1 mg/mL G418 disulfate salt (Sigma-Aldrich). Expression levels of Bcl-xL and Bcl-2 proteins were periodically measured with respect to that observed for non-transfected HeLa cells.

Treatment conditions and drug preparation

In order to test the activity of the synthesized products in the upcoming experiments, once purified, samples were prepared in DMSO at concentrations of 20 mM (stock solution) and 2 mM (working solution), and stored at -20 °C. For experiments involving cells, the 2 mM drug sample was pre-diluted in the corresponding culture media right before use. Adherent cells were plated at least one day before so that they were attached the moment the treatments were added, then culture media was changed, except in 96-well plate proliferation experiments.

For combination treatments, cells were incubated with the following inhibitors at the indicated concentration, 2 hours prior to the addition of the corresponding synthesized compound (Table 31):

Drug	Affected process	Target	Company	Working [c]
Verapamil	MDR transport	MDR efflux pumps	Sigma-Aldrich	1-10 µM
Elacridar	MDR transport	P-glycoprotein	Sigma-Aldrich	100 nM
Z-VAD-FMK	apoptosis	pan-caspases	Enzo Life Sciences	100 µM
Bafilomycin A1	autophagy	V-ATPase	Sigma-Aldrich	15 nM
Chloroquine	autophagy	lysosomal pH	Sigma-Aldrich	20 µM
Necrostatin-1	necroptosis	RIPK1	Sigma-Aldrich	200 µM
U0126	MEK pathway	MEK1/2	Calbiochem	10 µM
Cycloheximide	protein synthesis	60S ribosomal unit	Sigma-Aldrich	75 µM

Table 31. List of the inhibitors used in the present work in co-treatment with the synthesized compounds. Commercial suppliers and working concentrations are indicated.

Buffers and solutions

Unless otherwise indicated, the following solutions were prepared in milli-Q water and stored at 4 °C. Likewise, to make 1x solutions from the 10x stock, the dilution was carried out in milli-Q water by default if unspecified.

- *Annexin V binding buffer 10x:* 1.4 M NaCl, 25 mM $CaCl_2$, and 0.1 M HEPES, at pH 7.4.
- *Assembly buffer 10x (AB 10x):* 1 M MES, 10 mM EGTA, 10 mM $MgSO_4$, and 10 mM β-mercaptoethanol, at pH 6.7.
- *Extraction buffer (EB):* 0.52 M sucrose and 1 mM EGTA at pH 7.0.
- *HPEM buffer:* 25 mM HEPES, 60 mM PIPES, 10 mM EGTA, and 3 mM $MgCl_2$, at pH 6.6. Autoclaved before use.
- *Lower gel buffer:* 1.5 M Trizma base and 0.4% SDS at pH 8.8.
- *Mitochondria-free fraction lysis buffer:* 250 mM sucrose, 1 mM EDTA, 0.05% digitonin, 25 mM Trizma base, and 1 mM DTT, at pH 6.8.
- *Phosphate-buffered saline (PBS):* 8.1 mM Na_2HPO_4, 1.5 mM NaH_2PO_4, 137 mM NaCl, and 2.7 mM KCl, at pH 7.2.
- *Polymerization buffer:* 1.5 mM GTP and 1 mM β-mercaptoethanol in Assembly buffer 1x at pH 6.7.
- *Running buffer 10x (SDS-PAGE 10x):* 0.25 M Trizma base, 1.92 M glycine, and 1% SDS at pH 8.3. For 1x running buffer, it is diluted with distilled water.

- *Soluble protein loading buffer 4x (SPLB 4x):* 40% glycerol, 240 mM Tris/HCl pH 6.8, 8% SDS, 0.04% bromophenol blue, and 5% β-mercaptoethanol. Stored at -20 °C.
- *Tris-buffered saline 10x (TBS 10x):* 0.5 M Trizma base and 1.5 M NaCl at pH 7.6. Stored at RT. To prepare TBS-T 1x, it is diluted in distilled water with 1% Tween 20.
- *Transfer buffer 10x:* 0.25 M Trizma base and 1.92 M glycine at pH 8.3. For wet transference in WB, transfer buffer 10x is diluted with distilled water and 20% methanol.
- *Transport buffer (TB):* 0.4 M sucrose and 1 mM EDTA at pH 7.0.
- *Upper gel buffer:* 0.5 M Trizma base and 0.4% SDS at pH 6.8.
- *WCE-300:* 25 mM HEPES, 0.3 M NaCl, 1.5 mM $MgCl_2$, 0.2 mM EDTA, 0.1% Triton X-100, 20 mM β-glycerophosphate, and 100 µM sodium orthovanadate, at pH 7.7. Phosphatase and protease inhibitors (Thermo Fisher) were added right before use.

Antibodies

The following table encloses the primary (Ab-1) and secondary (Ab-2) antibodies used in Western blot, confocal microscopy immunofluorescence, and flow cytometry experiments (Table 32).

Antibody	Company	Host	Mw	Dilution	Incubation	Technique
Akt	Cell Signaling	rabbit	60	1:1000	O/N	WB
P-Akt	Cell Signaling	rabbit	60	1:1000	72 h	WB
α-tubulin	Thermo Fisher	mouse	50	1:150	1 h, rt	IF
β-actin	Sigma-Aldrich	mouse	42	1:15000	30 min, rt	WB
Bcl-2	Cell Signaling	rabbit	28	1:1000, 500	O/N, 30 min	WB, FC
P-Bcl-2	Cell Signaling	rabbit	28	1:1000	O/N	WB
Bcl-xL	Cell Signaling	rabbit	30	1:1000, 500	O/N, 30 min	WB, FC
procaspase 3	Cell Signaling	rabbit	35	1:1000	O/N	WB
procaspase 9	Cell Signaling	rabbit	47	1:1000	O/N	WB
cl-caspase 3	Cell Signaling	rabbit	17, 19	1:1000	72 h	WB
cl-caspase 9	Cell Signaling	rabbit	35	1:1000	72 h	WB
cytochrome c	Cell Signaling	rabbit	14	1:1000	72 h	WB
Erk1/2	Cell Signaling	mouse	42, 44	1:3000	O/N	WB
P-Erk1/2	Cell Signaling	mouse	42, 44	1:1000	O/N	WB
JNK2	Cell Signaling	rabbit	54	1:1000	O/N	WB
P-JNK	Cell Signaling	mouse	46, 54	1:2000	O/N	WB
Mcl-1	Santa Cruz	rabbit	40	1:500	O/N	WB
LC3A/B	Cell Signaling	rabbit	14, 16	1:1000, 200	O/N	WB, IF
MPM-2	Abcam	mouse	92	1:2000	O/N	WB
PARP	Cell Signaling	rabbit	89, 116	1:1000	O/N	WB
HRP-linked anti-mouse	Cell Signaling	horse	-	1:1000	1 h, rt	WB
HRP-linked anti-rabbit	Cell Signaling	goat	-	1:1000	1 h, rt	WB
CY3 anti-mouse	Jackson	sheep	-	1:100	1 h, rt	IF
Alexa488 anti-rabbit	Invitrogen	goat	-	1:500, 1000	2 h, 30 min	IF, FC

Table 32. List of the antibodies used in Western blot (WB), confocal microscopy immunofluorescence (IF), and flow cytometry (FC) experiments. The company, host, molecular weight (kDa), and dilutions are specified in each case. Incubations were carried out at 4 °C unless otherwise indicated. For Western blot, primary antibodies were diluted with 5% BSA or 5% non-fat dry milk in TBS-T, whereas secondary antibodies were diluted in TBS-T.

Proliferation assay

The anti-proliferative activity of the synthesized compounds was evaluated by a colorimetric reaction using tetrazolium salts XTT (Roche Molecular Biochemicals), MTT (Sigma-Aldrich), or WST-1 (Cayman Chemical), which are transformed by metabolically active cells into water-soluble (XTT and WST-1) or non-soluble (MTT) colored formazan crystals. Cells were seeded (10^3-10^4 cells per well) into flat-bottom 96-well plates in 100 µL volume per well one day in advance of being treated in case of adherent cells. Alternatively, non-adherent cells were treated the same day they were seeded. The tested drugs were prepared by serial dilutions in culture media and then, 10 µL were added to the cells with final concentration of DMSO lower than 0.05%. Negative controls with no drug were also included with the corresponding amount of DMSO.

After a 72-hour incubation, the proliferation was measured following the manufacturer´s specifications. First, reagents were added into each well as follows: 50 µL of XTT reaction mixture (50:1 of 2,3-bis(2-methoxy-4-nitro-5-sulfophenyl)-2H-tetrazolium-5-carboxanilide inner salt and the electron coupling reagent *N*-methylphenazonium methyl sulfate), 10 µL of previously filtered 5 mg/mL MTT in PBS, or 10 µL of WST-1 reaction mixture (1:1 of WST-1 developer reagent and electron mediator solution). The plates were incubated during 4 hours at 37 °C. The absorbance of XTT and WST-1 formazan crystals was measured at 450 nm with 650 nm reference wavelength, whereas for MTT reagent, a solubilization step is required. The plates were centrifuged at 1200 rpm for 5 min, media was removed, and the crystals were solubilized in 100 µL of DMSO in order to read the absorbance at 570 nm.

The compounds were tested at an initial concentration of 1 µM, and for those that inhibited cell proliferation by at least 50% with respect to control conditions in two independent experiments, the anti-proliferative activity was evaluated at final concentrations ranging from 10^{-5} M to 10^{-12} M, in order to calculate IC_{50} values. Each condition was seeded in triplicate and the experiments were repeated at least three times. IC_{50} values were calculated using SigmaPlot software using non-linear regression curves fitting the data, and expressed as mean ± SD.

Soft agar colony formation assay

The formation of HeLa cell colonies in agar in the presence of the selected treatments was conducted in 12-well plates.[529] First, a bottom layer (700 µL per well) of complete DMEM supplemented with 0.6% 2-hydroxyethylagarose (Agarose VII, Sigma-Aldrich) was prepared, waiting for the agarose to solidify for 1 hour at 4 °C. Over that matrix, HeLa cells were seeded at a concentration of 1000 cells per well in DMEM supplemented with 0.3% agarose containing the treatments (1 mL). The corresponding amount of DMSO was added to the untreated control. The cell layer was solidified at 4 °C for 15 min, then kept at 37 °C under typical culture conditions. One week later, each well was covered with a feeding layer containing the drugs in DMEM with 0.3% agarose (500 µL), solidified for 15 min at 4 °C. The effect of the treatments was evaluated at 1 nM, 5 nM, 10 nM, 50 nM, 100 nM, 500 nM, and 1 µM and the experiment was repeated four times. Pictures were taken under the scope (CCD Digital Camera Leica DFC 350 FX coupled with a light microscopy Zeiss Axioplan with phase contrast technique) 14 days after the cells were seeded. Then, colonies were stained with 100 µL per well of 5 mg/mL of MTT in PBS, incubated at 37 °C for 2 hours, and counted manually by two different observers. Results are expressed as mean ± SD.

Tubulin isolation

Microtubular protein (MTP) was isolated from bovine or porcine sources following Shelanski procedure with some modifications, by two cycles of polymerization/depolymerization at 37 °C and 4 °C, respectively.[531,532] In each isolation, we used four calf brains or ten pig brains, kindly donated by the slaughterhouse right after the animals were slaughtered, and transported at 4 °C in 350 mL of cold Transport Buffer (TB). The cleaning step was carried out in a 4 °C chamber to preserve the tissue in optimal conditions. The spinal bulb, meninges, and clots were manually removed, and once perfectly clean, the grey matter was cut into pieces avoiding the white matter as far as possible and submerged in cold TB. When the whole cortex is peeled, the drained grey matter (around 300 g) was mixed with Extraction Buffer (EB, 1 mL per g of grey matter).

The tissue was carefully homogenized using a potter (pinkish appearance) and subsequently centrifuged at 4 °C at 31000 rpm for 1 hour. The supernatant was diluted in Assembly Buffer 10x (AB, 1/10 of the s/n volume), 3.5 M glycerol, 0.5 mM GTP and 1 mM PMSF (prepared in absolute EtOH), and incubated at 37 °C. After 45 min, the mixture was centrifuged at 31000 rpm for 90 min, and the pellet (1st cycle of polymerization) was re-suspended in 12 mL of AB 1x and 1 mM GTP to be homogenized in a potter. The suspension was incubated during 30 min in ice and centrifuged at 32000 rpm for 30 minutes at 4 °C. GTP and PMSF were added to the supernatant (1st cycle of depolymerization) at final concentrations of 0.5 mM and 1 mM, respectively, and incubated at 37 °C for 30 min, then centrifuged again at 32000 rpm for 45 min at 37 °C. The resulting pellet (2nd cycle of polymerization) was cooled in ice for 5 min, re-suspended in 1.5 mL of 0.5 mM GTP in AB 1x, and aliquoted in 250 µL fractions. The vials were rapidly frozen in liquid N_2 and stored at -80 °C. The average yield is around 0.03-0.05% (90-150 mg of protein from 300 g of grey matter).

Tubulin polymerization inhibition assay (TPI)

Tubulin polymerization was measured by turbidity using bovine or porcine brain microtubular protein isolated as previously described. Tubulin was thawed as fast as possible at 20 °C, then kept in ice, and the whole experiment was carried out in an 18-20 °C room. The aliquots were re-suspended in 1 mL of polymerization buffer per vial, avoiding the formation of bubbles. It was stirred for 30 min at 4 °C very slowly and centrifuged at 50000 rpm and 4 °C for 30 min (2nd cycle of depolymerization). The supernatant containing the depolymerized tubulin was transferred to a clean tube and kept in ice. The experiment was conducted with 1.0 mg/mL microtubular protein (measured following Bradford procedure)[587] in polymerization buffer with or without the indicated ligands prepared in DMSO. The maximum amount of DMSO was 4%, which is reported not to interfere with the assembly process.[533] The samples were incubated at 20 °C for 30 min and cooled at 4 °C 10 more minutes. Tubulin polymerization was measured in Helios Alpha spectrophotometer (Thermo Fisher Scientific) by monitoring the turbidity increase observed at 450 nm when heating from 4 °C to 37 °C (after 5 min of stabilization at 4 °C). After around 20 min of stable readings, the temperature was switched back to 4 °C in order to corroborate whether the process was reversible.

Tubulin polymerization percentage was referred as the ratio between the amplitude obtained for the protein incubated with the drug and the control curve. Compounds were first assayed at 10 µM, and IC_{50} values were calculated for those that showed TPI percentages over 50% in two independent experiments. SigmaPlot software was used for calculations with mono-exponential curves fitting the experimental data.

Interaction with the colchicine binding domain

The interaction with tubulin was studied under the guidance of Dr. Fernando Díaz at CIB Margarita Salas (Madrid). The tubulin we used for this experiment was purified from calf brain following a modified Weisenberg procedure.[588] Right before the experiment, tubulin aliquots were rapidly thawed in ice and re-suspended in 10 mM NaP_i, 0.1 mM GTP at pH 7.0 (around 300 µL per 10 mg of tubulin). It was first loaded into a Sephadex G25 gel filtration chromatography in 0.9 x 25 cm column. After centrifugation at 50000 rpm for 10 min at 4 °C, tubulin was obtained as a clarified supernatant. Tubulin concentration was measured at 275 nm diluted with 10 mM NaP_i, 1% SDS at pH 7.0 (ε = 107000 $M^{-1}\,cm^{-1}$).[534]

The binding constants of the ligands to the colchicine domain were determined at 25 °C by displacement of MTC as an indirect method to detect the interaction. MTC binds to the colchicine site in tubulin, as evidenced by the tubulin-MTC complex X-ray structure.[156] MTC fluoresces with $\lambda_{excitation}$ = 350 nm and $\lambda_{emission}$ = 423 nm when bound to tubulin, whereas the fluorescence can be spared in its unbound state.[534] The scan of 10 µM MTC and 10 µM tubulin mixed in 10 mM NaP_i, 0.1 mM GTP at pH 7.0 was first recorded. Then, the ligands were added in increasing concentrations to that mixture and incubated for 30 min at 25 °C. Fluorescence emission spectra were monitored in a Fluoromax 2 fluorimeter (Horiba) from 360 nm to 550 nm, with 2 nm excitation and 5 nm emission slits. Alternatively, the experiment was conducted in black 96-well plates, and fluorescence emission was registered in a Varioskan Plate Reader (Thermo Fisher). The binding constant of MTC to the colchicine domain is known ($4.7 \cdot 10^5$ M^{-1}). Therefore, we calculated the fractional saturation values, and the binding constants were determined using Equigra V6.0 software, assuming unitary stoichiometry.[536] We used podophyllotoxin as a positive control.

Taking into account that the excitation wavelength is 350 nm, compounds that absorb in that wavelength are not optimal candidates for this experiment. We first scanned the absorption spectra of the compounds in 10 mM NaP_i buffer at pH 7.0 from 200 nm to 450 nm in a Helios Alpha spectrophotometer (Thermo Fisher Scientific).

Flow cytometry experiments

A. Cell cycle and apoptosis analysis

Cell cycle distribution was studied by analyzing the DNA relative content in PI-stained cells. Around 4-$8 \cdot 10^4$ cells were seeded onto 6-well plates and grown up to optimal confluency before adding the corresponding treatments at the selected concentrations. Following drug treatment, both cells in suspension and adherent were collected and brought together. Typically, each well is divided into two samples: one for cell cycle analysis and another for PI uptake or AnV/PI staining (see below). Those for cell cycle analysis were fixed overnight (at least) in 700 µL of 70% EtOH at 4 °C.

Samples were washed twice with PBS and centrifuged at 1200 rpm for 7 min between washes. The pellets were re-suspended in 0.2 mg/mL RNase A, 10 µg/mL PI (red fluorescence), and 0.5% NP-40 in 360 µL of PBS, and incubated in the dark at room temperature under agitation for 30 min, then analyzed with a Cytomics™ FC500 flow cytometer (Beckman Coulter), acquiring 10000 events within the eventual gate. Cell cycle analysis was performed using Cyflogic software, and apoptosis-like cell death was quantified as the percentage of cells in the $SubG_0/G_1$ region (hypodiploid peak). Experiments were repeated at least three times, and values are expressed as mean ± SD.

B. PI exclusion assay

PI uptake in non-fixed cells was used to evaluate cell membrane integrity. Cells were cultured under the same conditions described above. Pellets were re-suspended in 5 µg/mL PI (red fluorescence) in 400 µL of cold PBS, incubated in the dark at 4 °C for 5 min, and subsequently analyzed with a Cytomics™ FC500 flow cytometer (Beckman Coulter), acquiring 5000 events within the gated population. The analysis was carried out using Cyflogic software: the percentage of PI-positive cells was calculated as the population with increased PI uptake with respect to the basal fluorescence exhibited by cells under control conditions. Experiments were repeated at least three times, and values are expressed as mean ± SD.

C. Annexin V-FITC and PI staining

The quantification of apoptotic cells was carried out by monitoring phosphatidylserine (PtdSer) exposure at the outer leaflet of the plasma membrane. At the same time, cells were stained with PI. HeLa cells ($6 \cdot 10^4$) were seeded onto 6-well plates and incubated with the selected compounds at the indicated concentrations. Following drug treatment, detached and attached cells were harvested and washed with complete DMEM, centrifuging at 1200 rpm for 7 min between washes. The pellet was gently re-suspended in 350 µL of cold Binding buffer containing 4.2 µL of PI (red fluorescence) and 2.2 µL of Annexin V-FITC (Annexin V-FITC Apoptosis Staining Detection kit, Abcam, green fluorescence), and incubated in the dark for 5 min at 4 °C. Staurosporine (Sigma-Aldrich) was used as positive control at 0.5 µM for apoptosis induction. Green and red fluorescence was analyzed with a Cytomics™ FC500 flow cytometer (Beckman Coulter), acquiring 5000 events within the gated population. The analysis was carried out using Cyflogic software, considering AnV^-/PI^- (live cells), AnV^+/PI^- (early apoptosis), AnV^-/PI^+ (necrosis) and AnV^+/PI^+ (late apoptosis or necrosis secondary to apoptosis) populations. Experiments were carried out at least three times and results are expressed as mean ± SD.

D. Analysis of mitochondrial transmembrane potential ($\Delta\Psi_m$) and ROS levels

HeLa cells ($4 \cdot 10^4$) were seeded onto 6-well plates and grown in the presence or absence of the selected compounds. Cells were incubated with 0.5 nM $DiOC_6[3]$ and 2 µM DHE (Invitrogen) for 45 min at 37 °C to study mitochondrial transmembrane potential ($\Delta\Psi_m$) and ROS levels. $DiOC_6[3]$ is a green-fluorescent dye that detects mitochondrial membrane potential at low concentrations. DHE fluoresces red as a sensor of intercellular superoxide when oxidized.

Following incubation, cells were harvested and brought together, centrifuged at 1200 rpm for 7 min, and re-suspended in 350 µL of cold PBS. Additionally, the protonophore CCCP (10 µM) was used as a positive control to induce mitochondrial depolarization 30 min before adding the fluorescent dyes. Fluorescence was subsequently measured in a Cytomics™ FC500 flow cytometer (Beckman Coulter), acquiring 5000 events within the gated population. The analysis was conducted using Cyflogic software and depicted in an overlay as the shift in the average green and red fluorescence of the sample compared to the untreated cells. Experiments were performed at least three times.

E. Analysis of Bcl-xL and Bcl-2 expression

HeLa cells, WT and transfected with Bcl-xL and Bcl-2 were seeded onto 6-well plates following standard culture conditions, and grown up to optimal confluency. Cells were harvested, washed with PBS, and fixed at 4 °C for 30 min in 2% formaldehyde in PBS. The samples were centrifuged at 1200 rpm for 7 min between washes. Then, cells were washed with PBS staining solution (1% FBS, 1% BSA in PBS), and

blocked in ice for 15 min with 50% FBS, 1% BSA, and 0.2% saponin in PBS. Incubation with primary antibodies Ab-1 anti-Bcl-xL and anti-Bcl-2 rabbit polyclonal antibodies (1:500 in PBS staining with 0.2% saponin) was conducted for 30 min in ice. Samples were washed once with 0.2% saponin in PBS staining and incubated with Ab-2 Alexa488-conjugated goat anti-rabbit IgG (1:1000 in 0.2% saponin PBS staining, green fluorescence) for 30 min at 4 °C, and washed once with the same solution. The pellet was re-suspended in 400 µL of 0.2% saponin PBS staining, and subsequently analyzed in a Cytomics™ FC500 flow cytometer (Beckman Coulter).

Confocal microscopy immunofluorescence

A. Immunofluorescence of tubulin cytoskeleton

Sterile coverslips were coated by incubation with 0.01% poly-L-lysine solution for 1 hour at room temperature, then rinsed twice with sterile milli-Q water. Over 8-10·10^4 HeLa, HEK-293, or 20-25·10^4 HPNE cells were seeded on the coverslips in 35 mm individual plates and incubated up to 80% confluency. Culture media was replaced by fresh DMEM and cells were treated with the selected compounds. The corresponding amount of DMSO was added to the untreated negative control.

After incubation with the drugs, culture media was removed and coverslips were washed three times with cold HPEM buffer. Cells were fixed in 4% formaldehyde in HPEM buffer for 30 min at 4 °C and permeabilized with 0.5% Triton X-100 in HPEM buffer for 90 seconds at 4 °C. After washing four times with HPEM buffer, cells were incubated with Ab-1 anti-α-tubulin mouse monoclonal antibody (1:150 in PBS) for 1 hour at rt. Cells were washed four times with PBS and incubated in the absence of light with Ab-2 CY3-conjugated sheep anti-mouse IgG (1:100 in PBS) for 1 hour at RT (red fluorescence). After four washes with PBS, cell nuclei were stained with a drop of ProLong™ Gold antifade reagent with DAPI (blue fluorescence) to preserve fluorescence. The samples were kept at 4 °C in a humidified chamber in the dark, and analyzed in a Leica TCS SP5 confocal microscope. Negative controls lacking the primary antibody and alternatively, with an irrelevant primary antibody showed no fluorescence.

B. Visualization of LC3 puncta

As described above, over 8·10^4 HeLa cells were seeded onto poly-L-lysine coated coverslips. Cells were treated with the indicated compounds alone or in combination with bafilomycin A1, and incubated for 24 hours. After one PBS wash, cells were fixed in 4% formaldehyde in HPEM buffer for 30 minutes at 4 °C, then permeabilized with 0.5% Triton X-100 in HPEM buffer for 90 seconds at 4 °C. Coverslips were rinsed twice with PBS and then, cells were blocked for 1 hour at 4 °C in 2% BSA in PBS. The incubation with Ab-1 anti-LC3A/B rabbit polyclonal antibody (1:200 in PBS) was carried out at 4 °C overnight. After three washes with PBS, samples were incubated in the absence of light with Ab-2 Alexa488-conjugated goat anti-rabbit IgG (1:500 in PBS, green fluorescence) for 2 hours at 4 °C, followed by three PBS washes. Cell nuclei were stained with ProLong™ Gold antifade reagent with DAPI (blue fluorescence) to preserve fluorescence. The samples were kept at 4 °C in a humidified chamber in the dark, and analyzed by using a Leica TCS SP5 confocal microscope.

Rescue experiments

Cells were grown as specified for each type of experiment, and incubated with the compounds for a specific period of time. Then, both adherent and detached cells were brought together and washed three

times with PBS, with 5 min centrifugation at 1200 rpm between washes. The resulting pellets were re-suspended in complete media and seeded again.

Western blot

Following treatment, around 4-5·10^6 cells were harvested and brought together. Cells were washed twice with PBS at 4 °C, and centrifuged at 1200 rpm for 7 min between washes. The resulting pellet was re-suspended in 60-120 µL of WCE-300 lysis buffer, supplemented with phosphatase and protease inhibitors. After a 20-min incubation in ice, the samples were centrifuged at 14000 rpm for 18 min at 4 °C to provide the whole cell protein extract (supernatant). Protein concentration was measured by Bradford procedure at 595 nm first establishing a calibration curve with BSA.[587]

Protein lysate (20-80 µg) was denaturalized in SPLB by heating at 96 °C for 5 min. Proteins were subsequently separated by molecular weight in a polyacrylamide gel (8-15%) in SDS-PAGE under reducing conditions. Colorful protein ladder was run in parallel. After electrophoresis, proteins were transferred overnight at 4 °C to hydrophobic Immobilon-P PVDF membranes (Merck Millipore), previously activated in methanol for 5 min. Then, membranes were blocked with 5% BSA or 5% non-fat skimmed milk powder in TBS-T for at least 1 hour at RT. The incubation with primary antibodies listed in Table 32 was conducted at 4 °C for around 16 hours in most cases. After three 5-min TBS-T washes, membranes were incubated with HRP-conjugated secondary antibodies for 1 hour at RT. Then, protein bands were visualized in a ChemiDoc™ Imaging System (BioRad) using the enhanced chemoluminescence detection kit Amershamt™ ECL™ (GE Healthcare), and alternatively, SuperSignal™ West Femto (Thermo Fisher). Experiments were performed at least three times with independent protein lysates.

Separation of mitochondrial and cytosolic extracts

In order to analyze the release of cytochrome c from the mitochondria to the cytosol, separation of mitochondrial and cytosolic content was carried out as previously described.[589] Briefly, 4-5·10^6 cells were harvested and washed once with ice-cold PBS, then re-suspended in lysis buffer (see cytosol lysis buffer). Samples were immediately centrifuged at 12000 g for 5 min at 4 °C. Supernatants contain the cytosolic fraction free of mitochondria, whereas the pellet corresponds to the nuclear and mitochondrial fraction. Cytosolic extracts (40 µg) were subjected to Western blot electrophoresis in a 15% polyacrylamide gel as described above.

Time-lapse videomicroscopy

Over 10^4 HeLa cells were seeded into an 8 well chamber slide (Ibidi). Treated and non-treated cells were recorded by time-lapse microscopy using a Widefield Multidimensional Microscopy System Leica AF6000 LX, enclosed in an incubation chamber equipped with CO_2 and temperature controls. Frames were taken every 30 min for 72 hours, and three different fields were recorded for each well. The elapsed time is shown in the superior right corner of the video.

Tube formation assay

Tube formation assay was conducted during the stay at Dr. DeCicco-Skinner's laboratory, as previously described in the literature.[539] 3B-11 cells between the second and sixth passage were starved overnight in DMEM containing 0.2% FBS (Peak Serum), 1% PenStrep (Gibco), and 1% GlutaMAX (Gibco), and stained with 2 µg/mL calcein AM (Life Technologies) for 30 minutes prior to the assay. The cells were washed with

DPBS (Gibco), re-suspended in conditioned media from adipose tissue-derived stem cells, and filtered through a 100 µm strainer to discard clumps. Cells were homogeneously seeded in 24-well plates that had been previously coated with 220 µL of growth factor reduced basement membrane BME (Corning), avoiding the formation of bubbles at a concentration of $18 \cdot 10^4$ cells/well. Besides the selected treatments, control conditions were also set using the equivalent amount of DMSO. Pictures were taken after a 6-hour incubation at 37 °C under an Olympus SZX16 dissection scope, and then samples were fixed by incubation with 4% formaldehyde in DPBS for 15 minutes and stored at 4 °C. The tube network was quantified regarding nodes, meshes, and segments using ImageJ software (Angiogenesis Analyzer Plugin, HUVEC Fluo Analysis) by selecting different frames. The experiments were performed four times, and results are expressed as mean ± SD.

Statistical analysis

The experiments were repeated at least three times in different days with different passage number for experiments involving cells. Results are expressed as mean ± SD of the number of experiments indicated (*n*). Comparison between two different conditions was performed using Student's t-test with SigmaPlot 14.0 software. Statistical significance is indicated as *p* value <0.05 (*), <0.01 (**) or < 0.001 (***).

REFERENCES

1. Life expectancy. (2013). Available at: https://ourworldindata.org/life-expectancy.

2. Alberts, B. *et al.* Cancer. in *Molecular biology of the cell* 1091–1143 (Garland Science, 2008).

3. Stacker, S. A., Achen, M. G., Jussila, L., Baldwin, M. E. & Alitalo, K. Lymphangiogenesis and cancer metastasis. *Nat. Rev. Cancer* **2**, 573–583 (2002).

4. World Health Organization. (2018). Available at: https://www.who.int/health-topics/cancer.

5. Bray, F. *et al.* Global cancer statistics 2018: GLOBOCAN estimates of incidence and mortality worldwide for 36 cancers in 185 countries. *CA. Cancer J. Clin.* **68**, 394–424 (2018).

6. DeVita Jr, V. T. & Chu, E. A history of cancer chemotherapy. *Cancer Res.* **68**, 8643–8653 (2008).

7. Galmarini, D., Galmarini, C. M. & Galmarini, F. C. Cancer chemotherapy: a critical analysis of its 60 years of history. *Crit. Rev. Oncol. Hematol.* **84**, 181–199 (2012).

8. Alfarouk, K. O. *et al.* Resistance to cancer chemotherapy: failure in drug response from ADME to P-gp. *Cancer Cell Int.* **15**, 71 (2015).

9. Trédan, O., Galmarini, C. M., Patel, K. & Tannock, I. F. Drug resistance and the solid tumor microenvironment. *J. Natl. Cancer Inst.* **99**, 1441–1454 (2007).

10. Aylett, C. H. S., Löwe, J. & Amos, L. A. New Insights into the Mechanisms of Cytomotive Actin and Tubulin Filaments. *Int. Rev. Cell Mol. Biol.* **292**, 1–71 (2011).

11. Draber, P., Sulimenko, V. & Draberova, E. Cytoskeleton in mast cell signaling. *Front. Immunol.* **3**, 130 (2012).

12. Dumontet, C. & Jordan, M. A. Microtubule-binding agents: a dynamic field of cancer therapeutics. *Nat. Rev. Drug Discov.* **9**, 790–803 (2010).

13. Jordan, M. A. & Wilson, L. Microtubules as a target for anticancer drugs. *Nat. Rev. Cancer* **4**, 253–265 (2004).

14. Risinger, A. L., Giles, F. J. & Mooberry, S. L. Microtubule dynamics as a target in oncology. *Cancer Treat. Rev.* **35**, 255–261 (2009).

15. Luduena, R. F. Multiple forms of tubulin: different gene products and covalent modifications. *Int. Rev. Cytol.* **178**, 207–275 (1998).

16. Mandelkow, E. M., Mandelkow, E. & Milligan, R. A. Microtubule dynamics and microtubule caps: a time-resolved cryo-electron microscopy study. *J. Cell Biol.* **114**, 977–991 (1991).

17. Chrétien, D. & Wade, R. H. New data on the microtubule surface lattice. *Biol. Cell* **71**, 161–174 (1991).

18. Kollman, J. M., Polka, J. K., Zelter, A., Davis, T. N. & Agard, D. A. Microtubule nucleating gamma-TuSC assembles structures with 13-fold microtubule-like symmetry. *Nature* **466**, 879–882 (2010).

19. Chaaban, S. & Brouhard, G. J. A microtubule bestiary: structural diversity in tubulin polymers. *Mol. Biol. Cell* **28**, 2924–2931 (2017).

20. Amos, L. A. & Schlieper, D. Microtubules and Maps. *Adv. Protein Chem.* **71**, 257–298 (2005).

21. Nogales, E., Wolf, S. G. & Downing, K. H. Structure of the αβ tubulin dimer by electron crystallography. *Nature* **391**, 199–203 (1998).

22. Nogales, E., Whittaker, M., Milligan, R. A. & Downing, K. H. High-resolution model of the microtubule. *Cell* **96**, 79–88 (1999).

23. Löwe, J., Li, H., Downing, K. . & Nogales, E. Refined structure of αβ-tubulin at 3.5 Å resolution. *J. Mol. Biol.* **313**, 1045–1057 (2001).

24. Gigant, B. *et al.* The 4 A X-ray structure of a tubulin:stathmin-like domain complex. *Cell* **102**, 809–16 (2000).

25. Ravelli, R. B. G. *et al.* Insight into tubulin regulation from a complex with colchicine and a stathmin-like domain. *Nature* **428**, 198–202 (2004).

26. Vemu, A., Atherton, J., Spector, J. O., Moores, C. A. & Roll-Mecak, A. Tubulin isoform composition tunes microtubule dynamics. *Mol. Biol. Cell* **28**, 3564–3572 (2017).

27. Vicente-Blazquez, A. *et al.* Antitubulin sulfonamides: The successful combination of an established drug class and a multifaceted target. *Med. Res. Rev.* **39**, 775–830 (2019).

28. Alushin, G. M. *et al.* High-Resolution Microtubule Structures Reveal the Structural Transitions in alpha beta-Tubulin upon GTP Hydrolysis. *Cell* **157**, 1117–1129 (2014).

29. Ranaivoson, F. M., Gigant, B., Berritt, S., Joullie, M. & Knossow, M. Structural plasticity of tubulin assembly probed by vinca-domain ligands. *Acta Crystallogr.,Sect.D* **68**, 927–934 (2012).

30. Rose, A. S. *et al.* NGL viewer: web-based molecular graphics for large complexes. *Bioinformatics* **34**, 3755–3758 (2018).

31. Akhmanova, A. & Steinmetz, M. O. Control of microtubule organization and dynamics: two ends in the limelight. *Nat. Rev. Mol. Cell Biol.* **16**, 711–726 (2015).

32. Brouhard, G. J. & Rice, L. M. Microtubule dynamics: an interplay of biochemistry and mechanics. *Nat. Rev. Mol. Cell Biol.* **19**, 451–463 (2018).

33. Mollinedo, F. & Gajate, C. Microtubules, microtubule-interfering agents and apoptosis. *Apoptosis* **8**, 413–450 (2003).

34. van Haren, J. & Wittmann, T. Microtubule Plus End Dynamics - Do We Know How Microtubules Grow?: Cells boost microtubule growth by promoting distinct structural transitions at growing microtubule ends. *Bioessays* **41**, e1800194 (2019).

35. Howard, J. & Hyman, A. A. Dynamics and mechanics

of the microtubule plus end. *Nature* **422**, 753–758 (2003).

36. Akhmanova, A. & Steinmetz, M. O. Tracking the ends: a dynamic protein network controls the fate of microtubule tips. *Nat. Rev. Mol. Cell Biol.* **9**, 309–322 (2008).

37. Wang, H.-W. & Nogales, E. Nucleotide-dependent bending flexibility of tubulin regulates microtubule assembly. *Nature* **435**, 911–915 (2005).

38. Natarajan, K., Mohan, J. & Senapati, S. Relating nucleotide-dependent conformational changes in free tubulin dimers to tubulin assembly. *Biopolymers* **99**, 282–291 (2013).

39. Fedorov, V. A. *et al.* Mechanical properties of tubulin intra- and inter-dimer interfaces and their implications for microtubule dynamic instability. *PLOS Comput. Biol.* **15**, e1007327 (2019).

40. Nogales, E. & Wang, H.-W. Structural mechanisms underlying nucleotide-dependent self-assembly of tubulin and its relatives. *Curr. Opin. Struct. Biol.* **16**, 221–229 (2006).

41. Nogales, E. & Wang, H.-W. Structural intermediates in microtubule assembly and disassembly: how and why? *Curr. Opin. Cell Biol.* **18**, 179–184 (2006).

42. Barbier, P. *et al.* Stathmin and interfacial microtubule inhibitors recognize a naturally curved conformation of tubulin dimers. *J. Biol. Chem.* **285**, 31672–31681 (2010).

43. Buey, R. M., Diaz, J. F. & Andreu, J. M. The nucleotide switch of tubulin and microtubule assembly: a polymerization-driven structural change. *Biochemistry* **45**, 5933–5938 (2006).

44. Nawrotek, A., Knossow, M. & Gigant, B. The determinants that Govern microtubule assembly from the atomic structure of GTP-tubulin. *J. Mol. Biol.* (2011). doi:10.1016/j.jmb.2011.07.029

45. Brouhard, G. J. & Rice, L. M. The contribution of αβ-tubulin curvature to microtubule dynamics. *J. Cell Biol.* **207**, 323–334 (2014).

46. Rice, L. M., Montabana, E. A. & Agard, D. A. The lattice as allosteric effector: structural studies of alphabeta- and gamma-tubulin clarify the role of GTP in microtubule assembly. *Proc. Natl. Acad. Sci. U. S. A.* **105**, 5378–5383 (2008).

47. Grafmüller, A. & Voth, G. A. Intrinsic Bending of Microtubule Protofilaments. *Structure* **19**, 409–417 (2011).

48. Estévez-Gallego, J. *et al.* Structural model for differential cap maturation at growing microtubule ends. *Elife* **9**, e50155 (2020).

49. Quiniou, E., Guichard, P., Perahia, D., Marco, S. & Mouawad, L. An atomistic view of microtubule stabilization by GTP. *Structure* (2013). doi:10.1016/j.str.2013.03.009

50. Desai, A. & Mitchison, T. J. Microtubule polymerization dynamics. *Annu. Rev. Cell Dev. Biol.* **13**, 83–117 (1997).

51. Walker, R. A., Inoué, S. & Salmon, E. D. Asymmetric behavior of severed microtubule ends after ultraviolet-microbeam irradiation of individual microtubules in vitro. *J. Cell Biol.* **108**, 931–937 (1989).

52. Melki, R., Carlier, M. F., Pantaloni, D. & Timasheff, S. N. Cold depolymerization of microtubules to double rings: geometric stabilization of assemblies. *Biochemistry* **28**, 9143–9152 (1989).

53. Moudjou, M., Bordes, N., Paintrand, M. & Bornens, M. gamma-Tubulin in mammalian cells: the centrosomal and the cytosolic forms. *J. Cell Sci.* **109 (Pt 4**, 875–887 (1996).

54. Fernandez, N., Chang, Q., Buster, D. W., Sharp, D. J. & Ma, A. A model for the regulatory network controlling the dynamics of kinetochore microtubule plus-ends and poleward flux in metaphase. *Proc. Natl. Acad. Sci. U. S. A.* **106**, 7846–7851 (2009).

55. Prassanawar, S. S. & Panda, D. Tubulin heterogeneity regulates functions and dynamics of microtubules and plays a role in the development of drug resistance in cancer. *Biochem. J.* **476**, 1359–1376 (2019).

56. Saxton, W. M. *et al.* Tubulin dynamics in cultured mammalian cells. *J. Cell Biol.* **99**, 2175–2186 (1984).

57. Janke, C. & Bulinski, J. C. Post-translational regulation of the microtubule cytoskeleton: mechanisms and functions. *Nat. Rev. Mol. Cell Biol.* **12**, 773–786 (2011).

58. Verhey, K. J. & Gaertig, J. The tubulin code. *Cell Cycle* **6**, 2152–2160 (2007).

59. Gadadhar, S., Bodakuntla, S., Natarajan, K. & Janke, C. The tubulin code at a glance. *J. Cell Sci.* **130**, 1347–1353 (2017).

60. Wehenkel, A. & Janke, C. Towards elucidating the tubulin code. *Nat. Cell Biol.* **16**, 303–305 (2014).

61. Yu, I., Garnham, C. P. & Roll-Mecak, A. Writing and Reading the Tubulin Code. *J. Biol. Chem.* **290**, 17163–17172 (2015).

62. Redeker, V. Mass spectrometry analysis of C-terminal posttranslational modifications of tubulins. *Methods Cell Biol.* **95**, 77–103 (2010).

63. Lewis, S. A., Gu, W. & Cowan, N. J. Free intermingling of mammalian beta-tubulin isotypes among functionally distinct microtubules. *Cell* **49**, 539–548 (1987).

64. Leandro-Garcia, L. J. *et al.* Tumoral and tissue-specific expression of the major human beta-tubulin isotypes. *Cytoskeleton (Hoboken).* **67**, 214–223 (2010).

65. Roll-Mecak, A. Intrinsically disordered tubulin tails: complex tuners of microtubule functions? *Semin. Cell Dev. Biol.* **37**, 11–19 (2015).

66. Amos, L. A. Focusing-in on microtubules. *Curr. Opin. Struct. Biol.* **10**, 236–241 (2000).

67. Saillour, Y. *et al.* Beta tubulin isoforms are not interchangeable for rescuing impaired radial migration due to Tubb3 knockdown. *Hum. Mol. Genet.* **23**, 1516–1526 (2014).

68. Panda, D., Miller, H. P., Banerjee, A., Ludueña, R. F. & Wilson, L. Microtubule dynamics in vitro are regulated by the tubulin isotype composition. *Proc. Natl. Acad. Sci. U. S. A.* **91**, 11358–11362 (1994).

69. Fiore, M., Goulas, C. & Pillois, X. A new mutation in TUBB1 associated with thrombocytopenia confirms that C-terminal part of beta1-tubulin plays a role in microtubule assembly. *Clinical genetics* **91**, 924–926 (2017).

70. Tischfield, M. A. *et al.* Human TUBB3 mutations perturb microtubule dynamics, kinesin interactions, and axon guidance. *Cell* **140**, 74–87 (2010).

71. Feng, R. *et al.* Mutations in TUBB8 and Human Oocyte Meiotic Arrest. *N. Engl. J. Med.* **374**, 223–232 (2016).

72. Kavallaris, M. Microtubules and resistance to tubulin-binding agents. *Nat. Rev. Cancer* **10**, 194–204 (2010).

73. Song, Y. & Brady, S. T. Post-translational modifications of tubulin: pathways to functional diversity of microtubules. *Trends Cell Biol.* **25**, 125–136 (2015).

74. Magiera, M. M. & Janke, C. Post-translational modifications of tubulin. *Curr. Biol.* **24**, R351-4 (2014).

75. Magiera, M. M., Singh, P. & Janke, C. SnapShot: Functions of Tubulin Posttranslational Modifications. *Cell* **173**, 1552-1552.e1 (2018).

76. Fourest-Lieuvin, A. *et al.* Microtubule regulation in mitosis: tubulin phosphorylation by the cyclin-dependent kinase Cdk1. *Mol. Biol. Cell* **17**, 1041–1050 (2006).

77. Song, Y. *et al.* Transglutaminase and polyamination of tubulin: posttranslational modification for stabilizing axonal microtubules. *Neuron* **78**, 109–123 (2013).

78. Di Tommaso, P. *et al.* T-Coffee: a web server for the multiple sequence alignment of protein and RNA sequences using structural information and homology extension. *Nucleic Acids Res.* **39**, W13-7 (2011).

79. Soppina, V., Herbstman, J. F., Skiniotis, G. & Verhey, K. J. Luminal Localization of α-tubulin K40 Acetylation by Cryo-EM Analysis of Fab-Labeled Microtubules. *PLoS One* **7**, e48204 (2012).

80. Konno, A., Setou, M. & Ikegami, K. Ciliary and flagellar structure and function--their regulations by posttranslational modifications of axonemal tubulin. *Int. Rev. Cell Mol. Biol.* **294**, 133–170 (2012).

81. Wloga, D., Joachimiak, E. & Fabczak, H. Tubulin Post-Translational Modifications and Microtubule Dynamics. *Int. J. Mol. Sci.* **18**, 2207 (2017).

82. Dempsey, E. *et al.* Antimitotic herbicides bind to an unidentified site on malarial parasite tubulin and block development of liver-stage Plasmodium parasites. *Mol. Biochem. Parasitol.* **188**, 116–127 (2013).

83. Blume, Y. B., Nyporko, A. Y., Yemets, A. I. & Baird, W. V. Structural modeling of the interaction of plant α-tubulin with dinitroaniline and phosphoroamidate herbicides. *Cell Biol. Int.* **27**, 171–174 (2003).

84. Hoffman, J. C. & Vaughn, K. C. Mitotic disrupter herbicides act by a single mechanism but vary in efficacy. *Protoplasma* **179**, 16–25 (1994).

85. Stanton, R. A., Gernert, K. M., Nettles, J. H. & Aneja, R. Drugs that target dynamic microtubules: a new molecular perspective. *Med. Res. Rev.* **31**, 443–481 (2011).

86. Diaz, J. F. & Andreu, J. M. Assembly of purified GDP-tubulin into microtubules induced by taxol and taxotere: reversibility, ligand stoichiometry, and competition. *Biochemistry* **32**, 2747–2755 (1993).

87. Field, J. J., Díaz, J. F. & Miller, J. H. The binding sites of microtubule-stabilizing agents. *Chemistry and Biology* (2013). doi:10.1016/j.chembiol.2013.01.014

88. Zhao, Y., Mu, X. & Du, G. Microtubule-stabilizing agents: New drug discovery and cancer therapy. *Pharmacology and Therapeutics* (2016). doi:10.1016/j.pharmthera.2015.12.006

89. Magnani, M., Maccari, G., Andreu, J. M., Díaz, J. F. & Botta, M. Possible binding site for paclitaxel at microtubule pores. *FEBS J.* **276**, 2701–2712 (2009).

90. Barasoain, I. *et al.* Probing the pore drug binding site of microtubules with fluorescent taxanes: evidence of two binding poses. *Chem. Biol.* **17**, 243–253 (2010).

91. Naaz, F., Haider, M. R., Shafi, S. & Yar, M. S. Anti-tubulin agents of natural origin: Targeting taxol, vinca, and colchicine binding domains. *European Journal of Medicinal Chemistry* (2019). doi:10.1016/j.ejmech.2019.03.025

92. Cao, Y.-N. *et al.* Recent advances in microtubule-stabilizing agents. *Eur. J. Med. Chem.* **143**, 806–828 (2018).

93. National Cancer Institute. Available at: https://www.cancer.gov/.

94. SCHIFF, P. B., FANT, J. & HORWITZ, S. B. Promotion of microtubule assembly in vitro by taxol. *Nature* **277**, 665–667 (1979).

95. Ojima, I., Lichtenthal, B., Lee, S., Wang, C. & Wang, X. Taxane anticancer agents: a patent perspective. *Expert Opin. Ther. Pat.* **26**, 1–20 (2016).

96. Němcová-Fürstová, V. *et al.* Characterization of acquired paclitaxel resistance of breast cancer cells and involvement of ABC transporters. *Toxicol. Appl. Pharmacol.* **310**, 215–228 (2016).

97. Markman, M. Managing taxane toxicities. *Support. Care Cancer* **11**, 144–147 (2003).

98. Galsky, M. D., Dritselis, A., Kirkpatrick, P. & Oh, W. K. Cabazitaxel. *Nat. Rev. Drug Discov.* **9**, 677–678 (2010).

99. Cobham, M. V. & Donovan, D. Ixabepilone: a new treatment option for the management of taxane-resistant metastatic breast cancer. *Cancer Manag. Res.* **1**, 69–77 (2009).

100. Prota, A. E. *et al.* Structural basis of microtubule stabilization by laulimalide and peloruside A. *Angew. Chem. Int. Ed. Engl.* **53**, 1621–1625 (2014).

101. Mooberry, S. L., Tien, G., Hernandez, A. H., Plubrukarn, A. & Davidson, B. S. Laulimalide and isolaulimalide, new paclitaxel-like microtubule-stabilizing agents. *Cancer Res.* **59**, 653–660 (1999).

102. West, L. M., Northcote, P. T. & Battershill, C. N. Peloruside A: A Potent Cytotoxic Macrolide Isolated from the New Zealand Marine Sponge Mycale sp. *J. Org. Chem.* **65**, 445–449 (2000).

103. Hood, K. A. *et al.* Peloruside A, a novel antimitotic agent with paclitaxel-like microtubule- stabilizing activity. *Cancer Res.* **62**, 3356–3360 (2002).

104. Prota, A. E. *et al.* Molecular mechanism of action of microtubule-stabilizing anticancer agents. *Science* **339**, 587–590 (2013).

105. Khrapunovich-Baine, M. *et al.* Hallmarks of molecular action of microtubule stabilizing agents: effects of epothilone B, ixabepilone, peloruside A, and laulimalide on microtubule conformation. *J. Biol. Chem.* **286**, 11765–11778 (2011).

106. Liu, J. *et al.* In vitro and in vivo anticancer activities of synthetic (-)-laulimalide, a marine natural product microtubule stabilizing agent. *Anticancer Res.* **27**, 1509–1518 (2007).

107. Martino, E. *et al.* Vinca alkaloids and analogues as anti-cancer agents: Looking back, peering ahead. *Bioorg. Med. Chem. Lett.* **28**, 2816–2826 (2018).

108. Gigant, B. *et al.* Structural basis for the regulation of tubulin by vinblastine. *Nature* **435**, 519–522 (2005).

109. Wilson, L., Jordan, M. A., Morse, A. & Margolis, R. L. Interaction of vinblastine with steady-state microtubules in vitro. *J. Mol. Biol.* **159**, 125–149 (1982).

110. Lobert, S. & Correia, J. J. Energetics of vinca alkaloid interactions with tubulin. *Methods Enzymol.* **323**, 77–103 (2000).

111. Schutz, F. A. B., Bellmunt, J., Rosenberg, J. E. & Choueiri, T. K. Vinflunine: drug safety evaluation of this novel synthetic vinca alkaloid. *Expert Opin. Drug Saf.* **10**, 645–653 (2011).

112. Gerullis, H., Wawroschek, F., Köhne, C.-H. & Ecke, T. H. Vinflunine in the treatment of advanced urothelial cancer: clinical evidence and experience. *Ther. Adv. Urol.* **9**, 28–35 (2017).

113. Shah, N. N. *et al.* Vincristine Sulfate Liposomes Injection (VSLI, Marqibo®): Results From a Phase I Study in Children, Adolescents, and Young Adults With Refractory Solid Tumors or Leukemias. *Pediatr. Blood Cancer* **63**, 997–1005 (2016).

114. Gidding, C. E., Kellie, S. J., Kamps, W. A. & de Graaf, S. S. Vincristine revisited. *Crit. Rev. Oncol. Hematol.* **29**, 267–287 (1999).

115. Zhang, Y., Yang, S.-H. & Guo, X.-L. New insights into Vinca alkaloids resistance mechanism and circumvention in lung cancer. *Biomed. Pharmacother.* **96**, 659–666 (2017).

116. Wang, Y. *et al.* Structural Insights into the Pharmacophore of Vinca Domain Inhibitors of Microtubules. *Mol. Pharmacol.* **89**, 233–242 (2016).

117. Waight, A. B. *et al.* Structural Basis of Microtubule Destabilization by Potent Auristatin Anti-Mitotics. *PLoS One* **11**, e0160890–e0160890 (2016).

118. Sáez-Calvo, G. *et al.* Triazolopyrimidines Are Microtubule-Stabilizing Agents that Bind the Vinca Inhibitor Site of Tubulin. *Cell Chem. Biol.* **24**, 737-750.e6 (2017).

119. Doodhi, H. *et al.* Termination of Protofilament Elongation by Eribulin Induces Lattice Defects that Promote Microtubule Catastrophes. *Curr. Biol.* **26**, 1713–1721 (2016).

120. Smith, J. A. *et al.* Eribulin binds at microtubule ends to a single site on tubulin to suppress dynamic instability. *Biochemistry* **49**, 1331–1337 (2010).

121. Dabydeen, D. A. *et al.* Comparison of the activities of the truncated halichondrin B analog NSC 707389 (E7389) with those of the parent compound and a proposed binding site on tubulin. *Mol. Pharmacol.* **70**, 1866–1875 (2006).

122. Prota, A. E. *et al.* A new tubulin-binding site and pharmacophore for microtubule-destabilizing anticancer drugs. *Proc. Natl. Acad. Sci. U. S. A.* **111**, 13817–13821 (2014).

123. Hanauske, A. R. *et al.* Phase II clinical trials with rhizoxin in breast cancer and melanoma. The EORTC Early Clinical Trials Group. *Br. J. Cancer* **73**, 397–399 (1996).

124. Verma, S. *et al.* Trastuzumab emtansine for HER2-positive advanced breast cancer. *N. Engl. J. Med.* **367**, 1783–1791 (2012).

125. Hunter, F. W. *et al.* Mechanisms of resistance to trastuzumab emtansine (T-DM1) in HER2-positive breast cancer. *Br. J. Cancer* (2019). doi:10.1038/s41416-019-0635-y

126. Prota, A. E. *et al.* Pironetin Binds Covalently to αCys316 and Perturbs a Major Loop and Helix of α-Tubulin to Inhibit Microtubule Formation. *J. Mol. Biol.* (2016). doi:10.1016/j.jmb.2016.06.023

127. Yang, J. *et al.* Pironetin reacts covalently with cysteine-316 of α-tubulin to destabilize microtubule. *Nat. Commun.* **7**, 12103 (2016).

128. Alkadi, H., Khubeiz, M. J. & Jbeily, R. Colchicine: A Review on Chemical Structure and Clinical Usage. *Infect. Disord. Drug Targets* **18**, 105–121 (2018).

129. Borisy, G. G. & Taylor, E. W. The mechanism of action of colchicine. Colchicine binding to sea urchin eggs and the mitotic apparatus. *J. Cell Biol.* **34**, 535–548

(1967).

130. Uppuluri, S., Knipling, L., Sackett, D. L. & Wolff, J. Localization of the colchicine-binding site of tubulin. *Proc. Natl. Acad. Sci. U. S. A.* **90**, 11598–11602 (1993).

131. Andreu, J. M., Wagenknecht, T. & Timasheff, S. N. Polymerization of the tubulin-colchicine complex: relation to microtubule assembly. *Biochemistry* **22**, 1556–1566 (1983).

132. Skoufias, D. A. & Wilson, L. Mechanism of inhibition of microtubule polymerization by colchicine: inhibitory potencies of unliganded colchicine and tubulin-colchicine complexes. *Biochemistry* **31**, 738–746 (1992).

133. Dorléans, A. *et al.* Variations in the colchicine-binding domain provide insight into the structural switch of tubulin. *Proc. Natl. Acad. Sci. U. S. A.* **106**, 13775–13779 (2009).

134. David-Pfeuty, T., Simon, C. & Pantaloni, D. Effect of antimitotic drugs on tubulin GTPase activity and self-assembly. *J. Biol. Chem.* **254**, 11696–11702 (1979).

135. Prota, A. E. *et al.* The novel microtubule-destabilizing drug BAL27862 binds to the colchicine site of tubulin with distinct effects on microtubule organization. *J. Mol. Biol.* **426**, 1848–1860 (2014).

136. Lu, Y., Chen, J., Xiao, M., Li, W. & Miller, D. D. An overview of tubulin inhibitors that interact with the colchicine binding site. *Pharm. Res.* **29**, 2943–2971 (2012).

137. Zhou, J. & Giannakakou, P. Targeting microtubules for cancer chemotherapy. *Curr. Med. Chem. Anticancer. Agents* **5**, 65–71 (2005).

138. Dalbeth, N., Lauterio, T. J. & Wolfe, H. R. Mechanism of action of colchicine in the treatment of gout. *Clin. Ther.* **36**, 1465–1479 (2014).

139. Liantinioti, G., Argyris, A. A., Protogerou, A. D. & Vlachoyiannopoulos, P. The Role of Colchicine in the Treatment of Autoinflammatory Diseases. *Curr. Pharm. Des.* **24**, 690–694 (2018).

140. Sapra, S. *et al.* Colchicine and its various physicochemical and biological aspects. *Med. Chem. Res.* **22**, 531–547 (2013).

141. McLoughlin, E. C. & O'Boyle, N. M. Colchicine-Binding Site Inhibitors from Chemistry to Clinic: A Review. *Pharmaceuticals (Basel).* **13**, E8 (2020).

142. Álvarez, R., Medarde, M. & Peláez, R. New ligands of the tubulin colchicine site based on X-ray structures. *Curr. Top. Med. Chem.* **14**, 2231–2252 (2014).

143. Ambudkar, S. V, Kimchi-Sarfaty, C., Sauna, Z. E. & Gottesman, M. M. P-glycoprotein: from genomics to mechanism. *Oncogene* **22**, 7468–7485 (2003).

144. Dark, G. G. *et al.* Combretastatin A-4, an agent that displays potent and selective toxicity toward tumor vasculature. *Cancer Res.* **57**, 1829–1834 (1997).

145. Prota, A. E. *et al.* Structural basis of tubulin tyrosination by tubulin tyrosine ligase. *J. Cell Biol.* **200**, 259–270 (2013).

146. Massarotti, A., Coluccia, A., Silvestri, R., Sorba, G. & Brancale, A. The tubulin colchicine domain: a molecular modeling perspective. *ChemMedChem* **7**, 33–42 (2012).

147. McNamara, D. E., Senese, S., Yeates, T. O. & Torres, J. Z. Structures of potent anticancer compounds bound to tubulin. *Protein Sci.* **24**, 1164–1172 (2015).

148. Wang, Y. *et al.* Structures of a diverse set of colchicine binding site inhibitors in complex with tubulin provide a rationale for drug discovery. *FEBS J.* **283**, 102–111 (2016).

149. Canela, M.-D. *et al.* Antivascular and antitumor properties of the tubulin-binding chalcone TUB091. *Oncotarget* **8**, 14325–14342 (2017).

150. Marangon, J. *et al.* Tools for the rational design of bivalent microtubule-targeting drugs. *Biochem. Biophys. Res. Commun.* **479**, 48–53 (2016).

151. Bohnacker, T. *et al.* Deconvolution of Buparlisib's mechanism of action defines specific PI3K and tubulin inhibitors for therapeutic intervention. *Nat. Commun.* **8**, 14683 (2017).

152. Gaspari, R., Prota, A. E., Bargsten, K., Cavalli, A. & Steinmetz, M. O. Structural Basis of cis- and trans-Combretastatin Binding to Tubulin. *Chem* **2**, 102–113 (2017).

153. Zhou, P. *et al.* Potent Antitumor Activities and Structure Basis of the Chiral β-Lactam Bridged Analogue of Combretastatin A-4 Binding to Tubulin. *J. Med. Chem.* **59**, 10329–10334 (2016).

154. Cheng, J. *et al.* Structure of a benzylidene derivative of 9(10H)-anthracenone in complex with tubulin provides a rationale for drug design. *Biochem. Biophys. Res. Commun.* **495**, 185–188 (2018).

155. Zhao, W. *et al.* Structural Insights into the Inhibition of Tubulin by the Antitumor Agent 4β-(1,2,4-triazol-3-ylthio)-4-deoxypodophyllotoxin. *ACS Chem. Biol.* **12**, 746–752 (2017).

156. Field, J. J. *et al.* Zampanolide Binding to Tubulin Indicates Cross-Talk of Taxane Site with Colchicine and Nucleotide Sites. *J. Nat. Prod.* **81**, 494–505 (2018).

157. Jost, M. *et al.* Combined CRISPRi/a-Based Chemical Genetic Screens Reveal that Rigosertib Is a Microtubule-Destabilizing Agent. *Mol. Cell* **68**, 210-223.e6 (2017).

158. Niu, L. *et al.* Structure of 4'-demethylepipodophyllotoxin in complex with tubulin provides a rationale for drug design. *Biochem. Biophys. Res. Commun.* **493**, 718–722 (2017).

159. Arnst, K. E. *et al.* A Potent, Metabolically Stable Tubulin Inhibitor Targets the Colchicine Binding Site and Overcomes Taxane Resistance. *Cancer Res.* **78**, 265–277 (2018).

160. Dohle, W. *et al.* Quinazolinone-Based Anticancer Agents: Synthesis, Antiproliferative SAR, Antitubulin

Activity, and Tubulin Co-crystal Structure. *J. Med. Chem.* **61**, 1031–1044 (2018).

161. Zhou, P. *et al.* Design, synthesis, biological evaluation and cocrystal structures with tubulin of chiral β-lactam bridged combretastatin A-4 analogues as potent antitumor agents. *Eur. J. Med. Chem.* **144**, 817–842 (2018).

162. Yang, J. *et al.* The compound millepachine and its derivatives inhibit tubulin polymerization by irreversibly binding to the colchicine-binding site in β-tubulin. *J. Biol. Chem.* **293**, 9461–9472 (2018).

163. Yan, W. *et al.* SKLB060 Reversibly Binds to Colchicine Site of Tubulin and Possesses Efficacy in Multidrug-Resistant Cell Lines. *Cell. Physiol. Biochem.* **47**, 489–504 (2018).

164. Banerjee, S. *et al.* Heterocyclic-Fused Pyrimidines as Novel Tubulin Polymerization Inhibitors Targeting the Colchicine Binding Site: Structural Basis and Antitumor Efficacy. *J. Med. Chem.* **61**, 1704–1718 (2018).

165. Wang, Q. *et al.* Structural Modification of the 3,4,5-Trimethoxyphenyl Moiety in the Tubulin Inhibitor VERU-111 Leads to Improved Antiproliferative Activities. *J. Med. Chem.* **61**, 7877–7891 (2018).

166. Brindisi, M. *et al.* Structure-activity relationships, biological evaluation and structural studies of novel pyrrolonaphthoxazepines as antitumor agents. *Eur. J. Med. Chem.* **162**, 290–320 (2019).

167. Cury, N. M. *et al.* Structural Basis of Colchicine-Site targeting Acylhydrazones active against Multidrug-Resistant Acute Lymphoblastic Leukemia. *iScience* **21**, 95–109 (2019).

168. Naret, T. *et al.* 1,1-Diheterocyclic Ethylenes Derived from Quinaldine and Carbazole as New Tubulin-Polymerization Inhibitors: Synthesis, Metabolism, and Biological Evaluation. *J. Med. Chem.* **62**, 1902–1916 (2019).

169. Dohle, W. *et al.* Tetrahydroisoquinoline Sulfamates as Potent Microtubule Disruptors: Synthesis, Antiproliferative and Antitubulin Activity of Dichlorobenzyl-Based Derivatives, and a Tubulin Cocrystal Structure. *ACS omega* **4**, 755–764 (2019).

170. Zhang, Z. *et al.* Molecular mechanism of crolibulin in complex with tubulin provides a rationale for drug design. *Biochem. Biophys. Res. Commun.* **511**, 381–386 (2019).

171. Smedley, C. J. *et al.* Sustainable Syntheses of (-)-Jerantinines A & E and Structural Characterisation of the Jerantinine-Tubulin Complex at the Colchicine Binding Site. *Sci. Rep.* **8**, 10617 (2018).

172. Arnst, K. E. *et al.* Colchicine Binding Site Agent DJ95 Overcomes Drug Resistance and Exhibits Antitumor Efficacy. *Mol. Pharmacol.* **96**, 73–89 (2019).

173. Wang, Q. *et al.* Structure-Guided Design, Synthesis, and Biological Evaluation of (2-(1H-Indol-3-yl)-1H-imidazol-4-yl)(3,4,5-trimethoxyphenyl) Methanone (ABI-231) Analogues Targeting the Colchicine Binding Site in Tubulin. *J. Med. Chem.* **62**, 6734–6750 (2019).

174. Patterson, J. C. *et al.* VISAGE Reveals a Targetable Mitotic Spindle Vulnerability in Cancer Cells. *Cell Syst.* **9**, 74-92.e8 (2019).

175. Chen, H. *et al.* Structure-Activity Relationship Study of Novel 6-Aryl-2-benzoyl-pyridines as Tubulin Polymerization Inhibitors with Potent Antiproliferative Properties. *J. Med. Chem.* **63**, 827–846 (2020).

176. Arnst, K. E. *et al.* X-ray Crystal Structure Guided Discovery and Antitumor Efficacy of Dihydroquinoxalinone as Potent Tubulin Polymerization Inhibitors. *ACS Chem. Biol.* **14**, 2810–2821 (2019).

177. Li, Y. *et al.* Structural insights into the design of indole derivatives as tubulin polymerization inhibitors. *FEBS Lett.* **594**, 199–204 (2020).

178. Sharma, A. *et al.* Quinolin-6-Yloxyacetamides Are Microtubule Destabilizing Agents That Bind to the Colchicine Site of Tubulin. *Int. J. Mol. Sci.* **18**, 1336 (2017).

179. Ma, M. *et al.* Polymorphs, co-crystal structure and pharmacodynamics study of MBRI-001, a deuterium-substituted plinabulin derivative as a tubulin polymerization inhibitor. *Bioorg. Med. Chem.* **27**, 1836–1844 (2019).

180. Bueno, O. *et al.* High-affinity ligands of the colchicine domain in tubulin based on a structure-guided design. *Sci. Rep.* **8**, 4242 (2018).

181. Ning, N. *et al.* A Novel Microtubule Inhibitor Overcomes Multidrug Resistance in Tumors. *Cancer Res.* **78**, 5949–5957 (2018).

182. Niu, L. *et al.* Reversible binding of the anticancer drug KXO1 (tirbanibulin) to the colchicine-binding site of β-tubulin explains KXO1's low clinical toxicity. *J. Biol. Chem.* **294**, 18099–18108 (2019).

183. Zhongping, L. *et al.* The Structure of MT189-Tubulin Complex Provides Insights into Drug Design. *Lett. Drug Des. Discov.* **16**, 1069–1073 (2019).

184. Chen, J., Liu, T., Dong, X. & Hu, Y. Recent development and SAR analysis of colchicine binding site inhibitors. *Mini Rev. Med. Chem.* **9**, 1174–1190 (2009).

185. Gaukroger, K., Hadfield, J. A., Lawrence, N. J., Nolan, S. & McGown, A. T. Structural requirements for the interaction of combretastatins with tubulin: how important is the trimethoxy unit? *Org. Biomol. Chem.* **1**, 3033–3037 (2003).

186. Nguyen, T. L. *et al.* A common pharmacophore for a diverse set of colchicine site inhibitors using a structure-based approach. *J. Med. Chem.* **48**, 6107–6116 (2005).

187. Pettit, G. R., Cragg, G. M. & Singh, S. B. Antineoplastic agents, 122. Constituents of Combretum caffrum. *J. Nat. Prod.* **50**, 386–391 (1987).

188. Siemann, D. W., Chaplin, D. J. & Walicke, P. A. A review and update of the current status of the vasculature-disabling agent combretastatin-A4 phosphate (CA4P). *Expert Opin. Investig. Drugs* **18**,

189–197 (2009).

189. Delmonte, A. & Sessa, C. AVE8062: a new combretastatin derivative vascular disrupting agent. *Expert Opin. Investig. Drugs* **18**, 1541–1548 (2009).

190. Granata, R., Locati, L. D. & Licitra, L. Fosbretabulin for the treatment of anaplastic thyroid cancer. *Future Oncol.* **10**, 2015–2021 (2014).

191. Nishio, M. *et al.* Phase 1 study of ombrabulin in combination with docetaxel and cisplatin in Japanese patients with advanced solid tumors. *Jpn. J. Clin. Oncol.* **48**, 322–328 (2018).

192. Pettit, G. R. *et al.* Antineoplastic agents 393. Synthesis of the trans-isomer of combretastatin A-4 prodrug. *Anticancer. Drug Des.* **13**, 981–993 (1998).

193. Tron, G. C. *et al.* Medicinal Chemistry of Combretastatin A4: Present and Future Directions. *J. Med. Chem.* **49**, 3033–3044 (2006).

194. Borowiak, M. *et al.* Photoswitchable Inhibitors of Microtubule Dynamics Optically Control Mitosis and Cell Death. *Cell* **162**, 403–411 (2015).

195. Aprile, S., Del Grosso, E., Tron, G. C. & Grosa, G. In vitro metabolism study of combretastatin A-4 in rat and human liver microsomes. *Drug Metab. Dispos.* **35**, 2252–2261 (2007).

196. Malebari, A. M. *et al.* β-Lactam analogues of combretastatin A-4 prevent metabolic inactivation by glucuronidation in chemoresistant HT-29 colon cancer cells. *Eur. J. Med. Chem.* **130**, 261–285 (2017).

197. Chen, X. *et al.* Recent Developments on Phenstatins as Potent Antimitotic Agents. *Curr. Med. Chem.* **25**, 2329–2352 (2018).

198. Alvarez, R. *et al.* Isocombretastatins A: 1,1-diarylethenes as potent inhibitors of tubulin polymerization and cytotoxic compounds. *Bioorg. Med. Chem.* **17**, 6422–6431 (2009).

199. Hamze, A., Alami, M. & Provot, O. Developments of isoCombretastatin A-4 derivatives as highly cytotoxic agents. *Eur. J. Med. Chem.* **190**, 112110 (2020).

200. Chamberlain, M. C. *et al.* A phase 2 trial of verubulin for recurrent glioblastoma: a prospective study by the Brain Tumor Investigational Consortium (BTIC). *J. Neurooncol.* **118**, 335–343 (2014).

201. Brachmann, S. M. *et al.* Characterization of the mechanism of action of the pan class I PI3K inhibitor NVP-BKM120 across a broad range of concentrations. *Mol. Cancer Ther.* **11**, 1747–1757 (2012).

202. Campone, M. *et al.* Buparlisib plus fulvestrant versus placebo plus fulvestrant for postmenopausal, hormone receptor-positive, human epidermal growth factor receptor 2-negative, advanced breast cancer: Overall survival results from BELLE-2. *Eur. J. Cancer* **103**, 147–154 (2018).

203. Gul, N. *et al.* The MTH1 inhibitor TH588 is a microtubule-modulating agent that eliminates cancer cells by activating the mitotic surveillance pathway. *Sci. Rep.* **9**, 14667 (2019).

204. Athuluri-Divakar, S. K. *et al.* A Small Molecule RAS-Mimetic Disrupts RAS Association with Effector Proteins to Block Signaling. *Cell* **165**, 643–655 (2016).

205. Shan, B. *et al.* Selective, covalent modification of beta-tubulin residue Cys-239 by T138067, an antitumor agent with in vivo efficacy against multidrug-resistant tumors. *Proc. Natl. Acad. Sci. U. S. A.* **96**, 5686–5691 (1999).

206. Singh, J., Petter, R. C., Baillie, T. A. & Whitty, A. The resurgence of covalent drugs. *Nat. Rev. Drug Discov.* **10**, 307–317 (2011).

207. Arai, T. Inhibition of microtubule assembly in vitro by TN-16, a synthetic antitumor drug. *FEBS Lett.* **155**, 273–276 (1983).

208. Yoshino, H. *et al.* Novel sulfonamides as potential, systemically active antitumor agents. *J. Med. Chem.* **35**, 2496–2497 (1992).

209. Yoshimatsu, K., Yamaguchi, A., Yoshino, H., Koyanagi, N. & Kitoh, K. Mechanism of action of E7010, an orally active sulfonamide antitumor agent: inhibition of mitosis by binding to the colchicine site of tubulin. *Cancer Res.* **57**, 3208–3213 (1997).

210. Gupta, A. K. *et al.* Process for the preparation of cell proliferation inhibitors. (2004).

211. Wang, W. *et al.* MCL-1 degradation mediated by JNK activation via MEKK1/TAK1-MKK4 contributes to anticancer activity of new tubulin inhibitor MT189. *Mol. Cancer Ther.* **13**, 1480–1491 (2014).

212. de Almagro, M. C. & Vucic, D. Necroptosis: Pathway diversity and characteristics. *Semin. Cell Dev. Biol.* **39**, 56–62 (2015).

213. Galluzzi, L. *et al.* Cell death modalities: classification and pathophysiological implications. *Cell Death Differ.* **14**, 1237–1243 (2007).

214. Green, D. R. & Llambi, F. Cell Death Signaling. *Cold Spring Harb. Perspect. Biol.* **7**, (2015).

215. Chen, Q., Kang, J. & Fu, C. The independence of and associations among apoptosis, autophagy, and necrosis. *Signal Transduct. Target. Ther.* **3**, 18 (2018).

216. Kerr, J. F., Wyllie, A. H. & Currie, A. R. Apoptosis: a basic biological phenomenon with wide-ranging implications in tissue kinetics. *Br. J. Cancer* **26**, 239–257 (1972).

217. Duque-Parra, J. E. Note on the origin and history of the term 'apoptosis'. *Anat. Rec. B. New Anat.* **283**, 2–4 (2005).

218. Nagata, S. Apoptosis and Clearance of Apoptotic Cells. *Annu. Rev. Immunol.* **36**, 489–517 (2018).

219. Bock, F. J. & Tait, S. W. G. Mitochondria as multifaceted regulators of cell death. *Nat. Rev. Mol. Cell Biol.* **21**, 85–100 (2020).

220. Bolívar, B. E., Vogel, T. P. & Bouchier-Hayes, L. Inflammatory caspase regulation: maintaining balance between inflammation and cell death in health and disease. *FEBS J.* **286**, 2628–2644 (2019).

221. Janssens, S. & Tinel, A. The PIDDosome, DNA-damage-induced apoptosis and beyond. *Cell Death Differ.* **19**, 13–20 (2012).

222. Häcker, G. The morphology of apoptosis. *Cell Tissue Res.* **301**, 5–17 (2000).

223. Taylor, R. C., Cullen, S. P. & Martin, S. J. Apoptosis: controlled demolition at the cellular level. *Nat. Rev. Mol. Cell Biol.* **9**, 231–241 (2008).

224. Kasibhatla, S. *et al.* Analysis of DNA fragmentation using agarose gel electrophoresis. *CSH Protoc.* **2006**, pdb.prot4429 (2006).

225. deCathelineau, A. M. & Henson, P. M. The final step in programmed cell death: phagocytes carry apoptotic cells to the grave. *Essays Biochem.* **39**, 105–117 (2003).

226. Lauber, K. *et al.* Apoptotic cells induce migration of phagocytes via caspase-3-mediated release of a lipid attraction signal. *Cell* **113**, 717–730 (2003).

227. Vermes, I., Haanen, C., Steffens-Nakken, H. & Reutelingsperger, C. A novel assay for apoptosis. Flow cytometric detection of phosphatidylserine expression on early apoptotic cells using fluorescein labelled Annexin V. *J. Immunol. Methods* **184**, 39–51 (1995).

228. Lamkanfi, M., Declercq, W., Kalai, M., Saelens, X. & Vandenabeele, P. Alice in caspase land. A phylogenetic analysis of caspases from worm to man. *Cell Death Differ.* **9**, 358–361 (2002).

229. Pop, C. & Salvesen, G. S. Human caspases: activation, specificity, and regulation. *J. Biol. Chem.* **284**, 21777–21781 (2009).

230. Fuentes-Prior, P. & Salvesen, G. S. The protein structures that shape caspase activity, specificity, activation and inhibition. *Biochem. J.* **384**, 201–232 (2004).

231. Van Opdenbosch, N. & Lamkanfi, M. Caspases in Cell Death, Inflammation, and Disease. *Immunity* **50**, 1352–1364 (2019).

232. Yuan, S. & Akey, C. W. Apoptosome structure, assembly, and procaspase activation. *Structure* **21**, 501–515 (2013).

233. Boatright, K. M. *et al.* A unified model for apical caspase activation. *Mol. Cell* **11**, 529–541 (2003).

234. Ramirez, M. L. G. & Salvesen, G. S. A primer on caspase mechanisms. *Semin. Cell Dev. Biol.* **82**, 79–85 (2018).

235. Kroemer, G., Galluzzi, L. & Brenner, C. Mitochondrial membrane permeabilization in cell death. *Physiol. Rev.* **87**, 99–163 (2007).

236. Kale, J., Osterlund, E. J. & Andrews, D. W. BCL-2 family proteins: changing partners in the dance towards death. *Cell Death Differ.* **25**, 65–80 (2018).

237. Singh, R., Letai, A. & Sarosiek, K. Regulation of apoptosis in health and disease: the balancing act of BCL-2 family proteins. *Nat. Rev. Mol. Cell Biol.* **20**, 175–193 (2019).

238. Czabotar, P. E., Lessene, G., Strasser, A. & Adams, J. M. Control of apoptosis by the BCL-2 protein family: implications for physiology and therapy. *Nat. Rev. Mol. Cell Biol.* **15**, 49–63 (2014).

239. Yang, E. *et al.* Bad, a heterodimeric partner for Bcl-XL and Bcl-2, displaces Bax and promotes cell death. *Cell* **80**, 285–291 (1995).

240. Tait, S. W. G. & Green, D. R. Mitochondria and cell death: outer membrane permeabilization and beyond. *Nat. Rev. Mol. Cell Biol.* **11**, 621–632 (2010).

241. Czabotar, P. E. *et al.* Bax Crystal Structures Reveal How BH3 Domains Activate Bax and Nucleate Its Oligomerization to Induce Apoptosis. *Cell* **152**, 519–531 (2013).

242. Letai, A. *et al.* Distinct BH3 domains either sensitize or activate mitochondrial apoptosis, serving as prototype cancer therapeutics. *Cancer Cell* **2**, 183–192 (2002).

243. Jiang, X. & Wang, X. Cytochrome C-mediated apoptosis. *Annu. Rev. Biochem.* **73**, 87–106 (2004).

244. Muñoz-Pinedo, C. *et al.* Different mitochondrial intermembrane space proteins are released during apoptosis in a manner that is coordinately initiated but can vary in duration. *Proc. Natl. Acad. Sci.* **103**, 11573–11578 (2006).

245. Xiong, S., Mu, T., Wang, G. & Jiang, X. Mitochondria-mediated apoptosis in mammals. *Protein Cell* **5**, 737–749 (2014).

246. Kim, H.-E., Du, F., Fang, M. & Wang, X. Formation of apoptosome is initiated by cytochrome c-induced dATP hydrolysis and subsequent nucleotide exchange on Apaf-1. *Proc. Natl. Acad. Sci. U. S. A.* **102**, 17545–17550 (2005).

247. Dorstyn, L., Akey, C. W. & Kumar, S. New insights into apoptosome structure and function. *Cell Death Differ.* **25**, 1194–1208 (2018).

248. Renatus, M., Stennicke, H. R., Scott, F. L., Liddington, R. C. & Salvesen, G. S. Dimer formation drives the activation of the cell death protease caspase 9. *Proc. Natl. Acad. Sci. U. S. A.* **98**, 14250–14255 (2001).

249. Acehan, D. *et al.* Three-dimensional structure of the apoptosome: implications for assembly, procaspase-9 binding, and activation. *Mol. Cell* **9**, 423–432 (2002).

250. Wu, C.-C. *et al.* The Apaf-1 apoptosome induces formation of caspase-9 homo- and heterodimers with distinct activities. *Nat. Commun.* **7**, 13565 (2016).

251. Malladi, S., Challa-Malladi, M., Fearnhead, H. O. & Bratton, S. B. The Apaf-1*procaspase-9 apoptosome complex functions as a proteolytic-based molecular timer. *EMBO J.* **28**, 1916–1925 (2009).

252. Bratton, S. B. *et al.* Recruitment, activation and retention of caspases-9 and -3 by Apaf-1 apoptosome and associated XIAP complexes. *EMBO J.* **20**, 998–1009 (2001).

253. Segawa, K. *et al.* Caspase-mediated cleavage of phospholipid flippase for apoptotic phosphatidylserine exposure. *Science* **344**, 1164–1168 (2014).

254. Suzuki, J., Denning, D. P., Imanishi, E., Horvitz, H. R. & Nagata, S. Xk-Related Protein 8 and CED-8 Promote Phosphatidylserine Exposure in Apoptotic Cells. *Science (80-.).* **341**, 403 LP – 406 (2013).

255. Nagata, S., Sakuragi, T. & Segawa, K. Flippase and scramblase for phosphatidylserine exposure. *Curr. Opin. Immunol.* **62**, 31–38 (2019).

256. Wiens, G. D. & Glenney, G. W. Origin and evolution of TNF and TNF receptor superfamilies. *Dev. Comp. Immunol.* (2011). doi:10.1016/j.dci.2011.03.031

257. Dickens, L. S., Powley, I. R., Hughes, M. A. & MacFarlane, M. The 'complexities' of life and death: death receptor signalling platforms. *Exp. Cell Res.* **318**, 1269–1277 (2012).

258. Guicciardi, M. E. & Gores, G. J. Life and death by death receptors. *FASEB J. Off. Publ. Fed. Am. Soc. Exp. Biol.* **23**, 1625–1637 (2009).

259. Bodmer, J. L., Schneider, P. & Tschopp, J. The molecular architecture of the TNF superfamily. *Trends in Biochemical Sciences* (2002). doi:10.1016/S0968-0004(01)01995-8

260. Schneider, P. *et al.* Conversion of membrane-bound Fas(CD95) ligand to its soluble form is associated with downregulation of its proapoptotic activity and loss of liver toxicity. *J. Exp. Med.* **187**, 1205–1213 (1998).

261. Lee, E. W., Seo, J., Jeong, M., Lee, S. & Song, J. The roles of FADD in extrinsic apoptosis and necroptosis. *BMB Rep.* **45**, 496–508 (2012).

262. Peter, M. E. & Krammer, P. H. The CD95(APO-1/Fas) DISC and beyond. *Cell Death Differ.* **10**, 26–35 (2003).

263. Shi, Y. Caspase activation: revisiting the induced proximity model. *Cell* **117**, 855–858 (2004).

264. Yu, J. W. & Shi, Y. FLIP and the death effector domain family. *Oncogene* **27**, 6216–6227 (2008).

265. Lavrik, I. N. *et al.* CD95 stimulation results in the formation of a novel death effector domain protein-containing complex. *J. Biol. Chem.* **283**, 26401–26408 (2008).

266. Varfolomeev, E. *et al.* Molecular determinants of kinase pathway activation by Apo2 ligand/tumor necrosis factor-related apoptosis-inducing ligand. *J. Biol. Chem.* **280**, 40599–40608 (2005).

267. Lee, K.-H. *et al.* The role of receptor internalization in CD95 signaling. *EMBO J.* **25**, 1009–1023 (2006).

268. Kohlhaas, S. L., Craxton, A., Sun, X.-M., Pinkoski, M. J. & Cohen, G. M. Receptor-mediated endocytosis is not required for tumor necrosis factor-related apoptosis-inducing ligand (TRAIL)-induced apoptosis. *J. Biol. Chem.* **282**, 12831–12841 (2007).

269. Brenner, D., Blaser, H. & Mak, T. W. Regulation of tumour necrosis factor signalling: live or let die. *Nat. Rev. Immunol.* **15**, 362–374 (2015).

270. Morton, P. E. *et al.* TNFR1 membrane reorganization promotes distinct modes of TNFα signaling. *Sci. Signal.* **12**, eaaw2418 (2019).

271. Micheau, O. & Tschopp, J. Induction of TNF receptor I-mediated apoptosis via two sequential signaling complexes. *Cell* **114**, 181–190 (2003).

272. Harper, N., Hughes, M., MacFarlane, M. & Cohen, G. M. Fas-associated death domain protein and caspase-8 are not recruited to the tumor necrosis factor receptor 1 signaling complex during tumor necrosis factor-induced apoptosis. *J. Biol. Chem.* **278**, 25534–25541 (2003).

273. Csomos, R. A., Brady, G. F. & Duckett, C. S. Enhanced cytoprotective effects of the inhibitor of apoptosis protein cellular IAP1 through stabilization with TRAF2. *J. Biol. Chem.* **284**, 20531–20539 (2009).

274. Haas, T. L. *et al.* Recruitment of the linear ubiquitin chain assembly complex stabilizes the TNF-R1 signaling complex and is required for TNF-mediated gene induction. *Mol. Cell* **36**, 831–844 (2009).

275. Varfolomeev, E. *et al.* c-IAP1 and c-IAP2 are critical mediators of tumor necrosis factor alpha (TNFalpha)-induced NF-kappaB activation. *J. Biol. Chem.* **283**, 24295–24299 (2008).

276. Bertrand, M. J. M. *et al.* cIAP1 and cIAP2 facilitate cancer cell survival by functioning as E3 ligases that promote RIP1 ubiquitination. *Mol. Cell* **30**, 689–700 (2008).

277. Wajant, H., Pfizenmaier, K. & Scheurich, P. Tumor necrosis factor signaling. *Cell Death Differ.* **10**, 45–65 (2003).

278. Ea, C. K., Deng, L., Xia, Z. P., Pineda, G. & Chen, Z. J. Activation of IKK by TNFα Requires Site-Specific Ubiquitination of RIP1 and Polyubiquitin Binding by NEMO. *Mol. Cell* (2006). doi:10.1016/j.molcel.2006.03.026

279. Dempsey, P. W., Doyle, S. E., He, J. Q. & Cheng, G. The signaling adaptors and pathways activated by TNF superfamily. *Cytokine Growth Factor Rev.* **14**, 193–209 (2003).

280. Mahoney, D. J. *et al.* Both cIAP1 and cIAP2 regulate TNFα-mediated NF-κB activation. *Proc. Natl. Acad. Sci.* **105**, 11778 LP – 11783 (2008).

281. Schneider-Brachert, W. *et al.* Compartmentalization of TNF receptor 1 signaling: internalized TNF receptosomes as death signaling vesicles. *Immunity* **21**, 415–428 (2004).

282. Cabal-Hierro, L. & Lazo, P. S. Signal transduction by tumor necrosis factor receptors. *Cell. Signal.* **24**, 1297–1305 (2012).

283. Li, H., Kobayashi, M., Blonska, M., You, Y. & Lin, X. Ubiquitination of RIP is required for tumor necrosis factor alpha-induced NF-kappaB activation. *J. Biol. Chem.* **281**, 13636–13643 (2006).

284. O'Donnell, M. A., Legarda-Addison, D., Skountzos, P.,

Yeh, W. C. & Ting, A. T. Ubiquitination of RIP1 regulates an NF-kappaB-independent cell-death switch in TNF signaling. *Curr. Biol.* **17**, 418–424 (2007).

285. Declercq, W., Vanden Berghe, T. & Vandenabeele, P. RIP kinases at the crossroads of cell death and survival. *Cell* **138**, 229–232 (2009).

286. Hitomi, J. *et al.* Identification of a molecular signaling network that regulates a cellular necrotic cell death pathway. *Cell* **135**, 1311–1323 (2008).

287. Barnhart, B. C., Alappat, E. C. & Peter, M. E. The CD95 type I/type II model. *Semin. Immunol.* **15**, 185–193 (2003).

288. Li, H., Zhu, H., Xu, C. J. & Yuan, J. Cleavage of BID by caspase 8 mediates the mitochondrial damage in the Fas pathway of apoptosis. *Cell* **94**, 491–501 (1998).

289. Milhas, D. *et al.* Caspase-10 triggers Bid cleavage and caspase cascade activation in FasL-induced apoptosis. *J. Biol. Chem.* **280**, 19836–19842 (2005).

290. Korsmeyer, S. J. *et al.* Pro-apoptotic cascade activates BID, which oligomerizes BAK or BAX into pores that result in the release of cytochrome c. *Cell Death Differ.* **7**, 1166–1173 (2000).

291. Scaffidi, C. *et al.* Two CD95 (APO-1/Fas) signaling pathways. *EMBO J.* **17**, 1675–1687 (1998).

292. Lalaoui, N. & Vaux, D. L. Recent advances in understanding inhibitor of apoptosis proteins. *F1000Research* **7**, F1000 Faculty Rev-1889 (2018).

293. Huang, Y. *et al.* Structural basis of caspase inhibition by XIAP: differential roles of the linker versus the BIR domain. *Cell* **104**, 781–790 (2001).

294. Deveraux, Q. L. & Reed, J. C. IAP family proteins--suppressors of apoptosis. *Genes Dev.* **13**, 239–252 (1999).

295. MacFarlane, M., Merrison, W., Bratton, S. B. & Cohen, G. M. Proteasome-mediated degradation of Smac during apoptosis: XIAP promotes Smac ubiquitination in vitro. *J. Biol. Chem.* **277**, 36611–36616 (2002).

296. Eckelman, B. P., Salvesen, G. S. & Scott, F. L. Human inhibitor of apoptosis proteins: why XIAP is the black sheep of the family. *EMBO Rep.* **7**, 988–994 (2006).

297. Shiozaki, E. N. *et al.* Mechanism of XIAP-mediated inhibition of caspase-9. *Mol. Cell* **11**, 519–527 (2003).

298. Berthelet, J. & Dubrez, L. Regulation of Apoptosis by Inhibitors of Apoptosis (IAPs). *Cells* **2**, 163–187 (2013).

299. Du, C., Fang, M., Li, Y., Li, L. & Wang, X. Smac, a Mitochondrial Protein that Promotes Cytochrome c–Dependent Caspase Activation by Eliminating IAP Inhibition. *Cell* **102**, 33–42 (2000).

300. van Loo, G. *et al.* The serine protease Omi/HtrA2 is released from mitochondria during apoptosis. Omi interacts with caspase-inhibitor XIAP and induces enhanced caspase activity. *Cell Death Differ.* **9**, 20–26 (2002).

301. Chai, J. *et al.* Structural and biochemical basis of apoptotic activation by Smac/DIABLO . *Nature* **406**, 855–862 (2000).

302. Yang, Q.-H., Church-Hajduk, R., Ren, J., Newton, M. L. & Du, C. Omi/HtrA2 catalytic cleavage of inhibitor of apoptosis (IAP) irreversibly inactivates IAPs and facilitates caspase activity in apoptosis. *Genes Dev.* **17**, 1487–1496 (2003).

303. Edison, N. *et al.* The IAP-antagonist ARTS initiates caspase activation upstream of cytochrome C and SMAC/Diablo. *Cell Death Differ.* **19**, 356–368 (2012).

304. Mamriev, D. & Larisch, S. Another one bites the dust; ARTS enables degradation of Bcl-2 by XIAP. *Mol. Cell. Oncol.* **5**, e1441630 (2018).

305. Crawford, E. D. & Wells, J. A. Caspase substrates and cellular remodeling. *Annu. Rev. Biochem.* **80**, 1055–1087 (2011).

306. Brentnall, M., Rodriguez-Menocal, L., De Guevara, R. L., Cepero, E. & Boise, L. H. Caspase-9, caspase-3 and caspase-7 have distinct roles during intrinsic apoptosis. *BMC Cell Biol.* **14**, 32 (2013).

307. Coleman, M. L. *et al.* Membrane blebbing during apoptosis results from caspase-mediated activation of ROCK I. *Nat. Cell Biol.* **3**, 339–345 (2001).

308. Kothakota, S. *et al.* Caspase-3-generated fragment of gelsolin: effector of morphological change in apoptosis. *Science* **278**, 294–298 (1997).

309. Wen, L. P. *et al.* Cleavage of focal adhesion kinase by caspases during apoptosis. *J. Biol. Chem.* **272**, 26056–26061 (1997).

310. Ricci, J.-E. *et al.* Disruption of mitochondrial function during apoptosis is mediated by caspase cleavage of the p75 subunit of complex I of the electron transport chain. *Cell* **117**, 773–786 (2004).

311. Cheung, W. L. *et al.* Apoptotic phosphorylation of histone H2B is mediated by mammalian sterile twenty kinase. *Cell* **113**, 507–517 (2003).

312. Wen, W. *et al.* MST1 promotes apoptosis through phosphorylation of histone H2AX. *J. Biol. Chem.* **285**, 39108–39116 (2010).

313. Enari, M. *et al.* A caspase-activated DNase that degrades DNA during apoptosis, and its inhibitor ICAD. *Nature* **391**, 43–50 (1998).

314. Joza, N. *et al.* Essential role of the mitochondrial apoptosis-inducing factor in programmed cell death. *Nature* **410**, 549–554 (2001).

315. Li, L. Y., Luo, X. & Wang, X. Endonuclease G is an apoptotic DNase when released from mitochondria. *Nature* **412**, 95–99 (2001).

316. Galluzzi, L. *et al.* Molecular definitions of autophagy and related processes. *EMBO J.* **36**, 1811–1836 (2017).

317. Mizushima, N. & Komatsu, M. Autophagy: renovation of cells and tissues. *Cell* **147**, 728–741 (2011).

318. Rabinowitz, J. D. & White, E. Autophagy and metabolism. *Science* **330**, 1344–1348 (2010).

319. Sahu, R. *et al.* Microautophagy of cytosolic proteins by late endosomes. *Dev. Cell* **20**, 131–139 (2011).

320. Kaushik, S. & Cuervo, A. M. Chaperone-mediated autophagy: a unique way to enter the lysosome world. *Trends Cell Biol.* **22**, 407–417 (2012).

321. Khaminets, A., Behl, C. & Dikic, I. Ubiquitin-Dependent And Independent Signals In Selective Autophagy. *Trends Cell Biol.* **26**, 6–16 (2016).

322. Boya, P., Esteban-Martínez, L., Serrano-Puebla, A., Gómez-Sintes, R. & Villarejo-Zori, B. Autophagy in the eye: Development, degeneration, and aging. *Progress in Retinal and Eye Research* (2016). doi:10.1016/j.preteyeres.2016.08.001

323. Mizushima, N., Yoshimori, T. & Ohsumi, Y. The role of Atg proteins in autophagosome formation. *Annu. Rev. Cell Dev. Biol.* **27**, 107–132 (2011).

324. Suzuki, K. *et al.* The pre-autophagosomal structure organized by concerted functions of APG genes is essential for autophagosome formation. *EMBO J.* **20**, 5971–5981 (2001).

325. Axe, E. L. *et al.* Autophagosome formation from membrane compartments enriched in phosphatidylinositol 3-phosphate and dynamically connected to the endoplasmic reticulum. *J. Cell Biol.* **182**, 685–701 (2008).

326. Rubinsztein, D. C., Shpilka, T. & Elazar, Z. Mechanisms of autophagosome biogenesis. *Curr. Biol.* **22**, R29-34 (2012).

327. Yang, Z. & Klionsky, D. J. Mammalian autophagy: core molecular machinery and signaling regulation. *Curr. Opin. Cell Biol.* **22**, 124–131 (2010).

328. Alers, S., Löffler, A. S., Wesselborg, S. & Stork, B. Role of AMPK-mTOR-Ulk1/2 in the regulation of autophagy: cross talk, shortcuts, and feedbacks. *Mol. Cell. Biol.* **32**, 2–11 (2012).

329. Ganley, I. G. *et al.* ULK1.ATG13.FIP200 complex mediates mTOR signaling and is essential for autophagy. *J. Biol. Chem.* **284**, 12297–12305 (2009).

330. Bento, C. F. *et al.* Mammalian Autophagy: How Does It Work? *Annu. Rev. Biochem.* **85**, 685–713 (2016).

331. Proikas-Cezanne, T., Takacs, Z., Donnes, P. & Kohlbacher, O. WIPI proteins: essential PtdIns3P effectors at the nascent autophagosome. *J. Cell Sci.* **128**, 207–217 (2015).

332. Li, X., He, S. & Ma, B. Autophagy and autophagy-related proteins in cancer. *Mol. Cancer* **19**, 12 (2020).

333. Hanada, T. *et al.* The Atg12-Atg5 conjugate has a novel E3-like activity for protein lipidation in autophagy. *J. Biol. Chem.* **282**, 37298–37302 (2007).

334. Stolz, A., Ernst, A. & Dikic, I. Cargo recognition and trafficking in selective autophagy. *Nat. Cell Biol.* **16**, 495–501 (2014).

335. Johansen, T. & Lamark, T. Selective autophagy mediated by autophagic adapter proteins. *Autophagy* **7**, 279–296 (2011).

336. Noda, N. N. & Inagaki, F. Mechanisms of Autophagy. *Annu. Rev. Biophys.* **44**, 101–122 (2015).

337. Wong, P.-M., Puente, C., Ganley, I. G. & Jiang, X. The ULK1 complex: sensing nutrient signals for autophagy activation. *Autophagy* **9**, 124–137 (2013).

338. Ryter, S. W., Mizumura, K. & Choi, A. M. K. The Impact of Autophagy on Cell Death Modalities. *Int. J. Cell Biol.* **2014**, 502676 (2014).

339. Mukhopadhyay, S., Panda, P. K., Sinha, N., Das, D. N. & Bhutia, S. K. Autophagy and apoptosis: where do they meet? *Apoptosis* **19**, 555–566 (2014).

340. Marino, G., Niso-Santano, M., Baehrecke, E. H. & Kroemer, G. Self-consumption: the interplay of autophagy and apoptosis. *Nat. Rev. Mol. Cell Biol.* **15**, 81–94 (2014).

341. Luo, S. & Rubinsztein, D. C. Apoptosis blocks Beclin 1-dependent autophagosome synthesis: an effect rescued by Bcl-xL. *Cell Death Differ.* **17**, 268–277 (2010).

342. Levine, B., Sinha, S. & Kroemer, G. Bcl-2 family members: dual regulators of apoptosis and autophagy. *Autophagy* **4**, 600–606 (2008).

343. Lee, J.-S. *et al.* FLIP-mediated autophagy regulation in cell death control. *Nat. Cell Biol.* **11**, 1355–1362 (2009).

344. He, W. *et al.* A JNK-mediated autophagy pathway that triggers c-IAP degradation and necroptosis for anticancer chemotherapy. *Oncogene* **33**, 3004–3013 (2014).

345. Denton, D., Xu, T. & Kumar, S. Autophagy as a pro-death pathway. *Immunol. Cell Biol.* **93**, 35–42 (2015).

346. Anding, A. L. & Baehrecke, E. H. Autophagy in Cell Life and Cell Death. *Curr. Top. Dev. Biol.* **114**, 67–91 (2015).

347. Galluzzi, L. *et al.* Molecular mechanisms of cell death: recommendations of the Nomenclature Committee on Cell Death 2018. *Cell Death Differ.* **25**, 486–541 (2018).

348. Shen, H.-M. & Codogno, P. Autophagic cell death: Loch Ness monster or endangered species? *Autophagy* **7**, 457–465 (2011).

349. Gamrekelashvili, J., Greten, T. F. & Korangy, F. Immunogenicity of necrotic cell death. *Cell. Mol. Life Sci.* **72**, 273–283 (2015).

350. Holler, N. *et al.* Fas triggers an alternative, caspase-8–independent cell death pathway using the kinase RIP as effector molecule. *Nat. Immunol.* **1**, 489–495 (2000).

351. Orozco, S. & Oberst, A. RIPK3 in cell death and inflammation: the good, the bad, and the ugly. *Immunol. Rev.* **277**, 102–112 (2017).

352. Vercammen, D. *et al.* Inhibition of caspases increases the sensitivity of L929 cells to necrosis mediated by tumor necrosis factor. *J. Exp. Med.* **187**, 1477–1485 (1998).

353. Liu, Y. *et al.* RIP1/RIP3-regulated necroptosis as a target for multifaceted disease therapy (Review). *Int. J. Mol. Med.* **44**, 771–786 (2019).

354. Jun-Long, H. *et al.* Necroptosis Signaling Pathways in Stroke: From Mechanisms to Therapies. *Curr. Neuropharmacol.* **16**, 1327–1339 (2018).

355. Choi, M. E., Price, D. R., Ryter, S. W. & Choi, A. M. K. Necroptosis: a crucial pathogenic mediator of human disease. *JCI insight* **4**, (2019).

356. He, S. *et al.* Receptor interacting protein kinase-3 determines cellular necrotic response to TNF-alpha. *Cell* **137**, 1100–1111 (2009).

357. Vince, J. E. *et al.* IAP antagonists target cIAP1 to induce TNFalpha-dependent apoptosis. *Cell* **131**, 682–693 (2007).

358. Vandenabeele, P., Declercq, W., Van Herreweghe, F. & Vanden Berghe, T. The role of the kinases RIP1 and RIP3 in TNF-induced necrosis. *Sci. Signal.* **3**, re4 (2010).

359. Oberst, A. *et al.* Catalytic activity of the caspase-8–FLIPL complex inhibits RIPK3-dependent necrosis. *Nature* **471**, 363–367 (2011).

360. Cho, Y. S. *et al.* Phosphorylation-driven assembly of the RIP1-RIP3 complex regulates programmed necrosis and virus-induced inflammation. *Cell* **137**, 1112–1123 (2009).

361. Murphy, J. M. *et al.* The pseudokinase MLKL mediates necroptosis via a molecular switch mechanism. *Immunity* **39**, 443–453 (2013).

362. Sun, L. *et al.* Mixed lineage kinase domain-like protein mediates necrosis signaling downstream of RIP3 kinase. *Cell* **148**, 213–227 (2012).

363. Weinlich, R., Oberst, A., Beere, H. M. & Green, D. R. Necroptosis in development, inflammation and disease. *Nat. Rev. Mol. Cell Biol.* **18**, 127–136 (2017).

364. Cai, Z. *et al.* Plasma membrane translocation of trimerized MLKL protein is required for TNF-induced necroptosis. *Nat. Cell Biol.* **16**, 55–65 (2014).

365. Chen, X. *et al.* Translocation of mixed lineage kinase domain-like protein to plasma membrane leads to necrotic cell death. *Cell Res.* **24**, 105–121 (2014).

366. Wang, H. *et al.* Mixed lineage kinase domain-like protein MLKL causes necrotic membrane disruption upon phosphorylation by RIP3. *Mol. Cell* **54**, 133–146 (2014).

367. Dondelinger, Y. *et al.* MLKL compromises plasma membrane integrity by binding to phosphatidylinositol phosphates. *Cell Rep.* **7**, 971–981 (2014).

368. Vandenabeele, P., Galluzzi, L., Vanden Berghe, T. & Kroemer, G. Molecular mechanisms of necroptosis: an ordered cellular explosion. *Nat. Rev. Mol. Cell Biol.* **11**, 700–714 (2010).

369. Yang, Z. *et al.* RIP3 targets pyruvate dehydrogenase complex to increase aerobic respiration in TNF-induced necroptosis. *Nat. Cell Biol.* **20**, 186–197 (2018).

370. Zhang, D.-W. *et al.* RIP3, an energy metabolism regulator that switches TNF-induced cell death from apoptosis to necrosis. *Science* **325**, 332–336 (2009).

371. Zhang, Y. *et al.* RIP1 autophosphorylation is promoted by mitochondrial ROS and is essential for RIP3 recruitment into necrosome. *Nat. Commun.* **8**, 14329 (2017).

372. Yabal, M. *et al.* XIAP restricts TNF- and RIP3-dependent cell death and inflammasome activation. *Cell Rep.* **7**, 1796–1808 (2014).

373. Scherz-Shouval, R. & Elazar, Z. ROS, mitochondria and the regulation of autophagy. *Trends Cell Biol.* **17**, 422–427 (2007).

374. Pasparakis, M. & Vandenabeele, P. Necroptosis and its role in inflammation. *Nature* **517**, 311–320 (2015).

375. Kaczmarek, A., Vandenabeele, P. & Krysko, D. V. Necroptosis: the release of damage-associated molecular patterns and its physiological relevance. *Immunity* **38**, 209–223 (2013).

376. Dhuriya, Y. K. & Sharma, D. Necroptosis: a regulated inflammatory mode of cell death. *J. Neuroinflammation* **15**, 199 (2018).

377. Qiu, X., Zhang, Y. & Han, J. RIP3 is an upregulator of aerobic metabolism and the enhanced respiration by necrosomal RIP3 feeds back on necrosome to promote necroptosis. *Cell Death Differ.* (2018). doi:10.1038/s41418-018-0075-x

378. Chabner, B. *et al.* Antineoplastic agents. in *Goodman and Gilman's The Pharmacological Basis for Therapeutics* 1315–1403 (LL Brunton, New York: McGraw-Hill, 2006).

379. Mitchison, T. J. The proliferation rate paradox in antimitotic chemotherapy. *Mol. Biol. Cell* **23**, 1–6 (2012).

380. Komlodi-Pasztor, E., Sackett, D., Wilkerson, J. & Fojo, T. Mitosis is not a key target of microtubule agents in patient tumors. *Nat. Rev. Clin. Oncol.* **8**, 244–250 (2011).

381. Fürst, R. & Vollmar, A. M. A new perspective on old drugs: non-mitotic actions of tubulin-binding drugs play a major role in cancer treatment. *Pharmazie* **68**, 478–483 (2013).

382. Lunt, S. J. *et al.* Vascular effects dominate solid tumor response to treatment with combretastatin A-4-phosphate. *Int. J. cancer* **129**, 1979–1989 (2011).

383. Chaplin, D. J. & Hill, S. A. The development of combretastatin A4 phosphate as a vascular targeting agent. *Int. J. Radiat. Oncol. • Biol. • Phys.* **54**, 1491–1496 (2002).

384. Otani, M. *et al.* TZT-1027, an antimicrotubule agent, attacks tumor vasculature and induces tumor cell death. *Jpn. J. Cancer Res.* **91**, 837–844 (2000).

385. Tozer, G. M., Kanthou, C. & Baguley, B. C. Disrupting tumour blood vessels. *Nat. Rev. Cancer* **5**, 423–435 (2005).

386. Kanthou, C. & Tozer, G. M. Tumour targeting by microtubule-depolymerizing vascular disrupting agents. *Expert Opin. Ther. Targets* **11**, 1443–1457 (2007).

387. Pasquier, E., Honoré, S. & Braguer, D. Microtubule-targeting agents in angiogenesis: where do we stand? *Drug Resist. Updat.* **9**, 74–86 (2006).

388. Ahmed, B. *et al.* Vascular targeting effect of combretastatin A-4 phosphate dominates the inherent angiogenesis inhibitory activity. *Int. J. cancer* **105**, 20–25 (2003).

389. Porcù, E. *et al.* TR-644 a novel potent tubulin binding agent induces impairment of endothelial cells function and inhibits angiogenesis. *Angiogenesis* **16**, 647–662 (2013).

390. Samarin, J., Rehm, M., Krueger, B., Waschke, J. & Goppelt-Struebe, M. Up-regulation of connective tissue growth factor in endothelial cells by the microtubule-destabilizing agent combretastatin A-4. *Mol. Cancer Res.* **7**, 180–188 (2009).

391. Pollock, J. K. *et al.* Combretastatin (CA)-4 and its novel analogue CA-432 impair T-cell migration through the Rho/ROCK signalling pathway. *Biochem. Pharmacol.* **92**, 544–557 (2014).

392. Shen, C.-H. *et al.* Combretastatin A-4 inhibits cell growth and metastasis in bladder cancer cells and retards tumour growth in a murine orthotopic bladder tumour model. *Br. J. Pharmacol.* **160**, 2008–2027 (2010).

393. Rothmeier, A. S. *et al.* Investigation of the marine compound spongistatin 1 links the inhibition of PKCalpha translocation to nonmitotic effects of tubulin antagonism in angiogenesis. *FASEB J.* **23**, 1127–1137 (2009).

394. Bijman, M. N. A., van Nieuw Amerongen, G. P., Laurens, N., van Hinsbergh, V. W. M. & Boven, E. Microtubule-targeting agents inhibit angiogenesis at subtoxic concentrations, a process associated with inhibition of Rac1 and Cdc42 activity and changes in the endothelial cytoskeleton. *Mol. Cancer Ther.* **5**, 2348–2357 (2006).

395. Murtagh, J., Lu, H. & Schwartz, E. L. Taxotere-induced inhibition of human endothelial cell migration is a result of heat shock protein 90 degradation. *Cancer Res.* **66**, 8192–8199 (2006).

396. Lin, H.-L. *et al.* Combretastatin A4-induced differential cytotoxicity and reduced metastatic ability by inhibition of AKT function in human gastric cancer cells. *J. Pharmacol. Exp. Ther.* **323**, 365–373 (2007).

397. Schnaeker, E.-M. *et al.* Microtubule-dependent matrix metalloproteinase-2/matrix metalloproteinase-9 exocytosis: prerequisite in human melanoma cell invasion. *Cancer Res.* **64**, 8924–8931 (2004).

398. Kanthou, C. *et al.* The tubulin-binding agent combretastatin A-4-phosphate arrests endothelial cells in mitosis and induces mitotic cell death. *Am. J. Pathol.* **165**, 1401–1411 (2004).

399. Castedo, M. *et al.* Cell death by mitotic catastrophe: a molecular definition. *Oncogene* **23**, 2825–2837 (2004).

400. Brito, D. A. & Rieder, C. L. Mitotic checkpoint slippage in humans occurs via cyclin B destruction in the presence of an active checkpoint. *Curr. Biol.* **16**, 1194–1200 (2006).

401. Rieder, C. L. & Maiato, H. Stuck in division or passing through: what happens when cells cannot satisfy the spindle assembly checkpoint. *Dev. Cell* **7**, 637–651 (2004).

402. Caruso, R. *et al.* Mitotic catastrophe in malignant epithelial tumors: the pathologist's viewpoint. *Ultrastruct. Pathol.* **35**, 66–71 (2011).

403. Losada, A. Cohesin in cancer: chromosome segregation and beyond. *Nat. Rev. Cancer* **14**, 389–393 (2014).

404. Santaguida, S. & Musacchio, A. The life and miracles of kinetochores. *EMBO J.* **28**, 2511–2531 (2009).

405. Cheeseman, I. M. & Desai, A. Molecular architecture of the kinetochore-microtubule interface. *Nat. Rev. Mol. Cell Biol.* **9**, 33–46 (2008).

406. Rieder, C. L., Cole, R. W., Khodjakov, A. & Sluder, G. The checkpoint delaying anaphase in response to chromosome monoorientation is mediated by an inhibitory signal produced by unattached kinetochores. *J. Cell Biol.* **130**, 941–948 (1995).

407. Musacchio, A. & Salmon, E. D. The spindle-assembly checkpoint in space and time. *Nat. Rev. Mol. Cell Biol.* **8**, 379–393 (2007).

408. Musacchio, A. The Molecular Biology of Spindle Assembly Checkpoint Signaling Dynamics. *Curr. Biol.* **25**, R1002–R1018 (2015).

409. Lara-Gonzalez, P., Westhorpe, F. G. & Taylor, S. S. The Spindle Assembly Checkpoint. *Curr. Biol.* **22**, R966–R980 (2012).

410. Varetti, G. & Musacchio, A. The spindle assembly checkpoint. *Curr. Biol.* **18**, R591–R595 (2008).

411. Matson, D. R. & Stukenberg, P. T. Spindle poisons and cell fate: a tale of two pathways. *Mol. Interv.* **11**, 141–150 (2011).

412. Zhou, J., Yao, J. & Joshi, H. C. Attachment and tension in the spindle assembly checkpoint. *J. Cell Sci.* **115**, 3547–3555 (2002).

413. Clute, P. & Pines, J. Temporal and spatial control of cyclin B1 destruction in metaphase. *Nat. Cell Biol.* **1**, 82–87 (1999).

414. Peters, J.-M. The anaphase promoting complex/cyclosome: a machine designed to destroy. *Nat. Rev. Mol. Cell Biol.* **7**, 644–656 (2006).

415. Chang, L., Zhang, Z., Yang, J., McLaughlin, S. H. & Barford, D. Molecular architecture and mechanism of the anaphase-promoting complex. *Nature* **513**, 388–393 (2014).

416. Primorac, I. & Musacchio, A. Panta rhei: the APC/C at steady state. *J. Cell Biol.* **201**, 177–189 (2013).

417. Pines, J. Cubism and the cell cycle: the many faces of the APC/C. *Nat. Rev. Mol. Cell Biol.* **12**, 427–438 (2011).

418. Alfieri, C. *et al.* Molecular basis of APC/C regulation by the spindle assembly checkpoint. *Nature* **536**, 431–436 (2016).

419. Herzog, F. *et al.* Structure of the anaphase-promoting complex/cyclosome interacting with a mitotic checkpoint complex. *Science* **323**, 1477–1481 (2009).

420. Hornig, N. C. D., Knowles, P. P., McDonald, N. Q. & Uhlmann, F. The dual mechanism of separase regulation by securin. *Curr. Biol.* **12**, 973–982 (2002).

421. Nasmyth, K., Peters, J. M. & Uhlmann, F. Splitting the chromosome: cutting the ties that bind sister chromatids. *Science* **288**, 1379–1385 (2000).

422. Fabbri, F. *et al.* Mitotic catastrophe and apoptosis induced by docetaxel in hormone-refractory prostate cancer cells. *J. Cell. Physiol.* **217**, 494–501 (2008).

423. Cives, M. *et al.* Bendamustine overcomes resistance to melphalan in myeloma cell lines by inducing cell death through mitotic catastrophe. *Cell. Signal.* **25**, 1108–1117 (2013).

424. Michalakis, J. *et al.* Micromolar taxol, with or without hyperthermia, induces mitotic catastrophe and cell necrosis in HeLa cells. *Cancer Chemother. Pharmacol.* **56**, 615–622 (2005).

425. Gajate, C., Barasoain, I., Andreu, J. M. & Mollinedo, F. Induction of apoptosis in leukemic cells by the reversible microtubule-disrupting agent 2-methoxy-5-(2',3',4'-trimethoxyphenyl)-2,4,6-cycloheptatrien-1 -one: protection by Bcl-2 and Bcl-X(L) and cell cycle arrest. *Cancer Res.* **60**, 2651–2659 (2000).

426. Sakurikar, N., Eichhorn, J. M. & Chambers, T. C. Cyclin-dependent kinase-1 (Cdk1)/cyclin B1 dictates cell fate after mitotic arrest via phosphoregulation of antiapoptotic Bcl-2 proteins. *J. Biol. Chem.* **287**, 39193–39204 (2012).

427. Terrano, D. T., Upreti, M. & Chambers, T. C. Cyclin-dependent kinase 1-mediated Bcl-xL/Bcl-2 phosphorylation acts as a functional link coupling mitotic arrest and apoptosis. *Mol. Cell. Biol.* **30**, 640–656 (2010).

428. Zhou, L., Cai, X., Han, X., Xu, N. & Chang, D. C. CDK1 switches mitotic arrest to apoptosis by phosphorylating Bcl-2/Bax family proteins during treatment with microtubule interfering agents. *Cell Biol. Int.* **38**, 737–746 (2014).

429. Youle, R. J. & Strasser, A. The BCL-2 protein family: opposing activities that mediate cell death. *Nat. Rev. Mol. Cell Biol.* **9**, 47–59 (2008).

430. Hardwick, J. M. & Soane, L. Multiple functions of BCL-2 family proteins. *Cold Spring Harb. Perspect. Biol.* **5**, a008722 (2013).

431. Rolland, S. G. & Conradt, B. New role of the BCL2 family of proteins in the regulation of mitochondrial dynamics. *Curr. Opin. Cell Biol.* **22**, 852–858 (2010).

432. Harley, M. E., Allan, L. A., Sanderson, H. S. & Clarke, P. R. Phosphorylation of Mcl-1 by CDK1-cyclin B1 initiates its Cdc20-dependent destruction during mitotic arrest. *EMBO J.* **29**, 2407–2420 (2010).

433. Wertz, I. E. *et al.* Sensitivity to antitubulin chemotherapeutics is regulated by MCL1 and FBW7. *Nature* **471**, 110–114 (2011).

434. Chu, R., Terrano, D. T. & Chambers, T. C. Cdk1/cyclin B plays a key role in mitotic arrest-induced apoptosis by phosphorylation of Mcl-1, promoting its degradation and freeing Bak from sequestration. *Biochem. Pharmacol.* **83**, 199–206 (2012).

435. Choi, H. J. & Zhu, B. T. Upregulated cyclin B1/CDK1 mediates apoptosis following 2-methoxyestradiol-induced mitotic catastrophe: Role of Bcl-X(L) phosphorylation. *Steroids* **150**, 108381 (2019).

436. Choi, H. J. & Zhu, B. T. Role of cyclin B1/Cdc2 in mediating Bcl-XL phosphorylation and apoptotic cell death following nocodazole-induced mitotic arrest. *Mol. Carcinog.* **53**, 125–137 (2014).

437. Han, C. R., Jun, D. Y., Lee, J. Y. & Kim, Y. H. Prometaphase arrest-dependent phosphorylation of Bcl-2 and Bim reduces the association of Bcl-2 with Bak or Bim, provoking Bak activation and mitochondrial apoptosis in nocodazole-treated Jurkat T cells. *Apoptosis* **19**, 224–240 (2014).

438. Yamamoto, K., Ichijo, H. & Korsmeyer, S. J. BCL-2 is phosphorylated and inactivated by an ASK1/Jun N-terminal protein kinase pathway normally activated at G(2)/M. *Mol. Cell. Biol.* **19**, 8469–8478 (1999).

439. Eichhorn, J. M., Sakurikar, N., Alford, S. E., Chu, R. & Chambers, T. C. Critical role of anti-apoptotic Bcl-2 protein phosphorylation in mitotic death. *Cell Death Dis.* **4**, e834–e834 (2013).

440. Deng, X., Gao, F., Flagg, T. & May Jr, W. S. Mono- and multisite phosphorylation enhances Bcl2's antiapoptotic function and inhibition of cell cycle entry functions. *Proc. Natl. Acad. Sci. U. S. A.* **101**, 153–158 (2004).

441. Kim, R. Unknotting the roles of Bcl-2 and Bcl-xL in cell death. *Biochem. Biophys. Res. Commun.* **333**, 336–343 (2005).

442. Ito, T., Deng, X., Carr, B. & May, W. S. Bcl-2 phosphorylation required for anti-apoptosis function. *J. Biol. Chem.* **272**, 11671–11673 (1997).

443. Brichese, L., Barboule, N., Heliez, C. & Valette, A. Bcl-2 phosphorylation and proteasome-dependent degradation induced by paclitaxel treatment:

consequences on sensitivity of isolated mitochondria to Bid. *Exp. Cell Res.* **278**, 101–111 (2002).

444. Sloss, O., Topham, C., Diez, M. & Taylor, S. Mcl-1 dynamics influence mitotic slippage and death in mitosis. *Oncotarget* **7**, 5176–5192 (2016).

445. Thomas, L. W., Lam, C. & Edwards, S. W. Mcl-1; the molecular regulation of protein function. *FEBS Lett.* **584**, 2981–2989 (2010).

446. Topham, C. H. & Taylor, S. S. Mitosis and apoptosis: how is the balance set? *Curr. Opin. Cell Biol.* **25**, 780–785 (2013).

447. Cheng, B. & Crasta, K. Consequences of mitotic slippage for antimicrotubule drug therapy. *Endocr. Relat. Cancer* **24**, T97–T106 (2017).

448. Galán-Malo, P. *et al.* Cell fate after mitotic arrest in different tumor cells is determined by the balance between slippage and apoptotic threshold. *Toxicol. Appl. Pharmacol.* **258**, 384–393 (2012).

449. Hahnfeldt, P., Panigrahy, D., Folkman, J. & Hlatky, L. Tumor development under angiogenic signaling: a dynamical theory of tumor growth, treatment response, and postvascular dormancy. *Cancer Res.* **59**, 4770–4775 (1999).

450. Folkman, J. How is blood vessel growth regulated in normal and neoplastic tissue? G.H.A. Clowes memorial Award lecture. *Cancer Res.* **46**, 467–473 (1986).

451. Folkman, J. What is the evidence that tumors are angiogenesis dependent? *J. Natl. Cancer Inst.* **82**, 4–6 (1990).

452. Close, A. Antiangiogenesis and vascular disrupting agents in cancer: circumventing resistance and augmenting their therapeutic utility. *Future Med. Chem.* **8**, 443–462 (2016).

453. Kerbel, R. S. Inhibition of tumor angiogenesis as a strategy to circumvent acquired resistance to anti-cancer therapeutic agents. *Bioessays* **13**, 31–36 (1991).

454. Baluk, P., Hashizume, H. & McDonald, D. M. Cellular abnormalities of blood vessels as targets in cancer. *Curr. Opin. Genet. Dev.* **15**, 102–111 (2005).

455. Kanthou, C. & Tozer, G. M. Selective destruction of the tumour vasculature by targeting the endothelial cytoskeleton. *Drug Discov. Today Ther. Strateg.* **4**, 237–243 (2007).

456. Vasudev, N. S. & Reynolds, A. R. Anti-angiogenic therapy for cancer: current progress, unresolved questions and future directions. *Angiogenesis* **17**, 471–494 (2014).

457. Marmé, D. The impact of anti-angiogenic agents on cancer therapy. *J. Cancer Res. Clin. Oncol.* **129**, 607–620 (2003).

458. Ferrara, N. & Kerbel, R. S. Angiogenesis as a therapeutic target. *Nature* **438**, 967–974 (2005).

459. Siemann, D. W. *et al.* Differentiation and definition of vascular-targeted therapies. *Clin. Cancer Res.* **11**, 416–420 (2005).

460. Mita, M. M., Sargsyan, L., Mita, A. C. & Spear, M. Vascular-disrupting agents in oncology. *Expert Opin. Investig. Drugs* **22**, 317–328 (2013).

461. Tozer, G. M. *et al.* Combretastatin A-4 phosphate as a tumor vascular-targeting agent: early effects in tumors and normal tissues. *Cancer Res.* **59**, 1626–1634 (1999).

462. Dvorak, H. F., Nagy, J. A., Dvorak, J. T. & Dvorak, A. M. Identification and characterization of the blood vessels of solid tumors that are leaky to circulating macromolecules. *Am. J. Pathol.* **133**, 95–109 (1988).

463. Siemann, D. W. The unique characteristics of tumor vasculature and preclinical evidence for its selective disruption by Tumor-Vascular Disrupting Agents. *Cancer Treat. Rev.* **37**, 63–74 (2011).

464. Denekamp, J. Endothelial cell proliferation as a novel approach to targeting tumour therapy. *Br. J. Cancer* **45**, 136–139 (1982).

465. Tozer, G. M. *et al.* Blood vessel maturation and response to vascular-disrupting therapy in single vascular endothelial growth factor-A isoform-producing tumors. *Cancer Res.* **68**, 2301–2311 (2008).

466. Kliche, K., Jeggle, P., Pavenstädt, H. & Oberleithner, H. Role of cellular mechanics in the function and life span of vascular endothelium. *Pflugers Arch.* **462**, 209–217 (2011).

467. Siemann, D. W. & Horsman, M. R. Modulation of the tumor vasculature and oxygenation to improve therapy. *Pharmacol. Ther.* **153**, 107–124 (2015).

468. Konerding, M. A., Fait, E. & Gaumann, A. 3D microvascular architecture of pre-cancerous lesions and invasive carcinomas of the colon. *Br. J. Cancer* **84**, 1354–1362 (2001).

469. Hashizume, H. *et al.* Openings between defective endothelial cells explain tumor vessel leakiness. *Am. J. Pathol.* **156**, 1363–1380 (2000).

470. Eberhard, A. *et al.* Heterogeneity of angiogenesis and blood vessel maturation in human tumors: implications for antiangiogenic tumor therapies. *Cancer Res.* **60**, 1388–1393 (2000).

471. Tozer, G. M., Lewis, S., Michalowski, A. & Aber, V. The relationship between regional variations in blood flow and histology in a transplanted rat fibrosarcoma. *Br. J. Cancer* **61**, 250–257 (1990).

472. Pérez-Pérez, M.-J. *et al.* Blocking Blood Flow to Solid Tumors by Destabilizing Tubulin: An Approach to Targeting Tumor Growth. *J. Med. Chem.* **59**, 8685–8711 (2016).

473. Bayless, K. J. & Davis, G. E. Microtubule depolymerization rapidly collapses capillary tube networks in vitro and angiogenic vessels in vivo through the small GTPase Rho. *J. Biol. Chem.* **279**, 11686–11695 (2004).

474. Ding, X., Zhang, Z., Li, S. & Wang, A. Combretastatin

A4 phosphate induces programmed cell death in vascular endothelial cells. *Oncol. Res.* **19**, 303–309 (2011).

475. Williams, L. J. *et al.* An in vivo role for Rho kinase activation in the tumour vascular disrupting activity of combretastatin A-4 3-O-phosphate. *Br. J. Pharmacol.* **171**, 4902–4913 (2014).

476. Tozer, G. M. *et al.* Mechanisms associated with tumor vascular shut-down induced by combretastatin A-4 phosphate: intravital microscopy and measurement of vascular permeability. *Cancer Res.* **61**, 6413–6422 (2001).

477. Kanthou, C. & Tozer, G. M. Microtubule depolymerizing vascular disrupting agents: novel therapeutic agents for oncology and other pathologies. *Int. J. Exp. Pathol.* **90**, 284–294 (2009).

478. Vaupel, P. & Hockel, M. Blood supply, oxygenation status and metabolic micromilieu of breast cancers: characterization and therapeutic relevance. *Int. J. Oncol.* **17**, 869–879 (2000).

479. Kim, T. J. *et al.* Antitumor and antivascular effects of AVE8062 in ovarian carcinoma. *Cancer Res.* **67**, 9337–9345 (2007).

480. Wu, X.-Y., Ma, W., Gurung, K. & Guo, C.-H. Mechanisms of tumor resistance to small-molecule vascular disrupting agents: treatment and rationale of combination therapy. *J. Formos. Med. Assoc.* **112**, 115–124 (2013).

481. Nathan, P. *et al.* Phase I trial of combretastatin A4 phosphate (CA4P) in combination with bevacizumab in patients with advanced cancer. *Clin. Cancer Res.* **18**, 3428–3439 (2012).

482. Horsman, M. R. & Siemann, D. W. Pathophysiologic effects of vascular-targeting agents and the implications for combination with conventional therapies. *Cancer Res.* **66**, 11520–11539 (2006).

483. Rojiani, A. M., Li, L., Rise, L. & Siemann, D. W. Activity of the vascular targeting agent combretastatin A-4 disodium phosphate in a xenograft model of AIDS-associated Kaposi's sarcoma. *Acta Oncol.* **41**, 98–105 (2002).

484. Heath, V. L. & Bicknell, R. Anticancer strategies involving the vasculature. *Nat. Rev. Clin. Oncol.* **6**, 395–404 (2009).

485. Cesca, M., Bizzaro, F., Zucchetti, M. & Giavazzi, R. Tumor delivery of chemotherapy combined with inhibitors of angiogenesis and vascular targeting agents. *Front. Oncol.* **3**, 259 (2013).

486. Amano, M. *et al.* Phosphorylation and activation of myosin by Rho-associated kinase (Rho-kinase). *J. Biol. Chem.* **271**, 20246–20249 (1996).

487. Verin, A. D. *et al.* Microtubule disassembly increases endothelial cell barrier dysfunction: role of MLC phosphorylation. *Am. J. Physiol. Lung Cell. Mol. Physiol.* **281**, L565–L574 (2001).

488. Ridley, A. J. Rho GTPase signalling in cell migration. *Curr. Opin. Cell Biol.* **36**, 103–112 (2015).

489. Hori, K. & Saito, S. Microvascular mechanisms by which the combretastatin A-4 derivative AC7700 (AVE8062) induces tumour blood flow stasis. *Br. J. Cancer* **89**, 1334–1344 (2003).

490. Griggs, J., Metcalfe, J. C. & Hesketh, R. Targeting tumour vasculature: the development of combretastatin A4. *Lancet. Oncol.* **2**, 82–87 (2001).

491. Zhao, X. & Guan, J.-L. Focal adhesion kinase and its signaling pathways in cell migration and angiogenesis. *Adv. Drug Deliv. Rev.* **63**, 610–615 (2011).

492. Houle, F. & Huot, J. Dysregulation of the endothelial cellular response to oxidative stress in cancer. *Mol. Carcinog.* **45**, 362–367 (2006).

493. Nelson, C. M., Pirone, D. M., Tan, J. L. & Chen, C. S. Vascular endothelial-cadherin regulates cytoskeletal tension, cell spreading, and focal adhesions by stimulating RhoA. *Mol. Biol. Cell* **15**, 2943–2953 (2004).

494. Wojciak-Stothard, B. & Ridley, A. J. Rho GTPases and the regulation of endothelial permeability. *Vascul. Pharmacol.* **39**, 187–199 (2002).

495. Baluk, P., Morikawa, S., Haskell, A., Mancuso, M. & McDonald, D. M. Abnormalities of basement membrane on blood vessels and endothelial sprouts in tumors. *Am. J. Pathol.* **163**, 1801–1815 (2003).

496. Ley, C. D., Horsman, M. R. & Kristjansen, P. E. G. Early effects of combretastatin-A4 disodium phosphate on tumor perfusion and interstitial fluid pressure. *Neoplasia* **9**, 108–112 (2007).

497. Milosevic, M. F., Fyles, A. W. & Hill, R. P. The relationship between elevated interstitial fluid pressure and blood flow in tumors: a bioengineering analysis. *Int. J. Radiat. Oncol. Biol. Phys.* **43**, 1111–1123 (1999).

498. Lominadze, D. & Mchedlishvili, G. Red blood cell behavior at low flow rate in microvessels. *Microvasc. Res.* **58**, 187–189 (1999).

499. Álvarez, R. *et al.* Substitution at the indole 3 position yields highly potent indolecombretastatins against human tumor cells. *Eur. J. Med. Chem.* **158**, 167–183 (2018).

500. Medarde, M., Maya, A. B. S. & Pérez-Melero, C. Review ArticleNaphthalene Combretastatin Analogues: Synthesis, Cytotoxicity and Antitubulin Activity. *J. Enzyme Inhib. Med. Chem.* **19**, 521–540 (2004).

501. Maya, A. B. S. *et al.* Further naphthylcombretastatins. An investigation on the role of the naphthalene moiety. *J. Med. Chem.* **48**, 556–568 (2005).

502. Alvarez, C. *et al.* Synthesis and biological activity of naphthalene analogues of phenstatins: naphthylphenstatins. *Bioorg. Med. Chem. Lett.* **17**, 3417–3420 (2007).

503. Álvarez, C. *et al.* Naphthylphenstatins as tubulin ligands: Synthesis and biological evaluation. *Bioorganic Med. Chem.* (2008).

doi:10.1016/j.bmc.2008.08.040

504. Álvarez, C. *et al.* Diarylmethyloxime and hydrazone derivatives with 5-indolyl moieties as potent inhibitors of tubulin polymerization. *Bioorganic Med. Chem.* (2008). doi:10.1016/j.bmc.2008.04.054

505. Álvarez, R. *et al.* Endowing indole-based tubulin inhibitors with an anchor for derivatization: highly potent 3-substituted indolephenstatins and indoleisocombretastatins. *J. Med. Chem.* **56**, 2813–2827 (2013).

506. Liou, J.-P. *et al.* 4- and 5-Aroylindoles as Novel Classes of Potent Antitubulin Agents. *J. Med. Chem.* **50**, 4548–4552 (2007).

507. Senese, S. *et al.* Chemical dissection of the cell cycle: probes for cell biology and anti-cancer drug development. *Cell Death Dis.* **5**, e1462–e1462 (2014).

508. Michels, J. *et al.* A phase IB study of ABT-751 in combination with docetaxel in patients with advanced castration-resistant prostate cancer. *Ann. Oncol. Off. J. Eur. Soc. Med. Oncol.* **21**, 305–311 (2010).

509. Ma, T. *et al.* A phase I trial and in vitro studies combining ABT-751 with carboplatin in previously treated non-small cell lung cancer patients. *Chemotherapy* **58**, 321–329 (2012).

510. Rudin, C. M. *et al.* Phase I/II study of pemetrexed with or without ABT-751 in advanced or metastatic non-small-cell lung cancer. *J. Clin. Oncol.* **29**, 1075–1082 (2011).

511. Press, P. Sulfonic acids and their derivatives in Comprehensive Organic Chemistry. **3**, 331–350 (1979).

512. Montalbetti, C. A. G. N. & Falque, V. Amide bond formation and peptide coupling. *Tetrahedron* **61**, 10827–10852 (2005).

513. Hazlet, S. E. & Dornfeld, C. A. The Reduction of Aromatic Nitro Compounds with Activated Iron. *J. Am. Chem. Soc.* **66**, 1781–1782 (1944).

514. Liou, J.-P. *et al.* Synthesis and Structure−Activity Relationships of 3-Aminobenzophenones as Antimitotic Agents. *J. Med. Chem.* **47**, 2897–2905 (2004).

515. Bellamy, F. D. & Ou, K. Selective reduction of aromatic nitro compounds with stannous chloride in non acidic and non aqueous medium. *Tetrahedron Lett.* **25**, 839–842 (1984).

516. Bernstein, M. P., Bauschlicher, C. W. & Sandford, S. A. The infrared spectrum of matrix isolated aminoacetonitrile, a precursor to the amino acid glycine. *Adv. Sp. Res.* (2004). doi:10.1016/j.asr.2003.07.002

517. Pindur, U. & Kim, M.-H. First reactions of vinylindoles with diethyl mesoxalate, nitrosobenzene, and chlorosulfonyl isocyanate: New functionalized and [b]annellated indoles. *Tetrahedron* **45**, 6427–6438 (1989).

518. Meth-Cohn, O. & Stanforth, S. P. The Vilsmeier–Haack Reaction. *Compr. Org. Synth.* 777–794 (1991). doi:10.1016/B978-0-08-052349-1.00049-4

519. Čurillová, Z. *et al.* Synthesis and antiproliferative activity of 1-methoxy-, 1-(α-D-ribofuranosyl)- and 1-(β-D-ribofuranosyl)brassenin B. *Arkivoc* **8**, 85–104 (2008).

520. Morozova, S. E., Esikov, K. A., Dmitrieva, T. N., Malin, A. A. & Ostrovskii, V. A. Tetrachlorosilane–Sodium Azide System in the Synthesis of Tetrazole-Containing D,L-Tryptophane Derivatives. *Russ. J. Org. Chem.* **40**, 443–445 (2004).

521. Del Mazo, S. Nuevos antimitóticos basados en productos naturales. Master's thesis. (University of Salamanca, 2017).

522. Iranpoor, N., Firouzabadi, H., Nowrouzi, N. & Khalili, D. Selective mono- and di-N-alkylation of aromatic amines with alcohols and acylation of aromatic amines using Ph3P/DDQ. *Tetrahedron* **65**, 3893–3899 (2009).

523. Gwaltney, S. L. 2nd *et al.* Novel sulfonate analogues of combretastatin A-4: potent antimitotic agents. *Bioorg. Med. Chem. Lett.* **11**, 871–874 (2001).

524. Brameld, K. A., Kuhn, B., Reuter, D. C. & Stahl, M. Small Molecule Conformational Preferences Derived from Crystal Structure Data. A Medicinal Chemistry Focused Analysis. *J. Chem. Inf. Model.* **48**, 1–24 (2008).

525. Radkiewicz, J. L., McAllister, M. A., Goldstein, E. & Houk, K. N. A Theoretical Investigation of Phosphonamidates and Sulfonamides as Protease Transition State Isosteres. *J. Org. Chem.* **63**, 1419–1428 (1998).

526. Liu, X. ABC Family Transporters. *Adv. Exp. Med. Biol.* **1141**, 13–100 (2019).

527. Tsuruo, T., Iida, H., Tsukagoshi, S. & Sakurai, Y. Overcoming of vincristine resistance in P388 leukemia in vivo and in vitro through enhanced cytotoxicity of vincristine and vinblastine by verapamil. *Cancer Res.* **41**, 1967–1972 (1981).

528. Malingré, M. M. *et al.* Co-administration of GF120918 significantly increases the systemic exposure to oral paclitaxel in cancer patients. *Br. J. Cancer* **84**, 42–47 (2001).

529. Borowicz, S. *et al.* The soft agar colony formation assay. *J. Vis. Exp.* e51998 (2014). doi:10.3791/51998

530. Evangelio, J. A. *et al.* Fluorescent taxoids as probes of the microtubule cytoskeleton. *Cell Motil. Cytoskeleton* **39**, 73–90 (1998).

531. Shelanski, M. L., Gaskin, F. & Cantor, C. R. Microtubule assembly in the absence of added nucleotides. *Proc. Natl. Acad. Sci. U. S. A.* **70**, 765–768 (1973).

532. Dumortier, C., Gorbunoff, M. J., Andreu, J. M. & Engelborghs, Y. Different kinetic pathways of the binding of two biphenyl analogues of colchicine to tubulin. *Biochemistry* **35**, 4387–4395 (1996).

533. Han, Y. *et al.* Interaction of a fluorescent derivative of paclitaxel (Taxol) with microtubules and tubulin-colchicine. *Biochemistry* **35**, 14173–14183 (1996).

534. Andreu, J. M., Gorbunoff, M. J., Lee, J. C. & Timasheff, S. N. Interaction of tubulin with bifunctional colchicine analogues: an equilibrium study. *Biochemistry* **23**, 1742–1752 (1984).

535. Leynadier, D. *et al.* Tubulin binding of two 1-deaza-7,8-dihydropteridines with different biological properties: enantiomers NSC 613862 (S)-(-) and NSC 613863 (R)-(+). *Biochemistry* **32**, 10675–10682 (1993).

536. Díaz, J. F. & Buey, R. M. Characterizing ligand-microtubule binding by competition methods. *Methods Mol. Med.* **137**, 245–260 (2007).

537. Fernando Díaz, J. & Andreu, J. M. Kinetics of dissociation of the tubulin-colchicine complex. Complete reaction scheme and comparison to thermodynamic measurements. *J. Biol. Chem.* **266**, 2890–2896 (1991).

538. Cortese, F., Bhattacharyya, B. & Wolff, J. Podophyllotoxin as a probe for the colchicine binding site of tubulin. *J. Biol. Chem.* **252**, 1134–1140 (1977).

539. DeCicco-Skinner, K. L. *et al.* Endothelial cell tube formation assay for the in vitro study of angiogenesis. *J. Vis. Exp.* e51312 (2014). doi:10.3791/51312

540. Rodríguez-Enfedaque, A. *et al.* zVAD-fmk upregulates caspase-9 cleavage and activity in etoposide-induced cell death of mouse embryonic fibroblasts. *Biochim. Biophys. Acta - Mol. Cell Res.* **1823**, 1343–1352 (2012).

541. Klionsky, D. J. *et al.* Guidelines for the use and interpretation of assays for monitoring autophagy (3rd edition). *Autophagy* **12**, 1–222 (2016).

542. Boya, P., Esteban-Martínez, L., Serrano-Puebla, A., Gómez-Sintes, R. & Villarejo-Zori, B. Autophagy in the eye: Development, degeneration, and aging. *Prog. Retin. Eye Res.* **55**, 206–245 (2016).

543. Tanida, I., Minematsu-Ikeguchi, N., Ueno, T. & Kominami, E. Lysosomal turnover, but not a cellular level, of endogenous LC3 is a marker for autophagy. *Autophagy* **1**, 84–91 (2005).

544. Jahreiss, L., Menzies, F. M. & Rubinsztein, D. C. The itinerary of autophagosomes: from peripheral formation to kiss-and-run fusion with lysosomes. *Traffic* **9**, 574–587 (2008).

545. Klionsky, D. J., Elazar, Z., Seglen, P. O. & Rubinsztein, D. C. Does bafilomycin A1 block the fusion of autophagosomes with lysosomes? *Autophagy* **4**, 849–850 (2008).

546. Yoon, Y. H. *et al.* Induction of lysosomal dilatation, arrested autophagy, and cell death by chloroquine in cultured ARPE-19 cells. *Invest. Ophthalmol. Vis. Sci.* **51**, 6030–6037 (2010).

547. Mauthe, M. *et al.* Chloroquine inhibits autophagic flux by decreasing autophagosome-lysosome fusion. *Autophagy* **14**, 1435–1455 (2018).

548. Degterev, A. *et al.* Identification of RIP1 kinase as a specific cellular target of necrostatins. *Nat. Chem. Biol.* **4**, 313–321 (2008).

549. Ly, J. D., Grubb, D. R. & Lawen, A. The mitochondrial membrane potential (Δψm) in apoptosis; an update. *Apoptosis* **8**, 115–128 (2003).

550. Festjens, N., Vanden Berghe, T. & Vandenabeele, P. Necrosis, a well-orchestrated form of cell demise: signalling cascades, important mediators and concomitant immune response. *Biochim. Biophys. Acta* **1757**, 1371–1387 (2006).

551. Ríos Miguel, A. B. Obtención y evaluación de nuevas sulfamidas antitumorales. Bachelor's thesis. (University of Salamanca, 2015).

552. Aprile, S., Del Grosso, E. & Grosa, G. Identification of the human UDP-glucuronosyltransferases involved in the glucuronidation of combretastatin A-4. *Drug Metab. Dispos.* **38**, 1141–1146 (2010).

553. Laurence, C., Brameld, K. A., Graton, J., Le Questel, J.-Y. & Renault, E. The pKBHX Database: Toward a Better Understanding of Hydrogen-Bond Basicity for Medicinal Chemists. *J. Med. Chem.* **52**, 4073–4086 (2009).

554. Gennari, C., Gude, M., Potenza, D. & Piarulli, U. Hydrogen-Bonding Donor/Acceptor Scales in β-Sulfonamidopeptides. *Chem. – A Eur. J.* **4**, 1924–1931 (1998).

555. Álvarez, C. *et al.* Exploring the effect of 2,3,4-trimethoxy-phenyl moiety as a component of indolephenstatins. *Eur. J. Med. Chem.* **45**, 588–597 (2010).

556. Brancale, A. & Silvestri, R. Indole, a core nucleus for potent inhibitors of tubulin polymerization. *Med. Res. Rev.* **27**, 209–238 (2007).

557. Nobili, S., Landini, I., Mazzei, T. & Mini, E. Overcoming tumor multidrug resistance using drugs able to evade P-glycoprotein or to exploit its expression. *Med. Res. Rev.* **32**, 1220–1262 (2012).

558. Schwartz, E. L. Antivascular actions of microtubule-binding drugs. *Clin. Cancer Res.* **15**, 2594–2601 (2009).

559. Gascoigne, K. E. & Taylor, S. S. Cancer cells display profound intra- and interline variation following prolonged exposure to antimitotic drugs. *Cancer Cell* **14**, 111–122 (2008).

560. Yusuf, R. Z., Duan, Z., Lamendola, D. E., Penson, R. T. & Seiden, M. V. Paclitaxel resistance: molecular mechanisms and pharmacologic manipulation. *Curr. Cancer Drug Targets* **3**, 1–19 (2003).

561. Mackeh, R., Perdiz, D., Lorin, S., Codogno, P. & Poüs, C. Autophagy and microtubules – new story, old players. *J. Cell Sci.* **126**, 1071 LP – 1080 (2013).

562. Geeraert, C. *et al.* Starvation-induced hyperacetylation of tubulin is required for the stimulation of autophagy by nutrient deprivation. *J. Biol. Chem.* **285**, 24184–24194 (2010).

563. Köchl, R., Hu, X. W., Chan, E. Y. W. & Tooze, S. A. Microtubules Facilitate Autophagosome Formation and Fusion of Autophagosomes with Endosomes. *Traffic* **7**, 129–145 (2006).

564. Amenta, J. S., Sargus, M. J. & Baccino, F. M. Effect of microtubular or translational inhibitors on general cell protein degradation. Evidence for a dual catabolic pathway. *Biochem. J.* **168**, 223–227 (1977).

565. Wei, R.-J. *et al.* A microtubule inhibitor, ABT-751, induces autophagy and delays apoptosis in Huh-7 cells. *Toxicol. Appl. Pharmacol.* **311**, 88–98 (2016).

566. Wei, R.-J. *et al.* Inhibition of the formation of autophagosome but not autolysosome augments ABT-751-induced apoptosis in TP53-deficient Hep-3B cells. *J. Cell. Physiol.* **234**, 9551–9563 (2019).

567. Saetre, F., Hagen, L. K., Engedal, N. & Seglen, P. O. Novel steps in the autophagic-lysosomal pathway. *FEBS J.* **282**, 2202–2214 (2015).

568. Sarkar, S., Korolchuk, V., Renna, M., Winslow, A. & Rubinsztein, D. C. Methodological considerations for assessing autophagy modulators: a study with calcium phosphate precipitates. *Autophagy* **5**, 307–313 (2009).

569. Green, D. R. & Reed, J. C. Mitochondria and apoptosis. *Science* **281**, 1309–1312 (1998).

570. Shchepina, L. A. *et al.* Oligomycin, inhibitor of the F0 part of H+-ATP-synthase, suppresses the TNF-induced apoptosis. *Oncogene* **21**, 8149–8157 (2002).

571. Wong, C. H. *et al.* Simultaneous induction of non-canonical autophagy and apoptosis in cancer cells by ROS-dependent ERK and JNK activation. *PLoS One* **5**, e9996 (2010).

572. Li, X. *et al.* Targeting mitochondrial reactive oxygen species as novel therapy for inflammatory diseases and cancers. *J. Hematol. Oncol.* **6**, 19 (2013).

573. Park, W. H., Han, Y. W., Kim, S. H. & Kim, S. Z. An ROS generator, antimycin A, inhibits the growth of HeLa cells via apoptosis. *J. Cell. Biochem.* **102**, 98–109 (2007).

574. Chipuk, J. E., Bouchier-Hayes, L. & Green, D. R. Mitochondrial outer membrane permeabilization during apoptosis: the innocent bystander scenario. *Cell Death Differ.* **13**, 1396–1402 (2006).

575. Zamzami, N., Métivier, D. & Kroemer, G. Quantitation of mitochondrial transmembrane potential in cells and in isolated mitochondria. *Methods Enzymol.* **322**, 208–213 (2000).

576. Craig, R. W. MCL1 provides a window on the role of the BCL2 family in cell proliferation, differentiation and tumorigenesis. *Leukemia* **16**, 444–454 (2002).

577. Fulda, S. Tumor resistance to apoptosis. *Int. J. cancer* **124**, 511–515 (2009).

578. Igney, F. H. & Krammer, P. H. Death and anti-death: tumour resistance to apoptosis. *Nat. Rev. Cancer* **2**, 277–288 (2002).

579. Galluzzi, L. *et al.* Essential versus accessory aspects of cell death: recommendations of the NCCD 2015. *Cell Death Differ.* **22**, 58–73 (2015).

580. Yang, T. *et al.* Discovery of Tertiary Amine and Indole Derivatives as Potent RORγt Inverse Agonists. *ACS Med. Chem. Lett.* **5**, 65–68 (2014).

581. Noland, W. E. & Rieke, R. D. New Synthetic Route to 6-Nitroisatin via Nitration of 3-Indolealdehyde. *J. Org. Chem.* **27**, 2250–2252 (1962).

582. Zuse, A. *et al.* Sulfonate Derivatives of Naphtho[2,3-b]thiophen-4(9H)-one and 9(10H)-Anthracenone as Highly Active Antimicrotubule Agents. Synthesis, Antiproliferative Activity, and Inhibition of Tubulin Polymerization. *J. Med. Chem.* **50**, 6059–6066 (2007).

583. Samajdar, S., Becker, F. F. & Banik, B. K. Surface-mediated highly efficient regioselective nitration of aromatic compounds by bismuth nitrate. *Tetrahedron Lett.* **41**, 8017–8020 (2000).

584. Kudelko, A. & Wróblowska, M. An efficient synthesis of conjugated 5-aryl-1,3,4-oxadiazoles from 3-heteroarylacrylohydrazides and acid chlorides. *Tetrahedron Lett.* **55**, 3252–3254 (2014).

585. Lichti, U., Anders, J. & Yuspa, S. H. Isolation and short-term culture of primary keratinocytes, hair follicle populations and dermal cells from newborn mice and keratinocytes from adult mice for in vitro analysis and for grafting to immunodeficient mice. *Nat. Protoc.* **3**, 799–810 (2008).

586. Mollinedo, F. *et al.* Selective induction of apoptosis in cancer cells by the ether lipid ET-18-OCH3 (Edelfosine): molecular structure requirements, cellular uptake, and protection by Bcl-2 and Bcl-X(L). *Cancer Res.* **57**, 1320–1328 (1997).

587. Bradford, M. M. A rapid and sensitive method for the quantitation of microgram quantities of protein utilizing the principle of protein-dye binding. *Anal. Biochem.* **72**, 248–254 (1976).

588. Andreu, J. M. Large scale purification of brain tubulin with the modified Weisenberg procedure. *Methods Mol. Med.* **137**, 17–28 (2007).

589. Gajate, C., An, F. & Mollinedo, F. Rapid and selective apoptosis in human leukemic cells induced by Aplidine through a Fas/CD95- and mitochondrial-mediated mechanism. *Clin. cancer Res. an Off. J. Am. Assoc. Cancer Res.* **9**, 1535–1545 (2003).

APPENDIX

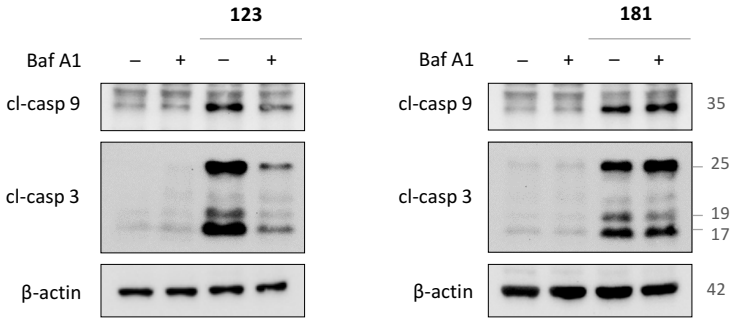

Figure I. Immunoblots of HeLa cell lysates: cleavage of caspases 9 and 3 after treatment with compounds **123** (1 µM) and **181** (100 nM) for 48 h, in combination or not with bafilomycin A1 (15 nM). β-actin was used as a loading control. Molecular weights are indicated in kDa.

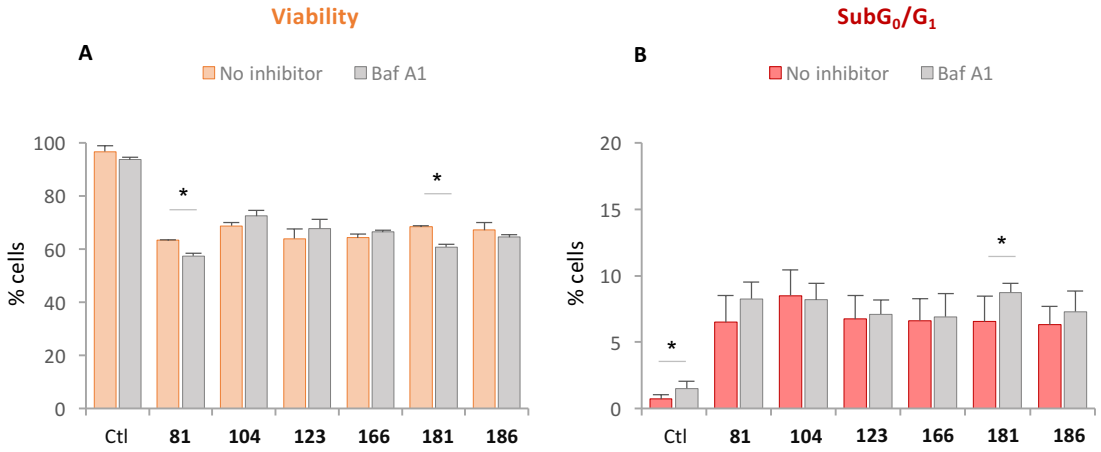

Figure II. HeLa cells in the absence (Ctl) or the presence of the lead compounds, in combination or not with the autophagy inhibitor bafilomycin A1 (15 nM). The compounds were tested at the working concentration: 100 nM except **123** at 1 µM, and incubated for 24 h. **A.** Percentage of **double negative An^-/PI^- cells** (viable cells) related to the dot plots in Figure III ($n = 3$; * $p < 0.05$). **B.** Quantification of the percentage of cells in the **$SubG_0/G_1$** region was measured by cell cycle analysis ($n = 5$).

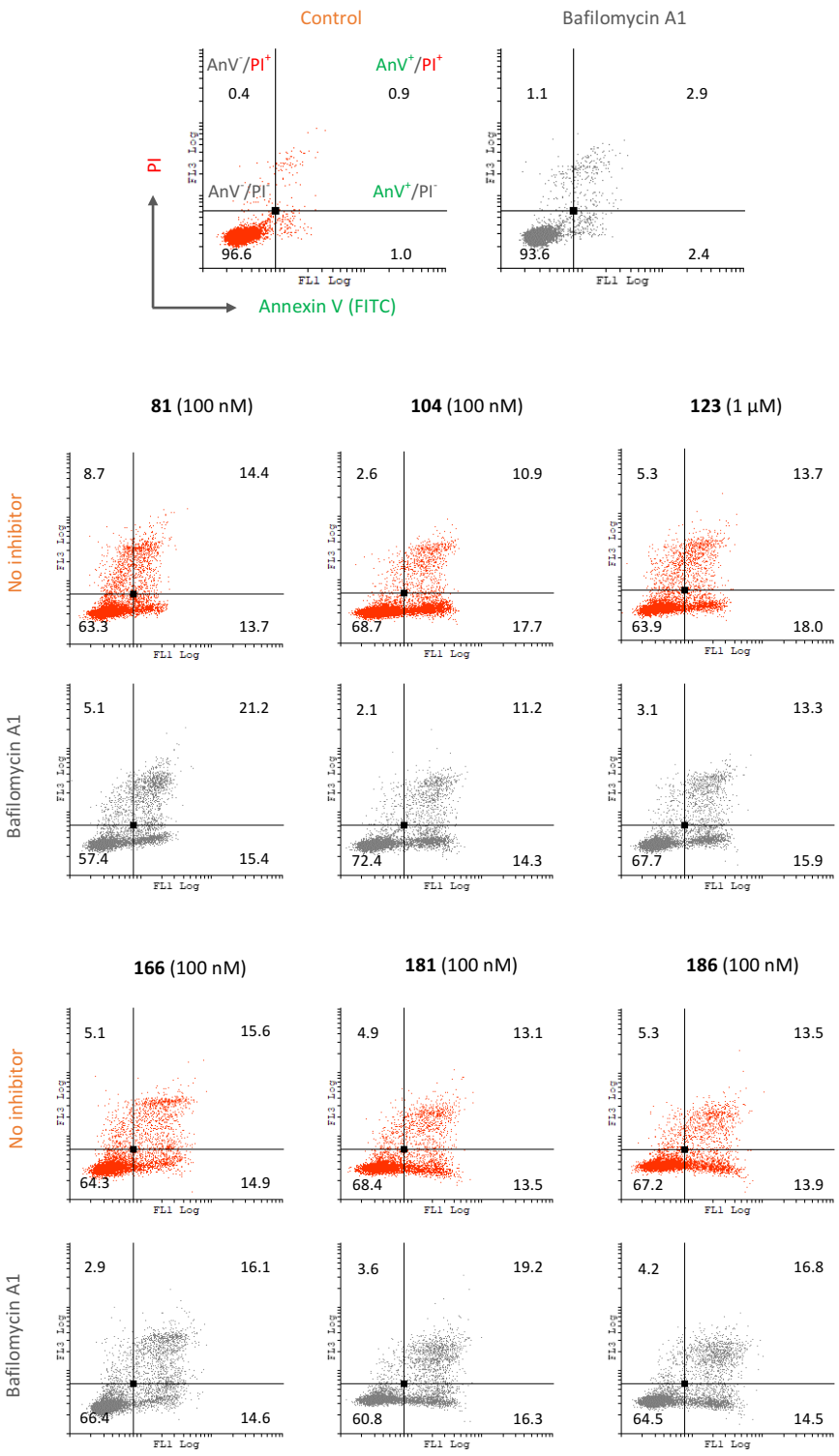

Figure III. Dot plots of non-permeabilized HeLa cells stained with **Annexin V-FITC** (green fluorescence, X axis) and **PI** (red fluorescence, Y axis). The cells were incubated without (**orange dot plots**) or with 15 nM bafilomycin A1 (**grey dot plots**) for 2 h prior to the addition of the lead compounds. The cells were analyzed after 24-h incubation with the indicated ligands. The population in each quadrant is expressed as the mean in percentage (n = 3) regarding the groups AnV^-/PI^- (live cells), AnV^+/PI^- (early apoptosis), AnV^-/PI^+ (necrosis) and AnV^+/PI^+ (late apoptosis or necrosis secondary to apoptosis). Dot plots are representative of three independent experiments.

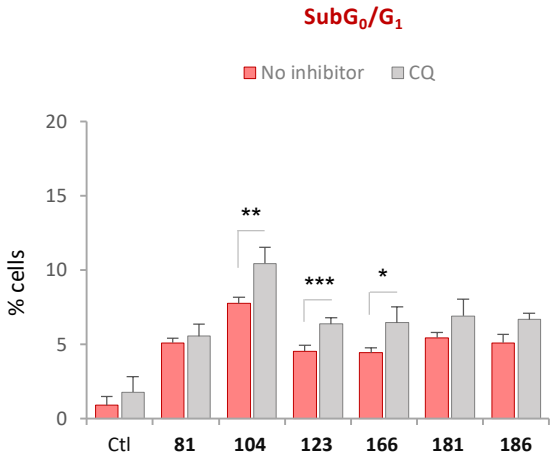

Figure IV. Quantification of the percentage of HeLa cells in the **SubG$_0$/G$_1$** region by cell cycle analysis after 24-h incubation with the lead compounds at 100 nM (except **123** at µM) in combination or not with 20 µM chloroquine (n = 4; * $p < 0.05$; ** $p < 0.01$; *** $p < 0.001$).

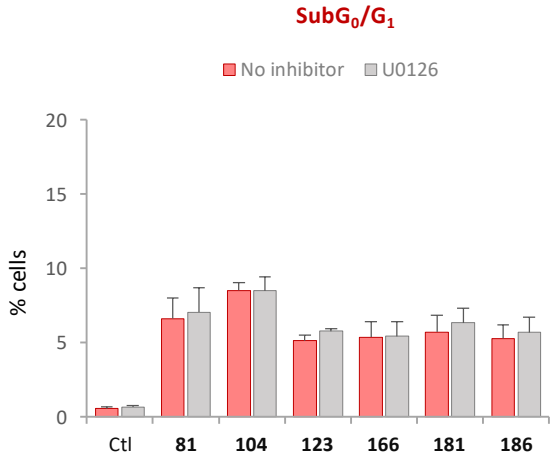

Figure V. Quantification of the percentage of HeLa cells in the **SubG$_0$/G$_1$** region by cell cycle analysis after 24-h incubation with the lead compounds at 100 nM (except **123** at µM) in combination or not with 10 µM U0126 (n = 4; there are no statistically significant differences).

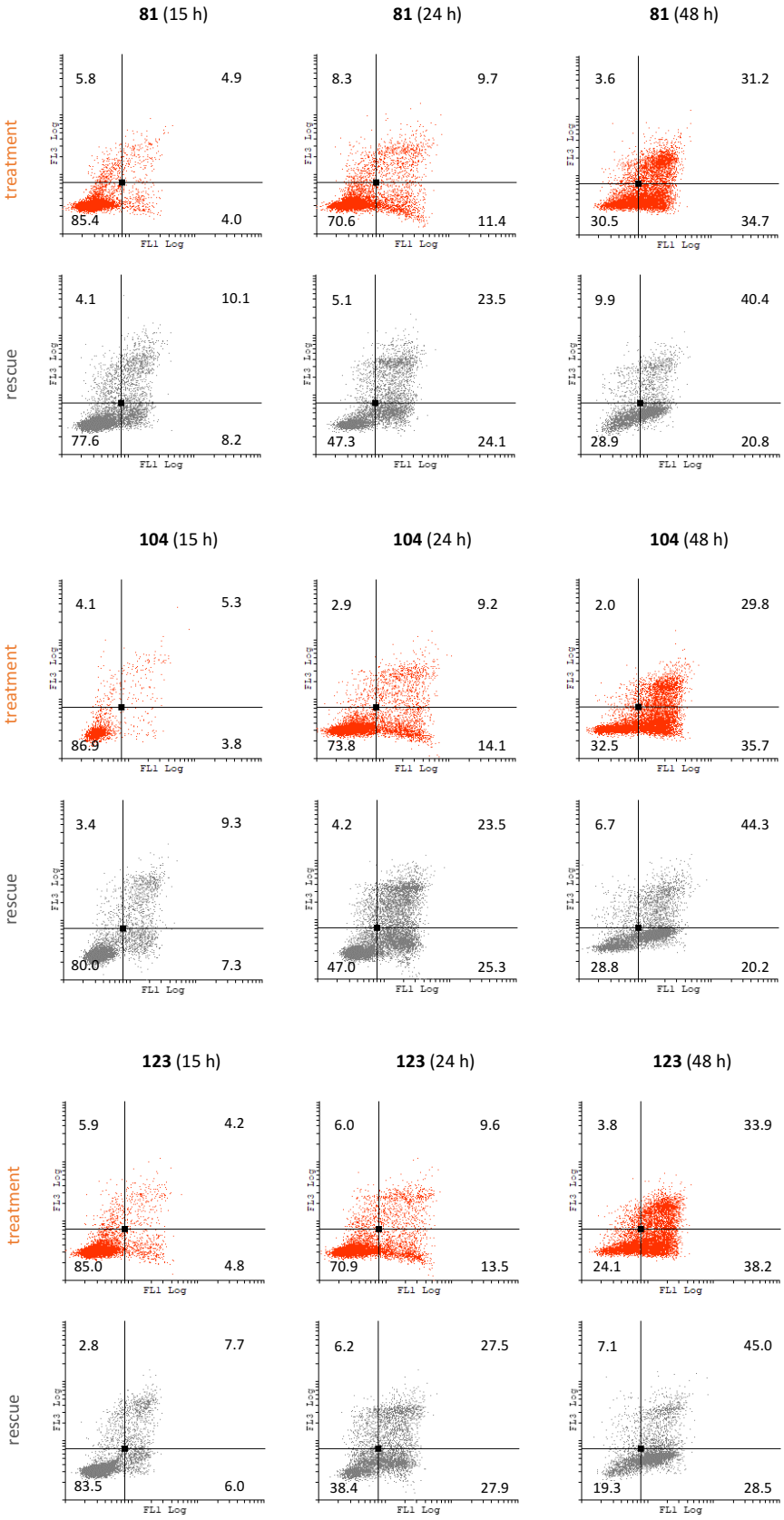

Figure VI. Continued

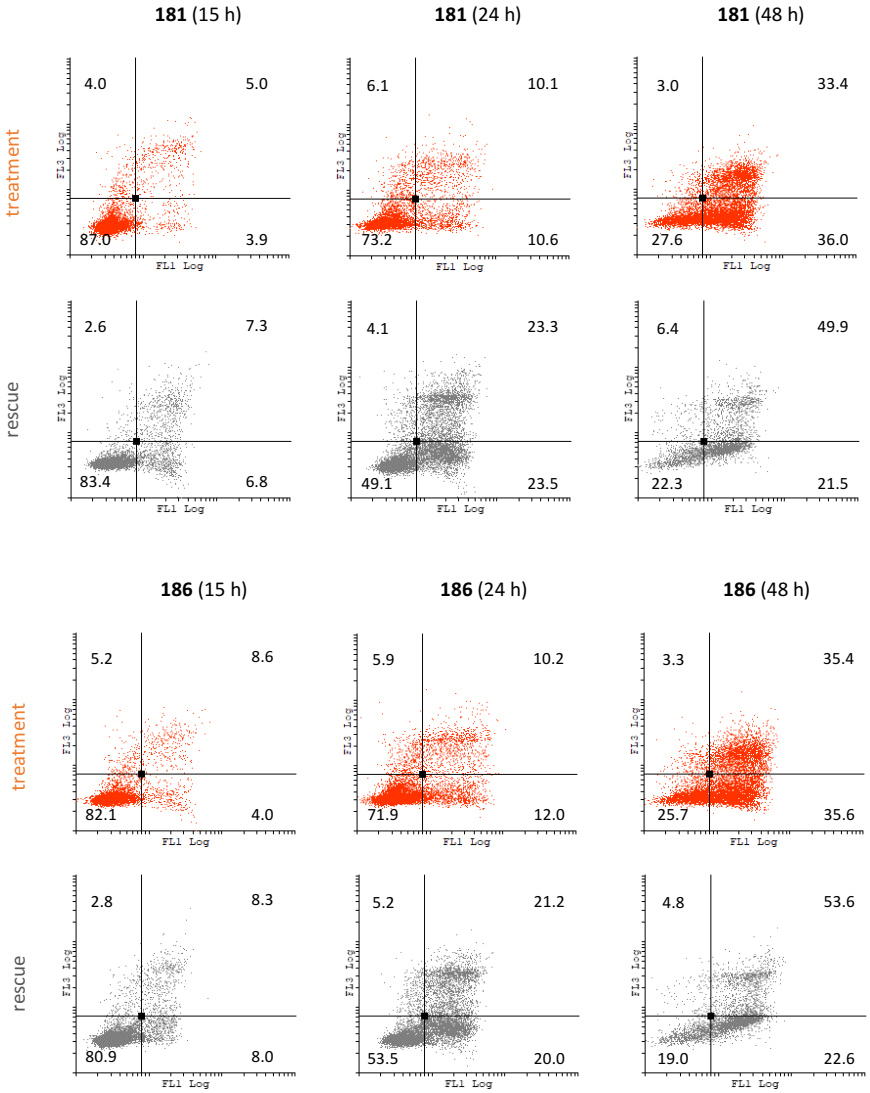

Figure VI. Dot plots of non-permeabilized HeLa cells treated with the lead compounds at 100 nM except for **123** (1µM), for 15 h, 24 h, or 48 h (treatment). The cells were washed three times with PBS and re-seeded in drug-free culture media, then analyzed 48 h after removing the treatment (rescue). According to their distribution along the X axis (**Annexin V-FITC**, green fluorescence) and the Y axis (**PI**, red fluorescence), cells can be categorized as AnV^-/PI^- (live cells), AnV^+/PI^- (early apoptosis), AnV^-/PI^+ (necrosis) and AnV^+/PI^+ (late apoptosis or necrosis secondary to apoptosis), expressed as the mean in percentage (n = 3). Dot plots are representative of three independent experiments.

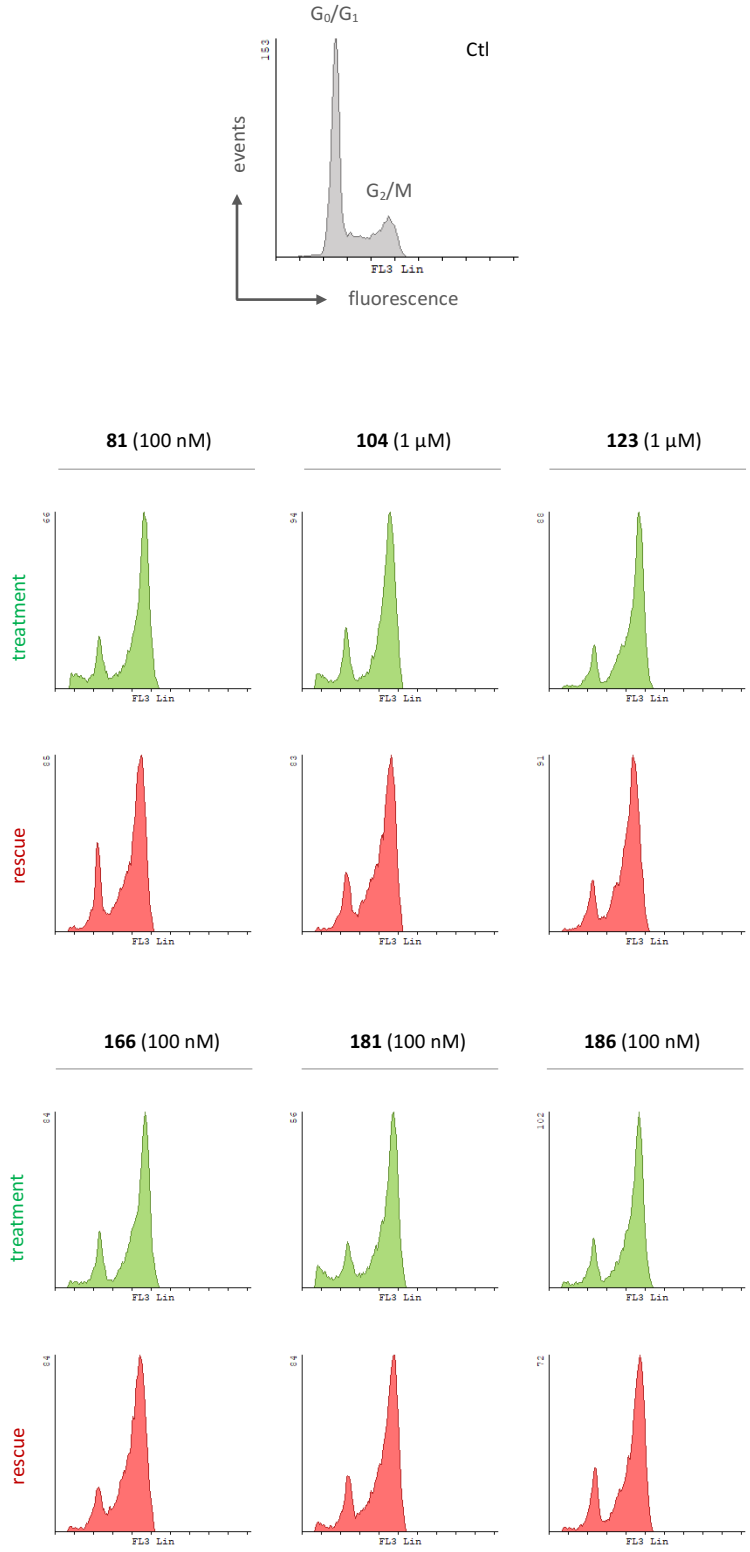

Figure VII. Cell cycle histograms of HPNE cells treated with the compound at the indicated concentrations for 7 days (green histograms). The cells were then repeatedly washed with PBS and cultured for 48 h in drug-free media (red histograms). The peaks corresponding to G_0/G_1 and G_2/M populations are indicated on the control histogram (Ctl, grey histogram). Flow cytometry profiles are representative of three independent experiments.

UNIVERSIDAD DE SALAMANCA

FACULTAD DE FARMACIA

Departamento de Ciencias Farmacéuticas

NUEVOS AGENTES ANTIMITÓTICOS BASADOS EN INDOL: DISEÑO, SÍNTESIS Y ESTUDIO DEL MECANISMO DE ACCIÓN ANTITUMORAL

MEMORIA PARA OPTAR AL GRADO DE DOCTOR

ALBA VICENTE BLÁZQUEZ

Bajo la dirección de

Dr. Faustino Mollinedo, Dr. Rafael Peláez

Centro de Investigaciones Biológicas Margarita Salas (CSIC)

2020

Contenidos

INTRODUCCIÓN

Tubulina como diana antitumoral

La tubulina es una proteína de células eucariotas que participa en procesos esenciales como la división celular, el transporte intracelular de vesículas o el mantenimiento de la forma celular. Esta proteína constituye una diana farmacológica validada como estrategia terapéutica en la quimioterapia antitumoral. Algunos de los fármacos antitumorales más extensamente utilizados de los aprobados por la FDA ejercen su acción por unión a tubulina (paclitaxel o algunos alcaloides de la vinca). La tubulina presenta un alto grado de conservación y apenas es susceptible de adquirir mutaciones que puedan afectar al desarrollo adecuado de sus funciones.

Los ligandos que se unen a tubulina presentan un mecanismo de acción citotóxico al impedir la correcta división de las células, que sufren apoptosis tras una parada sostenida en fase de mitosis. Algunos compuestos han mostrado de forma adicional un efecto antivascular (VDAs) al producir el colapso y oclusión de los pequeños vasos sanguíneos inmaduros que irrigan los tumores sólidos, induciendo necrosis en el centro del tumor por falta de aporte nutricional y de oxígeno. Este tipo de terapia antivascular está siendo ampliamente estudiada en ensayos clínicos en combinación con agentes citotóxicos clásicos, o inhibidores de angiogénesis, entre otros. Los fármacos dirigidos a tubulina suelen presentar problemas farmacocinéticos y también es frecuente la aparición de resistencia al tratamiento, generalmente mediada por transportadores de la familia MDR o por sobreexpresión de diferentes isotipos de tubulina. La expresión ubicua de tubulina da lugar a toxicidad *on-target* preferentemente en tejidos que presentan una alta velocidad de recambio, como por ejemplo la médula ósea.

Estructura y dinámica de los microtúbulos

La tubulina es una proteína heterodimérica formada por subunidades globulares α y β de unos 50 kDa cada una. La polimerización longitudinal de α,β-tubulina forma protofilamentos, cuya asociación lateral da lugar a microtúbulos. Los microtúbulos son, por tanto, estructuras cilíndricas que presentan un comportamiento altamente dinámico, con las subunidades β expuestas hacia el extremo-(+), en el que la asociación/disociación de heterodímeros es mucho más rápida que en el extremo-(-), que expone subunidades α (Fig. 1).

El proceso de polimerización depende de la hidrólisis de GTP. El dímero de tubulina consta de dos sitios de unión de nucleótidos: un sitio N (no intercambiable) en la subunidad α para unión de GTP y un sitio E (intercambiable) en la subunidad β para unión de GTP, GDP o GDP + P_i. Cada subunidad presenta dos regiones diferenciadas, la región globular que contiene el dominio GTPasa y el dominio de activación, y una cola hacia el exterior del microtúbulo, donde se concentran la mayor parte de modificaciones post-traduccionales (PTMs) y las diferencias entre isotipos de tubulina. La combinación de PTMs y cambios en la secuencia se conoce como el "código de tubulina" y está relacionado con el reconocimiento e interacción con proteínas asociadas a microtúbulos.

Los dímeros de tubulina con GTP en el sitio E son los que se incorporan al microtúbulo (Fig. 1). Al aproximarse al extremo de este, el nuevo dímero coloca el dominio de activación de la subunidad α cerca del dominio GTPasa de la subunidad β del último dímero incorporado. Esto conduce a su activación e hidrólisis de GTP a GDP. La región del microtúbulo que contiene GDP es más propensa a despolimerizar, pero se encuentra estabilizada por medio de los contactos laterales entre protofilamentos y la región de dímeros con GTP o GDP + P_i expuesta en los extremos, lo que se conoce como GTP-*cap* (Fig. 1).

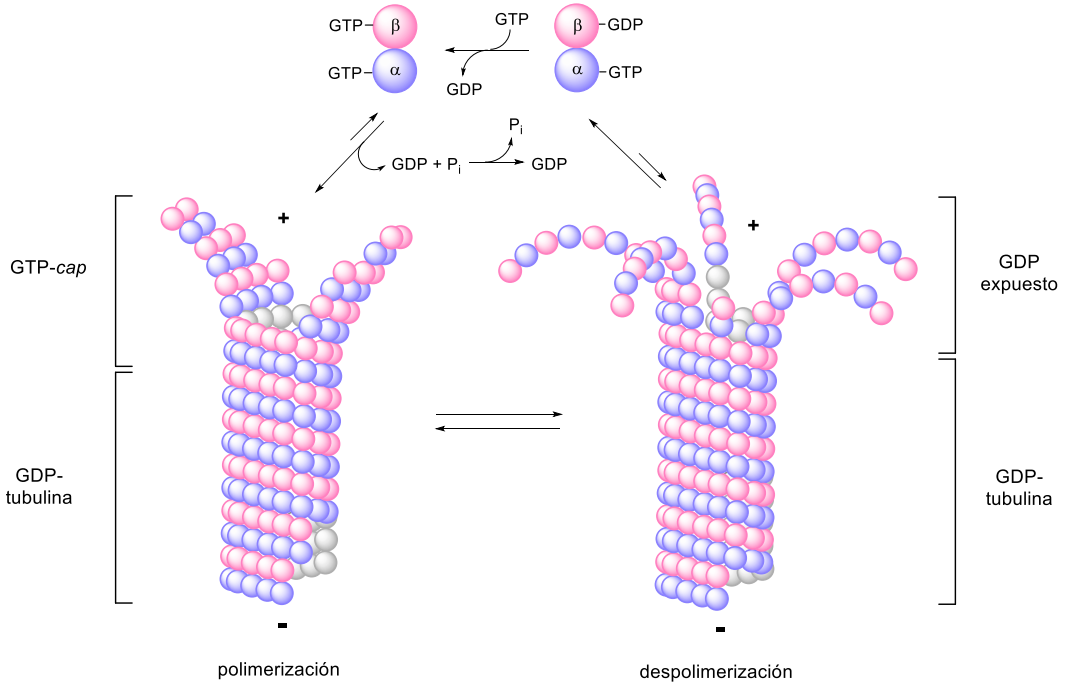

Figura 1. Esquema de los procesos de crecimiento y acortamiento de microtúbulos. El nucleótido del sitio E se intercambia en dímeros solubles, siendo GTP-tubulina la que se incorpora a los microtúbulos con la posterior hidrólisis del nucleótido. Los microtúbulos en crecimiento muestran un extremo cónico con una región GTP-*cap* que estabiliza la región con GDP, que es más propensa a despolimerizar. La exposición de GDP-tubulina en el extremo o estabilización insuficiente lleva a la pérdida de contactos laterales entre protofilamentos y despolimerización.

El dominio de colchicina

Se han descrito siete sitios adicionales de unión de ligandos en tubulina, divididos en base al efecto sobre la masa de microtúbulos en agentes estabilizantes de microtúbulos (MSAs) y agentes desestabilizantes de microtúbulos (MDAs). Los agentes estabilizantes engloban a los ligandos que se unen al sitio de paclitaxel y al sitio de laulimalida/pelorusido A. Los sitios de unión de agentes desestabilizantes incluyen el sitio de los alcaloides de la vinca, eribulina, maytansina, pironetina y colchicina. Independientemente de su acción estabilizante o desestabilizante, todos los compuestos que se unen a tubulina interfieren en la dinámica de los microtúbulos y, por tanto, impiden su correcto funcionamiento, actuando como agentes antimitóticos.

En este trabajo nos hemos centrado en el diseño de ligandos para su unión al dominio de colchicina. Este bolsillo de interacción constituye un entorno bastante hidrofóbico que se encuentra situado en la subunidad β, concretamente en la interfaz entre subunidades α y β del mismo dímero. Colchicina muestra un perfil de toxicidad elevado, por lo que no se emplea en la quimioterapia antitumoral. Se han descrito multitud de complejos de rayos X de tubulina con ligandos estructuralmente diversos que presentan diferentes modos de interacción. En base a estas estructuras, el sitio de unión de colchicina se suele dividir en tres zonas de interacción consecutivas (zonas 1, 2 y 3). Dentro de estos compuestos, la mayoría de ligandos interaccionan con las zonas 1 y 2 (Fig. 2, colchicina), muchos otros con las zonas 2 y 3 (Fig. 2, MI-181), y únicamente se conocen tres estructuras que interaccionen con las tres zonas de manera simultánea, aunque de forma parcial con al menos una de ellas (Fig. 2, ABT-751).

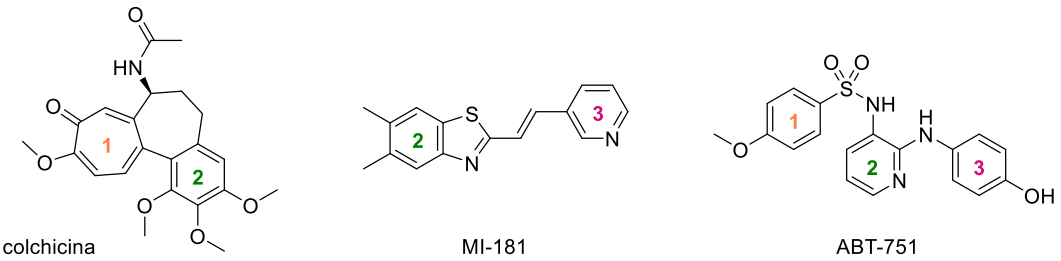

Figura 2. Estructuras químicas de tres ligandos que se unen al dominio de colchicina. Colchicina se une a las zonas 1 y 2, MI-181 se une a las zonas 2 y 3, y ABT-751 se une a las zonas 1, 2 y 3, aunque de forma parcial a la zona 3.

OBJETIVOS

El objetivo de este trabajo es obtener compuestos con propiedades antitumorales que se unan al dominio de colchicina en tubulina. Hemos planteado el diseño de varias familias estructurales de ligandos para su unión a las zonas 1-2, zonas 2-3, o zonas 1-2-3 en base a la información proporcionada por los modelos de rayos X y estudios de relación estructura-actividad. Esta aproximación pretende obtener compuestos con propiedades mejoradas para estudiar su mecanismo de acción antitumoral.

Primer objetivo. Diseño, síntesis y caracterización de nuevos compuestos para su unión al dominio de colchicina.

- ✓ Síntesis de sulfonamidas y tetrazoles para su unión a las zonas 1-2.
- ✓ Síntesis de sulfonamidas para su unión a las zonas 1-2-3.
- ✓ Síntesis de amidas, ureas y carbamatos para su unión a las zonas 2-3.
- ✓ Preparación de derivados de benzotiazol para su unión a las zonas 2-3.

Segundo objetivo. Estudio del potencial antitumoral y el mecanismo de acción de los compuestos resultantes del primer objetivo, así como el efecto de modificaciones estructurales en la actividad.

- ✓ Evaluación *in vitro* de la actividad antiproliferativa de los compuestos sintetizados frente a líneas celulares tumorales y no tumorigénicas para establecer modelos de relación estructura-actividad.
- ✓ Examinar el efecto de los compuestos en microtúbulos y estudiar si la tubulina es la diana farmacológica tras la respuesta observada.
- ✓ Estudiar si los compuestos presentan efectos antivasculares *in vitro* utilizando células endoteliales.
- ✓ Caracterizar el mecanismo de muerte celular tras el tratamiento: apoptosis (tipo I), autofagia (tipo II) o necrosis (tipo III).
- ✓ Evaluar si el efecto *in vitro* de los compuestos es reversible.

SULFONAMIDAS Y TETRAZOLES DIRIGIDOS A LAS ZONAS 1-2

Diseño de compuestos para su unión a las zonas 1-2

Hemos diseñado dos familias de compuestos buscando su interacción con las zonas 1 y 2 del dominio de colchicina en base a las estructuras de CA4, ABT-751 y A-293620 (Fig. 3). Estos nuevos ligandos están constituidos por un anillo de indol y un benceno polimetoxilado unidos por puentes de sulfonamida o tetrazol (Fig. 4).

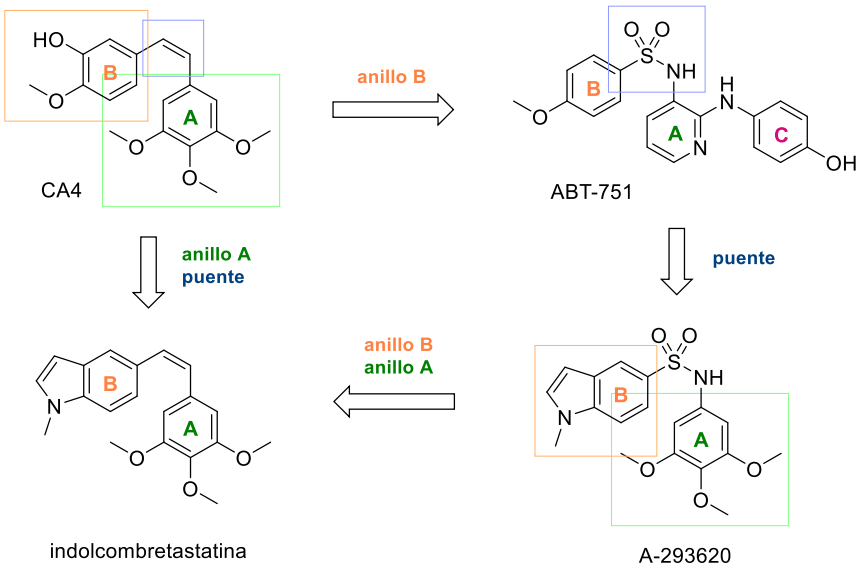

Figura 3. Estructuras químicas de CA4, ABT-751, A-293620 e indolcombretastatina. El anillo B aparece marcado en **naranja**, el anillo A en color **verde**, y el puente que conecta ambos anillos está indicado en **azul**.

Los compuestos que interaccionan en las zonas 1 y 2 del dominio de colchicina colocan sus anillos aromáticos en una disposición relativa *cisoide* y no coplanar. CA4 tiene dos fenilos unidos por un puente de olefina *Z* (Fig. 3). El anillo fenólico (anillo B) se une en la zona 1, y el anillo 3,4,5-trimetoxifenilo (anillo A) interacciona en la zona 2. La olefina *Z* dispone los anillos aromáticos de forma favorable para la interacción con la proteína, si bien es cierto que se isomeriza fácilmente a la olefina *E* que es termodinámicamente más estable y menos potente. Para evitar el problema de la isomerización, hemos sustituido la olefina por grupos sulfonamida o tetrazol (Fig. 4). Compuestos como ABT-751 o A-293620 también presentan grupos sulfonamida que mejoran la solubilidad acuosa (ABT-751 permite su administración por vía oral), y además colocan preferentemente los anillos aromáticos en disposiciones relativas *cisoides*. Los anillos de tetrazol suponen una alternativa rígida a las sulfonamidas.

El grupo fenólico de CA4 sufre metabolismo por conjugación. Por este motivo, decidimos sustituir el anillo B de CA4 por un anillo de indol (Fig. 4), presente en compuestos como A-293620 y otros indoles relacionados con CA4, como las indolcombretastatinas (Fig. 3). CA4 muestra una baja solubilidad acuosa, lo que suele solventarse mediante la formulación de profármacos sobre la posición fenólica. Al reemplazar este anillo por un indol, es necesario introducir sustituyentes polares o grupos solubilizadores en otras partes de la estructura para contrarrestar la pérdida del hidroxilo en términos de solubilidad. Decidimos explorar el efecto sobre la actividad de modificaciones en la posición 3 del anillo de indol (R_3) y sobre el nitrógeno de la sulfonamida (R_N).

En cuanto al anillo A, el grupo 3,4,5-trimetoxifenilo es común a varios ligandos del sitio de colchicina y se suele considerar importante para la actividad biológica. En este trabajo hemos planteado además utilizar otras alternativas a este anillo. Decidimos eliminar el metoxilo central en la posición 4 para contrarrestar el incremento de tamaño en la región del puente tras sustituir la olefina por grupos sulfonamida o tetrazol, explorando así el efecto sobre la actividad de grupos 3,5-dimetoxifenilo y 2,5-dimetoxifenilo (Fig. 4).

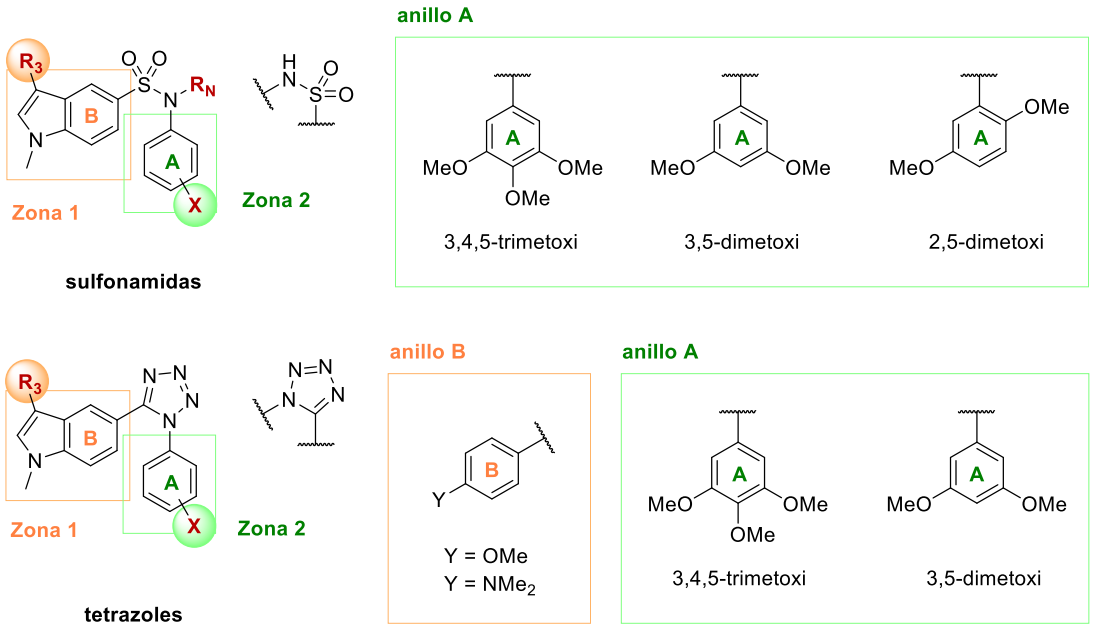

Figura 4. Estructuras generales de los compuestos diseñados para su unión a las zonas 1-2 del dominio de colchicina. Estos compuestos presentan grupos sulfonamida o tetrazol entre dos anillos aromáticos B y A. El **anillo B** es un grupo *N*-metil-5-indolilo, además de *p*-metoxifenilo y *N,N*-dimetilaminofenilo en el caso de tetrazoles. Para el **anillo A** hemos explorado bencenos con sustituciones 3,4,5-trimetoxi, 3,5-dimetoxi y 2,5-dimetoxi.

Síntesis de sulfonamidas 78-140 y tetrazoles 141-190

Las sulfonamidas se prepararon por reacción entre un cloruro de sulfonilo y diferentes aminas aromáticas en presencia de una base. Se utilizó trietilamina para reacciones en CH_2Cl_2 y $NaHCO_3$ para reacciones bifásicas en EtOAc/agua. La gran mayoría de las sulfonamidas preparadas presentan la sulfona en la posición 5 del anillo de indol, a excepción del compuesto **99**, que muestra una orientación cambiada con la sulfona unida al anillo de benceno. El compuesto **99** se preparó por reacción entre 1-metil-1*H*-indol-5-amina (**13**) y el cloruro de sulfonilo **6**. El resto de sulfonamidas se prepararon a partir del cloruro de sulfonilo en posición 5 de 1-formilindolina (**5**). En estos casos, tras la formación de la sulfonamida, se llevó a cabo la reducción del grupo formilo a metilo y la posterior aromatización del anillo de indolina a indol (Esquema 1).

Una vez obtenidas las indol sulfonamidas, se introdujeron diferentes sustituyentes en el nitrógeno del puente por sustitución nucleofílica con un derivado halogenado en ACN/KOH o DMF/K_2CO_3. Estos sustituyentes incluyen grupos metilo, etilo, acetonitrilo, acetato de etilo o bencilos. Además, se llevaron a cabo modificaciones en el anillo de indol comunes a las de los tetrazoles (Esquema 3).

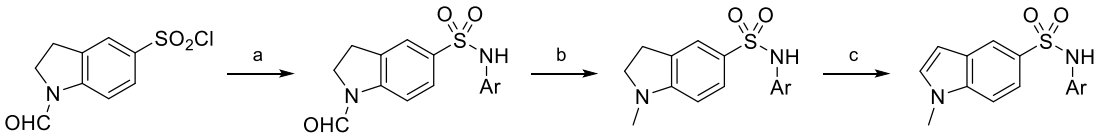

Esquema 1. Preparación de sulfonamidas. Reactivos y condiciones: (a) Ar-NH_2, EtOAc/H_2O y $NaHCO_3$ o CH_2Cl_2 y Et_3N, t.a., 4-19 h, N_2. (b) $NaBH_4$, Cl_3CCOOH, THF, 4 °C-t.a., 4-72 h, N_2. (c) DDQ, THF, 4 °C-t.a., 24-72 h, N_2.

Los compuestos con un anillo de tetrazol se obtuvieron a partir de las amidas correspondientes (Esquema 2). El enlace amida se formó por reacción entre un ácido carboxílico y una amina aromática en presencia de *p*-DMAP e hidrocloruro de EDC como catalizador de transferencia de fase. La conversión de amidas en tetrazoles se llevó a cabo a 80-90 °C en ACN con azida sódica y $SiCl_4$.

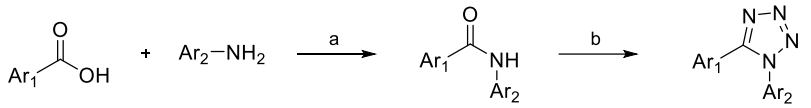

Esquema 2. Preparación de amidas y tetrazoles. Reactivos y condiciones: (a) i) Ar_1-COOH, EDC·HCl, *p*-DMAP, CH_2Cl_2, reflujo, 1-3 h, N_2; ii) Ar_2-NH_2, reflujo, 6 h-9 días, N_2. (b) NaN_3, $SiCl_4$, ACN, 80-90 °C, 3-6 días.

Una vez obtenidos los compuestos con puente de sulfonamida o tetrazol, se llevaron a cabo sustituciones electrofílicas aromáticas sobre la posición 3 del anillo de indol, altamente reactiva: bromaciones, introducción de grupos formilo y amida (Esquema 3). La reacción con NBS en CH_2Cl_2 dio lugar a compuestos bromados. El grupo amida se introdujo por reacción con CSI en 1,2-dicloroetano. Los derivados formilados se obtuvieron mediante la reacción de Vilsmeier-Haack utilizando $POCl_3$ y DMF. A partir de los compuestos con indol-3-carbaldehído se prepararon nitrilos mediante la formación previa de oximas, seguido de su acetilación y eliminación a 130 °C. La reacción de grupos formilo con ACN en medio básico dio lugar a la mezcla *E+Z* de propenonitrilos, separados mediante cromatografía preparativa (Esquema 3).

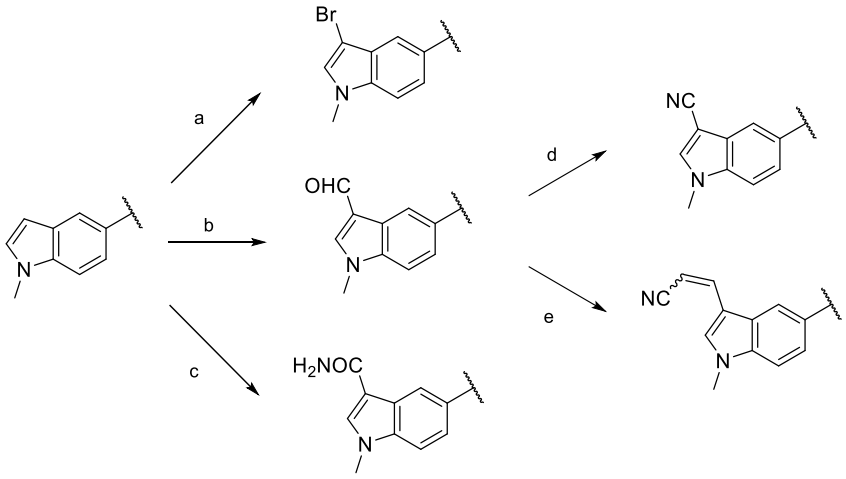

Esquema 3. Modificaciones sobre la posición 3 del anillo de indol. Reactivos y condiciones: (a) NBS, CH_2Cl_2, temperatura variable, 5 min-4 días. (b) i) $POCl_3$, DMF, 4 °C, 30 min, N_2; ii) derivado indólico, DMF, 4 °C, 5 min-2 h, N_2. (c) CSI, $C_2H_4Cl_2$, 4 °C-t.a., 3-24 h, N_2. (d) i) NH_2OH·HCl, piridina, MeOH, reflujo, 12-48 h, N_2; ii) Ac_2O, piridina, 130 °C, 30 h-4 días, N_2. (e) KOH, ACN, t.a., 6-7 días, N_2.

Actividad antiproliferativa: relación estructura-actividad

Los compuestos sintetizados fueron ensayados para determinar su actividad antiproliferativa *in vitro* frente a las líneas celulares tumorales humanas HeLa (adenocarcinoma de cérvix), HT-29 (adenocarcinoma colorrectal), HL-60 (leucemia mieloide aguda) y AGS (adenocarcinoma gástrico), además de la línea no tumorigénica humana de riñón HEK-293. Los compuestos mostraron CI_{50} en el rango submicromolar o nanomolar (ver páginas 134-135 para sulfonamidas y 138-139 para tetrazoles), con potencias similares o incluso superiores en algún caso a las de ligandos de referencia del sitio de la colchicina, como CA4. Las diferentes líneas celulares mostraron perfiles de sensibilidad muy similares entre ellas para cada compuesto evaluado.

Adicionalmente, se estudió el efecto sobre la proliferación de células HeLa en presencia de inhibidores de transportadores MDR (verapamilo y elacridar). Los resultados de CI_{50} bajo estas condiciones apenas mostraron diferencias con los obtenidos en ausencia de dichos inhibidores. Esto indicaría que, por lo general, los ligandos evaluados no son sustratos de este tipo de proteínas exportadoras, que es uno de los mecanismos de resistencia más frecuentes a fármacos que se unen a tubulina, como es el caso de paclitaxel.

Los resultados obtenidos para los compuestos con un puente de sulfonamida revelan la importancia del patrón de sustitución del anillo de benceno. Los ligandos con un anillo 3,4,5-trimetoxifenilo mostraron potencias en torno a un orden de magnitud superiores a los compuestos con un anillo 3,5-dimetoxifenilo, que a su vez resultaron más potentes que aquellos con 2,5-dimetoxifenilo. La bromación en posición 4 del anillo 2,5-dimetoxifenilo mejoró la actividad antiproliferativa de los compuestos. La metilación de la sulfonamida dio lugar a los compuestos más potentes dentro de cada serie, aunque el efecto de sustituyentes de mayor tamaño depende de la naturaleza el anillo de benceno. Independientemente de la presencia de sustituyentes en la sulfonamida o la sustitución del benceno, la introducción de grupos en posición 3 del anillo de indol presenta un efecto negativo sobre la actividad antiproliferativa de los compuestos.

La conversión del puente de amida en anillos de tetrazol mejoró notablemente la potencia de los compuestos. En esta familia de ligandos, el cambio de 3,4,5-trimetoxifenilo por 3,5-dimetoxifenilo no muestra un patrón claro sobre la actividad biológica, que difiere en función de los sustituyentes sobre el anillo de indol. Al igual que ocurre con las sulfonamidas, la introducción de sustituyentes sobre la posición 3 del anillo de indol reduce considerablemente la potencia de los compuestos. Además de este anillo, se estudió el efecto de 4-dimetilaminofenilo y 4-metoxifenilo, ambos menos potentes que los derivados indólicos, sobre todo aquellos con un anillo de 4-metoxifenilo. La orientación del anillo de tetrazol, especialmente en presencia de sustituyentes sobre el indol, también influye en el perfil antitumoral, siendo más potentes los compuestos que presentan el fenilo sobre la posición 1 del tetrazol.

En base a estos resultados se seleccionaron un total de seis compuestos representativos (Fig. 5), el más potente de cada una de las familias estructurales, para estudiar en mayor detalle el mecanismo de acción antitumoral de los compuestos y si las diferencias en la estructura se traducen en cambios significativos en la actividad farmacológica. Estos seis compuestos fueron evaluados también frente a las líneas celulares tumorales humanas SNU-1 (adenocarcinoma gástrico), RPMI-8226 y U266 (mieloma múltiple), la línea no tumorigénica murina 3B-11 y fibroblastos primarios de dermis de ratón, obteniendo en la mayoría de los casos valores de CI_{50} muy similares para cada compuesto.

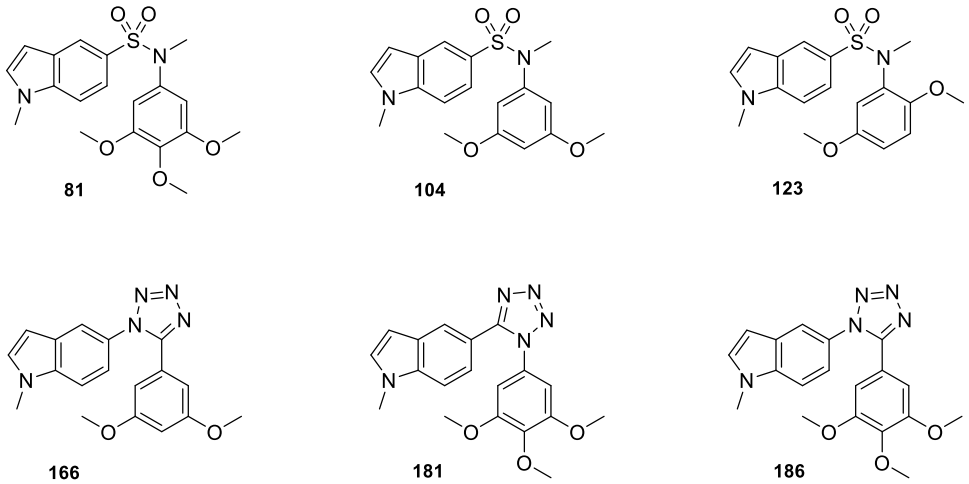

Figura 5. Estructuras químicas de los compuestos que fueron seleccionados para el estudio del mecanismo de acción antitumoral en este trabajo.

Mecanismo de acción: tubulina es la diana biológica

Los resultados de este trabajo indican que la combinación de un anillo *N*-metil-5-indol unido mediante puentes de sulfonamida o tetrazol a un benceno polimetoxilado conduce a compuestos capaces de interaccionar con el dominio de colchicina en tubulina, presentando propiedades antimitóticas y antivasculares.

Se estudió la distribución de las fases del ciclo celular para todos los compuestos a tres concentraciones (10 nM, 100 nM y 1 µM) y tres tiempos (24 h, 48 h y 72 h), a fin de evaluar si la potencia mostrada por los ligandos en este tipo de experimentos correlaciona con los valores de CI_{50} en ensayos de proliferación celular. Los compuestos que resultaron activos en los ensayos de proliferación celular también mostraron una parada del ciclo celular en G_2/M dependiente de la dosis de tratamiento y el tiempo de incubación. La acumulación de células en la región G_2/M (4n) procede de una parada en fase de mitosis, como se vio mediante el incremento de la señal para MPM-2 por *Western blot*. Tales hallazgos apuntan a un mecanismo de acción antimitótico. La correlación entre las concentraciones necesarias para producir una parada del ciclo celular y los valores de CI_{50} sugieren que la interrupción de la proliferación celular está relacionada con el efecto antimitótico.

Los experimentos de inmunofluorescencia indirecta marcando α-tubulina mostraron la desorganización del citoesqueleto de tubulina, compatible con un mecanismo desestabilizante de microtúbulos. Los ensayos bioquímicos *in vitro* realizados con tubulina aislada de cerebros bovinos mostraron la inhibición de la polimerización dependiente de la dosis utilizada para la mayoría de los compuestos ensayados (ver páginas 154-155), lo que estaría de acuerdo con el efecto observado por microscopía confocal. Algunos de los compuestos más potentes mostraron valores de CI_{50} frente a la polimerización *in vitro* de tubulina comparables al de CA4. Se llevaron a cabo experimentos de desplazamiento de MTC con algunos de los compuestos sintetizados, a fin de determinar si existe competición con dicho ligando por la unión al dominio de colchicina. MTC se emplea como sonda, ya que emite fluorescencia cuando se une a tubulina, de modo que la comparación del espectro de emisión de fluorescencia de MTC-tubulina con los espectros obtenidos al añadir concentraciones crecientes de ligandos permite determinar no solamente si existe unión al dominio de colchicina, sino también la afinidad de dicha interacción. De este modo confirmamos

la unión de varios compuestos al sitio de colchicina, con afinidades comparables a las de ligandos de referencia como MTC o podofilotoxina, incluso colchicina en algún caso. A pesar de que no se llevaron a cabo estos experimentos con todos los compuestos, podríamos asumir que todos los que inducen un efecto análogo a los que sí se ensayaron sobre la red de microtúbulos y el ciclo celular también se unirían al sitio de la colchicina dada la similitud estructural.

Los seis compuestos seleccionados como referencia mostraron un perfil antivascular en ensayos *in vitro* de formación de estructuras de tipo capilar. Estos ensayos se realizaron con la línea celular endotelial murina 3B-11. Los resultados obtenidos indican que los compuestos inhiben la formación de redes tubulares en función de la dosis empleada, efecto que correlaciona con las potencias observadas en ensayos de proliferación frente a esa misma línea celular.

Inducción de muerte celular tras el tratamiento

El estudio de los mecanismos de muerte celular tras el tratamiento con los ligandos seleccionados ha revelado que las células HeLa sufren principalmente apoptosis dependiente de caspasas. Tras la acumulación de células en G_2/M, se produjo un incremento dependiente del tiempo en la región $SubG_0/G_1$, que corresponde al pico hipodiploide de células que presentan fragmentación en el ADN, siendo este hecho indicativo de apoptosis. La respuesta apoptótica se produce tras la parada celular en mitosis, ya que la inhibición farmacológica de caspasas con Z-VAD-fmk impide la consecución de la muerte por apoptosis, pero no afecta al bloqueo mitótico. Estas observaciones están apoyadas por diferentes marcadores de apoptosis, además del *blebbing* de la membrana observado mediante microscopía *time-lapse*, característico de un fenotipo apoptótico. Tras el tratamiento, se detectó un incremento en los niveles de citocromo c citosólico liberado desde las mitocondrias, así como la aparición de los fragmentos activos de las caspasas 9 y 3. La activación de caspasas se acompaña de la escisión de PARP en un fragmento de menor tamaño, que es un marcador bioquímico indicativo de apoptosis. Los experimentos de citometría de flujo mostraron un incremento en el porcentaje de células positivas para Anexina V tras la incubación con los ligandos. Esta proteína interacciona con PtdSer, un fosfolípido de membrana que se reorganiza en la región externa de la membrana plasmática en respuesta a la activación de la cascada apoptótica, a modo de señal para su reconocimiento por células fagocíticas. La muerte celular observada en células HeLa tras el tratamiento con los ligandos puede prevenirse inhibiendo la función de caspasas efectoras con Z-VAD-fmk, lo que evidencia la dependencia de caspasas. La combinación con este inhibidor dio lugar a una caída drástica en los porcentajes de células positivas para Anexina V, de células en la región $SubG_0/G_1$ y la ausencia de fragmentación de PARP.

Por el contrario, no se encontró una contribución significativa de la muerte celular por necrosis. Los experimentos de videomicroscopía *time-lapse* no registraron la presencia de células necróticas. Aun así, se observó un incremento dependiente del tiempo en el porcentaje de células permeables a ioduro de propidio, siendo indicativo de daño en la membrana plasmática. Sin embargo, las células positivas a ioduro de propidio lo eran también a Anexina V. Este hallazgo, junto con el hecho de que la inhibición de caspasas inhibió la permeabilización de la membrana, indica que la aparición de células permeables a ioduro de propidio es una consecuencia de la respuesta apoptótica, y no se considera muerte por necrosis, sino apoptosis tardía o necrosis secundaria a apoptosis. Asimismo, el tratamiento conjunto con los ligandos y el inhibidor de RIPK1 necrostatina-1 no produjo cambios significativos en los porcentajes de células en la región $SubG_0/G_1$, por lo que puede considerarse que la necroptosis no contribuye a la muerte celular global en células HeLa.

El incremento en los niveles de LC3-II tras el tratamiento con los ligandos, junto con el efecto aditivo en combinación con bafilomicina A1, sugiere una cierta inducción en el flujo autofágico en células HeLa. Esto, sin embargo, no implica necesariamente que se esté produciendo la fusión de vesículas autofágicas y lisosomas para la degradación de su contenido. El co-tratamiento con los compuestos seleccionados y bafilomicina A1 mostró una serie de cambios en marcadores de muerte celular con respecto al efecto de los compuestos por separado. Se detectaron fluctuaciones en los porcentajes de células en la región $SubG_0/G_1$, en los marcajes con Anexina V y ioduro de propidio, y en los niveles de fragmentación de PARP. Aun así, la tendencia observada para cada uno de los tratamientos no fue la misma. Al emplear un inhibidor de autofagia distinto a bafilomicina A1, cloroquina, no observamos cambios en la fragmentación del ADN ni en la permeabilización de la membrana plasmática, indicando que la autofagia no desempeña un papel relevante respecto a la muerte celular global.

La cuantificación de las poblaciones hipodiploides en $SubG_0/G_1$ en diferentes líneas celulares tras el tratamiento con los ligandos seleccionados mostró que una parada sostenida en mitosis no es necesariamente suficiente para la inducción de la respuesta apoptótica. Se encontraron grandes diferencias entre líneas tumorales y líneas no tumorigénicas en cuanto a la fragmentación del ADN y la permeabilización de la membrana plasmática. Algunas de las líneas celulares mostraron sensibilidades similares a los tratamientos en ensayos de proliferación, en paralelo con una acumulación de células en la región G_2/M. Sin embargo, estos efectos antimitóticos no correlacionan con una respuesta apoptótica similar. Las diferentes líneas celulares estudiadas mostraron distinta propensión a la inducción de apoptosis. Es el caso de las líneas no tumorigénicas HEK-293, HPNE, BHK y L929, con porcentajes de células hipodiploides muy inferiores a los obtenidos para células tumorales HeLa, Mia PaCa-2, U2OS, AGS y SNU-1. La línea Huh-7, también tumoral, mostró un comportamiento más similar al de células no tumorigénicas. La escasa respuesta apoptótica no indica que las líneas celulares sean más resistentes *per se*, sino que viene dado por el mecanismo de acción de los compuestos. Así, las células HPNE sí sufren apoptosis en respuesta al fármaco estaurosporina, pero no en respuesta a fármacos que se unen a tubulina pese a una parada prácticamente total en mitosis.

Alteraciones relacionadas con la mitocondria en respuesta al tratamiento

El análisis de la fracción proteica libre de mitocondrias ha mostrado un incremento dependiente del tiempo en los niveles de citocromo c, que se libera desde el espacio intermembrana mitocondrial para la activación posterior de la caspasa 9. Estos resultados muestran la implicación de la mitocondria en la inducción de apoptosis tras el tratamiento con los ligandos seleccionados.

El marcaje con $DiOC_6[3]$ y DHE permite estudiar mediante citometría de flujo los cambios en el potencial mitocondrial transmembrana ($\Delta\Psi_m$) y en los niveles intracelulares de especies reactivas de oxígeno (ROS) en respuesta al tratamiento. Observamos un incremento en los niveles de ROS tras tiempos de incubación para los cuales no se observaron cambios en el potencial mitocondrial. A pesar de esta diferencia, la evolución en los niveles de ROS y en el potencial mitocondrial transmembrana sigue una tendencia en paralelo para los diferentes tiempos de incubación. Detectamos dos poblaciones diferenciadas de células HeLa a tiempos de incubación más largos: una población que presenta depleción o despolarización en $\Delta\Psi_m$, sugiriendo la pérdida de integridad de la membrana mitocondrial, y una segunda población aparentemente hiperpolarizada. Los cambios en $\Delta\Psi_m$ parecen sobrevenir no como un evento desencadenante de apoptosis, sino cuando ya existe activación del proceso.

En base a estos resultados, decidimos estudiar los cambios tras el tratamiento en los niveles de proteínas antiapoptóticas de la familia Bcl-2: Bcl-2, Bcl-xL y Mcl-1, que podrían estar implicadas en la interconexión entre la parada prolongada en mitosis y la inducción de muerte celular. Los resultados de *Western blot* mostraron una tendencia común para P-Bcl-2, Bcl-xL y Mcl-1; existe una inducción inicial transitoria en los niveles de dichas proteínas seguida de una depleción en los niveles detectados. Esta disminución se produce antes en el tiempo en el caso de Mcl-1. Esto sugiere que la fosforilación de Bcl-2 y el incremento en la expresión de Bcl-xL y Mcl-1 podría desempeñar un papel protector inicial, lo que estaría de acuerdo con la disminución de los niveles a medida que se induce la respuesta apoptótica.

Dado que muchos tumores sobreexpresan proteínas como Bcl-xL y Bcl-2, estudiamos si un incremento en la expresión de estas dos proteínas favorece la resistencia de las células al tratamiento. Para ello se utilizaron células HeLa transfectadas, que sobreexpresaban Bcl-xL o Bcl-2. La comparación de la respuesta de muerte celular en células transfectadas versus células *wild type* indica que estas dos proteínas pueden proteger a las células de la inducción de apoptosis, lo que se manifiesta con un retraso de aproximadamente un día en el incremento de células en la región $SubG_0/G_1$ y en una atenuación de la fragmentación de PARP, sobre todo en el caso de sobreexpresión de Bcl-2. Esta protección es parcial y no afecta a la parada mitótica y a la desorganización del citoesqueleto de tubulina.

Reversibilidad de la respuesta al tratamiento

En base a los resultados reflejados en estudios anteriores, que muestran cómo la parada mitótica no es irreversible sino un proceso que puede revertirse, decidimos estudiar si estos hallazgos eran también aplicables en el caso de los fármacos seleccionados. En este trabajo hemos mostrado que la acumulación de células HeLa en la región G_2/M en respuesta al tratamiento puede revertirse en función del tiempo previo de incubación con los ligandos. La recuperación de una distribución normal de las fases del ciclo celular está relacionada con la re-polimerización de los microtúbulos como evidenciaron los experimentos de microscopía confocal. Este proceso de re-polimerización de tubulina depende, al menos en parte, de la síntesis de proteínas.

En un principio, hipotetizamos que la posible reversibilidad del efecto antimitótico dependería del grado de apoptosis observado en las muestras. Sin embargo, los experimentos de rescate realizados en células que apenas presentan apoptosis (HEK-293 y HPNE) en respuesta al tratamiento indicaron que la parada mitótica puede no ser reversible a tiempos de incubación para los cuales no se observa muerte celular. Nuestros resultados en su conjunto sugieren que la reversibilidad del efecto antimitótico depende del período de incubación previo y el tiempo transcurrido entre la parada mitótica y el momento del rescate, en lugar de si existe o no inducción de apoptosis.

A nivel mitocondrial, observamos una serie de cambios principalmente en el potencial mitocondrial transmembrana, pero también en los niveles de ROS. Tras el rescate, se registró un cierto grado de hiperpolarización mitocondrial. A pesar de que inicialmente pensamos que esta condición podría suponer una protección de las células frente a un nuevo daño, vimos que las células HeLa totalmente recuperadas del efecto antimitótico inducido por incubaciones de 15 h con los ligandos, mostraron mayor sensibilidad frente a un nuevo ciclo de tratamiento con los mismos compuestos.

SULFONAMIDAS DIRIGIDAS A LAS ZONAS 1-2-3

Diseño de compuestos para su unión a las zonas 1-2-3

Para el diseño de compuestos dirigidos a las zonas 1-2-3 del dominio de colchicina tomamos como modelo estructural ABT-751 (Fig. 6). Esta sulfonamida presenta un perfil farmacocinético óptimo, permitiendo la administración oral, aunque la falta de eficacia *in vivo* hizo que no pasara a fase III de ensayos clínicos. ABT-751 está formado por tres anillos aromáticos: un anillo *p*-metoxifenilo (anillo B) que interacciona en la zona 1, una piridina 2,3-disustituida (anillo A) que se une a la zona 2 del dominio, y un anillo fenólico (anillo C) que presenta una interacción con la zona 3 de forma parcial.

La superposición de la pose de interacción de ABT-751 y otros ligandos como nocodazol sugiere que un patrón de sustitución diferente de la piridina central podría favorecer el acceso a la zona 3 (ver Fig. 29, página 79). En base a esto, decidimos sustituir el anillo A de ABT-751 con una sustitución 1,2 por anillos de 2,6-diaminopiridina y *m*-fenilendiamina, ambos con sustitución 1,3, manteniendo el anillo B de *p*-metoxifenilo para su interacción en la zona 1 y el puente de sulfonamida. Esto se hizo con el objetivo de explorar una geometría diferente intentando buscar una interacción con la zona 3. En cuanto al tercer anillo, elegimos grupos fenilo en base a su similitud con otros ligandos de la zona 3. Para permitir un acceso de forma completa a la zona 3, modificamos el grupo amino de ABT-751 entre los anillos A y C por conectores de diferente longitud con el objetivo de conferir flexibilidad y mejorar la solubilidad acuosa: bencilaminas, benzamidas, fenilacetamidas o fenilsulfonamidas (Fig. 6). Sobre este tercer anillo se exploraron también diferentes sustituyentes, ya que la zona 3 es una región menos hidrofóbica en comparación con las zonas 1 y 2.

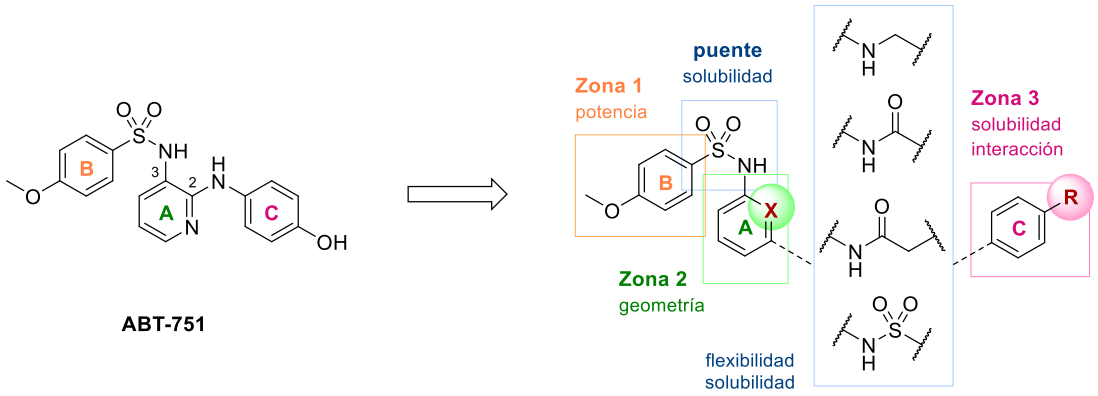

Figura 6. Propuesta estructural de compuestos para su interacción con las zonas 1-2-3 en base a la estructura de ABT-751. Se mantuvo el anillo de *p*-metoxifenilo como **anillo B**, unido mediante un puente sulfonamida a **anillos A** de piridina (X=N) o benceno (X=CH) con sustitución 1,3. Se exploraron varios conectores entre el anillo A y el **anillo C**.

Síntesis de sulfonamidas 35-77

Los compuestos propuestos se prepararon a partir de cloruro de 4-metoxibencenosulfonilo y *m*-fenilendiamina o 2,6-diaminopiridina (Esquema 4). Esta reacción se llevó a cabo en presencia de Et_3N o piridina como bases en CH_2Cl_2 o metanol. Al utilizar aminas bifuncionales, además de las monosulfonamidas, se obtuvieron también disulfonamidas por reacción de cada grupo amino con una molécula de cloruro de sulfonilo (Esquema 4). Esto se minimizó usando Et_3N en lugar de piridina.

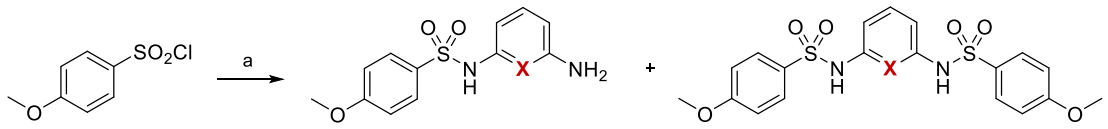

Esquema 4. Preparación de sulfonamidas. Reactivos y condiciones: (a) *m*-fenilendiamina o 2,6-diaminopiridina, Et_3N o piridina, CH_2Cl_2 o MeOH, t.a.-reflujo, 4-72 h, N_2.

Una vez formada la sulfonamida, se llevó a cabo la metilación del nitrógeno mediante sustitución nucleofílica. Primero se formó el anión en KOH y ACN o en condiciones de transferencia de fase, añadiendo después ioduro de metilo.

Para el acceso a la zona 3 del dominio de colchicina, se incorporó un tercer anillo aromático (anillo C) sobre el grupo amino libre. Este tercer anillo se unió por medio de grupos sulfonamida, amida o metilamina. La preparación de sulfonamidas se llevó a cabo de forma análoga a lo ya explicado anteriormente. En el caso de los grupos amida o metilamina, se intentaron dos aproximaciones diferentes (Fig. 7): i) la introducción del anillo C (Ar_3) una vez formada ya la sulfonamida (**ruta A**), o ii) la formación de la amida o metilamina con el **anillo A** de *m*-fenilendiamina o 2,6-diaminopiridina, formando en segundo lugar en enlace sulfonamida con el anillo B (Ar_1) (**ruta B**).

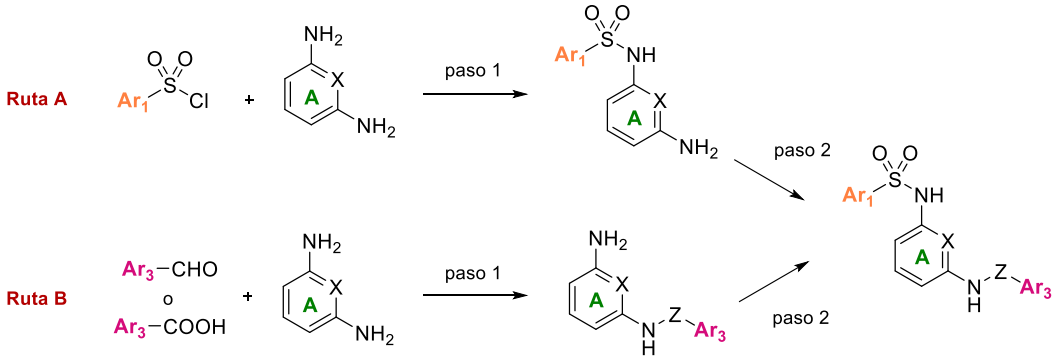

Figura 7. Formación de compuestos con tres anillos aromáticos. **Ruta A.** Formación del enlace sulfonamida en primer lugar, seguido de la incorporación del tercer anillo aromático (Ar_3). **Ruta B.** Aminación reductiva o formación de amidas con la diamina, seguido de la reacción con un cloruro de sulfonilo. Los grupos dirigidos a las zonas **1**, **2** y **3** están indicados en **naranja**, **verde** y **rosa**, respectivamente.

Tras testar diferentes condiciones, los mejores resultados en la reacción de aminación reductiva se obtuvieron mediante la reacción entre el aldehído y la amina en CH_2Cl_2 a reflujo para formar la imina, seguido de la reducción con $NaBH_4$ a temperatura ambiente en metanol.

Para obtener el enlace amida, se llevaron a cabo dos métodos sintéticos. En un caso se activó el ácido carboxílico con una carbodiimida (DCI o EDC) en presencia de *p*-DMAP en CH_2Cl_2 a reflujo o mediante irradiación en microondas a 130 °C, lo que redujo considerablemente los tiempos de reacción. Por otro lado, se formó el cloruro de ácido con $SOCl_2$, que se añadió después sobre la amina en CH_2Cl_2 con Et_3N a temperatura ambiente. A pesar de evaluar diferentes condiciones, los rendimientos obtenidos en las reacciones de formación de amidas no fueron demasiado elevados.

Sobre el anillo C se llevaron a cabo las modificaciones recogidas en el Esquema 5. Para la reducción de nitros aromáticos a anilinas se testaron tres condiciones de reacción: i) hidrogenación catalítica con Pd/C, ii) $SnCl_2 \cdot 2H_2O$, o iii) hierro en medio ácido, obteniendo en algún caso productos de hidrogenólisis. También se introdujo un bromo en *orto* del grupo amino mediante una reacción de sustitución electrofílica aromática con NBS. A partir de las anilinas se intentó la modificación para obtener ureas (X=O) y guanidinas (X=NH), aunque los resultados no fueron exitosos.

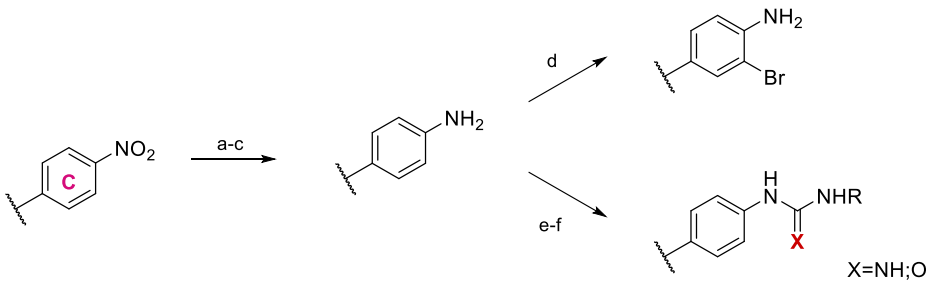

Esquema 5. Modificaciones a partir del grupo nitro sobre el **anillo C**. Reactivos y condiciones: (a) Pd/C, CH_2Cl_2/MeOH, t.a., 1-4 días, H_2. (b) $SnCl_2 \cdot 2H_2O$, EtOAc, t.a.-reflujo, 15 min-21 h, N_2. (c) Fe, HCl, AcOH/EtOH/H_2O, reflujo, 30 min-15 h, N_2. (d) NBS, CH_2Cl_2, 4 °C, 1-2 h, N_2. (e) KOCN o NH_2CN, agua/AcOH, 40-80 °C, 2-24 h, N_2. (f) BnNCO, CH_2Cl_2, reflujo, 24 h, N_2.

Los compuestos resultantes se evaluaron para determinar su actividad antiproliferativa frente a las líneas celulares tumorales HeLa, HT-29 y HL-60. Ninguno de ellos mostró inhibición del crecimiento a una concentración inicial de 1 µM.

AMIDAS, UREAS y CARBAMATOS DIRIGIDAS A LAS ZONAS 2-3

Diseño de compuestos para su unión a las zonas 2-3

Para el diseño de compuestos dirigidos a las zonas 2 y 3, nos basamos en las estructuras de CA4 y MI-181 (Fig. 8). MI-181 es una olefina *trans* con un anillo de benzotiazol y una piridina. El benzotiazol ocupa la zona 2 del dominio de colchicina, al igual que el grupo 3,4,5-trimetoxifenilo de CA4, mientras que el anillo de piridina interacciona en la zona 3.

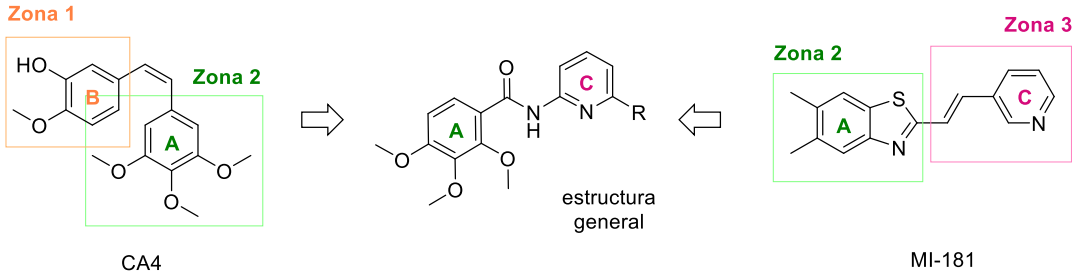

Figura 8. Estructuras químicas de CA4 y MI-181. En el centro se muestra la estructura general de los compuestos dirigidos a las zonas 2-3 como híbridos entre CA4 y MI-181. Como **anillo A** se utilizaron otros anillos polimetoxilados además de 2,3,4-trimetoxibenceno. El **anillo C** (piridinas u otros anillos aromáticos) se unió a través de grupos amida, ureas o carbamatos.

En lugar de benzotiazol, se utilizó un grupo 2,3,4-trimetoxifenilo (además de otras alternativas de bencenos polimetoxilados) para la unión a la zona 2. Los compuestos que interaccionan en las zonas 2 y 3 presentan una conformación extendida, por lo que en sustitución de la olefina *trans* de MI-181 utilizamos grupos amidas que muestran una geometría similar, incrementan la solubilidad acuosa y pueden establecer interacciones adicionales con la proteína. Además de amidas, también se evaluaron grupos urea o carbamato. Como anillo C exploramos principalmente piridinas con un amino adicional para su derivatización, pero también otro tipo de anillos aromáticos: benceno, naftaleno, isoxazol, etc.

Síntesis de compuestos 191-268

En primer lugar, se formó el enlace amida entre un ácido carboxílico y diferentes aminas aromáticas. Para ello, el ácido se trató con $SOCl_2$ obteniendo así el cloruro de ácido, que después se añadió sobre la amina en CH_2Cl_2 con Et_3N. En el caso de aminas bifuncionales con los grupos amino en posición relativa 1,3, se obtuvieron también diamidas (Esquema 6). Sobre el grupo amino libre se introdujeron diversas modificaciones utilizando una metodología sintética análoga a las reacciones ya descritas: grupos alquilo, amida, urea, carbamato.

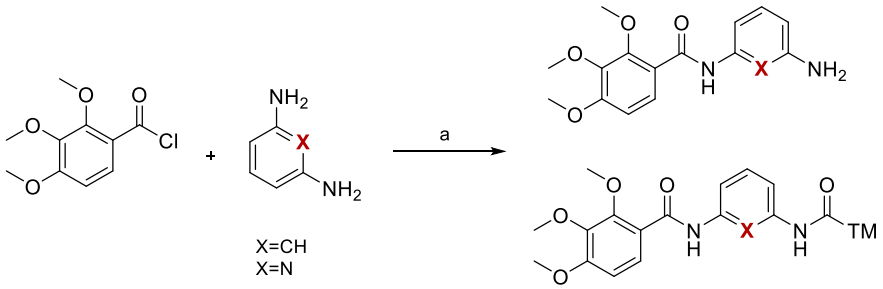

Esquema 6. Preparación de amidas. Reactivos y condiciones: (a) i) Ar-COOH, $SOCl_2$, t.a., 6-24 h. ii) R-NH_2, Et_3N, CH_2Cl_2, t.a., 5-15 h, N_2.

La reacción de cloruro de 2,3,4-trimetoxibenzoilo con aminas en posición 2 de nitrógenos de tipo piridina dio lugar a las imidas por reacción del mismo grupo amino con dos moléculas de cloruro de ácido. Esto pudo evitarse llevando a cabo la reacción con agentes de acoplamiento como EDC o DCI. Además de puentes amida, también se obtuvieron ureas por reacción de anilinas con isocianatos o carbamatos por reacción con cloroformiatos (Esquema 7).

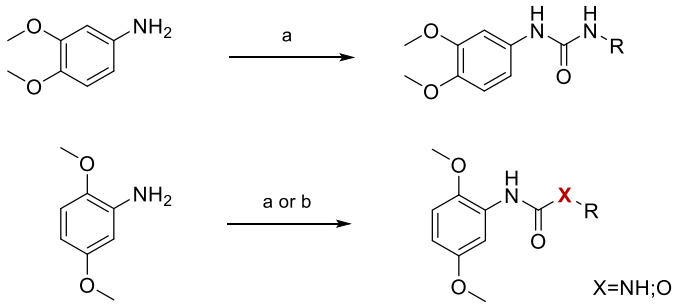

Esquema 7. Preparación de ureas y carbamatos. Reactivos y condiciones: (a) isocianato de etilo, fenilo o bencilo, CH_2Cl_2, t.a., 24 h-1 semana, N_2. (b) Cloroformiato de fenilo, Et_3N, CH_2Cl_2, t.a., 24 h, N_2.

Los compuestos se ensayaron frente a las líneas celulares tumorales HeLa, HT-29 y HL-60, pero no mostraron actividad antiproliferativa a una concentración de 1 µM.

BENZOTIAZOLES DIRIGIDOS A LAS ZONAS 2-3

Diseño de compuestos para su unión a las zonas 2-3

Esta familia de compuestos está basada en la estructura de MI-181, buscando una interacción similar con las zonas 2-3 del dominio de colchicina (Fig. 9). Como anillo A (zona 2) hemos mantenido el grupo 6-metilbenzotiazol, evaluando también el efecto de un bromo en posición 4. La olefina *trans* de MI-181 se sustituyó por grupos amida, urea, carbamato o alquilamina para dirigir el anillo C hacia la zona 3 manteniendo una conformación extendida. Para la zona 3 consideramos anillos de piridinas unidos por las posiciones 2, 3 o 4, además de fenilos y etilos.

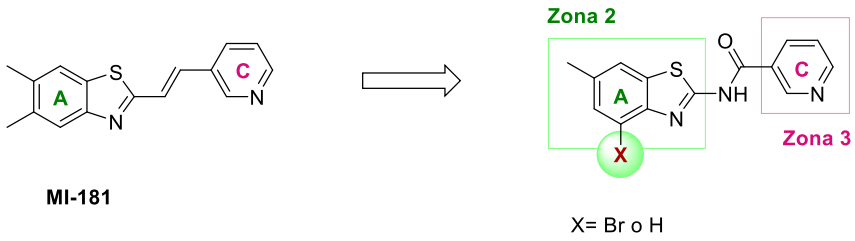

Figura 9. Propuesta estructural de compuestos para la interacción con las zonas 2-3 en base a MI-181. Se mantuvo un grupo 6-metilbenzotiazol como **anillo A**, unido mediante amidas, ureas, carbamatos o metilaminas al **anillo C** de piridina o benceno, además de grupos etilo.

Síntesis de compuestos 269-293

La formación de los diferentes tipos de enlace entre el benzotiazol y los grupos para la zona 3 se llevó a cabo siguiendo metodologías sintéticas análogas a las ya mencionadas para el resto de familias estructurales (Esquema 8). En el caso de los compuestos bromados en el benzotiazol, se obtuvo en primer lugar el compuesto **34** por reacción de 6-metilbenzo[d]tiazol-2-amina con NBS.

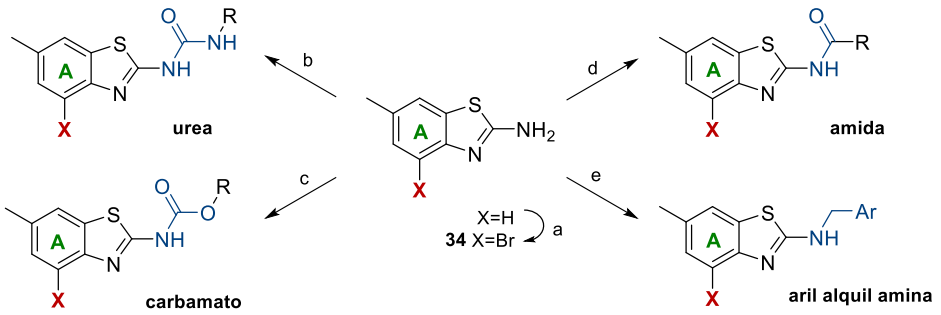

Esquema 8. Síntesis de derivados de benzotiazol. Reactivos y condiciones: (a) NBS, CH_2Cl_2, 4 °C, 4 h, N_2. (b) R-isocianato, CH_2Cl_2, t.a., 5 h-1 semana, N_2. (c) R-cloroformiato, Et_3N, CH_2Cl_2, t.a., 5-24 h, N_2. (d) i) $SOCl_2$, t.a., 24 h; ii) R-COCl, Et_3N, CH_2Cl_2, t.a., 3 h-5 días, N_2. (e) i) TsOH, Ar-CHO, tolueno, reflujo, 4-48 h, N_2; ii) $NaBH_4$, EtOH, t.a., 30 min-5 días, N_2.

Los compuestos sintetizados se ensayaron frente a las líneas celulares tumorales HeLa, HT-29 y HL-60 a una concentración de 1 µM. Únicamente el compuesto **270** 1-(4-bromo-6-metilbenzo[d]tiazol-2-il)-3-etilurea mostró actividad a esa concentración, con CI_{50} de 484.0 ± 23.1 nM frente a células HeLa.

CONCLUSIONES

En este trabajo se han obtenido nuevos compuestos antimitóticos como agentes prometedores en la terapia antitumoral. Los compuestos objeto de esta tesis se han diseñado con el fin de interaccionar con el dominio de colchicina en β-tubulina, que se suele dividir en tres regiones consecutivas en base a los modos de unión de ligandos en las estructuras de rayos X. Hemos sintetizado compuestos dirigidos a las zonas 1-2, 2-3 y 1-2-3 del dominio de colchicina. En vista a los resultados preliminares en ensayos de proliferación celular, se seleccionaron seis ligandos representativos para su evaluación biológica *in vitro* y el estudio de su mecanismo de acción como agentes antitumorales. En base a los resultados obtenidos en este trabajo podemos establecer las siguientes conclusiones:

i. Los procedimientos sintéticos utilizados son adecuados para preparar los compuestos objetivo, que han sido obtenidos con buenos rendimientos en la mayoría de los casos.

ii. La sustitución 1,3 del anillo central en sulfonamidas con tres anillos aromáticos basadas en ABT-751 no da lugar a compuestos activos en ensayos de proliferación celular *in vitro*.

iii. El reemplazo de la olefina *trans* en MI-181 por grupos amida, metilamina, urea o carbamato implica la pérdida de la actividad antiproliferativa. Compuestos híbridos con bencenos polimetoxilados como CA4 y piridinas como MI-181 unidos por grupos amida no presentan actividad citotóxica *in vitro*.

iv. La combinación de un *N*-metil-5-indolilo con bencenos polimetoxilados conectados por grupos sulfonamida o tetrazol da lugar a compuestos citotóxicos potentes. Estos ligandos presentan valores de CI_{50} en el rango nanomolar o submicromolar frente a diferentes líneas tumorales y no tumorigénicas, y células primarias. En la mayoría de los casos, su actividad antiproliferativa no se ve afectada por la inhibición farmacológica de glicoproteína-P, lo que sugiere que podrían no ser susceptibles a resistencias múltiples a fármacos *in vivo*. Las siguientes conclusiones se refieren a esta familia de compuestos.

v. En sulfonamidas, la posición de los grupos metoxilo en el anillo de benceno es crucial para la actividad biológica. El grupo clásico 3,4,5-trimetoxifenilo da lugar a los compuestos más potentes, seguidos de los ligandos con 3,5-dimetoxifenilo, que a su vez muestran mayor actividad citotóxica que aquellos con un anillo 2,5-dimetoxifenilo. La bromación en posición 4 de 2,5-dimetoxifenilo mejora la potencia. El patrón de sustitución 2,3,4-trimetoxi, junto con una orientación cambiada de la sulfonamida, no conduce a compuestos activos. Este anillo bencénico no es tan crítico en el caso de tetrazoles.

vi. La metilación de la sulfonamida incrementa la potencia, dando lugar a las sulfonamidas más potentes de cada serie, aunque la introducción de sustituyentes más voluminosos conlleva una reducción de la potencia. Las potencias de las sulfonamidas metiladas son comparables a las de tetrazoles con una posición análoga del nitrógeno en el puente. Los tetrazoles son considerablemente más potentes que sus precursores amida.

vii. La presencia de sustituyentes en la posición 3 del anillo de indol es perjudicial para la actividad. En tetrazoles, también evaluamos bencenos en reemplazo de *N*-metilindol. Los anillos de benceno sustituidos en la posición 4, aunque son menos potentes que los indoles, dan lugar a compuestos con potencias submicromolares, mejores en el caso de derivados dimetilamino que metoxilo.

viii. La diana biológica de los compuestos evaluados es tubulina. Estos ligandos actúan como agentes desestabilizantes de microtúbulos uniéndose al dominio de colchicina en α,β-tubulina con gran afinidad. Esto da lugar a desorganización en la red de microtúbulos, induciendo actividades antimitóticas y antivasculares. La actividad antitumoral de los compuestos es el resultado del mecanismo de acción antimitótico, causando efectos antiproliferativos *in vitro* con potencias similares entre líneas celulares.

ix. Los compuestos representativos inducen muerte celular apoptótica dependiente de caspasas en células HeLa tras una parada sostenida en mitosis, con rápida permeabilización de la membrana plasmática. A pesar de las similares potencias antiproliferativas de los compuestos frente a diferentes líneas celulares, la inducción de apoptosis es muy dependiente de cada línea celular. En términos generales, las líneas no tumorigénicas evaluadas muestran mayor resistencia a apoptosis que las líneas tumorales.

x. Hay un período de tiempo entre la alteración de los microtúbulos y la inducción irreversible de apoptosis durante el cual los efectos son reversibles. La parada mitótica puede revertirse al eliminar los compuestos del medio de cultivo mediante la re-polimerización del citoesqueleto de tubulina, que depende de la síntesis de proteínas. Aunque los porcentajes iniciales de las fases del ciclo celular se pueden recuperar de forma completa, las células HeLa se vuelven más sensibles a un ciclo adicional de tratamiento.

xi. La mitocondria está involucrada en la apoptosis inducida por este tipo de agentes, con una depleción en $\Delta\Psi_m$ posterior al incremento observado en los niveles de especies reactivas de oxígeno y a la liberación de citocromo c. Algunas proteínas de la familia Bcl-2, como Mcl-1, Bcl-xL y P-Bcl2 muestran una regulación positiva transitoria tras el tratamiento que podría tener un papel protector. Además, la sobreexpresión de Bcl-xL y Bcl-2 en células HeLa retrasa la respuesta apoptótica, aunque no previene completamente la inducción de muerte celular.

xii. El flujo autofágico se ve incrementado en células HeLa tras el tratamiento con los compuestos seleccionados, pero la autofagia no parece desempeñar un papel relevante en la muerte celular.